RILEM Bookseries

Viktor Mechtcherine
Kamal Khayat
Egor Secrieru *Editors*

Rheology and Processing of Construction Materials

RheoCon2 & SCC9

Springer

Rheology and Processing of Construction Materials

RILEM BOOKSERIES

Volume 23

RILEM, The International Union of Laboratories and Experts in Construction Materials, Systems and Structures, founded in 1947, is a non-governmental scientific association whose goal is to contribute to progress in the construction sciences, techniques and industries, essentially by means of the communication it fosters between research and practice. RILEM's focus is on construction materials and their use in building and civil engineering structures, covering all phases of the building process from manufacture to use and recycling of materials. More information on RILEM and its previous publications can be found on www.RILEM.net. Indexed in SCOPUS, Google Scholar and SpringerLink.

More information about this series at http://www.springer.com/series/8781

Viktor Mechtcherine · Kamal Khayat ·
Egor Secrieru
Editors

Rheology and Processing of Construction Materials

RheoCon2 & SCC9

Springer

Editors
Viktor Mechtcherine
Faculty of Civil Engineering
Technische Universität Dresden
Dresden, Sachsen, Germany

Kamal Khayat
Missouri University of Science
and Technology
Rolla, MO, USA

Egor Secrieru
Faculty of Civil Engineering
TU Dresden
Dresden, Sachsen, Germany

ISSN 2211-0844 ISSN 2211-0852 (electronic)
RILEM Bookseries
ISBN 978-3-030-22565-0 ISBN 978-3-030-22566-7 (eBook)
https://doi.org/10.1007/978-3-030-22566-7

Preface

Processing of building materials is the technological backbone in the modern construction industry. Tailored use of rheology-based processes is not only a vital key for solving current technical challenges, including mixing, transportation, casting, or pumping over extreme lengths and heights, but also for the design of emerging and highly innovative technologies, such as digital fabrication. These processes are carried out under a broad range of deformation rates, which result in the necessity of profound knowledge about material rheological behavior applying advanced experimental and numerical methods.

Following the motto "Mastering rheology-based processes," the 2nd International Conference on Rheology and Processing of Construction Materials (RheoCon2) and the 9th International RILEM Symposium on Self-Compacting Concrete (SCC9) were held on September 8 to 11, 2019, in Radebeul, Germany.

The RILEM SCC series of symposia started in 1999 in Stockholm, followed by Tokyo in 2001, Reykjavik in 2003, Chicago in 2005, Ghent in 2007, Montreal in 2010, Paris in 2013, and Washington, D.C. in 2016 with a steadily increasing number of papers, participants, and interests from across the globe. The first RheoCon conference was successfully organized in Paris in 2013 in conjunction with the RILEM SCC symposium.

By combining these two parallel and closely interconnected conferences, we succeeded in creating a platform for exchanging experience and ideas about the development, testing, applications, and numerical simulation of fresh properties of cement-based and other building materials with emphasis on rheological properties.

The SCC9 symposium was organized in recognition of Professor Kamal H. Khayat's impressive scientific research achievements, exceptional engagement and contribution to concrete rheology, in general, and self-compacting concrete, in particular, as well as his sustained leadership in technical societies and technology transfer.

The conference proceedings consist of 76 peer-reviewed papers. Topics covered include materials science and design, the effect of additions and admixtures on rheology, rheological testing, mixing, processing and casting, additive manufacturing, and 3D printing. Furthermore, contributions deal with rheology and flow

modeling of SCC as well as its durability, structural performance, and fiber reinforcement.

The three-day conference program comprised of a selected panel of seven keynote speakers, and over 110 oral and 15 poster presentations. With participants from more than 30 countries, the conference triggered a vibrant discussion on ongoing research, networking, and sharing of innovative visions on the bright and sustainable future of the construction industry.

The latest scientific findings from the Priority Program 2005 Opus Fluidum Futurum – Rheology of reactive, multiscale, multiphase construction materials, sponsored by the German Research Foundation (DFG), were also presented at the conference. The program was initiated in the early 2018, and it was a unique opportunity for the members who represent an interdisciplinary research community to actively participate in the tandem conference.

We would like to express our sincere gratitude to the Honorary Advisory Committee and the Scientific and Technical Committee for its support in putting together a high-caliber technical program, providing peer review to numerous papers and promoting the conference worldwide. Our gratitude also goes to members of the Organising Committee and especially to Ms. Shirin Fataei for their dedicated efforts to ensuring a successful international conference.

Our special thanks to the conference sponsors: BASF, Deutsche Bauchemie, CEMEX, KNIELE, Omya, Maschinenfabrik Gustav Eirich, Schleibinger Geräte Teubert u. Greim, Thermo Fisher Scientific and UltraTest. Their generous financial support is greatly acknowledged.

September 2019 Editors

Organization

Conference Chair

Viktor Mechtcherine, Germany

Honorary Advisory Committee

Geert De Schutter (Chair of SCC 2007), Belgium
Kamal H. Khayat (Chair of SCC 2010, 2016), USA
Nicolas Roussel (Chair of SCC 2013), France
Surendra P. Shah (Chair of SCC 2005, 2008), USA
Olafur H. Wallevik (Chair of SCC 2003), Iceland

International Scientific Committee

Hakim S. Abdelgader, Libya
Rolf Breitenbücher, Germany
Myoungsung Choi, Republic of Korea
Bart Craeye, Belgium
Geert De Schutter, Belgium
Khadija El Cheikh, Belgium
Tahir K. Erdem, Turkey
Vyacheslav Falikman, Russia
Shirin Fataei, Germany
Liberato Ferrara, Italy
Dimitri Feys, USA
Robert Flatt, Switzerland
Albrecht Gilka-Bötzow, Germany
Jacek Golaszewski, Poland
Annika Gram, Sweden
Steffen Grunewald, Netherlands
Michael Haist, Germany

Daniel Jansen, Germany
Steffen Jesinghausen, Germany
Helena Keller, Germany
Kamal H. Khayat, USA
Michael Khrapko, New Zealand
Jae H. Kim, Korea
Thomas Kränkel, Germany
Hans Krauss, Germany
Markus Krüger, Germany
Lei Lei, Germany
Marco Liebscher, Germany
Ludger Lohaus, Germany
Dirk Lowke, Germany
Zichen Lu, Germany
Pietro Lura, Switzerland
Viktor Mechtcherine (Chair), Germany
Behzad Nematollahi, Australia
Masahiro Ouchi, Japan
Arnaud Perot, France
Johann Plank, Germany
Ye Qian, Singapore
Nicolas Roussel, France
Manu Santhanam, India
Carsten Schilde, Germany
Wolfram Schmidt, Germany
Christof Schröfl, Germany
Rüdiger Schwarze, Germany
Egor Secrieru, Germany
Surendra P. Shah, USA
Kosmas Sideris, Greece
Dietmar Stephan, Germany
Neven Ukrainczyk, Germany
Gideon van Zijl, South Africa
Yannick Vanhove, France
Ksenja Vasilic, Germany
Jon Wallevik, Iceland
Timothy Wangler, Switzerland
Folker H. Wittmann, Germany
Ammar Yahia, Canada
Qiang Yuan, China

International Technical Committee

Sofiane Amziane, France
Harald Beitzel, Germany

Peter Billberg, Sweden
Mette Geiker, Norway
Shiho Kawashima, USA
Maria Konsta-Gdoutos, Greece
Changwen Miao, China
Anton Schindler, USA
Norbert Schroeter, Germany
Caijun Shi, China
Mohammed Sonebi, UK
Le Trung Thanh, Vietnam
Lars N. Thrane, Denmark
Nathan A. Tregger, USA
Olafur H. Wallevik, Iceland
Norbert Willenbacher, Germany

Local Organising Committee

Viktor Mechtcherine
Martina Awassi
Katrin Brothuhn
Shirin Fataei
Irina Ivanova
Egor Secrieru
Venkatesh N. Nerella

Contents

Materials Science and Design

Effect of Supplementary Cementitious Materials, Fillers and Chemical Admixtures on Rheology

Laboratory and In-Situ Rheological Testing

Mixing, Processing and Casting of Mortar and Concrete

Additive Manufacturing and 3D-Printing

Rheology and Workability of SCC

Mechanical Properties, Durability and Sustainability of SCC

Modelling and Numerical Simulations of Rheological Behaviour

RILEM Publications

The following list is presenting the global offer of RILEM Publications, sorted by series. Each publication is available in printed version and/or in online version.

RILEM Proceedings (PRO)

PRO 1: Durability of High Performance Concrete (ISBN: 2-912143-03-9; e-ISBN: 2-351580-12-5; e-ISBN: 2351580125); *Ed. H. Sommer*

PRO 2: Chloride Penetration into Concrete (ISBN: 2-912143-00-04; e-ISBN: 2912143454); *Eds. L.-O. Nilsson and J.-P. Ollivier*

PRO 3: Evaluation and Strengthening of Existing Masonry Structures (ISBN: 2-912143-02-0; e-ISBN: 2351580141); *Eds. L. Binda and C. Modena*

PRO 4: Concrete: From Material to Structure (ISBN: 2-912143-04-7; e-ISBN: 2351580206); *Eds. J.-P. Bournazel and Y. Malier*

PRO 5: The Role of Admixtures in High Performance Concrete (ISBN: 2-912143-05-5; e-ISBN: 2351580214); *Eds. J. G. Cabrera and R. Rivera-Villarreal*

PRO 6: High Performance Fiber Reinforced Cement Composites - HPFRCC 3 (ISBN: 2-912143-06-3; e-ISBN: 2351580222); *Eds. H. W. Reinhardt and A. E. Naaman*

PRO 7: 1st International RILEM Symposium on Self-Compacting Concrete (ISBN: 2-912143-09-8; e-ISBN: 2912143721); *Eds. Å. Skarendahl and Ö. Petersson*

PRO 8: International RILEM Symposium on Timber Engineering (ISBN: 2-912143-10-1; e-ISBN: 2351580230); *Ed. L. Boström*

PRO 9: 2nd International RILEM Symposium on Adhesion between Polymers and Concrete ISAP'99 (ISBN: 2-912143-11-X; e-ISBN: 2351580249); *Eds. Y. Ohama and M. Puterman*

PRO 10: 3rd International RILEM Symposium on Durability of Building and Construction Sealants (ISBN: 2-912143-13-6; e-ISBN: 2351580257); *Ed. A. T. Wolf*

PRO 11: 4th International RILEM Conference on Reflective Cracking in Pavements (ISBN: 2-912143-14-4; e-ISBN: 2351580265); *Eds. A. O. Abd El Halim, D. A. Taylor and El H. H. Mohamed*

PRO 12: International RILEM Workshop on Historic Mortars: Characteristics and Tests (ISBN: 2-912143-15-2; e-ISBN: 2351580273); *Eds. P. Bartos, C. Groot and J. J. Hughes*

PRO 13: 2nd International RILEM Symposium on Hydration and Setting (ISBN: 2-912143-16-0; e-ISBN: 2351580281); *Ed. A. Nonat*

PRO 14: Integrated Life-Cycle Design of Materials and Structures - ILCDES 2000 (ISBN: 951-758-408-3; e-ISBN: 235158029X); (ISSN: 0356-9403); *Ed. S. Sarja*

PRO 15: Fifth RILEM Symposium on Fibre-Reinforced Concretes (FRC) - BEFIB'2000 (ISBN: 2-912143-18-7; e-ISBN: 291214373X); *Eds. P. Rossi and G. Chanvillard*

PRO 16: Life Prediction and Management of Concrete Structures (ISBN: 2-912143-19-5; e-ISBN: 2351580303); *Ed. D. Naus*

PRO 17: Shrinkage of Concrete – Shrinkage 2000 (ISBN: 2-912143-20-9; e-ISBN: 2351580311); *Eds. V. Baroghel-Bouny and P.-C. Aïtcin*

PRO 18: Measurement and Interpretation of the On-Site Corrosion Rate (ISBN: 2-912143-21-7; e-ISBN: 235158032X); *Eds. C. Andrade, C. Alonso, J. Fullea, J. Polimon and J. Rodriguez*

PRO 19: Testing and Modelling the Chloride Ingress into Concrete (ISBN: 2-912143-22-5; e-ISBN: 2351580338); *Eds. C. Andrade and J. Kropp*

PRO 20: 1st International RILEM Workshop on Microbial Impacts on Building Materials (CD 02) (e-ISBN 978-2-35158-013-4); *Ed. M. Ribas Silva*

PRO 21: International RILEM Symposium on Connections between Steel and Concrete (ISBN: 2-912143-25-X; e-ISBN: 2351580346); *Ed. R. Eligehausen*

PRO 22: International RILEM Symposium on Joints in Timber Structures (ISBN: 2-912143-28-4; e-ISBN: 2351580354); *Eds. S. Aicher and H.-W. Reinhardt*

PRO 23: International RILEM Conference on Early Age Cracking in Cementitious Systems (ISBN: 2-912143-29-2; e-ISBN: 2351580362); *Eds. K. Kovler and A. Bentur*

PRO 24: 2nd International RILEM Workshop on Frost Resistance of Concrete (ISBN: 2-912143-30-6; e-ISBN: 2351580370); *Eds. M. J. Setzer, R. Auberg and H.-J. Keck*

PRO 25: International RILEM Workshop on Frost Damage in Concrete (ISBN: 2-912143-31-4; e-ISBN: 2351580389); *Eds. D. J. Janssen, M. J. Setzer and M. B. Snyder*

PRO 26: International RILEM Workshop on On-Site Control and Evaluation of Masonry Structures (ISBN: 2-912143-34-9; e-ISBN: 2351580141); *Eds. L. Binda and R. C. de Vekey*

PRO 27: International RILEM Symposium on Building Joint Sealants (CD03; e-ISBN: 235158015X); *Ed. A. T. Wolf*

PRO 28: 6th International RILEM Symposium on Performance Testing and Evaluation of Bituminous Materials - PTEBM'03 (ISBN: 2-912143-35-7; e-ISBN: 978-2-912143-77-8); *Ed. M. N. Partl*

PRO 29: 2nd International RILEM Workshop on Life Prediction and Ageing Management of Concrete Structures (ISBN: 2-912143-36-5; e-ISBN: 2912143780); *Ed. D. J. Naus*

PRO 30: 4th International RILEM Workshop on High Performance Fiber Reinforced Cement Composites - HPFRCC 4 (ISBN: 2-912143-37-3; e-ISBN: 2912143799); *Eds. A. E. Naaman and H. W. Reinhardt*

PRO 31: International RILEM Workshop on Test and Design Methods for Steel Fibre Reinforced Concrete: Background and Experiences (ISBN: 2-912143-38-1; e-ISBN: 2351580168); *Eds. B. Schnütgen and L. Vandewalle*

PRO 32: International Conference on Advances in Concrete and Structures 2 vol. (ISBN (set): 2-912143-41-1; e-ISBN: 2351580176); *Eds. Ying-shu Yuan, Surendra P. Shah and Heng-lin Lü*

PRO 33: 3rd International Symposium on Self-Compacting Concrete (ISBN: 2-912143-42-X; e-ISBN: 2912143713); *Eds. Ó. Wallevik and I. Níelsson*

PRO 34: International RILEM Conference on Microbial Impact on Building Materials (ISBN: 2-912143-43-8; e-ISBN: 2351580184); *Ed. M. Ribas Silva*

PRO 35: International RILEM TC 186-ISA on Internal Sulfate Attack and Delayed Ettringite Formation (ISBN: 2-912143-44-6; e-ISBN: 2912143802); *Eds. K. Scrivener and J. Skalny*

PRO 36: International RILEM Symposium on Concrete Science and Engineering – A Tribute to Arnon Bentur (ISBN: 2-912143-46-2; e-ISBN: 2912143586); *Eds. K. Kovler, J. Marchand, S. Mindess and J. Weiss*

PRO 37: 5th International RILEM Conference on Cracking in Pavements – Mitigation, Risk Assessment and Prevention (ISBN: 2-912143-47-0; e-ISBN: 2912143764); *Eds. C. Petit, I. Al-Qadi and A. Millien*

PRO 38: 3rd International RILEM Workshop on Testing and Modelling the Chloride Ingress into Concrete (ISBN: 2-912143-48-9; e-ISBN: 2912143578); *Eds. C. Andrade and J. Kropp*

PRO 39: 6th International RILEM Symposium on Fibre-Reinforced Concretes - BEFIB 2004 (ISBN: 2-912143-51-9; e-ISBN: 2912143748); *Eds. M. Di Prisco, R. Felicetti and G. A. Plizzari*

PRO 40: International RILEM Conference on the Use of Recycled Materials in Buildings and Structures (ISBN: 2-912143-52-7; e-ISBN: 2912143756); *Eds. E. Vázquez, Ch. F. Hendriks and G. M. T. Janssen*

PRO 41: RILEM International Symposium on Environment-Conscious Materials and Systems for Sustainable Development (ISBN: 2-912143-55-1; e-ISBN: 2912143640); *Eds. N. Kashino and Y. Ohama*

PRO 42: SCC'2005 - China: 1st International Symposium on Design, Performance and Use of Self-Consolidating Concrete (ISBN: 2-912143-61-6; e-ISBN: 2912143624); *Eds. Zhiwu Yu, Caijun Shi, Kamal Henri Khayat and Youjun Xie*

PRO 43: International RILEM Workshop on Bonded Concrete Overlays (e-ISBN: 2-912143-83-7); *Eds. J. L. Granju and J. Silfwerbrand*

PRO 44: 2nd International RILEM Workshop on Microbial Impacts on Building Materials (CD11) (e-ISBN: 2-912143-84-5); *Ed. M. Ribas Silva*

PRO 45: 2nd International Symposium on Nanotechnology in Construction, Bilbao (ISBN: 2-912143-87-X; e-ISBN: 2912143888); *Eds. Peter J. M. Bartos, Yolanda de Miguel and Antonio Porro*

PRO 46: ConcreteLife'06 - International RILEM-JCI Seminar on Concrete Durability and Service Life Planning: Curing, Crack Control, Performance in Harsh Environments (ISBN: 2-912143-89-6; e-ISBN: 291214390X); *Ed. K. Kovler*

PRO 47: International RILEM Workshop on Performance Based Evaluation and Indicators for Concrete Durability (ISBN: 978-2-912143-95-2; e-ISBN: 9782912143969); *Eds. V. Baroghel-Bouny, C. Andrade, R. Torrent and K. Scrivener*

PRO 48: 1st International RILEM Symposium on Advances in Concrete through Science and Engineering (e-ISBN: 2-912143-92-6); *Eds. J. Weiss, K. Kovler, J. Marchand, and S. Mindess*

PRO 49: International RILEM Workshop on High Performance Fiber Reinforced Cementitious Composites in Structural Applications (ISBN: 2-912143-93-4; e-ISBN: 2912143942); *Eds. G. Fischer and V. C. Li*

PRO 50: 1st International RILEM Symposium on Textile Reinforced Concrete (ISBN: 2-912143-97-7; e-ISBN: 2351580087); *Eds. Josef Hegger, Wolfgang Brameshuber and Norbert Will*

PRO 51: 2nd International Symposium on Advances in Concrete through Science and Engineering (ISBN: 2-35158-003-6; e-ISBN: 2-35158-002-8); *Eds. J. Marchand, B. Bissonnette, R. Gagné, M. Jolin and F. Paradis*

PRO 52: Volume Changes of Hardening Concrete: Testing and Mitigation (ISBN: 2-35158-004-4; e-ISBN: 2-35158-005-2); *Eds. O. M. Jensen, P. Lura and K. Kovler*

PRO 53: High Performance Fiber Reinforced Cement Composites - HPFRCC5 (ISBN: 978-2-35158-046-2; e-ISBN: 978-2-35158-089-9); *Eds. H. W. Reinhardt and A. E. Naaman*

PRO 54: 5th International RILEM Symposium on Self-Compacting Concrete (ISBN: 978-2-35158-047-9; e-ISBN: 978-2-35158-088-2); *Eds. G. De Schutter and V. Boel*

PRO 55: International RILEM Symposium Photocatalysis, Environment and Construction Materials (ISBN: 978-2-35158-056-1; e-ISBN: 978-2-35158-057-8); *Eds. P. Baglioni and L. Cassar*

PRO 56: International RILEM Workshop on Integral Service Life Modelling of Concrete Structures (ISBN 978-2-35158-058-5; e-ISBN: 978-2-35158-090-5); *Eds. R. M. Ferreira, J. Gulikers and C. Andrade*

PRO 57: RILEM Workshop on Performance of cement-based materials in aggressive aqueous environments (e-ISBN: 978-2-35158-059-2); *Ed. N. De Belie*

PRO 58: International RILEM Symposium on Concrete Modelling - CONMOD'08 (ISBN: 978-2-35158-060-8; e-ISBN: 978-2-35158-076-9); *Eds. E. Schlangen and G. De Schutter*

PRO 59: International RILEM Conference on On Site Assessment of Concrete, Masonry and Timber Structures - SACoMaTiS 2008 (ISBN set: 978-2-35158-061-5; e-ISBN: 978-2-35158-075-2); *Eds. L. Binda, M. di Prisco and R. Felicetti*

PRO 60: Seventh RILEM International Symposium on Fibre Reinforced Concrete: Design and Applications - BEFIB 2008 (ISBN: 978-2-35158-064-6; e-ISBN: 978-2-35158-086-8); *Ed. R. Gettu*

PRO 61: 1st International Conference on Microstructure Related Durability of Cementitious Composites 2 vol., (ISBN: 978-2-35158-065-3; e-ISBN: 978-2-35158-084-4); *Eds. W. Sun, K. van Breugel, C. Miao, G. Ye and H. Chen*

PRO 62: NSF/RILEM Workshop: In-situ Evaluation of Historic Wood and Masonry Structures (e-ISBN: 978-2-35158-068-4); *Eds. B. Kasal, R. Anthony and M. Drdácký*

PRO 63: Concrete in Aggressive Aqueous Environments: Performance, Testing and Modelling, 2 vol., (ISBN: 978-2-35158-071-4; e-ISBN: 978-2-35158-082-0); *Eds. M. G. Alexander and A. Bertron*

PRO 64: Long Term Performance of Cementitious Barriers and Reinforced Concrete in Nuclear Power Plants and Waste Management - NUCPERF 2009 (ISBN: 978-2-35158-072-1; e-ISBN: 978-2-35158-087-5); *Eds. V. L'Hostis, R. Gens, C. Gallé*

PRO 65: Design Performance and Use of Self-consolidating Concrete - SCC'2009 (ISBN: 978-2-35158-073-8; e-ISBN: 978-2-35158-093-6); *Eds. C. Shi, Z. Yu, K. H. Khayat and P. Yan*

PRO 66: 2nd International RILEM Workshop on Concrete Durability and Service Life Planning - ConcreteLife'09 (ISBN: 978-2-35158-074-5; ISBN: 978-2-35158-074-5); *Ed. K. Kovler*

PRO 67: Repairs Mortars for Historic Masonry (e-ISBN: 978-2-35158-083-7); *Ed. C. Groot*

PRO 68: Proceedings of the 3rd International RILEM Symposium on 'Rheology of Cement Suspensions such as Fresh Concrete' (ISBN 978-2-35158-091-2; e-ISBN: 978-2-35158-092-9); *Eds. O. H. Wallevik, S. Kubens and S. Oesterheld*

PRO 69: 3rd International PhD Student Workshop on 'Modelling the Durability of Reinforced Concrete' (ISBN: 978-2-35158-095-0); *Eds. R. M. Ferreira, J. Gulikers and C. Andrade*

PRO 70: 2nd International Conference on 'Service Life Design for Infrastructure' (ISBN set: 978-2-35158-096-7, e-ISBN: 978-2-35158-097-4); *Eds. K. van Breugel, G. Ye and Y. Yuan*

PRO 71: Advances in Civil Engineering Materials – 'The 50-year Teaching Anniversary of Prof. Sun Wei' (ISBN: 978-2-35158-098-1; e-ISBN: 978-2-35158-099-8); *Eds. C. Miao, G. Ye, and H. Chen*

PRO 72: First International Conference on 'Advances in Chemically-Activated Materials – CAM'2010' (2010), 264 pp., ISBN: 978-2-35158-101-8; e-ISBN: 978-2-35158-115-5, *Eds. Caijun Shi and Xiaodong Shen*

PRO 73: 2nd International Conference on 'Waste Engineering and Management - ICWEM 2010' (2010), 894 pp., ISBN: 978-2-35158-102-5; e-ISBN: 978-2-35158-103-2, *Eds. J. Zh. Xiao, Y. Zhang, M. S. Cheung and R. Chu*

PRO 74: International RILEM Conference on 'Use of Superabsorsorbent Polymers and Other New Additives in Concrete' (2010) 374 pp., ISBN: 978-2-35158-104-9; e-ISBN: 978-2-35158-105-6; *Eds. O. M. Jensen, M. T. Hasholt, and S. Laustsen*

PRO 75: International Conference on 'Material Science - 2nd ICTRC - Textile Reinforced Concrete - Theme 1' (2010) 436 pp., ISBN: 978-2-35158-106-3; e-ISBN: 978-2-35158-107-0; *Ed. W. Brameshuber*

PRO 76: International Conference on 'Material Science - HetMat - Modelling of Heterogeneous Materials - Theme 2' (2010) 255 pp., ISBN: 978-2-35158-108-7; e-ISBN: 978-2-35158-109-4; *Ed. W. Brameshuber*

PRO 77: International Conference on 'Material Science - AdIPoC - Additions Improving Properties of Concrete - Theme 3' (2010) 459 pp., ISBN: 978-2-35158-110-0; e-ISBN: 978-2-35158-111-7; *Ed. W. Brameshuber*

PRO 78: 2nd Historic Mortars Conference and RILEM TC 203-RHM Final Workshop – HMC2010 (2010) 1416 pp., e-ISBN: 978-2-35158-112-4; *Eds. J. Válek, C. Groot, and J. J. Hughes*

PRO 79: International RILEM Conference on Advances in Construction Materials Through Science and Engineering (2011) 213 pp., ISBN: 978-2-35158-116-2, e-ISBN: 978-2-35158-117-9; *Eds. Christopher Leung and K. T. Wan*

PRO 80: 2nd International RILEM Conference on Concrete Spalling due to Fire Exposure (2011) 453 pp., ISBN: 978-2-35158-118-6, e-ISBN: 978-2-35158-119-3; *Eds. E. A. B. Koenders and F. Dehn*

PRO 81: 2nd International RILEM Conference on Strain Hardening Cementitious Composites (SHCC2-Rio) (2011) 451 pp., ISBN: 978-2-35158-120-9, e-ISBN: 978-2-35158-121-6; *Eds. R. D. Toledo Filho, F. A. Silva, E. A. B. Koenders and E. M. R. Fairbairn*

PRO 82: 2nd International RILEM Conference on Progress of Recycling in the Built Environment (2011) 507 pp., e-ISBN: 978-2-35158-122-3; *Eds. V. M. John, E. Vazquez, S. C. Angulo and C. Ulsen*

PRO 83: 2nd International Conference on Microstructural-related Durability of Cementitious Composites (2012) 250 pp., ISBN: 978-2-35158-129-2; e-ISBN: 978-2-35158-123-0; *Eds. G. Ye, K. van Breugel, W. Sun and C. Miao*

PRO 84: CONSEC13 - Seventh International Conference on Concrete under Severe Conditions – Environment and Loading (2013) 1930 pp., ISBN: 978-2-35158-124-7; e-ISBN: 978-2- 35158-134-6; *Eds. Z. J. Li, W. Sun, C. W. Miao, K. Sakai, O. E. Gjorv and N. Banthia*

PRO 85: RILEM-JCI International Workshop on Crack Control of Mass Concrete and Related issues concerning Early-Age of Concrete Structures – ConCrack 3 – Control of Cracking in Concrete Structures 3 (2012) 237 pp., ISBN: 978-2-35158-125-4; e-ISBN: 978-2-35158-126-1; *Eds. F. Toutlemonde and J.-M. Torrenti*

PRO 86: International Symposium on Life Cycle Assessment and Construction (2012) 414 pp., ISBN: 978-2-35158-127-8, e-ISBN: 978-2-35158-128-5; *Eds. A. Ventura and C. de la Roche*

PRO 87: UHPFRC 2013 – RILEM-fib-AFGC International Symposium on Ultra-High Performance Fibre-Reinforced Concrete (2013), ISBN: 978-2-35158-130-8, e-ISBN: 978-2-35158-131-5; *Ed. F. Toutlemonde*

PRO 88: 8th RILEM International Symposium on Fibre Reinforced Concrete (2012) 344 pp., ISBN: 978-2-35158-132-2, e-ISBN: 978-2-35158-133-9; *Ed. Joaquim A. O. Barros*

PRO 89: RILEM International workshop on performance-based specification and control of concrete durability (2014) 678 pp., ISBN: 978-2-35158-135-3, e-ISBN: 978-2-35158-136-0; *Eds. D. Bjegović, H. Beushausen and M. Serdar*

PRO 90: 7th RILEM International Conference on Self-Compacting Concrete and of the 1st RILEM International Conference on Rheology and Processing of Construction Materials (2013) 396 pp., ISBN: 978-2-35158-137-7, e-ISBN: 978-2-35158-138-4; *Eds. Nicolas Roussel and Hela Bessaies-Bey*

PRO 91: CONMOD 2014 - RILEM International Symposium on Concrete Modelling (2014), ISBN: 978-2-35158-139-1; e-ISBN: 978-2-35158-140-7; *Eds. Kefei Li, Peiyu Yan and Rongwei Yang*

PRO 92: CAM 2014 - 2nd International Conference on advances in chemically-activated materials (2014) 392 pp., ISBN: 978-2-35158-141-4; e-ISBN: 978-2-35158-142-1; *Eds. Caijun Shi and Xiadong Shen*

PRO 93: SCC 2014 - 3rd International Symposium on Design, Performance and Use of Self-Consolidating Concrete (2014) 438 pp., ISBN: 978-2-35158-143-8; e-ISBN: 978-2-35158-144-5; *Eds. Caijun Shi, Zhihua Ou and Kamal H. Khayat*

PRO 94 (online version): HPFRCC-7 - 7th RILEM conference on High performance fiber reinforced cement composites (2015), e-ISBN: 978-2-35158-146-9; *Eds. H. W. Reinhardt, G. J. Parra-Montesinos and H. Garrecht*

PRO 95: International RILEM Conference on Application of superabsorbent polymers and other new admixtures in concrete construction (2014), ISBN: 978-2-35158-147-6; e-ISBN: 978-2-35158-148-3; *Eds. Viktor Mechtcherine and Christof Schroefl*

PRO 96 (online version): XIII DBMC: XIII International Conference on Durability of Building Materials and Components (2015), e-ISBN: 978-2-35158-149-0; *Eds. M. Quattrone and V. M. John*

PRO 97: SHCC3 – 3rd International RILEM Conference on Strain Hardening Cementitious Composites (2014), ISBN: 978-2-35158-150-6; e-ISBN: 978-2-35158-151-3; *Eds. E. Schlangen, M. G. Sierra Beltran, M. Lukovic and G. Ye*

PRO 98: FERRO-11 – 11th International Symposium on Ferrocement and 3rd ICTRC - International Conference on Textile Reinforced Concrete (2015), ISBN: 978-2-35158-152-0; e-ISBN: 978-2-35158-153-7; *Ed. W. Brameshuber*

PRO 99 (online version): ICBBM 2015 - 1st International Conference on Bio-Based Building Materials (2015), e-ISBN: 978-2-35158-154-4; *Eds. S. Amziane and M. Sonebi*

PRO 100: SCC16 - RILEM Self-Consolidating Concrete Conference (2016), ISBN: 978-2-35158-156-8; e-ISBN: 978-2-35158-157-5; *Ed. Kamal H. Kayat*

PRO 101 (online version): III Progress of Recycling in the Built Environment (2015), e-ISBN: 978-2-35158-158-2; *Eds. I. Martins, C. Ulsen and S. C. Angulo*

PRO 102 (online version): RILEM Conference on Microorganisms-Cementitious Materials Interactions (2016), e-ISBN: 978-2-35158-160-5; *Eds. Alexandra Bertron, Henk Jonkers and Virginie Wiktor*

PRO 103 (online version): ACESC'16 - Advances in Civil Engineering and Sustainable Construction (2016), e-ISBN: 978-2-35158-161-2; *Eds. T. Ch. Madhavi, G. Prabhakar, Santhosh Ram and P. M. Rameshwaran*

PRO 104 (online version): SSCS'2015 - Numerical Modeling - Strategies for Sustainable Concrete Structures (2015), e-ISBN: 978-2-35158-162-9

PRO 105: 1st International Conference on UHPC Materials and Structures (2016), ISBN: 978-2-35158-164-3, e-ISBN: 978-2-35158-165-0

PRO 106: AFGC-ACI-fib-RILEM International Conference on Ultra-High-Performance Fibre-Reinforced Concrete – UHPFRC 2017 (2017), ISBN: 978-2-35158-166-7, e-ISBN: 978-2-35158-167-4; *Eds. François Toutlemonde and Jacques Resplendino*

PRO 107 (online version): XIV DBMC – 14th International Conference on Durability of Building Materials and Components (2017), e-ISBN: 978-2-35158-159-9; *Eds. Geert De Schutter, Nele De Belie, Arnold Janssens and Nathan Van Den Bossche*

PRO 108: MSSCE 2016 - Innovation of Teaching in Materials and Structures (2016), ISBN: 978-2-35158-178-0, e-ISBN: 978-2-35158-179-7; *Ed. Per Goltermann*

PRO 109 (2 volumes): MSSCE 2016 - Service Life of Cement-Based Materials and Structures (2016), ISBN Vol. 1: 978-2-35158-170-4, Vol. 2: 978-2-35158-171-4, Set Vol. 1&2: 978-2-35158-172-8, e-ISBN : 978-2-35158-173-5; *Eds. Miguel Azenha, Ivan Gabrijel, Dirk Schlicke, Terje Kanstad and Ole Mejlhede Jensen*

PRO 110: MSSCE 2016 - Historical Masonry (2016), ISBN: 978-2-35158-178-0, e-ISBN: 978-2-35158-179-7; *Eds. Inge Rörig-Dalgaard and Ioannis Ioannou*

PRO 111: MSSCE 2016 - Electrochemistry in Civil Engineering (2016), ISBN: 978-2-35158-176-6, e-ISBN: 978-2-35158-177-3; *Ed. Lisbeth M. Ottosen*

PRO 112: MSSCE 2016 - Moisture in Materials and Structures (2016), ISBN: 978-2-35158-178-0, e-ISBN: 978-2-35158-179-7; *Eds. Kurt Kielsgaard Hansen, Carsten Rode and Lars-Olof Nilsson*

PRO 113: MSSCE 2016 - Concrete with Supplementary Cementitious Materials (2016), ISBN: 978-2-35158-178-0, e-ISBN: 978-2-35158-179-7; *Eds. Ole Mejlhede Jensen, Konstantin Kovler and Nele De Belie*

PRO 114: MSSCE 2016 - Frost Action in Concrete (2016), ISBN: 978-2-35158-182-7, e-ISBN: 978-2-35158-183-4; *Eds. Marianne Tange Hasholt, Katja Fridh and R. Doug Hooton*

PRO 115: MSSCE 2016 - Fresh Concrete (2016), ISBN: 978-2-35158-184-1, e-ISBN: 978-2-35158-185-8; *Eds. Lars N. Thrane, Claus Pade, Oldrich Svec and Nicolas Roussel*

PRO 116: BEFIB 2016 – 9th RILEM International Symposium on Fiber Reinforced Concrete (2016), ISBN: 978-2-35158-187-2, e-ISBN: 978-2-35158-186-5; *Eds. N. Banthia, M. di Prisco and S. Soleimani-Dashtaki*

PRO 117: 3rd International RILEM Conference on Microstructure Related Durability of Cementitious Composites (2016), ISBN: 978-2-35158-188-9, e-ISBN: 978-2-35158-189-6; *Eds. Changwen Miao, Wei Sun, Jiaping Liu, Huisu Chen, Guang Ye and Klaas van Breugel*

PRO 118 (4 volumes): International Conference on Advances in Construction Materials and Systems (2017), ISBN Set: 978-2-35158-190-2, Vol. 1: 978-2-35158-193-3, Vol. 2: 978-2-35158-194-0, Vol. 3: ISBN:978-2-35158-195-7, Vol. 4: ISBN:978-2-35158-196-4, e-ISBN: 978-2-35158-191-9; *Eds. Manu Santhanam, Ravindra Gettu, Radhakrishna G. Pillai and Sunitha K. Nayar*

PRO 119 (online version): ICBBM 2017 - Second International RILEM Conference on Bio-based Building Materials, (2017), e-ISBN: 978-2-35158-192-6; *Ed. Sofiane Amziane*

PRO 120 (2 volumes): EAC-02 - 2nd International RILEM/COST Conference on Early Age Cracking and Serviceability in Cement-based Materials and Structures, (2017), Vol. 1: 978-2-35158-199-5, Vol. 2: 978-2-35158-200-8, Set: 978-2-35158-197-1, e-ISBN: 978-2-35158-198-8; *Eds. Stéphanie Staquet and Dimitrios Aggelis*

PRO 121 (2 volumes): SynerCrete18: Interdisciplinary Approaches for Cement-based Materials and Structural Concrete: Synergizing Expertise and Bridging Scales of Space and Time, (2018), Set: 978-2-35158-202-2, Vol.1: 978-2-35158-211-4, Vol.2: 978-2-35158-212-1, e-ISBN: 978-2-35158-203-9; *Eds. Miguel Azenha, Dirk Schlicke, Farid Benboudjema and Agnieszka Knoppik*

PRO 122: SCC'2018 China - Fourth International Symposium on Design, Performance and Use of Self-Consolidating Concrete, (2018), ISBN: 978-2-35158-204-6, e-ISBN: 978-2-35158-205-3; *Eds. C. Shi, Z. Zhang and K. H. Khayat*

PRO 123: Final Conference of RILEM TC 253-MCI: Microorganisms-Cementitious Materials Interactions (2018), Set: 978-2-35158-207-7, Vol.1: 978-2-35158-209-1, Vol.2: 978-2-35158-210-7, e-ISBN: 978-2-35158-206-0; *Ed. Alexandra Bertron*

PRO 124 (online version): Fourth International Conference Progress of Recycling in the Built Environment (2018), e-ISBN: 978-2-35158-208-4; *Eds. Isabel M. Martins, Carina Ulsen and Yury Villagran*

PRO 125 (online version): SLD4 - 4th International Conference on Service Life Design for Infrastructures (2018), e-ISBN: 978-2-35158-213-8; *Eds. Guang Ye, Yong Yuan, Claudia Romero Rodriguez, Hongzhi Zhang and Branko Savija*

PRO 126: Workshop on Concrete Modelling and Material Behaviour in honor of Professor Klaas van Breugel (2018), ISBN: 978-2-35158-214-5, e-ISBN: 978-2-35158-215-2; *Ed. Guang Ye*

PRO 127 (online version): CONMOD2018 - Symposium on Concrete Modelling (2018), e-ISBN: 978-2-35158-216-9; *Eds. Erik Schlangen, Geert de Schutter, Branko Savija, Hongzhi Zhang and Claudia Romero Rodriguez*

PRO 128: SMSS2019 - International Conference on Sustainable Materials, Systems and Structures (2019), ISBN: 978-2-35158-217-6, e-ISBN: 978-2-35158-218-3

PRO 129: 2nd International Conference on UHPC Materials and Structures (UHPC2018-China), ISBN: 978-2-35158-219-0, e-ISBN: 978-2-35158-220-6;

PRO 130: 5th Historic Mortars Conference (2019), ISBN: 978-2-35158-221-3, e-ISBN: 978-2-35158-222-0; *Eds. José Ignacio Álvarez, José María Fernández, Íñigo Navarro, Adrián Durán and Rafael Sirera*

PRO 131 (online version): 3rd International Conference on Bio-Based Building Materials (ICBBM2019), e-ISBN: 978-2-35158-229-9; *Eds. Mohammed Sonebi, Sofiane Amziane and Jonathan Page*

RILEM Reports (REP)

Report 19: Considerations for Use in Managing the Aging of Nuclear Power Plant Concrete Structures (ISBN: 2-912143-07-1); *Ed. D. J. Naus*

Report 20: Engineering and Transport Properties of the Interfacial Transition Zone in Cementitious Composites (ISBN: 2-912143-08-X); *Eds. M. G. Alexander, G. Arliguie, G. Ballivy, A. Bentur and J. Marchand*

Report 21: Durability of Building Sealants (ISBN: 2-912143-12-8); *Ed. A. T. Wolf*

Report 22: Sustainable Raw Materials - Construction and Demolition Waste (ISBN: 2-912143-17-9); *Eds. C. F. Hendriks and H. S. Pietersen*

Report 23: Self-Compacting Concrete state-of-the-art report (ISBN: 2-912143-23-3); *Eds. Å. Skarendahl and Ö. Petersson*

Report 24: Workability and Rheology of Fresh Concrete: Compendium of Tests (ISBN: 2-912143-32-2); *Eds. P. J. M. Bartos, M. Sonebi and A. K. Tamimi*

Report 25: Early Age Cracking in Cementitious Systems (ISBN: 2-912143-33-0); *Ed. A. Bentur*

Report 26: Towards Sustainable Roofing (Joint Committee CIB/RILEM) (CD 07) (e-ISBN 978-2-912143-65-5); *Eds. Thomas W. Hutchinson and Keith Roberts*

Report 27: Condition Assessment of Roofs (Joint Committee CIB/RILEM) (CD 08) (e-ISBN 978-2-912143-66-2); *Ed. CIB W 83/RILEM TC166-RMS*

Report 28: Final report of RILEM TC 167-COM 'Characterisation of Old Mortars with Respect to Their Repair (ISBN: 978-2-912143-56-3); *Eds. C. Groot, G. Ashall and J. Hughes*

Report 29: Pavement Performance Prediction and Evaluation (PPPE): Interlaboratory Tests (e-ISBN: 2-912143-68-3); *Eds. M. Partl and H. Piber*

Report 30: Final Report of RILEM TC 198-URM 'Use of Recycled Materials' (ISBN: 2-912143-82-9; e-ISBN: 2-912143-69-1); *Eds. Ch. F. Hendriks, G. M. T. Janssen and E. Vázquez*

Report 31: Final Report of RILEM TC 185-ATC 'Advanced testing of cement-based materials during setting and hardening' (ISBN: 2-912143-81-0; e-ISBN: 2-912143-70-5); *Eds. H. W. Reinhardt and C. U. Grosse*

Report 32: Probabilistic Assessment of Existing Structures. A JCSS publication (ISBN 2-912143-24-1); *Ed. D. Diamantidis*

Report 33: State-of-the-Art Report of RILEM Technical Committee TC 184-IFE 'Industrial Floors' (ISBN 2-35158-006-0); *Ed. P. Seidler*

Report 34: Report of RILEM Technical Committee TC 147-FMB 'Fracture mechanics applications to anchorage and bond' Tension of Reinforced Concrete Prisms – Round Robin Analysis and Tests on Bond (e-ISBN 2-912143-91-8); *Eds. L. Elfgren and K. Noghabai*

Report 35: Final Report of RILEM Technical Committee TC 188-CSC 'Casting of Self Compacting Concrete' (ISBN 2-35158-001-X; e-ISBN: 2-912143-98-5); *Eds. Å. Skarendahl and P. Billberg*

Report 36: State-of-the-Art Report of RILEM Technical Committee TC 201-TRC 'Textile Reinforced Concrete' (ISBN 2-912143-99-3); *Ed. W. Brameshuber*

Report 37: State-of-the-Art Report of RILEM Technical Committee TC 192-ECM 'Environment-conscious construction materials and systems' (ISBN: 978-2-35158-053-0); *Eds. N. Kashino, D. Van Gemert and K. Imamoto*

Report 38: State-of-the-Art Report of RILEM Technical Committee TC 205-DSC 'Durability of Self-Compacting Concrete' (ISBN: 978-2-35158-048-6); *Eds. G. De Schutter and K. Audenaert*

Report 39: Final Report of RILEM Technical Committee TC 187-SOC 'Experimental determination of the stress-crack opening curve for concrete in tension' (ISBN 978-2-35158-049-3); *Ed. J. Planas*

Report 40: State-of-the-Art Report of RILEM Technical Committee TC 189-NEC 'Non-Destructive Evaluation of the Penetrability and Thickness of the Concrete Cover' (ISBN 978-2-35158-054-7); *Eds. R. Torrent and L. Fernández Luco*

Report 41: State-of-the-Art Report of RILEM Technical Committee TC 196-ICC 'Internal Curing of Concrete' (ISBN 978-2-35158-009-7); *Eds. K. Kovler and O. M. Jensen*

Report 42: 'Acoustic Emission and Related Non-destructive Evaluation Techniques for Crack Detection and Damage Evaluation in Concrete' - Final Report of RILEM Technical Committee 212-ACD (e-ISBN: 978-2-35158-100-1); *Ed. M. Ohtsu*

Report 45: Repair Mortars for Historic Masonry - State-of-the-Art Report of RILEM Technical Committee TC 203-RHM (e-ISBN: 978-2-35158-163-6); *Eds. Paul Maurenbrecher and Caspar Groot*

Report 46: Surface delamination of concrete industrial floors and other durability related aspects guide - Report of RILEM Technical Committee TC 268-SIF (e-ISBN: 978-2-35158-201-5); *Ed. Valerie Pollet*

Materials Science and Design

Influence of Waste Tire Rubber on Fresh and Hardened Properties of Self-Compacting Rubberized Concrete (SCRC)

Robert Bušić(✉) and Ivana Miličević

Department of Materials and Structures,
Faculty of Civil Engineering and Architecture Osijek, Osijek, Croatia
rbusic@gfos.hr

Abstract. This study investigates the influence of waste tire rubber on fresh and hardened properties of self-compacting concrete (SCC). Seven different SCC mixtures were designed: the reference mixture was made with natural aggregate and six SCC mixtures made with 5%, 10%, 15%, 20%, 25% and 30% replacement level of total aggregate volume. Natural fine aggregates were replaced by recycled waste tire rubber with maximum grain size of 4 mm. Flowability, viscosity, passing ability and porosity of fresh SCC mixtures were determined by means of slump flow, L-box, J-ring and air content – pressure method. Mechanical properties of hardened SCC were evaluated by means of compressive strength, flexural strength and static modulus of elasticity, while durability was expressed with two SCC hardened state properties, water permeability and gas permeability. The test results reveal that waste tire rubber affects the fresh and hardened SCC properties. With a higher amount of waste tire rubber in concrete mixtures, degradation in SCC fresh and hardened properties was observed. However, the addition of waste tire rubber up to 10% of total aggregate volume shows that it is possible to implement recycled rubber in SCC and to successfully satisfy both fresh and hardened SCC properties.

Keywords: Self-compacting concrete · Waste tire rubber · Fresh SCC properties · Mechanical properties · Durability

1 Introduction

During the last two decades, in order to preserve nature and natural resources, such as river and crushed stone aggregates, and due to rapidly increased number of waste tires in the world, civil engineering scientists are trying to implement waste tire rubber into different types of concrete. Only in Europe, the number of end of life tires has grown by 400 000 tonnes from year the 2004 to year 2013, and each year this number is getting higher [1]. On the other hand, concrete industry considered to be one of the biggest industries in the world, hence providing solutions to take care of waste tire rubber in a way of incorporating it into concrete. The main goal of all experimental investigations with self-compacting concrete (SCC) and waste tire rubber was to successfully replace fine and/or coarse aggregates and to retain desirable and necessary fresh and hardened concrete properties.

V. Mechtcherine et al. (Eds.): RheoCon 2019/SCC 2019, RILEM Bookseries 23, pp. 3–10, 2020.
https://doi.org/10.1007/978-3-030-22566-7_1

Up to date, many authors investigated fresh properties and hardened properties of self-compacting rubberized concrete (SCRC) [2–5]. They reported a reduction in fresh concrete properties and reduction of mechanical properties, when natural fine or coarse aggregates were replaced by waste tire rubber, citing reasons such as rubber rough surface and sharp edges which entraps air and increases the porosity of SCC [2, 3], lower modulus of elasticity of rubber compared to natural aggregates [4], etc. On the other hand, there were no experimental results on water permeability and gas permeability of SCRC at this moment and it is unquestionably that these durability properties of SCRC should get more attention. However, only a small number of authors investigated durability properties of traditional concrete with waste tire rubber, i.e. water and gas permeability, reporting an increase in water permeability [6–8] and gas permeability [6] with inclusion of rubber particles.

The objective of this work is to study the utilization of the waste tire rubber (crumb rubber - CR) in SCC as a partial replacement of natural crushed stone aggregates. Experimental research of fresh SCRC properties, i.e. flowability, passing ability and viscosity, and hardened SCRC properties in terms of mechanical properties and durability properties, were carried out in order to show a high potential for the waste tire rubber in concrete industry.

2 Experimental Part

2.1 Material Characteristics

In creation of SCC mixtures proportions, EFNARC dosage parameters were respected [9]. CEM I 42.5R type Portland cement having a specific gravity of 3.17 g/cm^3 and Blaine fineness of 4378 cm^2/g was used in the study, from the cement factory in Našice, Croatia, which was conform to EN 197-1:2012 standard [10]. Silica fume (SLF) obtained from Pocking, Germany was used as a mineral admixture in concrete production. SLF has a specific gravity of 2.19 g/cm^3 and a specific surface of 20.5 m^2/g. SF used in this laboratory investigation was conform to EN 13263-1:2009 standard [11]. Tap water from local water supply that complies with HRN EN 1008 standard was used [12]. In order to achieve desirable SCC fresh state properties, i.e. flowability and viscosity classes, superplasticizer Energy FM 500® was used as a chemical admixture. If necessary, the superplasticizer was adjusted at the time of mixing to achieve desirable slump flow values. Dolomite powder (size < 0.063 mm) from local quarry with specific gravity of 2.97 g/cm^3 and Blaine fineness of 5206 cm^2/g was used as filler. The density of cement, dolomite powder, and silica fume was tested according to ASTM C188-16 [13]. Natural sand and natural crushed aggregates with nominal sizes of 0–2 mm, 0–4 mm, 4 mm–8 mm and 8 mm–16 mm with a specific gravity of 2.58, 2.79, 2.88 and 2.88 g/cm^3, respectively, were used as fine (FA) and coarse aggregates (CA). Waste tire rubber, i.e. crumb rubber (CR), size 0.5 mm–3.5 mm, obtained from mechanical grinding of local waste tires, with a specific gravity of 1.05 g/cm^3, was used as a fine aggregate replacement (0–4 mm). The particle size gradation of FA, CA and CR was obtained through the sieve analysis according to HRN EN 933-1 [14] and it is given in Fig. 1.

2.2 Mixture Design

A total of 7 self-compacting concrete mixtures were tested in the fresh and hardened state, a reference mixture SCC-0CR with 0% of CR and 6 mixtures with 5%, 10%, 15%, 20%, 25% and 30% of CR as a replacement for natural fine aggregates (0 mm–4 mm) by volume. SCC mixture compositions are shown in Table 1.

Originally, an identical quantity of superplasticizer (SP) was used in the design of all SCC mixtures. During mixing, a loss in workability of mixture SCC-30CR was observed when 1.25% of SP was used. Therefore, the percentage of superplasticizer had to be increased from 1.25 to 1.5 for the mixture SCC-30CR.

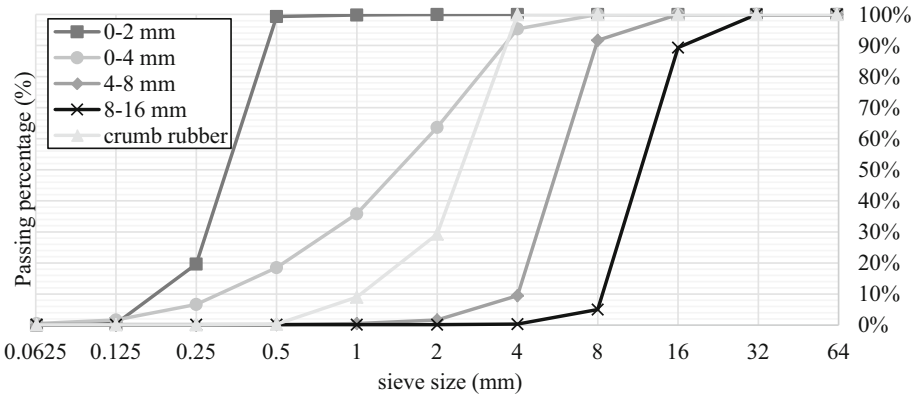

Fig. 1. Sieve analysis of natural aggregates and crumb rubber.

Table 1. Details of mix proportions in kg/m^3.

	SCC-0CR	SCC-5CR	SCC-10CR	SCC-15CR	SCC-20CR	SCC-25CR	SCC-30CR
Cement	405	405	405	405	405	405	405
Silica fume	45	45	45	45	45	45	45
Filler (dolomite)	80	80	80	80	80	80	80
w/c	0.4	0.4	0.4	0.4	0.4	0.4	0.4
SP (%)	1.25	1.25	1.25	1.25	1.25	1.25	1.50
Crumb rubber	0	32.82	65.63	98.45	131.26	164.08	196.90
0–2 mm	322.54	322.54	322.54	322.54	322.54	322.54	322.54
0–4 mm	610.38	523.18	435.99	348.79	261.59	174.39	87.20
4–8 mm	360.04	360.04	360.04	360.04	360.04	360.04	360.04
8–16 mm	450.05	450.05	450.05	450.05	450.05	450.05	450.05

2.3 Test Methods

Tests on fresh and hardened SCC were performed according to relevant European Standards. Slump flow, L-box ratio and J-ring test were executed according to HRN EN 12350-8:2010 [15], HRN EN 12350-10:2010 [16] and HRN EN 12350-12:2010 [17], respectively. The porosity was measured according to HRN EN 12350-7:2009 [18]. The passing ability of SCC was measured and classified through L-box and J-ring tests, while flowability and viscosity of SCC were measured and classified through the slump flow test. All specimens were demoulded 24 h after the casting and placed in a water tank for 4 weeks. Mechanical and durability properties were calculated from the average of three specimens and were determined after 28 days of water curing. Compressive strength of SCC specimens was tested on 150 mm × 150 mm × 150 mm 3 cubes and ∅150 × 300 mm cylinders according to HRN EN 12390-3:2009 [19]. Flexural strength was tested on 100 mm × 100 mm × 400 mm prisms according to HRN EN 12390-5:2009 [20]. Modulus of elasticity was tested on ∅150 × 300 mm cylinders according to HRN EN 12390-13:2013 [21]. Depth of penetration of water under pressure was tested on 150 mm × 150 mm × 150 mm 3 cubes according to HRN EN 12390-8:2009 [22]. Gas permeability was tested on ∅150 × 50 mm specimens produced by cutting from the cylinder specimens ∅150 × 300 mm, according to CEMBEREAU method recommended by RILEM [23] and according to HRN EN 993-4:2008 [24].

3 Test Results and Discussion

3.1 Fresh SCC Test Results

Results of testing the fresh SCC are given in Table 2. Aggregate segregation or bleeding of fresh SCC was not observed, therefore there was no need to carry out the sieve segregation test to determine the sieve segregation resistance.

Table 2. Test results of fresh SCC.

Mixture	Fresh density (kg/m^3)	p (%)	J-ring		Slump flow			L-box	
			PJ (mm)	Class	d (mm)	T500 (s)	Class	H_2/H_1 (PA2)	
SCC-0CR	2420.94	1.10	6.25	<10	690	1.45	SF2/VS1	0.87	>0.80
SCC-5CR	2305.48	1.20	9.50	<10	685	1.55	SF2/VS1	0.86	>0.80
SCC-10CR	2311.69	1.30	9.75	<10	670	1.71	SF2/VS1	0.81	>0.80
SCC-15CR	2278.17	2.00	11.00	>10	670	1.83	SF2/VS1	0.74	<0.80
SCC-20CR	2197.47	2.30	12.00	>10	685	1.86	SF2/VS1	0.78	<0.80
SCC-25CR	2155.26	2.80	13.75	>10	655	2.10	SF1/VS2	0.78	<0.80
SCC-30CR	2124.22	3.20	26.25	>10	620	2.36	SF1/VS2	0.77	<0.80

It can be seen from Table 2. that the implementation of CR as a fine aggregate replacement in SCC caused a reduction in fresh concrete density, flowability and passing ability, and an increase in viscosity and porosity, which is in accordance with several previous investigations carried out by different authors, where crumb rubber, grain size 0–4 mm, replaced fine aggregates in SCC [25–27]. The concrete porosity is almost 2 times higher when 30% of FA (grain size 0–4 mm) is replaced by CR (size 0.5 mm–3.5 mm). On the other hand, the fresh concrete density is reduced by 12% when the replacement level was increased from 0% to 30%. J-ring value is constantly decreasing when rubber content is increased. According to EFNARC Guidelines [9] the blocking step PJ should be less than 10 mm. With a replacement level of 5% and 10%, value of PJ is below 10 mm. On the other hand, PJ values exceed limit value when the replacement level is over 10%. L-box test results show a comparable picture. According to EFNARC Guidelines [9] the passing ability ratio H2/H1 should be between 0.8 and 1. H2/H1 values were between 0.8 and 1 when 5% or 10% of fine aggregates were replaced with CR, but when the replacement level was between 15% and 30%, values of H2/H1 were below 0.8. The passing ability of SCC with replacement level higher than 10% can be improved with an increase of superplasticizer dosage, and with utilization of different type of cement. The obtained L-box test results showed a pronounced scatter, likely because of the rapid concrete setting time caused by cement used in experiment (CEM I 42.5R), hence an investigation of SCC with CEM I 42.5N should be made, for the purpose of obtaining better results of passing ability tests of SCC with CR. With 30% of CR as a fine aggregate replacement, the slump flow diameter is reduced by 10%. However, when using 5% to 25% of crumb rubber the reduction in slump flow was almost negligible, according to test results given in Table 2. However, with a replacement level of 5%, 10%, 15% and 20% slump flow class SF2 was obtained, while in the case of higher replacement level the slump flow class was SF1. Results of slump flow test and its corresponding classes (SF1 and SF2) were in related to viscosity classes presented over T500 parameter. Up to 20% of replacement level T500 was under 2 s (VS1) and when replacement level was 25% and 30% T500 was over 2 s (VS2).

3.2 Hardened SCC Test Results

Results of testing hardened SCC mechanical and durability properties are given in Table 3 and Fig. 2.

Table 3. Mean values of mechanical and durability properties of tested SCC mixtures.

Mixture	$f_{ck,\ cube}$ (MPa)	$f_{ck,\ cyl}$ (MPa)	E (GPa)	f_b (MPa)	Depth of water (mm)	K (m^2)
SCC-0CR	83.86	66.30	49.26	7.38	2	2.27×10^{-17}
SCC-5CR	69.31	60.83	48.06	6.58	11	5.03×10^{-17}
SCC-10CR	57.56	42.73	41.94	6.27	13	5.07×10^{-17}
SCC-15CR	48.78	33.11	37.69	5.88	16	1.71×10^{-17}
SCC-20CR	40.04	25.04	36.28	5.07	16	1.88×10^{-17}
SCC-25CR	33.02	24.28	26.42	4.87	18	1.41×10^{-17}
SCC-30CR	27.77	18.96	23.68	4.46	22	1.35×10^{-17}

Compared to the reference mixture SCC-0CR, the reduction in compressive strength of cubic specimens was 17%, 31%, 42%, 52%, 61% and 67% with inclusion of 5%, 10%, 15%, 20%, 25% and 30% of CR. A similar trend, i.e. reduction in compressive strength with increasing amount of waste tire rubber, can be seen from the results of compressive strength of cylinder specimens. In this case a relative high drop in compressive strength can be seen for mixtures SCC-5CR and SCC-10CR. Regarding the modulus of elasticity, a reduction of 23% and 52% was obtained if 15% and 30% of fine aggregates were replaced with CR. In case of flexural strength, these reductions were 20% and 40%, respectively. All values of mechanical properties of SCC were reduced when CR replaced fine aggregates, probably because of the fact that CR has a lower modulus of elasticity than fine aggregates. However, all compressive strength values of cubic and cylinder specimens were over 17 MPa. Furthermore, most likely due to elastic behaviour of rubber particles, some test specimens with rubber did not experienced rapid collapse during the test. With a greater amount of CR, the depth of water penetration increased. Still, according to HRN 1128:2007 [28] classification, reference mixture and mixtures with up to 10% of CR can be classified as Class 3 concrete (VDP 3), while mixtures with CR over 10% can be classified as Class 2 concrete (VDP 2). The mean values of gas permeability coefficient (K) of SCC were within the range of $1.35 \times 10^{-17} - 5.03 \times 10^{-17}$. These values are in the middle of the range of values normally expected for structural concrete. During experimental investigation, in comparison with reference mixture SCC-0CR, higher values of gas permeability coefficient were obtained for replacement levels of 5% and 10%. However, the gas permeability coefficient was reduced when the replacement level was higher than 10%, meaning the gas permeability improved on a higher level of fine aggregate replacement.

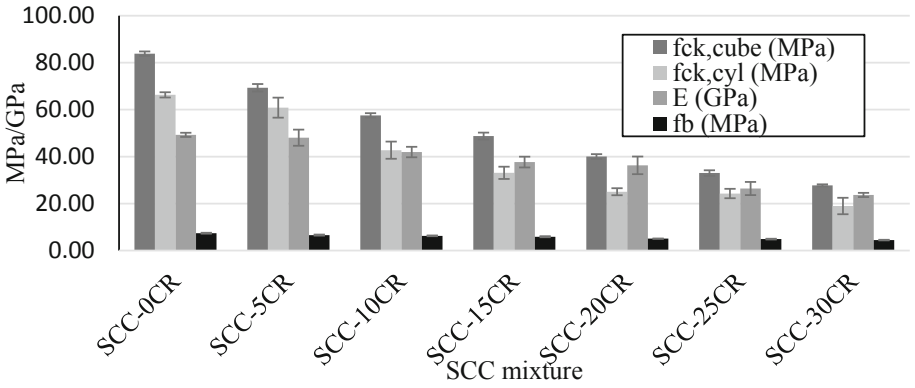

Fig. 2. Mechanical properties of SCC mixtures.

4 Conclusion

This paper presented an experimental investigation on fresh and hardened properties of self-compacting concrete with different amounts of fine aggregate being replaced with waste tire rubber, i.e. crumb rubber. Waste tire rubber was incorporated into SCC in different percentages of total aggregate volume, up to 30%. From the obtained results, several conclusions can be drawn:

- implementation of crumb rubber in SCC as a natural fine aggregate replacement caused a reduction in fresh concrete density, an increase in viscosity and a reduction in flowability and passing ability,
- at a replacement level of 30% the fresh concrete density is reduced by 12%,
- flowability and viscosity classes have been changed from SF2/VS1 to SF1/VS2 when 25% of natural aggregates were replaced with crumb rubber,
- up to 10% replacement level, the results of J-ring and L-box are still within desirable limits,
- partial replacement of fine aggregates with crumb rubber caused a reduction of all investigated mechanical properties of SCC, however compressive strength values of cylinder specimens were over 40 MPa at a 10% replacement level, which is promising for future investigation,
- considering durability properties of SCC, the depth of water penetration of cubic specimens constantly increased at increasing aggregate replacement level, and the gas permeability coefficient increased up to 10% replacement level and decreased from 15% to 30% replacement level,
- values of depth of water penetration and gas permeability coefficient are in the middle of the range of values normally expected for structural concrete, regardless of aggregate replacement level used in this experimental investigation.

Acknowledgements. This paper was supported by the Croatian Science Foundation under the project name UIP-2017-05-7113 Development of Reinforced Concrete Elements and Systems with Waste Tire Powder – ReCoTiP.

References

1. ETRMA (2015) End-of-life Tyre Report 2015
2. AbdelAleem BH, Hassan AAA (2018) Development of self-consolidating rubberized concrete incorporating silica fume. Constr Build Mater 161:389–397
3. Aslani F, Ma G, Yim Wan DL, Tran Le VX (2018) Experimental investigation into rubber granules and their effects on the fresh and hardened properties of self-compacting concrete. J Clean Prod 172:1835–1847
4. Najim KB, Hall MR (2012) Mechanical and dynamic properties of self-compacting crumb rubber modified concrete. Constr Build Mater 27(1):521–530
5. Bušić R, Miličević I, Šipoš T, Strukar K (2018) Recycled rubber as an aggregate replacement in self-compacting concrete—literature overview. Materials (Basel) 11(9):1729

6. Bjegović D, Baričević A, Serdar M (2011) Durability properties of concrete with recycled waste tyres. In: 12th international conference on durability of building materials and components Porto, Port., pp 1659–1667
7. Gupta T, Chaudhary S, Sharma RK (2016) Mechanical and durability properties of waste rubber fiber concrete with and without silica fume. J Clean Prod 112:702–711
8. Thomas BS, Gupta RC, Kalla P, Cseteneyi L (2014) Strength, abrasion and permeation characteristics of cement concrete containing discarded rubber fine aggregates. Constr Build Mater 59:204–212
9. EFNARC (2005) The European Guidelines for Self-Compacting Concrete
10. HRN EN 197-1:2012 Cement - Part 1: Composition, specifications and conformity criteria for common cements
11. HRN EN 13263-1:2009: Silica fume for concrete - Part 1: Definitions, requirements and conformity criteria
12. HRN EN 1008:2002 Mixing water for concrete – Specification for sampling, testing and assessing the suitability of water, including water recovered from processes in the concrete industry, as mixing water for concrete
13. ASTM (2011) C188-16, Standard Test Method for Density of Hydraulic Cement, vol 95, no Reapproved 2003, pp 37–39
14. HRN EN 933-1:2012: Tests for geometrical properties of aggregates – Part 1: Determination of particle size distribution – Sieving method
15. HRN EN 12350-8:2010: Testing fresh concrete - Part 8: Self-compacting concrete - Slump flow test
16. HRN EN 12350-10:2010: Testing fresh concrete - Part 10: Self-compacting concrete - L box test
17. HRN EN 12350-12:2010: Testing fresh concrete - Part 12: Self-compacting concrete - J-ring test
18. HRN EN 12350-7:2009: Testing fresh concrete - Part 7: Air content – Pressure methods
19. HRN EN 12390-3:2009: Testing hardened concrete - Part 3: Compressive strength of test specimens
20. HRN EN 12390-5:2009: Testing hardened concrete - Part 5: Flexural strength of test specimens
21. HRN EN 12390-13:2013: Testing hardened concrete - Part 13: Determination of secant modulus of elasticity in compression
22. HRN EN 12390-8:2009: Testing hardened concrete - Part 8: Depth of penetration of water under pressure
23. RILEM TC 116-PCD: permeability of concrete as a criterion of its durability (1999) Determination of the capillary absorption of water of hardened concrete. Mater Struct Constr 32:174–179, April 1999
24. HRN EN 993-4:2008: Methods of test for dense shaped refractory products – Part 4: Determination of permeability to gases
25. Ismail MK, Hassan AAA (2016) Use of metakaolin on enhancing the mechanical properties of self-consolidating concrete containing high percentages of crumb rubber. J Clean Prod 125:282–295
26. Uygunoğlu T, Topçu IB (2010) The role of scrap rubber particles on the drying shrinkage and mechanical properties of self-consolidating mortars. Constr Build Mater 24(7):1141–1150
27. Si R, Wang J, Guo S, Dai Q, Han S (2018) Evaluation of laboratory performance of self-consolidating concrete with recycled tire rubber. J Clean Prod 180:823–831
28. HRN 1128:2007: Concrete - Guidelines for the implementation of HRN EN 206-1

Novel Mix Design Methodology for Self-Compacting Steel-Fiber Reinforced Concrete Based on Rheological and Mechanical Concepts

Ángel de la Rosa[1(✉)], Elisa Poveda[1], Gonzalo Ruiz[1], and Héctor Cifuentes[2]

[1] ETS de Ingenieros de Caminos, C. y P., Univ. de Castilla–La Mancha, Ciudad Real, Spain
angel.delarosa@uclm.es
[2] ETS de Ingeniería, Universidad de Sevilla, Seville, Spain

Abstract. We describe a new methodology to calculate mix proportions of components for self-compacting steel-fiber reinforced concrete [*Construction and Building Materials* 189 (2018) 409–419]. The methodology is based on a previous one for plain self-compacting concrete by Prof. B. L. Karihaloo and co-workers, which has been expanded to include steel fibers while maintaining self-compactability of the concrete. The methodology has two key points. The first one is the rheological behavior of the fresh material, which leads to considering the effective viscosity of the suspension with fibers as a design parameter. By means of micromechanical models we estimate this parameter from the plastic viscosity of the cement paste and the volume fraction and aspect ratio of the fiber. The second one is the desired compressive strength of the composite material, which leads to setting water-cement ratio as the other design parameter. Besides, water-cement ratio influences the plastic viscosity value of the cement paste, together with the content of superplasticizer admixture. This rheological parameter has to be measured by means of rheometers or approximated by other simpler and cheaper instruments, like capillary viscometers (Cannon-Fenske or Marsh funnel). The methodology has been programmed numerically in MATLAB to make some practical design charts by means of which the quantities of the concrete components are calculated. The use of these design charts is explained with an example. The study also provides experimental validation in fresh and hardened state. The results show the robustness of the proportioning methodology.

Keywords: Self-compacting steel-fiber reinforced concrete · Mix design · Rheology · Plastic viscosity · Compressive strength

1 Introduction

Design methods for self-compacting steel-fiber reinforced concrete (SCSFRC) are scarce [1–4] and there are not specifics recommendations to ensure self-compactability of fiber concrete mixes. Recently, De la Rosa *et al.* [2] have proposed a new mix

V. Mechtcherine et al. (Eds.): RheoCon 2019/SCC 2019, RILEM Bookseries 23, pp. 11–18, 2020.
https://doi.org/10.1007/978-3-030-22566-7_2

proportioning methodology for SCSFRC based on the target plastic viscosity required for the mix in the fresh state and the target compressive strength for the hardened fiber concrete, which is outlined in this communication.

Plastic viscosity along with yield stress are the rheological parameters required to describe the Bingham model that approximates well the behavior of the SCC and SCSFRC in fresh state. However, yield stress is approximately constant in a wide range of values of plastic viscosity [5] and, then, SCFRC can be described by the plastic viscosity only. This was used by Abo Dhaheer *et al*. [6] for the development of a proportioning method for plain SCC. They select the water/cementitious materials ratio to achieve a desired strength class, measure the plastic viscosity of the cement paste for this *w/c* ratio and apply the Krieger and Dougherty equation to obtain the masses of the ingredients of a SCC for achieving a definite target viscosity of the fresh mix [6]. In this work, we extend their approach to SCSFRC. The inclusion of steel fibers is considered through the model proposed by Ghanbari and Karihaloo [5], which calculates the effect of the fibers on the plastic viscosity of the base concrete and thus allows regarding the fibers as another phase in the mix. An extensive experimental program was performed to validate the design methodology. Its development and explanation can be seen in detail in [2]; this communication provides an additional validation example. The procedure has been programmed numerically to generate practical and mix-design charts to determine the dosage of the components of SCSFRC. This methodology involves a drastic reduction of the number of trial and error designs necessary to obtain a concrete of these characteristics.

2 Mix Proportioning for SCSFRC

The proposed method is based on four concepts: the target compressive strength of SCSFRC, f_{cuf} (in cubic specimen of 100 mm side), the target effective plastic viscosity of SCSFRC, η_e, the measurement of the plastic viscosity of its cement paste, η_p, and the main fiber parameters to use (volume fraction of fiber, ϕ_f, and aspect ratio of the fiber, λ).

The compressive strength of concrete is mainly determined by setting the water to cementitious materials ratio, *w/c*. There are other factors that influence the strength, as the cement class and the type of aggregate [7]. However, the Abrams type relation is a widely-recognized rule that fits well in an extensive set of experimental data [6]. Equation (1) (in MPa) allows us to determine *w/c* from the target compressive strength. It should be noted that the use of steel fibers in SCC up to 1% by volume has a negligible effect on the compressive strength [8].

$$f_{cuf} = \frac{195}{12.65^{w/c}} \tag{1}$$

Then it is necessary to select the mass of superplasticizer to mass of cement ratio according to manufacturer's recommendation or previous test in a fresh state (drain flow time in the Marsh funnel could be an adequate test). Thus, it is possible to determine the plastic viscosity of the paste, η_p. It should be noted that the plastic viscosity may depend on the measuring instrument. Rotational rheometers, as cone-plate typology, provide

accurate measurements; however, capilar viscometers, which are cheaper and simpler apparatus, could be used to estimate η_p without too much loss of precision, due to the homogeneity of the suspension.

Fresh SCSFRC is a heterogeneous suspension that can be considered as two phase material formed by a solid phase (aggregates and fibers) suspended in a viscous fluid (cement paste) [5]. The increase of plastic viscosity of the cement paste can be estimated by means of a two-phase micro-mechanical model. Applying the model in stages, the first solid phase is the finest material (filler) in suspension in the fluid cement paste. The next stage incorporates the next coarser material into the first stage that is considered as the fluid viscous phase. This sequence is followed until all the solid constituents are included in the two-phase suspension. The plastic viscosity value of the suspension at stage i is calculated by Eq. (2) [5, 6]:

$$\eta_i = \eta_{i-1} f_i(\phi_i) \tag{2}$$

where η_{i-1} is the plastic viscosity of the previous stage, $i - 1$ (the first stage considered is the plastic viscosity of the cement paste, $\eta_p (= \eta_0)$; $f_i(\phi_i)$ is a function that estimates the increase of η_i produced by the solid phase with volume fraction ϕ_i. Thus, the plastic viscosity of the SCSFRC, η_e is:

$$\eta_e = \eta_p \prod_i^n f_i(\phi_i) \tag{3}$$

where n is the total number of solid phases with the last one corresponding to the rigid fibers. So that SCC to which fibers are added –or base SCC– is regarded as a suspension where aggregates are approached as rigid spheres, the equation proposed by Krieger-Dougherty [5, 6, 9], Eq. (4), can be use as a function to estimate the increase of plastic viscosity caused by the addition of solid phases:

$$f_i(\phi_i) = \left(1 - \frac{\phi_{\mathrm{i}}}{\phi_{i\max}}\right)^{-[\eta_i]\phi_{i\max}} \tag{4}$$

where $[\eta_i]$ is the intrinsic viscosity and $\phi_{i\max}$ is the maximum packing fraction of the solid phase i. This parameter can take theoretical values (equal to 0.524, 0.630 and 0.740, corresponding to filler, fine aggregate and coarse aggregate, respectively) or can be calculated taking into account the size and the distribution of the solid phase particles used in practice. The product $[\eta_i]\ \phi_{i\max}$ remains practically equal to 1.9 for rigid spherical particles in cementitious suspensions [5, 6]. Therefore, substituting Eq. (4) in Eq. (2), results in the viscosity of the base SCC, η_{eb}:

$$\eta_{eb} = \eta_p \left(1 - \frac{\phi_{LP}}{0.524}\right)^{-1.9} \left(1 - \frac{\phi_{FA}}{0.630}\right)^{-1.9} \left(1 - \frac{\phi_{CA}}{0.740}\right)^{-1.9} \tag{5}$$

being ϕ_{LP}, ϕ_{FA} and ϕ_{CA} the volume fraction of filler (or limestone powder, $i = 1$), fine aggregate ($i = 2$) and coarse aggregate ($i = 3$), respectively.

The last solid phase to include is the steel fiber whose shape differs from that aggregates. To estimate its effect on the plastic viscosity, it is assumed that the fibers are slender rigid solids that can translate and rotate but not undergo any elastic deformation, hypothesis that is met up to a maximum aspect ratio, λ (length of fiber/diameter of fiber), of 85 and a volume fraction of fiber, ϕ_f, lower than 2% (the method has been experimentally validated until a volume fraction less or equal than 1%). The values of the effective plastic viscosity of the base SCC, η_{eb}, and SCSFRC, η_e, can be estimated from the model proposed by Ghanbari and Karihaloo [5]:

$$\eta_e = \eta_{eb}\left[(1-\phi_f) + \frac{\pi\phi_f\lambda^2}{3\ln(2\lambda)}\right] \tag{6}$$

Equation (6) can be simplified in the Eq. (7) as is proposed in [2]:

$$\eta_{\mathrm{e}} = \eta_{eb}\left(1+\frac{\phi_f}{\phi_\lambda}\right) \text{ where } \phi_\lambda = \frac{3\ln(2\lambda)}{\pi\lambda^2} \tag{7}$$

ϕ_λ is a function of λ that tends to fall rapidly to zero with increasing λ. For values of λ greater or equal than 10, what is common in commercial steel fibers, this approximation is accurate.

Combining Eqs. (5) and (7) the effective plastic viscosity for SCSFRC, η_{eb}, is finally obtained:

$$\eta_e = \eta_p\left(1-\frac{\phi_{LP}}{0.524}\right)^{-1.9}\left(1-\frac{\phi_{FA}}{0.63}\right)^{-1.9}\left(1-\frac{\phi_{CA}}{0.74}\right)^{-1.9}\left(1+\frac{\phi_{\mathrm{f}}}{\phi_\lambda}\right) \tag{8}$$

By means of Eq. (7) the base SCC with its plastic viscosity value η_{eb} can be established. The resolution of this equation gives rise to the first design graph of the method (Fig. 1, upper graph) through which the value of η_{eb} can be obtained. Then it is only necessary to solve Eq. (5), which is resolved numerically in [6], to obtain the amount of filler (limestone powder), fine and coarse aggregates. The resolution of Eq. (5) originates the second design graph (Fig. 1, lower graph) through which amount of filler, fine and coarse aggregates are established. This entire methodology was programmed and automated in MATLAB, so it is only necessary entering the target values of parameters in the corresponding code line (f_{cu}, m_{SP}/m_c, η_{p}, η_{e}, λ and ϕ_f) and the two design graphs will be generated.

2.1 Range of Components

The addition of steel fibers in the SCC matrix requires decreasing the coarse aggregate content to ensure self-compactability [2, 4]. This methodology should be used only up to 1% of fibers, since Khayat *et al.* [4] indicate that self-compactability is hard to achieve beyond this fiber content.

As there are not specific guidelines for SCSFRC, this methodology follows the recommendations of IECA [10] (see Table 1) to establish the ranges of constituents of

SCSFRC, due to the fact that IECA recommendations reduce the amount of coarse aggregate and increase the upper limit of fine aggregate.

Table 1. Range of constituents for SCC following IECA recommendations [10].

Ingredients	Typical range
Powder, $m_c + m_{LP}$ [kg/m^3]	450–600
Water, m_w [kg/m^3]	150–210
Coarse aggregate, m_{CA} [kg/m^3]	650–900
Fine to total aggregate ratio, $m_{FA}/(m_{FA} + m_{CA})$	0.48–0.57
Water to powder ratio by volume, $V_w/(V_c + V_{LP})$	0.85–1.10

3 Example for Determining Mix Proportions of SCSFRC

In this section, we explain how to apply the mix design methodology calculating the mix proportions of a SCSFRC with these characteristics: f_{cuf} = 70 MPa, η_e = 30 Pa s (with hooked-end steel fibers, l_f = 35 mm, λ = 65, ρ_f = 7850 kg/m^3) and ϕ_f = 1%.

1. From Eq. 1, the compressive cubic strength of design corresponds to a *w/c* equal to 0.4.
2. Starting from a rheological test with the Marsh funnel and according to the manufacturer's recommendation, we select a m_{SP}/m_c ratio equal to 1.2%.
3. Measure the plastic viscosity of the cement paste by means of any viscometer (in this case, we use a Cannon-Fenske viscometer). For 100% CEM I 52.5 R-SR, *w/c* = 0.4, m_{SP}/m_c = 1.2% and assuming that there is 2% of trapped air bubbles, η_p = 0.086 Pa s.
4. For a SCSFRC with f_{cuf} = 70 MPa and η_e = 30 Pa s Fig. 1 allows us checking that ϕ_f = 1% is within the permissible range. Otherwise, η_e or ϕ_f has to be changed.
5. Obtain the value of η_{eb}, estimated graphically from Fig. 1 (upper subfigure) with the intersection between lines for η_e = 30 Pa s and ϕ_f = 0.01, which determines the inclined straight line that passes through it and the corresponding value for η_{eb}. In this case, η_{eb} = 3.1 Pa s.
6. Using Fig. 1 (lower subfigure), for η_{eb} = 3.1 Pa s and f_{cuf} = 70 MPa, the value of solid phases masses can be estimated by reading from each curve. Entering in the abscissa with η_{eb} every curve allows to determine the mass of the components:

   - Cementitious material, m_c (red curve): η_{eb} = 3.1 Pa s, m_c = 476.7 kg/m^3
   - Water, m_w: *w/c* (= m_w/m_c) = 0.4, m_w = 190.7 kg/m^3
   - Superplasticizer, m_{SP}: m_{SP}/m_c = 0.012, m_{SP} = 5.72 kg/m^3
   - Limestone powder, m_{LP} (blue curve): η_{eb} = 3.1 Pa s and m_c = 476.7 kg/m^3, m_{LP} = 121 kg/m^3
   - Fine aggregate, m_{FA} (green curve): η_{eb} = 3.1 Pa s, m_c = 476.7 kg/m^3 and m_{LP} = 121 kg/m^3, m_{FA} = 875 kg/m^3
   - Coarse aggregate, m_{CA} (magenta curve): η_{eb} = 3.1 Pa s, m_c = 476.7 kg/m^3 and m_{LP} = 121 kg/m^3 and m_{FA} = 875 kg/m^3, m_{CA} = 705 kg/m^3
   - Steel fiber, m_f: $m_f = \rho_f\, \phi_f$ = 78.5 kg/m^3

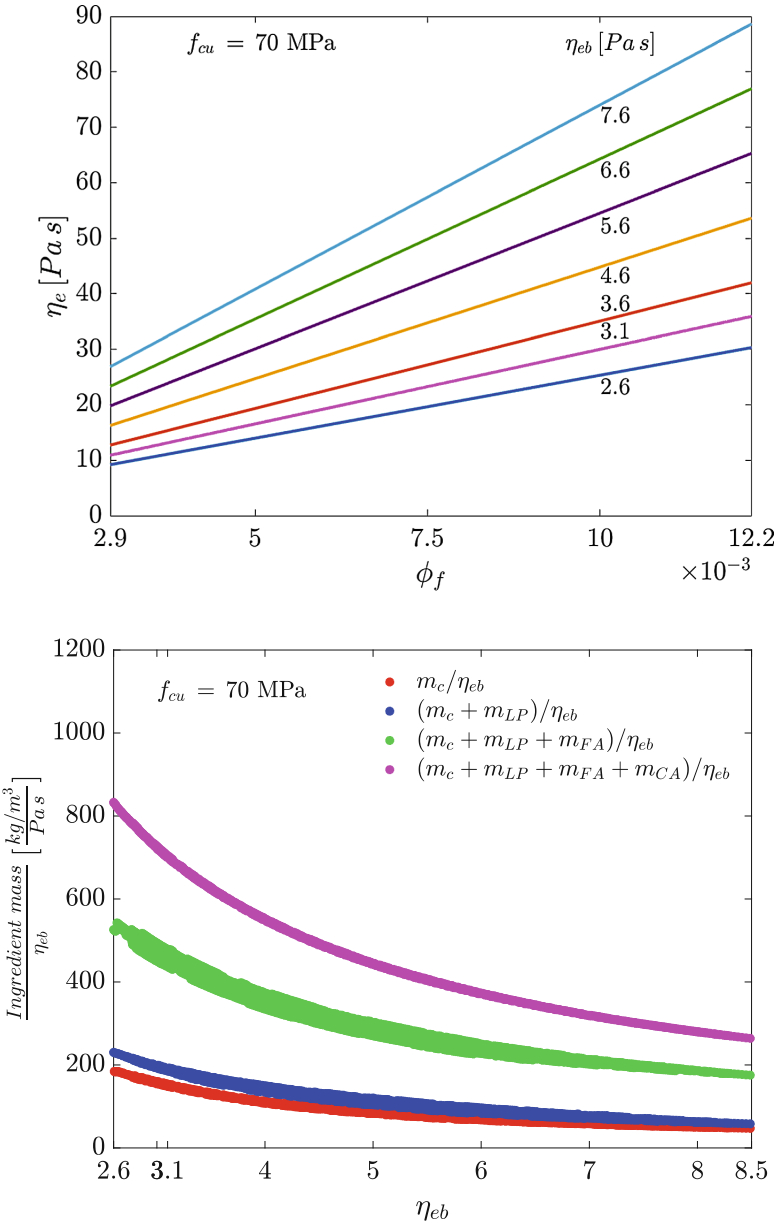

Fig. 1. Design graphs for SCSFRC, f_{cuf} = 70 MPa (Upper subfigure: permissible fiber range and calculus of η_{eb} from η_e value. Lower subfigure: design graph for calculating mix proportions of the solid phases). (Color figure online)

7. Calculate the total volume of the mix from the calculated ingredient mass and the densities of cement, superplasticizer, water, limestone powder, fine aggregate, coarse aggregate and fiber, that are, respectively: 3157 kg/m^3, 1058 kg/m^3, 1000 kg/m^3, 2641 kg/m^3, 2674 kg/m^3, 2679 kg/m^3 and 7850 kg/m^3. The total volume of SCSFRC for this composition is 1.003 m^3.
8. Calculate η_{eb} from volume fractions of solids suspended in the viscous phase:

$$\phi_{LP} = \frac{V_{LP}}{V_c + V_w + V_{SP} + V_{LP} + 0.02} = 0.111$$
$$\phi_{FA} = \frac{V_{FA}}{V_c + V_w + V_{SP} + V_{LP} + V_{FA} + 0.02} = 0.442$$
$$\phi_{CA} = \frac{V_{LP}}{V_c + V_w + V_{SP} + V_{LP} + V_{FA} + V_{CA} + 0.02} = 0.262$$

   According to Eq. 5, η_{eb} = 3.1 Pa s.
9. Determine η_e of SCSFRC using Eq. 8: η_e = 30 Pa s. If the error with respect to the target value of η_e is less than 5%, we accept the calculations and the mix design is concluded:

$$Error = 100\left|\frac{\eta_{ecalculated} - \eta_{etarget}}{\eta_{etarget}}\right| = 100\left|\frac{29.5 - 30}{30}\right| = 1.7\%$$

4 Experimental Results

The mix proportions calculated in the previous section have been actually used to produce a SCSFRC for validation purposes. The materials used are CEM I 52.5 R-SR, limestone powder composed of 98.5% natural calcium carbonate with a maximum size of 100 μm, natural round siliceous fine and coarse aggregates with a maximum size of 4 mm and 6.3 mm, respectively. A superplasticizer of poly-aril-ether based type (BASF MasterEase 5025) and an occluded air reducer (BASF MasterCast 212) were used too (the last one in a small proportion of 0.03 kg/m^3). The hooked-end steel fibers used are of the brand Bekaert Dramix 3D 65/35 GG, with l_f = 35 mm and $\lambda = 65$. Resistance to segregation, stability and air migration of SCSFRC were evaluated by the Slump Flow test (average diameter of the spread, d_m, and time needed to reach a spread of 500 mm, T_{500}), the passing ability by the L-Box test, according to EN 12350-8:2010 and EN 12350-10:2010, respectively. Its properties in fresh and hardened stated are summarized in Table 2.

Table 2. Properties of SCSFRC in fresh and hardened state (E is the modulus of elasticity, f_L is the flexural strength, f_{R1} and f_{R3} are the residual flexural strength for 0.5 mm and 2.5 mm of crack mouth opening, respectively – mean values, standard deviation in brackets).

Slump Flow test						
d_m [mm]	T_{500} [s]	f_{cuf} [MPa]	E [GPa]	f_L [MPa]	f_{R1} [MPa]	f_{R3} [MPa]
780	2.0	69.3 (1.6)	39.6 (2.3)	11.7 (1.4)	11.0 (1.3)	8.1 (1.1)

5 Summary and Conclusion

A new methodology is proposed to calculate mix-proportioning of SCSFRC based on the rheology of cement paste and on micro-mechanical constitutive models. From the adaptation of the Krieger and Dougherty equation to a suspension with steel fibers (adding the model of Ghanbari and Karihaloo for rigid fibers) we obtain the masses of the components of the SCSFRC. The data required are the target effective plastic viscosity, the compressive strength of the SCSFRC and the main steel fiber parameters, i.e. aspect ratio and fraction of fibers. Measuring the plastic viscosity of the cement paste through rheometers or estimating it with simpler and cheaper viscometers (like the Cannon-Fenske viscometer or the Marsh funnel) and using two design graphs (implemented in MATLAB) we can obtain the ingredient masses for any SCSFRC easily. An example is provided to explain how to use these design graphs and the equations involved, as well as its experimental validation in fresh and hardened states.

Acknowledgement. The authors acknowledge funding from the Ministerio de Ciencia, Innovación y Universidades through projects BIA2015-68678-C2-1R and International Campus of Excellence CYTEMA. Ángel de la Rosa acknowledges the fellowship FPI BES-2016-077458.

References

1. Grünewald S (2004) Performance-based design of self-compacting fibre reinforced concrete, PhD thesis. Delft, The Netherlands, Delf University of Technology
2. de la Rosa A, Poveda E, Ruiz G, Cifuentes H (2018) Proportioning of self-compacting steel-fiber reinforced concrete mixes based on target plastic viscosity and compressive strength: mix-design procedure & experimental validation. Constr Build Mater 189:409–419
3. Ferrara L, Park YD, Shah SP (2007) A method for mix-design of fiber-reinforced self-compacting concrete. Cem Concr Res 37(6):957–971
4. Khayat KH, Kassimi F, Ghoddousi P (2014) Mixture design and testing of fiber-reinforced self-consolidating concrete. Mater J 111(2):143–152
5. Ghanbari A, Karihaloo BL (2009) Prediction of the plastic viscosity of self-compacting steel fibre reinforced concrete. Cem Concr Res 39(12):1209–1216
6. Dhaheer MSA, Al-Rubaye MM, Alyhya WS, Karihaloo BL, Kulasegaram S (2016) Proportioning of self-compacting concrete mixed based on target plastic viscosity and compressive strength: Part I – mix design procedure. J Sustain Cem Based Mater 4:199–216
7. de Larrard F (1987) Formulation et Propiétés des Bétons á Trés Hautes Performances, PhD dissertation, Ecole Nationale des Ponts et Chaussées, Paris
8. Ruiz G, de la Rosa Á, Poveda E (2018) Model for the compressive stress-strain relationship of steel fiber-reinforced concrete for non-linear structural analysis. Hormigón y Acero 69 (S1):75–80
9. Krieger IM, Dougherty TJ (1959) A mechanism for non-newtonian flow in suspensions of rigid spheres. Trans Soc Rheol 3(1):137–152
10. Fernández-Gómez J (2005) Guía práctica para la utilización del hormigón autocompactante, Instituto Español del Cemento y sus Aplicaciones (IECA)

Innovative Use of Fine and Ultrafine GCC in Cementitious Systems

Pascal Gonnon(✉), Philipp Mueller, and Thomas Lys

Omya International AG, Oftringen, Switzerland
pascal.gonnon@omya.com

Abstract. Ground Calcium Carbonate (GCC) has been used for decades in construction to enhance performance-cost ratio of cement-based products such as grout, mortar or concrete. From dry-mortars to structural concrete, engineers associate GCC with cementitious materials (SCM) to optimize the fluidity, viscosity and reduce the carbon footprint of the mixtures. Nevertheless, the contribution of GCC to the flowability and viscosity of the cement-based systems as well as the range of GCC fineness available to optimize the packing density and strength are poorly appreciated. The benefits of specific GCC products are expected to be particularly useful in formulating concrete or mortar for digital fabrication. This paper will provide an overview of the best practice use of GCC products, aiming to stimulate interest for the material not only for use in digital fabrication with concrete.

Keywords: Ground Calcium Carbonate · Packing · LGsystem, LG10

1 Introduction

Due to environmental reasons and the growth of infrastructure development resulting in an enormous demand for cement, the workability and durability aspects of ecological mortar and concrete with high content of GCC has been investigated by many authors around the world [1–3]. It appears, that most of the related work on cement paste or mortars focuses on cement substitution, hydration, strength, heat release, low temperature curing or pore structure [4–6]. In many countries, the interest in GCC is also supported by the proposal of new valuable supplementary cementitious materials (SCMs) such as blast furnace slag, calcined clay or silica fume and the ongoing cement evolution with lower carbon footprint.

During the last decades, Omya International AG has been developing several methods to evaluate GCC materials as a functional mineral additive and to analyze the contribution of each individual component, i.e. cement, admixture, SCM and GCC to the performance of the system, in innovative underlayment systems, self-compacting concrete (SCC) and ultra-high-performance concrete (UHPC). Today, some of these methods are included in national provisions or standards [7]. This paper describes two methods, the LGsystem© to evaluate the point of saturation of a GCC material and the LG10© to determine the impact of a mineral addition (or a blend of several mineral additions) on system performance respectively.

V. Mechtcherine et al. (Eds.): RheoCon 2019/SCC 2019, RILEM Bookseries 23, pp. 19–26, 2020.
https://doi.org/10.1007/978-3-030-22566-7_3

2 The LGsystem©

To design and develop new formulations containing admixtures, nowadays, concrete and mortar producers often use CEM mortar as the rheological correlation between mortar and concrete has been established [8, 9]. Based on this existing know-how, the contribution of GCC quality and content to the rheological properties of the mortar can be measured by slump flow with a mini cone and flow time is determined thorough a V-Funnel. Depending on the composition of the formulation (binder and water content) as well as characteristics and compatibility of the components, it is possible to optimize GCC content to achieve best fluidity and viscosity. The evaluation can be completed with setting time and shrinkage.

2.1 Materials

The components of the mixtures are ordinary Portland cement (OPC) CEM I 42.5R CE HES, GCC, siliceous sand (EN 196-1), GCC, superplasticizer and water (Table 1). The superplasticizer is a liquid polycarboxylate (PCE). The selected GCC, Betocarb® HP, is a limestone-based functional filler with a Blaine surface area of 462 m^2/kg, a blue value of 0.3 g/kg and a CaCO3 content of 98.8%.

2.2 Experimental Method

The LGsystem© maintains a constant ratio of cement, water and admixture (Table 1). However, the dosage of superplasticizer (PCE) is adjusted to reach the targeted fluidity for the reference mixture.

The fluidity targets are: slump flow of 340 mm–400 mm and flow time of 4–10 s.

Table 1. CEM proportions with GCC.

Materials (g)	Reference	Test 1	Test 2	Test 3
Cement	380	380	380	380
GCC	200	300	400	500
Sand	1250	1150	1050	950
Superplasticizer	a	a	A	a
Water	190	190	190	190

"a" is the necessary superplasticizer quantity to achieve the flow target, defined for the reference.

Table 2. Results LGsystem©.

	Reference	Test 1	Test 2	Test 3
Slump flow (mm)	385	410	450	245
Flow time (sec)	12	7	6	47

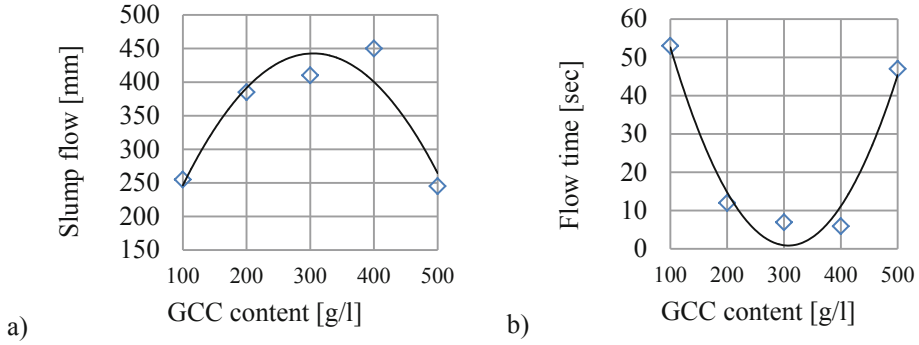

Fig. 1. (a) Fluidity, slump flow and (b) Fluidity, flow time.

Depending on GCC (i.e. Betocarb® HP) dosage, flowability and viscosity values are significantly improved as shown in Fig. 1a and b. This positive impact is a result of effective dispersion of the GCC particles in the mixture, leading to enhanced packing and improved interactions with the superplasticizer (PCE).

Table 3. Results LGsystem©.

	Reference	Test 1	Test 2	Test 3
Density	2.33	2.34	2.34	2.28
Strength 1D (MPa)	21	23	25	25
Strength 28D (MPa)	50	61	64	58

Based on the results shown in Tables 1 and 2, the selected GCC can effectively be used as a mineral plasticizer, in addition to partial sand replacement. The results shown in Table 3 confirm the packing improvement of the granular skeleton and the positive contribution to strength development. Therefore, it can be concluded that GCC is not an inert component (Type I addition).

Many authors have shown that GCC acts as the crystallization nucleus for the precipitation of portlandite. This effect accelerates the hydration of cement particles, particularly at lower water/cement ratio [10–12]. Since 1995, the French concrete standard (EN 2016) recognizes the activity of GCC (also defined as Limestone addition) using a k-value fixed at 25:100 for the Equivalent Binder calculation. In addition to its role of a mineral plasticizer, the example in Table 4 shows that for the common concrete exposure class XF1 (moderate water saturation, without de-icing agent), GCC can also be used for partial cement and sand replacement. The total fine content (cement and GCC) increases by 29.2% and the stability of the concrete is improved.

Table 4. Equivalent binder calculation.

	XF1
Minimum CEM I 42.5 content (kg)	294
CEM I (kg)	259
GCC (kg)	86
Total fine content (kg)	345
Growth of the total fine content (kg)	51
Cement reduction (kg)	35
Sand reduction (kg)	51
Equivalent binder C+k.A	294
A/A+C	0.25

Outside of France, the suitability of k-value is also established in the European concrete standard EN 206 for fly ash and silica fume when using CEM I conforming to EN 197-1.

In summary, the LGsystem® method allows the engineer to define the optimum GCC dosage in cement-based formulations. GCC is used as a Mineral Plasticizer® to optimize packing of the formulation and through this to enhance flow, stability and strength performance. In France, a k-value has been established and thus allows for the partial substitution of cement and sand.

3 The LG10© Method

Cementing materials or mineral additions, such as fly ash, blast furnace slag, pozzolana, limestone and silica fumes, have been used for many years to produce cement [13], mortars and concrete for civil engineering and building construction. In dedicated exposure classes, these mineral additions are incorporated to the concrete, according to the national concrete standard and in partial substitution of Portland cement. Durability factors, i.e. water/cement ratio, minimum cement content or compressive strength at 28 days are commonly used to assess concrete performance, while mineral addition contribution is typically expressed in term of the so-called k-value.

For economic and ecological reasons, it appears important to increase the amount of mineral addition and introduce new binders or cements. To protect the final user and maintain the quality of the concrete goods it is of utmost importance to properly evaluate the contribution of all components, i.e. cement, blast furnace slag, limestone etc. Furthermore, it is crucial to evaluate the combination of a given cement with one or many mineral additions on a regular basis. However, there is no good method available today for this evaluation.

Based on a new approach, Omya has developed the mortar test method LG10©. LG10© evaluates consistency and strength contribution of a single mineral addition or combination of several mineral additions. The two key parameters used in this method are (1) the proportion of mineral addition used to substitute cement (A/(A+C)) and

(2) the k-value of the mineral addition. The method allows the engineer to evaluate these parameters for a given cement at different age.

3.1 Materials

The components of the mixtures used in this method are OPC, siliceous sand (EN 196-1), the mineral addition to be evaluated and water.

3.2 Experimental Method

The mortar formulation shown is Table 5 is commonly used in industry to assess cements and particularly to determine compressive and flexural strength of the system.

Table 5. CEN mortar proportions.

Materials	Quantity
Cement (g)	450
Water (g)	225
Sand (g)	1350
Water/cement	0.50

3.2.1 LG10© - Reference

Starting from the CEN mortar shown in Table 5, the purpose of LG10© method is to formulate a plastic mortar using the following boundary conditions:

- constant total mass
- constant consistency
- variation of the W/C or W/(C+k*A), ranging from 60:100, 65:100 to 70:100.

Table 6. LG10© - Reference proportions.

W/C	60:10	65:100	70:100
Cement (g)	377	346	321
Water (g)	225	225	225
Sand (g)	1415	1446	1471
Total mass (g)	2017	2017	2017
W/C	0.60	0.65	0.70

The respective reference compositions are summarized in Table 6. It is worth noting that the total mass is kept constant at 2017 g. While water content is kept constant as well, the amount of sand is adjusted to account for the changing cement reduction as the W/C ratio ranges from 60:100 to 70:100.

3.2.2 Mixing and Casting

The consistency of each specimen is measured according to EN 1015-3 with flow table reported in mm. Targeted consistency is 200 mm ± 40 mm.

According to EN 196-1, the mortar is prepared by mechanical mixing and compacted in a prismatic mold 4 mm × 4 mm × 16 mm using a jolting apparatus. The casted mortars are stored in the mold in a moist atmosphere for 24 h and after demolding density is determined by a hydrostatic weighing method.

After that, all mortars are stored under water until strength testing is performed. At the required age, the mortars are taken from wet storage and broken in flexure. Each half prism is tested for strength compression.

3.2.3 LG10© with Mineral Addition

For each mineral addition, the engineer needs to define the rate of cement substitution and the k-value. The calculation of the amount of binary binder "Portland CEM I + mineral addition" to be tested is done with Eqs. (1) and (2).

$$C = \frac{y}{1 + k\left(\frac{x}{1-x}\right)} \tag{1}$$

$$A = \frac{y - C}{k} \tag{2}$$

- A = quantity of the mineral addition
- C = reduced cement content
- y = quantity of cement defined in Table 6
- k = k-value of the mineral addition
- x = A/(A+y) = rate of cement substitution.

3.3 LG10© with Ground Calcium Carbonate

3.3.1 Materials

The cement used is CEM I 42.5R. Main characteristics are C3A: 8.4%, C3S: 69.2%, C4AF: 6.9% and C2S: 9.4%, Blaine surface: 340 m^2/kg, Na2Oeq: 0.65%, S03: 2.8%, strength 1 day: 17 MPa, strength 28 days: 58 MPa.

Main characteristics of the selected GCC are Blaine surface: 385 m^2/kg, passing 63 µm: > 81%, methylene blue value: 0.4 g/kg, and calcium carbonate content: 98.3%.

The k-value is estimated at 25:100 and the maximum rate of cement substitution, A/(A+C) is 25:100. Based on Eqs. (1) and (2) and the recipes in Table 6, the Equivalent Binder proportion (Cement and GCC) is calculated for each W/C ratio and reported in Table 7.

Table 7. LG10© proportions with GCC.

W/C	60:10	65:100	70:100
Cement (g)	348	319	296
GCC (g)	116	106	99
Water (g)	225	225	225
Sand (g)	1328	1365	1397
Total mass (g)	2017	2017	2017
W/C	0.60	0.65	0.70

Table 7 shows that the total mass is kept constant at 2017 g. While water content is kept constant, the amount of sand is adjusted to account for the changing cement and GCC amounts as the W/(C+k*A) ratio ranges from 60:100 to 70:100.

3.3.2 Density, Flow and Strength

The results shown in Table 8 confirm that the GCC hypothesis of k-value (25:100) and A/(A+C) (25:100) are relevant. Compressive strength, flow and density of the Equivalent Binder formulations (cement + GCC) are equivalent or better than the ones for of the mixtures containing cement only without GCC.

Table 8. Results LG10© with GCC

Specimen W/C	60:10	65:100	70:100
Strength (MPa)	42.5	33.3	24.1
Density (g/l)	2.29	2.29	2.28
Flow (mm)	210	203	190
GCC W/C+k.A	60:10	65:100	70:100
Strength (MPa)	42.7	37.9	23.5
Density (g/l)	2.29	2.29	2.28
Flow (mm)	215	220	210

4 Summary and Conclusion

The novel methods LGsystem© and LG10© developed by Omya can be used to formulate and evaluate concrete and mortar mixtures using local ingredients (i.e. sand, cement, admixture) and specialty GCC materials (Betocarb® HP) as functional minerals and evaluate the right combination with other mineral additions. The methods have been applied successfully for the optimization of innovative underlayment, SCC and UHPC formulations with selected fine GCC materials being identified and used as mineral plasticizer. The methods allow the engineer to achieve typically desired properties such as flowability, viscosity, stability, early age strength at improved formulation cost due to a more effective use of SCMs.

Because digital fabrication typically uses mixtures containing smaller aggregates, paste volume must be increased and proper grading of the remaining components must be optimized. Rheological behavior of such mixtures is of importance and we believe that the methods presented in this article can support the efficient and successful development of formulations using selected GCC materials (such as Betocarb® HP or Betoflow® D) for digital fabrication applications.

References

1. Juhart J, David GA, Nickel C, Fischer G, Mittermayr F, Maydl P: Durable eco-concrete in Austria: Materials and mix design methods. Institute of Technology and Testing of Building Materials, Graz University of Technology, Austria
2. High or Ultra-High-performance concrete, United States, Patent Application Publication, Pub. No.: US 2012/0037045 A1
3. Huang W, Kazemi-Kamyab H, Sun W, Scrivener K: Effect of cement substitution by limestone on the hydration and microstructural development of ultra-high-performance concrete (UHPC). Cement and Concrete Composites
4. Vance K, Aguayo M, Oey T, Sant G, Neithalath N: Hydration and strength development in ternary portland cement blends containing limestone and fly ash or metakaolin. Cement & Concrete Composites
5. Bentz DP, Stutzman PE, Zunino F: Low-Temperature Curing Strength Enhancement in Cement-Based Materials Containing Limestone Powder. Materials and Structures
6. Arora A, Sant G, Neithalath N: Ternary blends containing slag and interground/blended limestone: Hydration, strength, and pore structure. Cement & Concrete Composites
7. Méthode LG7 – Limestone addition for concrete, NF P 18-508:2012
8. Schwartzentruber C (2000) Method of the concrete equivalent mortar
9. Erdem TK, Khayat KH, Yahia A (2009) Correling rheology of self-consolidating concrete to corresponding concrete-equivalent mortar
10. Hajiesmaeili A, Denarié E (2018) Next generation UHPFRC for sustainable structural applications. In: EPFL, DSCS 2018: 2nd international workshop on durability and sustainability of concrete structures, Russian Academy of Sciences, 6–7 June 2018
11. Fennis S, Walraven J, Den Uijl J (2013) Defined-performance design of ecological concrete. Mater Struct 46:639–650
12. Chen JJ, Kwan AKH, Ng PL, Li LG (2016) Packing density improvement through addition of limestone fines, superfine cement and condensed silica fume. J Mater Sci Chem Eng 4:29–36
13. Cement. Composition, specifications and conformity criteria for common cements

Use of Surfactant to Improve Properties of Crumb Rubbers in Concrete Products

Marupatch Jamnongwong[1(✉)] and Piti Sukontasukkul[2]

[1] Department of Civil Engineering, King Mongkut's University of Technology North Bangkok, Bangkok, Thailand
marupatch.j@eng.kmutnb.ac.th
[2] Construction and Building Materials Research Center, Department of Civil Engineering, King Mongkut's University of Technology North Bangkok, Bangkok, Thailand

Abstract. Use of crumb rubbers from waste tires in concrete applications can help reduce environmental impacts from the massive waste tires. However, several studies show that incorporating crumb rubbers into concrete can decrease the mechanical properties due to their low strength and stiffness, and poor interfacial bond with cement paste. Since crumb rubbers are considered a hydrophobic material, they tend to repel water and segregate from fresh cement paste. This causes poor bond strength between cement paste and crumb rubbers and provides negative effects on concrete strength. This study aims to improve the performance of concrete mixed with crumb rubber or rubberized concrete by increasing the crumb rubber surface wettability (i.e., reduce its water repellant ability). A surfactant (Tergitol NP-10) is applied to the crumb rubbers in order to reduce solid/liquid interfacial tension between the crumb rubber and water. This modification should allow better attachment and bond between crumb rubbers and cement paste and hence, improve the concrete mechanical properties. The specimens are prepared using non-modified and modified crumb rubbers at the rate of 3% to 10% by volume. Three experiments are a carried out: adhesive bond, compressive and flexural strength. Results show that the rubberized concrete mixed with modified crumb rubbers exhibit better bond and higher compressive and flexural strengths than those mixed with conventional crumb rubber.

Keywords: Concrete · Crumb rubber · Waste tires · Surfactant · Adhesive strength

1 Introduction

All over the world, over 1,000 million waste tires are generated every year from automobile industry [1–3]. The disposal of the massive waste tires creates major environmental problems because it needs enormous landfill spaces and may result in accidental fires with pollution emissions. Waste tires are also not biodegradable material, so the need of new space/landfill is increased by accumulated large number of waste tires every year.

Recycling the waste tires into crumb rubber for civil engineering applications can provide solutions to environmental as it reduces the amount of waste tires entering

V. Mechtcherine et al. (Eds.): RheoCon 2019/SCC 2019, RILEM Bookseries 23, pp. 27–35, 2020.
https://doi.org/10.1007/978-3-030-22566-7_4

landfills and reduces natural resource demand for concrete production by replacing mineral aggregates such as sand with crumb rubbers. Researchers have investigated the use of crumb rubber as a partial replacement of its mineral aggregates to produce concrete a so-called rubberized concrete or crumb rubber concrete (CRC).

The addition of crumb rubber from waste tires or proportional subtraction of mineral aggregates from concrete mix can improve energy absorption capacity [4–7], resistance to abrasion [8], resistance to freeze-thaw condition [8, 9] and performance under fire [8, 10] when compared against those of ordinary concrete. However, there are some drawbacks such as the reduction in compressive strength [11–17], tensile strength [14, 17, 18] and elastic modulus [4, 8, 10, 15, 19–22].

These inferior mechanical properties are partly due to the interface incompatibility between crumb rubber and inorganic materials like cement paste. Cement paste is a hydrophilic material, while the surface of crumb rubber is hydrophobic. The combination of both creates poor adhesion between crumb rubber and cement paste which impairing the mechanical properties of rubberized concrete and limiting its development and related application [23].

In recent years, a lot of research has been done to enhance the performance of rubber-modified concrete through surface treatment of crumb rubber. Mohammadi et al. treated the rubber surface with sodium hydroxide (NaOH) before mixing in concrete and found that the improvement in both compressive strength and flexural strength of the modified rubberized concrete [24]. Segre et al. indicated that the main role of NaOH is to clean rubber surface and soaking in NaOH solution for 24 h did not change the hydrophobic nature of rubber [25]. Zhang et al. treated the rubber surface with acrylic acid (ACA) and polyethylene glycol (PEG) in order to grafting hydrophilic groups on the surface and found that the slump, air-entrainment, compressive strength, flexural strength, and impact performance of modified rubberized concrete were obviously improved [26]. Ossolo and Wojcik treated the rubber surface with ultraviolet radiation and found that the flexural strength of rubberized concrete was improved [27].

Surfactant reduces the surface tension of liquids or the interfacial tension of two-phase systems due to adsorption at the surface or interface. A common structure of most surfactants is the presence of hydrophobic (non-polar) part on one side and hydrophilic (polar) part on the other side. As the concentration of a surfactant increases, adsorption takes place at the surface until it is fully overlaid, which corresponds to the minimum value of the surface tension. Micelles form in the volume phase above the transition concentration described as the critical micelle concentration (CMC). After this, micelles form in the volume phase. The groups of micelles with less affinity to the volume phase (usually the hydrophobic groups) are oriented inwards [28].

The present study aims to investigate the properties of concrete mixed with crumb rubbers which are treated to improve surface wettability (i.e., reduce its water repellant ability). A surfactant is applied to the crumb rubbers in order to reduce solid/liquid interfacial tension between the crumb rubber and water. This modification should allow better attachment and bond between crumb rubbers and cement paste and hence, improve the concrete mechanical properties.

2 Experimental Procedure

2.1 Materials

The cement used was ordinary Portland cement (type I). Natural river sand (medium sand) and crushed stone (size 3/8″) were used as fine and coarse aggregates, respectively. The water was tap water in the laboratory. Crumbed tire rubber (passing sieve #7) was selected as a replacement material for fine aggregates. Its characterization including average bulk specific gravity (dry), average bulk specific gravity (SSD), average apparent specific gravity and average absorption are 0.96, 0.97, 0.97 and 0.92% respectively. Rubber sheets with dimension of 20 mm × 60 mm × 5 mm. were used in the contact angle and adhesive bond strength with cement tests. Modifier for the pretreatment of rubber was 5% NaOH solution. And, in order to not only avoid the ionic interference to hydration reaction which is one of the major factors of strength in concrete matrix but also less toxic to human health and the environment, the nonionic surfactant (Tergitol NP-10) was selected as a modifier for rubber surface modification.

2.2 Rubber Modification

First, the crumb rubbers were cleaned with tap water and dried in 110 °C oven for 20 min. Secondly, they were soaked in 5% NaOH solution for 24 h, rinsed in water and dried in 110 °C oven for 20 min. After finishing the pretreatment process, the rubber surfaces were modified by soaking in surfactant solution (10, 100 and 1,000 CMC) for 2 h and then dried in 110 °C oven for 20 min to complete the process.

2.2.1 Hydrophobic Test Using Contact Angle Investigation

The change of the hydrophobic property at the rubber surface after the modification was measured by mean of the change in contact angle between water droplet and the surface of rubber using an image processing software (ImageJ).

2.2.2 Adhesive Bond Strength Test

The adhesive bond strength between rubber and cement is directly related to their interaction at the interfaces. In order to evaluate the effectiveness of surface modification of rubber, the adhesive bond test was setup as shown in Fig. 1a–b. In Fig. 1a, a rubber plate was embedded into a cement paste cube (50 mm × 50 mm × 50 mm.) by about 20 mm. during casting. The specimens were then cured in the standard curing conditions for 7 days. Figure 1b shows a testing device for measurement the adhesive bond strength between the rubbers and cement paste. On the upper side, the rubber plate was fixed on a stiff steel beam. At the bottom side, the cement specimen was tied on a wire which was connected with a bucket. Weight were slowly added to the bucket until the rubber plate began to pull out of the specimen. The weight that caused the rubber plate to pull out was considered a pull out force. The surface treatment method that provide the highest bond strength will be selected as a surface treatment for crumb rubber particle and used in the casting of rubberized concrete specimens.

Fig. 1. (a) Rubber plate was embedded in a cement paste and (b) A self-made test device for measurement the adhesive strength.

2.3 Specimen Preparation and Testing

For the control mix, the mix proportion was set at 1:2.45:1.81 (cement: coarse aggregate: fine aggregate) with water-cement ratio fixed at 0.51. For rubberized concrete, the fine aggregates were partially replaced with crumb rubber at the rate of 0%, 3%, 5%, 10% by volume fractions. The crumb rubbers were treated using the selected method as described in Sect. 2.2.

In mixing process, all ingredients were mixing in dry condition first for about 5 min and after the water was added, the mixing process continue for another 5 min. The fresh concrete was placed in a mold in three layers and each layer was compacted using a steel rod and vibrating table. After 24 h, the specimens were demolded and cured in a standard curing condition for 28 days before testing. Two test were carried out: the compressive strength (ASTM C39/C39M-09a) and flexural strength (ASTM C293-02).

3 Results and Discussion

3.1 Effect of Surfactant on the Hydrophobicity of Rubber Surface

The purpose of the surfactant is to reduce the hydrophobicity of the rubber which can be investigated by measuring the change of the contact angle between the rubber surface and the water droplet. Figure 2 presents the visual image of the contact angle testing before and after the rubber modification. It is clear that the contact angle is greatly reduced after modification. The rubber surface property changes from full hydrophobic to hydrophilic.

Figure 3 shows the change of the contact angle of rubber with different types of treatment. With pretreatment NaOH, the angle change slightly from 83.4° to 73.3°. After the modification using surfactant, significant decrease in angle was observed from

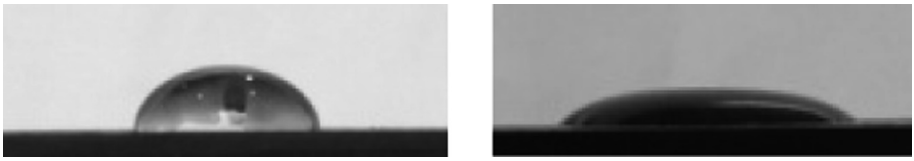

Fig. 2. Contact angle testing (a) before and (b) after the surface modification using NaOH and surfactant 1,000 CMC.

71.5° to 33.2° with the increase of the surfactant concentration from 10 to 1,000 CMC. This indicates that the surfactant particles can cover more thoroughly on rubber surface when surfactant concentration are higher.

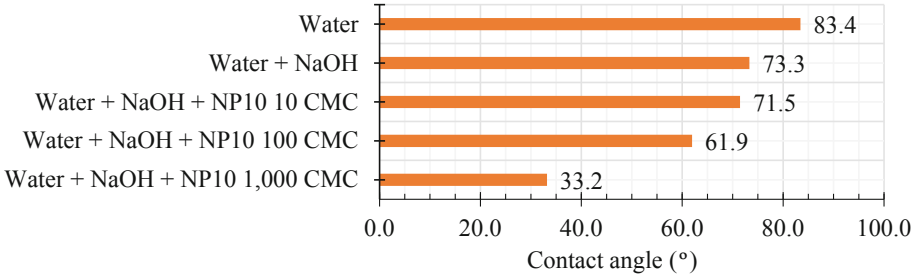

Fig. 3. Effect of surfactant on the contact angle of rubber surface with water.

Since surfactants are made from long molecules that contain a head (hydrophilic) and tail (hydrophobic). When the surfactant molecules meet crumb rubber, the tails are attached to the rubber surface as they are the same hydrophobic material. While the heads of the molecule are oriented outward to the surface rubber. Then modified crumb rubber presented hydrophilic property.

3.2 Effect of Surface Modification on Adhesive Bond Strength

The adhesive bond strengths between non modified and modified rubber sheets and cement paste are shown in Fig. 4. The adhesive bond strength between rubber and cement paste was found to be unchanged with the pretreatment with NaOH alone.

Significant improvement was observed with the modification by NaOH+NP10 as the bond strength increased from 0.053 MPa to 0.072 MPa (at NP10 concentration of 100 CMC). This proves that the surfactant can improve the interfacial bonding property between rubber and cement paste. However, when surfactant concentration reaches 1,000 CMC, the adhesive strength decreased slightly. The reduction is partly due to the thickening of surfactant at high concentration which cover the rubber surface and inhibit the bond between rubber and cement paste.

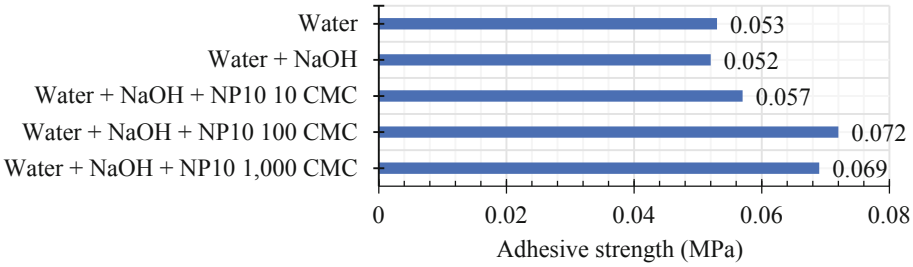

Fig. 4. Adhesive bond strength between rubber plate and cement paste.

In this case, the modification that provides the best result on adhesive bond strength is the surface treatment using NaOH+NP10 100 CMC and it was selected to produce the modified rubberized concrete for investigation on compressive and flexural strengths.

3.3 Effect of Surface Modification on Compressive Strength of CRC

Several studies show that incorporating crumb rubbers into concrete can reduce the mechanical properties due to their low strength and stiffness. In order to provide a sufficient compressive strength of the concrete, only small quantities of crumb rubber can be utilized. In our study, the replacement ratio is set at below 10% by volume of fine aggregate.

Figure 5 shows the compressive strength comparison between CRC with different rubber content with/without surface treatment modification. Comparing between groups of CRC without surface treatment, the compressive strength was found to decline rapidly with the increasing crumb rubber content (from 26.4 MPa to 18.1 MPa with the replacement ratio of 0% to 10%).

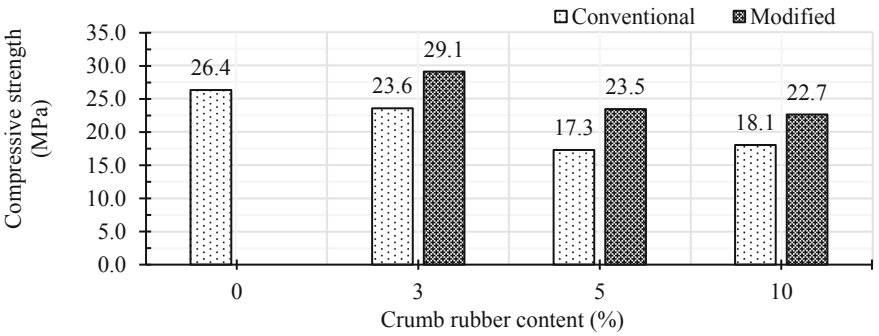

Fig. 5. The compressive strength of the CRC comparing to the rubber content.

On the other hand, with the modified crumb rubber, the compressive strength was found to increase by about 10.5% in the CRC with 3% replacement. However, the compressive strength then gradually decreased when the crumb rubber replacement rate was higher than 3%. Although the reduction in compressive strength of modified CRC was observed at higher crumb rubber content, they were still higher than those with non-modified CRC.

This proves that the surface modification of crumb rubber can reduce the adverse effect of crumb rubber on the compressive strength of concrete. Not only that, it also shows that with the right amount of the modified crumb rubber, the improvement in the compressive strength can also be observed.

3.4 Effect of Surface Modification on Flexural Strength of CRC

Figure 6 presents the comparison on the flexural strength of CRC with different crumb rubber content with/without surface modification. Similar to the compressive strength, the flexural strength of non-modified CRC was found to decrease gradually from 6.5 to 5.2 MPa. For the modified CRC, the flexural strength increased at the replacement rate of 3% then decrease gradually with higher crumb rubber content. The optimum crumb rubber replacement rate was found at 3% by volume of fine aggregate.

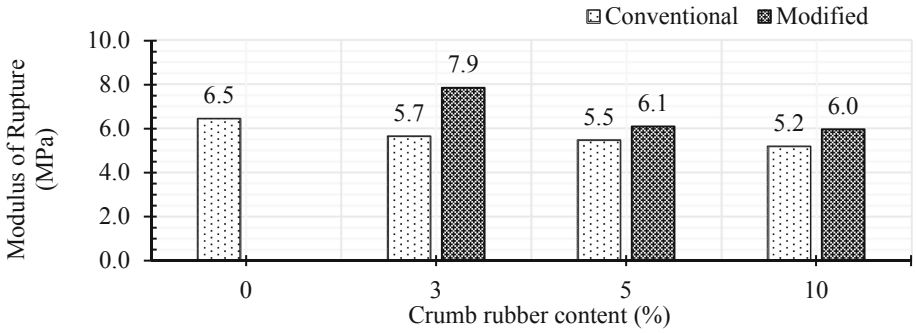

Fig. 6. The flexural strength of the CRC comparing to the rubber content.

4 Conclusion

Based on the obtained results, the following conclusions can be drawn:

(1) The surface modification of crumb rubber by nonionic surfactant turns the surface of the rubber to be more hydrophilic as seen by the reduction of the contact angle between the rubber surface and water droplet after the surface modification was applied.
(2) The rubber surface modification also enhances the adhesive bond strength. However, higher concentration of surfactant can reduce the efficiency of the surface modification.

(3) The mechanical properties of CRC with modified crumb rubber is found to be better than those of CRC with non-modified crumb rubber in every crumb rubber content. Higher compressive and flexural strengths are observed in the modified CRC group comparing with non-modified CRC group. The CRC with 3% of modified crumb rubber exhibits higher compressive and flexural strengths of CRC than the concrete without crumb rubber.

Acknowledgments. This research was supported by King Mongkut's University of Technology North Bangkok, Contact no. KMUTNB-62-NEW-03.

References

1. Onenç S, Brebu M, Vasile C, Yanik J (2012) Copyrolysis of scrap tires with oily wastes. J Anal Appl Pyrolysis 94:184–189
2. Arabiourrutia M, Lopez G, Elordi G, Olazar M, Aguado R, Bilbao J (2007) Product distribution obtained in the pyrolysis of tyres in a conical spouted bed reactor. Chem Eng Sci 62:5271–5275
3. Thomas BS, Gupta RC, Kalla P, Cseteneyi L (2014) Strength, abrasion and permeation characteristics of cement concrete containing discarded rubber fine aggregates. Constr Build Mater 59:204–212
4. Al-Tayeb MM, Bakar BHA, Ismail H, Akil HM (2012) Impact resistance of concrete with partial replacements of sand and cement by waste rubber. Polym Plast Technol Eng 51 (12):1230–1236
5. Cheng Z, Shi Z (2014) Vibration attenuation properties of periodic rubber concrete panels. Constr Build Mater 50:257–265
6. Grinys A, Sivilevičius H, Pupeikis D, Ivanauskas E (2013) Fracture of concrete containing crumb rubber. J Civ Eng Manag 19(3):447–455
7. Liu F, Chen G, Li L, Guo Y (2012) Study of impact performance of rubber reinforced concrete. Constr Build Mater 36:604–616
8. Bravo M, de Brito J (2012) Concrete made with used tyre aggregate: durability related performance. J Clean Prod 25:42–50
9. Richardson AE, Coventry KA, Ward G (2012) Freeze/thaw protection of concrete with optimum rubber crumb content. J Clean Prod 23(1):96–103
10. Pacheco-Torgal F, Ding Y, Jalali S (2012) Properties and durability of concrete containing polymeric wastes (tyre rubber and polyethylene terephthalate bottles): an overview. Constr Build Mater 30:714–724
11. Aiello MA, Leuzzi F (2010) Waste tyre rubberized concrete: properties at fresh and hardened state. Waste Manag 30(8–9):1696–1704
12. Al-Tayeb MM, Abu Bakar BH, Akil HM, Ismail H (2013) Experimental and numerical investigations of the influence of reducing cement by adding waste powder rubber on the impact behaviour of concrete. Comput Concr 11(1):11
13. Boudaoud Z (2012) Effects of recycled tires rubber aggregates on the characteristics of cement concrete. Open J Civ Eng 02(04):193–197
14. Ganjian E, Khorami M, Maghsoudi AA (2009) Scrap-tyre-rubber replacement for aggregate and filler in concrete. Constr Build Mater 23(5):1828–1836
15. Ghaly AM, Cahill JD IV (2005) Correlation of strength, rubber content, and water to cement ratio in rubberized concrete. Can J Civ Eng 32(6):1075–1081

16. Issa CA, Salem G (2013) Utilization of recycled crumb rubber as fine aggregates in concrete mix design. Constr Build Mater 42:48–52
17. Mohammed BS (2010) Structural behavior and m–k value of composite slab utilizing concrete containing crumb rubber. Constr Build Mater 24(7):1214–1221
18. Eldin NN, Senouci AB (1993) Rubber tyre particles as concrete aggregates. J Mater Civ Eng 5:478–497
19. Holmes N, Dunne K, O'Donnell J (2014) Longitudinal shear resistance of composite slabs containing crumb rubber in concrete toppings. Constr Build Mater 55:365–378
20. Onuaguluchi O, Panesar DK (2014) Hardened properties of concrete mixtures containing pre-coated crumb rubber and silica fume. J Clean Prod 82:125–131
21. Shu X, Huang B (2013) Recycling of waste tyre rubber in asphalt and Portland cement concrete: an overview. Constr Build Mater 67:217–224
22. Sukontasukkul P, Tiamlom K (2012) Expansion under water and drying shrinkage of rubberized concrete mixed with crumb rubber with different size. Constr Build Mater 29:520–526
23. He L, Ma Y, Liu Q, Mu Y (2016) Surface modification of crumb rubber and its influence on the mechanical properties of rubber-cement concrete. Constr Build Mater 120:403–407
24. Mohammadi I, Khabbaz H, Vessalas K (2016) Enhancing mechanical performance of rubberised concrete pavements with sodium hydroxide treatment. Mater Struct 49(3):813–827
25. Segre N, Monteiro PJM, Sposito G (2002) Surface characterization of recycled tire rubber to be used in cement paste matrix. J Colloid Interf Sci 248(2):521–523
26. Zhang H, Gou M, Liu X et al (2014) Effect of rubber particle modification on properties of rubberized concrete. J Wuhan Univ Technol Mater 29(4):763–768
27. Ossola G, Wojcik A (2014) UV modification of tire rubber for use in cementitious composites. Cem Concr Comp 52:34–41
28. Rosen MJ, Kunjappu JT (2012) Surfactants and interfacial phenomena, 4th edn. Wiley, New York

Structural Build-Up of Cementitious Paste Under External Magnetic Fields

Dengwu Jiao[1,2(✉)], Khadija El Cheikh[1], Karel Lesage[1], Caijun Shi[2], and Geert De Schutter[1]

[1] Magnel Laboratory for Concrete Research, Department of Structural Engineering, Ghent University, Ghent, Belgium
dengwu.jiao@ugent.be
[2] Key Laboratory for Green and Advanced Civil Engineering Materials and Application Technology of Hunan Province, College of Civil Engineering, Hunan University, Changsha, China

Abstract. Engineering application processes of fresh concrete include transporting, pumping, formwork casting, etc. Each process is a significant factor influencing properties of fresh and hardened concrete. However, many contradicting requirements of fresh concrete performances (such as structuration rate) exist in these operation processes. Therefore, advanced techniques need to be proposed to satisfy future challenges. Actively controlling the stiffness by applying external magnetic fields would be a potential solution for the contradicting requirements, and could make the pumping and casting processes smarter and more reliable. In the present paper, the effects of magnetic field strength and magnetizing time on structural build-up of cementitious paste are discussed. The results show that higher magnetic field strengths result in higher percolation time and lower phase angle at equilibrium state. However, the application of external magnetic fields with low flux density has little effects on the viscoelastic behaviour of cementitious paste. Under high magnetic field strengths, the viscous-liquid behaviour dominates the elastic-solid behaviour at early stage, while the solid-like behaviour becomes more dominant with magnetizing time.

Keywords: Cement paste · Structural build-up · Viscoelastic behavior · Magnetic fields

1 Introduction

The engineering application processes of concrete include transporting, pumping and formwork casting. Each process is a significant factor influencing the properties of fresh and hardened concrete. However, for the same concrete mixture proportion, once the concrete is prepared, its properties become uncontrollable to a certain extent. In this case, this concrete is transported and pumped according to its original properties, and the construction techniques will become the main barrier to improve the robustness of concrete. Thus, more attention should be paid to improvement of construction techniques. Indeed, many conflicts and contradictions in requirements of fresh concrete performances exist in different operation processes. For example, lower thixotropic

V. Mechtcherine et al. (Eds.): RheoCon 2019/SCC 2019, RILEM Bookseries 23, pp. 36–42, 2020.
https://doi.org/10.1007/978-3-030-22566-7_5

structural build-up is needed to overcome the major problem in resuming pumping operations if a short interruption is experienced (such as the delay of concrete truck) [1] and improve the interface properties during multi-casting process [2]. By contrast, higher structuration rate of fresh concrete is beneficial for reducing formwork pressure at the casting process [3, 4]. In this context, an innovative casting concept "SmartCast" has been proposed by De Schutter [5, 6] to overcome aforementioned problems. By actively controlling the rheology and stiffness, the structuration rate of fresh concrete could be adjusted artificially according to the requirements at different operation processes for the same concrete mixture, which could make the pumping and casting processes smarter and more reliable.

Applying an external magnetic field is a potential way to control the rheology of fresh concrete. However, cement pastes without magnetic additives have negligible response to magnetic field [7, 8]. In the present study, the structural build-up of cementitious paste containing nano-Fe_3O_4 was experimentally investigated under external magnetic fields. The time-sweep test with low shear strain within the linear viscoelastic region was conducted to characterize the structural build-up of cementitious paste. The current study provides a step forward in stiffness control of cement pastes. The results are some preliminary concepts that will contribute to actively controlling the rheology and stiffness of cementitious materials.

2 Experimental Program

2.1 Materials and Mix Proportions

CEM I 42.5 Portland cement (OPC) conforming to EN 196-1 [9] was used in this study. The chemical composition is shown in Table 1. Spherical iron oxide Fe_3O_4 nanoparticles with Fe_3O_4 purity higher than 98% were used. The average particle size and density of nano-Fe_3O_4 are 20 nm–30 nm and 4.95 g/cm^3, respectively. All samples were prepared using de-ionized water. The water-to-cement (w/c) mass ratio of cement paste medium was 0.4. The content of nano-Fe_3O_4 was fixed at 3% by the mass of cement paste.

Table 1. Chemical composition of Portland cement.

Components	% by mass
SiO_2	19.6
Al_2O_3	4.88
Fe_2O_3	3.14
CaO	63.2
MgO	1.8
SO_3	2.9

2.2 Testing Method

The structural evolution of cementitious paste was characterized by storage modulus and phase angle, obtained from small amplitude oscillatory shear (SAOS) test using a rotational parallel plate rheometer (MCR 102, Anton Paar, Austria). The disc diameter is 20 mm and the gap between the upper and lower plates is fixed at 1 mm. After the sample was prepared, it was poured on the lower plate. To obtain a repeatable initial state and eliminate possible influences during gap positioning, the sample was first pre-sheared at shear rate of 100 s^{-1} for 30 s and then rested for 10 s without external magnetic field. Afterwards, the oscillatory time-sweep test with constant frequency of 2 Hz and strain amplitude of 0.001% was immediately carried out for 180 s under given magnetic field. The magnetic flux densities were selected as 0 T, 0.08 T, 0.16 T, 0.24 T, 0.32 T, 0.5 T and 0.76 T. Each test was repeated for three times using fresh samples. During the rheological tests, the temperature was controlled at 20 °C ± 0.5 °C.

3 Results and Discussion

3.1 Storage Modulus

The evolution of storage modulus of cementitious pastes under various external magnetic fields are shown in Fig. 1. Without external magnetic fields, the storage modulus of cementitious paste gradually increased with resting time. The results are in agreement with those shown in [10–12]. Indeed, at rest, colloidal interactions due to van der Waals attractive forces lead to formation of flocculated structures. On the other side, C-S-H links and bridges between cement particles are enhanced with progress of cement hydration. Besides, the nano-Fe_3O_4 particles have a strong tendency to agglomerate due to their high magnetic properties [13–15]. As a result, the rigidity and stiffness of cementitious suspensions are increased, exhibiting a gradual increase in storage modulus. With the elapses of resting time, the storage modulus reached a steady increase, reflecting the transition from viscous behavior to elastic behavior.

It can be observed from Fig. 1 that the application of external magnetic field had a significant influence on the structural build-up of cementitious paste. After applying an external magnetic field, low storage modulus at early ages (45 s) and high storage modulus at longer magnetizing time were respectively observed. This indicates that applying the external magnetic field improved the liquid-like property and then the solid-like property was gradually enhanced with magnetizing time. The development of storage modulus was also dependent on the magnetic field strength. Indeed, low magnetic field such as 0.08 T and 0.16 T had little effects on the magnitude of storage modulus. After magnetizing for 180 s, the storage modulus increased by 1.4 and 2 times after applying magnetic field of 0.24 T and 0.5 T, respectively. In other words, the magnetorheological effect, describing the responsiveness of the suspension to external magnetic field, was only obvious at sufficiently high magnetic field strength. This is in agreement with the results obtained by Rankin et al. [16]. This behavior can be explained by the fact that the magnetic field-induced interparticle force is correlated to the particle distance. Indeed, the interparticle force induced by external magnetic field increases with decreasing distance between particles [17]. Under low magnetic

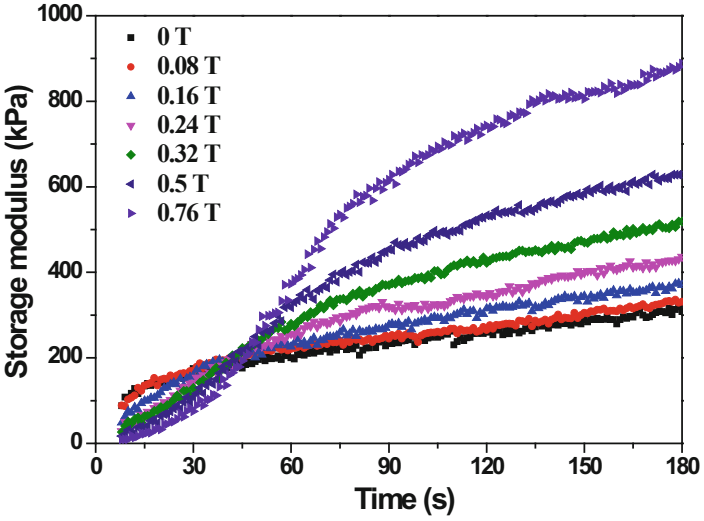

Fig. 1. Evolution of storage modulus of cementitious paste under various magnetic fields.

field, the nanoparticles aggregate into clusters. In this case, the mean distance between the clusters is large and the mean interparticle force is low, and the gap-spanning chains do not form [16]. With the magnetic field strength increases, the clusters grow and the gap is gradually narrowed. At sufficient large magnetic field, the gap-spanning clusters form. This is reflected by the large magnitude of storage modulus under external magnetic fields with high strength. In addition, the amount of nanoparticles contributed to clusters are increased with the increase of magnetic field strength. In a word, the increase of storage modulus is a result of enhancement in particle interactions due to more effective nanoparticles and higher magnetic forces. In the case of the improvement of liquid-like property at early ages, it will be discussed in the following part.

3.2 Phase Angle

The phase angle (δ) is used to describe the phase shift between the applied stress and resultant strain, which can be calculated by $\tan^{-1}$ (G″/G′). The viscous behavior dominates when $\delta > 45°$, and the elastic behavior dominates when $\delta < 45°$. The phase angle of cementitious paste as a function of time under various magnetic fields is shown in Fig. 2. As expected, the phase angle was significantly decreased and then stabilized, reflecting the transition from liquid behavior to elastic behavior. The time where the value of phase angle starts to stabilize can be defined as percolation time [18], which can be used to describe the time for colloidal particles to reach their equilibrium positions. It can be seen that the percolation time gradually increased with the increase of magnetic field strength. For example, the percolation time was about 20 s and 100 s under external magnetic field of 0 T and 0.5 T, respectively. In other words, it will need longer time for the magnetic nanoparticles to reach their stable

positions at higher magnetic fields. Besides, higher magnetic field strength resulted in lower phase angle at equilibrium state, indicating that higher structural strength was obtained at higher magnetic field.

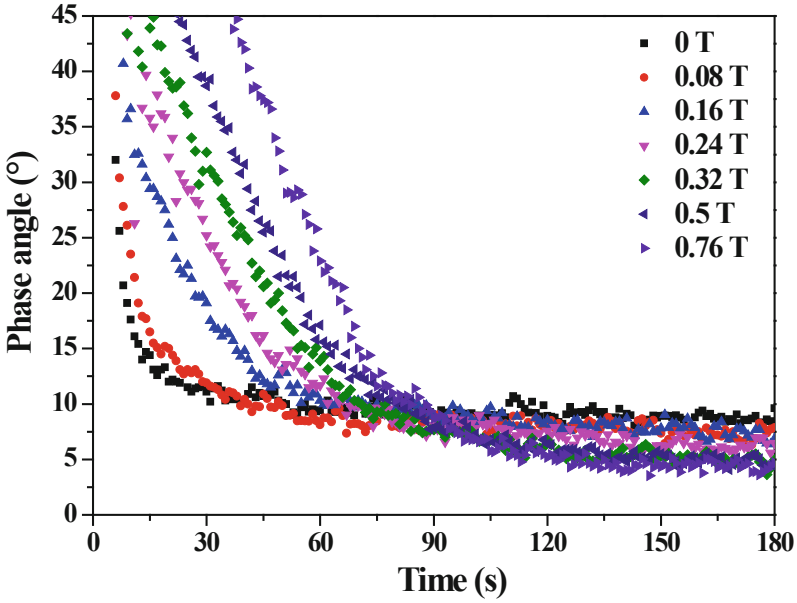

Fig. 2. Evolution of phase angle of cementitious paste under various magnetic fields.

From Fig. 2, it can be seen that the time when $G' = G''$ increased with increasing magnetic field strength. This means that the liquid-like behavior of cementitious paste was improved at the beginning after applying a high magnetic field. This can be explained by the nanoparticle movement under external magnetic field. In the absence of external magnetic fields, the nano-Fe_3O_4 particles were randomly distributed in the cement paste medium. After application of an external magnetic field, the magnetic dipoles in the nano-Fe_3O_4 will move to be aligned along the direction of magnetic field. During their displacements to form clusters, the nanoparticles create a sort of mechanical agitation, and then the C-S-H bridges and flocculated networks between cement particles are destroyed. Thus, the cement particles transform from flocculated state to dispersed state, and a more viscous behavior can be observed.

4 Conclusions

The effect of magnetic field strength on storage modulus and phase angle evolution of cement paste containing nano-Fe_3O_4 was studied. The results showed that:

(1) The application of external magnetic fields with low flux density had little effects on the structural build-up of cementitious paste.
(2) Higher magnetic field strengths resulted in higher storage modulus and percolation time, as well as lower phase angles at equilibrium state.
(3) The liquid-like property was improved at the beginning after applying magnetic field and the solid-like property became more dominant with magnetizing time.

Acknowledgement. The authors acknowledge the financial support given by the European Research Council (ERC) for the Advanced Grant Project 'SmartCast' (No. 693755) awarded to Prof. Geert De Schutter.

References

1. De Schutter G (2017) Thixotropic effects during large-scale concrete pump tests on site. In: 71st RILEM annual week & ICACMS 2017, Chennai, India
2. Roussel N, Cussigh F (2008) Distinct-layer casting of SCC: the mechanical consequences of thixotropy. Cem Concr Res 38:624–632
3. Ovarlez G, Roussel N (2006) A physical model for the prediction of lateral stress exerted by self-compacting concrete on formwork. Mater Struct 39:269–279
4. Roussel N (2006) A thixotropy model for fresh fluid concretes: theory, validation and applications. Cem Concr Res 36:1797–1806
5. De Schutter G, Lesage K (2018) Active control of properties of concrete: a (p)review. Mater Struct 51:123
6. De Schutter G, Lesage K, Mechtcherine V et al (2018) Vision of 3D printing with concrete - technical, economic and environmental potentials. Cem Concr Res 112:25–36
7. Nair SD, Ferron RD (2014) Set-on-demand concrete. Cem Concr Res 57:13–27
8. Jiao D, Shi C, Lesage K, et al (2018) Rheological behavior of cement paste under magnetic field. In: National civil engineering forum for graduate students (NCEF 2018)
9. EN TS 196-1 (2005) Methods of testing cement–Part 1: Determination of strength, European Committee for standardization, 26
10. Nachbaur L, Mutin J, Nonat A et al (2001) Dynamic mode rheology of cement and tricalcium silicate pastes from mixing to setting. Cem Concr Res 31:183–192
11. Roussel N, Ovarlez G, Garrault S et al (2012) The origins of thixotropy of fresh cement pastes. Cem Concr Res 42:148–157
12. Yuan Q, Zhou D, Khayat KH et al (2017) On the measurement of evolution of structural build-up of cement paste with time by static yield stress test vs. small amplitude oscillatory shear test. Cem Concr Res 99:183–189
13. Yazdi NA, Arefi MR, Mollaahmadi E et al (2011) To study the effect of adding Fe2O3 nanoparticles on the morphology properties and microstructure of cement mortar. Life Sci J 8:550–554
14. Sikora P, Horszczaruk E, Cendrowski K et al (2016) The influence of Nano-Fe_3O_4 on the microstructure and mechanical properties of cementitious composites. Nanoscale Res Lett 11:182
15. Jiao D, Shi C, Lesage K, et al (2018) Effects of external magnetic field on structural evolution of cement paste with nano-Fe_3O_4. In: 2nd international conference on UHPC materials and structures (UHPC 2018), Fuzhou, China, pp 344–348

16. Rankin PJ, Horvath AT, Klingenberg DJ (1999) Magnetorheology in viscoplastic media. Rheol Acta 38:471–477
17. Ginder JM (2003) Rheology controlled by magnetic fields, digital encyclopedia of applied physics
18. Mostafa AM, Yahia A (2016) New approach to assess build-up of cement-based suspensions. Cem Concr Res 85:174–182

Influence of Aggregate Particle Size Distribution on Mixing Behavior and Rheological Properties of Low-Binder Concrete

Markus Samuel Rebmann(✉) and Rafael Giuliano Pileggi

Department of Construction Engineering, Escola Politécnica, University of São Paulo, São Paulo, Brazil
markus.rebmann@lme.pcc.usp.br

Abstract. Particle Size Distribution (PSD) has impact on the workability of concretes because it affects the particle packing and particle mobility during flow. In continuous concrete production, keeping always the same PSD is not possible. So, it is important to understand how this variability affects concrete properties. The research described in this paper evaluated a more sustainable low-binder concrete, with focus on particle size variability of the aggregates. Applying particle packing and dispersion concepts, rheological control, use of limestone fillers and appropriate choice of material, a reference concrete with low binder consumption (3.7 kg/m^3/MPa) was developed. On this reference concrete, PSD variations were applied: a coarser and a finer version for each aggregate was tested and two levels of fines content were also evaluated. Mixing behavior and rheological properties were determined by a concrete mixing rheometer (Pheso Poli-USP) with planetary configuration. An acceptance criterion was established based on mixing torque and all concrete outside the limits had their water content adjusted until they met the specifications. After that, mechanical strength was evaluated at 28 days of age. The obtained results indicate that PSD variations affected both the mixing and flow of concrete. Especially higher fines content and presence of a finer natural sand increased the torque levels during the mixing process and shear cycles and lead to higher mixing power demand. The water correction, adopted to overcome the rheological changes, affected hardened state properties (up to 10% on compressive strength). As these findings are specific to the analyzed concrete and considered PSD variations, this research aimed to explain more generally the influence of the several variables. The surface area of the granular material, solids concentrations and mean distance between the fine and coarse particles are some quantitative parameters useful for predicting rheological aspects of concrete compositions.

Keywords: Low-binder concrete · Particle Size Distribution · Rheology · Mixing rheometer

V. Mechtcherine et al. (Eds.): RheoCon 2019/SCC 2019, RILEM Bookseries 23, pp. 43–51, 2020.
https://doi.org/10.1007/978-3-030-22566-7_6

1 Introduction

Particle Size Distribution (PSD) has impact on the workability of concretes because it affects the particle packing and particle mobility during flow [1, 2]. Variable fraction of crushed fines is another common source of aggregate PSD variation. Resulting surface area and PSD changes affect the rheological properties of the cementitious paste [3].

In continuous concrete production, keep always the same PSD is not possible. The concrete formulation needs to be robust enough to withstand PSD variations. Robustness studies are common in the self-compacting concretes (SCC) and, among other parameters, the PSD of aggregates and component quantity variations affect the rheological properties and robustness of SCC [4, 5].

The aim of this study was to evaluate the effect of ordinary granulometric changes of the aggregates on rheological properties of a concrete with low cement consumption, and the consequence on the compressive strength, if water adjustment is used to overcome rheological changes.

2 Experimental

2.1 Materials and Concrete Compositions

The work started with a previously adjusted reference concrete [6], with low cement content (200 kg/m^3), slump-flow of 680 mm, t_{50} = 4 s and 28 day cylindrical compressive strength of 52 MPa, resulting in low binder intensity (3.7 kg/m^3/MPa). Coarse crushed granite aggregates (C), crushed granite sand (CS) and fine natural quartz sand (NS) were used as aggregates. A high early strength Brazilian Portland cement (CPV-ARI) and two calcium carbonate fillers, well dispersed by a polycarboxylate superplasticizer (SP), formed the cement paste. The choice of this variety of materials sought to obtain a highly packed and dispersed concrete with low cement content.

On this reference concrete, a two-level fractional factorial design was applied to evaluate the influence of the Particle Size Distribution (PSD) of the three aggregates. For each aggregate, a coarser (labeled "+") and a finer (labeled "−") version was used. As the crushed aggregates are usually accompanied by a fraction of fine powder (<150 μm), this fraction was separated from all crushed aggregates by sieving. The so collected fine Granite Powders (GP) were mixed and then added to the concretes in two different amounts (high = "+"; low = "−"), constituting the fourth evaluated factor. The factor levels were established based on a data survey carried out on a large infrastructure project in Brazil [6]. The eight resulting concretes are described according to the evaluated factors in Table 1. The material consumption differentiates the eight concretes into two groups according to the volume of GP (Table 2).

PSD (Fig. 1) for aggregates, was obtained by Dynamic Image Analysis (Qicpic/Sympatec, dry free-fall dispersion) and for fines, Laser Diffraction was used (Helos/Sympatec, wet dispersion). Density and surface area are presented in Table 3.

Table 1. Factor levels of the tested concretes.

Concrete ID	Fineness modulus of aggregates			GP content (%w solids)
	Coarse (C)	Crushed sand (CS)	Natural sand (NS)	
Reference	7.16	3.77	1.31	3.85%
1	7.30	4.01	1.47	5.35%
2	7.30	4.01	1.16	2.35%
3	7.30	3.51	1.47	2.35%
4	7.30	3.51	1.16	5.35%
5	7.03	4.01	1.47	2.35%
6	7.03	4.01	1.16	5.35%
7	7.03	3.51	1.47	5.35%
8	7.03	3.51	1.16	2.35%

Table 2. Concrete compositions [kg/m^3].

Concrete ID	C	CS	NS	GP	Filler	Microfiller	Cement	Water	SP
Reference	1027	427	265	89	105	191	200	145	4,0
1, 4, 6, 7	1023	396	265	123	105	191	200	145	4,0
2, 3, 5, 8	1031	458	265	54	105	191	200	145	4,0

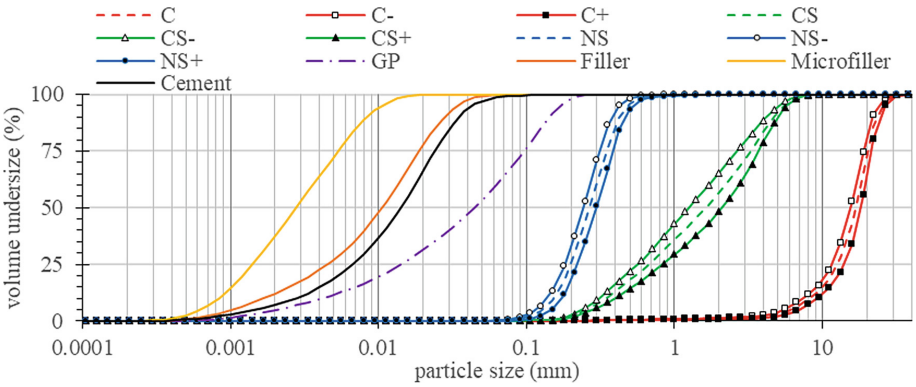

Fig. 1. Particle size distribution of the granular materials.

2.2 Mixing and Rheometry

For rheological measurements, a mortar/concrete rheometer (Pheso Poli-USP, Fig. 2) was used. This rheometer allows the direct measure of torque, up to 160 N.m with high accuracy (±0.1 N.m). A dedicated computer software controls the rotation speed and acquires the corresponding torques.

Batches of 17 L of concrete were mixed with the rheometer. The mixing behavior of the concretes was assessed by measuring the effort (torque) to maintain the rotation

Table 3. Physical characteristics of the granular materials.

Parameter		C	CS	NS	GP	Filler	Microfiller	Cement
Real Density (g/cm^3)[a]		2.70	2.70	2.65	2.70	2.79	2.80	3.09
SSA (m^2/g)[b]					1.34	1.16	3.73	1.54
VSA (m^2/cm^3)[c]	Ref	0.00058	0.0070	0.0252	3.63	3.24	10.4	4.76
	–	0.00064	0.0081	0.0279				
	+	0.00052	0.0060	0.0225				

[a]By helium gas pycnometry (Multipycnometer/Quantachrome);
[b]Specific Surface Area: by N_2 adsorption and BET-model (Belsorp max/Bel Japan);
[c]Volumetric Surface Area (VSA): for aggregates calculated from the PSD assuming a spherical particle model; for fines: calculated as SSA BET N_2/real density.

of the impeller constant (126 rpm) throughout the mixing procedure. The mixture followed the sequence (see top of Fig. 3): (1) positioning of impeller 1 mm from the bottom of the bowl; (2) introduction of dry mortar (fines and sands) into the bowl; (3) dry mortar homogenization; (4) addition of water with diluted superplasticizer; (5) initial wet mortar homogenization; (6) stop to scrape container walls; (7) final wet mortar homogenization; (8) mortar shear cycle; (9) positioning of impeller 30 mm from bottom of the bowl; (10) coarse aggregate addition; (11) concrete final homogenization; (12) concrete shear cycle.

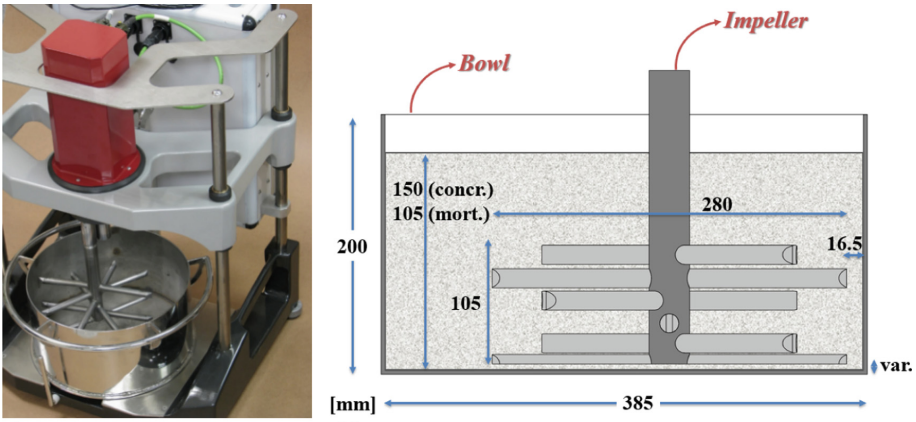

Fig. 2. (a) Rotational Rheometer Pheso Poli-USP for mortars and concretes, with bowl and impeller; (b) illustration showing the concrete container and the impeller with six double blades in helical configuration used in planetary setup for mixing and rheological tests. The distance from the bottom was 1 mm at mortar mixture and 30 mm at concrete mixture.

Immediately after mortar and concrete mixing, shear cycles were performed to evaluate the rheological behavior (with the same setup shown in Fig. 2). The shear cycle consists of increasing the speed of the impeller (from 6 rpm to 253 rpm) in 8 steps of 8 s each, and then slowing it down following the same steps. In each step, torques are measured 10 t/s. The first and last 10 data points are discarded, and a mean value of torque and rotational speed was calculated with the remaining points.

3 Results and Discussion

3.1 Effect of Granulometric Variations on Rheological Parameters

Figure 3 shows the torques during the mixing process. For reasons of graphic clarity only the reference and the most extreme cases are displayed. The results show that the mixing kinetics are similar but there are changes in torque levels. For instance, the torque at the end of concrete mixing (step 11) is almost 60% higher in concrete 4 than in concrete 5.

Several rheological parameters can be extracted from de mixing data and the shear cycles. Due to the limited space available in this paper, only four parameters will be considered: final torque and mixing energy from the mixing data; and viscosity and yield torque parameters from the concrete shear cycle (Table 4).

The yield torques presented low values, reflecting a well-dispersed paste present in adequate volume proportion. No significant relation to the studied parameters could be observed.

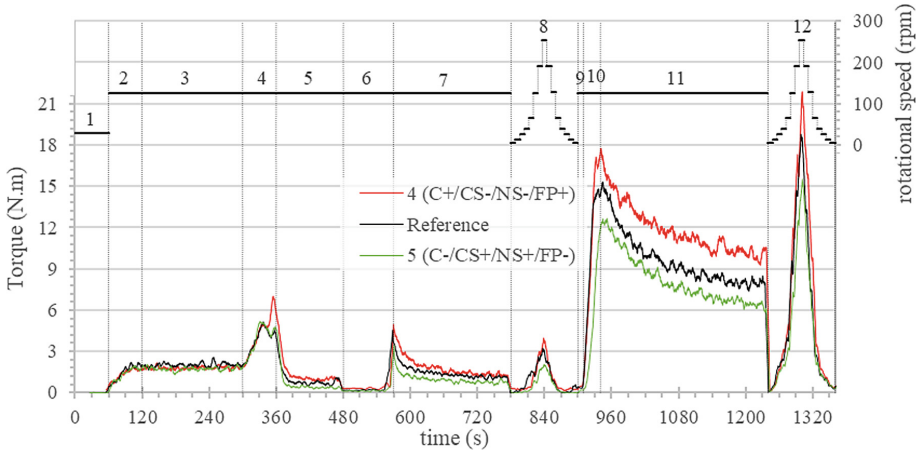

Fig. 3. Mixing rheometry: mixing steps and rotational speed showed at the top and torque of some selected concretes at the bottom.

Table 4. Rheological parameters.

Parameter	Concrete ID								
	Ref	1	2	3	4	5	6	7	8
T_{mix} (N.m)[a]	7.96	8.56	6.32	6.38	10.05	6.32	9.56	9.06	6.76
E_{mix} (N.m.s)[b]	3163	3385	2561	2514	3871	2591	3877	3590	2667
V_{ap} (N.m.s)[c]	4.38	4.52	3.77	3.15	4.99	3.59	5.02	4.62	3.73
T_0 (N.m)[d]	0.31	0.35	0.75	0.53	0.42	0.34	0.34	0.29	0.35

[a]Final concrete mixing torque (end of step 11);
[b]The energy of concrete mixing (area under the curve "toque *versus* time" for steps 10+11);
[c]Apparent viscosity parameter at the highest shear rate for concrete shear cycle (center of step 12);
[d]Concrete yield torque (torque at the lowest speed in the deceleration ramp of the concrete shear cycle (end of step 12).

For the other rheological parameters, variations of more than 20% were observed in some cases. ANOVA applied to the factorial design indicated that only the Granite Powder (GP) content and PSD of the Natural Sand (NS) significantly affected the rheological parameters, at 90% confidence level. Finer natural sand and higher granite powder content lead to an increase of torque levels. Of these two, the predominant factor is the powder content. For the adopted factor level variations, the powder content change led to rheological modifications about 3 to 5 more intense than the change in PSD of NS.

Linear regressions, adjusted to express the rheological parameters in terms of the fineness modulus of the natural sand and the volume of Granite Powder (expressed as a fraction of the total volume of dry materials), give R^2-values between 0.96–0.97. Both finer sand and higher fine powder volume increase the surface area of the particles in the system. Considering that the coarse aggregates and the crushed sand also contribute, though little, to the surface area, these can also be considered. Using these surface areas (SA_{agr} = surface area of all aggregates; SA_{GP} = surface area of granite powder) as variables, linear regressions equivalent to the previous ones were obtained:

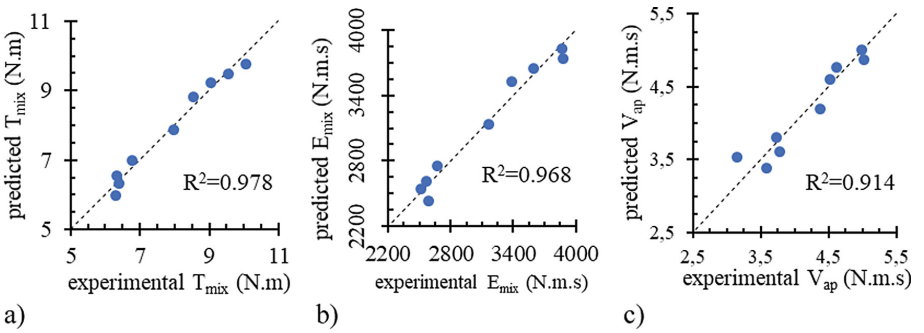

Fig. 4. Experimental data *versus* predicted values by linear regression models: (a) mixing torque at the end of concrete mixing; (b) mixing energy of concrete; (c) apparent viscosity value at maximum rotation.

$$T_{mix} = -0.34 + 944 \times SA_{Agr} + 27.6 \times SA_{GP}$$

$$E_{mix} = 271 + 301669 \times SA_{Agr} + 10463 \times SA_{GP}$$

$$V_{ap} = 0.69 + 399 \times SA_{Agr} + 11.8 \times SA_{GP}$$

Figure 4 shows how well these regressions do fit the experimental data.

So, the initial analysis of four factors could be reduced to only two: change of the surface area of the aggregates and change of the volume of granite powder (represented in the regression equations by its surface area in the system).

3.2 Effect of Water Adjustment Based on Rheological Criteria

In continuous concrete production, rheological variations are not welcome and so the current practice is to make corrections. Often this correction is performed by adjusting the water demand. Using the mixing torque as a parameter for rheological acceptance and adopting a range of ±15% as acceptance interval (6.8 N.m to 9.2 N.m), all concretes that did not fit this requirement were adjusted. Those with higher torques (4, 6 and 7) received an increase of water and those with lower torques (2, 3, 5 and 8) were produced again with less water. In Table 5 the mixing torques after the water adjustment and the corrected water content are presented.

Table 5. Concrete parameters, before and after water adjustment.

Parameter		Concrete ID								
		Ref	1	2	3	4	5	6	7	8
T_{mix} (N.m)[a]	after	-	-	8.2	8.7	9.5	8.2	9.5	9.3	9.3
Water (L/m^3)	after	-	-	142	141	148	142	147	146	141
Compressive strength (MPa)	after	51.9	50.8	53.8	52.9	48.7	53.7	49.4	49.6	52.5
$Dist_{fines}$ (μm)[b]	before	0.121	0.113	0.130	0.130	0.112	0.130	0.112	0.113	0.129
	after	-	-	0.123	0.121	0.117	0.123	0.116	0.115	0.122
$Dist_{coarse}$ (μm)[b]	before	115	133	112	107	114	116	120	118	98
	after	-	-	111	106	115	114	122	119	98

[a]Concrete mixing torque after adjusting water;
[b]Calculated mean particle distance for fine (<100 μm) and coarse particles (>100 μm).

The deviations of compressive strength (Table 5) from the reference value, induced by the granulometric variations, are in the order of −6.4% to +3.8% (5.2 MPa between the lowest and highest value). This is equivalent to the usual difference between mean and characteristic concrete strength when a standard deviation of 3.0 MPa is adopted (1.64 × 3.0 = 4.9 MPa). It is possible that a relevant part of the strength variation observed in continuous concrete production is induced by PSD changes like those evaluated here.

All previous findings are restricted to the tested composition and selected factor levels. Somewhat more general conclusions would be interesting. It is known that PSD changes affect the packing density and surface area [2]. The rheological changes lead to water volume adjustments which, together with the variable fine powder content, have an impact on the overall past volume and its solid concentration. These parameters affect the distance between the solid particles (space for mobility) of the concrete suspension, and this may possibly affect rheological properties.

The mean distances between the particles in a suspension can be calculated by distributing the excess volume of fluid (the fraction of the total fluid volume remaining after filling the packing porosity) across the area of the particles. Mathematically the mean distance *Dist* is calculated [1] by:

$$Dist = \frac{2}{VSA} \times \left[\frac{1}{V_s} - \left(\frac{1}{1 - P_{of}} \right) \right]$$

where *VSA* is the volumetric surface area, V_s is the volumetric fraction of solids in the suspension and P_{of} is the packing porosity of the particles. If *VSA* is given in m^2/cm^3, *Dist* results in μm.

This distance can be evaluated at two levels [1, 7]: paste, where only fine (<100 μm) particles are considered; and aggregates, where only the coarser particles are considered. For the paste, water is the fluid. For the aggregates, the paste plays the role of fluid.

These distances were calculated for all concretes (Table 5), before and after the water adjustment, and a linear regression model was fitted to the experimental mixing torques. Figure 5 shows how well mixing torques can be estimated by means of these two microstructural parameters.

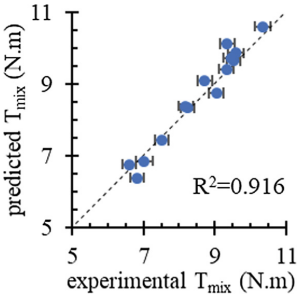

$$T_{mix} = 44.9 - 251 \times Dist_{fine} - 0.0506 \times Dist_{coarse}$$

Fig. 5. Prediction of mixing torque, based on fine and coarse particle mean distances.

4 Summary and Conclusion

This research evaluated the influence of granulometric variations of aggregates on rheological properties of a low-binder concrete. Mixing torque, mixing energy demand and apparent viscosity were affected by granulometric changes, in some cases up to over 20% compared to the reference concrete. Main factors are fine powder content

(coming from aggregate crushing) and fineness of the natural fine sand. Of these two, the predominant factor is the powder content. In the evaluated intervals, the powder content change led to rheological modifications about 3 to 5 more intense than the change in PSD of the sand. Granulometric variations of the coarser aggregates had no significant effects in the analyzed case.

When water correction was adopted as a strategy to overcome the rheological changes caused by the granulometric changes, consequences in the hardened state were observed. In the analyzed case, compressive strength varied in a range of 5.2 MPa, which is relevant, since in practice the difference between characteristic and mean concrete compressive strength is often in the range of 5 MPa–7 MPa.

Finally, it was shown that mixing torque can be estimated from the mean distances between the fine and coarse particles in the concrete suspension. A linear regression model, with $R^2 = 0.91$, was obtained. Such models have practical use for composition correction in a scenario with variable raw materials, for robustness simulations and for concrete optimizations.

Acknowledgment. The authors would like to thank FAPESP (The São Paulo Research Foundation) for financial support through the grant 2012/21134-2.

References

1. Funk JE, Dinger DR (1994) Predictive process control of crowded particulate suspensions: applied to ceramic manufacturing. Springer, New York
2. de Larrard F (1999) Concrete mixture proportioning: a scientific approach. E&FN Spon, London
3. Cepuritis R, Jacobsen S, Smeplass S, Mørtsell E, Wigum BJ, Ng S (2017) Influence of crushed aggregate fines with micro-proportioned particle size distributions on rheology of cement paste. Cem Concr Comp 80:64–79
4. Van Der Vurst F, Grünewald S, Feys D, Lesage K, Vandewalle L, Vantomme J, De Schutter G (2017) Effect of the mix design on the robustness of fresh self-compacting concrete. Cem Concr Comp 82:190–201
5. Zuo W, Liu J, Tian Q, Xu W, She W, Miao C (2018) Norm method to define and evaluate robustness of self-compacting concrete due to component quantity variations. Constr Build Mater 161:246–253
6. Rebmann MS (2016) Robustness of concrete with low Portland cement consumption: deviations in proportioning and particle size and morphological variability of the aggregates, PhD thesis, University of São Paulo (in Portuguese)
7. Romano R, Cardoso FA, Pileggi, RG (2011) Propriedades do concreto no estado fresco. In: Concreto: ciência e tecnologia, 1st edn. IBRACON, São Paulo

Suspensions Sedimenting in a Horizontal Annulus – A Model for Oilfield Cements in Horizontal Wells

Agathe Robisson[1(✉)], Teresa Liberto[1], and Elizabeth B. Dussan V.[2]

[1] Department of Civil Engineering, Vienna University of Technology, Vienna, Austria
agathe.robisson@tuwien.ac.at
[2] Watertown, USA

Abstract. We evaluate the settling of a suspension in an annular geometry, where the concentric pipes are placed horizontally. The geometry was chosen to mimic cement slurry bleeding (i.e. accumulation of fluid on top of the geometry due to the settling of particles) in horizontal oil and gas wells. We compare the behavior of ideal semi-dilute suspensions, such as polymer beads in oil, with real cement slurries, in cells of similar geometry. Despite the differences between the two systems, our results show striking similarities and explain the presence of weak points at the upper outer diameter, below the internal diameter and at the poles.

Keywords: Cement · Bleeding · Rheology · Horizontal well cementing · Sedimentation

1 Introduction and Motivation

With the development of shale gas wells in North America, the number of horizontal oil and gas wells has tremendously increased, related to their increased production [1]. A number of these wells needs to be cemented for hydraulic isolation purposes. In particular, the annulus between the rock that has been drilled and the pipe that brings hydrocarbons to the surface is filled with cement. It is critical that the cement completely fills the annulus to provide a seal. If the cement presents defects, gaps, cracks or does not properly bond to its confining environment (metallic pipe or rock), the cement sheath may not serve its purpose of hydraulic isolation. This, in turns, will affect the fracturing treatment, and eventually lead to a lower hydrocarbon production.

While a large number of studies have focused on the properties of the set cement (i.e. shrinkage and damage due to thermal stresses and earth movement) [2] as well as mud clean-up in the well [3], no study, from our knowledge, discussed cement placement and potential issues linked to slurry stability in a horizontal annulus geometry. The purpose of the present study is to emphasize the critical importance of

E. B. Dussan V.—Retired.

V. Mechtcherine et al. (Eds.): RheoCon 2019/SCC 2019, RILEM Bookseries 23, pp. 52–59, 2020.
https://doi.org/10.1007/978-3-030-22566-7_7

the cement slurry stability, and illustrates the difficulty of sealing a horizontal annular cavity with cement, as compared to a vertical annular cavity.

2 Materials and Methods

Two cement slurries were prepared with an OFITE blender [4]. In particular, the slurry #1 was prepared by pre-hydrating diutan gum in water and then slowly adding cement. The slurry #2 was prepared by pre-mixing water and plasticizer, and then slowly adding the cement. Magnesium oxide is added as an expanding agent to mitigate shrinkage (not studied here). The water-to-cement (w/c) ratio for both slurries was fixed at 0.4. Cement slurries were designed to have relatively low bleeding at room temperature.

The two suspensions were prepared by carefully weighting both the beads and the oil, and hand mixing.

The composition and properties of the four samples are detailed in Table 1.

Table 1. Cement slurries and suspensions data

	Slurry #1	Slurry #2	Suspension #1	Suspension #2
Composition	w/c = 0.4 dilutan: 0.0 2% bwoc $\Phi \approx 0.44$	w/c = 0.4 MgO: 10% bwoc plasticizer $\Phi \approx 0.44$	$\Phi = 0.01$	$\Phi = 0.05$
Average particle size	Cement $\approx$ 10 μm	Cement $\approx$ 10 μm	Beads $\approx$ 165 μm	Beads $\approx$ 165 μm
Rheological properties	Shear thinning High yield stress	Shear thinning Low yield stress	Newtonian	Newtonian
ASTM C232 bleeding	2 ml	3 ml		
Density	Cement $\approx$ 3.15 g/cc	Cement $\approx$ 3.15 g/cc	oil $\approx$ 0.83 g/cc beads $\approx$ 1 g/cc	oil $\approx$ 0.83 g/cc beads $\approx$ 1 g/cc

The cells with annular cavities for the cement slurries were custom-made of transparent (acrylic) plastic, with two pipes, assembled between two plates, creating an annular cavity of external diameter 120 mm, internal diameter 76 mm, and length 19 mm. The cells with annular cavities for the suspension were slightly larger with an external diameter of 140 mm, internal diameter of 76 mm, and a length of 20 mm.

Pictures were taken with a 70D Canon camera with a Sigma 18 mm–35 mm lens, with the camera facing the front of the cell. On all pictures, gravity points downwards.

Pictures were taken every second for the experiments with suspensions, and images presented here are made of 10 superposed images, taken over the course of 10 s. This technique of superposition enables the visualization of particle trajectories.

All tests were performed at room temperature.

3 Results and Discussion

3.1 Fresh Cement Settling in a Horizontal Annulus

Results obtained with the two cement slurry systems are presented in Figs. 1, 2 and 3. In all cases, we observed areas of the cells that were devoid of cement, and that were filled by a clear fluid (bleeding water).

Figures 1 and 2 show results obtained with the slurry #1 (diutan gum). Note that, although the pictures were taken 2 h after cement mixing and placement in the cell (to match the ASTM standard), defects started to appear almost immediately.

First, bleeding water accumulated at the top of the cell, on the upper part of the outer diameter. This is the highest point of the cell and therefore the logical place for bleeding water to go. We also observed cracks, of orientation between vertical and $\approx 45°$ inclination, starting from the upper outer diameter. Other cracks started from the inner diameter in the lower half of the cell. Surprisingly, these cracks are nearly horizontal, i.e. perpendicular to gravity. We have observed that, in some cases, once the bleeding process stops, some of these cracks close.

Moreover, bleeding water accumulating below the inner pipe can be seen in Fig. 2. The water was trapped here and could not travel up the cell, probably when cement gel strength was too high for water to create a path.

These results illustrate that even low bleeding cement can develop relatively strong defects when placed in a horizontal well.

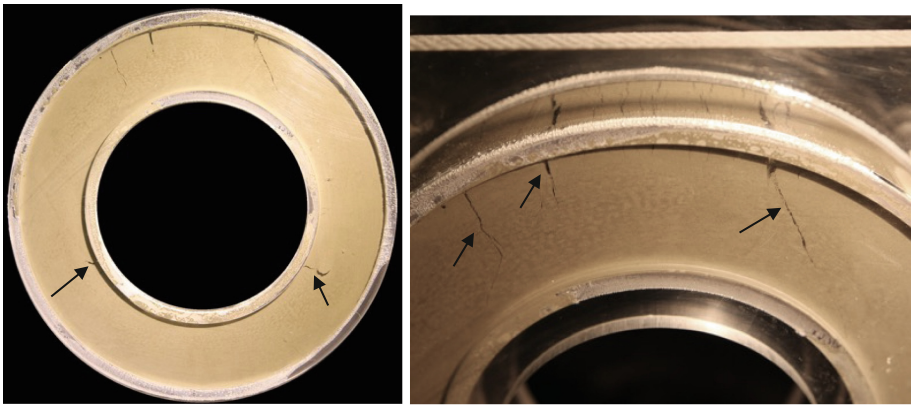

Fig. 1. Cement slurry #1 (diutan gum) - Whole cell front view and detailed view on defects in the upper part of cell – Black arrows show cracks.

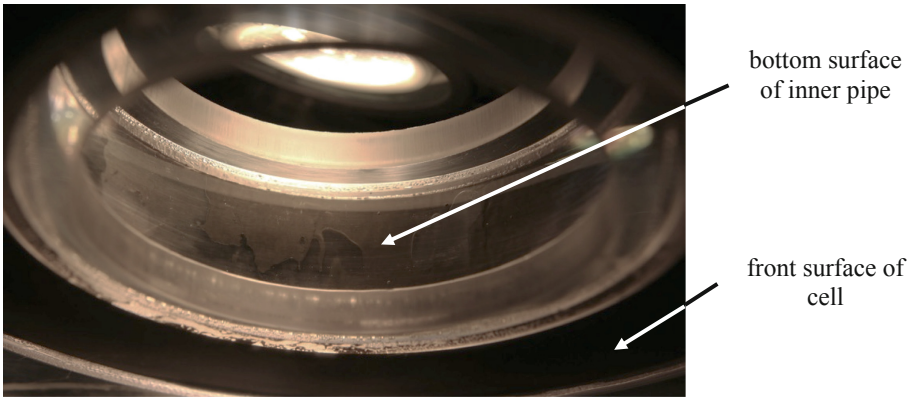

Fig. 2. Cement slurry #1 (diutan gum) - Detailed view on defects in the lower part of cell (below the inner pipe).

The cement slurry #2 shows a slightly higher bleeding capacity. In this case, no anti-settling additive (i.e. diutan gum) was used, while a plasticizer was added. In Fig. 3, we can distinguish a clear path for bleeding water flow. The picture was taken 10 min after placing the slurry in the cell.

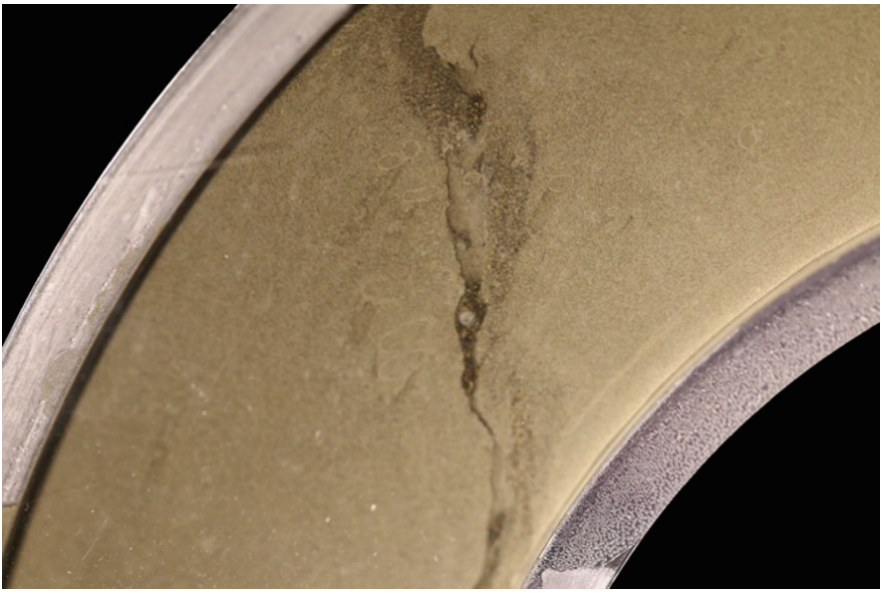

Fig. 3. Cement slurry #2 (higher bleeding capacity) - Detail of upper part of cell - Water flows up in a "crack".

3.2 Semi-dilute Suspension of Monodisperse Beads in Oil

To further investigate and quantify the above phenomena, we prepared suspensions of solid volume fractions $\Phi = 1\%$ and $\Phi = 5\%$ monodisperse beads in oil (Newtonian behavior). The beads have an average size of 165 μm, making Brownian motion and colloidal interactions negligible. This suspension was designed to strictly study the Stokes sedimentation of particles (sedimentation velocity is dictated only by hydrodynamics).

Figures 4 and 5 show the images taken on the cell filled with the $\Phi = 1\%$ and the $\Phi = 5\%$ suspensions, respectively, between times 300 s and 309 s.

In both suspensions, results show that the oil (fluid free of particles) accumulates at the top of the suspension, below the upper part of the outer diameter, as expected, while the particles settle down and accumulate at the bottom of the annular cavity. An oil layer also forms below, and along, the inner pipe. Near the tangent point of the inner diameter, accumulated oil visibly "breaks down" and starts traveling through the upper part of the suspension, towards the top of the cell.

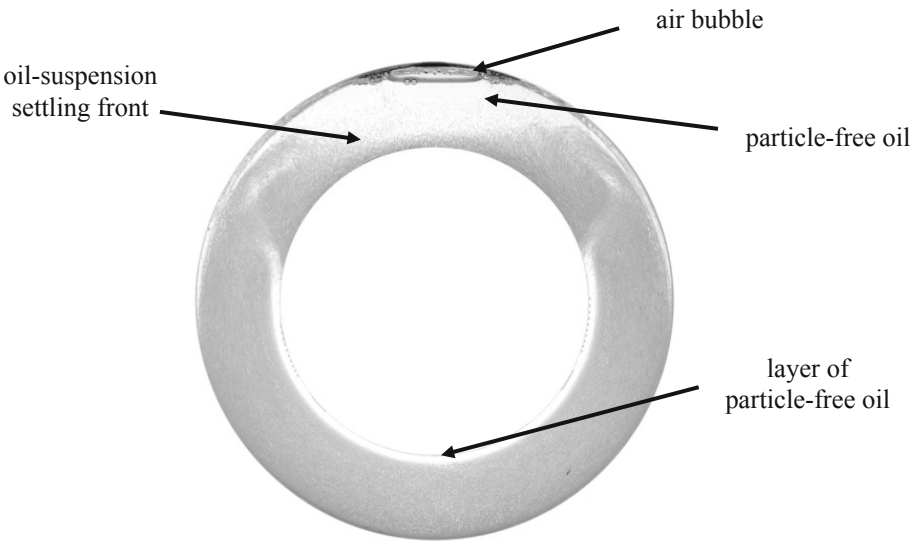

Fig. 4. Monodisperse beads in newtonian oil with $\Phi = 1\%$ settling in an horizontal annular cell. The image is composed of 10 superposed images at times $t = 300$ s–309 s.

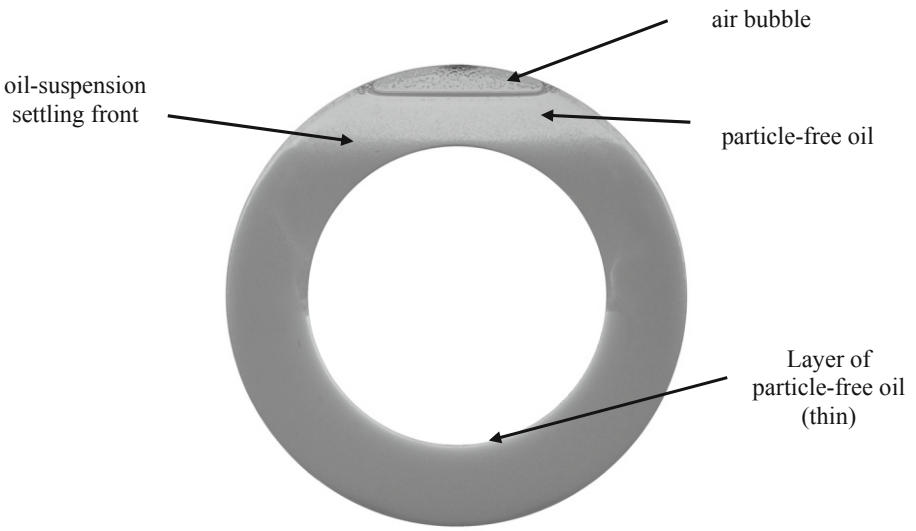

Fig. 5. Monodisperse beads in newtonian oil with $\Phi = 5\%$ settling in an horizontal annular cell. The image is composed of 10 superposed images at times $t = 300$ s–309 s.

These simpler systems seem in many ways far from being a model for a cement suspension. Indeed, in cement slurries, the suspension develops a yield stress due to colloidal interactions between the cement particles. Moreover, the solid volume fraction is high enough to create effective stresses, leading to gravity effects not only due to Stokes settling but also to consolidation [5]. Nevertheless, the patterns show striking similarities that help explain the behavior of cement slurries in horizonal annuli, as described below.

It is worthwhile noting that, in the suspensions, the clear fluid layer below the inner pipe forms a surprisingly constant thickness, stable in time (in the steady-state regime) and in space (along the lower inner pipe). The complete analysis is detailed in [6].

3.3 Comparison Between Semi-dilute Suspensions and Cement Slurries - Discussion

We claim that the above images emphasize, and illustrate, some of the phenomena that occur in the cement slurries. In a purely vertical container, including a vertical annulus, a settling suspension offers no surprise: the fluid travels up through the suspension until it reaches the top of the suspension, and mixes with the fluid already present there. In the current geometry, the fluid path is more complex, as shown in the graphical illustration of Fig. 6. Fluid rises throughout the suspension, collecting under all "downward facing surfaces" [7]. Simultaneously, the particles sink, collecting over all "upward facing surfaces".

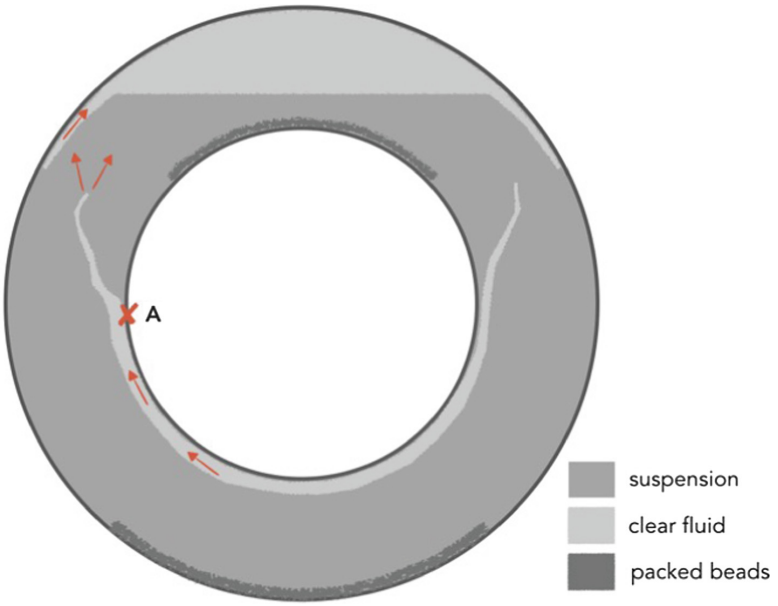

Fig. 6. Schematic of clear fluid flow and the formation of sediment in a suspension sedimenting in an horizontal annular cell.

In the case of a cement suspension, the relative movements of fluid and particles are also dictated by gravity. Water is clearly seen to accumulate below the inner pipe. In the case of the cement slurry, though, the progressive compaction/consolidation/gelling of the cement suspension may trap the fluid. This will compromise the bonding of the set cement in the pipe. Moreover, at the sides of the inner pipe, defects observed in the cement slurry also come from the bleeding water, separating from the inner pipe, and trying to make its way through the cement slurry to the top of the cell. This diluting of the cement is also likely to compromise the cement sheath integrity. Finally, the bleeding water accumulates to the top of the annular cavity, below the outer pipe. This gap, void of cement, also represents a potentially critical defect in the cement.

The fluid and particles movements near the sides of the inner pipe (near point A) present interesting features. In the upper part of the cell, particles in the suspension above the inner pipe settle down and accumulate on top of it. These particles will then slide from this surface into the suspension (around the sides, point A). Therefore, in this area, an avalanche of particles falling down will meet a flow of clear fluid flowing up. This creates the random patterns seen in all experiments. The point at which the fluid separates from the inner pipe will vary depending on the solid volume fraction, the bleeding ability of the slurry and its rheological properties (i.e. yield stress). Note that this critical point may be much lower from the side poles, at seen in Fig. 1. Moreover, if the cement slurry has gelled enough, the bleeding water, trying to escape upwards, will open a crack, that can be perpendicular to gravity, as observed in Fig. 1.

4 Summary and Conclusion

In this study, the sedimentation of suspensions is investigated in a horizontal annulus, making a direct comparison between two systems: cement slurries and Newtonian semi-dilute suspensions. The geometry was chosen to mimic cement slurry bleeding in horizontal oil and gas wells. We are especially interested in identifying the risks related to bleeding of cement in horizontal wells, but our results can also be extended to bleeding water accumulation below cables and large aggregates in concrete.

First, we investigated the effect of cement bleeding when placed in a horizontal annulus.

We saw bleeding water accumulating below the upper outer pipe and below the lower inner pipe, creating areas devoid of cement. At the sides, the bleeding water was observed to travel from the lower inner pipe back through the suspension. This also dilutes the cement slurry and may introduce long-term defects in the cement sheath.

Second, experiments on semi-dilute suspensions (monodisperse beads in Newtonian oil) clearly illustrated free fluid paths during a settling process and helped explain the behavior on cement slurries. In particular, we could explain the presence of cracks in cement slurries that opened perpendicular to gravity, an initially surprising result.

Our findings could have significant consequences on cement qualification for horizonal well cementing. Misleading conclusions could result upon from only examining the amount of water accumulated at the top of a column of cement, as recommended in the oilfield standard.

References

1. EIA report, Oil wells drilled horizontally are among the highest-producing wells, 4 November 2016
2. Ulm F-J, Abuhaikal M, Petersen T, Pellenq RJ-M (2015) Poro-chemo-fracture-mechanics: bottom-up: Application to risk of fracture design of oil and gas cement sheath at early ages. In: Bicanic N, et al (eds) Proceedings of the Computational Modelling of Concrete Structures, Euro-C 2015, Vol I, pp 61–71
3. Nelson EB, Guillot D (2006) Well Cementing, Schlumberger
4. Recommended Practice for Testing Well Cements, API Recommended Practice 10B-2sd Ed., April 2013
5. Tan T-S, Loh C-K, Yong K-Y, Wee T-H (1997) Modelling of bleeding of cement paste and mortar. Adv Cem Res 9(34):75–91
6. Robisson A, Dussan VEB (in preparation)
7. Acrivos A, Herbolzheimer E (1979) Enhanced sedimentation in settling tanks with inclined walls. J Fluid Mech 92(3):435–457

SCC for Sub-Saharan Africa Based on Local Raw Materials – Material Development, Optimisation, and Application Concept

Wolfram Schmidt(✉)

Bundesanstalt für Materialforschung und -prüfung, Berlin, Germany
wolfram.schmidt@bam.de

Abstract. Sub-Saharan Africa's (SSA) economies are developing at rapid pace. To keep up the verve, housing and infrastructure are urgent challenges, which demand for concrete technologies that can meet the demand. Considering the climate challenges that come along with concrete construction, for the growing African construction business, it is inevitable to use binders with lower carbon footprint and to use chemical admixtures that help reducing cement in concrete.

The use of superplasticizer (SP) and stabilising agents (STA) can enhance the concrete technology in SSA, since they can make concrete quality independent of the boundary parameters. However, the use of cement and concrete additives depends on their availability. Due to the partly poor infrastructure and the lack of chemical industries, in most regions in SSA, the use of admixtures is not yet always common practice. This amplifies the unfavourable framework for concrete construction such as fragmentary supply chains, high local cement prices, and unfavourable construction site facilities in this region significantly.

After providing a general overview of the peculiarities of the SSA boundary framework, and the recommendation of pre-mixed self-compacting concrete (SCC) compounds as a tool to overcome local challenges, a three-step SCC optimisation concept is recommended and experimentally proven based on readily available additives on the African continent. Eventually, the paper elaborates on alternative polysaccharide based rheology modifying agents from agricultural resources and waste materials with high potentials for high-performance concrete applications in SSA.

Keywords: Self-compacting concrete · Bio-based additions · Bio-based admixtures · Rheology · Supply chains

1 Introduction

Today, cement based materials are responsible for about 10% of the global carbon emissions [1], and the production of cement for concrete is increasing. Many solutions for more sustainable construction have been discussed and published, e.g. [2], but the global implementation is challenging and demands for education at all level [3].

In the developed countries of the Northern hemisphere, the application of innovative technologies is largely restricted by limited market growth potentials and policies and a regulative framework that prefers past technologies over innovation. In the

V. Mechtcherine et al. (Eds.): RheoCon 2019/SCC 2019, RILEM Bookseries 23, pp. 60–67, 2020.
https://doi.org/10.1007/978-3-030-22566-7_8

developing countries of the Southern hemisphere, the constraints are rather the limited economic power and technological capacities [4, 5]. For sub-Saharan African (SSA) economies, the lack of long-lasting established policies and standard frameworks, along with the tremendous innovation spirit the need to produce concrete a low cost and low carbon footprint provides a high potential to spearhead green construction technologies in the future [5–7].

Major technological challenges for concrete construction in SSA are lack of adequate supply chains, variable and uncertain raw materials supply, including varieties of cements that are imported from all over the world, extreme climatic conditions, and a wide range of application technologies from site-mixed concrete to ready-mixed concrete, whereas to date site-mixed concrete is clearly dominating [4]. On the construction site, typically, the only way to deal with the varying boundary conditions is to either add water to control the consistency or accept a large consistency scatter during casting, both effects negatively affect the hardened concrete performance. Hence, often the unfavourable technological boundary framework results in underperforming concrete to the disadvantage of the safety, the economy, and the environment [4].

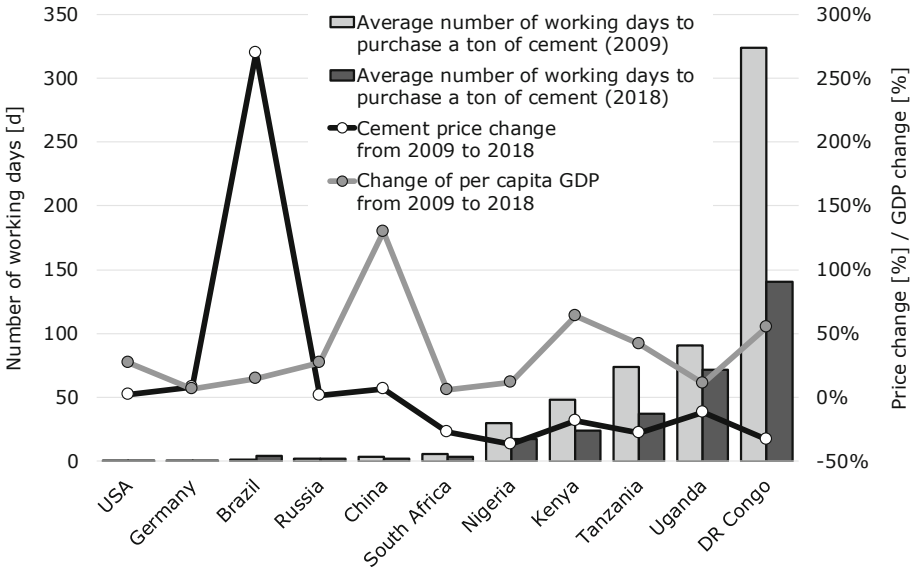

Fig. 1. Cement prices in various countries expressed in number of working days required for an average earner to purchase a ton of cement at local price in 2009 and 2018 compared to the changes of the per capita gross domestic product and cement price.

The impact of the negative concreting environment is amplified by the enormous need to save cement in SSA. Figure 1 shows the cement prices for a variety of African countries in comparison to countries from Europe, Asia and the Americas expressed in number of required working days for an average income earner to purchase a ton of cement. The data is based on average values from locally collected prices in urban and

rural areas, related to economic and demographic values based on UN data. It can be observed that the cement prices in the presented African countries have dropped, and at the same time the per capita gross domestic products (GDP) are have been increased. Nevertheless, despite the positive trend, in absolute values cement prices (approx. 6 to 12 USD/50 kg) remain high in Africa and the GDPs are low in comparison to most industrialised countries. As a result, the effort to obtain cement in Africa is significantly higher for an individual or a company than e.g. in Germany or the USA.

Due to the detrimental boundary framework, and the pressure to save cement, concrete in SSA often shows strongly scattering performance values, which is largely owed to the fact that varying cements are used and the water addition is linked to the required consistency and is thus uncontrolled. Self-compacting concrete (SCC), where the fresh concrete performance is mostly controlled by superplasticizer and the compaction is largely independent of the workers and the casting equipment, can be a solution to overcome the challenges. In the early days of SCC, the flow properties were just a vehicle to provide high concrete quality independent of the workers' skill as described by Ouchi [8]. Figure 2 shows that the same principle can be applied for the SSA boundary framework with the only difference that the challenges on many African construction sites go far beyond the low skill level of the workers.

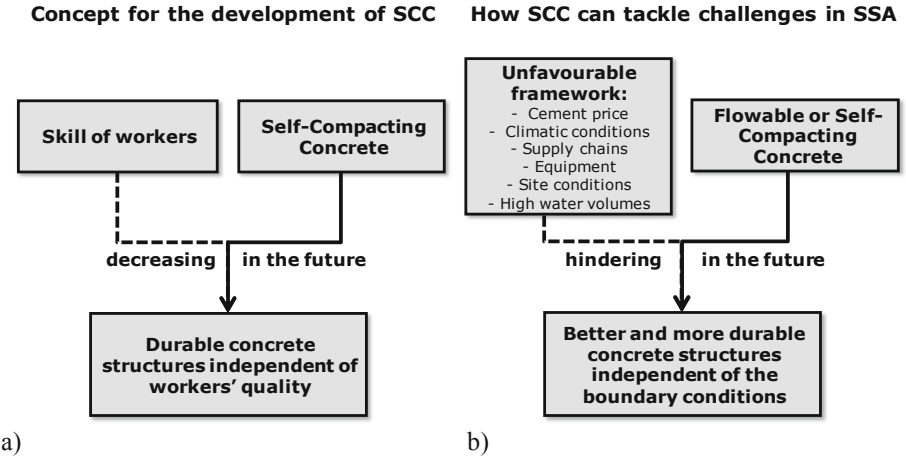

Fig. 2. Similarity between the situation that triggered the development of SCC in Japan after Ouchi [8] (a) and the situation in many regions of SSA (b).

From the perspective of the Northern hemisphere, the application of SCC typically comes along with higher complexity and lower reliability of the fresh concrete performances, particularly in the field of ready-mixed concrete. The reason is that standard concrete technologies have been well established in the daily construction for decades. This is different in most countries of SSA, where site concrete under varying conditions are standard. Here, standard concrete technologies are not more robust and easier to apply than SCC and the full potentials of SCC with its low w/p and high workability

can be tapped. In order to uncouple the performance of SCC from the construction site conditions, the SCC can be delivered as pre-mixed compound, already including powder type admixtures, fillers to minimise the cement content and sand, as illustrated in Fig. 3. On the construction site, only water and aggregates need to be added in the specified amount. Since the pre-mix can be well homogenised in advance and the robustness of the workability can be optimised by using superplasticizers and stabilising agents, so that there is no longer need for situation-specific water addition. The technological environment on the construction site remains unchanged with the only difference that bags with the pre-mixed compound would be stored on the construction site instead of cement bags, and no sand storage facilities would be required any more. However, the same labourers would do the same operations with the same equipment as before, yet, the concrete workability would be improved and the hardened concrete would show constant performance.

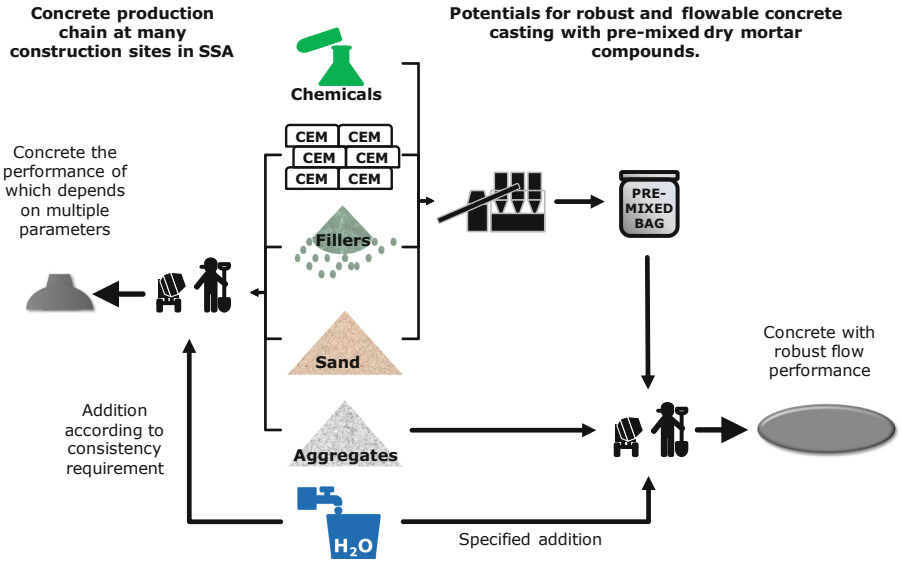

Fig. 3. Possible implementation strategy of robust flowable and self-compacting concrete as pre-mixed compound in comparison to currently applied standard concrete technologies.

2 Development of a Pre-mixed Self-compacting Concrete Compound

In order to prove the concept such a proposed binder compound was experimentally developed. The optimisation process is described in more details elsewhere [9].

In a first approach ordinary Portland cement was replaced by a variety of fillers as specified in Table 1. The water demand was determined according to the method proposed by Puntke [10, 11]. Figure 4a shows that for all replacement rates, no significant changes could be observed up to a replacement rate of 20%. In a second step

the water demand of mortars up to 2 mm sand was determined at varied paste to sand ratios. All pastes contained a 20% cement replacement with fillers. As can be seen for the different setups in Fig. 4b, the lowest binder volumes lie in the order of magnitude of 15%–30%. Since optimised particle packing is detrimental to flowability, the paste volume was fixed at 30%.

For the adjustment of admixtures, adsorption tests were conducted according to [12].

Table 1. Final mixture composition.

Material	Specification	Specific gravity
Ordinary Portland cement	CEM I 42.5 R	3.12
Limestone filler	-	2.74
Rice husk ash (Tanzania)	Low quality, uncontrolled burning	2.07
Coal fly ash (Tanzania)	Low quality, uncontrolled burning	2.06
Nat. pozzolan (Uganda)	Ground at BAM laboratory	2.50
Sand	Fractions 0-0.5/0.5-1.0/1.0-2.0	2.60
Aggregate	Fractions 2.0-4.0/4.0-8.0/8.0-16.0	2.60

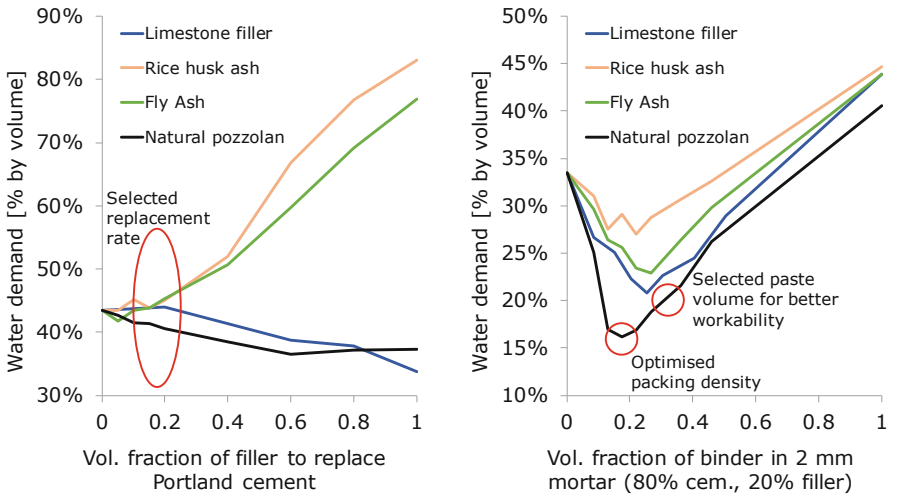

Fig. 4. Selection criteria for cement replacement by fillers (a) and binder to sand optimisation (b).

Table 2. Final mixture composition.

	Homogenized, pre-mixed dry mortar compound					To be added on-site	
Resulting SCC	Cement	Natural pozzolan	Sand 0–2 mm	Ligno sulfonate	Cassava starch	Water	Aggregate 2–16 mm
	385 kg/m^3	78 kg/m^3	944 kg/m^3	1.78% of cement	0.58% of cement	232 kg/m^3	650 kg/m^3

The experiments were done with a variety of plasticizers available in the African markets as well as one commercial PCE. Since for the final mixture a lignosulfonate (LS) should be used, it was found that for similar yield stress reduction as PCE, the water volume inevitably had to be increased depending on the filler used. Due to problems with strength evolution with the low-quality fly ash and rice husk ash, the final concrete optimisation was made with the natural pozzolan from Uganda. This pozzolan together with LS demanded for a water volume that corresponds to a w/c of 0.5. In order to stabilise the mixture and avoid bleeding and segregation, cassava starch based stabilising agent (STA) from Nigeria was added.

The final step was to minimise the mortar volume in concrete. The developed mortar compound was mixed with varied volumes of aggregates, and the threshold aggregate volume was determined at which the flow performance on concrete level significantly dropped. This step was conducted in a Contec Rheometer-4SCC.

The final mixture composition can be found in Table 2. Yield stress and plastic viscosities maintained stable over the first 20 min after mixing, and did not show significant variations in a temperature range between 5 °C and 40 °C. The compressive strength after 28 days was 56.2 MPa, after 90 days it was 68.4 MPa [9].

3 Local Superplasticizer and Stabilising Agent Alternatives

In order to produce high-performance concrete but also to use concrete with less cement by using cement more efficiently, rheology modifying admixtures are inevitable. However, the African continent is excluded from easy access to construction chemicals. Most admixtures have to be shipped over a long distance, which causes a limited choice and implies high prices.

More economic solutions can be found locally. Various polysaccharides show excellent rheology modifying properties, they occur in abundance in Africa and do not require complicated processing [13].

Acacia gum (GA), for example provides excellent plasticizing properties. Depending on the setup, they can even outperform highly efficient PCE type superplasticizers. Their performance depends strongly on the number of anionic charges, which again is determined by their provenience [14].

It could already be shown that GA can be used as superplasticizer for SCC [15], yet, its use has challenges, since GA acts as thickener and plasticizer depending upon the dosage and the w/c of the cementitious paste. Figure 5 shows a cement paste plasticized with PCE and GA. While unlike the PCE at w/c = 0.3 the GA cannot enhance the flow significantly, at *w/c* = 0.4 the paste segregates completely and much more than with PCE due to the high efficiency of the GA. Further research is required to study the mode of operation completely. For a robust application it might be inevitable to combine the polymers with additional stabilising agents. Various cost-efficient bio-based alternatives exist, e.g. potato or cassava starch or Triumfetta pendrata A. Rich [4, 14, 16].

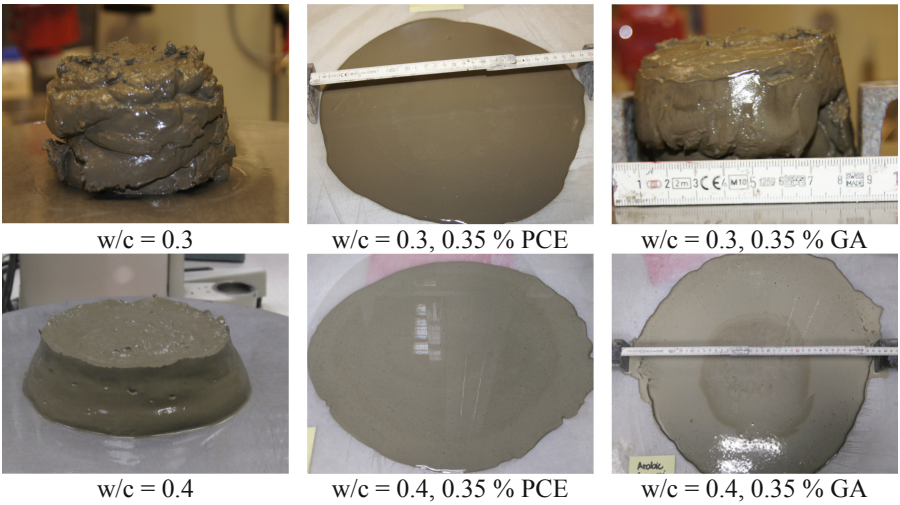

Fig. 5. Reference samples at w/c 0.3 and 0.4 (a); respective samples with 0.35% PCE (solids bwoc) (b); respective samples with 0.35% acacia gum (solids bwoc) (c).

4 Summary and Conclusions

For the implementation of future oriented, sustainable concrete technologies, the usage of chemical admixtures is inevitable to provide performance and to use cement in concrete most efficiently. The African continent could spearhead sustainable concrete technologies globally by maintaining its low carbon emission level while developing green and more modern technologies, but this require solutions for the current challenges in SSA.

SCC can help overcoming a variety of detrimental boundary conditions in SSA. For robust application, it can be implemented in the market as pre-mixed mortar compound to be amended by water and aggregates only.

A concept for SCC development with low cost constituents was shown in this paper. Additional potentials to overcome the restricted access to readily available construction chemicals on the continent were presented. Polysaccharides like acacia gum can be excellent, cost-efficient and sustainable rheology modifying admixtures, but further research is required to understand the mode of operation in more detail.

References

1. WBCSD (2016) Getting the Numbers Right, Project Emissions Report 2014
2. Scrivener K, John VM, Gartner EM (2017) Eco-efficient cements: potential economically viable solutions for a low-CO_2 cement-based materials industry, United Nations Environment Programme, Paris

3. Schmidt W, Alexander M, John V (2018) Education for sustainable use of cement based materials. Cem Concr Res 114:103–114
4. Schmidt W, Msinjili NS, Kühne H-C (2019) Materials and technology solutions to tackle the challenges in daily concrete construction for housing and infrastructure in Sub-Saharan Africa. Afr J Sci Technol Innov Dev 11(4):401–415. https://doi.org/10.1080/20421338.2017.1380582
5. Schmidt W (2016) Why Africa can spearhead innovative and sustainable cement and concrete technologies globally. In: Msinjili NS, Schmidt W (eds) KEYS knowledge exchange for young scientists: valorisation of industrial by-products for sustainable cement and concrete construction – improvement of solid waste management. BAM, Accra, pp 7–19
6. Schmidt W (2017) Potentials for sustainable cement and concrete technologies – comparison between Africa and Europe. In: Proceedings of the 1st international conference on construction materials for a sustainable future, Zadar, Croatia, 19–21 April 2017
7. Schmidt W, Falade F, Rogge A, Tchitnga R (2019) ISEE - innovation, science, engineering, education (pre-conference edition). Bundesanstalt für Materialforschung und -prüfung (BAM), Berlin, p 134
8. Ouchi M (1998) History of development and applications of self-compacting concrete in Japan. In: International workshop on self-compacting concrete, Kochi, Japan. JSCE, pp 1–10
9. Schmidt W, Msinjili NS, Uzoegbo HC, Makunza JK (2015) Admixture concepts for the Sub-Saharan African environment with indigenous raw materials. In: Malhotra VM (ed) SP-302 11th international conference on superplasticizers and other chemical admixtures in concrete, pp 491–505
10. Puntke W (2002) Wasseranspruch von feinen Kornhaufwerken. Beton 2002(5):242–248
11. Hunger M, Brouwers HJH (2009) Flow analysis of water-powder mixtures: application to specific surface area and shape factor. Cem Concr Comp 31(1):39–59
12. Schmidt W (2014) Design concepts for the robustness improvement of self-compacting concrete - effects of admixtures and mixture components on the rheology and early hydration at varying temperatures, PhD, Department of the Built Environment, TU Eindhoven, Netherlands, Bouwstenen 193
13. Schmidt W, Barucker-Sturzenbecher MJ (2019) Bio-based concrete, Berlin, p 7:51. https://vimeo.com/310549146
14. Schmidt W, Olonade KA, Tchetgnia Ngassam IL, Mbugua R, Athman Mwende C, Kühne H-C: Pflanzenbasierte Betonzusatzmittel für Hochleistungsbeton. 20. Baustofftagung ibausil, Weimar, vol 20, pp 1-874–1-885
15. Mwende Athman C (2018) Effectiveness of Gum Arabic as a superplasticizer in self-compacting concrete, MSc, Department of Civil Engineering, Pan African University
16. Schmidt W, Brouwers HJH, Kühne H-C, Meng B (2017) Interactions of polysaccharide stabilising agents with early cement hydration without and in the presence of superplasticizers. Constr Build Mater 139:584–593

Effect of Supplementary Cementitious Materials, Fillers and Chemical Admixtures on Rheology

Effect of Sodium Sulphate on Rheological Behaviour of Alkali Activated Slag Binders

Aparna Sai Surya Sree Nedunuri(✉) and Salman Muhammad

Department of Civil Engineering, Indian Institute of Technology Bombay, Bombay, India
naparna@iitb.ac.in

Abstract. Alkali-activated binders (AABs) are alternative binders to OPC which can reduce carbon emissions. AABs use a precursor (mostly a by-product) and alkaline activator that produces a binder having cementitious properties. However, a few drawbacks like faster setting time and high drying shrinkage hinders their application on a larger scale. The time available to work at ease with these materials depends on the kinetics of the reaction and rate of flocculation; which in turn is dependent on composition of the precursor, solid content, type of activator and activator dosage. The amount of calcium present in the precursor is one of the factors that govern the early reaction kinetics. Similarly, the concentration and type of alkali ions in the system have a significant effect on rheological behavior. In order to use AABs in large scale applications, it is essential to understand the effect of various parameters on the workability of mixtures. The objective of this study is to evaluate the effect of sulphate content on the rheological behavior of alkali-activated slag binders and it was found to have a significant effect on the evolution of yield stress and apparent viscosity.

Keywords: Yield stress · Apparent viscosity · Alkali activated binders · Sodium sulphate

1 Introduction

Ground granulated blast furnace slag, a by-product of steel industry is widely used as a supplementary cementitious material. Although the amount of glass present in ground granulated blast furnace slag is above 95%, its usage as a replacement to cement is limited owing to its latent hydraulic behaviour [1]. These materials can be used to their full potential (as an alternative to OPC) by activating them either by chemical or mechanical means. The first patent on alkali activation of slag dates back to 1908 by Kuhl and a significant laboratory work on cement consisting of slag and alkalis was contributed by Purdon in 1940. Since then, extensive research has been done related to alkali activated slag (AAS) binders [2]. AAS binders have a few drawbacks like high drying shrinkage and faster setting when compared to OPC binders. Early setting times of sodium silicate activated slag systems was attributed to the formation of primary C-S-H [3, 4]. On the other hand, sodium sulphate activated slag binders have delayed

V. Mechtcherine et al. (Eds.): RheoCon 2019/SCC 2019, RILEM Bookseries 23, pp. 71–78, 2020.
https://doi.org/10.1007/978-3-030-22566-7_9

setting time (attributed to low pH) and lower early age strength when compared to sodium silicate activated slag binders [5].

In case of Portland cement without gypsum, rapid reaction of C_3A with water results in significant loss of workability which is termed as "flash set". The reaction of C_3A with water at ordinary temperature forms metastable C_4AH_{19}, C_4AH_{13} and C_2AH_8 (hexagonal hydrates) and are converted to C_3AH_6 (cubic hydrate). To avoid flash set, a small amount of gypsum (less than 3%) is added to clinker. In the presence of gypsum, hydration of C_3A proceeds as $C_3A + 3C\bar{S}H_2 + 26H \rightarrow C_3A.3C\bar{S}.H_{32}$ (ettringite) and continues until the consumption of sulphate. The delayed setting of OPC in presence of gypsum is due to retardation of hydration of C_3A. The reason behind this phenomenon is debatable and can be either due to formation of ettringite layer around C_3A or due to adsorption of sulphate ions on reactive dissolution sites. However, the rate of hydration of C_3A in OPC is known to have significant effect on rheological behaviour. Greenberg et al. [6] are the first to study the influence of calcium sulphates on the rheology of cement paste. An attempt has been made in this study to increase the workable time of AAS binders by increasing the sulphate content of slag. This paper investigates the effect of sulphate content of precursor, activator dosage (% of Na_2O) and water to binder (w/b) ratio on the rheological behaviour and setting time of AAS binders.

2 Experimental Materials and Methods

Ground granulated blast furnace slag obtained from a steel plant located near Mumbai, India was used as a precursor. The oxide composition of slag as determined by ICP-AES is given in Table 1.

Table 1. Oxide composition (wt%) of slag.

Material	CaO	SiO_2	Al_2O_3	Fe_2O_3	MgO	Na_2O	K_2O
Slag	35.4	40.8	14.5	1.2	7.1	0.5	0.4

Slag was activated with activator solution having a molar modulus (molar ratio of SiO_2/Na_2O) of 1.5 which was prepared by mixing appropriate amounts of sodium silicate and 14 M NaOH solution. The sulphate content of slag was made to 1% and 2% (wt% of binder) by addition of laboratory grade sodium sulphate. Na_2O from sodium sulphate was accounted while calculating the amount of NaOH solution to be added to maintain the required activator dosage (% of Na_2O). 27 mixtures were prepared to investigate the effect of concentration of sulphate, % of Na_2O and water to binder ratio on the rheological behavior of AAS binders. Considered parameters and their levels are given in Table 2.

Table 2. Considered factors and their levels.

Parameter	Level 1	Level 2	Level 3
SO_3 content (wt %)	0	1	2
% of Na_2O	4	6	8
w/b ratio	0.40	0.45	0.50

Pastes were prepared by weighing appropriate quantities of slag, sodium sulphate, NaOH solution, sodium silicate and distilled water. Dry mixing of slag and sodium sulphate was done (priorly) for 2 min. The mixing regime as given in ASTM C 305 [7] was followed. After mixing for 2 min 30 s, the material was poured into building material cell of rheometer. Rheological measurements were performed on Anton Paar made MCR 102 rheometer after 5th min upon the addition of mix water. After pre-shearing at 300 s^{-1} for 90 s, the material was subjected to a linear ramp up shear profile (0 to 200 s^{-1} in 120 s) followed by linear ramp down (200 to 0 s^{-1} in 120 s). This cycle was repeated three times with a pause time of 5 s between adjacent cycles. Yield stress was obtained by fitting Herschel Bulkley equation to the downward curves of each cycle. Apparent viscosity (a ratio of shear stress to shear rate) at 125 s^{-1} was considered for comparison between the mixtures. Setting time of alkali activated binders was determined as per ASTM C 191 [8].

3 Results and Discussions

Yield stress values for all the considered AAS binders are shown in Fig. 1. It is observed that AAS binders with 1% SO_3 content are having relatively low yield stress values when compared to 0 and 2% SO_3 content. It is also observed that the mixtures (1% SO_3) are workable for more than 19 min whereas the binders with 0% and 2% SO_3 content are not even workable till 15 min (missing columns in Fig. 1(c)) which reflects that 1% SO_3 content enhanced the workability and workable times of AAS binders. The main effects plot of fitted means for yield stress measured at the end of third cycle (19 min) is shown in Fig. 2. The points to be noted from the plot are: (i) decrement in yield stress is observed with an increment in % of Na_2O and w/b ratio (ii) reduction in yield stress is observed with 1% SO_3 content when compared to AAS binders having 0% and 2%. Apparent viscosity measured at 125 s^{-1} shear rate for all the mixtures are presented in Fig. 3 and corresponding main effects (fitted means) plot is given in Fig. 4. It is observed that the apparent viscosity has decreased with decrease in activator dosage and with increase in w/b ratio and SO_3 content. Increment in SO_3 content from 1% to 2% resulted in an increase in yield stress and a decrease in apparent viscosity values. Greenberg et al. [6] observed an increase in yield stress and apparent viscosity of cement paste with increase in gypsum content from 3% to 7%. At lower SO_3 content, the dissolved sulphate ions might have reacted with aluminates and calcium dissolved from slag to form ettringite. Ettringite is found to be one of the main hydration products in sodium sulphate activated slag pastes [5, 9]. The formation of ettringite would have retarded the formation of primary C-S-H which is the main hydration product in sodium silicate activated slag binders that happens in the absence of sulphates [10]. At higher SO_3 concentration, the suspension might have reached supersaturation with respect to sulphates and would have led to rapid crystallization of gypsum (formed due to reaction of calcium and sulphate ions in the solution) [6]. Therefore, the observed stiffness in the paste can be attributed to the network formed by gypsum. This stiffening phenomenon which is caused due to crystallization of gypsum

in cement pastes is termed as plaster set or false set and plasticity can be recovered by continuous mixing unlike flash set [1, 6, 11]. Increased yield stress and decreased apparent viscosity is observed in mixtures having 2% SO_3 content and at lower activator dosages. This increase in yield stress might be due to formation of ettringite or gypsum. The dissolution of slag and the formation of Q^0 (monomers) would have resulted in decrease of viscosity. At higher activator dosages, the availability of free water is less and hence this would have resulted in higher viscosities with lower yield stress values. The formation of stable hydration products (if any) would also have resulted in increased apparent viscosity [12]. However, gypsum is not stable at pH above 13 and is highly stable at pH around 8 [13]. Therefore, the reason for increment in yield stress at higher SO_3 concentration needs further investigation. Reduction in yield stress and apparent viscosities with increment in water to binder ratio is due to decreased solid volume fraction [14, 15]. The viscosity of sodium silicate solution increases with increase in % of Na_2O at a constant molar modulus [16].

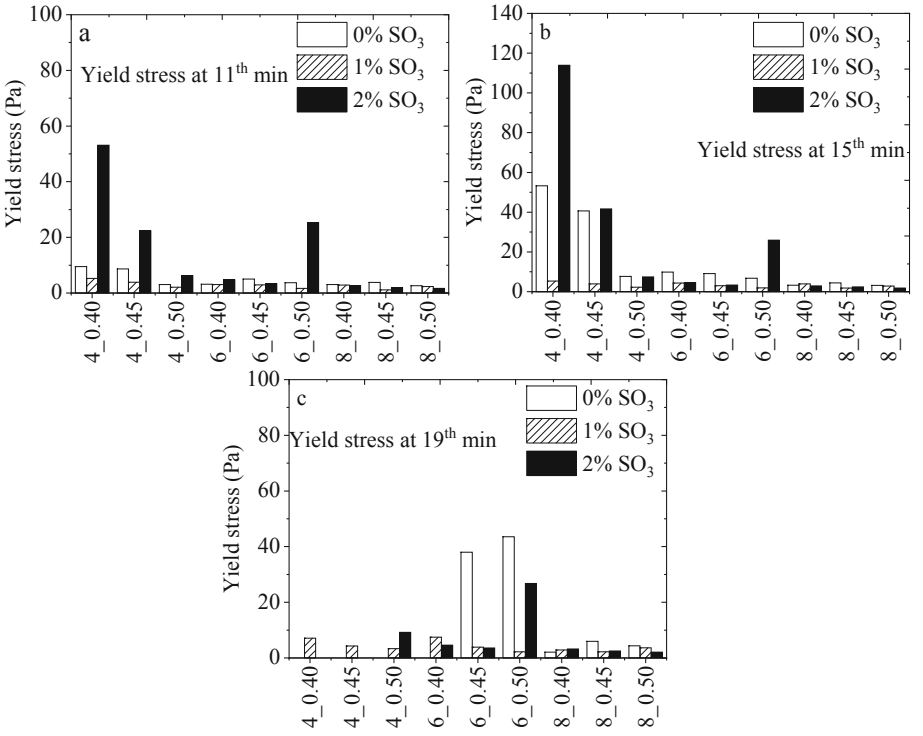

Fig. 1. Yield stress of AAS binder after (a) 11th min (b) 15th min (c) 19th min. 4_0.40 represents 4% of Na_2O and 0.40 w/b ratio.

From the results of yield stress (Fig. 2), it was observed there is a reduction in yield stress value by an average of 35% upon increasing the sulphate content of slag to 1%. The reduction in yield stress with increased amount of sulphates is attributed to

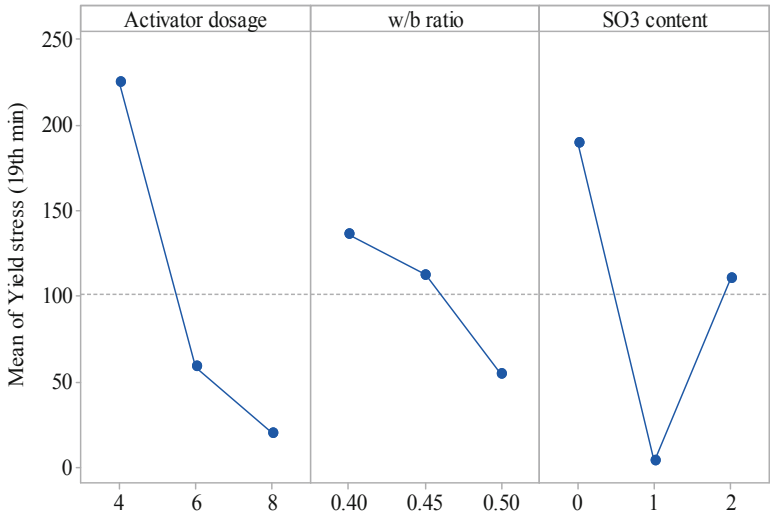

Fig. 2. Main effects plot (fitted mean) for the yield stress (Pa) measured after third cycle.

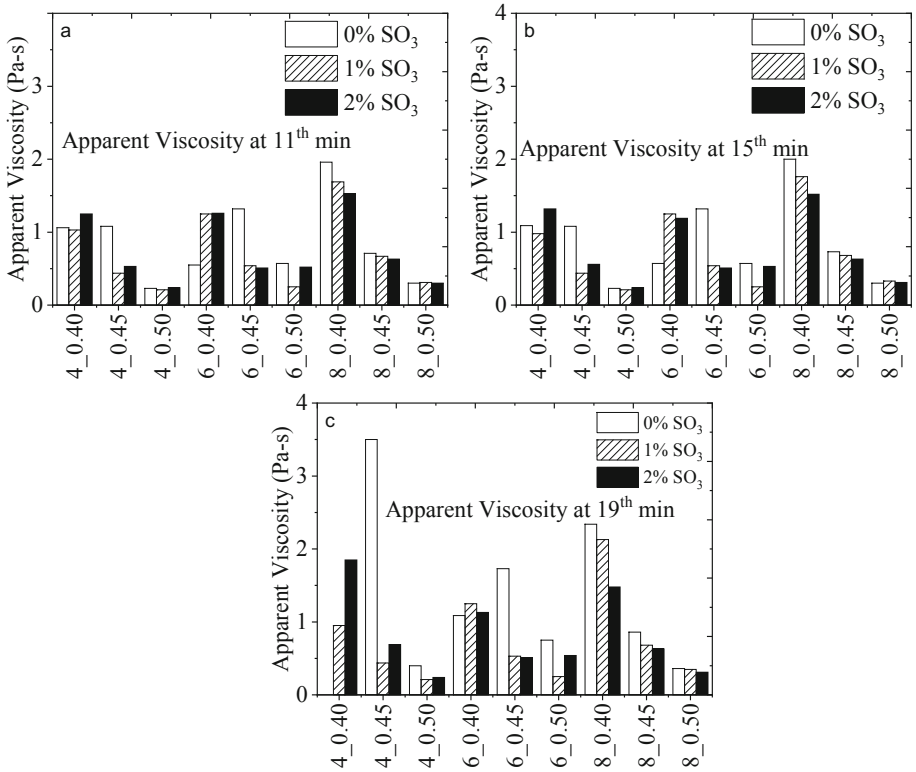

Fig. 3. Apparent viscosity of AAS binder after (a) 11th min (b) 15th min (c) 19th min. 4_0.40 represents 4% of Na_2O and 0.40 w/b ratio.

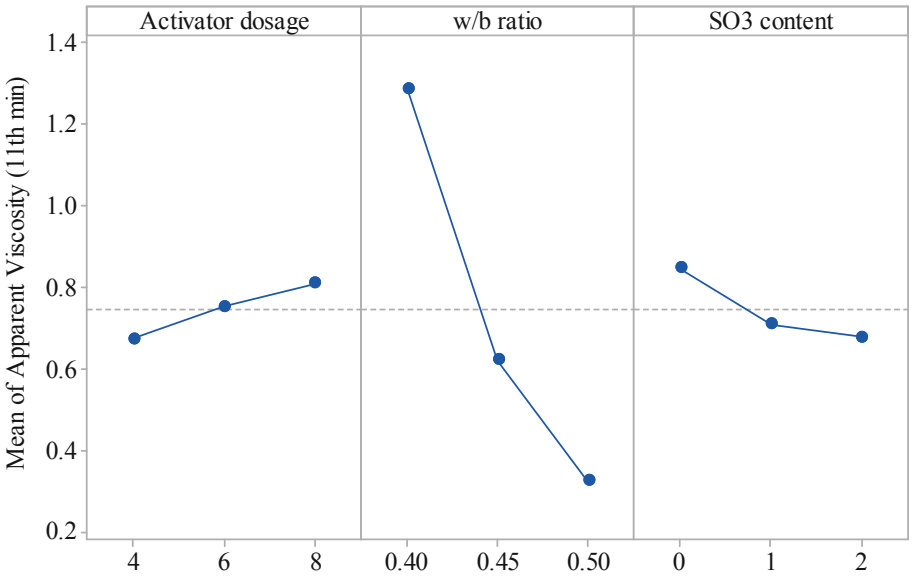

Fig. 4. Main effects plot (fitted mean) for apparent viscosity (Pa-s) measured after first cycle.

retardation effect. It was attempted to observe this retardation effect in terms of setting time. Setting time (which is the onset of rigidity) of alkali activated slag with 0% and 1% sulphates are shown in Fig. 5. Longer initial and final setting times were obtained with 1% when compared to 0% SO_3 content which might be due to retardation in the formation of primary C-S-H. This retardation effect is more predominant at lower activator dosages. The yield stress of the material is the one which resists the penetration of the needle. The needle penetrates if the yield stress of the material is less than the stress generated by the weight of needle. Therefore, the materials with high yield stress should exhibit shorter setting time when compared to the materials with low yield stress [17]. However, it is also observed that the mixtures having low activator dosage exhibited longer setting time and higher yield stress. Further study is necessary to understand the actual reason behind this phenomenon. Higher the activator dosage, higher is the concentration of OH^- ions due to which the dissolution of slag increases and this increases the reaction rate. Therefore, the mixtures with higher activator dosages exhibit shorter setting times when compared to lower activator dosage.

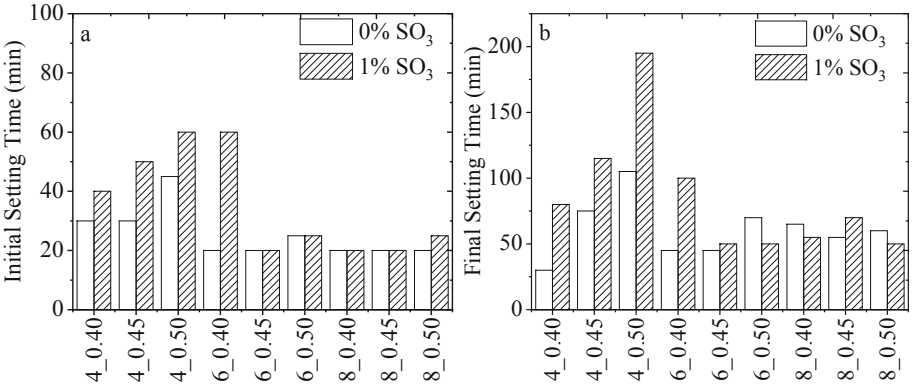

Fig. 5. (a) Initial setting time (b) Final setting time of AAS binders.

4 Conclusions

The rheological behavior of AAS binders was found to be dependent on the amount of sulphate content, w/b ratio, and activator dosage (% of Na_2O). The yield stress was found to decrease with increase in % of Na_2O and w/b ratio. Reduction in yield stress and apparent viscosity was observed with increment in SO_3 content from 0% to 1%, whereas an increase in yield stress was observed with further increment to 2%. The setting time was found to increase with increase in SO_3 content at lower activator dosages. The amount of SO_3 content was found to have a significant effect on the yield stress, apparent viscosity and setting time of AAS binders.

References

1. Taylor HFW (1997) Cement chemistry, 2nd edn. Thomas Telford Publishing, London
2. Pacheco-Torgal F, Castro-Gomes J, Jalali S (2008) Alkali-activated binders: a review. Part 1. Historical background, terminology, reaction mechanisms and hydration products. Constr Build Mater 22:1305–1314
3. Fernández-Jiménez A, Puertas F (2001) Setting of alkali-activated slag cement. Influence of activator nature. Adv Cem Res 13:115–121
4. Chang JJ (2003) A study on the setting characteristics of sodium silicate-activated slag pastes. Cem Concr Res 33:1005–1011
5. Rashad AM, Bai Y, Basheer PAM et al (2013) Hydration and properties of sodium sulfate activated slag. Cem Concr Compos 37:20–29
6. Greenberg SA, Meyer LM: Rheology of fresh Portland cement pastes. Influence of calcium sulfates (1963)
7. ASTM C305 (2014) Standard practice for mechanical mixing of hydraulic cement paste and mortars of plastic consistency
8. ASTM C191 (2018) Standard test methods for time of setting of hydraulic cement by Vicat needle
9. Mobasher N, Bernal SA, Provis JL (2016) Structural evolution of an alkali sulfate activated slag cement. J Nucl Mater 468:97–104

10. Wang S, Scrivener KL (1995) Hydration products of alkali activated slag Cement. Cem Concr Res 25:561–571
11. Ghosh SN (1983) Advances in cement technology, 1st edn. Pergamon Press, Oxford
12. Tattersall GH, Banfill PFG (1983) The rheology of fresh concrete. Pitman Publishing Inc, Boston
13. Liu K, Deng M (2015) Influence of pH on the formation of gypsum in cement materials during sulfate attack. Adv Cem Res 27:487–493
14. Struble L, Sun GK (1995) Viscosity of Portland cement paste as a function of concentration. Adv Cem Based Mater 2:62–69
15. Toutou Z, Roussel N (2006) Multi scale experimental study of concrete rheology: from water scale to gravel scale. Mater Struct 39:189–199
16. Vail JG, Wills J (1952) Soluble silicates - their properties and uses. Reinhold publishing corporation, New York
17. Lootens D, Jousset P, Martinie L et al (2009) Yield stress during setting of cement pastes from penetration tests. Cem Concr Res 39:401–408

Bio-Derived Rheology Modifying Agents for Cement-Based Materials

Mahzad Azima[1] and Zeynep Başaran Bundur[2(✉)]

[1] Department of Structural Engineering, Ghent University, Ghent, Belgium
[2] Civil Engineering Department, Ozyegin University, Istanbul, Turkey
zeynep.basaran@ozyegin.edu.tr

Abstract. In recent few years, significant development has been made in concrete technology to accommodate the requirements of high-performance concrete. Rheology Modifying Agents (RMAs) (such as superplasticizers) and Viscosity Modifying Agents (VMAs) have been developed as two alternative admixtures to obtain the required workability. However, these admixtures not only increased the environmental impacts of concrete production but also increased the unit cost of concrete. Following these concerns, several studies have been focusing on exploring more sustainable approaches in concrete production such as the use of bio-based admixtures in concrete production. Throughout the literature, bio-based polysaccharides (cellulose, chitosan, etc.) were found to be highly effective as VMAs. Long chain molecules of these polysaccharides stick to the water molecules, decrease their relative motion and forms a gel, so increase the yield stress and plastic viscosity. This behaviour reduces the bleeding and segregation, which results in robust highly workable concrete.

The interest in this study was motivated by the vital demand to introduce a greener and more sustainable VMA to improve the rheological properties of cement paste. To this end, bacterial cells proposed as VMAs for cement-based materials. The bacterial cells were directly incorporated into the mix of water without any additional intervention. The rheological measurements were implemented to evaluate the influence of cells on apparent viscosity and yield strength. In addition, the use of superplasticizers and fly ash on the performance of biological VMA were also investigated. Our results showed that the apparent viscosity and yield stress of the cement-paste mix were increased with the addition of the microorganisms. Moreover, bacterial cells were found to be compatible with the use of both fly ash and superplasticizers.

Keywords: Cement paste · Rheology · Viscosity · Yield stress · Microorganisms

1 Introduction

Recent development in concrete technology enabled the design of highly flowable concrete mixes with improved workability. These advanced mixes require incorporation of viscosity modifying agents (VMA) to reduce the possible segregation and

V. Mechtcherine et al. (Eds.): RheoCon 2019/SCC 2019, RILEM Bookseries 23, pp. 79–86, 2020.
https://doi.org/10.1007/978-3-030-22566-7_10

bleeding due to the use of superplasticizers. Commercially available polysaccharide VMAs on the market increasing the cost of SCC manufacturing, leading to a decreasing demand on the admixture. Thus, alternative bio-based VMAs could be listed as algae, bacterial cell walls or fermentation products such as extracellular polysaccharides (EPS) or diutan gum [1]. Sonobi [2] studied the effect of diutan gum on the rheology of cement-based materials containing fly ash compared to welan gum and found that both additive materials could increase the viscosity and yield stress. An extensive study was undertaken, using extracellular polysaccharides (EPS) from *Paenibacillus sp.* in cement paste as VMAs, which recorded and improvement in segregation, in lower dosages of EPS [3]. Pei et al. [4] showed that use of *Bacillus subtilis* cells walls could increase the viscosity of cement paste. However, extraction of cell walls again requires processing and labor. In fact, bacteria are known to be VMAs not only their complicated cell wall structure, they can influence rheology as being microswimmers [5].

While diverse biologically derived polysaccharides are VMAs, there is no knowledge of whether the direct addition bacterial cells with minimum manipulation could actually influence the rheology of cement paste. The main objective of this study was to evaluate the possible use of *Sporosarcina pasteurii* (*S. pasteurii*), *Bacillus megaterium* (*B. megaterium*), *Bacillus subtilis* (*B. subtilis*) and *Paenibacillus polymyxa* (*P. polymyxa*) cell as VMAs in cement paste. To achieve this goal, these gram-positive bacterial cells were grown in specified nutrient media and then harvested from the inoculum by centrifuging. Then, these cells were suspended in mixing water without any extra intervention and their influence on the rheology of cement paste was investigated.

2 Materials and Methods

2.1 Microorganism Growth

Four different type of bacterial strains, *S. pasteurii, B. megaterium, B. subtilis* and *P. polymyxa,* were used in this study. *S. pasteurii* (German Collection of Microorganisms and Cell Cultures-DMSZ 33) cells were cultured in a Urea-Corn Steep Liquor Medium (UCSL) at pH 9, which includes Tris base (15 g), urea (10 g) and Corn Steep Liquor (CSL) (15 g) to a liter of deionized water (DI). *P. polymyxa* cells were cultured in a nutrient medium including yeast extract (5 g), NaCl (5 g), and peptone (10 g) to 1-L DI water and the pH was adjusted to 7. Both *B. megaterium* (American Typical Cell Cultures- ATCC 14581) and *B. subtilis* (ATCC 6051) were grown in a medium containing Nutrient Broth (8 g) per 1 L DI water and pH was adjusted to 8. First, the nutrient media were sterilized at 121 °C for 45 min. Then, cells were added in 300 mL of sterilized liquid nutrient media and incubated aerobically with shaking conditions (210 rpm) at 30 °C. Then, the cells were collected from the culture by centrifuging at 6300 g for 15 min. Then the cells were washed twice by PBS (Phosphate buffered solution) and stored at 4 °C until testing.

2.2 Preparation of Cement Paste Samples

Cement paste samples were prepared containing Ordinary Portland Cement (OPC) CEM I 42.5 R, as the binder, accordingly to the norm EN 197-1. The mixtures were prepared at a w/c of 0.40 and 0.50. To determine the effects of superplasticizers and fly ash on the performance of the biological VMA, a polycarboxylate superplasticizer (by 0.1 kg/kg binder) and F-type fly ash (by 20% of the cement weight) was added to samples. To investigate the effect of microorganisms on the rheology of the cement paste, the abovementioned collected cells were directly added to the mixing water. The number of cells was adjusted in terms of percent weight of binder, such as 0.10% of the cement weight. The cement paste samples were manufactured according to ASTM C305-14.

2.3 Rheological Measurements

Rheological measurements were made at room temperature (23 °C) with ANTON PAAR RheolabQC rotational rheometer (Anton Paar, Graz, Austria). To ensure the homogeneity of the mixtures, a pre-shear stage where the shear rate was kept constant at 100 s^{-1} for another 60 s. Following the pre-shear stage, the analysis was conducted by decreasing the shear rate from 100 s^{-1} to 1 s^{-1} and the yield stresses and viscosity were recorded. The downcurve was chosen for evaluation of the rheological behavior of the samples. The rheological behavior of the cement paste was evaluated using the Bingham model (1). Where τ_0 is the yield stress (Pa), μ is the plastic viscosity (Pa.s), and $\dot{\gamma}$ is the shear rate (s^{-1}).

$$\tau = \tau_o + \mu\dot{\gamma} \tag{1}$$

An alternative model also should be considered, since the shear-thinning or shear-thickening behavior of mixes were unknown. A modified Bingham equation was also used to analyze shear-thickening cement paste samples (2), which could also explain the shear thinning behavior as well [6].

$$\tau = \tau + \mu\dot{\gamma} + c\dot{\gamma}^n \tag{2}$$

Where τ is the shear stress (Pa), τ_0 is the yield stress (Pa), μ is plastic viscosity, $\dot{\gamma}$ is the shear rate (s^{-1}) and c is a 2nd-degree parameter (Pa.s^2) [6].

2.4 Mini-Slump Test

The mini-slump test was conducted based on the measurement of the spread of cement paste placed into a cone-shaped mold on smooth plexiglass. For this approach, a specially manufactured stainless-steel cone with a height of 57.2 mm, an upper diameter of 19 mm and a lower diameter of 38.1 mm was used [7]. The cone was placed on the center of the plexiglass, and, immediately after mixing, the sample was filled into the cone. The cone was then lifted to let the cement paste flow. Then, the diameters at four right-angle positions were measured and the average diameter was calculated.

3 Results and Discussion

This study was undertaken to evaluate the possible use of bacterial cells as VMA in cement paste. Figure 1 summarizes the yield stress values calculated from Bingham model and relationship with yield stress and mini slump diameters. For cement paste samples without any FA or SP, incorporation of cells, except *P. polymxa,* resulted with a significant increase in the yield stress value regardless of the w/c (Fig. 1). Relatedly, the mini-slump diameters were found to be lower compared to control neat paste. Interestingly, the addition of *P. polymxa* cells to cement paste slightly decreased the yield stress compared to control neat paste. Incorporation of *P. polymxa* cells to FA amended cement paste improved its performance in terms of increasing the yield stress however the recorded yield stress was still lower than that was obtained when *B. megaterium* and *S. pasteurii* cells were incorporated. A similar influence was also observed *B. subtilis* was incorporated with FA where yield stress values were less than counterpart control neat paste.

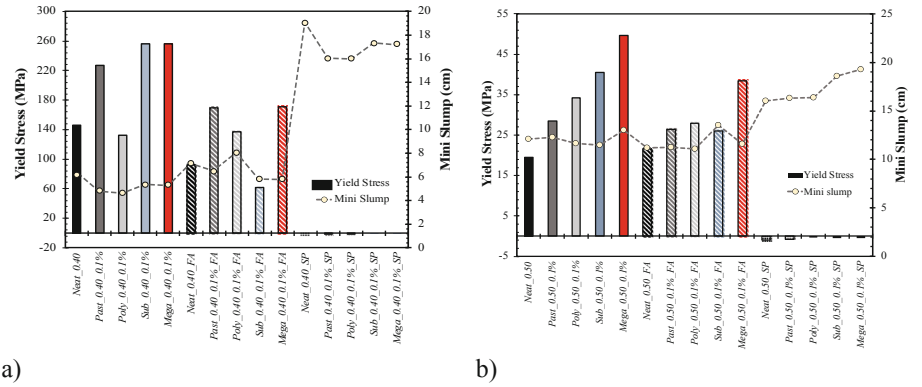

a) b)

Fig. 1. Yield stress and mini slump test results for cement paste samples with and without cells at w/c's of (a) 0.40 and (b) 0.50. Cell dosage was kept at 0.1% per weight of cement. Neat: Control paste; *Sub:* Cement paste containing *B. subtilis*; *Mega:* Cement paste containing *B. megaterium*; *Poly:* Cement paste containing *P. polymxa*; *Past:* Cement paste containing *S. pasteurii.*

The higher efficiency of *B. megaterium* from the rest of the cells could be explained by its cell size and composition. Yet, this strain was selected due to its size and thick cell wall, which presumably have a relatively high volume of polysaccharides and peptidoglycans. Thus, it might lead to higher water retention leading to a higher increase in yield stress and viscosity. Incorporation of SP leads to 0 yield stress and higher mini-slump values regardless of the w/c, which inhibits an accurate evaluation of yield stress in samples.

On a related note, there was a difference between mini-slump test results rand rheological analysis, which could be attributed to difference in applied shear rates. The mini-slump cone test was employed with a significantly lower shear rate than that was

imposed during the rheological analysis [8]. Considering the pseudo-plastic behavior of cement paste, the material response to these two different shear modes and rates was not the same.

Interestingly, incorporation of *P. polymxa* cells increased the yield stress of cement paste at a w/c of 0.50 (*see* Fig. 1(b)). Thus, at low w/c it might be possible that the material might not be able to flow immediately around the rotating vane at low shear rates thus leaving an air gap between the vane and the matrix. The presence of this gap reduces the shear stress transfer to the surrounding cement paste thus resulting with both lower yield stress and viscosity [9].

In general, all cement pastes exhibited a shear-thinning behavior (Fig. 2) regardless of the type of bacterial strain and addition of cells increased the viscosity of the cement paste regardless of the w/c used. This might be directly related to the expected action mechanism of bacterial cells as a VMA. Incorporation of polysaccharides and peptidoglycans in the cells structure resulting in an increasing intertwining of chains and leading to a higher water retention particularly at low shear-rates [10, 11]. In addition, these cells are negatively charged and it is known that they can interact with calcium [Ca^{+2}] ions present in the environment [12]. The cells could bind [Ca^{+2}] on the surface of cement particles along with the entrapped water between interwinding polysaccharides and peptidoglycans chains; thus, additionally increasing the viscosity of cement paste by increasing flocculation and agglomeration of the solids in the mix. However, with increasing shear rate the chains would break and releasing the water to the mix, leading to a more pronounced decrease in viscosity compared to low shear rates.

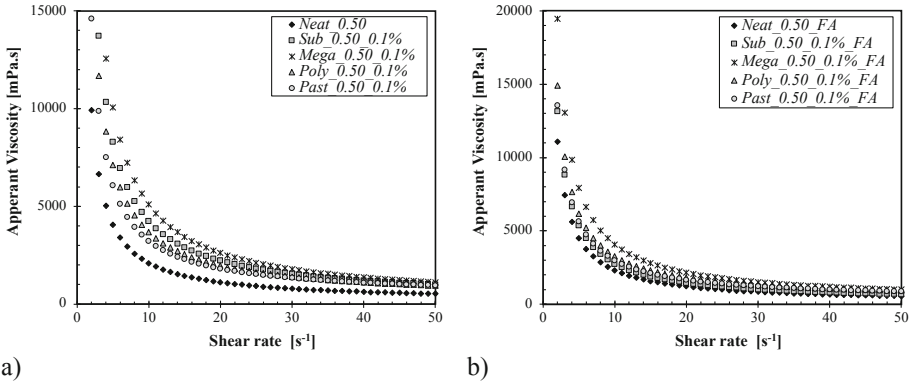

Fig. 2. Viscosity curves for cement paste samples without any additives. Cell dosage was kept at 0.1% per weight of cement with a w/c of (a) 0.40 and (b) 0.50. Neat: Control paste; *Sub:* Cement paste containing *B. subtilis*; *Mega:* Cement paste containing *B. megaterium*; *Poly:* Cement paste containing *P. polymxa*; *Past:* Cement paste containing *S. Pasteurii.*

Figures 3, 4 and 5 summarizes the apparent viscosity values calculated at shear rates of 17,20,27 and 34 s^{-1} for all samples with and without cells, which would be observed in casting and placing of concrete [13]. As expected, impact of *P. polymxa*

cells on viscosity was less pronounced compared to rest of the cell types. A similar influence was also observed when *B. subtilis* was incorporated to fly ash amended cement paste at low w/c. Even though, there is not a simple explanation regarding the complex interaction of microorganisms with fly ash at low w/c, the cells might influence the particle to particle interaction and induce a repulsive force with the F-type fly ash particles. Even though high plastic viscosity was expected in these low w/c mixes, the material might not able to flow immediately that could result with lower viscosity values [9].

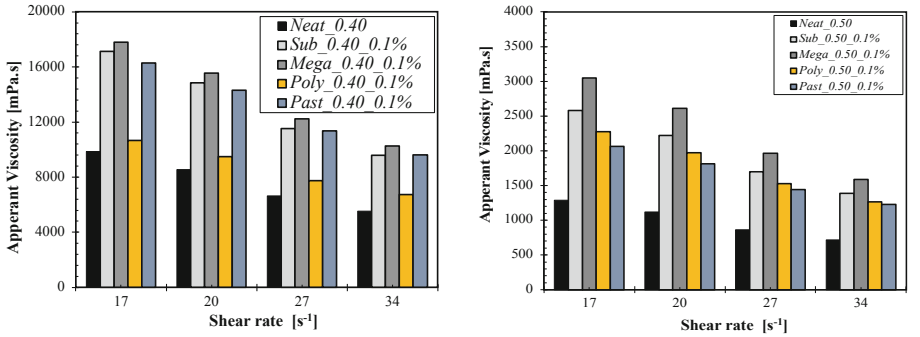

Fig. 3. Apparent viscosity values for samples at shear rates of 17, 20, 27 and 34 s^1. Cell dosage was kept at 0.1% per weight of cement with a w/c of (a) 0.40 and (b) 0.50. Neat: Control paste; *Sub:* Cement paste containing *B. subtilis*; *Mega:* Cement paste containing *B. megaterium*; *Poly:* Cement paste containing *P. polymxa*; *Past:* Cement paste containing *S. Pasteurii.*

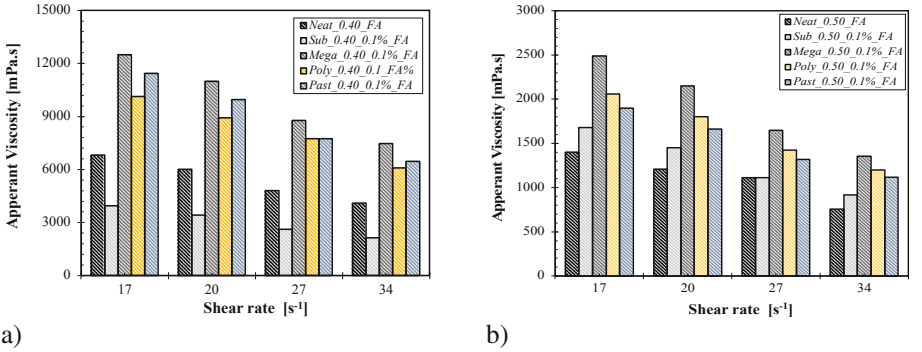

Fig. 4. Apparent viscosity values for samples at shear rates of 17, 20, 27 and 34 s^{-1}. Cell dosage was kept at 0.1% per weight of cement including fly ash with a w/c of (a) 0.40 and (b) 0.50. Neat: Control paste; *Sub:* Cement paste containing *B. subtilis*; *Mega:* Cement paste containing *B. megaterium*; *Poly:* Cement paste containing *P. polymxa*; *Past:* Cement paste containing *S. Pasteurii.*

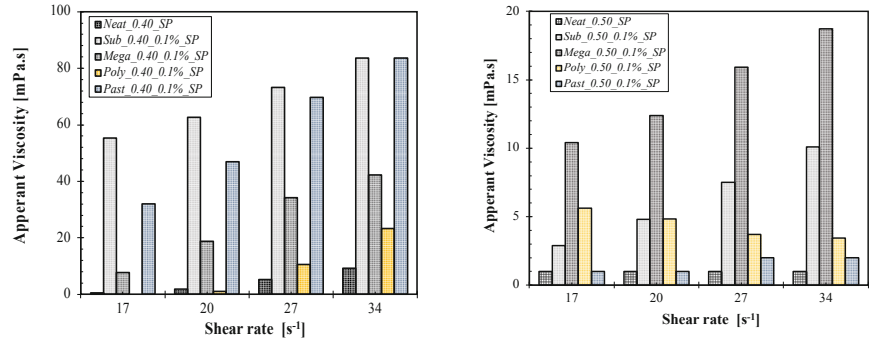

Fig. 5. Apparent viscosity values for samples at shear rates of 17, 20, 27 and 34 s^{-1}. Cell dosage was kept at 0.1% per weight of cement including superplasticizers with a w/c of (a) 0.40 and (b) 0.50. Neat: Control paste; *Sub:* Cement paste containing *B. subtilis*; *Mega:* Cement paste containing *B. megaterium*; *Poly:* Cement paste containing *P. polymxa*; *Past:* Cement paste containing *S. pasteurii*

Incorporation of superplasticizers completely changed the rheological behavior of cement paste samples regardless of the w/c used (see Fig. 5). The use of a very strong polycarboxylate superplasticizer resulted with a shear-thickening behavior rather than shear thinning behavior previously observed in rest of the samples. In this case, the shear-thickening cement paste behavior mix would not be simply explained by Bingham equation (see Sect. 2.3). Instead, a modified Bingham equation was used to analyze shear-thickening cement paste samples [6]. In addition, high flowability in these samples, particularly in neat control paste, lead excessive segregation which might interfere test results. This effect was also eliminated at low shears along with addition of cells.

Further rheological studies should be conducted with different instrument geometries and measuring methods to actually define the exact influence of cells on rheology. Although, it might not be possible to drive a quantitative statement in terms of increase in viscosity, we could still conclude that the bacterial cells, particularly *B. megaterium*, could serve as VMAs in cement-based materials.

4 Summary and Conclusion

This study represented the results of an extensive study undertaken to evaluate the possible use of microorganism VMA. The rheological behavior of cement paste samples including *P. polymxa, S. pasteurii B. megaterium* and *B. subtilis* cells were evaluated through rheological tests. Moreover, the compatibility of cells with the use of superplasticizer and fly ash, as well as the influence of w/c were investigated. Incorporation of cells increased the apparent viscosity regardless of the w/c used for the mixes. This influence was attributed to the interwinding of peptidoglycan chains leading to an increase in viscosity of mix water. The influence of cells was much more

pronounced at a w/c of 0.40 than it was at 0.50. *B. megaterium* cells showed a better performance among the strains tested considering their efficiency in increasing viscosity, compatibility with fly ash and superplasticizers. This novel study could be considered as a preliminary evaluation of a bio-based grout with improved rheology. Further studies have to be conducted to understand the other possible parameters of cells influencing the rheology such as the effect of cells on drag forces and particle-to-particle interaction. With the exploitation of these mechanisms will lead to the possible use of this grout in practice applications.

Acknowledgement. This research was conducted by financial assistance of the Scientific and Technical Research Council (TUBITAK) of Turkey Project: MAG-116M183. The authors also acknowledge BASF for providing the required chemical admixtures.

References

1. León-Martínez FM, Cano-Barrita PFDJ, Lagunez-Rivera L, Medina-Torres L (2014) Study of nopal mucilage and marine brown algae extract as viscosity-enhancing admixtures for cement based materials. Constr Build Mater 53:109–202
2. Sonebi M (2006) Rheological properties of grouts with viscosity modifying agents as diutan gum and welan gum incorporating pulverised fly ash. Cem Concr Res 36:1609–1618
3. Kahng GG, Lim SH, Yun HD, Seo WT (2001) Production of extracellular polysaccharide, EPS WN9, from *Paenibacillus sp.* WN9 KCTC 8951P and its usefulness as a cement mortar admixture. Biotechnol Bioprocess Eng 6:112–116
4. Pei R, Liu J, Wang S (2015) Use of bacterial cell walls as a viscosity-modifying admixture of concrete. Cem Concr Compos 55:186–195
5. Saintillan D (2012) Kinetic models for biologically active suspensions. Technical report. Department of mechanical science and engineering, University of Illinois at Urbana-Champaign, Urbana, Illinois
6. Feys D, Verhoeven R, De Schutter G (2008) Fresh self compacting concrete, a shear thickening material. Cem Concr Res 38:920–929
7. Khayat KH (1998) Viscosity-enhancing admixtures for cement-based materials — an overview. Cem Concr Compos 20:171–188
8. Khayat KH, Yahia A (1998) Simple field tests to characterize fluidity and washout resistance of structural cement grout. Cem Concr Aggregates 20:145–156
9. Koutný O, Snoeck D, Van Der Vurst F, De Belie N (2018) Rheological behaviour of ultra-high performance cementitious composites containing high amounts of silica fume. Cem Concr Compos 88:29–40
10. Lachemi M, Hossain KMA, Lambros V, Nkinamubanzi PC, Bouzoubaâ N (2004) Self-consolidating concrete incorporating new viscosity modifying admixtures. Cem Concr Res 34:917–926
11. Schmidt W, Brouwers HJH, Kühne HC, Meng B (2013) The working mechanism of starch and diutan gum in cementitious and limestone dispersions in presence of polycarboxylate ether superplasticizers. Appl Rheol 23:1–12
12. Stocks-Fischer S, Galinat JK, Bang SS (1999) Microbiological precipitation of $CaCO_3$. Soil Biol Biochem 31:1563–1571
13. Jennings HM, Saak AW, Shah SP (2001) New methodology for designing self-compacting concrete. Mater J 98(6):429–439

Influence of Cements Containing Calcareous Fly Ash on Rheological Properties of Fresh Mortars and Its Variability

Jacek Gołaszewski(✉), Tomasz Ponikiewski, and Aleksandra Kostrzanowska-Siedlarz

Faculty of Civil Engineering, Silesian University of Technology, Gliwice, Poland
jacek.golaszewski@polsl.pl

Abstract. In the research influence of cements containing calcareous fly ashes W as non-clinker constituent produced by different methods on rheological properties of mortars and its variability is presented. In comparison to mortars with CEM I mortars with cements CEM II/A-W, CEM II/B-W, CEM IV/B-W are characterized by worse workability and faster workability loss, the greater the more fly ash W is in cement. However, using cements CEM II/A-W, CEM II/B-W produced by intergrinding of the constituents or homogenization with ground fly ash W it is possible to obtain mixtures with acceptable rheological properties. Obtained results shows significant influence of properties of the fly ash W on the variability of rheological properties of cement CEM II/B-W mortars. However, if fly ashes W with a bulk density of less than 900 kg/m^3 are not used for the production of cement, it is possible to achieve variability of the rheological properties of mortars, to a level not deviating significantly from other types of cements.

Keywords: Rheology · Mortar · Calcareous fly ash · Plasticizer · Cement

1 Introduction

By using the mineral additives beneficial effects can be obtained: technical (in respect to concrete durability), economical (in respect to whole live cycle of construction) and ecological (due to reduction of cement or/and clinker content in cement). Mineral additives can be applied directly to the concrete or as the main constituent of common cement. Currently, standard EN 197-1 provides for the possibility of use as non-clinker constituent of cement, amongst others, calcareous fly ash (W). Calcareous fly ash is produced as a result of burning brown coal in conventional furnaces in large amount – in Poland about 5 million Mg every year is produced [1]. In a large studies [2], it was shown that among the calcareous fly ashes available in Poland, the most favourable properties due to their use in cement has fly ash from the Bełchatów power plant. That fly ash meets the requirements of the PN EN 197-1 in relation to the main constituents of common cement [3]. However, up to date fly ashes W are used as cement constituent to a limited extent. The main problem is a relatively small number of data regarding its influence on hardened concrete properties available. However, in extensive studies

V. Mechtcherine et al. (Eds.): RheoCon 2019/SCC 2019, RILEM Bookseries 23, pp. 87–96, 2020.
https://doi.org/10.1007/978-3-030-22566-7_11

[3–7], it has been shown that the use of fly ash from Bełchatów power plant as cement constituent generally does not adversely affect the properties of hardened concrete.

Important technological problem is the influence of fly ash W on workability of fresh concrete. In raw state fly ash W is characterized by high water demand and it makes it difficult to obtain a fresh concrete with the required and time-stable workability [3, 9–13]. It was shown in [11, 13], that high water demand of fly ash is cased, amongst others by large grains of asymmetrical shape and high porosity. Processing calcareous fly ash by removing these grains can reduce the water demand, which in turn can reduce its impact on the workability [3, 11–13]. It was shown in [11–13] that effective way of processing can be grinding by grinding. In that case large porous grains are broken down and negative influence of fly ash W on the workability may be reduced. Problematic due to controlling workability is the high variability of fly ash W chemical and physical properties. The impact of this variability on the rheological properties of the fresh concrete has not been the subject of extensive studies.

In the paper are presented and discussed the results of investigation into the influence of CEM II and CEM IV) cements containing a different amount of fly ashes W of various properties on rheological properties of mortars and its variability. In a broader aspect, the research contributes to popularize use of cements containing calcareous fly ash in concrete technology, what greatly benefits the environment protection.

2 Introduction

2.1 Research Plan and Variables

Research plan is shown in Table 1. As variable factors in research were adopted:

- cement type: CEM II/A-W, CEM II/B-W, CEM IV/B-W (W content in cement – 15%, 30% and 50% respectively, see Table 4),
- method of cement production: by intergrinding or by homogenization,
- processing of fly ash W: raw or ground fly ash W, homogenized cements,
- variability of fly ash W properties: type CEM II/B-W homogenized cements produced using 6 different batches of fly ash W (see Tables 3 and 4).

Homogenized cements were produced by homogenization of cement CEM I and separately prepared raw or ground fly ash W in ball – mill. Interground cements were produced by intergrinding of clinker, fly ash W, gypsum in a ball-mill. The fly ashes W were taken from the retention tanks through the course of three months.

Table 1. Research plan.

Homogenized cements		Interground cements
Raw W	Processed W	
CEM I	CEM I	CEM I (g)
CEM II/A-W hr	CEM II/A-W hp	CEM II/A-W g
CEM II/B-W hr [various fly ash W batches]	CEM II/B-W hp [various fly ash W batches]	CEM II/B-W g
CEM IV/B-W hr	CEM IV/B-W hp	CEM IV/B-W g

Table 2. Properties of cement and clinker.

	Ingredient, % of mass								Blain specific surface, cm^2/g
	SiO_2	Al_2O_3	Fe_2O_3	CaO	MgO	SO_3	K_2O	Na_2O	
CEM I	19	4.9	2.9	63	1.3	2.8	0.9	0.14	3630
Clinker	20	4.5	2.1	67	1.0	–	0.24	0.54	–

2.2 Materials and Mortar Composition

Properties of cement CEM I, clinker and fly ashes W used in research are presented in Tables 2 and 3. In Table 3 the documentation of variability of fly ashes properties is also presented. The composition of fly ashes and variability of their properties do not differ from those presented in [3]. Composition and properties of cement used are presented in Table 4. The proportions of mortars were based on standard mortar according to EN 196-1, but with *w/c* = 0.55.

Table 3. Properties of fly ash W.

Fly ash W	Loi	SiO_2	Al_2O_3	Fe_2O_3	CaO	SO_3	CaO_w	Fineness, %		Bulk density, kg/m^3
								Raw	Ground	
A	2.6	33.5	19.2	5.4	31.2	4.33	3.43	36.4	23	1098
B	3.4	35.4	21.9	6.1	25.6	4.22	1.24	35.4	13.3	749
C	1.8	40.2	24.0	5.9	22.4	2.49	1.46	55.6	22	1059
D	2.2	41.0	18.5	5.0	25.4	4.25	1.92	50.2	22	845
E	3.0	41.0	15.1	3.6	30.1	3.27	4.57	47.4	21	934
F	3.6	56.9	18.2	3.2	14.1	1.6	1.71	60.4	25	1058
Av	2.8	41.3	19.5	4.9	24.8	3.4	2.4	47.6	21.1	957.2
CV	25	20	16	25	25	34	55	21	19	15

Av - average value, CV - coefficient of variation

Table 4. Properties of cements.

Cement	Constituents, %				Density, g/cm^3	Water demand, %	Specific surface, cm^2/g
	CEM I	Clinkier	W	Gypsum			
Reference cements							
CEM I	100	–	–	–	3.09	27.6	3630
CEM I (g)	–	95	–	5	3.10	25.8	3810

(*continued*)

Table 4. (*continued*)

CEM II/A-W, CEM II/B-W, CEM IV/B-W (fly ash W batch - A)						
CEM II/A-W (hAr)	85	–	15	2.99	30	3640
CEM II/B-W (hAr)	70	–	30	2.95	31	3570
CEM IV/B-W (hAr)	50	–	50	2.85	32.2	3420
CEM II/A-W (hAp)	85	–	15	3.04	26.5	4020
CEM II/B-W (hAp)	70	–	30	2.99	28	4070
CEM IV/B-W (hAp)	50	–	50	2.92	30.2	4150
CEM II/A-W (gA)	–	81.1	14.3	3.04	27.6	4190
CEM II/B-W (gA)	–	67.7	29	2.98	30.4	4030
CEM IV/B-W (gA)	–	49.2	49.2	2.88	31.4	4000
CEM II/B-W (fly ash W batch - B, C, D, E, F)						
CEM II/B-W hBr	70	–	30	2.93	35.6	3930
CEM II/B-W hCr				2.93	29.8	3630
CEM II/B-W hDr				2.95	30.6	3580
CEM II/B-W hEr				2.96	31.0	3530
CEM II/B-W hFr				2.95	30.0	3180
CEM II/B-W hBp				2.95	34.2	4440
CEM II/B-W hCp				2.96	29.8	4030
CEM II/B-W hDp				2.99	30.8	4300
CEM II/B-W hEp				2.98	30.8	4230
CEM II/B-W hFp				2.98	29.8	3930

2.3 Testing Method

Rheological behaviour of mortar is usually described by parameters of the Bingham model - yield stress τ_o and plastic viscosity η_{pl} [14]. Schleibinger rotational Viskomat NT rheometer was used for measuring mortars rheological parameters. For this rheometer determined are yield value *g* (Nm) and plastic viscosity *h* (Nm s), corresponding to yield stress τ_o and plastic viscosity η_{pl} respectively. Theoretical basis and rules for rheological measurements are discussed widely in [15]. It is necessary to notice that studies on rheology of mortars and concretes indicate that results of rheological measurements obtained for mortars are suitable for prediction of fresh concrete rheology [16]. The mixer and mixing procedure of mortars were compliant with EN 196-1. After mixing mortars samples were transferred to rheometer and tested after 5 min and 90 min. The measurement procedure is presented in [17]. Mortars temperature was maintained 20 °C ± 1 °C using thermostatic device.

3 Test Results and Discussion

The effect of CEM II/A-W, CEM II/B-W and CEM IV/B-W cements on the rheological properties of mortars is shown on Fig. 1. In general, the use of cements with fly ash W in place of CEM I cement causes increase in yield value *g* and plastic viscosity *h* of mortars after 5 min and 90 min, thus worsening their workability. The yield value *g* and plastic viscosity *h* increase is the higher the more fly ash W is in cement, in the range dependent on the cement production method. The negative effect of cements containing fly ash W on the workability of mortars is clearly strongest when homogenized cements with raw fly ash W are used. In this case significant worsening of workability can be observed already when content of fly ash W in cement is only 15% (CEM II/A-W). This demonstrates the low usefulness of raw fly ash W as a component of homogenized cements. In the case of mortars with interground cements or cements homogenized with ground fly ash W the worsening of workability is moderate when amount of fly ash W is not higher than 30% (CEM II/A-W or CEM II/B-W). Workability worsening becomes significant when the amount of fly ash W is increased to 50% (CEM IV/B-W). This shows that using homogenized cements with ground fly ash W or interground cements it can be possible to develop mixtures with acceptable workability. However, even for these cements, the amount of W should not exceed 30%.

Comparing with study [13], the nature of the influence of fly ash W on the rheological properties of mortars when it is used as a cement constituent or as a type II additive is analogous. However, if fly ash W is used as the cement constituent, its negative influence on the rheological properties seems to be lower. Using fly ash W as a cement constituent enables to obtain the mortars (and concrete) with better workability when analogous amount of the same fly ash W is added directly to the mixture. It is probably caused by the additional grinding of the fly ash W during the process of cement production.

Influence of fly ash W batch on rheological properties of mortars with homogenized CEM II/B-W is shown on Fig. 2. In general, it has been confirmed, that the batch of fly ash W (and more specifically variation in fly ash W physicochemical properties) significantly influences rheological properties of mortars with cement CEM II/B-W.

Coefficient of variation CV of rheological parameters of mortars with CEM II/B-W due to fly ash W batch are given in Table 5. It is commonly assumed that if the CV for rheological parameters of mortar caused by given factor is higher than 10%, this factor probably influences the variability of rheological properties. If CV is higher than 15%, influence of this factor is very strong. It should be note, that as study [17] indicate, the average CV_{av} for a series of measurements of rheological parameters performed using Viskomat NT under the same conditions are 4,7% and 4.2% for the yield value g and the plastic viscosity h respectively. Taking the above into account, if the CV is higher than 10% and less than 15%, it means that the influence of variability of rheological properties of mortars is significant, but it does not hinder the control of workability of mixture. If the CV is higher than 15%, it should be considered that the variability of rheological properties of mortars is very significant, and hinders the control of mixture

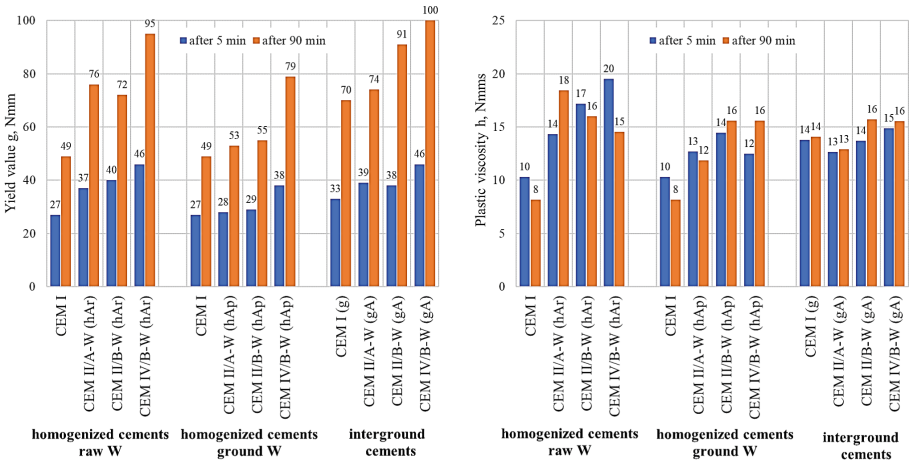

Fig. 1. Rheological properties of mortars made of cements, CEM II/A-W, CEM II/B-W and CEM IV/B-W. (a) Yield value, (b) Plastic viscosity.

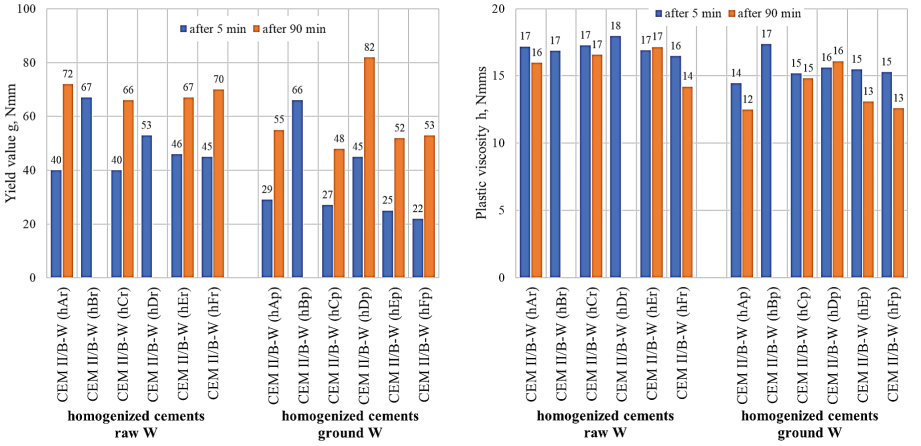

Fig. 2. Influence of fly ash W batch on rheological properties of mortars with CEM II/B-W cement. (a) Yield value, (b) Plastic viscosity.

workability. The variation of the yield stress g of mortars with cements CEM II/B-W both with raw and the processed fly ash W is clearly higher than 15% and influence of fly ash W batch should be assessed as very significant from technological point of view. It makes the industrial use of W as a component of cement problematic.

Table 5. Coefficients of variation of rheological parameters of CEM II/B-W mortars.

	CEM II/B-W with raw fly ash W				CEM II/B-W with ground fly ash W			
	g, Nmm		h, Nmms		g, Nmm		h, Nmms	
	5 min	90 min	5 min	90 min	5 min	90 min	5 min	90 min
CEM II/B-S with all fly ash W batches								
Av	48	69	17.1	16.0	35	58	15.6	13.8
CV	21%/	–	3%/	–	47%	24%	6%	11%
CEM II/B-S with fly ash W of bulk density >900 kg/m^3								
Av	43	69	17	16.0	26	52	15.1	13.2
CV	7%		2%	–	12%/	7%	3%	8%

Av - average value, CV - coefficient of variation

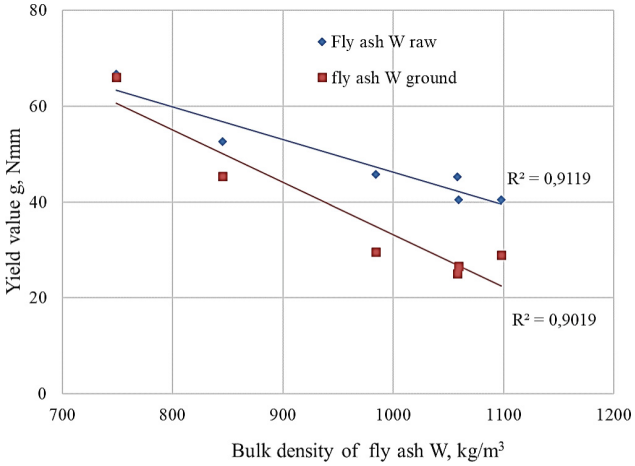

Fig. 3. Yield value g of CEM II/B-W mortars vs. volume density of fly ash W.

However, as relationship on Fig. 3 indicate, significant worsening of the rheological properties of mortars occurs when the fly ashes W used for cement production have a bulk density of less than 900 kg/m^3. It should be note, that bulk density is closely related to the conditions of combustion of coal or more accurately to temperature - the lower temperature, the lower amount of the glass phase and the greater the bulk density of the fly ash W. As consequence of lower amount of the glass phase is the higher water demand of fly ash W. If batches of fly ashes W with bulk density less than 900 kg/m^3 would not be used for the production of cement, it is possible to reduce its negative influence on rheological parameters of mortars and improvement in the uniformity of the rheological properties of CEM II/ B-W mortars (see Fig. 4 and Table 5).

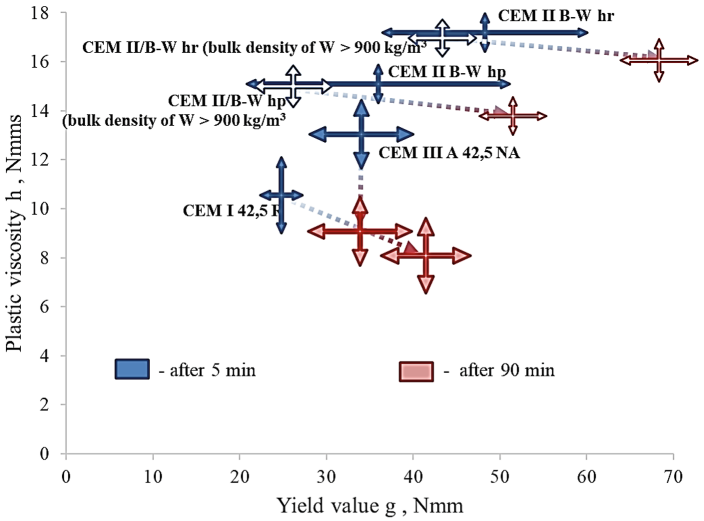

Fig. 4. Variation of rheological properties of mortars made of different cements.

Influence of fly ash W batch on variability of rheological properties of mortars can also be compared with the influence of batch of commercial cements on variability of rheological properties of mortars. According to [17] in the case of using CEM I and CEM III cements from the same source, but from different production batches over 2 months, the CV for rheological parameters ranged from 7% to 19% (see Fig. 4). As can be seen variability in rheological properties of CEM II/B-W mortars is significantly higher than for other types of cement. However, by using only fly ash W with bulk density less than 900 kg/m^3 variability of CEM II/B-W mortars can be reduced to a level not deviating significantly from other types of cement with additives.

4 Summary

Mortars with cements CEM II/A-W, CEM II/B-W and CEM IV/B-W have worse workability and higher workability loss than CEM I mortars. These effects are the stronger the more fly ash W is in cement. The presence of fly ash W in cement in an amount higher than 30% worsens the workability so much that its use as the main component of CEM IV cements is not possible. It was confirmed that the high variability of fly ash W properties may results in a very significant variability in rheological properties of cement mortars with CEM II/B-W cements.

Due to the definitely negative impact on workability of cements obtained by homogenizing with raw fly ash W, the production and use of these cements is not recommended. By using cements CEM II/A-W or CEM II/B-W produced by intergrinding or homogenizing with ground fly ash W it is possible to obtain mortars (and concretes) with tolerable workability properties. It should be noted, however, that the

mortars with these cements are characterized by higher workability loss than mortars with CEM I cements and higher variability in rheological properties.

In order to reduce the impact on workability, fly ash W for cement production should be carefully selected because of its properties. According to the research, using fly ash W of the bulk density higher than 900 kg/m^3, it is possible to obtain cements not differing significantly from other currently used cements in respect to variability of the rheological properties of mortars and influence on its workability.

Acknowledgement. This research was co-financed by the EU from the European Regional Development Fund no. POIG 01.01.02.-24-005/09 Innovative cementitious materials and concretes made with high calcium fly ashes.

References

1. Energy study 2014, reserves, resources and availability of energy resources 2013 (2014) Federal institute for geosciences and natural resources (BGR), Hanover
2. Baran T, Drożdż W (2013) Evaluation of properties of domestic calcareous fly ash and its processing methods. Roads Bridges - Drogi i Mosty 12:5–15
3. Dziuk D, Giergiczny Z, Garbacik A (2013) Calcareous fly ash as a main constituent of common cements. Roads Bridges - Drogi i Mosty 12:57–69
4. Czopowski E, Łaźniewska-Piekarczyk B, Rubińska-Jonczy B, Szwabowski J (2013) Properties of concretes based on cements containing calcareous fly ash. Roads Bridges - Drogi i Mosty 12:31–40
5. Drożdż W, Giergiczny Z (2013) The resistance of mortars and concrete with calcareous fly ash on alkaline corrosion. Roads Bridges - Drogi i Mosty 12:147–158
6. Dąbrowska M, Giergiczny Z (2013) Chemical resistance of mortars made of cements with calcareous fly ash. Roads Bridges - Drogi i Mosty 12:131–146
7. Gibas K, Glinicki MA, Nowowiejski G (2013) Evaluation of impermeability of concrete containing calcareous fly ash in respect to environmental media. Roads Bridges - Drogi i Mosty 12:157–172
8. Jóźwiak-Niedźwiedzka D, Sobczak M, Gibas K (2013) Carbonation of concretes containing calcareous fly ashes. Roads Bridges - Drogi i Mosty 12:223–236
9. Papadakis VG (2000) Effect of fly ash on Portland cement systems, Part II. High calcium fly ash. Cem Concr Res 30:1647–1654
10. Tsimas S, Moutsatsou-Tsima A (2005) HCFA as the fourth constituent in concrete: problems, solutions and perspectives. Cem Con Comp 27:231–237
11. Giergiczny Z, Synowiec K, Żak A (2013) Suitability evaluation of calcareous fly ash as an active mineral additive to concrete. Roads Bridges - Drogi i Mosty 12:83–97
12. Gołaszewski J, Kostrzanowska A, Ponikiewski T, Antonowicz G (2013) Influence of calcareous fly ash on rheological properties of cement pastes and mortars. Roads and Bridges - Drogi i Mosty 12:99–112
13. Gołaszewski J, Giergiczny Z, Ponikiewski T, Kostrzanowska-Siedlarz A, Miera P (2018) Effect of calcareous fly-ash processing methods on rheological properties of mortars. Periodica Polytech Civ Eng 62:643–652
14. Banfill PFG (2003) The rheology of fresh cement and concrete - a review. In: Proceeding of 11th international cement chemistry congress, Durban, South Africa
15. Roussel N (2011) Understanding the rheology of concrete. Woodhead Publishing, Sawston

16. Gołaszewski J, Kostrzanowska-Siedlarz A, Cygan G, Drewniok M (2016) Mortar as a model to predict self-compacting concrete rheological properties as a function of time and temperature. Con Build Mat 124:1100–1108
17. Gołaszewski J, Cygan G, Gołaszewska M (2018) Repeatability and reproducibility of measurement of rheological parameters of fresh mortars and concretes. In: Proceedings of 27th conferences and laboratory workshops on rheological measurement of building materials 2018, Regensburg, Germany

Early Properties of Portland Cements with Varied Set Regulators

Tamino Hirsch(✉), Tobias Dorn, and Dietmar Stephan

Building Materials and Construction Chemistry,
Technische Universität Berlin, Berlin, Germany
t.hirsch@tu-berlin.de

Abstract. The effects of variation of amount and type of calcium sulfate on the early behaviour of hydrating Portland cement were examined. Initial setting of pastes determined via the Vicat needle penetration method indicates that not only the amount but also the type of set regulator has a substantial impact on early properties of hydrating cement. The influence of the type not only depends on its concentration but also on the Portland cement clinker used. In the measurement of ultrasonic P-wave velocity of hydrating pastes, different stages of strength gain can be defined. The successive addition of set regulators changes the material properties in these stages in different ways. Examinations lead to the conclusion that differences in the prepared samples are mainly due to different solubility of calcium sulfate types, early ettringite formation and the amount of reacting aluminate phases of the clinker.

Keywords: Sulfate source · Setting · Early properties · 3D printing · Phase development

1 Introduction

Additive manufacturing with Portland cement-based materials gives rise to entirely new challenges to adjust the properties of the binder. Many possibilities exist to design a cement paste which shows enhanced features for the additive manufacturing. Long-kept customs for the design of cement should be evaluated to use all prospects for improved material properties for this new manufacturing. The calcium sulfate content of Portland cement is one of these conventions. One of the reasons to add calcium sulfates to cement is to prolong the handling time for the resulting cementitious products like mortar and concrete. Hence, the calcium sulfate is also referred as set regulator. For 3D printing, a faster setting is more needed than an extended handling time. Hence, the decrease of sulfate content could be a way to shorten setting time which would be cheaper than the use of additives. The present study compares the influence of amount and type of set regulator on two Portland cement clinkers.

V. Mechtcherine et al. (Eds.): RheoCon 2019/SCC 2019, RILEM Bookseries 23, pp. 97–105, 2020.
https://doi.org/10.1007/978-3-030-22566-7_12

2 Materials and Methods

Two Portland cement clinkers were used in this study (named as C1 and C2). Samples were ground on a laboratory ball mill with steel grinding media to a specific surface area of 4100 $cm^2/g \pm 100$ cm^2/g each (determined by the Blaine method [1]). The chemical composition of clinkers was examined via X-ray fluorescence (XRF; PHILIPS WD-RFA PW 2400) on powder and molten (borate flux) tablets (Table 1). The clinkers are relatively similar in their chemical composition besides the SO_3 content. This enables to keep the number of parameters manageable and to draw more defined conclusions. Two different set regulators were used. Natural anhydrite and flue-gas desulfurization gypsum (FGDG) were ground on a Pulverisette 5 (Fritsch GmbH) with steel milling media. The natural anhydrite was found to be pure anhydrite. The FGDG contains 91 wt% gypsum and additionally calcite, dolomite and quartz.

Clinker and set regulators were blended in an overheadroom shaker (REAX20/12, Heidolph Instruments) for three hours with rubber mixing agents at 33 min^{-1}. The mass of mixed material was kept constant to avoid differences in the intensity of mixing. The homogeneous blended samples were rested for at least 12 h to avoid influences because of heat generated during mixing procedure. Paste samples were prepared by mixing these homogenized powders with deionised water. The standard consistency for the blends was determined on the equivalent cement pastes [2]. Henceforth, water to cement ratios of 0.314 for C1 cements and 0.29 for C2 cements were selected for all experiments. Vicat needle penetration test was performed with an automated device (ToniSET, ToniTechnik GmbH) in a water bath at 21 °C ± 1 °C (in accordance with [2]). Ultrasonic P-wave velocity and temperature of samples were recorded by an IP-8 (UltraTest GmbH). For these experiments, samples were produced in the same way as in [2]. In-situ XRD was performed on samples mixed in a plastic container on a vortex mixer for one minute. The samples were placed in the sample carrier, covered by Kapton foil and measured at 21 °C ± 1 °C. Measurement was performed by a PANalytical Empyrean with Bragg-Brentano geometry. The radiation (Cu Kα) was generated with 40 kV and 40 mA, filtered by Ni and detected by a PiXcel^{1D}.

Table 1. Chemical composition and loss on ignition (LOI) of used clinkers in wt%.

	Al_2O_3	CaO	Fe_2O_3	K_2O	MgO	MnO	Na_2O	P_2O_5	SiO_2	SO_3	TiO_2	LOI
C1	4.99	64.90	3.11	1.39	1.69	0.05	0.32	0.08	20.27	1.48	0.22	0.64
C2	4.90	64.64	3.15	1.53	1.58	0.11	0.23	0.23	21.18	0.83	0.26	0.63

3 Results and Discussion

The Vicat method shows an increase in initial setting time with addition of set regulator (Fig. 1). With increasing addition, the further delay in setting time is successively decreasing. In the case of clinker C1, the addition of up to 0.6 wt% SO_3 leads to the

same setting time for anhydrite and FGDG. At higher addition, FGDG retards more effectively than anhydrite. However, the behaviour of C2 is different. Anhydrite is retarding more than FGDG at any examined concentration. These results are supported by Locher et al. [3] as it was reported that effectiveness of type of set regulator (in that study anhydrite or bassanite in only one, higher amount) can depend on the clinker.

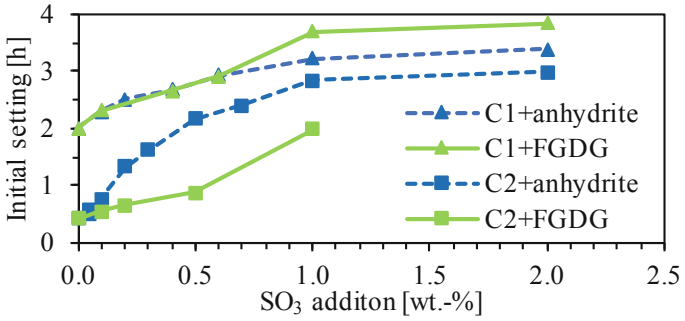

Fig. 1. Set regulator influence on initial setting via the Vicat method for two clinkers.

It can be observed from Fig. 1, that pure C1 and C2 + 0.50 wt% SO_3 by anhydrite exhibit nearby setting time. While for the same addition of FGDG, C2-based cement paste has lower setting time. Therefore, this cannot be interpreted in the way that the different behaviour of C1- and C2-based cement pastes is only because of the different sulfur content in the clinkers. Furthermore, the proportions of alkalis in the clinkers are comparable. This means that the amount of readily dissolvable alkali sulfates (Na_2SO_4, K_2SO_4) should be approximately same. Sulfur which is not bound in alkali sulfates is mainly incorporated into belite and alite and is therefore only available when these phases dissolve [4]. This means that the sulfate contribution of the two tested clinkers will be comparable at least in the first hours. Hence, the available sulfate cannot be same in the pastes of pure C1 and C2 + 0.50 wt% SO_3 by anhydrite.

The velocity of ultrasonic waves and the strength of the transmitting material correlate with each other. The higher the wave velocity the higher the strength. Several research studies showed that this principle is also applicable for the strength gain of usual cement pastes and also for 3D printable cement pastes [5]. The development of velocity over time presented in Fig. 2 depicts one principal shape and can be divided into the stages I to III. These three stages are assigned approximately as described by Kamada et al. [6]. In the first stage (I), all curves begin roughly at the same velocity value after pouring the sample into the measurement cell. The velocity rises with a comparatively high slope. Some of the samples perform a slight decrease and increase in slope during stage I. At the end of stage I, the slope decreases remarkably. Stage II leads initially again to an increase in slope of velocity curve which is slowly decreasing

to the end of stage II. The decrease in slope is continued in stage III and at the end of stage III, the velocity is only increasing at a very low rate. An intersection of curves with different SO_3 addition is defined as transition from stage II to stage III (in the present publication). This intersection and also the temporary decrease in slope between stage I and II is shown by all combinations of C1 or C2 with anhydrite or FGDG. In the transition of stage I to II, the mixtures of C2 and FGDG developed an additional intersection point.

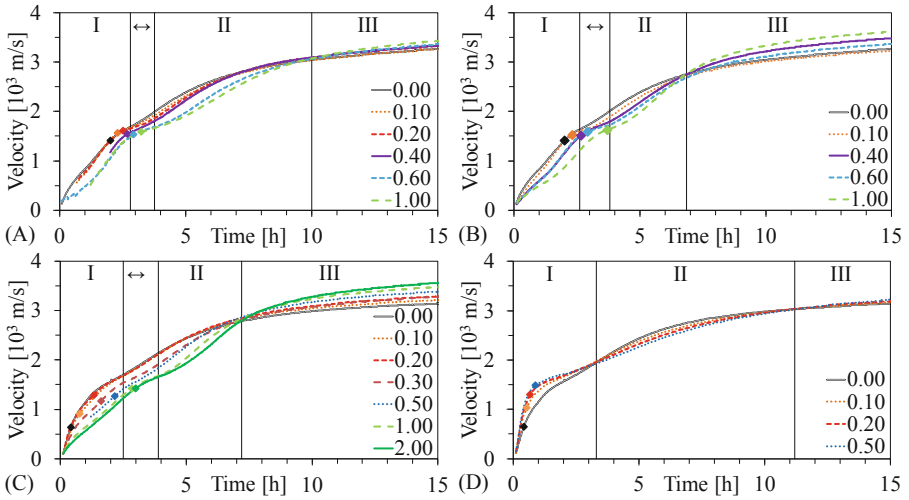

Fig. 2. Ultrasonic P-wave velocity in blends of (A) C1 + anhydrite, (B) C1 + FGDG, (C) C2 + anhydrite and (D) C2 + FGDG with different amounts of a set regulator in wt% SO_3 in respect to clinker. Borders of stages are marked by vertical lines. The border between stage I and II is shifting. The rotated square indicates initial setting.

The addition of SO_3 has several influences on the development of ultrasonic wave velocity. The mixes of C1 with anhydrite or FGDG and C2 with anhydrite generate lower velocity with increasing amount of SO_3 in stage I. The mixes of C2 and FGDG behave vice versa. The temporary loss in slope between stage I and II gets stronger with higher SO_3 content and occurs at later times for C1 + anhydrite, C1 + FGDG and C2 + anhydrite samples. The pure clinkers do not or only slightly show this bending in the curves. Nevertheless, all samples exhibit the transition between stage I and II. In the stages II and III, all combinations of clinkers and set regulators behave similar. In stage II, the velocity is lower for mixes with higher content of SO_3. Beginning with stage III, the samples with the highest SO_3 content have the highest ultrasonic wave velocity.

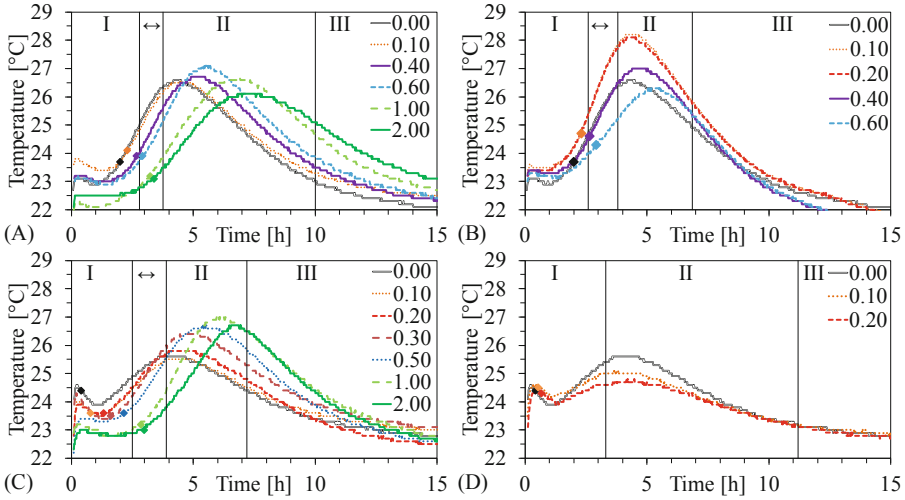

Fig. 3. Development of temperature in blends of (A) C1 + anhydrite, (B) C1 + FGDG, (C) C2 + anhydrite and (D) C2 + FGDG with different amounts of the set regulator in wt% SO_3 in respect to clinker. The measurement was performed simultaneously with the ultrasonic wave velocity measurement. Labels are as explained in Fig. 2.

The temperature development of mixes of clinkers and set regulators is shown in Fig. 3. All curves have one general appearance and are comparable to calorimetric curves. Nevertheless, it must be considered that these are temperature measurements and not heat measurements. The curves begin with a sharp rise of temperature which is attributed to the initial contact of the sample with the sensor and first dissolution and precipitation of phases. After this, the temperature of the samples decreases (development of a dormant period) and rises again to a second peak (main peak of cement hydration). Several changes in this general pattern are observed due to the set regulator. For all combinations of the two clinkers and two set regulators, an increase of the added amount of set regulator delays the time of second increase in temperature. For clinker C2 with anhydrite, the second peak gets sharper with rising amount of set regulator whereas the trend of the peak width is vice versa with FGDG. For C1, the addition of set regulator leads in both cases to broadening of the temperature peak. An increasing amount of anhydrite seems to lead initially to a small decrease, then an increase and later to a decrease in the height of the second peak. Both clinkers reach comparable absolute peak heights with anhydrite addition. For samples C1 + FGDG, the lowest concentration of FGDG leads to large increase in temperature which decreases with further addition of FGDG. For samples C2 + FGDG, a decrease in height can be observed at 0.10% SO_3. The absolute values of the peak heights with FGDG strongly depend on the clinker used. Compared to other mixes, C1 + FGDG develops a large second peak followed by lower temperature at a later time.

For all C1 pastes and that of C2 with higher addition of set regulator, initial set is shortly before the reduction in P-wave velocity slope at end of stage I and at the beginning of second temperature rise which indicates that the set is because of C-S-H

precipitation [7]. However, C2-based pastes with low set regulator addition seem to perform initial set due to another reason as initial setting happens longer before the reduction in P-wave velocity slope and at the end of the first temperature peak (Figs. 2 and 3).

By means of in-situ XRD, mixes of C1 or C2 with anhydride or FGDG were investigated wherein the SO_3 addition was 1 wt% (Fig. 4). The intensities of reflexes of the clinker phases are decreasing in time. The samples mixed with FGDG do not show reflexes of gypsum but samples with anhydrite exhibit its reflexes. Gypsum has a lower solubility [8, 9] but dissolves faster in water than anhydrite [10, 11] and because of this, the gypsum is completely dissolved after mixing. The intensities of anhydrite reflexes decrease with time. In C1 samples, after 23 h the phase can still be identified in low concentrations. For C2 samples, the peak has diminished after approximately 12 h. This can have two reasons: on the one hand, the higher sulfur content in C1 could supply additional sulfate which slows down the dissolution of anhydrite. On the other hand, the formation of reaction products can consume sulfate at a lower rate in the mix with C1. As concluded earlier, the sulfate contribution of the two clinkers will be comparable in the first hours. That is why most likely the reason for faster anhydrite dissolution with clinker C2 is a faster consumption of sulfate. This higher consumption of sulfate can be due to a faster formation of reaction products or due to precipitation of products which bind more sulfate. Both possibilities can lead to the faster setting of C2 measured via the Vicat method.

One of the early reaction products of Portland cement is ettringite. All plots show reflexes of ettringite which increase in their intensities in time. Most prominent is the reflex at 9.1° 2θ (Laue index 010). Dissolution of tricalcium aluminate and brownmillerite supply the aluminate for the formation of ettringite. While, sulfate can come from added calcium sulfate or the clinker. That is why, the development of the ettringite reflex intensity can be used as an indicator for the reacting amount of tricalcium aluminate and brownmillerite besides the decrease in the reflex intensities of these phases. Samples with C2 form ettringite faster than those with C1. This indicates that the faster formation of reaction products by C2 is because of more dissolving aluminate phases.

FGDG-containing samples show an earlier and more intense ettringite formation than that with anhydrite. The reason for this can be the higher sulfate supply by faster gypsum dissolution. As sulfate is an essential component of ettringite, a higher amount of sulfate in the early pore solution enables more ettringite to form. If there is not enough dissolved sulfate available, AFm phases are formed instead [12, 13]. AFm phases are solid solutions which incorporate sulfate but also other anions. One of these is carbonate which leads to strong stabilization of AFm. Hence, carbonate can replace sulfate while AFm formation. By this, sulfate is free to form more ettringite [14, 15]. As FGDG contains carbonates, such an effect is also possible in the presented mixes. Nevertheless, no change in the peak of the AFm phase monocarbonate is recognizable in Fig. 4. This could be because the effect is small or not occurring at all in the samples. The low crystallinity of AFm phases could possibly also mask this effect.

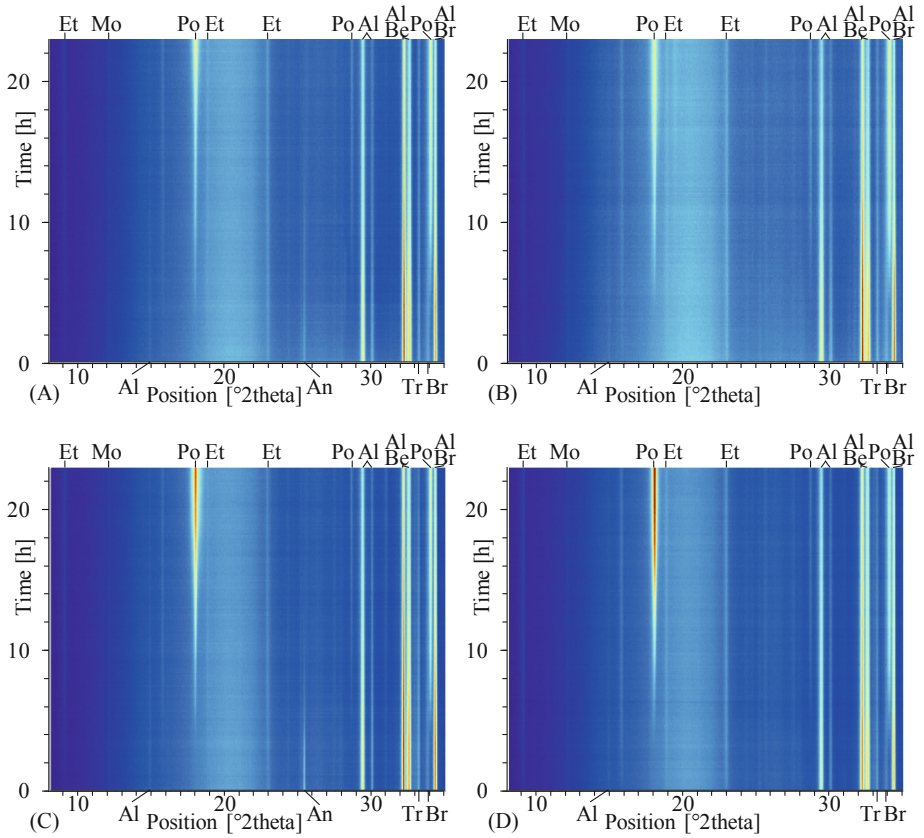

Fig. 4. In-situ XRD of hydration of blends with 1 wt% SO_3 out of set regulator. The panels present: (A) C1 + anhydrite, (B) C1 + FGDG, (C) C2 + anhydrite and (D) C2 + FGDG. Labels stand for: Al alite, An anhydrite, Be belite, Br brownmillerite, Et ettringite, Mo monocarbonate, Po portlandite, Tr tricalcium aluminate.

At early time, a strong formation of ettringite in the mix of C2 and FGDG can be observed. This can be the reason for the unique behaviour of these blends. In ultrasonic wave velocity, an acceleration with FGDG addition is observed in early time (stage I). Also, Kamada et al. [6] found that ettringite crystallization enhances the P-wave velocity. Nevertheless, the ettringite crystallization happens much later in their experiments although they use high-early-strength cement. Voigt et al. [16] concluded that the formation of ettringite enhances the P-wave velocity by filling the pore volume with solid matter. Compared to other products of cement hydration, ettringite has a large molar volume [17]. In this regard, ettringite crystallization raises the solid to liquid ratio of the paste and the transmission of mechanical waves is more effective and faster. On the other hand, ettringite forms needle-like to columnar crystals which grow mostly radial on the cement particles [18]. Such an arrangement could connect the particles in the paste and lead to a more rigid structure which can transmit ultrasonic

waves faster. This second possibility was neglected for conventional Portland cement in literature [16] but must be considered for the system presented here. Also, the moderate increase in initial setting time in the blends of C2 and FGDG is likely due to early ettringite formation. Possibly, ettringite crystals connect the cement grains strong enough to increase ultrasonic wave velocity, but the crystals are too weak to give high resistance to the Vicat needle. The weakness of (especially young) ettringite [19] and a needle-like morphology could lead to weakness against deformation in macro scale. In literature, it was concluded that if all early dissolved ions of tricalcium aluminate are used for ettringite formation, the maximum delay of setting is reached [3]. Nevertheless, this statement is too general. Large and early precipitation of ettringite can lead to faster initial setting.

Another reaction product is portlandite. In all samples, the time at which the portlandite reflexes are first seen is comparable. As the clinker phases react, the intensities of portlandite reflexes increase till the end of the measurements. In the C2 samples with anhydrite and with FGDG, the intensity of the portlandite reflex at 17.9° 2θ is at the end of the observed period much higher than in the C1 samples. As 17.9° is the basal reflex of (the hexagonal) portlandite, this peak cannot be used directly as an indicator for the amount of portlandite in the sample. Other reflexes of portlandite must be considered too. The reflexes at 28.6° and 33.9° do not show increases in intensity relative to C1 samples which are proportional to that of 17.9°. The most likely explanation is that the portlandite crystals grow in the C2 samples more platelet-like. By this, the relative intensities of the peaks are altered and the reflex at 17.9° becomes more pronounced.

4 Conclusion

A change in the added amount and type of calcium sulfate can effectively alter the early behaviour of a Portland cement paste. The amount of calcium sulfate gives rise to a comparatively easy change in stiffening in the examined combinations while the influence of the type of calcium sulfate is more complex. Anhydrite can retard less, equal or more than FGDG depending on the clinker and the amount of set regulator. Ettringite formation can play a key role in the early behaviour of Portland cement varied in set regulator. Early ettringite precipitation in high amount has been found to be interesting for applications which demand short setting time, like 3D printing. Variation of set regulator can pave the way for cement with more defined early properties and adjustment to most recent applications like 3D printing. Nevertheless, more research is needed to examine how the ettringite formation influences other properties and if the major mechanism is the connection of particles or filling of pore volume.

Acknowledgement. The authors are thankful to German Federal Ministry of Education and Research for funding this work in the scope of project BauProAddi (FKZ: 03XP0122A). Furthermore, acknowledgement goes to Opterra Zement GmbH for the supply of material and to Ms Charline Gruhn and Mr Falk Martin for their assistance in the laboratory.

References

1. EN 196-6:2010, Methods of testing cement – Part 6: determination of fineness
2. EN 196-3:2016, Methods of testing cement – Part 3: determination of setting times and soundness
3. Locher FW, Richartz W, Sprung S (1980) Erstarren von Zement, Teil II: Einfluss des Calciumsulfatzusatzes. ZKG Int 33:271–277
4. Herfort D (2002) Distribution of sulfates in Portland cement clinker. In: International RILEM TC 186-ISA workshop on internal sulfate attack and delayed ettringite formation, Villars, Switzerland, 4–6 September 2002, pp 18–27
5. Wolfs RJM, Bos FP, Salet TAM (2018) Correlation between destructive compression tests and non-destructive ultrasonic measurements on early age 3D printed concrete. Constr Build Mater 181:447–454
6. Kamada T, Uchida S, Rokugo K (2005) Nondestructive evaluation of setting and hardening of cement paste based on ultrasonic propagation characteristics. J Adv Concr Technol 3:343–353
7. Hesse C, Goetz-Neunhoeffer F, Neubauer J (2011) A new approach in quantitative in-situ XRD of cement pastes: correlation of heat flow curves with early hydration reactions. Cem Concr Res 41:123–128
8. Power WH, Fabuss BM, Satterfield CN (1964) Transient solubilities in the calcium sulfate-water system. J Chem Eng Data 9:437–442
9. Amathieu L, Boistelle R (1988) Crystallization kinetics of gypsum from dense suspension of hemihydrate in water. J Cryst Growth 88:183–192
10. Barton AFM, Wilde NM (1971) Dissolution rates of polycrystalline samples of gypsum and orthorhombic forms of calcium sulphate by a rotating disc method. Trans Faraday Soc 67:3590–3597
11. Klimchouk A (1996) The dissolution and conversion of gypsum and anhydrite. Int J Speleol 25:21–36
12. Quennoz A (2011) Hydration of C_3A with calcium sulfate alone and in the presence of calcium silicate. Doctoral thesis, Lusanne
13. Bergold ST, Goetz-Neunhoeffer F, Neubauer J (2017) Interaction of silicate and aluminate reaction in a synthetic cement system: implications for the process of alite hydration. Cem Concr Res 93:32–44
14. Matschei T, Lothenbach B, Glasser FP (2007) The AFm phase in Portland cement. Cem Concr Res 37:118–130
15. Matschei T, Lothenbach B, Glasser FP (2007) The role of calcium carbonate in cement hydration. Cem Concr Res 37:551–558
16. Voigt T, Malonn T, Shah SP (2006) Green and early age compressive strength of extruded cement mortar monitored with compression tests and ultrasonic techniques. Cem Concr Res 36:858–867
17. Lothenbach B, Kulik DA, Matschei T, Balonis M, Baquerizo L, Dilnesa B, Miron GD, Myers RJ (2019) Cemdata18: a chemical thermodynamic database for hydrated Portland cements and alkali-activated materials. Cem Concr Res 115:472–506
18. Schwiete HE, Ludwig U, Jäger P (1966) Investigations in the system 3 $CaO{\cdot}Al_2O_3$-$CaSO_4$-CaO-H_2O. Highway research board, Washington, D.C., pp 353–366
19. Scrivener KL, Pratt PL (1984) Microstructural studies of the hydration of C_3A and C_4AF independently and in cement paste. Proc Br Ceram Soc 35:207–219

Influence of Different Accelerators on the Rheology and Early Hydration of Cement Paste

Sarah Leinitz[1](✉), Zichen Lu[2], Simon Becker[3], Dietmar Stephan[2], Regine von Klitzing[3], and Wolfram Schmidt[1]

[1] Bundesanstalt für Materialforschung und -prüfung (BAM), Berlin, Germany
sarah.leinitz@bam.de
[2] Department of Civil Engineering, Technische Universität Berlin, Berlin, Germany
[3] Department of Physics, Technische Universität Darmstadt, Darmstadt, Germany

Abstract. Special applications like pumping, spraying or printing of concrete require the precise adjustment of very specific rheological properties at different time steps during the casting process. Superplasticizers such as polycarboxylate ethers (PCE) can be used to obtain the required flowability, which, possibly in combination with additional rheology modifying admixtures, generate the required specified consistency. However, after the application, the concrete should change the rheological properties immediately in order to avoid deformations at rest. Therefore, the use of accelerators can be effective. Accelerators influence the hydration of cementitious materials, and thus the rheological properties over the course of time and the setting.

In this paper, the influence of different accelerators on the rheology and early hydration of cement paste as well as the interaction of accelerator and PCE are presented. Methods like rheometry, needle penetration tests and practical tests like spread flow were applied. The used accelerators showed accelerating behavior on the cement pastes without and in the presence of PCE. At the same time an influence on the rheology could be observed. This effect was less in the mixes with PCE, especially at the highest water/cement ratio (w/c).

Keywords: Rheology · Cement paste · Accelerator · Superplasticizer · Setting

1 Introduction

The rheological properties of cementitious materials change very fast in the first minutes after water addition and they are important for special applications like spraying, pumping or printing of concrete [1]. Especially accelerators (ACCs) can cause rapid changes of the early properties. Therefore, it is necessary to understand the early hydration of those systems and the respective rheological behavior.

Accelerators affect the hydration rate and can shorten the setting time and/or increase early strength development [2]. However, in this study only setting accelerators were investigated. Typical accelerators are based on calcium chloride and

V. Mechtcherine et al. (Eds.): RheoCon 2019/SCC 2019, RILEM Bookseries 23, pp. 106–115, 2020.
https://doi.org/10.1007/978-3-030-22566-7_13

thiocyanate [3]. For applications, which are sensitive to chlorides, accelerators like calcium nitrate can be employed [4]. Calcium nitrate can be also used as a multifunctional concrete admixture with corrosion inhibiting and rheology modifying properties depending on the dosage [4]. Bost et al. [5] investigated different accelerators and found out that stabilized C-S-H seeds show acceleration of Portland cement hydration. Also, pure synthesized C-S-H seeds can accelerate cementitious materials, like Land and Stephan [6] presented. In the future, the combination of accelerators and superplasticizers plays an important role, due to the need of specific rheological properties at different time steps. While for example for printing and spraying often the concrete needs an initially flowable consistency but already a few minutes later a certain stability is required. In order to tailor the rheological properties for special applications, a lot of different superplasticizers as well as accelerators are available on the market. Since, fresh concrete properties become more and more important for future technologies, it is imperative to better understand the systematic behavior between superplasticizers and accelerators.

2 Experiments

Cement pastes with various water/cement ratios were used for the different investigations of early performance properties. The effect of accelerators was studied without and in the presence of superplasticizers.

2.1 Materials

Cement paste was made with Portland cement CEM I 42,5 R from HeidelbergCement, Germany and deionized water at 20 °C. Two different commercial accelerators, MasterSet AC 555 and X-Seed 100 by BASF were used to influence the setting of the paste. AC 555 is based on calcium nitrate and will be abbreviated with CN.

X-Seed (XS) contains C-S-H-seeds for the hydration acceleration. It additionally contains PCE to stabilize the solution. The superplasticizer that was used is a polycarboxylate ether provided by BASF. The physical properties of the materials are shown in Table 1.

Table 1. Physical properties of the used materials.

Name	Density [g/cm^3]	Solid content [%]	Mw [g/mol]
CEM I, 42.5 R	3.1	100	–
CN	1.39	55	–
XS	1.13	22	–
PCE	1.06 (bulk)	23	25000

2.2 Methods

2.2.1 Sample Preparation

The pastes were mixed in a mixer according to DIN EN 197-1. The mixing procedure is shown in Table 2. If contained in the mixture, PCE was always added before the accelerator. Certainly, the order of admixture addition can have a strong effect on the efficiency of each admixture. Here, it was important to understand the effect of the accelerators in robust reference systems. Thus, if contained, first the PCE was dosed and the accelerator was added with a considerable delay to ensure that the PCE was well dispersed in the paste.

Table 2. Mixing procedure.

Process	Mixing intensity	Mixing duration	
Dry homogenization of raw materials	140 min^{-1}	60 s	
Addition of water during mixing	140 min^{-1}	15 s	Addition of PCE
Mixing at low speed	140 min^{-1}	45 s	
Pause (manual return of caking material)	–	90 s	Addition of ACC
Homogenization at higher speed	285 min^{-1}	60 s	
Pause (manual return of caking material)	–	30 s	
Homogenization at higher speed	285 min^{-1}	120 s	
Pause	–	390 s	
Remixing at low speed	140 min^{-1}	30 s	

2.2.2 Spread Flow

Spread flow was performed using a Haegermann cone on a spread flow table. The used cone has a lower diameter of 100 mm and an upper diameter of 70 mm with a total height of 60 mm. The procedure for obtaining the spread flow was done according to DIN EN 1015-3:2007 [7].

The determined value is the average of the perpendicular diameters measured from the spread of the paste. The spread flow was measured for every mixture 15 min after addition of water, in order to avoid effects of the rapidly changing cement chemistry over the first minutes after contact of cement and water.

2.2.3 Rheometric Measurement

The rheometric investigations were conducted with a Couette type rheometer (Schleibinger, Viskomat NT) with a basket cell [8]. The chosen profile for the measurement is only 4.25 min to avoid long shearing and is shown in Fig. 1.

2.2.4 Setting Time

The setting time was determined with an automatic Vicat device with 11 slots. The material was filled in molds according to DIN EN 196-3. The needle penetration was

recorded over the course of time and the initial setting time was defined as the time when a penetration depth of 6 mm was reached.

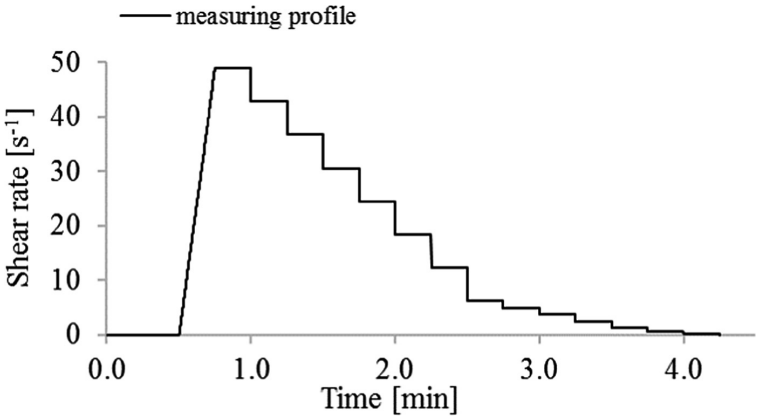

Fig. 1. Profile for rheometric measurement with Viskomat NT from Schleibinger.

3 Results and Discussion

3.1 Spread Flow

The results of the spread flow are presented in Fig. 2 and Fig. 3 without and in the presence of PCE, respectively. The figures show pastes with three different w/c ratios, without and in the presence of PCE, CN and XS.

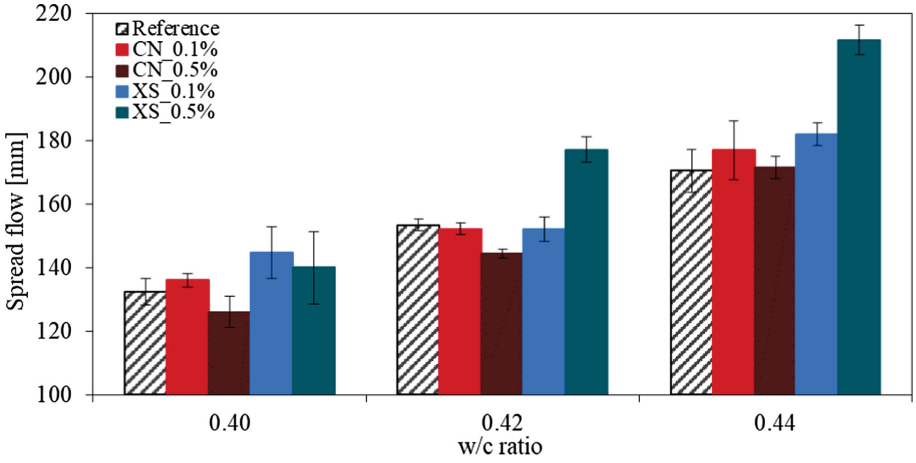

Fig. 2. Spread flow of pastes with different dosages of accelerator and depending on various w/c ratios.

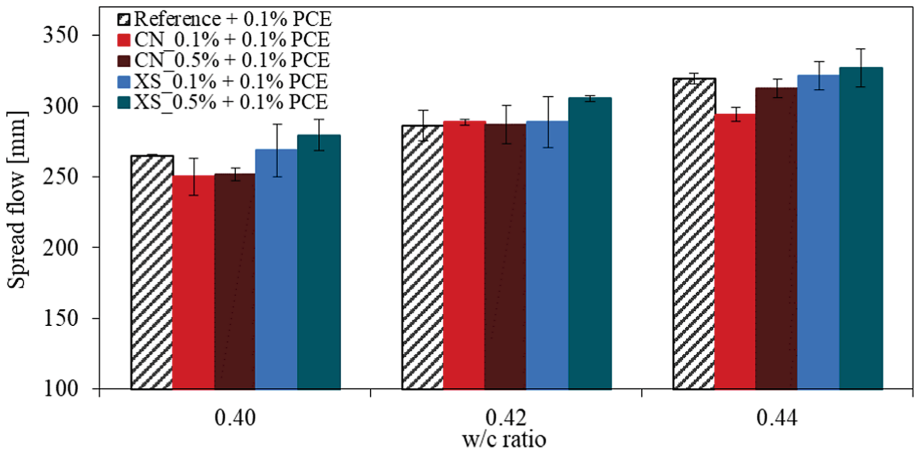

Fig. 3. Spread flow of pastes with different dosages of accelerator and depending on various w/c ratios in the presence of 0.1% PCE.

The reference mixes with *w/c* ratio = 0.40, 0.42, 0.44 have spread flows of 136 mm, 155 mm and 175 mm, respectively. It seems, that the difference between w/c ratio 0.40 and 0.42 is smaller than between 0.42 and 0.44. The accelerator XS increases the spread flow of the pastes. An additional increase of the dosage of XS leads to higher spread flow, which is caused by the contained PCE in the XS. This effect is even stronger with higher w/c ratios. In contrast, the addition of CN decreases these values.

By adding PCE to the reference systems, the diameters increase to 265 mm, 287 mm and 320 mm, respectively. With a combination of XS and 0.1% PCE the spread flow decreases with a low dosage of XS, but then increase again with 0.5% of XS and leads to the highest spread flow of 327 mm for w/c ratio 0.44. Due to the seeding effect of XS, the building of C-S-H is more prominent at low dosages and the reduction of the spread flow can be explained. However, high dosages of XS cause a higher total amount of ions in the system, which can be seen by higher flow values. The paste with CN in the presence of PCE show lower flowability. With increasing concentration of ACC to 0.5%, the spread flow also increases. However, the value for the reference mix with PCE cannot be reached again. A hypothesis for this observation can be, that the calcium nitrate brings more calcium ion in the system, which may slightly reduce the charges of the PCE and thus reduce their capacity to adsorb on surfaces, which eventually causes the reduced flowability. With higher amounts of CN, the nitrate content also increases prominently, and the nitrate can work like a sacrificial ion, which causes that more PCE could be adsorbed at outer surfaces, so that the polymers' efficiency can be increased.

3.2 Rheometric Results

From the measured rheometer data, a mean value of the last 10 measuring points of each plateau was calculated. The results of the rheometric measurements are given in the Figs. 4 and 5. Figure 4 provides information about the flow curve of the paste for the reference, mixes with CN and XS for three w/c ratios and three different dosages

(0.1%, 0.5%, 1.0%) of accelerator. For Fig. 4(a) it can be seen, that the addition of CN causes only a minimal change in the yield stress. There is no systematic change in the viscosity at shear rate range from 12 to 50 s^{-1} for the different dosages of CN depending on the w/c ratio. However, the range of the viscosities within one group of mixes with the same w/c ratio does not vary strongly. The highest viscosity is achieved for *w/c* ratio = 0.40 and the medium dosage (0.5%) of CN. The effect of the different w/c ratios is significantly stronger than the influence of the dosages of CN. This observation corresponds to the results of the spread flow presented in the Figs. 2 and 3.

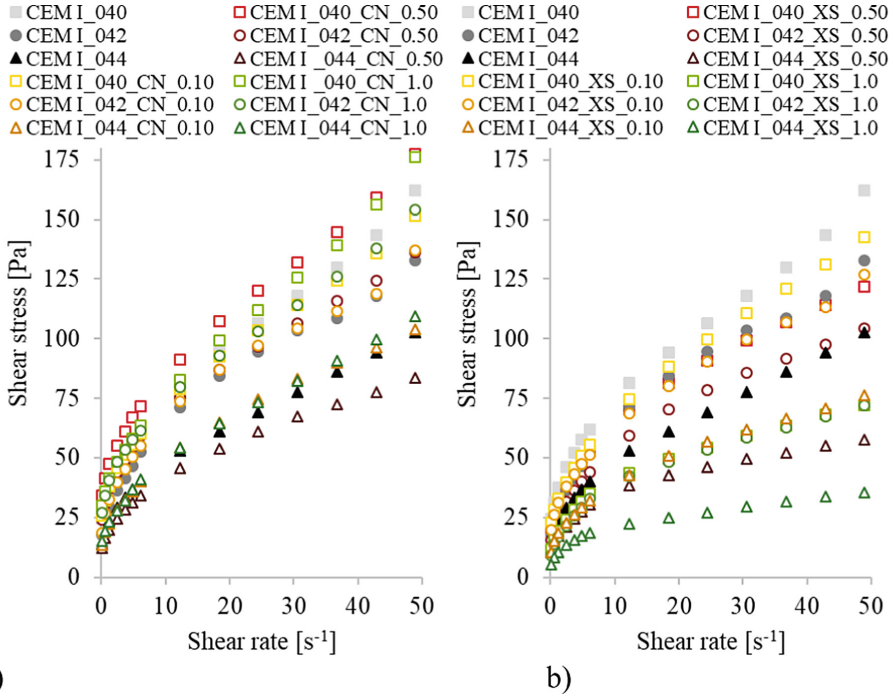

Fig. 4. Flow curves of pastes with different w/c ratios (0.40, 0.42, 0.44), various dosages of accelerator without PCE for (a) CN and (b) XS.

The flow curves in Fig. 4(b) show that XS has a higher influence on the rheology than CN. With an increasing dosage of XS, the apparent viscosity decreases compared to the reference mix without any accelerator. The dosages of XS can have effects that are in the order of magnitude of changes in the water content. The yield stress is generally lower with XS than for the mixes with CN. This is most likely caused by the PCE that is used to stabilize the particles.

Figure 5(a) displays the flow curves for the pastes in the presence of 0.1% PCE for CN and Fig. 5(b) for XS, respectively. Since in the presence of PCE for some mixes the additional PCE content from the XS caused severe segregation, here, only the results of a maximum dosage of 0.5% are presented. The highest yield stress and

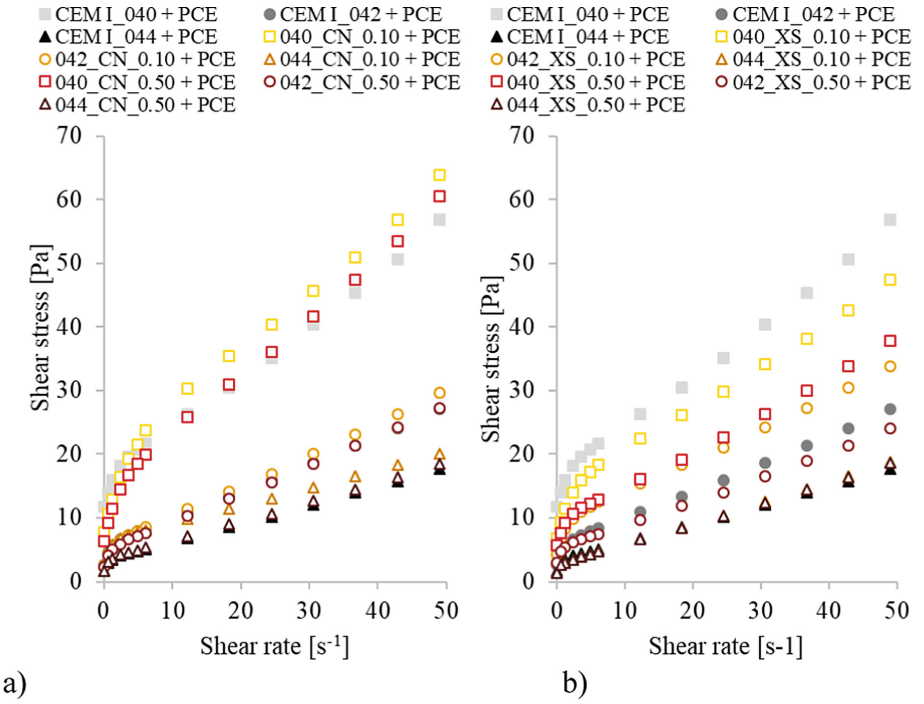

Fig. 5. Flow curves of pastes with different w/c ratios (0.40, 0.42, 0.44), various dosages of accelerator with 0.1% PCE for (a) CN and (b) XS.

viscosity for the mixes with ACC + PCE was reached for the mix with w/c ratio 0.40 and 0.1% CN and 0.1% PCE. The mix with w/c ratio 0.44 and 0.1% PCE leads to the lowest values. The higher the w/c ratio, the more overlapping can be observed for the flow curves for CN in the presence of 0.1% PCE. The flow curves in Fig. 5(b) show, that the viscosity decreases with increasing dosages of XS at w/c ratio 0.40. With higher water cement ratios, a similar behavior as CN can be observed. There is no big difference in the flow curves in Fig. 5 at the highest water amount. This is in line with former research, where it was shown that admixture interactions with PCE occur more pronounced at higher particle solid volume fractions [9]. This means, that the w/c ratio affects influence of the ACCs on the rheology in the presence of PCEs. This effect is relatively small for CN but prominent for the XS accelerator.

The fact that PCE is added to the systems, changes the rheological properties the most. However, there is a minor influence on rheology with calcium nitrate in comparison to XS, which could be explained already before. At the same time, it seems that the PCE from the XS may compete with the other PCE, which is responsible for the increase at low XS dosage and the decrease of the apparent viscosity at the higher dosage.

Figure 6 provides initial setting times of pastes with different w/c ratios (0.40, 0.42, 0.44), without and in the presence of PCE, CN and XS. The different w/c ratios influence the initial set. The higher the water amount, the higher the initial set. The set retardation effect of PCE on the systems without ACC is approximately 4 h regardless of the w/c.

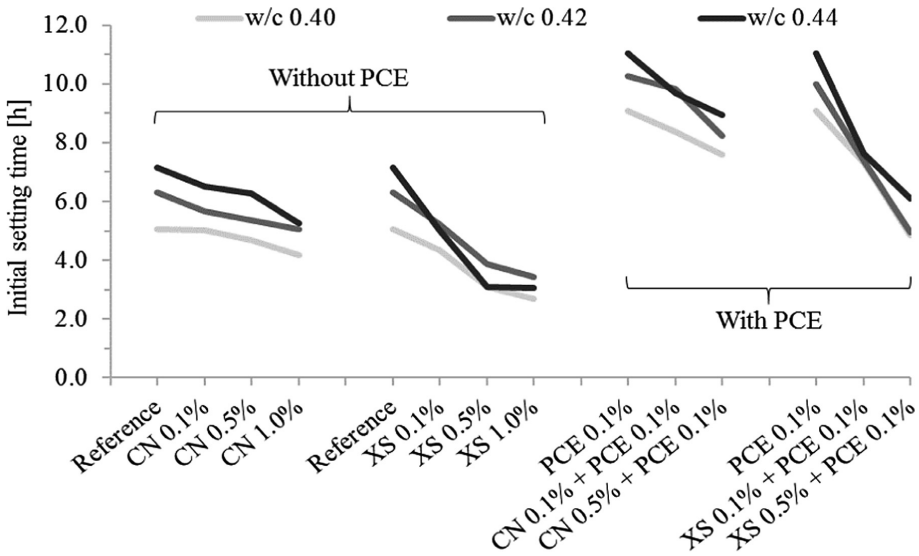

Fig. 6. Initial setting time of pastes with different w/c ratios (0.40, 0.42, 0.44), without and in the presence of PCE, CN and XS.

It can be observed that the use of accelerators causes faster initial setting for both ACCs. Increasing dosages of CN cause a set acceleration that is slightly stronger in the presence of PCE, for example at a dosage of 0.5% the initial set takes place approximately 1 h earlier, while in the presence of PCE the same dosage causes an approximately 2 h earlier setting. This effect can be caused by the supplementary adsorption surfaces available from the accelerator for PCE to be adsorbed, so that once the rapid C-S-H hydration sets in lower amounts of PCE interfere with the hydration. A similar effect was shown before for PCE in the presence of stabilizing agents that interfere with the cement hydration process [10, 11].

The accelerating effect with XS is stronger without and with PCE. For example, without PCE the dosage of 0.5% XS causes a set acceleration of approximately 3 h. In the presence of PCE the same dosage of XS causes an acceleration of 4.5 h. The latter acceleration is significantly stronger than in the system without PCE. Without PCE the retarding effect of the PCE incorporated only from the XS may overlap with the accelerating effect of the C-S-H seeds. In the presence of PCE the supplementary PCE from XS is negligible compared to the initial PCE dosage, thus, the effects of the additional polymers do not become effective, while the accelerating effect of C-S-H seeds remain unaffected. Hence without the overlapping retarding effect of the PCE from the XS, the effect of the C-S-H seeds on the set acceleration is more pronounced than without PCE.

4 Conclusions

The present study shows the accelerating effect of CN and XS. At the same dosage, XS causes a higher acceleration, but leads to stronger influence on the rheology of the pastes at very early age, which is induced by the contained PCE.

Without PCE increased dosages of CN showed influence on the apparent viscosity but yield stress was not significantly affected, which is confirmed by the spread flow results. However, for the comparable systems with XS, both apparent viscosity and spread flow were affected, which is caused by the incorporated PCE from the accelerator.

In the presence of PCE the effect of the accelerator on the rheology was strongly depending on the w/c. The higher the w/c the lower the accelerators' effect.

The systems without PCE have earlier setting times, but the relative set acceleration of both ACCs is stronger in the presence of PCE. XS has a stronger accelerating effect than CN, but without PCE its effect is overlapped by the retarding effect of the PCE molecules contained in the admixture as stabilizing agent.

Future experiments should also include the influence of the addition time of the different admixtures on rheology and setting. A better understanding of the effect of calcium nitrate can be obtained by zeta potential measurements. In addition, the use of pure C-S-H seeds without PCE as stabilizers is scheduled.

Furthermore, the influence of various temperatures and lower w/c ratios have to be considered, as well as the supplementary effects of coarser particles like sand and aggregates.

Acknowledgement. The author would like to thank the funding from German Research Association (DFG) for the project program *Opus Fluidum Futurum – Rheology of reactive, multiscale, multiphase construction materials (SPP 2005)* (Project number 387092747) and the supply of cement and superplasticizer from HeidelbergCement and BASF, respectively.

References

1. Roussel N (2012) Understanding the rheology of concrete. Woodhead Publishing, Sawston
2. Myrdal R (2007) Accelerating admixtures for concrete
3. Justnes H, Nygaard EC (1995) Technical calcium nitrate as set accelerator for cement at low temperatures. Cem Concr Res 25:1766–1774
4. Justnes H (2010) Calcium nitrate as a multifunctional concrete admixture. https://de.scribd.com/document/311682442/Calcium-Nitrate-as-a-Multifunctional-Concrete-Admixture
5. Bost P, Regnier M, Horgnies M (2016) Comparison of the accelerating effect of various additions on the early hydration of Portland cement. Constr Build Mater 113:290–296
6. Land G, Stephan D (2015) Controlling cement hydration with nanoparticles. Cement Concr Compos 57:64–67
7. DIN (2007) Methods of test for mortar for masonry - Part 3: determination of consistence of fresh mortar (by flow table). In: EN 1015-3, ed. European committee for standardization, Brussels
8. Vogel R (2008) A measuring cell for special mortars. Concr Plant + Precast Technol 1:124–126

9. Schmidt W, Brouwers HJH, Kühne H-C, Meng B (2014) Influences of superplasticizer modification and mixture composition on the performance of self-compacting concrete at varied ambient temperatures. Cement Concr Compos 49:111–126
10. Schmidt W, Brouwers HJH, Kühne H-C, Meng B (2017) Interactions of polysaccharide stabilising agents with early cement hydration without and in the presence of superplasticizers. Constr Build Mater 139:584–593
11. Stroh J, Schlegel MC, Schmidt W, Thi YN, Meng B, Emmerling F (2016) Time-resolved in situ investigation of Portland cement hydration influenced by chemical admixtures. Constr Build Mater 106:18–26

Effect of Mineral Additions on Rheology and Fresh Properties of Cement Pastes and Mortars

Dorota Małaszkiewicz(✉) and Mateusz Osipiuk

Faculty of Civil and Environmental Engineering,
Bialystok University of Technology, Bialystok, Poland
d.malaszkiewicz@pb.edu.pl

Abstract. In this study the following mineral additions were used as 10% by weight cement replacement: silica fume SF, two types of metakaolin MK1 and MK2, and limestone powder LP. One type of cement CEM I 42.5R and one high range water reducing (HRWR) admixture were used in all mixes. Fresh properties of mortars with natural postglacial sand 0/4 mm were examined by mini-cone test and rotational viscometer Viskomat XL. In this instrument, when the cylindrical sample container rotates, the mortar flows through the blades of the impeller and exerts a torque which is measured by a transducer. As a result of the measurement, a set of data expressing the resistance of the mix subjected to the stresses induced by the rotation of the impeller was obtained. By linear approximation of the obtained results from the down-curve, the flow line of the mixture was obtained and compared with the modified Bingham Equation, which allowed to determine the rheological parameters of the tested mortars. All additions except for LP decreased rheological properties of the tested pastes and mortars. Not only particle size distributions (PSD), cumulative percentages and specific surfaces of the powders influence water and admixture demand of cement-based composites. Also shape and texture of the individual particles have an effect on the rheological properties.

Keywords: Rheology of cement mortar · Silica fume · Limestone powder · Metakaolin

1 Introduction

The incorporating of supplementary cementitious materials (SCMs), especially pozzolanic materials, in concrete has a considerable effect on both fresh and hardened properties [1–3]. They are usually introduced as a partial cement replacement or they can be added over the cement contents to enhance the engineering properties of hardened material. They also influence fresh properties of cement composites [4, 5]. SCMs are usually powders finer than cement so they can improve cohesiveness of mixtures and reduce segregation risk by improving particle size distribution (PSD). Thus, the mineral additives are efficiently utilized as viscosity enhancers. Due to the negative effect of fine powders on water demand they usually decrease workability and high dosage of high range water reducing admixtures (HRWRA) is required to achieve

V. Mechtcherine et al. (Eds.): RheoCon 2019/SCC 2019, RILEM Bookseries 23, pp. 116–124, 2020.
https://doi.org/10.1007/978-3-030-22566-7_14

high flowability of concrete mixes [6–9]. But there are also available SCMs which result in reduction of water or HRWRA dosage to maintain the same rheological properties [10].

Rheology is used to determine the effect of changes in constituent materials and mixture proportions of cement-based materials and allows more complete description of the fresh properties compared to standard tests [11]. Rheological studies provide an information about behavior of materials in the plastic state and monitor the formation of the structure, which demonstrates the development of mechanical properties [12]. The flow behavior of the concentrated suspensions depends on the contact surface between solid particles and intermolecular forces such as van der Waals forces and steric forces [13]. The rheological parameters help to characterize the ease with which cement-based composites can be operated during mixing, placing, pumping, compacting and finishing. There is considerable evidence that the rheology of cement-based materials conforms to the Bingham model [12, 14]:

$$\tau = \tau_0 + \eta_{pl} \cdot \dot{\gamma} \tag{1}$$

where: τ_0 - the yield stress, describing the stress needed to initiate flow; η_{pl} - the plastic viscosity, which is a resistance of the material to flow; τ - the shear stress; $\dot{\gamma}$ - the shear rate.

Although at high shear rates or a very low water content non-linear behavior is observed and application of the Bingham model may lead to inaccurate results [11].

At least two measurements at considerably different shear rates are required to characterize a Bingham material [14, 15]. Devices that are based on rotational rheometry are often used to test cement mortars or concrete mixes [16]. Typically they are based on the measurement of the torque of an agitator of variable geometry. Changes of the rheological properties can be displayed qualitatively, but the results cannot be converted to the fundamental rheological units as it would for instance be possible with a coaxial cylinder rheometer. When applying a Bingham curve on the results according to the Eq. (1) with $\dot{\gamma}$ replaced by the rotation speed and τ replaced by the measured current, quantitative information about yield stress (g) and viscosity (h) of material can be obtained. Because the principle of measurement in rotational viscometers differs from coaxial viscometers, Bingham equation was modified by Tattersall and Banfill [15]:

$$M = g + hN \tag{2}$$

where: M - the torque; N - the rotation speed of the probe or the cylindrical vessel; g and h - constants. In this equation g (the intercept) is proportional to the yield stress τ_0 and h (the gradient) is proportional to the plastic viscosity η_{pl} of the material. The rheological parameters g and h are material constants. When the stress exceeds the yield stress value, the mixture starts to flow with the speed proportional to the plastic viscosity. The lower the plastic viscosity of the mixture, the higher is the speed of flow at a given load. But also the risk of segregation increases with the decrease of this parameter.

2 Experimental Program

2.1 Materials

The experimental program focused on the investigation of the rheological properties of cement mortars where 10% of cement mass was replaced by one additive. Four additives were used: two types of metakaolin MK1 and MK2, silica fume (SF) and limestone powder (LP). Tests were also performed on pastes composed of additive alone, no cement was added.

Specimens were prepared with Portland cement CEM I 42.5R conforming to the standard EN 197-1. According to the report provided by the manufacturer it has a Blaine fineness of 420 m^2/kg, insoluble residue 0.6% and LoI 3.2%. All the applied powders used as cement replacements were commercially available additions. They differed not only in PSD and specific area, but in the shape and texture of individual particles as well. The Table 1 presents the equivalent diameter for each accumulated percentage of particles and the measured surface area. The PSDs of each of the five powders as obtained using laser diffraction are given in Fig. 1.

Table 1. Properties of powders.

Property	CEM I	MK1	MK2	SF	LP
D_{10} [μm]	7.2	1.27	0.92	0.07	1.44
D_{50} [μm]	21.3	12.9	13.1	0.15	21.0
D_{90} [μm]	38.7	54.8	36.7	0.70	89.6
Specific surface BET [m^2g^{-1}]	–	13	16	28.7	1.1
Specific gravity [g cm^{-3}]	3.1	2.60	2.45	2.15	2.71

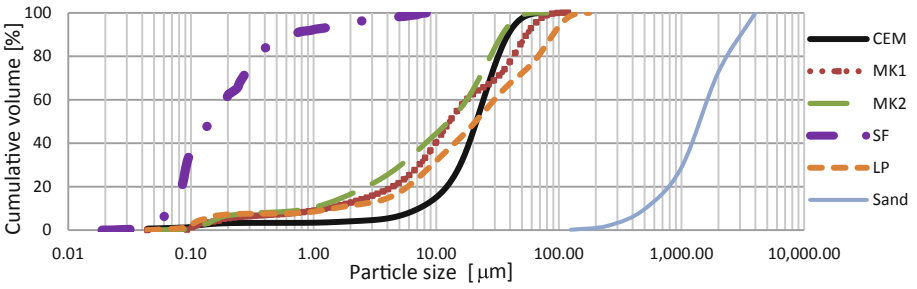

Fig. 1. Particle size distribution of the used powders and sand.

SEM images (Fig. 2) show the difference in particle size, shape and texture of the particular powders. Images were made using FEI Quanta 250 FEG SEM with different magnifications to show the details of the individual particles of the particular powders.

2.2 Experimental Procedure

The mini-cone test was conducted on pastes according to the procedure described in [17] to determine the water/solids (binder) volumetric ratio (V_w/V_b) for zero flow (β_p). Mini-cone flow tests with increasing V_w/V_b ratios were performed with the selected powder compositions and the relative slump Γ_p was calculated from the formula:

$$\Gamma_p = \left(\frac{d}{d_0}\right)^2 - 1 \tag{3}$$

where d – mean flow diameter, d_0 = 100 mm.

The intersection point of the linear regression of the function $\Gamma_p = f(V_w/V_b)$ with the y - axis is designated the β_p value.

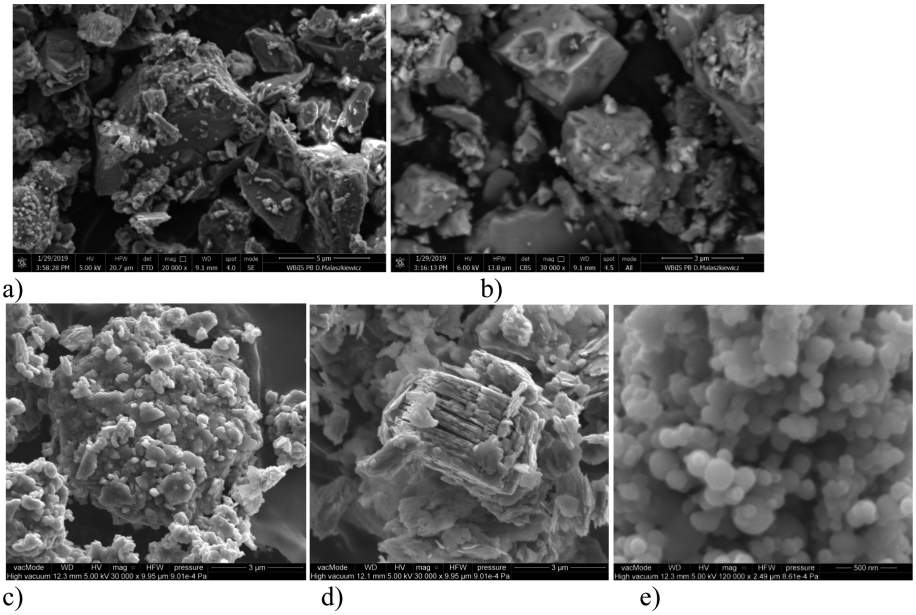

Fig. 2. SEM images of the powders (a) cement; (b) LP (c) MK1; (d) MK2; (e) SF.

The mini-cone test was also performed on mortars to determine the optimum HRWRA dosage. The paste:sand volumetric ratio (V_p/V_s) was constant for all mortars and equaled 1.22. It means that volume of paste amounted to 55% of mortar volume. The optimum admixture dosage was assumed for the mortar flow in the range 270 mm–300 mm. Because the rheological tests were performed also on mortars without admixture, the V_w/V_b at which the paste relative flow Γ_p = 0.56 (corresponds to flow diameter 125 mm) was assumed for all tested mortars. The equation of linear regression was used to determine V_w/V_b for Γ_p = 0.56.

Cement and the appropriate additive were first mixed in the mortar mixer (as specified in EN 196) at rotation speed 140 min^{-1} for about 30 s, than water containing the appropriate quantity of HRWRA was added and mixing continued for 60 s. Finally, sand was placed in the bowl. The total time of mixing was 3 min.

The rotational viscometer Viskomat XL (Schleibinger) was used to measure the rheological parameters corresponding to the yield stress and plastic viscosity. A fish-bone probe appropriate for mixes containing grains up to 8 mm was used. A measuring cylinder allows the measurement of a mixture of 3 dm^3. In this study the constant temperature of 20 °C ± 1 °C was kept during the tests. The test started after 10 min from the moment of mixing the constituent materials. The procedure consisted of the pre-mixing at maximum shear rate 0.5 s^{-1} (duration 420 s), the rest period (duration 60 s), increase of shear rate to 0.417 s^{-1} (25 min^{-1}) and keeping this rate for 30 s, and then ramp decrease of rate to 0.017 s^{-1} (1 min^{-1}). The rheological parameters g and h where calculated from the data logged during the final down-curve, which started 20 min after water addition. The measuring protocol is plotted in Fig. 3.

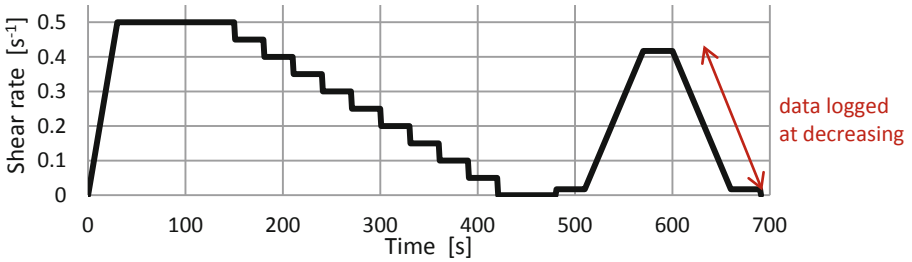

Fig. 3. Rheology measuring protocol - the variation of shear rate with time.

As a result of the measurement, a set of data expressing the resistance of the mix subjected to the stresses induced by the rotation of the impeller was obtained. By linear regression of the obtained results from the down-curve, the flow line of the mixture is obtained and compared with the modified Bingham Eq. (2), which allows to determine the rheological parameters of the tested fresh mortars.

3 Results and Discussion

3.1 Mini-Cone Test Results

The dependencies between the relative slump and V_w/V_b for all pastes and the equations of the linear regression of these dependencies are presented in Fig. 4. In order to achieve the desired slump flow, mixtures containing metakaolins and SF required larger amount of water, mainly because of the small particle size and increased surface area. The value of β_p doubled in the case of SF paste compared to the cement paste. Interesting situation was observed when two metakaolins were compared. Though PSDs are quite similar and cumulative percentages D_{10} and D_{50} are of the same order, the β_p for MK2 is almost

50% higher. A distinctive difference in the morphology of the individual particles could be responsible for such behavior. MK1 exhibited more rounded grains, while MK2 more lamellar structure, which significantly influenced the water demand.

Based on the results obtained on the pastes, the appropriate volumetric proportions $(V_w/V_b)_{125}$ corresponding to the mini-cone flow 125 mm were accepted for preparation of the mortars. The binder was either cement or cement with 10% mass replacement by the particular additive. Table 2 presents the volumetric and mass proportions between water and powders (binder). HRWR admixture was added gradually until the optimum flow of fresh mortar ranging from 270 mm to 300 mm was achieved (Fig. 5). The highest friction of admixture in relation to powders was required for the mortar with MK2, the lowest for the cement mortar and mortar with LP. Though PSDs of MK2 and SF differ significantly, both powders caused almost equally negative influence on workability in terms of flow and need for admixture. In the case of LP, the target flow was obtained at the first lowest dosage of the admixture. The observed differences in PSD and shape of the tested additions had an influence on the flow properties of pastes and mortars at the fresh state.

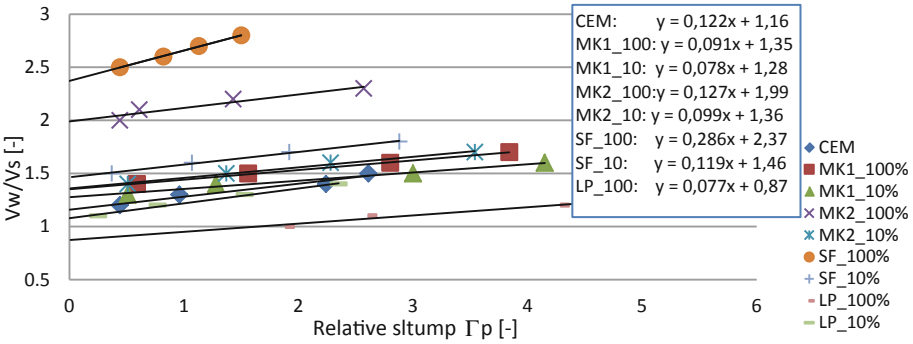

Fig. 4. Relative slumps of tested pastes.

Table 2. Volumetric and mass water: solids ratios for 125 mm flow.

	$(V_w/V_b)_{125}$	*w/b*
CEM I	1.23	0.40
MK1_10%	1.32	0.43
MK2_10%	1.42	0.47
SF_10%	1.53	0.51
LP_10%	1.16	0.38

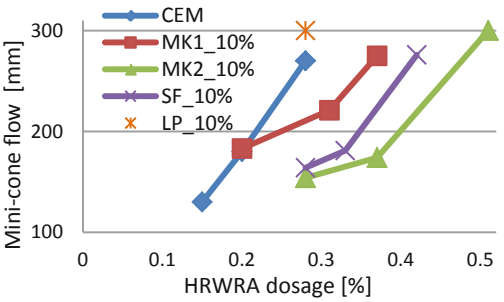

Fig. 5. Influence of dosage of HRWRA and powder type on flow value.

3.2 Rheological Properties

The torque and shear rate obtained from the rheometer for cement mortars with increasing admixture dosage and the linear functions determined for each set of the experimental results are plotted in Fig. 6. The examined mortars exhibited linear behavior and the Bingham model fitted well. The same procedure was performed for all tested fresh mortars. The results in terms of rheological parameters *g* and *h* are presented in Fig. 7a–b. As it was expected, with the increase of the admixture content the yield stress decreased and it was approaching zero at the target flow. In the cement mortar no significant change in viscosity was observed with the increase of admixture amount, while when LP was added - the viscosity improved even at the small admixture dosage (0.28%). Mortars with SF and MK1 exhibited significant decrease in shear stress even with the smallest HRWRA content, however the further increase in admixture dosing did not significantly affect the decrease in yield stress. Nevertheless, the progress in mini-cone flow was observed with the increase of admixture fraction. At the target dosage of admixture, a noticeable increase in viscosity was observed for mortars containing MK1 and SF. The lower plastic viscosity of fresh mortars containing MK1, MK2 and SF, especially without added admixture, compared to the cement and cement+LP mortars could be the result of higher water content (see Table 2). Yield stresses of mortars with no admixture added differed though they exhibited the same slump flow. The lowest yield stress was reported for mortars with MK1 and SF, the highest for LP. The differences in water:powders ratios could be responsible for such results. Generally LP improved workability even though D_{50} is the

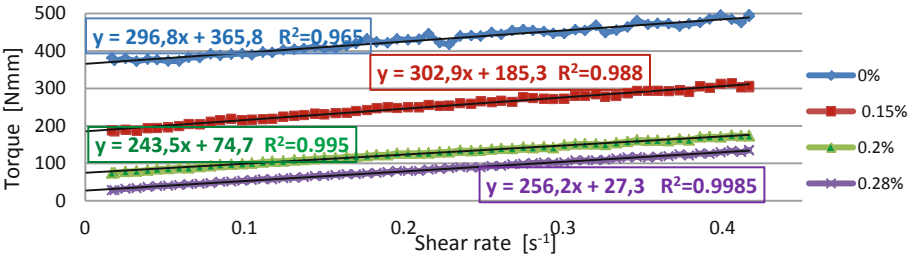

Fig. 6. Bingham model applied on rheograms of the cement mortar.

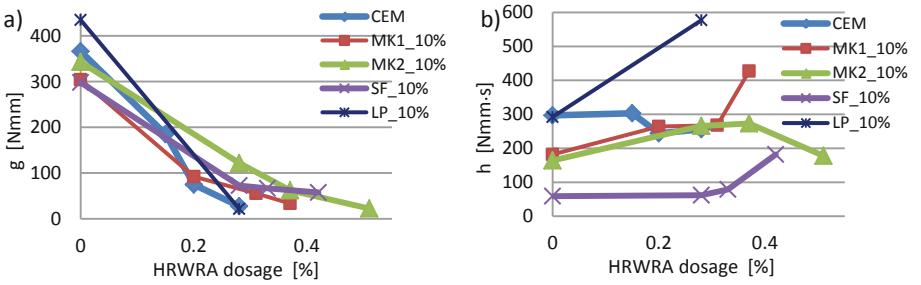

Fig. 7. Rheological parameters (a) yield stress expressed as *g*; (b) plastic viscosity expressed as *h*.

same as for cement and specific surface even higher. The difference in particle texture could be responsible for such behavior. LP particles are much smoother and regular compared to the cement particles.

4 Conclusions

The effect of four types of additives on the rheological properties of the fresh cement pastes and mortars was investigated. Both metakaolins and SF decreased workability. Higher water:powders proportions were required to maintain the same rheological properties as for the cement fresh mortar. Whereas LP improved fresh properties of paste and mortar. Not only PSDs, cumulative percentages and specific surface of the powders influence water and admixture demand of cement-based composites. Also shape and texture of the individual particles have an effect on the rheological properties.

Acknowledgement. The research was supported by the projects No. S/WBiIS/1/2016, and it was financially supported by the Ministry of Science and Higher Education, Poland.

References

1. Paiva H, Velosa A, Cachim P, Ferreira VM (2012) Effect of metakaolin dispersion on the fresh and hardened state properties of concrete. Cem Concr Res 42:607–612
2. Sfikas IP, Badogiannis EG, Trezos KG (2014) Rheology and mechanical characteristics of self-compacting concrete mixtures containing metakaolin. Constr Build Mater 64:121–129
3. García-Taengua E, Sonebi M, Hossain KMA, Lachemi M, Khatib J (2015) Effects of the addition of nanosilica on the rheology, hydration and development of the compressive strength of cement mortars. Compos Part B 81:120–129
4. Sua-iam G, Makul N (2015) Rheological and mechanical properties of cement–fly ash self-consolidating concrete incorporating high volumes of alumina-based material as fine aggregate. Constr Build Mater 95:736–747
5. Chen JJ, Fung WWS, Kwan AKH (2012) Effects of CSF on strength, rheology and cohesiveness of cement paste. Constr Build Mater 35:979–987
6. Gołaszewski J, Ponikiewski T, Kostrzanowska A (2011) Rheological properties of cement mixtures with high calcium fly ash. In: Proceedings of the international conference: non-traditional cement and concrete IV, Brno University of Technology, pp 410–419
7. Bentz DP, Ferraris CF, Galler MA, Hansen AS, Guynn JM (2012) Influence of particle size distributions on yield stress and viscosity of cement–fly ash pastes. Cem Concr Res 42:404–409
8. Senff L, Labrincha JA, Ferreira VM, Hotza D, Repette WL (2009) Effect of nano-silica on rheology and fresh properties of cement pastes and mortars. Constr Build Mater 23:2487–2491
9. Cassagnabere F, Diederich P, Mouret M, Escadeillas G, Lachemi M (2013) Impact of metakaolin characteristics on the rheological properties of mortar in the fresh state. Cem Concr Comp 37:95–107
10. Kim JH, Noemi N, Shah SP (2012) Effect of powder materials on the rheology and formwork pressure of self-consolidating concrete. Cem Concr Comp 34:746–753
11. Wallevik OH, Feys D, Wallevik JE, Khayat KH (2015) Avoiding inaccurate interpretations of rheological measurements for cement-based materials. Cem Concr Res 78:100–109

12. Sant G, Ferraris CF, Weiss J (2008) Rheological properties of cement pastes: a discussion of structure formation and mechanical property development. Cem Concr Res 38:1286–1296
13. Mueller S, Llewellin EW, Mader HM (2010) The rheology of suspensions of solid particles. Proc R Soc Math Phys Eng Sci 466:1201–1228
14. Banfill PFG (2006) Rheology of fresh cement and concrete. Rheol Rev 61–130
15. Tattersall GH, Banfill PFG (1983) The rheology of fresh concrete. Pitman, London
16. Schmidt W (2014) Design concepts for the robustness improvement of self-compacting concrete – effects of admixtures and mixture components on the rheology and early hydration at varying temperatures. Ph.D. thesis, Eindhoven University of Technology
17. The European Guidelines for Self-Compacting Concrete (2005) Specification, production and use. http://www.efnarc.org/publications.html

Effect of the Side Chain Density and Length of Polycarboxylate Ether Superplasticizers on the Thixotropic Structural Build-Up of Cement Paste

David Nicia(✉) and Dirk Lowke

Institute of Building Materials, Concrete Construction and Fire Safety, Technische Universität Braunschweig, Brunswick, Germany
d.nicia@ibmb.tu-bs.de

Abstract. Polycarboxylate ether superplasticizers (PCE) are of great importance to control interparticle interactions and hence the rheological properties of cement-based suspensions because their molecular structure can be modified according to the requirements. Nevertheless, the effect of individual parameters of the molecular structure on thixotropy is not yet fully understood. For a deeper understanding, specifically polymerized PCE with different side chain densities and side chain lengths were investigated. The effect of the molecular structure was studied by producing cement pastes with constant yield stress and determining the thixotropic structural build-up with a parallel plates rheometer.

The results indicate that thixotropy increases with decreasing side chain densities and decreasing side chain lengths. This might be explained by the fact that PCE molecules with low side chain densities adsorb faster and to a larger extent on cement particles surfaces. Consequently, less PCE molecules are left in the pore solution to enable permanent adsorption on newly formed and growing hydration products, leading to a decrease of steric repulsion and hence to an increase in thixotropy. Furthermore, thixotropy increases in case of lower side chain lengths. This effect might be related to a decreased PCE layer thickness on the cement particle surface, increasing the probability to be overgrown by hydration products.

Keywords: Rheology · Polycarboxylate ether superplasticizer (PCE) · Thixotropy · Structural build-up · Cement-based suspensions

1 Introduction

The rheological properties of fresh concrete determine its behavior during transport, handling, casting and setting. Concrete exhibits a thixotropic behavior [8, 14], which implies a decrease of yield stress and viscosity as a function of shear load, caused by structural breakdown, followed by a time-dependent recovery of both parameters due to structural build-up at rest. The thixotropic structural breakdown and build-up are attributed to changes in the particle agglomeration state caused by shear forces and time, being fully reversible [17]. The prediction of the thixotropic behavior of fresh

V. Mechtcherine et al. (Eds.): RheoCon 2019/SCC 2019, RILEM Bookseries 23, pp. 125–133, 2020.
https://doi.org/10.1007/978-3-030-22566-7_15

concrete is highly relevant for processing of modern concretes such as form filling ability [2], formwork pressure [14], pumping or 3D concrete printing [13, 16].

Polycarboxylate ether superplasticizers (PCE) are frequently used to improve the flow ability of cement-based suspensions due to the effective particle dispersion without further addition of water [6]. The dispersion effect is primarily based on steric repulsion of polymer molecules that adsorb on cement particles surfaces, counteracting attractive interparticle forces [12, 21]. PCE exhibit a large flexibility in molecular design enabling a precise control of rheological properties of cement-based suspensions [10, 23]. Existing investigations focused on the effect of PCE molecular structures on yield stress, with the result that yield stress decreases with increasing number density of carboxylic groups, decreasing side chain density, increasing side chains length and decreasing backbone length [20, 22, 23]. On the other hand, the effect of the PCE molecular structure on the thixotropic structural build-up is poorly explored.

2 Theoretical Background

2.1 Molecular Structure of PCE

PCE molecules consist of a backbone with numerous side chains that both can be synthesized individually. A simplified structural description of comb-shaped copolymers is proposed by [5] introducing the parameters n, N and P (Fig. 1a). n implies the overall number of repeating units in the PCE structure corresponding to the backbone length. N gives the number of monomers, usually carboxylic groups, in one repeating unit that incorporates one side chain. P represents the length of one side chain in the repeating unit.

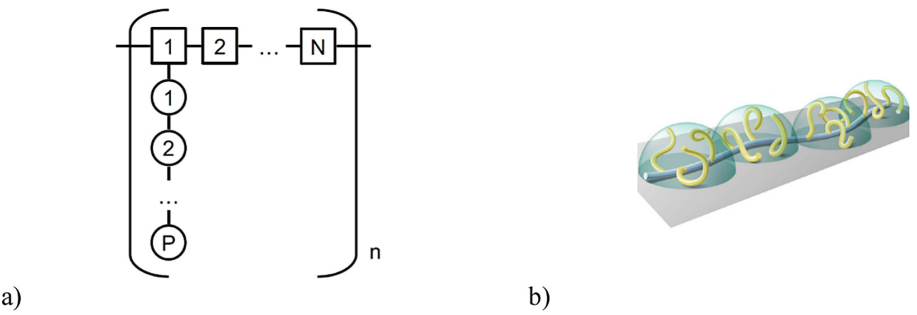

Fig. 1. (a) Classification of comb-shaped copolymers after [5] (b) Schematic representation of an adsorbed copolymer as a chain of spherical cores (from [9]).

2.2 Effect of the Molecular Structure of PCE on Particle Dispersion

The particle dispersing effect of PCEs in cement-based suspensions is related to the amount of molecules adsorbed on the particle surface, i.e., surface coverage (Fig. 1b) [9, 20, 22, 23]. The larger the surface coverage the higher the steric repulsion that

counteracts the attractive van der Waal forces. As a result, particles are effectively dispersed due to steric forces effecting a decrease in yield stress [6, 22]. Moreover, adsorption of PCE molecules depends on their molecular architecture and increases for higher numbers of anionic groups in the backbone (N-1, Fig. 1(a)) [12, 20, 22]. The overall dispersing effect of PCE molecules is related to the adsorbed layer density at full surface coverage that scales with molecular structure according to $P^{7/10}/N^{-1/10}$ and therefore mainly depends on the side chain length [5]. However, it has to be noted that for PCE amounts commonly used in practice, the surface coverage is incomplete, hence, the adsorbed fraction is a crucial parameter [6].

Cement-based suspensions are reactive systems with numerous effects perturbing the action of PCEs [4]. One important mechanism is the formation and growth of hydration products at the cement particle surface that can overgrow adsorbed PCE molecules (Fig. 2) [4]. As a result, less PCE molecules are available to modify inter-particle forces and hence yield stress increases. Therefore, a sufficient PCE deposit in the aqueous phase is necessary to enable permanent adsorption on the newly formed hydration products to obtain workability for the desired time period [11].

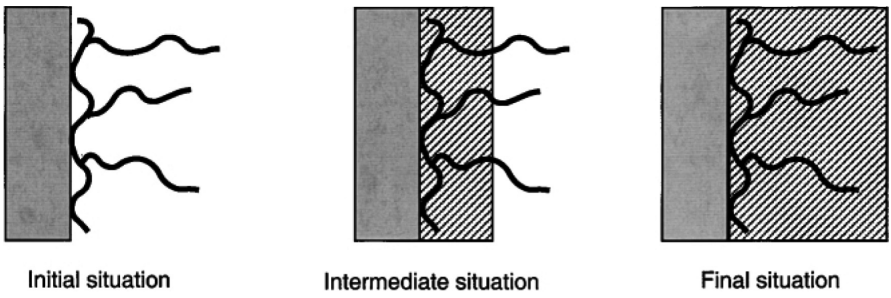

Fig. 2. Schematic illustration of a PCE molecule adsorbed on a hydrating clinker particle, gradually overgrown by reaction products (from [19]).

2.3 Thixotropic Structural Build-Up in the Presence of PCE

The thixotropic structural build-up of cement-based suspensions is controlled by colloidal surface interactions, particle bridging due to the formation of hydration products at contact points and strengthening of the particle network (Fig. 3) [17]. In the presence of PCE, the particle network exhibits lower strength and stiffness due to steric repulsion. Consequently, particle bridges break apart easier, i.e., at lower shear stress [3]. The extent of this phenomenon depends on the particle surface coverage with superplasticizer [7, 8]. Lower surface coverage leads to reduced steric interactions, allowing faster flocculation and therefore a higher thixotropy and vice versa (Fig. 3).

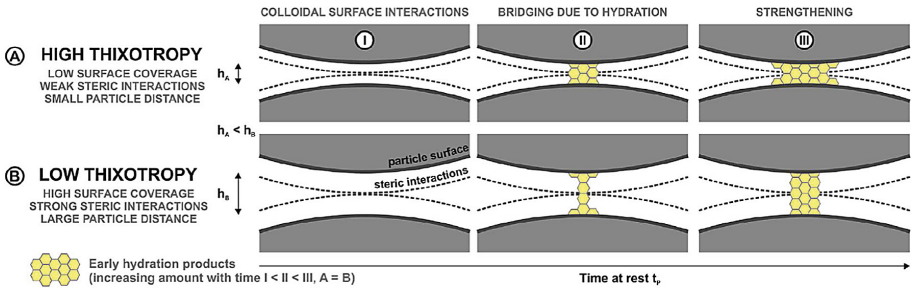

Fig. 3. Schematic illustration of the thixotropic structural build-up as a function of the PCE surface coverage (from [8]).

3 Experimental Programme, Materials and Methods

3.1 Concept

The investigations focus on the effect of (a) the side chain density and (b) the side chain length of PCE molecules on the thixotropic structural build-up of cement pastes at constant flow ability. In practical applications, the question usually rises how the structural build-up can be affected at a designated workability. For this purpose, all experiments were performed at equal yield stress (spread flow = 270 mm ± 5 mm; $\tau_{0D} \approx 9.6$ Pa acc. to [18]). The target spread flow was achieved by adjusting the PCE dosage for each batch.

3.2 Materials

In this study, six specifically polymerized PCEs with different side chain densities and side chain lengths were used. Qualitative information on the PCE structure are given in Table 1.

Table 1. Qualitative information on the molecular structures of the PCEs used.

Structural parameter	PCE SH	PCE SM	PCE SL	PCE LH	PCE LM	PCE LL
Side chain length	Short	Short	Short	Long	Long	Long
Side chain density	High	Medium	Low	High	Medium	Low

A commercially available ordinary Portland cement CEM I 42.5 R was used. The mineralogical composition (from XRD and Rietveld analysis) and the mean volumetric particle diameter $d_{v,50}$ (from laser granulometry) are given in Table 2. For each test one batch of 1 dm^3 cement paste was produced by mixing the constituents for 4 min in a standard EN 196-1 mixer [1] (Fig. 3). PCE was added directly into the mixing water (Table 3).

Table 2. Mineralogical composition and mean particle diameter $d_{v,50}$ of the cement used.

Cement type	C_3S [M.%]	C_2S [M.%]	C_3A [M.%]	C_4AF [M.%]	$CaSO_4$ [M.%]	CaO [M.%]	K_2SO_4 [M.%]	MgO [M.%]	$d_{v,50}$ [µm]
CEM I 42.5 R	70.9	10.8	5.1	11.1	5.9	1.1	0.4	0.4	15.3

Table 3. Mixing proportions of the cement paste.

Cement volume [dm^3/m^3]	Water (distilled) volume [dm^3/m^3]	w/c ratio	V_w/V_c [-]	Solid fraction Φ [vol.%]
526	474	0.29	0.90	0.53

3.3 Measurement of the Thixotropic Structural Build-Up

The thixotropic structural build-up was investigated using a parallel plates rheometer (Anton Paar MCR 502) with serrated plates (diameter: 50 mm; roughness: 0.5 mm). The measurement started 15 min after water addition. For a homogenization and to induce a structural breakdown, the material was subjected to a shear rate of 80 s^{-1} for a duration of 30 s, see shear profile in Fig. 4. Simultaneously, the spread flow was determined after preshearing the material for 30 s with a handmixer. In order to characterize the structural build-up at rest, the static yield stress was determined by applying low shear rates of 0.1155 s^{-1} for a duration of 6 s at different time intervals. The shear rate and shear time were chosen as a compromise in order to ensure a measureable static

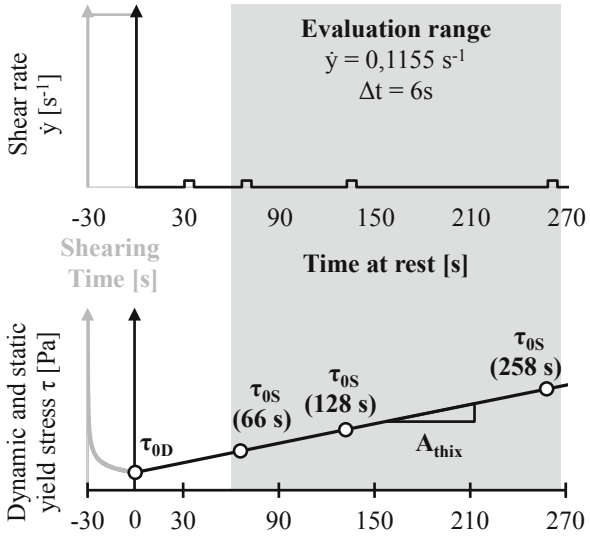

Fig. 4. Shear profile, evaluation range and definition of the thixotropic structural build-up A_{thix} as the increase of static yield stress τ_{0S} over time.

yield stress and to only slightly disrupt the structure. The low applied shear rate leads to an incomplete destructuration of the particle microstructure, which is why multiple static yield stress measurements are evaluated (Fig. 4). From the increase of static yield stress at rest as a function of time, the thixotropic structural build-up A_{thix}, was calculated as a measure of thixotropy [15], see evaluation range in Fig. 4.

4 Results and Discussion

4.1 Effect of the PCE Side Chain Density on Thixotropy

Figure 5a shows the thixotropic structural build-up A_{thix} of cement pastes for different side chain densities plotted separately for copolymers with short or long side chains.

The thixotropic structural build-up A_{thix} ranges from 0.14 Pa/s to 0.88 Pa/s indicating a distinct effect of the PCE molecular structure. In case of short side chains, thixotropy increases significantly with decreasing side chain density (Fig. 5a). However, the effect of the side chain density on thixotropy is much less pronounced for PCE molecules with long side chains. In case of PCE molecules with high side chain densities and long side chains, the cement pastes generally show a lower thixotropy compared to PCE molecules with a medium side chain density. Furthermore, thixotropy is reduced in case of low side chain densities compared to the medium side chain densities. Nevertheless, the results of different side chain densities have no clear effect on thixtropy in case of PCE molecules with long side chains.

The significant increase of A_{thix} with decreasing side chain density in case of short side chains might be caused by faster adsorption of PCE molecules. Since the anionic

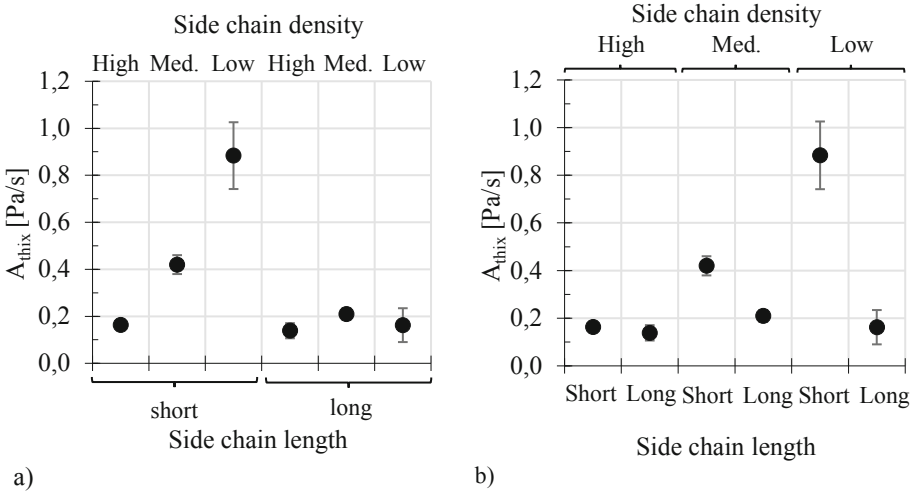

Fig. 5. (a) Thixotropic structural build-up A_{thix} of cement pastes with constant yield stress (spread flow 270 mm ± 5 mm) as a function of the side chain density for constant side chain lengths (b) Same data as in (a) plotted separately for different side chain densities to better visualize the effect of the side chain length.

charge in the backbone is less shielded by the side chains, it is likely that molecules could adsorb faster and to a larger extent [11, 12, 20, 22]. Consequently, less polymer molecules might be left in the pore solution to adsorb on the newly formed hydration products. This would result in weaker steric interactions and hence in an increase of thixotropy (Fig. 3).

4.2 Effect of the PCE Side Chain Length on Thixotropy

In Fig. 5b the thixotropic structural build-up A_{thix} is presented for different side chain lengths at constant side chain densities, respectively. This plot reveals that the thixotropy of the cement paste is generally higher for reduced side chain lengths.

Those observations may be explained by the fact that adsorbed PCE molecules with low side chain lengths are more likely to be overgrown by hydration products. As it is known, the adsorbed layer thickness decreases for lower side chain lengths [5] (Fig. 2). Consequently, the steric interactions of PCE molecules with short side chains might be lower because of the decreased layer thickness due to a thinner effective layer of copolymers on the particle surfaces compared to PCE molecules with longer side chains. Moreover, the lower steric repulsion would lead to a higher thixotropy since the particle distance is smaller (compare principle in Fig. 3).

5 Conclusion and Outlook

In this paper, the effect of the PCE side chain density and side chain length on the thixotropic structural build-up of cement paste was investigated. The results indicate that thixotropy is increased by lower side chain densities in case of PCE molecules with short side chains. However, when PCE molecules exhibit long side chains, the effect of the side chain density on thixotropy is less pronounced. Furthermore, short side chains are likely to increase thixotropy, independently of the side chain density of the PCE molecule.

The findings in case of PCE molecules with low side chain density may be explained by the fact that less PCE is left in the pore solution since the affinity for adsorption on the cement particle surface is increased. Therefore, less PCE is available to adsorb on newly forming and growing hydration products, causing a higher thixotropy because of less steric repulsion. The effect of increasing thixotropy due to short side chains might be the result of a decreased PCE layer thickness on the cement particle surface, leading to an increased probability to be overgrown by hydration products. Consequently, the steric repulsion decreases and thixotropy increases because of a reduced particle distance.

To further investigate this phenomenon, the TOC depletion method will be used to determine the residual amount of PCE in the pore solution. Furthermore, the surface coverage of cement particles with the individual PCE molecules will be determined to enable quantitative explanations of the phenomena observed.

References

1. EN 196-1 (2016) Methods of testing cement - Part 1: determination of strength
2. Ferrari L, Boustingorry P (2015) The influence of paste thixotropy on the formwork-filling properties of concrete. Special Publication, vol 302
3. Ferron RD, Shah S, Fuente E, Negro C (2013) Aggregation and breakage kinetics of fresh cement paste. Cem Concr Res 50:1–10
4. Flatt RJ, Houst YF (2001) A simplified view on chemical effects perturbing the action of superplasticizers. Cem Concr Res 31(8):1169–1176
5. Flatt RJ, Schober I, Raphael E, Plassard C, Lesniewska E (2009) Conformation of adsorbed comb copolymer dispersants. Langmuir ACS J Surf Colloids 25(2):845–855
6. Gelardi G, Mantellato S, Marchon D, Palacios M, Eberhardt AB, Flatt RJ (2016) Chemistry of chemical admixtures. In: Science and technology of concrete admixtures. Elsevier, pp 149–218
7. Lowke D (2014) Segregation resistance and robustness of self-compacting concrete. Optimization based on modelling interparticle interactions in cement based suspensions (in German). Beuth, Berlin, Wien, Zürich
8. Lowke D (2018) Thixotropy of SCC—a model describing the effect of particle packing and superplasticizer adsorption on thixotropic structural build-up of the mortar phase based on interparticle interactions. Cem Concr Res 104:94–104
9. Marchon D, Juilland P, Gallucci E, Frunz L, Flatt RJ (2017) Molecular and submolecular scale effects of comb-copolymers on tri-calcium silicate reactivity. Toward molecular design. J Am Ceram Soc 100(3):817–841
10. Nkinamubanzi P-C, Mantellato S, Flatt RJ (2016) Superplasticizers in practice. In: Science and technology of concrete admixtures. Elsevier, pp 353–377
11. Ohta A, Sugiyama T, Tanaka Y (1997) Fluidizing mechanism and applications of polycarboxylate-based superplasticizers. In: Malhotra VM (ed) International conference on superplasticizer, vol 5, pp 359–378
12. Plank J, Sachsenhauser B (2009) Experimental determination of the effective anionic charge density of polycarboxylate superplasticizers in cement pore solution. Cem Concr Res 39 (1):1–5
13. Reiter L, Wangler T, Roussel N, Flatt RJ (2018) The role of early age structural build-up in digital fabrication with concrete. Cem Concr Res 112:86–95
14. Roussel N (2005) Steady and transient flow behaviour of fresh cement pastes. Cem Concr Res 35(9):1656–1664
15. Roussel N (2006) A thixotropy model for fresh fluid concretes. Theory, validation and applications. Cem Concr Res 36(10):1797–1806
16. Roussel N (2018) Rheological requirements for printable concretes. Cem Concr Res 112:76–85
17. Roussel N, Ovarlez G, Garrault S, Brumaud C (2012) The origins of thixotropy of fresh cement pastes. Cem Concr Res 42(1):148–157
18. Roussel N, Stefani C, Leroy R (2005) From mini-cone test to Abrams cone test. Measurement of cement-based materials yield stress using slump tests. Cem Concr Res 35 (5):817–822
19. Sakai E, Daimon M (1997) Mechanisms of superplastification. In: Materials Science of Concrete IV, pp 91–111
20. Sakai E, Yamada K, Ohta A (2003) Molecular structure and dispersion-adsorption mechanisms of comb-type superplasticizers used in Japan. ACT 1(1):16–25

21. Uchikawa H, Hanehara S, Sawaki D (1997) The role of steric repulsive force in the dispersion of cement particles in fresh paste prepared with organic admixture. Cem Concr Res 27(1):37–50
22. Winnefeld F, Becker S, Pakusch J, Götz T (2007) Effects of the molecular architecture of comb-shaped superplasticizers on their performance in cementitious systems. Cement Concr Compos 29(4):251–262
23. Yamada K, Takahashi T, Hanehara S, Matsuhisa M (2000) Effects of the chemical structure on the properties of polycarboxylate-type superplasticizer. Cem Concr Res 30(2):197–207

Interaction of Superplasticizers with Cement from the Point of View of Colloid Chemistry

Johann Plank(✉) and Manuel Ilg

Chair for Construction Chemistry, Technische Universität München, Munich, Germany
sekretariat@bauchemie.ch.tum.de

Abstract. When cement is mixed with water, the clinker phases immediately start to dissolve and a large amount of ions is released into the pore solution. As a result, the ion concentration rapidly increases until the aqueous phase is supersaturated, at which first hydration products are precipitated. As the dissolution, crystallization and the initial hydration reactions all occur at the solid-liquid interface, it is appropriate to consider early cement hydration from the aspects of colloid and interface science.

Generally, fresh cement pastes constitute a thermodynamically unstable colloidal dispersion of mesoscopic particles and hydrate phases in water. The rheological properties (e.g. viscosity, yield stress) and the stability are affected by colloidal and interparticle interactions (e.g. Brownian effects, hydrodynamic and contact forces). However, the poor workability of cement suspensions can be attributed to attractive van der Waals forces between cationic and anionic surface areas. To overcome those forces, superplasticizers are added which disperse cement by imparting an electrostatic (polycondensates) or steric (polycarboxylates) effect. Superplasticizers can interact with cement via adsorption (=physisorption), chemisorption (=intercalation into early hydrate phases) or at low water-to-cement ratios even through repulsive depletion forces induced by the portion of non-adsorbed polymers remaining in the pore solution.

In light of this, the aim of the paper is to give an overview of the different kinds of interactions of superplasticizers with cement from a colloid chemistry point of view. It will be shown, to which thermodynamic parameters the adsorption process is subjected and how the chemical composition of the polymers affects the adsorption behavior. Additionally, experimental methods will be presented that are commonly applied for the investigation of cement-superplasticizer interactions (adsorption and zeta potential measurements). Finally, the role of non-adsorbed superplasticizer molecules on the dispersion of cementitious systems with high solid volume fractions will be discussed.

Keywords: Dispersion · Adsorption · Superplasticizer · Colloid chemistry · Adsorbed layer thickness

V. Mechtcherine et al. (Eds.): RheoCon 2019/SCC 2019, RILEM Bookseries 23, pp. 134–141, 2020.
https://doi.org/10.1007/978-3-030-22566-7_16

1 Dispersion Mechanism of Superplasticizers

Ordinary Portland cement comprises silicate (C_3S, C_2S) and aluminate phases (C_3A, C_4AF) as well as sulfate carriers (e.g. gypsum) for the regulation of the set behavior. When suspended in water, the clinker phases develop a heterogeneous surface charge which leads to the flocculation of the cement particles [1]. Thus, some of the mixing water is entrapped resulting in a high viscosity. However, the agglomerates can be dissipated by the addition of superplasticizers like polycondensates or polycarboxylates (PCEs) which modify the interparticle forces.

It is well established that polycondensates disperse cement through an electrostatic effect, while PCEs achieve dispersion through a combination of electrostatic and steric repulsive forces [2, 3]. To achieve dispersion the superplasticizers need to adsorb at the solid-liquid interface. After adsorption the particles exhibit a negative surface charge which provokes an electrostatic repulsion whose magnitude is much stronger for polycondensates due to their higher anionicity. The electrostatic stabilization of colloidal suspensions is described by the DLVO theory developed by Derjaguin, Landau, Verwey and Overbeek. According to this model, the dimension of the electrostatic effect depends on the electric charge and the Debye length that represents the thickness of the ion cloud surrounding the suspended particles. In contrast to polycondensates, PCEs additionally impart a steric effect induced by their polyethylene glycol side chains [2]. These non-ionic lateral chains protrude into the pore solution and prevent cement particles from approaching each other too close. The steric effect correlates with the thickness of the adsorbed polymer layer, as obvious from the Ottewill-Walker equation:

$$V_{\text{steric}}(a) = \frac{4\pi kTC_v^2}{3v_1^2\rho_2^2}(\psi_1 - \kappa_1)(\delta - a)^2\left(3R + 2\delta + \frac{a}{2}\right)$$

where C_v is the concentration of the adsorbed polymer, v_1 is the molecular volume of the solvent molecules, δ is the adsorbed layer thickness, ρ_2 is the density of the adsorbate (polymer), ψ_1 is the entropy, κ_1 is the enthalpy, R is the radius of the adsorbate, and a is the distance between two adsorbate particles.

The importance of the adsorbed layer thickness for the steric stabilization is supported by findings from Houst et al. who showed that PCEs with longer side chains are more powerful dispersants than those exhibiting shorter ones [4]. Therefore, knowing the layer thickness can help to better understand the differences in the performance characteristics of superplasticizers. Unfortunately, the experimental determination is not very easy because no direct measurement on cement particles is possible due to the continuous changes of their surface composition during the hydration reactions. So far, the layer thicknesses of only a limited number of PCE products have been assessed, most often by atomic force microscopy (AFM) using non-reactive substrates like quartz, mica or magnesium oxide (MgO) [5]. This method produced relatively low values for the layer thickness (1 nm–4 nm) which are far below the values calculated for ideally stretched side chains. For example, many common PCEs exhibit lateral side chains made up of 45 ethylene oxide units which in an ideally stretched conformation

would spread over ~12.5 nm. The low values for the layer thickness are often ascribed to compression of the polymer layer by the negatively charged AFM tip. Based on those results, it is argued that AFM is an appropriate method to determine the actual adsorbed layer thickness of PCEs. Thus, more reliable information from additional methods is required to obtain a better understanding of the actual dimensions of the adsorbed layer thickness.

Recently, molecular dynamics simulations (MDS) were carried out to investigate the adsorption behavior of PCEs (MPEG-, APEG- and IPEG-PCE) on MgO in synthetic cement pore solution [6]. It was found that the adsorbed conformation is sensitive to the initial orientation of the polymers against the MgO surface. To be more specific, a parallel orientation favored a train like conformation, whereas a perpendicular one was more beneficial for a loop or tail shaped adsorption mode. Depending on the chemical composition of the PCEs quite different conformations were obtained (Fig. 1). According to the results of the MD simulations, the MPEG-PCE adsorbs in a rather flat conformation (=train) covering a large surface area that results in a thin layer thickness. However, the APEG-PCE provokes a medium but dense polymer layer. The highest layer thickness was observed for the IPEG-PCE that adsorbs in a tail like conformation mode. By interconnecting these findings with results from adsorption and fluidity tests it was inferred that a layer thickness higher than 6 nm is necessary for a high dispersing efficacy at a standard dosage of the PCE [6].

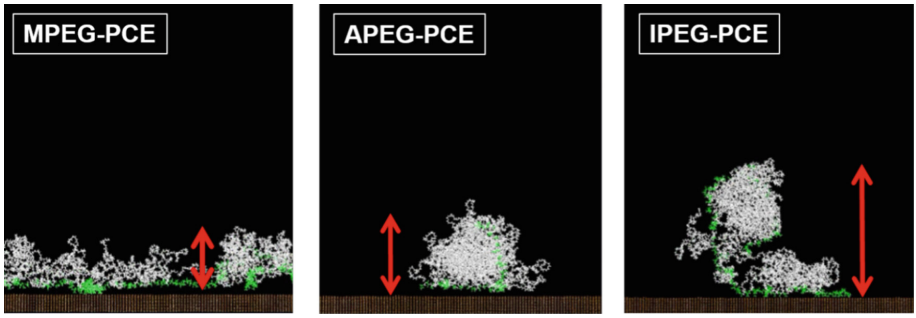

Fig. 1. Adsorbed conformations of different PCEs on MgO as obtained by MD simulations.

2 Adsorption Behavior of Superplasticizers

The working mechanism of superplasticizers relies on physical adsorption (=physisorption) of the anionic polymers on oppositely charged surface areas. Generally, adsorption is a dynamic process with three fundamental steps including the diffusion of the polymers to the solid-liquid interface, the physical attachment to the surface and the final rearrangement of the polymer layer until a maximum number of binding points is achieved [7]. From an energetic perspective, adsorption spontaneously occurs when the Gibbs free energy of adsorption ΔG is negative in sign. According to the Gibbs Helmholtz equation ($\Delta G = \Delta H - T \cdot \Delta S$) this is the case, when heat is released ($\Delta H < 0$) and/or the entropy of the system increases ($\Delta S > 0$). However, depending on

the molecular composition of the superplasticizer, enthalpy or entropy may be the prevalent parameter which instigates adsorption [8]. The experimental determination of ΔH and ΔS for polycondensates revealed that their adsorption is mainly driven by enthalpic contributions resulting from strong electrostatic interactions of the highly anionic polymers with the particle surface. For PCEs, adsorption primarily derives from a huge gain in entropy owed to the release of a large amount of ions and water molecules from the particle surface and the hydrate shell of the polymer [8].

The adsorption behavior of superplasticizers can be modified by the molecular weight, chemical composition and the overall polymer structure. It is well known, that differences in the adsorption properties entail quite diverging performance characteristics (e.g. slump retention capability). For instance, the high anionic character of polycondensates (e.g. BNS, MFS) favors an immediate and almost quantitative adsorption on cement. Consequently, the fluidity rapidly decreases within the first 30 min because no polymer remains in the pore solution to disperse newly formed hydration products. The adsorption properties of PCEs are influenced by the anionic charge amount and the side chain density. Principally, two generic types are differentiated (Fig. 2). PCE variants with a high side chain density and short side chains are favorable for ready mix concrete, whereas products with a high anionicity and a long side chain length are mainly used for precast concrete. The PCE with a low anionic charge amount initially adsorbs only in a small quantity (20%–30% of dosage). The reserve of polymer remaining in the pore solution can then gradually adsorb over time which leads to a long slump retention. Because of this mechanism, such PCEs require a relatively high dosage. Oppositely, PCEs for precast concrete adsorb in a high amount (70%–80%) which engenders a fast decrease of the initial fluidity due to a much smaller depot effect of the non-adsorbed polymers.

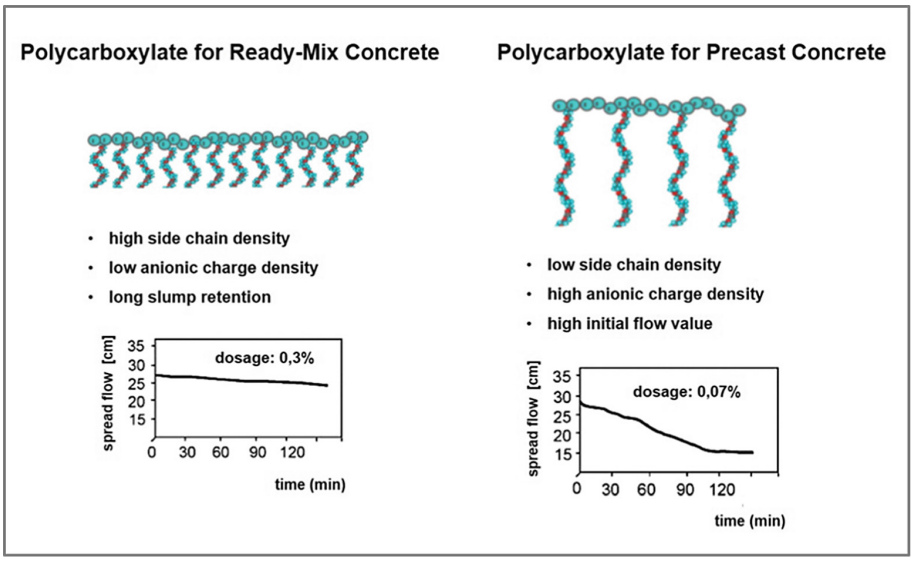

Fig. 2. Structural composition of PCEs applied in ready-mix and precast concrete.

3 Methods for Investigating Cement-Superplasticizer Interactions

Usually, the interaction of superplasticizers with cement is investigated by adsorption measurements using the depletion method. Here, the amount of polymer remaining in the pore solution after contact with cement at equilibrium condition is quantified by total organic carbon (TOC) analysis. Adsorbed amounts are determined for increasing polymer additions until a plateau value is reached (=saturated adsorption) signifying full surface coverage. Adsorption isotherms can be developed then by plotting the depleted amount of polymer as a function of the initial polymer concentration. The adsorption isotherms obtained for polycondensate and PCE based superplasticizers generally comply with the Langmuir adsorption model. However, it has to be noted that this analytical method is incapable of distinguishing the amount of polymer adsorbed via physical attraction from the portion which was consumed by absorption (=chemical intercalation) or precipitation. Therefore, data obtained from adsorption measurements should be interpreted in a prudent way since this method only gives an indication about the depleted amount of polymer.

Actual adsorption of superplasticizers can be corroborated by zeta potential measurements of cement slurries using the electroacoustic method. The zeta potential represents the electric potential at the shear plane between the Stern layer (stationary layer) and the diffuse ion layer of a colloidal particle. Though zeta potential does not correspond to the actual surface charge, it provides useful information about the colloidal stability and the working mechanism of superplasticizers. The typical zeta potential curves for a polycondensate and PCE based superplasticizer are illustrated in Fig. 3. As can be seen there, rising additions of the polycondensate gradually decreases the zeta potential to highly negative values (~ -55 mV) until to the saturated adsorption. At this point, the zeta potential remains constant because no polymer can adsorb on the surface anymore. The highly negative zeta potential induces an electrostatic repulsion of the cement particles.

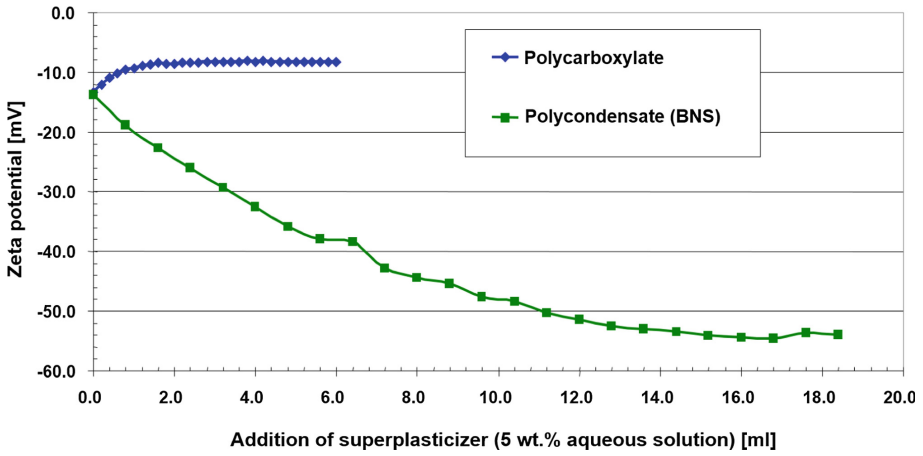

Fig. 3. Zeta potential of cement slurries admixed with different types of superplasticizers.

Adsorption of PCEs generally provokes an increase of the zeta potential. This can be attributed to a displacement of the shear plane by the polyethylene glycol side chains. PCEs with a long side chain length ($n_{EO} \geq 20$) move the shear plane to greater distances away from the cement surface thus causing a more positive value [9].

However, still the question remains on which surface areas superplasticizers adsorb. Yoshioka et al. found that a much higher quantity adsorbs on the aluminate phases (C_3A, C_4AF) than on the silicates (C_3S, C_2S) [2]. This was attributed to the different zeta potentials of the pure cement minerals. C_3A and C_4AF exhibit a positive zeta potential, whereas C_3S and C_2S develop a negative one. A further study revealed that also the adsorbed amount of superplasticizers on the surface of early hydration products is quite different [10]. High adsorbed amounts were especially found for those hydrate phases with a positive zeta potential (i.e. ettringite and mono sulfoaluminate). No adsorption occurred on syngenite, portlandite and gypsum because their zeta potential is zero or negative. This means that superplasticizers are mainly concentrated on surface areas where hydration products with a positive zeta potential crystallize. Thus, a mosaic structure results with an uneven distribution of the polymers on the surface area of the hydrating cement grain (Fig. 4) [10].

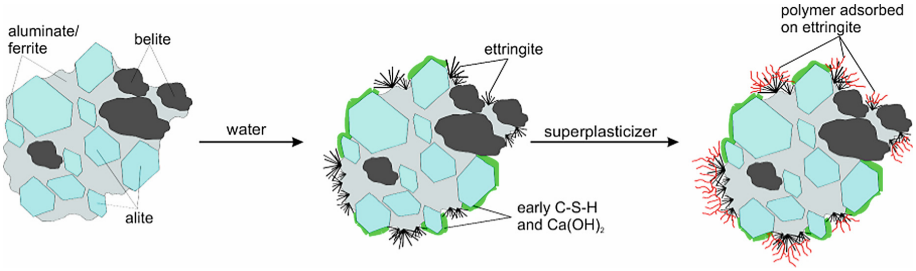

Fig. 4. Schematic presentation of the preferential adsorption sites of superplasticizers on a hydrating cement grain [10].

4 Chemisorption of Superplasticizers

Superplasticizers can interact with cement not only via surface adsorption, also intercalation (chemisorption) of a part of the polymer into the layered structure of calcium aluminate hydrates (C-A-H) may occur during cement hydration. This reaction is highly undesirable because after intercalation the polymer can no longer induce any fluidity. It was found that such intercalates (=organo-mineral phase) form instantaneously upon contact of cement with water when little or no sulfate is initially available for the hydration of C_3A [11]. For cements possessing a high content of alkali sulfates no intercalation was observed. The reaction patterns of C_3A are illustrated for different sulfate concentrations in Fig. 5. Generally, intercalation can be prevented by using alkali sulfates which immediately dissolve or by a delayed addition mode of the superplasticizer.

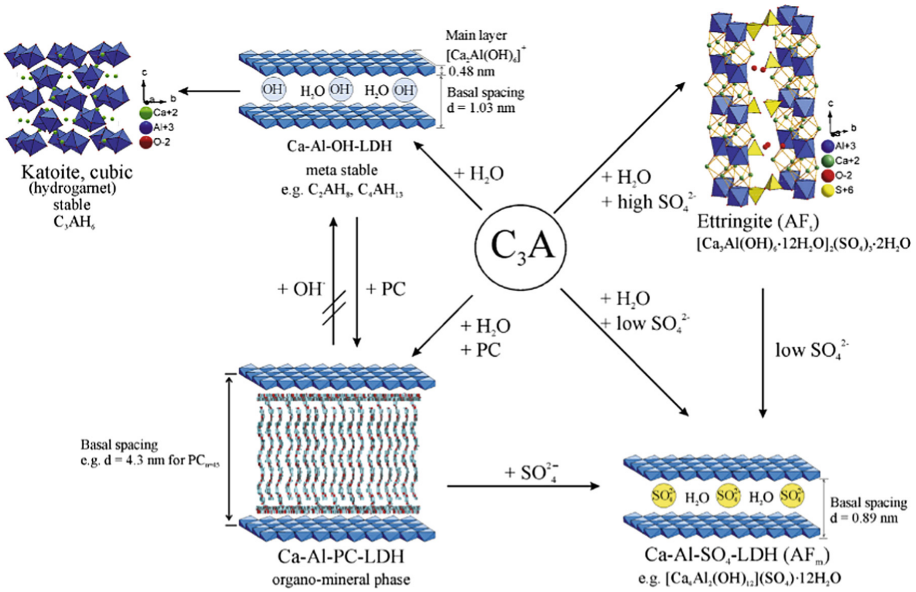

Fig. 5. Reaction patterns of C_3A hydrated at different sulfate concentrations in the absence and presence of a PCE superplasticizer [11].

5 Dispersion Forces at Low w/c-Ratios

Some studies suggest that at low w/c ratios the conventional models for dispersion like the DLVO theory and the Ottewill-Walker equation are no longer exclusively applicable. Instead, the portion of non-adsorbed polymers remaining in the pore solution seems to contribute to cement dispersion as well. This was first described by Sakai et al. who investigated the fluidity of low heat Portland cement – silica blends using different PCE superplasticizers at water-to-powder ratios from 0.16–0.32 [12]. According to their results, the paste fluidity at low w/p ratios (i.e. 0.16) cannot derive only from a steric effect of adsorbed PCE polymers, but is linked to non-adsorbed PCEs that remain in the pore solution. More recent studies showed that even specific non-ionic polymers and glycol compounds can augment the dispersing performance of PCEs at w/c ratios ≤ 0.30 [13]. It is assumed that such co-dispersants might induce repulsive depletion forces between the cement particles. However, more research is necessary to elucidate in more detail the role of non-adsorbed polymers to cement dispersion.

6 Summary

Superplasticizers can adsorb on cement, chemisorb into lamellar C-A-H phases or remain in the pore solution. The macroscopic properties of cement suspensions (e.g. rheology) are affected by those interactions. Adsorption of the superplasticizers on the

surface of the first hydration products is essential for cement dispersion. Depending on the chemical composition of the polymer dispersion is achieved by an electrostatic and/or steric effect. Chemisorption mainly occurs when cement is undersulfated. A low amount of highly soluble sulfates during the first seconds of the hydration of C_3A usually entails an intercalation of the superplasticizer into C-A-H phases. Thus, the polymer becomes ineffective and the fluidity decreases. However, non-adsorbed polymers that remain in the pore solution seem to contribute to cement dispersion especially at low w/c ratios.

References

1. Yoshioka K, Tazawa E, Kawai K, Enohata T (2002) Adsorption characteristics of superplasticizers on cement component minerals. Cem Concr Res 32:1507–1513
2. Yoshioka K, Sakai E, Daimon M, Kitahar A (1997) Role of steric hindrance in the performance of superplasticizers for concrete. J Am Ceram Soc 80:2667–2671
3. Flatt RJ (2004) Dispersion forces in cement suspensions. Cem Concr Res 34:399–408
4. Houst YF, Bowen P, Perche F, Kauppi A et al (2008) Design and function of novel superplasticizers for more durable high performance concrete (superplast project). Cem Concr Res 38:1197–1209
5. Flatt RJ, Schober I, Raphael E, Plassard C, Lesniewska E (2009) Conformation of adsorbed comb polymers dispersant. Langmuir 25(2):845–855
6. Hirata T, Ye J, Branicio P, Zheng J, Lange A, Plank J, Sullivan M (2017) Adsorbed conformations of PCE superplasticizers in cement pore solution unraveled by molecular dynamics simulations. Sci Rep 7:16599
7. Nylander T, Samoshina Y, Lindman B (2006) Formation of polyelectrolyte-surfactant complexes on surfaces. Adv Colloid Interfac 123–126:105–123
8. de Reese J, Plank J (2011) Adsorption of polyelectrolytes on calcium carbonate – Which thermodynamic parameters are driving this process? J Am Ceram Soc 94:3515–3522
9. Plank J, Vlad D, Brandl A, Chatziagorastou P (2005) Colloidal chemistry examination of the steric effect of polycarboxylate superplasticizers. Cem Int 2:100–110
10. Plank J, Hirsch C (2007) Impact of zeta potential of early cement hydration phases on superplasticizer adsorption. Cem Concr Res 37:537–542
11. Plank J, Dai Z, Keller H, von Hoessle F, Seidl W (2010) Fundamental mechanisms for polycarboxylate intercalation into C_3A hydrate phases and the role of sulfate present in cement. Cem Concr Res 40:45–57
12. Ushiro M, Atarashi D, Kawakami H, Sakai E (2013) The effect of superplasticizer present in pore solution on flowability of low water-to-powder cement paste. Cem Sci Concr Technol 67:102–107
13. Lange A, Plank J (2016) Contribution of non-adsorbing polymers to cement dispersion. Cem Concr Res 79:131–136

Improvement of UHPFRC-Rheology by Using Circular Shape Memory Alloy Fibres

Maximilian Schleiting[1(✉)], Alexander Wetzel[1], Florian Gerland[2], Thomas Niendorf[3], Olaf Wünsch[2], and Bernhard Middendorf[1]

[1] Department of Structural Materials and Construction Chemistry, University of Kassel, Kassel, Germany
schleiting@uni-kassel.de
[2] Department of Fluid Mechanics, University of Kassel, Kassel, Germany
[3] Institute of Materials Engineering, University of Kassel, Kassel, Germany

Abstract. Fibre reinforcement of Ultra-High Performance Concrete (UHPC) is linked to a reduction of the flowability of fresh concrete. Moreover, high fibre contents often promote agglomerations. Therefore, commonly a fibre content of about 1–2 vol.-% is used. A novel method is proposed to minimise the negative influence of high fibre contents on the rheological properties of fresh concrete without any significant deterioration of the mechanical properties of the hardened concrete. To achieve this, shape memory alloy (SMA) fibres made from nickel and titanium are proposed to be used. These SMA-fibres have the ability to transform into an imprinted geometry upon heating. During mixing, fibres with a circular geometry avoiding agglomerations are added and, therefore, the rheological properties of fresh concrete can be improved compared to straight fibre reinforced concrete. After mixing the UHPC, the shape memory effect is thermally activated while the concrete is still flowable. The fibres transform into their imprinted, straight geometry enhancing the properties of the hardened concrete. With this method we propose to combine the improved mechanical properties of a fibre reinforced UHPC with a good workability. The present work presents a first step towards achieving the final goals.

Keywords: UHPC · Concrete rheology · Fibre reinforcement · Shape memory alloys (SMA)

1 Introduction

High Performance (HPC) and especially Ultra-High Performance Concrete (UHPC) are specified by their high compressive strength up to 250 N/mm^2 and their durability. These characteristics are mainly obtained by a high packing density and a low water/binder ratio of about 0.20 to 0.25 [1]. In contrast to these advantages, the tensile- and flexural strength of the material decline significantly. Furthermore, in case of failure, the brittle material reacts abrupt and almost no post-failure behaviour is existent. To enhance the above mentioned properties, fibre reinforcement is a commonly used tool in building and construction [2, 3]. Usually, steel fibres of a maximum amount of about 1–2 vol.-% are added. A higher content of fibre reinforcement leads to a negative impact on the rheology and, thus, on the workability of the fresh concrete (Fig. 1) [1].

V. Mechtcherine et al. (Eds.): RheoCon 2019/SCC 2019, RILEM Bookseries 23, pp. 142–148, 2020.
https://doi.org/10.1007/978-3-030-22566-7_17

A novel method to combine the positive impact of fibre reinforcement on the mechanical properties of the hardened concrete with a good rheology and workability of the fresh concrete is the use of shape memory alloy (SMA) fibres. Shape memory alloys have the ability to transform into an imprinted geometry upon heating. This change in geometry is based on a fully reversible (temperature and stress dependent) phase transformation from austenite to martensite. The shape memory behaviour is revealed for many alloys, most important in terms of application for alloys based on nickel-titanium (NiTi) and copper [4–6].

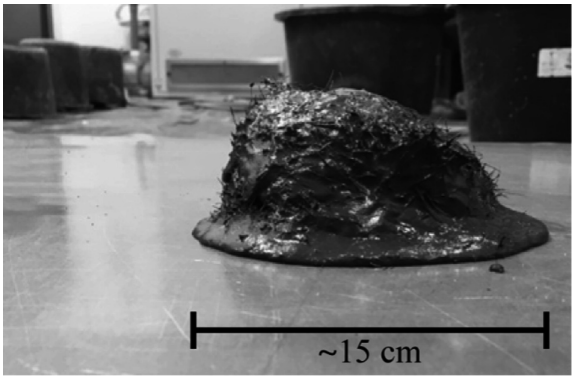

Fig. 1. Negative influence of high fibre contents on rheology of the fresh concrete. Contact of fibres lead to agglomerations and decrease the workability.

In the mixing procedure of the UHPC, fibres made of SMA are added in a shape that is favourable for the rheological properties of the fresh concrete. After filling the moulds, the UHPC is thermally treated to activate the shape memory effect. The fibres transform into their imprinted shape, which is favourable for the mechanical properties of the hardened concrete.

Results of the very first steps towards the final aim are detailed in the remainder. In this regard, the present work will evaluate the positive effect of circular formed (non-shape memory) fibres on the viscosity of fresh UHPC compared to UHPC containing the usually used straight fibres.

2 Materials and Methods

2.1 Materials

A basic UHPC mixture ("M3Q") is used for all tests. The mixture and its mixing procedure were developed in former investigations (SPP1182; Table 1) [7].

Table 1. Compounds of the used M3Q mixture

Material	kg/m^3	wt.%	Material	kg/m^3	wt.%
CEM I 52 R HS/NA	787	34.0	quartz powder	199	8.5
silica fume	169	7.2	superplasticizer	27	1.1
quartz sand	966	41.2	water	187	8.0
water/binder-ratio	0.21				

Mixing procedure contains one minute of homogenising the dry components. After addition of water and superplasticizer, mixing speed is doubled for two minutes until mixing break (two minutes). In case of producing specimen, the fibres are added in the break. Afterwards, mixing speed is decreased and the concrete is homogenised for another 5 min. In case of the rheology measurements, fibres are added manually before the tests to avoid sedimentation of the fibres in the mixing container.

To get a more detailed insight into the distribution and orientation of the fibres, the tests are additionally done using a silicon oil polydimethylsiloxane (PDMS) with the trade name *Korasilon® Fluid M 100,000*. The fibre free M3Q has a viscosity of about 100 Pa*s ± 30 Pa*s and a negligible yield point (<1 Pa). The silicon oil behaves Newtonian at a viscosity of about 110 Pa*s ± 4 Pa*s. Therefore, the flow characteristics of both materials are comparable.

For the investigations of the viscosity of both materials, circular and straight steel fibres are used. SMA fibres will be considered in follow-up work. An overview of the fibre characteristics for all fibres used is given in Table 2.

Table 2. Properties of the used steel fibre material.

Abbreviation	Length [mm]	Material diameter [mm]	Ring diameter [mm]	Geometry
S12_0.4	12	0.4	–	Straight
S10_0.4_c	10 (unfolded)	0.4	3	Circular
S25_0.5	25	0.5	–	Straight
S25_0.5_c	25 (unfolded)	0.5	4.1	Circular

2.2 Methods

The viscosity of the material and its workability are measured with a fine-grain rotation-viscometer “Viskomat NT” (350 ml) and a coarse-grain rotation-rheometer “eBT2” (20 l; both by Schleibinger).

The “Viskomat NT” works based on the Couette principle, i.e. the container, including the concrete, rotates around a stable measurement ball. In contrast, the “eBT2” works based on the Searle principle, i.e. the measurement balls rotate in a stable container with the concrete [8]. Both methods derive data characterising rotation speed [m/s] and torque [Nm]. Based on these data the shear rate [1/s] and shear stress [Pa] can be calculated. For the determination of the flow curve, a ramp profile with

increasing and decreasing speed is used. The corresponding flow curves can be compared and characteristic values can be deduced from the curves. A simulation-based evaluation method is used to determine the Bingham flow parameters (yield stress, plastic viscosity). The method can explain non-linear curves of the torque-velocity measurements from the complex flow conditions of the concrete rheometer type used here. No significant yield point (always < 1 Pa) is determined in any measurement. The concrete thus behaves Newtonian. To ensure a statistical relevance of the data, 5 measurements of the materials without fibres are done. Mixtures containing fibres are measured at least two times.

The flexural strength of the fibre reinforced samples is tested 7 days after casting and storage under standard conditions (20 °C, 65% rel. hum.) in a three point bending universal testing machine (150 kN Zwick/Roell) according standard DIN EN 12390-5 [9]; 6 prisms are tested for each condition, i.e. they contain the same fibres that are used for the viscosity measurements but are unfolded and, therefore, have a straight geometry. To get information about the post-failure behaviour the tests are done in displacement control with a testing speed of 0.01 mm/s. Specimen have a size of 160 mm × 40 mm × 40 mm (norm size).

Both tests are done for UHPC mixtures containing fibres characterised by fibre fractions of 0 and at least 2 vol.-% taking in account both feasibility of specimen and availability of material.

3 Results and Discussion

The circular fibres (S10_0.4_c) in the silicon oil (grey graphs in Fig. 2) do not show a significant improvement of the viscosity of the material compared to straight fibres (S12_0.4). The viscosity increases about the same rate with increasing fibre content as the viscosity of the mixture containing straight fibres. However, the calculated trend line for the mixture with straight fibres has a slightly higher slope than the trend line for the mixture containing circular fibres.

The results of the measurements with fibres in UHPC (black graphs in Fig. 2) show a more distinct difference in viscosity regarding fibre geometry as sand is present, additionally to the fibres, in the role of a major viscosity-influencing component. The viscosity of the UHPC mixtures containing circular fibres (S10_0.4_c) increases with increasing fibre content. The mixture with a fibre content of about 3 vol.-% has a viscosity of about 1.4 times higher than the reference without fibres. However, this increase is less pronounced compared to the viscosity of the mixtures containing straight fibres (S12_0.4). Viscosity increases about 1.8 times at a fibre content of 3 vol.-% compared to the reference without fibres. Furthermore, an abrupt increase in viscosity from 2.5 vol.-% to 3 vol.-% is recognisable.

Tests using the longer fibres (S25_0.5) are not done as the associated circular fibres (S25_0.5_c) sediment quickly (about a minute after pouring) at the bottom of the measurement container. Sedimented fibres are shown in Fig. 3. Consequently, no measurements with the long, straight fibres are done.

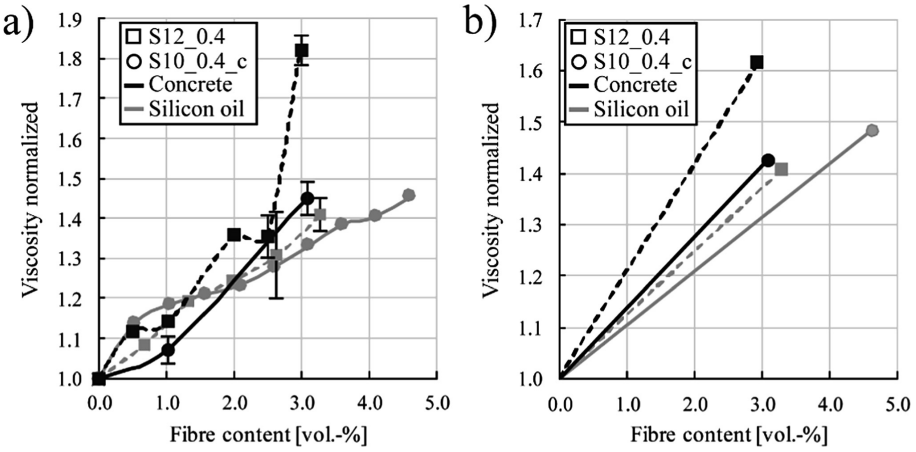

Fig. 2. Results of the viscosity measurements. (a) Viscosity normalised to the reference viscosity (no fibres). (b) Trend line for normalised viscosity. Measurements of material with straight fibres are done with the coarse-grain rheometer "eBT2", measurements of material with circular fibres are done with the fine-grain viscometer "Viskomat NT". Relative standard deviations over 5% are marked with error bars.

Fig. 3. Sedimentation of circular fibres (marked with arrows) with a diameter of 4.1 mm and a material diameter of 0.5 mm. Bubbles are present due to manual mixing of the material.

To highlight the importance of fibre length and of the fibre content in regards to the mechanical properties of the hardened concrete, tests have been conducted for both introduced fibre lengths that fit to the respective circular fibres. The results of the tests are shown in Fig. 4. The maximum flexural strengths of the specimens containing the short, straight fibres (S12_0.4) do not change significantly as a function of the fibre content (Fig. 4 a). For all fibre contents the flexural strength is about 8 N/mm^2. The post-cracking behaviour clearly is improved (Fig. 4b). A pseudo ductile failure

behaviour of the material is given for fibre contents of at least 1 vol.-%. Specimen containing long, straight fibres (S25_0.5) show a significant increase in maximum flexural strength (Fig. 4a) as well as an improved post-failure behaviour with increasing fibre content (Fig. 4c). The maximum flexural strength increases linearly with an increasing fibre content from about 8 N/mm^2 without any fibres to about 32 N/mm^2 at a fibre content of 2 vol.-%. The post-cracking behaviour guarantees a pseudo ductile failure behaviour for mixtures containing at least 0.5 vol.-%. These results clearly show the importance of high fibre contents as well as of high fibre aspect ratios in regards to the mechanical properties of fibre reinforced UHPC.

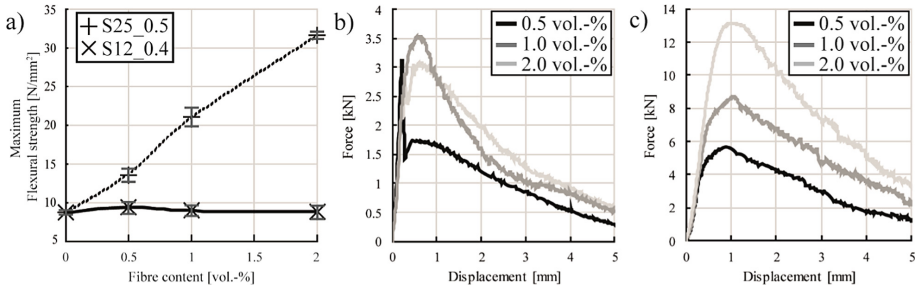

Fig. 4. Test results for the flexural strength and post-failure behaviour regarding different fibre geometries and contents. (a) Maximum flexural strength of fibre reinforced prisms with different fibre geometry and content. (b) Force/Displacement diagram for prisms reinforced with S12_0.4 fibres. (c) Force/Displacement diagram for prisms reinforced with S25_0.5 fibres. All diagrams show the average of 6 specimens.

4 Summary and Conclusion

The results of the viscosity measurements reveal that a circular geometry of the fibres improves the viscosity of UHPC reinforced with high fibre content and, therefore, the workability of the fresh concrete compared to straight fibres. In contrast, silicon oil does not show this significant divergence in viscosity induced by fibre geometry. This is thought to be based on the abundance of granular components in the concrete that support a network built by the fibres [10]. The characteristic behaviour of the concrete is seen in this study as an abrupt increase of the viscosity when increasing straight fibre content from 2.5 vol.-% to 3.0 vol.-%. Therefore, the use of circular shaped fibres is recommended for high fibre contents in UHPC as no abrupt increase is recognisable for the tested circular fibre fractions. In contrast, for low fibre contents (<2 vol.-%) the difference in the workability of fresh concrete is limited in regards to this specific fibre geometry.

A significant increase of the flexural strength of the associated prisms containing short fibres is not seen for the tested fibre contents. However, an improvement of the post-failure behaviour is existent for all specimen; a pseudo ductile behaviour is reached at a fibre content of at least 1 vol.-%. In contrast, the long, straight fibres lead to a significant increase of the flexural strength for all tested fibre contents. A pseudo ductile post-failure behaviour is given for all tested fibre contents as well.

However, rapid sedimentation of the fibres in shape of rings intended for superior workability of fresh concrete currently hinder further evaluation of these long fibres.

In summary, in light of the current results the functionality of shape memory alloy fibres, i.e. their ability to change shape upon heating, is assumed to be the pathway towards significantly increasing the amounts of fibres in UHPC without a significant deterioration of its workability. Based on this approach, it is expected to achieve much higher flexural and tensile strengths of UHPC than it is possible today. However, there are many aspects that have to be considered in future material design. The used circular fibres show a disadvantageous sedimentation behaviour. Thus, other geometries or materials have to be designed to avoid or minimise this issue. Furthermore, the retransformation of the fibres in UHPC has to be investigated, as the "final" geometry of the fibre is one of the essential factors for the mechanical properties of the hardened concrete.

References

1. Bornemann R, Schmidt M, Fehling E, Middendorf B (2001) Ultra-Hochleistungsbeton UHPC - Herstellung, Eigenschaften und Anwendungsmöglichkeiten. Beton- und Stahlbetonbau 96:459–467
2. Leutbecher T, Fehling E (2012) Behavior of ultra-high-performance concrete reinforced with reinforcing bars and fibers: minimizing fiber content. ACI Struct. J. 109:253–263
3. Naaman A (2003) Engineered steel fibers with optimal properties for reinforced cement composites. J Adv Concr Technol 1:241–252
4. Otsuka K, Wayman CM (1999) Shape memory materials. Cambridge University Press, Cambridge
5. Janke L, Czaderski C, Metavalli M, Ruth J (2005) Application of shape memory alloys in civil engineering structures - overview, limits, and new ideas. Mater Struct 38:578–592
6. Kaack M (2002) Elastische Eigenschaften von NiTi-Formgedächtnis-Legierungen, Ph.D.-Thesis. Ruhr-University Bochum, Bochum
7. SPP 1182 (2014) Sustainable building with ultra-high performance concrete. In: Schmidt M, Fehling E, Fröhlich S, Thiemicke J (eds) Kassel University Press, Kassel
8. Mezger T (2006) The rheology handbook, 2nd edn. Vincentz Verlag, Hannover
9. DIN EN 12390-5:2009 (2009) Testing hardened concrete – Part 5: flexural strength of test specimens
10. Martinie L, Rossi P, Roussel N (2010) Rheology of fiber reinforced cemetitious materials: classification and prediction. Cem Concr Res 40:226–234

Laboratory and In-Situ Rheological Testing

The Use of Parallel-Plate Rotational Rheometry to Determine the Superplasticizer to be Used in Cement Pastes Admixtures

Livia B. Agostinho[1(✉)], Eugenia F. da Silva[1], Luciana A. Farias[2], and Alexandre C. Pereira[2]

[1] Civil Engineering, University of Brasilia, Brasilia, Brazil
liviaborbagostinho@gmail.com
[2] Eletrobras Furnas Hydroelectric Company, Goiania, Brazil

Abstract. The usual test to obtain the better superplasticizer (SP) to be used and also their content in the admixture is the Marsh cone test, but it demands a lot of material to perform it. On other hand, the use of the parallel-plate rotational rheometry allows achieving those answers using very few materials and in a fast way. In this research, three different pastes were tested to see which one had the longer workability period, performing oscillatory time sweep test. This test allows observing the behavior of the elastic component (G′) in the time, fact that some authors correlated with the setting time. After choosing the SP that obtained the best behavior over time, flow tests in pastes with different amounts of additive were performed to obtain the saturation point. With the viscosity results, it was possible to analyze when the SP no longer influences this parameter. It was observed that very few materials were used in these tests, an important factor when working with expensive or rare materials. Determining the superplasticizer that did not indicate delay in casting time and their saturation point, could guarantee that the additive did not affect the compatibility between materials in the admixture.

Keywords: Rheology · Superplasticizer · Saturation point · Cement paste

1 Introduction

More and more researchers have been working with innovative materials to improve some properties of cementitious compounds, such as compressive strength, sulfate attack, cracking, among others. Some of these materials may be plentiful on the market, such as construction waste, waste from other industrial processes. However, in some cases these innovative materials can be expensive or even rare materials. In these cases, it is necessary to make tests that requires a small amount of material.

Currently, with the advent of high strength concrete it is almost impossible to produce concrete without the use of superplasticizing additives (SP). For self-compacting concrete, for example, the optimum dosage of SP is fundamental to guarantee the properties of the mixture.

V. Mechtcherine et al. (Eds.): RheoCon 2019/SCC 2019, RILEM Bookseries 23, pp. 151–159, 2020.
https://doi.org/10.1007/978-3-030-22566-7_18

To be classified as self-compacting, concrete must have adequate characteristics such as fluidity and workability. The cement pastes have great influences on these characteristics, becoming important the development of researches to determine the rheological parameters necessary to the proper characterization of these pastes and, consequently, to enable a correct proportioning of self-compacting concrete.

The use of the Marsh cone has been a reliable way to determine the point of saturation of additives in pastes and mortars besides the ease of execution and reliability of the results. However, for the execution of the test, an amount of about one liter of material is demanded. On the other hand, with the use of the rotational paste rheometer, only about 100 mL of material is mixed, but the quantity effectively that is going to be used is much smaller (around 10 mL).

1.1 Rheological Measurements

Also known as a static or flow test, this methodology consists of applying a force or deformation and determining the strength of the material to this applied stress. By varying the shear rate or shear stress, one can plot the flow curve and hence the appropriate rheological state equations. The rheological properties are thus obtained: viscosity and yield stress [1].

Performing an oscillatory test with a rotational rheometer means that the rotor (top plate or cone) is no longer rotating continuously in one direction, but is alternately shifted in a small-angle sine-time function to the right and left. The sample placed in the shear gap is forced to deform according to a similar sinusoidal function, generating resistance tensions in the sample.

In a stress controlled rheometer a small-amplitude oscillatory shear stress is applied and the resulting deformation is measured. Rheological parameters such as modulus and viscosity are computed and the modulus is transformed into elastic (or storage) modulus and viscous (or loss) modulus. The elastic modulus G′ quantifies the elastic deformation of the (recoverable) material, and the viscous modulus G″ quantifies the viscous dissipation (more like a liquid behavior) [2].

Thus, a material can be readily identified as an elastic solid or a viscous liquid. Flocculated suspensions (suspensions whose particles adhere forming a three-dimensional network) typically exhibit elastic behavior at low shear rate and viscous behavior at high rate. On the other hand, dispersed suspensions typically show viscous behavior at all stress levels. The measurement of G′ and G″ using the oscillatory shear allows to differentiate the two types of suspension. The cement paste is considered as a viscoelastic material because it contains elastic and viscous behavior under applied shear stress [3].

2 Materials and Methods

The Brazilian type cement CPV-ARI was chosen due to the quantity of clinker and because it is frequently used in high strength concretes (HSC) in Brazil. Table 1 shows the chemical composition of Portland cement used in this research.

Table 1. Chemical composition of Portland cement and silica fume.

Material	Chemical composition (%)									
	SO_3	MgO	SiO_2	Fe_2O_3	Al_2O_3	CaO	Free CaO	$CaSO_4$	Na_2O	K_2O
Cement	3.28	4.36	24.41	3.02	7.09	53.44	2.16	2.16	0.29	0.77

The values of the chemical and physical properties were within the limits established by the Brazilian standard NBR 16697. The insoluble residue content was low, with no evidence of pozzolanic material. The levels of free calcium oxide and magnesium oxide were at acceptable levels (2.16% and 4.6%, respectively) and, probably, did not cause expansive cement reaction due to the later hydration of these compounds (CaO and MgO).

A kind of an experimental Glenium superplasticizer additive was used. It is a white viscous liquid with ether carboxylate as chemical basis, specific gravity between 1.067 g/cm^3 and 1.107 g/cm^3 and 30% of solid contents.

The Nanosilica used in the research was an aqueous and translucent solution with stabilized colloidal silica with 30% solid contents. NS amorphous particles have a negative surface charge, are discontinuous, slightly rough, spherical in shape and narrow particle size distribution, specially designed for use in cement-based materials. Other properties of the studied NS are shown in Table 2.

Table 2. Properties of the colloidal nano-silica used in this work.

Colloidal nano-silica properties	
Nano-silica content (%)	30.0
Density (g/cm^3)	1.20
Na_2O content (%)	0.55
Particle size (nm)	3 to 40
Surface area (m^2/g)	80.0

Figure 1 shows the rotational rheometer model AR G2 by TA Instruments coupled to a computer for data acquisition used to perform the rheological tests. The geometry of parallel plates with 40 mm diameter was used. The top plate had grooves while a textured adhesive was applied on the lower plate to guarantee internal shear and prevent sliding between the plates and the sample, as shown in Fig. 2(a) and (b), respectively. Figure 2(c) shows the radius and gap dimensions schematically.

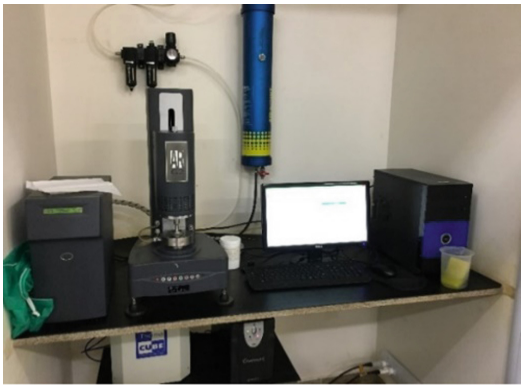

Fig. 1. Rotational Rheometer AR G2.

The parallel plate geometry was chosen according to the characteristics of the cement paste, especially the viscosity, and also the possibility of accommodating suspensions with different particle sizes by adjusting the gap and obtaining high shear rates. The gap is recommended to be at least 10 times greater than the sample maximum particle size whereas TA INSTRUMENTS [4] suggests a minimum height of 1% of the geometry diameter.

Fig. 2. Characteristics of the used geometry: (a) Slotted top plate; (b) Bottom plate with textured adhesive; (c) Plate radius (R) and distance between plates (h or gap).

All tests were performed in a temperature-controlled room at 23 °C ± 2 °C with the equipment also programmed to perform the tests at the same temperature. The equipment control showed that the temperature remained within this range for all tests.

First, the sample is placed in the equipment, and the top plate is lowered down to the required distance between the parallel plates (gap), which was 1 mm for performed all tests. The bottom plate has a load cell capable of measuring the normal stress in the sample throughout the test.

The preparation of the samples for all rheological tests consisted of weighing the materials in precision scale to two decimal places, where the cement and liquid materials were measured separately. The mixtures were prepared manually using a spatula for 1 min, followed by mechanical mixing using a digital IKA RW 20 mixer at a rotational speed of about 2500 rpm, for three minutes.

The oscillatory test had duration of 7 h, displacement of 10^{-4} rad and frequency of 1 Hz.

On the other hand, the flow test consisted of a cycles composed of three ramps each cycle. First, the shear rate increased from zero to 400 s^{-1} in the acceleration ramp, and then, from 400 s^{-1} to zero in the deceleration ramp. Each ramp lasted 60 s with 30 measurements captured (one point every two seconds); therefore, each cycle lasted two minutes totaling six minutes for the three cycles of each trial.

Only the results of last four of the six trials were analyzed since the mixture is still in the process of homogenization and adherence to the parallel plates in the first cycle. In the second cycle, after the sample became homogeneous, it is possible to collect data representative of the rheological parameters (initial yield stress and viscosity), and the third cycle was performed to confirm the data obtained in the previous cycle. The last two cycles represent the repeatability required for statistical analysis.

In a flow test, the viscosity versus shear rate curves show that the viscosity tends to stabilize, at high rates. Similar to other models, the Herschel-Bulkley model assumes viscosity as a variable independent of the shear rate. However, because this assumption is only valid at high shear rates, the present work assumed the viscosity values at the maximum shear rates to calculate the means of the four flow curves.

3 Analysis and Results

The main result to be analyzed for the choice of the additive that best behaves in relation to the setting time is the oscillatory time sweep test, which has a long duration and makes it possible to identify the agglomeration force of the paste. Observing the behavior of the elastic component (G′) in the time, some authors correlate changes on the curve's behavior with the setting time. In the time sweep test, a curve of the elastic component G′ is obtained as a function of time. The curves for the studied pulps are shown in Fig. 3.

An author [5], explained the interpretation of the time sweep test in a simple way, explaining that there is a rapid increase of G′ during the first 40 min of hydration, after starting the test in low value, due to the rupture of the structure during the pre-strain sweep test (Region I). After this period, Region II begins, whose growth rate of the elastic component (G′) is slower, that is, during this period the hydration is slower.

The circles inserted in Fig. 3, whose elastic component is distributed in logarithmic scale, show the beginning of Region III, which present an intense increase of the elastic component caused by the higher rate of hydration, being able to be associated with the setting time [6]. For 1.0% of the Glenium EXPA additive, it occurred about 180 min after the start of the assay, but when the content was increased to 1.2% this time increased to approximately 230 min.

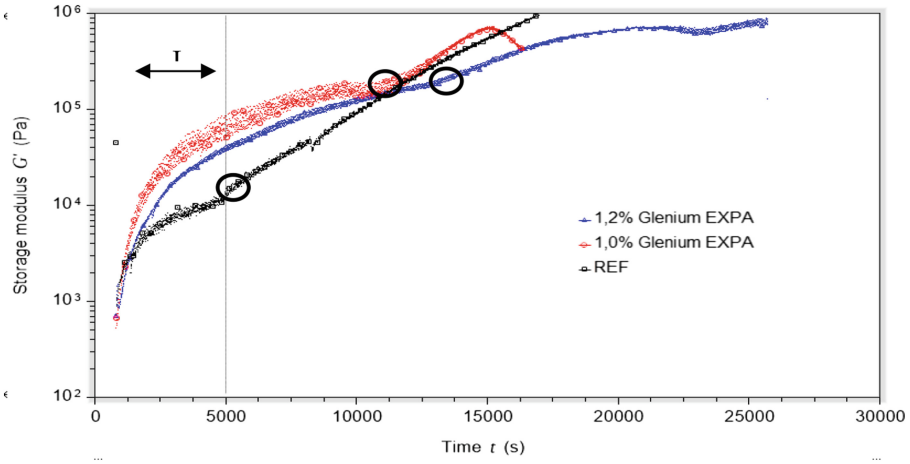

Fig. 3. Evolution of the elastic component (G′) of the pastes containing 1% and 1,2% of the superplasticizing additives Glenium and the reference paste.

After selecting the superplasticizer additive that obtained the best behavior over time (the one that presented no delay on setting time), flow tests were performed to determine the best dosage not exceeding the saturation limit of the superplasticizer additive.

The tests of the most critical mixture, were carried out, that means those with high values of viscosity and yield stress. In order to perform the test accurately it is necessary to respect the limitations of the equipment in the acquisition of data.

To determine the saturation content of the chosen SP (experimental Glenium), a flow test sequence was performed with pastes with w/c of 0.4, varying the SP content of: 0.5%, 1.0%, 1.5%, 2.5%, 3.0%, 4.0% and the reference (0.0%). With the viscosity results, it is possible to analyze when the SP no longer influences this parameter, indicating the saturation point of the additive.

The flow test consisted of three cycles composed of two ramps each cycle. First, the shear rate increased from zero to 400 s^{-1} in the acceleration ramp, and then, from 400 s^{-1} to zero in the deceleration ramp. Each ramp lasted 60 s with 30 measurements captured (one point every two seconds); therefore, each cycle lasted two minutes totaling six minutes for the three cycles of each trial (Fig. 4).

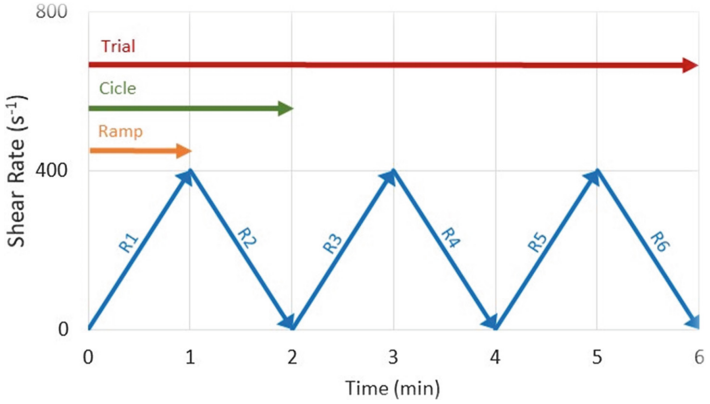

Fig. 4. Flow test schema.

The shear rate viscosity curve as well as the increase of the values obtained at high rates (those used for viscosity determination) are shown in Fig. 5.

It is possible to observe that the dosage curves of 2.5% and 3.0% practically overlap, whereas the curve of 4.0% presents values higher than the dosages mentioned above. This increase in viscosity of 4.0% may be due to the excess of SP that no longer helps in the plasticity of the mixture, impairing its performance.

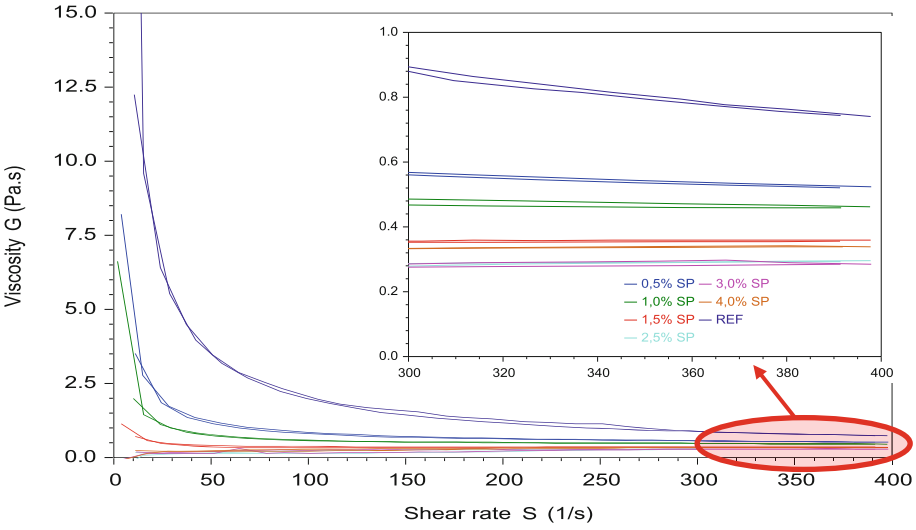

Fig. 5. Graph of viscosity x rate of shear and the increase of viscosity values at high rates.

From the viscosity data at high shear rates of the last four ramps tested it was possible to trace the viscosity curve (Pa.s) by additive content (%) data in an evolution chart of the SP effect shown in Fig. 6. In this graph, a modeling was done adjusting the points using a polynomial curve whose R^2 was equal to 0.96, considered a good adjustment of the curve to the presented data.

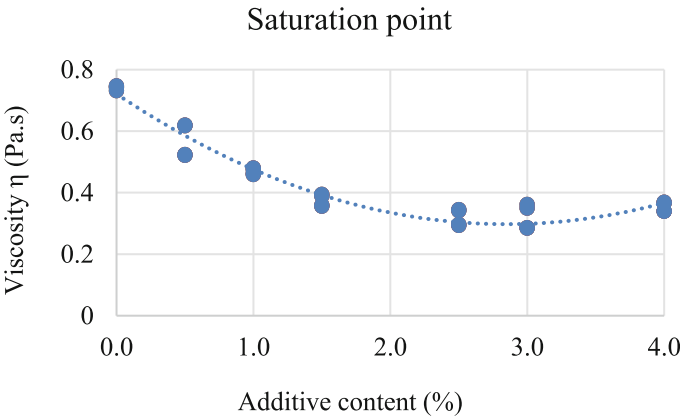

Fig. 6. Viscosity evolution graph by SP content obtained by flow tests.

To determine the saturation point of the SP, the point of inflection of the curve was determined, that is, the point where the additive ceases to have an effect on the viscosity (decreasing its value). In the case of the Glenium additive, this calculated value was 2.7%.

4 Summary and Conclusion

With two easy tests performed, it was able to determine the approximate setting time and the saturation point of the chosen superplasticizer. Little amount of material was spent and a reliable result was obtained. When studding high strength or rare materials it is important to think about how much material will be spent, and with the use of the rotation rheometer it is possible to decrease dramatically the quantity of materials used in preliminary tests.

Determining the superplasticizer that did not indicate delay in casting time and their saturation point, could guarantee that the additive did not affect the compatibility between materials in the admixture. A comparison between the Marsh cone and the rheometer tests for the saturation point of the SP is proposed for future trials.

Acknowledgement. The authors thank University of Brasilia and Furnas Central Hydropower S.A. for the partnership in this research. Thanks are also given to The National Council for Scientific and Technological Development (CNPq) for the financial support and BASF for the donation of the superplasticizer.

References

1. Quarcioni VA (2008) Influence of hydrated lime on the initial ages of Portland cement hydration - paste study. Doctoral thesis, Escola Politécnica da Universidade de São Paulo
2. Dinkgreve M et al (2016) On different ways of measuring the yield stress. J Non-Newton Fluid Mech 238:233–241
3. Chen C, Struble LJ, Zhang H (2006) Using dynamic rheology to measure cement-admixture. J ASTM Int 3(3):1–13
4. TA Instruments (2010) AR-G2/AR 2000ex Rheometers - Operator's ManualNew CastleTA Instruments
5. Betioli AM, Gleize PJP, Silva DA, John VM, Pileggi RG (2009) Effect of HMEC on the consolidation of cement pastes: isothermal calorimetry versus oscillatory rheometry. Cem Concr Res 39(5):440–445
6. Schultz MA, Struble LJ (1993) Use of oscillatory shear to study flow behavior of fresh cement paste. Cem Concr Res

Rheology and Build-Up of Fresh SCC Pastes Evaluated with the Mini-slump Cone Test

Gonzalo Barluenga[1(✉)], Irene Palomar[1], Cynthia Guardia[1], Hugo Varela[1], and Francisco Hernandez-Olivares[2]

[1] Department of Architecture, University of Alcala, Madrid, Spain
gonzalo.barluenga@uah.es
[2] Department of Building Construction and Technology, Technical University of Madrid, Madrid, Spain

Abstract. SCC are composed by a larger amount of paste than conventional concrete in order to achieve larger flowability without segregation. SCC pastes are typically very fluid, showing large spread diameters in consistency tests, while exhibiting high viscosity values.

In this study, a mini-slump cone test is used to evaluate the fresh properties of SCC pastes with different supplementary cementitious materials (SCM), as limestone filler (LF), colloidal nanosilica (NS) and metakaolin (MK). Two amounts of NS were studied and different amounts of Superplasticizer (SP) were considered to achieve self-compacting ability. The mini-slump test has been implemented with a video acquisition setup that records the spread diameter and allows to follow the velocity of deformation of the fresh paste. The basic rheological parameters were calculated using simple analytical models obtained from the literature. The effects of the type and amount of SCM and the level of SP were analyzed. Several cones were filled in each batch and tested at different times after cast, comparing samples at rest with other stirred before testing. The comparison of both results allowed to identify the structural build-up and the reversible/irreversible processes that take place in the fresh SCC pastes and the effect of SCM and SP.

Keywords: Rheology · Build-up · SCC · Supplementary cementitious materials · Mini-slump cone

1 Introduction

Supplementary cementitious materials (SCM) are commonly used in SCC mixtures for engineering and architectural applications. Recycling of industrial wastes, reduction of carbon footprint and the increase of certain hardened properties are behind their extended use. SCM are also responsible of changes in SCC fresh properties, especially increasing shear yield stress and requiring to modify either w/c ratio or superplasticizer (SP) amount to achieve the necessary SCC flowability. However, these solutions do not have the same effect on other fresh state properties, such as structural build-up that can be very useful to reduce formwork pressure. In some cases, the increase of SP has been found to be a better option [1] while in others this increase has been reported to be

V. Mechtcherine et al. (Eds.): RheoCon 2019/SCC 2019, RILEM Bookseries 23, pp. 160–167, 2020.
https://doi.org/10.1007/978-3-030-22566-7_19

undesirable [2]. The ability to build up a structure at rest before setting occurs has been defined as thixotropy for cementitious materials [3], and would depend on several mixing parameters [2].

The effect of SCM on SCC fresh properties can be evaluated through the paste rheological parameters, yield stress and viscosity, calculated with models [4–6] from testing parameters. Spread diameter and final stop time, measured using simple field tests as mini-cone slump test, has showed good correlations to rheological parameters [7–10]. Furthermore, the difference between the samples left at rest a certain time and stirred before tested spread diameters, which corresponds to the reversible structural build-up, can be used to quantify thixotropy [7].

In this study, the pastes from SCC compositions including SCM as limestone filler (LF), Metakaolin (MK) and Nanosilica were evaluated using the mini-cone slump test. Several cones were tested at different times after mixing, comparing samples left at rest to other stirred before testing. The aim was to evaluate the effect of SCM and composition proportions on SCC pastes reversible structural build-up.

2 Materials and Test Procedures

SCC paste compositions are summarized in Table 1, which correspond to SCC mixtures without aggregates. A reference paste containing a CEM I 42.5R cement, limestone filler (LF), water and policarboxilate superplasticizer (SP) was designed. Afterwards, LF was replaced by Metakaolin (MK) and colloidal Nanosilica (NS), 2.5% or 5% by weight of cement. Further information of the components used has been previously published [11].

Table 1. Paste SCC compositions (in g), water to cement ratio (w/c) and fresh density (D).

	Cement	Filler	NS	MK	SP	Water[a]	w/c[b]	D (kg/m^3)
PL1	965	360	-	-	9.65	313	0.32	2074
PL1.5MK2.5	965	336	-	24	14.50	344	0.36	2076
PL1.25NS2.5	965	336	109	-	12	259	0.36	2058
PL1.75NS5	965	312	218	-	16.89	143	0.32	2104
PL2.75NS5	965	312	218	-	26.54	174	0.36	2098

[a]Liquid water added

[b]Considering both liquid water and water from liquid components (SP and NS)

A mini-cone slump test with 50 mm height, 70 mm upper diameter and 100 mm lower diameter was used to evaluate SCC paste samples. Spread slump diameter (ϕ_{max}), time to reach a diameter of 200 mm (T_{200}) and the time to stop flowing or final time (T_f) were measured. Several cones were filled from each batch and tested at different times from 0 to 120 min after mixing, comparing samples at rest with other stirred before testing.

3 Experimental Results and Analysis

Figure 1 plots the flow test results of SCC and their correspondent SCC pastes. SCC spread diameter varied between 690 mm and 780 mm and T_{500} between 3 and 6 s. Pastes showed larger variability, especially regarding ϕ_{max}, varying from 220 mm to 390 mm.

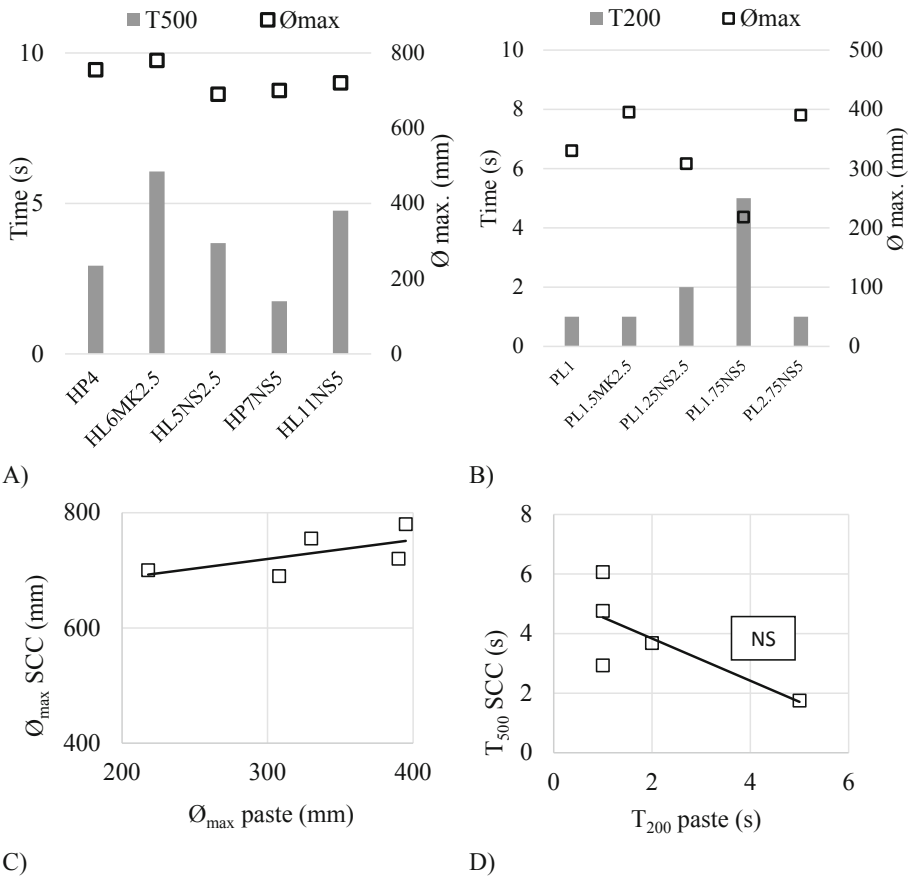

Fig. 1. Flow tests results. (A) Slump flow diameter (ϕ_{max} SCC) and time to reach 500 mm (T_{500}) of SCC samples. (B) Mini-cone Spread diameter (ϕ_{max} paste) and time to reach 200 mm (T_{200}) of SCC paste samples. (C) Relation between Slump flow diameter of SCC samples and Mini-cone Spread diameter of SCC paste samples. (D) Relation between T_{500} of SCC samples and T_{200} of SCC paste samples.

A good correlation between diameter spread was observed between SCC and pastes (Fig. 1C), which confirms that SCC flowability depends mainly on paste rheological properties. Regarding spread final time, only pastes with NS showed a linear relationship between T_{200} of pastes and T_{500} of SCC.

Table 2 summarizes ϕ_{max} at different times from 0 to 120 min after mixing of SCC paste samples left at rest (R) and stirred (S) for 30 s before testing. The initial irreversible build-up (initial setting) corresponded to the reduction of ϕ_{max} for the stirred samples.

Table 2. Mini-cone Spread diameter (in cm) of samples at rest and stirred before tested at Testing times (T in min). In grey, initial irreversible build-up.

	T0	T5		T10		T15		T20		T30		T60		T90		T120	
		R	S	R	S	R	S	R	S	R	S	R	S	R	S	R	S
PL1	34	29	33	28	38	24	32	23	33	21	34	11	31	10	**25**	-	-
PL1.5MK2.5	39	41	41	39	40	40	39	39	39	35	40	33	40	24	36	-	-
PL1.25NS2.5	31	35	32	26	30	27	30	21	28	20	28	10	**27**	10	22	10	20
PL1.75NS5	22	16	24	12	25	11	24	10	24	10	**23**	10	19	10	13	10	10
PL2.75NS5	39	37	41	35	38	35	39	34	42	32	38	28	38	28	36	22	36

R = Sample at rest

S = Sample Stirred for 30 s before tested.

■ = initial irreversible build-up (related to initial setting time)

Figure 2 plots the relation between the spread diameter and the sample height of the SCC samples at the different testing times and conditions. A reduction in time of the spread diameter occurred in all cases, showing a general pattern composed by 4 stages, which can be observed following the lateral profiles of the tested samples. Stage 1 corresponded to very fluid pastes, with spread diameter larger than 300 mm and a negligible height; Stage 2 showed a linear relation between 0–40 mm height and 300 mm–100 mm diameter. A third stage corresponded to a cylindrical profile of the sample when only a height decrease occurred, followed by a last stage with a slight height descend and a cone shape profile. The reduction of diameter implies a build-up of a structural resistance to flow [3]. When the samples at rest showed build-up but the stirred samples did not, a reversible build-up can be assumed.

Figure 3 plots the evolution in time of the spread diameter and the final spread time of SCC pastes samples at rest. Two main patterns can be identified. Samples of reference mixtures and two compositions with NS showed a significant reduction both of diameter and of the final time. Samples with larger amount of NS and lower w/c ratio showed a faster spread reduction and a larger final time reduction. It can be highlighted that the spread time reached zero when the sample did not spread anymore (stages 3 and 4 according to Fig. 2). On the other hand, samples with MK and 5% of NS with larger amount of SP showed a negligible reduction of spread diameter while a large increase of final time.

According to several models published in the literature [4, 5], spread diameter can be correlated to the Yield stress (τ_0). Figure 4A shows the evolution in time of Yield Stress of pastes calculated with Roussel model [4] (Fig. 4B). It can be observed that samples with 5% of NS with lower amount of SP showed a fast increase of Yield stress. Reference mixture and paste with 2.5% of NS delay 30 min their Yield Stress increase.

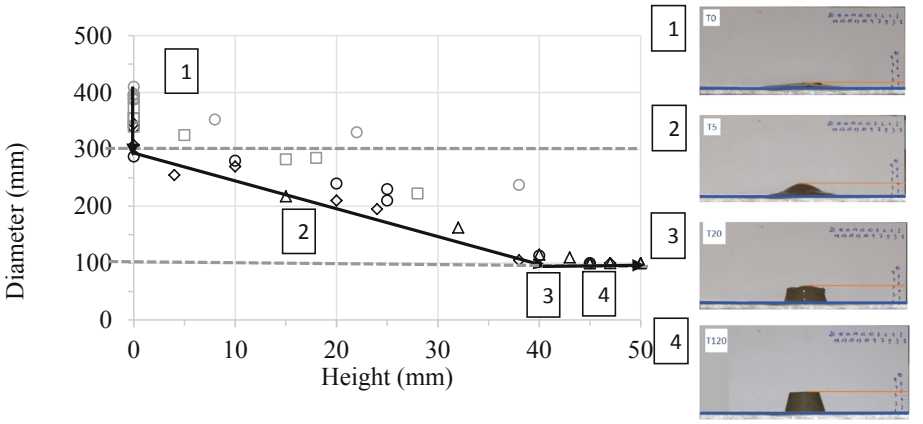

Fig. 2. Relation between Mini-cone Spread diameter and height of SCC paste samples considering the evolution in time (build-up). On the right, lateral shape profiles and height measurements of the build-up process.

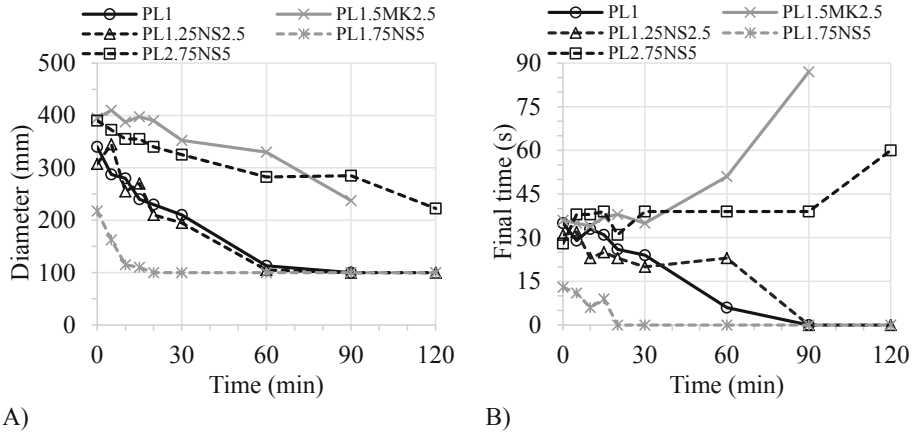

Fig. 3. Evolution in time of (A) the spread diameter and (B) the final time of SCC paste samples at rest.

Samples with MK and 5% of NS with larger amount of SP showed a small increase. The build-up process can be also quantified using the thixotropy parameter (A_{thix}) which corresponds to the Yield curve slope, calculated according to Roussel model [3]. Figure 4C presents the A_{thix} values, showing larger thixotropy values for mixtures with larger Yield stress increase. It can be observed that the paste with 2.5% of NS suffers a change of the slope at 60 min, when the irreversible build-up process began (Table 2). In the other two cases, the reversible build-up was completed before irreversible build-up occurred.

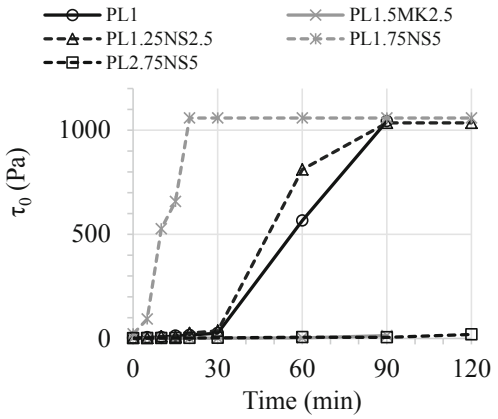

A)

B)

$$\tau_0 = \frac{225\rho g V^2}{128\pi^2 R^5}$$

	A_{thix} (Pa/min)
PL1	16.96
PL1.5MK2.5	0.12
PL1.25NS2.5	25.82
PL1.75NS5	49.02
PL2.75NS5	0.12

C)

$$\tau_0(t) = \tau_{00} + A_{thix}t$$

Fig. 4. (A) Evolution in time (build-up) of Yield Stress of SCC paste samples at rest calculated from the paste density (ρ) and volume (V) and the spread radius (R), according to (B) Roussel's model [4]. (C) Thixotropy parameter A_{thix} calculated from (A), according to [3].

Figure 5 plots the evolution in time due to reversible build-up of viscosity (μ) calculated from the final time (T_f) and final spread diameter (D_f), according to Tregger's model [5]. It can be observed that paste with 5% of NS with lower amount of SP was the first to increase μ, followed by reference and paste with 2.5% NS. Paste with MK and with 5% NS with larger amount of SP showed a slight increase.

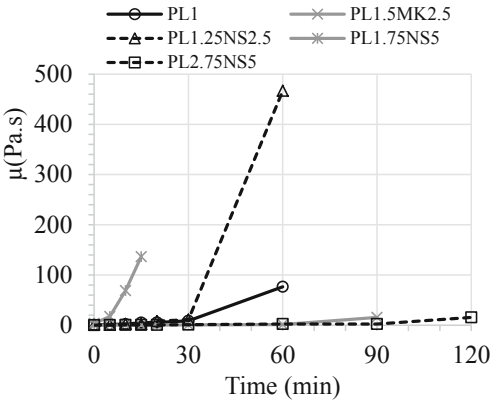

A)

B)

$$\tau_0 = 2.75\text{x}10^{9}\ D_f^{-5.81}$$

$$\mu/\tau_0 = 6.41\text{x}10^{-3}T_f - 1.94\text{x}10^{-3}$$

Fig. 5. Evolution in time (build-up) of Viscosity of SCC paste samples at rest calculated from the final time (T_f) and final spread diameter (Df), according to (B) Tregger's model [5].

4 Concluding Remarks

An experimental study on the effect of different supplementary cementitious materials (SCM) as limestone filler (LF), nanosilica (NS) and metakaolin (MK) on the rheological parameters of pastes for SCC was carried out using the mini-cone slump test. Several cones were tested at different times after mixing, comparing samples left at rest to other stirred before testing. The main conclusions of the study were:

- Although all the pastes come from SCC compositions with similar flowability, the rheological values differ among the compositions tested.
- All the samples measured at rest suffered a reduction of the spread diameter and an increase of viscosity in time. However, only the reference paste and those with NS and lower amount of SP showed a significant increase of Yield stress. The increase for samples with MK and with NS with larger amounts of SP was negligible.
- The increase of Yield stress of samples at rest before stirred samples began a reduction of the spread diameter means a reversible structural build-up of the fresh paste that can be quantified by the thixotropy parameter A_{thix}.
- Structural build-up also produced a notable increase of paste viscosity.
- The structural build-up of the SCC pastes under study was measured on mixtures with NS but not in samples with MK, and was affected by the amount of SP. Lower w/c ratio and larger amounts of NS accelerated the structural build-up, increasing the thixotropy parameter.

Acknowledgement. Financial support was provided by NanoCompaC (*BIA2016-77911-R*), funded by the Spanish Ministry of Economy and Competitiveness. Some of the components were supplied by BASF Construction Chemicals Spain S.L, Omya Clariana S.L, and Portland Cement Vaderrivas.

References

1. Ferron RP, Gregori A, Sun Z, Shah SP (2007) Rheological method to evaluate structural buildup in self-consolidating concrete cement pastes. ACI Mater J 104(3):242–250
2. Lowke D (2018) Thixotropy of SCC—a model describing the effect of particle packing and superplasticizer adsorption on thixotropic structural build-up of the mortar phase based on interparticle interactions. Cem Concr Res 104:94–104
3. Roussel N (2007) Rheology of fresh concrete: from measurements to predictions of casting processes. Mater Struct 40:1001–1012
4. Roussel N, Stefani C, Leroy R (2005) From mini-cone test to Abrams cone test: measurement of cement-based materials yield stress using slump tests. Cem Concr Res 35:817–822
5. Tregger N, Ferrara L, Shah SP (2008) Identifying viscosity of cement paste from mini-slump test. ACI Mater J 105(6):558–566
6. Bouvet A, Ghorbel E, Bennacer R (2010) The mini-conical slump flow test: analysis and numerical study. Cem Concr Res 40:1517–1523

7. Khayat KH, Omran AF, Naji S, Billberg P, Yahia A (2012) Field-oriented test methods to evaluate structural build-up at rest of flowable mortar and concrete. Mater Struct 45:1547–1564
8. Choi MS, Lee JS, Ryu KS, Koh KT, Kwon SH (2016) Estimation of rheological properties of UHPC using mini slump test. Constr Build Mater 106:632–639
9. Tan Z, Bernal SA, Provis JL (2017) Reproducible mini-slump test procedure for measuring the yield stress of cementitious pastes. Mater Struct 50:235
10. Jalal M, Teimortashlu E, Grasley Z (2019) Performance-based design and optimization of rheological and strength properties of self-compacting cement composite incorporating micro/nano admixtures. Compos Part B 163:497–510
11. Barluenga G, Puentes J, Palomar I (2013) Early age and hardened performance of cement pastes combining mineral additions. Mater Struct 46(6):921–941S

About the Influence of Shear-Induced Particle Migration and Sedimentation on the Measurement Results of Concrete Rheometers

Christian Baumert(✉) and Harald Garrecht

Institute of Construction Materials, Universität Stuttgart, Stuttgart, Germany
christian.baumert@iwb.uni-stuttgart.de

Abstract. Concrete chemistry is an integral component in the development of eco-concretes, easily compactible concretes, high-strength and very durable concretes. It is always necessary to adapt the fresh and hardened concrete properties to the respective application. In order to be able to develop a specific mix design, two essential requirements have to be taken into account. Firstly, mixing technology must also be reproduced on a laboratory scale. Secondly, the fresh concrete properties must ideally be determined in absolute units. A so-called intensive mixer is preferred in order to map the various mixing technologies used in practice. The shear intensity and thus the machine's Froude number can be changed over a wide range. A rheometer, which uses so-called absolute measuring tools, enables the calculation of the fresh concrete properties in absolute units. The KNIELE KKM-RT 22.5/15 integrates a rheometer into an intensive mixer. This unique combination is extended by a device for pre-shearing and homogenization of the mixture. In this article it will be shown that the mix is segregated during classic pre-shearing and that the subsequent measurements deliver too low raw data. The rheological parameters calculated from these raw data are too low and do not describe the concrete correctly. Pre-shearing with the newly developed device eliminates this fundamental problem of other concrete rheometers.

Keywords: Concrete · Rheology · Shear-induced particle migration · Sedimentation

1 Introduction

Concrete rheometers offer the possibility to vary the shear intensity and thus to map different loads in practice (transport; pumps, paving). Several round robin tests have shown that different concrete rheometers correctly determine the order of the tested concretes with regard to their fresh concrete properties. But unfortunately, the calculated rheological properties in absolute properties showed unacceptably large differences.

According to [2] these massive deviations must be based on the violation of one or more main hypotheses for rheological measurements.

V. Mechtcherine et al. (Eds.): RheoCon 2019/SCC 2019, RILEM Bookseries 23, pp. 168–173, 2020.
https://doi.org/10.1007/978-3-030-22566-7_20

– No-slip condition on the surfaces of the measuring devices
– Laminar flow equilibrium in the shear gap
– Homogeneity of the sample material

A rough or slightly profiled surface effectively prevents the sample from sliding on the measuring instruments. The falsification of the measured values by a slight profiling of the surface is given, is however certainly insignificant in order of magnitude, and can be excluded as reason for the deviations with the round tests. However, there are considerable uncertainties with regard to flow and material homogeneity. The structure of a resting concrete makes the pre-shearing of the material immediately before the measuring process unavoidable. The extent of the associated shear-induced particle migration is controversially discussed in the literature. [4] sees this as the main source for incorrectly determined fresh concrete properties. [2] was able to prove this effect for a mortar with a fast upward ramp in a speed-controlled test. In addition, [3] states that even sedimentation-stable mixtures can sediment under the influence of shear stress during the test.

2 The Solution Approach

The laboratory mixer KNIELE KKM-RT 22.5/15 has been developed to implement the development of mortars and concretes quickly and practically. For the first time, it is possible to produce mortars and concretes with infinitely variable mixing intensities in a so-called intensive mixer and subsequently carry out rheological measurements in the mixer.

After the concrete has been mixed, it is up to the customer to decide whether to use the mixing tool or additional measuring tools to determine the properties of the fresh concrete. Using the mixing tools, it is possible to evaluate the raw data of the rheological measurements. Since no defined surfaces can be defined for the mixing tools, the measured values have a relative character and can be used to check the individual batch. A conversion into absolute units is also not possible and reasonable via conversion factors. If the mixing tools are exchanged for the measuring tools via quick-change devices, the fresh concrete properties can be calculated in absolute units. Compared to the well-known concrete rheometers, the KNIELE KKM-RT 22.5/15 has a special feature. A hard rubber spiral is mounted on the outer cylinder, which transports the mix vertically upwards during rotation and conveys it through openings in the outer cylinder into the shearing gap. This enables the mandatory pre-shearing to be achieved with active homogenization of the mix.

The internal drive, a high-torque synchronous motor, drives the measuring cylinder. The speed is measured by a high-resolution rotary encoder, the torque by a frequency converter which works according to the direct torque principle. The outer cylinder is driven by the motor for the outer agitator and is fixed in position by a motor brake during the actual measurement. The pre-shearing itself does not take place via the inner cylinder, but via the spiral (Fig. 1). The result is the 3-dimensional circulation and the pre-shearing of the material and one of the main hypotheses for the conversion to absolute units is fulfilled. During the circulation of the material with the spiral, the moisture sensor integrated in the bottom flap determines the moisture content of the

material in a partial volume directly in front of the moisture probe. Since the measured values fluctuate only minimally during the circulation process, it is permissible to assume uniform moisture distribution in the material to be mixed and thus homogeneity.

3 Test Procedure

In order to demonstrate the influence of shear-induced particle migration, an easily compactable concrete was developed according to BASF's Smart Dynamic concept and subjected to two different measurement regimes (Table 1).

Table 1. Composition of the investigated easily compactable concrete.

	[kg/m^3]
CEM III/A 42.5 N	292
Limestone s&h easyflow	98
Superplasticizer BASF ACE 430	2,2
Stabilizer BASF Rheomatrix	0,88
Water	175
Gravel 8/16	381,5
Gravel 2/8	606,3
Sand 0/2	783,8

In the first measuring mode (traditional), the pre-shearing (duration 5 s) takes place at the maximum shear rate of the following test via the inner measuring cylinder. During the measuring process itself, the shear rate is gradually reduced (every 5 s). This procedure corresponds to the classical measuring regime of a concrete rheometer. In the second measuring mode (spiral), the pre-shearing takes place via the spiral for 30 s before the measuring process and before each speed change. Thus, with this measuring mode, a homogenized material is present at the beginning of each speed change (Fig. 2).

3.1 Selection of Measurement Data

After each speed change, a flow equilibrium must first form in the shear gap. However, since this process is superimposed by the shear-induced particle migration, the assumption was made that the flow equilibrium is reached 1 s after each speed reduction. The mean values for the torque were determined at all shear rates in the period 1 s–2 s after each speed change. The idle torque of the drive and the torque component caused by the bottom surface of the measuring cylinder in the concrete must be subtracted from these raw data. For this purpose, the drive part of the mixer was moved upwards until only the bottom surface of the measuring cylinder had contact with the concrete. Then the individual speed stages were run down and mean values for the required torque were calculated. The raw data, reduced by these two

proportions, thus allow the reference only to the outer surface of the measuring cylinder.

According to [1] it is currently not possible to determine which concrete rheometer outputs the correct absolute values. As all boundary conditions for determining the yield point of the LCPC box are fulfilled in absolute units according to the current state of knowledge, it was specified as a reference. With a flow distance of L = 62 cm, the yield point is approx. 70 Pa.

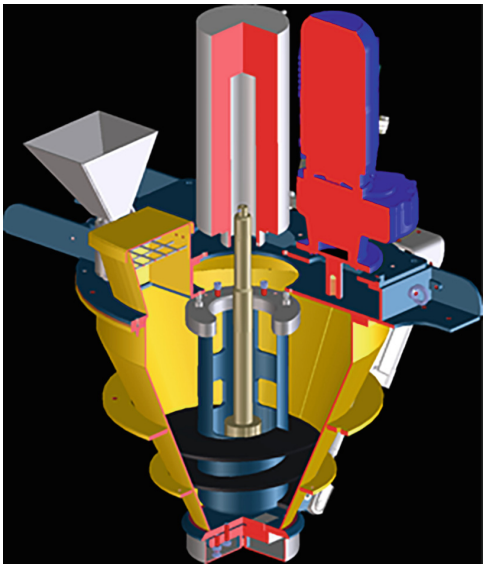

Fig. 1. Insight into the KNIELE KKM-RT 22.5/15 with measuring tools incl. spiral. The spiral enables three-dimensional circulation without segregation.

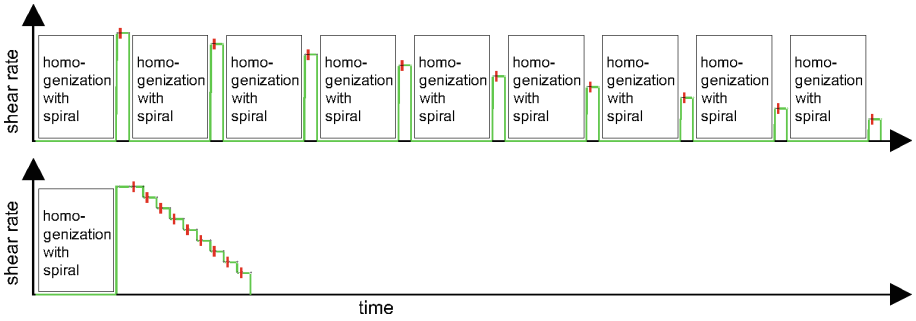

Fig. 2. Measuring-regime with the spiral of the KNIELE mixer (top) and according to conventional specifications (bottom). With the KNIELE, the inner measuring tool is stopped during the rotation of the spiral. In the classic mode, pre-shearing and measurement are performed with the inner cylinder. The spiral is not used. For identical starting situations the samples would be sheared with the spiral for 30 s before the test.

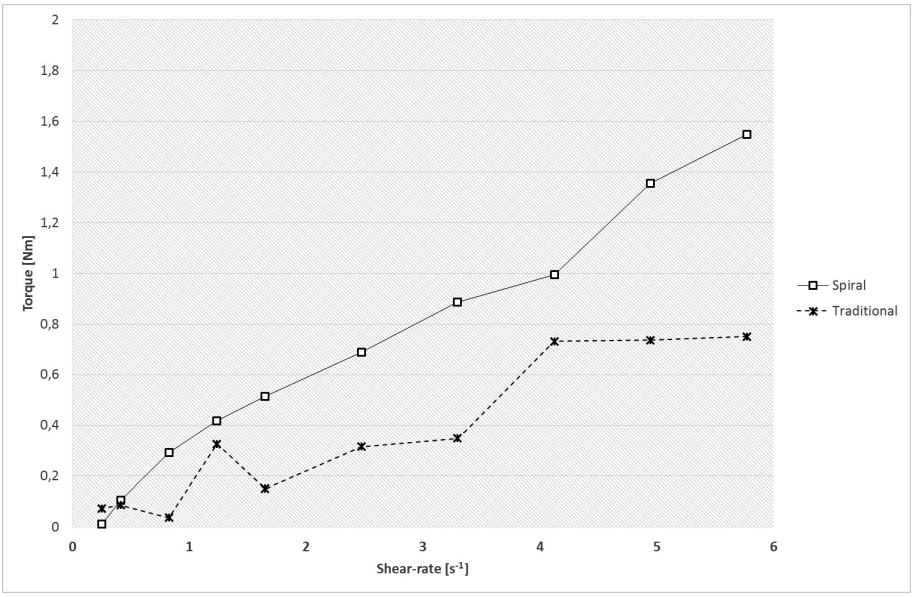

Fig. 3. Comparison between the traditional flow curve (pre-shear with spiral at the beginning) and the flow curve for the pre-shear with the spiral before each speed step.

3.2 Conversion of Raw Data into Absolute Units

In order to convert the machine data speed and torque into values in absolute units, Reiner Riwlin's method was chosen. The mean values of the torques in the interval 1 s–2 s after speed change were selected as input data for both measuring modes (Fig. 3). This interval was chosen because the assumption was made that after a two second segregation by the shear induced particle migration is not yet pronounced. After 1 s (without evaluation), however, it can be assumed that the shear in the shear gap is homogeneous.

Table 2. Results for the two measuring regimes after Reiner Riwlin.

	Spiral	Traditional
Yield stress in [pa]	23,141	0,010
Viscosity in [pa]	51,767	30,300
Deviation for viscosity (basis Traditional)	+71%	0%
Coefficient of determination R^2	0,995	0,944
Min. speed without shear-localisation [rad/s]	0,542	0,000

The pre-shearing before the actual measurement by the measuring tool leads to a low calculated viscosity. If the sample is homogenized by the spiral on the outer cylinder before each speed change, the calculated viscosity increases by 71%.

A yield stress of approx. 70 Pa was determined with the LCPC box. The solution shown in the table above with a yield stress of almost zero must therefore be rejected. The classical measuring regime with the evaluation according to Reiner Riwlin is therefore not suitable to describe the investigated concrete with regard to fresh concrete properties. The evaluation with pre-shearing by means of a spiral provides only a yield point of 23 Pa and thus still deviates considerably from the LCPC box.

3.3 Interpretation

The differences in Table 2 can be explained by the literature [2–4]. Due to the very rapid shear-induced particle migration, the measured values are often determined in practice on non-homogeneous samples. Yield stress and viscosity are therefore considerably underestimated. [4] rated this process probably as the greatest source of error in the determination of rheological properties on cementitious samples.

With the measuring device of the KNIELE KKM-RT 22.5/15 segregation can be effectively countered for the first time and the measurement of values can be carried out in absolute units. The calculated yield stress of the tested concrete is below the reference value of approx. 70 Pa even with the new measuring regime. This can probably also be attributed to the speed-controlled operation that is usual for concrete rheometers. The yield stress is extrapolated to zero using the rheological model. According to [5] “this method should only be used for simple QA tests, but no longer for modern research and development”. The KKM-RT 22.5/15 will therefore expand its range of functions in the future. Alternatively, the shear stress is specified and the yield point is thus determined directly as the measured value.

Acknowledgement. Special thanks are owed to the DFG for funding the IWB as part of the DFG 2005 priority project.

References

1. Roussel N (2012) From industrial testing to rheolgical parameters for concrete. In: Roussel N (ed) Understanding the rheology of concrete. Woodhead Publishing, Seiten, pp 83–95
2. Ovarlez G (2012) Introduction to the rheometry of complex suspensions. In: Roussel N (ed) Understanding the rheology of concrete. Woodhead Publishing, Seiten, pp 23–62
3. Ovarlez G et al (2010) Three-dimensional jamming an flows of soft glassy materials. Nat Mater 9:115–119
4. Hafid H, et al (2010) Estimating measurement artifacts in concrete rheometers from MRI measurement on model materials. RILEM Book Series, vol 1, pp 127–137
5. Mezger T (2012) Das Rheologie Handbuch, vol 4. Vincentz Network, Auflage

On-Board Concrete Rheology Measurements Using an In-Drum Sensor System: Early Stages

Xavier Berger[1(✉)], Pierre Siccardi[1], Robin Jean[1], Marc Jolin[1], Denis Beaupre[2], and Benoît Bissonnette[1]

[1] Research Centre on Concrete Infrastructures (CRIB), Department of Civil and Water Engineering, Université Laval, Québec, Canada
xavier.berger.l@ulaval.ca
[2] Command Alkon Canada, Québec, Canada

Abstract. Consistent quality in concrete production is an essential requirement in the ready-mix concrete industry. Insuring batch-to-batch uniformity is, in fact, an ever-present challenge. Moreover, modern concretes mixture designs often have complex behaviors in their fresh states, and yet the focus is on the slump (related to the *yield stress*) only, presenting an incomplete picture when one wants to assess the properties of various types of concrete. A second parameter known to be highly informative in this situation is the *plastic viscosity* of the fresh concrete. Few authors have assessed the potential of rheology measurements with a ready-mix truck. After a short introduction on sustainability, the aim of the first part of this conference paper is to offer a review of the different methodologies and results available on rheology measurements in/with a ready-mix truck. The second part is focused on the description of the in-drum sensor system used in this project. Finally, methodology and results about the slump evaluation with the in-drum sensor system are presented.

Keywords: Rheology measurement · Ready-mix truck · Quality control · Supplementary cementitious material · Sustainability

1 Introduction and Project Overview

Concrete technology has greatly improved over the years. Thus, modern mixes designs are far from the simple mix of cement, aggregates and water. Yet, QC-testing tools did not follow the concrete technologies development trend. In consequence, using engineered concretes often present a daily challenge in the industry.

Concrete is the most utilized construction material, it is unique in the way it is produced, transported and then cast in formwork of varying shapes and sizes. Thanks to the approach of Barcelo et al. [1], it is possible to estimate concrete annual production based on the annual cement consumption. In the USA, according to U.S. Geological Survey [2], the cement apparent consumption reached 96.8 million tons in 2017. With concretes produced having a cement content from 10% to 15% (by mass), it means concrete production reached about 775 million of tons. In order to meaningfully improve the total concrete production, it is relevant to evaluate the leading means of production. The U.S. Geological Survey [2] estimates that the ready-mix industry

V. Mechtcherine et al. (Eds.): RheoCon 2019/SCC 2019, RILEM Bookseries 23, pp. 174–181, 2020.
https://doi.org/10.1007/978-3-030-22566-7_21

bought 70% to 75% of the cement over the last years. That represents about 450 to 680 million tons of concrete. Obviously, it is the direction to follow in order to have a significant impact on the global concrete production.

It is not a new idea to say that improvements in the concrete industry must translate in decreasing its own greenhouse gas emissions. Today, the Organisation for Economic Co-operation and Development (OECD) estimates that about 9% of the worldwide greenhouse gas emissions are due to concrete [3]. While concrete has itself a low level of embodied CO_2, the source of the environmental challenge is the very large volume of concrete annually produced [1]. Cement and aggregates consumption are the main challenges in green concrete production. The OECD projects that the estimated 27 billion tons of aggregates used worldwide in 2017 will double by 2060 [4].

Modern concrete mixture designs have complex behaviors in their fresh state (for ex.: self-consolidating concretes or pumpable concretes) that often calls for more precise and specialized Quality Control-testing (QC-testing) upon arrival on the job site in order to determine their compliance with the specifications [5]. In the field, it is common to focus on the slump value (related to the *yield stress*) only, but it draws an incomplete picture when one wants to assess the fresh properties of various types of concrete. A second parameter highly significant in these situations is the *plastic viscosity* of the fresh concrete [6], especially SCC. Unfortunately, to this day, the on-site assessment of the plastic viscosity is seldom conducted and where it is, it is assessed by empirical tests such as the T_{50} or the V-funnel and rarely with a rheometer, a rather complex device which can hardly be used on a day-to-day basis on job-site. At the same time, QC-testing is considered costly, time consuming and often the source of animated discussion because of potential human factor errors. Luckily, a few authors did assess the potential of rheology measurements with a ready-mix truck [7–10]. Most of the time, the methodology used is based on the energy required to drive the ready-mix truck drum. Nevertheless, recent development of an in-drum sensor system opens the door to many new possibilities [11]. Tests have shown the potential to measure concrete plastic viscosity as the sensor goes through concrete during drum rotation [10]. To explore the capabilities and reach of such a technology, *Université Laval* has initiated a research program in collaboration with *Command Alkon*, the company that markets the sensor system.

2 Rheological Measurement Methods

2.1 Background

On one hand, concrete rheology is the most "scientific" description of the concrete flow in comparison to empirical tests. On the other hand, it is an experimental challenge to obtain the fundamental rheological parameters of concrete. Although many models exist to describe the flow of concrete [12], the Bingham model is most often use to describe the concrete behavior [13] given its ease of use in experimental R&D. Indeed, it allows to describe the concrete flow by the yield stress (τ_0) and the plastic viscosity (η_{pl}) as per Eq. 1.

$$\tau = \tau_0 + \eta_{pl}\dot{\gamma} \tag{1}$$

With τ = shear stress (Pa) and $\dot{\gamma}$ = shear stress rate (s^{-1}).

Several designs of rotational rheometers were developed over the years. In practice, the torque and the rotational velocity are recorded, and results are expressed in arbitrary units. Coaxial and parallel plate rheometers have geometries that allow the use of equations to transform these arbitrary units in fundamental units, Pa and Pa.s for the yield stress and the plastic viscosity respectively. Rheometers with complex geometries require the use of a reference material with known rheological properties to do a calibration [5]. An extensive experimental program has been conducted to compare different rheometers and it was concluded that rheological parameters are, after all, dependent to the apparatus used [14, 15]. To this day, measurement of the fundamental rheological properties themselves is very complex. However, the measurement of the fundamental rheological properties may be unnecessary to develop a relevant job-site QC-testing tool for fresh concrete.

Tattersall [5] developed a mixer equipped to measure the power consumption during mixing to use as a rheometer. The theoretical development is detailed in [5]. As soon as the flow in the mixer is laminar, the relationship between the *rotational speed* and the *power consumption* can be expressed as a quadratic equation and the relationship between the power and the torque allows to write the following equation:

$$T = G + HN \tag{2}$$

With T = torque (N.m) and N = rotational speed (RPM).

Using the similitude between Eqs. 1 and 2 and as per Tattersall theoretical development [5], the (arbitrary unit) parameter G is relative to the yield stress and the (arbitrary unit) parameter H is relative to the plastic viscosity. Such a practical approach could be enough to characterise the concrete flow from a practical point of view. Applying this concept to an on-board measurement method seems to be the way to use the rheological measurements concepts in the field.

2.2 On Board Rheology Measurements

This section highlights two concepts used to assess rheological parameters of concrete with a ready-mix truck. In the first studies, the power consumption during mixing is used to obtain the parameters with a ready-mix truck. Because trucks are equipped with a hydraulic system to drive the drum rotation, hydraulic pressure (related to the torque) is measured. Characteristic's concrete flow curves are obtained by plotting the inlet hydraulic pressure for a range of drum rotational speed. Then the concrete flow can be represented by Eq. 3; G_h and H_h are respectively the yield stress and the plastic viscosity, in arbitrary units.

$$P_{inlet} = G_h + H_h N \tag{3}$$

With P_{inlet} = inlet hydraulic pressure (Pa) and N = drum rotational speed (RPM). Subscript "h" refers to the hydraulic system used to determine the rheological parameters.

Daczco [7] presented a study on the potential of using of a ready-mix truck in order to measure concrete rheology. By using a linear curve fit on the data collected by varying the drum rotation speed and monitoring the hydraulic pressure, he showed that it may be experimentally possible to assess the rheological parameters. However, only two concretes mix designs were studied. A few years later, Amziane et al. [8] studied nine different concretes with various consistency. It was observed that a ready-mix truck is a good tool to obtain flow curves of concrete, the flow curves are sensitive enough to capture variations in material behavior. The yield stress obtained with the ready-mix truck is well correlated with the one obtained with a rheometer; however, plastic viscosity correlation was not satisfactory. The authors [8] reported that a more precise pressure gauge and a velocity recording system is required in order to improve the rheology measurement with the truck. Later, Ferraris et al. [9] used a proprietary system to record the hydraulic pressure and the drum rotational speed and studied twenty-one different concretes. They confirmed that yield stress can be determine with an instrumented ready-mix truck and that it is well correlate with the yield stress obtain with a rheometer. However, plastic viscosity correlation is unfortunately still not satisfactory. Experimental issues, different procedures and systems reported in the literature can lead to unprecise assessments of the best way to measure rheology with a ready-mix truck. Even if full rheology measurement using a ready mix-truck is not yet attained, this approach is still promising (Ferraris et al. [9]). An extensive study needs to take place to finally judge clearly on the practical value of the power consumption concept to measure concrete rheology with a ready-mix truck. Taking into account these findings will obviously help to reach this goal.

A less explored concept is based on drag force measurement. Mokéddem [16] worked on rheology measurement inside a concrete mixer with a probe (the Visco-probe© system). The relative motion of the probe and the concrete creates a force on the probe which is assumed dependent on the rheological properties of the material. The author details the theoretical development to link the yield stress and the plastic viscosity to the drag force and the probe speed [16]. It is possible to identify an affine relation between the drag force and the probe speed (Eq. 4):

$$F = G_f + H_f N \tag{4}$$

With F = drag force (N) and N = probe velocity (m/s). Subscript "f" refers to the drag force concept used to determine the rheological parameters.

In Eq. 4, G_f and H_f are respectively relative to the yield stress and plastic viscosity (arbitrary units). Beaupre et al. [11] also developed a sensor system (Fig. 1) to measure concrete rheology *inside* a ready-mix truck. By varying the speed of the drum, the force recorded by the probe changes and the rheology can be measured. To allow the comparison of the results with similar devices of different size and shape, the force is transformed to an equivalent pressure [17]. Exploring the potential of this sensor-system will be the first step of this project.

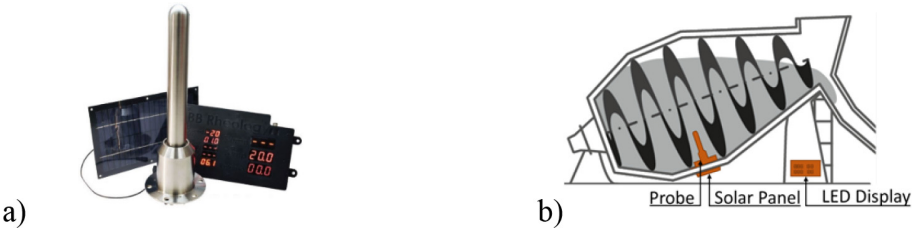

Fig. 1. (a) Probe, display and solar panel [image by Command Alkon] and (b) Probe system overview (adapted from [18]).

3 Set-Up

The sensor system used in this project is composed of the probe, a solar panel, a display, a tablet, a data acquisition system and a communication system. The probe is installed in the drum and the power comes from the solar panel. The data acquisition system records the probe data, then it is logged to a database. A hydraulic pressure gauge is installed on the hydraulic line to the drum motor and a rotational speed sensor is fixed to the motor. Both sensors outputs are also recorded by the data acquisition system.

4 Slump Evaluation by the Sensor System

The slump test is a standard acceptance tools so, any onboard system that allows its evaluation during the transport and at the job site is relevant. The sensor system described was designed to assess the slump using calibration tables. In fact, it is currently commercialised for this purpose. At this time, the calibration table used correlates the pressure applied on the probe with the measured slump. Tests at *Université Laval* have been made to validate the relevance of the calibration table logged in a concrete producer system based in Québec City and to compare results obtained with literature data. The procedure used to build the in-house calibration table was similar to the one introduced by Beaupré et al. [17]. At the beginning of the test, concrete was purposely very stiff (no slump), then water is gradually added to change consistency; that is called the *re-tempering methods*. For each concrete consistency, two technicians performed slump test (ASTM C143/143M-15a [19]) separately and another technician records the pressure when the drum rotational speed is below 3 RPM. The results obtained are reproduced in Fig. 2.

No curve-fit is purposely applied to this data set because of the inconsistencies especially at the boundaries of the calibration table. Tentatively, a linear interpolation between two points is used to estimate the slump. As expected, the pressure is inversely proportional to the slump measured. Also, the relationship obtained is similar to the calibration table logged in probes used by the concrete producer, especially for a slump over 150 mm. However, it was not possible to reach a slump over 200 mm during our testing. The slight difference between *Université Laval* calibration and the producer

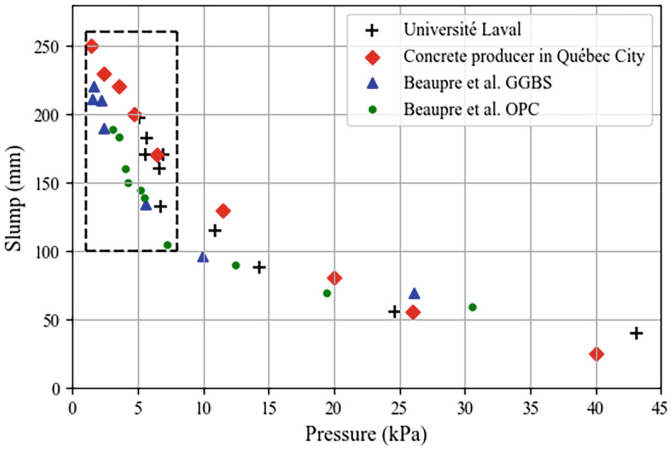

Fig. 2. Calibration tables from literature [17], concrete producer in Québec City and the one obtained at Université Laval.

calibration for slumps ranging from 30 mm to 150 mm could be explained by the difference in concrete mix design.

It was found that whatever the calibration table used, a small difference in recorded pressure can lead to a significant difference in the slump estimation for the dotted box region on Fig. 2. Therefore, it is necessary to study the precision of the pressure measured by the sensor system. From this analysis, it will be possible to determine a range of slumps value relative to a pressure measurement, which is more rigorous than a unique value of slump. In fact, this is currently a lack in the slump estimation procedure with this sensor-system. Figure 2 also compares literature results [17] with the concrete producer calibration table in Québec City and the outcomes of *Université Laval* tests. As expressed previously, concrete mix design has an effect of the calibration table to be selected. In consequence, it is not possible to use a generic calibration table to estimate slumps for all concretes mix-designs.

5 Case Study

This case study was conducted on a precast concrete project. In order to estimate the slump of ternary blends concrete mix using the sensor system, a calibration table has been previously elaborated. For this project, concrete must be delivered with a slump value of 220 mm ± 30 mm. The main objective is to compare the measured slump obtained through the conventional test (ASTM C143/143M-15a [19]) with the slump estimated by the sensor system. Measured slump versus estimated slump are represented in Fig. 3.

The solid line represents the equality between the estimated and the measured slump. The dashed lines represent a ±10 mm zone around the estimated and measured slump equality. About 75% of the estimated slump values are included in this area. This means that 75% of the slump values are estimated with an absolute difference of

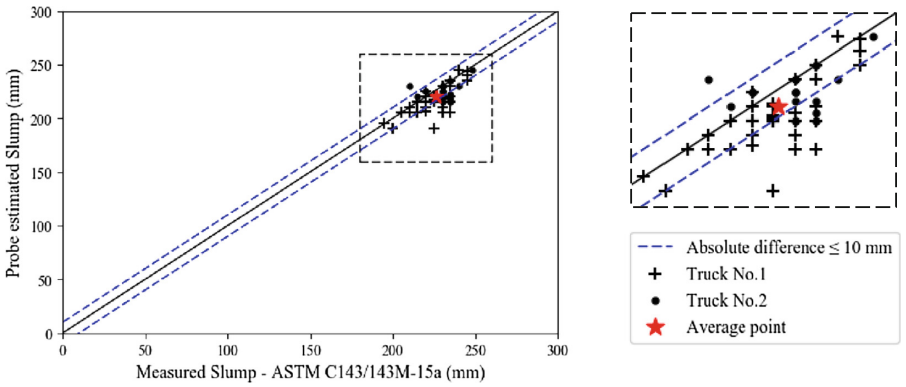

Fig. 3. Measured slump Vs. estimated slump.

less than 10 mm. Moreover, given the ±30 mm threshold acceptance on this job-site, using the sensor system value of slump would have led to similar acceptance. This result is quite good, but it could be better with a proper adjustment of the calibration table. The center of gravity of the scatter plot allows to highlight that the average of the estimated slumps is slightly below the average of the measured slumps. So, the initial calibration table could be adjusted thanks to the production data set gathered. Specifics calibration table appears necessary for a specific mix design. However, the methodology presented here could be used to optimize a default calibration set for any new mix design. The first part of this case study highlight that the sensor system could be a very interesting device for slump estimation as soon as the calibration table is set accurately. So, the next step will be to determine statistically how many loads must be followed to establish a properly adjusted calibration table.

6 What Is Next?

An instrumented ready-mix truck is an efficient mean to obtain the concrete yield stress (slump), but work is still needed to determine the concrete plastic viscosity. For further developments, a complete understanding of the testing procedure and mechanisms involved must take place. In fact, this is an important challenge of the project introduced in the paper. Nevertheless, the slump test is currently the most common test to control concrete on job-site. Any tool that allows automatic slump evaluation such as the sensor system described here is a significant improvement in the ready-mix concrete production. Hopefully, the findings of this promising project will promote the use of modern concrete mixture designs especially with regards to the use of large volumes of SCM, recycle aggregates and the use of recycled water; three types of constituents that are known to cause difficulties in *maintaining* and *controlling* the workability of fresh concrete up to the point of delivery.

7 Acknowledgement

This project is supported by Collaborative Research and Development Grants. The authors would like to thank Command Alkon and Béton Provincial for the financial, technical and logistic support, the NSERC for funding, BPDL for the access to the precast factory and Mathieu Thomassin for his implication.

References

1. Barcelo L, Kline J, Walenta G, Gartner E (2014) Cement and carbon emissions. Mater Struct 47(6):1055–1065
2. Ober JA (2018) Mineral commodity summaries. U.S Geological Survey, Reston, p 204
3. OECD (2018) Highlight - Global Material Resources Outlook to 2060
4. OECD (2019) Global Material Resources Outlook to 2060
5. Tattersall GH, Banfill PF (1983) The rheology of fresh concrete. Pitman Books Limited, Great Britain
6. Wallevik OH, Feys D, Wallevik JE, Khayat KH (2015) Avoiding inaccurate interpretations of rheological measurements for cement-based materials. Cem Concr Res 78:100–109
7. Daczko JA (2000) A proposal for measuring rheology of production concrete. Concr Int 22 (5):47–49
8. Amziane S, Ferraris CF, Koehler E (2005) Measurement of workability of fresh concrete using a mixing truck. J Res Natl Inst Stan Technol 110(1):55
9. Ferraris CF, Cooley R, Grein J, Peltz MA, Topputo M, Verdino S (2007) Feasibility of using a concrete mixing truck as a rheometer, Orlando, Florida, NISTIR 7447
10. Beaupre D (2012) Rheological probe to measure concrete workability. In: 37th Conference on our world in concrete & structures, Singapore
11. Beaupre D, Chapdelaine J, Chapdelaine F (2017) Probe and method for obtaining rheological property value, U.S. Patent No.: US 2017/0108421 A1
12. ACI (2007) Report on Measurements of Workability and Rheology of Fresh Concrete
13. Ferraris CF (2006) Concrete rheology: knowledge and challenges. In: 2nd International RILEM symposium on advances in concrete through science and engineering, Quebec, Canada
14. Ferraris CF, Brower LE, Banfill P, Beaupré D, Chapdelaine F, de Larrard F, Domone P (2001) Comparison of concrete rheometers: international Test at LCPC, Nantes, France in October 2000, NISTIR 6819
15. Beaupré D, Chapdelaine F, Domone P, Koehler E, Shen L, Sonebi M, Struble L, Tepke D, Wallevik J, Wallevik O (2004) Comparison of concrete rheometers: international tests at MBT, Cleveland OH, USA in May 2003, NISTIR 7154
16. Mokéddem S (2012) Contrôle de la rhéologie d'un béton et de son évolution lors du malaxage par des mesures en ligne à l'aide de la sonde Viscoprobe. Thèse de Doctorat, Ecole Centrale de Nantes (ECN)
17. Beaupre D (2012) Mixer-mounted probe measures concrete workability. Concr Int 34(9):46–49
18. Ambrosetti M D.R.L. Under license CC BY-SA 4.0. https://commons.wikimedia.org/wiki/File:Operation_of_a_truck_mixer.gif#filehistory
19. ASTM C143/C143M-15a (2015) Standard Test Method for Slump of Hydraulic-Cement Concrete, ASTM International, West Conshohocken, PA. www.astm.org

Experimental Developments of the Squeeze Flow Test for Mortars

Fábio A. Cardoso(✉), Franco A. Grandes, Victor K. Sakano, Andressa C. A. Rego, Fábio C. Lofrano, Vanderley M. John, and Rafael G. Pileggi

Department of Construction Engineering - Escola Politécnica, University of São Paulo, São Paulo, Brazil
fabio.cardoso@lme.pcc.usp.br

Abstract. Squeeze flow rheological technique is based on the compression of a cylindrical sample between parallel plates and is used to determine the flow properties of food, pharmaceuticals, composites, suspensions, including cementitious materials. This work summarizes the main experimental developments on squeeze-flow for the evaluation of mortars that have been performed in Brazil for the last 15 years and supported the creation of the Brazilian standard test method applied to rendering and masonry mortars (ABNT NBR 15839:2010). The paper exemplifies possible test setups (configuration, geometry, velocity, roughness) for different types of mortars and situations, the use of porous substrate (ceramic or concrete blocks) as the bottom plate, and a method to measure phase separation induced by the. A complementary instrumentation (interfacial pressure mapping) for the assessment of pressure evolution during flow is also presented – forming the pressure mapped squeeze flow method (PMSF) – which allows for identification of transitions in flow type and localized pressure peaks resulting from microstructural changes like particle jamming. The technique was also employed to study and develop laboratory mixing methods for mortars, as the resulting flow curves are very sensitive to the material's agglomeration state. Finally, rheological parameters of mortars by squeeze-flow and rotational rheometry were compared showing that yield stress have some degree of agreement, whereas viscosity values from these techniques are complex to be related.

Keywords: Mortar · Squeeze flow · Phase separation · Pressure distribution · Mixing

1 Introduction

Inorganic mortars, besides being a fundamental portion of concretes, are also products widely used for many functions. The rheological requirements associated with the various uses and processing combinations are diverse as well [1]. In this sense, squeeze-flow testing has been applied as an alternative/complementary technique to assess the flow behavior of building materials. Besides its ease of implementation, the geometry change during gap reduction makes the method particularly interesting, as it creates flow conditions similar to those involved in processing and application of

V. Mechtcherine et al. (Eds.): RheoCon 2019/SCC 2019, RILEM Bookseries 23, pp. 182–190, 2020.
https://doi.org/10.1007/978-3-030-22566-7_22

mortars like pumping, spreading, finishing, squeezing between bricks, extrusion and more recently 3D printing processes [1–4]. The method is very versatile allowing various geometric configurations, plate roughness, gaps and displacement rates to better simulate diverse technological situations [2, 5]. During squeeze, suspensions may undergo phase separation depending on material's susceptibility and flow conditions [1, 2]. This phenomenon is crucial as it affects localized solid content and consequently the rheological behavior of mortars even in a more complex way, since they are multiphasic heterogeneous materials with micro and macroscopic particles. Therefore, phase separation should be considered for a better interpretation of squeeze flow behavior [1, 2], preferably with complementary techniques that can provide information regarding this associated effect. The present paper aims to highlight a group of developments about the test for mortars that improved experimental possibilities and comprehension of some phenomena closely related to this type of flow; plus, a practical use of the test for evaluation and development of mixing methods. Most results present in this work are of factory-produced rendering mortars (Brazilian or European) [1, 5–8] and a few are of mortars formulated in the university's laboratory [2, 6]. Further details of mortars' features and methods can be found in the references. All squeeze flow tests were displacement-controlled with constant velocity (0.1 mm/s or 3 mm/s).

2 Squeeze Flow Configurations and Plate Roughness

Figure 1 shows the two main geometric configurations employed: (a) constant area and (b) constant volume. The first has the advantage of maintaining a constant surface area of the material in contact with the moving top plate, facilitating stress determination, but susceptible to edge effects when the material is extruded outwards. On the other hand, in the constant volume configuration the material is always in between the plates with no edge effects other than the boundary of the spreading sample. However, determination of stress must always be performed, which for mortars may not only be a matter of volume conservation since entrained air is compressible and can even collapse; in addition diameter/height ratio changes more significantly throughout the test (when compared to CA), which can induce transition of flow type – from elongational to shear – because this ratio is one the main parameters that influences the flow [1, 5, 7, 8]. Nevertheless, both configurations are useful and have some degree of similarity with processing and application conditions of mortars and other cement-based materials.

In Fig. 2 the influence of the geometric configuration can be seen both with smooth and rough plates. For the same displacement, normal stress tends to be higher for CA than for CV, since for the first, diameter/height ratio is higher which induces more shear and overall resistance to flow. Most curves of this particular mortar are characterized by a strain-hardening behavior at small displacements, with absence of a more pronounced viscous or plastic behavior stage [1]. At 3 mm/s (graphic b), final displacements achieved (test with 1000 N) are larger than those at 0.1 mm/s because liquid-solid phase separation (filtration phenomenon) is more intense at slower rates. Therefore, CV_smooth curve displays some viscous or plastic stage. The other main

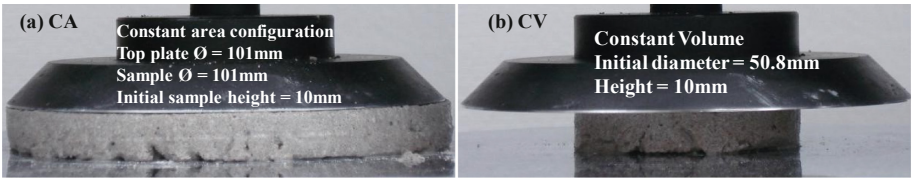

Fig. 1. Squeeze-flow configurations: (a) Constant area a 101 mm top plate; (b) Constant volume with a 101 mm top plate and sample initial diameter of 50.8 mm. In both cases, bottom plate was 200 mm in diameter (adapted from [5]).

parameter that affects the predominant flow type is plate roughness: the higher the friction at the interface, more shear flow; whereas, more slip results in more elongation. This is the reason why squeeze flow curves with rough plates (SiC emery paper) have higher stresses and smaller final displacements [5]. The manifestation of strain-hardening at such large gaps (small displacements) when compared to the maximum particle size of the mortar (2 mm) is caused by phase separation that increases solid content in the central region [1, 2, 5, 6]. These results from the variations of configuration and interfacial roughness, indicate that shear induced during squeeze flow of mortars was associated to phase separation in this case. Confirmation was obtained by phase separation experimental data from [5] measured as described in Fig. 4.

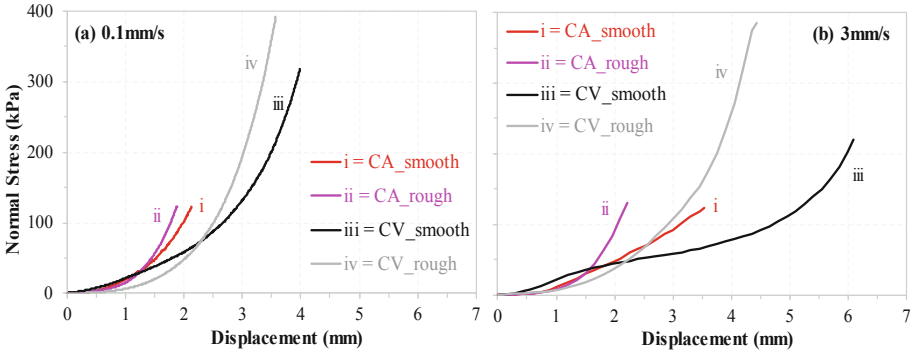

Fig. 2. Squeeze-flow results of mortar Alfa with constant area (CA) and constant volume (CV) using smooth metallic plates and emery paper. (a) 0.1 mm/s; (b) 3 mm/s (adapted from [5]). For CV stress, nominal constant volume of the samples was considered.

3 Assessment of Pressure Distribution and Phase Separation

Pressure distribution at mortar-plate interfaces was evaluated by a dynamic pressure mapping system (I-Scan, Tekscan Inc.) [2]. Figure 3 shows the evolution of pressure distribution of two similar mortars, except for the use of MHEC (methyl hydroxyethyl cellulose ether admixture - Tylose 10012P6) in mortar coded as CE. This technology provided evidence of phase separation effects on the squeeze flow behavior, proving

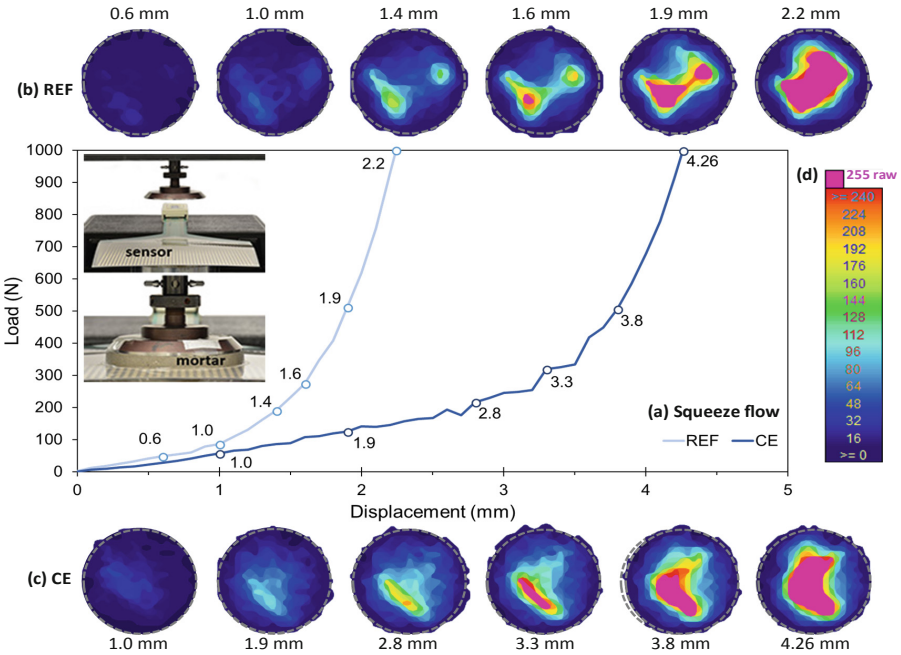

Fig. 3. Squeeze-flow and pressure distribution results of mortars REF (without MHEC cellulose ether) and CE (with MHEC) tested at 0.1 mm/s (adapted from [2]).

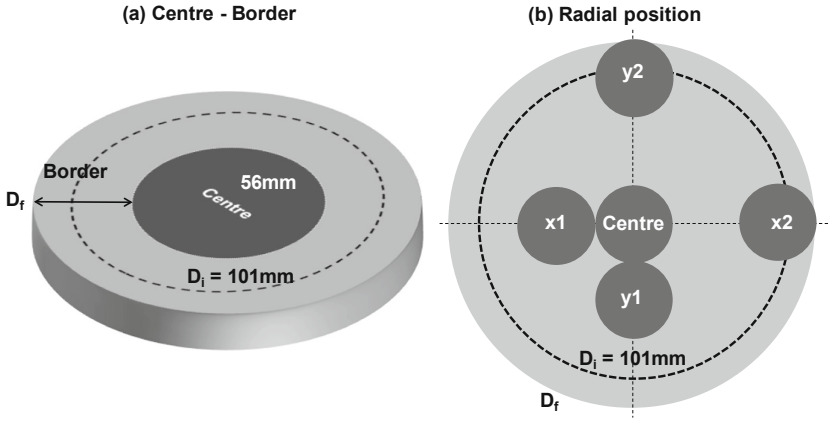

Fig. 4. Geometric configurations used to divide fresh mortar samples for the phase separation evaluation after squeeze flow tests: (a) Centre – Border, (b) Radial position. Each portion was microwave dried for 20 min (unpublished results from [6]).

that strain-hardening at gaps much larger than the maximum particle size is caused by formation of drier microstructures, when the liquid percolates radially the packing of particles [1, 2]. Hence, localized pressure peaks are formed due to particle jamming,

and at the end of this microstructural change, the solid content of the center (and pressure) are much higher than in the border, as proved by phase separation tests [2]. The use of viscosity enhancing admixtures, like cellulose ethers, increases the viscosity of water thus improving its drag capacity, which tends to reduce (or eliminate) the relative flow between liquid and particles [2]. The consequences of this effect can be seen by the occurrence of strain-hardening and localized pressure increase only at higher displacements for mortar CE. This is the reason for the employment of such admixtures in compositions submitted to pumping and spraying, situations where phase separation is undesired. The other important contribution of the PMSF is the determination of profiles in radial position (not shown in this work), which allows the comparison with models and the identification of flow type (elongation, shear, plastic or frictional) and possible transitions that can occur [2]. Knowing the actual flow type is crucial to apply the proper rheological model.

As mentioned, a method for quantification of phase separation was developed based on division of the squeezed mortar in different portions and quantifying their water content by microwave drying [2, 5–7]. Figure 5 exemplifies results combining squeeze flow with pressure mapping and phase separation quantification in order to illustrate how the mortar flow occurs when liquid migration is intense. Mortar K is a composition very keen to this phenomenon since it has no admixture whatsoever and the sand's particle size distribution is very narrow. With a very thin paste and a very permeable particle packing this composition is highly susceptible to filtration rather than flowing as a homogeneous fluid, especially when tested at slow rate [1, 2, 6]. As a result, pressure concentration and strain-hardening occur early in the test and the resulting microstructure is a central part with solid content considerably higher than the nominal and even higher than the border. Yet possible and probable, paste-aggregate phase separation is still to be experimentally proved.

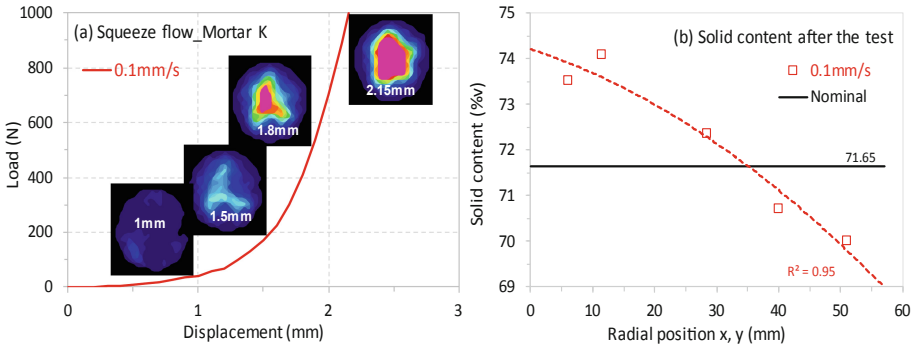

Fig. 5. (a) Squeeze-flow and pressure distribution results of mortar K tested at 0.1 mm/s. (b) Radial solid content (%v) distribution of mortar K after the test assessed by microwave drying [6].

4 Squeeze Flow Over Porous Substrates

In practical applications mortars are applied over different substrates with varying characteristics such as roughness, porosity and water absorption capacity. As demonstrated local variations of water content are important and can adversely affect the flow behavior and homogeneity of the material. Nevertheless, when applied to a wall for example a rendering mortar interacts with the substrate and the increase in consistency within an appropriate time frame is required to allow cutting, leveling and finishing procedures. Therefore, an experimental apparatus was developed, and mortars tested over a ceramic block after different resting times and compared with the standard test, as illustrated in Fig. 6 [6]. Results show that the mortar changes much faster when it loses water to the porous block, with strain-hardening occurring for very small displacements. Such adaptations of the squeeze flow method can be very useful for evaluation of different substrates and development of mix-designs tailored for various environmental conditions, which can be simulated in the laboratory before going to pilot field tests.

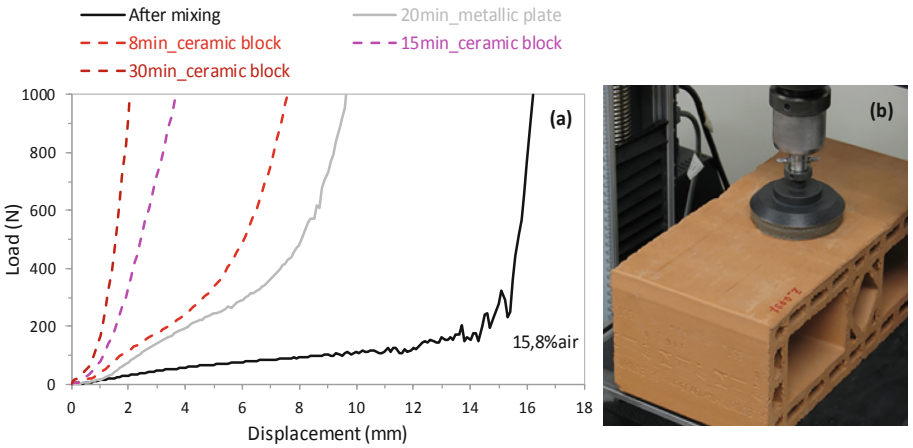

Fig. 6. (a) Squeeze-flow results of mortar Zeta tested at 0.1 mm/s and initial height of 20 mm: solid lines - immediately after mixing and after 20 min resting over the metallic bottom plate; dashed lines - after different resting times over ceramic blocks. (b) Picture of the setup used with the ceramic blocks. (unpublished results from [6]).

5 Evaluation and Development of Mixing Procedures

Due to the geometric restriction, compressive displacement and induction of phase separation that are inherent to squeeze flow, the test is highly sensitive to the agglomeration and homogenization states of the suspensions [2, 4, 8]. These characteristics make the technique very interesting to evaluate the mixing condition of mortars and, hence, the efficiency of mixing procedures and equipment. Using the test, differences in flow behavior have been identified between mortars produced by manual

procedure, mechanical mixing according to ABNT 13276 (valid standard procedure until 2016) and a mechanical two-step water addition procedure, as shown in Fig. 7(a). More efficient procedure (Two-step > ABNT 13276 > Manual) produced more flowable mortars and provided smaller variation between batches, due to the higher energy provided to disperse agglomerates and homogenize the constituents [7]. Further research resulted in the creation of a more efficient new Brazilian standard procedure for mortars (ABNT 16541/2016), as evidenced by Fig. 7(b) [8].

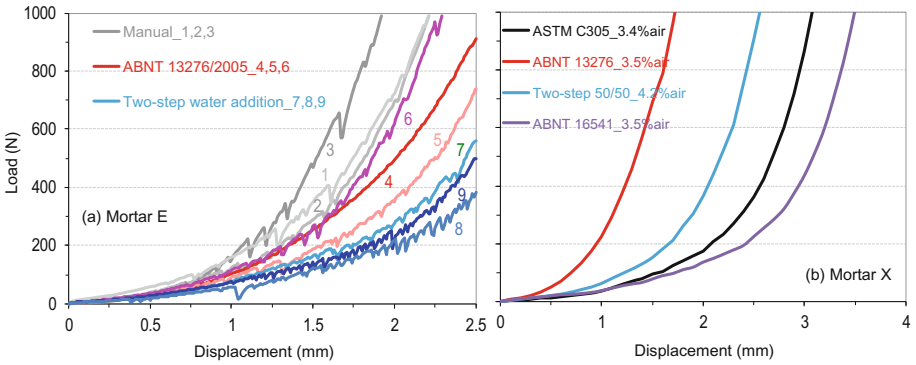

Fig. 7. (a) Squeeze flow results for Mortar E prepared by different mixing procedures: manual mixing with a spatula, mechanical mixing according to standard ABNT 13276/2005 and two-step 50/50% water addition. The batches were prepared 3 times each and the mortar tested at 0.1 mm/s (adapted from [7]). (b) Mortar X prepared following 4 different procedures, including the one described by the new Brazilian standard ABNT 16541/2016, which is more efficient as it is based on two-step water addition (75% + 25%) concept with one minute at high rotation speed in between the steps [8].

6 Rheological Parameters from Rotational Rheometry and Squeeze Flow

A systematic comparison between rotational shear and squeeze-flow for evaluating the rheological behavior of several mortars (Fig. 8) showed encouraging agreement in ranking the mortars' yield stress with a good linear correlation, with some differences depending if whether the material behavior was more visco-plastic or granular [1].

7 Conclusions

Squeeze flow technique has been showing great potential for the rheological evaluation of cement-based and other building materials due its ease of implementation and, especially, because it fills a gap of flow conditions and association with relevant phase separation phenomenon that other methods are not able to provide. For simple and controlled shear evaluation with no geometry change, rotational rheometry is more appropriate, but squeeze flow can be an important complementary test for specific

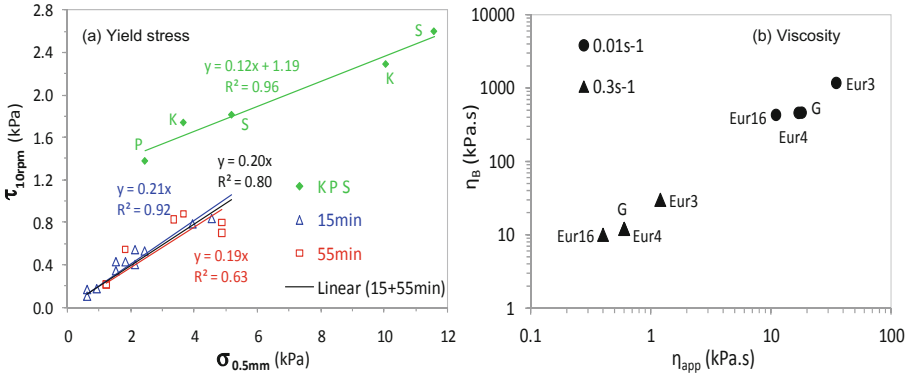

Fig. 8. (a) Comparison of yield stresses of several mortars: rotational shear stress at using Viskomat rheometer vs. squeeze (normal) stress at 0.5 mm. (b) Biaxial extensional viscosity (η_B) from squeeze flow testes of mortars with no phase separation vs. shear apparent viscosity (η_{app}) from Viskomat shear cycles (adapted from [1]).

situations, including 3D printing related processes. The reported developments and associated experimental techniques are important tools for complete rheological evaluation of such complex materials as cement-based mortars and other similar suspensions, fiber-containing and composites.

For some mortars with no segregation it was possible to compare shear and extensional viscosities with a good linear correlation and Trouton ratios between 20 and 40. But for most mortars, phase separation during squeeze flow and also in rotational tests makes this correlation more complex to be performed since different flow conditions are obtained.

Acknowledgement. FAPESP (2011/00948-9, 2012/18952-5), CAPES, CNPq, ABAI and CONSITRA.

References

1. Cardoso FA, John VM, Pileggi RG, Banfill PFG (2014) Characterisation of rendering mortars by squeeze-flow and rotational rheometry. Cem Concr Res 57:79–87
2. Grandes FA, Sakano VK, Rego ACA, Cardoso FA, Pileggi RG (2018) Squeeze flow coupled with dynamic pressure mapping for the rheological evaluation of cement-based mortars. Cem Concr Compos 92:18–35
3. Toutou Z, Roussel N, Lanos C (2005) The squeezing test: a tool to identify firm cement-based material's rheological behaviour and evaluate their extrusion ability. Cem Concr Res 35:1891–1899. https://doi.org/10.1016/j.cemconres.2004.09.007
4. Nair SAO, Alghamdi H, Arora A, Mehdipour I, Sant G, Neithalath N (2019) Linking fresh paste microstructure, rheology and extrusion characteristics of cementitious binders for 3D printing. J Am Ceram Soc 102:3951–3964. https://doi.org/10.1111/jace.16305

5. Cardoso FA, Lofrano FC, John VM, Pileggi RG (2014) Influence of experimental parameters of the squeeze-flow test on the rheological behaviour and phase segregation of cement mortars. Trans Nordic Rheol Soc 22:79–85
6. Cardoso FA, Pileggi RG (2013) Phase separation in mortars: development of measuring method and influence on rheological behavior. FAPESP Post-Doc Scientific Report 2011/00948-9, no. 1, São Paulo (Unpublished results from internal document)
7. Cardoso FA, Campora FL, Pileggi RG, John VM (2018) Evaluation of mortar mixing procedures using squeeze flow test. In: Proceedings of the International RILEM workshop on rheological measurements of cement-based materials, Arras, pp 18–22
8. Cardoso FA, de França MS, Campora FL, Pileggi RG (2019) Development of the new Brazilian standard mixing procedure for mortar preparation in laboratory. In: 15th International Congress on the Chemistry of Cement, Prague (accepted)

Measuring the Impact Behavior of Fresh Mortars by Pressure Mapping

Victor K. Sakano[1], Franco A. Grandes[1], Fábio A. Cardoso[1(✉)], Fábio L. Campora[2], Roberto C. O. Romano[1], and Rafael G. Pileggi[1]

[1] Department of Construction Engineering - Escola Politécnica, University of São Paulo, São Paulo, Brazil
fabio.cardoso@lme.pcc.usp.br
[2] Brazilian Association of Mortar Industries, São Paulo, Brazil

Abstract. Mortars and concretes are subjected to diverse rheological situations during their processing and application. Their behavior can be predicted for most situations by rotational rheometry and/or squeeze flow. However, very high strain rates that occur during impact are very difficult to be properly simulated using these methods. Especially for rendering mortars, impact behavior (during manual or spray application) is important not only regarding productivity and rebound issues but also because the initial mortar-substrate contact extension strongly affects the interfacial bond strength, which is one of the renders most critical hardened properties. The present work introduces initial developments towards an impact rheometry technique intended primarily for cementitious and other suspensions used in construction. The technique is based on a pressure mapping system that measures area and force with a thin and flexible sensor at 100 Hz. Mortars were applied manually, by continuous spraying, and by free fall. Results showed that in manual application, pressures up to 50 kPa took place, whereas in the mechanical procedure the pressure values were considerably lower (>5 kPa) since the force is distributed in small portions of material by the spray. Some of these results can be useful to compare projection techniques and equipment, for the development of nozzles, and to set free fall drop heights to better simulate manual applications and even allow more realistic molding procedures for mortar-substrate tensile bond tests.

Keywords: Mortars · Manual application · Spraying · Impact · Pressure mapping

1 Introduction

In Brazil, rendering mortars are traditionally applied manually, but mechanical projection procedures have been growing in civil industry due to technical and economic benefits. Since both types of application demand different rheological behaviors, a more thorough understanding is imperative to increase productivity, by avoiding rebound issues after the material is launched, and enhance mortar adhesion on the substrate, for high-quality finishing.

After collision, the immediate spreading of mortars on the base is related to impact energy against the surface. If the rheological behavior is not adequate to the imposed

V. Mechtcherine et al. (Eds.): RheoCon 2019/SCC 2019, RILEM Bookseries 23, pp. 191–199, 2020.
https://doi.org/10.1007/978-3-030-22566-7_23

energy, pathological problems may occur after hardening. For instance, adhesion in fresh state and bond strength after hardening between mortar and base can be observed due to voids created in the interface that reduces contact area [1]. Mortars deform at high rates at the moment of impact, which makes it difficult to simulate this phenomenon through rheological techniques commonly used to evaluate this family of materials, such as squeeze flow and rotational rheometry. Thus, some methods were developed to quantify kinetic energy in the impact, like the use of a free fall "drop box" to simulate material projection with known energy [1, 2], instrumentation of a target with accelerometers, to determine impact velocity [1], and sprayer speed assessment through image analysis [3]. Still, these techniques only evaluate the kinetic energy before the impact. So, it is important to develop a methodology to monitor the behavior of the mortar during impact.

Dynamic interfacial pressure mapping is an innovative technology, and has been employed in different industries and services, like automotive, medical and dental, for example. It allows for high-frequency real-time measurements, providing detailed and accurate data about the interfacial pressure distribution in a considerable area. A recent work have already employed this technology in parallel with squeeze flow tests to assess the pressure distribution in mortars [4], developing a method called pressure mapped squeeze flow (PMSF). In this context, the aim of this paper is to introduce initial developments towards an impact rheometry technique for cementitious materials based on pressure mapping.

2 Experimental

2.1 Mortars

This study evaluated 6 different types of mortars commonly employed in Brazilian construction, which main characteristics are presented in Table 1.

Table 1. Characteristics of studied mortars: product description; proportion of sand and fines in mass; volume of admixture; and volumetric content of air and water.

Mortar	cement : hyd.lime : sand ratio	Dry materials			Fresh mortars	
		Sand (%m)	**Fines** (%m)	**Admixture** (ml)	**Air** (%vol)	**Water** (%vol)
A	**1:1:6**	82.1	17.9	-	3.2	22.8
B	**1:1:6**	80.1	19.9	-	4.8	22.6
C	**1:0:6**	87.8	12.2	10	9.0	22.8
D	**1:0:6**	87.8	12.2	10	19.0	20.7
E	Factory produced rendering mortar for spray application				27.5	17.2
F	Factory produced masonry mortar				8.1	18.3

Fine fractions of mortars C and D were composed only by cement and the addition of different types of air entraining admixtures. In mortars A and B, aside from cement,

hydrated lime types CHIII and CHI are respectively used. Mortars E and F are factory produced commercial products.

2.2 Mortar Application

Two application methods were analyzed: manual and continuous spraying, as shown in Fig. 1. For both methods, it was asked for the operator to replicate the exact movement used for applying the mortars on a real situation. In all cases, the material was thrown over the sensor to fully cover the measurement area.

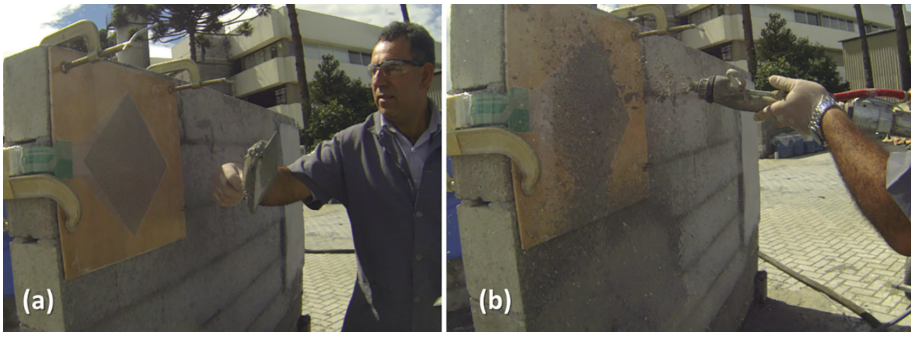

Fig. 1. Evaluated methods for mortar application: (a) manual; and (b) continuous spray.

2.3 Dynamic Pressure Mapping

For monitoring of the pressure distribution at impact of the mortars, the Flexiforce 5250 sensor (Tekscan) was used, with a maximum capacity of 69 kPa (Fig. 2a).

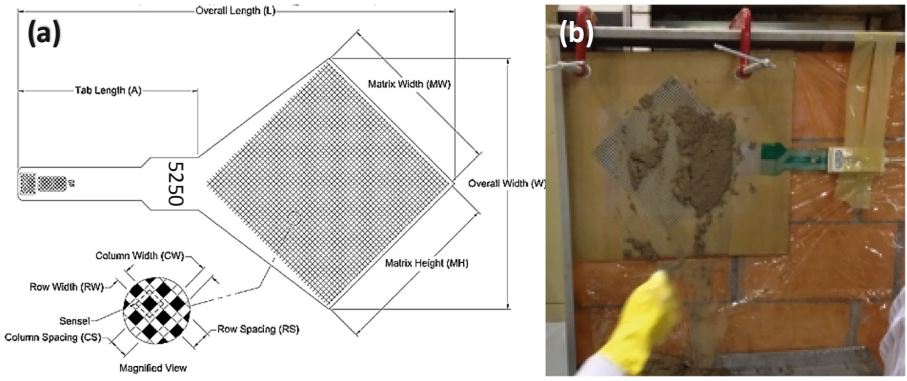

Fig. 2. (a) Illustration of the sensor and (b) wood-sensor assembly and the apparatus for acquiring data fixed on the masonry panel.

To analyze the moment of collision between mortar and surface, maximum sampling rate of the equipment was used (100 Hz), thus each frame of pressure distribution corresponds to an interval of 0.01 s. The sensor was glued onto a wooden board to facilitate its attachment to the masonry panel (Fig. 2b). In addition, the sensor was covered by a plastic film to protect it and facilitate cleaning after testing. The sensitivity was set to 35 (on a scale from 0 to 40) and sensor calibration was performed using squeeze flow tests of the mortars in the same sensitivity [4].

2.4 Free Fall Pneumatic Launcher

As a way of controlling the kinetic energy, a device to launch mortars by free fall was created, which allows adjustment of the variables involved, such as height, launch angle and gate opening velocity. The dynamic pressure mapping sensor is positioned over the base to assess the moment of impact, as illustrated in Fig. 3. After preliminary tests, the height of the container was set as 1 m and an amount between 0.9 kg and 1 kg of mortar was molded in a circular truncated cone, originally used for flow table sample preparation. A styrofoam shield was placed on the back of the container to ensure that the mortar hit the center of the sensor.

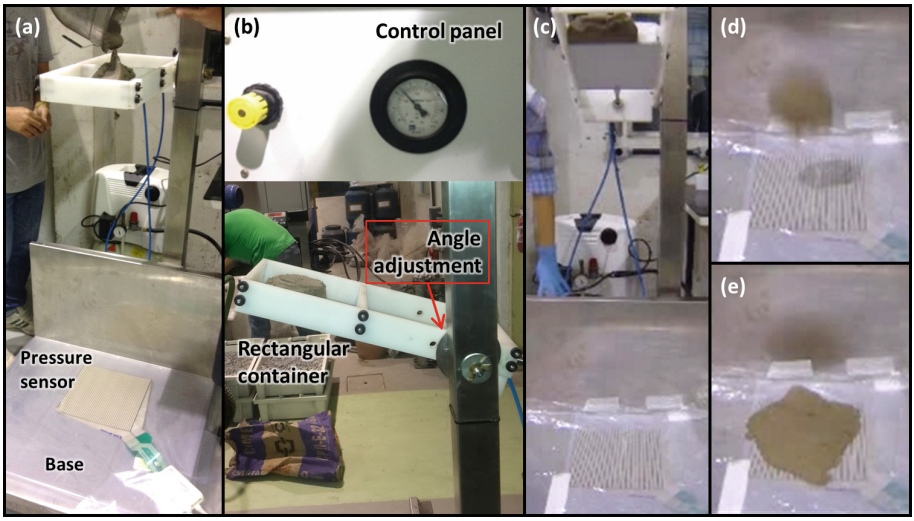

Fig. 3. Free fall pneumatic launcher developed: (a) wide base with a pressure sensor and a metal column with inserts to adjust heights; (b) detail of the control panel of the pneumatic device for opening and closing the retractable plate at adjustable speed, and rectangular container with angle adjustment; and example of a test with (c) the opening of the gate; (d) mortar falling towards the base; (e) sample over the sensor after impact.

3 Results and Discussion

3.1 Pressure Distribution of Mortars Applied Manually

As the event occurs over a short period of time, the pressure distributions resulting from the impact of mortar B over the sensor is shown in a sequence of three frames in Fig. 4. At the start of the impact (Fig. 4a), the central region shows high values, due to the concentrated mass hitting the sensor in one big portion. Subsequently (Fig. 4b, c), the material is spread, with increasing contact area and relatively lower pressure levels. The results presented are in raw units of the equipment.

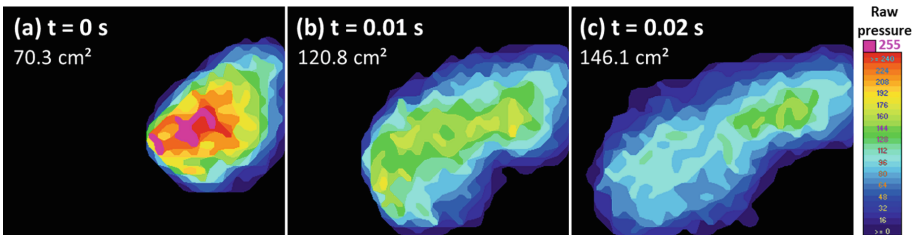

Fig. 4. Pressure (in raw units) evolution during impact of mortar B applied manually.

To compare different tests more directly, it is also possible to display the maximum pressure levels obtained in each part of the sensor. Figure 5 shows the results of the maximum pressure caused by 3 separate manual launches of mortars A, B, C and D on the surface instrumented with the sensor, also highlighting the air content of each mortar. In this figure the results are shown in engineering units (kPa) and the calibration procedure based on squeeze flow test can be found in [4].

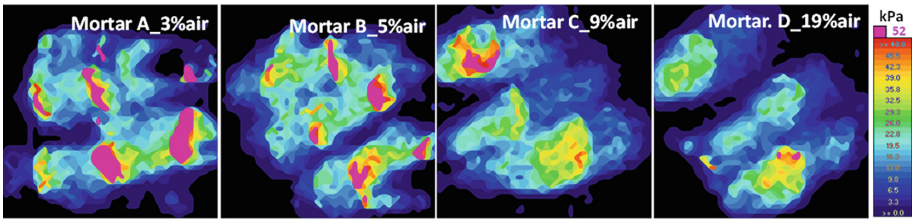

Fig. 5. Impact pressure (in kPa) peaks of mortar A, B, C and D caused by 3 consecutive manual application and air content of each mortar.

The impact points of the launched mortars display high pressure, and, in some cases, sensor saturation is reached (pink regions), representing values higher than 50 kPa. This occurs because a large quantity of material is thrown and kept together until the collision. The effect of mortar air content is also observed by the decrease of maximum pressure area with increasing air, especially when comparing extreme values

(3% and 19% of air content), with no region of sensor saturation being present for mortar D. The air is deformable, so it absorbs the impact and reduces the pressure during collision.

3.2 Comparison Between Manual and Spray Application

To compare application methods, mortar E was applied by both techniques, manual and spray. The results illustrate the maximum pressures attained during manual application (Fig. 6a), continuous spray (Fig. 6b), and leveling after spray (Fig. 6c).

The impact pressure levels are much higher for manual application (Fig. 6a), with most of the contact area subjected to pressures above 20 kPa. The behavior is similar to that seen in Sect. 3.1, caused by the large amount of mortar at the impact. On the other hand, smaller impact pressures are obtained for continuous spray (mainly <5 kPa).

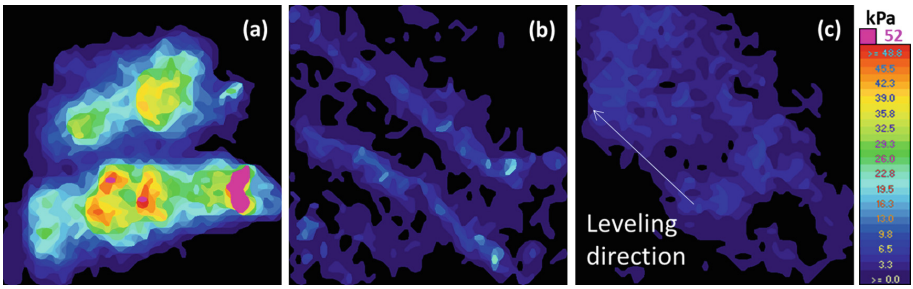

Fig. 6. Impact pressure peaks during application procedures with mortar E. (a) manual application; (b) continuous spray; and (c) leveling with a ruler right after spray application.

The spraying process separates the fresh mortar into small portions, which are projected by the pressurized air, resulting in more uniform impact pressure. This may be the reason why this type of application provides better coatings, with better filling and less rebound also with a better substrate-mortar bond strength after hardening. With manual application, on the other hand, the higher impact energy ends up generating an elastic response that hinders the initial adhesion of the mortar to the substrate with the appearance of interfacial defects [1, 3].

After the continuous spray application of mortar on the surface, the leveling process, in which material is tightened with a ruler to regularize and adjust thickness, was also evaluated (Fig. 6c). This stage enhances the contact between the mortar and the substrate. It is found that, even though it does not reach high levels, the pressure throughout the applied area is uniform and tends to decrease defects at the interface, improving contact and adherence. The possibility of measuring these different steps enables the comparison of materials, tools, methods and practices, consequently providing improvement opportunities for each processing stage related to the application of mortars.

3.3 Evaluation of the Impact of Mortar by Free Fall Pneumatic Launcher

Mortars E and F were analyzed using the free fall launcher. Results are shown in Fig. 7, and for each mortar two sets of figures are illustrated: on top, free fall sequence of the mortar from the release moment to right after the impact; beneath, pressure distribution of the first 4 frames of the impact. Air content of each mortar is also presented, as well as the activation area of the sensor and the total load at each moment. Results were calibrated using a squeeze flow test performed on one of the mortars. The saturation values are underestimated and therefore the total load values provide a notion of the order of magnitude of pressure and charge involved but are not totally accurate. A proper calibration form for impact testing has yet to be developed.

By the images, it is observed that mortar F presented more pronounced growth area rate than mortar E, probably because of its lower air content. The maximum loads for each mortar were different: 500 N (mortar F) and 372 N (mortar E). This probably depends on how the material collides with the surface and impact energy. Since the

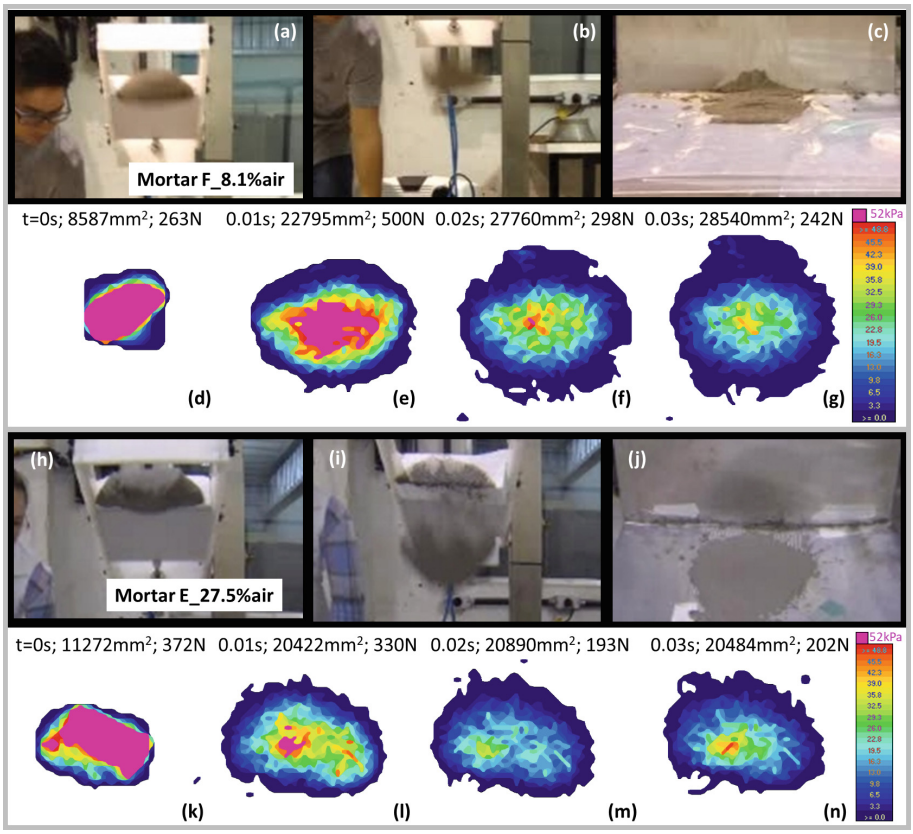

Fig. 7. Results for mortars F (a–g) and E (h–n): (a–c) and (h–j) free fall sequence images from the release to impact; (d–g) and (k–n) sequence of pressure distribution after the impact on the surface on the first 0.04 s.

volume of the material is the same, the energy is related to the mass of the material and, consequently, to the air content (which affects density) of each one. As observed previously, the air content contributes with energy dissipation, thus the higher the air content in the mortar, the lower is the pressure and impact energy.

Images (d) and (k) present overloaded areas of the sensor due to pressure range limits, thus the calculated force (in N) values are underestimated. Comparing these results with manual application, it is verified that pressure concentration is more intense in this test because not only the mass is larger, but also the angle of impact is more orthogonal to the hit plane. For the manual application, even though mass was also kept together when launched, the mortar was thrown with a certain angle (simulating practical condition) inducing further spread on impact, thus only the initial part of the mortar hit the substrate with more energy.

4 Conclusion

Dynamic pressure mapping system presents great technological potential to be used in the monitoring of processes with a high deformation rate, such as the impact of mortars either by manual or spray application processes. Results show that the sensor was able to differentiate application systems, allowing high-rate data acquisition. However, there is a very large variation in pressure distribution levels, depending on the type of mortar and application method. Manual application resulted in pressure levels roughly 10 times higher than those caused by spray application, which led to more homogeneous distributions due to a scattering effect, that generates smaller portions of mortar during launching.

Since the pressures for spray application are very low, higher sensor sensitivity may be advised for these cases. In addition, a sensor with a relatively small area for this kind of process was used and the sprayed mortar filled it out very quickly; a larger area to increase sampling and continuity of the process could be interesting. Additionally, an equipment was developed to standardize the process through free fall launching, allowing control over some variables (height; angle; etc.).

This methodology has potential to be developed towards an impact rheometry technique for both technological and scientific purposes, however some limitations still must be addressed. Higher data acquisition frequency than used in this work must be used to allow assessment of detailed information regarding very short-period phenomena that take place during impact. The other main challenge is the determination of strain rate and rheological parameters with an irregular and variable shaped elasto-viscoplastic material as the mortars analyzed.

5 Acknowledgments

The authors thank the support from the Brazilian research funding agencies FAPESP (project 2012/18952-5) and CNPq, also ABAI (Brazilian Association of Mortar Industries), CONSITRA (Brazilian consortium for the development of mortar technology) and Votorantim Cimentos.

References

1. do Antunes RPN (2005) Influence of rheology and impact energy on the bond strength of mortar coatings. Doctoral Thesis, University of São Paulo (in Portuguese)
2. Carasek H (1996) Adherence of Portland cement based mortars to porous substrates - evaluation of intervening factors and contribution to the study of the bonding mechanism. Doctoral Thesis, University of São Paulo (in Portuguese)
3. Fernandes HC (2007) Estimation of projection energy of mortars sprayed by compressed air. Masters Dissertation, University of São Paulo (in Portuguese)
4. Grandes FA, Sakano VK, Rego ACA, Cardoso FA, Pileggi RG (2018) Squeeze flow coupled with dynamic pressure mapping for the rheological evaluation of cement-based mortars. Cem Concr Compos 92:18–35

Evaluation of Fresh Adhesive Mortars Through Various Rheological and Imaging Techniques

Alessandra L. Fujii-Yamagata[1(✉)], Fábio A. Cardoso[2], Anne Daubresse[3], Evelyne Prat[3], and Mohend Chaouche[1]

[1] Laboratoire de Mécanique et Technologie, École Normale Supérieure Paris-Saclay, Cachan, France
alessandra@fujii-yamagata.com
[2] Department of Construction Engineering, Escola Politécnica, University of São Paulo, São Paulo, Brazil
[3] Centre d'Innovation Parexgroup, St Quentin Fallavier, France

Abstract. Adhesive mortars are meant to glue tiles and during application they are applied with a toothed comb to ensure that the proper amount of material is distributed over the substrate, also to ease the later tile placement. Throughout the application, different types of strains and stresses are imposed to adhesive mortars, and one method is not enough to fully characterize their behavior. Thus, in this investigation various techniques were used to evaluate the mortar's fresh properties. Bulk and interfacial oscillatory rheology combined with MRI characterizations were used to understand the rheological properties evolution and skin formation over time simulating the waiting period until the tile is emplaced. Squeeze flow measurements at different waiting times were used to indicate mortars behavior during tile placement and were complemented with small depth-of-field optical microscopy technique to obtain the visualization of the contact between mortar and tiles. The experimental variable studied was the content of cellulose ether – widely used admixture in adhesive formulations as viscosity and water retaining enhancer – and the applied methodology was able to assess the effects of the admixture by covering a wide range of the required fresh properties of adhesive mortars.

Keywords: Adhesive mortar · Skin · Interfacial rheology · MRI · Optical microscopy

1 Introduction

Adhesive mortars are construction materials meant to glue tiles. During their application, different strains and stresses are imposed requiring from the mortars different fresh state properties to obtain good performance. The mortar needs to have easiness of application and attach to the substrate, form clear strips, be easily squeezed when the tile is placed and maintain it adhered to the wall during hardened state. With different requirements, only a single method is not enough to characterize the important rheological properties of adhesive mortars.

V. Mechtcherine et al. (Eds.): RheoCon 2019/SCC 2019, RILEM Bookseries 23, pp. 200–208, 2020.
https://doi.org/10.1007/978-3-030-22566-7_24

Not only the rheological properties of the mortar evolve over time, but the interface will have a particularly important role, since this thin layer may control the contact, and consequently the adhesion. To understand this role, mortar's bulk and interfacial properties on adhesion were assessed by different techniques. Firstly, to characterize the properties of the material over time, time sweep of small amplitude oscillatory measurements and squeeze flow at different waiting times were performed. Then, to characterize the mortar's interfacial properties, MRI was used to obtain the free water distribution over time and interfacial rheology technique was used to measure the interface's rheological properties. Finally, to verify how these properties affected contact generation between the mortar and tile, small depth-of-field optical microscopy technique was used. Due to cellulose ether influence on rheological properties of the bulk and interface, the impact of this admixture was the main variable evaluated in this study.

2 Materials and Formulations

This work employed basic compositions of adhesive mortars with cement CEM I 52,5 N CE CP2 NF from Lafarge, normalized sand PE2LS from FULCHIRON, Redispersible Polymer Powder from Momentive and an organic modifier (CE: hydroxyethyl methyl cellulose) from Dow Chemicals. The formulations used in this study are shown in Table 1.

Table 1. Formulations of adhesive mortars with different cellulose ether content (wt%).

Formulations	CEM I	Sand	Latex	CE	Water/powder	Entrained air
0.1 % CE	30 %	67.40 %	2.5 %	0.1 %	0.34	13 %
0.25 % CE	30 %	67.25 %	2.5 %	0.25 %		20 %
0.4 % CE	30 %	67.10 %	2.5 %	0.4 %		22 %

3 Methods

3.1 Magnetic Resonance Imaging (MRI)

MRI was used to obtain the free water distribution through the depth of an uncovered adhesive mortar fresh sample. The equipment used was an Ascend 400 WB from *Bruker* with a static magnetic field of 9.4 T. To obtain the 1D distribution, the mortar was put in a glass cylindrical holder of 8 mm diameter and 4 mm height with the top uncovered to allow water evaporation. The signal obtained was from a horizontal cut through all the sample depth. Data acquisition was done every five minutes for two hours. The room temperature was kept at 23 °C ± 1 °C and 30% RU.

3.2 Bulk and Interfacial Oscillatory Rheometry

A rheometer (MCR301 from Anton Paar) was used to perform the measurements with a vane geometry. The rotational strain amplitude was defined as 0.05%, at the linear viscoelastic region in strain sweep tests. The mortars were prepared according to the mixing procedure described by European standard EN-196-1. After mixing, the mortar was put in the rheometer cup, the excess material was removed with the use of a spatula and the cup was put in the machine for the test. The environmental conditions of the room were kept at 23 °C ± 1 °C and 50% RU; the rheometer temperature was kept at 23 °C ± 1 °C. All tests were repeated 2 or 3 times. The bulk oscillatory measurements were performed with the Vane measuring probe fully immersed in the rheometer cup.

The interfacial results are based on Gibb's definition of "excess property" [1]. The evolution of interfacial properties was obtained through two measurements: one in which the vane geometry is partially immersed (3 mm) including the interface and another with the geometry fully immersed in the bulk [2]. The excess property is obtained by the difference between the measurement at 3 mm and at the bulk.

For the measurements at 3 mm, the same test parameters of the bulk measurements were used, but with probe partially immersed. The 3 mm depth was chosen to be smallest as possible to minimize bulk effects, but large enough compared to grain size, about 6 times. The bulk properties subtraction allows a closer approach to the real interfacial properties. In this investigation, low amplitude storage modulus (G') was defined as [2]:

$$G_{interface} = G_{3mm} - G_{bulk} \tag{1}$$

The sample preparation and test conditions were the same for both bulk and interfacial measurements.

3.3 Squeeze Flow

Squeeze flow measurements were performed with an MCR 301 rheometer from Anton Paar with a cross hatched geometry with a diameter of 50 mm and a cup of 52 mm. Each adhesive mortar formulation was mixed in a planetary mix according to EN-196-1. The mortar samples were applied with the help of an aluminum tool in a cylindrical shape of 6 mm height and 40 mm diameter. The samples were put to rest for different waiting time, simulating mortars of different open time: 0 and 20 min. After this time, the sample was put in the rheometer for the squeeze test, where it was compressed at an imposed velocity of 1 mm/s for 3 mm. The test set up is illustrated in Fig. 1a and the typical load in Fig. 1b.

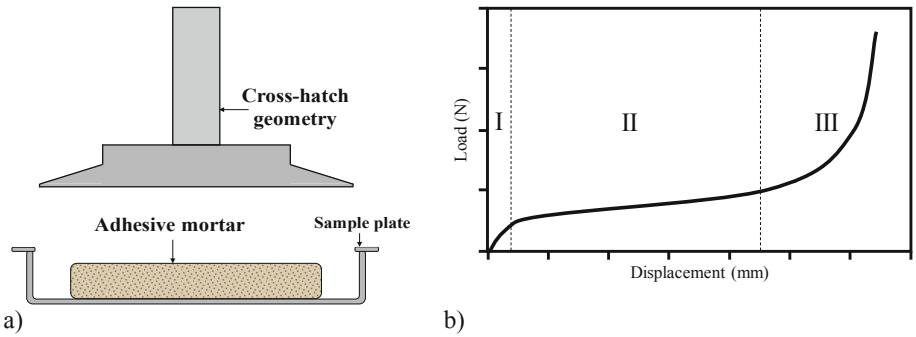

Fig. 1. (a) Scheme of squeeze flow montage – the geometry press (b) Typical load vs. displacement curve of a displacement-controlled squeeze flow test, illustrating the material's behavior. *Adapted from* [3].

3.4 Small Depth-of-Field Optical Microscopy

Small depth-of-field optical microscopy was used in order to obtain the contact generated between the tile and the mortars. This new technique focalizes in the region of the contact with a small depth-of-field microscope and observe the wetted and unwetted regions. The mortars were applied to prexiglass substrate of 5 cm × 5 cm with a toothed trowel, after different open times, another prexiglass was applied and compressed with a weigh of 2 kg for 30 s. Then, the samples were placed in a Digital Microscope Keyence VHX with VH-Z100R lens where the contact was observed.

4 Results

4.1 MRI

Figure 2a shows the MRI results for the formulation with lower CE content, 0.1% CE-A, where the moisture distribution through the depth is fairly homogeneous. In comparison to other samples, the signal intensity along the whole sample reduces considerably during the first 2 h. This indicates that the mortar loses water from the surface by evaporation, but the moisture inside is able to move and re-homogenize.

The result of the 0.25% CE formulation is shown in Fig. 2b. A low signal layer linearly grows toward the inner part of the sample as a function of elapsed time and the dark blue area indicates a dry layer. The material that is located below this dryer zone has a more intense signal, showing that underneath the mortar keeps its moisture content. This result is different from 0.1% CE, where the material does not form these two zones of dry and moisturized mortar, staying homogeneous from the top to the bottom of the sample with higher mitigation of the water signal measured on the bottom of the sample for longer times. The nature of CE explains these results, as it forms an aqueous phase with higher viscosity that reduces water mobility [4, 5],

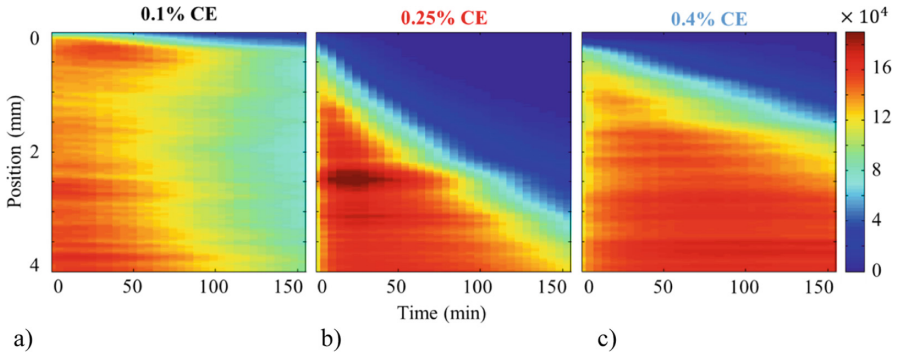

Fig. 2. MRI 1D 1st echo map signal vs time for a sample of cylindrical mortar samples exposed to air on the top: (a) 0.1% CE, (b) 0.25% CE and (c) 0.4% CE. (Color figure online)

consequently inhibiting water flow towards the mortars surface. This means that as the mortar with higher CE content started to lose water from the surface, a layer of dryer material formed; this drying layer grew down the surface, but the material below this layer retained its moisture.

4.2 Bulk and Interfacial Rheology

In Fig. 3a, G′ evolution over time of formulations with different CE content are shown. In the graph, equal colors represent a repetition. In the first minutes, the formulation with 0.25% CE is the lowest, then 0.4% CE in the middle, and 0.1% CE the highest. The reduction of initial G′ values of 0.1% to 0.25% is related to entraining effect of CE, from 13% to 20%. For 0.4% however, air entrainment seems to have almost saturated and entrained air obtained was 22%. The air entrainment effect is diminished at higher concentrations, the polymer thickening effect starts to influence, and G′ becomes higher for higher CE-A content.

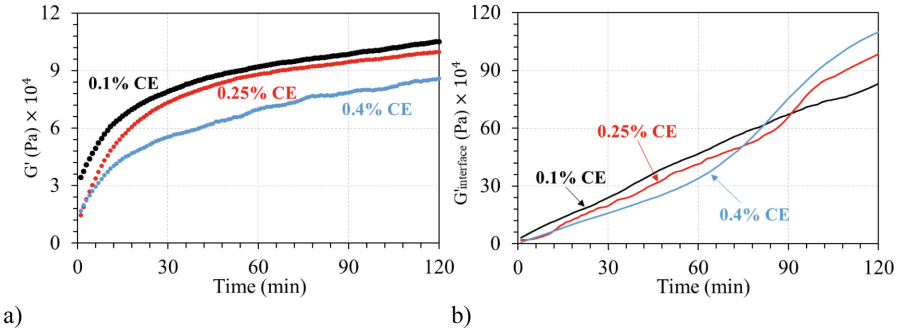

Fig. 3. (a) Bulk storage modulus evolution over time for the formulations with different CE content and (b) Interfacial storage modulus evolution over time for the formulations with difference CE content.

After around 8–10 min, an inversion of G′ values occur. The formulation with higher CE content, 0.4% CE-A, became lower than 0.25% CE-A, and maintained lower values during the 2 h of the test. This low value is probably related to the CE's ability to delay structuring of cement particles [8]. Weyer et al. [7] showed that the adsorption of the polymers onto the cement clinker phases inhibits the formation of Ca(OH)2. This is related to CE's strong influence on C-S-H precipitation, leading to a decrease in the amount of initial C-S-H nuclei, delaying the formation of a continuous C-S-H shell around the C3S grain, and delaying the formation of a thicker and more permeable C-S-H layer.

When CE is added to a cementitious matrix, a gradual reduction of C3A dissolution rate is observed; this is also associated with AFt and hydroxy-AFm precipitation [7, 8]. Often the increase of viscosity generated by CE is associated with hydration retardation, however, Pourchez et al. [9] results have shown that the assumption of a diffusion barrier induced by the high viscous solution of cellulose ethers is not relevant.

In Fig. 3b, interfacial storage loss evolution over time is shown for the formulations with different CE content. In the graph, it is possible to observe how initially, in the first 60 min, as CE content is increased, the evolution rate of G′ interface is reduced. Then, at around 75 min for 0.25% CE and 60 min for 0.4% CE, an inflection occurs and the higher the CE content, the higher the G′ interface achieves. These results show the transition from a water/solids dominance to polymer properties dominance [2].

4.3 Squeeze Flow Behavior

Squeeze flow curves of the adhesive mortars formulations at different waiting times are shown in Fig. 4a and b. Most of the curves present a similar behavior to typical squeeze flow curve shown in Fig. 1b, some curves only achieve the first – elastic deformation – and second stage – plastic deformation or viscous flow – without the strain hardening stage. With an open time of 0 min, the curves present a tendency of higher CE content, higher normal forces achieved. This result agrees with the thickening effect of CE.

At a waiting time of 20 min, however, the formulation 0.1% CE, which contains the smallest CE content, present higher normal force at the end of the test than 0.25% CE. Thus, g_0.1% CE-A consolidation seems to be evolving at a higher rate than the other samples.

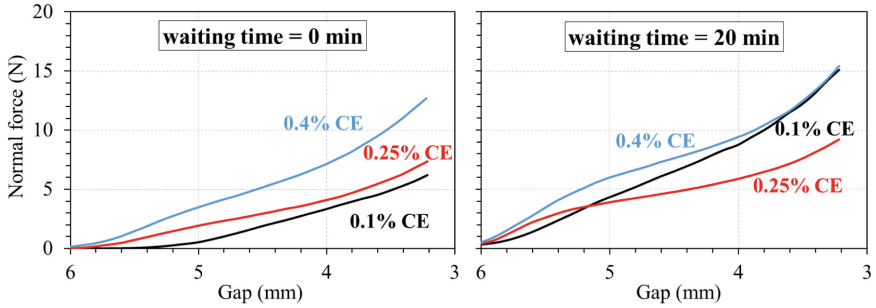

Fig. 4. Squeeze flow curves of the mortars with different CE content for a waiting time of 0 min (a) and 20 min (b).

These results can be related to the structure building delay that was observed in bulk properties evaluation, as CE content is increased, the storage modulus of the formulations is reduced. Also, as observed in MRI results, the fresh material that is observed under the dryer layer of the formulations with higher CE content can also lead to easier squeeze, since this fresh layer could more easily flow during the compression.

In the formulation 0.1% CE, the material's behavior can be related to phase segregation, since with lower CE content, the mortar tends to have easier liquid phase movement and intensified particle friction, where the paste migrates to the outer part of the sample, leaving a drier material in the middle of the sample. Higher CE content increases the paste viscosity and reduces the impact of this effect [6].

The 0.4% CE formulation, with even higher CE content, also presented the linear formation of the dry layer material evolving with time toward the inner layers of the sample, similarly to 0.25% CE-A. However, the growing rate was less than the other sample and after 2 h the dry layer was only 1.5 mm thick, which is smaller than the 3 mm seen for 0.25% CE. The slower growing rate and final thickness of the dry zone may be related to the higher CE content (0.4%), which intensifies polymer film formation that creates a barrier to water evaporation. This result reinforces CE's water retention ability, and by its increase, less water is lost from the mortars.

4.4 Contact Generation

In Fig. 5, contact visualization of mortar after 5 min and 20 min waiting is shown for the formulations with different CE content at the rib and between ribs. From the Fig. 5a, it is possible to observe that at the region of the rib, in the formulation with 0.25% CE have spots of non-contact due to the skin formation, and for 0.4% there is even a more spots of non-contact. For both formulations, there is very good contact at the region between the ribs. For 0.1% CE, there is an even distribution of smalls dots of non-contact in both at the rib and between ribs and the contact is very homogenous.

For a waiting time of 20 min, the contact is poor for the formulation with 0.1% CE and the ribs were poorly squeezed, resulting in no material between the ribs. With an increase of CE content to 0.25%, the contact in both region at the rib and between ribs are better. In the region between ribs, it is possible to verify a line of entrapped air between the ribs. With even higher CE content of 0.4% CE, due to skin formation, the contact at the ribs is poor with very small areas of wet tile, however, at the region between the ribs, the mortar was able to tile the material very well. These results show that as CE content is increased, a skin is formed with fresh material underneath that is released during squeeze, generating good contact between the ribs.

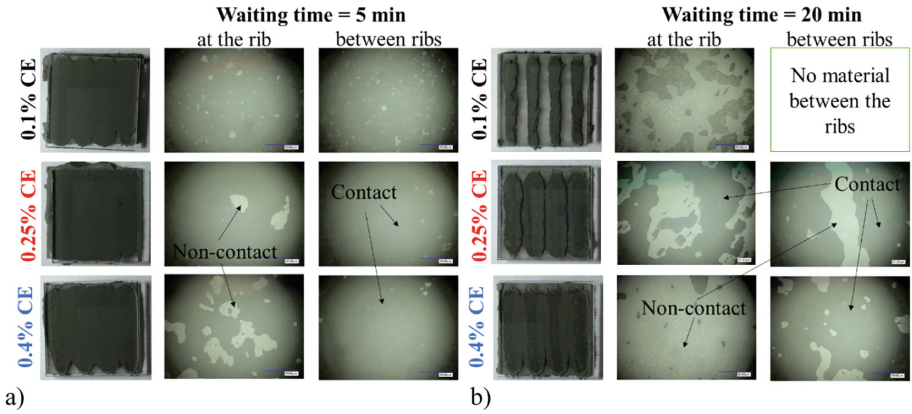

Fig. 5. Contact visualization between mortar and prexiglass tile for the different CE content formulation at the rib and between ribs regions after different waiting times: (a) 5 min and (b) 20 min.

5 Summary and Conclusion

The present study aimed to understand the relationship between rheological and adhesive properties as a function of CE content. Bulk oscillatory measurements and squeeze flow were used to evaluate the properties of the material over time. Squeeze flow results indicated a faster evolution of the formulation with lower CE content as its samples needed higher stresses to be compressed for longer waiting time. Then, interfacial rheology and MRI measurements were performed to characterize the skin and measure the mortar's formulation rheological properties. The results indicated the formation of a dryer layer for the formulation with 0.25% and 0.4% CE, and a higher interfacial storage modulus values the higher the CE content. Finally, small depth-of-field optical microscopy technique assessed the contact generated between the mortar and a tile for the different waiting times indicating that, despite the dryer layer (skin), as CE content was increased, when squeezed, fresh material was released and generated good contact in between the ribs zone. Through different techniques, it was possible to observe the change of evolution and behavior of the mortars which influenced the mortar-substrate contact generation.

Acknowledgement. The authors acknowledge ParexGroup for financing this project. CNPq – Brazil for F.A. Cardoso's post-doc grant. Vincent Sarou-Kanian for MRI experiments.

References

1. Gibb JW (1928) The collected works. Green & Co., Longmans
2. Fujii-Yamagata A, Cardoso FA, Daubresse A, Prat E, Chaouche M (2019) Skin formation in adhesive mortars evaluated by MRI and interfacial rheology. Cem Concr Compos 99:251–261
3. Cardoso FA, John VM, Pileggi RG (2009) Rheological behavior of mortars under different squeezing rates. Cem Concr Res 39:748–753
4. Khayat KH (1998) Viscosity-enhancing admixtures for cement-based materials—an overview. Cem Concr Compos 20:171–188
5. Patural L, Govin A, Grosseau P, Ruot B, Devès O (2009) The effect of cellulose ethers on water retention in freshly-mixed mortars. In: 11th 2009 International conference and exhibition European ceramic society pp 85–87
6. Cardoso FA, Fujii AL, Pileggi RG, Chaouche M (2015) Parallel-plate rotational rheometry of cement paste: Influence of the squeeze velocity during gap positioning. Cem Concr Res 75:66–74
7. Weyer HJ, Müller I, Schmitt B, Bosbach D, Putnis A (2005) Time-resolved monitoring of cement hydration: influence of cellulose ethers on hydration kinetics. Nucl Instrum Methods Phys Res Sect B Beam Interact Mater Atoms 238:102–106. https://doi.org/10.1016/j.nimb.2005.06.026
8. Agrawal AM, Manek RV, Kolling WM, Neau SH (2004) Water distribution studies within microcrystalline cellulose and chitosan using differential scanning calorimetry and dynamic vapor sorption analysis. J Pharm Sci 93:1766–1779. https://doi.org/10.1002/jps.20085
9. Pourchez J, Grosseau P, Ruot B (2010) Changes in C3S hydration in the presence of cellulose ethers. Cem Concr Res 40:179–188. https://doi.org/10.1016/j.cemconres.2009.10.008

Evaluation of Structural Build-Up Rate of Cementitious Materials by Means of Constant Shear Rate Test: Parameter Study

Irina Ivanova(✉) and Viktor Mechtcherine

Institute of Construction Materials,
Technische Universität Dresden, Dresden, Germany
irina.ivanova@tu-dresden.de

Abstract. Accurate characterisation of static yield stress evolution with time enables correct evaluation of the structural build-up rate for cement-based materials. This parameter is fundamentally important for many construction processes, including conventional in-situ concrete construction, various digital fabrication techniques, well cementing, etc. The paper at hand presents a parameter study on determination of structural build-up by means of constant shear rate test. It is shown, how the choice of single or multiple samples as well as different constant shear rates and pre-shear regimes influences the apparent time-dependent static yield stress evolution of cementitious materials and, hence, the accuracy of structural build-up rate evaluation. Respective recommendations for decreasing error in measurements of static yield stress are provided.

Keywords: Rheology · Cementitious materials · Structural build-up · Static yield stress

1 Introduction

One of the most widely used techniques for the static yield stress (SYS) measurements is constant shear rate (CSR) test, in which a low constant value of shear rate is applied to a material until the moment, when shear stress reaches its peak or plateau value. This peak or plateau value is attributive to the flow onset and is considered as SYS of material at its particular age. A number of such measurements can be performed while the structure of material builds up. Eventually, the obtained SYS values are plotted versus the age of material, and this characteristic curve is used to calculate structural build-up rate [1–5].

Despite the fact that CSR test has been used for years by many researchers, the reasons behind the selection of particular parameters of the applied procedures are rarely discussed.

The aim of this research was to analyse and quantify the differences in structural build-up rate, induced by the following parameters of the testing protocol: single-batch or multiple-batch approach, different constant shear rates, various pre-shear regimes.

V. Mechtcherine et al. (Eds.): RheoCon 2019/SCC 2019, RILEM Bookseries 23, pp. 209–218, 2020.
https://doi.org/10.1007/978-3-030-22566-7_25

2 Materials and Methods

Portland cement CEM I 42.5 R produced by HeidelbergCement AG and sand 0–2 mm produced by Ottendorf-Okrilla GmbH & Co.KG were used in this study. Sand 0–2 mm was dried to constant mass and sieved in laboratory conditions in order to obtain narrow fractions of 0.5–1 mm and 1–2 mm. Narrow fractions were used to ensure uniform particle size distribution of aggregate in the tested mortars.

For performing rheological measurements, cement paste with water-to-binder ratio (w/b) of 0.4 (later referred to as "paste") and cementitious mortar with the same w/b and 30% vol. of sand (later referred to as "mortar") were prepared. Mixture compositions, their average workability (estimated by means of Haegermann flow table test) and Bingham parameters are given in Table 1.

Table 1. Compositions of the materials under investigation.

Parameter	Value	
	For paste	For mortar
Characteristics of mixture		
w/b	0.4	0.4
Aggregate amount [% vol.]	–	30
Dosage of component [kg] per 1 L of mixture		
CEM I 42.5 R	1.384	0.969
Sand 0.5–1 mm	–	0.398
Sand 1–2 mm	–	0.398
Water	0.554	0.388
Workability and Bingham parameters		
Spread [mm] (no strokes/after 15 strokes)	160/235	140/225
Plastic viscosity [Pa · s]	3.9	4.6
Yield stress [Pa]	60	120

Mixing and testing of samples were conducted according to the procedure presented in Table 2. For each experiment 1 L batch of material was prepared using laboratory mixer conforming to EN 196-1.

HAAKE MARS II Rheometer with building material cell and a temperature control module were used to perform rheological measurements [5].

Pre-shear in the main experiments was conducted as follows: 15 rotational steps from 0.1 to 10 s^{-1} in 30 s, rotation at 10 s^{-1} for 10 s, 15 rotational steps from 10 to 0.1 s^{-1} in 30 s. Before proceeding with SYS measurements, it was ensured that there is no significant deviations in Bingham parameters of the samples of the same material. Coefficient of variation (CoV) of Bingham parameters did not exceed 5% for paste and 7% for mortar. SYS measurements were conducted by means of constant shear rate test at the age of 20, 40, 60, 80 and 100 min for paste and at the age of 20, 40, 60 and 80 min for mortar (SYS at 100 min could not be measured due to the torque limitation of the rheometer). The temperature of all samples was maintained at 20 °C.

Table 2. Testing procedure.

Step	Time [h:min:s]	Rotational velocity of mixer	Action
1	−00:01:00	1	Homogenizing dry component (s)
2	00:00:00	0	Adding water to dry component (s)
3	00:00:15	1	Mixing
4	00:01:00	0	Stopping the mixer, scrapping the material adhering to the wall and bottom part of the bowl, placing it back to the centre of the bowl
5	00:02:30	2	Mixing
6	00:03:30	0	Repeating Step 4
7	00:04:00	2	mixing
8	00:06:00	–	Flow test on the Haegermann flow table in accordance with EN 1015-4
9	00:09:00	–	Filling rheometer cell
10	00:10:00	–	Pre-shear and determination of Bingham parameters
11	00:11:00	–	Resting time
12	00:20:00–01:40:00	–	SYS measurements

Calculation of structural build-up rate A_{thix} was conducted using Perrot's model [6], since it ensured more precise fit for a number of the obtained results in comparison to Roussel's model [7], and therefore increased accuracy of the parameter study.

3 Comparison Between Single-batch and Multi-batch Approaches

In the majority of studies on the SYS evolution of cementitious materials, single-batch approach has been used to perform one series of measurements. It means that a single sample is prepared and then tested at its various ages in order to obtain values of SYS plotted versus the age of material. Rotor is installed into the sample after its preparation and stays inside during the whole testing period. The choice of this approach is driven by its practicability (using single sample ensures fast achievement of the results), however, it implies the risk of getting inaccurate values of SYS due to multiple disturbance of the material.

In multi-batch approach, a new sample is prepared for every investigated age, then the rotor is installed in material and kept inside until performing a single SYS measurement. Consequently, each test is conducted at entirely undisturbed sample, which presumably shall provide more accurate values of SYS.

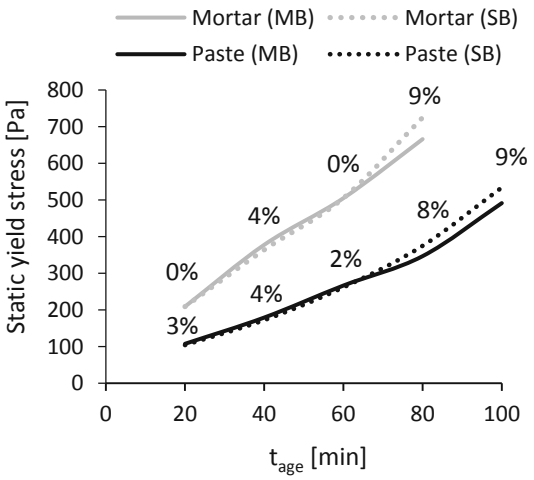

Fig. 1. Comparison of single- and multi-batch approaches for determination of structural build-up rate of paste and mortar.

Yet, this approach is notably more time-consuming and may implement another error due to possible deviations in the quality of separately prepared batches of the same material.

In the present research, structural build-up rates obtained with single-batch and multi-batch approaches were compared for paste and mortar. When using single batch, attention was paid that the measurement is stopped immediately after obtaining a peak value of shear stress in order to prevent excessive disturbance of the sample. All tests were conducted at the applied shear rate of 0.15 s^{-1}. The results are presented in Fig. 1 and Table 3.

Table 3. Structural build-up rate determined with single- and multi-batch approaches.

Tested material	A_{thix} [Pa/min]		Difference
	Single-batch	Multi-batch	
Paste	2.6	2.4	8%
Mortar	5.6	5.8	4%

It was found that percentage difference between the individual values of SYS obtained with both approaches did not exceed 9% for both paste and mortar. The difference between the values of structural build-up rate was equal to 8% for paste and 4% for mortar. For rheological measurements such differences can be considered insignificant, so it can be concluded that the single-batch approach enables correct evaluation of structural build-up rate by means of CSR test and is therefore more preferable due to its high time efficiency.

4 Effect of Applied Constant Shear Rate

In SYS measurements it is important to ensure that the test is performed at the lowest possible CSR in order to simulate static conditions. At the same time, attention shall be paid that, firstly, the selected CSR is achievable for a particular material at all ages of interest and, secondly, that this CSR can be reached in relatively short time, since otherwise the resulting SYS cannot be attributed to the age, at which the test started [5].

In order to study the effect of the applied CSR on structural build-up rate and test duration (time from the start of the test to obtaining the peak value of shear stress), CSR was varied as follows: 0.05, 0.10, 0.15, and 0.20 s^{-1}. These values are higher in comparison with the ones usually reported by the other researcher due to the different rotor geometry of HAAKE Mars II Rheometer. All tests were performed using single-batch approach. The obtained results are shown in Figs. 2 and 3 and in Table 4.

Table 4. Structural build-up rate determined with various constant shear rates.

Tested material	A_{thix} [Pa/min] at applied shear rates					CoV
	0.05 s^{-1}	0.10 s^{-1}	0.15 s^{-1}	0.20 s^{-1}	Average	
Paste	3.0	2.7	2.7	3.5	3.0	13%
Mortar	6.0	6.0	5.6	4.6	5.6	12%

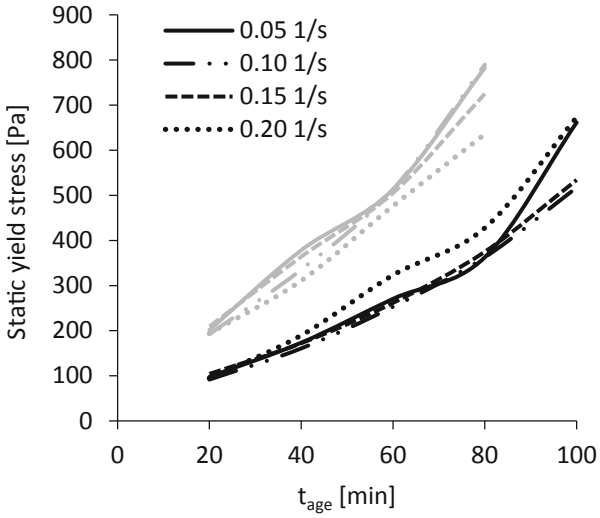

Fig. 2. Effect of the applied constant shear rate on structural build-up rate of paste (in black) and mortar (in grey).

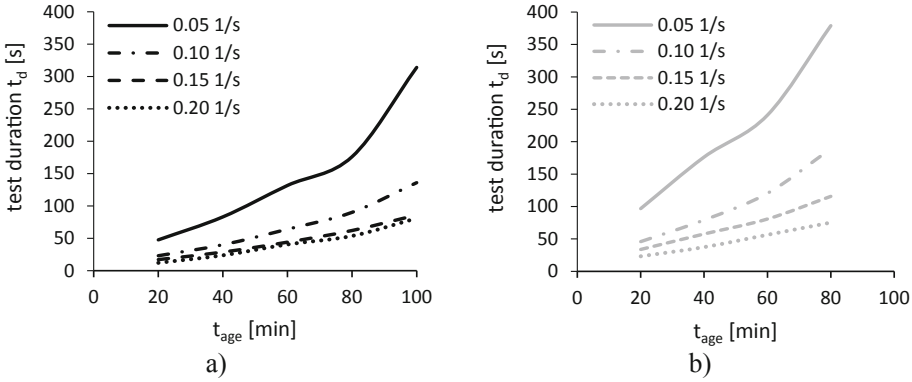

Fig. 3. Effect of applied constant shear rate on test duration for (a) paste and (b) mortar.

The key findings are provided below:

- CoV for individual values of SYS determined at identical age of sample varied in the range of 6–14% for the paste and in the range of 3–10% for the mortar. These variations did not follow any particular pattern, i.e. no correlation between the changes in applied CSR and obtained SYS values was found.
- CoV of structural build-up rate was equal to 13% for the paste and to 12% for mortar.
- Test duration prominently depends on the applied CSR, i.e. a lower applied CSR leads to a longer test duration, since more time is required to break the resistance of material to exerted load. Test duration also increases with the age of sample.

It can be concluded that the selection of the applied CSR shall mainly be based on the preferable test duration, while the test duration might be established depending on the hydration rate of the tested material. E.g. for rapid hardening cements, cements with accelerating additives or for binders containing calcium aluminate cements, test duration shall be shorter in comparison to ordinary or retarded systems, so that the obtained SYS value correctly represents the state of the tested material at each age.

5 Effect of Pre-shear

Pre-shearing a sample of a cementitious material prior to SYS test is a standard protocol used by researchers [1, 3, 6, 8]. However, in some cases this step may seem to be unnecessary, especially when the structural build-up rate shall be measured under conditions close to reality, in which no purposeful shearing of material usually occurs after its placement.

In order to analyse the effect of pre-shearing on the measured structural build-up rate, the following regimes were applied: no pre-shear; pre-shear at the age of 10 min at maximum shear rate of 10 s^{-1}; pre-shear at the age of 10 min at maximum shear rate of 30 s^{-1}; pre-shear at the age of 19 min at maximum shear rate of 10 s^{-1}. The tests were

performed for mortar, the applied CSR was equal to 0.15 s^{-1}. In case of no pre-shear, approximated value of SYS at the age of 80 min was used for A_{thix} calculation. The obtained results are presented in Figs. 4 and 5 and Table 5.

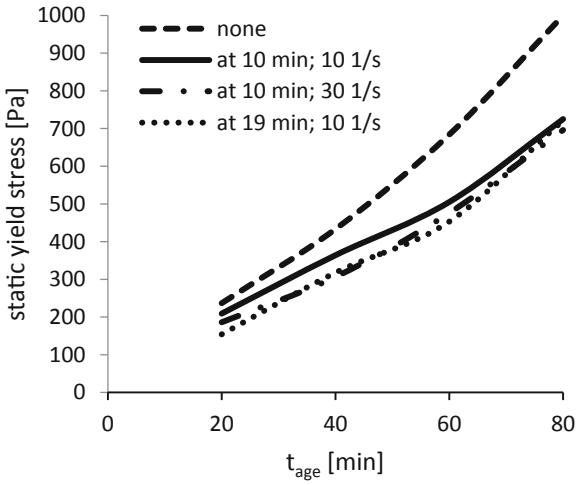

Fig. 4. Effect of pre-shear on structural build-up rate of mortar.

CoV of structural build-up rate was equal to 20% when comparing all investigated cases.

In case of applying various pre-shear regimes, the difference between SYS values is the most prominent at the first measuring point (CoV equals 15% at 20 min) and then decreases with time (CoV was equal to 9, 5 and 2% at the age of 40, 60 and 80 min, respectively).

It shall be pointed out that late pre-shear or pre-shear at higher shear rate lead to lower SYS values at the early ages and, therefore, to higher resulting A_{thix} values.

This may provide an impression of more rapid structural build-up in the material, which, however, occurs not due to intrinsic differences in thixotropic behaviour but due to restoration of structure disturbed by pre-shear. However, in this particular research the difference between A_{thix} values was not significant (CoV = 7%).

Table 5. Structural build-up rate determined after applying various pre-shear regimes

Tested material	A_{thix} [Pa/min] after applying various pre-shear regimes					CoV
	None	At 10 min; 10 s^{-1}	At 10 min; 30 s^{-1}	At 19 min; 10 s^{-1}	Average	
Mortar	7.7	5.1	5.2	5.8	6.0	20%
Mortar	–	5.1	5.2	5.8	5.4	7%

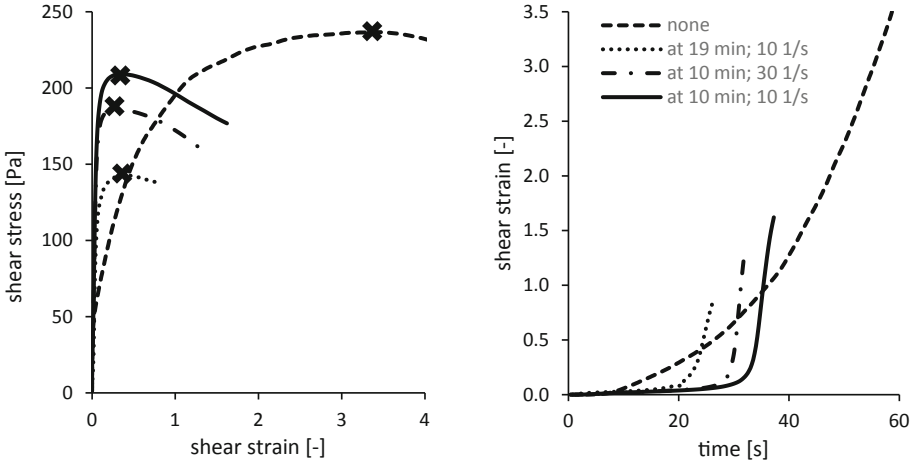

Fig. 5. Effect of pre-shear on determination of shear strain at the first measurement point (mortar age of 20 min).

Another issue which was observed in this set of experiments, was pronouncedly different pattern of strain growth during the first measurement of SYS in case of no pre-shear; see Fig. 5. In this case, the sample was characterised by significantly smaller shear stress required to reach the elastic limit, in comparison to pre-sheared samples of the same material. Furthermore, the measured critical strain attributed to SYS for non-pre-sheared sample (3.4 units) was considerably higher than for pre-sheared samples (0.3–0.5 units). This result cannot represent the actual state of the tested material, since the mortar which was not subject to pre-shearing should exhibit a faster structural build-up, hence, the shear stress at elastic limit should be higher, as well as the region of plastic deformations should not be considerably wider.

Supposedly, the measured difference in strain is not caused by various shear histories of samples, but develops due to different positioning of rotor in the tested material. In case of no pre-shear, the rotor is installed in the sample and then never moved before the first SYS measurement. This results into formation of some space in the rotors' vicinity. That is why no significant resistance of material is detected from the start of the test in comparison to pre-sheared samples.

It can be concluded that pre-shear ensures the correct positioning of the rotor before the first measurement and, hence, provides more accurate determination of shear strain and elastic limit, if required. However, considerable decrease in structural build-up rate due to pre-shear must also be taken into account. Since such variation in strain was observed only for the first measurement point, it can be suggested to apply a zero SYS measurement instead of pre-shear. This would enable proper rotor positioning without considerable disturbance of the sample's structure. Since the general purpose of evaluating the structural build-up rate is prediction of the material's behaviour in in-situ conditions, a general recommendation might be to keep the shear history of the tested sample as close as possible to its expected state on site.

6 Conclusions

In this research work, the differences in the structural build-up rate resulting from using different procedures in the constant shear rate test were quantified and discussed.

A comparison between single- and multi-batch approaches showed that the structural build-up rate of both cement paste and mortar did not undergo significant changes. Therefore, single batch of material can be used for its evaluation, ensuring both time efficiency of experiments and reliable results.

The variation in the selected constant shear rate (CSR) in the range from 0.05 to 0.20 s^{-1} lead to 12–13% variation in the structural build-up rate of cement paste and mortar. While such variation is not critical, it still may be recommended to use identical CSR for comparative experiments, especially in cases, when high level of precision must be ensured. It shall be also taken into consideration that lower CSRs lead to longer test durations. Hence, the selected CSR shall represent a compromise between as static as possible conditions and feasibility to obtain SYS values for all ages of interest with the test durations, which can be considered representative for each particular age of the sample. The authors suggest that test durations shall be selected depending on particular material under investigation and its rate of structural build-up.

Finally, variation of pre-shear regime showed that if a sample is not pre-sheared, 20% higher structural build-up rate was obtained in comparison to pre-sheared samples. Changes in the age, at which pre-shear was applied, or the maximum shear rate of pre-shear had no prominent effect on the structural build-up rate of the pre-sheared samples. It was also found that in case no pre-shear was applied, the measurements of shear strain at the first point were incorrect due to improper contact between the rotor and the material. In order to ensure accurate determination of the structural build-up rate in static conditions, it was proposed to apply an additional constant shear rate step instead of intensive pre-shear.

Acknowledgements. This work is a part of I. Ivanova's PhD research. The project is funded by German Research Foundation (DFG) within the priority program SPP 2005 Opus Fluidum Futurum – Rheology of reactive, multiscale, multiphase construction materials. The authors also express sincere gratitude to HeidelbergCement AG for providing Portland cement used in this study.

References

1. Roussel N, Ovarlez G, Garrault S, Brumaud C (2012) The origins of thixotropy of fresh cement pastes. Cem Concr Res 42(1):148–157
2. Mahaut F, Mokéddem S, Chateau X, Roussel N, Ovarlez G (2008) Effect of coarse particle volume fraction on the yield stress and thixotropy of cementitious materials. Cem Concr Res 38:1276–1285
3. Yuan Q, Zhou D, Li B, Huang H, Shi C (2018) Effect of mineral admixtures on the structural build-up of cement paste. Constr Build Mater 160:117–126
4. Khayat KH, Omran AF, Naji S, Billberg P, Yahia A (2012) Field-oriented test methods to evaluate structural build-up at rest of flowable mortar and concrete. Mater Struct 45:1547–1564

5. Nerella VN, Beigh MAB, Fataei S, Mechtcherine V (2019) Strain-based approach for measuring structural build-up of cement pastes in the context of digital construction. Cem Concr Res 115:530–544
6. Perrot A, Rangeard D (2015) Pierre A (2015) Structural built-up of cement-based materials used for 3D- printing extrusion techniques. Mater Struct 49:1213–1220
7. Roussel N (2006) A thixotropy model for fresh fluid concretes: theory, validation and applications. Cem Concr Res 36(10):1797–1806
8. Omran AF, Khayat KH, Elaguab YM (2012) Effect of SCC mixture composition on thixotropy and formwork pressure. J Mater Civ Eng 24(7):876–888

Comparing Phase Development and Rheological Properties of OPC Paste Within the First Hour of Hydration

Cordula Jakob[1(✉)], Daniel Jansen[1], Ursula Pott[2], and Jürgen Neubauer[1]

[1] GeoZentrum, Mineralogy, FAU Erlangen-Nuernberg, Erlangen, Germany
cordula.jakob@fau.de
[2] Building Materials and Construction Chemistry, TU Berlin, Berlin, Germany

Abstract. In this paper the very early hydration of ordinary Portland cement at 20 °C and 30 °C is investigated, focussing on the first hour after the addition of water. The development of the rheological behaviour of cement paste during hydration is compared with the kinetics determined by quantitative in-situ X-ray diffraction (QXRD) and heat flow calorimetry. For both temperatures the cumulative heat correlates very well with the evolution of ettringite content over the first hour of hydration. The precipitation rate of ettringite is strongly influenced by temperature. This results in a higher formation rate of ettringite already in the first minutes after mixing at 30 °C. Analogously the temperature affects the rheological behaviour of the cement paste. The measured torque values are also higher for 30 °C from the first point of investigation on. Furthermore, the increasing torque can be linked to the rise in the ettringite content at both temperatures. The formation of other hydrate phases influencing the development of the rheological behaviour within the observed time frame cannot be proven with the data at hand. Therefore, it can be assumed that ettringite content is the determining mineral for the early workability of cement pastes.

Keywords: Hydration kinetics · Rheology · Ettringite formation · Temperature · OPC

1 Introduction

The transformation of the cement paste from a suspension to a plastic state, which results in the loss of workability, is of great interest in industry as well as in science. Special application fields like the construction of super-tall buildings or the 3D-printing make particular demands on the performance of cementitious systems. The rheological performance of the concrete, especially in the initial period after mixing, has to be regulated uniquely for the respective application. In case of super-tall buildings the concrete has to maintain its workability and stability during extended periods of high-pressure pumping without blockage, bleeding or segregation [1]. The respective time frame for these desired properties usually concerns the first hour after mixing. A deeper understanding of the ongoing processes in this early period of cement hydration within

V. Mechtcherine et al. (Eds.): RheoCon 2019/SCC 2019, RILEM Bookseries 23, pp. 219–227, 2020.
https://doi.org/10.1007/978-3-030-22566-7_26

the paste and their influence on the rheological behaviour of the paste are indispensable for controlling the workability of both cement paste and concrete.

In the literature the setting time which can be determined by Vicat is mainly attributed to the silicate reaction [2, 3]. The strong solidification is linked to the coalescence of the clinker grains caused by the formation of C-S-H [3].

Whereas the determining factors which influence the slight loss of workability before setting are still not agreed upon. Roussel et al. [4] state that, analogous to the rigidification stage, C-S-H is the decisive hydrate phase which "bridges" the particles and leads to flocculation. In contrast Uchikawa et al. [2] relate the rheological development at the beginning of hydration to ettringite formation. Due to the investigations of the interaction between cement and polycarboxylate-ether based superplasticizers (PCE) Winnefeld et al. [5] concluded that ettringite formation and its dispersion in the fresh cement paste controls the workability in this early stage of hydration.

To investigate this special period with regard to the working mechanisms behind the loss of workability the experiments were performed at two different temperatures. The hydration kinetics are strongly influenced by this factor [6]. Therefore, it is possible to compare these differences with the rheological behaviour of the cement paste which is also affected by temperature.

2 Materials and Methods

2.1 Materials

For the experiments a commercial ordinary Portland cement (OPC) CEM I 42.5 R was used. The quantitative phase content was analysed by means of quantitative X-ray powder diffraction (QXRD) coupled with the external standard G-Factor method [7]. Minor phase enrichment experiments [8, 9] were conducted to ensure an accurate quantification and identification of all phases. Additionally, the chemical composition determined by X-ray fluorescence analysis (XRF). The mineralogical and the chemical composition is shown in Table 1.

Table 1. Phase content (QXRD) and chemical composition (XRF) of CEM I.

Phase	wt.-%	Oxide	wt.-%
alite	57.4	CaO	63.0
belite	14.0	SiO_2	20.5
C_3A_{cub}	6.6	Al_2O_3	5.7
C_3A_{orth}	3.1	Fe_2O_3	2.5
anhydrite	2.5	MgO	1.6
bassanite	2.5	Na_2O	0.2
gypsum	<0.1	K_2O	0.8
arcanite	0.7	SO_3	3.3
calcite	3.4	TiO_2	0.3
		LOI	1.9

2.2 Sample Preparation and Mixing

For hydration a water to cement ratio (w/c) of 0.36 was employed. For all experiments except the heat flow calorimetry 650 g cement and deionized water were mixed in a KitchenAid 5K45. The mixing routine started with 58 rounds per minute (rpm) for 15 s. The speed was then increased at first up to 125 rpm for 45 s and after that up to 220 rpm for 30 s. In the following 90 s the mixing was stopped and the sides of the bowl were scraped off. The break was followed by a last mixing at 220 rpm for 60 s. Before mixing the cement and the deionized water were equilibrated at the experimental temperatures for at least 4 h. Two experimental temperatures were used: 20.0 °C ± 0.5 °C and 30.0 °C ± 0.5 °C.

2.3 Heat Flow Calorimetry

A TAM Air calorimeter (TA Instruments) was used to measure the heat flow evolution of the mixes at 20.0 °C ± 0.2 °C and 30.0 °C ± 0.2 °C. A custom made InMixEr [10] device was utilized which allows equilibration, injection of water and mixing inside the calorimeter. This experimental setup enables the proper detection of the heat flow directly from the time of mixing on. Cement and water were mixed to a paste at 860 rpm for 1 min. For both temperature three measurements were performed. Raw data were corrected according to the time resolution of the calorimeter.

2.4 In-situ QXRD

In order to examine the phase evolution in the first hours of the cement hydration in-situ XRD measurements were performed. After mixing the cement paste was transferred into a PVC sample holder and placed into a custom-made heating and cooling device which ensures a constant experimental temperature (20.0 °C ± 0.2 °C and 30.0 °C ± 0.2 °C). The sample was covered by a 7.5 µm thick Kapton® polyimide film to avoid water evaporation and CO_2 intake of the paste. The diffraction patterns were recorded by a Bruker AXS D8 Advance diffractometer in Bragg-Brentano geometry every 10 min from 7° to 55° 2Θ and a step width of 0.0236° 2Θ. Three preparations were measured for both temperatures over a time frame of 5 h. The Rietveld analysis was performed using the software TOPAS 5.0 (Bruker AXS). The external standard G-Factor method [7] was used to gain absolute amounts of the crystalline phases present in the paste.

2.5 Rheology

A speed controlled rotational rheometer Viskomat NT (Schleibinger) was used to perform the rheological measurements. During the measurement the cement paste flows around the stationary paddle and generates a torque, which can be measured. The measuring range of the torque is between 0 and 500 Nmm and the range of the speed is between 0.001 rpm and 400 rpm. The rheometer has an angle accuracy of 2 * 10E−2°. The used geometry is a fish bone paddle. For the investigation of the early cement hydration measurements were performed at 20.5 °C ± 0.5 °C and 30.0 °C ± 0.5 °C.

For this purpose, a velocity of 2 rpm was applied for 30 s. Since the first formed crystals should not be destroyed, pre-shear was waived. For each measurement a new sample was prepared and stored at the experimental temperature. During the measurement, one data point was recorded every second. The last five data points were used to calculate the mean.

3 Results

3.1 Heat Flow Calorimetry

The heat flow development of the cement paste at two different temperatures (20.0 °C ± 0.2 °C and 30.0 °C ± 0.2 °C) is shown in Fig. 1a. Both samples show very high initial heat flows followed by a steady decline. For 30 °C the initial heat flow reaches 187 mW/g_{cement} and is therefore 60 mW/g_{cement} higher than at 20 °C. Due to the mixing inside the calorimeter the initial heat flow can be considered significant. Before the heat flow rises again it reaches a relative minimum in both systems. This induction period is characterised by a low but detectable heat flow (for both temperatures approx. 0.5 mW/g_{cement}). At 30 °C the acceleration period starts earlier and the incline is steeper than at 20 °C. Hence the second maximum associated with the silicate reaction is reached earlier for the higher temperature. Also the third maximum related to the aluminate reaction (sulfate depletion) appears 5 h earlier for the 30 °C sample. For the higher temperature the maxima of the two reactions are located in close proximity, whereas at 20 °C they are separated by 5 h.

3.2 In-situ QXRD

In Fig. 1b the development of the phases related to the silicate reaction are shown over a time frame of 5 h. The phase contents of alite at different temperatures shows no significant difference in the first 1.5 h of hydration. For both temperatures no

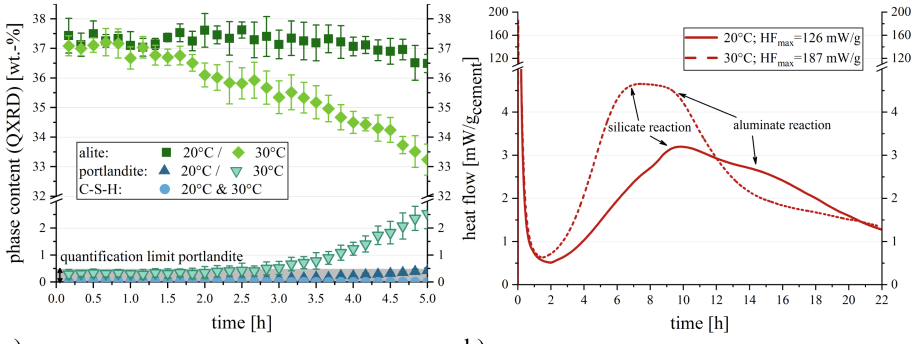

Fig. 1. (a) Heat flow development of CEM I at 20 and 30°C (*w/c* = 0.36). (b) Development of phase contents relating to the silicate reaction within the first 5 h of hydration at 20 °C and 30 °C (*w/c* = 0.36). The quantification limit of portlandite is greyed out.

dissolution can be observed up to 1.5 h. Afterwards the alite content in the paste decreases for the 30 °C sample. At 20 °C the amount of alite stays constant until about 3 h after the addition of water and then begins to decrease slowly.

Over the first few hours of hydration the determined amount of portlandite lies below the quantification limit of 0.5 wt.-%. At 20 °C there are no certain observable peaks of portlandite in the diffraction pattern until 3.5 h. At 30 °C the portlandite content exceeds the limit of quantification at around 2 h. A steadily increasing precipitation rate of portlandite can be observed afterwards. The 20 °C system shows a slightly increasing portlandite content only after 3.5 h.

For the Rietveld refinement the C-S-H model published by Bergold et al. [11] was used. However, this is only valid for the dimeric or "long-range ordered" C-S-H. The monomeric or "short-range ordered" C-S-H which precipitates at first can't be detected by this model [12]. Hence it isn't surprising that no C-S-H precipitation can be noticed for both temperatures over the whole time frame, even though it has to be expected from the portlandite precipitation and alite dissolution [13, 14].

The evolution of the phases associated with the aluminate reaction are shown in Fig. 2. Figure 2a relates to the anhydrous phases and Fig. 2b to the corresponding hydrate phases. No considerable alteration of the amount of C_3A and anhydrite can be observed in Fig. 2a over the whole time frame at both temperatures. Merely the initial dissolution of C_3A (expected value at the time of mixing is 7.1 wt.-%) seems to be higher for 30 °C. However, in terms of the measurement accuracy this difference is close to be not significant. The highly soluble sulfates like bassanite and arcanite are completely dissolved within the first 10 min and therefore not shown in the graph.

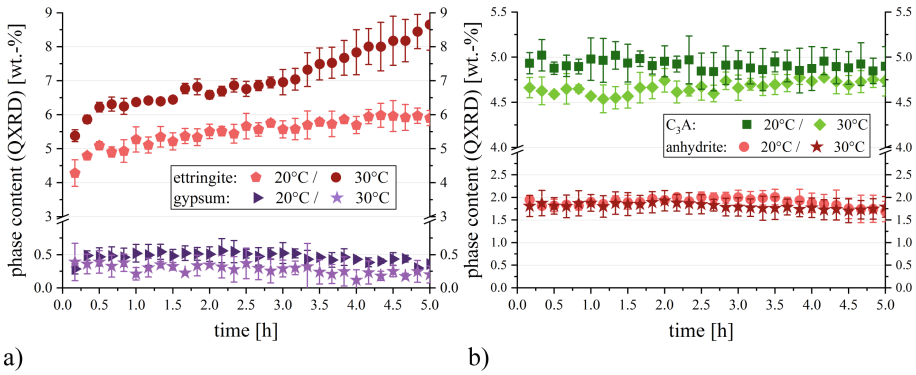

Fig. 2. Development of phase contents relating to the aluminate reaction within the first 5 h of hydration at 20 °C and 30 °C (*w/c* = 0.36). (a) The anhydrous phases and b) the hydrate phases of the reaction. Expected values at the time of mixing: C_3A = 7.1 wt.-% and anhydrite = 1.8 wt.-%.

At both temperatures the precipitation of nearly 0.5 wt.-% gypsum can be observed within the first 10 min of hydration. In terms of the measurement accuracy the gypsum content evolves equally. Over the whole time frame no significant changes in the amount are observable.

Already within the first 10 min a substantial precipitation of ettringite can be detected for both temperatures. At 20 °C the amount of ettringite reaches 4.3 wt.-% and even 5.3 wt.-% for 30 °C. At 20 °C a further increase of the ettringite content to nearly 5 wt.-% within the first 20 min can be observed, followed by a period of a reduced but constant precipitation rate. At 30 °C the fast initial precipitation of ettringite lasts until 30 min after the addition of water and an ettringite content of 6.2 wt.-% is reached. Afterwards the ettringite precipitation rate is reduced but constant until 3 h and then increases again.

3.3 Rheology

In Fig. 3 the results of the rheological measurements over a time frame of one hour are shown. At both temperatures an increasing torque with progressing hydration time can be observed. The measurements at 30 °C shows higher torque values after 6 min up to 45 min. Already after 6 min the torque is higher than for 20 °C and increases much faster during the hydration at 30 °C.

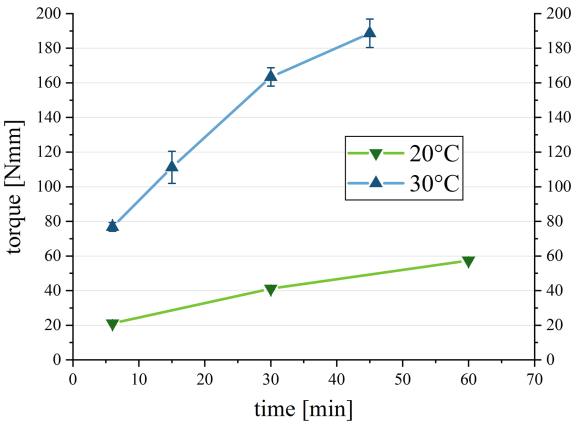

Fig. 3. Development of the measured torque during the first hour of hydration at 20 °C and 30 °C (*w/c* = 0.36). Standard deviation of torque measurements at 20 °C is smaller than the size of symbols.

4 Discussion

To investigate the influence of hydrate phases on the rheological properties in the first hour of hydration the evolution of ettringite precipitation and the rheological measurements at 20 °C and 30 °C are shown in Fig. 4. Additionally, the heat of hydration calculated from the heat flow is presented for both temperatures. The early stage of hydration is the critical time frame for several industrial applications like the pumping of concrete. In this period according to the present data there is no evidence of another developing hydrate phase other than ettringite. Gypsum precipitates in the very first minutes (slightly over sulphated OPC) and afterwards shows no significant changes in

its very low amount. Furthermore, there are no decisive differences in the amount of the precipitated gypsum between both temperatures. Therefore, it can't be responsible for the steady increase of the torque with progressive hydration. In case of the silicate reaction there is no evidence for an ongoing dissolution of C_3S as well as the precipitation of portlandite or C-S-H in this period. This is already stated in literature and called the induction period.

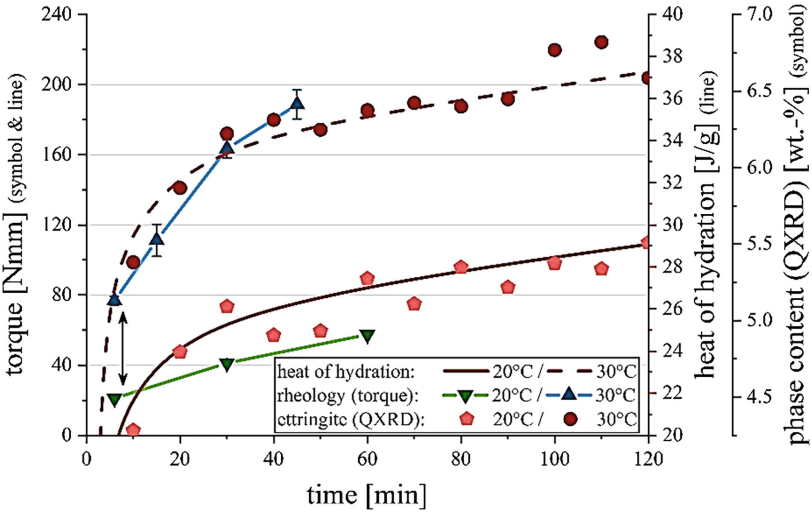

Fig. 4. Comparison of rheological behaviour, heat of hydration and ettringite content during the first two hours of hydration at 20 °C and 30 °C (*w/c* = 0.36). Standard deviation of ettringite: 0.2 wt.-%. Standard deviation of torque measurements at 20 °C is smaller than the size of symbols.

Only the ettringite content shows a steady, continuous increase in the considered period and its precipitation rate is strongly influenced by the temperature. The degree of reaction is higher for the 30 °C system at any point in time, as evident from the heat of hydration plotted in Fig. 4. The aluminate hydration, especially the formation of ettringite strongly influenced by temperature as shown in Fig. 2b. The significant faster formation of ettringite within the first 30 min at 30 °C which leads to the higher initial heat release in Fig. 1. These findings for the influence of temperature on the hydration of cement are in agreement with the results reported by Hesse et al. [6].

The heat of hydration shown in Fig. 4 correlates perfectly well with the formation of ettringite. In addition, the increase of the ettringite content in the paste correlates with the rising torque of the rheological measurement. The higher initial ettringite precipitation coincides with the higher torque of the first rheological measurement at 30 °C compared to 20 °C. Also the ascent of the torque is considerably higher at the higher temperature and correlates nicely with the development of ettringite content at both temperatures.

Therefore, it can be assumed that ettringite as only forming hydrate phase is accountable for the rheological development in the first hours of hydration. This was also reported by Uchikawa et al. [2]. Due to the high amount of water incorporation into the ettringite structure (45.9 wt.-% of water) and the formation of additional surface area through ettringite formation the evident loss of workability indicated by the increasing viscosity in this period can be explained.

5 Conclusion

The whole hydration process of Portland cement is influenced by temperature. The aluminate reaction, especially the ettringite formation is strongly depending on this factor within the first hours of hydration.

Up to 1 h the rheological behaviour is related to the formation of ettringite. The faster loss of workability at higher temperatures is caused by the faster hydration progress and especially by the increased amount of precipitated ettringite. The formation of ettringite can be correlated with the rheological torque measurements. The existence of an early monomeric C-S-H phase forming in the first minutes of hydration cannot be excluded with the data at hand. Whether the amount of this phase is sufficient for flocculation as described by Roussel et al. [4] should be the scope of further studies. With regard to the constant phase content of alite within the 1st h of hydration there is no evidence of another evolving hydrate phase influencing rheology in the 1st h of hydration which indicates that the formation of ettringite is the deciding factor concerning the early rheological behaviour.

6 Acknowledgement

The authors would like to thank the German Research Foundation (DFG) for funding the priority program *Opus Fluidum Futurum – Rheology of reactive, multiscale, multiphase construction materials (SPP 2005)* (STE 1086/181; NE 813/7-1) and HeidelbergCement for providing the material.

References

1. Nehdi ML (2013) Only tall things cast shadows: opportunities, challenges and research needs of self-consolidating concrete in super-tall buildings. Constr Build Mater 48:80–90
2. Uchikawa H, Ogawa K, Uchida S (1985) Influence of character of clinker on the early hydration process and rheological property of cement paste. Cem Concr Res 15:561–572
3. Ylmén R, Jäglid U, Steenari B-M, Panas I (2009) Cement and concrete research early hydration and setting of portland cement monitored by IR, SEM and Vicat techniques. Cem Concr Res 39:433–439
4. Roussel N, Ovarlez G, Garrault S, Brumaud C (2012) The origins of thixotropy of fresh cement pastes. Cem Concr Res 42:148–157

5. Winnefeld F, Zingg A, Holzer L, Pakusch J, Becker S (2009) Ettringite-superplasticizer interaction and its impact on the ettringite distribution in cement suspensions. In: Ninth ACI international conference superplast. Other chem. tenth ACI international conference on recent advances in concrete technology Sustainable Issues, Sevillia, Spain, p 420.1–420.17
6. Hesse C, Goetz-Neunhoeffer F, Neubauer J, Bräu M, Kutschera M (2009) In situ XRD analysis for clarification of the progress of hydration reactions on model cement with reduced phase content at defined temperatures. In: 17th International Baustofftagung - Tagungsbericht, F.A. Finger-Institut für Baustoffkunde, Weimar, pp 289–296
7. Jansen D, Goetz-Neunhoeffer F, Stabler C, Neubauer J (2011) A remastered external standard method applied to the quantification of early OPC hydration. Cem Concr Res 41:602–608
8. Struble L (1985) The effect of water on maleic acid and salicylic acid extractions. Cem Concr Res 15:631–636
9. Gutteridge WA (1979) On the dissolution of the interstitial phases in Portland cement. Cem Concr Res 9:319–324
10. Hertel T, Neubauer J, Goetz-Neunhoeffer F (2016) Study of hydration potential and kinetics of the ferrite phase in iron-rich CAC. Cem Concr Res 83:79–85
11. Bergold ST, Goetz-Neunhoeffer F, Neubauer J (2013) Quantitative analysis of C-S-H in hydrating alite pastes by in-situ XRD. Cem Concr Res 53:119–126
12. Bergold ST, Goetz-Neunhoeffer F, Neubauer J (2015) Mechanically activated alite: new insights into alite hydration. Cem Concr Res 76:202–211
13. Garrault-Gauffinet S (2012) The rheology of cement during setting. In: Roussel N (ed) Understanding the rheology of concrete, 1st edn. Woodhead Publishing, Cambridge, pp 96–113
14. Jansen D, Naber C, Ectors D, Lu Z, Kong XM, Goetz-Neunhoeffer F, Neubauer J (2018) The early hydration of OPC investigated by in-situ XRD, heat flow calorimetry, pore water analysis and ^{1}H NMR: learning about adsorbed ions from a complete mass balance approach. Cem Concr Res 109:230–242

Challenges in Rheological Characterization of Cement Pastes Using a Parallel-Plates Geometry

Aida Margarita Ley-Hernández(✉) and Dimitri Feys

Department of Civil, Architectural and Environmental Engineering, Missouri University of Science and Technology, Rolla, MO, USA
alwy2@mst.edu

Abstract. Cement-based materials are characterized as complex suspensions that may experience a thixotropic behavior caused by physical and chemical phenomena. The characterization and understanding of the rheological properties of cement-based materials have become essential with the introduction of 3D printing in field of civil engineering. Therefore, there is a need to accurately measure such properties to obtain repeatable and consistent results. To measure the rheological properties, different geometries are available, such as vane, parallel-plates, or coaxial cylinders: These are the most used for cement-based materials. Although, there are no specific guidelines on how to select the appropriate geometry for the material that will be tested. Proper understanding of the advantages and disadvantages as well as the limitations of each geometry should be taken into account. Since parallel-plates is a common tool used to evaluate fresh cement-based materials, due to its simplicity, the small sample volume required and the variable gap that can simulate the distance between the aggregates. This paper discusses the major challenges and issues encountered when using parallel-plates geometry to measure the rheological properties of cement-based suspensions under shear. Some issues such as wall slip, sample spill, dryness, particles sedimentation, non-uniform shear rate applied, etc. can be prevented but the user should be aware of these problems.

Keywords: Parallel-plates · Rheology · Cement-based materials · Challenges

1 Introduction

Digital printing has been recently introduced into the field of civil engineering offering significant advantages, such as construction without using a formwork, which allows for a greater freedom of shape, a faster construction process and cost savings. This technology comes with engineering challenges, as some of the requirements that the formwork used to fulfill, e.g. support of the concrete, are now imposed onto the material [1]. Therefore, the proper characterization and understanding of the rheological properties of cement-based materials has become essential to successfully print the material. Cementitious pastes are characterized as complex suspensions that contain a wide particle size distribution, which are on the boundary between colloidal and non-colloidal particles. This broad distribution of polydisperse particles influences various

V. Mechtcherine et al. (Eds.): RheoCon 2019/SCC 2019, RILEM Bookseries 23, pp. 228–236, 2020.
https://doi.org/10.1007/978-3-030-22566-7_27

interaction forces depending of the size of the particles, the volume fraction in the mixture and external forces. Therefore, these pastes may experience thixotropic behavior caused by physical and chemical phenomena [2–5]. To measure the rheological properties of cement pastes, different geometries are available, such as vane, parallel-plates, or coaxial cylinders: These are the most used for cement-based materials. However, there are no specific guidelines on how to select the appropriate geometry for the material that will be tested. Proper understanding of the advantages and disadvantages as well as the limitations of each geometry should be considered. In the case of parallel-plates, which is a common tool to use to evaluate fresh cement-based materials. This due to its simplicity, the small sample volume required, surface roughness and the variable gap that can simulate the distance between the aggregates when testing. It has been shown that the rheological properties of cement-based materials are highly sensitive to variations in geometry used to test, gap size and friction characteristics of the shearing surfaces [6]. The object of this paper is to discuss some challenges encountered when using parallel-plates geometry in cement pastes.

2 Materials and Methods

2.1 Materials

A commercially available type I/II ordinary Portland cement complying with ASTM C150/C150M specifications was used to produce the cement paste mixtures with a water-to-cement ratio (w/c) of 0.45. A polycarboxylate-based superplasticizer (SP) with a solid content of 25.8% was incorporated to obtain a dispersed system with a mini-slump flow spread of 330 mm ± 10 mm. The specific gravity of the cement and the SP is 3150 kg/m^3 and 1032 kg/m^3, respectively.

2.2 Mixing Procedure

The mixtures were prepared in 1.0 l batches in a small Hobart mixer using two speed positions. The mixing sequence consisted on introducing first the water and then the cement into the bowl and wait for 30 s. The mixer was started at slow speed (140 rpm ± 5 rpm) for 30 s to homogenize the materials. After that, the mixer was stopped for 30 s and the mixture was manually homogenized by scraping the walls of the mixing bowl. After this scraping period, SP was added and the mixing continued for 120 s. Immediately after mixing, the mini-slump flow of the mixture was measured and all rheological testing was performed at 15 min after the contact with water.

2.3 Rheological Measurements

The rheological measurements were performed at a constant temperature of 20 °C using sandblasted parallel plates (PP) geometry, unless stated otherwise, in an Anton Paar MCR 302 rheometer. The plates were 50 mm in diameter and the gap was varied from 0.25 mm to 1.5 mm. Sandpaper disks (#60 grit) of 50 mm were used in some cases to minimize slippage between the plates and the sample. To avoid evaporation of

water from the sample a temperature-controlled hood was typically placed on the top of the system. To compare the rheological properties measured with different geometries, a serrated concentric cylinder (CC) was used with an inner radius (R_i) of 13.33 mm, outer radius (R_o) equal to 14.56 mm and the height of the vertical part of the inner cylinder is 40.00 mm. The testing procedure was executed at 15 min after the contact of water with cement. First, the sample was pre-sheared at 100 s^{-1} for 120 s to minimize measurements artifacts caused by breakdown of internal structure and to impose a reference state [7]. Then a linearly decreasing shear rate ramp, from 100 s^{-1} to 10 s^{-1} was imposed over a period of 30 s. The rheological properties were determined using the transformation equation for parallel plates geometry, similar to the Reiner-Riwlin equations used for concentric cylinders. The equation transforms the relative units into a relationship between shear rate and shear stress. The intercept of torque (T) and angular velocity (Ω) curve (G) is transformed into yield stress (YS) using Eq. 1. The plastic viscosity (PV) of the pastes was determined using the slope of the curve (L) and transformed using Eq. 2. Similarly, CC data was transformed using the Reiner-Riwlin for concentric cylinder equation described in [7].

$$T = G + L\Omega$$

$$\tau_0 = \frac{3G}{2\pi R^3} \tag{1}$$

$$\mu_p = \frac{2HL}{\pi R^4} \tag{2}$$

where:

T = *Torque (Nm)*
Ω = *Angular velocity (rad/s)*
τ_0 = *yield stress (Pa)*
μ_p = *plastic viscosity (Pa s)*
R = *radius of plate (m)*
H = *gap between the plates (m)*

3 Results and Discussion

3.1 Evaporation of Water (Drying)

A series of cement pastes mixtures were produced in a previous study [8], where the influence of using a temperature-controlled hood to prevent drying of the sample was found to be critical for prolonged testing procedures. Table 1 shows results from the mixtures with a water-powder ratio (w/p) of 0.35 containing slag (dose by mass 25%), silica fume (SF-5%) and attapulgite clay (Att clay-0.5%). The evolution of the rheological properties over time are expressed as the change in yield stress and plastic viscosity, from 15 min to 45 min, with and without hood. The variation in the rheological properties over time is significantly smaller when the hood is engaged, except for the plain cement

system. The reason of such discrepancy is unknown. The percentage change when using or omitting the hood is higher when the mixtures are composed by additional powders besides cement, this behavior can be due the increased surface area provided by the powders. Additional surface area will have a higher water demand and the effect of the evaporation will be more critical in these systems.

Table 1. Time-evolution of rheological properties of pastes with and without hood.

Mixture	YS (Pa/min)			PV (Pa s/min)		
	Hood	No hood	% Change	Hood	No hood	% Change
CEM	0.563	0.285	–49	0.006	0.004	–29
Slag + Att clay	0.032	0.162	407	0.003	0.010	180
SF + Att clay	0.006	0.215	3191	0.001	0.014	693
Slag + SF + Att clay	0.016	0.246	1425	0.002	0.021	888

3.2 Gap Size

This section discusses the effect of different gap sizes between the sandblasted parallel plates on the rheological properties of cement pastes. According to literature, the selection of the gap size to obtain consistent results should be at least an order of magnitude larger than the maximum particle size [9, 10]. The ideal gap size depends on other factors such as the depth of the serration of the plate, shear rate and the plate diameter [11]. Figure 1 illustrates the shear stress values at a constant shear rate at 1, 0.5 mm and 0.25 mm gap up to 120 s, followed by a flow curve. Since the optimum gap size also depends on the shear rate, in the case of a small gap size, such as 0.25 mm, larger shear rates can cause instabilities due to a likelihood of experiencing secondary flows and an increased possibility of the particles to get in contact with the shearing surfaces [12]. Therefore, the results at 0.25 mm show more scattering and a possible sample spill could have occurred causing a reduction of the plastic viscosity due to the higher shear rates induced by a smaller gap. The results in Table 2 show that increasing the gap size from 0.5 mm to 1 mm decreases the plastic viscosity. This can be explained as the effect of confinement of the samples is reduced when the gap size is increased. This behavior was also observed in previous studies [6, 11]. Yield stress values are not reported since the models used for linear and non-linear fitting led to negative values, which have no physical meaning.

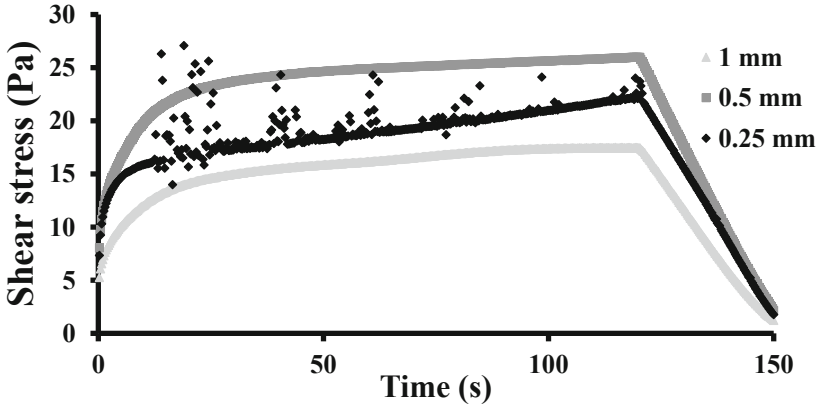

Fig. 1. Shear stress vs time curve for different gap sizes with sandblasted parallel plates.

Table 2. Rheological properties using different gap size.

Gap (mm)	PV (Pa s)
1.0	0.188
0.5	0.269
0.25	0.234

3.3 Wall Slip

Yield stress and viscosity measurements might be influenced by the friction between the sample and the shearing surfaces. Previous studies have shown that a smooth shearing surface increases the possibility of experiencing slippage, flow localization and plug flow [13–15]. Slippage occurs when cement particles move away from the smooth wall of the shearing surface, causing a decrease in particle concentration, producing a lubrication effect enhancing the flow and resulting in erroneous estimations of the rheological properties. This phenomenon is more pronounced to develop at stresses near to the yield stress [16]. In order to prevent the lubrication layer to form, the use of texture or roughness on the shearing surfaces is desired, to a certain extent. This depends on the nature and size of the dispersed particles [6].

3.4 Geometry Comparison and Surface Condition

To evaluate the influence of different geometries on the rheological properties of cement pastes, two geometries were used and the average of three replicates was considered. Figure 2 shows the shear stress vs time for CC, PP and PP with sandpaper (PP-SP), and the flow curves with the different geometries. The results in Fig. 2(a), show during the pre-shear, when using the PP geometry, an increase in shear stress at a

constant shear rate (100 s^{-1}), which does not agree with the literature. CC show a decreasing shear stress due to structural breakdown [7]. In order to avoid any potential slippage between the sample and the rheometer surfaces, sandpaper disks were used to increase the friction between the sample and the shearing surfaces. PP-SP shows similar behavior as CC in the pre-shear period, but the values of the rheological properties were significantly lower. The behavior of the flow curves with different geometries and surface roughness is illustrated in Fig. 2(b). The results of PP geometry show higher viscosity compared to the other systems, but the yield stress was not reported since the flow curve intercepted the shear stress axis in the negatives range. PP-SP rheological properties are lower, not agreeing with reported in previous studies [11] where viscosity increases when surfaces roughness increases. This discrepancy may be due to a measurement artifact that occurs when the true gap (h) is larger than the apparent gap (h_a) calibrated by apparent contact of the plates [17, 18]. However, this reasoning cannot fully explain why the viscosity is 3 to 4 times lower for the PP-SP compared to the CC and PP, respectively. The transformation function for the slope of the T-Ω to the plastic viscosity (Eq. 2) shows linear dependence on the gap size (H).

Table 3 shows the rheological properties and the standard deviation of the cement paste measured using different geometries and plate roughness.

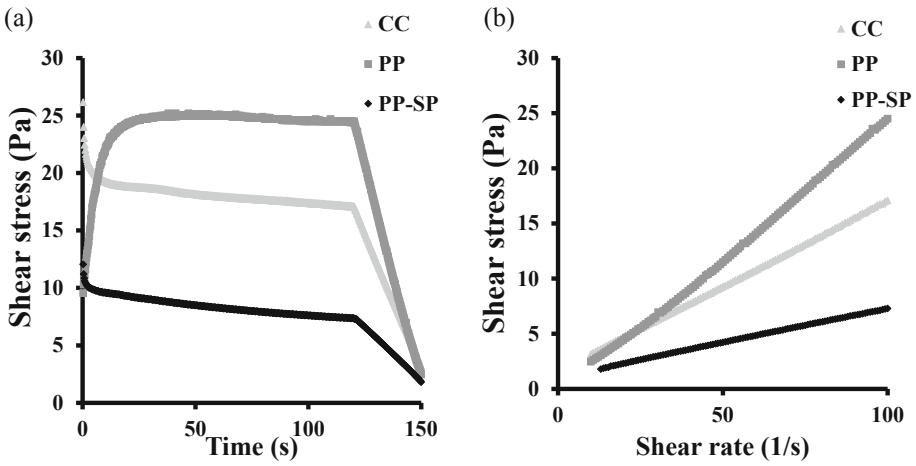

Fig. 2. (a) Shear stress vs time curve (b) Flow curves with different geometries.

Table 3. Rheological properties of cement paste using different geometries.

Geometry	YS (Pa)	ST DEV	PV (Pa s)	ST DEV
CC	1.654	0.072	0.160	0.001
PP	–	–	0.253	0.014
PP-SP	0.840	0.136	0.059	0.004

3.5 Other Challenges

Additional issues can also be included in the list of possible ways that the rheological measurements can go astray, invalidating any further interpretation of data. One important point is the sample volume. In PP geometry, torque is very sensitive to the surface contact of the sample and the shearing plates. Underfill is more susceptive than overfill to an uneven shearing of the sample, but in both cases those problems cause errors on the measurements [17]. Figure 3(a) shows a sample spill after the testing procedure was executed. This phenomenon occurred due to a high shear rate applied to the sample (300 s^{-1}), therefore a proper shear rate must be selected that is relevant for the application of the material, and leads to minimal errors. Another issue is sedimentation of the particles: When particles settle, the water in the mixture migrates to the top, causing bleeding. Figure 3(b) illustrates a sample of cement paste exhibiting bleeding, which results in lower rheological properties. In case a sample is susceptible to bleeding, a concentric cylinder geometry is usually recommended [17], but that does not guarantee adequate measurements either.

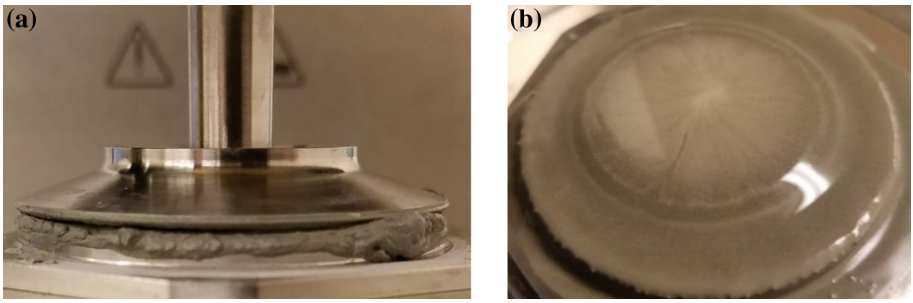

Fig. 3. (a) Sample spill, (b) Bleeding of the sample after measuring.

4 Conclusions

- Some of the challenges encountered when measuring the rheological properties of cement-based materials using parallel plates geometry are drying of the sample, varying gap size, wall slip, particle sedimentation and surface conditions. However, some of these issues are inherent to the nature of the sample. Therefore, a proper selection of the rheometer geometry and setup details is of paramount importance in order to get reliable, accurate and reproducible data.
- The evaporation of water is highly critical in systems containing additional powder due to the additional surface area, having higher demand leading to a higher rate of increase of the rheological properties over time. The use of evaporation protection, such as a temperature-controlled hood, is recommended.
- Increasing the gap size from 0.5 mm to 1 mm between the sample and the shearing surfaces, decreases the plastic viscosity, since the confinement of the particles is reduced.
- Wall slip can be prevented enhancing the texture of the shearing surfaces.

- CC geometry appeared to be more appropriate to measure the rheological properties for the cement paste with a w/c of 0.45.
- The use of PP with rough sandpaper disks may cause a measurement artifact due to inaccuracies during the determination of the gap or secondary flows.
- PP geometry is more sensitive to changes in the sample volume causing uneven shear rates and errors during the measurement. Also, it is more susceptible to obtain less repeatable rheological properties when the sample has a risk for bleeding.

Acknowledgements. The research team would like to acknowledge the University of Missouri Research Board (UMRB) and the Center for Infrastructure Studies (CIES) at Missouri S&T for the financial support and the use of the equipment.

References

1. Marchon D, Kawashima S, Bessaies-Bey H, Mantellato S, Ng S (2018) Hydration and rheology control of concrete for digital fabrication: potential admixtures and cement chemistry. Cem Concr Res 112:96–110
2. Hattori K (1990) A new viscosity equation for non-Newtonian suspensions and its application. In: Proceeding of the RILEM colloquium on properties of fresh concrete. Chapman and Hall, pp 83–92
3. Wallevik JE (2003) Rheology of particle suspensions: fresh concrete, mortar and cement paste with various types of lignosulfonates. Fakultet for ingeniørvitenskap og teknologi
4. Wallevik JE (2009) Rheological properties of cement paste: thixotropic behavior and structural breakdown. Cem Concr Res 39(1):14–29
5. Roussel N, Lemaître A, Flatt RJ, Coussot P (2010) Steady state flow of cement suspensions: a micromechanical state of the art. Cem Concr Res 40(1):77–84
6. Nehdi M, Rahman MA (2004) Estimating rheological properties of cement pastes using various rheological models for different test geometry, gap and surface friction. Cem Concr Res 34(11):1993–2007
7. Wallevik OH, Feys D, Wallevik JE, Khayat KH (2015) Avoiding inaccurate interpretations of rheological measurements for cement-based materials. Cem Concr Res 78:100–109
8. Lunkad PR (2018) Simultaneous enhancement of fluidity and thixotropy of vibration-free concrete. Masters Theses 7767
9. Banfill PFG (2003) Rheology of fresh cement and concrete – a review. In: 11th international cement chemistry congress, Durban
10. Shaughnessy R III, Clark PE (1988) The rheological behavior of fresh cement pastes. Cem Concr Res 18(3):327–341
11. Vance K, Sant G, Neithalath N (2015) The rheology of cementitious suspensions: a closer look at experimental parameters and property determination using common rheological models. Cem Concr Compos 59:38–48
12. Ferraris CF, Gaidis JM (1992) Connection between the rheology of concrete and rheology of cement paste. Mater J 89(4):388–393
13. Banfill PFG (2006) Rheology of fresh cement and concrete . Rheol Rev 61–130
14. Bhatty JI, Banfill PFG (1982) Sedimentation behavior in cement pastes subjected to continuous shear in rotational viscometers. Cem Concr Res 12(1):69–78
15. Mannheimer RJ (1983) Effect of slip on the flow properties of cement slurries. In: Annual meeting papers, division of production. American Petroleum Institute

16. Barnes HA (1995) A review of the slip (wall depletion) of polymer solutions, emulsions and particle suspensions in viscometers: its cause, character, and cure. J Nonnewton Fluid Mech 56(3):221–251
17. Ewoldt RH, Johnston MT, Caretta LM (2015) Experimental challenges of shear rheology: how to avoid bad data. In: Complex fluids in biological systems. Springer, New York, pp 207–241
18. Connell RW, Greener J (1985) J Rheol 29(2):209

Correlation Between "Very Early" Age Fracture Performance and Evolution of Rheological Properties of High Performance Fiber Reinforced Cementitious Composites with Adapted Rheology

Francesco Lo Monte[1], Gabriele Zago[1], Marco Cucchi[2], and Liberato Ferrara[1(✉)]

[1] Department of Civil and Environmental Engineering (DICA), Politecnico di Milano, Milan, Italy
liberato.ferrara@polimi.it
[2] Laboratory for Testing Materials Buildings and Structures, Politecnico di Milano, Milan, Italy

Abstract. The tremendous advances in concrete technologies our society is witness of, do not only provide the construction industry with new advanced materials and processing/manufacturing techniques, but also require the performance of cement based materials to be investigated not only in its structural service state, but also throughout its *very early* and *early* age life.

Tailored successful placement and development of mechanical performance, even in the first hours of life, can affect the structural durability and discriminate about the successful accomplishment of the structural performance throughout the service life. In this paper reference is made to a High-Performance Fibre-Reinforced Cementitious Composite, formulated with adapted rheology to ease its placement and most of all to achieve a tailored alignment of the fibres through the casting flow.

The development of tensile and shear fracture properties in the first hours (up to three) after the first contact between cement and water has been studied with an ad-hoc designed test set-up. The knowledge of such properties is of the utmost importance to foster the use of these kind of advanced cement based materials with adapted rheology in precast construction, where the design of transient situations, including demoulding and handling, may play a crucial role, also in the sight of optimizing the productivity.

In a quality control framework, the development of tensile and shear fracture properties of the investigated materials in the considered time frame have been also correlated to the evolution of rheological properties, so far evaluated through a mini-slump flow tests.

Keywords: Rheology · Tensile strength · Shear strength · Very early age properties · 3D printing

V. Mechtcherine et al. (Eds.): RheoCon 2019/SCC 2019, RILEM Bookseries 23, pp. 237–245, 2020.
https://doi.org/10.1007/978-3-030-22566-7_28

1 Introduction

Concrete and, more generally, cementitious materials are the most used materials in construction owing to many advantageous inherent features, such as relatively low cost, high durability, good fire performance, "tailorability" and on-site free shaping.

Despite concrete is considered as a traditional material, it has experienced an intensive process of continuous improvement in the last decades, leading to the formulation of very advanced material, as examples High- and Ultra-High Performance Concretes (HPC), Self-Compacting Concretes (SCC) and Ultra-High Durable Concretes (UHDC, [1, 2]).

In the very last years, a further drive to concrete development has been represented by *concrete 3D printing*, which aims at combining the free on-site shaping typical of cementitious materials with the digital fabrication, in order to reduce construction time and cost, while increasing the overall quality and work safety [3].

All these improvements have their roots in the enhancement of concrete rheology brought in by SCC and UHPC technologies, which allow very low water-to-cement ratios and, consequently, very dense and resistant materials. Adapted concrete rheology also fosters the introduction of different types of fibers, even in relevant amount (up to 3% by volume), thus providing extraordinary toughness and ductility to concrete. The formulation of strain-hardening concrete in tension is nowadays something quite easy to be reached.

In most cases, rheology is the key *very early* age property (namely, in the first few hours after casting), since it has to be tailored in order to guarantee concrete pouring and air expulsion without vibration, while avoiding fibers and aggregates segregation. Furthermore, shrinkage should be limited, so to reduce possible micro-cracking during hardening, this being detrimental for stiffness and durability. *Concrete 3D printing*, however, gives a major role also to *very early* age tensile, shear and compressive strengths, since they govern, together with rheology of course, the overall manufacturing process. In *concrete 3D printing*, this has a direct impact on deposition layout and velocity, and vertical inclination.

Starting from the study by Mettler et al. [4], an experimental approach is described in this paper for the assessment of the very early age fracture behaviour of concrete, focusing on the time evolution of tensile and shear strengths, in the very first hours after casting. The final aim is to apply such approach for the study of *3D-printable* concretes.

2 Very Early Age Properties

2.1 Rheology

As well known, fresh concrete can be addressed as a yield stress fluid, characterized by a minimum value of stress to be applied in order to active irreversible deformation and to trigger flow [5]. In particular, concrete behaves as a Bingham fluid, *i.e.*, once the yield limit τ_{lim} is attained, tangential stress τ is linearly proportional to the shear rate $\dot{\gamma}$ through the plastic viscosity μ_p (namely, $\dot{\gamma} = 0$ for $\tau < \tau_{lim}$ and $\tau = \tau_{lim} + \mu_p \cdot \dot{\gamma}$ for $\tau \geq \tau_{lim}$ [6–9]).

The rheological parameters (yield stress and plastic viscosity) can be evaluated by means of different types of rheometers (depending on aggregate sizes) or via far simpler (but less exhaustive) procedures such as slump test [9]. The determination of the rheological properties of concrete, however, is made rather tricky by the thixotropic behavior, inducing a variation of fresh properties with time, and by the shear rate effect [10–14].

Rheological properties are very important for practical applications [15, 16], as an example in the case of self-compacting and fiber-reinforced concretes, and especially in rather new technologies, first of all *concrete 3D printing*. In the case at hand, a preliminary investigation has been conducted based on slump test, which provides an indirect indication about the yield stress.

2.2 Tensile and Shear Strengths

Tensile strength is generally considered as secondary property in concrete, since the mechanical performance of reinforced concrete structures usually relies on the tensile behavior of reinforcing bars. On the other hand, the increasing attention to fiber-reinforced concrete, durability and advanced manufacturing processes, makes fracture behavior of concrete a key parameter. Shear behavior should be also properly addressed, since, even though mainly linked to tensile strength, it can be influenced by aggregate interlock and by the formation of compressed struts confined by fibers (if any). In the particular case of *concrete 3D printing*, shear behavior is instrumental in directly addressing the problem of layer-to-layer bond, in which the orientation of fiber is the main influencing parameter.

3 Test Setup and Materials

3.1 Testing Devices

In order to investigate the evolution of tensile and shear strengths with time, in the very first hours after casting, two special test setups have been manufactured according to the schemes reported in Fig. 1 (plan view and picture of the actual systems, [17]).

The molds are made of transparent polycarbonate so to check during loading if significant stratification takes place through the specimen thickness.

The tensile test device consists of two separate rectangular molds (grey and white in Fig. 1a, top). The opening between the two parts is narrowed at mid-length by two semi-circular elements so to locally reduce the cross-section and consequently localize the fracture. As shown in Fig. 1a (bottom), small pins have been introduced in the lateral faces of each of the two molds, in order to limit as possible concrete-to-mold slippage.

Similarly, the shear test device consists of two separate rectangular molds (grey and white in Fig. 1b, top). In this case no pins have been introduced, since slippage should not occur, being the fracture plane parallel to the direction of motion.

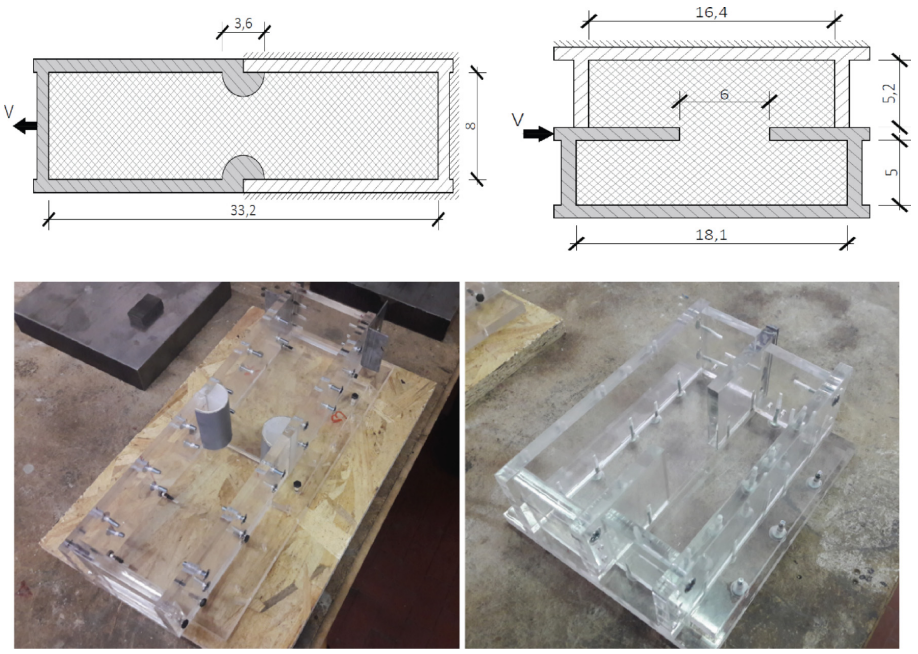

Fig. 1. Setups for tension (left) and shear (right) tests. (dimensions in cm).

Both tests were displacement-controlled thanks to a small electromechanical actuator, and load has been measured via a 600 N-capacity load-cell. The displacement velocity adopted was equal to 0.05 mm/s and 0.10 mm/s for tensile and shear tests, respectively.

It is worth noting that friction during the motion of the movable molds (grey part in Fig. 1a–b, top) is non-negligible with respect to the strength of fresh concrete. Hence, friction coefficient has been evaluated experimentally, by applying two separate weighs on the two molds of each device and performing the test. The thus estimated friction contribution has been then deducted from the force-displacement curves.

In this preliminary investigation aimed at assessing the effectiveness of the experimental procedure, slump has been assessed via a small cone (top diameter = 70 mm, bottom diameter = 100 mm, height = 65 mm) before each strength test, so to have an indirect indication about yield stress evolution.

3.2 Materials

The mixes planned for the experimental investigations are reported in Table 1. In particular, Mix M120 with 120 kg/m^3 of steel fiber has been recently studied, while the other 3 concretes, with decreasing amounts of fiber, will be tested in the next months, in order to deepen the effect of fiber content on the variation with time of *very early* age properties.

Table 1. Concrete mixes.

	M120	M80	M40	M00
CEM II 42.5 [kg/m^3]	**600**	600	600	600
Slag [kg/m^3]	**500**	500	500	500
Water [kg/m^3]	**200**	200	200	200
Superplasticizer [L/m^3]	**33**	33	33	33
Sand 0–2 mm [kg/m^3]	**982**	982	982	982
Steel fiber [kg/m^3]	**120**	80	40	0

Concrete has been cast by firstly mixing for 1 min cement and slag (slowly pouring water in the latter 30 s) and then adding the superplasticizer. Afterwards, sand and fibers have been introduced, both of them after 2 min of mixing. Finally, concrete has been mixed for 3 min. Then concrete has been quickly poured in the mold, in order to force the material to pass through the future fracture plane so fostering fibers alignment.

4 Test Results

4.1 Slump Test

Slump tests have been performed in the range of 0 min–200 min after casting, and the spread diameter in two orthogonal directions has been measured. A schematic representation of slump test spread is provided in Fig. 2a, while its average depth is reported in Fig. 2b for different time durations after casting. From Fig. 2b it is clear that (1) already at 3 h after casting slump spread is negligible and (2) the experimental dots lie in a curve with upward concavity. From preliminary experimental results on the other 3 mixes, it seems that the evidence (1) depends mainly on cement mortar (no significant difference being observed among the concretes), while the outcome (2) depends on fiber content, since downward concavity has been observed for far lower fiber content.

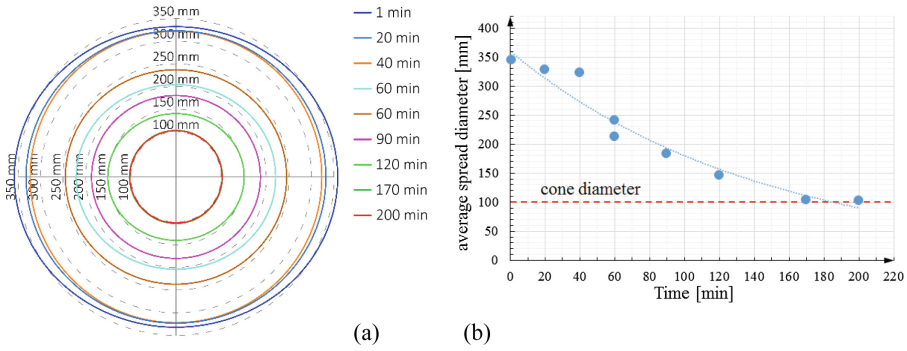

Fig. 2. Slump test: (a) schematic representation of slump spread and (b) average spread as a function of time after casting.

4.2 Tensile Strength

Tensile tests have been performed in the range 40 min–200 min after casting, since for smaller time durations concrete was too fluid for providing any tensile resistance.

In Fig. 3a the typical failure of the specimen is represented. Thanks to the reduced resistant area, failure always occurred at the mid-span section. The analysis of the fracture surface showed that a very good alignment of the fibers along the axis of the specimens and just a slight downward segregation of the same fibers.

A critical point, however, is represented by the non-homogeneous hydration of the specimen, usually faster at the exposed top surface.

In Fig. 3b, the nominal stress – displacement curves are reported, while in Fig. 4a and b, tensile strength and fracture energy are shown as functions of time duration after casting. Fracture energy has been computed as integral of the whole nominal stress – displacement curve. As expected, both properties increase with time, tensile strength with an exponential law, while fracture energy with a logarithmic trend.

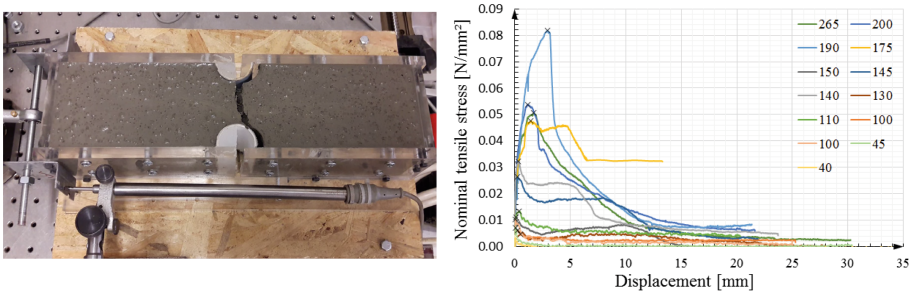

Fig. 3. Tensile test: (a) specimen at failure and (b) nominal stress – displacement curves for different time durations after casting.

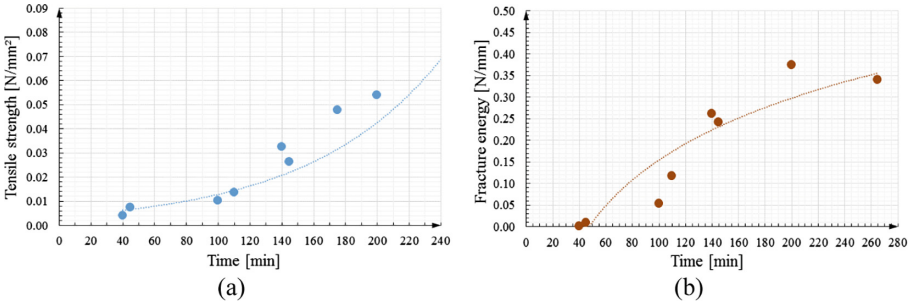

Fig. 4. Tensile test: (a) strength and (b) fracture energy at different time durations.

4.3 Shear Strength

Shear tests have been performed approximatively in the range 40 min–200 min after casting. In Fig. 5a one of the typical failure mode of the specimen is represented.

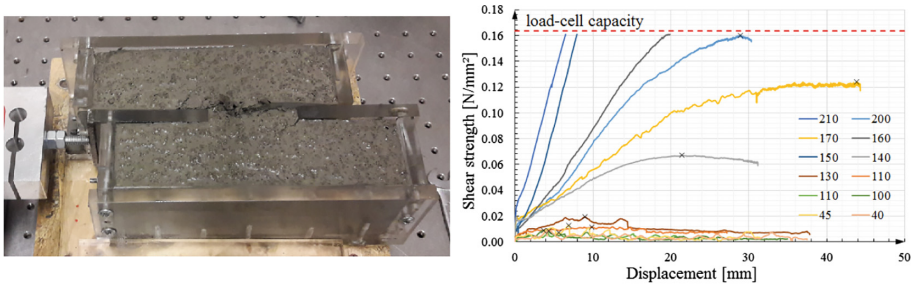

Fig. 5. Shear test: (a) specimen at failure and (b) nominal stress – displacement curves for different time durations after casting.

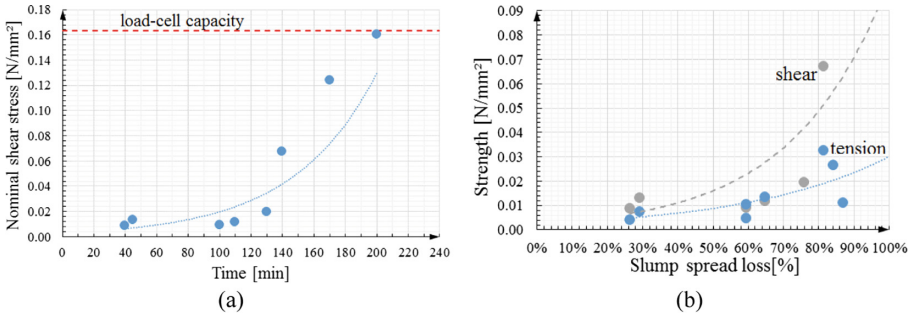

Fig. 6. Plot of (a) nominal stress – displacement curves in shear test for different time durations after casting, and (b) tensile and shear strength against slump spread loss (η_{slump}).

Failure modes in shear appear to be slightly more complex than in tension, due to a tension-compression induced by the formation of inclined concrete struts in some cases.

The analysis of the fracture surface showed a very good alignment of the fibers across the fracture, and a non-homogeneous hydration of the specimen has been observed as well. In Fig. 5b, the nominal stress – displacement curves are shown for different times after casting, while in Fig. 6a shear strength evolution with time is reported. Shear strength appeared to increase with an exponential law as for tensile

strength, even though more rapidly in both absolute and normalized terms. In Fig. 6b, tensile and shear strength are plotted as functions of the slump spreading loss, expressed as:

$$\eta_{slump} = \left(d^{t}_{spreding} - d_{cone}\right) / \left(d^{t_o}_{spreding} - d_{cone}\right)$$

where $t_o = 0$ min.

5 Concluding Remarks and Outlooks

A testing procedure has been developed to assess the *very early* age properties of concrete, by evaluating slump flow, tensile and shear strengths. The tailored test setups consist of polycarbonate molds in which concrete is poured just after mixing and then directly tested at a given time duration after casting. Mechanical characterization is accompanied by mini slump tests, whose results are linked to concrete yield stress.

Tensile and shear strength tests in the range 40 min–200 min after casting have been performed, showing an exponential increase with time, sharper in the case of shear behavior. Fracture energy showed a logarithmic increase with the time.

Further investigations on mixes with different amounts of fiber together with rheometer tests will allow (1) to better highlight the direct role of fiber in the evolution of the mechanical behavior and (2) to correlate the development of rheological and mechanical properties. Finally, a setup for compression test in under evaluation, this being instrumental for the detection of the failure envelope of concrete. This information could allow to monitor the evolution of the fracture process in concrete.

Acknowledgements. The activity described in this paper has been performed in the framework of the project "Rethinking coastal defence and Green-energy Service infrastructures through enHancEd-durAbiLity high-performance cement-based materials-ReSHEALience", funded by the European Union Horizon 2020 research and innovation programme under GA No. 760824.

References

1. Lo Monte F, Mezquida-Alcaraz EJ, Navarro-Gregori J, Serna P, Ferrara L (2019) Characterization of the tensile behaviour in UHPC. In: Proceedings of 5th NBSC workshop, 19–20 September 2019. Politecnico di Milano, Milan
2. Cuenca E, Roig-Flores M, Serna P, Ferrara L (2019) Use of nano-additions to improve the durability of UHPFRCs developed in the ReSHEALience project. In: Proceedings of 5th NBSC workshop, 19–20 September 2019. Politecnico di Milano, Milan
3. Flatt RJ, Wangler T (eds) (2018) Digital concrete 2018. In: Cement and concrete research special issue, vol 112, pp 1–136
4. Mettler LK, Wittel FK, Flatt RJ, Herrmann HJ (2016) Evolution of strength and failure of SCC during early hydration. Cem Concr Res 89:288–296
5. Kovler K, Roussel N (2011) Properties of fresh and hardened concrete. Cem Concr Res 41:775–792

6. Tatersall GH, Banfill PGF (1983) The rheology of fresh concrete. Pitman, London
7. De Larrard F (1999) Concrete mixture proportioning. E & FN Spon, London
8. Hu C, de Larrard F (1996) The rheology of fresh high performance concrete. Cem Concr Res 26(2):283–294
9. Murata J (1984) Flow and deformation of fresh concrete. Mat. Struct. 98:117–129
10. Wallevik JE (2009) Rheological properties of cement paste: thixotropic behavior and structural breakdown. Cem Concr Res 39(1):14–29
11. Billberg P (2005) Development of SCC static yield stress at rest and its effect on the lateral form pressure. In: Shah SP (ed) Proceedings of the 2nd North American conference on the design and use of SCC and the 4th international RILEM symposium on SCC, 30 October–3 November 2005, Chicago
12. Jarny S, Roussel N, Rodts S, Le Roy R, Coussot P (2005) Rheological behavior of cement pastes from MRI velocimetry. Cem Concr Res 35:1873–1881
13. Assaad J, Khayat K, Mesbah H (2003) Assessment of thixotropy of flowable and selfconsolidating concrete. ACI Mater J 100(2):99–107
14. Roussel N (2006) A thixotropy model for fresh fluid concretes: theory, validation and applications. Cem Concr Res 36(10):1797–1806
15. Perrot A, Pierre A, Vitaloni S, Picandet V (2015) Prediction of lateral form pressure exerted by concrete at low casting rates. Mater Struct 48:2315–2322
16. Subramaniam KV, Wang X (2010) An investigation on microstructure evolution in cement paste through setting using ultrasonic and rheological measurements. Cem Concr Res 40:33–44
17. Zago G (2018) Characterization of fracture properties of FRCCs at very early ages, MSc thesis, Politecnico di Milano, DICA. (in Italian)

Investigation of the Early Cement Hydration with a New Penetration Test, Rheometry and In-Situ XRD

Ursula Pott[1(✉)], Clemens Ehm[1], Cordula Jakob[2], and Dietmar Stephan[1]

[1] Building Materials and Construction Chemistry, TU Berlin, Berlin, Germany
u.pott@tu-berlin.de
[2] GeoZentrum Nordbayern, Mineralogy, FAU Erlangen-Nuernberg, Erlangen, Germany

Abstract. To gain more information about the relationship between early cement hydration and rheological behavior of the corresponding cement paste, a new penetration test device, with the name "Multipurpose Incremental Loading device" (MILD), has been developed. The construction and the mechanical properties of the device are described in detail. Furthermore, the implementation of a measurement and first results will be discussed, and the new device is compared with the standardized Vicat test. In addition, a comparison of the measurement results with rheological investigations is made and the results of quantitative in-situ XRD and calorimetry are integrated for a deeper understanding. We show that it is possible to get more information about the structure formation with the new device than with the Vicat test. Moreover, a comparison with the rheological properties of a cement paste was done. Both methods show two periods with different rheological behavior. During the first two hours the paste shows a slow increase of viscosity which is followed by a strong increase. The results of the penetration test and the rheometer are linked with the formation of hydration products and the heat flow development. This comparison shows that the link between the two periods is the beginning of the acceleration period. Finally, it is concluded that it is possible to get precise information about the early cement hydration with a penetration test.

Keywords: Penetration test · Early cement hydration · Phase formation · Rheology

1 Introduction

The early cement hydration and the developing rheological and mechanical properties of the fresh material have a significant impact on many applications of cementitious products. Nevertheless, the complex processes especially during early cement hydration are barely understood. However, in many areas, it is important to know in detail how a fresh paste or concrete will behave, and which properties can be expected. The relationships between the processes of early cement hydration and the rheological properties of a cement paste are of importance in view of the increasing development of

V. Mechtcherine et al. (Eds.): RheoCon 2019/SCC 2019, RILEM Bookseries 23, pp. 246–255, 2020.
https://doi.org/10.1007/978-3-030-22566-7_29

3D printing of concrete [1, 2]. There are several commonly used penetration tests in the field of civil engineering like the Vicat needle, the Hilti nail gun and the Gillmore needle. Moreover, there are two different types of penetration tests. Some devices measure the penetration resistance at a given speed and other devices measure the penetration depth at a given load [3]. In this paper, we will compare the new device with the most widely used and standardized Vicat test. This method measures the penetration depth whereas the Multipurpose Incremental Loading device (MILD) measure the penetration resistance. Penetration tests can also be considered as rheological investigations [4]. During penetration tests where the penetration depth is measured, the needle is hindered from further penetration by the yield point of the paste. Consequently, the resistance to needle penetration at a given speed is also affected by the yield point [3]. For this study, the chemical processes of early cement hydration are particularly important. These processes is described by Jansen et al. [5].

2 Materials

2.1 Materials

Ordinary Portland cement (OPC, CEM I 42.5 R) provided by HeidelbergCement was used and its chemical and mineral composition are given in Table 1. The specific surface measured by Blaine is 3699 $cm^2/g \pm 23$ cm^2/g and deionized water was used.

Table 1. Phase content (QXRD) and chemical composition (XRF).

Phase	wt%	Phase	wt%	Oxide	wt%	Oxide	wt%
Alite	57.4	Anhydrite	2.5	CaO	64.33	Na_2O	0.20
Belite	14.0	Bassanite	2.5	SiO_2	20.51	K_2O	0.74
C_3A_{cubic}	6.6	Gypsum	–	Al_2O_3	5.28	SO_3	2.96
$C_3A_{orth.}$	3.1	Calcite	3.4	Fe_2O_3	2.49	TiO_2	0.29
Arcanite	0.7			MgO	1.4		

2.2 Sample Preparation

Cement paste was prepared with 650 g cement and a water to cement ratio of 0.36 under 20.0 °C ± 0.3 °C and a relative humidity of 65%. A stand mixer (Kitchen Aid, Type 5K45) was used to prepare the sample with the following process: The mixing procedure started after the water addition. It started at level 1 (58 rounds per minute (rpm)) for 15 s. After that the speed was increased to level 4 (125 rpm) for 45 s and then level 10 (220 rpm) for 30 s. This was followed by a 90 s break to rid the edges of the bowl of cement paste. The last step involves mixing at level 10 for another 60 s.

3 Methods

3.1 Multipurpose Incremental Loading Device (MILD)

3.1.1 Construction

The MILD was designed and built at the TU Berlin. With this device two different measurements can be performed. The first one is a compressive strength test for small sample cubes and the second one is a penetration test with constant penetration speed. In this paper, we will focus on the penetration test of cement past. The device is combined by the following parts: The stepper motor drive, the pistil with the penetration needle, the casing of electronic control unit, the sample table and the cantilever under the table (Fig. 1a). The stepper motor drives the vertically mounted revolving ball spindle (propulsion accuracy > 200 μm). On the spindle, a head is attached with a stamp plate, which can move up and down. In this stamp different needles can be clamped (Fig. 1b). The downward movement forces the needle into the sample, which is located on the sample table. The table is fitted on a cantilever. On the top of the cantilever are electrical conductors through which an electric current flow. Stretching the cantilever also stretches the conductor. As a result, the voltage and thus the resistance increases. Once calibrated, this allows the measurement of the applied force by the analysis of the resistance. Through the progress of hydration, the resistance to penetration of the sample increases. This increasing force is measured as a function of time.

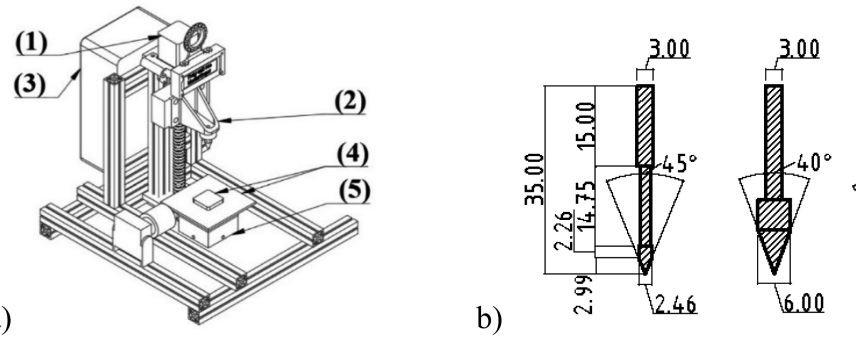

Fig. 1. (a) MILD (1) stepper motor drive (2) needle (3) electronic control unit (4) sample table (5) cantilever under the table (b) needle 1 (left), needle 2 (right).

3.1.2 Implementation

For a measurement a mould with a diameter of 9 cm and a height of 3 cm was filled with cement paste directly after mixing. The measurement started 10 min after water addition. The head with the needle automatically goes up and down (speed: 0,7 mm/s). However, the sample has to be moved manually, and the needle must be cleaned after each measurement. The maximum force that can be measured is 100 N.

3.1.3 Error Analysis

When developing a prototype, taking errors into account is essential. A correct interpretation of the results can only be ensured by a comprehensive examination of the errors. A major error during a measurement is the fact that the table, which is fixed on a cantilever, travels under the load. Due to the force exerted by the needle on the mould and thus on the table and the cantilever, the table moves downwards by a certain length. Therefore, the needle does not reach the set depth, but only the depth minus the deformation of the cantilever. Consequently, it is possible that the force at the exact depth would be greater than the force at the indeed depth. To evaluate this error, the deformation of the cantilever is recorded prior to each measurement. A calculation has shown that this leads to an error of 0.5%. The measurements of the cantilever are dependent on the temperature. Since the device is operated in an air-conditioned room this error is negligible. Another error can be caused by the stepper motor drive system. There is a speed range where the motor runs smoothly. If the motor is forced to move in very high or low speeds it is possible that the motor skip steps. Due to test runs with high and low speeds, it is expected that this error is negligibly small in the performed experiments. Since the MILD is a prototype, further errors may occur which have not been considered before. For this reason, a maximum error of 0.5 is increased tenfold, so that an error of 5.0% is assumed.

3.2 Vicat

The method for the determination of the initial and the final setting of a cement paste is a standardized procedure (EN 196-3) [6]. According to this standard, the procedure must be carried out at the w/c-ratio determined by the standard stiffness, defined by the same standard, which was in this case at a w/c-ratio of 0.31. To ensure comparability with the other tests of this work, it has deviated from the standard and the Vicat method was carried out at a w/c-ratio of 0.36. In addition, the sample preparation was carried out as described in Sect. 2.2. Initial and final setting were determined as described in the standard.

3.3 Rheology

The rheological measurements are carried out using a speed controlled rotational rheometer (Viskomat NT, Schleibinger, Germany). During a measurement the cement paste flows around the stationary paddle and generates a torque, which can be measured. The measuring range of the torque is between 0 and 500 Nmm and the range of the speed is between 0.001 rpm and 400 rpm. The used geometry is a fish bone paddle. For the investigation of the early cement hydration longer measurements were performed. For this purpose, a velocity of 0.001 rpm was run every half hour. Since the first formed crystals should not be destroyed, pre-shear was waived. For each measurement a new sample was prepared and stored at 20 °C.

3.4 In-Situ QXRD

In order to examine the phase evolution in the first hours of the cement hydration in-situ XRD measurements were performed (20 °C ± 0.2 °C). The sample was covered by a 7.5 µm thick Kapton® polyimide film to avoid water evaporation and CO_2 intake of the paste. The diffraction patterns were recorded every 10 min by a Bruker AXS D8 Advance diffractometer in Bragg-Brentano geometry from 7° to 55° 2Θ and a step width of 0.0236° 2Θ. Three preparations were measured over a time frame of 6 h. The Rietveld analysis was performed using the software TOPAS 5.0 (Bruker AXS). The external standard G-Factor method [7] was used to gain absolute amounts of the crystalline phases present in the paste.

3.5 Heat Flow Calorimetry

A TAM Air calorimeter was used to measure the heat flow evolution of the system at 20 °C ± 0.2 °C. A custom made InMixEr [8] device was used which allows equilibration, injection of water and mixing inside the calorimeter. This experimental setup enables the proper detection of the heat flow directly from the time of mixing on. Cement and water were mixed to a paste at 860 rpm for 1 min. Three measurements were performed.

4 Results and Discussion

4.1 MILD

Two needle sizes were tested, and the results are shown in Fig. 2. The trend line can be determined by using a power-law formula of the type $f(x) = a * x^b$ [9, 10]. It is easy to see that the reproducibility of both needle geometries is very good. As expected, the figure shows that the needle geometry is directly related to the duration of the measurement. The smaller the surface of the needle, the longer a measurement takes. It can be clearly seen that the early period of the measurement can't be described by an exponential function. Based on the results, one can therefore recognize two different periods. In the first period, the force shows a rather small increase and after a certain time, the force increases significantly faster. The second period can be described by an exponential function. A distinction in these two periods was also done by Mantellato et al. [10]. At this point, it can be stated that needle 1 is advantageous if a longer period is interesting. On the other hand, it is less sensitive during the first hours of cement hydration. In this period needle 1 shows almost a plateau. Needle 2 is advantageous if the early cement hydration is important. In the first period it shows a steady increase. The influence of the surface and the angle of the needle tip must be further investigated.

4.2 Comparison to Vicat

Figure 3 shows the result of a Vicat-test and the fitted curves of the MILD. Based on the Vicat-test the initial setting (IS) and the final setting (FS) can be determined. The IS occurs after about 4.8 h and ends after 6.5 h. Up to a time of about 4.5 h, nothing can

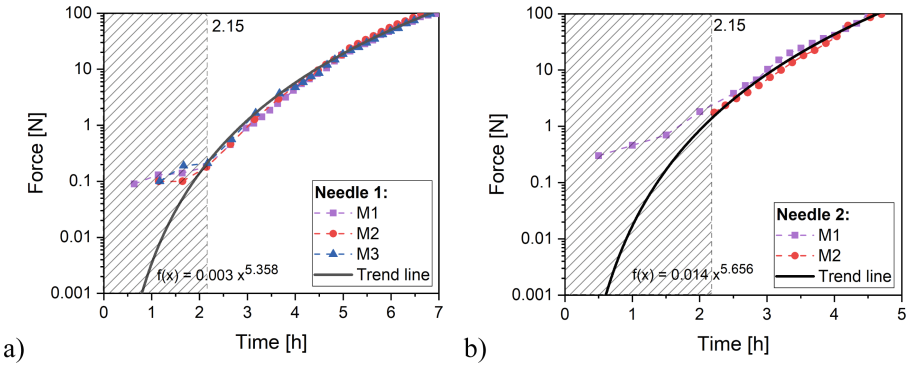

Fig. 2. Results of the MILD test in a logarithmic scale.

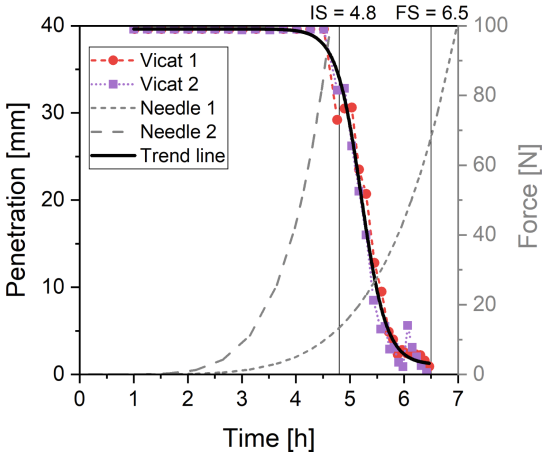

Fig. 3. Results of a Vicat-test and the MILD.

be measured with the Vicat method. The surface of the needle is too small and fully penetrates the paste. From the IS the penetration decreases, which ends with the FS.

In comparison one can get more information about the structure formation and the following increase of the strength and viscosity with the results of the MILD. In the test results of the MILD no significant points can be seen at the time of the initial and final setting determined by Vicat. For that reason, one can conclude that the setting according to Vicat is not caused by a signification change of the structure [11].

4.3 Rheological Measurements

The rheological measurements were carried out up to 4 h after water addition and with a speed of 0.001 rpm. Saake et al. found out that at low speeds it is possible to measure

the elastically deformation of the first formed hydration products till they reach their elastic limit and the bonds start to break [12]. Such a measured curve can be seen in Fig. 4a. Based on this investigation, we assume that we can use this method to measure the microstructure formation (mainly ettringite). However, the peak as shown in Fig. 4a can't be seen so clearly in every measurement. For this reason, the mean of the five last values is used for the evaluation. The results of the rheological measurement show an increasing curve with two different periods (Fig. 4b). The first period starts after the water addition and ends after about 2.15 h. This period is characterized by a rather slow increase in torque and thus in viscosity. The second period starts after about 2.15 h. This period shows a large increase in torque over time. It is interesting to see that the rheological measurement shows the same kink at about 2.15 h like the MILD results.

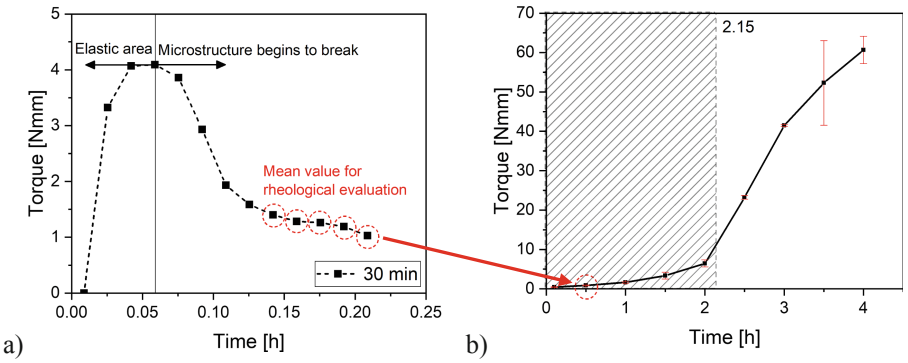

Fig. 4. (a) Result of a rheological measurement after 30 min at a speed of 0.001 rpm (b) Rheological measurement of a cement paste at 20 °C at a speed of 0.001 rpm.

4.4 In-Situ XRD and Calorimetry

Figure 5 shows the phase development measured by in-situ QXRD and the heat flow evolution of the cement paste during the first 6 h of hydration. In the first 2.15 h no significant decrease in the amount of alite can be observed. Afterwards it shows a steadily increasing reaction rate. In the first hours there is no significant precipitation of portlandite. The determined contents are below the detection limit of 0.5 wt%. Over the whole measured time frame no C-S-H-Phase can be detected, even though it can be expected from the dissolution of alite and portlandite precipitation. This is caused by the used phase model published by Bergold et al. [13] for the Rietveld refinement which is just capable for the dimeric or "long-range ordered" C-S-H. The earlier precipitated monomeric or "short-range ordered" C-S-H can't be detected by this model [14], but occurs simultaneously with alite dissolution and portlandite precipitation [15].

The onset of the acceleration period of the silicate reaction is related to the beginning of the second heat flow event. After a very high initial heat flow and a subsequent period of low heat release the heat flow starts to increase at 2.15 h. The experimental results so far show no evolution in the silicate reaction (dissolution of alite respectively precipitation of CH and C-S-H) in the first 2.15 h. Alite content is

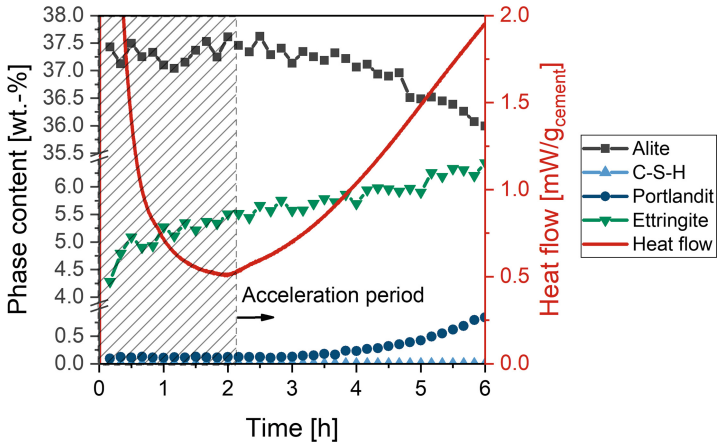

Fig. 5. Alite, C-S-H, portlandite and ettringite (QXRD) and heat flow (calorimetry).

constant up to 2.15 h. The only phase which develops considerably during this period is the hydration product of the aluminate reaction, ettringite. The precipitation of ettringite starts directly after the addition of water. After around 2.15 h the second period starts. Ettringite content is still increasing during that period. Now alite is dissolving after about 2.15 h and the formation of portlandite can be detected after 3.5 h indicating the start of the formation of C-S-H.

5 Conclusion

5.1 Advantages of the New Penetration Test Device

In this study a new penetration test device was investigated. Based on the results, the development of early cement hydration can be better investigated than with the standardized Vicat test. It is possible to measure the early and sensitive phase formation with a penetration test device and to determine the beginning of the acceleration period. By being able to use different needle geometries very sensitive changes in cement hydration can be measured. The results correlate perfectly with those of other measurement methods such as rheometry, QXRD and calorimetry (Fig. 6). Consequently, this device can lead to a better understanding of early cement hydration.

5.2 Comparison with the Formation of Hydration Products

According to the present data two periods of different rheological regimes can be observed by either MILD or rheometer as shown in Fig. 6. Period 1 (0–2.15 h) with low slope for MILD and rheometer measurements is due to formation of ettringite. Period 2 (2.15 h–6 h) with high slope for MILD and rheometer measurements is correlated with ongoing formation of ettringite and additionally related to the C-S-H formation (indicated by dissolution of alite).

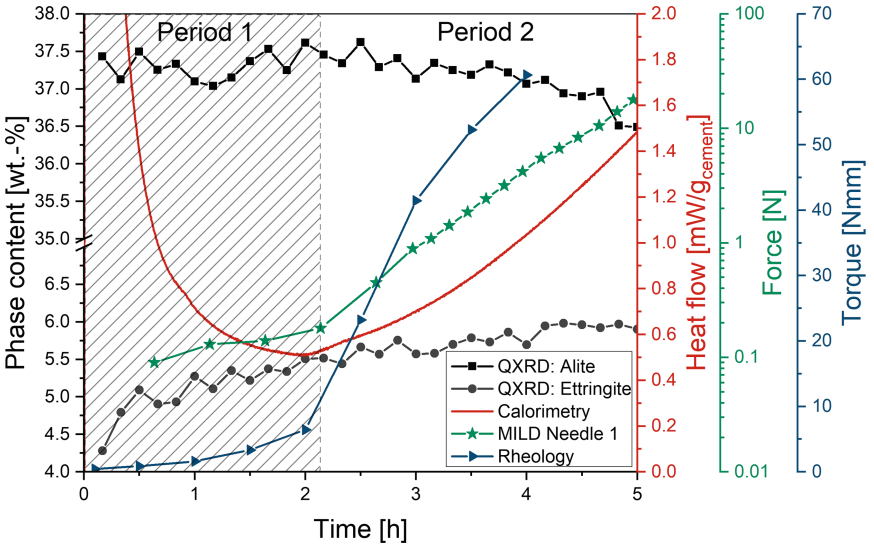

Fig. 6. Conclusion of the results of QXRD, calorimetry, MILD and rheometry.

Acknowledgement. The author would like to thank the German Research Foundation (DFG) for funding the priority program Opus Fluidum Futurum – Rheology of reactive, multiscale, multiphase construction materials (SPP 2005) (STE 1086/181; NE 813/7-1) and HeidelbergCement for providing the materials.

References

1. Wangler T, Lloret E, Reiter L, Hack N, Gramazio F, Kohler M, Bernhard M, Dillenburger B, Buchli J, Roussel N, Flatt RJ (2016) Digital concrete: opportunities and challenges. RILEM Tech Lett 1:67–75
2. Roussel N (2018) Rheological requirements for printable concretes. Cem Concr Res 112:76–85
3. Lootens D, Jousset P, Martinie L, Roussel N, Flatt RJ (2009) Yield stress during setting of cement pastes from penetration tests. Cem Concr Res 39:401–408
4. Boujlel J, Coussot P (2012) Measuring yield stress: a new, practical, and precise technique derived from detailed penetrometry analysis. Rheol Acta 51:867–882
5. Jansen D, Naber C, Ectors D, Lu Z, Kong X-M, Goetz-Neunhoeffer F, Neubauer J (2018) The early hydration of OPC investigated by in-situ XRD, heat flow calorimetry, pore water analysis and ^{1}H NMR: learning about adsorbed ions from a complete mass balance approach. Cem Concr Res 109:230–242
6. Deutsches Institut für Normung (2017) Prüfverfahren für Zement: Teil 3: Bestimmung der Erstarrungszeiten und der Raumbeständigkeit; Deutsche Fassung EN 196-3:2016
7. Jansen D, Goetz-Neunhoeffer F, Stabler C, Neubauer J (2011) A remastered external standard method applied to the quantification of early OPC hydration. Cem Concr Res 41:602–608

8. Hertel T, Neubauer J, Goetz-Neunhoeffer F (2016) Study of hydration potential and kinetics of the ferrite phase in iron-rich CAC. Cem Concr Res 83:79–85
9. Flatt RJ, Larosa D, Roussel N (2006) Linking yield stress measurements: spread test versus Viskomat. Cem Concr Res 36:99–109
10. Mantellato S, Palacios M, Flatt RJ (2019) Relating early hydration, specific surface and flow loss of cement pastes. Mater Struct 52:5
11. de Oliveira Romano RC, Hark Maciel M, Pileggi RG, Alba Cincotto M (2017) Monitoring of hardening of Portland cement suspensions by Vicat test, oscillatory rheometry and isothermal calorimetry. Appl Rheol 27:28–37
12. Saak AW, Jennings HM, Shah SP (2001) The influence of wall slip on yield stress and viscoelastic measurements of cement paste. Cem Concr Res 31:205–212
13. Bergold ST, Goetz-Neunhoeffer F, Neubauer J (2013) Quantitative analysis of C-S–H in hydrating alite pastes by in-situ XRD. Cem Concr Res 53:119–126
14. Bergold ST, Goetz-Neunhoeffer F, Neubauer J (2015) Mechanically activated alite: new insights into alite hydration. Cem Concr Res 76:202–211
15. Jansen D, Goetz-Neunhoeffer F, Lothenbach B, Neubauer J (2012) The early hydration of Ordinary Portland Cement (OPC): an approach comparing measured heat flow with calculated heat flow from QXRD. Cem Concr Res 42:134–138

Use of Combined Rheo-NMR to Investigate the Relationship Between the Molecular and Mechanical Properties of Early Cement Paste Hydration

Nonkululeko W. Radebe, Karl-Friedrich Ratzsch, Christopher O. Klein, and Manfred Wilhelm(✉)

Institute for Chemical Technology and Polymer Chemistry, Karlsruhe Institute of Technology, Karlsruhe, Germany
{nonkululeko.radebe,manfred.wilhelm}@kit.edu

Abstract. The in-situ combination of rheological measurements with solid-state NMR as a second characterization method is used to gain unique information about molecular dynamics and structure of time-dependent phenomena. This study aims to show the application of low field benchtop ^{1}H NMR relaxometry combined with rheology to investigate the hydration and hydration kinetics of cement pastes. Here the relationship between the storage modulus, G′ and transverse, T_2, ^{1}H-NMR relaxation rates in different water environments that exist during early hydration of cement paste at different water to cement ratios is presented. In addition, the rate of rigidification and percolation time are determined from the dynamic time sweeps at a strain within the linear viscoelastic region.

Keywords: Cement paste · SAOS · Proton mobility · Rheo-NMR

1 Introduction

Small amplitude oscillatory shear (SAOS) testing can be used to monitor the structural build-up of cement paste at rest [1, 2]. During the SAOS test, a sample is exposed to a continuous sinusoidal excitation of either a given deformation or a given shear stress. The mechanical response of either shear stress or deformation, respectively of the material is measured to evaluate the structural build-up of the material. When the applied excitation is very low, and the material therefore is still within the linear viscoelastic regime, the test will not interfere with the structure of the material and can be considered a non-destructive method. Consequently, SAOS can be used to mechanically probe the material microstructure at rest. A SAOS test result in the material functions of G′(t, ω, γ_o) and G″(t, ω, γ_o) to describe the material within the viscoelastic region [3]. For this reason, SAOS tests provide very useful and convenient rheological characterization of complex fluids such as cement paste. Cement paste can be studied at many different levels in time and length scale ranging from the molecular structure in nanometres to large e.g. steel reinforced structures in the metres range. At each level, there are different phases that exist in the material from the calcium-silicate-hydrate (C-S-H) gel structure

V. Mechtcherine et al. (Eds.): RheoCon 2019/SCC 2019, RILEM Bookseries 23, pp. 256–265, 2020.
https://doi.org/10.1007/978-3-030-22566-7_30

to coarse aggregates within the centimeter range. In this work, we aim to probe the microstructural changes of cement paste during the first few hours of hydration by monitoring the changes in the ^{1}H magnetisation transverse relaxation [4–7] within a given pore volume. The physical metamorphosis in the form of structuration is addressed with rheology and the hydration chemistry with nuclear magnetic resonance (NMR) relaxation analysis. NMR relaxometry is a non-destructive and non-invasive method for pore water analysis. Mobile water within a less confined space will have slow relaxation times and more confined water will have faster relaxation times. Rheo-NMR is a unique tool that simultaneously measures the mechanical behaviour, using a strain-controlled rheometer, and the relaxation properties with a low-field NMR spectrometer [8]. The rheology corresponds to macromolecular properties at a timescale of seconds and the molecular mobility in the form of ^{1}H transverse relaxation time takes place at a timescale that is between 50 μs and several hundred ms. This unique combination leads to new insights into the relationship between macroscopic rheometric observables and microscopic molecular dynamics. With this Rheo-NMR combination, Räntzsch et al. [9] characterized and quantified the crystallization of iPP at different temperatures.

2 Experiments

2.1 Materials

Portland cement type CEM I 42,5 R was used in together with distilled water. A mass of 3.5 g was used for each mixture. The plain cement paste was mixed by hand during 2 min and then placed into the plate geometry. Reproducibility is possible within a logarithmic scale.

2.2 Oscillatory Rheology

A conventional strain-controlled rheometer (ARES G2, TA-Instruments) is used to perform oscillatory rheological measurements of the cement paste as a function of time (and at various water to cement (w/c) ratios. A plate-plate geometry (d = 25 mm) is used. The plate gap was kept in the range on 1.5 mm. Two types of oscillatory shear tests were carried to investigate the appropriate ranges in the strain amplitude (γ_o) and angular frequency ω of cement pastes by SAOS tests, i.e. oscillatory amplitude sweep test and oscillatory frequency sweep test. The linear (SAOS) region was tested by performing an oscillatory stress sweep from $\gamma_o = 4 \times 10^{-5}$ to $\gamma_o = 0.5$. Thereafter an angular frequency sweep varying from 6.28 rad/s–314 rad/s was performed as seen in Fig. 1. The linear region is dependent on the frequency, the temperature and the state of the sample. The temperature was kept constant at 22 °C ± 0.1 °C using a Peltier system. Thereafter, a series of time sweeps were done by measuring the amplitude of the waveform associated to the shear stress as a function of hydration time (t) [10], presented as the storage modulus, G′, as a function of time.

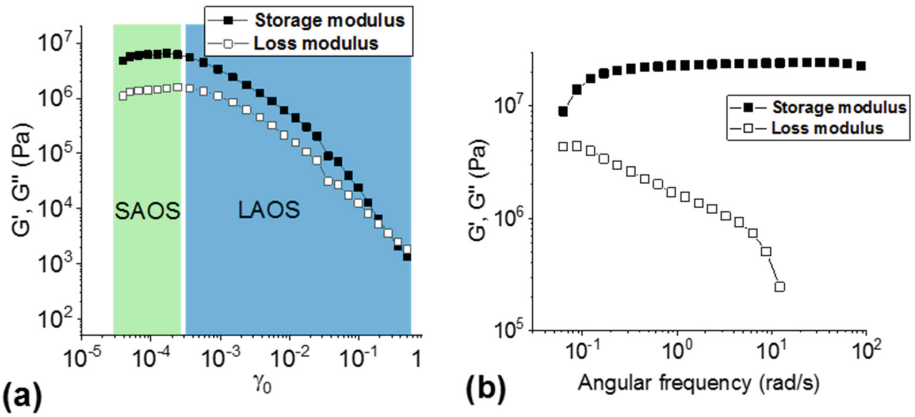

Fig. 1. (a) Oscillatory strain sweep of fresh cement paste 62.8 rad/s and *w/c* = 0.40 (b) Oscillatory frequency sweep of fresh cement pastes at 0.05% strain and *w/c* = 0.40.

2.3 NMR Measurements

A Bruker Minispec mq20 ND-Series, with a 0.5 T magnetic field operating at a ^{1}H resonance frequency of 19.95 MHz was used for NMR measurements. The probe was temperature-controlled 23 °C–25 °C via a thermostated gas flow. The sample was placed in a 22 cm × 0.9 cm glass tube. It was filled to a height of 1.5 cm. In order to get the T_2 distribution, longitudinal proton magnetization decays because of the NMR signal relaxation were measured by means of a combined magic sandwich echo (MSE) and Carr, Purcell, Meiboom, Gill (CPMG) pulse sequence as seen in Fig. 2(a).

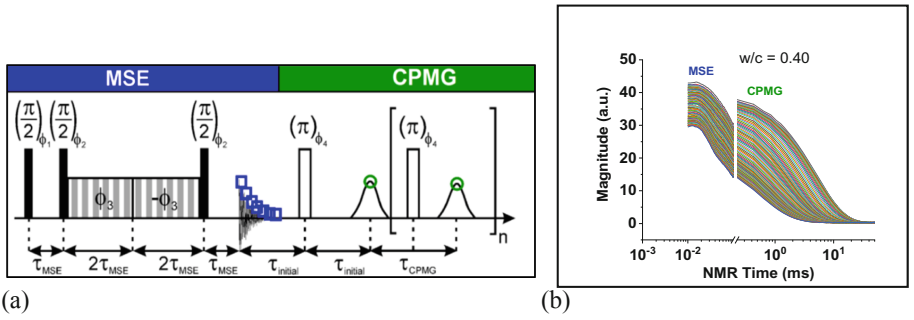

Fig. 2. (a) Combined MSE-CPMG pulse sequence [11] and (b) example of acquired raw data.

The MSE refocuses the initial transverse magnetization of the complete sample over the dead time of the NMR probe after a 90° pulse [11]. The magnetization is measured as the echo refocuses the magnetization of the protons in the sample. Therefore, the relative intensity can give an indication of the amount of protons that have evaporated and those remaining in the sample as hydration products or confined

water [12]. The CPMG refocuses the more mobile protons in the sample. The acquired relaxation curve (Fig. 2) was evaluated regarding the relative intensity of the MSE and CPMG decay curve. For this, a combined Gaussian-exponential (Eq. 1) and bi-exponential (Eq. 2) decay function was used, respectively.

$$I_{\mathrm{mse}}(t) = I_{soild}^{\left(-\frac{t-t_0}{T_{2,solid}}\right)^2} - I_{C-S-H}^{-t/T_{2,C-S-H}} \tag{1}$$

$$I_{cpmg}(t) = I_{gel\,pore}^{-t/T_{2,gel\,pore}} + I_{mobile\,water}^{-t/T_{2,mobile\,water}} \tag{2}$$

2.4 Rheo-NMR Measurements

A plate-plate geometry (d =13 mm) used and an oscillatory strain amplitude 0.05%, ω = 6.28 rad/s is applied to the cement paste. The parallel-plate tool was built in-house from machinable ceramics (Vitronit of Vitron Spezialwerkstoffe GmbH, Germany), see schematic in Fig. 3.

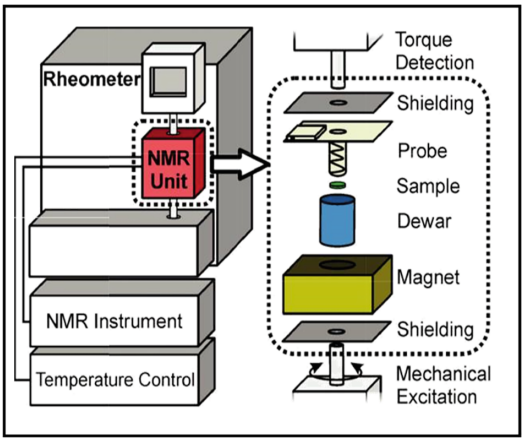

Fig. 3. Schematic overview of the developed Rheo-NMR setup in the TA ARES rheometer.

3 Results and Discussion

3.1 SAOS and Offline NMR

Oscillatory time sweep tests were carried out at an angular frequency of 6.28 rad/s and strain of 0.3%. The values of G′, G″ and were monitored continuously, as shown in Fig. 4. Each test was started 2.5 min after the cement made contact with the water and it

lasted for 90 min. 30 s was given to mounting the sample and starting the experiment after mixing. The storage modulus at $t = 0$ in Fig. 4(a) is related to the water content in each sample. The sample with the highest water content ($w/c = 0.48$) is the least viscous and has a G′ of 10^4 Pa. At around 10 s of hydration time, the modulus begins to increase for all the samples at a similar rate. The increase is expected because with time the sample hardens and therefore becomes more and more elastic. It is important to mention that sedimentation for the higher w/c ratio ($w/c = 0.48$), sedimentation was not observed. This phenomenon is expected to be seen with a decrease in the G′ or a build-up of water on the bottom plate. After 90 min, the storage modulus for all three samples has increased to 10^6–10^7 Pa. This corresponds to the increase in the rigidity of the samples caused by structural build up. Structural build up is a complex physiochemical process [13] and needs to be described both physically and chemically. The latter is addressed by means of offline ^{1}H NMR relaxometry. For this, we prepared a water to cement ratio (w/c) of 0.40 and measured the T_2 values corresponding to different water environments as seen in Fig. 4(b). It is important to note that an oscillatory time sweep is limited because the sample becomes more and more solid-like at which point the flow properties are no longer measurable.

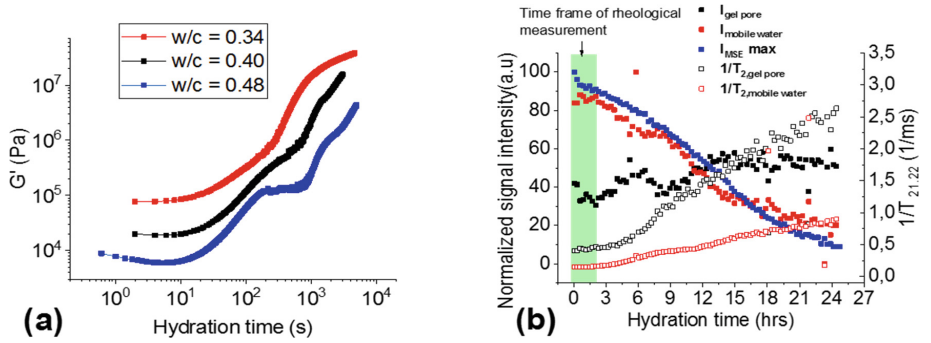

Fig. 4. (a) The evolution of the storage modulus (G′) for cement pastes subjected to 0.3% strain and 1 Hz frequency using 25 mm plate-plate and (b) evolution of the signal intensity and $1/T_{2,\ gel\ pore}$ over 24 h after water is added to the cement paste w/c = 0.40.

The MSE relative signal intensity as seen in Fig. 4(b) is indicative of the total amount of protons within the sample. It decreases by approximately a third in 24 h. This indicates that there is a loss in protons. This could be explained by evaporation of water due to the set-up. To eliminate this effect, an enclosed tube with a total height of 2 cm and can be fitted inside the 20 cm × 9 mm glass tube. The NMR signal is processed and interpreted such that there are four populations of water [14]. However, it is important to note that not all can be distinctly seen within the first 24 h of hydration as some products are only beginning to form after this time. The first is attributed to the Gaussian part of the MSE FID as a spin-spin relaxation rate in the order of 100 ms^{-1} [4]. Table 1 shows that after 24 h in the MSE part, this component has formed. It is attributed to the ^{1}H chemically combined in the solid crystalline

phases of calcium hydroxide and ettringite. From Table 1, $1/T_{2,solid}$ has increased by almost 4 fold but is lower than 100 ms^{-1}. From this we can assume that the solid phases have begun to form after 24 h but have not fully formed. The second is between 12,5 ms^{-1}–8,3 ms^{-1} which can be associated with the calcium-silicate-hydrate interlayers. Similarly $1/T_{2,C\text{-}S\text{-}H}$ is lower than the expected range of C-S-H interlayers and could be attributed to the above-mentioned reason. The third part is the water in the gel pores with T_2 rates in the range of 3,3 ms^{-1}–2 ms^{-1} as seen in Table 2 for $1/T_{2,gel\ pore}$. Any rate lower than the abovementioned times is considered to be due to 'mobile water'.

Table 1. A table showing the changes in the initial MSE echo as normalized signal intensity and relaxation rates of a sample with a *w/c* = 0.40 over 24 h.

	MSE after 5 s	MSE after 24 h
I_{solid}	100 (a.u)	66.6 (a.u)
I_{C-S-H}	100 (a.u)	43.6 (a.u)
$1/T_{2,solid}$	16.7 (ms^{-1})	62.5 (ms^{-1})
$1/T_{2,C-S-H}$	2.28 (ms^{-1})	6.67 (ms^{-1})

Table 2. A table showing the changes in the CPMG decay as normalized signal intensity and relaxation rates. This shows the heterogeneity of a sample with a *w/c* = 0.40 over 24 h.

	CPMG after 5 s	CPMG after 24 h
$I_{gel\,pore}$	42.1 (a.u)	50.9 (a.u)
$I_{mobile\,water}$	84.0 (a.u)	20.2 (a.u)
$1/T_{2,gel\,pore}$	0.40 (ms^{-1})	2.63 (ms^{-1})
$1/T_{2,mobile\,water}$	0.15 (ms^{-1})	0.90 (ms^{-1})

3.2 Rheo-NMR – Plate-Plate Geometry

In this part of the work it was attempted to investigate the relationship between water mobility and the increase in the storage modulus. Figure 5(a) shows cement paste of different w/c ratios subjected to the same strain as in Fig. 4(a). There is a notably large difference in the $t = 0$ moduli. At $t = 0$ the G′ is between 10^6 and 10^7 Pa as compared to the 10^4 and 10^5 Pa of Fig. 4(a). There are a few differences in the preparation, which could lead to this difference. The first is that a sample is 5 min old by the time the Rheo-NMR experiment starts compared to the 2 min of offline rheology, because the NMR assembly can only be mounted after placement of the sample. The second is the material of the parallel-plate geometry is ceramic for Rheo-NMR and stainless steel for rheology. Ceramic is likely to absorb some water and therefore dry the sample before measurement begins. Lastly, the temperature control of the RheoNMR setup is

achieved by an airflow, leading to an increased loss of water esp. in the outer region of the plate-plate sample geometry. The increase of the G′ begins 10 and 100 s, which is comparable to the samples, measured offline. Within the same time frame the G′ has increased to 10^7 Pa–10^8 Pa, which is higher than that seen in Fig. 4(a).

Figure 5(b) is an overlay of the G′ and the relaxation rate due to partially bound water. Here it is clear the increase in G′ is not visibly related to the relaxation rate. The values within 2 h are comparable to those seen in Fig. 4(b) for offline ^{1}H NMR relaxometry.

However, the signal intensities drop significantly from both the MSE and the CPMG part. As previously mentioned, this is due to a loss in protons attributed to evaporation.

Figure 6 shows correlated Rheo-NMR data. This can give information about the change in G′ and relaxation rate of a cement paste sample over time that is under a specific oscillatory strain at a specific frequency. The initial increase in G′, seen in Fig. 5, is not combined with an increase in relaxation rate. This could mean that the formation of hydration products is not related to the increase in the G′ within the first 1 min (highlighted in yellow Fig. 5(b). Therefore, it can be concluded that in this period, physical interactions are dominant. These interactions could be explained using percolation theory and can be described with a percolation time (t_{perc}) as introduced by Mostafa and Yahia [15]. The percolation time describes the resting period needed for colloidal particles to reach their favourable and equilibrium positions [16].

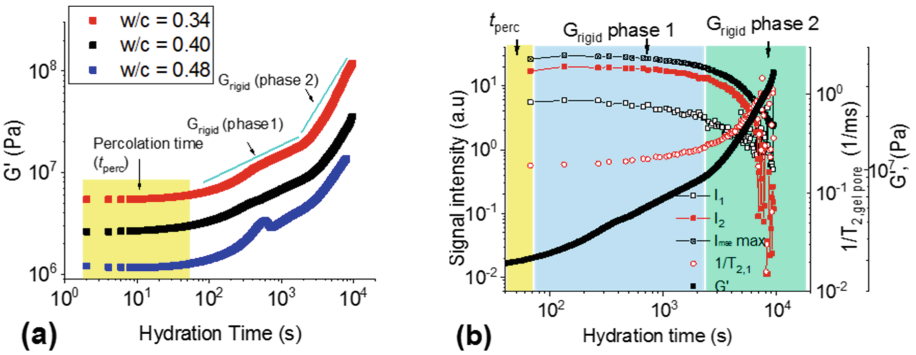

Fig. 5. (a) Evolution of the storage modulus (G′) for three species of different water content subjected to 0.05% strain at 1 Hz using 13 mm plate-plate (Rheo-NMR) and (b) Evolution of $1/T_{2,1}$ and mechanical structure (G′) over 2 h for *w/c* = 0.40. (Color figure online)

The t_{perc} can represent the time needed to build-up a percolated elastic network and allow transition from liquid to solid. In this work, t_{perc} is the time at which the G' and the relaxation rate relationship is pronounced. For all three cement pastes, t_{perc} is approximately 1 min. After the initial steep increase seen in Fig. 6, the curve slope decreases. At this point, the structural build up is due to the combined effects of colloidal structuration from interparticle interactions and chemical rigidification. Chemical rigidification is hardening of cement due to the formation of hydration

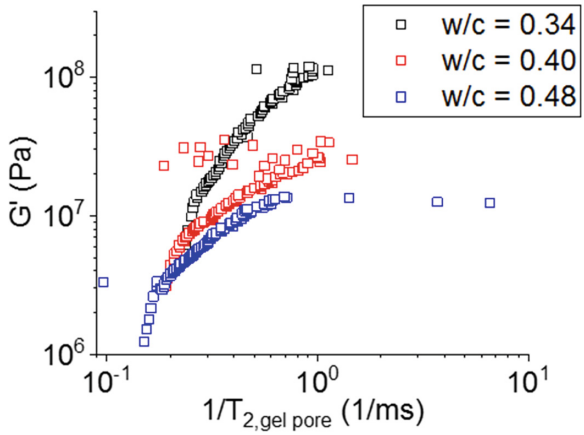

Fig. 6. Correlated G′ and $1/T_{2,gel\ pore}$ over 2 h for *w/c* = 0.34, 0.40 and 0.48.

products. The chemical rigidification rate (G_{rigid}) in Pa/s can therefore be determined as the relationship between G′ and the hydration time from Fig. 5(a). Furthermore, the relationship between G′ and the relaxation rate can be described as an apparent viscosity at rest.

In Table 3, the G_{rigid} in phase 1 and 2 decreases with an increase in water to cement ratio. For the paste with the lowest water content (*w/c* = 0.34) the rigidification rate increases by three times from the first phase to the second phase. The other two cement paste samples rigidification rate only increases by 50%. This indicates that less water leads to faster formation of chemically bound protons in the form of hydrates. This is further confirmed by the steep increase in the relaxation rate of *w/c* = 0.34 in Fig. 6. Furthermore, the apparent viscosities follow the same pattern as the rigidification rate. The sample with the lowest water content has the highest viscosity and therefore presumably more strength.

Table 3. G_{rigid} and apparent viscosity of three cement pastes.

	G_{rigid} phase 1(Pa/s)	G_{rigid} phase 2(Pa/s)	'Apparent' viscosity (Pa.s)
0.34	4719	1415	$1{,}54 \times 10^5$
0.40	1920	3666	$2{,}81 \times 10^4$
0.48	1027	1733	$2{,}49 \times 10^4$

4 Conclusions

The new and unique combination of rheological testing and ^{1}H NMR relaxometry on hydrating cement pastes is a promising tool to investigate the relation between macroscopic structure formation and the underlying chemical processes leading to

changes in the water mobility on a broad timescale. From this study, it is clear the proton mobility is partially responsible for the increase in the storage modulus, G′. The process of percolation followed by rigidification. It is yet unclear if the percolation time has a direct relationship with the w/c ratio because in this work, the t_{perc} are all within the same time range. The comparability of results to known findings on separately conducted measurements is currently limited to the initial period of setting, because of the uneven sample drying of the open plate-plate sample geometry. However, it is possible with this method to quantitatively describe structural build up. A new, closed toolset with coutette geometry is currently being developed, and should greatly alleviate the problem of drying. By eliminating the effect of evaporation, a more reliable quantification can be presented and give more accurate insight on the predicted strength of the cement paste.

Acknowledgments. The authors thank the Deutsche Forschungsgemeinschaft (DFG) SPP 2005 "Opus Fluidum Futurum" for funding.

References

1. Yuan Q, Lu X, Khayat KH, Feys D, Shi C (2017) Small amplitude oscillatory shear technique to evaluate structural build-up of cement paste. Mater Struct 50:112
2. Yuan Q, Zhou D, Khayat KH, Feys D, Shi C (2017) On the measurement of evolution of structural build-up of cement paste with time by static yield stress test vs. small amplitude oscillatory shear test. Cem Concr Res 99:183–189
3. Hyun K, Wilhelm M, Klein CO, Cho KS, Nam JG, Ahn KH, Lee SJ, Ewoldt RH, McKinley GH (2011) A review of nonlinear oscillatory shear tests: analysis and application of large amplitude oscillatory shear (LAOS). Prog Polym Sci 36:1697–1753
4. Muller ACA, Scrivener KL, Gajewicz AM, McDonald PJ (2013) Densification of C-S-H measured by 1H NMR relaxometry. J Phys Chem C 117:403–412
5. McDonald PJ, Gajewicz AM, Morrell R (2017) The characterisation of cement based materials using T2 1H nuclear magnetic resonance relaxation analysis. Meas Good Pract Guid 144. http://www.npl.co.uk/content/ConPublication/7369
6. Valori A, McDonald PJ, Scrivener KL (2013) The morphology of C-S-H: lessons from 1H nuclear magnetic resonance relaxometry. Cem Concr Res 49:65–81
7. McDonald PJ, Rodin V, Valori A (2010) Characterisation of intra- and inter-C-S-H gel pore water in white cement based on an analysis of NMR signal amplitudes as a function of water content. Cem Concr Res 40:1656–1663
8. Ratzsch K-F, Friedrich C, Wilhelm M (2017) Low-field Rheo-NMR: a novel combination of NMR relaxometry with high end shear rheology. J Rheol 61:905–917
9. Räntzsch V, Özen MB, Ratzsch KF, Stellamanns E, Sprung M, Guthausen G, Wilhelm M (2018) Polymer crystallization studied by hyphenated rheology techniques: Rheo-NMR, Rheo-SAXS, and Rheo-Microscopy. Macromol Mater Eng 1800586:1–14
10. Varshney A, Gohil S, Chalke BA, Bapat RD, Mazumder S, Bhattacharya S, Ghosh S (2017) Rheology of hydrating cement paste: crossover between two aging processes
11. Maus A, Hertlein C, Saalwächter K (2006) A robust proton NMR method to investigate hard/soft ratios, crystallinity, and component mobility in polymers. Macromol Chem Phys 207:1150–1158

12. Ey H (2011) PhysRevB.3.684 331:1–19. papers2://publication/uuid/A5160E39-7EC8-4CF6-9067-DF471DB15367
13. Mostafa AM, Yahia A (2017) Physico-chemical kinetics of structural build-up of neat cement-based suspensions. Cem Concr Res 97:11–27
14. Bortolotti V, Fantazzini P, Mongiorgi R, Sauro S, Zanna S (2012) Hydration kinetics of cements by time-domain nuclear magnetic resonance: application to Portland-cement-derived endodontic pastes. Cem Concr Res 42:577–582
15. Mostafa AM, Yahia A (2016) New approach to assess build-up of cement-based suspensions. Cem Concr Res 85:174–182
16. Coussot P (2005) Rheometry of pastes, suspensions, and granular materials: applications in industry and environment. Wiley, Hoboken

Calibration of ASTM C230 Cone for Measuring Flow Diameter of Self-flowing Mortar According to the EFNARC Recommendation

Shamir Sakir[1], Sudharshan N. Raman[1,2(✉)], A. B. M. Amrul Kaish[3], and Azrul A. Mutalib[1]

[1] Smart and Sustainable Township Research Centre (SUTRA), Faculty of Engineering and Built Environment, Universiti Kebangsaan Malaysia, Bangi, Selangor, Malaysia
snraman@gmail.com
[2] Centre for Innovative Architecture and Built Environment (SErAMBI), Faculty of Engineering and Built Environment, Universiti Kebangsaan Malaysia, Bangi, Selangor, Malaysia
[3] Department of Civil Engineering, Infrastructure University Kuala Lumpur, Kajang, Selangor, Malaysia

Abstract. Proper design of mixing proportions is the key factor to appreciate the benefits and advantages of self-compacting concrete (SCC). Determining a proper water-to-powder ratio is a crucial step in designing SCC. Mini slump flow test of mortar, as recommended by the EFNARC, is popularly used to check the water-to-powder ratio in the design process. The dimensions of the EFNARC recommended cone is slightly different from the widely available ASTM C230 cone. This study is an attempt to find a correlation between the test results of these two cones. Using the same fresh mixtures, two sets of data were collected using both cones. The correlation factor was determined using these data and verified by theoretical calculation. A proper correlation will allow the use of ASTM cone in the design of SCC. As the ASTM recommended cone is commonly available in most concrete laboratories, its application in SCC related studies will reduce the need of fabrication of new equipment, as well as, using the same cone to test the slump flow of both conventional workability and self-compacting mortar will allow the experts to come up with simplified test procedures and guidelines for the fresh property of mortar for the whole workability range.

Keywords: Concrete · Mortar · Self-compacting mortar · Slump flow · Workability

1 Introduction

Self-compacting concrete (SCC) has emerged to ensure the durability of concrete structures, as there is a strong correlation between the durability and sufficient compaction of concrete [1]. Additional advantages (i.e.: reduced labour and time

V. Mechtcherine et al. (Eds.): RheoCon 2019/SCC 2019, RILEM Bookseries 23, pp. 266–272, 2020.
https://doi.org/10.1007/978-3-030-22566-7_31

requirements, ease of concreting in densely reinforced members, narrow sections and complex shaped places, noise reduction, smooth surface finish, etc.) has made SCC popular in the industry very quickly. The global market of SCC was of USD 8.74 billion in 2016 and expected to reach USD 11.67 billion by 2023 [2]. This huge market demand and its potential of growth have attracted many researchers to investigate different aspects of SCC.

SCC is distinguished from the conventional concrete by its filling ability, passing ability and segregation resistance. Such concrete must have excellent deformability, low risk of blockage and good stability [3]. To ensure these properties, mix design of SCC requires much more expertise than its conventional counterpart. Okamura et al. [4] established the guidelines for mixing proportions of SCC. Later, most of them were included in the "Specification and guidelines for self-compacting concrete" by the European Federation, EFNARC and after that, in the "European guidelines for self-compacting concrete" [5, 6]. The recommended design procedure requires flow tests of mortar to adjust the water-to-powder ratio and superplasticiser dosage of SCC. The guideline provides detailed specification of the flow measuring cone and acceptable limits of flow diameter of mortar.

The dimensions of the EFNARC recommended cone for measuring flow diameter of mortar for SCC are very close to the dimensions of the cone recommended by ASTM C230 [7] for measuring flow of conventional mortar. Figure 1 shows the dimensions of both cones. The base and top diameters for both cones are same, 100 mm and 70 mm respectively. Only difference is in the height, 60 mm for EFNARC cone and 50 mm for ASTM C230 cone [6, 7]. As an apparatus of a basic test, ASTM C230 cone is widely available in civil engineering laboratories that follow ASTM standards. On the contrary, the cone recommended by EFNARC is available in the laboratories where SCC has been studied or European standards are followed, as this cone is used in EN 1015-3 [8]. Besides the availability issue, the similar dimensions of these two cones causes confusion sometimes.

This present study is focused to find a correlation between these two cones. Flow diameters of the same mortar mixtures were measured by both cones, according to EFNARC guideline. Then the diameters were compared to find a correlation factor. The correlation factor was verified by theoretical calculations. A similar study was conducted by Roussel et al. (2005) to find a correlation between the plastic yield value and flow spread of cement-based materials [9]. At first, the relationship was developed and verified using smaller sized ASTM C230 cone for cement pastes and grouts. Then the proposed correlation was applied to the Abrams cone and fresh concrete [9].

A correlation between these two cones will allow the researchers to conduct experiments on the SCC using ASTM C230 cone. As ASTM has not provided any guideline for self-flowing mortar yet, this correlation will be helpful to many researchers. Besides that, this correlation will eliminate the chances of confusion between two cones.

2 Theoretical Relationship

This section presents theoretical derivation of a correlation factor between the cones, considering their volumes. The thickness of the mortar flow spread is considered constant in both cases.

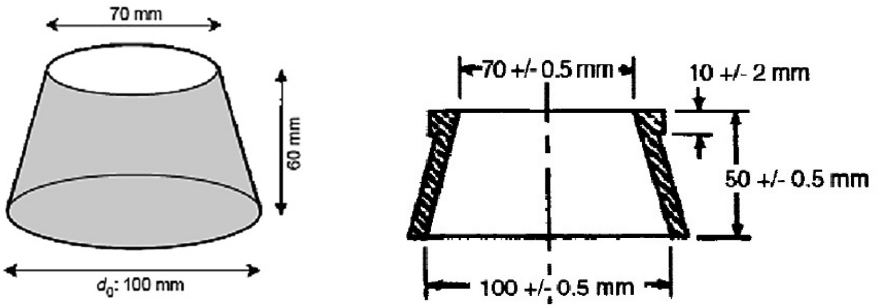

Fig. 1. Dimensions of cone recommended by (a) EFNARC [6] and (b) ASTM C230 [7].

Volume of ASTM cone, $V_A = \frac{1}{8}\pi\left((100)^2 + (70)^2\right) \times 50\,\text{mm}^3 = 292,560.8\,\text{mm}^3$
Volume of EFNARC cone, $V_E = \frac{1}{8}\pi\,(100)^2 + (70)^2) \times 60\,\text{mm}^3 = 351,073.0\,\text{mm}^3$
So,

$$\begin{gathered} \frac{V_A}{V_E} = 0.833 \\ \text{or, } V_A = 0.833\,V_E \\ \text{or, } \tfrac{1}{4}\pi D_A^2 T = 0.833\,\tfrac{1}{4}\pi D_E^2 T \\ \text{or, } D_A^2 = 0.833 D_E^2 \\ \text{or, } D_A = 0.913 D_E \end{gathered} \tag{1}$$

Where,

V_A = Volume of ASTM C230 cone.
V_E = Volume of EFNARC cone.
D_A = Flow diameter measured by ASTM C230 cone.
D_E = Flow diameter measured by EFNARC cone.
T = Thickness of flow spread of mortar.

3 Experimental Program

3.1 Materials

Ordinary Portland cement (OPC) of grade 42.5 MPa was used. Sand was local river sand with a maximum aggregate size of 2 mm. A superplasticiser (SP) was added to

enhance flowability. To produce stable mixture with high dosage of SP, commercially available silica fume (SF) was added in some mixtures.

3.2 Mix Proportions

Binder-to-sand ratio of 1:1.5 (w/w) and water-binder ratio of 0.40 were used in all the mixes. The SP content were varied from 0.6%–1.5% by weight of the binder. In some samples, 10%–12% of OPC was replaced with silica fume. Table 1 shows the detailed mix proportions of the mortar mixtures.

3.3 Test Methods

Cementitious mortar samples were produced using the same mixing machine. First, the cement and sand were mixed separately. Then all the water and superplasticiser were added to the mixer. The solid mixture was added bit by bit to the mixer while the machine was running. A longer mixing time was used to enhance the dispersion of fine particles, thus decreasing the yield stress and plastic viscosity. After mixing, tests on workability were conducted. Mini slump flow test and mini V-funnel test were performed according to the EFNARC Guidelines [6]. Mini slump flow test was repeated in the same process using the cone described in ASTM C230 for comparison [7]. Figure 2 shows the measurement of diameters of the mortar spread using both cones.

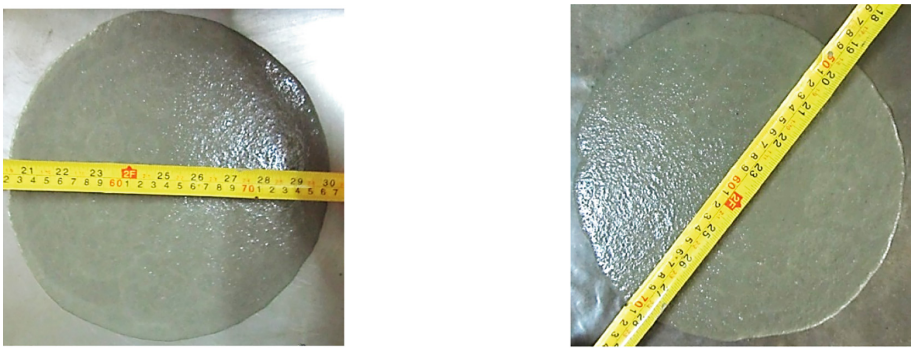

(a) (b)

Fig. 2. Measuring flow diameter of spread by (a) EFNARC cone and (b) ASTM C230 cone.

3.4 Results

The diameters obtained from both type of cones were plotted in a graph in two axes to find a trend line. The slope of the trend line gives the multiplying factor of diameter from EFNARC cone to get equivalent diameter of ASTM cone test. To optimise between flow and stability of the mortar mix, EFNARC recommends slump flow of 240 mm–260 mm and V-funnel flow time of 7 s–11 s [6]. To keep consistent with these criteria, only the mixtures with a flow diameter of 221 mm–308 mm, measured

by EFNARC cone and flow time of 3.2 s–13.0 s were considered in this calibration. To represent the powder with supplementary cementitious materials, two mixtures with 10% and 12% silica fume were included as well.

Figure 3 shows the plot and corresponding trend line. It gives the correlation factor of 0.884, which is very close to the theoretical factor of 0.913. The difference between these two factors is only 3%. The R^2 value of 0.815 indicates a good representation of experimental points by the regression line. The figure also shows that, both types of powder (100% OPC and OPC with 10%–12% SF) give similar relationship between the diameters, measured by two types of cones.

Table 1. Mixing proportions and fresh properties of mortar.

s/b	w/b	SP (%)	SF (%)	D_A [mm]	D_E [mm]	V-funnel flow time [sec]
1.50	0.40	0.70	0	233	254	8.4
1.50	0.40	0.80	0	201	221	9.7
1.50	0.40	0.70	0	263	300	8.4
1.50	0.40	0.70	0	240	268	9.5
1.50	0.40	0.60	0	265	308	3.2
1.50	0.40	0.65	0	244	279	6.1
1.50	0.40	0.70	0	243	278	8.0
1.50	0.40	0.75	0	268	280	8.8
1.50	0.40	0.70	0	219	248	11.5
1.50	0.40	1.20	10	233	273	10.8
1.50	0.40	1.50	12	218	260	13.0

Note: s/b and w/b represent sand-to-binder and water-to-binder ratio respectively, while SP and SF represent the dosage of superplasticiser and silica fume respectively. D_A and D_E indicate the flow diameter from ASTM C230 and EFNARC cones respectively.

3.5 Discussion

The theoretical and experimental correlation factors are very close. The cone described in ASTM C230, which is commonly available in most of the laboratories, can be used to check the flowability of mortar instead of EFNARC cone. The mortar mixtures with 10–12% SF in binder had the similar relationship as the mortars with 100% OPC binder. So, this correlation is independent of binder type.

As there are chances of some experimental error, the theoretically derived factor is considered as more reliable. So, 0.913 is the recommended correlation factor of the flow diameters, measured by ASTM C230 and EFNARC cones. The corresponding desirable flow diameter should be 219 mm–237 mm for tests with ASTM C230 cone, for a stable and self-compacting mortar mixture, which can be used to produce SCC.

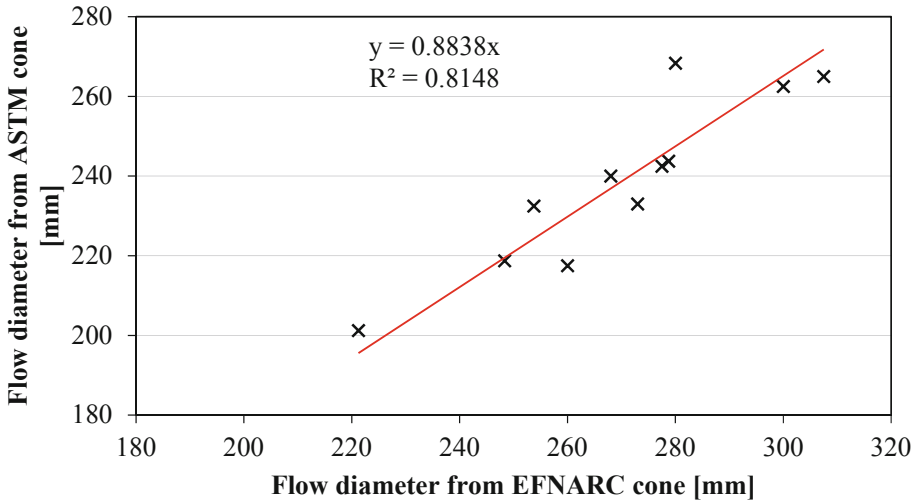

Fig. 3. Correlation of the EFNARC and ASTM C230 cones.

4 Concluding Remarks

The findings of this analysis shows a consistent correlation between the diameters of flowable mortar measured with both type of cones. The correlation factor of 0.913 and corresponding allowable range of 219 mm–237 mm for flow diameter can be used while testing with ASTM C230 cone. This correlation will enable us to measure the flow diameter of conventional mortar and self-compacting mortar with the ASTM recommended cone. Using the same apparatus to measure the flow of both types of mortar will open the window of unified guidelines and recommendations for fresh properties of mortar. Utilisation of available equipment for mix design of SCC will make it easier for the professionals and scholars, as well as, will add to the popularity of SCC.

Acknowledgements. The authors are grateful to Universiti Kebangsaan Malaysia for supporting this research through the UKM Impak Perdana Grant (DIP-2017-002).

References

1. Güneyisi E, Gesoglu M, Ghanim H, İpek S, Taha I (2016) Influence of the artificial lightweight aggregate on fresh properties and compressive strength of the self-compacting mortars. Constr Build Mater 116:151–158
2. Markets and Markets (2017) Self-compacting concrete market by type (powder, viscosity, combination), application (drilled shafts, columns, metal decking, concrete frames), end user (oil & gas construction, infrastructure, building & construction), region - global forecast to 2026, Mark. Res. Rep. https://www.marketsandmarkets.com/Market-Reports/self-compacting-concrete-market-226178048.html. Accessed 2 Feb 2019

3. Erdem TK, Khayat KH, Yahia A (2009) Correlating rheology of self-consolidating concrete to corresponding concrete-equivalent mortar. ACI Mater J 106:154–160
4. Okamura H, Ozawa K, Ouchi M (2000) Self-compacting concrete. Struct Concr 1:3–17
5. Self-compacting concrete European project group, The European guidelines for self-compacting concrete, BIBM, CEMBUREAU, ERMCO, EFCA, EFNARC (2005). http://www.efnarc.org/pdf/SCCGuidelinesMay2005.pdf
6. EFNARC, specification and guidelines for self-compacting concrete, European federation of specialist construction chemicals and concrete systems, Syderstone, Norfolk, UK (2002). http://scholar.google.com/scholar?hl=en&btnG=Search&q=intitle:Specification+and+Guidelines+for+Self-Compacting+Concrete#0
7. ASTM C230/C230 M-14 (2014) Standard specification for flow table for use in tests of hydraulic cement. ASTM International, West Conshohocken
8. BS EN 1015-3 (1999) Methods of test for mortar for masonry. Determination of consistence of fresh mortar (by flow table), Br. Stand
9. Roussel N, Stefani C, Leroy R (2005) From mini-cone test to Abrams cone test: measurement of cement-based materials yield stress using slump tests. Cem Concr Res 35:817–822

Thixotropy-Dependent Form Filling Ability of Cement Paste

Mareike Thiedeitz(✉), Thomas Kränkel, and Christoph Gehlen

Centre for Building Materials, Technical University of Munich, Munich, Germany
mareike.thiedeitz@tum.de

Abstract. The form filling ability of fresh concrete is not only dependent on its rheological parameters yield stress and viscosity but on thixotropy as well. Currently, there are not many investigations regarding the effect of thixotropic structural build up on the form filling behaviour of concretes. The thixotropy of fresh concrete is mainly dependent on the thixotropic character of its cementitious paste. Thus, form filling experiments on cementitious suspensions were performed investigating their workability in dependence of their rheological parameters as preliminary tests for the workability prediction of fresh concretes. For this reason, cementitious pastes with equal solid content but varying yield stress and thixotropy were tested. Rotational rheometer measurements to investigate the rheological key parameters yield stress, viscosity and thixotropy were combined with formfilling tests in a L-shaped model formwork. With increasing thixotropy, flow distance in the formwork and thus form filling ability of the cementitious suspensions decreased. The conducted experimental series therefore is the base to enhance the prediction of form filling behaviour of fresh concrete.

Keywords: Rheology · Thixotropy · Time-dependent structural build up · Form filling ability · Structural parameter

1 Introduction and Motivation

The rheological behavior of cementitious materials can be tested by either conducting rheometric or empirical stoppage tests [1]. Rheometric measurements provide more accurate information about the rheological parameters such as yield stress, viscosity and structural build-up, indeed the costs for rheometric devices are quite high [2–4]. Empirical stoppage tests meanwhile are cheap and easy to handle which makes them more suitable for in-situ measurements. The correlation of empirical stoppage tests with rheological parameters yield stress and viscosity was e.g. investigated in [5] and is even used in common standardizations. Empirical stoppage tests are the mini-slump flow test acc. to EN 1015-3 with a calculation of the rheological parameter yield stress acc. to [6] and the slump flow test acc. to EN 12350-8, the L-Box test acc. to EN 12530-10 or tests with the LCPC-Box acc. to [4]. The correlation of the measured rheological parameters with the real flow behavior of concrete is of practical interest: A correct prediction of the flowability enables engineers to a more appropriate estimation on bleeding and

V. Mechtcherine et al. (Eds.): RheoCon 2019/SCC 2019, RILEM Bookseries 23, pp. 273–280, 2020.
https://doi.org/10.1007/978-3-030-22566-7_32

segregation behavior, reduction of wall pressure for formwork calculations and the form filling ability especially through tight or densely reinforced formworks [7–10]. Especially for high fluidity concretes such as Self Compacting Concrete (SCC) or High Performance Concretes (HPC), the correlation of the rheological parameters yield stress, viscosity and thixotropy with the real flow behavior is necessary for the correct prediction of concrete placement processes. Because of that rotational rheometer experiments with cement pastes were combined with form filling tests in an L-shaped model formwork. The measured flow distances in the model formworks were afterwards related to the calculated rheological parameters. By varying the thixotropy without varying the other rheological parameters it could be shown that the thixotropy has a huge impact on the flowability of concrete and thus the form filling process. The calculation of the form filling ability by using the common equations does not predict the flow behavior of the cementitious paste in the correct way. The presented experimental series thus can be seen as the start point on more detailed investigations of the effect of thixotropy on the form filling of concrete.

2 Structural Build up and Breakdown in Cementitious Suspensions

The rheology of cementitious suspensions is mainly defined by the interaction forces of its colloidal particles: The sum of attractive forces, namely Van-der-Waals-forces, electrostatic attraction and Brownian motion and repulsive forces like electrostatic repulsion and steric hindrances caused by admixtures defines the network clustering of colloidal particles and thus the microstructure of the cement paste [11–13]. Following, the strength of the particle network defines the stress that has to be overcome to make the suspension flow called yield stress $\tau_{0,d}$ as well as the viscosity during flow. At very low shear, suspensions exhibit nearly only elastic properties, but gain a viscous part with increasing shear [14, 15]. The Bingham-regression states “easy flow” which means a linear proportion between the applied shear and the stress response of the paste as well as a defined yield stress at zero shear which has to be overcome to start yielding [16]. Indeed, this regression is just a simplified approximation which is especially not fitting at low shear rates and for densely packed suspensions: At low shear rates, if the applied shear is too low to prevent attractive interparticle forces, microstructure is rebuilt which increases the apparent viscosity η and moreover the yield stress over time, namely the static yield stress $\tau_{0,s}$. This phenomenon is called thixotropy. Thixotropy is the reversible time dependent change in both yield stress and viscosity in the cementitious suspension due to changes in the particle network [17–22]. Under applied shear, interparticle bonds are destroyed. Thus, particle networks deflocculate causing a decrease in viscosity. At rest, particle networks are rebuilt with time due to the attractive interparticle forces. The total rate of thixotropy thus always is the sum of structural build-up and breakdown. Under low shear, only a percentage of the total thixotropy rate occurs [23]. The dependence of the viscosity on the thixotropy was expressed e.g. by Coussot as

$$\eta = \eta_0(1+\lambda^n); \frac{d\lambda}{dt} = \frac{1}{\theta} - \alpha\dot{\gamma}\lambda \tag{1}$$

with θ being the flocculation time and λ the ratio between structural build-up and breakdown. The equation states that from a start viscosity η_0 the apparent viscosity η increases with a structural parameter λ. λ meanwhile is the time derivative of the flocculation time, a structural parameter α and the shear rate $\dot{\gamma}$. Moreover, not only the apparent viscosity η but the static yield stress $\tau_{0,s}$ is dependent on the thixotropy as well: At rest, starting from the dynamic yield stress $\tau_{0,d}$ the evolution of static yield stress $\tau_{0,s}$ can be expressed as

$$\tau_0(t) = \tau_{0,d} + A_{thix} * t \tag{2}$$

With time, static yield stress increases. The investigation of the increase in static yield stress over time thus can be calculated as A_{thix}. What has to be taken into account is that it is insufficient to only predict yield stress and viscosity of a material without considering its time-dependent development (i.e. the thixotropy).

2.1 Form Filling Ability of Cementitious Materials

For cheap and easy testing procedures, empirical stoppage tests such as slump flow test or L-Box test especially for SCC are state of the art. These empirical stoppage tests are viable for yield stress fluids following the theory that flow occurs when the yield stress is surpassed and flow stops as soon as yield stress in the system is higher than the apparent stress in the paste or the concrete in dependence of the shear. Especially for SCC, the L-Box test is a common acceptance test for the evaluation of the flow performance. It is standardized in EN 12350-10. For the calculation of rheological parameters the Bingham approximation is normally used [1, 4, 7, 24]. With a known volume of filled paste (defined by the height h_0, the flow distance L and the Box width l_0), the density ρ and yield stress of the material, the flow distance in an L-Box can be calculated acc. to [7] using Eq. (3)

$$L = \frac{h_0 \rho g l_0}{2\tau_0} + \frac{l_0^2 \rho g}{4\tau_0} \ln\left(\frac{l_0}{l_0 + 2h}\right) \tag{3}$$

For low thixotropic materials the results are viable. Nevertheless, as soon as the apparent flow is too slow for generating shear rates for a complete structural breakdown, the Bingham approximation is not applicable anymore. First investigations by Chaparian et al. show that the implication of thixotropic behavior in the deduction of viscosity and yield stress based on the results of the form filling procedure give more precise results [1]. Still missing is the actual knowledge about the effect of thixotropy on the prediction of form filling processes. For such a prediction e.g. in simulations using Computational Fluid Dynamics (CDF), the effect of thixotropy especially in dependence on the shear rate and the time of flow should be known as a clear parameter.

3 Materials and Methods

3.1 Materials and Mix Design

Ordinary Portland Cement CEM I 42,5 R acc. to EN 197-1 was mixed with demineralized water. The temperature of the water was adjusted to result in a cement paste temperature of 20 °C. All cement pastes possessed a solid concentration $\phi = 0.45$; subsequently the water to cement ratio w/c was set to 0.393. A polycarboxylate ether (PCE) based superplasticizer was used in an appropriate amount for the targeted variation of the yield stress. The yield stress was calculated by the approximation acc. [6] for three different slump flow values of 200 ± 5 mm, 250 ± 5 mm and 275 ± 5 mm. The viscosity modifying agent (VMA) was added for the variation of thixotropy: For each paste, one reference cement paste without VMA was prepared with its original thixotropy. In addition to that, two more cement pastes with VMA contents of 0.375 wt% and 0.500 wt% by cement were prepared to rise the thixotropy of the system without changing other rheological parameters. For each measurement 1.5 l of paste were mixed. More detailed information are given in Table 1.

Table 1. Cement paste mixtures.

Mixture	ϕ [–]	Cem. [kg/m^3]	Water [kg/m^3]	PCE [wt% o.c.]	VMA [wt% o.c.]	Slump flow[mm]
0.45_0	0.45	2092.65	824.02	0.35	0.000	$200 \pm 5/250 \pm 5/275 \pm 5$
0.45_0.75	0.45	2092.65	824.02	0.97	0.375	$200 \pm 5/250 \pm 5/275 \pm 5$
0.45_1.0	0.45	2092.65	824.02	1.70	0.500	$200 \pm 5/250 \pm 5/275 \pm 5$

The cement pastes were prepared using a mortar mixer "ToniMix 6210" with a mix program according to EN 196-1. The rheological measurements were performed using an Anton Paar Rheometer MCR 502. For the static yield stress measurements as well as the dynamic profile a vane-in-cup system with a six-bladed vane device was used. Due to the very low rotational velocities during the static experiments, shear was assumed to only occur at the circumference of the vane in order to simplify the calculation of the related shear rates. For the calculation of the dynamic parameters, the shear stress was assumed using the Reiner-Riwlin equation with a plug flow.

3.2 Experimental Procedure of Rheometric Measurements

Cement pastes were prepared with a mixing time of 4 min acc. to EN 196-1. Superplasticizer and VMA were added after 90 s of mixing time. After mixing, the cement pastes were left at rest until 12:30 min. after water addition in order to reduce early hydration reaction effects during the rheological experiments. Before the measurements started, each paste was mixed for 30 s. with a standard drilling machine with a propelling screw to set a comparable controlled preshear state for each mixture (Fig. 1).

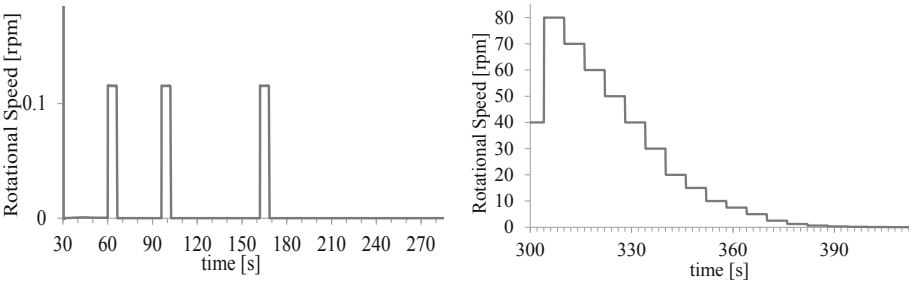

Fig. 1. Left: Static profile. Right: Dynamic profile for the Vane measurements.

Directly after preshear, the paste was filled into the vane cup. The rheometric measurements started 15 min. after water addition with the static profile after another preshear of 30 s at 80 rpm. After the preshear, a 30 s. resting period was conducted followed by an immediate rotational speed of 0.1155 rpm for 6 s. For the calculation of the static yield stress, two resting periods of 60 and 120 s were set. During the resting time the cement paste rebuilt its thixotropic structure, thus the measured peak of yield stress increased over time. The peak of measured shear stress during shear was evaluated as static yield stress and the slope of static yield stress over the time was calculated as thixotropy. After the static measurement, the cement paste was presheared in the vane cup with a rotational speed of 40 rpm for 10 s. After the preshear, the dynamic profile was performed with 19 stepwise decreasing rotational speeds from 80 rpm until 0.02 rpm with a shear time of 6 s per step. For each step, the equilibrium torque was taken and calculated as shear stress acc. to the Reiner Riwlin equation.

3.3 Experimental Procedure of Form Filling Tests

The L-Box invented for the cement paste flowability experiments possesses modified dimensions in comparison to the standardized L-Box-test. It can be seen in Fig. 2. The horizontal section of the L-Box has a width of 50 mm and the length of 1200 mm with a clearance height of 50 mm. The L-Box tests are conducted at low speed that free flow is assumed. The top of the horizontal section thus can be assumed as open. The vertical section exhibits a width of 50 mm, a depth of 45 mm and a total height of 540 mm. Both sections were separated with a gate.

The cement paste was left at rest for 08:30 min after mixing and remixed again for 30 s at 12:30. Directly after the 30 s of preshear, 0.5 l of the cement paste was filled in the L-box with a closed gate within a time 30 s. The paste then was left at rest for 30 s before opening the gate. To avoid inertia effects, the gate was lifted during a time of 5 s 14 min after addition of water. At the same time, slump flow was measured acc. to [6]. The flow distance was measured at flow stoppage and the height at the gate entrance was taken as h_0.

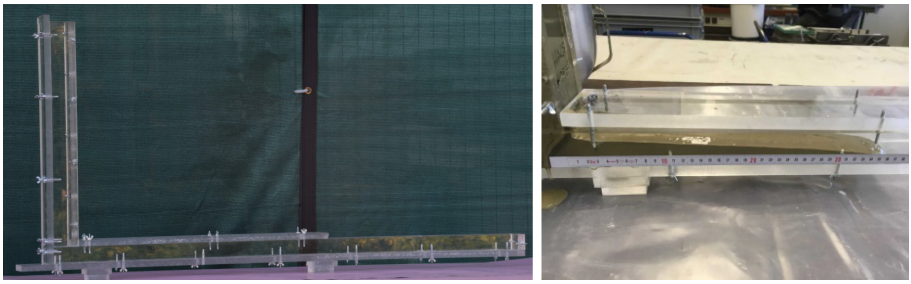

Fig. 2. Used L-Box for the form filling procedure.

4 Experimental Results and Discussion

For each cement paste three different VMA contents were tested. With the given VMA content of 0, 0.375 and 0.500% o.c. three different thixotropies were adjusted. Moreover each cement paste was set at a slump flow of 200, 250 and 275 mm (see Table 1). With the given recipes, conducting the rheological measurements three different thixotropy rates were evaluated considering the increase in static yield stress $\tau_{0,s}$ over time. The values for the thixotropy can be seen in Table 2.

Table 2. Results of measured cement pastes.

SF [mm]	200 ± 5			250 ± 5			275 ± 5		
	A_{thix} [Pa/s]	*Flow* [mm]	$\tau_{0,calc}$ [Pa]	A_{thix} [Pa/s]	*Flow* [mm]	$\tau_{0,calc}$ [Pa]	A_{thix} [Pa/s]	*Flow* [mm]	$\tau_{0,calc}$ [Pa]
Series 1	0.082	395	16.8	0.082	501	13.3	0.084	535	10.9
Series 2	0.267	325	17.7	0.359	422	15.8	0.198	500	11.6
Series 3	0.325	272	24.5	0.525	401	16.6	x	x	x

With this setup three different thixotropies were investigated at similar yield stresses, assuming the same slump flow and the yield stress calculation acc. [6]. In Fig. 3, the dependence of the flow distance on the thixotropy is shown. Generally, with decreasing slump flow the flow distance decreases as expected. Meanwhile, with increasing thixotropy, the flow distance decreases. This is viable for each testing series of different adjusted slump flows.

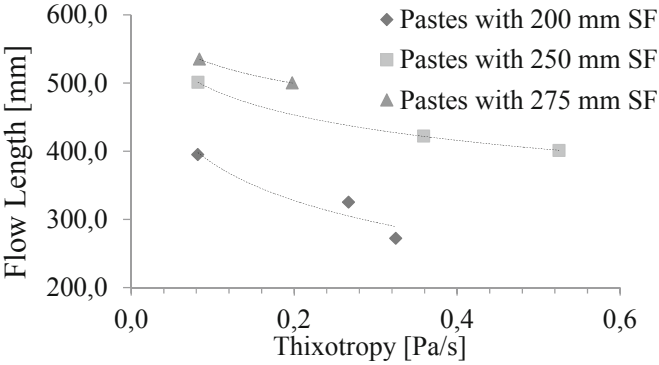

Fig. 3. Effect of the thixotropy on the flow distance.

5 Conclusions

This paper focuses on the investigation of the effect of thixotropy on the form filling ability of cementitious pastes. The experimental results can be seen as preliminary measurements for following experimental procedures. With an adjusted manipulation of only the thixotropy of the pastes (whereas yield stress and viscosity remain almost constant) its effect on the form filling behavior was investigated. It could be stated that with increasing thixotropy the flow distance in the L-Box decreases. For a clear quantification of the relationship between the thixotropy of the paste and the related form filling behavior, more detailed and extensive experimental programs have to be conducted. In these experimental programs it has to be taken in mind that normally not the whole structural build up takes place but a percentage depending on the apparent shear rate in the system during flow motion. Due to that, a quantification of the thixotropic structural build up of the pastes should not be limited to measurements at rest but extended to low shear. These investigations are currently started. The presented experimental results nevertheless are a good base for the ongoing research.

Acknowledgements. The experimental program was conducted as part of the DFG project 313773090 in the frame of the DFG priority program 2005 “Opus Fluidum Futurum”. The author kindly thanks the DFG for the support of this priority program.

References

1. Chaparian E, Nasouri B (2018) L-box—a tool for measuring the “yield stress”: a theoretical study. Phys Fluids 30(8):83101
2. Yammine J, Chaouche M, Guerinet M, Moranville M, Roussel N (2008) From ordinary rhelogy concrete to self compacting concrete: a transition between frictional and hydrodynamic interactions. Cem Concr Res 38(7):890–896

3. Hafid H, Ovarlez G, Toussaint F, Jezequel PH, Roussel N (2015) Assessment of potential concrete and mortar rheometry artifacts using magnetic resonance imaging. Cem Concr Res 71:29–35
4. Roussel N (2007) The LCPC BOX: a cheap and simple technique for yield stress measurements of SCC. Mater Struct 40(9):889–896
5. Kraenkel T (2018) Research report: rheology and workability Testing of Deep Foundation COncrete in EUrope and the US
6. Roussel N, Stefani C, Leroy R (2005) From mini-cone test to Abrams cone test: measurement of cement-based materials yield stress using slump tests. Cem Concr Res 35 (5):817–822
7. Nguyen TLH, Roussel N, Coussot P (2006) Correlation between L-box test and rheological parameters of a homogeneous yield stress fluid. Cem Concr Res 36(10):1789–1796
8. Roussel N, Gram A, Cremonesi M, Ferrara L, Krenzer K, Mechtcherine V, Shyshko S, Skocec J, Spangenberg J, Svec O, Thrane LN, Vasilic K (2016) Numerical simulations of concrete flow: a benchmark comparison. Cem Concr Res 79:265–271
9. Mechtcherine V, Gram A, Krenzer K, Schwabe J-H, Shyshko S, Roussel N (2014) Simulation of fresh concrete flow using Discrete Element Method (DEM): theory and applications. Mater Struct 47(4):615–630
10. Thrane LN (2007) Form filling with self-compacting concrete. Lyngby, Technical University of Denmark, Danish Technological Institute. Dissertation
11. Genovese DB (2012) Shear rheology of hard-sphere, dispersed, and aggregated suspensions, and filler-matrix composites. Adv Coll Interface Sci 171–172:1–16
12. Bentz DP, Ferraris CF, Galler MA, Hansen AS, Guynn JM (2012) Influence of particle size distributions on yield stress and viscosity of cement–fly ash pastes. Cem Concr Res 42 (2):404–409
13. Snabre P, Mills P (1996) I. Rheology of weakly flocculated suspensions of rigid particles. J Phys III 6(12):1811–1834
14. Sun Z, Voigt T, Shah SP (2006) Rheometric and ultrasonic investigations of viscoelastic properties of fresh Portland cement pastes. Cem Concr Res 36(2):278–287
15. Choi M, Park K, Oh T (2016) Viscoelastic properties of fresh cement paste to study the flow behavior. Int J Concr Struct Mater 10(3):65–74
16. Bingham EC (1916) An investigation of the law of plastic flow. Bull Bur Stan 13(266): 309–353
17. Goodeve CF (1938) General theory of thixotropy and viscosity
18. Lapasin R, Papo A, Rajgelj S (1983) The phenomenological description of the thixotropic behaviour of fresh cement pastes. Rheologica Acta 22(4):410–416
19. Barnes HA (1997) Thixotropy—a review. J Nonnewton Fluid Mech 70(1–2):1–33
20. Coussot P, Nguyen QD, Huynh HT, Bonn D (2002) Viscosity bifurcation in thixotropic, yielding fluids. J Rheol 46(3):573–589
21. Mujumdar A, Beris AN, Metzner AB (2002) Transient phenomena in thixotropic systems. J NonNewtonian Fluid Mech 102(2):157–178
22. Mewis J, Wagner NJ (2009) Thixotropy. Adv Colloid Interface Sci 147–148:214–227
23. Thiedeitz M, Kränkel T, Gehlen C (2019) Thixotropic structural build-up of cement pastes at low shear rates
24. Shan Z, Yu Z, Shi J (2015) Experimental investigation of flow of fresh self-compacting concrete in improved L-box. Constr Build Mater 84:30–38

Mixing, Processing and Casting of Mortar and Concrete

Comparative Study on the Effect of Mixer Type on Properties of Self-compacting Mortar

Bart Craeye[1,2(✉)], Wim Bastiaens[3], Erik Coppens[3], Dirk Van Houdt[4], Wilfried Gijbels[5], and Thomas Rondou[6]

[1] Faculty of Applied Engineering - EMIB Research Group, University of Antwerp, Antwerp, Belgium
bart.craeye@uantwerpen.be
[2] Industrial Sciences and Technology - DUBiT Research Unit, Odisee University College, Aalst, Belgium
[3] ONDRAF/NIRAS, Brussels, Belgium
[4] Belgoprocess, Dessel, Belgium
[5] Betonadvies Gijko, Sint-Niklaas, Belgium
[6] Belgian Building Research Institute, Brussels, Belgium

Abstract. For the realisation of safe, permanent and sustainable solutions for the management of short-lived low and intermediate level radioactive waste in Belgium, this radwaste is placed in concrete caissons and subsequently encapsulated with mortar to form a monolith, placed in a near surface disposal facility. This high-performance self-compacting mortar consists of an inert calcareous matrix (filler and sand), blast furnace slag cement, microsilica and naphthalene sulfonate superplasticizer (dry-powder type and liquid-based type), with a water/cement ratio of approximately 0.36. As considerable amount of this cementitious material is needed, it is necessary to come to an easily manageable and repeatable mixing and casting procedure.

Therefore, an intensive experimental program was conducted to evaluate the effect of different mixer types on the consistency of fresh state (slump flow, V-funnel, air content and volumetric weight), the hardened properties at different ages (both compressive and flexural strength, modulus of elasticity and coefficient of thermal expansion) and porosity accessible to water (including segregation risk). Four different mixers were considered in this study, with different working principle and capacity: (i) forced action pan mixer, (ii) ring pan mixer, (iii) paddle mixer (ploughshare), and (iv) twin shaft mixer. For durability related reasons, porosity and segregation risk have a decisive effect on the choice of mixer to be used for further (upscaled) research.

It was found that the mixing procedure, scale and type has an impact on the previously mentioned properties of the self-compacting mortar. Lowest porosity is obtained by means of ploughshare mixer in combination with dry superplasticizer, while the lowest segregation risk is obtained for TS mixer, regardless the type of superplasticizer.

Keywords: Self-compacting mortar · Mixer type · Fresh and hardened properties

V. Mechtcherine et al. (Eds.): RheoCon 2019/SCC 2019, RILEM Bookseries 23, pp. 283–293, 2020.
https://doi.org/10.1007/978-3-030-22566-7_33

1 Introduction

The Belgian Agency for Radioactive Waste and Enriched Fissile Materials (ONDRAF/NIRAS) has come up with a reference design for ensuring a safe, permanent and sustainable solution for the management of short-lived low and intermediate level radioactive waste (category A waste) in Belgium. The radwaste is placed in pre-cast concrete caissons and subsequently encapsulated with mortar to form a monolith, placed in a near surface disposal facility [1]. Therefore, a high-performance self-compacting mortar was developed using an inert calcareous matrix, blast furnace slag cement, microsilica and naphthalene sulfonate superplasticizer. As considerable amount of self-compacting mortar is needed (approximate 20,000 m^3) for this reference design, it is necessary to come to an easily manageable and repeatable mixing and casting procedure. Therefore, an intensive experimental program was conducted to evaluate the effect of different mixer types. Porosity and segregation risk have a decisive effect on the choice of mixer to be used for further (upscaled) research.

Self-compacting mortars are suitable for the construction of thin elements, for repair applications, for casting sheet piles, where it was proven that the modified mixtures performed equally well compared to the reference concrete mixtures and comparable structural needs were fulfilled [2]. Another application is the use of self-compacting mortar poured in a preplaced coarse aggregate skeleton (e.g. for cofferdam section and mass concrete applications), using the self-weight of the mortar to achieve the filling of the gaps. High flowability and limited bleeding is required [3]. Self-compacting mortar is also extremely suitable for (repair) work done in locations where it is difficult to vibrate, e.g. in narrow spaces [4].

Producing self-compacting concrete is more complex than traditional vibrated mixes and the mixing method could significantly change or improve the workability of the concrete [5]. It is known that higher mixing time is required for high-performing and self-compacting mixes, but a reduction can be obtained by increasing the fine particle content, optimizing the granular skeleton and using microsilica [6]. Intensive mixers or higher mixing speed is needed for ultra-high performant and self-compacting mixes to shorten the required mixing time [7]. However, an excessive speed can lead to overmixing and higher chance of segregation. A delayed addition of the superplasticizer, leads to an improved workability, especially when a low water-to-cement ratio is used [7]. High mixing intensity results in a more homogenous paste while mixing at low intensity leads to increase in porosity but improved workability [8]. Due to the low water contents relative to the powder contents and high additive dosages, more energy is required for the production of self-compacting concrete to distribute the raw materials evenly. Mixing times of 240 s are not rare in a ready mixed concrete plants [9].

2 Experimental Details

2.1 Mortar Composition

In this experimental program, two self-compacting mortars are being tested, as listed in Table 1. In real applications, this or an equivalent composition will be used to directly encapsulate the category A radwaste and cast in a prefabricated concrete caisson without additional compaction/vibration. The self-compactability of the mixes is obtained by using sufficient amount of powder (blast furnace slag cement, limestone filler and microsilica) and sand separated in different fractions (Table 1). Two types of naphthalene sulfonate superplasticizer were considered: (i) a dry powder-type and (ii) a liquid-based type (40% concentration), used respectively in the 'premix' and 'wet mix' as mentioned further on.

Table 1. Composition of the self-compacting mortar: premix and wet mix. *w = water, *c = cement, *b = binder (cement + microsilica), *p = powder (cement + microsilica + limestone filler), *sp = superplasticizer – NFS = naphthalene formaldehyde

	PREMIX	WET MIX
Component	**kg/m³**	**kg/m³**
CEM III/C 32.5 N-SR	637	637
Limestone filler	101	101
Microsilica	39	39
Limestone sand (<0.1 mm)	91	91
Limestone sand (0.1-0.5 mm)	404	404
Limestone sand (0.5-1.0 mm)	299	299
Limestone sand (1.0-2.0 mm)	412	412
Water	229	219
Dry Superplasticizer NFS	6	-
Liquid Superplasticizer NFS 37.5 con%	-	16**

Density [kg/m³]	2218
w/c [-]	0.36
w/b [-]	0.34
w/p [-]	0.29
sp/c	1.0%

2.2 Mixing Procedure

Four different mixers were considered in this study (Fig. 1 and Table 2), with different working principle and capacity: (i) forced action pan mixer (FAP), (ii) ring pan mixer (RP), (iii) paddle mixer (ploughshare-PS), and (iv) twin shaft mixer (TS). The mixers have different (mixing) volume and different mixing times are used. According to DIN-EN206-1 and [11] one high performant mixer (FAP), two performant mixers (PS and TS) and one regular mixer (RP) were considered. Depending on the mortar composition (premix vs. wet mix, Table 1) and the mixer type, the mixing procedure (Table 3) is adjusted to obtain a self-compacting, homogeneous, non-segregating and highly flowable fresh mix.

Table 2. Mixer type.

Mixer type	Equipment	Code	Volume	Mixing volume	Mixing time	DIN-EN206-1
Forced action pan	Creteangle CF	FAP	52 L	20 L	10′	High Performant
Ring pan	GSG	RP	70 L	40 L	15′	Regular
Paddle/Ploughshare	Lödige FM130	PS	130 L	60 L	6′	Performant
Twin shaft	BHS DKX0.06	TS	–	60 L	6′	Performant

Table 3. Mixing procedure.

Mixing procedure	Time wet mix	Time premix	FAP	RP	PS	TS
Add all dry components	0 s	0 s	30 rpm	–	130 rpm	30 rpm
Add 90% of mixing water	0 s–60 s	0 s–60 s	60 rpm	–	130 rpm	50 rpm
Continued mixing	60 s–90 s	60 s–180 s	60 rpm	–	130 rpm	50 rpm
Add superplasticizer	90 s–120 s	–	60 rpm	–	130 rpm	50 rpm
Continued mixing	120 s–180 s	–	60 rpm	–	130 rpm	50 rpm
Add 10% of mixing water	180 s	180 s	100 rpm	–	130 rpm	50 rpm
Continued mixing	180 s–end	180 s–end	100 rpm	–	130 rpm	50 rpm
End			600 s	900 s	360 s	360 s

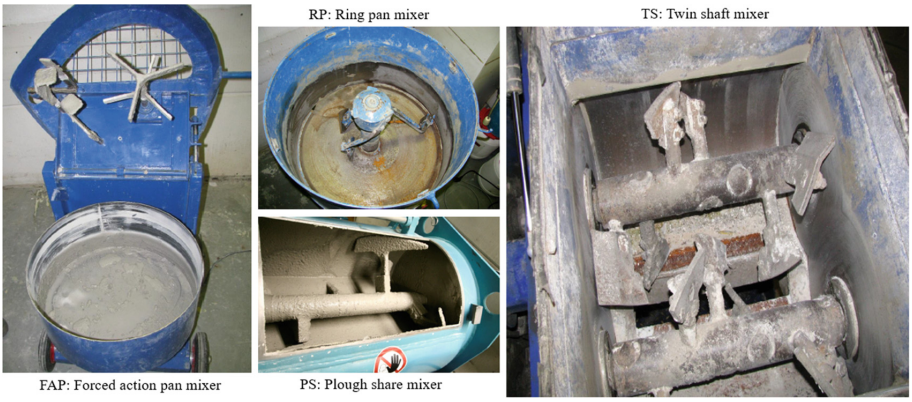

Fig. 1. Four mixers used in this study: forced action pan, ring pan, plough share and twin shaft.

2.3 Testing: Characterization of Fresh and Hardened Properties

In total 19 mixes were made and evaluated: 9 premixes (3 using FAP, 2 using RP, 2 using PS, 2 using TS) and 10 wet mixes (3-2-2-3 for FAP-RP-PS-TS respectively). The effect of different mixer types is evaluated by means of the consistency of the fresh mix, the mechanical properties and the microstructure and porosity. In Table 4 a summary of the test program is given. Some additional remarks are listed below:

- The slump flow is determined by means of a mini-cone (height: 60 mm, upper diameter 70 mm, lower diameter 100 mm, as mentioned in [12]);
- V-funnel is performed immediately after mixing, and once more after 5 min. Therefore, a mini V-funnel was used, as mentioned in [12];
- Prisms with dimensions 40 mm × 40 mm × 160 mm were cast for strength determination (both in compressive and flexural behaviour), determination of modulus of elasticity and coefficient of thermal expansion. Only the 28-day results will be discussed in this paper. Curing is performed under water at 20 °C;
- The porosity will be evaluated by means of water absorption test and determination of the water accessible porosity. Therefore, a cylindrical specimen (height 500 mm, diameter 100 mm) is cast. After one day of hardening, the specimen is cut into three

Table 4. Testing program on fresh and hardened concrete.

Fresh mix characterization	Verified property	Code
Slumpflow	Flow-ability in unconfined conditions [mm]	EN 1015-3
V-funnel	Flow time and viscosity [s]	EN 12350-9
Air	Volume of air voids [%]	EN 1015-7
Volumetric weight	Density of fresh mix [kg/m^3]	EN 1015-6
Mechanical properties	**Verified property**	**Code**
Compressive strength	Capacity to withstand axial directed pushing stress [MPa]	EN 196-1
Flexural tensile strength	Highest tensile stress-moment of rupture in flexure [MPa]	EN 196-1
Modulus of elasticity (secans)	Slope of stress-strain curve-elastic deformation region [GPa]	EN 13412
Thermal properties	**Verified property**	**Code**
Coefficient of thermal expansion	Thermal deformation under temperature variation [μm/(m°C)]	EN 1770
Microstructure characterization	**Verified property**	**Code**
Water accessible porosity	Segregation in hardened samples [-] Water absorption – porosity [vol.%]	–

parts, only selecting the upper and lower part, and cured under water at 20 °C, until full saturation. The weight is determined above (G_{sat}) and under water (G_1). Afterwards the samples are dried until constant mass is achieved and the weight is determined once more (G_{dry}). The water accessible porosity ratio (WAP-ratio) is determined by using (Eq. 1). By means of the WAP index, the segregation risk can be evaluated, as a value of 1,0 means no segregation (equal porosity of both upper and bottom half).

$$WAP\text{-}ratio = \frac{\varepsilon_{upper}}{\varepsilon_{lower}} = \frac{\left(\frac{G_{sat}-G_{dry}}{G_{sat}-G_1}\right)_{upper}}{\left(\frac{G_{sat}-G_{dry}}{G_{sat}-G_1}\right)_{lower}} \quad (1)$$

3 Results and Discussion

3.1 Fresh Properties

A mean slump flow of 285 mm is found for all mixes. For the premixes, the FAP or PS mixer does not have an effect on the flowability. However, using RP mixers leads to an increase, while using TS mixer leads to a significant decrease in slump flow. For the wet mixes, no remarkable difference is noticeable.

Using dry or wet superplasticizer does not have an effect on the results of the V-funnel time. Most remarkable finding is the fact that lower flow time can be expected in case of PS mixing, and a higher flow time in case of RP mixing. Furthermore, V-funnel time increases with approximately 2 s after 5 min for all mixes.

A higher air content (and reduced fresh density) is found for the PS and TS mixers, when comparing premixes and wet mixes. This effect did not appear for the FAP and RP mixers. When using liquid plasticizer, no effect on air content or density were found comparing the different mixers (Table 5 and Fig. 2).

Table 5. Air content and fresh density of the different mixes.

Mixes	A.C. [%]	ρ [kg/m^3]
FAP-P1-2-3	2.1 ± 0.1	2303 ± 3
FAP-W1-2-3	1.9 ± 0.1	2294 ± 12
RP-P1-2	1.5 ± 0.4	2307 ± 6
RP-W1-2	1.6 ± 0.4	2316 ± 10
PS-P2-4	2.5 ± 0.3	2279 ± 11
PS-W2-3	1.5 ± 0.1	2308 ± 25
TS-P2-3	3.4 ± 1.0	2267 ± 11
TS-W1-2-3	2.0 ± 0.2	2322 ± 4

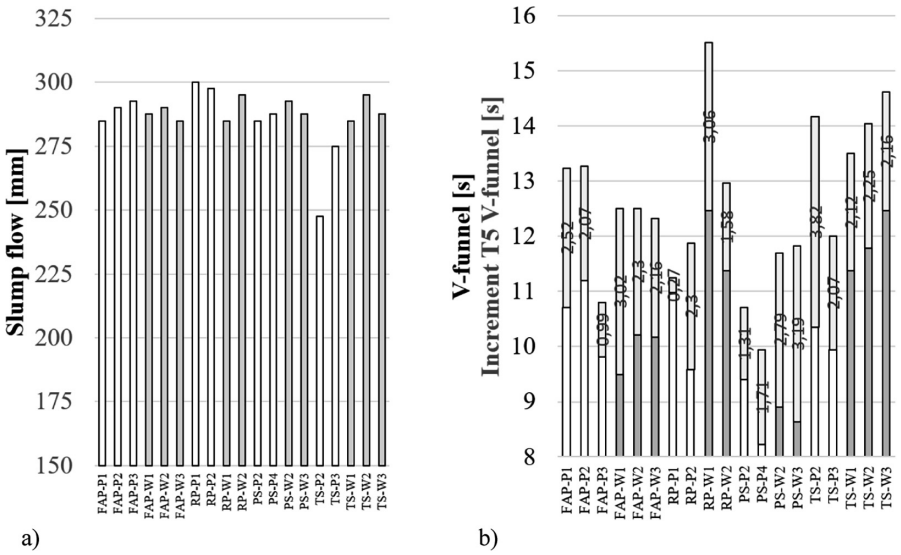

Fig. 2. (a) Slump flow and (b) V-funnel (immediate and after 5 min) of the different mixes.

3.2 Mechanical and Thermal Properties

The compressive strength of the mortar samples after 28 days of hardening is significantly affected by (i) the type of superplasticizer and (ii) the type of mixer. For the premix comparable strength is obtained when using FAP, PS or TS mixers, although higher air content was found in the samples of the PS and TS mixes, as mentioned in Sect. 3.1. However, higher air content can contribute to lower flexural strength which was found for these two performant mixers. The highest flexural strength was obtained by using the high performant FAP mixer. Using RP mixer slightly decreases the compressive strength, and has a significant negative effect on the flexural strength.

For the wet mixes the results are somehow different: using FAP mixer, the compressive and flexural strength decreases compared to the premixes. Compressive strength does not change significantly for the PS and TS mixers, but flexural behavior does increase using liquid plasticizer. Once more, the decreased air content can be the major contributor to this effect. For the RP mixer, increase in both compressive and flexural strength was found (Fig. 3).

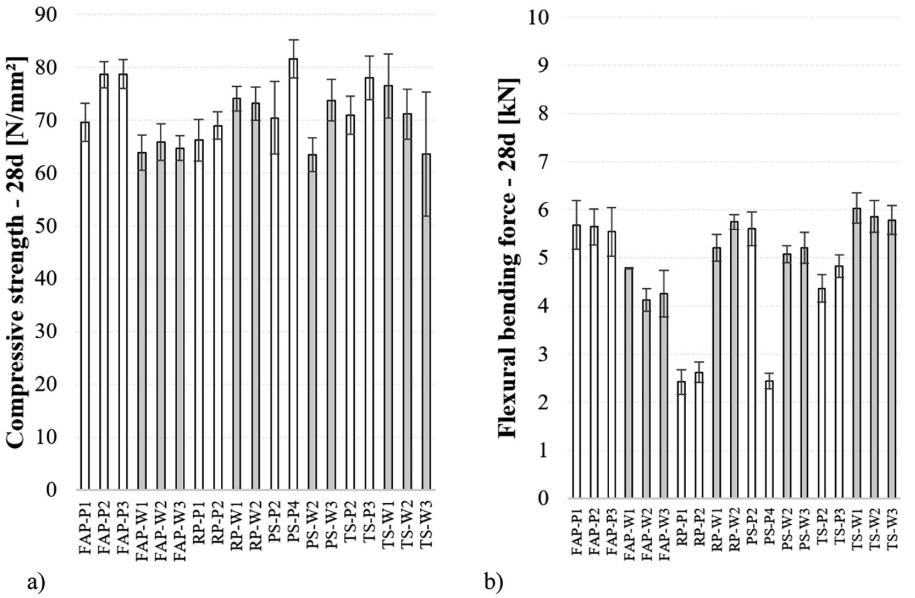

Fig. 3. (a) 28d-compressive strength and (b) 28d-flexural rupture force of the different mixes.

The modulus of elasticity and coefficient of thermal expansion of samples prepared with FAP mixer is higher in case powder-type superplasticizer is added: 6.96 vs. 6.79 μm/m°C and 33.39/35.50 GPa vs. 31.62/33.67 GPa (28/90 days results). However, more research is needed to evaluate the effect of mixer type and type of superplasticizer on the elastic behavior and (thermal) deformation of these self-compacting mortars.

3.3 Porosity

To evaluate the segregating potential of the mixes and the effect of the mixer, the water accessible porosity ratio (WAP-ratio) is determined as mentioned in Sect. 2.3 and (Eq. 1). Especially the wet mixes experience higher segregation in case FAP, RP or PS mixers are used. Mixes prepared with TS mixer experience almost no segregation. The water absorption of the upper and bottom part samples for the different wet mixes are:

- FAP: 9.6 vol.% vs. 7.3 vol.% -> WAP = 1.26
- RP: 9.1 vol.% vs. 7.2 vol.% -> WAP = 1.22
- PS: 10.1 vol.% vs. 7.5 vol.% -> WAP = 1.29
- TS: 7.5 vol.% vs. 7.6 vol.% -> WAP = 0.99

Clearly the upper parts have higher porosity compared to the bottom parts, except for the TS mixes, which was already observed immediately after casting.

For the mixes with dry superplasticizer, (i) the difference between upper part and bottom part is much smaller (meaning: lower segregation risk, WAP decreases), and (ii) the absolute values of water absorption is lower (meaning: lower porosity for mixes with dry superplasticizer):

- FAP: 7.4 vol.% vs. 7.2 vol.% -> WAP = 1.03
- RP: 8.7 vol.% vs. 7.5 vol.% -> WAP = 1.14
- PS: 6.9 vol.% vs. 6.5 vol.% -> WAP = 1.05
- TS: 7.5 vol.% vs. 7.6 vol.% -> WAP = 0.99

Lowest porosity is obtained by means of PS mixer in combination with dry superplasticizer, and the lowest segregation risk is obtained for TS mixer, regardless the type of superplasticizer. Using RP mixer leads to the highest segregation risk for the premix, and PS mixer for the wet mix (Fig. 4).

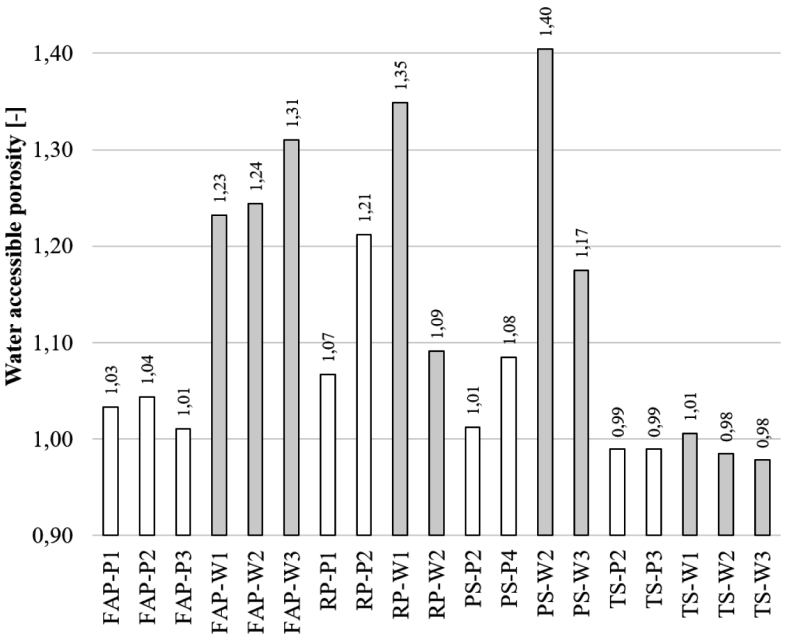

Fig. 4. Water accessible porosity and segregation potential of all mixes.

4 Summary and Conclusion

The effect of different mixer types on the consistency of fresh state, the hardened properties and porosity accessible to water of a self-compacting high-performance mortar was extensively studied. This mortar consists of an inert calcareous matrix (filler and sand), blast furnace slag cement, microsilica and naphthalene sulfonate superplasticizer, with a water/cement ratio of approximately 0.36. Four different mixers were considered in this study, with different working principle and capacity: (i) forced action

pan (FAP) mixer, (ii) ring pan (RP) mixer, (iii) paddle mixer (ploughshare - PS), and (iv) twin shaft (TS) mixer. It was found that the mixing procedure, scale and type has an impact on the previously mentioned properties of the self-compacting mortar:

- The type of mixer and the type of used superplasticizer (dry powder-type of liquid) has an remarkable impact on the consistency of the fresh mix:
  - RP mixing leads to an increase, while TS mixing leads to a decrease in slumpflow;
  - Lower V-funnel flow time can be expected in case of PS mixing, and a higher flow time in case of RP mixing;
  - A higher air content is found for the PS and TS mixers, when comparing premixes and wet mixes. This effect did not appear for the FAP and RP mixers.
- The compressive strength is significantly affected by the type of mixer and the type of superplasticizer(dry or liquid).
- Lowest porosity is obtained by means of PS mixer in combination with dry superplasticizer, and the lowest segregation risk is obtained for TS mixer, regardless the type of superplasticizer.
- Further research is performed with paddle mixer (ploughshare) with a volume of 1.1 m^3, in combination with dry powder-type superplasticizer. This combination led to the most satisfying results on behalf of fresh, mechanical and porosity related properties, as presented in this paper.

References

1. ONDRAF/NIRAS (2019) Internal report NIROND-TR 2011-01, Version 3
2. Lappa ES et al (2003) Self-compacting, high-strength and steel fibre reinforced mortar for pre-cast sheet piles. In: Proceedings PRO33: self-compacting concrete – SCC 2003, RILEM, Reykjavik
3. Vieira M et al (2010) Self-compacting mortar for mass concrete application with PAC technology. In: Proceedings of SCC 2010, RILEM, Montreal
4. Courard L, Bissonnette B (2007) Compatibility performance as a fundamental requirement for the repair of concrete structures with self-compacting repair mortars. In: Proceedings PRO54: self-compacting concrete – SCC 2007, RILEM, Ghent
5. Cazacliu B (2016) Mixing self-compacting concrete: mixers, mixing methods, mixing time, IFSTTAR
6. Chopin D et al (2004) Why do HPC and SCC require a longer mixing time? Cem Concr Res 34:2237–2243
7. Dils J et al (2012) Influence of mixing procedure and mixer type on fresh and hardened properties of concrete: a review. Mater Struct
8. Geiker MR et al (2007) Effect of mixing on properties of SCC. In: Proceedings PRO54: self-compacting concrete – SCC 2007, RILEM, Ghent
9. Lowke D, Schiessl P (2005) Effect of mixing energy on fresh properties of SCC. In: Proceedings self-compacting concrete – SCC 2005, RILEM, Chicago

10. Rondou T (2015) Dosage installation IPM – NIRAS Dessel (in Dutch), internal report PN003 THRO/WIGI/JPO, Betonadvies Gijko, Technum-Tractebel Engineering, Kemp BV, Belgoprocess, ONDRAF/NIRAS
11. Beitzel H (2010) Optimisation of the mixing process for producing self-compacting high-performance concrete. In: Proceedings of SCC 2010, RILEM, Montreal
12. Ghafari E et al (2013) Development of ultra-high performance self-compacting concrete. In: Proceedings of self-compacting concrete – SCC 2013, Chicago

Effect of Electromagnetic Pulsation on the Rheological Properties of Mortars During Pumping

Inka Dreßler(✉), Patrick Varady, Hans-Werner Krauss, and Dirk Lowke

Institute of Building Materials, Concrete Construction and Fire Safety, TU Braunschweig, Brunswick, Germany
i.dressler@ibmb.tu-bs.de

Abstract. The basic understanding of the underlying mechanisms and the coherences between material properties and processing parameters, which are prerequisite for a better understanding and prediction of pumpability of concrete, mortar or suspensions, is an objective of numerous research activities. Current investigations aim to actively control the pumping process, hence being able to prevent blockages. Although much progress has been made in this research field recently, generally applicable models for the prediction of pumpability under consideration of the rheological properties of the material to be pumped as well as the process parameters are not available.

Experimentally determined properties of the bulk material investigated in a small scale pumping test will be presented. We evaluated the effect of an externally applied alternating electromagnetic field with varying frequencies on the pumpability of the mortars regarding changes in pressure in the pipe as well as viscosity and yield stress of the bulk material. For the tests, two mortars with a constant solid volume fraction based on limestone powder (non-reactive) or ordinary portland cement (reactive) as solid phase have been investigated. Moreover, the lubrication layer formed at the interface between pipe and material during pumping, being the main influencing factor on pumping of cementitious materials, will be examined. The effect of the alternating electromagnetic field on the lubrication layer was experimentally simulated with a sliding pipe rheometer. Results for the bulk material and the lubrication layer will be compared. Moreover, the practical applicability of electromagnetic pulsation on the pumpability will be discussed.

Keywords: Electromagnetic field · Sliding pipe rheometer · Pumpability · Rheology

1 Introduction

Pumping enables an efficient transport of fresh concrete over long distances within a pipe. The technique of pumping is widely known for decades. Today, approximately 45% of ready-mixed concrete volume in Germany is transported via pumping [1], which is in the same order of magnitude as in other industrial nations.

V. Mechtcherine et al. (Eds.): RheoCon 2019/SCC 2019, RILEM Bookseries 23, pp. 294–302, 2020.
https://doi.org/10.1007/978-3-030-22566-7_34

Several studies [2, 3] assess that the lubrication layer formed in the vicinity of the wall of the pipe dominates the pumping behavior. Lubrication layer has a lower viscosity and yield stress than the bulk material [4] because of higher paste content [5].

This research investigates an active method to change the properties of the lubrication layer and the bulk material with an alternating electromagnetic field (EMF). The EMF varies in frequency and is induced via coils applied on the pipe. In [6] it was found that applying suitable EMF in a 1000 m full-scale pumping test improved pumpability of concrete, which came along with a severe reduction of pumping pressure. In this paper this effect will be examined in regard to a fundamental physical explanation on a particle level. In addition, the effect of the EMF on the lubrication layer in a sliding pipe rheometer and the bulk material in a pumping circuit at laboratory scale will be investigated.

2 Principle of Electromagnetic Fields

An electromagnetic force $\vec{F}$[N] acts on a particle with charge q [C] moving with velocity $\vec{v}$ [m/s] due to an external electric field $\vec{E}$ [V/m] and magnetic field $\vec{B}$ [V_s/m^2]:

$$\vec{F} = q \cdot \vec{E} + q \cdot \vec{v} \times \vec{B}$$

In a cylindrical coil, fed by an alternating current, a magnetic field occurs which realigns permanently according to the current flux. The resulting force is independent from the direction of current flux into the center of the coil.

A change in the magnetic flux through a surface ϕ_{mag} (surface integral of the normal component of magnetic field $\vec{B}$) will cause an electric voltage U_{ind} [V] and herewith an electric field orthogonal to the magnetic field:

$$U_{ind} \sim -\frac{\partial \phi_{mag}}{dt}$$

In addition, an electric field moves charged particles into the direction of field. The electric field varies due to variations in frequencies and in field intensity. Moreover, a realignment occurs due to the realignment of the magnetic field.

Therefore, material which is pumped through coils (moving charged particles) experiences a permanent as well as an oscillating force in the inlet and outlet of the coils. The intensity of the electric and magnetic field decreases with greater depth in the coil and depends on frequency but also on material properties (magnetic and relative permeability). Herewith the effect of the electromagnetic field on the material is assumed to be higher in the vicinity of the wall compared to the bulk material.

3 Material and Mixing Procedure

The composition of the mortar mixtures under investigation are given in Table 1. For the pumping circuit (PC) batches of 70 L were prepared using an intensive mixer (R08 W, Eirich). Here the solid material (limestone powder (LSP) and/or cement (CEM) and sand) was placed into the mixing container and during the first 30 s of mixing water and superplasticizer were added. The mixing pan rotated with 1.2 m/s and the counter-current mixing tool rotated with 0.37 m/s. The total mixing time was 180 s. For sliding pipe rheometer (SPR) experiments batches of 10 L were prepared with a handheld mixer (Collomix Duo with counter-rotating mixing paddles). Therefore, water and superplasticizer were mixed and placed into a mixing container. While mixing the latter the solid material was added for 60 s and then the material was stirred for another 120 s. After a pause of 60 s for manual homogenization the material was mixed for further 60 s.

Table 1. Compositions of the limestone powder (LSP) and cement (CEM) mortars under investigation in the sliding pipe rheometer (SPR) and the pumping circuit (PC).

Material	Density [kg/m^3]	LS-SPR [kg/m^3]	LS-PC [kg/m^3]	CEM-SPR [kg/m^3]	CEM-PC [kg/m^3]
CEM I 42.5 (d_{50} = 12.9 µm)	3100	0	0	625.0	555.5
LSP (d_{50} = 4.5 µm)	2700	604.8	604.8	60.5	121.0
Sand 0/2	2650	1360.3	1360.3	1360.3	1360.3
Superplasticizer [M.-%]	1050	00.02	0.35	1.30	1.30
V_{Sand}/V_{Powder} [-]		1.1	1.1	1.1	1.1
water/cement [-]		–	–	0,39	0,44
Φ_s [vol.-%]		48	48	48	48

4 Method and Experiment

4.1 Experimental Overview

Three batches of both mortars were executed for each EMF-setting in the pumping circuit (PC):

- LSP/CEM-PC: without EMF
- LSP/CEM-PC-EMF: with EMF after 5 min of pumping

In the sliding pipe rheometer (SPR) three batches were tested as well:

- LS/CEM-SPR: without EMF
- LS/CEM-SPR-EMF: with EMF (pre-shearing without EMF)

4.2 Pumping Circuit at Lab-Scale

A small scale pumping circuit was used under laboratory conditions, Fig. 1. The vertical polyvinyl chloride pipe length was l = 2000 mm with an inner diameter of 36 mm. The total pumping distance was 4200 mm. Behind the screw pump, which pumped constantly at 1 m^3/h ± 0,05 m^3/h, inductors were applied on the outer pipe wall (6 coils, I = 3 A, U = 7 V, f = 125 Hz – 500 Hz), covering a total distance of 550 mm. The inductors were controlled by an electronic device called Fluid Liner. The pipeline was equipped with two pressure sensors (at the beginning and the end of the vertical pipe) and one temperature sensor.

After 5, 15 and 25 min of pumping a sample was taken from the pumping circuit to determine the spread flow as a measure for yield stress. Moreover, after 5 and 25 min samples were taken for rheometer tests using Viskomat XL (Schleibinger). In a linear upward ramp from 0 rpm to 60 rpm torque [Nmm] was measured and the torque-speed slope of the curve [Nmm/rpm] was taken as measure for the plastic viscosity of the material. In addition, for one LS-PC (without EMF) and one LS-PC-EMF a focused beam reflectance measurement (FBRM, G400, Mettler-Toledo) probe was used to track changes in particle size distribution during the pumping process.

4.3 Sliding Pipe Rheometer

A sliding pipe rheometer according to Kasten [7] was used, which enables a reliable estimation of the relationships between pumping pressure and discharge rates for a given pipe geometry. The pressure P [bar], which was prevalent when the pipe was sliding downwards, as well as the speed of the sliding pipe were measured. With the known pipe diameter the discharge rate Q [m^3/h] was calculated.

After mixing the pipe was filled and three downward slides of the pipe were conducted to pre-shear the material. Then various weights were applied (2.5 kg, 22.5 kg, 42.5 kg, with minimum of three slides per weight) to vary the velocity and herewith the pressure.

From the P-Q-curve two parameters a and b were calculated. Parameter a [bar] is a parameter related to yield stress of the material in the vicinity of the wall (y-intercept), parameter b [bar * h/m^3] is the slope of the P-Q-curve and is a parameter related to plastic viscosity in the same region:

$$P = a + b \cdot Q$$

Here, a sliding pipe rheometer with a steel pipe was used with an inner diameter of 125 mm and a total length of 1300 mm, Fig. 2. 6 coils were applied on the pipe to induce an alternating EMF controlled with the same device as the coils in the pumping circuit.

5 Results and Discussion

The results from experiments conducted with (mainly) bulk material from the pumping circuit are shown in Fig. 3. Plastic viscosity and spread flow values of the material extracted from the pumping circuit were normalized to 100% for the first measurement (t = 5 min) to display parameter changes over time (referred to as relative viscosity and relative spread flow). The average measured values are summarized in Table 2.

Table 2. Averaged results and standard deviations σ of spread flow and slope of torque-speed-curve (viscosity related) for limestone (LSP) and cement (CEM) mortar from the pumping circuit.

Material	Spread flow [cm]						Torque-speed-slope [Nmm/rpm]			
	5 min	σ_{5min}	15 min	σ_{15min}	25 min	σ_{25min}	5 min	σ_{5min}	25 min	σ_{25min}
LSP-PC	16.0	0.8	15.7	0.9	15.0	1.1	3.3	0.7	3.5	0.5
LSP-PC-EMF	17.5	1.1	17.2	1.1	15.6	0.9	2.2	0.3	2.6	0.2
CEM-PC	19.6	1.4	18.6	1.1	18.2	0.9	7.6	1.0	6.4	0.2
CEM-PC-EMF	23.2	1.1	22.1	0.9	20.2	0.4	6.4	0.3	6.3	0.2

During pumping an increase in yield stress was observed, expressed by a reduction of spread flow for CEM and LSP mortars (Fig. 3 bottom). For (very fine) LSP this effect may be agglomeration due to attractive intermolecular and surface forces. The reduction of yield stress in cement based materials has been observed by other authors [8] as well. Structural build-up and stiffening of the cement paste may be the cause for a reduced spread flow. Moreover, temperature increase (which occurs during pumping due to permanent friction and induction of shear) leads to an acceleration of hydration reactions [9]. The increase in yield stress was significantly higher (CEM) or tended to be higher (LSP) with activated EMF (Fig. 3 bottom, light and dark grey symbols at the time of 15 and 25 min).

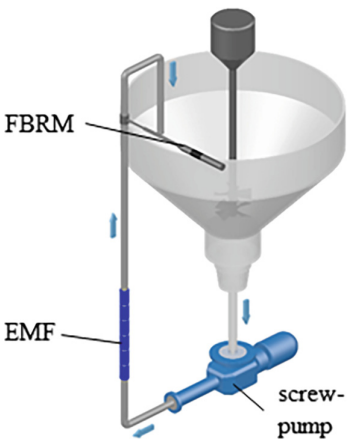

Fig. 1. Pumping circuit.

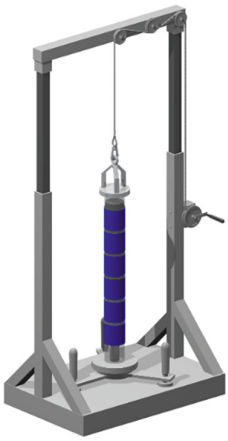

Fig. 2. Sliding pipe rheometer.

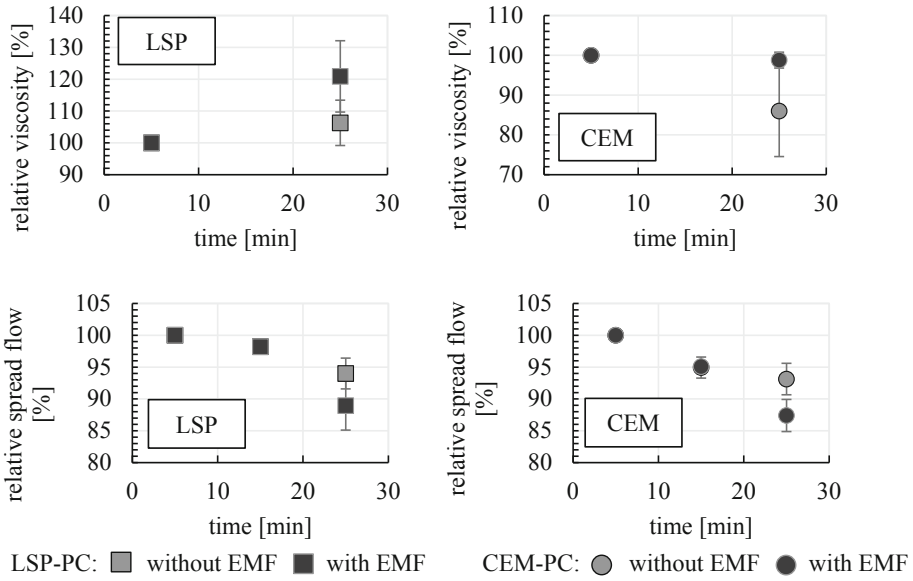

Fig. 3. Averaged results of relative viscosity and relative spread flow of limestone powder (LSP) and cement (CEM) mortar extracted from the pumping circuit after various time of pumping (n = 3).

The plastic viscosity of the bulk material increased during pumping in case of LSP mortars, whereas it decreased for cement mortar (Fig. 3 top). An increase in plastic viscosity may occur due to further agglomeration. A reduction of plastic viscosity of cement based materials has been observed previously (e.g. by [10]). This may be attributed to the redispersion of coagulated or flocculated cement particles due to permanent shearing. When EMF was activated, higher plastic viscosity were determined for pumped CEM and LSP mortars (Fig. 3 top, light and dark grey symbols at the time of 25 min). The hypothesis of LSP agglomeration with active EMF as a main reason for higher viscosity was supported by FBRM-measurements: an increase of the median agglomerate size d_{50} with active EMF in the lubrication layer of pumped LSP mortar was observed, Fig. 4. However, it must be pointed out that the base level of the mean particle size varies slightly in the beginning of the test. As expected, a larger mean agglomerate size resulted in an increase of viscosity. When the EMF was not acting on the particles, the mean particle size did not change. Pressure sensors revealed a reduction of pressure in the pipe over time. With EMF the reduction was more pronounced by 3% (LSP mortar) and 7% (CEM mortar) compared to pumping tests without EMF.

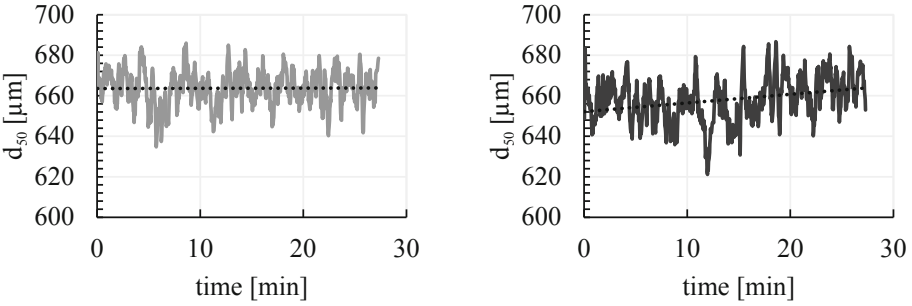

Fig. 4. Median agglomerate size d_{50} of limestone powder mortar during pumping without (left) and with EMF (right).

The averaged measured curves of the pressure-discharge rate relationship determined with the sliding pipe rheometer are shown in Fig. 5. The average and standard deviations of parameters *a* and *b* are given in Table 3. The parameter *a* (yield stress related parameter of the lubrication layer, intercept with y-axes) was lower for both mortars when the EMF was activated. The parameter *b* (viscosity related parameter of the lubrication layer, slope of the curve) was for both materials higher with activated EMF, although the effect was not very pronounced for CEM mortar. Both diagrams reveal an interception point of the two curves, meaning that there is a range of (low) discharge rates when an EMF seems reasonable and economically feasible to apply. In [6] a reduction of pressure in the pipe was mentioned with activated EMF. It may be that the concrete in [6] was pumped with EMF at low discharge rates (before the material specific intersection point) and herewith an reduction in pressure was observed. Though, one has to consider the deviating boundary conditions from the own conducted experiments such as piston vs. screw pump.

However, for the sliding pipe rheometer and the pumping circuit a (relative) increase in viscosity of both, the lubrication layer and the bulk material, was observed when EMF was active. This may be due to enhanced agglomeration of the particles. Forces acting due to the EMF may result into an increased particle mobility and herewith into an accelerated agglomeration process.

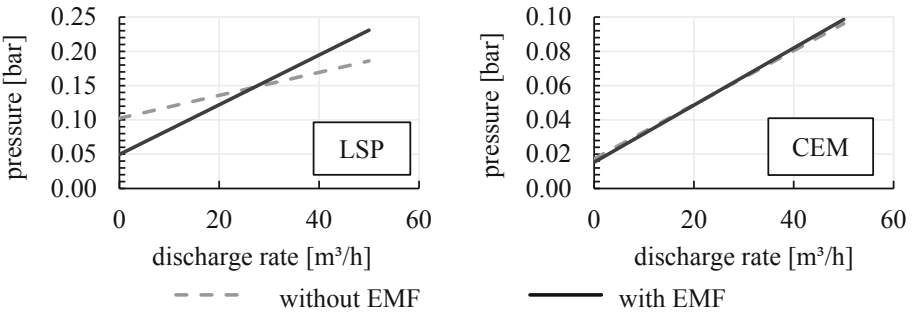

Fig. 5. Averaged pressure-discharge rate curves obtained from sliding pipe rheometer for limestone powder (LSP) and cement (CEM) mortar (n = 3).

Table 3. Average values and standard deviations σ of parameters a (y-intercept) and b (slope) describing pressure-discharge rate-curve in the sliding pipe rheometer (n = 3).

Setting	LSP-SPR				CEM-SPR			
	a [mbar]	σ_a	b [bar * h/m^3]	σ_b	a [mbar]	σ_a	b [bar * h/m^3]	σ_b
Without EMF	102.2	26.2	1.7	0.7	17.3	4.8	1.6	0.1
With EMF	49.6	32.9	3.1	1.4	15.3	4.8	1.7	0.3

Changes in yield stress related parameter from sliding pipe rheometer tests at low discharge rates seems to be in contradiction with results from the pumping circuit tests. Though, the lubrication layer thickness is known to increase with higher discharge rates [3]. Moreover, a lower packing density in the vicinity of a wall may be achieved if particle radii are larger [11]. Assumed that agglomeration was prevalent due to the EMF this would lead to a reduced packing density in the vicinity of the wall. As a consequence, the locally higher fluid volume content may be responsible for an apparently reduced yield stress at low discharge rates. For higher discharge rates more material from the inner part of the pipe is part of the measured (sheared) lubrication layer, hence the effect is much less pronounced.

6 Conclusion and Outlook

The following conclusions were obtained from this study:

- The application of an alternating EMF can lead to an increase in viscosity of bulk material and lubrication layer material for both, limestone powder and cement mortar.
- When EMF was active the increase (bulk material) resp. decrease (lubrication layer) in yield stress was more pronounced compared to measurements without EMF.
- EMF is likely to promote the agglomeration of both tested particle systems and causes herewith a change in rheological properties. For practical causes it is reasonable to use EMF for low discharge rates since the pumping pressure is reduced. However, to fully explain the results observed in full scale tests [6] more research is required.

In the future it is relevant to investigate various EMF-settings (e.g. frequency band, pipe material) and their effect on a broader range of materials. Moreover particular properties of the base material should be related to the observed effects (such as polarization [12]).

Acknowledgement. The authors appreciate the provision of the SPR by Leibniz University of Hannover.

References

1. Secrieru E, Butler M, Mechtcherine V (2014) Prüfen der Pumpbarkeit von Beton - Vom Labor in die Praxis. Bautechnik 91(91):797–811
2. Choi M, Roussel N, Kim Y, Kim J (2013) Lubrication layer properties during concrete pumping. Cem Con Res 45:69–78
3. Khatib R (2013) Analysis and prediction of pumping characteristics of high-strength self-consolidating concrete, PhD-thesis, Université de Sheerbrooke
4. Kaplan D, de Larrard F, Sedran T (2005) Design of concrete pumping circuit. ACI Mater J 102:110–117
5. Jacobsen S, Haugan L, Hammer TA, Kalogiannidis E (2009) Flow conditions of fresh mortar and concrete in different pipes. Cem Con Res 39:997–1006
6. Choi MS, Kim YS, Kim JH, Kim J, Kwon SH (2014) Effects of an externally imposed electromagnetic field on the formation of a lubrication layer in concrete pumping. Constr Build Mater 61:18–23
7. Kasten K (2010) Gleitrohr-Rheometer: Ein Verfahren zur Bestimmung der Fließeigenschaften von Dickstoffen in Rohrleitungen, PhD-thesis, TU Dresden
8. Secrieru E, Cotardo D, Mechtcherine V, Lohaus L, Schröfl C, Begemann C (2018) Changes in concrete properties during pumping and formation of lubricating material under pressure. Cem Con Res 108:129–139
9. Nehdi M, Al Martini S (2009) Estimating time and temperature dependent yield stress of cement paste using oscillatory rheology and genetic algorithms. Cem Con Res 39:1007–1016
10. Jang KP, Kwon SH, Choi M, Kim Y, Park C, Shah S (2018) Experimental observation on variation of rheological properties during concrete pumping. Int J Concr Struct Mater 79:1–15
11. Zok F, Lange F (1991) Packing density of composite powder mixtures. J Am Ceram Soc 74:1880–1885
12. De Schutter G, Lesage K (2018) Active control of properties of concrete: a (p)review. Mater Struct 123:1–16

Influence of Aggregate Volume Fraction on Concrete Pumping Behaviour

Shirin Fataei(✉), Egor Secrieru, and Viktor Mechtcherine

Institute for Construction Materials,
Technische Universität Dresden, Dresden, Germany
shirin.fataei@tu-dresden.de

Abstract. The paper at hand quantifies the influence of aggregate volume fraction on pumping behaviour of concretes with distinct flow behaviours, i.e. plug or shear flow type. For this purpose, conventionally vibrated concretes (CVC), and self-compacting concretes (SCC) containing different volume fraction of aggregates are designed, and their rheological properties are investigated. The results indicate that the concrete pumpability, in terms of delivery rate for a given pressure, decreases by at least 30% for 10% increase in aggregates content by volume. The relative decrease in pumpability is more pronounced for CVC. Furthermore, it is shown that under certain experimental conditions the rheological properties of the lubricating layer (LL) can be approximated to those of the constitutive mortar in pumped concrete. Accordingly, the measurements on constitutive mortar can be used as a basis for the analytical prediction of pumping pressure. The obtained knowledge is a prerequisite for evaluating flow-induced particle migration (FIPM) during pumping and LL formation.

Keywords: Pumping · Rheology · Lubricating layer · Aggregate volume fraction · Flow-induced particle migration

1 Introduction

Pumping is the most efficient transportation and casting method for concrete, especially in the case of large construction sites. The pumping behaviour of concrete is determined by an appropriate design of its composition under consideration of rheological properties of both concrete bulk and lubricating layer (LL) forming at the pipe wall-concrete interface [1–3]. The rheological properties of LL play a crucial role in concrete pumpability. Choi et al. [3] suggested that the LL and the constitutive mortar of the pumped concrete show similar rheological behaviour. However, Le et al. [4] reported that the paste content and the maximum aggregate size of LL are not identical to those of the constitutive mortar. The last was explained by flow-induced particle migration (FIPM) in fresh concrete at the high shear rates which alters the composition and rheological properties of the LL [5, 6]. Moreover, Phillips et al. [7] and Jo et al. [8] highlighted that the FIPM is the underlying mechanism for the formation of LL that governs the concrete flow through the pipeline. With the migration of coarser particles toward the centreline, the surplus paste moves toward the pipe wall and contributes to

V. Mechtcherine et al. (Eds.): RheoCon 2019/SCC 2019, RILEM Bookseries 23, pp. 303–310, 2020.
https://doi.org/10.1007/978-3-030-22566-7_35

the formation of LL [8]. While the impact of aggregate shape and size on concrete rheology and pumpability has been extensively studied [9, 10], the influence of the volume fraction of aggregates on concrete pumping behaviour and FIPM has not been explicitly quantified so far.

The objective of the work at hand is to experimentally evaluate the influence of aggregate volume fraction on concrete pumpability, in terms of delivery rate for a given pressure. In what follows, the concrete is considered as a two-phase suspension consisting of a non-Newtonian fluid and poly-dispersed particles [5, 8, 11]. The obtained knowledge will be applied to qualitatively and quantitatively analyse the FIPM and LL formation at high shear rates characteristic for pumping.

2 Experimental Investigation

2.1 Materials and Mixture Design

Two concrete types were examined: conventionally vibrated concrete (CVC) and self-compacting concrete (SCC). For each concrete type, three mixture compositions were designed to purposefully investigate the influences of aggregates volume fraction and constitutive mortar rheology on concrete pumping behaviour as well as on rheological properties of the forming lubricating layer (LL). The compositions of concretes and constitutive mortars are given in Table 1.

Table 1. Compositions of concrete mixtures under investigation.

Materials		Density [kg/m^3]	Dosage [kg/m^3]					
			C42	C47	C52	S37	S42	S47
Constitutive mortar	CEM III/A 42.5 N	2990	425	388	351	392	361	330
	Fly ash	2200	–	–	–	239	220	201
	Quartz powder	2677	57	52	47	52	48	44
	Quartz sand 0.06/0.2	2650	57	52	47	52	48	44
	Quartz sand 0/1	2650	456	416	376	420	387	354
	Water	1000	211	192	173	180	166	152
	SP	1056	3.48	3.18	2.87	11.14	10.26	9.38
Aggregates	Quartz sand 1/2	2650	210	235	260	185	210	235
	Quartz sand 2/4	2650	210	235	260	185	210	235
	Quartz gravel 4/8	2650	290	325	360	255	290	325
	Quartz gravel 8/16	2650	403	451	500	355	403	451
w/b [-]			0.50	0.50	0.50	0.30	0.30	0.30
SP % bwoc			0.72	0.72	0.72	2.85	2.85	2.85
Vol. agg. (>1 mm) [%]			42	47	52	37	42	47
Concrete flow table [mm]			640	545	450	–	–	–
Concrete slump flow [mm]			–	–	–	720	680	600
Mortar flow table [mm]			260	260	240	–	–	–
Mortar slump flow [mm]			–	–	–	300	290	250

Each mixture was given a specific name, e.g. C47 is a CVC and S42 is a SCC with an aggregate volume of 47% and 42%, respectively. For simplicity, the constitutive fine mortar with a max. aggregate size of one mm and the "coarse" aggregates larger than one mm are referred as "mortar" and "aggregates".

2.2 Experimental Measurements

The rheological properties of concrete bulk were determined using a wide coaxial gap concentric cylinder viscometer ConTec 5 [12]; see Fig. 1a.

The pressure-flow rate relationship (P–Q curve) for the concretes under investigation was determined using a portable in-situ device Sliding Pipe Rheometer (Sliper) which has previously proven reliable to estimate the required pumping pressure for specific flow rates in full-scale pumping experiments [13, 15]; see Fig. 1b.

The constitutive mortar was sieved out of concrete using a mesh opening size of one mm under the assumption that the largest particle in the forming LL is within this range. The new approach is in contrast to the previous research by the same group described in [9] where a two mm sieve was applied. The comparison of the results will be published elsewhere. The HAAKE MARS II rheometer equipped with a special cell and measuring geometry were used to determine the rheological parameters of the constitutive mortar instead of the forming LL; see Fig. 1c.

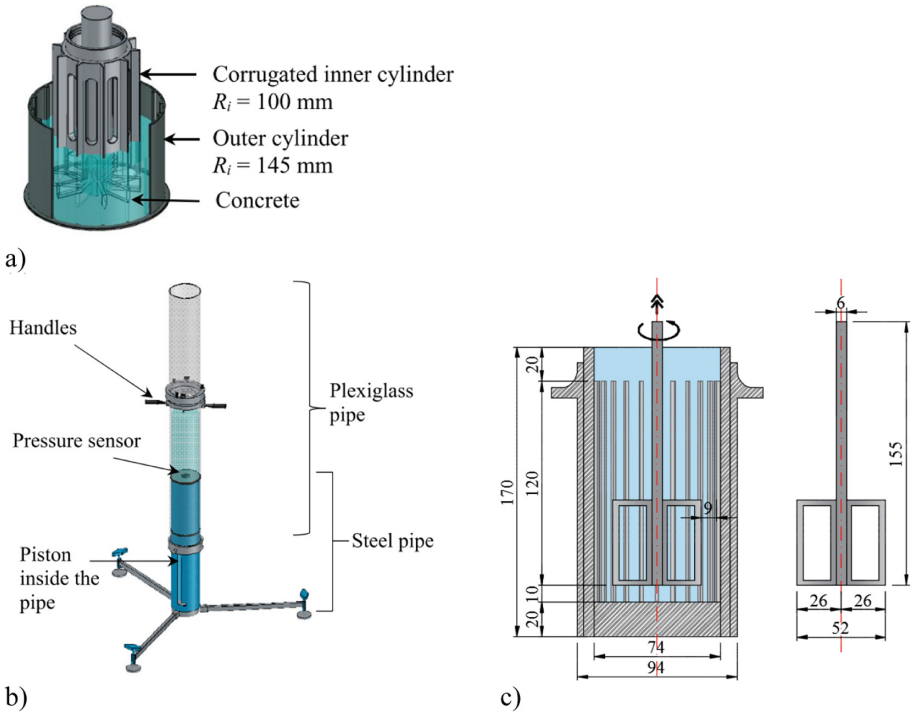

Fig. 1. (a) ConTec 5 viscometer geometry [13], (b) Sliper setup [9] and (c) unit cell and rotor for HAAKE MARS II rheometer (units in [mm]) [14].

2.3 Analytical Approach for Predicting Pumping Pressure

The movement of concrete in a pipe can be generalised as a combination of shearing of LL, partial shearing of concrete bulk and plug flow [16]. The discharge rate Q is computed by integrating the velocity profiles over the area of the pipe cross-section, see Eq. 1:

$$Q = \int_{R_{LL}}^{R} 2\,\pi \cdot r\, v_{LL}(r)dr + \int_{R_P}^{R_{LL}} 2\,\pi\, r\, v_s(r)dr + \int_{0}^{R_P} 2\,\pi \cdot r\, v_P dr$$
$$Q = \frac{3600\,\pi}{24 \cdot \mu_{LL}\,\mu} \cdot \left[\begin{array}{l} 3\,\Delta P\,\mu \cdot \left(R^4 - R_{LL}^4\right) - 8\,\tau_{LL} \cdot \mu\left(R^3 - R_{LL}^3\right)\ldots \\ +3\,\Delta P \cdot \mu_{LL} \cdot \left(R_{LL}^4 - R_P^4\right) - 8\,\tau \cdot \mu_{LL} \cdot \left(R_{LL}^3 - R_P^3\right) \end{array} \right] \quad (1)$$

where v_{LL} [m/s], v_S [m/s] and v_P [m/s] are the velocities in LL, sheared and plug regions of concrete bulk, respectively. R [m], R_{LL} [m] and R_P [m] represent the pipe, LL and plug radii. τ_{LL} [Pa] and μ_{LL} [Pa·s] are the yield stress and plastic viscosity of LL; τ [Pa] and μ [Pa·s] are the corresponding values of concrete bulk. ΔP [Pa/m] indicates the pressure loss per meter length. The average LL thickness e, with $e = R - R_{LL}$, is calculated for each measured P–Q values from Sliper acc. to Eq. 1. These values can be later applied for prediction of pressure in full-scale pumping. The viscosity of the fluid phase (mortar) and the volume fraction of particles (aggregates) are the most decisive parameters in the diffusive flux model and FIPM [7, 8]. Thus, the objective of the analytical approach is to investigate the link between the estimated thickness of LL and the former two parameters.

3 Results and Discussion

3.1 Rheological Properties of Constitutive Mortar and Concrete Bulk

Figure 2 depicts the Bingham parameters, i.e. yield stress and plastic viscosity, of the concretes and constitutive mortars under investigation. An increase in the aggregate volume fraction by 5%, i.e. from 42% to 47% for CVC and from 37% to 42% for SCC has a minor effect on Bingham parameters of the constitutive mortars. However, an increase in aggregate content by further 5% causes a pronounced increase in both yield stress (except S47) and plastic viscosity values, primarily due to the water demand of the extra aggregates and the detrimental impact on mixture workability.

In contrast, the impact of aggregate content on rheological properties of the concrete bulk is straightforward: The additional solid inclusions hinder the flowability of the entire system. Hence, both yield stress and plastic viscosity values significantly increase. Furthermore, the influence of additional aggregate volume on rheological parameters is more pronounced in CVC mixtures. It can be reasoned by the fact, that the CVC mixtures contain by default a lower paste volume in comparison to SCC. In the case of C52, the volume fraction of all particles larger than 0.06 mm reaches

$\phi = 0.68$, while the dense packing fraction is $\phi_c = 0.80$ resulting in $\phi/\phi_c = 0.85$. Therefore, the viscosity value of C52 approaches the critical region after which an exponential increase is expected [11]. By decreasing the total paste amount in the system, the stress transfer during deformation is prone to drift from hydrodynamic to frictional interaction [17].

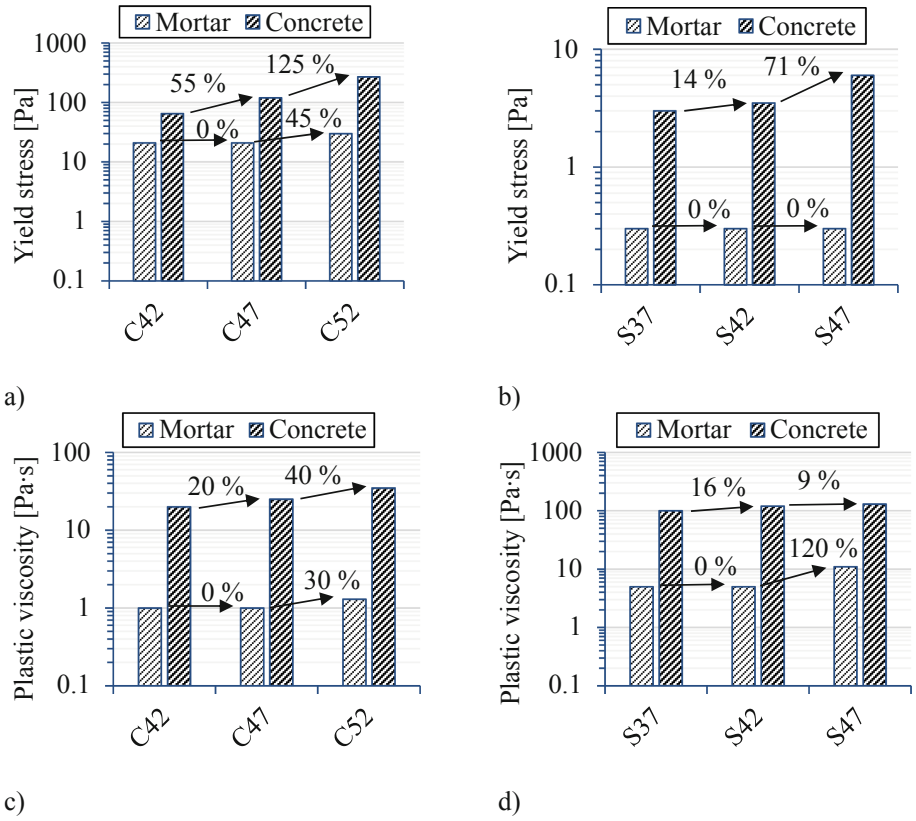

Fig. 2. Evolution of Bingham parameters (a)-(b) yield stress and (c)-(d) plastic viscosity for the concretes and constitutive mortars under investigation.

3.2 Pumping Pressure vs. Aggregate Volume Fraction

Figure 3 summarises the *P*–*Q* values for the concretes under investigation. The results are directly obtained from measurements with Sliper. The outcomes clearly indicate that the concrete pumpability reduces by at least 30% for 10% increase in aggregate volume for SCC and by almost 60% for CVC. This reduction in pumpability can be traced back to the larger changes in the rheological parameters for both concrete bulk and constitutive mortars in case of CVC. Indeed, the yield stress and to a larger extent the viscosity parameters have a strong impact on pumping pressure; see Eq. 1.

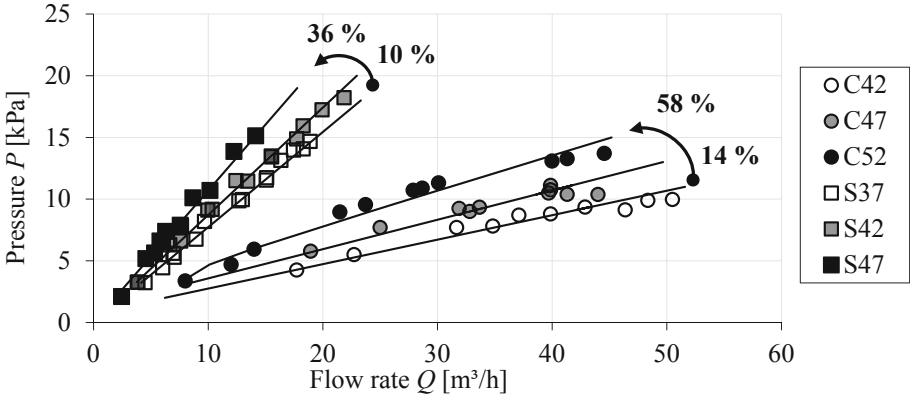

Fig. 3. Comparison between *P*–*Q* values determined by the Sliper.

In Table 2 the results for the analytical thickness of LL are shown. These values depend on mixture composition and represent a "concession" between the actual LL thickness, i.e. a very thin and aqueous film at the concrete-pipe interface, and the thickness of the layer whose properties can be rheologically determined based on the constitutive mortar. In the opinion of the authors, the general assumption of a constant LL thickness for any mixture type [18] is inaccurate and compromises the prediction of *P*–*Q*.

Table 2. Analytical thickness *e* of LL.

Concrete mixture	C42	C47	C52	S37	S42	S47
e [mm]	1.13	0.96	1.16	1.58	1.37	2.81

3.3 Link to Flow-Induced Particle Migration

The viscosity of mortar and volume fraction of aggregates are crucial parameters to affect FIPM [7, 8]. It can be assumed that the intensity of FIPM and thickness of LL increase with the viscosity value (directly proportional) and diminish with increasing aggregate volume fraction (inversely proportional). Moving from C42 to C47, the volume of aggregates was increased by 5% without any notable changes in viscosity value of the LL (constitutive mortar), and as expected, the thickness of LL decreased; see Table 2. In the case of C47 and C52, the volume fraction of aggregates was increased by 5% again. This further increase in the aggregate content caused an increase in the LL viscosity by 30%. Since the analytical thickness of LL for the C52 mixture also increased, it can be stated that the influence of viscosity is dominating. Both assumptions are congruent also for SCC mixtures, S37, S42 and S47.

4 Summary and Outlook

As a first step in investigating the underlying mechanisms of the flow-induced particle migration (FIPM) and lubricating layer (LL) formation, the authors quantify the influence of aggregate volume fraction on pumping behaviour for concretes showing distinct flow behaviours. Moreover, the analytical approach to predict the pressure-flow rate relationship (P–Q curve) is used to estimate the thickness of the LL required for prediction of pumping pressure. The following conclusions can be drawn:

- The impact of increasing aggregate content on concrete bulk rheology is straightforward: The additional solid inclusions reduce the flowability of the entire system and therefore also the pumpability;
- In case of the constitutive mortar, an increase in the aggregate content by 5%, i.e. from 42% to 47% by volume for CVC and from 37% to 42% for SCC, has a minor effect on Bingham parameters. However, a further increment by 5% in aggregate volume causes an increase in both yield stress and plastic viscosity values, primarily due to the supplementary water demand of the added aggregate amount;
- The necessary concrete pumping pressure rises by more than 30% for 10% increase in aggregates volume fraction for self-compacting concrete (SCC) and by almost 60% for conventionally vibrated concrete (CVC);
- The accuracy of the analytical approach for prediction of concrete pumping pressure [16] can be further improved under consideration of the LL analytical thickness;
- The intensity of FIPM and thickness of LL are assumed to increase with increasing viscosity of fine mortar and diminish with increasing aggregate volume fraction;
- For analytical prediction of pumping pressure, the rheological properties of the LL can be approximated to those of the constitutive mortar.

Acknowledgement. This paper is a part of the first author's PhD dissertation. The research is funded by German Research Foundation (DFG) within the priority program SPP 2005: Opus Fluidum Futurum – Rheology of reactive, multiscale, multiphase construction materials. The authors gratefully acknowledge the supply of binder by HeidelbergCement AG and admixtures by BASF Construction Solutions GmbH.

References

1. Kaplan D, De Larrard F, Sedran T (2005) Design of concrete pumping circuit. ACI Mater J 102:110–117
2. Feys D, De Schutter G, Verhoeven R (2012) Parameters influencing pressure during pumping of self-compacting concrete. Mater Struct 46:533–555
3. Choi M, Roussel N, Kim Y, Kim J (2013) Lubrication layer properties during concrete pumping. Cem Concr Res 45:69–78
4. Le HD, Kadri E, Aggoun S, Vierendeels J, Troch P, De Schutter G (2015) Effect of lubrication layer on velocity profile of concrete in a pumping pipe. Mater Struct 48:3991–4003

5. Spangenberg J, Roussel N, Hattel JH, Stang H, Skocek J, Geiker MR (2012) Flow induced particle migration in fresh concrete: theoretical frame, numerical simulations and experimental results on model fluids. Cem Concr Res 42:633–641
6. Feys D, Khayat KH, Perez-schell A, Khatib R (2014) Development of a tribometer to characterize lubrication layer properties of self- consolidating concrete. Cem Concr Compos 54:40–52
7. Phillips RJ, Armstrong RC, Brown RA, Graham AL, Abbott JR (1992) A constitutive equation for concentrated suspensions that accounts for shear- induced particle migration. Phys Fluids A Fluid Dyn 4:30–40
8. Jo SD, Park CK, Jeong JH, Lee SH, Kwon SH (2012) A computational approach to estimating a lubricating layer in concrete pumping. Comput Mater Contin 27:189–210
9. Secrieru E, Fataei S, Schröfl C, Mechtcherine V (2017) Study on concrete pumpability combining different laboratory tools and linkage to rheology. Constr Build Mater 144:451–461
10. Kwon SH, Jang KP, Kim JH, Shah SP (2016) State of the art on prediction of concrete pumping. Int J Concr Struct Mater 10:75–85
11. Guazzelli É, Pouliquen O (2018) Rheology of dense granular suspensions. J Fluid Mech 852:P11–P173
12. Heirman G, Hendrickx R, Vandewalle L, Van Gemert D, Feys D, De Schutter G, Desmet B, Vantomme J (2009) Integration approach of the Couette inverse problem of powder type self-compacting concrete in a wide-gap concentric cylinder rheometer. Cem Concr Res 39:171–181
13. Secrieru E (2018) Pumping behaviour of modern concretes – Characterisation and prediction. PhD thesis, TU Dresden
14. Mechtcherine V, Secrieru E, Schröfl C (2015) Effect of superabsorbent polymers (SAPs) on rheological properties of fresh cement-based mortars—development of yield stress and plastic viscosity over time. Cem Concr Res 67:52–65
15. Kasten K (2010) Gleitrohr – Rheometer, Ein Verfahren zur Bestimmung der Fließeigenschaften von Dickstoffen in Rohrleitungen, TU Dresden
16. Kwon SH, Park CK, Jeong JH, Jo SD, Lee SH (2013) Prediction of concrete pumping: part II—analytical prediction and experimental verification. ACI Mater J 110:657–668
17. Browne RD, Bamforth PB (1977) Tests to establish concrete pumpability. ACI J Proc 74:93–203
18. Choi MS, Kim YJ, Jang KP, Kwon SH (2014) Effect of the coarse aggregate size on pipe flow of pumped concrete. Constr Build Mater 66:723–730

Effect of Mixing Procedure on the Rheological Properties and Hydration Kinetics of Portland Cement Paste

Danila Fabiane Ferraz[1,2(✉)], Ariane C. R. Martho[1], Elizabeth G. Burns[1], Roberto C. O. Romano[2], and Rafael G. Pileggi[2]

[1] GCP Applied Technologies, Sorocaba, Brazil
danila.f.ferraz@gcpat.com
[2] Department of Civil Construction Engineering, University of São Paulo, São Paulo, Brazil

Abstract. The mixing procedure used to make paste, mortar or concrete has an important influence on the hydration kinetics and rheological properties of cementitious materials. In this study, different shear mixing procedures were studied to evaluate the effect on the kinetics of hydration for Portland cement paste by isothermal calorimetry over 72 h. The rheological properties of the same pastes in terms of yield stress (Pa) and apparent viscosity (Pa.s) were also studied with the same mixing procedures: manual, 2500 rpm and high shear mixing at 10000 rpm. To compare the heat flow over the time of each mixing procedure with the stiffening, an oscillatory rheometry evaluation with continuous flow was carried out. All the tests were carried out in triplicate and the variability was evaluated.

The results show important differences in terms of enhancement of height of the main heat evolution peak and reduction of the induction period when the paste was mixed at 10000 rpm (high shear), moreover, the oscillatory rheometry showed that the high shear mixing reduced the stiffening time of the mix compared to manual mixing and 2500 rpm mixing.

Keywords: Chemical reaction · Rheology · Portland cement · Superplasticizer · Mixing procedure

1 Introduction

Rheological properties of the cement paste, and the kinetics of hydration reaction are influenced by the mixing procedure and admixture usage. Among the different factors influencing the behavior of a paste on fresh state, the homogeneity in the mixing of a suspension is certainly one of the most important. Non-homogeneous paste, mortar or concrete will result in lower mechanical strength due to high amount of voids/porosity, thus reducing the concrete lifetime [3]. Fine materials in suspension agglomerate very easily due to interparticle interactions, hence the chemical admixtures are used to disperse the cement particles and reduce the yield stress of the cementitious suspensions [3]. This leads to a reduction on the amount of water in the mix at equal flow, thereby reducing porosity and increasing strength [4].

V. Mechtcherine et al. (Eds.): RheoCon 2019/SCC 2019, RILEM Bookseries 23, pp. 311–319, 2020.
https://doi.org/10.1007/978-3-030-22566-7_36

The use of superplasticizers permits the development of repulsive forces due to the adsorption of the polymers on the surface of the cement particles. This way, the mixing procedure combines the mechanical dispersion effect in combination with the repulsion caused by the admixture [6]. The admixture used in this work is a polycarboxylate based superplasticizer; the main purpose is increasing the fluidity of the paste. The procedure used to make cementitious suspensions also plays an important role; the characteristics of the fresh state of paste, mortar and concrete are dependent on mixing [9].

The aim of this study is to evaluate the influence of different mixing procedures on the hydration kinetics of Portland cement paste, and the rheological behavior, which is characterized as yield stress (Pa), apparent viscosity (Pa.s) and stiffening of the paste by oscillatory rheometry evaluation to investigate the properties of the agglomerated and dispersed state, each mixing procedure was evaluated with (dispersed) and without (agglomerated) admixtures.

2 Materials

A commercially available blended cement type CP V of the local region (Brazil) was studied, collected directly at the cement plant. A polycarboxylate-based superplasticizer admixture, MiraFlow 973 (GCP Applied Technologies), was used in combination with this cement to keep the particles dispersibility and increase the paste fluidity. The dosage of the admixture was fixed at 0.35%, considering the paste dispersion comparing with non-dispersed mix.

3 Methods

3.1 Cement Characterization

Particle Size Distribution: equipment used: Malvern Instruments model Mastersizer 2000/2000E. The test was performed wet, in absolute ethyl alcohol.

X-ray Fluorescence (XRF): according to ISO/FDIS 29581-2:2009 (E) – equipment used: Panalytical model Minipal Cement, from melt pellets on a Claisse model M4 melting machine using melt-based lithium tetraborate/ lithium metaborate mixtures MAXXIFLUX (66.67% $Li_2B_4O_7$, 32.83% $LiBO_2$ and 0.50% LiBr), with a ratio of 1 g of sample: 6.75 g of flux.

X-ray Diffraction (XRD): according to ASTM C1365-06 (2011), using an equipment Rigaku model Windmax 1000, operating on copper Kα radiation with 40 kV–20 mA and scanning of 2°/min. Identification of the compounds was performed using Panalytical X-pert HighScore Plus software (version 3.0) and diffraction patterns provided by the International Center for Diffraction Data (ICDD), the calculations were done by using Rietveld methods.

Figure 1 presents the cement particle size distribution. Table 1 shows the chemical species of the binder obtained by X-ray fluorescence and the mineralogical composition obtained by X-ray diffraction and applying the Rietveld refinement method.

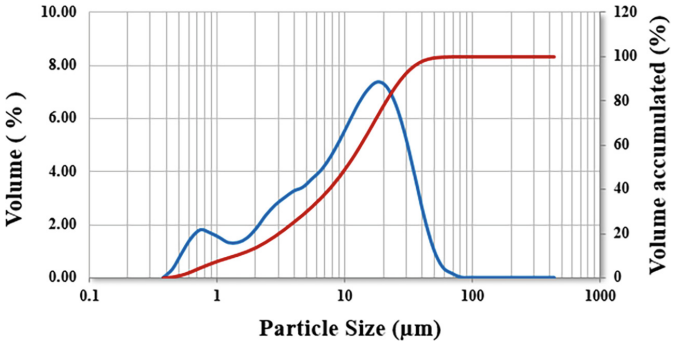

Fig. 1. Particle size distribution of the cement sample

Table 1. Chemical composition by fluorescence of X-ray and mineralogical composition by diffraction of X-ray calculated by Rietveld

Analyte, %	XRF
SiO_2	18.60
Al_2O_3	4.78
Fe_2O_3	2.48
CaO	61.27
MgO	5.31
SO_3	2.99
Na_2O	0.19
K_2O	0.85
TiO_2	0.21
P_2O_5	0.12
Mn_2O_3	0.14
SrO	0.05
Cr_2O_3	<0.01
ZnO	<0.01
L.O.I (950°C)	3.09
Total	100.1
Alk_{eq} ($Na_2O + 0.658K_2O$)	0.75

Analyte, %	XRD
Alite	66.8
Belite	9.6
Brownmillerite	5.4
C3A_cubic	3.5
C3A_ortho	1.3
Periclase	4.9
Calcite	3.5
Gypsum	3.5
Hemihydrate	1.5

3.2 Paste Mixing Procedure

Dry cement powder was weighed in a beaker and the water plus admixture in another: the water/cement ratio was maintained at 0.4. The water was added to the cement immediately before running each mixing speed: manual (with a spatula), 2500 rpm and 10000 rpm, for one minute. The suspensions were used in the rotational and oscillatory rheometry and isothermal conduction calorimetry tests. The mixer used for 2500 rpm is a Fisatom and for the 10000 rpm is a high shear mixer (Makita).

Rotational and Oscillatory Rheometry: The cementitious pastes were added to an Anton-Paar rheometer, model MCR302. The tests were performed using cross-hatched stainless-steel parallel plate geometry with diameter of 25 mm (PP25/P2), to guarantee shear without slipping during the tests. The stepped flow test was used for the determination of rheological parameters and the type of behavior under different shear conditions. The shear rate was kept constant for 10 s at each step and the shear stress and viscosity as a function of the shear rate was measured from a mean of the last 5 s [2]. The oscillatory rheometry was used to evaluate the evolution of the gain of consistency over the time of each paste without damaging the structure in formation, for this the oscillatory frequency was maintained at 1 Hz and deformation at 10-4. The test was performed for 15000 s.

Isothermal Conduction Calorimetry: carried out using an equipment TAM AIR, TA Instrument. The results of this technique allow the evaluation of the kinetics of the chemical reactions that occur during the first 72 h of hydration of the cement [1].

4 Results and Discussion

The results obtained from rotational rheometry are usually presented in the form of shear stress versus shear rate graphs, but for this work, the results are presented in terms of apparent viscosity, yield stress for a given dose of admixture.

As the tests are performed in two steps (acceleration and deceleration), the result obtained in the deceleration was used, since the material had already undergone the condition of greater imposed shear and there is a natural tendency of re-agglomerate. The apparent viscosity was estimated at the maximum shear rate. A well dispersed suspension should have low yield stress and apparent viscosity.

The variation in the apparent viscosity and in the yield stress of the pastes is indicated as a function of the type of mixing procedure. There are different ways to get these values. One of them is from the application of rheological modeling, such as from Herschel-Bulkley, Casson, Bingham, et al. [8]. In these cases the viscosity obtained is plastic, but care must be taken with the model parameters, as they often result in negative flow values, very low plastic viscosity and very high modeling errors [9]. Another way of comparing the values is to collect raw data directly in the graph. In this scenario, the values of apparent viscosity was obtained at the maximum shear rate applied in the test, since it is the state of greater dispersion of the particles. In the graph of stress vs. shear rate, viscosity is the ratio of both. The yield stress was quantified as the shear stress value at the lowest rate used in the test: as the tests were performed in two stages (acceleration and deceleration) the results of the deceleration step were adopted, since the material had already passed through the higher imposed shear condition, and there is a natural tendency for re-bonding. Results of both, viscosity and yield stress, are presented in Figs. 2 and 3. On the left are the results obtained for the pastes mixed without admixture and on the right with the polycarboxylate-based admixture.

The repeatability of each mixture was monitored evaluating three times each composition (three different batches); the error bars represent one standard deviation.

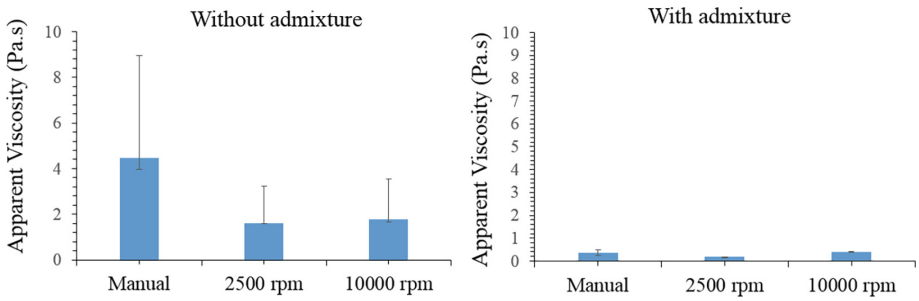

Fig. 2. Left: apparent viscosity without admixture; Right: apparent viscosity with admixture (error bars represent one standard deviation)

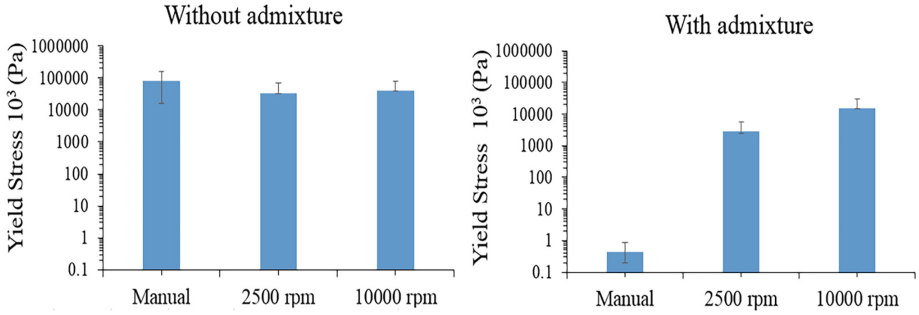

Fig. 3. Left: yield stress without admixture; Right: yield stress with admixture (error bars represent one standard deviation)

Comparing the three mixing regimes, the manual mixing is sub-optimal. The agglomerates are not all broken, and the admixture is unable to stabilize a new, more fluid, situation. On the other hand, the 10000 rpm mixing also produces higher viscosity. In this case "over mixing" is breaking down the agglomerates, creating surface area beyond the ability of this amount of admixture to stabilize. The amount of admixture and the shear force from 2500 rpm mixing are well-matched, leading to a fluid, well-stabilized system.

The results for yield stress are intriguing. Higher shear creates higher dynamic yield stress, which relates to lower slump. This high shear mixing, likely too high for optimum admixture performance, liberated a lot of cations, as revealed in the calorimetry data. The higher yield stress may be due to the accelerated dissolution of ions from cement under high shear conditions. This condition may cause poor polycarboxylate adsorption to rapidly dissolving cement phases. From another perspective, the early products of cement hydration (ettringite) may be enhanced, and decrease the fluidity of the mixture, increasing the yield stress.

The rotational rheometry for characterization of cementitious pastes and evaluation of rheological behavior is an important tool for the cementitious materials studies, but which can only draw correct conclusions if the mixture is suitable. The Fig. 4 shows the influence of the mixing procedure on the heat flow of each mix. In these cases, there was no variability among the three tests of each mixing condition. The intensity of mixing shows the most significant differences on the heat flow results, the manual and 2500 rpm mixes showed similar behavior on the mixes without admixture, but the 10000 rpm showed an important reduction on the induction period. This is likely due to exposing more cement surface to water. When admixture is used, the induction period decreased with increasing intensity mixing. Exposing more cement surface area also caused more sulfate and aluminate to dissolve in a short period of time. The soluble salts react more quickly, as is observed in the calorimetry [2 and 5]. In addition, increased induction times are observed on the pastes with admixture when compared to the without admixtures one (Fig. 5) [6]. The polycarboxylates in the admixture adsorb on the surface, and this slows the rate of cement hydration by protecting the cement surface [9].

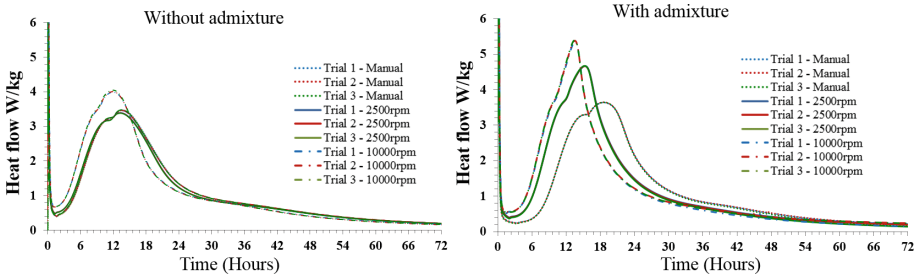

Fig. 4. Calorimetry - heat flow of the different mixing procedures with and without admixture

The oscillatory rheometry showed increase on the variability of the hand mixed paste with admixture when compared to the no admixture paste, the 10000 rpm paste with admixture showed higher storage modulus over the time (Fig. 6). Development of a storage modulus is diagnostic of a network forming – in this case cement hydration and likely growth of ettringite needles.

The early development of the network is consistent with deagglomeration of the cement particles by high shear mixing and consequent polycarboxylate adsorption and hydration. The differences between high shear mixing with and without polycarboxylate suggests the presence of admixture influences the pathway as well as the kinetics of cement hydration.

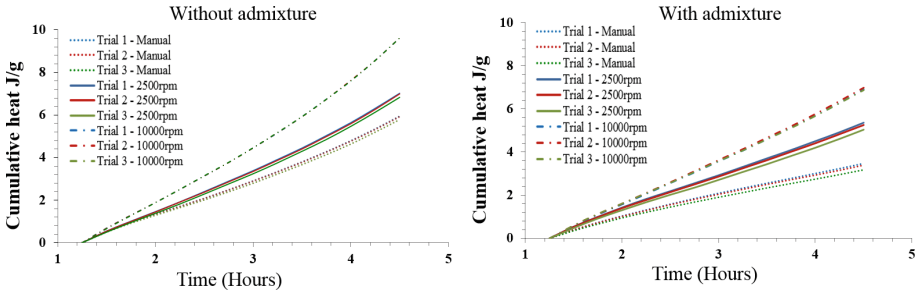

Fig. 5. Cumulative of the different mixing procedures with and without admixture

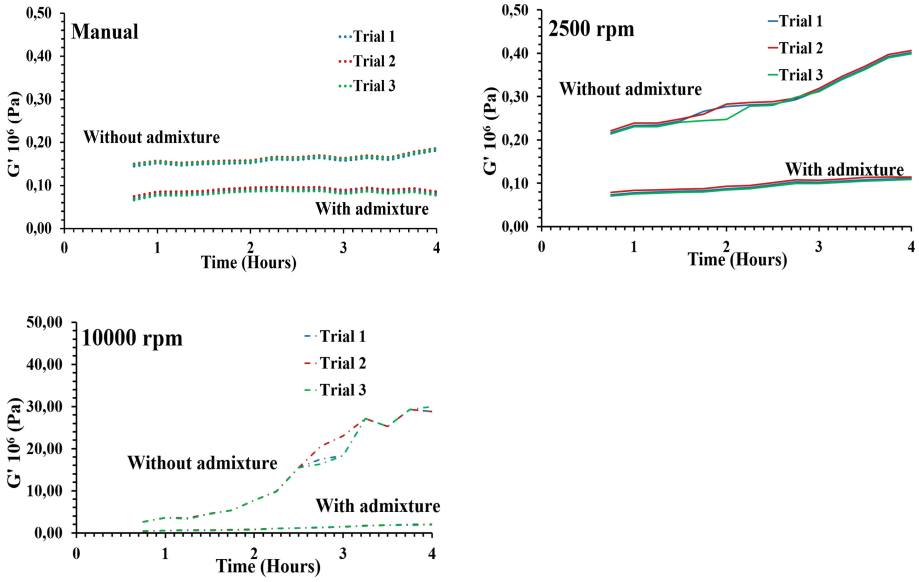

Fig. 6. Stiffening of different mixing procedures with and without admixture

The correlation between stiffening (G′) and cumulative heat flow was evaluated on Fig. 7, based on the results the high shear mixing at 10000 rpm showed higher variability between the three trials by using the admixture, but the pastes without admixture did not show significative differences between the three trials.

Based on this, a combined evaluation of calorimetry and stiffening is shown in the Fig. 7, once the hydrated microstructure (the stiffening step) is very affected.

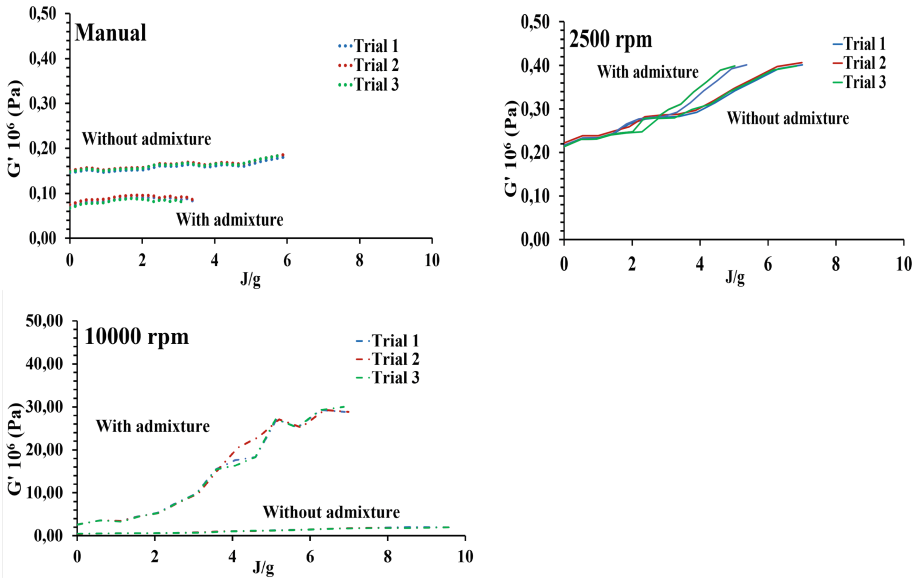

Fig. 7. Stiffening (G′) correlation with cumulative heat (J/g) Manual, 2500 rpm and 10000 rpm.

5 Conclusion

Selection of an appropriate mixing procedure is necessary in the evaluation of cement paste. Experimental results can be affected by the mixing and the data could be misleading. This study helps to our understanding of the rheological behavior of the pastes mixed with different shear intensity in the presence and in the absence of admixture.

The hydration kinetics of each paste were compared, showing longer induction periods for pastes made with admixtures. The values of Yield Stress and Viscosity of the 10000 rpm mixes showed higher values than the 2500 rpm, ascribed to more through breakdown of the initial cement particles, followed by both faster hydration and in the presence of polycarboxylate more adsorption. This is likely due to exposing more cement surface to water. When admixture is used, the induction period decreased with increasing intensity mixing. The behavior of the aluminates peaks was also affected by the admixture that accelerates the gypsum solubility, thus the aluminates is available to react; higher the mixing shear, these phenomena is potentialized.

The mixing procedure is an important step not only for the rheological properties evaluation, but also for the hydration kinetics and stiffening development of the paste, especially for the pastes containing admixtures it's an step to be very well studied, thus other studies evaluating the mixing on concrete is needed.

References

1. Aleixo DM (2011) Influência do cloreto de magnésio na hidratação de cimento Portland para cimentação de poços de petróleo. Dissertação de Mestrado, Habitação: Tecnologia das edificações-IPT, p 200
2. Bertioli AM, Cincotto MA, John VM, Pileggi RG (2008) Relação entre o comportamento reológico e os fenômenos físico-químicos no início da hidratação do cimento Portland com adição de filler. ENTAC, Fortaleza
3. Han D, Ferron RD (2015) Effect of mixing method on microstructure and rheology of cement paste. Constr Build Mater 93:278–288
4. Han D (2014) Flow behavior and microstructure of the cement-based materials. The University of Texas at Austin, Austin, TX
5. Hanehara S, Yamada K (1998) Interaction between cement and chemical admixture from the point of cement hydration, absorption behavior of admixture, and paste rheology. Cem Concr Res 29:1159–1165
6. Juilland P, Kumar A, Gallucci E, Flatt RJ, Scrivener KL (2012) Effect of mixing on the early hydration of alite and OPC systems. Cem Concr Res 42:1175–1188
7. Nehdi M, Rahman MA (2004) Estimating rheological properties of cement pastes using various rheological models for different test geometry, gap and surface friction. Cem Concr Res 34:1993–2007
8. Romano RCO, Pileggi RG (2017) Use of rheological models for the evaluation of cement pastes with air-entraining agent in different temperatures. In: 26th nordic rheology society, vol 25, pp 341–348. Copenhagen (2017)
9. Uchikawa H, Hanehara S, Sawaki D (1995) Influence of kind and added timing organic admixture type and addition time on the composition, structure, and property of fresh cement paste. Cem Concr Res 25:353–364

Development of SCC Placement Methodology for the Monolithic Construction of Slab-to-Wall Members Using Formwork Pressure and Time of Set-Based Modeling

Boris Haranki[1(✉)] and Ufuk Dilek[2]

[1] Westinghouse Electric Company, LLC, Charlotte, NC, USA
haranlb@westinghouse.com
[2] Wood PLC, Charlotte, NC, USA

Abstract. This paper discusses the use of Self Consolidating Concrete (SCC) in a unique approach for the construction of combined slabs and wall members commonly encountered in modular construction in new nuclear facilities required to be cast monolithically. Use of vibrators or other tools for surface set determination was not feasible due to lack of access in the 20 m steel-composite module walls. In addition, a material "upwell" in the slab segments during the vertical rise of SCC in the steel-composite module wall was not desired and needed to be managed. Therefore, the rate of rise, time of set, and formwork pressure-related considerations needed to be properly managed for the apparently "fluid" SCC mixture in the combined slab-to-wall placement to prevent upwell and/or high formwork pressures while avoiding cold joint/bond issues. This paper discusses the unique engineering approach to the construction challenges and related testing performed to overcome these challenges and manage the engineering properties in a critical slab-to-wall placement. Engineering considerations and the field trials in preparation for a 71 h, monolithic 1415 m^3 placement in critical areas in a new nuclear facility are discussed. Among the testing performed in preparation for the placement was the filling of 3 m, and 6 m tall mock-ups to measure formwork pressures at intended placement rates. Floor-to-wall mock-ups were performed consisting of an exposed horizontal section and a vertical section to observe upwell tendency as well as verify set or cold joint occurrence by subsequent saw cutting. Multiple time of set determination testing of the SCC mixture at different concrete temperatures were performed with the purpose of developing time of set curves to be used in the development of a placement plan.

The engineering evaluation and input was particularly of value in the successful completion of the 1415 m^3 placement lasting 71 h.

Keywords: Self Consolidating Concrete · Nuclear construction · Time of set · Cold joint · Formwork pressures

V. Mechtcherine et al. (Eds.): RheoCon 2019/SCC 2019, RILEM Bookseries 23, pp. 320–328, 2020.
https://doi.org/10.1007/978-3-030-22566-7_37

1 Introduction

This paper presents a study in which SCC is used in a unique application for the monolithic construction of combined slabs and tall steel-composite wall members in new nuclear facilities. The study aimed to develop a methodology for managing multiple attributes with the development of a time of set curve over a wide range of temperatures and a prediction of maximum lateral formwork pressures based on mixture-specific measured data from mock-ups. Constructability challenges associated with the placement of monolithic slab-to-steel-composite-wall transitions free of cold joints, without upwell, and the development of time of set curves, are discussed. As part of this effort, on-site trials in mock-ups, formwork pressure measurement, time of set determination over a wide range of temperatures, and subsequent evaluation or confirmation of cold joint formation through saw cutting were performed in preparation for the actual placement.

Use of a developed linear equation to predict maximum lateral formwork pressures and time of set curves over a wide range of temperatures allowed for detailed planning of stoppage times at the different critical points during the 71 h, monolithic 1415 m^3 placement in critical areas in a new nuclear facility. An isometric view of this structure is shown in Fig. 1.

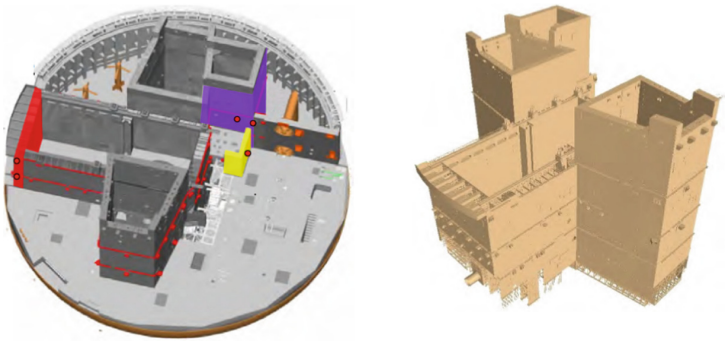

Fig. 1. Isometric views of the structure with and without outside floor.

2 Overview

This paper provides an overview of the development of a predictive model to estimate maximum lateral formwork pressures and determination of time of set curves for a specific SCC mixture for use in the 71 h, monolithic construction of critical areas in a new nuclear facility. The details of the technical challenges associated with this unique approach are covered in the five subsections below.

2.1 Details of the Mixture Design

The materials used in the specific SCC mixture consisted of ASTM C150M [1] Type II cement. Part of the cement is replaced with a lower specific gravity ASTM C618 [2] Class F fly ash at 2.25 for increased paste volume and stability. Granite ASTM C33M [3] coarse aggregate with a specific gravity of 2.97 for radiation shielding as well as ASTM C33M [3] fine aggregate with fineness modulus of 2.70 and specific gravity of 2.63 were used. A commercially available ASTM C494M [4] polycarboxylate high range water reducer (HRWR) was used to increase flowability; an ASTM C494M [4] Type S viscosity modifying agent (VMA) was used to enhance viscosity; and an ASTM C260M [5] air entraining agent (AEA) was used to reduce bleeding potential and help prevent the formation of pockets of water beneath the large embed plates at the finish surfaces. Proportions are summarized in Table 1. The SCC mixture had an ASTM C1611M [6] slump flow specification range of 610 mm ± 65 mm, an air content range of 5% ± 1.5%, and a design w/cm ratio of 0.39.

Table 1. SCC mixture proportions.

Material	Quantity
Cement	268 kg/m^3
Fly ash	178 kg/m^3
Fine aggregate	832 kg/m^3
Coarse aggregate	892 kg/m^3
Water	172 kg/m^3
AEA	65 ml/100 kg
VMA	520 ml/100 kg
HRWR	350 ml/100 kg

2.2 Development of Time of Set Curves

The time of set curves were developed by performing ASTM C403M [7] tests in a wide range of ambient temperatures in order to understand the initial and final setting characteristics of the specific SCC mixture. The ambient temperatures for which the ASTM C403M [7] time of set tests were performed ranged from 8 °C to 26 °C.

The resulting data from the individual ASTM C403M [7] tests was combined and a regression analysis was performed on the combined data using the model below. The curves were developed for the purpose of estimation of the initial and final time of set at other concrete temperatures where no performed ASTM C403M [7] data exists as a placement aid tool under various ambient conditions. The coefficient of regression for the developed equation was $R^2 = 0.9941$ for the initial time of set and $R^2 = 0.9977$ for the final time of set.

$$Time\ of\ Set\ (hrs) = A \cdot T_c^B\ ,$$

where T_c is the temperature of the mortar.

Figure 2 shows the evaluation of the model against the data from experimental results:

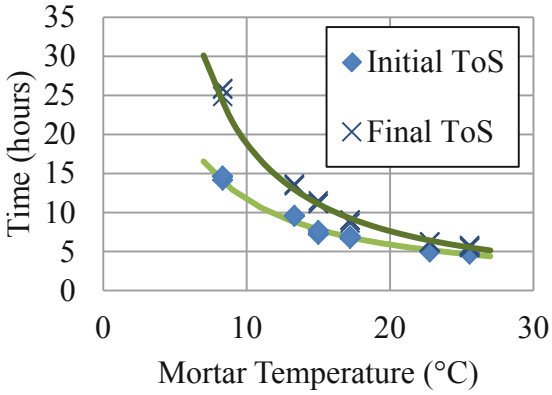

Fig. 2. ASTM C403M curves for initial and final time of set.

2.3 Tall Mock-Ups and Pressure Measurements

The design specification limited the maximum pressure of the concrete acting on the steel-composite walls of the modules to 50 kPa and required placement specifics to be determined by mock-up testing as required by ACI 347 [8]. For formwork pressure determination, Honeywell ABH015PGC5B3 pressure sensors rated for 0 kPa to 100 kPa were used to measure the lateral pressures as the mock-up modules were filled with the SCC mixture. The spacing of the installed sensors was 60 cm from the bottom of the forms, and the location of the bottom sensor (S1) was offset by 15 cm from the bottom of the forms. The pressure sensors were connected to a Campbell Scientific CR800 strain indicator which was used to monitor the data as gathered by the pressure transducers.

First, a 12 m long, 4 m tall mock-up was built to understand the effects of 0.3 m and 0.6 m lifts with a rest time of about 30 min in between lifts on the lateral formwork pressures. A vertical partitioning steel wall was installed within the mock-up to partition the segments that were placed at different lift heights. The maximum lateral formwork pressures recorded by the pressure sensors were about 10 kPa for the segment of the mock-up that was filled in 0.3 m lifts, and about 19 kPa for the segment that was filled in 0.6 m lifts, both of which were less than the specified maximum allowed pressure of 50 kPa. Both pressures represented 10% and 27% of the "hydrostatic pressure" which is the assumed liquid head based on an equivalent liquid unit weight of concrete.

Based on the pressure results, a second 6-m tall mock-up was built to determine the influence of 0.9 m lifts on the lateral pressures with similar rest times in between lifts. The maximum lateral pressure recorded by the pressure sensors in the second 6 m tall mock-up was 33 kPa, 23% of the maximum hydrostatic pressure, which was less than the specified maximum allowed pressure of 50 kPa. This is shown on Fig. 3 below.

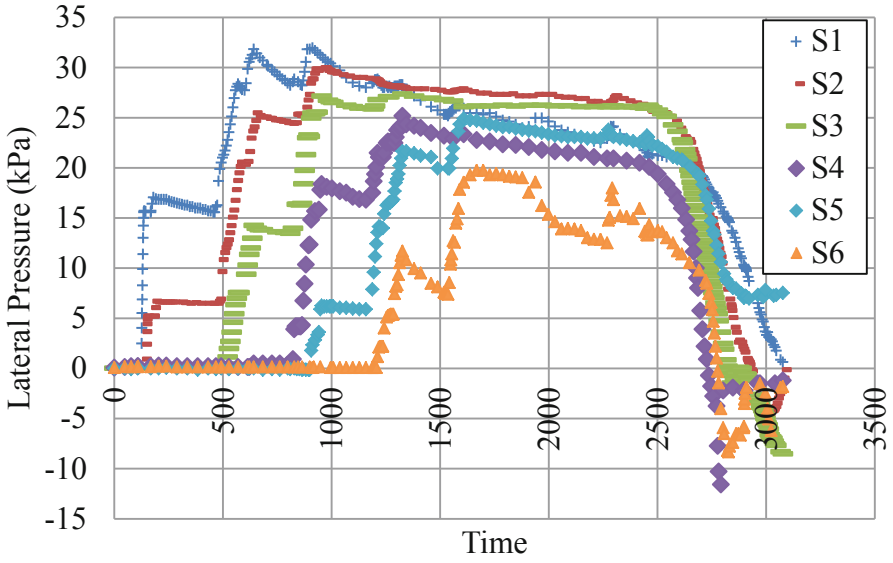

Fig. 3. Lateral formwork pressures exerted by 0.9 m lifts.

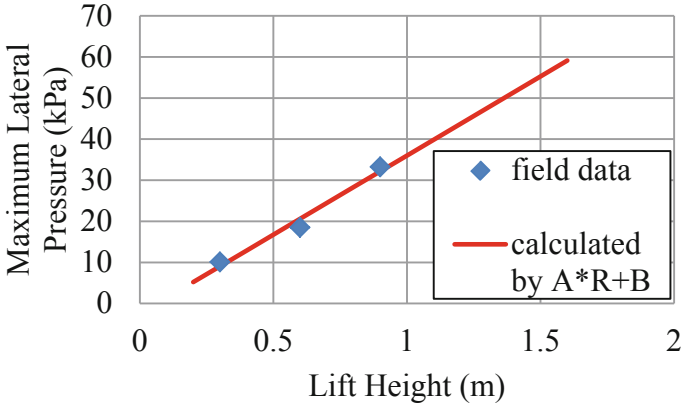

Fig. 4. Relationship maximum formwork pressures and lift heights with 30 min rest intervals.

The maximum lateral formwork pressures measured during the mock-up trials were combined and a linear equation was developed to estimate the maximum lift height necessary to not exceed the specified 50 kPa, while maintaining similar rest times of about 30 min in between lifts. This linear model is in Fig. 4 below. Based on the linear model, this maximum lift height was determined to be about 1.3 m with an R^2 value of 0.9758.

2.4 Floor-to-Wall Mock-Ups

Concurrently, a third round of mock-ups were built to model the actual elements in construction of the monolithic, combined floor concrete and wall sections. The mock-up shown in Fig. 5 below was designed to simulate the restrictions and configurations of the actual design and to allow for removal of the plywood forms for visual inspections and saw cutting. The mock-up allowed for utilization of the developed ASTM C403 [7] time of set curves and evaluation of a cold joint occurrence at the horizontal-to-vertical interface by subsequent saw cutting and coring. In addition, the vertical portion of the mock-up was made high enough for the purpose of evaluating upwell at the finished horizontal surfaces. Preventing upwell in the slabs at several elevations was critical due to the small tolerances at the finished floors required for the installation of steel liner plates.

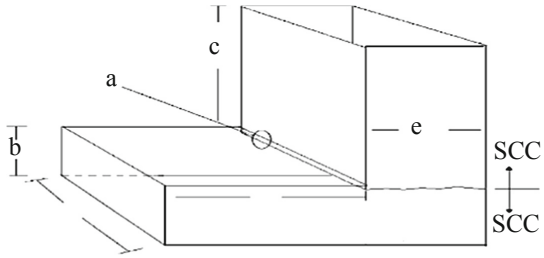

Legend
a = 40 mm recess
b = 0.6 m
c = 3 m
d = 2.5 m
e = 0.8 m
f = 1.2 m

Fig. 5. Floor-to-wall mockup.

The timing of the concrete placement in the floor-to-wall mockup was planned based on the ambient and concrete temperatures during placement and the corresponding developed ASTM C403 M [7] time of set curves. The in-place temperatures were measured with commercially available handheld infrared thermometers and the corresponding initial and final time of sets were read off the developed ASTM C403 M [7] time of set curves.

The concrete placement and stopping times were carried out as follows:

1. The horizontal portion of the mockup was filled with SCC.
2. The in-place temperature was measured and initial as well as final set times were estimated from the predeveloped ASTM C403 M [7] time of set curves.
3. First stop occurred.
4. Thirty (30) min before reaching initial set (as determined by the predeveloped ASTM C403M [7] time of set curves), SCC was placed inside the vertical portion of the mockup, about 30 cm. This was done for the purpose of "resetting the clock" or renewing the exposed concrete surface inside the vertical portion of the mockup and avoid a cold joint at the horizontal-to-vertical transition. The concrete on the exposed horizontal surfaces at this time could support the weight of several persons and the surface of the concrete was reported to be pliable which was important for occurrence of bond to consecutive lift. The value of the time of set information to best gage timing of consecutive lifts is best pointed out in ACI 237R [9], which

states: “Because of its thixotropic characteristic, SCC can be placed onto previously placed SCC that has gelled but has not yet achieved initial set” which forms the basis of placement delayed to achieve the “no-upwell” but occurring prior to time of set.
5. Second stop occurred.
6. When the concrete at the horizontal portion of the mock-up reached final set as determined by the predeveloped ASTM C403 M [7] time of set curve, the concrete placement inside the vertical portion of the mock-up was resumed. Upwell was prevented by allowing the concrete in the slab portion to reach this “fixed” volume state. Implementation of this regime with engineering input provided accomplishing this segmented placement during one placement.
7. The vertical portion was filled at the previously estimated 0.9 m lifts with the prescribed rest time in between lifts until the top was reached. No upwell was observed at the exposed horizontal portion of the mock-up. The intersection between the horizontal and the vertical portions of the mock-up were not purposely roughened or cleaned.

2.5 Saw Cutting and Verification of Cold Joint Formation

After form removal, placement lines were observed for each lift on both the horizontal and the vertical portions of the mock-up, which was attributed to the wait time in between lifts. It can be expected that visually apparent lift lines may occur when consecutive layers flow over each other without vibratory action to knit the lifts together. A vertical saw cut was performed from the top of the mockup to the bottom and the saw cut surfaces were exposed for the purpose of evaluating the depth of the placement lines into the concrete mass. A placement line is visible on the formed surface but it disappears about 25 mm into the concrete mass. This finding was attributed to the possibility of the formwork providing some restraint to the cohesive mixture and friction which does not exist in the body of the member.

In addition to the saw cut, drilled cores from several locations on the formed surfaces at the intersection between the horizontal and vertical portions of the mockup were obtained, prepared, and tested per ASTM C42M [10]. The purpose of coring was to determine the compressive strength, the possibility of quantifying effects of a possible joint or discontinuity, and to confirm overall quality of the in-place concrete under the proposed placement regime. Core testing confirmed the monolithic nature of the member and acceptable compressive strength levels above the required strength. The compressive strengths all met the required f’c and no discernible difference was noted compared to baseline cores within the body of the member.

2.6 Placement Planning, Verification of Time of Set, and Pressure Data

The information gathered from the mock-ups, pressure measurements, and the developed ASTM C403M [7] time of set curves were used in the detailed planning of rate of rise, lift size, and stoppage times at the different slab-to-wall transitions for the monolithic placement in critical areas in the new nuclear facility. For the actual placement, the start time for depositing the first lift of concrete inside the steel-composite wall modules

was planned at 1 h (instead of 30 min as performed during the mock-ups) prior to the concrete in the horizontal slab portion reaching initial set. This extended time was to account for re-priming of pumps and any other unforeseen delays.

No upwell was observed at the exposed horizontal slab surfaces during filling of the 20 m high steel-composite module walls per the engineered regime.

After the initial 30 cm concrete lift inside the steel-composite module walls was deposited to "reset the clock or renew the surface", the subsequent concrete lift heights were planned for 1.3 m with at least 30 min rest time in between lifts based on the findings of the study. Pressure sensors were installed in one of the vertical steel panels of the steel-composite module and used to monitor lateral pressure in real-time. The lateral pressures peaked well below the maximum allowed 50 kPa at 29 kPa using the planned 1.3-m lifts. However, it was also acknowledged that during the actual construction process the rest times in between lifts was at times well over the planned 30 min due to delays and likely the reason for the lower-than-expected pressures.

3 Summary and Conclusions

Construction of monolithic members consisting of multiple slab-to-wall transitions can be achieved with the use of SCC whenever initial and final times of sets are understood.

The value of the time of set information is best pointed out in ACI 237R [9], which states: "Because of its thixotropic characteristic, SCC can be placed onto previously placed SCC that has gelled but has not yet achieved initial set". Therefore, recommendations were developed based on subsequent lift being placed prior to reaching initial time of set but wait occurring long enough to avoid upwell. By understanding the time of set characteristics of the SCC mixture, the contractor has the information necessary to develop placement specifics for a monolithic structure, free of cold joints, and without upwell at the unformed surfaces. The time of set determination should be done a wide range of temperatures to be prepared for ambient conditions encountered during the concrete placement.

Mock-ups are helpful when performed to establish proper rate of rise and manage formwork pressures as well as other objectives such as the ones presented here. The relationship between SCC lift thicknesses and maximum lateral pressures could be represented with a linear relationship in this particular study for the specific set of parameters such as the wait time and the mix utilized. The study was instrumental in executing a successful placement. The findings of this study can be utilized as long as the mixture proportions and the rest times in between lifts remain somewhat similar. Other placement specific studies with differing lift heights, wait times, mixtures, admixtures or other factors can be developed based on project and placement specifics. In this case, if the placement is temporarily suspended and concrete is allowed to rest in between lifts for extended periods of time, the linear relationship overestimates the lateral pressures.

References

1. ASTM C150/C150M-09 (2009) Standard Specification for Portland Cement. ASTM International
2. ASTM C618-08a (2008) Standard Specification for Coal Fly Ash and Raw or Calcinated Natural Pozzolan for Use in Concrete. ASTM International
3. ASTM C33/C33M-08 (2008) Standard Specification for Concrete Aggregates. ASTM International
4. ASTM C494/C494M-10a (2010) Standard Specification for Chemical Admixtures for Concrete. ASTM International
5. ASTM C260/C260M-10a (2010) Standard Specification for Air-Entraining Admixtures for Concrete. ASTM International
6. ASTM C1611/C1611M-09b (2009) Standard Test Method for Slump Flow of Self-Consolidating Concrete. ASTM International
7. ASTM C403/C403M-08 (2008) Standard Test Method for Time of Setting of Concrete Mixtures by Penetration Resistance. ASTM International
8. ACI 347-04 (2004) Guide to Formwork for Concrete. American Concrete Institute
9. ACI 237R-07 (2007) Self-Consolidating Concrete. American Concrete Institute
10. ASTM C42/C42M-10 (2010) Standard Test Method for Obtaining and Testing Drilled Cores and Sawed Beams of Concrete. ASTM International

Influence of Segregation on Materials Component in Fresh Concrete Due to Vibration

Kazuaki Nishimura[1(✉)] and Yoshitaka Kato[2]

[1] FLOWRIC Co., Ltd., Tokyo, Japan
nishi237835@gmail.com
[2] Department of Civil Engineering, Tokyo University of Science, Tokyo, Japan

Abstract. Variations in the degree of deterioration of a concrete structure are caused by variations in concrete quality and environmental impacts. Moreover, variations in concrete quality are also influenced by the segregation of fresh concrete due to vibration and bleeding. Considering this background, the degree of segregation of fresh concrete and its factors caused by vibration were experimentally investigated. As a result, it is found that the gravel settled due to the vibration while compacting the fresh concrete, whereas the cement paste rose up. Moreover, the longer the vibration time, the larger the amounts of risen cement paste and settled gravel. In addition, it is concluded that the mortar apparent viscosity and the inter-gravel average distance influenced the segregation of fresh concrete due to vibration.

Keywords: Segregation · Vibration · Viscosity

1 Introduction

The durability of concrete structures depends on the quality of cover concrete, which is a primary factor affecting the deterioration caused by chloride ions, carbon dioxide, oxygen and water. Further, the quality of cover concrete is influenced by the types of materials and mix proportions. However, the degree of deterioration of each part of the same concrete structure varies, even if the structure is made using the same mix proportions.

Variations in the degree of deterioration of a concrete structure are caused by variations in concrete quality and environmental impacts. Moreover, variations in concrete quality are also influenced by the segregation of fresh concrete due to vibration and bleeding. For example, Gao et al. [1] reported that the permeability of chloride ions at the top element was larger than that at the bottom in the case of vibration time of more than 15 s. Considering this background, the degree of segregation of fresh concrete and its factors caused by vibration were experimentally investigated.

V. Mechtcherine et al. (Eds.): RheoCon 2019/SCC 2019, RILEM Bookseries 23, pp. 329–337, 2020.
https://doi.org/10.1007/978-3-030-22566-7_38

2 Experiment on Degree of Segregation

2.1 Test Method

In this study, the degree of segregation of fresh concrete was measured by the estimating mix-proportions method. This method is shown in Fig. 1.

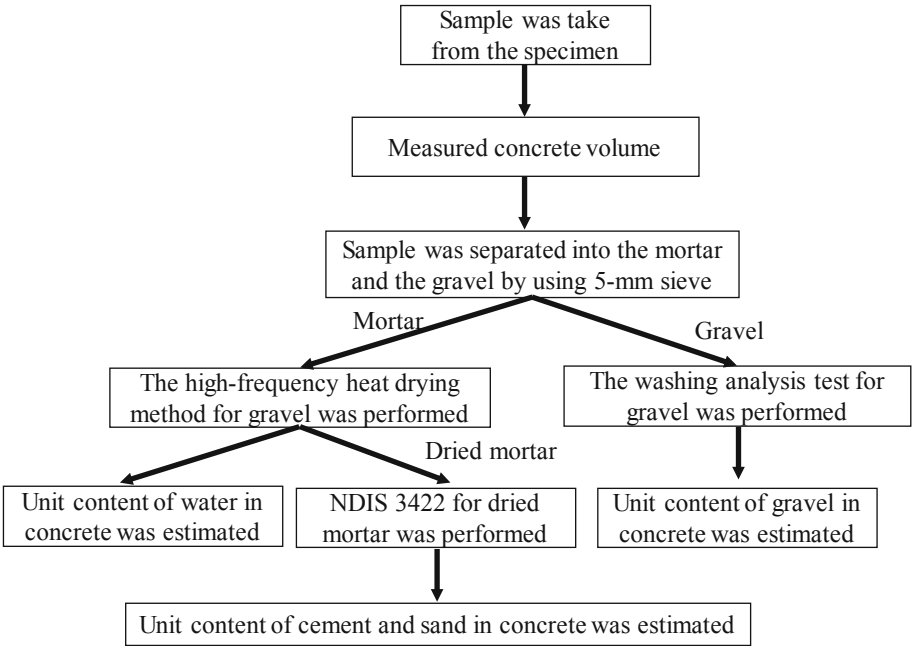

Fig. 1. Method of estimating mix-proportions.

First, a metal mold with the size of 150 mm × 150 mm × 400 mm was filled with fresh concrete. After the concrete had been compacted using an internal vibrator, a sample was taken from the specimen and used for estimating the mix proportions. Next, the sample was separated into mortar and gravel by using a 5-mm sieve. The washing analysis test for gravel was performed according to past research [2], and the unit content of gravel in concrete was estimated. The high-frequency heat drying method for fresh mortar was performed according to past research [3], and the unit content of water in concrete was estimated. Non-Destructive Inspection (NDIS) 3422 for dried mortar was performed, then the unit content of cement and sand in concrete was estimated. These calculation formulae are shown in Eqs. (1) to (6).

$$UC_G = \frac{M_G/\rho_{Gd} \times \rho_{Gs}}{V_M + V_G} \tag{1}$$

$$UC_W = \frac{W_d/\rho_W}{V_M + V_G} \times 1000 \tag{2}$$

$$X = \frac{UM_C}{UM_C + UM_S} \times 100 \tag{3}$$

$$\frac{W_d}{V_M}/\rho_W + UM_C/\rho_C + UM_S/\rho_{Ss} = 1 \tag{4}$$

$$\begin{aligned} UM_C &= \frac{1000 - UC_W}{1/\rho_C + (1 - \rho_{Ss})/(X/100 \times \rho_{Ss})} \\ UM_S &= \frac{1000 - W}{1/\rho_{Ss} + X/100/(\rho_C \times (1 - X/100))} \end{aligned} \tag{5}$$

$$\begin{aligned} UC_C &= UM_C \times \frac{(1000 - UC_G/\rho_{Gs})}{1000} \\ UC_S &= UM_S \times \frac{(1000 - UC_G/\rho_{Gs})}{1000} \end{aligned} \tag{6}$$

where, UC: estimated material unit content in concrete (kg/m^3), UM: estimated material unit content in mortar (kg/m^3), V: material volume (m^3), M: material weight after oven-drying (kg), ρ_s: material density in saturated surface-dry condition (kg/m^3), ρ_d: material density after oven-drying (kg/m^3), X: percentage of cement content in mortar (%), subscript W: water, subscript C: cement, subscript S: sand, subscript G: gravel.

It is assumed that the average UC of all samples of each material in the specimen equals the unit content after mixing. Therefore, the index of degree of segregation was calculated using Eq. (7).

$$\text{volume fraction} = \frac{\text{UC at each place}}{\text{average UC of all sample of each material in the specimen}} \tag{7}$$

2.2 Materials, Mix Proportions, and Vibration Time

Concrete was made using ordinary Portland cement (density: 3.15 g/cm^3, Blaine fineness: 3410 cm^2/g), river sand (density in saturated surface-dry condition: 2.65 g/cm^3, fineness modulus: 2.73), and crushed sandstone gravel with G_{max} of 20 mm (density in saturated surface-dry condition: 2.72 g/cm^3, density in oven-dry condition: 2.67 g/cm^3, fineness modulus: 6.74). The concrete mix proportions are shown in Table 1. The vibration time was 15 s for the tests in Sect. 2.3, and was 5 s, 15 s and 60 s for the tests in Sect. 2.4.

Table 1. Mix proportion.

W/C (%)	s/a (%)	Unit (kg/m^3)				Unit (g/m^3)		Slump (cm)	Air (%)
		Water (W)	Cement (C)	Sand (S)	Gravel (G)	A_1	A_2		
40	45	165	413	774	976	10	907	9.5	5.5
50	45	165	330	805	1014	9	792	9.0	5.5
60	45	165	275	826	1040	10	275	9.5	4.5

A_1: Air-entraining admixture, A_2: Air-entraining and water reducing admixture

2.3 Influence of Segregation on Materials Components in Fresh Concrete Due to Vibration During Compacting

The measurement results for the vibration time of 15 s are shown in Fig. 2.

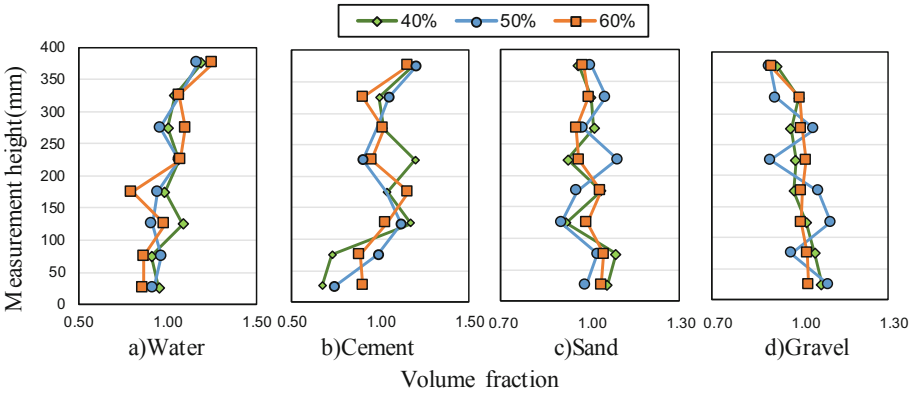

Fig. 2. Influence of segregation on unit volume of concrete due to vibration.

UC_W and UC_C increased with increase in measurement height, whereas UC_G decreased with increase in measurement height. It is thought that the gravel settled due to the vibration while compacting the fresh concrete, whereas the cement paste rose up.

2.4 Influence of Vibration Time on Cement Paste and Gravel Volume Fraction

From the results of Sect. 2.3, UC_W, UC_C and UC_G changed with measurement height. Makoto [4] reported that the water content (W/C) of risen cement paste hardly changed due to vibration during compaction. Based on this report, UC_C was estimated from the measured UC_W and W/C. Therefore, UC_W and UC_G were measured in this section. In all cases, W/C was 50%. The influences of vibration time on UC_W and UC_G are shown in Fig. 3.

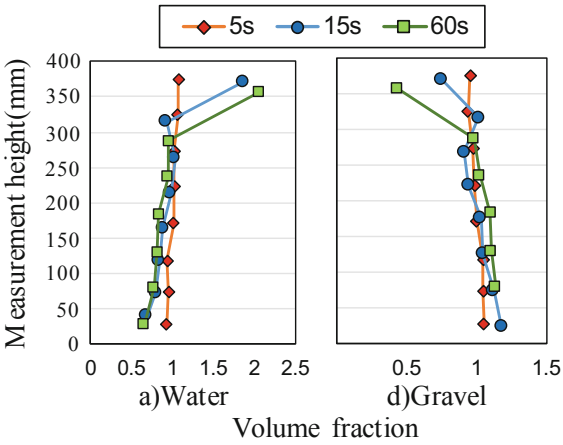

Fig. 3. Influence of the vibration time on cement paste and gravel volume fraction.

The difference between the maximum value and the minimum value of UC_W and UC_G is larger in the order of 60 s, 15 s, and 5 s. It is thought that the longer the vibration time, the larger the amounts of risen cement paste and settled gravel.

3 Influence of Mortar Viscosity on Segregation

3.1 Test Method

According to the results of Sect. 2, in order to understand the segregation behavior of fresh concrete due to vibration during compaction, it is necessary to understand the behavior of cement paste or gravel; this study focused on gravel. It was assumed that the concrete consisted of mortar as the liquid phase and gravel as the solid phase. Therefore, the equilibrium of forces of the solid in liquid was expressed by Eq. (8). Assuming that the velocity of the solid was constant, the acceleration of the solid was 0. From the resulting Eq. (9), the drag coefficient changed as given by Eq. (10).

$$\begin{aligned} &ma = F_b - F - D \\ &\therefore \frac{4}{3}\pi r^3 \rho_p a = \rho_f V g - \rho_p V g - \frac{1}{2} C_D \rho_f v^2 \pi r^2 \end{aligned} \tag{8}$$

$$Re = \frac{2rv\rho_f}{\mu} \tag{9}$$

$$C_D = \begin{cases} \frac{24}{Re} (Re < 2) \\ \frac{10}{\sqrt{Re}} (2 < Re < 500) \\ 0.44 (500 < Re < 10^5) \end{cases} \tag{10}$$

where, C_D: drag coefficient, m: weight of mock gravel (kg), a: acceleration of mock gravel (m/s^2), F_b: buoyancy acting on mock gravel (N), F_b: gravity acting on mock gravel (N), D: drag force acting on mock gravel (N), r: radius of mock gravel (m), v: rise rate of mock gravel (m/s), ρ_p: density of mock gravel (kg/m^3), ρ_f: density of mortar (kg/m^3), g: gravitational acceleration (m/s^2), V: volume of mock gravel (m^3), μ: mortar apparent viscosity (Pa•s), Re: Reynolds number. Therefore, the mortar apparent viscosity, expressed as an index of the behavior of gravel, is given by Eq. (11).

$$\mu = \begin{cases} \frac{(\rho_f - \rho_p)g}{6\pi r v} \left(Re < 2\right) \\ \frac{\left\{(\rho_f - \rho_p)Vg\right\}^2}{12\rho_f \pi^2 r^3 v^3} \left(2 < Re < 500\right) \\ \frac{(\rho_f - \rho_p)g}{0.22\rho_f \pi r^2 v^2} \left(500 < Re < 10^5\right) \end{cases} \tag{11}$$

Reynolds number was less than 2 for all mix-proportions. In order to simulate the behavior of gravel, a new test method was proposed. The test equipment is shown in Fig. 4, and the test procedure was as follows.

(1) The mock gravel was secured to the bottom of the equipment with a magnet.
(2) Mortar was placed in the equipment.
(3) The mock gravel was released while vibrating the mortar, and the rate of rise of the mock gravel was measured.

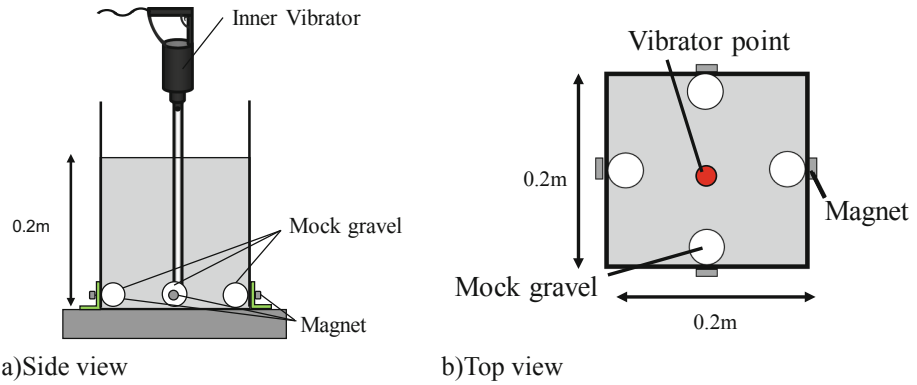

Fig. 4. Equipment of measuring mortar viscosity.

Banfil [5] reported that concrete viscosity was changed by vibration during compaction. Therefore, the influence of acceleration by the vibrator during compaction on the mortar apparent viscosity was experimentally investigated. The results are shown in Fig. 5. The mortar apparent viscosity decreased with the increase of acceleration of the vibrator, and finally became a constant.

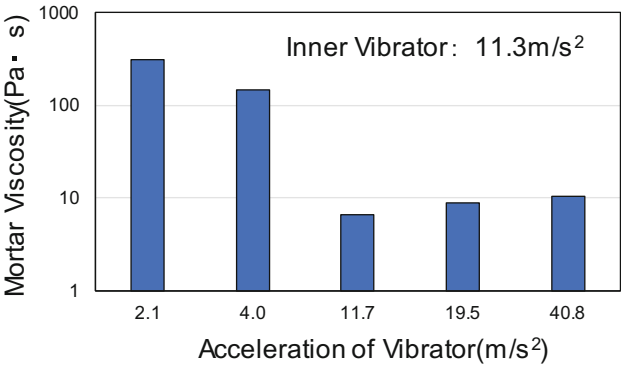

Fig. 5. Influence of Acceleration of vibrator on mortar viscosity.

3.2 Results and Discussion

In order to understand the relationship between the mortar apparent viscosity and the degree of segregation of fresh concrete, the degree of gravel settlement was used as the index of the degree of segregation of fresh concrete. The degree of gravel settlement was expressed by the difference between the maximum value and the minimum value of gravel volume fraction ($G_{Max-Min}$). The influence of W/C on mortar apparent viscosity is shown in Fig. 6, and the degree of gravel settlement is shown in Table 2.

Table 2. The degree of gravel settlement.

W/C(%)	40	50	60
$G_{max-min}$	0.15	0.2	0.13

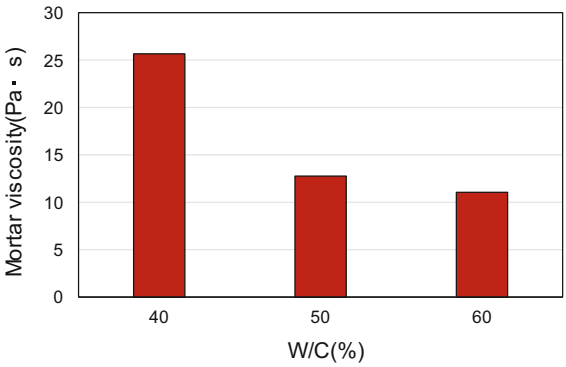

Fig. 6. Influence of W/C on mortar viscosity.

The mortar apparent viscosity increased with an increase in W/C. However, regardless of W/C, $G_{Max-Min}$ was constant. It is considered that the degree of gravel settlement is influenced not only by mortar apparent viscosity but also by the sedimentable distance of gravel. Therefore, the settlement distance of gravel during vibration, calculated from the mortar apparent viscosity, was compared with the average distance between gravel particles calculated by Eq. (12).

$$L = \sqrt{r^2\pi/(A/100)} - r \tag{12}$$

where, L: inter-gravel average distance (m), A: gravel volume in concrete (%).

The inter-gravel average distance and the settlement distance of gravel during vibration at 15 s are shown in Table 3. In all cases, the settlement distance is much larger than the inter-gravel average distance.

Table 3. Inter-gravel distance and settlement velocity of gravel while vibrating.

W/C(%)	40	50	60
Inter-gravel average distance (mm)	4.8–19.2	4.5–18.1	4.3–17.4
Settlement velocity of gravel while vibrating at 15 s (mm)	18–292	36–576	42–676

From these results, it is concluded that the mortar apparent viscosity and the inter-gravel average distance influenced the segregation of fresh concrete due to vibration.

4 Conclusion

As a result of this study, the following findings were obtained.

1. It is thought that the gravel settled due to the vibration while compacting the fresh concrete, whereas the cement paste rose up.
2. It is thought that the longer the vibration time, the larger the amounts of risen cement paste and settled gravel.
3. It is concluded that the mortar apparent viscosity and the inter-gravel average distance influenced the segregation of fresh concrete due to vibration.

References

1. Gao X, Zhang J, Yue S (2019) Influence of vibration-induced segregation on mechanical property and chloride ion permeability of concrete with variable rheological perrformance. Constr Build Mater 194:32–41
2. Kozo O, Yasushi K, Hiromichi M (2006) Mixture change of concrete by passing between rebar. J JSCE Div E 62(1):119–128

3. Taku M, Koichi H, Hideaki T, Yoshikatsu N (2004) Investigation of various factors on estimation of unit water volume by high-frequency heat drying method. In: Japan society of civil engineers 2004 annual meeting, pp 297–298
4. Makoto K, Hiroshi T (1983) Segregation phenomena of concrete with various chemical admixtures due to vibrating compaction. J Soc Mater Sci Jpn 32(353):33–39
5. Banfil PFG, Teixeira MAOM, Craik RJM (2011) Rheology and vibration of fresh concrete: predicting the radius action of poker vibration from wave propagation. Cem Concr Res 41:932–941

Study of the Mixing Completion in Concrete Production by Means of an on-Board Sensor System

Pierre Siccardi[1(✉)], Xavier Berger[1], Robin Jean[1], Marc Jolin[1], Benoît Bissonnette[1], and Denis Beaupré[2]

[1] Department of Civil and Water Engineering, Research Centre on Concrete Infrastructures (CRIB), Université Laval, Québec, Canada
pierre.siccardi.l@ulaval.ca
[2] Command Alkon Canada, Québec, Canada

Abstract. The second industrial revolution has been accompanied by the massive use of concrete. However, rejected loads or demolitions of new structures due to poor quality indicates that quality control still needs to be improved. Furthermore, with the advent of the third industrial revolution, the industry needs more advanced production systems; for example, high-tech implementation processes like 3D concrete printing will require continuous rheology control systems. In that respect, to answer today's and tomorrow's questions, *Université Laval* has initiated a research program using an on-board sensor system for ready-mix concrete production to monitor real-time concrete fresh properties.

One research interest of the program lies in the study of the completion of mixing, a crucial step to obtain quality concrete: after loading the materials, the driver adjusts the water and admixtures introduced while mixing to obtain the desired consistency. This article aims to highlight the path taken to determine the completion of mixing based on the probe assessment.

Recent tests focused on the measurement of homogeneity by monitoring the pressures exerted on the probe. To better understand what happens in the drum, this step has necessarily involved viewing and studying the behavior of the material during mixing. Moreover, tests brought to light distinctive patterns in the pressures detected by the probe which could be synonym of segregation. Also, methods based on artificial intelligence to anticipate the completion of mixing are already under analysis and appear extremely promising.

Finally, the ambition is to develop an automatic adjustment program that would add water and admixtures through an automatic gate. Resources consumption could be decreased, thus reducing the economic and environmental impact of the concrete production while improving concrete quality.

Keywords: Concrete production · Completion of mixing · On-board sensor system · Adjustment · Quality control

V. Mechtcherine et al. (Eds.): RheoCon 2019/SCC 2019, RILEM Bookseries 23, pp. 338–345, 2020.
https://doi.org/10.1007/978-3-030-22566-7_39

1 Introduction

The second industrial revolution was accompanied by the massive use of concrete. To meet the needs of this revolution, essentially mass production, the means have evolved to produce concrete quickly, in large quantities and with a minimum quality control to meet specifications in the field, and all this at the lowest possible price/costs. However, rejected concrete loads or (partial) demolitions of new structures due to poor concrete quality indicates that quality control still needs improvements.

Furthermore, to deal with environmental and economic considerations, concrete producers have to increasingly integrate recycled aggregates and supplementary cementitious materials (SCMs) in their mix-designs. For instance, on the new Champlain Bridge, a massive bridge project in Montréal, Canada, concrete producers are forced to use 30% of SCMs in all the concrete mixtures. However, intrinsic composition fluctuations of the SCMs often generate significant rheological variations of the fresh concrete, which makes the use of these products sometimes challenging on the jobsites.

In a longer-term perspective, with the advent of the third industrial revolution being the era of mass personalization, the industry needs more advanced production systems. For example, high-tech implementation processes such as 3D concrete printing may require continuous rheology control systems.

In that respect, to answer today's and tomorrow's questions, *Université Laval* has initiated a research program using an electronic on-board sensor system for ready-mix concrete production to monitor real-time concrete fresh properties inside the drum. In collaboration with *Command Alkon*, the company that markets the embedded system, this multi-faceted project aims to develop and explore the capabilities of the system.

One research interest of the program lies in the study of the completion of mixing, a crucial step to obtain quality concrete. After loading the materials in a mixer truck, the driver adjusts the water and admixtures introduced while mixing to obtain the desired consistency. This article aims to highlight the path taken to determine the completion of mixing based on the probe assessment.

2 The Homogeneity Measurement

2.1 Relevance

Whether if it is in a dry or a wet-batch concrete plant, concrete homogenization is a costly operation in terms of energy: it involves using mixers of high electricity power consumption (or fuel engines at high RPM in case of dry-batch) during mixing. According to Frey and Kim [1], fuel consumption during mixing can be up to twenty-two times greater than when idling or at low engine load. Moreover, this operation is time consuming and the plant managers try to minimize it to optimize the concrete production. Thus, besides having an obvious economic goal, the project ties within a sustainable development scope to reduce mixing duration and thus fuel consumption.

The discussion about homogeneity would be incomplete without mentioning the inconveniences caused by inhomogeneity. Segregation issues, for example, affect both

aesthetic and performance of concrete structures: in the best-case scenario, honeycombs impair the concrete surface only, but in the worst case, it can lead to large dimensions of un-encapsulated reinforcing bars. Having an *automated homogeneity measurement tool* would help avoiding segregation issues that are detrimental for the construction industry, and to a wider extent, the user safety.

2.2 In the Literature

Homogeneity is far from being a trivial concept. Chopin [2] defines two scales of observations: macroscopic and microscopic. Macroscopic homogeneity, on the one hand, corresponds to the distribution of coarse constituents in the mix, which requires little mixing time (20 s to 30 s) [2–4]. This aspect can be experimentally evaluated by characterizing the distribution variation of the coarse components by sampling and performing particle size distribution, as well as compressive strength and slump tests.

Microscopic homogeneity, on the other hand, is related to the optimization of the granular arrangement, i.e. the dispersion of fine elements. In the past, Johansson [3] quantified microscopic homogeneity by measuring the cement content per sample, while Vandanjon et al. [4] conducted accelerated carbonation tests and radioactive tracing of fly ash. Chopin [2] has observed the evolution of the rheological properties of fresh concrete since, according to the compressible packing model, the viscosity and the ratio of the solid volume to the maximum compactness of the granular skeleton are linked [5]. In addition, Chopin [2] completed the characterization of microscopic homogeneity by deicer salt scaling tests. It should be noted, however, that according to the authors, the above-mentioned tests have not made possible a clear quantification of the microscopic homogeneity. In addition, most are indirect test methods, which shows the need to establish a direct and efficient method to evaluate the concrete micro-homogeneity.

The idea of an in-line method to detect concrete homogeneity and workability is not new. The first attempt to evaluate workability during mixing by Purrington and Loring [6] dates back to 1928 [7]. Since then, several systems have been developed to monitor concrete evolution in the mixer. Those technologies can be divided into two families: the one based on the power consumption of the mixer, and the other based on a drag force exerted on a probe.

Since the 1960s, most concrete plant mixers have been equipped with ammeter or wattmeter to monitor power consumption [8]. These values give an image of the force applied by the concrete on the mixer paddles. The advent of high-performance concrete and self-consolidating concrete was accompanied by increased problems in mixing. Thus, efforts on identifying the completion of mixing using the wattmeter were made to help improving the concrete production [2, 9]. Then, some researches were conducted to assess workability by measuring the power consumption at various mixing speeds [10, 11]. Finally, trials were done to do the same in a ready-mix truck by observing the hydraulic pressure from the drum system [12, 13].

The main problem of the above-cited examples of in-line monitoring systems is the equipment dependence: the information of interest partly relies on mechanical parts subjected to wear for example. This aspect makes their response dependent on time and type of mixer. This observation led to the development of drag force-based probes:

MFM probe and Viscoprobe™, for example, already make possible the evaluation of the rheology of self consolidating concrete inside the mixer [14].

Whether it comes from a power consumption or a drag force monitoring system, curves adopt a similar shape as can be seen in Fig. 1.

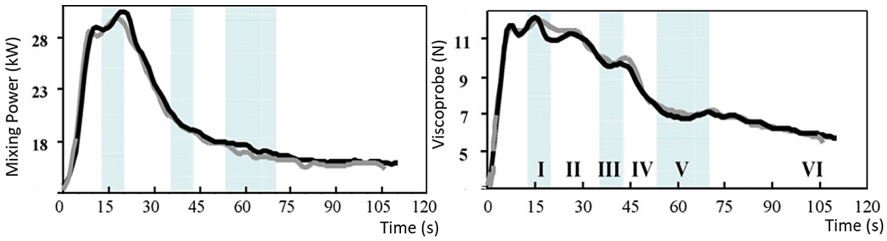

Fig. 1. (a) Power consumption and (b) force measured by Viscoprobe™ evolutions with time during the mixing cycle of two self consolidating concretes of the same mix-design (adapted from Cazacliu [8]).

Following a sudden increase due to the introduction of materials in the mixer, the power (or drag force) gradually decreases until a plateau is reached, which translates to continuous efforts of the concrete on the system and therefore overall homogeneity. Moreover, distinctive stages (in white and blue) can be outlined in Fig. 1; each number correspond to a different state in the granular media such as "sand coating" or "suspension forming" (for more details, see [8]).

In the same way that he defines two levels of homogeneity, Chopin [2] associates two distinct powers with regards the homogenization of the mixture, as presented in Fig. 2.

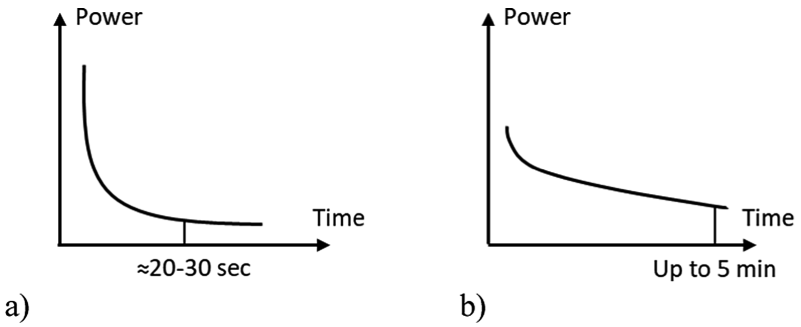

Fig. 2. (a) Power consumption for the distribution of the coarse constituents in the mixer and (b) Power consumption for the distribution of fine elements in the mixer (adapted from Chopin [2]).

As mentioned previously, spatial distribution of the coarse constituents to achieve macroscopic homogeneity is quite a rapid process as presented by Fig. 2a. Chopin [2] attributed an arctangent relationship to fit this observation. On the opposite, dispersion of fine elements may be a longer task (see Fig. 2b) and was fitted by a negative exponential.

3 On-Board Sensor System

3.1 System Overview

The system is essentially based on a stainless-steel probe, visible in the center of Fig. 3a, directly attached to the inner surface of the truck mixer as shown in Fig. 3b.

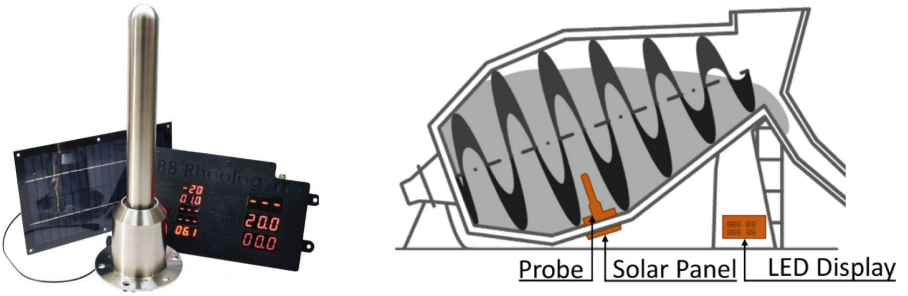

a) b)

Fig. 3. (a) Detail of the embedded system for concrete properties control (courtesy of Command Alkon) and (b) installation on the ready-mix truck (adapted from [15]).

The system has been developed over the last ten years by Denis Beaupré, a former *Université Laval* professor expert in concrete rheology. Due to its location in the mixer, the probe system travels through the fresh concrete during the rotation of the mixer. Thanks to the force exerted by the concrete on the probe, the system already allows to assess certain properties such as the volume of concrete in the mixer, its slump or its temperature [16, 17] and it is currently used as is commercially. The values are displayed on a led panel installed on the truck and are sent to a remotely accessible database.

3.2 Homogeneity Measurements with the System

Recent tests focused on the assessment of homogeneity by monitoring the force exerted on the probe. By a simple calculation with the probe projected area, the force is converted into a pressure (for more details, see [18]), and can then be plotted as a function of time as presented in Fig. 4. An exponential curve fit can then be drawn to fit the experimental data as presented in Fig. 4, in order to define the fluidity point, a point defined as the transition from a hard paste to a granular suspension (soft paste) [19].

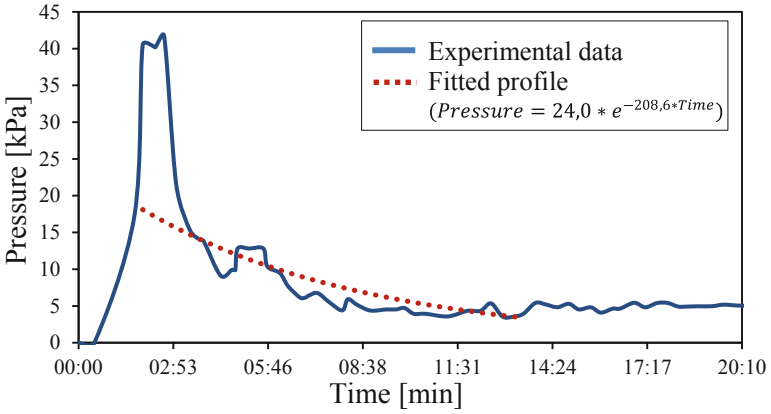

Fig. 4. Typical curve of the probe pressure as a function of time with an exponential fitted profile.

However, some tests brought to light distinctive patterns in the pressures detected by the probe. Figure 5a presents a cross section of the drum with the probe position at two different rotation angles (A and B) i.e. two different probe travel distances on the same drum rotation during one experiment. Figure 5b displays the pressure monitored for position A and B: two distinct levels of pressure can be distinguished but the exact origin of this difference is currently unknown. One hypothesis concerns the concrete homogeneity, and more precisely segregation. For example, if the probe travels though a sand pocket instead of a homogeneous concrete, material density and so forces exerted on the probe would be different. The system could thus detect concrete segregation and alert the production manager afterwards.

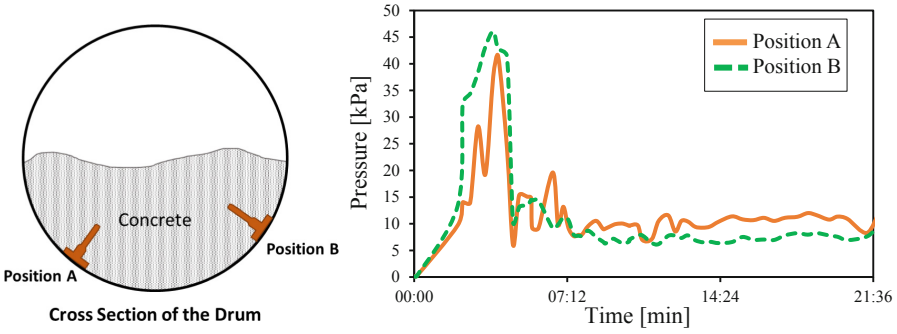

Fig. 5. (a) Details of the probe positions for data acquisition and (b) probe pressure function of time for two different probe travel distances along the same drum rotation.

Nevertheless, the difference in pressures could also derive from the concrete flow inside the drum. Fluid velocity or direction of flow for example can affect the forces applied on the probe, leading to a pressure differential, function of the position of the probe. However, knowledge about the concrete motion inside the mixer is still missing. Thus, to better understand what happens in the drum, a video pole was built to record and study the behavior of the material inside the drum during mixing. The video pole consists of an action camera combined with LED stripes to provide sufficient light in the drum. The camera and lights are then attached to the end of a telescopic pole.

Equipped with a reliable probe system and with promising early observations, an experimental program to detect multi-scale homogeneity by means of the on-board system will follow. Macro-homogeneity will be assessed by compressive strength tests, slump tests and sieve analysis as it has been done in previous projects [2–4].

The modus operandi for micro homogeneity determination is currently under conception: visual techniques ranging from binocular magnifier to Scanning Electron Microscopy (SEM) are planned to be used on air-entrained self-consolidating concrete made with ternary binder. Major elements of interest are the fly ash dispersion and air bubbles network. Moreover, image analysis tools should help to quantify the micro homogeneity.

4 Conclusions and Outlook

Although only a few tests have been done so far, the completion of mixing seems to be detectable based on the probe assessment which is very encouraging. Many methods, tests and planning are to be defined. The unknowns are numerous, but a positive outcome of the project is expected.

Moreover, methods based on artificial intelligence to anticipate the completion of mixing are already under analysis and appear to be very promising. The aim of this aspect of the project is to help operators and speed up the decision process during adjustment.

Finally, the ambition is to develop an automatic adjustment program that would add water and admixtures through an automatic gate. Resources consumption could be decreased, thus reducing the economical and environmental impact of the concrete production while improving the overall concrete quality.

Acknowledgement. The authors would like to acknowledge Command Alkon Canada and Béton Provincial for their financial and technical support, Mathieu Thomassin for his help during the project, Antoine Gagnon for his helpful comments concerning the article and the Natural Sciences and Engineering Research Council of Canada for its funding.

References

1. Frey HC, Kim K (2009) In-use measurement of the activity, fuel use, and emissions of eight cement mixer trucks operated on each of petroleum diesel and soy-based B20 biodiesel. Transp Res Part D: Transp Environ 14(8):585–592

2. Chopin D (2003) Malaxage des bétons à hautes performances et des bétons auto-plaçants: optimisation du temps de fabrication, Nantes
3. Johansson A (1971) The relationship between mixing time and type of concrete mixer
4. Vandanjon PO, de LARRARD F, Dehousse B, Villain G, Maillot R, Laplante P (2000) Homogeneisation des betons en centrale de fabrication discontinue. Influence du temps de malaxage et du mode d'introduction des additions minerales. Bulletin des laboratoires des Ponts et Chaussées :35–46
5. De Larrard F (2000) Structures granulaires et formulation des bétons. Laboratoire Central des Ponts et Chaussées
6. Purrington W, Loring H (1928) The determination of the workability of concrete. In: Proceedings of american society testing materials
7. Tattersall GH (1991) Workability and quality control of concrete. CRC Press, Boca Raton
8. Cazacliu B (2008) In-mixer measurement to describe the mixture kinetics during concrete mixing. In: Proceedings of sixty international on mixing in industrial process industries, I SMIP VI
9. Nishiyama N (1994) Controlling the consistency of high-performance concrete by mixing torque in the ready-mixed concrete plant. Spec Publ 149:633–648
10. Nordenswan E, Käppi A (2007) A new online method of measuring the workability of self-compacting concrete. In: Proceedings of 5th RILEM symposium on SCC, Ghent
11. Lê ND (2007) Amélioration de la régularité du béton en production. Thèse de docteur de l'École Nationale des Ponts et Chaussées, Spécialité: Structures et Matériaux
12. Amziane S, Ferraris CF, Koehler EP (2005) Measurement of workability of fresh concrete using a mixing truck. J Res Natl Inst Stand Technol 110(1):55
13. Daczko JA (2000) A proposal for measuring rheology of production concrete. Concr Int 22 (5):47–49
14. Mokéddem S (2012) Contrôle de la rhéologie d'un béton et de son évolution lors du malaxage par des mesures en ligne à l'aide de la sonde Viscoprobe. Ecole Centrale de Nantes (ECN)
15. Ambrosetti M DensityDesign Research Lab. Editor. Under license CC BY-SA 4.0/Adaptation. https://creativecommons.org-/licenses/by-sa/4.0/
16. Beaupré D (2012) Mixer-mounted probe measures concrete workability. Concr Int 34:2–5
17. Beaupré D (2012) Rheological probe to measure concrete workability. In: The 37th conference on our world in concrete & structure, Singapore
18. Beaupre D, Chapdelaine J, Chapdelaine F (2017) Probe and method for obtaining rheological property value. U.S. Patent Application No 14/886,436
19. Cazacliu B, Roquet N (2009) Concrete mixing kinetics by means of power measurement. Cem Concr Res 39(3):182–194

Pumping Process of High Strength Self-consolidating Concrete in the Construction of Skyscraper

Peiyu Yan(✉), Jianguo Han, Mengyuan Li, and Yu Liu

Department of Civil Engineering, Tsinghua University, Beijing, China
yanpy@tsinghua.edu.cn

Abstract. Lots of skyscrapers are or will be built in China. High strength self-consolidating concrete is used to construct composite steel concrete pillars and shear walls of core tube. It is introduced how to prepare high strength self-consolidating concrete with local raw materials and the controlling index for the workability of fresh concrete pumped to different heights. The pumpability of fresh concrete was evaluated in laboratory and in-site using normal workability evaluation methods and Sliper, a newly developed instrument to estimate pumpability of fresh concrete. A simulating pumping process of high strength self-consolidating concrete was done to investigate its performance using an experimental pumpline circuit with the total length of 2300 m. C100 concrete was pumped one time to the height more than 1000 m and cast without vibration in Shenzhen, China. Super-highly pumping of C70 self-consolidating concrete is widely performed now in the construction projects of skyscraper in China.

Keywords: High strength SCC · Pumpability · Workability · Super-high pumping

1 Introduction

Lots of skyscrapers are or will be built in China. There are 5 in China in top 10 skyscrapers worldwide. 88 skyscrapers higher than 200 m are completed in 2018 in China, accounting for 61.5% of the total 143 ones completed worldwide in 2018. There are 19 in China in total 34 top high rising buildings under construction, which will be completed in 2019. The mainstream structure form of these skyscrapers is steel reinforced concrete (SRC) pillars and reinforced concrete (RC) shear wall of core tube. 90 completed skyscrapers adopted concrete structure, accounting for 62.9% of the total 143 ones. Therefore, huge amount of high strength concrete must be transported vertically by pumping process to the elevation and cast into the mould. Self-consolidating concrete (SCC) with long-time workability maintaining property is prepared to satisfy the requirement of pumping under the condition of very high altitude and very long distance.

Excellent pumpability of fresh concrete is the precondition of a successful high-rising pumping of concrete. Some parameters of concrete workability are used to evaluate the pumpability of concrete in worksite. For example, slump of plastic

V. Mechtcherine et al. (Eds.): RheoCon 2019/SCC 2019, RILEM Bookseries 23, pp. 346–352, 2020.
https://doi.org/10.1007/978-3-030-22566-7_40

concrete is measured to calculate its pressure lose along the pipeline during the pumping process. The slump of self-consolidating concrete is too large to character its variation of workability as well as pumpability. Other parameters of fresh self-consolidating concrete need to determine and the corresponding method need to establish to character its pumpability. A newly developed instrument, Sliper, can be used to measure the property of lubrication layer on the wall of pipeline and evaluate the pumpability of concrete [1].

Ping-an Finance Center is located in Shenzhen, Guangdong Province, China. It is a skyscraper of 600 m high. There are 8 steel reinforced concrete pillars at 4 corners of the building as the main bearing structure. C70 high strength concrete is prepared to cast the pillars till 400 m high. C60 high strength concrete is prepared to cast the pillars higher than 400 m and the shear wall. C35 concrete is used for floor. The highest pumping altitude of concrete is 555 m. A simulating casting of C100 concrete to a height of more than 1000 m was done based on this building.

2 Preparing, Pumping and Casting of High Strength SCC in the Construction Project of Ping-an Finance Center

P II 52.5 Portland cement, S95 GGBS and class I fly ash was used as binder. The specific surface area of cement is 374 m^2/kg. The 3 d and 28 d compressive strength of cement is 29.5 MPa and 57.4 MPa. The water requirement ratio, the loss on ignition and the residue on 45 μm sieve of fly ash is 93%, 3.2% and 9.4%, respectively. 5 mm - 20 mm crushed limestone and river sand with fine module of 2.6 was used as coarse and fine aggregate. Clay and clay lump of coarse aggregate is 0.4% and 0.2%, respectively. Its flakiness and elongation index is 4% and its crushing value is 4.7%. Clay and clay lump of fine aggregate is 1.4% and 0.4%, respectively. Polycarboxylate superplasticizer (SP) with the solid content of 20% and water-reducing ratio of 25% was used. The mix proportions of the concretes used under and over 200 m is shown in Tables 1 and 2 respectively. Some parameters of concrete mixture used to guide its mix proportion design is shown in Table 3. The binder content and paste ratio of concrete used for upper part over 200 m is higher than that used for lower part under 200 m. Very high sand ratio is used to improve the flowability of SCC. The pumpability of concrete can be improved by this way.

Table 1. The mix proportion of self-compacting concrete used under 200 m (kg/m^3).

	Cement	GGBS	Fly ash	Sand	Stone	Water	SP
C70	350	120	70	839	860	155	6.48
C60	300	110	80	875	860	160	4.9

Table 2. The mix proportion of self-compacting concrete used over 200 m (kg/m^3).

	Cement	GGBS	Fly ash	Sand	Stone	Water	SP
C70	390	120	80	773	870	163	7.08
C60	360	140	60	824	830	170	5.88

Table 3. Some parameters of concrete mixture.

	Under 200 m				Over 200 m			
	Binder content (kg/m^3)	W/B	Paste ratio (%)	Sand ratio (%)	Binder content (kg/m^3)	W/B	Paste ratio (%)	Sand ratio (%)
C70	540	0.30	32.9	49.4%	590	0.29	35.3	47.0%
C60	490	0.33	31.8	50.4%	560	0.31	35.1	49.8%

The requirement of workability of fresh concretes is shown in Table 4. The real measuring results of fresh concretes arrived at the worksite show that its slump flow is in the range of 700 mm ± 50 mm and there is not slump flow loss in 3 h; the decrease of slump flow after J-ring test is no larger than 50 mm and there is no separation and bleeding. A pump with an exit pressure of 50 MPa was used. The variation of pumping pressure with pumping height is shown in Fig. 1. The pumping pressure increased with the increase of building altitude. The highest pumping pressure was not beyond 25 MPa. The slump flow of concrete pumped to the casting site mainly decreased less than 40 mm (Fig. 2). The concrete mixture was very flowable after long distance and large height of pumping. The prepared concrete mixture was pumped smoothly with a reasonable speed to the casting site in the super-high rising tower, cast and consolidated with or even without a little vibration.

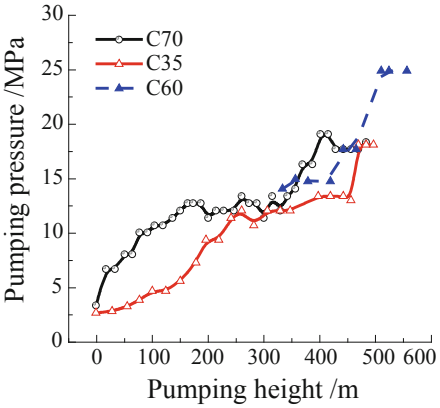

Fig. 1. Pumping pressure of concrete.

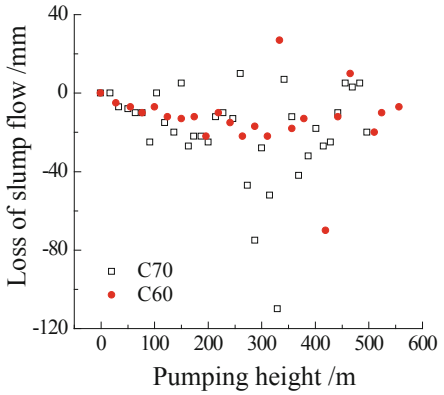

Fig. 2. Loss of slump flow of concrete after pumping.

The adiabatic temperature rising curve of C70 concrete is shown in Fig. 3. The total adiabatic temperature rising of concrete was 48.8 °C. The autogenous shrinkage curve of C70 concrete is shown in Fig. 4. The autogenous shrinkage of concrete can be divided into two distinct stages, a rapidly increasing stage of about 350×10^{-6} in the first hydrating day and a gently increasing stage of less than 200×10^{-6} in the later

Table 4. The requirement of workability of fresh concrete.

	Slump flow (mm)	Decrease of slump flow after J-ring test (mm)	Flowing time through V-vessel (s)	Keeping of slump flow (mm)		Ratio of separation (%)	Bleeding ratio under pressure (%)
				2 h	3 h		
C70	650–750	≤ 50	≤ 10	≥ 680	≥ 660	≤ 15	≤ 35
C60	650–750	≤ 50	≤ 10	≥ 680	≥ 660	≤ 15	≤ 35

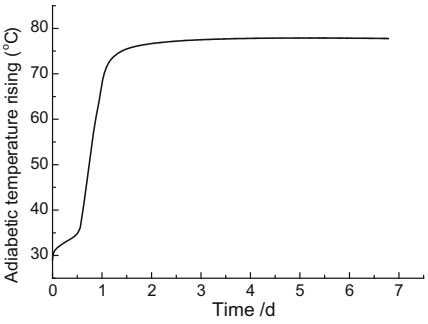

Fig. 3. The adiabatic temperature rising curve of C70 concrete.

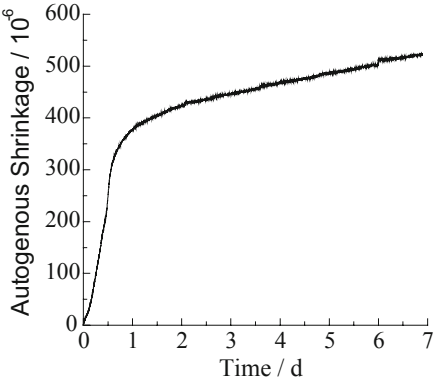

Fig. 4. The autogenous shrinkage curve of C70 concrete.

time till 7 days. The total autogenous shrinkage of C70 concrete prepared for SRC columns of a super-high rising tower is almost 520×10^{-6}.

More than 46 000 m^3 C70 and C60 self-compacting concrete was used in two years to cast the huge SRC pillars and shear wall in the construction project of Ping-an Finance Center. The average compressive strength of C70 and C60 concrete is 79.86 MPa and 73.95 MPa, respectively. The standard deviation of compressive strength of C70 and C60 concrete is 7.58 MPa and 4.85 MPa, respectively. The quality of concrete is very satisfactory.

3 The Evaluation of Pumpability of Concrete Using Sliper

Sliper is an instrument for evaluation of pumpability of concrete [2]. Based on Mechtcherine's research, the relationship of pressure P and flow rate Q of concrete during pumping tested with Sliper is obtained as:

$$P = A + BQ \tag{1}$$

The yield stress $\tau_{0,LL}$ and the equivalent of effective viscosity η_{LL} of lubrication layer on the wall of pipeline is as:

$$\tau_{0,\mathrm{LL}} = \frac{dA}{4l} \tag{2}$$

$$\eta_{LL} = \frac{B\pi d^3}{16l} \tag{3}$$

where l and d are the length and diameter of Sliper pipe.

Kaplan [3] indicated that the pumping pressure of concrete under the condition of slip flow is as:

$$P = \frac{4L}{D}\tau_{0,LL} + \frac{16L}{\pi D^3}\cdot\eta_{LL}\cdot\frac{Q}{e} + \rho\cdot g\cdot h \tag{4}$$

The pumping pressure of concrete under the condition of slip-plus-shear flow is as:

$$P = \frac{4L}{D}\left(\frac{\frac{Q}{900\pi D^2 e} - \frac{D}{8\mu_c}\tau_{0,LL} + \frac{D}{6\mu_c}\tau_0}{1 + \frac{D}{8\mu_c}\eta_{LL}}\eta_{LL} + \tau_{0,LL}\right) + \rho\cdot g\cdot h \tag{5}$$

where μ_c and τ_0 is the plastic viscosity and yield stress of concrete, h is pumping height, L and D are the length and diameter of pumpline.

Table 5. The properties of fresh concrete measured at worksite.

Concrete	Slump flow (mm)	Flowing time through V-vessel (s)	ρ (kg·m^{-3})	τ_0 (Pa)	μ_c (Pa·s)	$\tau_{0.LL}$ (Pa)	η_{LL} (Pa·s·m^{-1})
1	680	9.19	2 357	276.5	65.9	0.63	900.14
2	790	3.26	2 391	282.1	55.6	1.25	1167.97
3	705	7.22	2 427	111.7	25.7	0.63	1322.60

Table 6. The pumping parameters and predicted pumping pressures of concrete.

Concrete	L (m)	H (m)	P_0 (MPa)	P_1 (MPa)	P_2 (MPa)
1	392	292	9	10.6	10.6
2	410	310	9	12.5	12.2
3	456	356	9	15.1	12.7

The rheological properties of C60 concrete to be pumped to different altitudes were measured by Sliper and ICAR concrete rheometer at the construction worksite of a skyscraper. The workability of concrete measured at worksite is shown in Table 5.

The mix proportion of C60 concrete was same with Table 2. The diameter of pipe was 150 mm. The flow rate of concrete was about 25 m^3 estimated by the valve opening of pump machine. The pumping pressure of concrete was calculated by its properties measured at worksite and read from the gage of machine (Table 6).

P_0 is the reading from the gage of machine, P_1 is the calculating result of Eq. (4) and P_2 is the calculating result of Eq. (5). The yield stress of SCC is very low. Therefore, there is a shear flow even under the condition of low flow rate. Just measuring the properties of lubrication layer on the wall of pipe and predicting the pumping pressure of concrete may result an excessive value. The Eq. (5) should be used to estimate the pumping pressure of SCC considering simultaneously the rheological properties of concrete and lubrication layer. It can be seen that the prediction pumping pressure by Kaplan's equations is lower than real readings from the gage on the machine. It is conservative.

4 Full-Scale Test of C100 Concrete Pumped to the Altitude of over 1000 m

A full-scale test of super-high rising pumping of high strength concrete was done at the worksite of Ping-an Finance Center. C100 concrete was prepared. Its mix proportion is shown in Table 7 and its properties are shown in Table 8. The vertical pumping height was 555 m. The length of horizontal pipeline at ground was 243 m. The length of horizontal pipeline at 83th floor and 99th floor was 723 m and 749 m, respectively. The total length of pipeline with the diameter of 150 mm was more than 2300 m (Elbows had been conversed to straight pipe according to Chinese standard). It can simulate the pumping height of more than 1000 m. A pump with an exit pressure of 50 MPa was used.

Table 7. The mix proportion of C100 concrete (kg/m^3).

P. II 52.5 cement	Silica fume	Microsphere FA	River sand	5-20 mm stone	Water	SP
460	60	140	727	970	120	23.1

Table 8. The properties of C100 concrete prepared in laboratory.

Mechanical properties of hardened concrete				Slump flow of fresh concrete		
Age	3 d	28 d	56 d	0 h	1 h	2 h
Compressive strength (MPa)	94.2	128.2	130.4	765 mm	790 mm	760 mm
Elastic module (GPa)	44.6	48.1	48.7			

The slump flow of fresh concrete was 790 mm when it was just out of mixer, 850 mm when it arrived worksite after about 1 h of transportation time and 750 mm at the top of tower after another 1 h of pumping time. The exit pressure of concrete was

41.2 MPa. The concrete is very flowable and can be leveling without vibration at the top of tower. The 28 d compressive strength of concrete sample prepared and cured at field was 114.6 MPa.

5 Conclusion

High strength self-consolidating concrete was manufactured with local raw materials. It can be pumped vertically to the top of super-high rising tower and cast with a little vibration or even without vibration.

Sliper can evaluate the rheological properties of lubrication layer on the wall of pipeline. The pumping pressure can be estimated conservatively using Kaplan's equation based on the measuring results of Sliper.

A full-scale test was done. C100 concrete was pumped to the altitude of higher than 1000 m and cast without vibration.

Acknowledgments. The authors would like to acknowledge the financial support of National Key R&D Program of China (2017YFB0310101) and National Natural Science Foundation of China (No. 51678343).

References

1. Kasten (2010) Gleitrohr–Rheometer, Ein Verfahren zur Bestimmung der Fließeigenschaften von Dickstoffen in Rohrleitungen, Ph.D. thesis, TU Dresden. (in German)
2. Mechtcherine V, Nerella VN, Kasten K (2014) Testing pumpability of concrete using Sliding Pipe Rheometer. Constr Build Mater 53:312–323
3. Kaplan D, Larrard FD, Sedran T (2005) Design of concrete pumping circuit. ACI Mater J 102:110–117

Additive Manufacturing and 3D-Printing

Hardened Properties of 3D Printable Ultra-High Performance Fiber-Reinforced Concrete for Digital Construction Applications

Ravendran Arunothayan[1], Behzad Nematollahi[1(✉)], Shin Hau Bong[1], Ravi Ranade[2], and Jay Sanjayan[1]

[1] Center for Sustainable Infrastructure, Swinburne University of Technology, Hawthorn, VIC, Australia
bnematollahi@swin.edu.au
[2] University at Buffalo, State University of New York, New York, USA

Abstract. The current progress of 3D concrete printing technique is hampered by the limited range of printable concretes and reinforcing methods. To tackle both limitations, a 3D printable ultra-high performance fiber-reinforced concrete (UHPFRC) was developed in this study with using locally available materials for digital construction applications. The hardened properties of the developed 3D printable UHPFRC, including density, compressive strength and flexural strength were experimentally measured. The effect of testing directions on the compressive and flexural strengths of the 3D printed UHPFRC was also investigated. A conventionally mold-cast UHPFRC counterpart mix was also made for comparison purposes. The results showed that the compressive strength of the printed UHPFRC samples exhibited an anisotropic behavior, depending on the loading direction. However, the flexural strength of the printed UHPFRC samples was comparable in lateral and perpendicular directions. The results also showed that the density and compressive strength of the printed UHPFRC specimens were relatively lower than those of the mold-cast samples. However, the flexural strength of the printed UHPFRC specimens was higher than that of the mold-cast specimens.

Keywords: 3D concrete printing · UHPFRC · Ultra-high performance fiber-reinforced concrete · Extrusion · Mechanical properties

1 Introduction

Application of Additive Manufacturing (AM) technologies such as 3D concrete printing (3DCP) has the potential to unlock unprecedented transformations in the construction industry. The layer-by-layer deposition process in 3DCP allows "free-form" construction without the use of expensive formwork, which boosts the geometrical freedom and produces less construction waste, while saving the construction cost and time. The most widely known 3DCP technology is extrusion-based technique, which is comparable to the fused deposition modeling (FDM) method. In this

V. Mechtcherine et al. (Eds.): RheoCon 2019/SCC 2019, RILEM Bookseries 23, pp. 355–362, 2020.
https://doi.org/10.1007/978-3-030-22566-7_41

technique, a low-slump cementitious material is extruded from a nozzle mounted on a gantry, a crane or a robotic arm to print a concrete structure layer-by-layer [1].

One of the main restrictions of the extrusion-based 3DCP is the severely limited scope of available concretes that are suitable for the 3DCP technique. The conventional concrete in its current form is not suitable for printing applications, due to the setting characteristics of ordinary Portland cement (OPC). Application of other materials for the extrusion-based 3DCP such as geopolymer concrete [2–7], earth-based mortar [8], high-performance fiber-reinforced concrete (HPFRC) [9, 10] and ultra-high performance concrete (UHPC) [11] has already been reported in the literature.

Another key limitation of the extrusion-based 3DCP technique is incorporation of conventional steel reinforcements in the 3D printing process. As a possible solution, the conventional steel bars may be (partially or completely) replaced with short-fibers, which reduces the reliance on the conventional steel bars for cracking control (due to shrinkage and temperature changes), and in some cases provides some load bearing and deflection capacities. For instance, polypropylene (PP) micro fibers were used in the developed 3D printable HPFRC to reduce shrinkage and deformation in the plastic state [9, 10]. The results of a previous study of the authors showed that the 3D-printed geopolymers containing 0.75% and 1.00% (by volume) of PP fibers exhibited deflection-hardening behavior in bending. Bos et al. [12] used short straight steel fibers to improve ductility of the normal strength 3D printed concrete.

This study aims to systematically develop a 3D printable ultra-high performance fiber reinforced concrete (UHPFRC) with using locally available raw materials to tackle both the above-mentioned obstacles. The very high compressive strength of the printable UHPFRC enables size efficiency to 3D print complex concrete structures with slender, thereby lightweight cross sections [13]. In addition, the very high flexural strength in conjunction with a deflection-hardening behavior of the printable UHPFRC significantly reduces the reliance on the conventional steel bars. It should be noted that no fiber was used in the 3D printable UHPC reported in Gosselin et al [11] study. In addition, the reported printable UHPC had a proprietary mix design specifically developed and supplied by Lafarge-Holcim. This paper reports the hardened properties of the developed 3D printable UHPFRC, including density, compressive strength and flexural strength. The results were also compared with those of the conventionally mold-cast UHPFRC counterpart. Effect of the testing direction on the compressive and flexural strengths of the developed 3D printable UHPFRC was also investigated.

2 Experimental Process

2.1 Materials and Mix Proportions

The binder consisted of OPC and silica fume. The General Purpose (Type GP) Portland cement, conforming to AS 3972, was supplied by Geelong Cement, Australia. The densified silica fume, having a surface area of 18 m^2/g, was supplied by Doral Pty Ltd, Australia. Three types of sieve graded silica sands - each of different particle sizes - were used in this study. The average particle sizes (D_{50}) of fine, medium and coarse sands were 176 μm, 498 μm and 840 μm, respectively. A Polycarboxylate ether-based

superplasticizer (SP) supplied by BASF, Australia was used to adjust the workability. The short straight steel fibers (13 mm in length, 0.2 mm in diameter, with ultimate tensile strength of 2500 MPa) were supplied by Bekaert, Belgium. Sodium carboxymethyl cellulose (CMC) powder supplied by DKS Co. Ltd, Japan was used as a viscosity modifying agent to increase buildability of the mix.

Mix proportions were permuted with the aim of achieving the highest particle packing density. Sand-to-cement ratio was taken as 1.4 as recommended by Wille et al [14]. The mix proportions of the 3D-printable UHPFRC are presented in Table 1. Several trials have been conducted before arriving at the final mix proportions providing satisfactory extrudability and buildability characteristics.

Table 1. Mix proportions of 3D printable UHPFRC.

Binder		Sand			Tap water	SP[a]	Steel fiber	CMC
Cement	Silica fume	Fine	Medium	Coarse				
0.7	0.3	0.4	0.3	0.3	0.16	0.015	2%	0.001

Note: All numbers are mass ratios of the binder weight, except the fiber content (volume fraction).
[a]Superplasticizer.

2.2 Mixing, Casting, Printing, and Curing of Specimens

A 20L Hobart mixer was used for mixing. First, dry materials were mixed for 5 min. Around 75% of the tap water was gradually added and the mixing was continued for 5 additional minutes. The remaining tap water was mixed with the superplasticizer and then gradually added to the mix. The mixing was continued for 6–9 min until sufficient workability was achieved for the fibers to disperse uniformly. The fibers were then gradually added for 8–10 min. Finally, the CMC powder was added and mixed for an additional minute. The total mixing time ranges between 25–30 min.

Figure 1 presents the schematic illustration of the extrusion process. A small-scale custom-made printer was used in this study with a piston type extruder with a rectangular nozzle opening of 30 mm × 15 mm. The extruder was a metallic cylinder of 50 mm in diameter and 600 mm in length. Two layers of 280 mm long filaments were printed with a print-time interval (delay time) of 2 min. The specimens were sealed inside a container for 24 h to reduce excessive water loss during the setting. In addition, 25 mm cubes and prisms with the dimensions of 25 mm × 25 mm × 280 mm were conventionally cast for comparison purposes. The conventionally mold-cast specimens were covered with plastic sheets and de-molded after 24 h. Figure 2 presents a sample specimen of two-layer printed filament using the aforesaid method.

An elevated temperature curing procedure was adopted in this study to accelerate the hydration reactions. At the end of 24 h, all specimens were transferred to a water tank and cured in the room temperature (20 °C) for 7 days. Then, the specimens were put inside an oven and heat cured for 4 days in water at 90 °C, followed by 2 days in air at 90 °C. According to Ranade et al. [15], the 14-day compressive strength of the

samples cured in accordance with the above-said curing regime is equivalent to the 90-day compressive strength of the samples cured in the ambient temperature (20 °C).

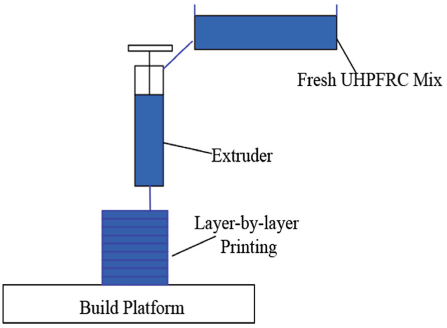

Fig. 1. Schematic illustration of the extrusion-based 3DCP process.

Fig. 2. Two-layer printed UHPFRC filaments.

2.3 Testing of Specimens

At the end of the accelerated curing process, the printed specimens were ground in all directions to have flat surfaces for compression and bending tests. All specimens were weighed on the testing day to calculate the hardened density of the mold-cast and 3D printed UHPFRC specimens.

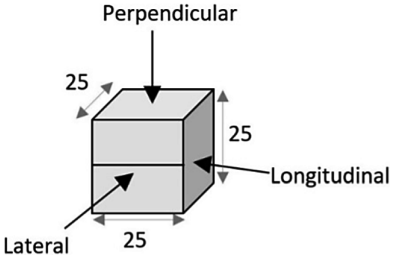

Fig. 3. The testing directions for compression tests of the printed specimen.

To measure the compressive strength of the printed UHPFRC, 25 mm cube specimens were extracted from the printed filaments and loaded in three directions as shown in Fig. 3. At least six specimens were tested for each direction. To measure the compressive strength of the mold-cast UHPFRC, at least six 25 mm mold-cast cube specimens were tested in perpendicular direction only. A constant load rate of 0.33 MPa/s was applied for the compression tests.

To measure the flexural strength of the printed UHPFRC, 280 mm × 25 mm 25 mm printed specimens were tested in perpendicular and lateral directions. At least

six specimens were tested for each direction. To measure the flexural strength of the mold-cast UHPFRC, at least six mold-cast specimens with the dimensions of 280 mm × 25 mm × 25 mm were tested in perpendicular direction only. A three-point bending test setup with a span of 160 mm and a displacement control rate of 1 mm/min was used for the bending tests.

3 Results and Discussion

3.1 Density

The mean hardened density of the printed UHPFRC mix was 2345 kg/m^3 and that of the mold-cast UHPFRC mix was 2395 kg/m^3. The mean density of the mold-cast UHPFRC mix was slightly higher than that of the 3D printed UHPFRC mix. This phenomenon can be attributed to the 3D printing characteristics, such as free flowing nature of the material in the lateral direction and its vulnerability to entrap air voids in the absence of vibration, as compared to the conventional mold-casting approach.

3.2 Compressive Strength

Figure 4 presents the results of the compression tests. An anisotropic behavior was observed in the compressive strength of the printed UHPFRC, depending on the loading direction. Similar outcomes were reported elsewhere for normal strength concrete [16], high performance concrete [10] and geopolymer [2].

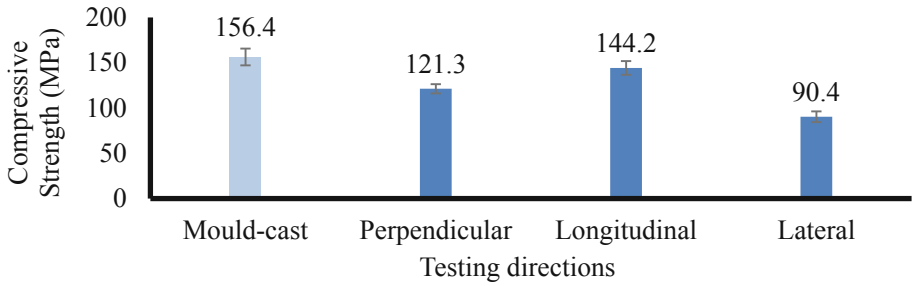

Fig. 4. Results of the compression tests of 3D printed and mold-cast UHPFRC.

For the printed UHPFRC mix, the highest mean compressive strength was recorded in the longitudinal direction. The pressure exerted during the extrusion process contributes to improved compaction of the UHPFRC mix in the longitudinal direction. The mean compressive strength in the lateral direction was the lowest, because the material was free to expand and settle in this direction. Also, there was no external pressure applied in the lateral direction, and hence the compaction is comparatively weaker in this direction than the longitudinal and perpendicular directions. The mean compressive strength in the perpendicular direction was in between the compressive strength in the

lateral and longitudinal directions. Compaction in the perpendicular direction was exerted by the pressure applied by the weight of the adjacent layer printed above.

The mean compressive strength of the mold-cast UHPFRC mix was at least 8% higher than the highest mean compressive strength achieved in the printed UHPFRC mix (the longitudinal direction). As compared to the conventional mold-casting approach, the porosity increment due to free expansion in the lateral direction and/or lack of vibration in the 3DCP process could have contributed to the reduction of the compressive strength of the printed UHPFRC mix.

3.3 Flexural Strength

The flexural test results are presented in Fig. 5. In contrast to the compressive strength of the printed UHPFRC, the flexural strength of the printed UHPFRC did not significantly vary with respect to the direction of testing. This behavior does not comply with the previous studies where the primary load resisting component was either the OPC concrete [9, 10, 16] or geopolymer concrete [2]. The central bottom area where the highest tensile stresses occur was compacted superiorly in the perpendicular direction compared to the lateral direction, and hence the variation in the results was anticipated. However, in the printed UHPFRC, the major contributor in resisting the flexural loads is steel fibers, not the concrete. The fiber orientation along the longitudinal direction is identical, irrespective of the direction of load application (perpendicular or lateral). Therefore, the resistance shown against the highest tensile stresses is identical.

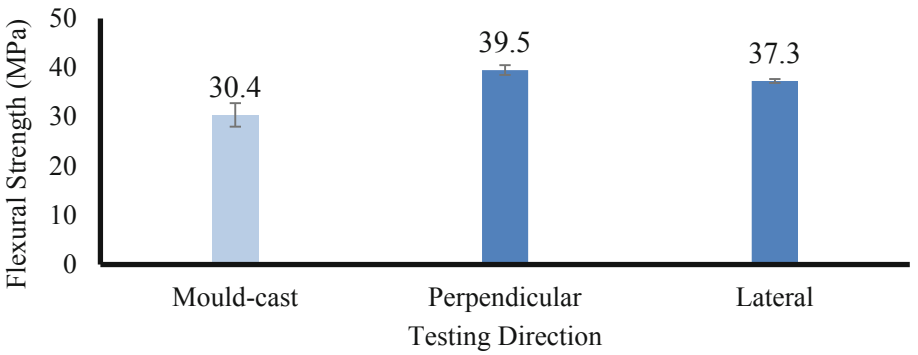

Fig. 5. Results of the flexural tests of 3D printed and mold-cast UHPFRC.

It can also be noted from Fig. 5 that the mean flexural strength of the printed samples was 20–30% higher than that of the mold-cast samples. This behavior is in contrast to the compressive strength results, where the printed specimens exhibited lower compressive strength than the mold-cast samples. This behavior can be attributed to the printing process of the UHPFRC mix. As the pressure is exerted in the longitudinal direction during printing, the steel fibers tend to align in the direction of concrete flow (the longitudinal direction). The printing nozzle size of 15 mm - which is

only slightly larger than the length of steel fiber (13 mm), aligns the fibers in 2D orientations. On the other hand, the mold-cast specimens show random arrangement of fibers in 3D orientations. This effect contributes to the increase in the flexural strength of the printed specimens in comparison to the mold-cast specimens.

4 Conclusion

This paper presented the results of a study on the development of a 3D printable UHPFRC mix. The hardened properties of the printed UHPFRC mix were compared with those of the mold-cast counterpart mix. The following conclusions are drawn:

(1) The anisotropic behavior of the compressive strength of the printed UHPFRC is an inherent property of the extrusion-based 3D concrete printing process. Longitudinal direction showed the highest compressive strength, while the lateral direction showed the lowest. The strength in the perpendicular direction fell in between the other two directions.
(2) The compressive strength of the mold-cast counterpart UHPFRC mix (156.4 MPa) was slightly higher than the highest compressive strength of the printed UHPFRC mix (144.2 MPa). As compared to the conventional mold-casting approach, the porosity increment due to free expansion in the lateral direction and/or lack of vibration in the 3DCP process could have contributed to the reduction of the compressive strength of the printed UHPFRC mix.
(3) In contrast to the compressive strength, the flexural strength of the 3D printed UHPFRC mix did not show an anisotropic behavior with respect to the testing direction. This is because the flexural strength of the printed UHPFRC depends on the fiber orientation of the specimens. Regardless of the direction of flexural testing, the fiber orientation would always be along the longitudinal direction (the printing direction). Therefore, the flexural strengths in both lateral and perpendicular directions were comparable.
(4) The flexural strength of the mold-cast counterpart UHPFRC mix was 18%–23% lower than that of the printed UHPFRC mix. This strength reduction can be attributed to the random orientation of fibers in the mold-cast specimens, unlike the 2D orientations of the fibers along the longitudinal direction in the printed specimens. The nozzle size and the exerted pressure during the extrusion process influenced the fiber orientation in the printed samples.

Acknowledgement. The authors would like to gratefully acknowledge the support by the Australian Research Council Linkage Infrastructure Grant LE170100168 and Discovery Early Career Researcher Award DE180101587.

References

1. Nematollahi B, Xia M, Sanjayan J (2017) Current progress of 3D concrete printing technologies. In: Proceedings of the international symposium on automation and robotics in construction (ISARC), Vilnius Gediminas Technical University, Taipei
2. Nematollahi B, Xia M, Bong SH, Sanjayan J (2018) Hardened properties of 3D printable 'one-part' geopolymer for construction applications. In: Proceedings of the 1st RILEM international conference on concrete and digital fabrication 'digital concrete 2018', Zurich, Switzerland, pp 190–199
3. Bong SH, Nematollahi B, Nazari A, Xia M, Sanjayan J (2019) Method of optimization for ambient temperature cured sustainable geopolymers for 3D printing construction applications. Materials 12(6):902
4. Nematollahi B, Xia M, Sanjayan J, Vijay P (2018) Effect of type of fiber on flexural and inter-layer bond strength of extrusion-based 3D printed geopolymer concrete. Mater Sci Forum 939:155–162
5. Nematollahi B, Xia M, Vijay P, Sanjayan J (2019) Properties of extrusion-based 3D printable geopolymer for digital construction applications. In: 3D concrete printing technology. Elsevier, Butterworth-Heinemann, Imprint, Paperback, pp 371–388. ISBN 9780128154816
6. Nematollahi B, Vijay P, Sanjayan J, Nazari A, Xia M, Nerella VN, Mechtcherine V (2018) Effect of polypropylene fiber addition on properties of geopolymers made by 3D printing for digital construction. Materials 11(12):2352
7. Bong SH, Nematollahi B, Nazari A, Xia M, Sanjayan J (2018) Fresh and hardened properties of 3D printable geopolymer cured in ambient temperature. In: Proceedings of the 1st RILEM international conference on concrete and digital fabrication 'digital concrete 2018', Zurich, Switzerland, pp 3–11
8. Perrot A, Rangeard D, Courteille E (2018) 3D printing of earth-based materials: processing aspects. Constr Build Mater 172:670–676
9. Le TT, Austin SA, Lim S, Buswell RA, Gibb AGF, Thorpe T (2012) Mix design and fresh properties for high-performance printing concrete. Mater Struct 45(8):1221–1232
10. Le TT, Austin SA, Lim S, Buswell RA, Law R, Gibb AGF, Thorpe T (2012) Hardened properties of high-performance printing concrete. Cem Concr Res 42(3):558–566
11. Gosselin C, Duballet R, Roux Ph, Gaudillière N, Dirrenberger J, Morel Ph (2016) Large-scale 3D printing of ultra-high performance concrete–a new processing route for architects and builders. Mater Des 100:102–109
12. Bos F, Bosco E, Salet T (2018) Ductility of 3D printed concrete reinforced with short straight steel fibers. Virtual Phys Prototyp 14:1–15
13. Nematollahi B, Saifulnaz RM, Jaafar MS, Voo YL (2012) A review on ultra high performance 'ductile' concrete (UHPdC) technology. Int J Civ Struct Eng 2(3):994
14. Wille K, Naaman AE, Parra-Montesinos GJ (2011) Ultra-high performance concrete with compressive strength exceeding 150 MPa (22 ksi): a simpler way. ACI Mater J 108(1):46–54
15. Ranade R, Stults MD, Li VC, Rushing TS, Ronth J, Heard WF (2011) Development of high strength high ductility concrete. In: Proceedings of the 2nd international RILEM conference on strain hardening cementitious composites, Rio de Janeiro, Brazil, pp 1–8
16. Sanjayan J, Nematollahi B, Xia M, Marchment T (2018) Effect of surface moisture on inter-layer strength of 3D printed concrete. Constr Build Mater 172:468–475

Properties of 3D-Printable Ductile Fibre-Reinforced Geopolymer Composite for Digital Construction Applications

Shin Hau Bong[1], Behzad Nematollahi[1(✉)], Ming Xia[1], Ali Nazari[1], Jay Sanjayan[1], and Jinlong Pan[2]

[1] Centre for Sustainable Infrastructure, Faculty of Science, Engineering and Technology, Swinburne University of Technology, Hawthorn, VIC, Australia
bnematollahi@swin.edu.au
[2] School of Civil Engineering, Southeast University, Nanjing, China

Abstract. Two main limitations of extrusion-based 3D concrete printing process are the incorporation of conventional steel bars and the limited range of printable concretes. To tackle both limitations, this paper investigates feasibility of developing a 3D-printable ductile fibre-reinforced geopolymer composite (DFRGC) for digital construction applications. Instead of the conventional cement binder, a "just-add-water" geopolymer binder was used for production of the 3D-printable DFRGC, which considerably improves its sustainability performance and commercial viability in the construction industry. A series of experiments including bulk density, apparent porosity, compression, and flexural tests were conducted to characterize the mechanical properties of the 3D-printable DFRGC. The effect of number of printed layers on the mechanical properties of the 3D-printable DFRGC was also investigated. Further, dependency of the compressive strength of the printed sample on the testing direction was also evaluated. The developed 3D-printable DFRGC exhibited deflection-hardening behaviour in flexure with high modulus of rupture of up to 10.2 MPa and deflection capacity of up to 5.3 mm. Therefore, the feasibility of developing 3D-printable deflection-hardening ductile geopolymer composites was established. The results also showed that the compressive and flexural performances of the 3D-printed DFRGC specimens depended on the testing direction and number of printed layers.

Keywords: 3D concrete printing · Extrusion · Just-add-water geopolymer · Deflection-hardening · High ductility · Digital construction

1 Introduction

One of the key limitations of extrusion-based 3D concrete printing (3DCP) techniques is the very limited range of available concretes that are suitable for the 3D printing process. Therefore, it is urgently needed to expand the range of printable concretes. The other main limitation of the extrusion-based 3DCP is incorporation of conventional steel reinforcement into 3D-printing process [1]. As a possible solution, conventional

V. Mechtcherine et al. (Eds.): RheoCon 2019/SCC 2019, RILEM Bookseries 23, pp. 363–372, 2020.
https://doi.org/10.1007/978-3-030-22566-7_42

steel bars might be partly or completely substituted by short-fibre reinforcement. Ductile fibre-reinforced cementitious composite (DFRCC) is a special class of fibre-reinforced cementitious composites (FRCCs) that has higher deflection capacity at peak load in comparison with other FRCCs and characterized by deflection-hardening behaviour in bending after first-cracking, accompanied by multiple fine cracks. Multiple cracking leads to development in properties such as ductility, toughness, fracture energy, deformation capacity under bending [2]. Therefore, DFRCCs can be considered as a kind of self-reinforced cementitious composites to reduce or even eliminate the need for conventional steel bars in 3D-printed concrete structures, which results in more efficiency and freedom for extrusion-based 3DCP process.

However, there is generally high amount of ordinary Portland cement (OPC) in the mixture design of DFRCC, which results in high autogenous shrinkage, heat of hydration, and cost. In addition, production of OPC is a highly energy and emissions industry. The associated increase in the CO_2 emissions as well as embodied energy due to manufacture of OPC apparently compromise sustainability credential of DFRCC [2]. Recently, the authors of this study have developed a green ductile fibre-reinforced geopolymer composite (DFRGC) with complete replacement of the OPC binder by a geopolymer binder [2, 3]. Geopolymer is a sustainable alternative binder to OPC. It is produced by alkaline activation of fly ash and slag, which are being industrial by-products of coal power stations and iron manufacture, respectively [4]. The developed DFRGC demonstrated a deflection-hardening behaviour in flexure with high modulus of rupture of up to 11.5 MPa and very high deflection capacity of up to 40 mm [2, 3].

The other main limitation of the extrusion-based 3DCP is the very limited range of available concretes that are suitable for the 3D printing process. To tackle both limitations, this study reports a feasibility study of developing a 3D-printable DFRGC for digital construction applications. Appropriate 3D-printable mix proportions were determined through experiments, utilizing knowledge obtained from development of cast-in-mould DFRGC, which satisfied the requirements for extrusion-based 3DCP process. A series of experiments including bulk density, apparent porosity, compression in different directions, and flexural tests were conducted to characterize the mechanical properties of the developed 3D-printable DFRGC.

2 Materials and Methods

2.1 Materials and Mixture Proportions

The low calcium (Class F) fly ash and granulated ground blast furnace slag (henceforth referred to as slag) were supplied by Cement Australia Pty Ltd., Australia and Building Products Supplies Pty Ltd., Australia, respectively. The sand with a D50 of 176 μm and D10 of 108 μm was supplied by TGS Industrial Sands Pty Ltd., Australia. Anhydrous sodium metasilicate powder with SiO_2/Na_2O mass ratio of 0.9 supplied by Redox Pty Ltd., Australia was used as the solid alkaline activator. Oil-coated PVA fibres supplied by Kuraray Co. Ltd., Japan were used. The properties of the PVA fibre are present in Table 1.

Table 2 presents mixture proportion of the 3D-printable DFRGC. Several trials were performed before arriving at the final mix proportions presented in Table 2. The geopolymer precursor was composed of fly ash and slag with the fly ash to slag mass ratio of 1.0. Sucrose powder with a 0.2% by mass of geopolymer precursor was used as a retarder to increase the setting time of the mixture. Sodium carboxymethyl cellulose (CMC) powder supplied by DKS Co. Ltd, Japan was used as a viscosity modifying agent (VMA) to achieve appropriate rheological properties for extrusion-based 3DCP process.

Table 1. Properties of PVA fibre.

Fibre type	Diameter (μm)	Length (mm)	Young's modulus (GPa)	Elongation (%)	Density (g/cm^3)	Nominal strength (MPa)
RECS 15	40	8	41	6	1.3	1600

Table 2. Mixture proportion of 3D-printable DFRGC.

Geopolymer precursor[a]	Activator	Water	Sand	Retarder[b]	VMA[c]	Fibre
1.0	0.08	0.3	0.05	0.002	0.0006	0.020[d]

Note: All numbers are mass ratios of the precursor weight (fly ash + slag) except fibre content (volume fraction).
[a] Mixture of fly ash and slag with fly ash to slag mass ratio of 1.0.
[b] Sucrose powder.
[c] Sodium carboxymethyl cellulose.
[d] PVA fibre.

2.2 Mixing, Printing and Curing of 3D-Printable DFRGC

To prepare the DFRGC mixture, the fly ash, slag, solid activator, sand and sucrose powder were added to a Hobart mixer and dry mixed for 3 min. The water was then gradually added to the mixer and the mixing was continued for about 12 min. After the matrix ingredients were thoroughly mixed to achieve the desired fresh state, the fibres were gradually added to the mixer to ensure uniform fibre dispersion and the mixing was continued for another 12 min. The CMC powder was finally added to the mixer and mixed for about 5 min to obtain suitable rheological properties for extrusion-based 3DCP process.

The extrusion-based 3DCP process was simulated by using a small-scale custom-made 3D printer (Fig. 1). A piston-type extruder was developed for this 3D printer to extrude the fresh material through a metallic cylinder. A 3D-printed 45° nozzle with a rectangle opening of 30 mm × 15 mm was attached to the end of the extruder.

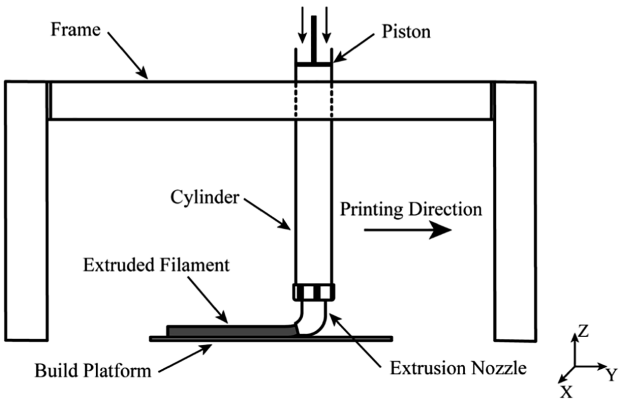

Fig. 1. Schematic drawing of the small-scale custom-made 3D printing apparatus.

The fresh DFRGC mixture was gradually filled into the extruder and a moderate external vibration was applied to the extruder to ensure the mixture inside the extruder received adequate compaction. The specimens were printed by moving the extruder in the horizontal direction at a constant speed of 35 mm/s. Two groups of specimens denoted as DFRGC-1L and DFRGC-2L were prepared in this study. DFRGC-1L specimens consisted of only one printed layer with the dimensions of 350 mm (L) × 30 mm (W) × 15 mm (H), while DFRGC-2L specimens consisted of two printed layers with the dimensions of 350 mm (L) × 30 mm (W) × 30 mm (H). For DFRGC-2L specimens, the second layer was printed on top of the first printed layer after 2 min.

All printed specimens were kept in the laboratory environment at ambient temperature (23 °C ± 3 °C) for the first 24 h and then cured in an oven at 60 °C for another 24 h to accelerate the geopolymerisation reactions. After the end of heat curing period, all specimens were removed from the oven and stored in the laboratory for ambient temperature curing until the day of testing. All specimens were tested seven days after printing.

2.3 Characterization Methods

Compression tests were conducted to determine the compressive strength of the printed DFRGC specimens. For DFRGC-1L specimens, at least three specimens with the dimensions of 30 mm (L) × 30 mm (W) × 15 mm (H) were sawn from the printed filament and tested in one of the two directions, namely lateral and longitudinal directions. For DFRGC-2L specimens, at least three cubic specimens with the dimension of 30 mm were sawn from the printed filaments and tested in one of the three different directions, namely longitudinal, lateral and perpendicular directions (Fig. 2). All specimens were tested by using a universal testing machine under a loading control of 0.33 MPa/s. It should be noted that surfaces of the printed specimens loaded in different directions were ground to have a smooth and flat surface while testing.

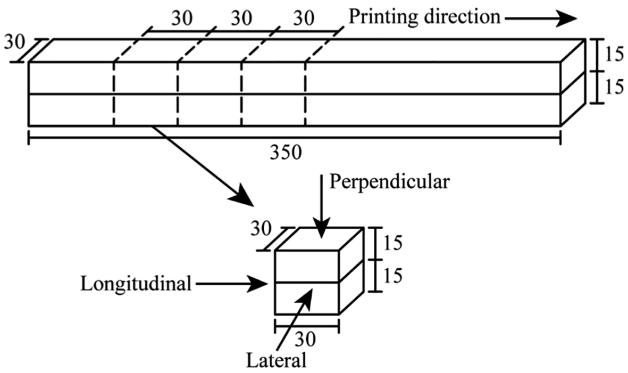

Fig. 2. Testing directions of two-layer DFRGC specimens in compression.

The flexural performance of the 3D-printed DFRGC specimens were evaluated by conducting four-point bending test. In this regard, both DFRGC-1L and DFRGC-2L specimens were only tested in perpendicular direction (Fig. 3) with the mid-span measuring 100 mm under displacement control at the rate of 1.0 mm/min. At least two specimens were tested for each group. The resulting load versus mid-span deflection data of each specimen were used to plot the flexural stress versus mid-span deflection curves.

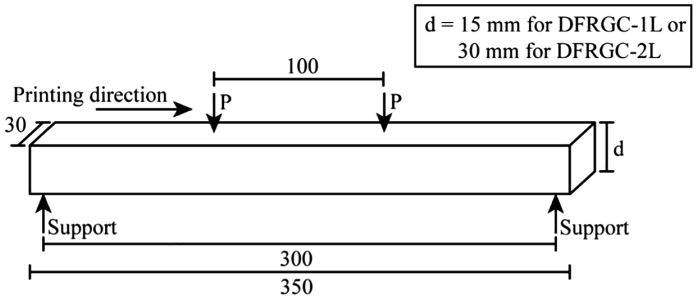

Fig. 3. Testing direction of 3D-printed DFRGC specimens in flexural.

The apparent porosity and bulk density of the printed DFRGC specimens were measured at 7 days in accordance with ASTM C20-00 (2015). In this regard, at least seven specimens were extracted from DFRGC-1L and DFRGC-2L specimens for the measurements.

3 Results and Discussion

3.1 Compressive Strength

The compressive strengths of the 3D-printed DFRGCs in different directions are presented in Table 3. The compressive strength of 3D-printed DFRGCs exhibited anisotropic behaviour depending on the testing direction. Previous studies also reported anisotropic behaviour of printed OPC-based and geopolymer-based mortars with respect to the compressive strength [5–12]. As shown in Table 3, in DFRGC-1L specimens the compressive strength in lateral direction was 37% higher than that in longitudinal direction. In DFRGC-2L specimens, the highest compressive strength was obtained in perpendicular direction followed by lateral direction and longitudinal direction. This anisotropic behaviour is most likely influenced by the fibre orientation in the 3D-printed DFRGCs. The fibre orientation in the printed specimens was evaluated by using a digital microscope. As can be seen in Fig. 4, significant amounts of fibres in the printed specimens were aligned parallel to the printing direction, which is consistent with the result reported by Ogura et al. [13] and Nematollahi et al. [14]. Since the preferential orientation of the fibres is parallel to the printing direction, the fibres help in crack bridging upon action of compressive force in the perpendicular and lateral directions [14]. In DFRGC-2L specimens the compressive strength in perpendicular direction was higher than that in lateral direction which may be because the fresh DFRGC mixture received some level of pressure in the perpendicular direction during the setting process due to the self-weight of the concrete [5]. The fibres do not aid in the compressive strength in longitudinal direction. This is because, as mentioned above, the fibres are mainly aligned parallel to the extrusion direction, which implies that they lie in the same plane as the loading direction when tested longitudinally.

Table 3. Compressive strength of 3D-printed DFRGCs.

Specimen ID	Compressive strength (MPa)		
	Perpendicular direction	Lateral direction	Longitudinal direction
DFRGC-1L	N/A	34.5 ± 3.1	25.1 ± 3.0
DFRGC-2L	49.8 ± 1.8	39.0 ± 1.7	29.1 ± 3.5

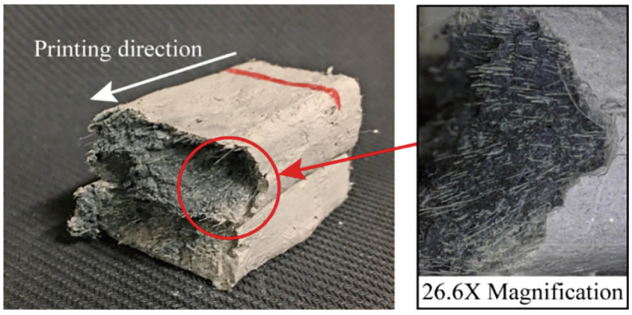

Fig. 4. Fibre orientation in 3D-printed DFRGC.

3.2 Flexural Performance

The flexural stress vs. mid-span deflection curves of the 3D-printed DFRGC specimens are presented in Fig. 5. As can be seen in this figure, all 3D-printed DFRGC specimens, regardless of the number of printed layers, exhibited deflection- hardening behaviour.

The first cracking point is defined as the point where nonlinearity in the load–deflection curve becomes obvious. According to ASTM C1018 (1997), this point is designated as limit of proportionality (LOP). In this study, the method proposed by Kim et al. [15] is adopted to identify the LOP in the load-deflection curves. The load value at LOP and its corresponding deflection value are designated as P_{LOP} and δ_{LOP}. The ultimate flexural strength commonly known as modulus of rupture (MOR) is defined as the point where softening happens after the LOP. The load value at MOR and its corresponding deflection value are designated as P_{MOR} and δ_{MOR}. According to ASTM C1609 (2012), the first crack-strength (f_{LOP}) and the modulus of rupture (MOR) for each printed DFRGC specimens can be determined from the following equations:

$$f_{LOP} = \frac{P_{LOP} \times L}{b \times d^2} \tag{1}$$

$$MOR = \frac{P_{MOR} \times L}{b \times d^2} \tag{2}$$

where L = 300 mm is the distance between the supporting rollers (span length), and b = 30 mm is the width of the specimen and d = 15 mm in DFRGC-1L and 30 mm in DFRGC-2L specimens is the height of the specimen.

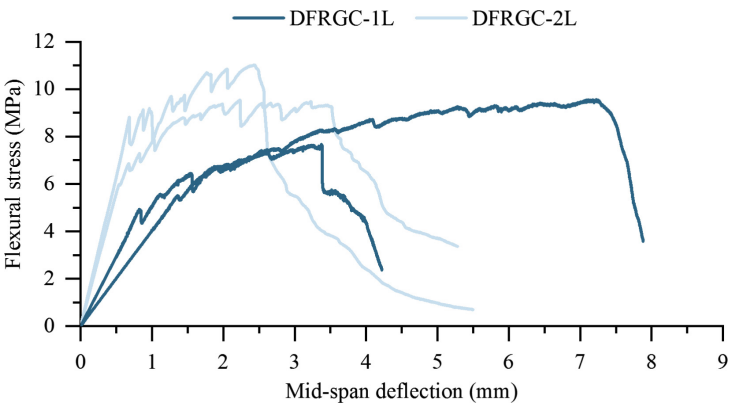

Fig. 5. Flexural stress vs. mid-span deflection curves of 3D-printed DFRGCs.

The f_{LOP}, MOR and their corresponding deflections of each printed DFRGC group are summarized in Table 4. In order to achieve deflection hardening with multiple cracking behaviour, the MOR of the composite must exceed the f_{LOP} of the composite.

If this condition is satisfied, multiple cracking with increasing load occurs and an immediate stress drop after first cracking is prevented [2]. As can be seen in Table 4, in all 3D-printed DFRGCs, regardless of the number of printed layers, the MOR of the composite was significantly higher than the f_{LOP}; thereby, the condition for deflection hardening behaviour is satisfied.

Table 4. Flexural test results of 3D-printed DFRGCs.

Specimen ID	First-crack strength f_{LOP}; (MPa)	First-crack deflection δ_{LOP}; (mm)	Modulus of rupture MOR; (MPa)	Deflection at peak load δ_{MOR}; (mm)
DFRGC-1L	5.2 ± 0.3	1.09 ± 0.3	8.6 ± 0.9	5.3 ± 1.9
DFRGC-2L	7.4 ± 1.4	0.61 ± 0.1	10.2 ± 0.8	2.9 ± 0.5

According to Table 4, the first-crack strength and modulus of rupture of the DFRGC-2L specimens were 42% and 19%, respectively higher than those of the DFRGC-1L specimens. In the case of testing flexural specimens in perpendicular direction, the mid-span of the bottom layer governs the flexural strength where the maximum tensile stress takes place. The bottom layer in DFRGC-2L specimens was most likely well compacted due to self-weight of the top layer, resulting in higher load capacity of the bottom layer, thereby the higher flexural strength of DFRGC-2L as compared to DFRGC-1L specimens.

As can be seen in Table 4, regardless of the number of printed layers, the deflection at peak load is significantly higher than the first-crack deflection. Although the DFRGC-1L specimens had lower first-crack strength and modulus of rupture than those of DFRGC-2L specimens, the deflection capacity (the deflection at peak load) of DFRGC-1L specimens was significantly (80%) higher than that of DFRGC-2L specimens. One of the underlying reasons for the significant difference in the deflection capacities (δ_{MOR}) of DFRGC-1L and DFRGC-2L specimens lies in their different MOR/f_{LOP} ratios. According to Table 4, the MOR/f_{LOP} ratio of the DFRGC-1L specimens is 1.65 which is about 20% higher than that of the DFRGC-2L specimens (1.38). According to Kanda and Li [16], the higher the MOR/f_{LOP} ratio led to the greater the possibility of deflection-hardening behaviour, and therefore results in the higher deflection capacity of the composite.

3.3 Apparent Porosity and Bulk Density

The apparent porosity and bulk density of 3D-printed DFRGCs were presented in Table 5. The apparent porosity of 3D-printed DFRGCs was about 28% regardless of the number of printed layers. Such high porosity can be due to the inclusion of short polymeric fibres which results in a fibre-induced increase in entrapped air in the mixture, and thereby higher porosity of the mixture [14]. As can be seen in Table 5, the bulk density of 3D-printed DFRGCs was about 1500 kg/m^3 regardless of the number of printed layers. Such low bulk density is due to the high apparent porosity of the 3D-printed DFRGCs.

Table 5. Apparent porosity and bulk density of 3D-printed DFRGCs.

Specimen ID	Apparent porosity (%)	Bulk density (kg/m^3)
DFRGC-1L	28.2 ± 1.0	1513 ± 23
DFRGC-2L	28.4 ± 0.6	1526 ± 14

4 Conclusion

A 3D-printable ductile fibre-reinforced geopolymer composite (DFRGC) exhibiting deflection-hardening behaviour in flexure accompanied by multiple fine cracks was developed in this study. The 3D printed DFRGC samples exhibited compressive strength of 25.1–49.8 MPa, modulus of rupture of 8.6–10.2 MPa, and deflection capacity of 2.9–5.3 mm, depending on the number of printed layers and testing direction. The following conclusions can be drawn:

(1) Regardless of the number of printed layers, the compressive strength of the 3D-printed DFRGC exhibited anisotropic behaviour, depending on the testing direction. The anisotropic behaviour is highly influenced by the orientation of fibres. In DFRGC-2L specimens (consisted of 2 layers), the highest compressive strength was obtained in perpendicular direction followed by lateral direction and longitudinal direction.
(2) The orientation of the fibres in the 3D-printed DFRGC specimens was found to be mainly parallel to the printing direction. Therefore, the fibres only helped in crack bridging upon action of compressive force in the perpendicular and lateral directions, but not in the longitudinal direction (parallel to the printing direction).
(3) The number of printed layers affected flexural performance of the 3D-printed DFRGC. The first-crack strength and modulus of rupture of the DFRGC-2L specimens (consisted of 2 layers) were higher than those of the DFRGC-1L specimens (consisted of only one layer). On the other hand, the deflection capacity of DFRGC-1L specimens was significantly higher than that of DFRGC-2L specimens.
(4) Regardless of the number of printed layers, the apparent porosity and bulk density of the 3D-printed DFRGCs were about 28% and 1500 kg/m^3. Such high porosity can be due to the inclusion of short polymeric fibres which results in a fibre-induced increase in entrapped air in the mixture, and thereby higher porosity of the mixture. Such low bulk density is due to the high apparent porosity of the 3D-printed DFRGCs.

Acknowledgement. The authors gratefully acknowledge the support by the Australian Research Council Linkage Infrastructure Grant LE170100168, Discovery Grant DP170103521 and Discovery Early Career Researcher Award DE180101587.

References

1. Nematollahi B, Xia M, Sanjayan J (2017) Current progress of 3D concrete printing technologies, ISARC. In: Proceedings of the international symposium on automation and robotics in construction. Vilnius Gediminas Technical University, Department of Construction Economics & Property
2. Nematollahi B, Sanjayan J, Shaikh FUA (2014) Comparative deflection hardening behavior of short fiber reinforced geopolymer composites. Constr Build Mater 70:54–64
3. Nematollahi B, Sanjayan J, Shaikh FUA (2014) Influence of the type of activator combinations on the deflection hardening behavior of geopolymer composites. In: SHCC3 3rd international RILEM conference on strain hardening cementitious composites, proceedings. RILEM Publications SARL 2014, pp 105–112
4. Nematollahi B, Sanjayan J, Shaikh FUA (2015) Synthesis of heat and ambient cured one-part geopolymer mixes with different grades of sodium silicate. Ceram Int 41(4):5696–5704
5. Sanjayan JG, Nematollahi B, Xia M, Marchment T (2018) Effect of surface moisture on inter-layer strength of 3D printed concrete. Constr Build Mater 172:468–475
6. Nematollahi B, Xia M, Bong SH, Sanjayan J (2018) Hardened properties of 3D printable 'one-part'geopolymer for construction applications. In: RILEM international conference on concrete and digital fabrication. Springer, pp 190–199
7. Bong SH, Nematollahi B, Nazari A, Xia M, Sanjayan J (2019) Method of optimisation for ambient temperature cured sustainable geopolymers for 3D printing construction applications. Materials 12(6):902
8. Bong SH, Nematollahi B, Nazari A, Xia M, Sanjayan JG (2018) Fresh and hardened properties of 3D printable geopolymer cured in ambient temperature. In: RILEM international conference on concrete and digital fabrication. Springer, pp 3–11
9. Nematollahi B, Xia M, Sanjayan J, Vijay P (2018) Effect of type of fiber on inter-layer bond and flexural strengths of extrusion-based 3D printed geopolymer. In: Materials science forum. Trans Tech Publications, pp 155–162
10. Marchment T, Xia M, Dodd E, Sanjayan J, Nematollahi B (2017) Effect of delay time on the mechanical properties of extrusion-based 3D printed concrete. In: Proceedings of the international symposium on automation and robotics in construction, Taipei, Taiwan
11. Nematollahi B, Xia M, Vijay P, Sanjayan JG (2019) Properties of extrusion-based 3D printable geopolymers for digital construction applications. In: 3D concrete printing technology. Elsevier, pp 371–388
12. Marchment T, Sanjayan JG, Nematollahi B, Xia M (2019) Interlayer strength of 3D printed concrete: influencing factors and method of enhancing. In: 3D concrete printing technology. Elsevier, pp 241–264
13. Ogura H, Nerella V, Mechtcherine V (2018) Developing and testing of strain-hardening cement-based composites (SHCC) in the context of 3D-printing. Materials 11(8):1375
14. Nematollahi B, Vijay P, Sanjayan J, Nazari A, Xia M, Naidu Nerella V, Mechtcherine V (2018) Effect of polypropylene fibre addition on properties of geopolymers made by 3D printing for digital construction. Materials 11(12):2352
15. Kim DJ, Naaman AE, El-Tawil S (2008) Comparative flexural behavior of four fiber reinforced cementitious composites. Cem Concr Compos 30(10):917–928
16. Kanda T, Li VC (2006) Practical design criteria for saturated pseudo strain hardening behavior in ECC. J Adv Concr Technol 4(1):59–72

Rheology of 3D Printable Lightweight Foam Concrete Incorporating Nano-Silica

Seung Cho(✉), Jacques Kruger, Algurnon van Rooyen, Stephan Zeranka, and Gideon van Zijl

Structural Department, Civil Engineering, Stellenbosch University, Stellenbosch, South Africa
scho@sun.ac.za

Abstract. Lightweight foam concrete (LWFC) has relatively high workability, or low static and dynamic shear resistance in the fresh state. It is also sensitive to applied pressure. These limitations present challenges for 3D printing of LWFC, through its pumping and extrusion, and bearing pressure of subsequent layers. The associated risks of 3D printing LWFC is therefore twofold, altering the LWFC properties during the printing process, and insufficient buildability. Inclusion of appropriate nanoparticles, with high surface area to volume ratio, is proposed here to influence the microstructure of the cementitious composite in the fresh and hardened state, in order to increase the shear resistance, and limit the impact of the 3D printing process on its density. Nano-SiO_2 (nS) particles with a diameter smaller than 30 nm and 99.5% purity are incorporated into LWFC at 2% and 3% by weight of cement. Rheometer results indicate increased shear resistance and thixotropic behavior. Conservative buildability prediction based on the thixotropic properties is validated by 3D printed nLWFC building height of a circular hollow column.

Keywords: Rheology · Thixotropy · Foam concrete · 3D printing · Nanomaterials

1 Introduction

A compelling case has been made for the construction of medium storey residential buildings from lightweight foam concrete, given the recent advancement of its mechanical properties and durability performance [1]. Given the advantages of digital construction (DC), in an industrialized construction context, 3D printing of LWFC is investigated here. 3DP requires less workable concrete for shape retention, while an appropriate flowability is required when agitated during pumping. The desirable microstructural flocculation, de-flocculation and re-flocculation processes of concrete are captured by the thixotropy. The flocculation and re-flocculation by a physical (coagulation) and chemical (hydration) process increase the viscosity, and de-flocculation by shear-thinning property of thixotropy decreases the viscosity during agitation. This shear stress history dependent phenomenon is, in particular, required

V. Mechtcherine et al. (Eds.): RheoCon 2019/SCC 2019, RILEM Bookseries 23, pp. 373–381, 2020.
https://doi.org/10.1007/978-3-030-22566-7_43

for 3D printable concrete. Nanoparticle incorporation is believed to modify the static and dynamic shear yield stress in a time scale relevant to 3D printing of concrete structures.

High fly ash (FA) content lightweight foam concrete (LWFC) was proposed and developed by Kearsley [2]. Water content governs the rheological behavior and stability of the entrapped foam [1, 3]. Too low water content causes degradation of the foam, while excess water causes segregation. For foam stability, appropriate water demand of the base mix, i.e. the mix before the foam is added, can be determined through slump flow tests (ASTM C230/C230 M) [4]. Kearsley [2] proposed the favourable base mix spread to be in the range 220 mm to 250 mm.

Once the foam is added to the base mix, LWFC is typically highly self-levelling, which presents a challenge for it to be 3D printed successfully. While the pumping part might be successful, given the low dynamic yield stress of fresh LWFC, shape retention once deposited, and subsequently bearing upper layers without significant deformation or plastic yield, requires sufficiently high shearing resistance shortly after deposition. 3D printability is postulated to be improved by the inclusion of nanoparticles, which have a high surface-to-volume ratio. This increases static shear yield strength by enhanced inter-particle attraction and increased packing density. After agitation, for instance, by 3D printing, the rate of re-flocculation, a physical process of rebuilding a favourable inter-particle arrangement, is increased by nanoparticles for the same reason. In this paper, SiO_2 nanoparticles with 99.5% purity and 150 $\pm$ 30 g/m^2 specific surface area are used at different dosages (2% and 3% by weight of cement) in a LWFC mix, to study their influence on 3D printability.

Kruger [5] recently presented an analytical buildability model for 3DP of concrete based on a lower bound theorem considering material failure according to a Mohr-Coulomb criterion. The model predicts the maximum number of layers that can be 3D printed before plastic shear flow occurs and causes collapse. The model is in a function of the geometry of the printed filament, printing speed, thixotropic parameters R_{thix} (re-flocculation rate) and A_{thix} (structuration rate) which describe the evolution of dynamic and static yield stress, τ_D and $\tau_S(t)$ shown in Fig. 1. The bi-linear thixotropy model amends the linear proposed by Roussel [6]. The buildability model compares the gravity of upper layers with the shear resistance evolution of the critical layer. Once the strength is exceeded by the weight of the upper layers, collapse is considered to be imminent.

In this paper, 3D printability and buildability of LWFC with and without small dosages of $nSiO_2$ are studied.

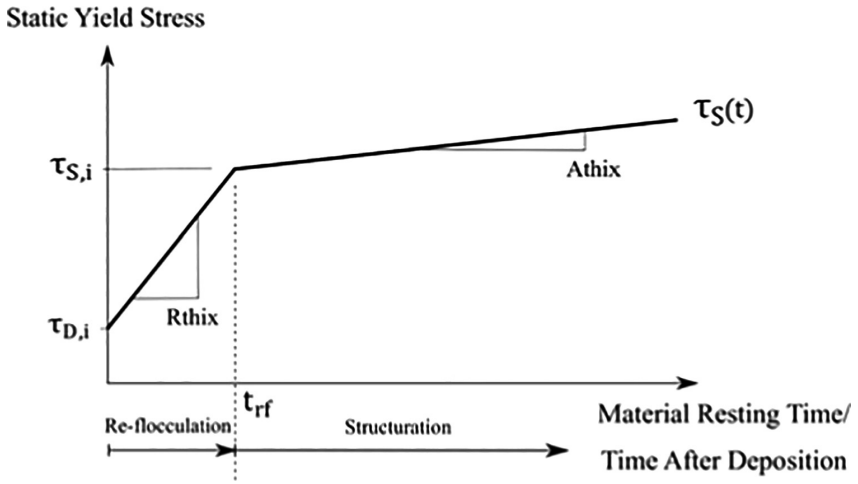

Fig. 1. Shear yield stress development model with a function of time [7].

2 Experimental Procedures

2.1 Material Mix Design

The mix constituents of LWFC in Table 1 are adapted from [1, 3]. To enhance thixotropy for viable 3D printing, SiO_2 nanoparticles with 99.5% purity and 150 ± 30 g/m^2 specific surface area, are added at dosages of 2% and 3% (of cement mass). To ensure foam stability, slump flow tests as proposed by [2] are performed according to ASTM C230/C230 M [4]. The initial setting times of the LWFC present upper limits to the printing time scale. Here, the Vicat penetration testing method (SANS 50196-3) [8] is used in a climate-controlled room at 23 ± 2 °C and 65 ± 5% RH.

Table 1. Mix composition of LWFC.

Constituents	Type	Mass (kg)	Adjusted mix (kg)*
Cement (SANS 50197-1:2013) [9]	CEM II 52.5 N	506.2	524.8
Fly ash (SANS 50450-1:2014) [10]	Class S	506.2	524.8
Water		369.6	330.6
Fibres	Polypropylene	4.095	4.095
Foam		18.00	19.80
Nano SiO_2	20–30 nm particle size	2, 3% by cement mass	2% by cement mass

*Adjusted mix to reduce total water content, denoted *2% $nSiO_2$ new*

2.2 Rheology Testing

The rheological parameters are characterised with a rotational cylinder type rheometer, RHM-3005/3009, developed by the Germann Instruments ICAR (Fig. 2). The 60 s

stress growth test at 0.124 s^{-1} shear rate as per Fig. 1b is performed to record the static and dynamic yield stress after different resting periods, including 0 s, 10 s, 20 s, 30 s, 60 s, 120 s, and up to an hour, or a reasonable fraction of the initial setting time.

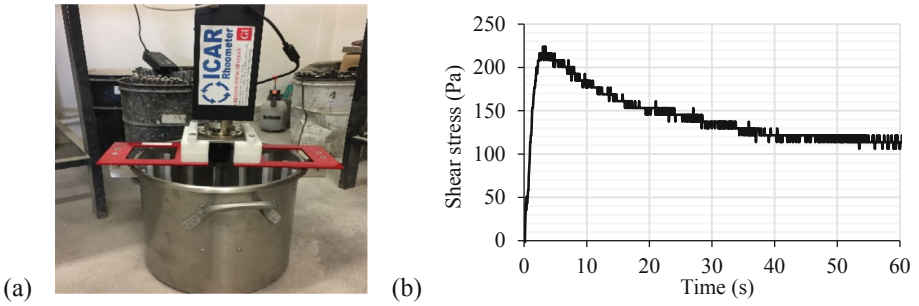

Fig. 2. (a) ICAR rheometer setup and (b) typical stress growth test result showing the static yield stress at the peak and the dynamic yield stress at the post-peak plateau.

By plotting the recorded static and dynamic yield stresses after different resting time intervals, the short-term (R_{thix}) and longer-term (A_{thix}) shear strength evolution model of thixotropy developed by Kruger [7] (Fig. 1) is obtained.

2.3 3D Printing Validation

To validate 3D printability of LWFC, the reference and rheologically modified LWFC is 3D printed with an industrial-grade gantry type 3D printer of roughly 1 m^3 build volume at Stellenbosch University. Using a 25 mm diameter circular nozzle, a 250 mm diameter circular hollow column is printed until plastic flow, and the number of layers recorded. Print parameters are summarised in Table 2.

Table 2. Summarised 3D print parameters.

Print parameter	Value
Layer height (h)	10 mm
Printed layer width (w)	32 mm
Path length per layer (l)	785 mm
Printing speed (v)	40 mm/s
Aspect ratio (h/w)	0.33

3 Experimental Results

3.1 Fresh State Property Measurements

The flow table spread and initial setting times are summarised in Table 3, showing that the addition of $nSiO_2$ reduces the slump flow diameter and initial setting time of LWFC. This is accredited to the high surface area-to-volume ratio of the nanoparticles [11].

Table 3. Slump flow and initial set results.

Base mix	d_1 (mm)	d_2 (mm)	d_{ave} (mm)	$t_{initial\ set}$ (min)
0% $nSiO_2$	239	238	238.5	570
2% $nSiO_2$	233	230	231.5	390
3% $nSiO_2$	228	229	228.5	420
2% $nSiO_2$ new	165	166	165.5	Not recorded

Stress growth rheometer test results are shown in Fig. 3. Both the static and dynamic yield stresses are significantly increased by the $nSiO_2$. The static and dynamic yield stresses are 78.02 Pa and 61.63 Pa for the mix without $nSiO_2$, and increase to 224.2 Pa and 120.0 Pa for 2%, and 386.2 and 291.6 for 3% $nSiO_2$. Despite the 187% and 208% improvement in static shear strength for 2% and 3% $nSiO_2$ respectively, the mixes are still considered to be too flowable for 3D printing. Considering the high total water content of the mixes of 26.4% by mass and 37.0% by volume, an adjusted mix with 23.6% total water content by mass and 33.1% by volume was prepared and tested (see Tables 1 and 2, denoted *2% $nSiO_2$ new*). The static and dynamic yield stresses are increased to 1169.9 and 649.7 Pa respectively – Fig. 3b.

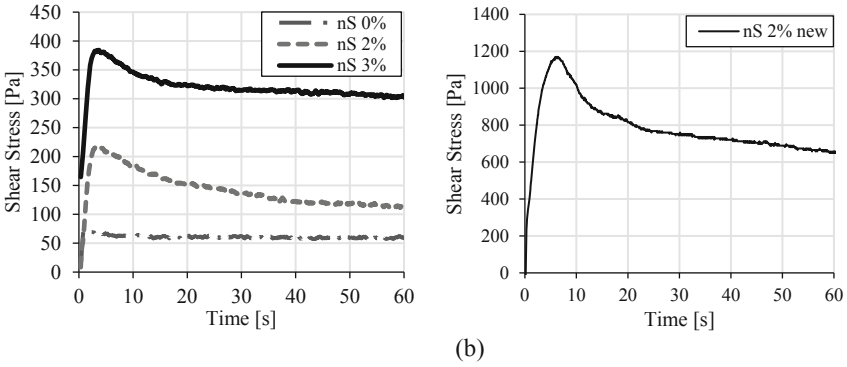

Fig. 3. Stress growth test results of (a) the initial test set and (b) the mix adjusted to have less total water content, denoted *2% $nSiO_2$ new*.

Apart from increased static and dynamic shear stresses, the rate of re-flocculation after agitation has stopped is of importance. Thereby, resistance is quickly recovered after 3D printing, in order to bear the weight of subsequent layers. For this reason, the stress growth tests are repeated after various waiting times after agitation, and the results summarised in Table 4. In Fig. 4, full stress-growth evolution graphs are plotted for a subset of the tests summarized in Table 4. The results in Fig. 4a show little or no strength recovery with increased resting time. Note that plotting the static yield stresses in Table 4 as a function of resting time should produce the bilinear response shown in Fig. 1, as proposed by Kruger [7], for each mix. However, negative Rthix and Athix gradients are obtained from the data in Table 4, for the original and adjusted (*2% SiO_2 new*) mixes.

In analyzing this unusual result, close inspection of the rheometer tests revealed that the highly adhesive LWFC tends to stick to the vane blades. Also, the sheared zone along the vane circular path in the rheometer cylinder does not recover during the waiting time before the next stress growth curve test is performed. Both these phenomena may lead to incorrect results, whereby little or no shear resistance is met along the shearing circumference, and the measured torque is dominated by the inertia of the LWFC within the circumference adhered to the vane blades, as illustrated in Fig. 4c.

To test this postulation, two stress growth tests were repeated for waiting periods of 30 and 60 min respectively. Instead of leaving the vane undisturbed during the resting period within the rheometer, the vane was removed from the container to scrape off the adhering LWFC, and subsequently lightly tamp the LWFC mix in the container, before returning the vane and repeating the test immediately, for both 30 and 60 min rest periods. These results are shown in Fig. 4b. Also shown on the same graph, are the originally measured stress-growth curves without the intervention to remove the adhered material. Significantly higher static and dynamic yield stresses are found for the adjusted stress-growth test method. Execution of the full series of tests with the adjusted test method is underway, but not completed in time for this publication.

Table 4. Static and dynamic yield stress (in brackets). All units are in Pa.

Intervals (sec)	0	10	30	60	120	1800	3600
0% $nSiO_2$	78 (46.5)	70.1 (46.5)	60.6 (43.5)	50.8 (42.2)	63.6 (39.9)	64.0 (32.5)	78.8 (47.3)
2% $nSiO_2$	224.2 (105.9)	113.8 (82.3)	98.1 (86.0)	98.1 (82.0)	98.1 (74.4)	105.9 (82.3)	121.7 (90.2)
3% $nSiO_2$	386.2 (291.6)	299.5 (252.2)	260.1 (228.6)	244.3 (220.7)	244.3 (220.7)	252.2 (228.6)	299.5 (236.5)
2% $nSiO_2$ new	1169.9 (649.7)	347.1 (228.9)	232.3 (200.8)	213.6 (189.9)	197.2 (173.5)	270.34 (230.9)	458.2 (355.7)

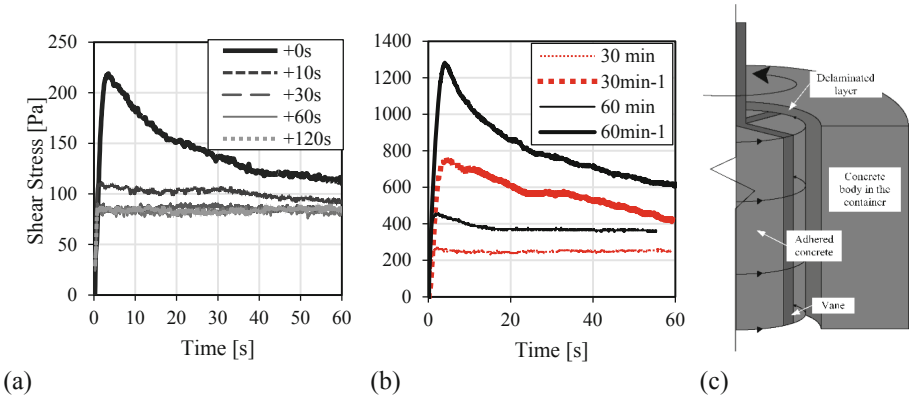

Fig. 4. Stress growth curves (a) showing slight re-building at different waiting time intervals, and (b) significant re-building at two-time intervals with an adapted rheometer test procedure. (c) Illustration of the adherence of LWFC to the vane blades, and a delaminated shear plane, leading to erroneous rheometer test results.

3.2 3D Printing Validation

The density alteration through printing is recorded before and after the printing process. The average wet densities changed from 1435.2 kg/m^3 and 1445.8 kg/m^3 respectively for 2% $nSiO_2$ and 3% $nSiO_2$, to 1455.7 kg/m^3 and 1461.0 kg/m^3 after the printing. Thus, the density alteration is insignificant, at less than 1.5%. However, the density of the *2% $nSiO_2$ new* mix was 1648.1 kg/m^3 before and 1720.3 kg/m^3 after printing. This indicates that the lower slump flow (see Table 3) for this mix indeed led to the destabilisation of the foam, and increased density. While the density can still be accepted as representing a LWFC, it exceeds the target wet density for this study. Continued efforts to optimise the LWFC to retain foam stability while achieving printability, are underway.

Based on the measured print parameters summarised in Table 2 and the static and dynamic yield strength, the maximum 3D printable height is predicted to be 3 and 6 layers for 2% and 3% $nSiO_2$ respectively. As shown in Fig. 5, 4 and 6 layers for the 2% and 3% $nSiO_2$ LWFC mixes respectively could be 3D printed at the said printer settings, before plastic yield occurred of the bottom layer.

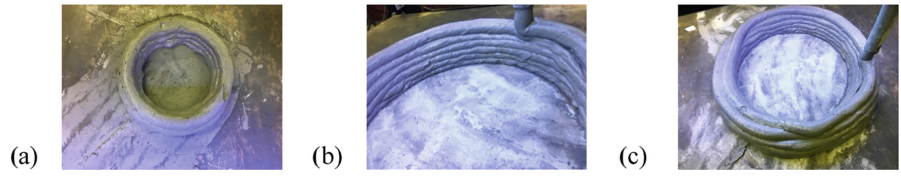

Fig. 5. (a) 2% $nSiO_2$ LWFC 3D printing validation with 4 successful layers, (b) 3% $nSiO_2$ LWFC 3D printing with 6 successful layers and (c) global failure of the printed wall due to plastic yielding, causes print path alteration.

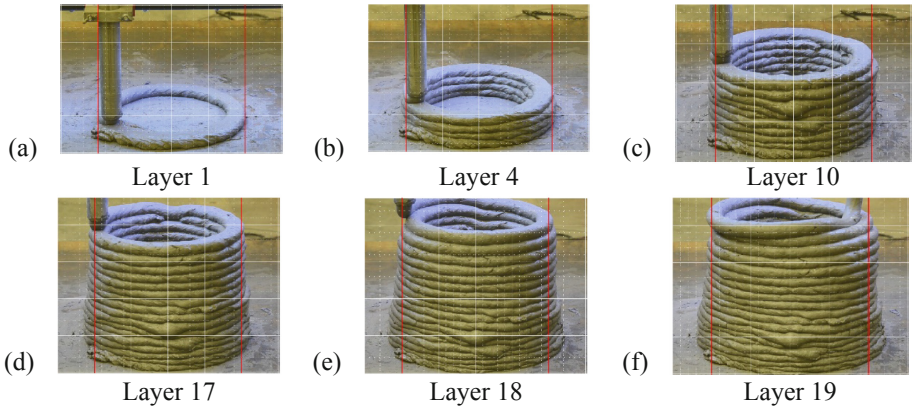

Fig. 6. (a)–(c) new 2% $nSiO_2$ 3D printing validation process and (d)–(f) gradual failure.

The *2% $nSiO_2$ new* LWFC mix, noted to be of higher density in the previous section, is predicted to be stable for up to twelve 3D printed layers with the said print settings and based on its rheological properties. Figure 6 shows the 3D printing progress. Significant deformation radially and axially is observed in Fig. 6d. Layer 17, which is considered to be the onset of plastic yield. Note that printing irregularities observed in the 5th and 8th layers are due to stoppage of the nozzle at those positions, leading to excess material deposition.

4 Conclusion and Future Work

This paper reports results of a study on the fresh properties of LWFC, and their improvement by the inclusion of nanoparticles, in order to improve 3D printability and buildability. The following conclusions are drawn:

- Improved rheological behaviour is achieved by the inclusion of small quantities of nano SiO_2. This is most clearly demonstrated through stress growth rheometer test results, showing significant increased static and dynamic yield stresses.
- Re-flocculation, or rebuilding of LWFC after agitation appears to be improved by the addition of small quantities of $nSiO_2$. This conclusion is based on limited test results, after modifying the rheometer test procedure to compensate for the highly adhesive nature of LWFC. To confirm this result, a full series of rheometer stress growth tests after various, increasing rest time periods must be performed, using the adapted test procedure. As an alternative, a different rheometer and vane are currently under investigation for better suitability to rheometer testing of LWFC.
- Reduced total water content in LWFC appears to improve thixotropy. However, the stability of foam in the more viscous base mix was compromised, and led to an increased wet density. Optimisation of the water content and foam stability in LWFC are subject to continued investigation.
- 3D printed cylinders validated the improved buildability of LWFC containing $nSiO_2$. More layers could be 3D printed at a fixed set of 3D printer parameters with LWFC containing $nSiO_2$ than the reference LWFC without nanoparticles. For the modified LWFC mix with lower total water content and 2% $nSiO_2$, a significantly higher cylinder (17 layers versus 6 layers) could be 3D printed. Distinction between the increased density and reduced water content as mechanisms of the significantly improved buildability remains to be investigated.

References

1. Dunn TPA, van Zijl GPAG, van Rooyen AS (2018) Investigating a reinforced lightweight foamed concrete walling system for low-rise residential buildings in moderate seismic regions. J Build Eng 10:663–670
2. Kearsley EP, Mostert D (2005) Designing mix composition of foamed concrete with high fly ash contents. In: Proceedings of the international conference on the use of foamed concrete in construction

3. de Villiers J (2015) Bond behaviour of deformed steel reinforcement in lightweight foamed concrete, Master thesis, Stellenbosch University
4. ASTM C230/C230 M:2014 (2014) Standard specification for flow table for use in tests of hydraulic cement
5. Kruger J, Zeranka S, van Zijl G (2019) 3D concrete printing: a lower bound analytical model for buildability performance quantification. Autom constr 106:102904. https://doi.org/10.1016/j.autcon.2019.102904
6. Roussel N (2006) A thixotropy model for fresh fluid concretes: theory, validation and applications. Cem Concr Res 36:1797–1806
7. Kruger J, Zeranka S, van Zijl G (2019) An ab initio approach for thixotropy characterisation of (nanoparticle-infused) 3D printable concrete. Constr Build Mater 224:372–386. https://doi.org/10.1016/j.conbuildmat.2019.07.078
8. SANS 50196-3:2006 (2006) Methods of testing cement. Part 3: determination of setting times and soundness
9. SANS 50197-1:2013 (2013) Cement. Part 1: composition, specifications and conformity criteria for common cements
10. SANS 50450-1:2014 (2014) Fly ash for concrete. Part 1: definition, specifications and conformity criteria
11. Paul SC, van Rooyen AS, van Zijl GPAG, Petrik LF (2018) A review of nanoparticles in cement-based materials. Constr Build Mater 189:1019–1034

Study on the Influence of Accelerators on the Hydration of Portland Cement and Their Applicability in 3D Printing

Tobias Dorn(✉), Tamino Hirsch, and Dietmar Stephan

Building Materials and Construction Chemistry, Technische Universität Berlin, Berlin, Germany
t.dorn@tu-berlin.de

Abstract. As extrusion based additive manufacturing (AM) has the potential of becoming the largest evolution in the construction industry in the 21st century, the control of early cement hydration becomes more and more important. This study focuses on the control of the compressive strength development of a CEM I 52.5R via the addition of different dosages of K_2CO_3, Na_2CO_3, $Ca(NO_3)_2$ and Triethanolamine (TEA) which all act as accelerators in cement hydration. Further, the influence of the above-mentioned substances on the hydration products formed during the first 24 h of hydration and their applicability in extrusion-based 3D printing processes was examined. The initial and final setting time as well as the compressive strength after 1, 2, 7 and 28 d were tested. The formation of hydration products during the first 24 h was studied using continuous in-situ XRD and calorimetric measurements. The early compressive strength development of the accelerated cement was tested, using a newly developed measuring device, starting at 20 min after the initial hydration. It was shown, that by adding the above-mentioned accelerators the initial setting time and the compressive strength development of the cement paste can be precisely adapted to the printing process. It could further be shown that the used accelerators strongly influence the hydration processes of the cement pastes and the crystallinity of some hydration products.

Keywords: Additive manufacturing · Cement hydration · Acceleration

1 Introduction

AM describes a process in which a component is built in a layer-wise fashion, fully automatically and directly from a digital model. In construction such a process bears several potential advantages, e.g. a higher degree of design freedom. As the focus in the development of 3D printing in construction lies on the development of extrusion-based processes [1], the development of printable mortars, of which the main characteristics have been defined by Lim et al. [2], is of great importance. In order to achieve a printable material, the printability, defined as the ease and reliability of depositing material through a deposition device and the buildability, defined as the resistance of deposited wet material to deformation under load, must be optimized. These material parameters are competing factors in that a high printability reduces the buildability of

V. Mechtcherine et al. (Eds.): RheoCon 2019/SCC 2019, RILEM Bookseries 23, pp. 382–390, 2020.
https://doi.org/10.1007/978-3-030-22566-7_44

the printed material [3]. The introduction of an accelerator into the mortar shortly before the extrusion might make it possible to combine a good printability with a fast structural buildup of the material after deposition. Thus a thorough understanding of the effects of accelerating admixtures on the early hydration of ordinary Portland cement is required in regard of the development of printable materials. In this study, the influence of TEA, $Ca(NO_3)_2$, K_2CO_3 and Na_2CO_3, on the setting and hardening behavior as well as the compressive strength development was tested. Further, the additives mentioned above have been studied in regard to their influence on the hydration process and in regard to their influence on the hydration products formed within the first 24 h of hydration.

2 Experimental

2.1 Materials

A CEM I 52,5 R (ft), produced by Opterra, was used in this study. The chemical composition of the cement was determined by X-Ray fluorescence (XRF) and is presented in Table 1. The chemical admixture specifications are listed in Table 2.

Table 1. Composition of CEM I 52.5 R (ft) determined by XRF.

	Al_2O_3	CaO	Fe_2O_3	K_2O	MgO	MnO	Na_2O	P_2O_5	SiO_2	SO_3	TiO_2	LOI	Sum
wt.%	4.9	62.5	3	1.2	2.2	0.1	0.3	0.1	19.2	3.3	0.2	2.5	99.1

Table 2. Specifications of the used admixtures.

Admixture	Purity (wt.%)	Producer	Evap. water (wt.%)
TEA	≥ 95	VWR chemicals	–
$Ca(NO_3)_2 * 4\ H_2O$	≥ 97	Alfa Aesar	31.4
K_2CO_3	≥ 99	VWR chemicals	0.8
Na_2CO_3	≥ 99	Roth	0.9

2.2 Cement Paste and Mortar Preparation

Deionized water has been used in all experiments. The evaporable water of the admixtures was determined by drying to mass constancy at 110 °C (Table 2) and was subtracted from the mixing water. For the standardized testing of the cement water requirement, the initial and final setting time and for the testing of the early development of compressive strength using the multipurpose incremental loading device (MILD) [4], the cement paste was prepared according to [5]. For XRD and isothermal calorimetry experiments, the cement pastes were prepared with a water-cement ratio (w/c) of 0.33 which equals the water requirement of the cement. For these experiments, the cement pastes were prepared using a vibration mixer on which all samples were mixed through intense vibration for 60 s.

2.3 Testing of the Cement Water Requirement and the Initial and Final Setting Time

The cement water requirement and the initial and final setting time of the reference sample was tested according to [5]. The initial and final setting time was further determined in dependence of different admixture concentrations using the w/c of 0.33 determined for the reference sample. The admixtures were added to the cement together with the mixing water in which they were dissolved prior to the start of the experiment.

2.4 Testing of the Early Age Compressive Strength Development

The early compressive strength development of the reference sample and four accelerated samples was tested using the MILD which uses a cantilever to precisely measure the force which is applied to the sample by a piston [4]. Before the measurements the cement paste was filled in cubic molds with an edge length of 2 cm, compacted for 60 s and cautiously removed from the molds. The MILD recorded the force which was required to compress each cube to 70% of its original edge length while compressing the samples with a velocity of 1 mm/s. The testing started at 20 min after the initial contact with water. Measurements were conducted every three minutes.

2.5 Testing of the Later Age Compressive Strength Development

The compressive strength at 1 d, 2 d, 7 d and 28 d of the reference and the accelerated samples was tested based on [6].

2.6 In-Situ X-Ray Diffraction (XRD)

All in-situ XRD measurements were performed on a PANalytical Empyrean in Bragg-Brentano geometry equipped with a temperature-controlled sample stage set to 22 °C, using CuK_{α}-radiation. A Kapton film (gauge 7.5 µm) was used to protect the samples from surface drying and atmospheric CO_2.

2.7 Isothermal Conduction Calorimetry

The heat of hydration of all samples was determined using an isothermal heat flow calorimeter (MC-Cal 100P, C3 Prozess- und Analysetechnik) at a measurement temperature of 20 °C. For each sample, 1.32 g of cement and 0.44 g of water were used. The corresponding amount of accelerator was dissolved in the mixing water 24 h before the measurement started. After the paste preparation, the plastic flasks in which the measurement took place were sealed and placed into the calorimeter. The heat of hydration was recorded every 60 s for 168 h. The onset of the acceleration period was defined as discussed by von Daake and Stephan [7]. In the case of the sample accelerated with $Ca(NO_3)_2$ the linear regression of the acceleration period was made between 2.5 and 3.5 mW/g as the minimum heat flow during the induction period lies above 2 mW/g.

3 Results and Discussion

3.1 Initial and Final Setting Time

The dependence of the initial and final setting time on the concentrations of the different tested accelerators is depicted in Fig. 1. At dosages below 0.02 wt.%, TEA acts as a retarder and at dosages between 0.02 wt.% and 1 wt.% as a setting accelerator. An excess amount of Na_2CO_3, K_2CO_3 and $Ca(NO_3)_2$ does not further accelerate the cement hydration towards the initial setting. As with the concentrations of 4 wt.% K_2CO_3 and Na_2CO_3, 2.33 wt.% $Ca(NO_3)_2$ and 0.1 and 1 wt.% TEA early initial setting is achieved these concentrations have been selected for further analysis of their mechanisms of action.

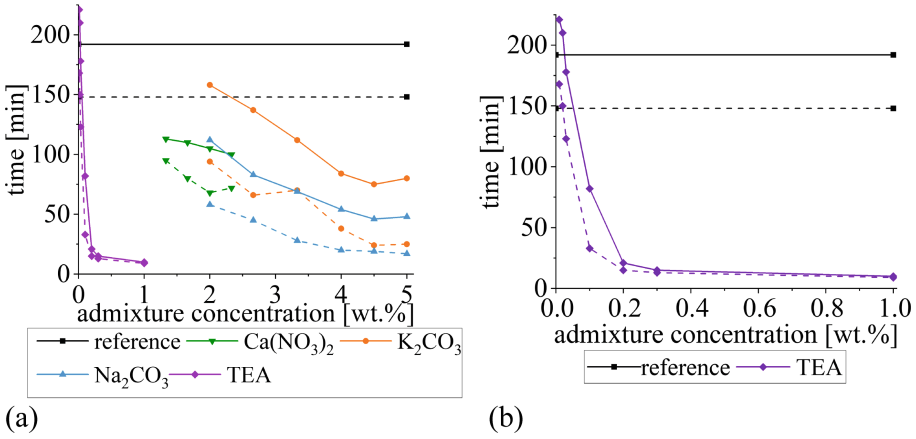

Fig. 1. (a) Vicat needle test results dependent on admixture concentration; (b) Detailed view of the Vicat needle test results of the samples accelerated with TEA; dashed line: initial setting; solid line: final setting.

3.2 Heat of Hydration, Heat Flux and Crystalline Phase Development

The heat of hydration (Fig. 2), reveals that within the first 60 min of hydration all accelerated samples evolve more heat than the reference sample. Thus, a significant influence of the accelerators on the mechanism of early hydration, which is dominated by the formation of ettringite as the main hydrate phase of the initial reaction [8], can be deducted from these results. After one week, the amount of evolved hydration heat is significantly less for the samples to which carbonates and TEA in the dosage of 1 wt.% have been added (Fig. 2).

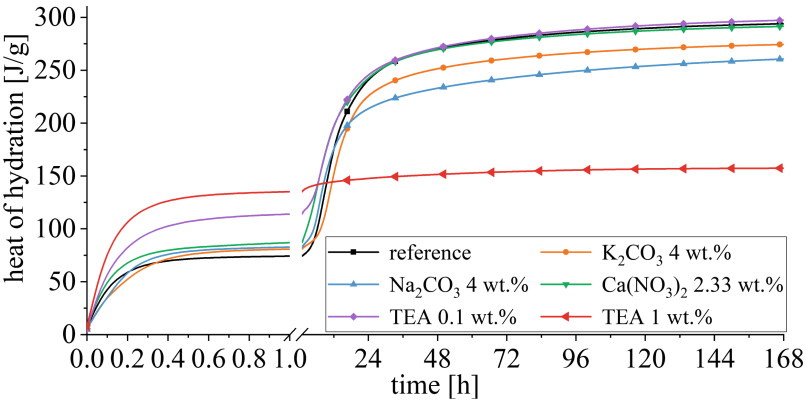

Fig. 2. Hydration heat developed during the first 168 h of hydration.

In the reference sample, the onset of the acceleration period lies at 2.7 h (Table 3) and the reduction of the 024 alite reflex intensity is starting at approximately 6 h of hydration (Fig. 3A) with the maximum rate of its reduction being in good correspondence to the second heat flow maximum of calorimetry. At the first decline of the alite 024 reflex intensity, the 001 CH reflex is starting to develop. This matches the mechanism of cement hydration explained by Bullard et al. [8] who state that after a period of slow reaction fast hydration of C_3S and the formation of C-S-H phases are occurring. In the system analyzed in the presented study this mechanism of hydration seems to be altered by the addition of the accelerating admixtures. TEA at the dosage of 0.1 wt.% leads to an onset of the acceleration period at 2.5 h (Table 3), promotes the formation of ettringite (Fig. 3E), and leads to a higher evolution of hydration heat within the first 60 min of hydration as discussed above. It can thus be concluded that TEA has an activating effect on the hydration of C_3A contained in the analyzed cement. Comparable results have already been found by Ramachandran [9]. Further, it can be stated that 0.1 wt.% of TEA does not significantly delay the alite hydration in the analyzed sample. Concerning the reduced amount of portlandite accessible to XRD, Yan-Rong et al. [10] state that this is a result of a TEA-Ca^{2+} complexation, which introduces TEA into the CH crystallization process, alters the CH morphology and reduces the content of crystalline CH. For the sample accelerated with 1 wt.% TEA the second maximum of heat flux which is commonly associated with the hydration of alite, the formation of C-S-H phases and CH [8] could not be detected within 168 h of hydration. In Fig. 3F the intensity of the 024 alite reflex is staying on a constant level indicating that the amount of unhydrated alite is not decreasing within 24 h of hydration. After 5 min of hydration, the time it takes to prepare the sample and start the measurement, a significant amount of ettringite has already be formed. No further mineral formation or dissolution seems to occur. An acceleration of the initial reaction by TEA and long retardation of the second heat flux maximum is well known in the literature. According to [9] and [11], the retarding effect of TEA at high dosages on the C_3S hydration can be explained with a barrier-hypotheses of the calcium aluminate hydrates formed at the beginning of hydration, inhibiting the hydration of C_3S. As in

this study, a second heat flux maximum could not be detected within the first week of hydration it appears that TEA supressed any further hydration of alite and belite in this period of time. The addition of $Ca(NO_3)_2$ to the cement paste leads to a higher reaction rate, during the period of slow reaction (Fig. 3B). This implies an elevated activity of hydration and precipitation processes in that stage, compared to the reference sample. Further an early onset of the acceleration period (Table 3), and in good correspondence to that, an early 024 alite reflex intensity reduction and 001 portlandite as wells as 010 ettringite reflex intensity increase was observed.

Table 3. Onset of the acceleration period determined from the recorded heatflux according to [7].

Accelerator	Onset acceleration period (h)
Reference sample	2.7
$Ca(NO_3)_2$	2.3
Na_2CO_3	2.8
K_2CO_3	5.2
TEA (0.1 wt.%)	2.5
TEA (1 wt.%)	–

The mechanism responsible for the accelerating effect of $Ca(NO_3)_2$ could not be deducted from the presented results but the findings are well in line with results presented by Abdelrazig et al. [12]. They state that an early portlandite and gypsum formation result from a change in the solubility product criteria caused by the Ca^{2+} ions added to the hydrating cement by the dissolved $Ca(NO_3)_2$.

For the samples accelerated with Na_2CO_3 and K_2CO_3 even though the heat of hydration which evolved within the first 30 min of hydration is slightly elevated compared to the reference sample (Fig. 2), no ettringite could be detected by XRD in the Na_2CO_3 accelerated sample and only a small amount of ettringite could be detected in the K_2CO_3 accelerated sample. Thus, the addition of Na_2CO_3 and K_2CO_3 seems to alter the hydration process of the tested cement towards another hydration product. The addition of Na_2CO_3 and K_2CO_3 reduced the amount of CH accessible to XRD. Results from XRD measurements indicate, that during the first 24 h of hydration $CaCO_3$ has crystallized.

Further, the two phases monocarboaluminate (Mc) and hemicarboaluminate (Hc) could be detected. The detection of $CaCO_3$ is in line with findings from Janotka et al. [13], who states that an excess of CO_3^{2-} ions in the paste mixture, as a consequence of Na_2CO_3 addition, renders C-S-H phases and CH unstable and lets them quickly transform to $CaCO_3$. The detection of Ms and Hc also corresponds to results in the literature [14, 15]. Matschei et al. state, that carbonate AFm phases are thermodynamically more stable than hydroxy or sulfate phases which explains the occurrence of Hc and Mc in the presence of CO_3^{2-} ions. Further research will be necessary to explain the strongly reduced ettringite formation in the presence of K_2CO_3 and the missing ettringite formation in the presence of Na_2CO_3 respectively.

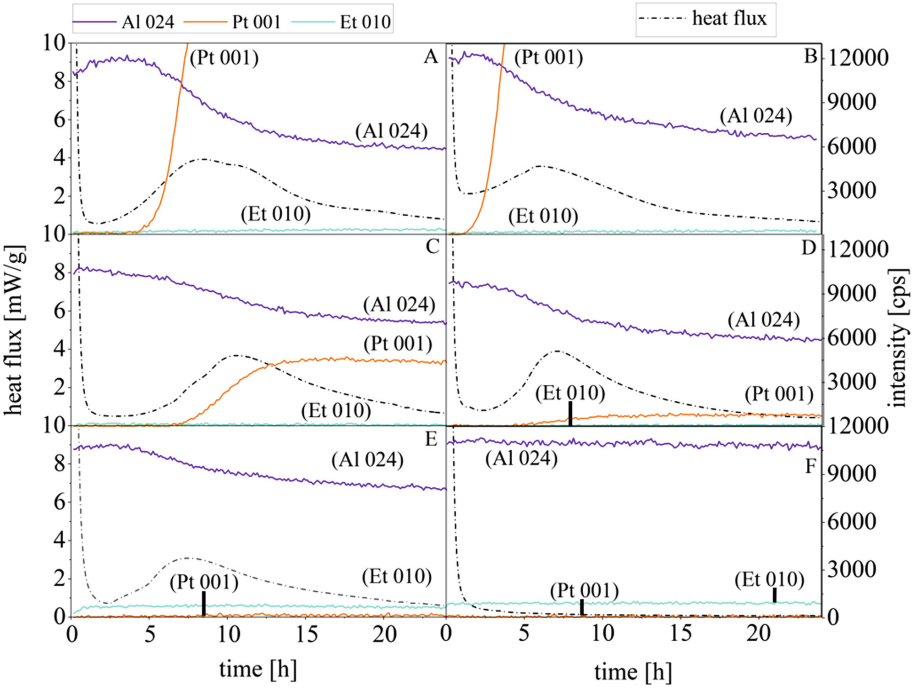

Fig. 3. Evolution of the X-ray reflex intensities of alite (Al) 024, portlandite (Pt) 001 and ettringite (Et) 010. Heat flux from isothermal calorimetry during the first 24 h of hydration. A - reference, B - $Ca(NO_3)_2$ 2.33 wt.%, C - K_2CO_3 4 wt.%, D - Na_2CO_3 4 wt.%, E - TEA 0.1 wt. %, F - TEA 1 wt.%.

3.3 Compressive Strength Development

Compared to the reference sample, high early age compressive strengths can be achieved with all tested accelerating admixtures (Fig. 4a). The effect of the accelerating admixtures on the later age compressive strength development starting at 1 d is illustrated in Fig. 4b. At 1 d, all added accelerators have a decreasing effect on the compressive strength. After 2 d $Ca(NO_3)_2$ enhances the compressive strength and after 28 d the sample accelerated with 0.1 wt.% TEA reaches the same compressive strength as the reference sample. For both tested carbonates and the sample accelerated with 1 wt.% TEA norm compliant mortar prisms could not be achieved as the mortar started setting while being filled into the molds.

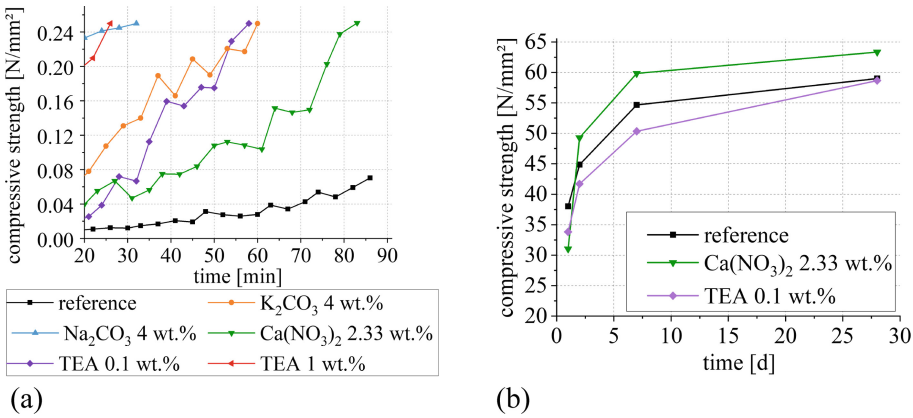

Fig. 4. (a) Development of the early age compressive strength determined with the MILD; (b) Compressive strength development according to [6].

4 Conclusions

The results presented in this study are limited to the analysis of the hydration mechanism of one cement in the presence of different accelerating admixtures. In the tested cement, TEA at the dosage of 1 wt.% accelerates the formation of ettringite during the first minutes of hydration and seems to inhibit any further hydration reaction afterwards. At the dosage of 0.1 wt.%, TEA negatively affects the crystallinity of CH, accelerates the early hydration, contributes actively to the early compressive strength development within the first 80 min of hydration and retards the compressive strength development at later ages. $Ca(NO_3)_2$ at the dosage of 2.33 wt.% accelerates the dissolution of C_3S and the formation of portlandite implying an accelerated formation of C-S-H phases. Further it seems to accelerate the formation of ettringite and contributes to the early and later age compressive strength development. K_2CO_3 and Na_2CO_3 contribute to the formation of $CaCO_3$, Hc and Mc in the tested cement. This might result from the introduction of CO_3^{2-} ions into the hydrating cement paste. The addition of Na_2CO_3 and K_2CO_3 at the dosage of 4 wt.% strongly accelerates the setting time determined on a cement paste using the Vicat needle test and causes flash-setting in a mortar paste prepared according to [6]. K_2CO_3 delays the acceleration period and the hydration of alite. Further research using pure clinker phases will be required as to clarify the effect of the accelerating admixtures on each single clinker phase.

Acknowledgement. The authors acknowledge the German Federal Ministry of Education and Research for funding this work in the scope of project BauProAddi (FKZ: 03XP0122A).

References

1. Labonnote N, Rønnquist A, Manum B, Rüther P (2016) Additive construction: state-of-the-art, challenges and opportunities. Autom Constr 72:347–366
2. Lim S, Buswell R, Le TT, Wackrow R, Austin SA, Gibb AGF, Thorpe T (2011) Development of a viable concrete printing process. In: Proceedings of the 28th international symposium on automation and robotics in construction, (ISARC2011), Seoul, South Korea, 29th June–2nd July 2011, pp 665–670
3. Soltan DG, Li VC (2018) A self-reinforced cementitious composite for building-scale 3D printing. Cem Concr Compos 90:1–13
4. Pott U, Ehm C, Jakob C, Stephan D (2019) Investigation of the early cement hydration with a new penetration test, rheometry and in-situ XRD. In: 2nd international RILEM conference, rheology and processing of construction materials (RheoCon2), Dresden, Germany, 08th–11th September 2019
5. EN 196-3:2016 (2017) Methods of testing cement. Part 3: determination of setting times and soundness
6. EN 196-1:2016 (2016) Methods of testing cement. Part 1: determination of strength
7. von Daake H, Stephan D (2016) Setting of cement with controlled superplasticizer addition monitored by ultrasonic measurements and calorimetry. Cem Concr Compos 66:24–37
8. Bullard JW, Jennings HM, Livingston RA, Nonat A, Scherer GW, Schweitzer JS, Scrivener KL, Thomas JJ (2011) Mechanisms of cement hydration. Cem Concr Res 41:1208–1223
9. Ramachandran VS (1976) Hydration of cement—role of triethanolamine. Cem Concr Res 6:623–631
10. Yan-Rong Z, Xiang-Ming K, Zi-Chen L, Zhen-Bao L, Qing Z, Bi-Qin D, Feng X (2016) Influence of triethanolamine on the hydration product of portlandite in cement paste and the mechanism. Cem Concr Res 87:64–76
11. Jachiet M, Azéma N, Le Saoût G, Garcia-Diaz E, Kocaba V (2018) Influence of triethanolamine on cement pastes at early age of hydration. Adv Cem Res 30:159–171
12. Abdelrazig BEI, Bonner DG, Nowell DV, Dransfield JM, Egan PJ (1999) The solution chemistry and early hydration of ordinary portland cement pastes with and without admixtures. Thermochim Acta 340–341:417–430
13. Janotka I, Mojumdar SC (2007) Degree of hydration in cement paste and C_3A-sodium carbonate-water systems. J Therm Anal Cal 90:645–652
14. Kuzel H-J, Pöllmann H (1991) Hydration of C_3A in the presence of $Ca(OH)_2$, $CaSO_4{\cdot}2H_2O$ and $CaCO_3$. Cem Concr Res 21:885–895
15. Matschei T, Lothenbach B, Glasser FP (2007) The role of calcium carbonate in cement hydration. Cem Concr Res 37:551–558

Predication of Strength-Based Failure in Extrusion-Based 3D Concrete Printing

Roshan I. Jayathilakage(✉), Pathmanathan Rajeev, and Jay Sanjayan

Department of Civil and Construction Engineering,
Swinburne University of Technology, Melbourne, Australia
rjayathilakage@swin.edu.au

Abstract. Extrusion-based concrete 3D printing is an emerging construction technique to build the desired structure layer by layer without using any type of formwork. Hence, the printable concrete requires to achieve adequate strength to support the self-weight and subsequent layers in short period of time. This paper aims to identify the strength-based failure limits of 3D printing concrete through experimental and numerical procedure. The 3D Printing experiments were carried out to obtain the height of failure (i.e., number of printed layers before failure). The important rheological parameters of 3D printable concrete mixes were estimated experimentally and used in a numerical simulation as well as in theoretical equations to compare the results. The strength-based failure criterion for 3D printed object was developed and validated numerically using FLAC 3D (i.e., Fast Lagrangian Analysis of Continua). The time-dependent material behaviour was considered in the numerical analysis and the failure mode and the failure heights were modelled and compared with the experimental values. It was found that the experimental results and the numerical simulation results are comparable and the numerical simulation can be used as a reliable tool to decide the rheological parameters of 3D printing concrete for preventing the strength based failure.

Keywords: Concrete 3D printing · Rheology · Yield stress · Viscosity · Thixotropy

1 Introduction

3D concrete printing is an innovative and promising construction automation technology for manufacturing large-scale concrete structural elements without the use of formwork. Also, the 3D printing can be used to build geometrically complex shapes easily and precisely. The layer-based extrusion method is the commonly used printing method, which extrudes concrete layers to build large scale objects. The advantage of this method is that different sizes of particles as well as the additives like fibre can be included in the printing material [1]. Also, the smoothness of the constructed surfaces can be achieved adequately by constraining the extruded flow in vertical and horizontal directions to trowel surfaces.

Therefore, the concrete used in 3D printing should have special characteristics in order to cater the extrudability and buildability of layers and adequate stiffness to

V. Mechtcherine et al. (Eds.): RheoCon 2019/SCC 2019, RILEM Bookseries 23, pp. 391–399, 2020.
https://doi.org/10.1007/978-3-030-22566-7_45

support the above layers [2]. The printable concrete is expected to be flowable as self-compacting concrete or sprayed concrete during pumping. Therefore, the printable concrete can be conveyed effectively and efficiently through the pumps without any blockage. However, the printable concrete should have the ability to form layers without any significant deformation due to self-weight before setting after extrusion. Hence, the rheology of printable concrete plays a vital role, in order to develop concrete mixes that are easily flowable and extrudable during printing process and buildable after printing.

In this paper, experimental procedure was followed to print a circular structure layer by layer, using 3D printing concrete. The failure mode and the failure height were observed experimentally. The validation of the failure mode and the failure height were done using numerical simulation (FLAC 3D software). Time-dependent Mohr-Coulomb failure criterion was considered to model the material failure. Therefore, the time dependent cohesive stress and the time dependent elastic modulus were estimated experimentally. A non-conventional method was trialed to assess the time dependent elastic modulus values in the current study. The experimental results were compared with the numerical results and the available analytical models in literature.

1.1 Rheology of 3D Printing Concrete

Concrete mixes used in 3D printing concrete applications commonly considered as visco-plastic Bingham material where the flow only occurs when subject to a shear stress larger than a critical value, i.e., the yield stress (τ_y). After initiating the flow, the shear stress (τ) is proportional to the shear rate ($\dot{\gamma}$). The gradient of the shear stress vs. shear rate curve is the plastic viscosity value (μ) of the material. Simply, the Bingham model [3] gives the stress vs. shear rate behavior of material used in concrete 3D printing.

However, concrete is a thixotropic material where the yield stress of the material increase with the resting time after completion of the mixing. This phenomena is happening due to the buildup of an internal structure in the material as a result of flocculation process of cement particles [4]. The model developed by Perrot et al. [5] explains the evolution of yield stress, $\tau_y(t)$, with resting time, t, as in Eq. 1, where the parameter, A_{thix}, is the thixotropic build rate which assumed as a constant for a considered material. The τ_{y0} is the initial yield stress at zero resting time and t_c termed as the characteristic time which mainly used for curve fitting of experimental values with the model:

$$\tau_y(t) = A_{thix} \cdot t_c\left(e^{t/tc} - 1\right) + \tau_{y0} \tag{1}$$

The model shows a linear yield stress increase for low resting times and will increase exponentially for higher resting times with a smooth transition from linear to an exponential curve.

1.2 Buildability

After the extrusion process, the printed layer should sustain its own weight and have an initial yield stress to overcome the stress due to gravity. The bottom layer should sustain the gravity induced stresses of printed layers above. However, as mentioned earlier, the material yield stress increase with the resting time and this is an important characteristic in concrete which is useful in building the structure layer by layer.

When the layer by layer construction continues, the stresses induced in the bottom layers converts to extensional stresses and are dominant [6]. If the total build height of the structure is, H, the bottom layer induces should have a minimum yield stress of $\rho gH/\sqrt{3}$ (where g is gravity and ρ is density of concrete) [7]. The requirement for the A_{thix} (i.e., the rate of increase in yield stress) to prevent the strength-based failure, neglecting the initial yield stress can be written as $A_{thix} \geq \rho g\dot{H}/\sqrt{3}$, where $\dot{H}$ is the build rate of the structure. Simply, the yield stress after time 't' at the bottom layers should satisfy the following condition as in Eq. 2 to prevent the strength based failure:

$$\tau_y(t) \geq \rho g\dot{H}t/\sqrt{3} \tag{2}$$

The Eq. 2 is based mainly on the strength of the material and can predict the strength based failure. Depending on the layer width (δ) of the printed layer and the modulus of elasticity (E) of the material, a critical failure height (H_c) and a critical elastic modulus (E_c) can be defined as in [7], where the buckling failure is dominant if exceeds H_c, and material should have an elastic modulus higher than E_c to prevent buckling failure. The critical buckling failure height (H_c) and the critical elastic modulus (E_c) can be calculated using the Eqs. 3 and 4 respectively:

$$H_c = \left(2E\,\delta^2/3\rho g\right)^{1/3} \tag{3}$$

$$E_c = 3\rho g H^3/2\,\delta^2 \tag{4}$$

2 Experimental Work

In this study, experimental work was carried out to characterize the concrete material flow properties and to identify the failure models for 3D printed structures. Time-dependent yield stress and the time-dependent elastic modulus were evaluated using experimental procedure. Afterwards, 3D printing of circular hollow sections were performed until the failure occurred.

2.1 Material and Mix

A mix was prepared using general purpose cement according to AS3972 type I which is similar to ASTM C595/C595M. The sand used for the mix was graded sand with coarse aggregate which have 16/30 gradation (maximum particle size of 1.18 mm) and fine aggregate of 30/60 gradation (maximum particle size of 600 μm). The mix proportions used for the mix is shown in Table 1.

Table 1. Mix proportion (weight proportions as ratios of the cement weight).

Cement	Silica fume	Coarse sand	Fine sand	Total sand	Water	Superxplasticizer (ml/100 g of binder)	Retarders (ml/100 g of binder)
1	0.11	0.56	1.11	1.67	0.25	0.9	0.6

Initially, dry mixing was done for about 5 min. After adding water slow mixing was done up to 5 min, and high-speed mixing was done about 10 min after adding superplasticizers and retarders.

2.2 Measurement of Yield Stress Evolution with Time

Yield stress evolution was measured using a vane shear apparatus as in [8], according to the standard ASTM D4648/D4648M. Vane shear apparatus was originally used to measure the shear strength of clayey soils but, implemented in the current study to measure the yield stress of mixes as a cost effective measurement technique rather than implementing high cost rheometer measurements. The vane used has a height of 70 mm and a width of 90 mm.

Shear strength or yield stress measurements were taken for 15 min time intervals from 0 to 60 min.

2.3 Measurement of Elastic Modulus Evolution with Time

A different non-conventional approach was followed in the current study to achieve the elastic modulus variation with time. Rather than testing cylindrical samples, printed samples were tested in compression to get the stress-strain behavior, and to determine the elastic modulus. Printed samples which have similar dimensions to a printed layer (i.e., 10 mm thickness and 30 mm width and length) was used for the compression testing. In this study, as a start, no restrains were applied for the length of the sample. In future, different end restrictions and more accurate load measurements will be done.

Three compression test trials were done for three samples at the same time period to get the average values. Material preparation, extrusion and preparation of the desired sample took 15 min to complete after adding water to the mix. A very low displacement rate (0.5 mm/min) was applied for the samples. The test continued up to 2.5 mm vertical deformation of the sample (25% strain limit) result in 5 min to complete a single test. Therefore, the elastic modulus at 20 min and at more than 20 min time can only be considered. It is difficult to determine the elastic modulus experimentally at 0 min with the above conditions.

Finally, using the stress-strain plots, the elastic modulus will be calculated considering the 5% strain limit of the sample.

2.4 Mohr-Coulomb Failure Model Parameters for 3D Printable Concrete

Mohr-Coulomb parameters and the dilation angle can be found from the direct shear test method. A complete description of the direct shear test method and how to

implement it to measure the above mentioned parameters for 3D printing concrete was published by the authors elsewhere [9].

However, it should be mentioned that measuring the time dependent cohesion value is not practical using the direct shear test due to the extended time gap between mixing of the material and the shearing of the material. In the study [9], it was found that the cohesion stress is equivalent to the yield stress of the material. Therefore, the time dependent yield stress values obtained from the vane shear test were considered as the cohesion values of the mix.

2.5 3D Concrete Printing of Circular Section

A hollow cylindrical structure with 300 mm inner diameter was printed. Three trials were conducted to achieve an average failure height. A 30 mm circular nozzle was used for printing and the layer thickness was kept as 10 mm. A printing speed of 2244 mm/min was used, which gives a 0.42 min time gap between two consecutive layers.

3 Numerical Simulation for Layer by Layer Construction

FLAC 3D software [10] was used as the numerical simulation tool which uses Finite Difference Method (FDM) for analysis. For the numerical simulation of the printed layers, the stress–strain behavior of a layer before failure was considered. Therefore, the elastic modulus, E(t), of the fresh mix should be determined as an input parameter for the numerical simulation. In a study done previously [11], it was found that the elastic modulus of the fresh 3D printing material increase linearly with time. Hence, the time-dependent behavior of elastic modulus also was considered in the current study. In the same study [11], time-dependent linear Mohr-Coulomb failure criteria was considered as the failure criteria of the fresh material. It can be written as in Eq. 5 where c(t), σ_n and $\emptyset$ are cohesion, normal stress and the friction angle of the material respectively:

$$\tau_y(t) = c(t) + \sigma_n \tan \emptyset \tag{5}$$

The cohesion value was found as a time-dependent value, and the friction angle as a time-independent value from the study [11]. Therefore, time-dependent cohesive stresses and the friction angle value of the fresh material were considered as main input parameters for the model.

Poisson ratio (υ), density of the material (ρ) and the dilation angle (ψ) are also some input parameters for the numerical model which are time-independent [11].

The cylindrical-shell mesh in FLAC 3D was used to form primitive-based grid points and zones to model the printed layers [10]. Full circular section was considered for the modelling and the boundary condition for the bottom most face (contacting face with the print bed) was fixed in the model. The height of a layer kept as 10 mm as in the experiment and the initial width as 30 mm (i.e. equal to the nozzle sizes used). The time-dependent properties for each layer were input by a user-defined algorithm.

The FISH language, which specifically used in FLAC 3D software was used to write and input the required commands.

The Mohr-Coulomb failure criteria used in FLAC 3D is a composite Mohr-Coulomb criterion with tension cutoff. When implementing the Mohr-Coulomb failure criteria in FLAC 3D software, initial elastic stresses will be calculated using Hooke's law and using the total strain increments in the initial time steps. Principal stresses σ_1, σ_2 and σ_3 and the corresponding directions are then calculated. If the stresses σ_1, σ_2 and σ_3 $(\sigma_1 \leq \sigma_2 \leq \sigma_3)$ violates the composite yield criteria shown in Eqs. 6 and 7 given below, the shear yielding or tensile yielding may occur.

$$f^s = -\sigma_1 + \sigma_3 \frac{1+\sin\emptyset}{1-\sin\emptyset} - 2c\sqrt{\frac{1+\sin\emptyset}{1-\sin\emptyset}} \tag{6}$$

$$f^t = \sigma_3 - \sigma_t \tag{7}$$

In Eqs. 6 and 7, $f^s = 0$ is Mohr-Coulomb failure envelop and $f^t = 0$ is tensile failure envelop. σ_t in Eq. 7 is the tensile strength which have a maximum value ($\sigma_{t,max}$) of $c/\tan\emptyset$. Note that the compressive stresses will be considered as negative in the FLAC analysis. A graphical interpretation and a detailed description of the failure criteria can be found in FLAC 3D documentation [10]:

After deciding whether the principal stress points are in shear failure domain or in tensile failure domain, a set of different equations will be used to calculate the principal stresses in plastic state [10].

4 Results and Discussion

Figure 1(a) and (b) shows the vane shear test results and the results for elastic modulus variation with time respectively.

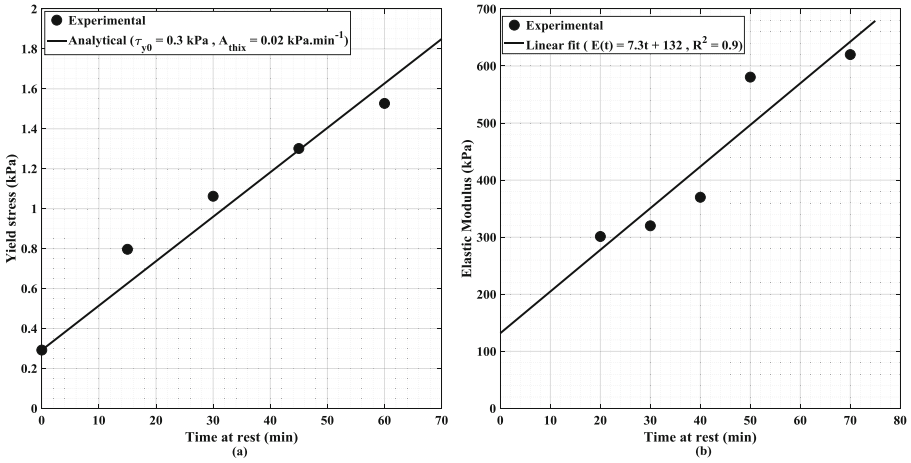

Fig. 1. (a) Vane shear test results (b) Elastic modulus variation with time.

It can be seen from the results in Fig. 1(a), that the initial yield stress of the material is 0.3 kPa which is a very low value compared with the mix used in [11]. This type of low yield stress material was selected in the study to enforce a strength-based failure rather than a buckling failure. This will be discussed in later sections.

As mentioned previously, the cohesion value is taken as equivalent to the shear yield stress values achieved from the vane shear test. From the direct shear test, it was found that the friction angle ($\emptyset$) and the dilation angle (ψ) are 42 and 0.7° respectively.

The printing experiment and the collapsing of the structure from 1st trial are shown in Fig. 2(a) and (b) respectively. The comparison of the failure layer number from each trial of the experiments are given in Table 2.

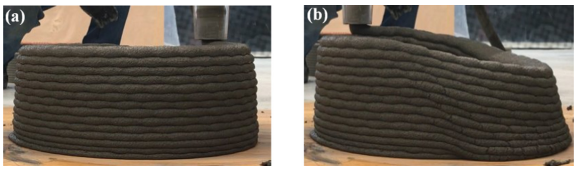

Fig. 2. (a) Printing experiment (b) Collapsing of the structure.

Table 2. Printing experiment result comparison.

Trial no	Failure layer no
1	14.0
2	13.0
3	13.0
Average	13.0
Standard deviation	0.5
RSD (%)	3.8

In numerical simulation, two types of failure mechanisms are indicated by a standard Mohr-Coulomb plasticity state plot: shear failure and tensile failure (Eqs. 6 and 7). Each type is designated by a different color. The state of each zone can be checked after the convergence criteria in each time-step. The state of the zone describes whether the zone exceeded the shear strength at past (i.e. in previous time-step) and denote as 'shear-p'. This means that the principal stresses fall below the shear yield limit as shown in Eq. 6. Otherwise, the state of the zone gives whether the stresses are exceeding the shear strength in the current time-step as 'shear-n'. The same notation for tension limits (i.e. tension-p or tension-s) will be used in the plasticity state plot. If the shear strength limit exceeds (i.e. principal stresses falls below the shear yield function as in Eq. 6) in a particular zone, plastic flow will occur. This will result in higher deformation of the zones and can consider as failure.

Figure 3 shows the plastic state plots after constructing 5 number of layers and at failure. In Fig. 3(a), no failure occurs at the bottom most layer after constructing 5 layers. This denotes as 'None' in the plot. It should be noted that the default value of σ_t

is considered as zero in FLAC 3D. Therefore, tensile failure limit already exceeds in each layer (except the bottom most layer due to its fixed boundary conditions at the base). Hence, 'tension-p' or exceeding the tensile limit at previous time-step is shown. However, exceeding the tensile limit will not result in failure of the structure. Figure 3 (b), shows the failure of the bottom layer after exceeding the shear failure limit as shown in Eq. 6. Shear failure limit exceeded at the previous step (shear-p) when constructing the 15^{th} layer in the numerical simulation. It can be seen that the plastic flow has occurred up to 9^{th} layer. However, the bottom most layer fails in shear at 15^{th} layer construction initiating the plastic flow. Therefore, we can predict the failure layer number is 14 from the numerical simulation.

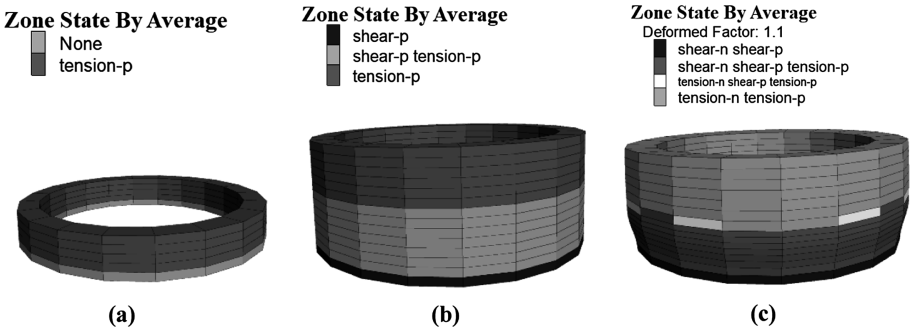

Fig. 3. Numerical simulation results for (a) Zone state after 5 layers (b) Zone state at failure (c) Zone state at plastic deformation.

Also, it is interesting to note that the failure height of the print structure achieved form Eq. 2 is around 4 layers, which is an under-estimation of the failure height. However, for rough estimations of strength-based failure in square cross sections, this may be useful [7].

5 Conclusions

In this paper, the stability of the 3D printed concrete structure is modelled numerically and validated with experimental results. The time dependent concrete material model was developed using laboratory experimental results and implemented in numerical simulation. The failure mode observed during 3D printing is purely strength-based failure for the mix used and the geometry considered in this study. The buckling mode of the structure cannot be seen during printing. Following conclusions can be made from the current study:

- Time-dependent Mohr-Coulomb failure criteria and FLAC 3D numerical simulations can be used effectively to predict the strength-based failure of 3D printing concrete.

- The strength-based failure criteria which purely based on yield stress (Eq. 2), underestimates the failure height of the structure.
- To predict the buckling failure height, accurate measurements of time-dependent elastic modulus should be implemented. Measuring the stress and strain of a printed layer by applying a compression load would be a useful method to determine the elastic modulus of the material.

References

1. Wolfs R, Salet T, Hendriks B (2015) 3D printing of sustainable concrete structures. In: Proceedings of IASS annual symposia, vol 2. International Association for Shell and Spatial Structures (IASS), pp 1–8
2. Lim S, Buswell RA, Le TT, Austin SA, Gibb AG, Thorpe T (2012) Developments in construction-scale additive manufacturing processes. Autom Constr 21:262–268
3. Bingham EC (1922) Fluidity and plasticity, vol 2. McGraw-Hill, New York
4. Roussel N, Ovarlez G, Garrault S, Brumaud C (2012) The origins of thixotropy of fresh cement pastes. Cem Concr Res 42(1):148–157
5. Perrot A, Rangeard D, Pierre A (2016) Structural built-up of cement-based materials used for 3D-printing extrusion techniques. Mater Struct 49(4):1213–1220
6. Roussel N, Coussot P (2005) "Fifty-cent rheometer" for yield stress measurements: from slump to spreading flow. J Rheol 49(3):705–718
7. Roussel N (2018) Rheological requirements for printable concretes. Cem Concr Res 112:76–85
8. Le TT, Austin SA, Lim S, Buswell RA, Gibb AG, Thorpe T (2012) Mix design and fresh properties for high-performance printing concrete. Mater Struct 45(8):1221–1232
9. Jayathilakage R, Sanjayan J, Rajeev P (2019) Direct shear test for the assessment of rheological parameters of concrete for 3D printing applications. Mater Struct 52(1):12
10. Itasca F (2000) Fast Lagrangian analysis of continua. Itasca Consulting Group Inc., Minneapolis
11. Wolfs R, Bos F, Salet T (2018) Early age mechanical behaviour of 3D printed concrete: Numerical modelling and experimental testing. Cem Concr Res 106:103–116

Quantifying Constructability Performance of 3D Concrete Printing via Rheology-Based Analytical Models

Jacques Kruger(✉), Stephan Zeranka, and Gideon van Zijl

Division for Structural Engineering and Civil Engineering Informatics, Stellenbosch University, Stellenbosch, South Africa
pjkruger@sun.ac.za

Abstract. 3D printing of concrete (3DPC) is a developing automation technology that can promote further industrialisation in the construction industry. 3DPC has complex rheological requirements, namely low material viscosity for ease of pumping but high viscosity for constructability. Greater emphasis is therefore placed on the rheology of cement-based composites used for 3DPC compared to conventional construction techniques. Thixotropic materials demonstrate the material performance required for 3DPC. This research presents the work of Kruger et al., who developed a bi-linear thixotropy model [1] specifically for 3DPC materials. This model demonstrates the degree of thixotropy of a material and the static yield shear stress evolution after it has been extruded. A buildability model [2] predicts the maximum number of filament/printing layers achievable, which is based on the bi-linear thixotropy model. Lastly, a rheology-based filament shape retention model [3] determines the maximum height of a filament layer where no plastic yielding at a material point will occur. The three aforementioned models are applied in this research in order to quantify the constructability of 3DPC by only conducting rheology tests and no mechanical tests. A circular hollow column is 3D printed that validates the models presented in this research. The buildability model predicted 52 filament layers whereas 54 layers were obtained experimentally before failure, yielding a conservative 3DPC construction height prediction of 3.7%.

Keywords: 3D concrete printing · Rheology · Buildability · Shape retention · Modelling

1 Introduction

3D printing of concrete (3DPC) entails the pumping and extrusion of concrete in its plastic state. Printable concrete requires a balance between pumpability at low viscosity (to avoid high pump pressures) and buildability at high viscosity, while retaining the homogeneity of the concrete during the pumping and extrusion phase. A feasible range in printable concrete viscosity therefore exists, as depicted in Fig. 1. Due to the conflicting requirements of pumpability and buildability of 3DPC, different approaches have been developed to characterise 3DPC, most notably based on rheological or mechanical properties in the fresh state (green strength).

V. Mechtcherine et al. (Eds.): RheoCon 2019/SCC 2019, RILEM Bookseries 23, pp. 400–408, 2020.
https://doi.org/10.1007/978-3-030-22566-7_46

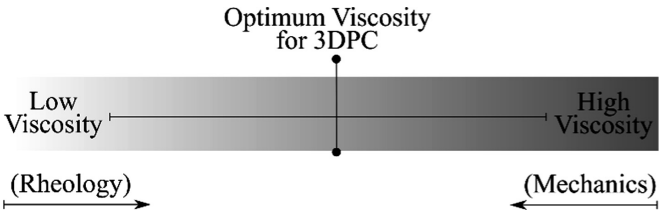

Fig. 1. Viscosity range of a 3D printable concrete indicating rheological characterisation preferred for low viscosities and mechanical characterisation for high viscosities.

State of the art literature on 3DPC modelling is mainly based on the mechanical characterisation of materials. Suiker [4] proposed a mechanistic buildability model for 3DPC that requires a material's green strength properties as input parameters. Similarly, Wolfs et al. [5] developed a numerical model for 3DPC based on green strength properties. However, this research builds on current 3DPC literature that is based on rheological characterisation [6].

Kruger et al. [1] developed a bi-linear thixotropy model specifically for 3DPC. Thixotropic material behaviour is deemed the most appropriate for 3DPC as a distinct difference exists between the static and dynamic yield shear stress. Thus, the material's viscosity decreases while being agitated during the pumping process and then increases after the agitation is removed. The model defines the re-flocculation rate (R_{thix}) that is a measure of the degree of thixotropy of a material. Buildability [2] and filament shape retention [3] models are incorporated that are also based on rheological characterisation.

This research applies these models in practice in order to demonstrate the relative ease with which the constructability process of 3DPC can be quantified by only characterising the rheology of a material. This is achieved by performing a rheological characterisation of the standard 3DPC material at Stellenbosch University (SU) and thereafter 3D printing a circular hollow column to validate the models.

2 Analytical Models

2.1 Bi-linear Thixotropy Model

A novel bi-linear thixotropy model for 3DPC is developed by Kruger et al. [1]. This model builds on the thixotropy model that is proposed by Roussel [7] by accounting for both re-flocculation (R_{thix}) and structuration (A_{thix}) mechanisms, as indicated in Fig. 2. R_{thix} is mainly a physical process resulting from interparticle forces, specifically interatomic and intermolecular forces on a particle's surface, and typically reaches equilibrium in a few hundred seconds. A_{thix} is mainly a chemical process that is influenced by the early formation of hydration products, consequently yielding a decrease in concrete plasticity. The study by Kruger et al. [1] found that R_{thix} is a better indicator of thixotropic behaviour suitable for 3DPC than A_{thix}.

The practical aspect of the model is that it portrays a material's static yield shear stress evolution after it has been extruded from the nozzle as a function of resting time. Thus, the shear history is accounted for, which is then immediately followed by re-flocculation and thereafter structuration. The shear history incorporates the shearing action induced by the pump and hose during the 3DPC process. Due to this shearing action, a material's microstructure is broken down from the static to dynamic yield shear stress that is denoted by $\tau_{D,i}$ in Fig. 2. After cessation of the agitation i.e. when the material exits the nozzle, Brownian motion will result in re-flocculation of the particles consequently rebuilding the material's original microstructure before shear was induced, denoted as $\tau_{S,i}$ which is the material's initial static yield shear stress. Thereafter the material structurates until the hydration process comes into full effect. A material's shear strength can be obtained as a function of resting time with the following equations:

$$\tau_S(t) = \tau_{D,i} + R_{thix} \cdot t \quad for \quad [t \leq t_{rf}] \tag{1}$$

$$t_{rf} = \frac{\tau_{S,i} - \tau_{D,i}}{R_{thix}} \tag{2}$$

$$\tau_S(t) = \tau_{S,i} + A_{thix} \cdot (t - t_{rf}) \quad for \quad [t > t_{rf}] \tag{3}$$

Where $\tau_S(t)$ is the static yield shear stress of the material at time (t) after deposition and t_{rf} the time period over which re-flocculation occurs as illustrated in Fig. 2.

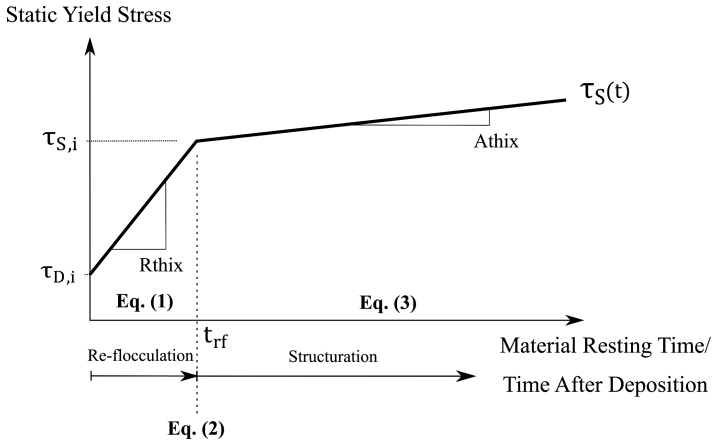

Fig. 2. Bi-linear thixotropy model that depicts the static yield shear stress evolution as a function of material resting time after deposition.

2.2 Buildability Model

An analytical model is developed by Kruger et al. [2] that quantifies the buildability performance of a material for 3DPC, in particular the maximum number of layers

achievable before failure occurs. This model only accounts for physical nonlinearity i.e. plastic yielding of the bottom critical filament layer and not geometrical nonlinearity such as elastic buckling. The resistance provided by the material against plastic yielding, namely the static yield shear stress, is incorporated via Eqs. 1 to 3. Thus, the buildability model is primarily based on rheology and not on green strength. An a priori check is performed to determine which one of the final two Eqs. 5 or 6, is to be employed:

$$\textit{If} \qquad \frac{d}{dt}\left(\frac{\rho \cdot g \cdot h_l \cdot v \cdot 10^{-3}}{2 \cdot l_p \cdot F_{AR}} \cdot t\right) \geq \frac{\tau_{S,i} \cdot R_{thix}}{\tau_{S,i} - \tau_{D,i}} \tag{4}$$

$$\textit{Then use} \qquad N_L = -\left[\frac{\tau_{D,i}}{\left(\frac{R_{thix} \cdot l_p}{v}\right) - \left(\frac{\rho \cdot g \cdot h_l}{2.10^3 \cdot F_{AR}}\right)}\right] \tag{5}$$

$$\textit{Else use} \quad N_L = -\left[\frac{\tau_{S,i} + \left(\frac{A_{thix} \cdot \left(\tau_{D,i} - \tau_{S,i}\right)}{R_{thix}}\right)}{\left(\frac{A_{thix} \cdot l_p}{v}\right) - \left(\frac{\rho \cdot g \cdot h_l}{2.10^3 \cdot F_{AR}}\right)}\right] \tag{6}$$

Where ρ is the material density (kg/m^3), g the gravitational constant (m/s^2), h_l the filament layer height (mm), v the printing speed (mm/s), l_p the print path length per layer (mm), N_L the number of filament layers and F_{AR} the strength correction factor based on the aspect ratio of the filament layer.

Concrete in its plastic state demonstrates similar behaviour to cohesive soils, i.e. both possess less capacity in tension than in compression. In this case, failure in compression is due to relative movement of particles resulting in shear failure and not by crushing of constituents. This pressure-dependent shear failure is best defined by the Mohr-Coulomb failure criterion. However, more material parameters are required to employ this failure criterion, such as cohesion (c) and interparticle friction (φ). Both are functions of time that will consequently require more laborious data acquisition. Therefore, a simplified approach is adopted that focuses on the principle stress state within a filament layer. As depicted in Fig. 3a, the aspect ratio of a filament layer will determine the stress state, in particular a uniaxial or triaxial stress state, provided that sufficient friction is present to prevent slip. The area wherein a triaxial stress state is present is referred to as being confined. For an aspect ratio of 2, failure typically occurs in the middle of the specimen due to uniaxial stress conditions that yield maximum shear stress. This is evident in unconfined uniaxial compression tests (UUCT) whereby failure is depicted by the Tresca criterion, or maximum shear stress theory, and also forms the lower bound of the Mohr-Coulomb failure criterion. Confinement increases as the aspect ratio of a filament layer decreases, consequently yielding higher apparent compressive strengths relative to the strength at an aspect ratio of 2 [8], as depicted in Fig. 3b. This is synonymous to reaching the upper bound of the Mohr-Coulomb failure criterion, known as the Rankine or maximum normal stress theory. The model is

simplified by incorporating strength correction factors (F_{AR}) that are normalised to unity at an aspect ratio of 2, as depicted in Fig. 3b.

In essence, the vertical building rate obtained from print-specific parameters is equated to the strength development curve depicted in Fig. 2. This yields Eqs. 5 and 6, however, the vertical building rate that is expressed in terms of normal stress is converted to the equivalently induced shear stress by means of the Mohr-Coulomb failure criterion. In order to negate additional material tests, the lower bound Tresca failure criterion is adopted. Confinement within filament layers, which has a significant influence on the total bearing capacity, is accounted for by means of strength correction factors for various filament layer aspect ratios. More detailed information is presented in [2].

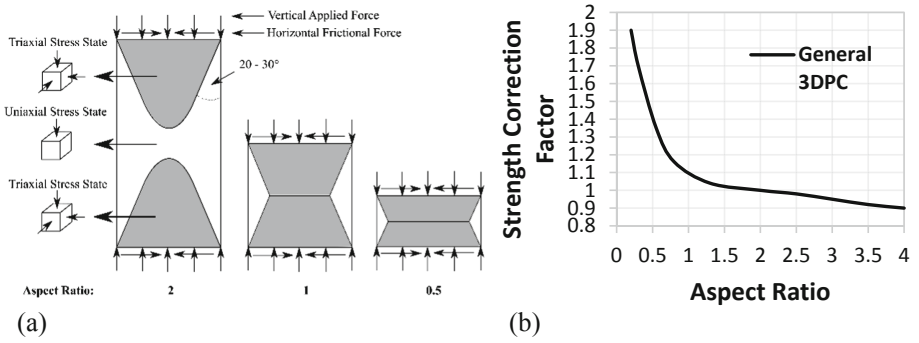

Fig. 3. (a) Confinement within filament layers of different aspect ratios and (b) strength correction factors (F_{AR}) for various filament aspect ratios.

2.3 Shape Retention Model

Kruger et al. [3] developed a quasi-static analytical model to determine the maximum filament layer height whereby plastic yielding at any material point will not occur under self-weight, thus preventing significant deformation after extrusion. Filament shape retention is not only a prerequisite for good buildability performance, but also for adequate surface aesthetics of 3DPC elements. The model is based on the dynamic yield shear stress ($\tau_{D,i}$). Therefore, material shear history is of crucial importance to obtain accurate predictions.

A cross-section segment of a filament layer is illustrated in Fig. 4. Plane strain behaviour is assumed due to the continuous lateral support provided in the longitudinal direction of the filament layer. As for the buildability model, it is assumed that sufficient friction is present to induce confinement in the bottom part of the filament layer, as depicted in Fig. 4a. Consequently, a horizontal stress termed σ_2 is induced. The plane strain conditions specify that $\sigma_3 = \upsilon \cdot (\sigma_1 + \sigma_2)$, where υ is the material's Poisson's ratio. The vertically induced stress due to self-weight is $\sigma_1 = \rho \cdot g \cdot h_l$. By assessing the maximum and minimum stress combinations on a Mohr circle, the following shape retention expressions are presented for failure zones 1, 2 and 3 in Fig. 4b respectively:

$$H_{max} = \frac{2 \cdot \tau_{D,i}}{\rho \cdot g} \tag{7}$$

$$H_{max} = \frac{2 \cdot \tau_{D,i} \cdot (1 - \upsilon)}{\rho \cdot g} \tag{8}$$

$$H_{max} = \frac{2 \cdot \tau_{D,i}}{(1 - \upsilon) \cdot \rho \cdot g} \tag{9}$$

Where H_{max} is the maximum filament layer height at which plastic deformations will not occur. By interpreting Eqs. 7 to 9 parametrically, it can be seen that Eq. 8 will always govern. More detailed information is presented in [3].

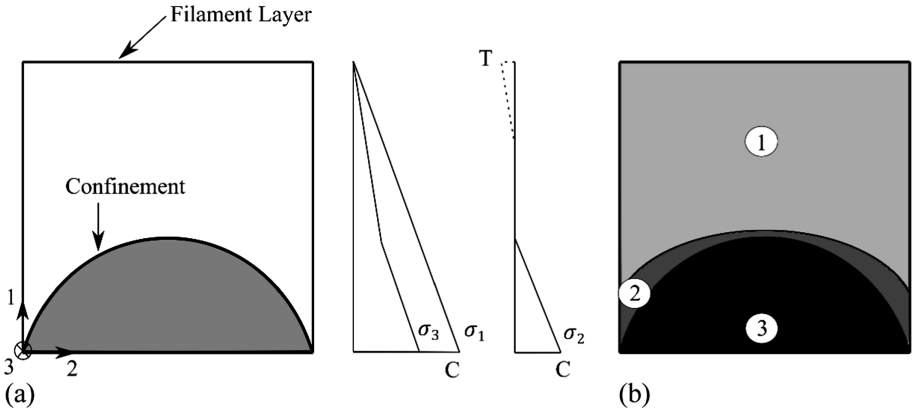

Fig. 4. (a) Cross-section of a filament layer with confinement in the bottom and corresponding principle stresses indicated to the right, and (b) three failure zones within a filament layer.

3 Experimental Procedure

The standard 3DPC mix at SU, given in Table 1, is employed in this research. Initially a 20L batch is prepared for the rheological characterisation via the Germann ICAR rheometer. A stress growth test is performed at various material resting time intervals. This test involves the application of a constant shear rate and the shear stress measured as a function of time. The shear induced via the pump process is approximately replicated with the rheometer by correlating the rheometer's vane speed to that of the pump's screw. The shear induced via the hose is taken into account by correlating the rheometer shear duration to the time it takes material to exit the nozzle. A shear rate of $1s^{-1}$ is obtained based on a rotational speed of 0.2 rev/s. The shear duration is equal to 60 s based on a hose length of 3.5 m and a print speed of 60 mm/s. This is a simplified approach to yield roughly the same induced shear by the rheometer as during the printing process. This shear rate and duration is used for all rheological measurements. A stress growth test is performed at the following resting intervals (s): 0, 10, 20, 30, 40, 50, 60,

90, 120, 180, 1200, 2400 and 3600. A single-batch approach is followed; however, it is acknowledged that segregation may occur on the vane's perimeter at higher concrete ages. R_{thix} and A_{thix} are then calculated and the static yield shear stress evolution curve plotted. More details regarding the test procedure can be obtained in [1].

The buildability (Eqs. 4–6) and shape retention (Eqs. 7–9) models are applied after the rheological characterisation and data processing have been executed. A circular hollow column with diameter 250 mm is 3D printed until failure occurs. A 25 mm diameter circular nozzle is used at a deposition height of 10 mm to yield a layer width and height of 30 mm and 10 mm respectively. The concrete density, obtained by filling a known volume (1 L) and measuring the sample's mass, is 2150 kg/m^3. The Poisson's ratio is assumed to be 0.3, following the work and assumptions made by Wolfs et al. [5] and Suiker [4]. Based on the aforementioned data, l_p is calculated as 785 mm and F_{AR} as 1.7 from Fig. 3b.

4 Results and Discussions

The static yield shear stress evolution curve as well as the thixotropy parameters are indicated in Fig. 5. The material has a re-flocculation rate of 6.88 Pa/s, which is more than 6 times that of its structuration rate of 1.08 Pa/s. The material is regarded as highly thixotropic. The buildability model (Eq. 6) predicted that 52 filament layers would be obtained. The governing expression of the shape retention model (Eq. 8) predicted a maximum stable filament layer height of 76 mm.

The 3D print is illustrated in Fig. 6. 54 filament layers are obtained in 12 min at a layer height of 10 mm; thus, a total height of 540 mm is obtained. Plastic yielding of the bottom filament layers instigated global failure of the printed element. No filament layer deformation is observed, except for a slight undulating pattern on the printed element's surface due to irregular pump frequencies.

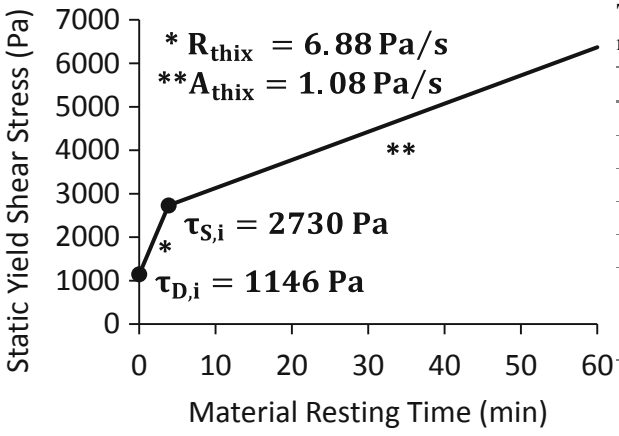

Fig. 5. Static yield shear stress evolution curve depicting the initial static and dynamic yield shear stresses as well as the re-flocculation and structuration rates.

Table 1. Standard SU 3DPC mix constituent quantities.

Constituent	kg
Cement	579
Fly ash	165
Silica fume	83
Fine aggregate	1167
Water	261
Superplasticizer	1.48%, by binder mass

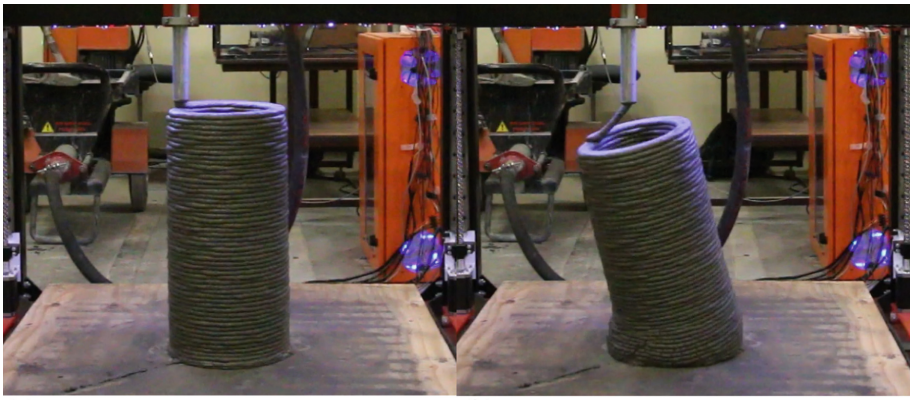

Fig. 6. (a) 3D printed circular hollow column just before failure occurs and (b) plastic yielding of bottom filament layers results in global failure of the printed column.

The models presented by Kruger et al. [1–3] are thus validated. The buildability model in particular predicted a conservative building height of 3.7% lower than the actual, stable 3D printed column height. This is the most accurate prediction by the model to date, as previously an underprediction of 8.3% was achieved [2].

5 Conclusion

The models developed by Kruger et al. for thixotropy, buildability and shape retention of 3DPC elements are presented in this research. These models are practically applied in order to demonstrate their ease of use by only characterising a material's rheology. After the print-specific and material parameters were determined, the models predicted a maximum of 52 filament layers before failure occurs as well as a maximum stable filament layer height of 76 mm. Failure of the 3D printed 250 mm diameter circular hollow column occurred after the deposition of 54 layers at a layer height of 10 mm. A good surface finish was obtained due to insignificant filament deformation after extrusion. The buildability model predicted a building height of 3.7% lower than the actual, stable 3D printed column height.

Acknowledgement. The authors gratefully acknowledge Mr Seung Cho's assistance with the experimental work. This research is funded by The Concrete Institute (TCI) and the Department of Trade and Industry of South Africa under THRIP Research Grant TP14062772324.

References

1. Kruger PJ, Zeranka S, van Zijl GPAG (2019) An ab initio approach for thixotropic characterisation of (nanoparticle-infused) 3D printable concrete. Constr Build Mater 224:372–386

2. Kruger PJ, Zeranka S, van Zijl GPAG (2019) 3D concrete printing: a lower bound analytical model for buildability performance quantification. Autom. Constr. 106:10294
3. Kruger PJ, Zeranka S, van Zijl GPAG (2019) A rheology-based quasi-static shape retention model for digitally fabricated concrete
4. Suiker ASJ (2018) Mechanical performance of wall structures in 3D printing processes: theory, design tools and experiments. Int J Mech Sci 137:145–170. https://doi.org/10.1016/j.ijmecsci.2018.01.010
5. Wolfs RJM, Bos FP, Salet TAM (2018) Early age mechanical behaviour of 3D printed concrete: Numerical modelling and experimental testing. Cem Concr Res 106:103–116. https://doi.org/10.1016/j.cemconres.2018.02.001
6. Roussel N (2018) Rheological requirements for printable concretes. Cem Concr Res 112:76–85. https://doi.org/10.1016/j.cemconres.2018.04.005
7. Roussel N (2006) A thixotropy model for fresh fluid concretes: Theory, validation and applications. Cem Concr Res 36:1797–1806. https://doi.org/10.1016/j.cemconres.2006.05.025
8. Lamond JF, Pielert JH (2006) Significance of tests and properties of concrete and concrete-making materials. ASTM International, West Conshohocken ISSN 9780803155206

Extrusion of Lightweight Concrete: Rheological Investigations

Carla Matthäus(✉), Daniel Weger, Thomas Kränkel, Luis Santos Carvalho, and Christoph Gehlen

Center for Building Materials,
Technical University of Munich, Munich, Germany
c.matthaeus@tum.de

Abstract. Lightweight concrete enables the production of monolithic exterior wall components with sufficient thermal insulation even under Central European climatic conditions. If, in addition, additive manufacturing by extrusion is used for production, these components can be further improved by installing air chambers to increase thermal insulation of the component or varying wall thicknesses to reduce material demand. Furthermore, it is beneficial to use lightweight aggregate concrete (LAC) instead of e.g. aerated concrete due to its higher robustness with regard to the pumping process. However, LAC differs from normal concrete as the porous lightweight aggregates absorb water and thereby change the characteristics of the fresh mixture. This applies in particular if the concrete is put under pressure during production, e.g. during pumping. This paper focusses on the effect of rheological parameters (especially plastic viscosity) on the pumpability of LAC. We found for the tested mixtures, pumped with an eccentric screw mortar pump, that pumpability was independent of the yield stress. Plastic viscosity, on the other hand, had a decisive effect on the pumpability of the LAC. By varying the total water to binder ratio, we found a significant effect on the pumpability, which is in line with the effect of the plastic viscosity. Furthermore, alternative concrete additives can affect the flow in the pipe, as is known from normal concrete. Our experiments show that limestone powder influences the pumpability independently of plastic viscosity and yield stress. With our results, we contribute to the development of a lightweight, 3D printable concrete.

Keywords: Additive manufacturing · Extrusion · Lightweight aggregate concrete · 3D-Printing · Rheology

1 Introduction

Computer-aid as well as robotic-aid systems have revolutionized entire production and engineering processes. While in many branches of industry additive manufacturing (AM) is already state-of-the-art, the development in the construction industry is still in an early stage. However, in recent years, the research activity in the area of AM has increased significantly [1]. In concrete construction, the AM method extrusion is used

V. Mechtcherine et al. (Eds.): RheoCon 2019/SCC 2019, RILEM Bookseries 23, pp. 409–416, 2020.
https://doi.org/10.1007/978-3-030-22566-7_47

as the construction speed is already comparatively high [1]. The extrusion technique realizes a digitally designed object by stacking layers of fresh concrete. It creates new opportunities in construction industry: free-formed buildings, integration of functionality, or reduced consumption of resources, among others [2, 3]. However, using regular concrete for extrusion limits those possibilities. For example, the need of insulation materials in Central European climate zones lowers the freedom of design, as insulation still has to be added manually. In addition, it deteriorates the recyclability of the construction. Using lightweight concrete might overcome those obstacles. Lightweight concrete has a low thermal conductivity and induces less weight on the system due to its low density (according to EN 206:2016-11 [4] between 800 kg/m^3 and 2,000 kg/m^3).

For extrusion, the material has to fulfil contradicting requirements: To convey the material to the nozzle (by pumping), the material needs a certain workability. Contrary, to retain its shape and to bear the weight of subsequent layers, the material needs a sufficient green strength as soon as it leaves the nozzle. Combining these contradicting material properties in one material is challenging. This paper contributes to the material development by analyzing the pumpability of lightweight aggregate concrete regarding its rheological properties.

There are three types of lightweight concrete: lightweight aggregate concrete (LAC), aerated concrete and no-fines concrete. Due to its higher robustness during pumping, this paper focuses on LAC. LAC contains a similar composition as normal concrete, but the aggregates are partially or fully substituted by porous lightweight aggregates.

In order to understand pumpability, we must first look at the behavior of normal concrete. According to Rössig normal concrete can be categorized as Bingham substance, for which the pumpability is defined by shear viscosity and shear stress if the pipe diameter and the pumping velocity are known [5]. However, further research has shown that most concretes flow as a plug (bulk material in the center of the pipe) and form a lubrication layer on the peripheral of the pipe [6–9]. This material behavior is known as the flow-induced particle migration (migration of coarser aggregates to the center) [6]. Plastic viscosity of the fresh concrete and the paste content of the total mixture affect this migration and therefore, the formation of a lubrication layer [10]. This has a significant influence on the pumpability. For LAC, the water absorption of the aggregates can lead to a significant divergence in its pumping behavior. This is one of the main differences to normal concrete. If the porous lightweight aggregates are not soaked before mixing, the LAC might behave as a time-dependent rheopectic fluid [5]. However, pre-wetting the lightweight aggregates leads to a nearly time-independent Bingham behavior [5]. After extrusion (exiting the nozzle) re-absorption of water might occur. The water leaves the aggregates because the encapsulated air inside the aggregates relaxes. Therefore, the behavior of LAC submitted to a pumping pressure is not only compressible but also elastic [11]. This might be an advantage over normal concrete, where cracks might occur due to the lack of formwork which prevents drying out [12].

2 Materials and Methods

2.1 Materials

Investigations were performed with lightweight concretes with a density between 950 kg/m^3 and 1,250 kg/m^3. The concretes were based on Ordinary Portland Cement (OPC) and Portland Limestone Cement (PLC). Expanded glass granulate with a maximum grain size of 2 mm were used as light aggregate. The particle size distribution of the lightweight aggregates was kept constant for all experiments. For some concrete compositions a polycarboxylate ether (PCE) based superplasticizer, fly ash (*F*) or limestone powder (*LSP*) was added, respectively. The particle size distribution of the OPC and the fly ash was comparable.

2.2 Water Content

In addition to the mixing water w, the water absorbed by the light aggregates w_A must be taken into account. The total amount of water w_t is therefore $w_t = w + w_A$. As the water absorption by light aggregates depends on both the prevailing pressure p and the time of exposure t_e, the total amount of absorbed water cannot be clearly predicted. The water absorption at atmospheric pressure for different exposure times $w_{A,atm}(t_e)$ is often provided by the manufacturer. It can be regarded as lower limit for water absorption during pumping: $w_{A,atm}(t_e) \leq w_A(t_e, p) \leq w_{A,max}(\Phi_{void})$. Φ_{void} is the open void fraction of the light aggregates and limits the maximum amount of water that can be absorbed. Since the composition of the light aggregates and the mixing regime are kept constant throughout the investigations, the water absorption of the light aggregates is always the same at the beginning of the pumping process. As a simplification, the presumed constant, but unknown amount of water absorption is not subtracted. Hence, the total water to binder b ratio (by mass) $w_t/b = (w + w_A)/(c + f + LSP)$ is used for comparison.

2.3 Mix Design

The yield stress was varied by a targeted addition of PCE (wt% w.r.t. cement). For the investigation of the plastic viscosity at a constant yield stress, a part of the mass of the cement was replaced by fly ash. For the evaluation a replacement of 20 wt% and 40 wt% was considered. In order to keep the paste content constant, the water content was adjusted and taken into account in the evaluation. This enabled systematic variation of the plastic viscosity and quantification of its effect on pumpability. In addition, the influence of the material composition on the pumpability was investigated by a variation of the w_t/b ratio (0.46–0.63) and a partial cement replacement by limestone powder as filler material (0–20 wt%). Furthermore, we compare two LACs with similar rheological properties and similar w_t/b ratio: *O_L20* contains 20 wt% LSP w.r.t. cement and *O_PCE* 0.2 wt% PCE w.r.t. cement to achieve comparable rheological properties (see Table 2).

2.4 Methods

In order to analyze the correlations, the LAC compositions were examined both rheologically and with regard to their pumpability. All tests were conducted at laboratory atmosphere. We kept a uniform mixing order to eliminate confounding effects:

- Mix dry aggregate and 2/3 of water (pre-wetting): 1 min
- Rest (pre-wetting/water absorption): 4 min
- Add cement (and if applicable, mineral additives): 1 min
- Add last 1/3 of water (and if applicable, PCE), mixing: 45 s
- Open mixer and scratch out concrete from the sides and blade: 30 s
- Further mixing: 45 s

Following a 30 s remix (at 14 min 30 s) to break a potentially formed inner structure of the concrete, the determination of the rheological properties began 15 min after addition of water to the cement. Therefore, we used a rotational rheometer (MCR 502, Anton Paar) and a vane-in-cup measuring device with a six-bladed vane paddle (height 60 mm and radius 20 mm) and a vane-cup with ribbed surface (radius 35 mm) to prevent wall slipping. We measured the torque values in nine descending rotational speed steps, 10 s each (80, 60, 40, 20, 10, 5, 3, 2 and 1 rpm). Before starting the measurement with 80 rpm the concrete rested for 50 s (from 15 min to 15 min 50 s) to simulate the procedure between filling the concrete pump and starting the pumping process. To analyze the rheological properties dynamic yield τ_0 stress and plastic viscosity μ, we used the equilibrium value of steps 40 rpm, 20 rpm, 10 rpm, 5 rpm and 3 rpm in combination with Bingham model based on Reiner-Riwlin-Equation as well as assumption of plug flow [13]. The steps 80 rpm, 60 rpm, 2 rpm and 1 rpm must be neglected, because not every concrete showed equilibrium values in these steps.

The results of the rheometer were compared to real pump tests. The designed mixtures were pumped in the actual 3D printer setting. We used an eccentric screw mortar pump with a diameter of 90 mm with a frequency controlled motor speed. Thereupon, we pumped the material through a mortar hose with 25 mm inner diameter, a length of 5 m and a difference in height of approximately 2 m. Before every examination of the pumpability, the pump was wetted with water in order to ensure a uniform lubrication of the wall. The mortar pump was always activated at a control frequency of 10 Hz and if the material did not leave the hose within 90 s, the control frequency was accelerated to 18.5 Hz. If the material still was not pumpable, the control frequency was increased to 26.2 Hz at 150 s. If the material was easily pumpable and material left the hose within the first 60 s, the control frequency was reduced to 3–6 Hz. Temperature was measured before and after pumping. Pumpability can be described in terms of the ratio of pumping pressure to flow rate. These values could not be recorded by the device. Therefore, the frequency controlled motor speed of the concrete pump s, the time until material emerged from the hose t, and the change of fresh concrete's temperature during the pumping process ΔT were taken into account. The mixtures were examined in accordance to these criteria and given a score (1 very good – 6 very bad, see Table 1). Their overall pumpability score Ps was calculated by $Ps = \frac{1}{3}s + \frac{1}{3}t + \frac{1}{3}\Delta T$.

Table 1. Pumpability criteria.

Ps	1 very good	2 good	3 medium	4 poor	5 bad	6 very bad
S [Hz]	<10	10	18.5	26.2	33.3	>34
T [s]	≤ 60	60–120	120–180	180–240	240–360	>360
ΔT [°C]	$\leq 1, 9$	2–4, 9	5–9, 9	10–14, 9	15–19, 9	>20

3 Results and Analysis

3.1 Rheological Properties

Table 2 gives an overview over the measured and calculated values of significant concrete compositions. The ratio between paste volume V_p and volume of aggregates V_A was always kept constant at $V_P/V_A = 1.0$.

Table 2. Concrete compositions and rheological properties.

Label	O_1	O_PCE	O_F0	O_F20	O_F40	O_L20	O_L5	P_1	P_2
Cement type	OPC	OPC	OPC	OPC	OPC	OPC	OPC	PLC	PLC
Add./repl. [wt%] w.r.t. cement	–	PCE 0.2	–	F 20	F 40	LSP 20	LSP 5	–	–
w_t/b [-]	0.63	0.57	0.51	0.49	0.47	0.56	0.51	0.52	0.57
Pl. viscosity [Pas]	3.2	2.9	4.6	5.8	7.6	2.8	4.5	4.7	1.8
Yield stress [Pa]	218	103	47	51	53	103	119	220	162
Pumpability	1.9	2.0	4.0	4.3	4.7	1.3	3.3	3.0	1.5

3.2 Effect of Yield Stress

The influence yield stress on pumpability can exemplarily be shown at compositions *O_1* and *O_PCE* (see Table 2). The plastic viscosity of both compositions is in the range of 3.0 Pas ± 0.2 Pas. Even though the yield stress varies significantly (218 Pa to 103 Pa), the pumpability is almost the same for both mixtures (score 1.9 and 2.0). The results exhibit that pumpability seems to be independent of changes in yield stress. This could be due to the fact that the effect of yield stress is negligible after transition from the solid into the flow state of the material, which was the case while pumping. Overcoming the yield stress by the pumping pressure, plastic viscosity should influence the flow resistance of the material.

3.3 Effect of Viscosity

For the rheological analysis we varied the plastic viscosity by replacement of cement by 0 wt%, 20 wt% and 40 wt% fly ash (*O_F0*, *O_F20* and *O_F40*, see Table 2) at constant yield stress (50 Pa ± 3 Pa). Figure 1 (left) shows the plastic viscosity depending on the w_t/b ratio. Increasing the fly ash content results in a decrease of w_t/b. With decreasing w_t/b the plastic viscosity increases. This can be explained by the

increase of the solid concentration of the paste. This leads to a decreasing distance and thus, an increasing interparticle friction as origin for viscosity of the paste. Figure 1 (middle) shows the pumpability depending on the w_t/b ratio. There, the pumpability score increases with increasing w_t/b and hence, with decreasing viscosity, see Fig. 1 (right). This is in line with results for normal concrete, see [14]. The effect of plastic viscosity on pumpability is due to its effect on the migration of particles [6].

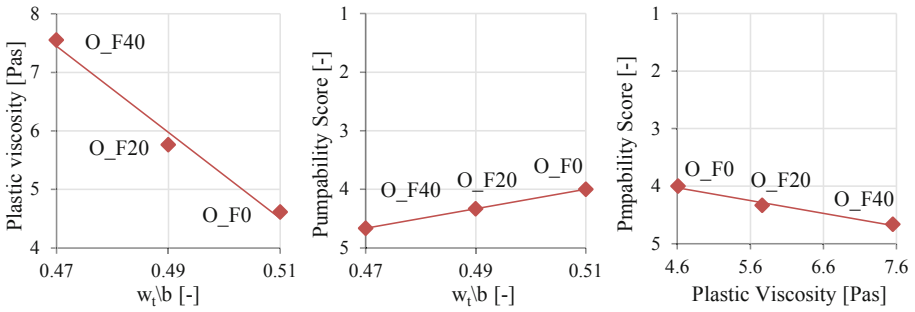

Fig. 1. Relation between viscosity, pumpability and w_t/b (τ_0 = 50 Pa ± 3 Pa).

4 Effect of Material Composition

In a first step, we vary the w_t/b ratio of OPC, see red diamonds, Fig. 2. An increasing w_t/b resulted in an enhanced pumpability score due to a decreased viscosity (see Sect. 3.3). Nevertheless, too high w_t/b ratios can lead to segregation.

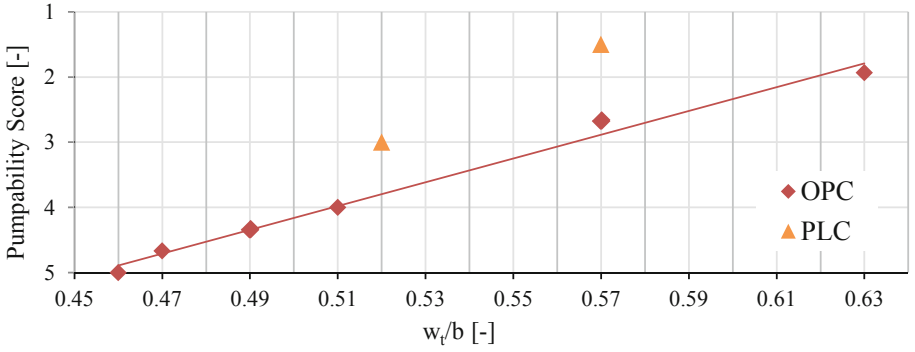

Fig. 2. Relation between pumpability and w_t/b for OPC and PLC.

This also applies for other types of cement. Comparing exemplarily two PLC compositions *P_1* and *P_2* (see yellow triangles and Table 2), *P_1* had a w_t/b of 0.52 and a pumpability score of 3.0 while *P_2* had a w_t/b of 0.57 and a pumpability score of

1.5. The results show that the pumpability of PLC is increased to OPC at comparable w_f/b. This positive effect of the limestone can be confirmed in Fig. 3 (left), which shows the pumpability score of two concretes with similar plastic viscosity (2.9 Pas ± 0.1 Pas), yield stress (103 Pa ± 0.4 Pa), and w_f/b (0.56 ± 0.01). There, we exhibit an increase of the pumpability score from 1.3 to 1.9 with increasing limestone content of 0 to 20 wt%.

Figure 3 (right) compares an OPC, a modified OPC and a PLC with similar plastic viscosity (4.6 Pas ± 0.1 Pas) and w_f/b (0.51 ± 0.01), but with different yield stress (47 Pa, 119 Pa and 220 Pa from left to right). The OPC *O_L5* was modified adding the same limestone powder, which is contained in PLC, partly to the OPC. The results show once more an enhanced pumpability score with increased limestone content. As discussed in Sect. 3.2 yield stress has no influence. Therefore, limestone content is also in this case the driving force for the effect.

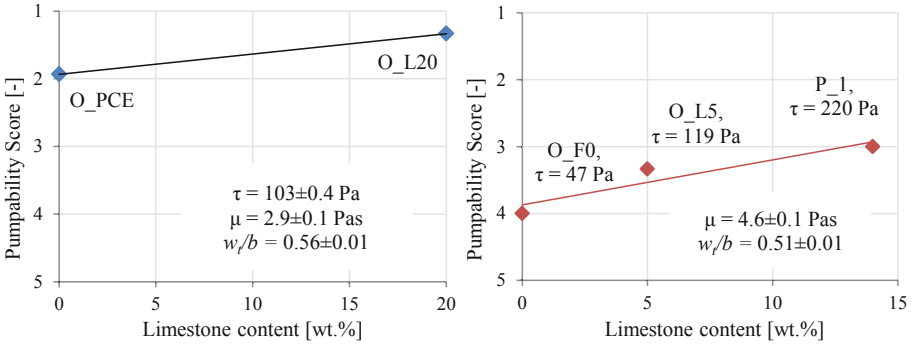

Fig. 3. Relation between pumpability and limestone content [wt% by cement] for OPC and PLC at similar plastic viscosity μ and w_f/b in each case.

In all cases, the pumpability enhances at approximately constant plastic viscosity. Therefore, the plastic viscosity of the LAC as the only parameter is not sufficient to predict the pumpability. Our results show, that the plastic viscosity as well as the amount of limestone significantly affect the pumping behavior of LAC. Their mechanism of action can be assumed to be the same as for normal concrete (influencing the formation of a lubrication layer), but must be examined in further investigations.

5 Summary and Conclusion

The aim of this paper was to assess a correlation between the rheological parameters yield stress and plastic viscosity of the lightweight aggregate concrete and its pumping performance. We found that pumpability was not affected by the yield stress, but plastic viscosity directly affected the pumpability of lightweight aggregate concrete (decrease in plastic viscosity results in improved pumpability). According to [14], the plastic viscosity influences the migration of coarser particles on the fringe of a pipe into the

shear and plug flow region, which contributes mostly to the formation of a lubrication layer. Further research is necessary to validate this hypothesis for LAC. Furthermore, we found, that evaluating the plastic viscosity as the only parameter is not sufficient for the prediction of pumpability but additives (exemplarily limestone powder) had a significant effect on the pumping performance at similar plastic viscosity. Further research will be executed, whether the formation of a lubrication layer is presumably the driving force for this phenomenon, see [7–9]. Being able to estimate the pumpability, the further phases of extrusion can be analyzed and an overall optimization of the lightweight aggregate concrete for 3D printing is possible. In first tests, many of the mixes were suitable for extrusion in terms of buildability. However, a systematic material optimization in order to achieve increased process speed will be part of further research.

References

1. Bos F, Wolfs R, Ahmed Z, Salet T (2016) Additive manufacturing of concrete in construction: potentials and challenges of 3D concrete printing. Virtual Phys Prototyp 11 (3):209–225. https://doi.org/10.1080/17452759.2016.1209867
2. de Schutter G, Lesage K, Mechtcherine V, Nerella VN, Habert G, Agusti-Juan I (2018) Vision of 3D printing with concrete—technical, economic and environmental potentials. Cem Concr Res 112:25–36. https://doi.org/10.1016/j.cemconres.2018.06.001
3. Salet TAM, Wolfs RJM (2016) Potentials and challenges. In: 3D Concrete printing proceedings of the 2nd international conference on progress in additive manufacturing (Pro-AM 2016), pp 8–13
4. EN 206:2016-11 Concrete – Specification, performance, production and conformity
5. Rössig M (1974) Fördern von Frischbeton, insbesondere von Leichtbeton, durch Rohrleitungen. Forschungsbericht des Landes Nordrhein-Westfalen Nr. 2456. Westdeutscher Verlag
6. Secrieru E, Butler M, Mechtcherine V (2014) Prüfen der Pumpbarkeit von Beton - Vom Labor in die Praxis. Bautechnik 91(11):797–811. https://doi.org/10.1002/bate.201400072
7. Jacobsen S, Mork J, Lee S, Haugan L (2008) Pumping of concrete and mortar - state of the art. In: COIN project report, vol 5, pp 1–44
8. Kaplan D, deLarrard F, Sedran T (2005) Avoidance of blockages in concrete pumping process. ACI Mater J 102(3):183–191
9. Choi M, Roussel N, Kim Y, Kim J (2013) Lubrication layer properties during concrete pumping. Cem Concr Res 45:69–78. https://doi.org/10.1016/j.cemconres.2012.11.001
10. Mechtcherine V, Venkatesh N, Kasten K (2014) Testing pumpability of concrete using Sliding Pipe Rheometer. Constr Build Mater 53:312–323
11. Faust T (2003) Leichtbeton im konstruktiven Ingenieurbau. Wiley, Hoboken
12. Roussel N (2018) Rheological requirements for printable concretes. Cem Concr Res 112:76–85. https://doi.org/10.1016/j.cemconres.2018.04.005
13. Koehler E, Fowler D (2004) Development of a Portable Rheometer for Fresh Portland Cement Concrete
14. Secrieru E (2017): Pumping behaviour of modern concretes - Characterisation and prediction, Schriftenreihe des Institutes für Baustoffe (2). ISBN 978-3-86780-562-9

Enhancing Strength of Powder-Based 3D Printed Geopolymers for Digital Construction Applications

Behzad Nematollahi(✉), Ming Xia, and Jay Sanjayan

Centre for Sustainable Infrastructure, Faculty of Science, Engineering and Technology, Swinburne University of Technology, Hawthorn, VIC, Australia
bnematollahi@swin.edu.au

Abstract. The authors of this study have recently succeeded to formulate geopolymer as a printing material to be used in commercially available powder-based 3D printers for the manufacture of '*free-form*' components with complex geometries without the use of expensive formwork. This study focusses on post-processing methods to increase the strength of powder-based 3D printed geopolymers. The effects of curing medium, curing temperature, curing time and loading direction on the compressive strength of the printed geopolymers were investigated. The printed samples were cured in two different sodium (Na)-based and potassium (K)-based alkaline solutions at two different curing temperatures (ambient-temperature (23 °C) and 60 °C) for 7 days and 28 days. The compressive strength of the post-processed geopolymer samples was measured in two different loading directions. The results showed that the post-processed printed geopolymer specimens cured in the Na-based solution exhibited higher compressive strength than that of the specimens cured in the K-based solution. This is true regardless of the curing temperature, curing time and loading direction. In addition, the 28-day compressive strength of the ambient-temperature-cured post-processed printed geopolymer samples was comparable to the 7-day compressive strength of the heat-cured samples. This is true regardless of the curing medium and loading direction.

Keywords: Geopolymer · Powder-based 3D printing · 3D concrete printing · Post-processing · 3D printed geopolymer

1 Introduction

In the recent years, several attempts have been made to develop 3D Concrete Printing (3DCP) technology for construction applications owing to its potential use for direct construction of buildings and other complex structures of virtually any shape without the use of expensive formwork. Elimination of the formwork would result in considerable cost savings, as the formwork represents 35% to 60% of the cost of construction of concrete structures. In addition, the elimination of formwork also reduces the number of wastages in construction, thereby improves sustainability in construction, since the formwork represents a significant source of waste as all of it is discarded sooner or later [1]. Currently, two different 3DCP techniques, namely extrusion-based

V. Mechtcherine et al. (Eds.): RheoCon 2019/SCC 2019, RILEM Bookseries 23, pp. 417–425, 2020.
https://doi.org/10.1007/978-3-030-22566-7_48

and powder-based techniques have been explored in the construction industry. The authors of this paper have recently developed several 3D printable geopolymer formulations suitable for extrusion-based 3DCP applications [2–6].

The powder-based 3DCP is an off-site process designed for manufacturing precast components. This method is capable of producing building components with complex and intricate shapes. Figure 1(a) schematically illustrates the powder-based 3DCP process. First, a thin layer of powder is spread over the powder bed surface. Subsequently, binder droplets are selectively applied on the powder layer by a print-head, causing powder particles to bind to each other. Repeating the described steps, the built part is completed and removed after a certain drying time. Finally, unbound powder is removed by using an air blower.

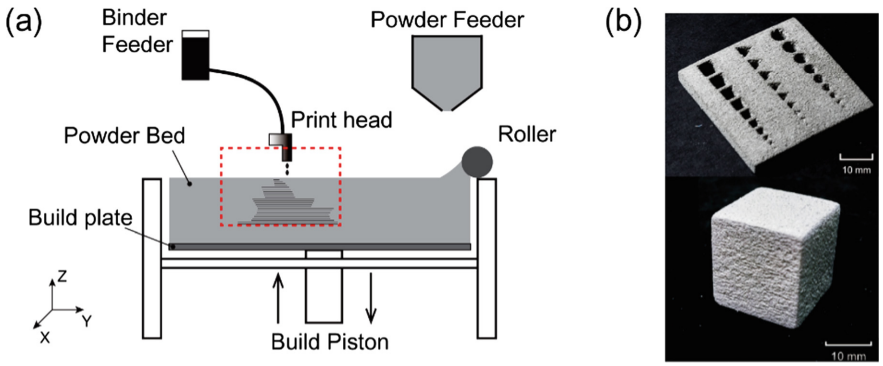

Fig. 1. (a) Schematic illustration of the powder-based 3DCP process, (b) 3D printed geopolymer specimens.

Although the powder-based 3DCP technique can offer several advantages in the construction industry, there are a number of challenges to be overcome before the technique is fully utilized. One of the main challenges is that the proprietary printing materials that are typically used in the commercially available powder-based 3D printers are not suitable for the construction applications. To tackle this limitation, the authors of this study have been working on developing innovative methodologies for formulating conventional Portland cement/ geopolymer based materials which can be used in the commercially available powder-based 3D printers for construction applications. Geopolymer is a sustainable alternative to conventional Portland cement. It is synthesized by alkaline activation of fly ash and/or slag, being industrial by-products of coal power stations and iron manufacture, respectively. The authors of this paper have recently developed several slag/fly ash-based geopolymer formulations suitable for powder-based 3DCP applications [7–11].

The strength of powder-based 3D printed Portland cement/geopolymer specimens immediately after completion of the de-powdering process, often referred to as “green” strength, is typically very low due to the inherent high porosity of the powder bed, which is not suitable for construction applications. Therefore, further post-processing methods are required to enhance the “green” strength of the 3D printed Portland

cement/geopolymer specimens, making them suitable for construction applications. In the authors' previous study [12], different heat curing regimes have been used to enhance the "green" strength of the powder-based 3D printed geopolymers. However, the developed post-processing method based on the heat curing may limit the in-situ application of the developed powder-based 3D printed geopolymers. Therefore, the first objective of this study is to investigate the effect of curing temperature (heat-curing versus ambient-temperature-curing) on the compressive strength of the powder-based 3D printed geopolymers. Effect of type of activator solution (i.e., curing medium) was not investigated in the authors' previous study [12]. Hence, the second objective of this study is to evaluate the effects of the type of curing medium on the compressive strength of 3D printed geopolymers.

2 Experimental Procedures

2.1 Materials

A printable geopolymer powder previously developed by the authors [9] was used in this study. It was a mixture of slag (supplied by Building Products Supplies Pty Ltd., Australia), silicate-based activator (supplied by Redox Pty Ltd., Australia) and fine silica sand (supplied by TGS Industrial Sands Pty. Ltd., Australia). An aqueous solvent (Zb® 63, Z-Corp, USA) was used as a liquid binder for the powder-based 3DCP process. Further details regarding the preparation of the printable geopolymer powder and the liquid binder can be found in [9].

Two different sodium (Na)-based and potassium (K)-based activator solutions were used as the curing mediums. The Na-based activator solution (denoted as "Na-solution") was composed of Na_2SiO_3 solution (71.4% w/w) and NaOH solution (28.6% w/w). The Na_2SiO_3 solution was N Grade with a modulus (M_s) of 3.22 (where M_s = SiO_2/ Na_2O, Na_2O = 8.9 wt% and SiO_2 = 28.6 wt%, balance H_2O). The NaOH solution was prepared with a concentration of 8.0 M using NaOH beads of 97% purity and tap water. The K-based activator solution (denoted as "K-solution") was composed of potassium silicate (K_2SiO_3) solution (71.4% w/w) and potassium hydroxide (KOH) solution (28.6% w/w). The K_2SiO_3 solution was KASIL 2236 Grade with a modulus (M_s) of 2.22 (where M_s = SiO_2/ K_2O, K_2O = 11.0 wt% and SiO_2 = 24.5 wt%, balance H_2O). The KOH solution was prepared with a concentration of 8.0 M using KOH flakes of 90% purity and tap water.

It should be noted that in the authors' previous study [12], tap water was used as the curing medium. The result showed that the compressive of the printed samples immersed in tap water at 60 °C for 7 days was only 2.2 MPa, which was due to the low presence of OH^- ions in tap water, causing inefficient dissolution and formation of hydroxyl species and oligomers. Therefore, the polymerization or condensation reaction could not be established properly leading to the low compressive strength. Thus, tap water is not an effective curing medium for post-processing of 3D printed geopolymers.

2.2 3D Printing of Geopolymer Specimens

In this study, 20 mm × 20 mm × 20 mm cubic geopolymer specimens were printed using ZPrinter® 150. The ZPrinter® 150 is a commercial powder-based 3D printer manufactured by Z-Corp, USA with a specific resolution of 300 × 450 dpi, a build volume of 182 mm × 236 mm × 132 mm, and a build speed of 2–4 layers/minute. The printed samples were left undisturbed within the powder bed of the printer at room temperature for 2 h and then unbound powder was removed using compressed air. Further details of ZPrinter® 150 and the printing process can be found in [9].

2.3 Post-processing and Testing Methods

After the de-powdering process, the printed cubes were divided into two groups denoted as "heat-curing" and "ambient-temperature-curing". For the "heat-curing" group, the printed cubes were immersed in the two curing mediums inside separate containers. Details of the curing mediums are given in Sect. 2.1. The containers were sealed and placed in an oven at 60 °C ± 3 °C for 7 days. After completion of the heat curing period, the containers were removed from the oven and the heat-cured samples were taken out from the curing mediums and kept undisturbed until become cool and dry. For the "ambient-temperature-curing" group, the printed samples were similarly immersed in the two curing mediums, but the sealed containers were kept at ambient temperature (23 °C ± 3 °C) for 7 and 28 days. At the end of the curing period, the ambient-temperature-cured samples were taken out from the curing mediums and kept undisturbed until become dry. The heat-cured specimens were tested at 7 days, while the ambient-temperature-cured samples were tested at 7 and 28 days. The compressive strengths in both X-direction (i.e., the binder jetting direction) and Z-direction (i.e., layer stacking direction) were measured under load control at the rate of 0.33 MPa/s. A population of 10 samples for each testing direction was used.

3 Results and Discussions

3.1 Heat-Curing

Figure 2 shows the 7-day compressive strength of the heat-cured printed samples in two loading directions. The error bars in the presented results are based on 95% confidence level and the numerical values on top of the bars are the mean strengths. The 7-day compressive strength of the printed specimens cured in the "Na-solution" was about 26%–31% higher than that of the specimens cured in the "K-solution", depending on the testing direction. This may be attributed to several factors, such as the modulus and ion size of the activator. The modulus (molar ratio of SiO_2 to Na_2O) of the "Na-solution" is 1.74, while the modulus (molar ratio of SiO_2 to K_2O) of the "K-solution" is 1.56. Therefore, according to Xu and Van Denventer [13], a higher extent of dissolution is expected for the samples cured in the "Na-solution" than in the "K-solution", leading to the higher strength of the Na-based cured samples. The smaller ionic size of Na^+ than K^+ also favors the ionic pair reaction with the smaller silicate

oligomers, thus enhancing the bond strength, which in turn improves the strength of the Na-based cured samples [13].

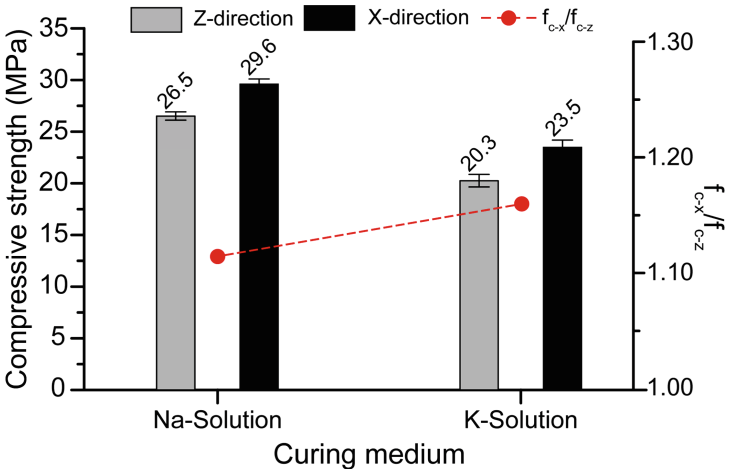

Fig. 2. The 7-day compressive strength of the heat-cured 3D printed geopolymer samples. Note: f_{c-x}/f_{c-z} shows the ratio of compressive strength in X-direction to the compressive strength in Z-direction.

As shown in Fig. 2, an anisotropic phenomenon was observed in the compressive strength of the printed geopolymers depending on the loading directions. The compressive strength was always higher in the X-direction than in the Z-direction, regardless of type of the curing medium. The observed anisotropic phenomenon may be related to bond strength between the layers. According to Lowke et al. [14], the water content in the green samples significantly oscillates in accordance with a higher water content in the top region of the layer and a significantly lower content in the bottom region. Thus, the inter-layer water gradient will cause a weak bond between the layers. As shown in Fig. 2, the f_{c-x}/f_{c-z} (i.e. the ratio of compressive strength in X-direction to the compressive strength in Z-direction) was 1.12 for the "Na-solution" cured specimens, and the f_{c-x}/f_{c-z} increased to 1.16 for the "K-solution" cured specimens. Therefore, it can be said the anisotropic behavior was more pronounced in the "K-solution" cured specimens than in the "Na-solution" cured samples.

3.2 Ambient-Temperature-Curing

Figure 3 shows the 7-day and 28-day compressive strengths of the ambient-temperature-cured samples. The error bars in the presented results are based on 95% confidence level and the numerical values on top of the bars are the mean strengths. Similar to the heat-cured specimens (Fig. 2), the compressive strength of the ambient-temperature-cured printed specimens cured in the "Na-solution" was about 14%–29% higher than that of the specimens cured in the "K-solution", depending on the testing

direction and age of testing. The reason for the higher strength of the "Na-solution" cured specimens compared to the "K-solution" cured specimens is explained in Sect. 3.1.

For the ambient-temperature-cured specimens, the compressive strength exhibited similar anisotropic behavior, depending on the testing direction. The compressive strength was always higher in the X-direction than in the Z-direction, regardless of the curing medium and curing time. For the "Na-solution" cured specimens, the f_{c-x}/f_{c-z} decreased from 1.12 to 1.10 (from 7 days to 28 days), and for the "K-solution" cured specimens, the f_{c-x}/f_{c-z} decreased from 1.24 to 1.22 (from 7 days to 28 days). It is necessary to note that the "K-solution" introduced significantly higher anisotropic behavior in the compressive strength results as compared to the "Na-solution". It is also worth noting that the increase of age of specimen (from 7 days to 28 days) slightly (less than 10%) reduced the observed anisotropic behavior in the compressive strength results.

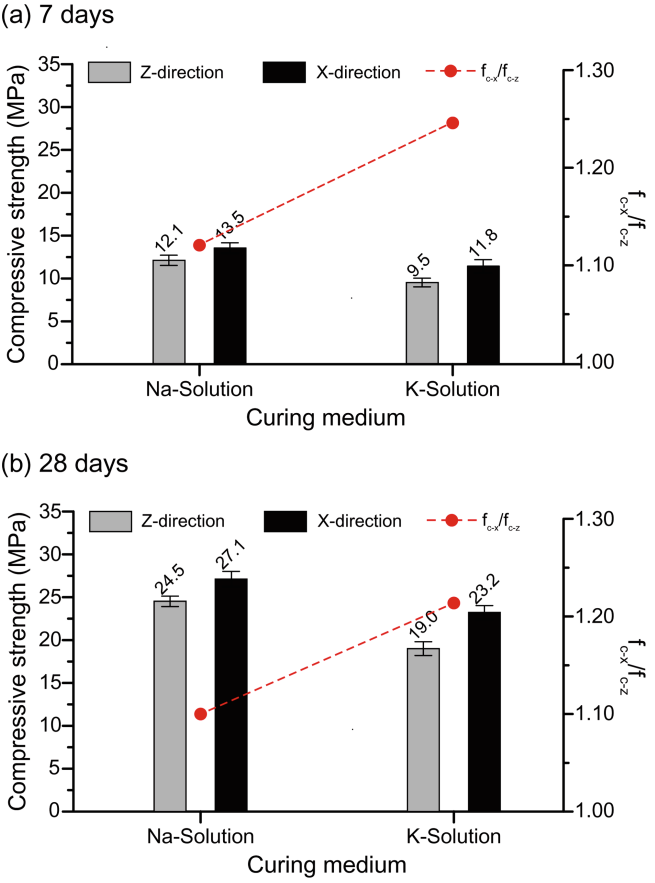

Fig. 3. The compressive strength of the ambient-temperature-cured 3D printed geopolymers at (a) 7 days and (b) 28 days. Note: f_{c-x}/f_{c-z} shows the ratio of compressive strength in X-direction to the compressive strength in Z-direction.

As can be seen in Fig. 3, the 28-day compressive strength of the ambient-temperature-cured printed samples was almost twice as high as the 7-day compressive strength. This is true regardless of the testing direction and curing medium. This significant increase is due to the continued geopolymerisation process in the presence of the alkaline activator solution. A similar result was reported for the conventionally mold-casting geopolymers, where the longer curing time increased the compressive strength [15, 16].

Comparison between Fig. 3(b) and Fig. 2 showed that the 28-day compressive strength of the ambient-temperature-cured samples was up to 8% lower than the 7-day compressive strength of the heat-cured samples. This established the feasibility of the newly developed post-processing method based on the ambient-temperature curing for enhancing the strength of powder-based 3D printed geopolymers, which requires significantly less energy, yet provides comparable strength compared to the post-processing method based on the heat-curing. At the same time, it enhances the in-situ and broader applications of the developed powder-based 3D printed geopolymers in the construction industry as compared to the post-processing method based on the heat-curing.

4 Conclusions

This study investigated the effects of different curing mediums, curing temperatures, curing times, and loading directions on the compressive strength of the digitally fabricated geopolymers using the powder-based 3D printing process. The results established the feasibility of enhancing the strength of powder-based 3D printed geopolymers by curing in the alkaline solutions at the ambient-temperature, which is more viable and less energy-intensive as compared to the curing at elevated temperature. The newly developed post-processing method at ambient-temperature promotes wider applications of the developed powder-based 3D printed geopolymers in the construction industry. The following specific conclusions are drawn:

(1) The compressive strength of the printed geopolymers cured in the Na-based alkaline solution was about 14%–31% higher than that of the specimens cured in the K-based solution, depending on the curing temperature, curing time and loading direction.
(2) An anisotropic phenomenon was observed in the compressive strength of the printed geopolymers, depending on the loading directions. The compressive strength in X-direction was always higher than in Z-direction. This is true regardless of the curing temperature, curing medium and curing time. However, the curing in the K-based solution introduced significantly higher anisotropic behavior in the compressive strength of the printed geopolymers as compared to the curing in the Na-based solution.
(3) The 28-day compressive strength of the ambient-temperature-cured printed geopolymers was almost twice as high as the 7-day compressive strength. This is true regardless of the testing direction and curing medium.
(4) (a) The 7-day compressive strength of the ambient-temperature-cured printed geopolymers was about 50%–54% lower than the 7-day compressive strength of the heat-cured printed geopolymers. The significantly higher 7-day strength of the

heat-cured samples is due to the higher reaction rate of geopolymer at elevated temperature as compared to the ambient temperature. (b) However, the 28-day compressive strength of the ambient-temperature-cured printed geopolymers was comparable to the 7-day compressive strength of the heat-cured printed geopolymers. Both (a) and (b) are true regardless of the curing medium and testing direction.

References

1. Nematollahi B, Xia M, Sanjayan J (2017) Current progress of 3D concrete printing technologies, ISARC. In: Proceedings of the international symposium on automation and robotics in construction, Vilnius Gediminas Technical University, Department of construction economics & property, Taipei, pp 260–267
2. Nematollahi B, Xia M, Sanjayan J, Vijay P (2018) Effect of type of fiber on inter-layer bond and flexural strengths of extrusion-based 3D printed geopolymer. In: Materials science forum, vol 939. Trans Tech Publ, pp 155–162
3. Nematollahi B, Praful V, Sanjayan J, Nazari A, Xia M, Naidu Nerella V, Mechtcherine V (2018) Effect of polypropylene fiber addition on properties of geopolymers made by 3D printing for digital construction. Materials 11(12):2352
4. Bong SH, Nematollahi B, Nazari A, Xia M, Sanjayan J (2019) Method of optimization for ambient temperature cured sustainable geopolymers for 3D printing construction applications. Materials 12(6):902
5. Bong SH, Nematollahi B, Sanjayan J, Xia M, Nazari A (2018) Fresh and hardened properties of 3D printable geopolymer cured in ambient temperature. RILEM international conference on concrete and digital fabrication, vol 19. RILEM Bookseries. Springer, Cham, pp 3–11
6. Nematollahi B, Xia M, Sanjayan BS-HJ (2018) Hardened properties of 3D printable 'one-part' geopolymer for construction applications. RILEM international conference on concrete and digital fabrication, vol 19. RILEM Bookseries. Springer, Cham, pp 190–199
7. Xia M, Nematollahi B, Sanjayan J (2019) Printability, accuracy and strength of geopolymer made using powder-based 3D printing for construction applications. Autom Constr 101:179–189
8. Xia M, Sanjayan J (2017) Post-processing methods for improving strength of geopolymer produced using 3D printing technique. In: ICACMS. international conference on advances in construction materials and systems, Chennai
9. Xia M, Sanjayan J (2016) Method of formulating geopolymer for 3D printing for construction applications. Mater Des 110:382–390
10. Xia M, Nematollahi B, Sanjayan J (2018) Compressive strength and dimensional accuracy of Portland cement mortar made using powder-based 3D printing for construction applications. RILEM international conference on concrete and digital fabrication, vol 19. RILEM Bookseries. Springer, Cham, pp 245–254
11. Xia M, Nematollahi B, Sanjayan J (2018) Influence of binder saturation level on green strength and dimensional accuracy of powder-based 3D printed geopolymer. In: Materials science forum, vol 939. Trans Tech Publ, pp 177–183
12. Xia M, Sanjayan J (2018) Methods of enhancing strength of geopolymer produced from powder-based 3D printing process. Mater Lett 227:281–283
13. Xu H, Van Deventer J (2000) The geopolymerization of alumino-silicate minerals. Int J Miner Process 59:247–266

14. Lowke D, Dini E, Perrot A, Weger D, Gehlen C, Dillenburger B (2018) Particle-bed 3D printing in concrete construction-possibilities and challenges. Cem Concr Res 112:50–65
15. Nematollahi B, Sanjayan J, Shaikh FUA (2015) Synthesis of heat and ambient cured one-part geopolymer mixes with different grades of sodium silicate. Ceram Int 41:5696–5704
16. Wongsa A, Sata V, Nematollahi B, Sanjayan J, Chindaprasirt P (2018) Mechanical and thermal properties of lightweight geopolymer mortar incorporating crumb rubber. J Cleaner Prod 195:1069–1080

Rheology and Structural Rebuilding of One-Part Geopolymer Mortar in the Context of 3D Concrete Printing

Biranchi Panda(✉), Nisar Ahamed Noor Mohamed, and Ming Jen Tan

Singapore Centre for 3D Printing,
School of Mechanical and Aerospace Engineering,
Nanyang Technological University, Singapore, Singapore
biranchi001@e.ntu.edu.sg

Abstract. The employment of automation in construction has not yet reached its full potential. 3D concrete printing is one of the promising construction techniques which has drawn a lot of attention due to its unique benefit in terms of higher productivity, faster construction processes, geometrical freedom, and cost-efficiency. With the number of 3D printing projects increasing rapidly, the demand for accurate measurement of concrete fresh property is also increasing. Therefore, in this paper rheology and structural rebuilding properties are investigated to understand printability and buildability attributes of one-part geopolymer mixtures. A custom made geopolymer binder was designed for extrusion-based 3D printing and the fresh geopolymer was tested in different resting time to reveal the structural rebuilding property via measurement of compressive green strength. The material test result shows that the green strength increases with fresh concrete age, as does the static yield strength.

Keywords: 3D printing · Geopolymer · Rheology and structural rebuilding

1 Introduction

With increase in technological advancements, automation in the construction industry is becoming more common, as illustrated by advanced prefab, precast technologies and more recently, by the digital construction (DC) process which is commonly known as 3D concrete printing (3DCP) [1, 2]. In the construction practice, digital design using computer-aided design (CAD), building information modelling (BIM) tools are already well developed and the step from designing to digital manufacturing is now benefiting higher productivity, faster construction processes, higher geometrical freedom, efficient use of raw materials, etc. The most widespread approach of 3DCP is the contour crafting method [3], where contours of any vertical elements are produced by extruding concrete filaments in a layer with a print head linked to concrete pump. Since the print head gradually builds up the complete structure, it is thus feasible to vary the composition and filament direction according to specific local requirements. A schematic diagram of 3DCP process at NTU, Singapore is shown in Fig. 1 [4].

V. Mechtcherine et al. (Eds.): RheoCon 2019/SCC 2019, RILEM Bookseries 23, pp. 426–431, 2020.
https://doi.org/10.1007/978-3-030-22566-7_49

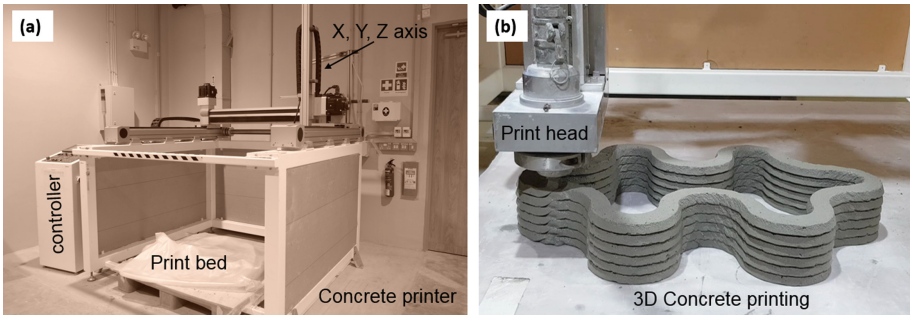

Fig. 1. (a) 4-axis concrete gantry printer, (b) 3D concrete printing (3DCP) process.

Despite a steadily growing number of researchers and private enterprises active in this field, 3DCP is still in its infancy. Fundamental scientific understanding of the relations between design, material and process is slowly evolving while the material formulation has been highly explored in the literature [5–7], describing printable properties such as extrudability, open time and buildability. Building materials with a high yield strength and low viscosity are usually preferred in 3DCP, where the yield stress is linked to the shape retention and buildability characteristics and viscosity is an indication of the ease of mortar extrusion. The main challenge exists in controlling the structuration rate of the material without disturbing its flow properties so that the extruded layers can be deposited in a layer-by-layer manner [8].

Although the use of two-part geopolymer systems has been studied previously [4, 9], no detailed studies on the use of one-part geopolymers in 3D printing have been reported until now. Therefore, this paper aims to study the formulation of one-part geopolymers and provide an assessment of their fresh properties in terms of thixotropy and structural rebuilding to evaluate the 3D printability performance.

2 Materials and Methods

Class F fly ash (FA) conforming to ASTM C618 and ground granulated blast furnace slag (GGBS), supplied by EnGro Corporation Ltd. (Singapore) were used to prepare printable one-part geopolymer binder according to the author's previous study [9]. Other than FA and GGBS, the solid alkaline activator used in this study was prepared by blending potassium silicate powder (49.50 wt% SiO_2, 42.54 wt% K_2O and remaining H_2O) together with potassium hydroxide (KOH) powder to reach the desired modulus (MR) of 1.5 [10]. For the preparation of geopolymer mortars, fine river sand with a maximum particle size of 1.18 mm was used along with tap water (0.35 water-to-binder ratio). Geopolymer was prepared by dry mixing FA: GGBS (70:30 by mass) with silicate powder and sand in an 8-L Hobart laboratory mixer. 0.10 activator-binder ratio and 0.85 aggregate-to-binder ratio was maintained for smooth extrusion of geopolymer through a rectangular nozzle, as described in [9].

To obtain the static yield stress, stress growth test was performed by applying deformation at a constant shear rate of 0.1 s^{-1}. During this test, the shear stress

progressively developed to a maximum value and then stabilized at an equilibrium value. The static yield stress was defined as the peak shear stress value. In this study, thixotropy was measured via viscosity recovery test by applying different shear rates of (i) 0.01 s^{-1} for 60 s, (ii) 300 s^{-1} for 30 s and (iii) 0.01 s^{-1} for 60 s at three different time intervals corresponding to the material state (i) initially at rest, (ii) shearing/extrusion and (iii) again at rest, as used in previous studies [11]. The apparent viscosities were measured during these three intervals to understand the recovery behaviour of the different geopolymer mixes.

Uniaxial unconfined compression tests were performed on cylindrical samples with 70 mm diameter and 140 mm height to measure the green strength as described in [12]. Each test was conducted close to 60–70 s to neglect effects of thixotropic build-up and their average values were presented in terms of force and displacement (F-d) diagram. In this paper, we have used the custom made four axis gantry printer (see Fig. 1(a)) that can print concrete components of one cubic meter volume. During printing, the printer speed and pump flow rate were optimized to ensure continuous flow and good shape retention of the extrudates.

3 Results and Discussion

Figure 2(a) shows the yield stress of the geopolymer mortar, which is sufficient enough (>200 Pa) for shape retention of the extruded geopolymer, as confirmed in Fig. 2(c). The geopolymer behaves as shear thinning fluid since the apparent viscosity decreases with increasing shear rate (Fig. 2(b)) and this is the most common behaviour of non-Newtonian fluids. Such high yield stress and low viscosity properties of the geopolymer seems to be an excellent combination for 3DCP application. The high yield stress enables the material to maintain the shape of the extrudates same as nozzle diameter, while the low viscosity is helpful for ease of extrusion without significant issue of clogging or discontinuity in the flow.

Apart from yield stress and viscosity, thixotropy of the printable materials is an important attribute which is quantified in terms of viscosity recovery in this paper. Viscosity recovery compares and indicates the viscosity recover ability of the material *before*, *during* and *after* the extrusion process. Figure 3 shows the recovery plot of the printable one-part geopolymer used in this study. Due to van der Waals force of attraction one-part geopolymer possesses excellent thixotropy and is able to recover 40%–50% of the original viscosity in stage (III) compared to the material at rest in stage (I). The importance of viscosity recovery can be visualized in terms of good shape retention since some building materials are unable to recover its original viscosity due to lack of thixotropy and flocculation phenomena.

Following thixotropy, measurement of structural rebuilding [13] is needed for estimating buildability of the printable geopolymer. In this paper, compressive green strength is used to reveal material rebuilding or hardening rate which happens due to flocculation and chemical reaction (poly-condensation) [14]. The typical force-displacement (F-d) curves are shown in Fig. 4(a) for concrete age t = 5 to 60 min. It is clearly observed that the load initially increases approximately linearly as the vertical displacement increases. After this initial path, the increment of loading decreases as

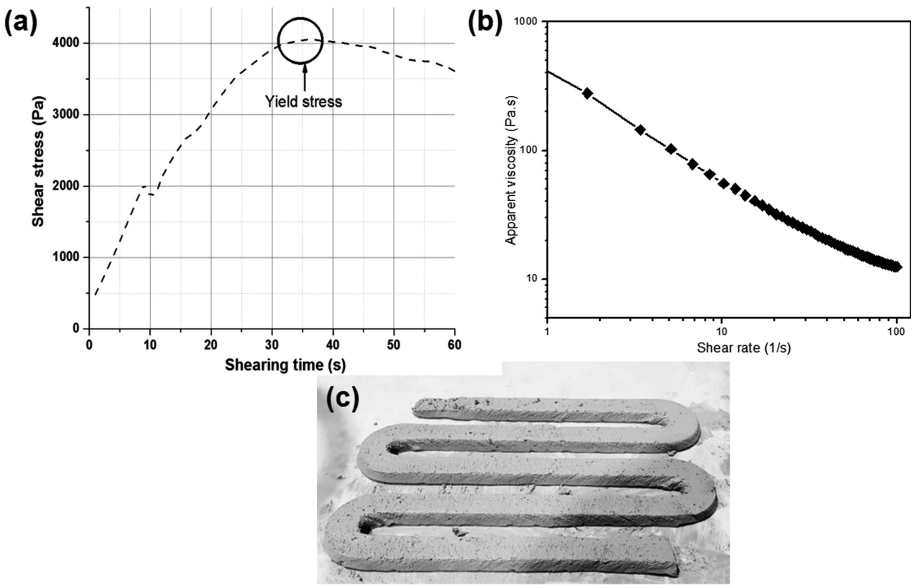

Fig. 2. (a) Static yield stress, (b) shear thinning and (c) continuous extrusion of one-part geopolymer mortar.

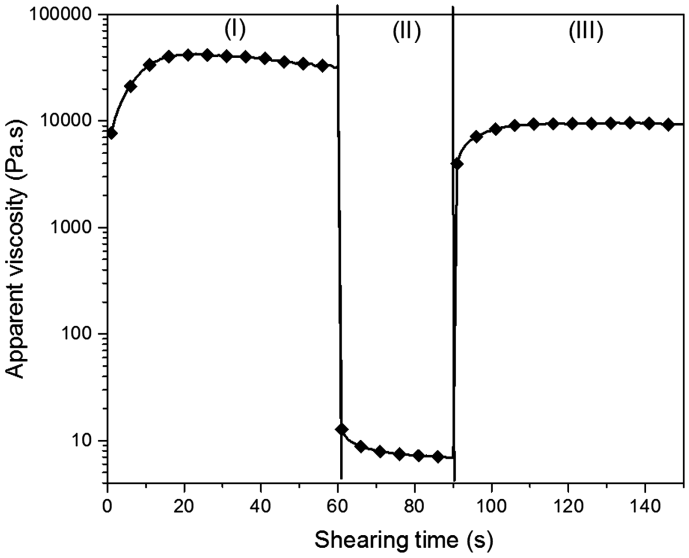

Fig. 3. Viscosity recovery of one-part geopolymer mortar.

deformations grow. The younger specimens (i.e. t = 5 min) show an increment in load with increasing deformations, up to a certain plateau. The older specimens (i.e. t = 60 min), on the other hand, show a load decrease after the initial peak, again to a certain limit. This difference in behaviour is attributed to different material failure because a distinct failure plane is observed for older samples whereas younger samples fail by "barreling" effect as shown in Fig. 4(b). The F-d diagram shows material load bearing capacity with different resting time however the strength development mechanism remains unclear. We found that in conventional liquid based geopolymer, the early age strength development is mostly due to rapid reaction product formation [14], but in the case of one-part geopolymer, it can be attributed to the combined effect of thixotropy and geopolymer reaction. The main difference between the strength development by thixotropy and rigidification (hardening by reaction) is that thixotropy effect can be easily break down by shearing action whereas rigidification is a permeant effect.

Therefore, despite high yield stress (stiffness) the developed one-part geopolymer was suitable for extrusion-based printing even after 30 minutes since initially it exhibits thixotropic effect but later due to material rigidification, the geopolymer mortar was not extrudable. This rapid hardening behaviour is well suited for large scale concrete printing without the need of any chemical accelerators.

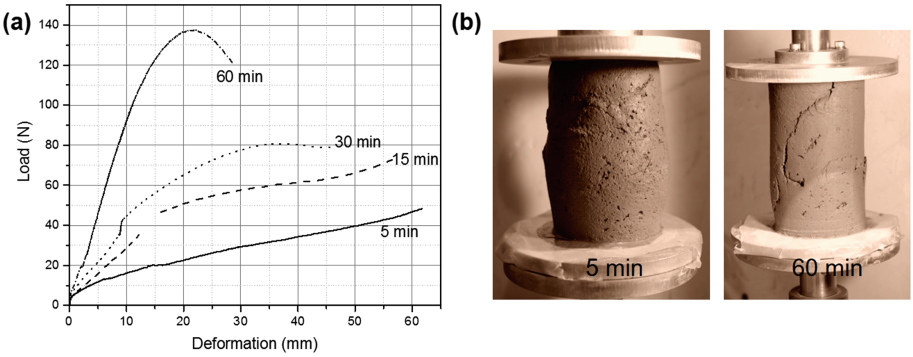

Fig. 4. (a) Force-displacement curve and (b) failure patterns of one-part geopolymer mortar.

4 Conclusions

In this paper, for the first time one-part geopolymer mortar is characterized for extrusion-based 3D concrete printing application. The extruded geopolymer exhibits high yield stress and shear thinning behaviour, thus making it as an ideal material for concrete printing. Thixotropy of the geopolymer, measured in terms of viscosity recovery reveals 40%–50% recovery ability which is reflected in terms of shape retention of the filaments deposited on the print bed. From the experimental results of green compressive strength, the printable (one-part) geopolymer was found to be extrudable till 30–45 min from the time of mixing with the activator.

References

1. Tay YWD, Panda B, Paul SC, Noor Mohamed NA, Tan MJ, Leong KF (2017) 3D printing trends in building and construction industry: a review. Virtual Phys Prototyp 12(3):261–276
2. Ogura H, Nerella V, Mechtcherine V (2018) Developing and testing of strain-hardening cement-based composites (SHCC) in the context of 3D-printing. Materials 11(8):1375
3. Khoshnevis B, Yuan X, Zahiri B, Zhang J, Xia B (2016) Construction by Contour Crafting using sulfur concrete with planetary applications. Rapid Prototyp J 22(5):848–856
4. Panda B, Unluer C, Tan MJ (2018) Investigation of the rheology and strength of geopolymer mixtures for extrusion-based 3D printing. Cement Concr Compos 94:307–314
5. Buswell RA, de Silva WL, Jones SZ, Dirrenberger J (2018) 3D printing using concrete extrusion: a roadmap for research. Cem Concr Res 112:37–49
6. Hojati M, Radlińska A, Nazarian S, Pinto Duarte J, Memari AM, Meisel N, Bilén S (2018) Synthesis and 3D printing of one-part geopolymer mortar. In: 1st RILEM international conference on concrete and digital fabrication, Zurich, Switzerland
7. Nematollahi B, Xia M, Bong SH, Sanjayan, J (2018) Hardened properties of 3D printable 'one-part'geopolymer for construction applications. In: RILEM international conference on concrete and digital fabrication. Springer, Cham, pp 190–199
8. Roussel N (2018) Rheological requirements for printable concretes. Cem Concr Res 122:76–85
9. Panda B, Singh GB, Unluer C, Tan MJ (2019) Synthesis and characterization of one-part geopolymers for extrusion-based 3D concrete printing. J Clean Prod 220:610–619
10. Davidovits J (2008) Geopolymer chemistry and applications. Geopolymer Institute
11. Panda B, Ruan S, Unluer C, Tan MJ (2019) Improving the 3D printability of high-volume fly ash mixtures via the use of nano attapulgite clay. Compos B Eng 165:75–83
12. Panda B, Hui LJ, Tan MJ (2019) Mechanical properties and deformation behaviour of early age concrete in the context of digital construction. Compos B Eng 165:563–571
13. Reiter L, Wangler T, Roussel N, Flatt RJ (2018) The role of early age structural build-up in digital fabrication with concrete. Cem Concr Res 112:86–95
14. Steins P, Poulesquen A, Diat O, Frizon F (2012) Structural evolution during geopolymerization from an early age to consolidated material. Langmuir 28(22):8502–8510

Rheology of Fresh Concrete: Historical Perspective and Glance in the Future

Surendra P. Shah[1,2(✉)] and Jae Hong Kim[3]

[1] Department of Civil and Environmental Engineering, Northwestern University, Evanston, IL, USA
s-shah@northwestern.edu
[2] Center for Advanced Construction Materials, University of Texas at Arlington, Arlington, TX, USA
[3] Department of Civil and Environmental Engineering, Korea Advanced Institute of Science and Technology, Daejeon, Republic of Korea
jae.kim@kaist.ac.kr

Abstract. Conventional casting and placement of concrete involves fragmented tasks such as reinforcement arrangements, formwork assembling and dismantling later, and concrete pouring. Recent study on the automation in construction reports that the fragmented construction can be possibly replaced by continuous operations such as 3D printing. The use of continuous operations can reduce the time of construction and consequently construction expenses. Control of the rheology of fresh cement-based materials is the key technology to realize the continuous casting of cement-based materials. Various precursors of 3D printing are summarized, and basic understanding toward the continuous casting is provided in terms of the rheology.

Keywords: 3D printing · Slipform · Extrusion · Viscosity

1 Introduction

Automation in construction industry is essential to improve its efficiency in time and finance. Difficult tasks to be manually handled can be also accomplished with an automated machine in construction. Among them, the continuous casting of cement-based materials is one of the promising technologies. The continuous casting potentially (1) eliminates need for formwork; (2) increases the rate of construction; (3) increases design freedom; and (4) makes the quality less vulnerable to human error.

2 Additive Manufacturing

The continuous operation of cement-based materials has been used for fiber reinforced cementitious composite board. Those application include Hatschek processing for asbestos (now cellulose and polyvinyl alcohol) fiber-cement composite sheets and spray-suction technique with short glass fiber reinforcement. Figure 1 shows a schematic of the Hatschek processing [1]. A slurry-form cement-based material together with cellulose fibers is supplied on screens passing through multiple bins. A conveyor

V. Mechtcherine et al. (Eds.): RheoCon 2019/SCC 2019, RILEM Bookseries 23, pp. 432–439, 2020.
https://doi.org/10.1007/978-3-030-22566-7_50

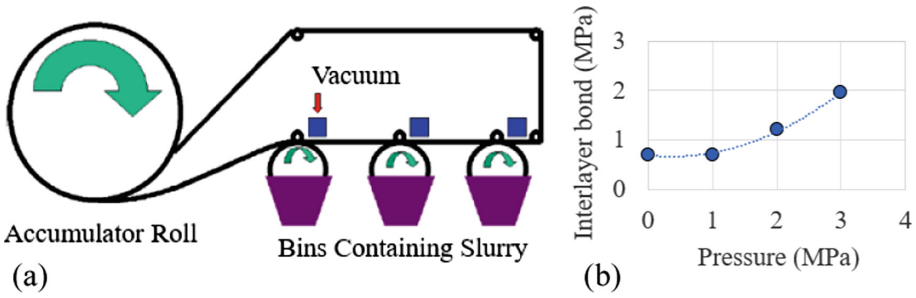

Fig. 1. Hatschek processing: (a) A schematic of the additive manufacturing and (b) external pressure applied to enhance the interlayer bond strength.

belt continues to accumulate a monolayer on the screens until the desired thickness is achieved. The resultant board is therefore a layered cementitious composite board.

The weak interlayer bond between the additive monolayers was a technical issue, which caused delamination and durability problem related to freezing-and-thawing phenomenon. Immediately after the boards were formed, external pressure was applied to enhance the interlayer bond and its mechanical properties [2]. The external pressure induced free water in the slurry-form material to propagate through the interlayer, and the interlayer bonds were homogenized. Figure 1(b) shows the effect of external pressure applied to increase the interlayer bond strength. The research on Hatschek processing gives a demonstration of the weak points and a possible solution of additive manufacturing with cementitious materials.

Slipform construction is one of the widely applied continuous castings. Slipform paving production rates are typically 60 m/h to 90 m/h for the 250 mm thick surface course (slab). The slab needs to keep its original shape without any formwork, and so 'no-slump' concrete is usually fed to the slipform paving machine. Continuously additive paving is homogenized with internal vibrators in the machine as shown in Fig. 2. A powerful vibrating produces a shape-stable slab. However, excessive vibration along the line of the vibrators causes loss of air content, internal bleeding and segregation, where concrete is susceptible to deterioration processes such as freezing-and-thawing damage.

Tailoring the fresh properties of concrete materials eliminates the internal vibrators without sacrificing the homogenization of the additive paving. The use of various additives such as fly ash and nanoclay enabled the continuously additive paving [3, 4]. The concrete was self-consolidating through the slipform processing, and then its shape stability was quickly obtained (by addition of nanoclay) while short forming guides support the stationary mix.

A precision of 3D printing of cement-based materials is extrusion. The extrusion processing (die forming) applies external pressure for the flow of the material as shown in Fig. 3(b). The extrusion material must be formable enough to go through a die and cohesive (that is stiff) enough so as to maintain shape stability after its forming like the slipform paved concrete. Fiber reinforcement is necessary to provide sufficient

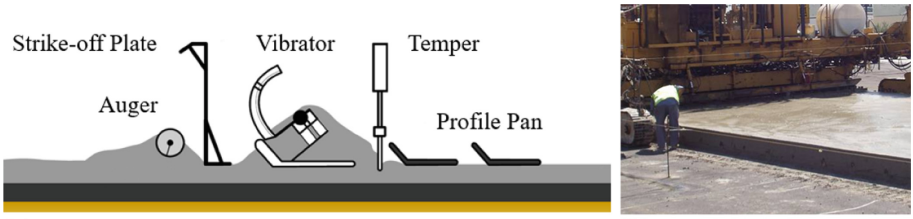

Fig. 2. Slipform paving: (a) A schematic of the operation, ©Steve Muench, Pavement interactive, and (b) the final product.

ductility. Meta cellulose was originally used for composing the fiber reinforced cementitious composites. Incorporating PVA (polyvinyl alcohol) fibers up to 2% made the composites a strain-hardening material, which results in homogenization without macro cracks [5, 6]. Extrusion with nanoclay replacing meta cellulose improved cohesion and consequently homogenization of the extruded materials [7].

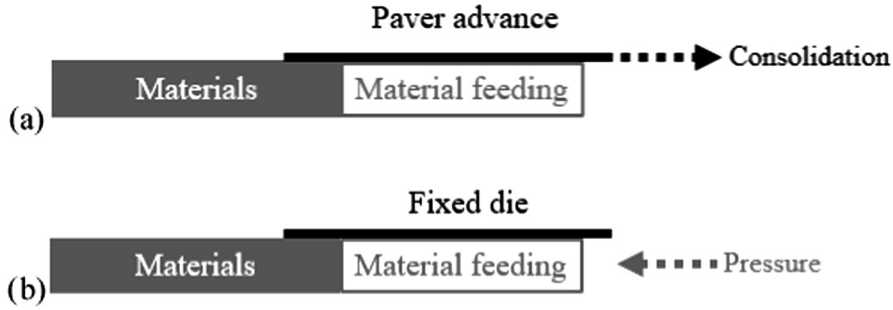

Fig. 3. Schematics of the continuous casting: (a) Slipform paving and (b) extrusion.

Recent advances in 3D printing extend the application of the continuous casting of cement-based materials [8]. Figure 4 shows various examples of the 3D printing by layered extrusion. We need the material to flow with minimum energy; the material

Fig. 4. 3D printing by layered extrusion: (a) Eindhoven University of Technology and (b) Andrey Kudenko, a contractor; and (c) Yingchuang Building Technique (Shanghai) Co., Ltd. (Winsun).

needs to be homogenized; and its shape stability is quickly achieved at rest. A stiffer material is good for the shape stability, but a higher extrusion energy is required. The problem of interlayer homogenization (the weak interlayer bond) arises in addition to a concern of extruding sound continuously additive monolayers. Several tens of minutes can make the interlayer 'cold joint' while the time to receive an overlay depends on the dimension of a structure.

Figure 5(c) shows the other example of 3D printing by slipform processing. The conventional slipform construction has been successfully applied to develop high-rise piers and towers as shown in Fig. 5(b). A slipform incrementally moves up at 25 mm to 30 mm, and the slipformed column grows at 4 m to 8 m per day. The smart dynamic casting reduced the time of casting, and a free-form 4 m high column stood up within 2 h approximately [9]. The continuously additive concrete shows a workability enough to be homogenized, and the concrete at rest takes a quality shape stability to sustain its self-weight [10].

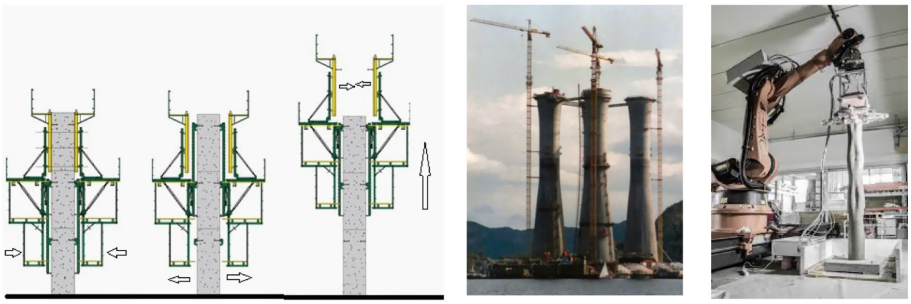

Fig. 5. Slipform processing: (a) slipform construction; (b) off shore oil platform in Norway; and (c) smart dynamic casting of free-form concrete structures - ETH Zürich.

3 Performance and Characterization for the Continuous Casting Materials

The continuous casting of cement-based materials needs delicate control of its workability to shorten the period of the continuous operations. Developing the precise performance requirements depends on the developing processes and machines, but important considerations can be given as follows:

- Flow should be with minimum energy. The flow in an equipment, from a hopper to a nozzle/slipform, needs to be such that no segregation takes place.
- Homogenization on the continuously additive materials and their interlayers is critical.
- Discontinuity such as plastic and autogenous cracking could be prevented by fiber reinforcement and mineral/chemical admixtures. Self-consolidating of the materials is also critical for the slipform processing. Otherwise, external vibration and pressure needs to be applied.

- Shape stability. The form (extruding guide or slipform) for the additive materials is removed within a few minutes. A high degree of thixotropy and cohesion is certainly required to obtain the designed shape of a structure.

Rheology, in particular thixotropy, and cohesion are therefore critical material properties for the continuous casting of cement-based materials. Considerable work has been done to understand the rheology and thixotropy for different applications.

A higher thixotropy of fresh concrete was beneficial for reducing the form pressure (the lateral pressure exerted by fresh concrete). Note the form work pressure is very similar to the pressure exerted by subsequent layers on the previous layer. The use of the pressure response model allows us to understand the thixotropic effect on form pressure [11, 12]. The model defines the lateral pressure response when a unit concrete is subjected to the vertical pressure $\Delta\sigma_V$ at time t'. The instantaneous response ratio β and the delayed response ratio α characterize the dissipation of the lateral pressure,

$$\Delta\sigma_L(t,t') = \alpha(t,t')\beta(t')\Delta\sigma_V(t') \tag{1}$$

as shown in Fig. 6. Water gives 1.0 for the product of α and β, which implies the hydrostatic pressure regardless of time passing. A higher-thixotropic SCC gives a faster decrease in the value of α and β. Their change with time can be linearized by

$$\alpha(t,t') = 1 - a^2 t'(t-t') \tag{2}$$

and

$$\beta(t') = 1 - bt' \tag{3}$$

where a fast decrease in α or β is parameterized with a higher value for instantaneous or delayed parameter, a or b, respectively. The instantaneous response (β) was more significantly affected by the admixtures, and its variation dominated for determining the maximum value of form pressure.

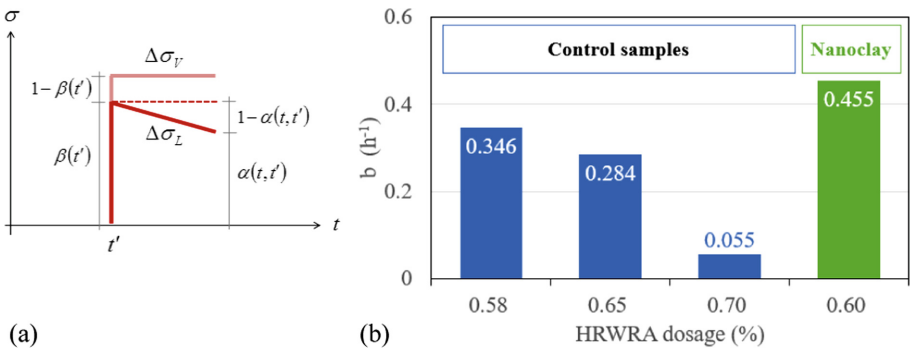

Fig. 6. Analytical model for evaluating form pressure: (a) Pressure response model and (b) the effect of nanoclay.

The form pressure exerted by self-consolidating concrete (SCC) is relatively high and long-lasting compared to ordinary slump-based concrete. Incorporating nanoclay particles accelerated the rate of thixotropy of SCC at rest, which results in a fast dissipation of form pressure [13]. Figure 6(b) shows the effect of the additive. The control mixes showed a lower b with a higher dosage of HRWRA, which indicates a higher form pressure. The small addition (0.33% per cement mass) of nanoclay highly increased the parameter compared with the control mixes.

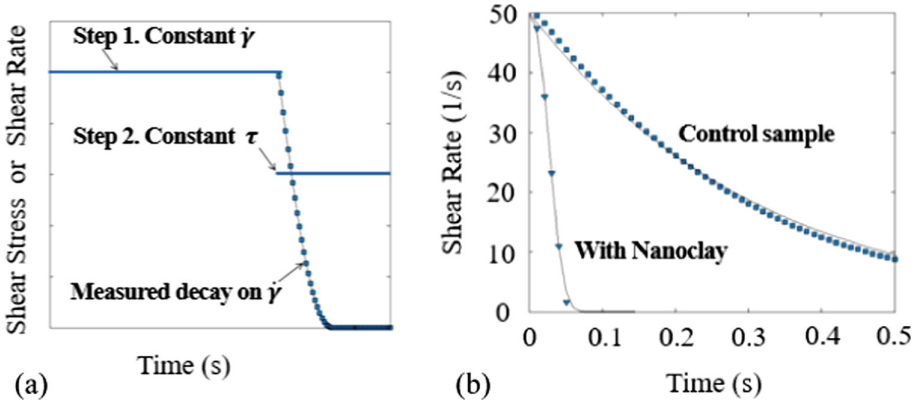

Fig. 7. The shear stress-controlled protocol to characterize the thixotropic rebuilding: (a) Strain rate decay during creep and (b) The effect of nanoclay.

Figure 7 shows the thixotropic behavior of the nanoclay-added pastes, where a rheological protocol was designed to quantitatively evaluate its effect. A constant high shearing was applied into a sample. That may assume the rate of shear strain under pumping. A constant shear stress below the yield stress of a sample was then sustained while the decay in shear rate was measured. The decay implies the rate of structural recovery, and it was fitted well with the following exponential model,

$$\dot{\gamma}(t) = \dot{\gamma}_0 \exp\left(-\left(\frac{t}{\tau}\right)^r\right) \tag{4}$$

where τ is an average relaxation time and r is a dimensionless exponent. For an aqueous mono-dispersed suspension, $r = 1$ with a single relaxation time. A polydisperse colloidal or granular suspension is characterized by a distribution of the relaxation time, and the width of the distribution can be described by r. In many cases, the stretched exponents obtain $0 < r < 1$. A lower relaxation time indicated a higher structural recovery, and the small dosage (0.50% per cement mass) of nanoclay dominated the rheology of the sample as shown in Fig. 7(b).

The thixotropy of cement-based materials is explained by cement flocculation. A larger flocculated-particles network in a suspension increase its viscosity. Separation of flocculated particles by shearing the suspension brings an opposite result. Flocculation of cement particles could be observed by a laser backscattering technique. The dimensional information of suspended cement particles was obtained at a controlled rate of shear strain [14]. Flocculation was observed at a low rate of shear strain (1 s^{-1} with 35 mm parallel-plates geometry), as shown in Fig. 8, while deflocculation of the replicated sample was observed at a high rate. In addition, it was also found that the cement flocculation (within short time period) can be reversible: Repeated change of shear rate test, with considerable duration of each step, reported a stable-reversible floc size at a certain shear rate [15]. The stable floc size was much higher than the mean size of cement particle, measured by the conventional laser diffraction. The reversibility of flocculation and resultant thixotropy are essential for the homogenization on the continuously additive materials. A higher flocculation with the use of the nanoclay was also reported in a separate study [16].

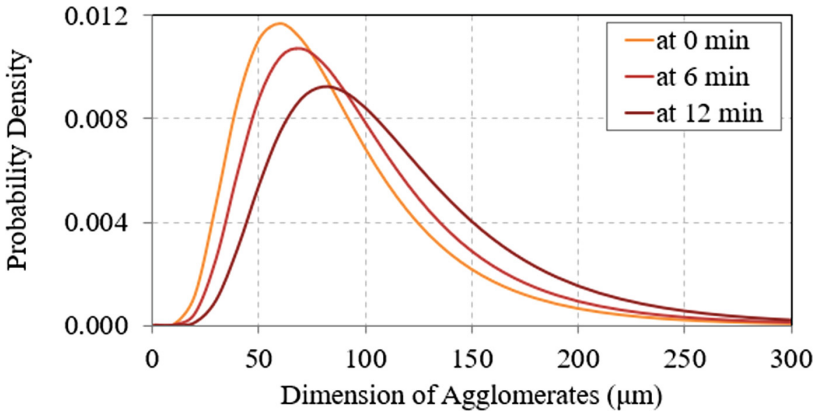

Fig. 8. Cement flocculation at a low rate of shear strain.

4 Conclusions

The continuous casting of cement-based materials does not use the conventional formwork system. Formwork and concrete placement are replaced by additive manufacturing (casting), and as a result the time of casting is dramatically shortened. The thixotropy is one of the contributions to the shape stability of extruded/slip-formed concrete while stiffening by the cement hydration contributes to its strength development later. Understanding and characterizing the thixotropy and other factors influencing the development of shape (or green strength) have been considered critical in the development of 3D printing.

References

1. Kuder KG, Shah SP (2009) Importance of processing in advanced cement-based products. American Concrete Institute, ACI Special Publication, pp 1–16
2. Kuder KG, Shah SP (2003) Effects of pressure on resistance to freezing and thawing of fiber-reinforced cement board. ACI Mater J 100:463–468
3. Pekmezci BY, Voigt T, Kejin W, Shah SP (2007) Low compaction energy concrete for improved slipform casting of concrete pavements. ACI Mater J 104:251–258
4. Shah SP, Pakula M, Tregger N (2010) Influence of micro- and nanoclays on fresh state of concrete. Transp Res Rec J Transp Res Board 2141:68–74
5. Shao Y, Shah SP (1997) Mechanical properties of PVA fiber reinforced cement composites fabricated by extrusion processing. ACI Mater J 94:555–563
6. Shao Y, Qiu J, Shah SP (2001) Microstructure of extruded cement-bonded fiberboard. Cem Concr Res 31:1153–1161
7. Kuder KG, Shah SP (2007) Rheology of extruded cement-based materials. ACI Mater J 104:283–290
8. Wangler T, Lloret E, Reiter L, Hack N, Gramazio F, Kohler M, Bernhard M, Dillenburger B, Buchli J, Roussel N, Flatt R (2016) Digital concrete: opportunities and challenges. RILEM Tech Lett 1:67
9. Lloret E, Reiter L, Wangler T, Gramazio F, Kohler M, Flatt R (2017) Smart dynamic casting: slipforming with flexible formwork-inline measurement and control. In: Proceedings of 2nd concrete innovation conference, Tromsø, Norway
10. Reiter L, Wangler T, Roussel N, Flatt R (2018) The role of early age structural build-up in digital fabrication with concrete
11. Kim JH, Beacraft MW, Kwon SHH, Shah SPP (2011) Simple analytical model for formwork design of self-consolidating concrete. ACI Mater J 108:38–45
12. Kwon SH, Shah SP, Quoc TP, Kim JH, Lee Y (2010) Intrinsic model to predict formwork pressure. ACI Mater J 107:20–26
13. Kim JH, Beacraft M, Shah SP (2010) Effect of mineral admixtures on formwork pressure of self-consolidating concrete. Cem Concr Compos 32:665–671
14. Yim HJ, Kim JH, Shah SP (2013) Cement particle flocculation and breakage monitoring under couette flow. Cem Concr Res 53:36–43
15. Kim JH, Yim HJ, Ferron RD (2016) In situ measurement of the rheological properties and agglomeration on cementitious pastes. J Rheol 60:695–704
16. Ferron RD, Shah S, Fuente E, Negro C (2013) Aggregation and breakage kinetics of fresh cement paste. Cem Concr Res 50:1–10

Processing of Set on Demand Solutions for Digital Fabrication in Architecture

Anna Szabo[1(✉)], Lex Reiter[2], Ena Lloret-Fritschi[1,2], Fabio Gramazio[1], Matthias Kohler[1], and Robert J. Flatt[2]

[1] Gramazio Kohler Research, NCCR Digital Fabrication, ETH Zurich, Zurich, Switzerland
szabo@arch.ethz.ch
[2] Institute for Building Materials, NCCR Digital Fabrication, ETH Zurich, Zurich, Switzerland

Abstract. Digital fabrication with concrete holds potential to rationalize the production of large-scale mass-customized shapes in architecture. However, these digital technologies have manifold requirements for concrete compared to ordinary casting due to the relatively long production time combined with the need for fast strength build-up after placing. Thus, first, a large retarded batch of concrete is prepared to provide extended open time for fabrication. Then, the retarded concrete is accelerated on demand in small increments over the course of the experiment.

This paper discusses suitable set on demand compositions to increase the buildability of three specific processes, Smart Dynamic Casting (SDC), Digital Casting (DC) and layered extrusion as they have similar requirements for concrete during fabrication. SDC and DC need low yield stress upon acceleration for casting and all three of them require consistent, rapid strength evolution for building.

Two significantly different material compositions, a SCM and an UHPFRC are studied using two formulated accelerators. The overall hydration and strength build-up kinetics are investigated with calorimetry, slow penetration and uniaxial compression measurements. It was found that the rate of yield stress evolution can be customized with both mortars by using different dosages of accelerator and that the onset of strength build-up depends on the type of mortar formulation. The proposed acceleration method is a promising approach to increase the fabrication speed and the possible building height for a given mix design in applications like SDC, DC or layered extrusion.

Keywords: Set on demand · Acceleration · Yield stress evolution · Slow penetration, feedback

1 Introduction

In the era of the third industrial revolution a shift towards digital fabrication technologies can be witnessed in the construction sector [1]. These digital processes hold the potential to enable mass customization that increases the efficiency of building, lowers environmental impact providing enlarged design space at the same cost [2].

V. Mechtcherine et al. (Eds.): RheoCon 2019/SCC 2019, RILEM Bookseries 23, pp. 440–447, 2020.
https://doi.org/10.1007/978-3-030-22566-7_51

Amongst these technologies, the field of digital concrete processing is receiving growing interest both in research and in practice [3]. One of the key challenges of these digital concrete technologies is that they often require set on demand material solutions with customized acceleration methods that can activate increments of a large retarded batch over a longer timeframe. This paper focuses on three specific digital concrete processes, Smart Dynamic Casting, Digital Casting and layered extrusion and aims to address this challenge to offer a suitable material composition increasing their potential to produce large-scale elements within the timeframe of a workday.

Smart Dynamic Casting is a robotic slip forming process. It can produce a set of different geometries by using a robot to move a single formwork continuously filled with concrete along a digitally defined path at a speed defined by the strength evolution of the concrete [4]. The accelerated increments of concrete are casted into the formwork with low enough yield stress for filling and high enough yield stress to avoid segregation. Then, as their strength evolves they reach the process window and can be slipped out. The yield stress of the concrete in the process window is low enough to avoid fracturing and high enough to support the weight of the newly casted material above it [5].

Digital Casting is the numerically controlled spatial deposition of a set on demand material enabling the use of stationary weakly supported or unsupported formworks [3]. A low yield stress is required upon filling the formworks with the accelerated material, then, a fast rate of strength evolution is needed for minimizing the formwork pressure during building.

Layered extrusion uses the principal of 3D printing to fabricate an element layer by layer with an extruded concrete filament. Upon extrusion, the accelerated concrete must have enough yield stress to keep the extruded shape and then the material has to build strength immediately to support the subsequent layer on top.

As the desired building speed and undisturbed hydration kinetics could not be achieved with the previously used commercially available accelerator [6], alternative solutions were explored using two custom accelerators prepared in-house. The paper focuses on the characterization of these accelerators and evaluates their potential for SDC, DC and layered extrusion through different mix compositions.

2 Materials and Methods

A self-compacting mortar (SCM – S mix) and an UHPFRC (U mix) formulation based on [7] were tested during the experiments with the composition shown in Table 1. Both mixes are retarded with sucrose, contain a commercial PCE based superplasticizer and are mixed in a Hobart mixer adding water to solids. The mixing sequence starts with dry-mixing at low speed (1 min for S, 3 min for U), followed by water and admixture addition and mixing at low speed (7 min for S, 15 min for U), forming the retarded base mix (S and U).

Acceleration occurs 1 h after water addition for both mixes and is achieved using two formulated accelerators prepared at ETHZ, accelerator A for S mix and accelerator B for U mix. The accelerators are mixed with the retarded base mix for 5 min, forming the accelerated mixes (S_A and U_B).

Table 1. SCM and UHPFRC mix designs and flow characteristics adapted for extended experimental time and delayed acceleration at 1 h from water addition.

Retarded base mix	Mix S			Mix U		
Sand (0–4 mm)	1367.6					
Quartz sand (0.125–0.5 mm)				616.4		
Alkali res. glass fibres (10–15 mm)				7.4		
Cement (CEM I 52.5R or N)	622.9 (R)			547.5 (N)		
Silica fume (BASF Masterlife SF100)	32.8			191.6		
Limestone 5–15 µm d50% (Betocarb-HP)				183.1		
Limestone 3 µm d50% (Betoflow-D)				419.1		
Water	262.3			221.8		
Superplasticizer (BASF ACE 30)	1.6			6.0		
Sucrose 99.5% purity D(+)	0.69			1.3		
$Ca(NO_3)_2$				0.03		
Accelerator	Mix S_A			Mix U_B		
Dosage (m_accelerator/m_CEM)	5.3%	7.6%	10.0%	4.7%	7.0%	9.3%
Yield stress [Pa]						
Retarded base mix	526			2.9		
Accelerated mix	16	51	257	15	24	83

The spread flow is measured for all compositions immediately after the end of mixing with a Hagermann mini slump cone. Yield stress is calculated according to [8]. Isothermal calorimetry (I-Cal8000) is conducted to provide qualitative information about the hydration kinetics of both retarded and accelerated samples. Further, slow penetration measurements according to [9] are performed on accelerated mixes using a Zwick universal testing machine with a conical penetration tip (30 mm height and 10 mm radius) at a penetration rate of 20 mm/h. These tests are complemented by displacement controlled (0.2 mm/s) uniaxial compression tests on cylindrical samples (height 140 mm, diameter 70 mm) on the same accelerated compositions, to relate penetration measurements to compressive strength and yield stress [9].

3 Results

3.1 Calorimetry

The results of the calorimetry measurements represented in Fig. 1 show that both the S and U retarded base mixes have the onset of hydration delayed by at least 8 h. With the addition of accelerator (S_A, U_B) the main peaks of hydration occur at earlier time, more so for higher accelerator addition. Additionally, the initial heat release of the first hour is significantly higher with the U_B compositions, however it drops back to a similarly low level as observed for S_A mixes in the second and third hours.

The relative position of the main hydration peaks with all accelerated S_A and U_B compositions remain unchanged compared to the respective retarded U and S. In the

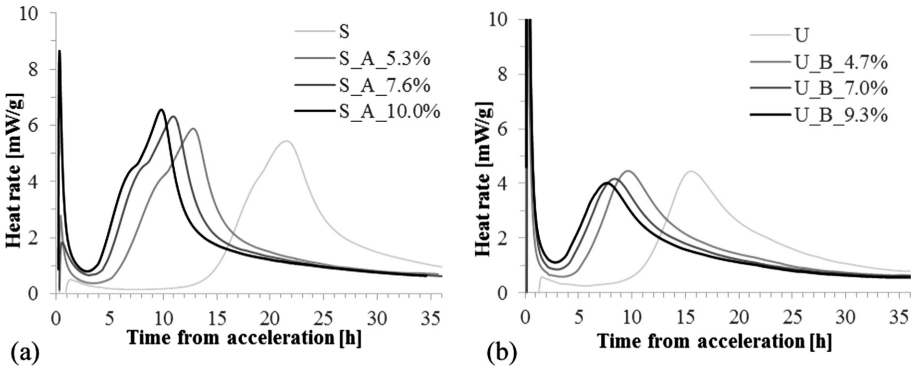

Fig. 1. (a) Hydration kinetics of the S mix and its accelerated S_A compositions with different dosages (b) Same measurements of the U mix and its accelerated U_B compositions.

case of U and U_B only a single hydration peak appears while the different silicate and aluminate main reaction peaks of S and S_A can be identified.

3.2 Slow Penetration Tests

The penetration force recorded with slow penetration tests in Fig. 2 increases with material age for all accelerated S_A samples according to a scaling with approximately 1.5 as exponent. Penetration force increases faster for increasing accelerator dosage and the force increase occurs immediately from the time of casting. The uniaxial compression and penetration force have similar values at the same measuring time.

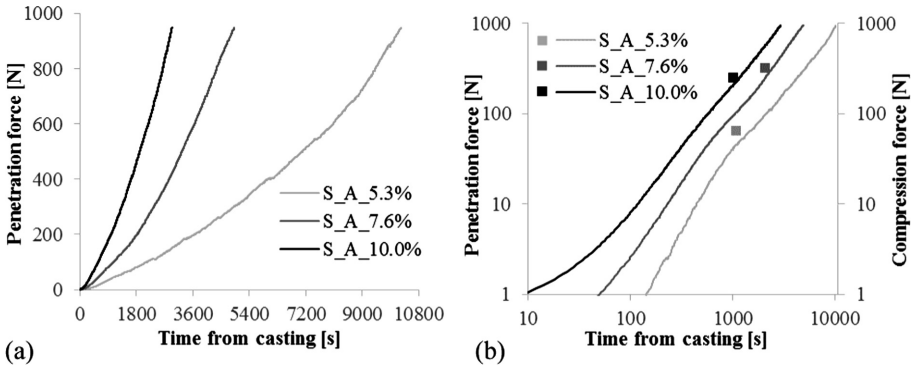

Fig. 2. (a) Penetration force measured with slow penetration tests on S_A samples prepared with different accelerator amounts (b) Comparison of the discrete measurement of the uniaxial compression test and the continuous slow penetration with all S_A compositions.

Compared to the slow penetration tests of the S_A mix variants where an immediate rapid increase of penetration resistance can be observed, the U_B compositions

on Fig. 3 show a delayed onset of strength build up, resulting in a higher exponent of the force evolution (approximately 3.5). The acceleration is more efficient at higher dosages and results in faster strength evolution than observed with the S_A mixes. The uniaxial compression test measurements of the respective U_B material compositions are closer to the slow penetration forces obtained at same material age than previously with the S_A mixes.

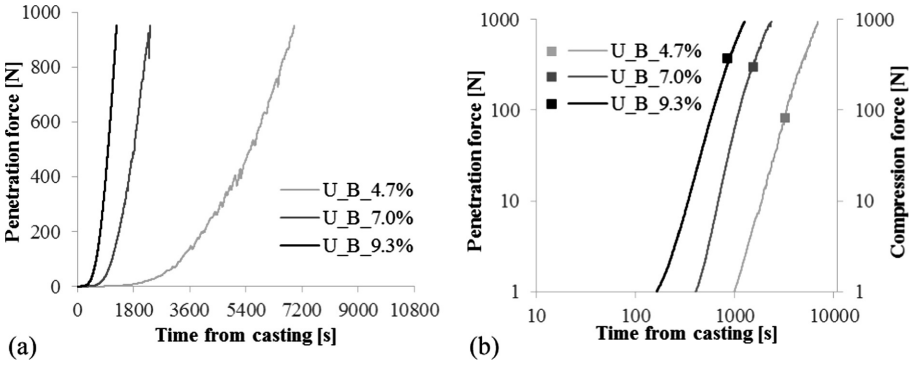

Fig. 3. (a) Slow penetration tests performed on all U_B samples prepared with different accelerator amounts. (b) Comparison of the uniaxial compression test and the slow penetration with all U_B compositions.

In Fig. 4 a linear relation can be observed between the compression force obtained with the uniaxial compression test and the penetration force recorded at the same time with the slow penetration measurement. This relation is also evident when compressive stress (compressive force at failure divided by cylinder cross-section area) is compared to penetration stress (penetration force divided by base surface of the penetration tip) and the ratios of the penetration and the compression stresses range from 8.9 to 13.7 with all possible mix compositions. Further, all uniaxial compressive test failures indicate a plastic failure (Table 2).

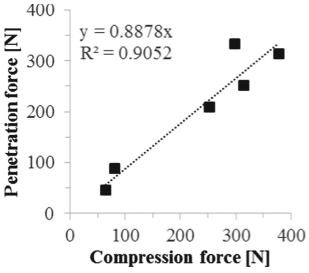

Fig. 4. Relation between compression force and penetration force at the same time measured with all mix compositions

Table 2. Stresses calculated from the forces recorded at penetration and compression tests.

	$\sigma_{penetration}$ [kPa]	$\sigma_{compression}$ [kPa]	$\frac{\sigma_{penetration}}{\sigma_{compression}}$
S_A_5.3%	149	16.8	8.9
S_A_7.6%	803	81.9	9.8
S_A_10.0%	664	65.6	10.1
U_B_4.7%	284	21.0	13.5
U_B_7.0%	1060	77.6	13.7
U_B_9.3%	997	98.2	10.2

4 Discussion

The calorimetry measurements of the accelerated S_A and U_B mixes show that by adding the accelerator, the retardation of the main hydration peak is largely negated. The first hour upon acceleration is interesting to study in digital fabrication processes relying on early strength build up to support the newly placed material on top, however, mortars cannot be characterized quantitatively with isothermal calorimetry in that timeframe [5]. Nevertheless, it can be observed that the heat rate between 1 h after acceleration and the time of onset of silicate hydration is substantially increased compared to the retarded mix and more so for increasing accelerator dosages. While the previously used, commercially available accelerator, designed for direct addition with the mixing water, suggested the occurrence of early sulphate depletion based on calorimetry results and showed decreased efficiency in delayed addition [6], with the formulations used in this study the later hydration steps remain unaffected (silicate hydration is largely unchanged and sulphate depletion occurs at similar times). Both accelerators showed a wider range of acceleration potential in the same timeframe without disturbing the hydration kinetics.

Qualitatively early age hydration is in good agreement with the respective slow penetration tests showing a yield stress increase depending on the accelerator dosage, the time to reach a certain strength scaling approximately with the inverse square of dosage. This means that strength build-up is sensitive to the amount of accelerator used, but can be varied in a wide range with small changes thereof.

The slow penetration test was shown to be able to capture the yield stress evolution of cement pastes [9] and it shows the same potential with the S_A and U_B mixes (plastic failure), as penetration and compressive stress scale largely linearly in the measuring range [9], indicating repeatability in this range. This linear relationship is particularly useful to discriminate changes to the rate of build-up that may go unnoticed with discrete measurements, such as the apparent induction time until the onset of yield stress increase occurring in the U_A compositions.

Quantitatively, the slow penetration test can be transformed into a yield stress according to these equations [10] with α as a pre-factor relating the penetration stress to the yield stress, using the linear regression from Fig. 4 as basis for the stress ratio:

$$\tau_0 = \frac{\sigma_{compression}}{\sqrt{3}}, \tau_0 = \frac{\sigma_{penetration}}{\alpha} \Rightarrow \alpha = \frac{\sigma_{penetration}\sqrt{3}}{\sigma_{compression}} \approx 19$$

For cement pastes, the empirical factor relating penetration force to yield stress was found to be 200 Pa/N [9], while for the mortars in this study a factor of 170 Pa/N is found. Using this factor, we can assess the accelerated mortars with respect to the requirements of the building processes. For typical formworks in SDC, a yield stress of approximately 5000 Pa is required when the formwork is removed (filling level 35 cm). This is achieved at a penetration force of 30 N. The time to reach this force and the possible vertical building rate v are reported in Table 3. For weak formworks the same approach may be chosen, the target penetration force depending on the formwork strength. For simplicity we consider the same target of 30 N. For layered extrusion,

self-support is required from the time of placing, hence the rate of yield stress increase is critical. S_A features an instantaneous yield stress increase that is adequate for layered extrusion, the rate of yield stress increase and possible vertical building rate being calculated in the interval between 1 and 2 min after placing and reported in Fig. 5. Due to the long time until yield stress increase, U_A is not adequate for layered extrusion. For these calculations only, the strength-based criteria are considered [10]:

$$\tau_{0,min} = \frac{\rho g h}{\sqrt{3}} \; and \; \dot{\tau}_{0,min} = \frac{\rho g v}{\sqrt{3}}$$

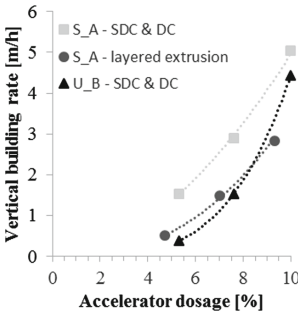

Fig. 5. Vertical building rate with different dosages of accelerator for all three studied digital fabrication processes.

Table 3. Vertical building rates calculated from strength-based criteria.

	Time to reach 30 N pen. resistance [s]	Building rate v SDC & DC [m/h]	Yield stress build up rate $\dot{\tau}_0$ [kPa/h]	Building rate v Layered extrusion [m/h]
S_A_5.3%	820	1.54	4.96	0.38
S_A_7.6%	435	2.90	20.0	1.53
S_A_10.0%	250	5.04	57.8	4.44
U_A_4.7%	2480	0.51	–	–
U_A_7.0%	850	1.48	–	–
U_A_9.3%	445	2.83	–	–

Both S_A and U_B show great potential to increase the buildability of digital fabrication processes up to several m/h, while keeping the initial low yield stress needed for casting. While the less abrupt yield stress increase of S_A compositions allows an easier detection of the process window, the higher exponent of yield stress increase is more favourable to deal with friction in small cross-sections in slip casting [5]. It should be kept in mind that friction between the formwork walls and the hardening concrete depends also on other factors and requires specific tests for the respective compositions. For digital casting, the U_B type of formulations appear suited with strong formworks as the long-term build-up is faster, while S_A are favourable for weak formworks due to immediate yield stress increase. While not designed for layered extrusion S_A fulfils the requirement of fast yield stress build-up and technological solutions to increase the initial yield stress could be found.

Finally, the studied concrete compositions are suitable for the experimental setup with the custom mixing reactor due to their yield stress increase without the immediate loss of workability.

5 Summary and Conclusion

Two significantly different material compositions, a traditional SCM and an UHPFRC formulation were used with customised accelerators in a set on demand system aiming to fulfil the material requirements of Smart Dynamic Casting, Digital Casting and layered extrusion. Both types of accelerated mortars showed low initial yield stress for casting upon activation and then a controlled rapid strength increase to support the weight of the newly casted material on top. The rate of strength build-up could be customized allowing for faster vertical building rate than before with both different mortars by changing the accelerator dosage without causing early sulphate depletion. Additionally, the onset of yield stress increase was also qualitatively related to the dosage.

With slow penetration tests the non-linear strength build-up of rapid-hardening mortars could be captured and related to yield stress. Thus, these continuous penetration tests hold the potential to serve as integrated feedback that can increase the robustness of digital fabrication processes aiming to produce elements at one-to-one architectural scale.

Acknowledgement. The research is pursued in the interdisciplinary framework of the National Competence Centre of Research (NCCR) Digital Fabrication funded by the SNSF at ETH Zürich. The authors thank Heinz Richner, Andi Reusser for technical assistance. The authors are also grateful for the constructive discussions with Tim Wangler.

References

1. Naboni R, Paoletti I (2015) Advanced customization in architectural design and construction. SpringerBriefs Appl. Sci. Technol., no. 9783319044224, pp i–iv
2. Wangler T et al (2016) Digital concrete: opportunities and challenges. RILEM Tech Lett 1:67
3. Wangler T (2018) Digital concrete processing: a review
4. Lloret Fritschi E (2016) Smart dynamic casting - a digital fabrication method for non-standard concrete structures
5. Reiter L, Wangler T, Roussel N, Flatt RJ (2018) The role of early age structural build-up in digital fabrication with concrete. Cem Concr Res 112(May):86–95
6. Szabo A, Reiter L, Lloret-Fritschi E, Gramazio F, Kohler M, Flatt RJ (2019) Adapting smart dynamic casting to thin folded geometries, vol 19
7. Hajiesmaeili A, Denarié E (2018) Next generation UHPFRC for sustainable structural applications. Am Concr Inst 326(June):58.1–58.10
8. Roussel N (2007) Rheology of fresh concrete: from measurements to predictions of casting processes. Mater Struct Constr 40(10):1001–1012
9. Reiter L, Wangler T, Roussel N, Flatt RJ (2019) Continuous characterization method for structural build-up. In: RheoCon2 conference and SCC9 symposium
10. Roussel N, Coussot P (2005) Fifty-cent rheometer' for yield stress measurements: from slump to spreading flow. J Rheol 49(3):705–718

Residence Time Distributions in Continuous Processing of Concrete

Timothy Wangler[1(✉)], Fabio Scotto[1,2], Ena Lloret-Fritschi[1,2], and Robert J. Flatt[1]

[1] Physical Chemistry of Building Materials, Institute for Building Materials, ETH Zurich, Zurich, Switzerland
wangler@ifb.baug.ethz.ch
[2] Gramazio Kohler Research, Institute for Technology in Architecture, ETH Zurich, Zurich, Switzerland

Abstract. Digital fabrication with concrete introduces new challenges in terms of continuous processing of concrete. To enable increased vertical building rates, accelerators are dosed at a nozzle reactor unit directly before placement in many of these processes. The details of this mixing process have large implications for the behavior of the system and the success of the process. The measurement of residence time distribution (RTD) is a potentially useful tool in understanding these processes and diagnosing pathological behavior of reactors. In this study, the RTD of the Smart Dynamic Casting (SDC) reactor is measured, and implications for this process and other digital fabrication processes are considered.

Keywords: Concrete · Digital fabrication · Processing · Residence time distribution

1 Introduction

Digital fabrication with concrete has seen rapid growth in recent years, after first being introduced into the public consciousness more than two decades ago by Prof. Berokh Khosnevis [1]. Concrete is a material that lends itself well to digital fabrication processes such as 3-D printing; it is a material that can be easily handled as a fluid, placed, hold its shape, and then transform into a solid material that can bear a load. As concrete digital fabrication processes are vertical building processes, it is usually necessary that concrete builds strength upon placement, otherwise it will eventually collapse as more material is added [2], or it will collapse by buckling, depending on the geometry of the component being built [3, 4]. The maximum yield stress that can be achieved without any form of set control usually does not allow build heights much higher than about three quarters of a meter [5], although some highly thixotropic mixes do allow significant building heights. These mixes, however, may lend themselves to problems with pumping, so set control (generally by hydration control) initiated at the nozzle is usually required.

Hydration control can be effected in a number of ways, but the most widely used method is the use of chemical admixtures, in particular retarders and accelerators [6].

V. Mechtcherine et al. (Eds.): RheoCon 2019/SCC 2019, RILEM Bookseries 23, pp. 448–456, 2020.
https://doi.org/10.1007/978-3-030-22566-7_52

A properly dosed combination of these can produce an almost set-on-demand system, where the start of the onset of hydration is controlled enough to enable high vertical building rates in digital fabrication. The Smart Dynamic Casting (SDC) system, developed at ETH Zurich [7], is a system of a vertically moving formwork, where self-compacting concrete enters the top of the formwork in the fluid state, and exits when it is hardening and can bear a load. The concrete can still be shaped, either at the exit, or within the formwork itself, if the formwork can change its shape digitally [8]. Hydration control is effected by retarding a large batch of concrete, which is then pumped into a mixing unit, or reactor, where an accelerator is then dosed, and the concrete exits the reactor and enters the formwork, where it begins to hydrate. This reactor, and the details of the mixing inside, form a vital part of the SDC system, and indeed this process is important for all digital fabrication processes with concrete that mix an accelerator just before deposition, which is recommended to ensure that hardening does not occur in the processing line [9]. Besides SDC, only one other study also demonstrated a successful continuous inline mixing system of acceleration, in this case in a concrete extrusion system [10]. This research aims to address this process as a vital unit operation for future concrete digital fabrication processes by examining the residence time distribution for the SDC process, and using it as a model to advise further development in all similar digital fabrication processes with concrete.

2 Residence Time Distributions

The average residence time τ_R of a material continuously flowing through a vessel of volume V is simply this volume divided by the volumetric flowrate Q:

$$\tau_R = \frac{V}{Q} \tag{1}$$

In continuous mixing processes, two major canonical models in mixing behavior exist [11]: (1) the plug flow reactor (PFR) model, and (2) the continuous stirred tank reactor (CSTR) model, both depicted in Fig. 1. It should be noted for the purpose of analysis that concrete is considered an incompressible fluid, and the volume of accelerator added is considered as negligible in comparison to the volume of concrete being pumped.

To describe mixing behavior inside these reactors, usually a tracer injection experiment is carried out; that is, a tracer is injected into the feed stream of the reactor (either a pulse injection or a step increase), and then its exiting behavior is analyzed. This can be described by the washout function, *W(t)*:

$$W(t) = \text{probability that a particle has a residence time less than } t \tag{2}$$

In an ideal PFR, two materials are injected into a reactor simultaneously in piston flow down the length of the reactor. The materials mix and react along the length of the reactor, before being discharged at a time equal to the mean residence time. When one imagines two “packets” of material entering the reactor simultaneously, they would

also exit simultaneously. If one were to suddenly increase the concentration of a tracer, then, a sudden increase of that concentration would appear at exactly the mean residence time. Thus, *W(t)* for a PFR is equal to a step function, or

$$\begin{aligned} W(t) &= 1, \quad t < \tau_R \\ W(t) &= 0, \quad t > \tau_R \end{aligned} \tag{3}$$

In an ideal CSTR, the reactants are injected into the reactor, which is continuously agitated to get perfect mixing, and the concentration of all reactants and products is equal at the exit and throughout the entire reactor. In such a reactor, "packets" of material do not have equal residence times as in a PFR, because the assumption of complete uniformity due to perfect mixing means that these "packets" will have variable residence times. The washout function for such a reactor is exponential:

$$W(t) = e^{-\frac{t}{\tau_R}} \tag{4}$$

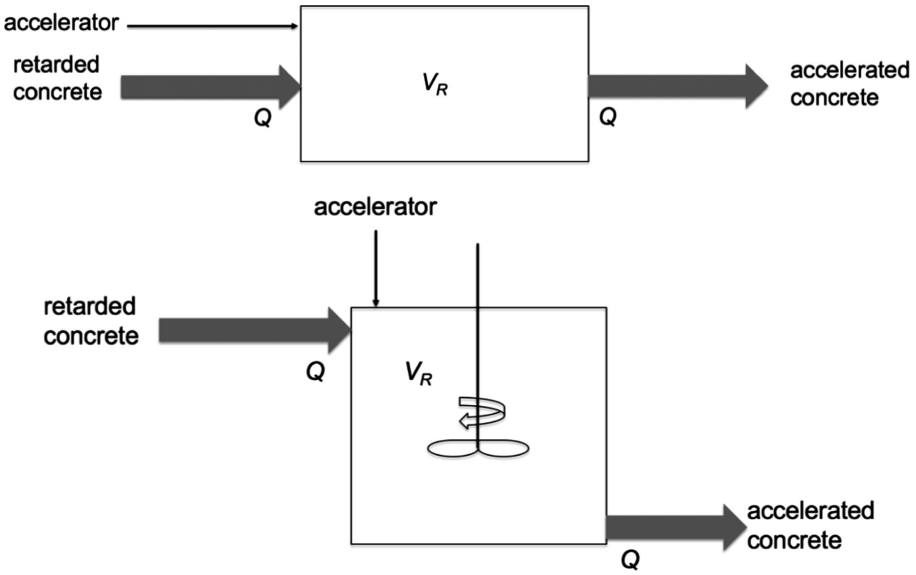

Fig. 1. (Top) Schematic showing a plug flow (piston flow) reactor in digital concrete processing. (Bottom) Schematic showing a continuous stirred tank reactor in digital concrete processing. Mean residence time for both reactors is simply the volumetric flowrate Q divided by the reactor volume V_R.

Figure 2 illustrates the corresponding washout functions for the two reactor types.

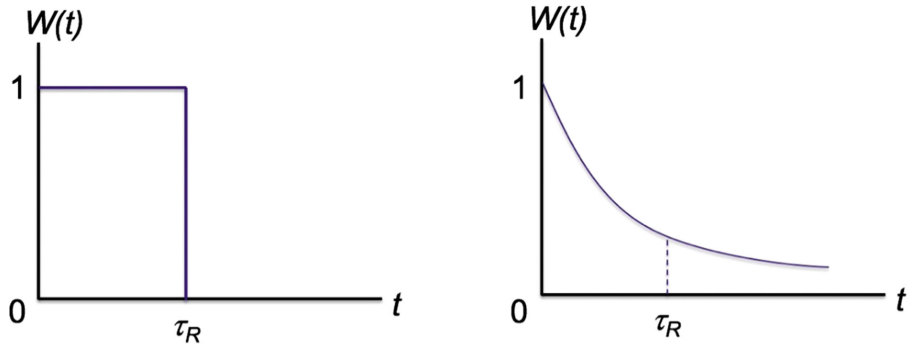

Fig. 2. Washout functions for PFR (left) and CSTR (right). A step function for the PFR shows that in piston flow, all particles have the same residence time, while an exponential function for the CSTR shows that all particles do not, even if both theoretically could have the same average residence time τ_R.

3 Experimental

3.1 Materials

For the experiments, standard SDC mix design based on [8] was used. Briefly, a pumpable mortar (max grain size 4 mm) made with CEM I 52.5R and 8% microsilica (w/b = 0.34), is dosed with a PCE superplasticizer to get proper rheology and retarded with sucrose to get an open time of 8 h. The accelerator normally used is a calcium nitrate based accelerator added at a dosage of 8% w/w binder. To measure the RTD, a pigment suspension of 15% w/w chromium oxide (Colortherm Green GN-M from Harold Scholz & Co. GmbH) was used. The pigment suspension was injected at a volumetric rate equal to that of the accelerator for each experiment.

3.2 Experiment

Similar to the SDC process, the retarded concrete was pumped using a PFT Swing L mortar pump (progressive cavity pump) through a funnel-shaped reactor where the accelerator or the pigment was injected via a peristaltic pump. The reactor is equipped with a rotating pin mixer to agitate the material and enable mixing, with the speed constant at 80 RPM. The material pumps through the reactor and becomes self-compacting after mixing, allowing it to flow down the chute at the top of the reactor and into the formwork. Two experiments were carried out, corresponding to two different reactor sizes: 1.414 L and 0.707 L. The reactors were both of similar heights and the pin mixers had identical geometries; only the reactor diameter (and pin length) was varied between the two. Experiments were carried out as step-increase-decrease experiments, where the accelerator line was replaced by the pigment line until a stable

pigment concentration could be detected visually, and the lines were then switched back to observe the decrease in pigment concentration. The concrete was collected in prismatic molds of 100 cm^2 cross sectional area for the larger reactor, and 50 cm^2 for the smaller reactor. The pump rate was determined for each experiment to correspond to a fill rate of 12 mm/min, thus 0.12 L/min and 0.06 L/min for the large and small reactors, respectively, and corresponding to a mean residence time of $\tau_R = 11.8$ min for both experiments. The system is depicted schematically in Fig. 3. The tracer washout behavior was analyzed in the step decrease portion of the curve.

3.3 Analysis

The concrete collected in the molds was then sliced at various points corresponding to various times in the experiment and the concentration of pigment was analyzed by polishing slices (further cut down to ca. 5 cm^2 to fit in the microscope) and carrying out quantitative EDX analysis on an FEI Quanta 200 3D Scanning Electron Microscope equipped with an EDX detector and software capable of quantitative analysis. For the analyses, 10 areas at 4000X magnification (approximately 2 mm^2 total analysis area) on a sample were selected, where no aggregates were present. The collection time for each spectrum was 1 min, and the chromium concentration was then determined by the software by peak area analysis and was averaged across the 10 areas for each sample.

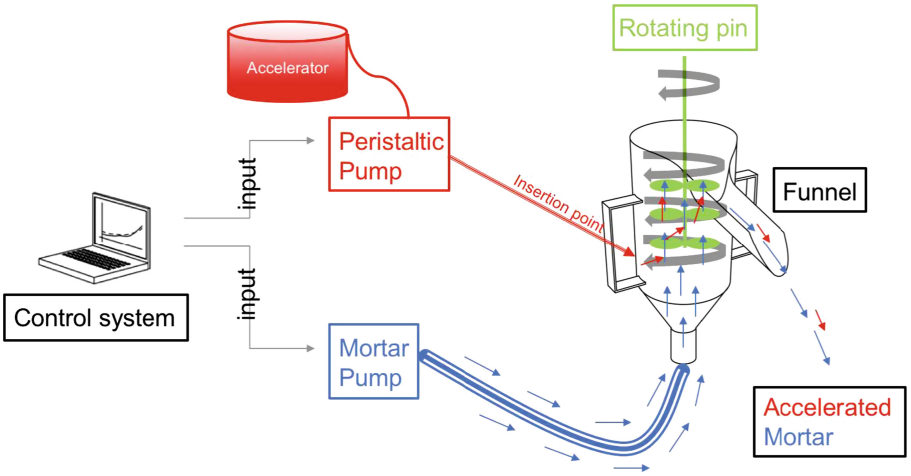

Fig. 3. Schematic showing the experimental setup. A control system coordinated the mortar pump and peristaltic accelerator/pigment pump. (figure from [12]).

4 Results

Figure 4 shows the step up and down curve for the large reactor, and Fig. 5 for the smaller reactor. The point where the pigment line was replaced (the beginning of the washout curve) is noted on each plot. Also noted on each plot is the mean residence time after pigment removal.

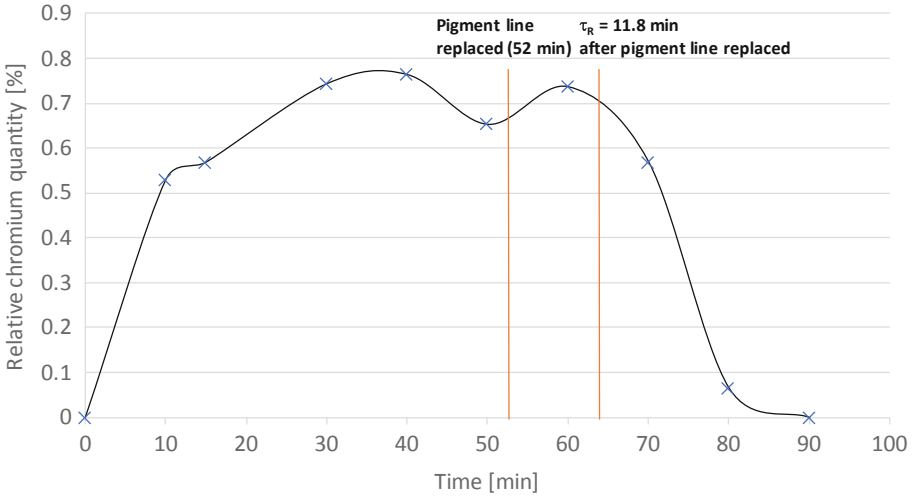

Fig. 4. Pigment tracer vs. time in step increase-decrease experiment. Pigment line inserted at t = *0*, and removed at t = 52 (beginning washout curve). Mean residence time indicated on plot.

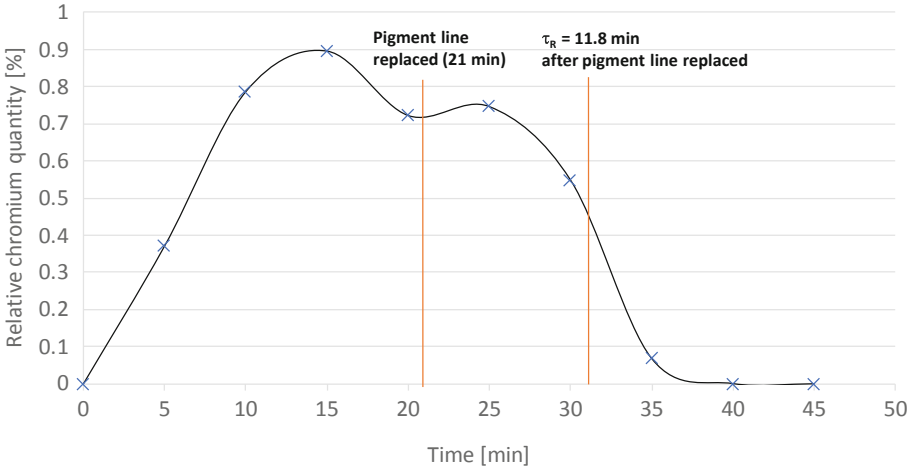

Fig. 5. Pigment tracer vs. time in step increase-decrease experiment. Pigment line inserted at t = 0, and removed at t = 21 (beginning washout curve). Mean residence time indicated on plot.

5 Discussion

The negative step change experiment is the typical method used to analyze RTDs, due to its simplicity and ease of execution [13]. Therefore, for this experiment, we examine only the washout curve upon removal of the pigment line.

For processes of digital fabrication with concrete, such as SDC, one would desire a consistent residence time that would ensure adequate mixing and no hardening occurring inside of the reactor. A distribution such as that encountered in a CSTR (Fig. 2) would thus be more undesirable, as regardless of reactor volume, some material remains in the reactor longer than others, and in processes such as these, where mixing energy can impact reactivity, this can be problematic.

The experiments depicted in Figs. 4 and 5 demonstrate that in SDC processing, there is clearly not PFR behavior. In piston flow (PFR) behavior, the washout curve would show an immediate decrease in concentration to zero at the mean residence time τ_R, shown on both curves. Clearly, for both reactor sizes, the washout curve continues beyond this. In the case of the large reactor, it continues for at least 1.5x the mean residence time, and for the small reactor, 0.5x the mean residence time. The reasons for this difference between the curves are not clear, but are likely related to the details of the pumping procedure (pumping is running in a pulsating manner) combined with the geometry of the funnels. It should also be stated that the pigment concentration seems to be oscillatory rather than stable, and this also likely has to do with these details as well. The extended length of the washout curve for the large reactor indicates that more backmixing is occurring in this reactor, which with the larger volume is a reasonable assumption. While neither the PFR nor the CSTR idealizations describe the behavior of these reactors, a combination of the two is often used in the practice, and indeed, could be used to describe the behavior of both of these reactors, which is done in a separate study.

The implications of the reactor behavior for design are significant. When sizing this reactor, one must consider that it must have an adequate residence time to ensure proper mixing, but not such a long residence time that hardening occurs prematurely, according to the process requirements. Mixing energy and duration have a direct impact on rheology and reactivity of cement [14], thus extended time of any material in the reactor could lead to potential problems of this sort. While this would favor designing for PFR behavior, the CSTR is what is required in reality, as this design is the only design that ensures adequate mixing necessary for proper dispersion of the accelerator within the concrete.

The mixing procedure itself is rather complex and difficult, as it is the mixing of a very small volume fraction of a complex fluid into a very large volume fraction of another complex fluid, with fast dispersion required to eliminate highly reactive steep concentration gradients. Even if both fluids have similar rheologies, a static mixing approach (more closely approximating PFR behavior) would be unadvised. However, a detailed examination of mixing times as they relate to this process with respect to both static and various types of active mixing is recommended as a topic of further research. In any case, this highlights how the rheological requirements of the concrete play an important role in reactor behavior. In a process such as SDC, where the concrete must be very fluid (self compacting) upon discharge, the mixer behavior would be expected to be different compared to a process such as extrusion, where the concrete must have a high yield stress; for example, a low yield stress fluid such as in SDC would be expected to produce higher backmixing.

A final implication that should be noted is what this means for scaleup. Digital fabrication processes with concrete currently tend to run at one speed, but demands for process versatility may call for systems that are capable of pumping at variable speeds to compensate for variable printhead speeds or variable design geometries. In a fixed volume reactor, again, ensuring adequate mixing at high processing rates and ensuring no premature hardening at low processing rates will determine these boundaries, and thus versatility of a system with respect to scaleup.

6 Conclusion

In this study, a first look at residence time distributions for nozzle mixing in a continuous concrete process was undertaken via tracer experiments using pigments. For the SDC process, the reactor behavior does not conform to either PFR or CSTR behavior, but somewhere in between, and requires further analysis as to how this impacts the acceleration of hydration required for successful processing. Implications for digital concrete processing in general were considered, especially with respect to reactor sizing and scaleup.

Acknowledgments. This work was carried out in the context of a bachelor thesis at ETH Zurich by the students Davide Biondini and Roberto Gharib. Microscopy work was supported by Asel Maria Aguilar Sanchez from the chair of Physical Chemistry of Building Materials in the Institute for Building Materials at ETH Zurich. The authors also acknowledge the support of Heinz Richner and Andreas Reusser of the Institute for Building Materials. The authors also acknowledge Lex Reiter (ETH Zurich Physical Chemistry of Building Materials) for his contribution in the initial development of the reactor. This work was primarily financially supported by the Swiss National Science Foundation and the National Centre for Competence in Research in Digital Fabrication in Architecture.

References

1. Khoshnevis B (2004) Automated construction by contour crafting—related robotics and information technologies. Autom Constr 13:5–19
2. Perrot A, Rangeard D, Pierre A (2015) Structural built-up of cement-based materials used for 3D-printing extrusion techniques. Mater Struct 49(4):1213–1220
3. Wolfs RJM, Bos FP, Salet TAM (2018) Early age mechanical behaviour of 3D printed concrete: numerical modelling and experimental testing. Cem Concr Res 106:103–116
4. Roussel N (2018) Rheological requirements for printable concretes. Cem Concr Res 112:76–85
5. Wangler T, Lloret E, Reiter L, Hack N, Gramazio F, Kohler M, Bernhard M, Dillenburger B, Buchli J, Roussel N, Flatt R (2016) Digital concrete: opportunities and challenges. RILEM Tech Lett 1:67–75
6. Reiter L, Palacios M, Wangler T, Flatt RJ (2015) Putting concrete to sleep and waking it up with chemical admixtures. Special publication, vol 302
7. Lloret E, Shahab AR, Linus M, Flatt RJ, Gramazio F, Kohler M, Langenberg S (2015) Complex concrete structures: merging existing casting techniques with digital fabrication. Comput Aided Des 60:40–49

8. Lloret-Fritschi E, Scotto F, Gramazio F, Kohler M, Graser K, Wangler T, Reiter T, Flatt RJ, Mata-Falcón J (2018) Challenges of real-scale production with smart dynamic casting. In: Wangler T, Flatt RJ (eds) First RILEM international conference on concrete and digital fabrication – digital concrete. Springer, Cham, pp 299–310
9. Reiter L, Wangler T, Roussel N, Flatt RJ (2018) The role of early age structural build-up in digital fabrication with concrete. Cem Concr Res 112:86–95
10. Esnault V, Labyad A, Chantin M, Toussaint F (2018) Experience in online modification of rheology and strength acquisition of 3D printable mortars. In: Wangler T, Flatt RJ (eds) First RILEM international conference on concrete and digital fabrication – digital concrete. Springer, Cham, pp 24–38
11. Nauman EB, Buffham BA (1983) Mixing in Continuous Flow Systems. Wiley, New York
12. Biondini D, Gharib R (2018) Smart dynamic casting: reactor characterization, Bachelor Thesis, ETH Zurich
13. Nauman EB (2004) Residence time distributions. In: Handbook of industrial mixing. Wiley, pp 1–17
14. Han D, Ferron RD (2015) Effect of mixing method on microstructure and rheology of cement paste. Constr Build Mater 93:278–288

Post-processing Techniques to Enhance Strength of Portland Cement Mortar Digitally Fabricated Using Powder-Based 3D Printing Process

Ming Xia(✉), Behzad Nematollahi, and Jay Sanjayan

Centre for Smart Infrastructure and Digital Construction, Faculty of Science, Engineering and Technology, Swinburne University of Technology, Hawthorn, VIC, Australia
mxia@swin.edu.au

Abstract. The authors of this study have recently succeeded to formulate a Portland cement-based mortar as a printing material for use in commercially available powder-based 3D printers to build '*free-form*' concrete components with complex geometries for construction applications. This study focusses on post-processing methods to enhance the strength of cement mortar specimens digitally fabricated using the powder-based 3D printing technique. The effects of type of curing medium (tap-water vs. saturated-limewater), curing time (7 days vs. 28 days), and loading direction (binder-jetting direction vs. layer-stacking direction) on the compressive strength of the printed samples were investigated. The results showed that the compressive strength of the printed samples cured in either tap-water or saturated-limewater was significantly higher than that of the 'green' samples. However, the 7-day and 28-day compressive strengths of the saturated-limewater-cured samples were 26% and 17%, respectively higher than those of the corresponding tap-water-cured samples. The results also showed that the compressive strength of the 3D printed cement mortar specimens depended on the loading direction. However, the degree of anisotropy in the compressive strength was reduced with the increase of curing time.

Keywords: 3D concrete printing · Post-processing · Digital construction · Powder-based technique · 3D printed cement

1 Introduction

Three-dimensional (3D) printing, also known as additive manufacturing (AM) is a group of emerging techniques for fabricating a wide range of structures with complex geometries from digital models. The process involves printing successive layers of materials that are formed on top of each other. Several industries including aerospace, automotive, biomedical have already explored the benefits of adopting this technology as an integral part of their product manufacturing process [1].

Recently, the construction industry has started to embrace the AM techniques [2–4]. Compared to conventional construction processes, the AM techniques have the advantages of (1) reducing the labor requirements which would result in a decreased construction cost and an increased level of safety, (2) reducing on-site construction

V. Mechtcherine et al. (Eds.): RheoCon 2019/SCC 2019, RILEM Bookseries 23, pp. 457–464, 2020.
https://doi.org/10.1007/978-3-030-22566-7_53

time by operating at a constant rate, (3) minimizing the chance of errors by highly precise material deposition, and (4) increasing architectural freedom which would enable more sophisticated designs for structural and architectural purposes [5].

One of the AM techniques adopted by the construction industry is known as the powder-based 3D concrete printing (3DCP) technique, which is categorized in three groups according to the type of materials used: (1) selective binder (cement) activation; (2) selective paste intrusion; and (3) binder jetting [6]. The powder-based 3DCP technique is an off-site process designed to manufacture precast components. This method is capable of producing *free-form* building elements with complex geometries without the necessity for using formworks. In the construction industry, there is a high demand for such components which with the currently available construction techniques can only be made with using expensive formwork systems. The authors believe that the powder-based 3DCP technique is highly suitable for small-scale building components such as panels, permanent formworks and interior structures that then can be assembled on site [5, 7].

Figure 1(a) schematically demonstrates the powder-based 3DCP technique. A thin layer of powder is spread over the powder bed surface. Subsequently, binder droplets are selectively applied on the powder layer by a print-head, causing powder particles to bind to each other. Repeating the described steps, the built part is completed and removed after a certain drying time and unbound powder is removed by using an air blower. One of the advantages of this technique is that overhanging structures can be made without the necessity for using a supporting structure. Examples of technologies developed based on the powder-based 3DCP technique include D-shape [8] and Emerging Objects [9].

Although the powder-based 3DCP technique can offer several advantages in the construction industry, there are several challenges to be overcome before the technique is fully utilized. One of the main challenges is that the proprietary printing materials that are typically used in the commercially available powder-based 3D printers are not suitable for the construction applications. To date, only a limited range of cementitious materials have been explored for the powder-based 3DCP technique, such as rapid hardening Portland cement (RHPC) [10], calcium aluminate cement (CAC) [11], magnesium oxychloride cement (also known as Sorel cement) [12], fiber reinforced cement polymer [9], magnesium potassium phosphate cement [13] and calcium sulfoaluminate (CSA) cement [14]. Therefore, it is urgently needed to increase the limited scope of printing materials for the powder-based 3DCP technique. To tackle this limitation, the authors of this study have been working on developing innovative methodologies for formulating geopolymer/Portland cement-based materials which can be used in the commercially available powder-based 3D printers for construction applications [15–17]. The 3D printed samples using the developed geopolymer-based and Portland cement-based powders are presented in Figs. 1(b) and (c), respectively.

In the authors' previous study [15], a Portland cement-based powder was developed for the powder-based 3DCP process. The strength of the 3D printed samples immediately after completion of the de-powdering process, often referred to as the "green" strength, was typically less than 5 MPa, which is not enough for the construction applications. The author's investigation showed the strength of the "green" samples was not increased when they were left at the ambient temperature for up to 90 days

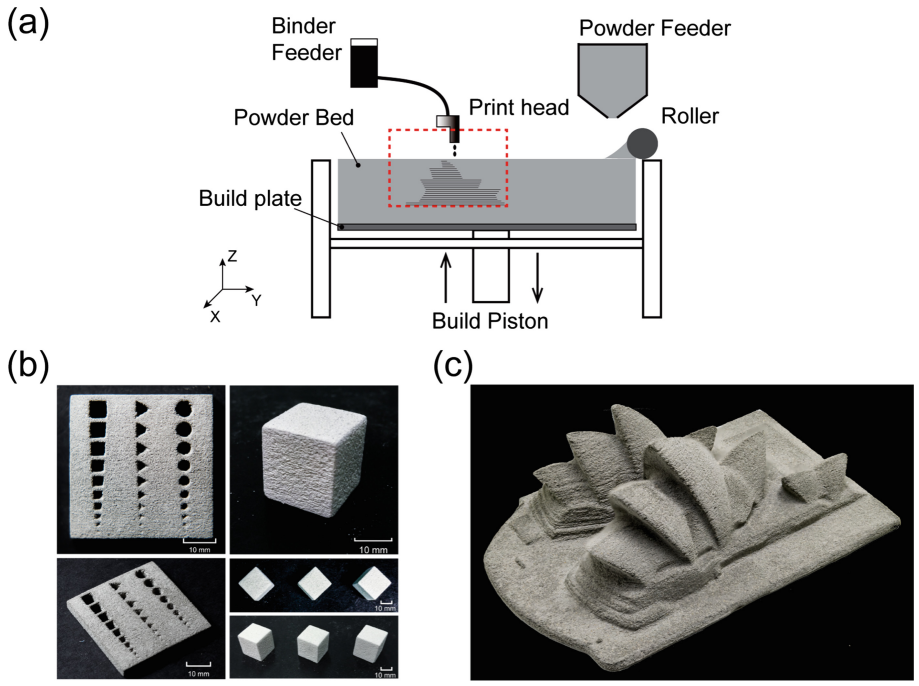

Fig. 1. (a) Schematic illustration of powder-based 3DCP, (b) 3D printed samples using geopolymer-based powder, (c) 3D printed samples using Portland cement-based powder.

without any post-processing. This can be due to the inherent high porosity of the powder bed and insufficient water content for continuation of the hydration process. Therefore, the focus of this study is on post-processing methods to enhance the strength of the 3D printed Portland cement mortar samples to make them suitable for construction applications. In this context, the effects of type of curing medium and curing time on the strength of the printed samples were investigated. In addition, the effect of loading direction on the strength of the printed samples was also studied.

2 Experimental Procedures

2.1 Materials

A printable Portland cement powder previously developed by the authors [11] was used in this study. The powder was a mixture of Portland cement (conforming to the Australian Standard, AS 3972 general purpose (Type GP) cement), high purity fine silica sand (supplied by TGS Industrial Sand Ltd., Australia) and a small amount of an accelerating additive. Further details regarding the preparation of the printable Portland cement-based powder can be found in [7, 15]. A commercial aqueous solvent known as Zb® 63 supplied by the printer's manufacture (Z-Corp, USA) was used in this study as the liquid binder. Details of the Zb® 63 liquid binder can be found in the authors' previous work [7].

2.2 3D Printing Process

A commercial powder-based 3D printer (ZPrinter® 150) manufactured by Z-Corp, USA was used in this study. Details of the ZPrinter® 150 can be found in the authors' previous work [7]. In this study, the powder layer thickness was set to 0.1016 mm. The binder saturation level was 135% and a shell to core ratio 1:2 was selected in this study. The binder saturation is defined as the ratio between the volume of deposited liquid binder (V_{Binder}) and the volume of pores in the powder bed (V_{Pores}). Two sub-variables of the binder saturation are employed in the powder-based 3D printers, namely 'shell' and 'core'. The 'shell' refers to the region comprising the edges of the sample and parts of the interior area within the edges of the sample. The 'core' refers to the remaining interior areas within the edges of the sample. 20 mm cube samples were printed for the compressive strength test. The printed samples were kept within the powder bed at the room temperature for 2 h and then the unbounded powder was removed via a compressed air.

2.3 Post-processing and Testing Methods

After the de-powdering process, the printed samples were divided into two groups denoted as "tap-water-curing" and "saturated-limewater-curing". The saturated limewater was prepared by adding and slightly stirring two grams of $Ca(OH)_2$ powder in one liter of tap water and. For the "tap-water-curing" group, the printed cubes were immersed in a sealed container containing tap water, while for the "saturated-limewater-curing" group, the printed cubes were immersed in a sealed container containing saturated limewater. Both containers were kept at the ambient temperature (23 °C ± 3 °C) for 7 and 28 days. At the end of the curing period, the cured samples were taken out from the curing mediums and kept undisturbed until become dry. The compressive strength of the cured samples was measured at 7 and 28 days. However, the compressive strength of the green samples was tested 2 h after the end of the printing process (i.e., after the de-powdering process). The compressive strengths in both X-direction (i.e., the binder-jetting-direction) and Z-direction (i.e., layer-stacking-direction) were measured under load control at the rate of 0.33 MPa/s. A population of 10 samples for each testing direction was used.

3 Results and Discussions

3.1 "Tap-Water-Curing" Group

Figure 2 shows the 7-day and 28-day compressive strengths of the tap-water-cured samples. The compressive strengths of the green samples are also presented in this figure. The error bars in the presented results are based on 95% confidence level and the numerical values in the middle of the bars are the mean strengths.

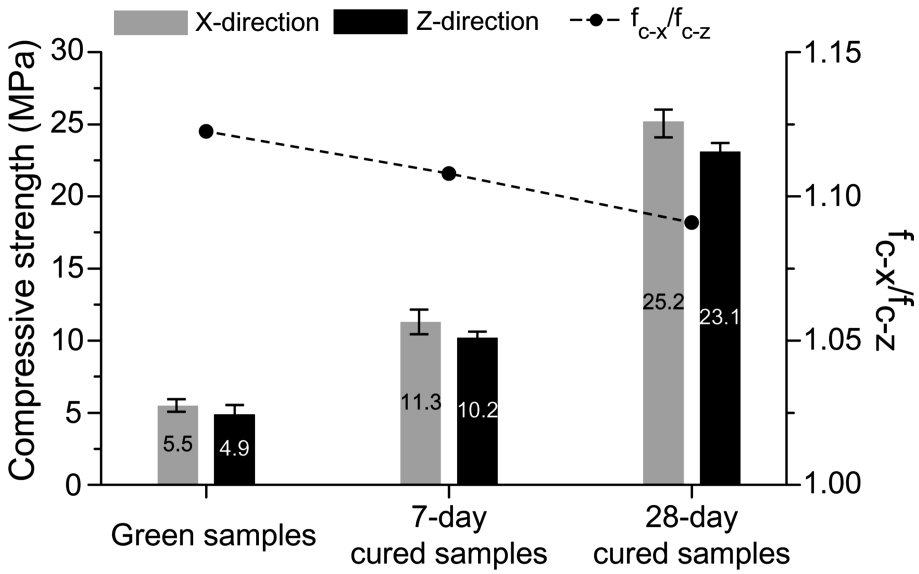

Fig. 2. Compressive strengths of the 3D printed Portland cement mortar cured in "tap water" for 7 days and 28 days. Note: The green compressive strength was tested 2 h after the printing process. The f_{c-x}/f_{c-z} shows the ratio of compressive strength in X-direction to the compressive strength in Z-direction.

As can be seen in Fig. 2, the compressive strength of the post-processed printed samples cured in tap water was significantly higher than that of the green samples. The 7-day compressive strength of the tap-water-cured printed samples was about 2.1 times higher than the compressive strength of the green samples. In addition, according to Fig. 2, the longer the curing time, the higher the strength gain. The 28-day compressive strength of the tap-water-cured printed samples was more than 2.2 times higher than the 7-day compressive strength. This is true regardless of the loading directions. This significant increase in the strength is due to the continued hydration of the un-reacted cement particles in presence of the tap water.

As shown in Fig. 2, an anisotropic phenomenon was observed in the compressive strength of the printed samples depending on the loading directions. Regardless of the age of testing, the mean compressive strength was always higher in the X-direction than in the Z-direction. The anisotropy in compressive strength might be related to the bond strength between the printed layers. According to Lowke et al. [14], in the green samples, the water content significantly oscillates in accordance with a higher water content in the top region of the layer and a significantly lower content in the bottom region. Thus, the intralayer water gradient will cause a weak bond between layers. As can be seen in Fig. 2, it is worth noting that the f_{c-x}/f_{c-z} (i.e. the ratio of compressive strength in X-direction to the compressive strength in Z-direction) decreased from 1.12 to 1.09 with the increase of the curing time, which implies that the degree of anisotropy in the compressive strength was reduced with the increase of curing time. The reason for this can be explained by the improved inter-layer bond strength resulting from the continued hydration of the un-reacted cement particles in the curing process.

3.2 "Saturated-Limewater-Curing" Group

Figure 3 shows the compressive strength of the green samples, as well as the 7-day and 28-day compressive strengths of samples cured in the saturated limewater. The error bars in the presented results are based on 95% confidence level and the numerical values in the middle of the bars are the mean strengths. The 7-day compressive strength of the post-processed printed samples cured in saturated limewater was about 2.6 times higher than the compressive strength of the green samples. In addition, the 28-day compressive strength of the saturated-limewater-cured printed samples was about 2.1 times higher than the 7-day compressive strength. This is true regardless of the loading direction.

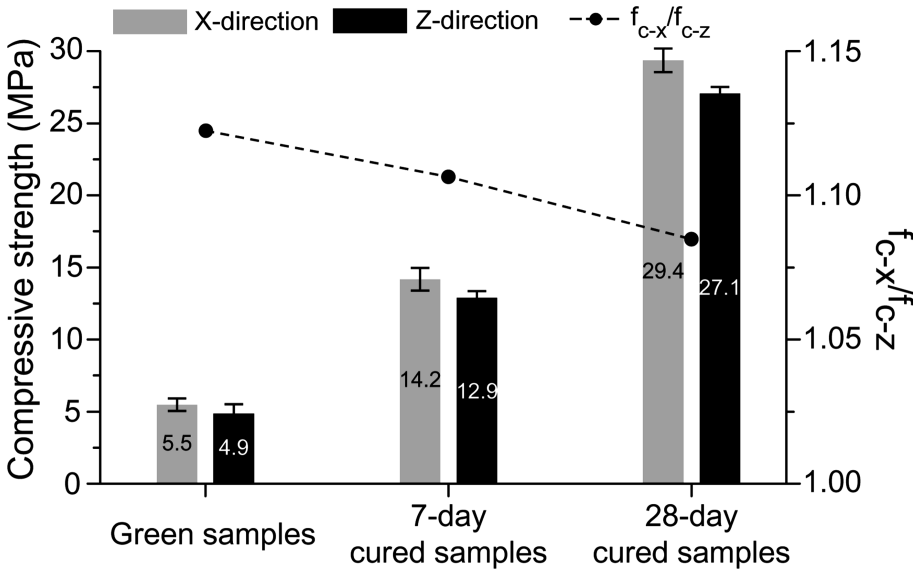

Fig. 3. Compressive strengths of the 3D printed Portland cement mortar cured in saturated limewater. Note: The green compressive strength was tested 2 h after the printing process. The f_{c-x}/f_{c-z} shows the ratio of compressive strength in X-direction to the compressive strength in Z-direction.

Comparison between Figs. 2 and 3 shows that all the printed samples cured in the saturated limewater generally acquired higher strength than those cured in tap water. This is true regardless of the curing time and loading direction. Irrespective of the loading direction, the 7-day and 28-day compressive strengths of the saturated-limewater-cured samples were 26% and 17%, respectively higher than those of the corresponding tap-water-cured samples. Since the concentration of Ca^{2+} in the

saturated limewater is high and CH is quite soluble in the cementitious materials, as cement hydration proceeded with time, less dissolution and leaching of CH occurred in the saturated-limewater than the tap water, therefore resulted in the higher compressive strength of the saturated-limewater-cured samples [18].

The compressive strength of the saturated-limewater-cured samples also exhibited similar anisotropic behavior, depending on the testing direction. The mean compressive strength was always higher in the X-direction than in the Z-direction, regardless of the age of testing. Similar to the printed samples cured in the tap water, the f_{c-x}/f_{c-z} also decreased with the increase of the curing time, indicating that the degree of anisotropy in the compressive strength was reduced with the increase of the curing time.

4 Conclusions

The present study investigated the effects of two different curing mediums, curing times and loading directions on the compressive strength of the printed Portland cement mortar samples made using the powder-based 3D concrete printing process. The post-processed printed specimens exhibited a 28-day compressive strength of 23.1 MPa–29.4 MPa, depending on the type of curing medium and testing direction. The 28-day compressive strength of the post-processed printed specimens was 4.2 to 6.0 times higher than the compressive strength of the green samples (4.9 MPa–5.5 MPa). The high strength of the post-processed printed samples archived in this study using the developed post-processing methods at the ambient temperature significantly enhances the commercial viability and promotes applications of the developed powder-based 3D printed Portland cement mortars in the construction industry. The following conclusions can be drawn:

(1) Tap water and saturated limewater are both effective post-processing curing mediums to enhance the strength of 3D printed Portland cement mortars. The significantly higher strength of the post-processed printed samples is due to the continued hydration of the un-reacted cement particles in the presence of either tap water or saturated limewater.
(2) Among the two curing mediums investigated in this study, saturated limewater was more effective in enhancing the strength of 3D printed Portland cement mortars. This is due to the less CH leaching and dissolution in the saturated limewater, which favored the continuous cement hydration process.
(3) An anisotropic phenomenon was observed in the compressive strength of the printed Portland cement mortars, depending on the loading direction. The compressive strength in X-direction (i.e., the binder-jetting-direction) was always higher than in Z-direction (i.e., layer-stacking-direction). This is true regardless of the curing medium and curing time.
(4) The fc–x/fc–z (i.e., the ratio of compressive strength in X-direction to the compressive strength in Z-direction) decreased with the increase of curing time. Therefore, it is concluded that the degree of anisotropy in the compressive strength was reduced with the increase of curing time. This is true regardless of the curing medium. This reduction in the degree of anisotropy is attributed to the improved inter-layer bond strength, resulted from the continuous hydration of the un-reacted cement particles in the curing process.

References

1. Wohlers T (2016) Wohlers report 2016, Wohlers Associates, Inc
2. Sanjayan J, Nematollahi B (2019) 3D concrete printing for construction applications. In: Sanjayan J, Nazari A, Nematollahi B (eds) 3D concrete printing technology. Elsevier, pp 1–11. https://doi.org/10.1016/B978-0-12-815481-6.00001-4
3. Wangler T, Lloret E, Reiter L, Hack N, Gramazio F, Kohler M, Bernhard M, Dillenburger B, Buchli J, Roussel N (2016) Digital concrete: opportunities and challenges. RILEM Tech Lett 1:67–75
4. Wu P, Wang J, Wang X (2016) A critical review of the use of 3-D printing in the construction industry. Autom Constr 68:21–31
5. Nematollahi B, Xia M, Sanjayan J (2017) Current progress of 3D concrete printing technologies. In: ISARC. proceedings of the international symposium on automation and robotics in construction, Vilnius Gediminas Technical University, Department of construction economics & property, Taipei, pp 260–267
6. Lowke D, Dini E, Perrot A, Weger D, Gehlen C, Dillenburger B (2018) Particle-bed 3D printing in concrete construction–possibilities and challenges. Cem Concr Res 112:50–65
7. Xia M, Sanjayan J (2016) Method of formulating geopolymer for 3D printing for construction applications. Mater Des 110:382–390
8. Dini E (2014) D_Shape, vol 2014. http://www.d-shape.com
9. Rael R, San Fratello V (2011) Developing concrete polymer building components for 3D printing. In: ACADIA. 31st annual conference of the association for computer aided design in architecture, Banff
10. Gibbons GJ, Williams R, Purnell P, Farahi E (2010) 3D printing of cement composites. Adv Appl Ceram 109:287–290
11. Maier AK, Dezmirean L, Will J, Greil P (2011) Three-dimensional printing of flash-setting calcium aluminate cement. J Mater Sci 46:2947–2954
12. Cesaretti G, Dini E, De Kestelier X, Colla V, Pambaguian L (2014) Building components for an outpost on the Lunar soil by means of a novel 3D printing technology. Acta Astronaut 93:430–450
13. Cao X, Li Z (2019) Factors influencing the mechanical properties of three-dimensional printed products from magnesium potassium phosphate cement material. In: Sanjayan JG, Nazari A, Nematollahi B (eds) 3D concrete printing technology, Butterworth-Heinemann, pp 211–222
14. Ingaglio J, Fox J, Naito CJ, Bocchini P (2019) Material characteristics of binder jet 3D printed hydrated CSA cement with the addition of fine aggregates. Constr Build Mater 206:494–503
15. Xia M, Nematollahi B, Sanjayan J (2018) Compressive strength and dimensional accuracy of Portland cement mortar made using powder-based 3D printing for construction applications. In: RILEM international conference on concrete and digital fabrication, RILEM bookseries, vol 19. Springer, Cham, pp 245–254
16. Xia M, Nematollahi B, Sanjayan J (2018) Influence of binder saturation level on green strength and dimensional accuracy of powder-based 3D printed geopolymer. In: Materials science forum, vol 939, Trans Tech Publ, pp 177–183
17. Xia M, Nematollahi B, Sanjayan J (2019) Printability, accuracy and strength of geopolymer made using powder-based 3D printing for construction applications. Autom Constr 101:179–189
18. Bullard JW, Jennings HM, Livingston RA, Nonat A, Scherer GW, Schweitzer JS, Scrivener KL, Thomas JJ (2011) Mechanisms of cement hydration. Cem Concr Res 41:1208–1223

Rheology and Workability of SCC

Rheology Study of Fresh Self-compacting Concrete Made Using Recycled Fine Aggregates

Monalisa Behera[1,2(✉)], Ashwani K. Minocha[1,2], Sriman K. Bhattacharyya[2,3], and Mohammad R. Rahman[1]

[1] CSIR-Central Building Research Institute, Roorkee, India
monalisabehera7@gmail.com
[2] Academy of Scientific and Innovative Research (AcSIR), Ghaziabad, India
[3] Department of Civil Engineering, Indian Institute of Technology, Kharagpur, India

Abstract. The paper herein presents the results of an experimental work carried out to investigate the rheological behaviour of self-compacting concrete (SCC) mixes, which were produced by replacing natural sand with recycled fine aggregate (RFA) and using supplementary cementitious materials. A cross-vane rotating type rheometer has been used to evaluate the rheological parameters of the mixes. A total of 5 different SCC mixes having varying RFA content (0%, 50% and 100%) and binder composition (30% fly ash with 10% silica fume and 40% fly ash without silica fume) have been investigated. The results showed that the yield stress of the SCCs increased with increase in the RFA content in the mixes, and it reduced when fly ash content was increased keeping RFA content constant. The mixes with 100% RFA content resulted in very high shear stress and it increases at higher rate with respect to time. Bingham parameters were obtained and linear correlation with high correlation coefficient value were found, which confirmed that the fresh self-compacting concrete having RFA can be properly modelled as a Bingham fluid. The thixotropy of the SCCs was evaluated in terms of breakdown area and drop in apparent viscosity. A strong correlation is found between breakdown area and drop in apparent viscosity at vane rotation speed from 0.1 rps to 0.4 rps.

Keywords: Rheology · Recycled fine aggregate · SCC · Thixotropy · Bingham model

1 Introduction

Concrete has become the principal construction material in the growing infrastructure development across the globe. Because of its several advantages, SCC utilization in construction industry has started growing rapidly [1]. SCC is a flowing concrete that can be compacted even into congested reinforcement places without vibrators. SCC require a higher powder content, hence demanding a large amount of cement with one or more mineral admixtures. Cement replacement by optimum mineral admixtures can

V. Mechtcherine et al. (Eds.): RheoCon 2019/SCC 2019, RILEM Bookseries 23, pp. 467–475, 2020.
https://doi.org/10.1007/978-3-030-22566-7_54

result in economical benefits and provide other advantages in terms of enhanced durability [2]. In SCC there is lesser coarse aggregate than the fine aggregates. Hence, demand of cementitious materials and fine aggregates has increased. Therefore, there is need to meet this growing demand by using supplementary cementitious materials (SCM) and RFA in concrete. It will address the sustainability and environmental issues of the concrete [3].

Performance and quality of SCC depends on its properties in the fresh state. Hence, various test methods has been developed to measure the fresh properties of SCC. Most of these methods are empirical in nature. Rheology of SCC in terms of more fundamental parameters that is yield stress and plastic viscosity give a better representation of its fresh properties. SCC is characterized by low yield stress and moderate viscosity [4]. Most of the studies on SCC incorporating recycled aggregate are focused on the basic properties of hardened concrete and only verify that workability criteria for the fresh SCC are fulfilled. Thus, most of the literatures report filling ability, passing ability and segregation resistance through empirical tests such as slump flow, L-box, V-funnel, J-Ring and sieve segregation [5]. However, very few studies are available on rheological properties of SCC with RFA. It has been reported that the rheological behavior of SCC is non-linear and the shear stress increases with increasing shear rate showing shear thickening behavior [6]. Shear thickening becomes important in some concrete process practically occurring at high shear rates, like mixing and pumping [7].

In view of this, the present study focuses on the rheology of fresh SCC made using RFA. The rheological parameters were evaluated using a cross-vane type ICAR rheometer. Yield stress of various fresh SCC mixes is evaluated to see the effect of RFA. SCMs such as FA and SF are used to replace cement. The flow behavior of fresh concrete is presented in form of Bingham model for various SCC mixes. More experiments are underway to study the shear thickening behavior of the SCC mixes with RFA and therefore it is not presented in this research. The thixotropy and structural breakdown was evaluated to see the effect of RFA and SCMs which is required for successful accomplishment and performance of the intended application of such concrete.

2 Experimental Work

2.1 Materials Used

Ordinary Portland cement (OPC) of 43 grade confirming to IS: 8112 [8], FA confirming to IS:3812 [9] and SF confirming to IS:15388 [10] have been used in this study. FA has been used at 30% and 40% and SF has been used at 10% respectively to replace the cement content and to contribute towards the more fine content. Natural coarse aggregate were the crushed stones of 12.5 mm maximum size and local river sand was used as fine aggregate for control mixes. RFA is used at various replacement levels as a substitute for fine aggregate. Figure 1 shows the particle size distribution of both the fine aggregates. The RFA can bee seen to be finer than natural fine aggregate (NFA). RFA is also found to be rough and had an irregular shape as it is produced through the crushing process. Water absorption of RFA was 11%, which is very high compared to

the 1% of NFA. It is mainly due to the more fines and adhered paste on fine aggregate surface. Chemical admixtures like high range water reducer (HRWR) and viscosity modifying agent (VMA) are used to control the flowability and viscosity of SCC mixes. HRWR was a polycarboxylate ether based superplasticizer having specific gravity 1.08 and VMA had specific gravity 1.01.

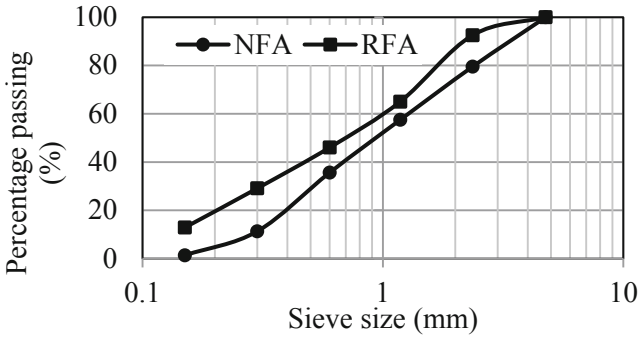

Fig. 1. Gradation curve of fine aggregates.

2.2 Mix Design and Methodology

The mix design of SCC was carried out as per the EFNARC guideline [11]. The mixes were targeted for a slump flow of 650 mm and a compressive strength of 40 MPa. The powder content was kept constant in all the mixes. The water to binder ratio was maintained at 0.9 by volume. The paste volume was fixed at ∼35% and the remaining volume comprised of aggregates. Fine aggregate was replaced by RFA at 0%, 50% and 100% by volume. Mix proportion of the SCCs is given in Table 1. Mix 1, 2 & 3 have 30% FA and 10% SF while Mix 4 & 5 has 40% FA in it. The mixing was carried out in a laboratory pan mixer. The materials were dry mixed first for 2 min and then water was added in two steps. Half of the total mixing water was added first to the dry mixture for uniform wetting. Superplasticizer and VMA are added into the second half of water and then mixed into the wet mixture. The mixing is continued for about 6-8 min until a uniform consistency was obtained, the concrete was left to rest for 2 min and again mixed for additional 2 min. Finally, the mixed concrete was poured out and filled into the rheometer container. Then the mix was tested for their fresh state properties.

2.3 Concrete Rheological Measurements

The rheology of the SCC was measured by a portable concrete rheometer manufactured by ICAR. The container used for the test was of 286 mm diameter and 40 L capacity. The blade of the rheometer was cross vane type having 127 mm diameter and 127 mm height. Two different tests were carried out with the rheometer: a stress growth test and a flow curve test.

Table 1. Mix details of SCCs (kg/m^3).

Constituent		Mix1	Mix2	Mix3	Mix4	Mix5
Cement		313.5	313.5	313.5	315.1	315.1
Fly ash		156.7	156.7	156.7	210.1	210.1
Silica fume		52.3	52.3	52.3	–	–
Natural Coarse aggregate		749.7	749.7	749.7	749.7	749.7
Fine aggregate	NFA	920.1	463.8	–	927.8	–
	RFA	–	364.8	729.6	–	729.6
Water (free)		174.1	174.1	174.1	174.1	174.1
SP (%)		1.0	1.0	1.0	0.7	0.8
VMA (%)		0.20	0.19	0.20	0.20	0.20
w/powder ratio (by vol.)		0.9	0.9	0.9	0.9	0.9

2.3.1 Stress Growth Test

The stress growth test was carried out immediately after the vane was immersed into the concrete. In this test, the vane is rotated at a constant speed and build-up in torque is measured continuously. The maximum torque observed during the test corresponds to the static yield stress of the SCC mix. The test was performed at different time intervals to monitor the change in behavior of the mixes with time.

2.3.2 Flow Curve Test

Flow curve test was performed after stress growth test is completed. This test determines the behavior of SCC mixes in terms of shear stress at different shearing rate measured in the form of relative parameters that is torque and rotational speed. For this study, breakdown speed which imparts pre-shearing to the SCC was 0.5 rps for 20 s time, number of points was kept 7, time per point was 5 s, initial and final speed was 0.5 rps and 0.05 rps respectively. With this setting, the vane initially rotates at a speed of 0.5 rps for 20 s. After this, torque measurements were taken at seven different speed points by reducing the speed stepwise from 0.50 rps to 0.05 rps. The average speed and torque readings for each step/speed are plotted and used to compute the rheological parameters.

3 Results and Discussions

3.1 Yield Stress

Yield stress of all the mixes were determined by performing stress growth test using ICAR concrete rheometer. Figure 2(a) shows the static yield stress of various SCC mixes with respect to time. It is seen that there is increase of static yield stress over time for all replacement levels of RFA. There was not much increase in stress during first 10 min. But, after this there was a rapid increase in the stress for all mixes and it was more pronounced for the mixes having 100% RFA. This is attributed to the rough surface texture and irregular shape of RFA that provides better interlocking leading to increased inter particle friction. Also the higher water absorbing nature of RFA makes

the concrete more and more stiff with time, thus requiring higher torque to shear the same mix. It is also seen that SCC mix with 50% RFA (Mix 2) has only slightly higher static yield stress values than Mix 1 and Mix 4 with NFA. And they show similar trend of static yield stress growth with time. Therefore, a replacement of NFA with RFA up to 50% can be easily done without affecting its rheological performance.

The initial static yield stress of Mix 3 containing 100% RFA is about 3 times more than the control mix (Mix 1) containing NFA. This is because of the more friction produced by the RFA due to their rough surface morphology and irregular shapes. Moreover, Mix 4 and Mix 5 having 40% FA as powder shows that mix with RFA has static yield stress values similar to the mix with NFA. Mix 3 and Mix 5 have 100% RFA and Fig. 2(a) shows that the Mix 3 having 30% FA requires higher stress to yield than Mix 5 having 40% FA. This is mainly due to the ball-bearing effect introduced as a result of spherical shape of FA particles.

3.2 Rheological Model

Torque measurements were taken at different rotational speed of vane by performing flow curve test in concrete rheometer as described earlier. The obtained torque and rotational speed data are then processed to evaluate yield stress and viscosity of the SCC mixes. The Reiner-Riwlin equation has been used to obtain shear stress and shear rate from the raw data of the rheometer flow curve test. An attempt is made here to express the flow behavior of the various SCC mixes using the well-known Bingham model. Figure 2(b) shows the shear rate and shear stress relationship of the SCC mixes along with the Bingham models for all the mixes. It can be seen that the yield stress of the mixes increases when NFA (Mix 1 and Mix 4) is replaced with RFA (Mix 3 and Mix 5). The viscosity was found to increase when RFA is used for the mix containing SF (Mix 1 and Mix 3), while, it decreased when no SF is used (Mix 4 and Mix 5) keeping the SCM level same in both the systems. Analyzing the mixes with 100% RFA, it is seen that the Mix 3 containing SF has higher viscosity than Mix 5 without SF. This clearly shows the more viscous imparting nature of SF. It is because of the extremely finenature and higher surface area of the SF. The linear model expressed here is seen to fit the rheological behavior of the mixes properly which confirmed that the fresh SCC containing RFA can be suitably modeled as a Bingham fluid.

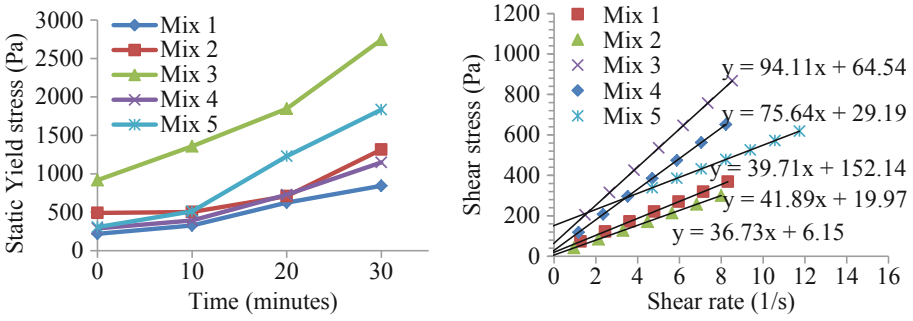

Fig. 2. (a) Static yield stress of various SCC mixes with time (b) Flow curve of various SCC mixes and Bingham model.

3.3 Thixotropy

Thixotropy of the SCC mixes was determined by analyzing the stress growth test results and it is evaluated through the method recommended by Legrand [12] and Ahari et al. [13]. In this method, initial torque (T_i) and equilibrium torque (T_e) are determined at a particular rotation speed from the stress growth curve as shown in Fig. 3.

T_i and T_e are determined by performing stress growth test at different rotational speed (0.1 to 0.5 rps). The T_i and T_e values for each rotational speed are plotted and power law best fit are drawn through the plotted values of both T_i and T_e. Figure 4(a) shows the best fit plot of Mix 1. Then, the area enclosed between the T_i and T_e curves is calculated by integration. This area gives the quantified value of the degree of thixotropy in terms of breakdown area. The breakdown area is calculated for the various SCC mixes and is presented in Fig. 4(b). The breakdown area is seen to increase with the increase of RFA content in the SCC mix. 50% replacement of RFA does not much effect the thixotropy of the SCC but at 100% replacement the thixotropy is greatly increased and this is evident from the increase of breakdown area to ~3 times for Mix 3 in comparison to the Mix 1.

Breakdown area is strongly dependent on the factors that affect initial torque and equilibrium torque values measured during the stress growth test. When FA content is increased from 30% to 40% in the SCC mix, it brings down the difference between the initial torque and equilibrium torque. This reduces the area enclosed and thereby reducing the breakdown area of the mixes having more FA content. Therefore, it is found that the Mix 3 has a breakdown area of ~45% less than the Mix 1 and Mix 5 has this value ~35% less than the Mix 3. This can be attributed to the spherical shape, smooth surface texture of the grains, low porosity of the particles and lower fineness of the FA.

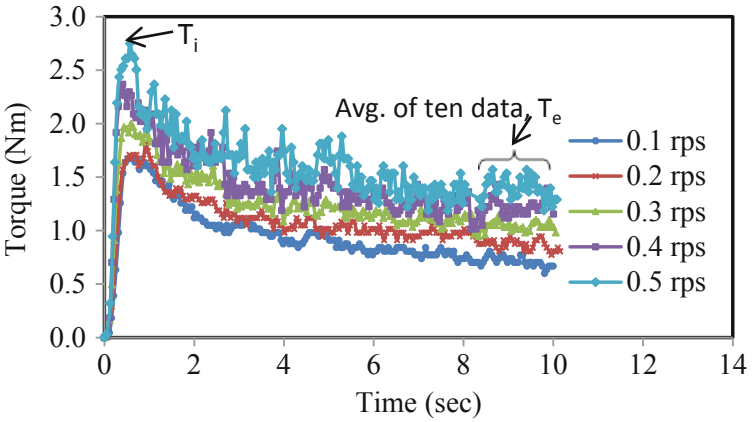

Fig. 3. Stress growth curve of Mix 1 at different rotational speed.

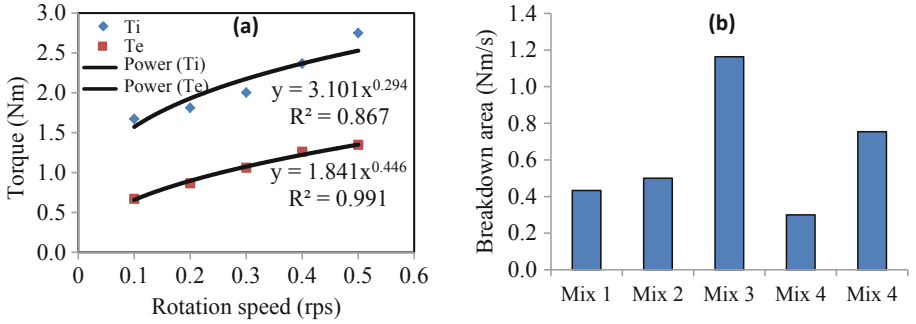

Fig. 4. (a) Best fit curve of initial and equilibrium torque for Mix 1 (b) Breakdown area of various SCC mixes.

The drop in apparent viscosity is calculated by dividing the difference between T_i and T_e by the corresponding rotational speed for which T_i and T_e has been obtained. It was calculated for 4 different speeds from 0.1 rps to 0.4 rps. Drop in apparent viscosity is an approach to assess the amplitude of the time-dependent phenomenon [13]. Figure 5 shows the relationship between breakdown area and drop in apparent viscosity at different rotational speeds. The high correlation coefficient (R^2) values ranging from 0.83 to 0.99, reveals that there is a good correlation of drop in apparent viscosity with breakdown area and it can be used to determine the thixotropy of the SCC mixes.

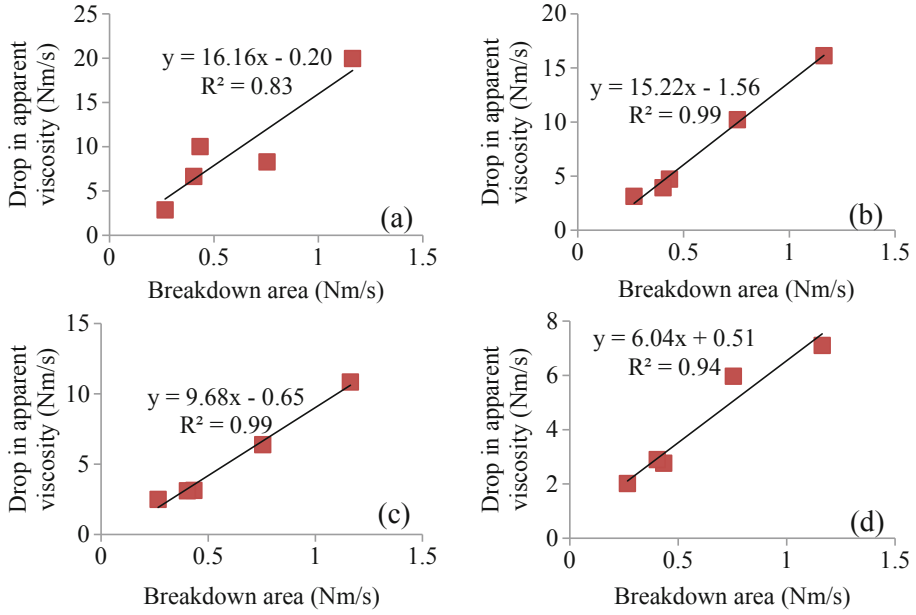

Fig. 5. Relationship between breakdown area and drop in apparent viscosity at different rotational speed (a) 0.1 rps (b) 0.2 rps (c) 0.3 rps (d) 0.4 rps.

4 Conclusions

The rheological properties of the SCC made using RFA have been investigated. Based on the results obtained in this study, the following conclusions can be drawn:

- The static yield stress increases with time for all mixes and it increase more rapidly in case of SCC containing 100% RFA likely due to higher water absorption capacity of RFA and more friction caused by the rough surface texture and interlocking of the irregular shaped RFA.
- The replacement of fine aggregate with RFA increased the viscosity of the mixes containing SF while, it decreased when no SF is present in the SCC.
- Bingham model is found suitable to describe the flow behavior of all SCC mixes.
- Breakdown area increased with increase of RFA in SCC due the irregular shape and rough surface morphology of the RFA while it decreased with increase in FA content because of the spherical shape and smooth texture of FA.
- A strong correlation exists between breakdown area and drop in apparent viscosity and drop in apparent viscosity can be used to assess the amplitude of the time-dependent thixotropy phenomenon.

Acknowledgement. The paper forms part of CSIR R&D program (Govt. of India) and funded by CSIR- Central Building Research Institute, Roorkee. It is published with the kind permission of the Director, CSIR-Central Building Research Institute, Roorkee, India.

References

1. Nataraja MC, Gadkar A, Jogin G (2018) A simple mix proportioning method to produce SCC based on compressive strength requirement by modification to IS 10262:2009. Indian Concr J 92(1):15–22
2. Behera M, Minocha AK, Bhattacharyya SK, Rahman MR (2018) Studies on the flow properties of self-compacting concrete with recycled fine aggregate. In: Proceedings of the 11th structural engineering convention, Kolkata, India, 19–21 December, CT129–CT137
3. Behera M, Bhattacharyya SK, Minocha AK, Deoliya R, Maiti S (2014) Recycled aggregate from C&D waste & its use in concrete – a breakthrough towards sustainability in construction sector: a review. Constr Build Mater 68:501–516
4. Khayat KH (2000) Optimization and performance of air-entrained, self compacting concrete. ACI Mater J 97(5):526–535
5. Safiuddin MD, Salam MA, Jumaat MZ (2011) Effects of recycled concrete aggregate on the fresh properties of SCC. Archiv Civ Mech Eng 11(4):1023–1041
6. Feys D, Verhoeven R, De Schutter G (2009) Why is fresh self-compacting concrete shear thickening? Cem Concr Res 39:510–523
7. Güneyisi E, Gesŏglu M, Algin Z, Yazici H (2016) Rheological and fresh properties of self-compacting concretes containing coarse and fine recycled concrete aggregates. Constr Build Mater 113:622–630
8. IS: 8112 (2013) Ordinary Portland cement, 43 Grade–specification, BIS, India
9. IS: 3812 (2013) Pulverized fuel ash—specification. Part 1 For use as pozzolana in cement, cement mortar and concrete, BIS, India

10. IS: 15388 (2003) Silica fume—specification, BIS, India
11. EFNARC (2005) The European guidelines for self-compacting concrete- specification, production and use
12. Legrand C (1971) Contribution of study of the rheology of fresh concrete, Ph.D thesis, Universite Paul Sabatier de Toulouse, France, p 150
13. Ahari RS, Erdem TK, Ramyar K (2015) Thixotropy and structural breakdown properties of self-consolidating concrete containing various supplementary cementitious materials. Cem Concr Comp 59:26–37

Experimental Study of Formwork Tightness as a Function of Rheological Properties of SCC

Chizya Chibulu(✉), Khadija El Cheikh, Mert Y. Yardimci, and Geert De Schutter

Magnel Laboratory for Concrete Research, Ghent University, Ghent, Belgium
chizya.chibulu@ugent.be

Abstract. Several studies relating formwork pressure to rheology exist, however the relationship between rheology and leakage through formwork joints remains to be investigated. In practice, standard documents are used to define formwork tightness requirements, typically using a qualitative approach. To try bridge this gap in knowledge, we developed a test set-up to study tightness of formwork joints under pressure as a function of varying rheological properties. Coupled with standard rheology tests, this new test set-up provides means of linking flow rate, formwork pressure, flow area, and the rheological properties. The study seeks to provide insight on measurable governing parameters and thus inform formwork tightness requirements in a more quantifiable manner.

This paper presents a test set-up designed to study the flow of fresh paste through small openings. It highlights a preliminary study on the pressure-driven flow of limestone paste through a bottom orifice in a cylindrical container. While this new device may not be directly representative of the actual conditions in formwork, it provides a good base for a fundamental study that can then be extrapolated to a more representative test operation. Preliminary results show a linear relationship between the flow rate and the applied pressure. The results also show that increasing the flow area by a factor of 2.33 had a higher impact than an increase in yield stress and viscosity by a factor of 2.54 and 3.80 respectively. However, more tests need to be carried out to obtain clear trends.

Keywords: Formwork tightness · Formwork pressure · Leakage · Rheology · SCC

1 Introduction

Over the past years, there has been increasing interest amongst researchers to understand and characterize the behaviour of self-compacting concrete (SCC). Despite this growing trend, contractors generally still have problems with practical aspects of construction. There are still many gaps in knowledge that need to be explored in order to adequately resolve these issues. Due to the high fluidity of SCC, one of the main challenges cited by contractors is the increase in formwork pressure and leakage between formwork panels [1]. To avoid formwork collapse or excessive surface defects, stiffer forms and supplementary sealing actions are required, making the use of SCC unappealing. Although various studies on formwork pressure have been done [2–6], the relationship between

V. Mechtcherine et al. (Eds.): RheoCon 2019/SCC 2019, RILEM Bookseries 23, pp. 476–481, 2020.
https://doi.org/10.1007/978-3-030-22566-7_55

rheology and leakage of cement grout through formwork joints remains to be investigated. Leakage of cement grout at the formwork joints could result in poor surface quality or even honeycombing in more severe cases. Water and fine particles (cement, powders and fine sand) are drained away, leaving unacceptable surface defects [1]. The unfortunate thing is that these sub-standard results are only discovered after the formwork is removed and the concrete has already set.

Formworks provide support and confinement to concrete as it transitions from its fresh state to a solid mass. To prevent or minimise leakage of fresh concrete, the contact surfaces of adjacent formwork panels must be as close as possible. In practice it is difficult to obtain a perfect connection between two adjacent panels, thereby leaving a gap between the joints. The width of the gap between the formwork panels affects the nature of flow through the joint, as well as the quantity and composition of the material leaking through. Generally, the leaked material is composed of cement milk, paste, or mortar, depending on the width of the gap. The ease with which the concrete flows through the formwork joints is also dependent on rheological properties of the bulk fluid. Mixtures with higher slump for example have been reported to exhibit more leakage [7]. The problem of formwork leakage is thus one that involves both hydrodynamics and rheology. The nature of the problem is that of flow of a material (cement paste in this case) through a confined space (the formwork joint). Numerous studies of this nature (confined flow) have been carried out in many fields outside the scope of concrete technology. For example, the flow of pastes through an orifice [8], the simultaneous discharge of liquid and grains from a silo [9], or flow of colloidal suspensions through small orifices [10].

In the present study, the theory of confined flow through small openings was used to develop a device to study the flow of cementitious materials (pastes and mortars) through formwork joints. This was coupled with design concepts of a previously developed portable device for evaluating formwork pressure [11]. While this new device may not be directly representative of the actual conditions in formwork and SCC, it provides a good base for a fundamental study that can then be extrapolated to a more representative test operation. It is a first step in an ongoing research to develop a method of characterization of rheological properties of SCC in relation to leakage behaviour and thus aid in the quantification of formwork tightness requirements. To begin our study, we decided to investigate the confined flow of pastes through an opening. As mentioned, when leakage of fresh concrete between formwork joints occurs, it is generally the liquid and paste material that make up the composition of the leaked fluid. From another perspective, concrete is a composite material that can be understood as a concentrated suspension of solid particles (aggregates) in a viscous liquid (cement paste) [12]. It would thus be beneficial in this case to understand how the cement paste, as the liquid medium, behaves under the various influencing conditions before the complexities of aggregates are included. It is understood that the results and trends observed for pure pastes may not hold when aggregates are incorporated into the mix design as this may cause a filtration effect. However, the data obtained from the investigations on pastes can be used to guide further studies on mortar and concrete.

2 Device to Study Formwork Tightness

A small-scale system was developed for the purpose of studying leakage as a function of pressure, rheological properties, and flow area. The system consists of a vertical steel column of circular cross section, diameter 100 mm. The top plate of the test cylinder is connected to an air compressor that supplies a regulated amount of air pressure into the device. The bottom plate of the test cylinder consists of interchangeable plates with various slit sizes so studies on the effect of different flow areas and geometries can be done. Figure 1 shows a schematic of the set-up. The test cylinder is filled with paste to a height of approximately 310 mm. A specified overhead pressure is then applied for approximately 1 min to allow for the pressure in the system to stabilise. Once this stable pressure value is achieved, the slit at the bottom of the cylinder is opened, allowing the material to flow. The mass flow rate is captured using an electronic balance equipped with data acquisition software. A calibrated pressure sensor is placed at the top plate of the column to monitor the actual pressure that is being applied and correlate it to the resulting flow rate. The overhead pressure can be varied to simulate different casting rates. In this study, pressures of 0.1 bar, 0.2 bar, 0.3 bar, 0.4 bar were applied to the system in order to imitate different casting pressures.

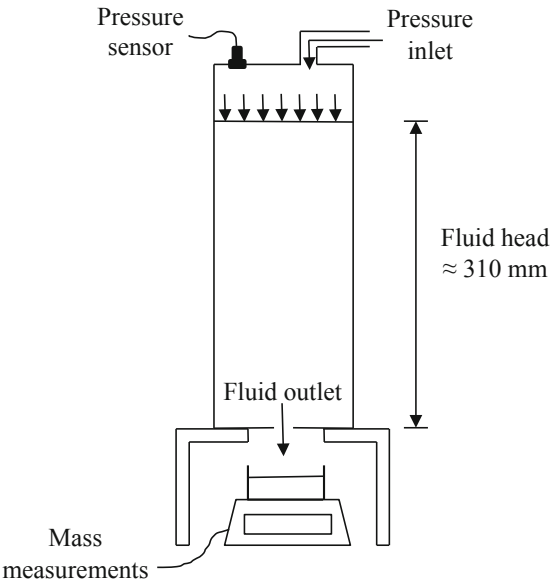

Fig. 1. Schematic of test set up.

The effect of varying rheological properties can be investigated by varying the mix design of the test fluid, keeping all other test variables constant. The rheological properties of the pastes can be modified by using workability boxes and a 'vectorised rheograph' approach [13]. Thixotropic effects can also be investigated by leaving the

material in the device for a set amount of time before initiating flow through the opening. As a first step, tests were conducted on limestone filler pastes. This removed the complexity of time dependency and allowed us to be more acquainted to the equipment and develop a test protocol. Two different limestone filler pastes were prepared. The material properties of the pastes are shown in Table 1.

Table 1. Material properties.

	W/LF	Density [kg/m^3]	Yield stress [Pa]	Viscosity [Pa·s]
LF1	0.40	1780	62.56	0.80
LF2	0.33	1900	158.48	3.04

To study the effect of flow area, two different slit sizes with rectangular geometry were used. The flow area of the two slits are 25.75 mm^2 (A1) and 60 mm^2 (A2), with dimensions of 1 mm × 25.75 mm and 2 mm × 30 mm for A1 and A2 respectively. For these tests, the rheological properties were kept constant by using the same limestone filler paste (LF2). The results are designated as LF2_A1 and LF2_A2 for the two respective flow areas.

3 Preliminary Results and Analysis

The overhead pressure applied to the system was measured and plotted. Typical values are shown in Fig. 2a. The three curves on both graphs of Fig. 2 represent three repetitions of the same test. The results show that the pressure remained relatively constant in the duration of the test, and thus an average value of pressure could be obtained. This average value of the three pressure readings was then taken as the actual pressure applied to the system. The mass of material flowing out of the slit was recorded in real time. Figure 2b shows a typical plot of the mass evolution. The curves show a linear increase implying a constant flow rate. The slope of the mass-time graph (Fig. 2b) gives the mass flow rate $\dot{m}$. The volumetric flow rate Q, was then calculated by dividing by the density of the paste ρ:

$$Q = \frac{\dot{m}}{\rho}$$

The volumetric flow rate (expressed in L/min) was then plotted against the pressure applied in the system. Figure 3a shows the results of the two different limestone mixes, keeping the flow area constant. The results show a linear relationship between the flow rate and the pressure for both pastes. The paste LF1 exhibits higher flow rates for a given pressure than LF2. The results show that for an increase in yield stress by a factor of 2.54 and viscosity by 3.80, the flow rate increased by a factor of 1.41% ± 10% at any given pressure. Similar results were obtained by increasing the flow area from 25.75 mm^2 to 60 mm^2. Figure 3b shows the results of the effect of increasing the flow area on the flow rate for a given paste. A linear relationship between flow rate and

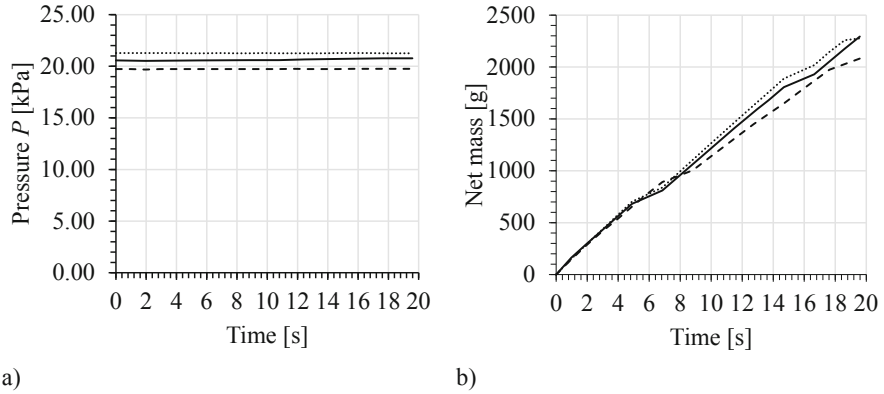

Fig. 2. (a) Typical pressure readings during test, (b) typical evolution of net mass during test.

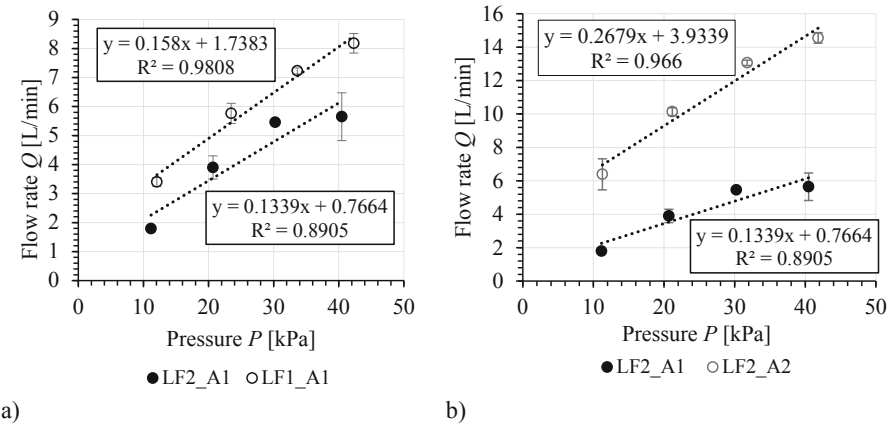

Fig. 3. Flow rate, Q as a function of applied pressure, P; (a) effect of rheological properties on flow rate, (b) effect of flow area on flow rate.

pressure was also obtained. Increasing the flow area by a factor of 2.33 resulted in a 2.67% ± 30% factor increase in the flow rate. In this instance, increasing the flow area had a larger impact on the flow rate than the increase in rheological properties. However, more tests need to be carried out to observe clear trends.

These preliminary experiments give promise to further understanding the phenomenon of leakage. With further testing, the goal is to obtain a theoretical expression that links flow rate to rheological properties and flow area. For instance, for a given change in yield stress and viscosity, the flow rate can be expected to change by a predicted factor.

4 Summary and Conclusion

This paper presents a test set-up designed to study the flow of SCC through a slit. It highlights a preliminary study on the pressure-driven flow of limestone paste through a bottom orifice in a cylindrical container. Although this is only a first step in an on-going study, the results already show the capabilities and information that can be extracted from such an experimental programme. More tests need to be carried out before meaningful correlations can be made. However, with these preliminary results it can be seen that test set-up is able to register the changes in flow rate due to a change in the input parameters.

Acknowledgement. The authors acknowledge the support given by the European Research Council (ERC) for the Advanced Grant Project 'SmartCast' (No. 693755) awarded to Prof. Geert De Schutter.

References

1. De Schutter G (2013) Damage to concrete structures. CRC Press, Ghent
2. Billberg P (2012) Understanding formwork pressure generated by fresh concrete. In: Roussel N (ed) Understanding the rheology of concrete. Woodhead Publishing Limited, Cambridge, pp 296–330
3. Khayat K, Assaad J, Mesbah H, Lessard M (2005) Effect of section width and casting rate on variations of formwork pressure of self-consolidating concrete. Mater Struct 38(1):73–78
4. Koehler EP (2014) Thixotropy of SCC and its effects on formwork pressure. American Concrete Institute, Cambridge
5. Omran AF, Khayat KH (2017) Effect of formwork characteristics on SCC lateral pressure. J Mater Civil Eng 29(5):04016293
6. Ovarlez G, Roussel N (2006) A physical model for the prediction of lateral stress exerted by self-compacting concrete on formwork. Mater Struct 39(2):269–279
7. Cools T, Van Gysel A, Van Itterbeeck P (2016) Tightness requirements for SCC formwork. s.l., s.n
8. Toplak T, Tabuteau H, De Bruyn JR, Coussot P (2007) Gravity draining of a yield-stress fluid through an orifice. Chem Eng Sci 62(23):6908–6913
9. Cervantes-Álvarez AM, Hidalgo-Caballero S, Pacheco-Vázquez F (2018) The simultaneous discharge of liquid and grains from a silo. Phys Fluids 30(4):043302
10. Hildago RC (2018) Flow of colloidal suspensions through small orifices. Phys Rev 97:012611
11. Khayat KH, Omran A (2009) SCC Formwork Pressure, Quebec, s.n
12. Castro AL, Liborio JB (2006) Initial rheological description of high performance concretes. Mater Res 9(4):405–410
13. Wallevik OH, Wallevik JE (2011) Rheology as a tool in concrete science: the use of rheographs and workability boxes. Cem Concr Res 41:1279–1288

The Effect of Fiber Geometry and Concentration on the Flow Properties of UHPC

Florian Gerland[1(✉)], Maximilian Schleiting[2], Thomas Schomberg[1], Olaf Wünsch[1], Alexander Wetzel[2], and Bernhard Middendorf[2]

[1] Department of Fluid Dynamics, University of Kassel, Kassel, Germany
florian.gerland@uni-kassel.de
[2] Department of Building Materials and Construction Chemistry, University of Kassel, Kassel, Germany

Abstract. The economic relevance of fiber-reinforced concrete has increased steadily throughout the years. Fiber reinforcement improves the mechanical properties of concrete structures, but at the same time has the disadvantage of worsening the workability of fresh concrete. In order to better understand the influence of the fibers on the fresh concrete properties, rheological measurements were carried out on suspensions with fibers of typical rod-shape and atypical ring-shape with volume fractions up to 3.3% and 4.8% respectively. The study is carried out on UHPC as a matrix fluid as well as on a silicone oil as a substitute fluid with comparable flow properties. Investigation on a substitute fluid has the advantage of excluding interferences caused by thixotropy and interaction with granular components.

The measurements were carried out with ball probe systems and evaluated with a numerical simulation-based procedure in such a way that objective physical Bingham material parameters could be determined. It was found that due to the weak interaction of the fibers, the increase in viscosity with the fiber volume fraction is linear and independent of the fiber geometry. For the same reason, no significant yield stress has been detected.

Keywords: Concrete rheometry · Fiber geometry · Flow properties · Viscosity · Fiber volume fraction

1 Introduction

With the increasing economic relevance of fiber-reinforced concrete, understanding the systematic effects of fiber addition on the flow behavior of fresh concrete and thus on its workability is of increasing importance. With regard to the flexural strength of the concrete components, it is desirable to maximize the fiber content [1]. The other side of the coin, in fact, is that the workability of the fresh concrete can drastically deteriorate through the addition of fibers. It may be a long-term goal to use fibers made of iron-based shape memory alloys (SMA). Such fibers can be mixed while in a geometry which is advantageous for the fresh concrete properties. Later, the activation (e.g. by heat) results in a change in shape which is advantageous for the solid-state properties.

V. Mechtcherine et al. (Eds.): RheoCon 2019/SCC 2019, RILEM Bookseries 23, pp. 482–490, 2020.
https://doi.org/10.1007/978-3-030-22566-7_56

In that way, it could be possible to improve the durability and safety of concrete components by significantly increasing the fiber volume fraction and thus increasing the strength of the components and their resistance to cracking. The applicability of SMA-fiber-reinforced concrete for pre-stressing [2] and to dissipate energy [3] has already been proven.

It is known that suspensions containing spherical particles exhibit a linear increase in viscosity with respect to the matrix fluid at low particle volume fractions [4]. As of a critical particle concentration, the viscosity increases over-proportionally. For spherical particles, a yield point is usually perceived above 50 vol-% of particles. Similar effects are known for suspensions of non-spherical (mostly rod-shaped) particles, but usually effects ascribed to concentrated suspensions occur at much lower volume fractions. The reason is that slender fibers form a high connectivity at a significantly lower volume fractions, which can be described by the fiber coordination number and negatively influences the rheological behavior [5, 6].

For fiber-reinforced concrete, only a few publications investigate the effect of fibers on flow behavior in detail. Ghanbari and Karihaloo investigated the plastic viscosity of self-compacting fiber-reinforced concrete (rod-shaped fibers) at concentrations up to 2 vol-%. They found that the relative viscosity related to fiber-free concrete increases linearly with the volume fraction and as a function of the aspect ratio of the fibers [7, 8]. Martinie et al. [9] investigated the influence of fibers on the development of the yield stress of UHPC. The result shows, that the yield stress started to occur from a critical packing density, which is a function of both the volume fraction and the fiber aspect ratio.

Abdallah et al. [10] investigated the influence of various hooked-end fiber geometries on the post-cracking behavior and reported in this context a minor influence on the workability of the concrete independent of geometry and fiber content. The authors used fibers with an aspect ratio of 65 at concentrations up to 1 vol-%. Soroushian and Bayasi [11] investigated the relative effect of fibers of different hooked-end, crimped and straight geometries at a volume fraction of 2% and aspect ratios around 60. They determined no significant differences in slump, inverted slump-cone and subjective workability tests. Guerini et al. [12] compared stiff fibers with end hooks with flexible fibers of different geometry at volume fractions up to 1% in ordinary concrete of classes C45 and C50. The authors stated that the processability deteriorates for both rigid and flexible fibers with increasing fiber length.

When measuring the properties of fresh concrete, some particularities need to be considered. Feys et al. [13] showed that rheometer types used in wide fields of rheometry have weaknesses when applied for cement pastes and concretes, which are basically due to the fact that the granular constituents are in the order of magnitude of the relevant device's geometry. Examples are wall slipping or plug flow as well as particle migration and segregation. Compensation efforts such as changing the device geometry (increasing the gap, attaching lamellas, etc.) almost ever come along with the drawback, that there is normally no longer a simple shear flow. The necessary corrections in the evaluation are then accompanied by the disadvantage that the actual (physical) shear rates and/or shear stresses are not necessarily represented. Therefore, the measurements only have comparative value, e.g. to assess the flow properties of samples or batches in the same measuring instrument. A device type specially

developed for granular suspensions such as concrete and cement paste is the ball probe system [14]. Devices of this type drive a ball specimen on a circular path through the sample located in a cylindrical container and measure the resulting flow resistance as a function of the rotational velocity. An advantage of this design is the avoidance of plug flow. However, the flow state is not described analytically, which is why a direct determination of the objective material parameters (yield point and plastic viscosity) is not possible directly. Thus, a comparison of the measurement results of devices with different dimensions is only feasible to a limited extent. Fleischmann [14] proposes an evaluation approach for such devices based on simplifications for Bingham fluids. This method, however, cannot explain nonlinear effects which appear in the measurement data for pronounced yield stress fluids. In former work of the author an alternative evaluation method for Bingham fluids based on numerical simulation of the flow in the rheometer and dimensional analysis of the flow problem has been developed (Gerland et al., submitted for publication). It could be demonstrated its good agreement with measurement data, its ability to determine objective and absolute material parameters and therefore the direct comparability of measurement results from devices of different dimensions. It should be noted that the geometry of the measuring instruments applied does not principally prevent wall slippage. However, wall slippage was not observed in any of our investigations neither with silicone oil nor with UHPC.

A determination of the physical material parameters and thus a quantitative comparability of the measurement results obtained by devices of different dimensions can be made by evaluating a general relationship of the torque M

$$M = l^2 \mu \Omega D \left(a_0 + a_1 \left[\frac{\tau_y R}{\mu \Omega D} \right]^{a_2} \right) \tag{1}$$

and the plastic viscosity μ, the yield stress τ_y, the radius of the ball's circular path R, its diameter D, the rotational velocity Ω as well as the geometry-specific coefficients a_0, a_1, a_2.

Geiker et al. [15] investigated the influence of the measuring procedure on the measuring results of a Vane type concrete rheometer under a staircase velocity profile. They determined that each velocity level must be maintained sufficiently long until a stationary stress condition is obtained. Our evaluation method for ball measuring systems is subject to the assumption that the flow is always quasi-stationary. This is ensured by selecting a velocity control in the form of a continuous ramp with sufficiently low acceleration. On fluids with known properties it was proven that the acceleration is sufficiently small by matching the measured values with steady state numerical simulations for the whole velocity range of investigation.

The aim of this work is to compare the influence of atypical fiber geometries on the flow behavior of fresh concrete with common rod-shaped fibers using the example of ring-shaped fibers.

2 Experimental Procedures

The constituents of concrete are natural products that are subject to fluctuations in their chemical and physical properties. These fluctuations may affect the flow properties of the mixture. Those effects as well as flow effects due to the interaction of fibers with granular components of the concrete should be excluded. Hence, to be able to attribute the measured variables exclusively to the influence of the fibers, the measurements were carried out on a silicone oil as a substitute medium. It exhibits Newtonian flow behavior in the investigated shear rate range and its flow properties are comparable with the concrete applied in this paper. The silicone oil is polydimethylsiloxane (PDMS) with the trade name *Korasilon® Fluid M 100,000*. Since the oil is transparent, it additionally allows visual assessment of the orientation and sedimentation of the fibers. Additional experiments with concrete were carried out to evaluate the transferability to concrete. A fine-grained fresh UHPC was investigated under addition of varied fiber content of two different fiber geometries. The concrete composition corresponds to the standard formulation of SPP 1182 [16]. Both the ratio of granular constituents to each other and the proportion of liquid constituents were kept constant. In both fluids, the model fluid and the UHPC, conventional rod-shaped steel fibers were compared with ring-shaped fibers, each under varying volume fraction. The rod-shaped fibers were of length $l = 12$ mm and diameter $D = 0.4$ mm (corresponding to $l/D = 30$). The ring-shaped fibers were of almost the same length (10 mm) and the same diameter and had a ring diameter of approx. 3 mm. Both geometries are sketched in Fig. 1.

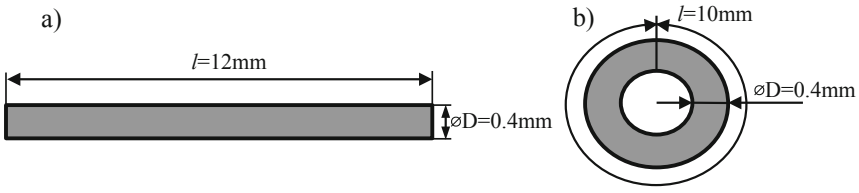

Fig. 1. Investigated fiber geometries. Rod-shaped (a) and ring-shaped (b) fibers.

Two rheometers of the spherical measuring system type were used to measure the flow properties of the fiber suspensions: *Viskomat NT* and *eBT2* (both from Schleibinger GmbH). The devices differ in dimensions, especially in sphere size and sample volume.

The determined material parameters are global flow quantities which only have a physical meaning if the assumption of a continuum in the sense of sufficient homogeneity of the sample is guaranteed during their measurement and application. It must therefore be ensured that the fibers are sufficiently small compared to the measuring geometry, i.e. the measuring sphere. For ring-shaped fibers, the characteristic dimension is the ring diameter. At 3 mm, it is sufficiently small compared to the ball diameter of the Viskomat NT (20 mm). For rod-shaped fibers, the characteristic length is the fiber

length. Therefore, a measurement in the Viskomat NT is unsuitable here. Instead, we carried out the measurements for this fiber geometry in eBT2 (ball diameter 80 mm).

At the beginning of the measurements, the fiber-free matrix liquid with a volume of 0.43 *l* (Viskomat NT) resp. 14.7 *l* (eBT2) was filled into the sample container of the measuring device.

To vary the fiber content, the fibers were successively mixed into the matrix liquid in defined portions of 14 g (Viskomat NT) resp. 785 g (eBT2). When mixing the fibers, care was taken to ensure a visually homogeneous fiber distribution. As silicone oil is transparent, we were able to assess the whole sample volume. In the case of concrete only the surface could be assessed during mixing.

The measurements were carried out at least twice for each volume fraction and a repeat homogenization was carried out immediately before the repeat. When homogenizing, it was made sure that there was no pre-orientation of the fibers at the beginning of the measurement (anisotropic fiber distribution). The orientation of the fibers was visually evaluated and compared before and after the measurements. It was also examined by observation at the container bottom whether fiber sedimentation occurs to a significant extent.

3 Results

3.1 Preliminary Studies

In the investigations on concrete it had to be ensured that a temporal influence of the hardening of the cement on the flow properties of the mixture (thixotropy) is excluded. The measurements on the sample were repeated five times over a total period of 36 min after the end of the mixing process. Before each measurement, the sample was homogenized by manual mixing to prevent sedimentation of the granular components. During this period no measurable yield point was observed and the viscosity of the sample remained approximately constant, as Fig. 2 demonstrates.

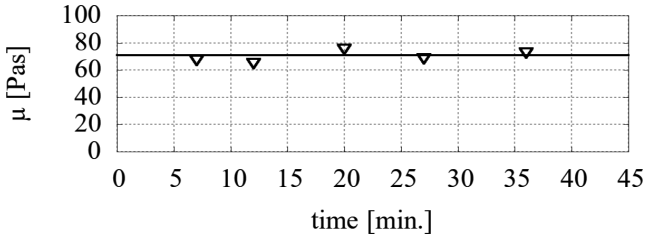

Fig. 2. Viscosity of the applied UHPC over time after the end of the mix.

The subsequent measurements on concrete with successive addition of fibres were carried out within 25 min after mixing, which is why the influence of time-dependent effects for these measurements can be excluded.

In a further pre-study, it was observed that the ring-shaped fibers in the silicone oil first completely sank to the bottom of the sample container of the rheometer after more than eight minutes. Very little sedimentation was observed within the 120 s measurement period. Especially at the level of the sphere, no reduction of the fiber concentration was observed. It was also noted that the rod-shaped fibers sediment. However, the sedimentation rate is slow compared to the duration of the measurement, so that the effect of the sedimentation is negligible for this fiber type as well.

Both measuring instruments record the torque applied to the measuring ball as a function of the rotational speed. This information is used to evaluate the Bingham material parameters by adapting the model curve from Eq. (1) to the measurement data using the least square method. Figure 3 shows the result of this procedure using the example of silicone oil with different fiber volume fractions.

3.2 Influence of Fibers on the Flow Behavior

The results of the rheometric measurements of the suspension of silicone oil with ring-shaped resp. rod-shaped fibers as well as of concrete with ring-shaped fibers are compared in Fig. 4. Yield stress could not be observed in any of the measurements. Before adding the fibers, the base viscosity of the oil and the concrete was measured. The viscosity of the silicone oil was $\mu_{base} = 112$ Pas, and that of the concrete was $\mu_{base} = 71$ Pas. The data in Fig. 4 has been related to μ_{base} of the actual matrix fluid, i.e. $\mu_{rel} = \mu_{fiber}/\mu_{base}$.

The error bars in Fig. 4 show the maximum and minimum values of a measurement series, the symbol shows the average of all repetitions. The scattering range in measurements with rod-shaped fibers (max. ± 8%) is slightly higher compared to those with ring-shaped fibers (max. ± 3%).

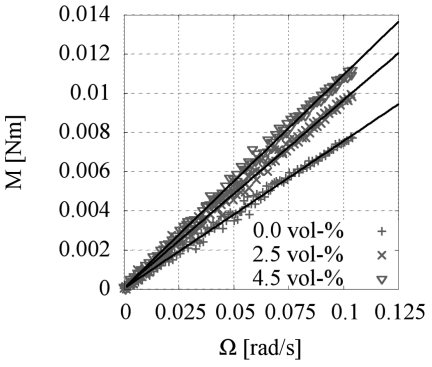

Fig. 3. Evaluation of the flow properties from the measured torque-speed-relation for different volume fractions of ring-shaped fibers suspended in PDMS.

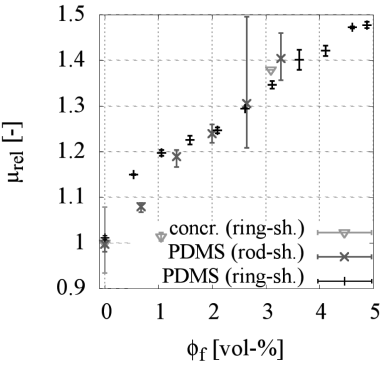

Fig. 4. Relative viscosity of the investigated suspensions as function of the fiber volume fraction. Symbols represent arithmetic mean and error bars show minimum and maximum value of each series.

The comparison of the experiments based on silicone oil suggests that in the investigated volume fraction range less than 5% (rings) resp. less than 4% (rods), no measurable influence of the fiber geometry on the flow behavior is present. In the experiments it could be observed that only sporadic fiber-fiber contacts occur and that there is no continuous inter-fiber network even at the maximum investigated volume fraction, i.e. the suspension is dilute or semi-dilute. In suspensions of this category, fluid-particle interaction forces dominate and, in the range of low particle-Reynolds numbers, flow resistance due to viscous friction dominates [17]. Both particle types follow the flow similarly well (comparable shear stresses) and their surface and volume are almost identical. Therefore, the drag force per fiber must also be comparable. Since there are similar numbers of fibers per unit volume of liquid at the same volume fraction, the momentum loss of the liquid caused by this force, which is directly related to an apparently increased viscosity, is almost identical, as observed in Fig. 4.

In both cases, the relationship between the increase in viscosity and the fiber volume fraction is approximately linear. This is in agreement with the analytical considerations of Einstein [18] for spherical particles at low concentrations. Although the measurement results on concrete show higher scatter throughout the measurement range compared to those on silicone oil, they suggest in comparison that there is the same linear correlation between viscosity increase and volume fraction. This hypothesis is also supported by the absence of a measurable yield point, which is as well attributed to the first occurrence of continuous fiber-fiber contacts [6, 9].

3.3 Fiber Orientation

Both the ring-shaped and the rod-shaped fibers revealed a pronounced orientation very quickly during the measurement. However, this did not show any discernible influence on the measured variables even after immediate repetition of the measurement without repeated homogenization. The orientation of the rod-shaped fibers before and after the measurement in silicone oil is illustrated in Fig. 5. The ring-shaped fibers oriented to a lesser extent than the rod-shaped fibers.

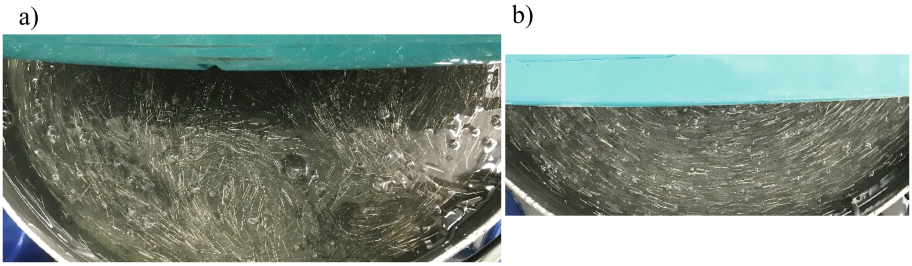

Fig. 5. Orientation of rod-shaped fibers in silicone oil before (a) and after (b) the measurement in eBT2.

4 Summary and Conclusion

In the present manuscript, the influence of fibers of the same length and diameter in rod-shaped and ring-shaped geometry at varying volume fractions in silicone oil and UHPC was compared. Regarding the geometry, no significant difference in the development of the suspension viscosity could be found. In all cases, the increase in viscosity is linearly related (proportional) to the volume fraction and is of the same rate. A pronounced yield stress was not detected in any case. The maximum fiber volume fraction was approx. 4.8% (rings) and 3.3% (rods). Even at the highest fiber concentrations examined, no continuous fiber-fiber contacts were discernable. The linear relation between viscosity and volume fraction can be explained by the dominant fluid-particle interaction forces, which are of similar size for ring-shaped and rod-shaped fibers of the same dimensions. All investigated suspensions thus fulfill the characteristics of a dilute suspension. The fact that this is also the case for unusually high volume concentrations of more than 3.3% for rod-shaped fibers in fiber-reinforced concretes can be explained by the relatively low aspect ratio of 30 and for silicone oil also by the absence of further granular particles which would favor a contact network. A higher than proportional increase in viscosity and the occurrence of a yield point, resulting in significant reduction in workability, can only be expected when a continuous fiber contact network occurs at higher volume concentrations. The bulk density of the fibers in ring-form is reduced compared to the rod-shape. Thus, the critical volume fraction for ring-shaped fibers is higher than for rod-shaped fibers. This critical volume fraction will be investigated in future investigations.

In the dilute suspensions investigated here, a strong orientation of the fibers according to the flow can be observed. This can be used to produce anisotropic material properties with fiber reinforcement similar to reinforcement steel.

References

1. Wu Z, Shi C, He W, Wu L (2016) Effects of steel fiber content and shape on mechanical properties of ultra high performance concrete. Constr Build Mater 103:8–14
2. Moser K, Bergamini A, Christen R, Czaderski C (2005) Feasibility of concrete prestressed by shape memory alloy short fibers. Mater Struct 38:593–600
3. Shajil N, Srinivasan SM, Santhanam M (2013) Self-centering of shape memory alloy fiber reinforced cement mortar members subjected to strong cyclic loading. Mater Struct 46:651–661
4. Stickel JJ, Powell RL (2005) Fluid mechanics and rheology of dense suspensions. Ann Rev Fluid Mech 37:129–149
5. Toll S (1993) Note: on the tube model for fiber suspensions. J Rheol 37:123–125
6. Orgéas L, Dumont P, Corre SL (2015) Rheology of highly concentrated fiber suspensions. In: Ausias G (ed) Rheology of non-spherical particle suspensions. Elsevier, New York, pp 119–166
7. Ghanbari A, Karihaloo BL (2009) Prediction of the plastic viscosity of self-compacting steel fibre reinforced concrete. Cem Concr Res 39:1209–1216
8. Grünewald S (2012) Fibre reinforcement and the rheology of concrete. In: Roussel N (ed) Understanding the rheology of concrete. Woodhead Publishing, Sawston, pp 229–256

9. Martinie L, Rossi P, Roussel N (2010) Rheology of fiber reinforced cementitious materials: classification and prediction. Cem Concr Res 40:226–234
10. Abdallah S, Fan M, Zhou X, Le Geyt S (2016) Anchorage effects of various steel fibre architectures for concrete reinforcement. Int J Concr Struct Mater 10:325–335
11. Soroushian P, Bayasi Z (1991) Fiber-type effects on the performance of steel fiber reinforced concrete. ACI Mater J 88:129–134
12. Guerini V, Conforti A, Plizzari G, Kawashima S (2018) Influence of steel and macro-synthetic fibers on concrete properties. Fibers 6:47
13. Feys D, Cepuritis R, Jacobsen S, Lesage K, Secrieru E, Yahia A (2017) Measuring rheological properties of cement pastes: most common techniques, procedures and challenges. RILEM Tech Lett 2:129–135
14. Fleischmann F (2014) Ein Beitrag zur Bestimmung der rheologischen Eigenschaften Selbstverdichtender Betone mit dem Kugel-Messsystem, Ph.D Dissertation, Ruhr-Universität Bochum
15. Geiker MR, Brandl M, Thrane LN, Bager DH, Wallevik O (2002) The effect of measuring procedure on the apparent rheological properties of self-compacting concrete. Cem Concr Res 32:1791–1795
16. Schmidt M, Fehling E, Fröhlich S (eds) (2014) Nachhaltiges Bauen mit ultra-hochfestem Beton: Ergebnisse des Schwerpunktprogrammes 1182, Kassel Univ. Press, Kassel
17. Crowe CT, Schwarzkopf JD, Sommerfeld M, Tsuji Y (2012) Multiphase flows with droplets and particles, 2nd edn. CRC Press, Boca Raton
18. Einstein A (1911) Berichtigung zu meiner Arbeit: Eine neue Bestimmung der Moleküldimensionen. Ann Phys 339:591–592

Rheological Characterization of Self-compacting Concrete Pastes with Polymeric Admixtures

Irene Palomar[1](✉), Gonzalo Barluenga[1], Cynthia Guardia[1], Ma Cruz Alonso[2], and Marina Álvarez[3]

[1] Department of Architecture, University of Alcala, Madrid, Spain
irene.palomar@uah.es
[2] Eduardo Torroja Institute for Construction Sciences, IETcc–CSIC, Madrid, Spain
[3] Computer Languages and Systems and Software Engineering Department, Technical University of Madrid, Madrid, Spain

Abstract. Multipurpose admixtures such as superplasticizers (SP), viscosity modifying agents (VMA) and superabsorbent polymers (SAP) are polymers commonly used in self-compacting concrete (SCC). Their main effect is positive for SCC fresh properties, minimizing some technical barriers of SCC production and cast in-place technology. However, they also affect fresh SCC rheological properties. This study addresses the rheological behaviour of fluid SCC pastes, modified with SP, VMA, SAP and their combined effects and interactions. A cement-limestone filler blended paste and two water-to-binder ratio (w/b) were designed as a reference mixture. Three dosages of VMA and SAP, 0.2%, 0.4% and 1.0% of cement weight, were investigated. The kinetics of water uptake of VMA and SAP admixtures were compared using the tea bag test in neutral pH and alkaline pH solutions. Additionally, SP was added to achieve a similar slump flow with final spread diameters of 300 mm and 400 mm, on pastes with and without VMA and SAP. The rheological parameters of the fresh pastes were tested with the mini-cone slump test. Final spread diameter, final height and time to final spread were measured after the mixing. It was found that the effectiveness of SP on the final spread diameter depended on the w/b ratio of reference paste. On the other hand, VMA increased the time to final spread, while slightly reducing the final spread diameter. SAP affected the maximum diameter due to water absorption kinetics and an increase of w/b ratio was needed to achieve similar spread diameters. It was observed that the combined use of SP and VMA or SAP affected the measured parameters. The particular effects of SP, VMA and SAP admixtures on the rheological parameters depended on w/b ratio, the amount of polymer and the combination of components.

Keywords: Rheology · Fluid paste · Limestone filler · Polymeric admixtures · Fresh SCC

V. Mechtcherine et al. (Eds.): RheoCon 2019/SCC 2019, RILEM Bookseries 23, pp. 491–499, 2020.
https://doi.org/10.1007/978-3-030-22566-7_57

1 Introduction

Polymers such as superplasticizers (SP), viscosity modifying agents (VMA) and superabsorbent polymers (SAP) are multipurpose admixtures commonly used for self-compacting concrete (SCC). Their main effect is beneficial for SCC fresh properties, minimizing some technical barriers of SCC cast in-place and construction technology. However, they also affect other rheological properties, which would affect fresh SCC workability and pumpability [1].

Due to wide variations in their composition, SCC can show different rheological properties and fresh performance. In order to reduce SCC energy consumption, supplementary cementitious materials (SCM) as limestone filler (LF) can be used [2]. Cement suspension blended with LF has been reported to show a reduction in yield stress without changes in its viscosity [3, 4]. LF can be included as a viscosity enhancement agent in mixes with large amounts of SP [5]. SP produces a remarkable effect decreasing fresh SCC yield stress. However, its effect is highly affected by the type of SP, water content and interactions with other components [6]. VMA is usually considered the best option for increasing the viscosity and stability of SCC [7, 8], although their effect on thixotropy and structural build-up is less studied [9]. SAPs are used as multifunctional admixtures, due to their high absorption capacity, included rheology modifier [10, 11].

This study aims to assess the rheological behaviour of fluid cement-limestone filler blended SCC pastes, modified with SP, VMA, SAP and their combined effects and interactions. The fresh pastes were tested measuring spread diameter, height and final time. The mechanisms behind yield stress, viscosity and thixotropy of SCC with these admixtures were investigated as they still need to be understood [12]. The mini-cone slump test is a simple field test suitable for fluid SCC pastes evaluation and the experimental parameters can be correlated to yield stress and viscosity [13–15].

2 Experimental Program

2.1 Materials and Mixtures

Figure 1 shows the design of fluid SCC pastes tested. A reference cement-limestone filler blended mixture (CEM I 42.5 R) with two water-to-binder ratios (w/b) was designed (CA). Three polymeric admixtures were used: a polycarboxylic ether superplasticizer (SP) in aqueous solution, a polyether-methylcellulose-based viscosity modified agent (VMA) and a poly(acrylamide-co-acrylate)-based superabsorbent polymer (SAP). Three dosages of VMA and SAP – 0.2%, 0.4% and 1.0% of weight of cement - were tested (Fig. 1a). Then, SP was added to achieve similar final spread diameters of 300 mm and 400 mm, on pastes with or without VMA and SAP (Fig. 1b). The dry components, included the SAP, were mixed first and the water was added afterwards. The total mixing time did not exceed 5 min in any case.

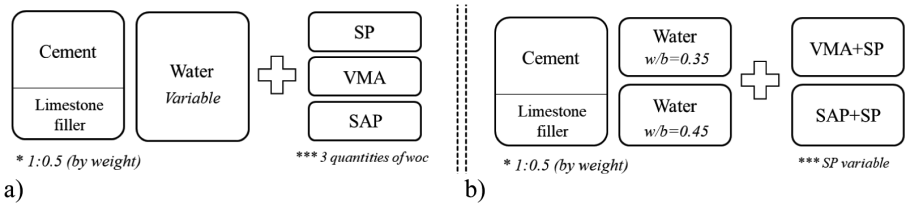

Fig. 1. Mixtures under study (a) with polymeric admixtures and (b) their combinations.

2.2 Experimental Methods and Preliminary Characterization

The experimental program involved measuring the average mass of fluid absorbed by dry VMA and SAP (teabag test) and the final spread diameter, height and time with the mini-cone slump flow test [14]. The teabag test was conducted with tap water (neutral pH) and cement pore solution (alkaline pH) [11]. Figure 2a shows the results of the teabag test. The water uptake of VMA showed a similar trend independently of the solution pH, 12 g/g and 9 g/g respectively, whereas SAP was highly affected, 32 g/g on neutral pH and 12 g/g on alkaline pH. The mini-cone used to measure the SCC pastes rheological parameters had an upper diameter of 70 mm, a lower diameter of 100 mm and a height of 50 mm. Each flow test was carried out on a dry methacrylate surface while recorded by a digital camera, in order to obtain the final diameter spread (D_f) and time to final spread (t_f). A picture of the final height (h_f) was also taken. These experimental parameters have been correlated to yield stress and viscosity [13–15]. Figure 2b relates the final spread diameter and height by a power law [13]. Thereafter, only D_f and t_f results were considered.

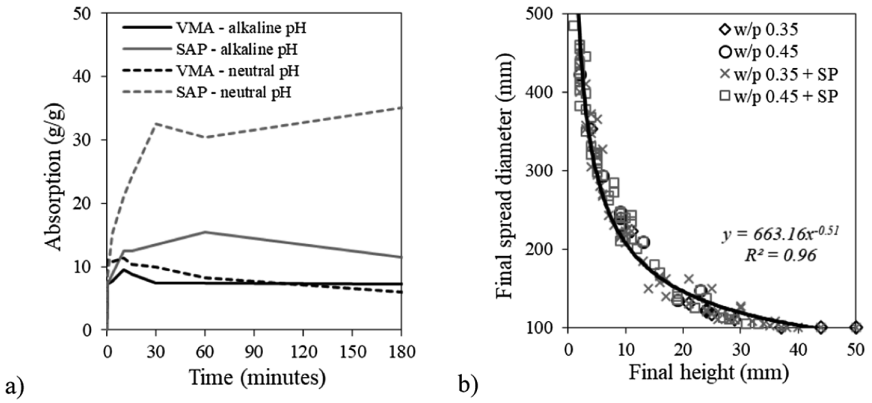

Fig. 2. (a) Teabag absorption results. (b) Final spread diameter and height of SCC pastes.

3 Experimental Results and Discussion

3.1 Mini-slump Flow Tests: Final Spread Diameter and Final Time

Figure 3 relates the paste components to the flow-test parameters. Figure 3a relates final spread diameter (D_f) to water-to-binder ratio (w/b), showing an S shape curve. A minimum and maximum w/b value can be identified.

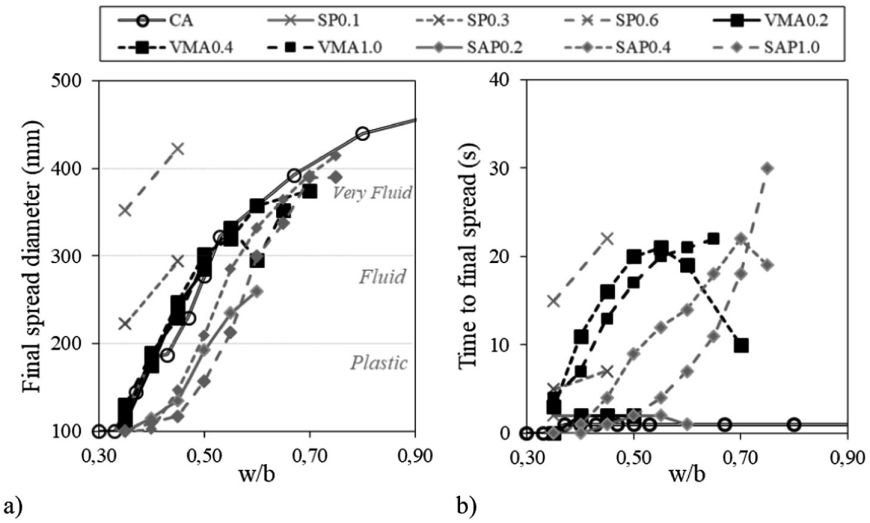

Fig. 3. Relationship among w/b (a) final diameter spread and (b) time to final spread.

Three groups of pastes can be observed, depend on paste compositions: with SP; CA and with VMA; and with SAP. As expected, SP increased significantly spread diameter, whereas SAP reduced it [10]. In general, D_f of 300 mm to 400 mm was achieved on all pastes with or without polymeric admixtures. However, the amount of water depended on the chemical structure and the amount of components, especially if SP is added. Figure 3b relates water-to-binder ratio (w/b) to time to final spread (t_f). The reference mixture (CA) and the samples with lower amount of polymeric admixtures (SP0.3, VMA0.2 and SAP 0.2) showed negligible t_f values. Nevertheless, t_f ranged from 4 s to 30 s when the amount of polymeric admixtures (SP/VMA/SAP) was increased, depending on the amount of polymer: SP above 0.3% and VMA and SAP above 0.4% modified t_f until a maximum value was reached. This peak was related to the w/b, which increased until a certain amount of water. SAP samples needed more water to reach the maximum t_f due to the kinetics of water uptake. Others authors have reported that the availability of free water for SAP mixtures influenced rheological parameters [10]. Summarizing, w/b was a flowability key parameter for polymeric admixtures. In mixtures with VMA w/b affected t_f, while in pastes with SP and SAP modified D_f and t_f.

Figure 4 presents the flow-test experimental results of pastes with VMA and SAP mixed with SP, for w/b ratios of 0.35 (Fig. 4a and b) and 0.45 (Fig. 4c and d). The increase in the amount of SP, increased D_f (Fig. 4a and c) and t_f (Fig. 4b and d), until a limit of efficiency, above which more SP did not increase D_f. The effectiveness of SP on spread diameter was higher for lower w/b. In addition, more SP is needed to reach similar diameter when the amount of the other polymeric admixture (VMA/SAP) was increased, especially for SAP samples, because SAP counteracted the effect of SP on yield stress [10]. In general, all samples with SP reached a minimum diameter of 300 mm (fluid pastes), except SAP1.0. Pastes with 0.35 w/b VMA0.2, VMA0.4 and SAP0.2 reached 400 mm (very fluid pastes) while for 0.45 w/b all the pastes with VMA and SAP0.2 achieved these values. Regarding t_f, two trends were identified: a linear relationship between SP amount and final time until a plateau or until a relative maximum per mixture was reached. Lower w/b ratio affected similarly the relation between SP and t_f, ranged from 0 s to 60 s, except for VMA0.4 + SP0.6 and SAP0.4 + SP0.6 that had a peak at 80 s and 110 s, respectively. On the other hand, a higher w/b ratio (0.45) slowed down CA + SP and SAP1.0 + SP. The other mixtures reached values between 50 s and 80 s, excluding VMA1.0 + SP that exceeded 120 s. Summarizing, the effect of SP on VMA and SAP blended-mixtures depended on SP range effectiveness, amount and type of admixture and w/b ratio.

3.2 Effect of SP, VMA and SAP on the Rheological Behavior of Fluid SCC Pastes

Figure 5 plots the influence of SP, VMA and SAP on the rheological behavior of fluid SCC pastes. The increase of yield stress and viscosity were assessed through the decrease of final diameter spread and the variation of time to final spread, respectively [13–15]. Reference mixture (CA) without SP reached a D_f of 120 mm and 210 mm at 0.35 and 0.45 w/b ratio, respectively, and in both cases final time was almost zero. Therefore, larger w/b reduced yield stress and did not affect viscosity, which agrees other studies [3]. The addition of SP increased linearly D_f up to 420 mm and t_f up to 25 s, though a minimum amount of 0.3% was needed. SP reduced significantly yield stress and increased viscosity. These results are in disagreement with other studies reported in the literature. There are studies were SP reduced the viscosity of SCC [5] and others where SP did not affect viscosity of cement-limestone filler paste [4]. VMA did not varied D_f of reference mixture for both w/b, whereas t_f increased above 13 s at 0.45 w/b ratio when 0.4% or 1.0% of VMA was added. Accordingly, VMA did not affect yield stress, while increased viscosity for higher w/b. An increase in both yield stress and viscosity of cement and blended cement–limestone pastes has been reported [5, 7]. SAP reduced slightly the final diameter for higher w/b (0.45) and did not modify significantly t_f. This slight yield stress and viscosity variations for w/b 0.45 may be explained due to water absorption kinetics. Increasing w/b ratio has been reported as a key parameter for changing in rheological behavior of cement mortars with SAP [10].

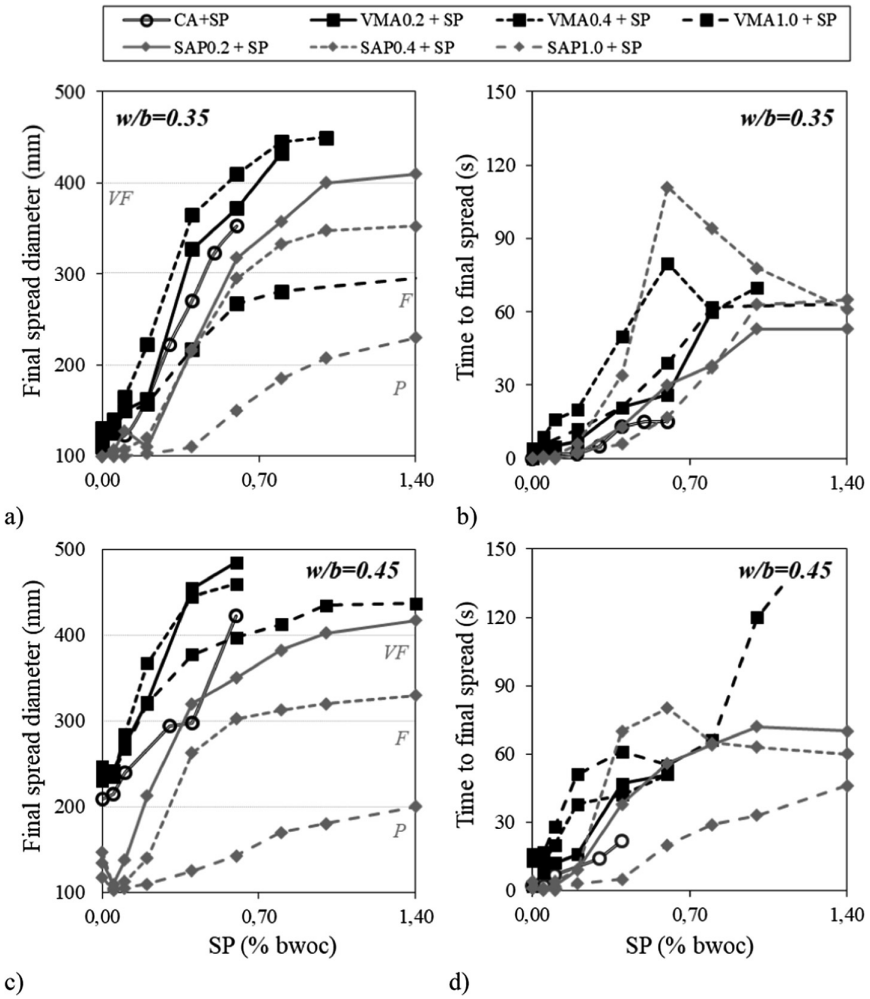

Fig. 4. Relationship among SP (a), (c) final diameter spread and (b), (d) time to final spread of two water-to-binder ratio fluid SCC pastes.

3.3 Combined Effects and Interactions of Polymeric Admixtures

Figure 6 plots the combined effects and interactions of polymeric admixtures on the rheological behavior of fluid SCC pastes. The rheological behavior was assessed through the ratio ($\Delta\text{Ø}/t_f$) relating slump diameter variation ($\Delta\text{Ø} = D_f - D_i$ in mm) and stopping time (t_f in seconds). Regardless w/b, reference mixture (CA) remained constant at 20 mm/s when SP ranged from 0.4% to 0.6%. In general, the combination of VMA and SP showed less variability (5 mm/s–20 mm/s), especially at 0.45 w/b, which agrees with other studies [6–8]. The combinations of SAP with SP showed the largest variability on D_f and t_f values, due to the larger effect of several parameters as the amount of polymer, % of SP and w/b, as was seen in Figs. 3 and 4 [10]. A minimum

value of 2.50 mm/s was reached for 0.40% of SAP and SP between 0.4%–0.6% regardless w/b. A maximum of 50 mm/s was observed when a small amount of SAP, SP and water was included (SAP0.2 + SP 0.2 + w/b 0.35).

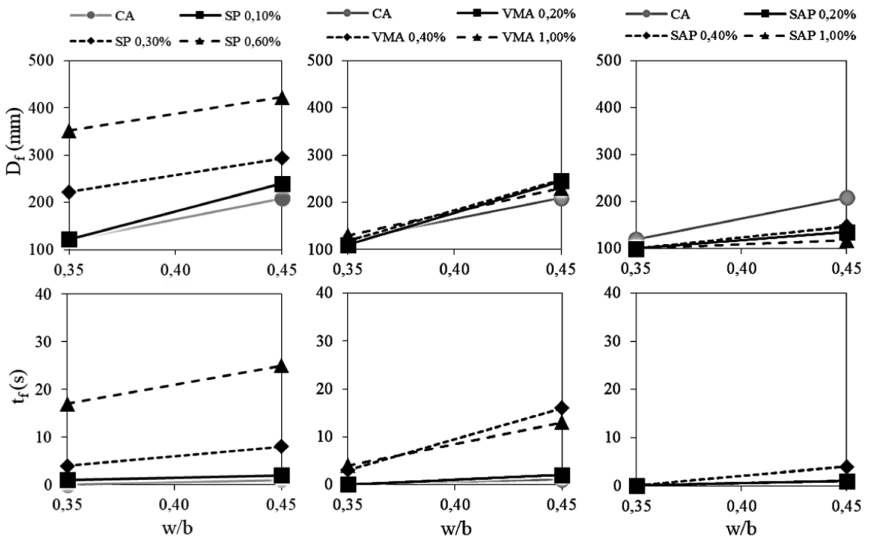

Fig. 5. Effect of polymeric admixtures (SP, VMA and SAP) on final diameter (D_f) and time to final spread (t_f).

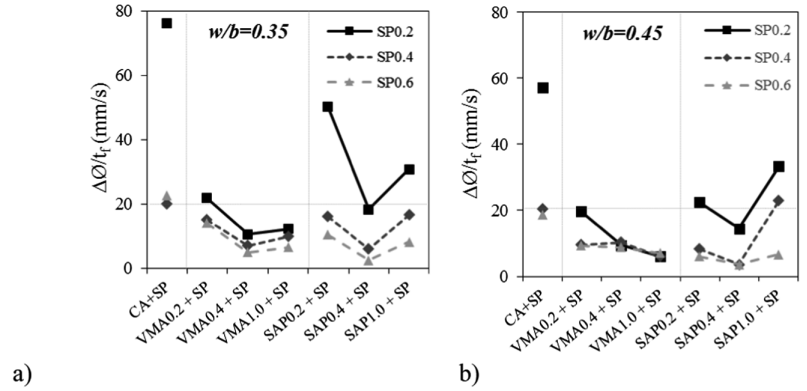

Fig. 6. Slump diameter (ΔØ) and stopping time (t_f) (a) at 0.35 and (b) 0.45 w/b ratio.

4 Summary and Conclusions

The effect of polymeric admixtures, a superplasticizer (SP), a viscosity modifying agent (VMA) and a superabsorbent polymer (SAP), on the rheological behavior of fluid SCC cement/limestone filler pastes was assessed. Yield stress and viscosity were related to

final spread diameter (D_f) and time to final spread (t_f) with mini-cone test. The main findings can be summarized as follows:

- SP increased D_f and t_f and its effectiveness was higher at lower w/b ratio; VMA affected t_f, although at certain minimum proportions (0.4% VMA of weight of cement and 0.45 w/b); and SAP reduced D_f at higher w/b ratio and significantly increased t_f.
- VMA combined with SP showed a synergetic effect, increasing significantly D_f and t_f. On the other hand, SAP showed a dominant behavior regarding SP, reducing D_f and increasing t_f, especially for SAP0.4 + SP0.6 at 0.35 w/b ($t_f = 110\,s$).
- In general, VMA combined with SP produced less variations in $\Delta Ø/t_f$ values than SAP + SP samples, which were highly dependent on water content and polymer dosage. Thus, the use of polymeric admixtures to achieve a tailor-made SCC is not as simple as the sum of their independent effects on rheology.

Acknowledgements. Financial support was provided by NanoCompaC (*BIA2016-77911-R*), funded by the Spanish Ministry of Economy & Competitiveness and postdoctoral fellowship (Ayuda Postdoctoral/Modalidad A/2017), funded by UAH (Spain). Some of the components were supplied by BASF Construction Chemicals Spain S.L, Omya Clariana S.L, and Portland Cement Vaderrivas.

References

1. Barluenga G et al (2017) Quality control parameters for on-site evaluation of pumped self-compacting concrete. Constr Build Mater 154:1112–1120
2. Barluenga G, Palomar I, Puentes J (2013) Early age and hardened performance of cement pastes combining mineral additions. Mater Struct 46(6):921–941
3. Vance K et al (2015) Rheological evaluations of interground and blended cement–limestone suspensions. Constr Build Mater 79:65–72
4. Santos FN et al (2017) Rheological study of cement paste with metakaolin and/or limestone filler using Mixture Design of Experiments. Constr Build Mater 143:92–103
5. Shadkam HR et al (2017) An investigation of the effects of limestone powder and Viscosity Modifying Agent in durability related parameters of self-consolidating concrete (SCC). Constr Build Mater 156:152–160
6. Asghari AA, Feys D, De Schutter G (2018) Mix design factors of self-consolidating cement paste affecting the magnitude of variations in rheological properties induced by the addition time of PCE-superplasticizer. Constr Build Mater 159:269–276
7. Schwartzentruber LDA, Le Roy R, Cordin J (2006) Rheological behaviour of fresh cement pastes formulated from a self compacting concrete. Cem Concr Res 36(7):1203–1213
8. Khayat KH, Mikanovic N (2012) Viscosity-enhancing admixtures and the rheology of concrete. In: Roussel N (ed) Understanding the rheology of concrete, 1st edn. Woodhead Publishing, Cambridge, pp 209–228
9. Ma S, Qian Y, Kawashima S (2018) Experimental and modeling study on the non-linear structural build-up of fresh cement pastes incorporating viscosity modifying admixtures. Cem Concr Res 108:1–9

10. Mechtcherine V, Secrieru E, Schröfl C (2015) Effect of superabsorbent polymers (SAPs) on rheological properties of fresh cement-based mortars—Development of yield stress and plastic viscosity over time. Cem Concr Res 67:52–65
11. Snoeck D, Schröfl C, Mechtcherine V (2018) Recommendation of RILEM TC 260-RSC: testing sorption by superabsorbent polymers (SAP) prior to implementation in cement-based materials. Mater Struct 51:116–123
12. Shah SP, Lomboy GR (2015) Future research needs in self-consolidating concrete. J Sustain Cem-Based Mater 4(3–4):154–163
13. Roussel N, Coussot P (2005) Fifty-cent rheometer for yield stress measurements: from slump to spreading flow. J Rheol 49(3):705–718
14. Tregger N, Ferrara L, Shah SP (2008) Identifying viscosity of cement paste from mini-slump-flow test. ACI Mater J 105(6):558–566
15. Ferrara L et al (2012) On the identification of rheological properties of cement suspensions: rheometry, computational fluid dynamics modeling and field test measurements. Cem Concr Res 42(8):1134–1146

Effect of Limestone Powder Addition Quality on SCC Rheology

Damien Rangeard[1,2(✉)], Arnaud Perrot[3], and Malalasoa Rodomond[2]

[1] Laboratoire CBTP, Research and Development Department, Noyal-Sur-Vilaine, France
damien.rangeard@lcbtp.com
[2] INSA Rennes, Rennes, France
[3] UBS, IRDL, Lorient, France

Abstract. Limestone powder is increasingly used as a supplementary cementitious composites in order to reduce the environmental impact of concrete. Limestone powder can simultaneously improve the rheological behaviour of the paste, increases the solid volume fraction and reduces the shrinkage of the concrete. The quality of limestone fillers is quarry-dependent and varies with the mineralogy of the original limestone rock. The filler produced can thus contain small but significant amount of different kinds of impurities.

In this study, the change in SCC rheology (yield stress value) induced by the variation in quality of the limestone filler (coming from the same quarry) is analysed.

In a first part, mineralogical analyses are performed in order to identify the nature of chemical species present in the limestone filler in addition to calcite. Then, the effect of calcite content in the limestone filler on the yield stress of limestone suspension is investigated using conventional rheometry.

The results highlight the presence of a critical content of impurities above which the yield stress of the limestone filler shows a dramatic increase. This high value of the yield stress implies a complete redefinition of the SCC mix-design.

Finally, a simple rheological test, based on cone penetration test, is proposed in order to quickly evaluate the quality of the filler before its introduction into the production process. This test can be used as a quality control procedure in order to define whether there is a need to change the mix design of SCC.

Keywords: Concrete · Rheology · Limestone powder · Yield stress

1 Introduction

Mineral admixtures such as silica fume, fly ash, metakaolin, limestone powder and so on are increasingly used in concrete formulation. The use of these supplementary cementitious materials limits the environmental impact of concrete by decreasing the cement content. Among these additions, limestone-based fillers are widely used because of their availability and because their addition is not detrimental to the qualities of hardened concrete (strength, durability) [1, 2]. Many studies have been carried out on limestone powder effect and have pointed out the underlying mechanisms acting

V. Mechtcherine et al. (Eds.): RheoCon 2019/SCC 2019, RILEM Bookseries 23, pp. 500–507, 2020.
https://doi.org/10.1007/978-3-030-22566-7_58

during cement hydration from fresh to hardened state: filler, CSH nucleation seeds, cement dilution and chemical effects. The filler effect is directly linked to the limestone powder particle size regarding to the cement particle size. Improvement of the particle packing is greater when the limestone filler particle size distribution is finer than the one of the cement: in that case, limestone particles fill the void between cement grains and increase the density of cement based materials [3]. The addition of fine limestone powder provided more nucleation seeds for the precipitation of hydration products. This effect is well known and largely documented [2, 5]. The dilution effect is linked to the quantity of limestone used as cement replacement. For a same W/C ratio, replacing cement by limestone powder decreases the quantity of particles with hydraulic or pozzolanic properties and in consequence increase the volume of water able to react with cement [2, 4, 5]. The chemical effect of limestone is linked to its particles size and to the content of alumina in cement. For small particle size, surface energy increases and chemical reactivity of limestone powder increases [2, 6]. So, the particle size of limestone powder is a key parameter for all of its actions in cement based material.

At fresh state, limestone powder addition has also an effect on the workability. Studies have shown contradictory results on this point. Researchers showed that the addition of limestone powder leads to an increase in yield stress and therefore decreases concrete workability, while others showed that the addition of limestone powder leads to a decrease in yield stress and therefore an increase in workability [7, 8]. Nevertheless, it seems that particle size distribution plays a major role in such system [15, 16].

In this paper, we analyse the origin of the change of the rheology of a SCC at the fresh state induced by variation in limestone filler. An exhaustive characterisation of the limestone powder used in the SCC mix, including mineralogical and rheological tests, is carried out in order to identify the origin of the variation in concrete rheology. Finally, a simple rheological test is proposed to quickly and simply evaluate the ability of the filler to be introduced or not in the concrete production plant.

2 Materials and Concrete Formulation

The cement used in this study is a CEM I 52.5 provided by Lafarge cement (Saint Pierre La Cour factory, France). The density of the cement was 3.15 g/cm^3. The specific surface area was 3390 cm^2/g, and the average particle size about 10 μm.

A washed river sand 0/4 mm with fineness modulus of 2.91 and density of 2.64 g/cm^3 was used as fine aggregate. Coarse aggregates consist of crushed hornfel rocks with granulometry 6.3/10, and density of 2.7 g/cm^3.

A high range water reducing admixture (superplasticizer) was used with a superplasticizer/cement mass ratio of 1.2%. This admixture is in liquid form of contains 20% of solid polymer extract.

The limestone filler is obtained from crushed and ground natural limestone rocks. The carry is located in Vendée (France). The specific surface area of the limestone filler was 5000 cm^2/g, and the average grain size was about 5 μm. The methylene blue value determined according EN 933-9 was 2.7 g/kg.

The water/binder ratio used was 0.35. The coarse/fine aggregates ratio was 1, and the limestone powder content was 55% of the cement mass.

3 Limestone Powder Effect

3.1 Rheology of Fresh Concrete

Eight samples of concrete using the mix design presented in Sect. 2 were tested. The only difference between the 8 samples comes from the limestone powder specimen, referenced from A to H. Those specimens come from the same quarry but have been produced at different time.

After mixing, the rheology of the concrete is evaluated using conventional slump test. For specimen made with B to H limestone powder, the concrete is self-consolidating showing spread flow value ranging from 710 mm to 740 mm. However, for the concrete made with batch A, the concrete presents a plastic consistency with slump flow value of 145 mm.

Yield stress value of the material can be derived from the results of the slump test, as described by [9, 10]. Using the model developed by Pierre et al. [9] for a spread flow, the yield stress value of concrete with B to H powder limestone range between 18 Pa to 24 Pa, while the development for a slump flow lead to a value of the yield stress higher than 2 000 Pa for the concrete made with batch A.

3.2 Limestone Powder Characteristics

As the only difference between the eight samples comes from the batch of limestone, an extensive characterization of the 8 batch A to H is performed. The particle size distribution was measured using a laser particle size analyzer after dispersion of the material in ethanol. The specific surface area was measured using Blaine apparatus according to the standard EN 196-6, and the methylene blue value (MBV) was determined according to the standard EN 933-9.

As can be seen in Table 1, those classical characteristics (grading, methylene blue value, specific surface area) do not show any significant difference between the different batches.

The 8 batches of limestone powder were observed using Scanning Electron Microscopy-Energy Dispersive Spectroscopy (SEM-EDS). The results of EDS, showned in Fig. 1, highlight as expected a high percentage of Ca in all samples. The presence of silica and, in a lesser content of aluminum, are also systematically observed. In reference A, trace of potassium were also observed. The content in calcium is significantly lesser in reference A than in the other references. The presence of silicon, potassium and aluminum atoms suggests the presence of alumino silicate of the phyllosilicate family.

In order to identify the nature of the impurities present in the sample in addition to the limestone, the materials are first treated with chlorhydric acid in order to remove the limestone. X Ray Diffraction (XRD) analysis is then performed on the remaining particles. The XRD patterns were obtained using a Philips PW 3710 X-ray

Table 1. Limestone powder characteristics

Batch	D_{50} (μm)	D_{90} (μm)	Specific Area (cm^2/g)	MBV (g/kg)
A	5.8	25.1	4760	3.3
B	5.0	20.4	5250	2.7
C	5.3	21.8	4350	3.4
D	4.8	22.1	4880	2.6
E	4.9	22.5	5500	3.2
F	6.0	19.9	4320	3.1
G	3.7	20.5	5500	2.8
H	4.2	25.5	4929	3.3

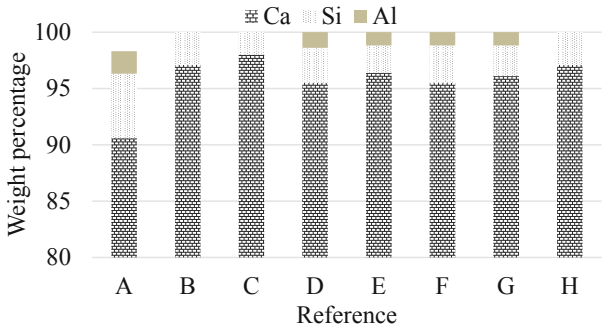

Fig. 1. Results of SEM-EDS analysis.

diffractometer with Bragg–Brentano geometry using Ni-filtered Cu Kα radiation. The recorded XRD patterns for the limestone powder A and F were showed in Fig. 2. The two diffraction patterns are similar, reflecting the same crystal composition of the two samples. The crystal phases are quartz, and clay minerals (illite and kaolinite).

3.3 Rheological Behavior of Limestone Powder

Previous mineralogical analyses have shown the presence of clay in the limestone powder. As these materials are very sensitive to water, their presence, even in small quantities, can impact the rheological behavior of concrete.

In a first time, the idea is to work on limestone suspensions in order to evaluate forces between limestone particles at a microscale. Rheological measurements are performed for water/limestone powder ratio ranging between 15% and 40%. Water and limestone powder were mixed in a planetary Hobart mixer, in two steps: 5 min at 140 rpm and 5 min at 280 rpm. After mixing, the measurement of the yield stress is performed using an Anton Paar Rheolab QC rheometer with a vane geometry. The measurement procedure is the same as the one presented by Perrot et al. [11]. The yield stress versus water content for sample A and F are plotted in Fig. 3a. Both samples

show significantly different yield stresses for the same water content (about one order of magnitude). Assuming that, in the concrete mix, the amount of water mobilized by the cement hydration is about 30% of the cement weight, and that the aggregates mobilized 1% of their weight (water absorption coefficient), the water available for the limestone powder correspond to 30% of the limestone weight. Figure 3b shows the yield stress of each limestone powder at a water content of 30% versus the percentage of impurities, defined as 100% – percentage of Ca identified by SEM-EDS analysis.

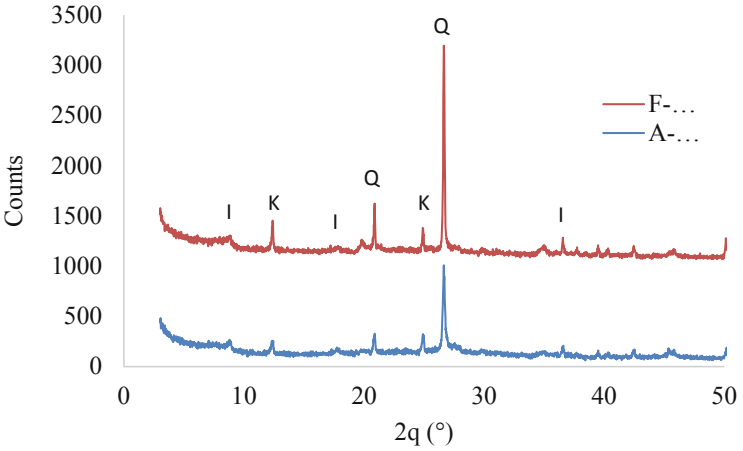

Fig. 2. XRD patterns on residue obtained after acid chlorhydric treatment.

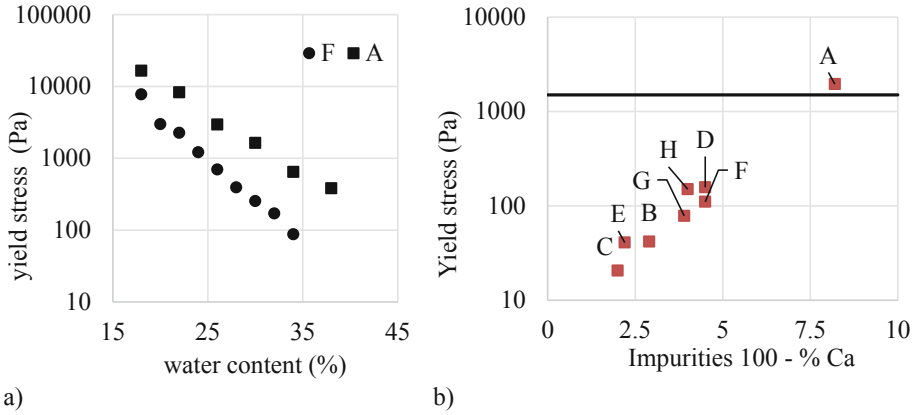

Fig. 3. Yield stress of limestone powder. (a) Yield stress versus water content – samples A and F, (b) Yield stress for a water content of 30%.

The analysis of the results allows to draw a direct link between the yield stress of limestone suspensions and the % of impurities. Reference A limestone, with the lower percentage of calcium and thus the maximum percentage of 'impurities' presents

significantly higher yield stress. This high sensitivity to small amount of impurities is due to the nature of impurities, constituted by clay minerals.

This difference in yield stress can lead to a difference in behavior from liquid to plastic behavior. This frontier between those two kinds of behavior is widely defined as the liquid limit in geotechnical engineering. It has been established that the liquid limit of a soil corresponds to a yield stress close to 2 kPa [11, 12]. This limit is reported in Fig. 3b, and allows to notice that for limestone powder A, the behavior at a water content of 30% (such as in the concrete mix) is in the plastic zone behavior, while for all other limestone samples the behavior at the same water content is clearly in the zone of liquid behavior.

4 Simple Test to Evaluate Limestone Powder Suitability for SCC Mix-Design

As previously observed, small variation in limestone powder composition can induce dramatic variation in limestone suspension rheology and thus in SCC rheology. This mineralogical variability cannot be detected using conventional characterization tests. Moreover, it is largely easier to perform simple rheological test in comparison with EDS analysis. The measurement of the limestone powder yield stress at a water content close to the one at which it will be submitted in concrete is fundamental to prevent detrimental rheological evolution of the concrete. The limestone powder has to be at a liquid state, i.e. with a yield stress value lower than 2 kPa.

The proposed test is based on cone penetration test that has already been used to measure the shear strength of mineral suspensions [12–14]. The stabilization of the cone is obtained when the friction force developed at the contact material/cone balances the weight of the cone. The yield stress τ is thus defined by the following equation:

$$\tau = \frac{W}{\pi \sin\left(\frac{\beta}{2}\right) h^2 \sqrt{1 + \tan(\frac{\beta}{2})^2}} \tag{1}$$

where W is the weight of the cone, β the cone tip angle and h the penetration depth.

The comparison of yield stress values measured from vane test and from cone penetration test on limestone powder A, presented in Fig. 4, shows that the results obtained from both methods are in good agreement.

For tested the validity of a limestone powder, the determination of the yield stress can therefore be easily and quickly carried out on site by mixing the limestone powder at the required water content and measured the penetration depth of the cone conventionally used in geotechnical engineering for the determination of the Atterberg limits.

Figure 3b shows that the cone penetration is able to isolate the batch A that provides a yield stress higher than 2 kPa that should not be used in the SCC mix-design presented in Sect. 2.

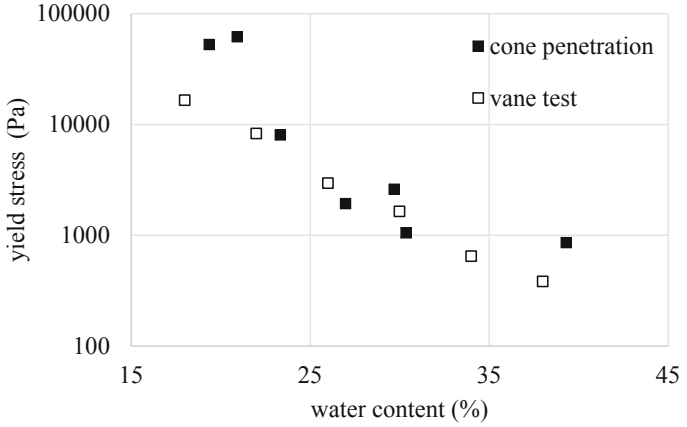

Fig. 4. Yield stress obtained from vane test and from cone penetration test.

5 Conclusions

In this paper, we have analyzed the variation of a SCC rheology generated by the variation of limestone powder characteristics. The mineralogical analysis performed on limestone coming from the same quarry have shown that a slight variation of impurities content can affect significantly the rheology of the filler suspension and as a consequence detrimentally affect the concrete workability. Its behavior can shift from liquid to plastic, and thus completely modified the behavior of the mix concrete. This change of behavior cannot be apprehended from conventional test, and need to be determined at the scale of the yield stress of the limestone.

To evaluate quickly and simply if a limestone powder is suitable to be used in SCC formulation, a simple rheological test based on cone penetration has been proposed and validated for the introduction of the filler in the concrete production process.

References

1. He H, Courard L, Pirard E (2012) Particle packing density and limestone fillers for more sustainable cement. Key Eng Mater 517:331–337
2. Wang D, Shi C, Farzadnia N, Shi Z, Jia H, Ou Z (2018) A review on use of limestone powder in cement-based materials: mechanism, hydration and microstructures. Constr Build Mater 181:659–672
3. Schutter GD (2011) Effect of limestone filler as mineral addition in self-compacting concrete. In: 36th conference on our world in concrete & structures, Singapore, 14–16 August 2011
4. Martin C, Pilippe L, Erick R (2006) Efficiency of mineral admixtures in mortars – Quantification of the physical and chemical effects of fine admixtures in relation with compressive strength. Cem Concr Res 36:264–277
5. Poppe AM, Schutter GD (2003) Effect off lime stone on the cement hydration in SCC. In: 3rd international symposium of SCC, pp 558–566

6. Kakali G, Tsivilis S, Aggeli E, Bati M (2000) Hydration products of C3A, C3S and Portland cement in the presence of CaCO3. Cem Concre Res 30:1073–1077
7. Wang D, Shi C, Farzadnia N, Shi Z, Jia H, Ou Z (2018) A review on effects of limestone powder on the properties of concrete. Constr Build Mater 192:153–166
8. Demirhan S, Turk K, Ulugerger K (2019) Fresh and hardened properties of self consolidating Portland limestone cement mortars: effect of high volume limestone powder replaced by cement. Constr Build Mater 196:115–125
9. Pierre A, Lanos C, Estelle P (2013) Extension of spread-slump formulae for yield stress evaluation. App Rheol 23(6):36–44
10. Roussel N, Coussot P (2005) "Fifty-cent rheometer" for yield stress measurements: from slump to spreading flow. J Rheol 49(3):705–718
11. Perrot A, Rangeard D, Levigneur A (2016) Linking rheological and geotechnical properties of kaolinite materials for earthen construction. Mater Struct 49:4647
12. Koumoto T, Houlsby GT (2001) Theroy and practice of the fall cone test. Geotechnique 51:701–712
13. Lootens D, Jousset P, Martinie L, Roussel N, Flatt RJ (2009) Yield stress during setting of cement pastes from penetration tests. Cem Concre Res 39:401–408
14. Wang D, Zentar R, Abriak N, Xu W (2013) Shear strength behavior of cement/lime solidified Dunkirk sediments by fall cone tests and vane shear test. Geotech Test J 36:155–162
15. Kashani A, San Nicolas R, Qiao GG, Van Deventer JSJ (2014) Modelling the yield stress of ternary cement–slag–fly ash pastes based on particle size distribution. Powder Technol 266:203–209
16. Vance K, Kumar A, Sant G, Neithalath N (2013) The rheological properties of ternary binders containing Portland cement, limestone, and metakaolin or fly ash. Cem Concr Res 52:196–207

Rheological and Mechanical Properties of Alkali-Activated Hybrid Matrix for Self-consolidating Concrete

Yasser Rifaai[1,2(✉)], Ammar Yahia[1], Ahmed Mostafa[1], Salima Aggoun[2], and El-Hadj Kadri[2]

[1] Department of Civil Engineering, Université de Sherbrooke, Sherbrooke, Canada
yasser.rifaai@usherbrooke.ca
[2] Laboratory L2MGC, University of Cergy Pontoise, Cergy Pontoise, France

Abstract. The objective of this study is to evaluate the flow behavior, build-up kinetics, and mechanical properties of an alkali-activated hybrid matrix using different concentrations of NaOH. The investigated mixtures showed different rheological behaviors depending on the NaOH concentration. The combination of Portland cement and fly ash contributed to the formation of a rigid network when the activator is used at a concentration of 2 mol/L. At this low concentration, the chemical reaction seems to be strongly accelerated. This resulted in an increase in the yield stress, plastic viscosity, and rigidification rate of the mixtures. However, when the concentration of NaOH increased to 14 mol/L, only cement contributed to the development of rigidity, and fly ash did not show any contribution. This resulted in relatively low yield stress, plastic viscosity, and rigidification rate. Moreover, the obtained test results revealed that the compressive strength of mortar mixtures made with cement - fly ash hybrid matrix is higher than that of fly ash-based mortar mixtures.

Keywords: Geopolymer · Hybrid matrix · Rheology · Compressive strength · Self-consolidating concrete

1 Introduction

Concrete is one of the most used materials in the world after water. Currently, concrete consumption reached 190 m^3 per second [1], i.e. 6 billion m^3 per year. Since cement is the basic material of concrete production, concrete becomes a very polluting material, because one ton of cement can cause the emission of one ton of CO_2 [2]. To reduce the environmental impact of concrete, many researchers have been interested to develop and use materials that can partially or completely replace cement [3]. For example, geopolymers with promising results in both fresh [4] and hardened states [5] have been developed. Geopolymers are generally derived from industrial waste, which considerably contributes to reducing the CO_2 footprint of the construction industry. This alternative is very attractive in designing self-consolidating concrete (SCC) and reduce its clinker factor. SCC is a new class of concrete characterized by a relatively higher volume of paste.

V. Mechtcherine et al. (Eds.): RheoCon 2019/SCC 2019, RILEM Bookseries 23, pp. 508–516, 2020.
https://doi.org/10.1007/978-3-030-22566-7_59

The objective of this study is to evaluate the feasibility of replacing cement by a geopolymer to the proportion of self-consolidating concrete (SCC). The experimental study was carried out on paste and equivalent SCC mortar mixtures. Both fresh properties and compressive strength development were evaluated. This aims to optimize a hybrid matrix that can be used to proportion SCC with adequate rheological and mechanical properties.

2 Experimental Program

2.1 Material and Mixture Proportion

A General Use cement (GU) complying with the ASTM C150M specifications was used to proportion cement paste and mortar mixtures investigated in this study. In addition, fly ash class F (FA) complying with the ASTM C618-17 specifications was used as a precursor of geopolymer pastes. NaOH is well known to have a less environmental impact than other activators, such as sodium silicate (Na_2SiO_3) [6]. The NaOH solution is prepared by dissolving the NaOH in water at a temperature of 20 °C. The paste mixtures were proportioned with a constant solid fraction of 0.442, which is equivalent to cement paste mixtures having a water-to-cement ratio (W/C) of 0.40. On the other hand, the mortar mixtures were proportioned with a solid fraction of paste of 0.442, a sand/binder ratio of 1.5, and a NaOH concentration of 2 mol/L. Various mortar specimens were prepared according to ASTM C305 and ASTM C109 specifications and used to evaluate compressive strength development at different ages. The specimens were kept in closed boxes at an ambient temperature of 23 °C. The compressive strength was measured according to ASTM C109 after 3, 7 and 28 days. The mixing procedure was carried out in accordance with the ASTM C1738M specifications. The samples were conserved in sealed containers to prevent water evaporation and kept at a temperature of 25 °C ± 2 °C.

2.2 Tests Methods

Rheological measurements were carried out on paste mixtures proportioned with a fixed solid fraction of 0.442. In the case of fly ash paste mixtures, this solid fraction is equivalent to a liquid/solid ratio (L/S) of 0.5, by weight. The rheological measurements were carried out using a coaxial cylinders rheometer. All measurements were carried out 10 min after the first contact between cement and water and at a temperature of 25 °C. The experimental protocol is presented in Fig. 1. The rheological parameters were estimated using the modified Bingham model:

$$\tau = \tau_0 + \mu_p \dot{\gamma} + C\dot{\gamma}^2 \quad (1)$$

τ_0 is the yield value (Pa), μ_p is the plastic viscosity (Pa.s), and C is the pseudo-plastic constant: linear when C = 0, shear-thinning for C < 0, or shear-thickening for C > 0.

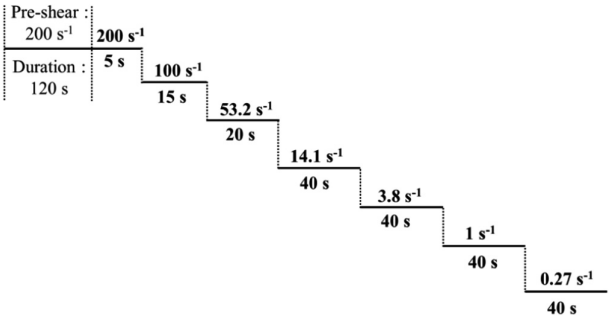

Fig. 1. Protocol of rheological measurements.

The viscoelastic properties of investigated mixtures were determined using oscillatory rheometric tests. Strain sweep tests were carried out to determine the linear viscoelastic domain (LVED), which is characterized by a constant shear modulus G′, and critical strain [7]. The applied strain is:

$$\gamma = \gamma_0 \sin \omega t \tag{2}$$

Where γ_0 is the shear strain varying from 0.0001% to 100% and ω is the angular frequency fixed at 10 rad/s.

The build-up kinetic was determined from time sweep tests using the experimental protocol presented in Fig. 2. Mostafa and Yahia [8] proposed a dispersing method that consists in combining rotational shear and oscillatory shear at large amplitude (Large Amplitude Oscillatory Shear LAOS). Then, the second phase consists of applying a Small Amplitude Oscillatory Shear (SAOS) to monitor the evolution of G′ and G″ with time while remaining in the LVED. In this study, the rigidification rate, which is the slop of the evolution of G′ with time in the elastic state, is determined [9].

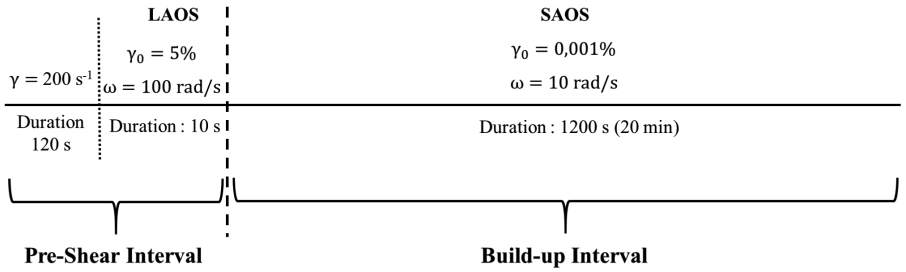

Fig. 2. Time sweep protocol.

The NaOH concentration was optimized to secure an appropriate setting time of paste mixtures according to ASTM C191 specifications. The targeted setting time of paste in depicted by the duration period needed to carry out rheological measurements,

which is approximately 70 min. Thus, all concentrations of NaOH that lead to a setting time lower than 70 min were excluded.

3 Results and Discussion

3.1 Optimization of NaOH Concentration

As mentioned earlier, NaOH concentrations were optimized to ensure a setting time higher than 70 min. The initial setting time value of the mixtures proportioned with 100% GU and 100% FA are summarized in Table 1. On the other hand, the results of hybrid mixtures proportioned with 50% GU and 50% FA, by volume, are summarized in Fig. 3. On the other hand, the selected concentrations of NaOH are presented in Table 2.

Table 1. Initial setting time of fly ash and cement paste mixtures.

		Initial setting time (min)	
		100% GU (W/C = 0.40)	100% FA (L/S = 0.4, by weight)
NaOH (mol/L)	0	280	No setting
	8	6	180
	14	6	≈7 days

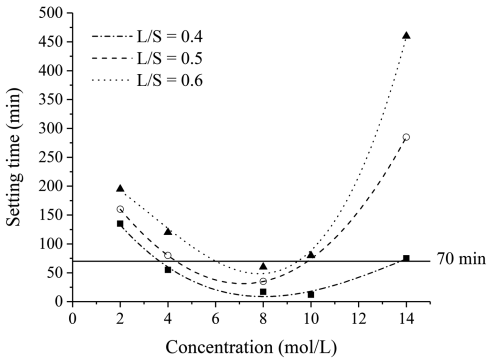

Fig. 3. Initial setting time of hybrid matrix cement-fly ash.

Table 2. Concentrations of NaOH used for rheological measurements.

	GU	FA	GU-FA
0 mol/L	✓	✓	✓
2 mol/L	X	✓	✓
14 mol/L	X	✓	✓

3.2 Rheological Parameters

The selected NaOH concentrations (Table 2) were used to prepare cement paste mixtures using GU, FA, and hybrid system (GU + FA) systems. Based on the modified Bingham model, the rheological parameters of the investigated mixture are summarized in Fig. 4.

The combined GU+FA system resulted in higher yield stress and plastic viscosity values than those obtained with FA suspensions. Furthermore, the increase in NaOH concentration increased the yield stress (Fig. 4a) and plastic viscosity (Fig. 4b) for GU+FA systems. This can be due to the reactivity of cement and the presence of NaOH activator. Indeed, the presence of NaOH can accelerate the hydration process of cement [10], hence contributes to increasing the yield stress and the plastic viscosity of the GU+FA suspension.

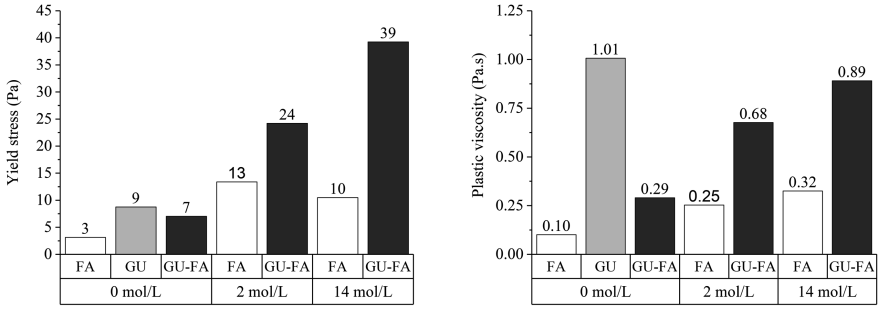

Fig. 4. Evolution of Bingham modified parameters with NaOH concentration (a) Yield stress (b) Plastic viscosity.

As can be observed in Table 3, the investigated mixtures exhibited shear-thinning behaviors in the case of 0 mol/L and 2 mol/L of NaOH. However, the mixture made with 14 mol/L showed a Bingham behavior (C = 0). The use of cement did not modify the shear-thinning aspect of the hybrid matrix in the case of 0 mol/L and 2 mol/L.

Table 3. Pseudoplastic behavior (constant C) of fly ash and hybrid paste mixtures.

	0 mol/L	2 mol/L	14 mol/L
Constant C (GU + Fly ash)	−0.001	−0.0018	≈0
Constant C (Fly ash)	−0.0003	−0.0007	≈0
Interpretation	Shear-thinning behavior		Binghamian behavior

3.3 Strain Sweep Results

As can be observed in Fig. 5, in the case of reference mixtures (0 mol/L), the suspensions proportioned with GU and GU+FA systems exhibited less critical strain than

those proportioned with FA. The increase in NaOH concentration resulted in an increase of critical strain, reflecting higher dispersion of suspensions, regardless of the type of suspension. However, the greater effect was observed with FA suspensions. This can be due to the higher dissolution process of FA suspension [11], which increase the concentration of negative monomers in the suspension (Si – OH^-). In the case of hybrid matrix GU+FA, the increase in NaOH concentration from 2 mol/L to 14 mol/L did not result in a further increase in critical strain. This suggests that the higher dissolution process of FA is balanced by the higher hydration kinetics of cement in the presence of NaOH, thus resulting in maintaining a constant critical strain.

In the case of storage modulus, for given cementitious materials (FA and GU+FA), the incorporation of 2 mol/L increased the storage modulus compared to reference mixture. This can be due to the combined effect of higher hydration process of cement and geopolymerization process of FA. However, the increase in NaOH concentration to 14 mol/L reduced the storage modulus, especially in the case of FA system (Fig. 5b). This can be explained by the higher dissolution process of FA. In this case, the contribution of FA is limited, and only cement contribute to the rigidity of the network, hence resulting in lower rigidity at 14 mol/L.

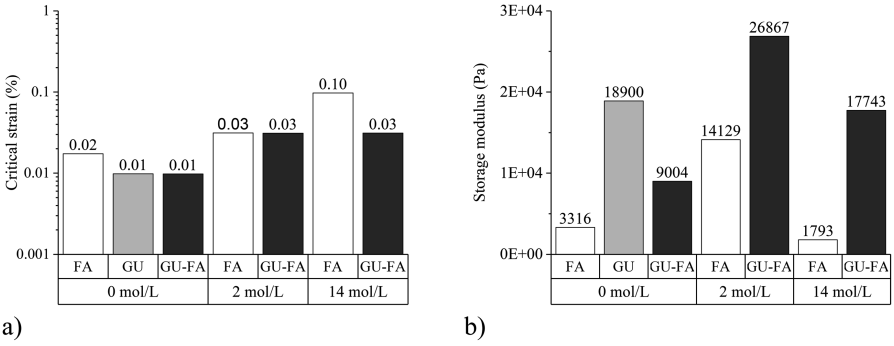

Fig. 5. Evolution of viscoelastic properties with NaOH concentration (a) critical strain (b) Storage modulus ($\gamma < \gamma_{critical}$).

3.4 Time Sweep Results

The use of GU cement resulted in a higher rigidification rate compared to FA and GU+FA systems (Fig. 6) in the case of reference mixtures (0 mol/L of NaOH). On the other hand, the use of 2 mol/L increased the rigidification rate of FA and GU+FA suspensions. This can be due to the increased chemical reaction processes of GU and FA. However, the increase in NaOH concentration from 2 mol/L to 14 mol/L decreased the rigidification rate for both FA and GU+FA suspensions. In this case, rigidification rate can be related exclusively to the contribution of GU, especially in presence of such high NaOH concentration of 14 mol/L that can increase the hydration kinetics, since FA does not contribute to rigidity because of the higher dissolution rate.

3.5 Compressive Strength

The variation of compressive strength development with age of investigated mixtures is shown in Fig. 7. As can be observed, the matrix composed of 100% GU developed the highest compressive strength, regardless of the age of the matrix. However, the lowest compressive strength values were obtained with the matrix proportioned with FA. The combination of FA with GU resulted in relatively higher compressive strength values, but lower than those obtained with GU alone. The difference in compressive strength values between GU matrix and other matrices can be due to the curing conditions of mortar cubes. Indeed, geopolymers require, in general, high curing temperature (around 60 °C) to help strength development [12]. Therefore, further studies will be carried out to optimize the curing temperature for hybrid matrices that can be used to achieve compressive strengths close to those of cement mixtures.

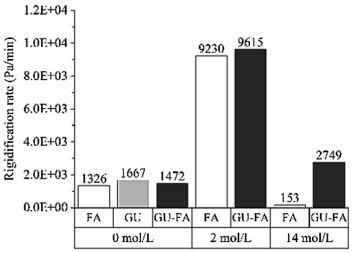

Fig. 6. Evolution of the rigidification rate with NaOH concentration.

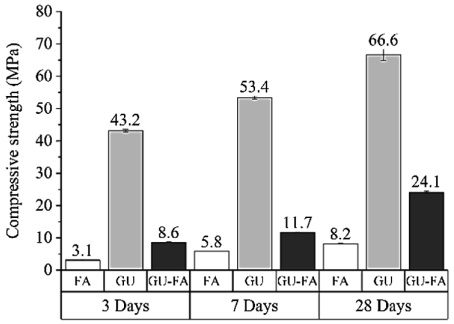

Fig. 7. Evolution of compressive strength with age.

- GU specimens were prepared using water (0 mol/L of NaOH)
- FA and GU-FA specimens were prepared using 2 mol/L of NaOH
- All samples were cured at ambient temperature

4 Conclusions

The flow behavior, build-up kinetics, and mechanical properties of an alkali-activated hybrid matrix (FA and GU+FA) were evaluated. Based on the resulted presented in this paper, the following conclusions can be pointed out:

1. Optimum NaOH concentrations to achieve a proper setting time of FA and GU+FA matrices are determined.
2. The GU+FA hybrid systems have higher yield stress and plastic viscosity values than those obtained with FA suspensions, regardless of the concentration of NaOH.
3. The FA and GU+FA hybrid systems proportioned with 2 mol/L of NaOH exhibit shear-thinning behaviors, while those proportioned with 14 mol/L behave as Bingham flow.
4. The GU+FA hybrid systems proportioned with 2 mol/L showed higher rigidification rate than those made with FA. However, the increase in NaOH concentration from 2 mol/L to 14 mol/L decreased the rigidification rate for both FA and GU+FA suspensions.
5. The FA and GU+FA hybrid system developed lower compressive strength than the reference mixture, regardless of the concentration of NaOH. Further studies are ongoing to optimize curing conditions to enhance strength development.

References

1. Planetoscope - Statistiques Production mondiale de béton (2018). https://www.planetoscope.com/matieres-premieres/1374-production-mondiale-de-beton.html
2. Criado M, Palomo A, Fernández-Jiménez A, Banfill PFG (2009) Alkali activated fly ash: effect of admixtures on paste rheology. Rheol Acta 48(4):447–455
3. Davidovits J (1991) Geopolymers – Inorganic polymeric new materials. J Therm Anal Calorim 37(8):1633–1656
4. Favier A, Hot J, Habert G, Roussel N, d'Espinose de Lacaillerie J-B (2014) Flow properties of MK-based geopolymer pastes. A comparative study with standard Portland cement pastes. Soft Matter 10(8):1134
5. Davidovits J (1994) Properties of geopolymer cements. In: First international conference on alkaline cements and concretes, pp 131–149
6. Habert G, D'Espinose De Lacaillerie JB, Roussel N (2011) An environmental evaluation of geopolymer based concrete production: Reviewing current research trends. J Clean Prod 19 (11):1229–1238
7. Mezger T (2006) The rheology handbook : for the users of rotational and oscillatory rheometers
8. Mostafa A, Yahia A (2015) Performance evaluation of different rheometric shearing techniques to disperse concentrated cement suspension. Appl Rheol 25(3):1–9
9. Mostafa AM, Yahia A (2016) New approach to assess build-up of cement-based suspensions. Cem Concr Res 85:174–182
10. Juenger CG, Jennings HM (2002) Effects of high alkalinity on cement pastes, no 98, pp 251–255

11. Khale D, Chaudhary ÆR (2007) Mechanism of geopolymerization and factors influencing its development: a review. J Mater Sci 42(3):729–746
12. Ridtirud C, Chindaprasirt P, Pimraksa K (2011) Factors affecting the shrinkage of fly ash geopolymers. Int J Miner Metall Mater 18(1):100–104

Effects of Nanoclays on SCC Paste Rheology

Hugo Varela[1(✉)], Gonzalo Barluenga[1], Irene Palomar[1], and Alberto Sepulcre[2]

[1] Department of Architecture, University of Alcala, Madrid, Spain
hugo.varela@edu.uah.es
[2] Department of Building Construction and Control, Technical University of Madrid, Madrid, Spain

Abstract. Self-compacting concrete is an efficient and advantageous technology that increases cast in place speed while reduces energy consumption and health risks. However, some difficulties regarding pumping and lateral pressure on the formwork still limits its widespread use. A promising alternative for reducing the formwork pressure is the use of nanocomponents. Among them, nanoclays such as sepiolite, attapulgite, and montmorillonite can modify the rheological properties of fresh concrete, increasing early age thixotropy and structural build-up. These nanoclays have different morphology and nature, but similar size or BET surface area. In order to evaluate the effect of nanoclays on early rheology of SCC pastes, an experimental study was carried out. A reference paste with ordinary Portland cement blended with limestone filler, 3:1 by weight, was designed and two water-to binder ratios (w/b), 0.35 and 0.45, were considered. Then, four types of nanoclays were incorporated: attapulgite, montmorillonite and two types of sepiolite, one in powder form and the other dispersed in water. Water adsorption was tested using the tea-bag method in tap water and alkaline pore water. Paste consistency was measured by slump flow adjusted using a high range water reducing admixture (HRWRA). The rheological behaviour of the mixtures was tested using the mini-slump flow test. The final spread diameter and time to final spread after mixing were assessed. The aim of this study is to understand and evaluate the effect of nanoclays on the rheological parameters of pastes with cement and limestone filler, which may improve the rheology and the structural build-up at rest, overcoming the problems identified for SCC.

Keywords: SCC paste · Nanoclays · Rheological properties · Water reducing admixture · Water to binder ratio

1 Introduction

Self-compacting concrete (SCC) shows some difficulties regarding pumping and lateral pressure on the formwork and due to its large fluidity, which still limits its widespread use. Regarding pumping, a shear thickening behaviour has been described, limiting the use of conventional concrete evaluation tools [1, 2]. Formwork pressure is related to the material fresh state performance. Rheological properties, as yield stress (dynamic and static), viscosity and thixotropy, are essential properties of fresh SCC and can modify

V. Mechtcherine et al. (Eds.): RheoCon 2019/SCC 2019, RILEM Bookseries 23, pp. 517–524, 2020.
https://doi.org/10.1007/978-3-030-22566-7_60

its form of spreading. Thus, controlling these properties is necessary to overcome SCC cast in place issues.

According to some studies, Nanoclays can modify SCC rheological properties [3, 4]. Besides, nanoclays combined with a high range water reducing admixture (HRWRA) can increase static yield stress and reduce dynamic yield stress, enhancing the effective thixotropy [5]. According to some authors [6–8], nanoclays showed more affinity with water and HRWRA than cement particles, because nanoclays have a BET surface area (S_{BET}) 17 times larger than cement [9]. That also explained the necessity of low nanoclays content by cement weight, being more than 2% unpractical to control the rheological parameters.

This paper presents a study on the effects of nanoclays on the rheological properties of cement paste in order to modify yield stress and viscosity in the fresh state. The aim is to characterize different types of nanoclays and their effects on the rheology of fluid cement pastes with limestone filler and two contents of w/b and different amounts of HRWRA.

2 Experimental Program

2.1 Materials Compositions

The cement/limestone filler pastes used in the experimental program are summarized in Table 1. It consisted of CEM I 42.5 R, limestone filler, water, high range water reducing admixture (HRWRA) in policarboxilate based and nanoclays. Cement was blended with limestone filler, 3:1 by weight. Two water to binder ratios (w/b) were considered, 0.35 and 0.45. To reach the paste fluidity required for SCC compositions a HRWRA was used, ranging between 0.05% to 2% by cement weight. Four nanoclays (2% by cement weight) were used with distinct morphology and nature, but similar size or S_{BET}; attapulgite (At), montmorillonite (Mmt), and two types of sepiolite, one in powder form (Sep) and other dispersed in water (Sew).

Table 1. Compositions of the fluid cement pastes under study (components in g)

	Ca 035	CaAt 035	CaMmt 035	CaSew 035	CaSep 035	Ca 045	CaAt 045	CaMmt 045	CaSew 045	CaSep 045
CEM I 42,5R	850	850	850	850	850	850	850	850	850	850
Limestone Filler	425	425	425	425	425	425	425	425	425	425
Water *a	446	446	446	386	446	574	574	574	514	574
HRWRA *b	0–2%					0–1%				
At*d	-	17	-	-	-	-	17	-	-	-
Mmt*d	-	-	17	-	-	-	-	17	-	-
Sew *c;d	-	-	-	17*	-	-	-	-	17*	-
Sep*d	-	-	-	-	17	-	-	-	-	17
w/b	0.35	0.35	0.35	0.35	0.35	0.45	0.45	0.45	0.45	0.45

*a Liquid water added.

*b HRWRA was employed as an increment dosage scale, by cement weight.

*c water of the components (HRWRA and SEW) was also taken into account. Sew solid residue was 22%.

*d Nanoclays S_{bet}: 144 m^2/g (At); 138 m^2/g (Mmt); 284 m^2/g (Sew); and 316 m^2/g (Sep).

2.2 Experimental Methods

Water Adsorption of nanoclays was tested using the tea-bag method, in tap water (pH = 5–6) and alkaline water (pH = 12–14), which corresponds to the pore water of a cement paste [10]. After filling the tea-bag with 0.3 g of nanoclay, the sample was submerged in water. At times previously determined between 0 and 20 min, the teabag was extracted, the surface moisture was removed with a dry cloth and the weight was measured. Adsorption water was calculated as the difference of teabag weights.

The fresh state properties of the pastes used in the study were characterized using a mini-cone with dimensions 100 mm × 70 mm × 50 mm (upper diameter-lower diameter-height) [11]. Mini-cone was filled with fresh paste and then it was lifted. The paste flowed until reaching the final spread diameter. Final spread diameter, time of final spread, final height and fresh density were measured and were recorded with a webcam. These experimental parameters can be used to assess rheological properties of paste, as yield stress and viscosity [12]. Spread diameter and height can be related to Yield Stress while final spread flow time can be related to viscosity [11]. Flow curves were produced for different w/b ratio and amount of HRWRA.

3 Experimental Results

The experimental results are comprised by three groups of tests: Water adsorption of nanoclays in two different pH water; flowing tests of cement pastes only with water and flowing tests of cement pastes with HRWRA for two w/b (0.35 and 0.45).

Figure 1 plots the water adsorption experimental results obtained with the tea-bag tests in alkaline and tap water. Water adsorption is related to the water surface retention of nanoclays. It can be observed that the adsorption was different depending on the pH of the liquid. Larger differences among the nanoclays under studied were observed for alkaline water. Sepiolite dispersed in alkaline water showed the highest adsorption value and attapulgite the lowest. Sepiolite in powder form and montmorillonite showed values in between, but sepiolite adsorbed a bit more than montmorillonite.

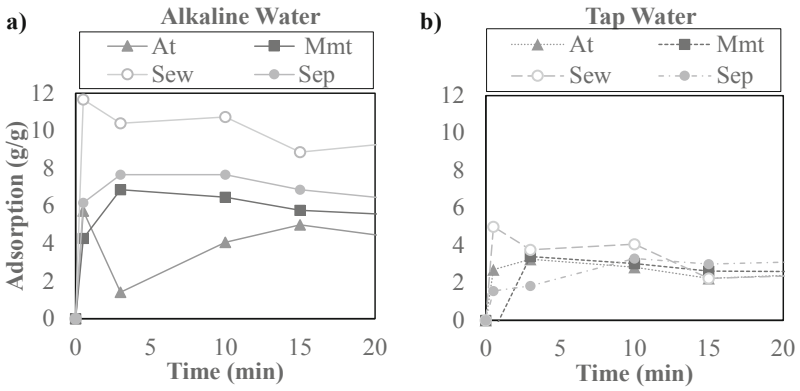

Fig. 1. Nanoclays results of water adsorption test in (a) Alkaline water; (b) Tap water.

Figure 2 shows (a) the final time and (b) spread diameter of pastes with nanoclays and different w/b. Final time values (Fig. 2a) were very short regardless the type of nanoclay used. Figure 2b shows a similar trend of the spread diameter among reference, At, Mmt and Sew mixtures. Sep showed a different behavior. It required larger w/b to reach the same spreading. During this test, pastes did not show final spread flow time that can be related to viscosity.

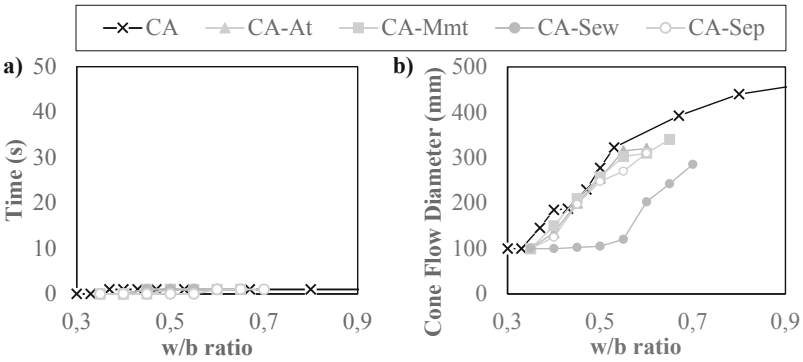

Fig. 2. Time to final spread and cone flow diameter vs w/b ratio.

Figure 3 presents the experimental results obtained with mini-slump flow test in samples with HRWRA and two w/b (0.35 and 0.45). Pastes with 0.35 w/b (Figs. 3a and b) showed three patterns regarding final time and final spread diameter. Reference paste and paste with At needed a low amount of HRWRA to spread over 300 mm. However At required larger time to reach the final spread diameter than all the other pastes. Both sepiolites with HRWRA produced similar spreads and needed almost twice HRWRA amount than At to spread over 300 mm. Moreover, these mixtures reached the final spread time slightly before At. Pastes with Mmt required three times the amount of HRWRA than At to reach over 300 mm. However, Mmt was the nanoclay with less time to reach the final spread.

Figure 3c and d show the final time and spread diameter of pastes with 0.45 w/b. It can be observed that the increase of w/b produced a significant change in the paste flow parameters. The differences observed for 0.35 w/b were dramatically reduced for 0.45. Regarding final time (Fig. 3c), it can be observed that Mmt and sepiolites needed considerably less HRWRA to reach similar final times to 0.35 w/b. In contrast, At showed slight differences on HRWRA effectiveness with different w/b. Regarding spread diameter (Fig. 3d) all nanoclays needed similar amount around 0.4% of HRWRA to reach 300 mm diameter, that was the same used for At with 0.35 w/b.

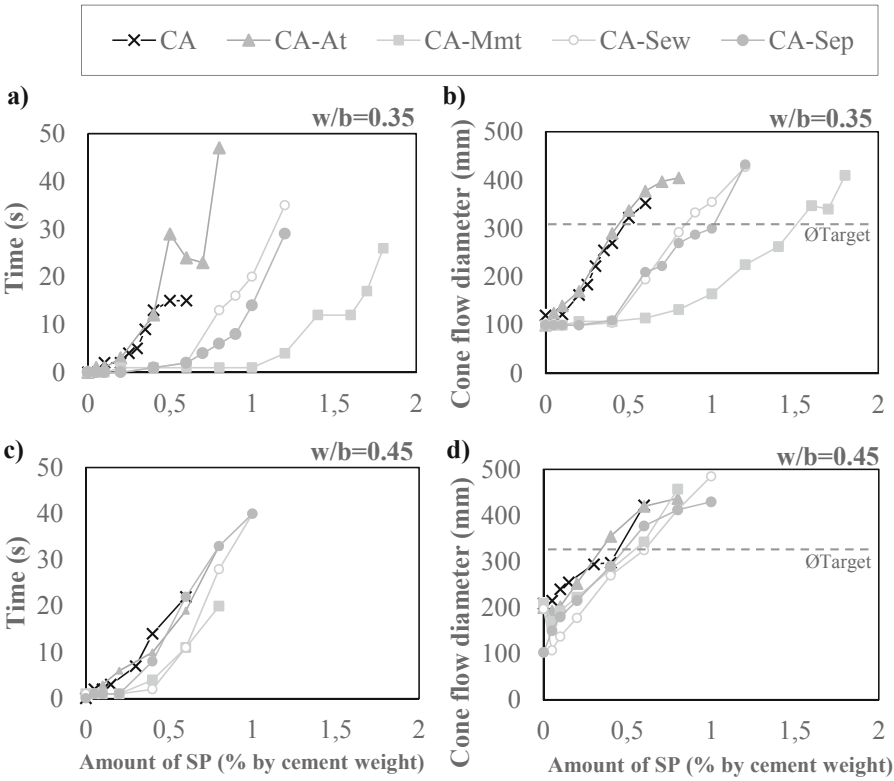

Fig. 3. Experimental results of mini-cone slump test. (a) Time vs %SP* with *w/b* = 0.35; (b) Diameter vs %SP* with *w/b* = 0.35; (c) Time vs %SP* with *w/b* = 0.45; (d) Diameter vs %SP* with *w/b* = 0.45. *(by cement weight)

4 Discussion

The use of different Nanoclays in cement pastes have produced different effects in fresh state rheological properties, related to water adsorption, water pH, and the interaction between nanoclays and HRWRA.

Nanoclays adsorption showed different values when submerged in tap or alkaline water, which corresponds to the pore water of a cement paste. Sep (sepiolite in powder form) had difficulties to spread only with water due to its morphology (needle shape) and size (larger particle size than Attapulgite (At) [9]. On the other hand, Sew (sepiolite dispersed in water) spread better in water because it incorporates a dispersing agent. As nanoclays had not viscosity (final time practically zero) it can be said that flow depended only on water effect.

The replacement of water as flow agent by a HRWRA produced the main differences observed among nanoclays. Attapulgite was able to spread with lower amount of HRWRA due to its lower requirement of water adsorption than the other nanoclays, as shown in Fig. 1. Mmt required three times the amount of HRWRA to reach the same

diameter as At, which points out that Mmt reduced HRWRA effectiveness [6–8]. The effect of HRWRA on flowability of pastes with sepiolite showed an intermediate behavior, because both needed a dispersant agent to be functional in cement pastes. It can be highlighted that, in contrast to pastes without HRWRA, the time to final spread was larger in pastes with HRWRA. In this case, nanoclays showed viscosity, although the nanoclay morphology, size and S_{BET} may influence the results [9], due to their flocculation capacity [3].

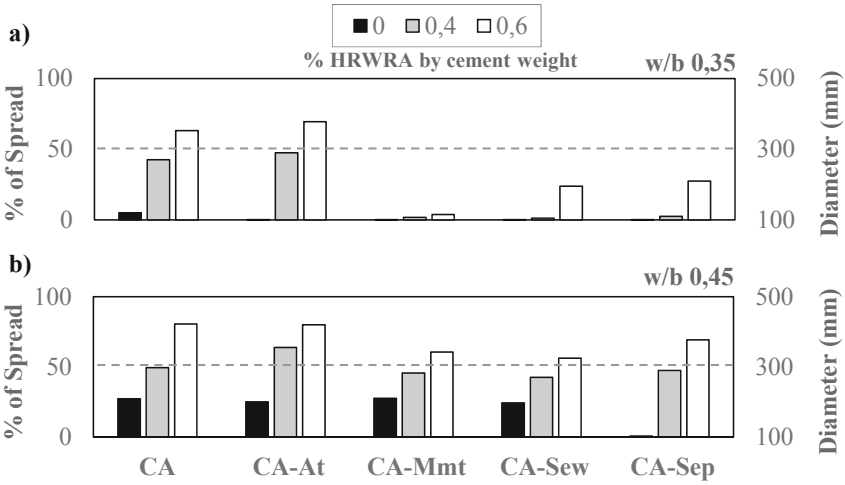

Fig. 4. Comparison of the effect of HRWRA on the of spread diameter increase %. (a) *w/b* = 0.35; (b) *w/b* = 0.45.

Figure 4 shows a comparison of the effect of HRWRA on the of spread diameter increase for two w/b. Diameter spread has been reported to be related to yield stress [11]. Pastes with 0.35 (Fig. 4a) showed that HRWRA was only effective for reference (CA) and paste with Attapulgite (At). With w/b of 0.45, HRWRA had a large effectiveness in all cases, with similar values for all the nanoclays under study, due to their saturation of water. Hence, Mmt and sepiolites require a minimum value of w/b to saturate before HRWRA can be effective. Furthermore, as shown in Fig. 3, this saturation also produces a reduction of final spread time, which can be related to paste viscosity [12]. However, it has been reported that is better to use HRWRA to reach the required spreading than water [13].

5 Conclusions

This paper presents a study on fluid cement pastes with limestone filler, two water to binder ratios (w/b) and different amounts of high range water reducing admixture (HRWRA). Four types of nanoclays were incorporated and their effect on rheological properties at early age (EA) was assessed. The main conclusions of the study were:

- Regarding cement pastes only with water and without HRWRA, sepiolite in powder form produced lower spread diameter (related to higher yield stress). This effect can be explained considering the entanglement of sepiolite needle shape particles. Whereas Sepiolite dispersed in water did not show this reduction. The use of HRWRA, remediated this undesired effect.
- For pastes with w/b of 0.35, attapulgite (At) showed similar spread diameters as reference paste, although raises the final time, which can be related to viscosity. On the contrary, sepiolites and montmorillonite required larger amounts of HRWRA to achieve similar spread diameters. Montmorillonite (Mmt) required the largest amounts of HRWRA to achieve flowability, due to the larger adsorption of admixture related to its plate shaped particles.
- Lower w/b pastes suffered larger effects of the nanoclay type on rheological parameters. When w/b was raised, all the nanoclays behaved similar. It seems that nanoclays require a level of water saturation to take advantage of HRWRA effectivity. This effect was moderate for sepiolites and extremely important for Montmorillonite.

Acknowledgement. Financial support was provided by NanoCompaC (*BIA2016-77911-R*), funded by the Spanish Ministry of Economy and Competitiveness. The authors greatly acknowledge the support of the companies TOLSA GROUP S.A, BASF construction chemicals, Omya Clariana and Cementos Portland Valderrivas.

References

1. Barluenga G, Giménez M, Rodríguez A, Rio O (2017) Quality control parameters for on-site evaluation of pumped self-compacting concrete. Constr Build Mater 154:1112–1120
2. Lomboy GR, Wang X, Wang K (2014) Rheological behavior and formwork pressure of SCC, SFSCC, and NC mixtures. Cem Concr Compos 54:110–116
3. Tregger NA, Margaret EP, Shah SP (2010) Influence of clays on the rheology of cement pastes. Cem Concr Res 40(3):384–391
4. Quanji Z, Lomboy GR, Wang K (2014) Influence of nano-sized highly purified magnesium alumino silicate clay on thixotropic behavior of fresh cement pastes. Constr Build Mater 69:295–300
5. Qian Ye, De Schutter Geert (2018) Enhancing thixotropy of fresh cement pastes with nanoclay in presence of polycarboxylate ether superplasticizer (PCE). Cem Concr Res 111:15–22
6. Tan H, Qi C, Ma B, Li X, Jian S (2015) Effect of polycarboxylate superplasticiser adsorption on fluidity of cement–clay system. Mater Res Innov 19(5):S5-423–S5-428
7. Ng S, Plank J (2012) Interaction mechanisms between Na-montmorillonite clay and MPEG-based polycarboxylate superplasticizers. Cem Concr Res 42:847–854
8. Lei L, Plank J (2014) A study on the impact of different clay minerals on the dispersing force of conventional and modified vinyl ether based polycarboxylate superplasticizers. Cem Concr Res 60:1–10

9. Murray HH (2007) Structure and composition of the clay minerals and their physical and chemical properties. In: applied clay mineralogy occurrences, processing and application of kaolins, bentonites, palygorskite-sepiolite, and common clays, 1st edn, Elsevier, Amsterdam, pp 7–31
10. Mechtcherine V, Secrieru E, Schröfl C (2015) Effect of superabsorbent polymers (SAPs) on rheological properties of fresh cement-based mortars – Development of yield stress and plastic viscosity over time. Cem Concr Res 67:52–65
11. Roussel N, Coussot P (2005) Fifty-cent rheometer for yield stress measurements: from slump to spreading flow. J Rheol 49:705–718
12. Tregger N, Ferrara L, Shah SP (2008) Identifying viscosity of cement paste from mini-slump-flow test. ACI Mater J 105(6):558–566
13. Ferron R, Gregori A, Sun Z, Shah SP (2007) Rheological method to evaluate structural build-up in self- consolidating concrete cement paste. ACI Mater J 104(3):242–250

Mechanical Properties, Durability and Sustainability of SCC

Revised Macro-cracking Criterion for Massive Non-reinforced Self-compacting Concrete Structures Under Thermal Load Based on Extensive Experimental Testing and Field Observations

Bart Craeye[1,2,3(✉)], Lou Areias[6], Maarten Van Geet[4], and Saeid Babaei[1,5]

[1] Faculty of Applied Engineering - EMIB Research Group, University of Antwerp, Antwerp, Belgium
bart.craeye@uantwerpen.be
[2] Industrial Sciences and Technology, Odisee University College, Aalst, Belgium
[3] Magnel Laboratory for Concrete Research, Ghent University, Ghent, Belgium
[4] ONDRAF/NIRAS, Brussels, Belgium
[5] SCK.CEN/EURIDICE, Mol, Belgium
[6] MeMC, Vrije Universiteit Brussel, Brussels, Belgium

Abstract. The Supercontainer is a reference concept of the Belgian Agency for Radioactive Waste and Enriched Fissile Materials (ONDRAF/NIRAS) for the post-packaging of vitrified high-level waste and spent fuel destined for deep geological disposal. The behaviour of this massive concrete structure was studied using macro-scale modelling, based on extensive experimental testing at lab-scale and validated by means of an experimental program, using realistic scale models. One of the objectives of this study was to predict and overcome possible cracking of the different cementitious layers in the container.

The experimental program used half-scale models of the Supercontainer constructed in two main phases: (i) the construction of a non-reinforced concrete buffer with an inner cavity using a self-compacting concrete mixture, and (ii) the embedment of a heat-emitting source in the cavity of the buffer to simulate the heat-emitting conditions of a real overpack. This paper provides a brief discussion of the test setup used in the experimental program as well as the instrumentation, concrete mixing and the casting process during the two construction phases of the experiment. The macro-cracking criterion used to predict cracking onset and evolution in the cementitious layers is critically reviewed by comparing the simulated tangential and axial stresses in the axi-symmetrical container with in-situ experimental measurements.

Keywords: Massive concrete structures · Macro-cracking criterion · Real-scale testing

L. Areias—Former SCK.CEN/EURIDICE, Belgium.

V. Mechtcherine et al. (Eds.): RheoCon 2019/SCC 2019, RILEM Bookseries 23, pp. 527–535, 2020.
https://doi.org/10.1007/978-3-030-22566-7_61

1 Introduction and Objectives

As part of the long-term management of high-level and heat-emitting radioactive waste, ONDRAF/NIRAS developed a reference design concept for the post-packaging of this waste (Fig. 1). This so-called Supercontainer (SC) consists of a canister containing the high-level waste, an (optional) outer steel envelope, a concrete buffer, a cementitious filler and a carbon-steel overpack forming a hermetically closed seal around the canister [1, 2]. The buffer provides passivation of the carbon steel overpack and offers radiation protection during handling and transport. The construction of a SC consists of four main stages [2], as shown in Fig. 1.

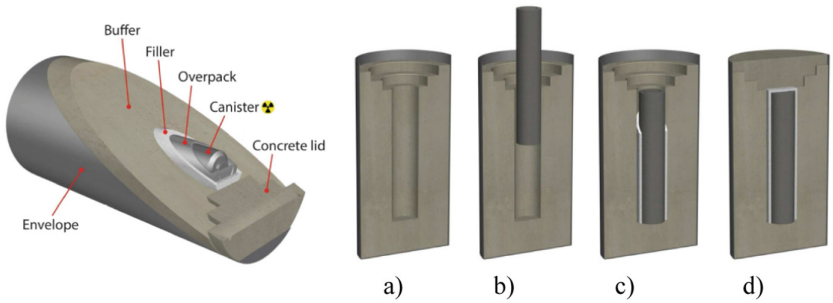

Fig. 1. The Belgian Supercontainer concept and its main construction phases: (a) construction of the buffer and outer envelope, (b) insertion of the overpack, (c) casting of the filler, and (d) installation of lid.

The feasibility to construct the SC is being evaluated through a number of scaled macro-models tested and validated using various measurement techniques. To investigate the feasibility of the SC concept at large scale, two half-scale tests have been performed. The term 'half-scale' refers to the size of the test mock-up, which has a true horizontal scale but is limited in height to approximately half of a real SC.

The first half-scale test (HST1), performed in 2009, demonstrated to a far extent that the SC can be constructed using available industrial techniques [3]. However, micro-cracks formed on the surface of the concrete buffer during the heating phase. The absence of a dedicated crack-monitoring system precluded defining the exact time of initiation, evolution and depth of penetration of these micro-cracks.

To build further on the knowledge acquired in HST1, a second test (HST2) was performed in 2013, which is the focus of this article. The primary objectives of this test were (i) to further investigate the feasibility of constructing the SC, and (ii) to advance our understanding of the thermo-mechanical behaviour of the self-compacting cementitious (concrete and mortar) materials. Other objectives included (iii) modifying operational aspects of concrete mixing and casting to prevent the formation of a transition casting joint as observed in HST1, (iv) testing a new filler composition with reduced modulus of elasticity to lower the risk of cracking in the buffer, and

(v) deploying state-of-the-art monitoring to detect and predict the onset of cracking and evolution in the concrete and filler during Phase 2.

The experimental mock-up weighed approximately 32 tons and consisted of two main construction phases. Phase 1 carried out the construction of a non-reinforced concrete buffer using a self-compacting concrete (SCC) mixture. This construction phase created a concrete buffer with an inner cavity large enough to hold a carbon steel overpack, as specified in the conceptual design. In Phase 2, a pre-heated carbon steel overpack was inserted into the existing cavity of the buffer and the free space in the cavity was subsequently filled with a cementitious filler especially developed for the test. The preheated overpack contained a heat source to simulate the heat emitted by a real canister.

2 Test Set-Up

2.1 Dimensions and Formwork

Figure 2a shows a cross-section of the concrete buffer constructed for the HST2. A detailed description of the half-scale test appears in [3, 4]. The formwork consists of a cylindrical-shape metal construction comprising a base, an inner conical section and an outer shell. The formwork is designed for casting the buffer in an upright position (Phase 1), which reduces the risk of damaging the instrumentation and provides a stable environment during the test. The T-shaped inner mould creates a cavity inside the buffer to allow the insertion of the pre-heated carbon steel overpack (Phase 2).

Fig. 2. (a) Cross-section of the buffer, dimensions in [m], (b) General view on mould during installation, (c) View of inside of formwork, (d) Carbon steel overpack containing heat source.

2.2 Instrumentation

The test used a state-of-the-art monitoring installation to measure relevant parameters including temperature, ambient wind velocity, pressure, strain and displacements in all three directions, as well as digital image correlation (DIC) and acoustic emission (AE) to monitor the onset and evolution of cracking in the buffer and filler.

DIC is an optical technique that allows the identification of displacements between subsequent images taken by a pair of cameras [5] (Fig. 3b), based on a digitally generated black and white pattern fixed on a predefined area. Usually, the first image is taken in a non-deformed state while subsequent images are taken at different proceeding load stages, enabling detection of micro-cracks with a crack opening resolution of approximately 12.5 ± 5 µm.

AE utilizes the transient elastic waves emitted by the tip of a crack during propagation and provides information on the density of cracks, the geometric location and depth of the cracking [5]. These waves are detected by piezoelectric sensors mounted on the surface of the concrete and are transformed into electric waveforms. By means of AE it is possible to determine the onset of cracking. The combination of these two non-destructive methods offers a powerful tool to study crack formation and evolution in concrete [5].

Three windows in the outer steel mould provided access to the DIC measurements during the first 29 days of hardening of the concrete buffer (Fig. 3a). The same figure shows the grey digital image installed in window 2, two days after casting of the buffer, and four AE sensors located at each corner of the window.

Fig. 3. (a) Outer mould showing three access windows for the DIC measurements and printed digital image together with four AE receivers installed at window W2, (b) Typical DIC set-up.

2.3 Self-compacting Concrete/Mortar: Composition, Mixing, Casting-Pumping and Time Schedule

The test used two types of self-compacting concrete mixes: (i) a self-compacting concrete for the buffer (Phase 1); and (ii) a self-compacting mortar for the filler and lid (Phase 2). The reference mix proportions of both compositions appear in Table 1.

Table 1. Composition of the self-compacting concrete (buffer) and mortar (filler) for 1 m^3 of mix, in [kg].

Dry components	Buffer	Filler
CEM I 42.5N LH LA HSR	350	235
Limestone filler	100	400
Limestone 0/4	840	1350
Limestone 2/6	327	–
Limestone 6/14	559	–
Water	175	235
Superplasticizer (PCE)	8	3,5
VMA	0,17	–
W/C-ratio	0,50	1,00
W/P-ratio	0,39	0,37
C/P-ratio	0,78	0,37

The concrete mixing facilities consisted of a forced-type concrete mixer with a capacity of 2 m^3 for the concrete and filler. In total, the concrete mixture supplied for the buffer was 12 m^3, while the filler and lid required 3 m^3, prepared in 6 $\times$ 2 m^3 batches for the buffer and 2 $\times$ 1.5 m^3 batches for the filler and lid, respectively. The time between the different batch-pumping activities was kept to a minimum to improve the quality and aesthetics of the concrete and to avoid undesired casting-joints between batches. During pumping, a flexible hose was lowered to the base of the formwork and lifted upwards during casting until the formwork was filled entirely. Once the casting and pumping processes ended, the top of the formwork was sealed by means of a non-adhesive foil to improve curing conditions. The consistency of the fresh mixes was evaluated in order to optimize the workability of the fresh mixes. The goal was to have a fresh, non-segregating (evaluated visually) mix with a minimal slump flow value of 600 mm. In order to further characterize the behaviour of the self-compacting concrete and mortar mixes, different thermal maturity-related and mechanical properties were determined, including: cube compressive and tensile strength at different ages, both in flexural as well as in splitting behaviour.

The autogenous shrinkage and the heat production in adiabatic environment (until the age of 168 h of hardening) were determined according to the procedures described in [6]. Thermal properties were obtained from previous studies [6]. These properties were implemented in the material database of the HEAT/MLS simulation tool. An overview of the obtained results of the fresh and hardened concrete properties can be found in [4].

Monitoring started as soon as casting ended at the start of Phase 1. Approximately 144 h after the start of Phase 1, the T-shaped inner mould was removed, exposing the hollow cavity in the buffer. The outer stainless steel formwork was removed after approximately 696 h. The temperature in the buffer reached a high of 60 °C and continued generating heat for a period of approximately 672 h. Phase 2 started approximately 66 days after the start of Phase 1.

2.4 Macro-scale Modelling and Macro-cracking Criterion

The numerical simulation were carried out using the finite element program HEAT/MLS. This tool performs advanced thermal and mechanical computations particularly linked to a material database and is well suited to calculates stress and the strength in concrete structures. However, the effects of moisture transport and moisture changes were not included in the simulation tool. The experimentally determined thermal, mechanical and maturity-related properties of the buffer and filler were implemented in the material database. Also the actual and registered boundary conditions (e.g. type of formwork, use of insulation, registered ambient wind velocity, registered heat emitted by the overpack) were incorporated. The finite element tool simulates the hydration process in the concrete structure and calculates the stresses and the strength in the structure. It is possible to simulate the internal stress development inside the cementitious layers in three axi-symmetrical directions. According to [6] the main stresses generated in the Supercontainer are the internal axial (z-direction) and tangential (y-direction) stresses.

The most significant question is whether the tensile stresses in the buffer, due to the developed thermal gradients inside the structure, and taking into account the autogenous deformation, the visco-elastic behaviour of the concrete and the thermal load of the overpack, will exceed the tensile strength of the concrete buffer, giving rise to early-age macro-cracking. A stress based macro-cracking criterion is defined for the estimation of the macro-cracking potential, as mentioned in [6, 7].

$$\frac{S_{y,z}}{\gamma_{cr} \cdot f_{ct}} \leq 1 \tag{1}$$

It can be assumed that tensile cracking will occur in real structures if the ratio expressed by Eq. (1) exceeds 1. By calculating the thermo-mechanical stress development inside the buffer at any point (by means of the HEAT/MLS finite element modelling: axial stresses S_y and tangential stresses S_z), and by determining the axial tensile strength in laboratory of the concrete used for the buffer (e.g. by performing splitting tensile strength tests, knowing $f_{ct} = 0{,}85 \cdot f_{ct,spl}$), the cracking index γ_{cr} can be empirically determined by comparing the cracking criterion with the onset and evolution of the macro-cracking of the outer concrete buffer layers (visualized by means of DIC/AE techniques), where the cracking potential is at its highest [6]. In literature, there is discussion about the value of this index: for normal strength concrete a value between 0,7 [7] and 0,9 [8] is assumed, for high strength concrete 0,6 is depicted [8] and for real massive structures 0,5 is highlighted by [8]. For the HST2 the cracking index γ_{cr} is set at 0.5.

3 Results and Discussion

Simulations using HEAT/MLS predicted the absence of early-age thermal cracking behaviour during Phase 1 of the test. This was in line with visual inspections of the buffer during Phase 1, prior to the start of the heating phase, which confirmed the complete absence of cracks both in the axial and tangential directions as well as at the surface and inside the concrete. DIC measurements further confirmed these observations, as shown in Fig. 4a. These findings also agree with earlier results reported in [2, 6], which concluded that the construction of the buffer in Phase 1 can be completed without inducing any macro-cracking behaviour.

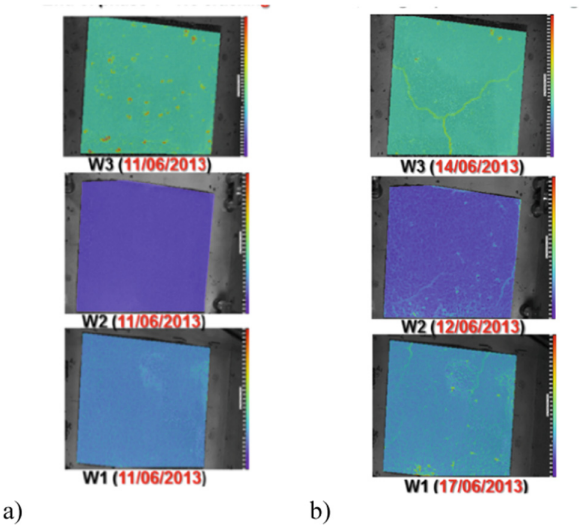

Fig. 4. (a) DIC images showing absence of cracks just before the start of Phase 2, (b) same images showing crack initiation after start of Phase 2.

Shortly after the start of Phase 2 on 11/06/2013, the DIC/AE monitoring installation detected the first micro cracks in the middle window W2, at approximately 20 h after the start of Phase 2, as shown in Fig. 4b. The first cracks in W1 and W3 appeared later, at respectively 144 h and 72 h. Post processing analysis of the acquired digital images indicated a general tendency for the width of the cracks to increase with time. The initial width of the cracks varied between 15 µm at detection and reached peak values of 55 µm (approximately 200 h after start of Phase 2) during the test [5].

HEAT/MLS simulations using a cracking index γ_{cr} of 0.5 yielded the highest (tangential) tensile stresses and (axial) cracking potential in the mid-region of the buffer (level W2, Fig. 5) at an approximate time of 331 h after the start of Phase 2 (Fig. 5, point C). As shown, the tensile cracking ratio (Eq. (1)) exceeds 1 after 96 h (point B). After 24 h (point A) a significant build-up of tensile stress (and cracking potential) is evident, which corresponds with the time of onset of cracking determined by the

DIC/AE monitoring installation. After 660 h, the tensile stresses evolve towards a constant value and the tensile cracking ratio becomes inferior to 1 (point D). There is a noticeable resemblance between the DIC/AE test measurements and the results of the thermo-mechanical simulations. However, exact determination of the time of onset of cracking by means of the thermo-mechanical HEAT/MLS is not possible. One plausible explanation for this is the absence of hygral modelling (moisture transport) in the HEAT/MLS simulations. In fact, prior to Phase 2, the outer stainless steel envelope was removed, thereby enabling transport of water out of the buffer under thermal load. Transport of water out of the buffer can give rise to a build-up of additional internal stresses and lead to cracking. Additional research taking into account the hygral behaviour of the buffer is recommended to better characterize the macro-cracking criteria of the buffer.

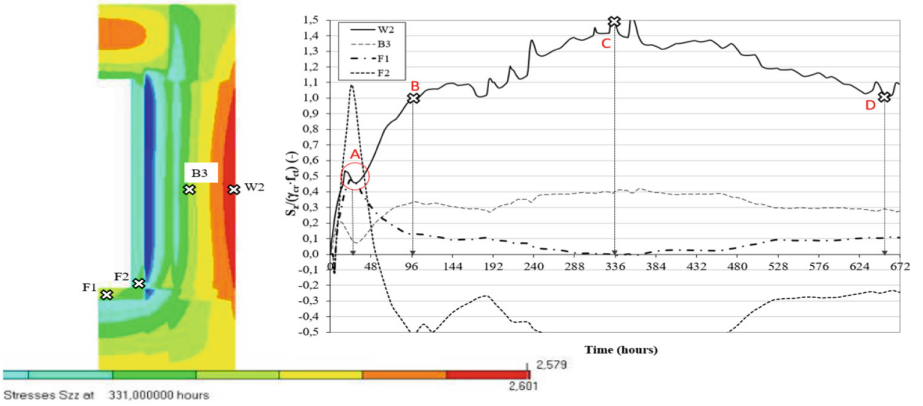

Fig. 5. Results of HEAT/MLS simulations of Phase 2: contour plot after 331 h and time graph of the cracking potential evolution.

References

1. Wacquier W, Van Humbeeck H (2009) B&C concept and Open Questions, ONDRAF/NIRAS internal report 2009-0146
2. Craeye B, De Schutter G, Wacquier W, Van Humbeeck H, Van Cotthem A, Areias L (2011) Closure of the concrete supercontainer in hot cell under thermal load. Nucl Eng Des 241:1352–1359
3. Areias L (2011) Construction and Testing of First Half-Scale Test, EURIDICE internal report
4. Areias L (2014) Surface tests to evaluate the feasibility to construct the Belgian Supercontainer, EURIDICE internal report EWETOPDEU-041, p 128
5. Iliopoulos S, Aggelis DG, Pyl L, Vantomme J, Van Marcke P, Coppens E, Areias L (2015) Detection and evaluation of cracks in the concrete buffer of the Belgian Nuclear Waste container using combined NDT techniques. Constr Build Mater 78:369–378
6. Craeye B (2010) Early-age thermo-mechanical behaviour of the supercontainers for radwaste disposal, Doctoral thesis Ghent University

7. Rostásy FS, Krauss M, Budelmann H (2002) Planungswerkzeug zur Kontrolle der frühen Rissbildung in massigen Betonbauteilen, Bautechnik 79, Ernst & Sohn Verslag
8. Koenders E (2018) Macro modelling: temperature and stresses, Multi-Scale Modelling of Concrete Course, TUDelft

Experimental Investigation on Mechanical Properties of Fiber Reinforced Lightweight Self-consolidating Concrete

Ali Ehsani Yeganeh(✉), Farzad Kouroshnezhad, Sina Dadsetan, Khandaker M. A. Hossain, and Mohamed Lachemi

Civil Engineering, Ryerson University, Toronto, ON, Canada
ali.ehsaniyeganeh@ryerson.ca

Abstract. This paper presents the results of an experimental investigation on the mechanical property of different types of fiber reinforced lightweight self-consolidating concrete (FRLWSCC) with three different types of fiber: High-Density Poly Ethylene (HDPE), Crumb Rubber (CR) and Polyvinyl Alcohol (PVA). Three developed mixes were compared in terms of compressive strength, flexural strength, stress-strain development, splitting tensile capacity, ductility, energy absorption capacity and stiffness with the lightweight self-consolidating concrete (LWSCC) without any fiber. For each category of tests, 20 samples were produced and tested. The results of the performed tests showed that the addition of fibers reduced compressive strength. In case of lightweight mixes with HDPE and PVA fibers, the reduction of compressive strength was more than 15%. However, all the fibers increased the flexural strength capacity with higher deflection at failure, meanwhile all type of fibers increased the number of cracks and reduced crack width at failure stage. Additionally, the splitting tensile capacities of FRLWSCC mixes were higher than LWSCC without fiber. All the FRLWSCCs showed a higher ability to absorb more energy. All FRLWSCC samples had a higher ductility capacity and exhibited a relatively lower stiffness.

Keywords: Lightweight self-consolidating concrete · Fibers · Compressive strength · Flexural behaviour · Energy absorption

1 Introduction

Concrete is the most common material in construction around the world [1]. During the past decades, extensive research has been carried out on self-consolidating concrete (SCC) products and it has been evolved since. New developments of SCC production accomplished high quality of concrete in construction. Introduction of fibers and lightweight aggregate are two of the latest innovations in production of SCC. This new type of concrete known as fiber reinforced lightweight self-consolidating concrete (FRLWSCC) has the flowability of SCC and a lower self-weight, which leads to lower dead load of structures with higher durability and improved mechanical properties [2]. The lower density of lightweight self-consolidating concrete (LWSCC) is obtained by replacement of normal aggregates by lightweight aggregates. The concrete weight is in

V. Mechtcherine et al. (Eds.): RheoCon 2019/SCC 2019, RILEM Bookseries 23, pp. 536–543, 2020.
https://doi.org/10.1007/978-3-030-22566-7_62

a range of 1400 kg/m^3 to 2000 kg/m^3, while maximizes the structural efficiency by reducing the total dead load of a structure and seismic inertia mass [3, 4].

Due to a high porosity, lightweight aggregates should be used in saturated surface dry (SSD) condition. Therefore, LWSCC has high internal curing and better quality of aggregate-paste contact zone (ITZ) compared to traditional concrete, this leads to reduction of concrete cracking and improvement of mechanical properties [5]. The introduction of a fiber into LWSCC is one of the most effective methods to improve the performance of concrete with regard to direct tensile load, splitting tensile strength, bending load capacity, deformation and deflection before failure, crack propagation resistance, energy absorption capacity, shrinkage and increase of the concrete strain capacity [6–8].

The effect of the addition of different types of fibers into normal concrete and SCC such as High-Density Polyethylene (HDPE), Polyvinyl Alcohol (PVA) and Crumb Rubber (CR) has been extensively investigated by different researchers [9–11], However, there are a lack of studies addressing the mechanical properties and characteristics of fiber reinforced lightweight self-consolidating concrete. The purpose of this research is to investigate mechanical properties of lightweight self-consolidating concrete incorporating different types of fibers and to evaluate their effect. This paper presents mechanical properties of three FRLWSCCs by highlighting different types of fibers compared to a control SCC mixture.

2 Experimental Program

2.1 Material Properties

All FRLWSCC mixes consist of CSA type 10 or ASTM type 1 Portland cement, fly ash (FA) type C according to ASTM C618 [12] and dry-densified silica fume (SF). Additionally, ADVA Cast 575 conforming to ASTM C494 types A and F [13] was used as high range water reducer (HRWR). Lightweight blast furnace slag aggregates were used for both coarse and fine aggregates with maximum nominal sizes of 10 mm and 4.75 mm, respectively. Both coarse and fine aggregates were submerged in the water for 72 h and then in room temperature for another 24 h to obtain saturated surface dry density (SSD) condition. Due to high porosity properties of both coarse and fine aggregates, after the total period of 96 h, coarse aggregates had water absorption of 13.42% with bulk specific gravity of 1.6 (kg/m^3) and fine aggregates had a water absorption of 9.64% with bulk specific gravity of 2.0 (kg/m^3).

For this study, three different types of fibers including High Density Polyethylene (HDPE), and Polyvinyl Alcohol (PVA) and Crumb Rubber (CR) were used. The geometrical and mechanical properties of fibers are presented in Table 1.

2.2 Mix Design

Four mixes of LWSCC were designed based on paste volume with constant water to cementitious material (w/b) ratio of 0.3. The mixture proportions are provided in Table 2. The slag coarse and fine aggregates were weighted in SSD condition and

Table 1. Geometrical and mechanical properties of fibers

Fiber type	Length (mm)	Specific gravity (Kg/m^3)	Melting point (°C)	Diameter (Microns)
PVA	8	1.3	225	38
HDPE	0.1	0.96	135	5
Crumb rubber	0.4	0.9	N/A	2

introduced first into the mixer and mixed with 75% of water for 2 min at normal speed, then the rest of cementitious materials including fly ash, silica fume and cement were added and mixed for another 5 min. HRWRA was slowly added to the mix with the remaining 25% water and mixed for another 5 min. Finally, fibers added into the mixer and mixed for 15 min. The same procedure was applied for control LWSCC mix as well without mixing period for fibers.

Table 2. Fiber reinforced lightweight SCC mix designs

Concrete mix	w/b	Cement	Fly ash (Class C)	Silica fume	Water	Coarse aggregates (SSD)	Fine aggregates (SSD)	HRWR kg/m^3	Fiber kg/m^3
All Ingredients are calculated based on 1 part of cement									
1% HDPE-FRLWSCC	0.30	1.00	0.16	0.09	0.38	0.99	1.61	4.75	9.2
1% CR-FRLWSCC	0.30	1.00	0.16	0.09	0.38	0.99	1.61	4.75	9.2
0.5% PVA-LWSCC	0.30	1.00	0.16	0.09	0.38	0.99	1.62	4.75	6.5
LWSCC	0.30	1.00	0.15	0.09	0.37	1	1.61	4.75	0

2.3 Fresh Properties of FRLWSCC

The workability of the FRLWSCC mixes were evaluated with the slump flow test while flowability, passing ability and segregation resistance were evaluated by slump cone, L-box, V-funnel tests, respectively according to ASTM standards - ASTM C1611 [14].

2.4 Experimental Procedure

A total of twenty flexural strength prism specimens for each mix design with length, height and width of 304 mm by 80 mm by 50 mm respectively were casted to obtain the average flexural strength based on ASTM C78 [15]. All samples were tested at 28 days under four-point bending load. To obtain concrete strain, a concrete strain gauge was attached to the compression surface of each specimen.

A total of forty cylindrical specimens with dimensions of 100 mm diameter and 200 mm height were casted for each mix design. Twenty cylindrical specimens were used to measure the average compressive strength according to ASTM C39 [16] to record the concrete strain, three concrete strain gauges were attached at the angle of 120 deg vertically to the cylindrical specimens. Twenty cylindrical specimens were used to measure average splitting tensile capacity according to ASTM C496 [17]; two concrete strain gauges were the attached to the surface of cylindrical specimens one vertically and one horizontally.

3 Results and Discussion

Compression test was carried out on total of twenty cylindrical specimens and experimentally obtained average stress versus average concrete compressive strain for all four mix designs are shown in Fig. 1(a). LWSCC and CR mixes had highest compressive strength of 52 MPa compared to HDPE and PVA lightweight mixes. CR lightweight mix reached the highest compressive strain of 3494 μmm/μmm compared to its counterpart mixes. Addition of PVA and HDPE fibers reduced the compressive strength while they increased the concrete compressive strain for the CR lightweight mix they increased both compressive strength and concrete compressive strain. Details of maximum compressive strength and compressive strain for all mixes are provided in Table 3.

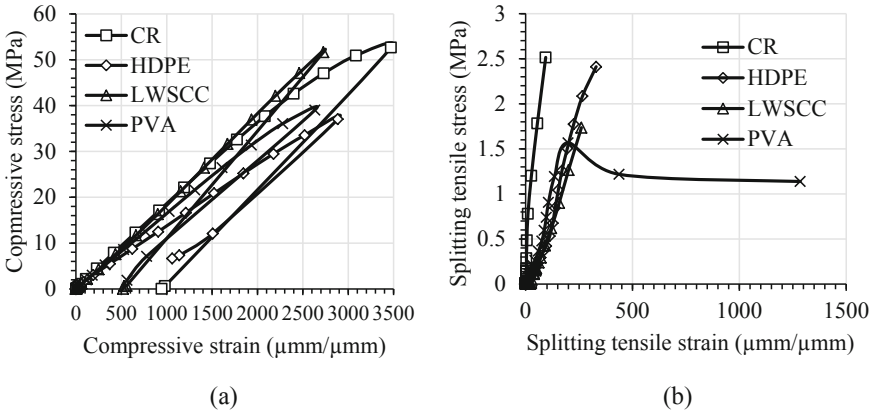

Fig. 1. (a) Average compressive stress vs. compressive strain (b) splitting tensile stress vs. splitting tensile strain.

A total of the twenty cylindrical specimens were tested for splitting tensile strength. The average splitting tensile stress vs average splitting tensile strain for all tested samples are shown in Fig. 1(b). CR and HDPE light weight mixes obtained the highest splitting tensile strength of 2.51 MPa and 2.41 MPa respectively compared to its counterparts mixes, both CR and HDPE fibers increased the ultimate tensile capacity

by more than 40% while the addition of PVA fiber to the lightweight mix reduced the splitting tensile strength compared to the LWSCC control mix. PVA lightweight mix showed the highest splitting tensile strain of 1285 μmm/μmm with increase of more than 350% compared to CR, HDPE and LWSCC due to geometric characteristics and fiber bridging of PVA. Maximum values of ultimate splitting tensile loads are obtained from the experimental tests with corresponding maximum splitting tensile stress and strain values for all mixes are provided in Table 4.

Table 3. Summary of ultimate compressive load, compressive strength and compressive strain.

Specimens	Ultimate compressive load (kN)	Ultimate compressive strength (MPa)	Ultimate compressive strain (μmm/μmm)
CR	415	52	3494
HDPE	303	39	3195
LW	420	53	2905
PVA	308	38	2632

Table 4. Summary of ultimate splitting tensile load, splitting tensile strength and tensile strain.

Specimens	Ultimate splitting tensile load (kN)	Ultimate splitting tensile strength (MPa)	Ultimate splitting tensile strain (μmm/μmm)
CR	100	2.51	120
HDPE	81	2.41	376
LW	65	1.73	330
PVA	70	1.56	1285

The ratio of the splitting tensile to the compressive strengths for all four mixes were mostly influenced by their compressive strengths, as the ratio increased with the increase of compressive strength except for the CR mix as shown in Fig. 2. Fibers material characteristics and geometry affected the ratio of the splitting tensile to the compressive strengths, as shown in Fig. 2. LWSCC ratio linearly increased but PVA and HDPE had nonlinear ratio increase and the CR ratio is almost constant.

A total of twenty prisms were tested under four-point bending load to obtain the average flexural strength and flexural deflection for all mixes. CR and HDPE FRLWSCCs had the highest flexural load capacity and flexural strength (approximately 2 kN and 3 MPa, respectively) compared to LWSCC and PVA mixes. PVA lightweight mix obtained the highest flexural deflection of 0.6 mm and all mixes had relatively similar flexural strain 300 μmm/μmm as shown in Fig. 3(a–b). Summary of ultimate flexural load, deflection, flexural strength and flexural strain is presented in Table 5.

Ductility, energy absorption, stiffness and modulus of elasticity was calculated for all four mixes based on obtained experimental result from flexural test. The stiffness was calculated from the slope of the flexural load-deflection curve. Energy absorption

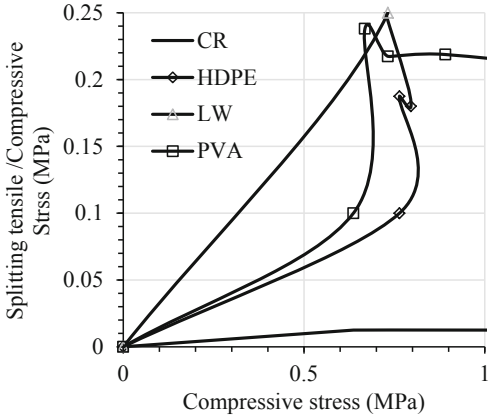

Fig. 2. Ratio of splitting tensile to compressive strength vs compressive strength.

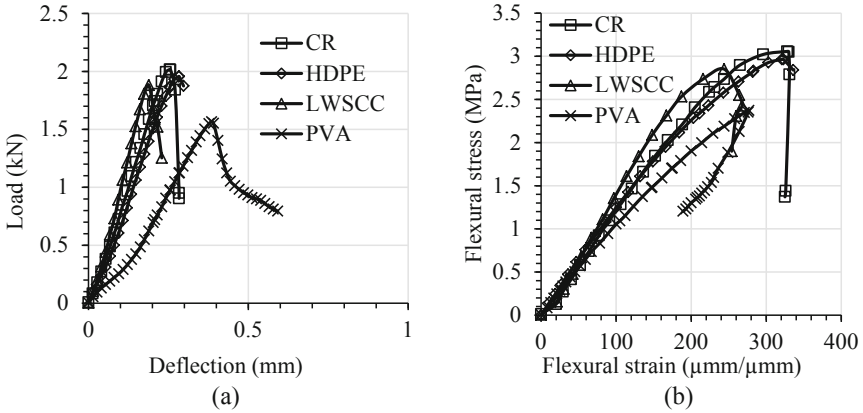

Fig. 3. (a) Load-deflection (b) flexural stress vs flexural strain behaviours.

Table 5. Ultimate flexural load, deflection, flexural strength and flexural strain.

Specimens	Ultimate flexural load (kN)	Ultimate flexural deflection (mm)	Ultimate flexural strength (MPa)	Ultimate flexural strain (μmm/μmm)
CR	2.01	0.28	3.05	330
HDPE	1.95	0.3	2.98	336
LWSCC	1.88	0.23	2.86	244
PVA	1.55	0.6	2.35	276

was obtained from the area under the flexural load-deflection curve up to the post peak flexural strength of 85% of the ultimate load. Ductility was illustrated as the ratio of deflection at 85% of ultimate load after the peak load was passed to 85% of ultimate load before peak load. Modulus of elasticity was calculated as the slope of flexural stress-strain curve. PVA mixes had the lowest stiffness of 3.11 kN/mm compared to all counterpart mixes. All fibre reinforced mixes showed higher energy absorption capacity and higher ductility compared to control LWSCC mix due to the presence of fiber. All mixes had similar modulus of elasticity except the HDPE mix which had a higher modulus of elasticity compared to other mixes. Results of stiffness, energy absorption capacity, ductility and modulus of elasticity calculations are summarized in Table 6.

Table 6. Summary of stiffness, energy absorption, ductility and modulus of elasticity.

Specimens	Stiffness (kN/mm)	Energy absorption (J)	Ductility	Modulus of elasticity (GPa)
CR	7.64	0.31	1.19	7.53
HDPE	6.27	0.32	1.23	11.25
LWSCC	8.86	0.2	1.18	9.37
PVA	3.11	0.3	1.34	8.83

4 Conclusions

The following conclusions are drawn from the study:

- The presence of fibers reduced the compressive strength and ultimate compressive load capacity of lightweight self-consolidating concrete except for CR fiber which had about the same compressive strength.
- All types of fiber increased splitting tensile and compressive strain capacity of LWSCC mixes. Due to PVA fiber geometry the tensile strain capacity of the lightweight mix increased by more than 350%.
- The use of HDPE and CR fibers increased the splitting tensile strength of lightweight mixes while PVA fibers reduced the splitting tensile strength, but sudden and brittle failures was avoided with PVA specimens.
  Material characteristics and geometry of fibers had an influence on the ratio of the splitting tensile to the compressive strengths of FRLWSCCs. The ratio of the splitting tensile to the compressive strengths increased at the increasing of compressive strength.
- Introduction of fibers increased the ultimate flexural load and flexural strength capacity of the lightweight mixes except PVA reduced both the ultimate flexural load and flexural strength capacity of FRLWSCCs.
- All types of fiber reduced the stiffness of FRLWSCCs while increased the energy absorption capacity and ductility.

Acknowledgement. The authors acknowledge the support of Lafarge Canada for providing the lightweight aggregates.

References

1. Ehsani Yeganeh A (2016) Structural behaviour of reinforced high performance concrete columns subjected to monotonic axial loading. In: 5th international structural speciality conference, London, Canada, pp 695–705
2. Khayat KH, Roussel Y (2000) Testing and performance of fiber-reinforced self-consolidating concrete. Mater Struct 33(6):391–397
3. ACI Committee 211 (2004) Standard practice for selecting proportions for structural lightweight concrete (ACI 211.2)
4. Corinaldesi V, Moriconi G (2015) Use of synthetic fibers in self-compacting lightweight aggregate concretes. J Build Eng 4:247–254
5. Hossain KMA, Ahmed S, Lachemi M (2011) Lightweight concrete incorporating pumice based blended cement and aggregate: mechanical and durability characteristics. Constr Build Mater 25:1186–1195
6. Gonen T (2015) Mechanical and fresh properties of fiber reinforced self-compacting lightweight concrete. Sci Iranica 22:313–318
7. Hossain KMA, Lachemi M (2007) Mixture design, strength, durability, and fire resistance of lightweight pumice concrete. ACI Mater J 104(5):449–457
8. Yehia S, Douba A, Abdullahi O, Farrag S (2016) Mechanical and durability evaluation of fiber-reinforced self-compacting concrete. Constr Build Mater 121:120–133
9. Grzymski F, Musiał M, Trapko T (2019) Mechanical properties of fibre reinforced concrete with recycled fibres. Constr Build Mater 198:323–331
10. Pešicá N, Zivanovic S, Garcia R, Papastergiou P (2016) Mechanical properties of concrete reinforced with recycled HDPE plastic fibres. Constr Build Mater 115:362–370
11. Doukakis JP (2013) Lightweight self consolidating fibre reinforced concrete. The State University of New Jersey
12. ASTM C618-17a, ASTM C618 (2017) Standard specification for coal fly ash and raw or calcined natural pozzolan for use in concrete, 17a ed. American Society for Testing and Materials. West Conshohocken, Pennsylvania, USA
13. ASTM C494/C494M-17 (2017) Standard specification for chemical admixtures for concrete. American Society for Testing and Materials, West Conshohocken, Pennsylvania, USA
14. ASTM C1611/C1611M (2018) Standard test method for slump flow of self-consolidating concrete. American Society for Testing and Materials, West Conshohocken, Pennsylvania, USA
15. ASTM C78/C78M (2010) Standard test method for flexural strength of concrete (using simple beam with third-point loading)
16. ASTM C39 (2003) Standard test method for static modulus of elasticity and Poisson's ratio of concrete in compression. American Society for Testing and Materials, West Conshohocken, Pennsylvania, USA
17. ASTM C496 (1996) Standard test method for splitting tensile strength of cylindrical concrete specimens. Society for Testing and Materials, West Conshohocken, Pennsylvania, USA

Utilization of Copper Slag in Self-compacting Concrete - Strength and Permeation Properties

Nikita Gupta(✉) and Rafat Siddique

Civil Engineering, Thapar Institute of Engineering and Technology, Patiala, India
nikitagupta.7l4@gmail.com

Abstract. The aim of this research was to prepare and evaluate the properties of self-compacting concrete mixes by replacing fine aggregates with copper slag. Copper slag is an industrial by-product of copper manufacturing industry. Various concrete mixes with constant water to- binder (w/b) ratio of 0.42 were produced, and the replacement level of fine aggregates by 0%, 20%, 40% and 60% copper slag were utilized for the purpose of evaluating the performance of SCC. The mechanical and the chloride migration property of the self-compacting concrete mixes were determined after 28 days of standard curing period. The fresh properties of SCC mixes were also studied. Results indicated that the properties of self-compacting concrete could be highly enhanced incorporating copper slag but in selective percentage of fine aggregate.

Keywords: Self-compacting · Copper slag · Performance · Mechanical · Permeation

1 Introduction

Mounting urbanisation and industrialization globally has led to two main challenges. One is the generation and disposal of a large amount of industrial by-products like iron slag, fly ash, copper slag, rice husk ash; the other is the scarcity of the natural resources available for the construction industry like natural aggregates. The only solution to counter these problems will be the utilization of industrial by-products in concrete. This will serve fruitful both economically as well as environmentally. One such by-product is copper slag that is produced by the copper manufacturing industry. To produce every ton of copper slag, approximately 2.2 tonnes to 3 tonnes of slag is produced [1]. Published literature confirms the usage of copper slag in normally vibrated concrete [2–6] apart from high strength concrete [7, 8]. Self-compacting concrete (SCC) is an innovative type of concrete that does not requires any type of vibration and is able to flow and compact under its own self-weight. The (only) disadvantages of using SCC mixes are its high cost depending on the materials involved and the quality control of mixes. The employment of copper slag as a replacement of natural aggregates in SCC will prove to be beneficial both in terms of cost cutting as well as conserving the environment. Limited literature has been published for SCC incorporating copper slag as fine aggregate replacement. Sharma et al. [9] has used copper slag varying from 0% to 100% as sand replacement in SCC mixes. Incorporation of copper slag up to 60% as

V. Mechtcherine et al. (Eds.): RheoCon 2019/SCC 2019, RILEM Bookseries 23, pp. 544–551, 2020.
https://doi.org/10.1007/978-3-030-22566-7_63

sand substitution improved the compressive strength and splitting tensile strength. In the present research, an extensive experimental programme was used to prepare and evaluate the fresh and hardened concrete properties of SCC incorporating 0%, 20%, 40% and 60% of fine aggregates replaced with copper slag. The fresh properties included slump flow, T_{500} slump flow, V-funnel and L-box were determined and checked with the EFNARC 2005 [10] requirements for all batches of SCC mixes. Compressive strength and splitting tensile strength were determined at 7 and 28 days of curing. Rapid chloride permeability test was conducted in order to evaluate the permeation property of SCC mixes at 28 days of curing.

2 Experimental Program

Ordinary Portland cement (OPC) grade 43 conforming to BIS 8112-1989 [11] was used. Tables 1 and 2 show the chemical composition and physical properties of OPC. Coarse aggregates of maximum 12 mm size were used in SCC mixes as per EFNARC [10]. The specific gravity and fineness modulus of coarse aggregates used were 2.65 and 6.09 respectively. River sand was procured from Pathankot; conforming to zone II as per BIS 383:1970 [12]. Figure 1 gives the particle size distribution of copper slag and sand. The specific gravity and fineness modulus of fine aggregates used were 2.55 and 2.19 respectively. Class F-Fly ash was collected from an adjacent thermal power plant located in Ropar, Punjab. The sum of constituents SiO_2, Al_2O_3 and Fe_2O_3 was found to be greater than 70%, which confirmed the criterion of class F fly ash as per ASTMC 618 [13]. Copper slag was procured from Taj Abrasive Industry, India. It is black in colour and has glassy texture. The main constituents of copper slag are Fe_2O_3 and SiO_2. The specific gravity and fineness modulus of copper slag was 3.51 and 3.11 respectively. Auramix-400 was used as a superplasticiser. It is a low viscosity and high water reducing admixture that is based on polycarboxylic ether polymer along with long lateral chains. It has light yellow coloured appearance and minimum pH of 6. The alkali content is generally less than 1.5 g Na_2O equivalent/L of admixture. The volumetric mass of Auramix-400 is 1.09 kg/L and contained nil amount of chloride content.

Table 1. Chemical composition of OPC and Copper slag (%).

Content	OPC	Copper slag
CaO	64.67	3.31
SiO_2	21.45	33.62
Al_2O_3	6.87	3.65
FeO	3.17	55.60
SO_3	1.95	1.12
MgO	1.16	1.51
K_2O	0.60	0.82
Na_2O	0.13	0.37

Table 2. Physical properties of ordinary Portland cement.

Colour	Grey
Initial Setting time (min)	80
Final Setting time (min)	226
Specific gravity	3.01
Consistency	29%
Soundness (mm)	1

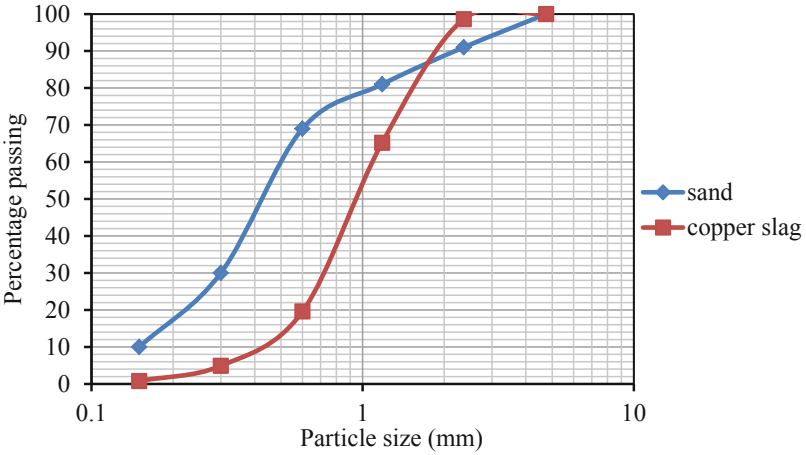

Fig. 1. Particle size distribution of sand and copper slag.

Each ingredient was measured using weighing balance and mixed in the pan mixture. Firstly, the dry materials like sand, copper slag, coarse aggregates were added initially. Then cement along with fly ash was added in the mixer. After this, 60% of water was introduced and the pan mixture was rotated for about 2 min till proper homogeneity was achieved. Rest 40% of water was added along with the dosage of super plasticiser in the mixture and was mixed for more 2 min. Immediately after SCC mixes were prepared in the mixture, the fresh properties were determined and checked with the EFNARC [10] requirements for all the batch of SCC mixes. A number of trial mixes were done in order to satisfy the requirements of EFNARC [10]. SCC mixes were prepared with and without copper slag and tested for fresh, strength and chloride migration properties. Final mix design of SCC with and without copper slag is given in Table 3.

Compressive strength of SCC mixes was determined as per BIS 516-1959 [14] using 150 mm size cube on compression testing machine. Splitting tensile strength was determined using BIS 5816-1999 [15] on cylinder of size 150 mm diameter and 300 mm length. Cylinders of 100 mm diameter and 200 mm length were casted and cured for 28 days. Slices of 100 mm diameter and 50 mm thick were cut from the casted cylinder and tested for rapid chloride permeability test according to ASTM C 1202 [16]. A total of 60 samples were tested for strength and permeability properties.

Table 3. Design mix of SCC.

Mix	0CS-SCC	20CS-SCC	40CS-SCC	60CS-SCC
Cement (kg/m^3)	400	400	400	400
Fly Ash (kg/m^3)	100	100	100	100
Sand (kg/m^3)	960	768	576	384
Copper Slag (%)	0	20	40	60
Coarse Aggregate (kg/m^3)	760	760	760	760
w/c ratio	0.42	0.42	0.42	0.42
Admixture (%)	1.2	1.2	1.2	1.2

CS-Copper Slag (0, 20, 40, 60 are the percentages of replacement of copper slag with sand)

3 Results and Discussion

3.1 Fresh Properties

The fresh properties like slump flow, T_{500} slump, V-funnel and L-box were determined and checked with the EFNARC [10] requirements for all batches of SCC mixes as given in Table 4.

Table 4. Results of fresh properties of SCC.

Property	No. of specimens to be tested for each mix	Standard deviation/mean (COV %)			
		0CS-SCC	20CS-SCC	40CS-SCC	60CS-SCC
Slump flow (mm)	5	7.07/685 (1.03)	7.91/730 (1.08)	10.61/735 (1.44)	9.35/750 (1.25)
V-funnel (s)	5	0.41/7.55 (5.40)	0.13/6.78 (1.92)	0.14/5.78 (2.46)	0.07/5.01 (1.42)
L-box	5	0.01/0.82 (0.86)	0.02/0.85 (2.76)	0.01/0.95 (0.57)	0.01/0.98 (0.92)

The slump flow diameter increased as the content of copper slag increased due to the glassy texture and low water absorption characteristic of copper slag grains. The slump flow of all mixes was in the range of 685 mm–750 mm; which is Slump Flow class 2 (SF2) according to EFNARC [10]. However, signs of bleeding and segregation were observed for SCC mixes incorporating 60% copper slag (Fig. 2). This was because of the higher specific gravity of copper slag as compared to that of sand. This was in agreement with the research conducted by [2, 7]. Also, this increased the density of SCC mixes incorporating copper slag. The density of SCC mix with 100% sand was 2466 (kg/m^3), while that of SCC mix incorporating 60% copper slag was 2636 (kg/m^3). The use of air entrainment agents can be used to reduce bleeding and segregation in concrete mixes [17].

Fig. 2. Slump flow of 60CS-SCC.

T_{500} values decreased as the content of copper slag increased. The reason for the decrease of values was the lack of bond of the constituents of SCC mixes [18]. V-funnel results showed a declining trend as the copper slag percentage increased. The V-funnel time taken by the SCC mix with 100% sand was 7.55 s while for SCC mix with 60% copper slag was 5.01 s. VF1 was the viscosity class for all the SCC mixes as per EFANRC [10]. Viscosity decreased as the amount of copper slag increased due to the glassy and smooth texture of slag grains. L-box ratio ranges from 0.82 to 0.98 for the SCC mixes containing 0% to 60% copper slag. Three re-bars were used for measuring the L-box ratio and all the SCC mixes were under PA2 class. Thus, all the fresh properties were well in accordance with the limits prescribed in the code. The flowability increased with the addition of copper slag.

3.2 Compressive Strength

Figure 3 shows the compressive strength of all SCC mixes varying from 0% to 60% at curing ages of 7 days and 28 days. The compressive strength results of SCC mixes incorporating copper slag were found to be similar or higher than that of mixes without copper slag [19, 20]. The compressive strength of the control mix was 35.63 MPa at 28 days curing. Compressive strength increased in SCC mixes incorporating up to 20% copper slag at 7 curing days and 28 curing days. The gain in strength was due to the angular shape of copper slag grains that improved the bond of the concrete matrix. A maximum strength of 38.55 MPa was observed for SCC mix incorporating 20% copper slag. However, a decline in compressive strength was observed when SCC mixes incorporated 40% and 60% copper slag as sand replacement. However, decay in values of compressive strength was not less than that of control concrete with sand. Due to the glassy texture and low water absorption property of copper slag, decrease in strength was observed [2].

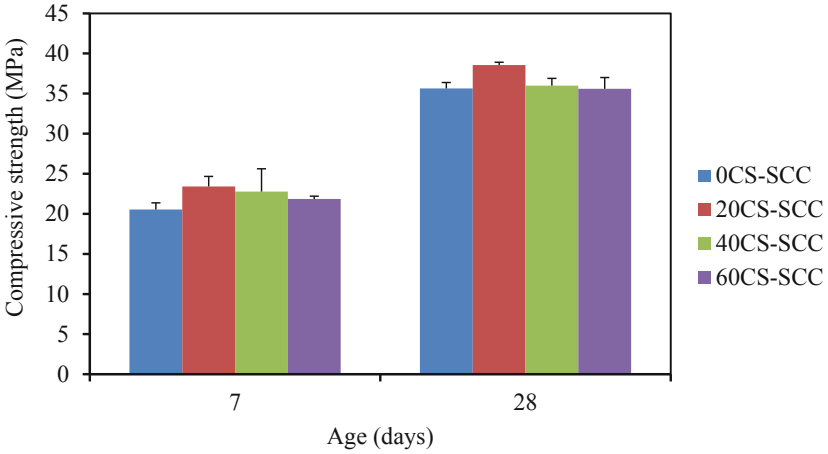

Fig. 3. Compressive strength of SCC mixes at 7 days and 28 days of curing.

3.3 Splitting Tensile Strength

The splitting tensile strength development of SCC mixes with and without copper slag at 7-days and 28-days curing is presented in Fig. 4. Splitting tensile strength improved as the content of copper slag increased from 0% to 60%. The splitting tensile strength of SCC mix without copper slag was found to be 2.13 MPa at 28 days curing. The gain in strength was 36.15%, 59.62% and 61.03% for SCC mix with 20%, 40% and 60% copper slag at 28 days curing. Due to the angular edges of slag grains, bond of the concrete matrix improved; thereby increasing the strength of SCC mixes incorporating copper slag. Similar results were presented by [9]; the splitting tensile strength decreased beyond 80% copper slag addition.

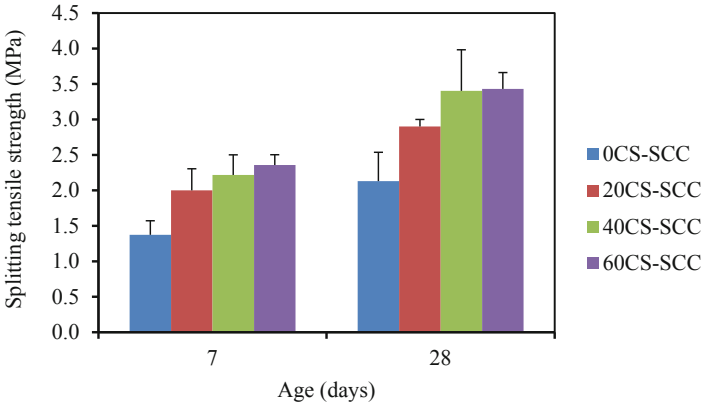

Fig. 4. Splitting tensile strength of SCC mixes at 7 and 28-days curing.

3.4 Rapid Chloride Permeability Test

Table 5 gives the values of SCC mixes with and without copper slag at 28 days curing age. As per ASTM C 1202 [16], rapid chloride permeability values are ranged from very low permeability (100–1000) to low (1000–2000), moderately (2000–4000) and high permeability (more than 4000) range. In the present study, all values were found between 800 coulombs - 1800 coulombs; thus showing very low to low range of chloride permeability. The charge decreased up to 20% copper slag replacement. However, it increased for SCC mixes incorporating 40% and 60% copper slag. The results were similar to that of the research findings of [21]. RCPT values decreased for concrete mixes from 0% to 30% copper slag substitution and then increased up to 60% copper slag replacement. From the research findings of [22], it was inferred that the effect of copper slag on RCPT are higher at later ages like 90 days curing period.

Table 5. RCPT values of SCC mix at 28 days curing age.

Design mix	Chloride permeability values (Coulombs)
0CS-SCC	1269
20CS-SCC	876
40CS-SCC	1729
60CS-SCC	1229

4 Conclusions

The utilization of copper slag as partial replacement of sand provides environmental as well as technical benefits. Copper slag is excluded from the hazardous waste lists of the United States Environmental Protection Agency as well as the United Nations (UN) Basel Convention on the Transboundary Movement of Hazardous Waste and its Disposal [23]. Improvement in compressive strength up to 20% replacement and splitting tensile strength up to 60% replacement in SCC mixes incorporating copper slag confirmed its successful utilization in concrete technology. Copper slag helped in reducing the pores of concrete matrix. Chloride migration property of SCC mixes enhanced with the addition of copper slag.

References

1. Gorai B, Jana RK, Premchand (2003) Characteristics and utilisation of copper slag-review. Resour Conserv Recycl 39(4):299–313
2. Al-Jabri KS, Al-Saidy AH, Taha R (2011) Effect of copper slag as a fine aggregate on the properties of cement mortars and concrete. Constr Build Mater 25(2):933–938
3. Dos Anjos MAG, Sales ATC, Andrade N (2017) Blasted copper slag as fine aggregate in Portland cement concrete. J Environ Manage 196:607–613

4. Ayano T, Sakata K (2000) Durability of concrete with copper slag fine aggregate. ACI Spec Publ 192:141–158
5. Madheswaran CK, Ambily PS, Dattatreya JK, Rajamane NP (2014) Studies on use of copper slag as replacement material for river sand in building constructions. J Inst Eng (India): Ser A 95(3):169–177
6. Mavroulidou M (2017) Mechanical properties and durability of concrete with water cooled copper slag aggregate. Waste Biomass Valor 8(5):1841–1854
7. Al-Jabri KS, Hisada M, Al-Oraimi SK, Al-Saidy AH (2009) Copper slag as sand replacement for high performance concrete. Cem Concr Comp 31(7):483–488
8. Wu W, Zhang W, Ma G (2010) Optimum content of copper slag as a fine aggregate in high strength concrete. Mater Des 31(6):2878–2883
9. Sharma R, Khan RA (2017) Fresh and mechanical properties of self compacting concrete containing copper slag as fine aggregates. J Mater Eng Struct 4(1):25–36
10. EFNARC (2005) The European Guidelines for Self-Compacting Concrete
11. Indian Standard (2013) IS 8112, Ordinary Portland Cement 43 grade -specification, New Delhi, India
12. Indian Standard (1971) IS 383, Specification for coarse and fine aggregates from natural sources for concrete, New Delhi, India
13. ASTM (American Society for Testing and Materials) (2005) ASTM C 618, Standard Specification for Coal Fly Ash and Raw or Calcined Natural Pozzolan for Use in Concrete
14. Indian Standard (1959) IS 516, Methods of test for strength of concrete, New Delhi, India
15. Indian Standard (1999) IS 5816, Splitting tensile strength of concrete - method of test, New Delhi, India
16. ASTM (American Society for Testing and Materials) (2011) ASTM C1202-10, Standard Test Method for Electrical Indication of Concrete's Ability to Resist Chloride Ion Penetration
17. Obe RKD, de Brito J, Mangabhai R, Lye CQ (2017) Use of copper slag as concrete sand, sustainable construction materials: copper slag. Woodhead Publishing, Sawston, pp 87–163
18. Gesoglu M, Guneyisi E, Ozbay E (2009) Properties of self-compacting concretes made with binary, ternary, and quaternary cementitious blends of fly ash, blast furnace slag, and silica fume. Constr Build Mater 23(5):1847–1854
19. Shoya M, Nagataki S, Tomosawa F, Sugita S, Tsukinaga Y (1997) Freezing and thawing resistance of concrete with excessive bleeding and its improvement. ACI Spec Publ 170:879–898
20. Hwang CL, Laiw JC (1989) Properties of concrete using copper slag as a substitute for fine aggregate. ACI Spec Publ 114:1677–1696
21. Thomas BS, Damare A, Gupta RC (2013) Strength and durability characteristics of copper tailing concrete. Constr Build Mater 48:894–900
22. Najimi M, Pourkhorshidi AR (2011) Properties of concrete containing copper slag waste. Mag Concr Res 63(8):605–615
23. de Brito J, Saikia N (2013) Construction and demolition waste aggregates, recycled aggregate in concrete. Springer, London, pp 81–113

Characterization of Non-proprietary UHPC for Use in Rehabilitation/Strengthening Applications

Ana Mafalda Matos[1(✉)], Sandra Nunes[1], Carla Costa[2], and José L. Barroso-Aguiar[3]

[1] CONSTRUCT-LABEST, Faculty of Engineering, University of Porto, Porto, Portugal
ana.matos@fe.up.pt
[2] High Institute of Engineering of Lisbon (ISEL), Lisbon Polytechnic Institute, Lisbon, Portugal
[3] School of Engineering, University of Minho, Guimarães, Portugal

Abstract. UHPFRC has become one of the most promising cement-based materials for the next generation of infrastructures because of its good workability, outstanding mechanical properties, and excellent durability. A promising field of application is the rehabilitation and/or strengthening of existing reinforced concrete structures, in which a new layer of UHPFRC replaces the deteriorated concrete (cracked, carbonated, chloride attack, etc.). The combination of the UHPFRC as protective layer, which can be reinforced, provides a simple and efficient way of increasing the durability (extending the service life), the stiffness and structural resistance capacity while keeping compact cross sections. A study was carried out to test a non-proprietary UHPC mix containing equilibrium catalyst to determine whether this new mix is a viable option for rehabilitation/strengthening applications. Several mechanical properties and durability were assessed, such as early age E-modulus development and autogenous shrinkage, compressive strength evolution in time, uniaxial tensile strength, water absorption by capillarity, chloride ion penetration, alkali-silica reactivity and sulphates attack resistance. Test results show that new UHPC developed present equivalent performance to other UHPCs cured under normal curing conditions.

Keywords: UHPFRC · Early age E-modulus · Autogenous shrinkage · Uniaxial tensile strength · Durability

1 Introduction

Ultra-High Performance Fibre Reinforced Composites (UHPFRC) refer to the family of composite materials containing a large amount of short steel fibres evenly embedded in an ultra-compact cementitious matrix (hereafter, UHPC) with a high content of the binding phase including cement and supplementary cementitious materials (SCMs) and a very low water to binder ratio (w/b < 0.2). The main principles for UHPFRC design are reduction in porosity, improvement in microstructure, enhancement in homogeneity

V. Mechtcherine et al. (Eds.): RheoCon 2019/SCC 2019, RILEM Bookseries 23, pp. 552–559, 2020.
https://doi.org/10.1007/978-3-030-22566-7_64

and increase in toughness. The raw materials, the curing regimes and the fibres content are the main factors that control the mechanical properties and durability of UHPFRC [1]. The raw materials of UHPFRC include a cementitious component (typically, cement and silica fume), fine inert fillers, quartz sand ($d_{max} < 1$ mm), superplasticizer, and fibres. It has been shown that granulated blast furnace slag, fly ash, metakaolin, limestone powder, rice husk ash can be used to replace silica fume in UHPC [2]. Fibres used in UHPFRC are often high-strength micro steel fibres with length of 13 mm and diameter of 0.2 mm. Considering the high cost and complexity of curing processes, such as heat curing and autoclave curing, use of conventional materials and common technology, such as conventional casting and room temperature curing has been preferred by several authors in order to facilitate the production and applications of UHPFRC.

Most current applications of UHPFRC in new structures are accomplished by factory pre-fabrication and on-site assembling, such as very slender and lightweight elements for pedestrian footbridges and highway bridges, and architecturally and aesthetically appealing structures. On-site fabrication of UHPFRC is mainly limited to rehabilitation and strengthening purposes. The main advantage of UHPFRC in this context is that it can play a double function (water tightness and strengthening) while enabling short-time interventions. Although UHPFRC is being utilized in several applications around the world, it still faces some challenges for wider implementation. A PhD research programme is currently underway at the Faculty of Engineering, Porto University, Portugal (FEUP), aiming to address some of those challenges, namely:

1. To develop a rational and accurate method for the mixture design and optimization of UHPC
2. To use locally available supplementary cementitious materials (including industrial residues) for partial replacement of cement and silica fume, in order to reduce the materials cost of UHPC, while achieving a minimum compressive strength of 150 MPa after normal curing regime
3. To mitigate autogenous shrinkage of UHPC to minimize early ages cracking risk (which might impair its durability), particularly when the deformations are restrained as is the case in rehabilitation/strengthening applications.

2 Experimental Programme

2.1 Materials Characterization and Mixture Proportions

The cement used in this study is ordinary Portland cement (CEM I 42.5 R), in accordance with the standard EN 197-1. Silica fume (SiO_2 content > 90v%) with a specific surface area of 19632 m^2/kg (BET method) and limestone filler (98v% $CaCO_3$) having a specific surface of 550 m^2/kg (Blaine method) were used to increase the compactness of the matrix. The aggregate phase consisted of a mixture of siliceous natural sand (1 mm maximum size) and a spent equilibrium catalyst, generated by Sines Refinery, Portugal (ECat). Chemically, the ECat is essentially an aluminosilicate which main active phase is Y-zeolite, a crystalline aluminosilicate with a structure

consisting of tunnels and cages that leads to a high (internal and external) surface specific area. Due to its aluminosilicate chemical composition, ECat has a potential pozzolanic activity; hence, is likely to be used as a cement-based material additive. Results of modified Chapelle test method (according to French standard NF P18-513) reveal that 1540 mg and 1577 mg of $Ca(OH)_2$ are consumed per g of ECat and per g of SF, respectively, suggesting that both materials have high pozzolanic activity. Moreover, the high specific surface of the ECat (150070 m^2/Kg, BET method) with water affinity promotes significant water absorption (about 30%, by mass). Thus, this residue is used in the current work as an internal curing agent in UHPFRC. A polycarboxylate-based superplasticizer (SP) was also used, with a solid content of 40%. High strength short steel fibres with 0.2 mm in diameter and 13 mm in length (l_f/d_f = 65) were used as reinforcement. The tensile strength and modulus of elasticity of the fibres are 2750 MPa and 200 GPa, respectively.

The design of experiments (DOE) approach (combining statistical and mathematical methods of experiment design, regression analysis and optimisation techniques) was employed to reduce the effort necessary to achieve the target engineering properties of the UHPC, namely, self-compatibility, low autogenous shrinkage, improved durability and high mechanical performance, as described in [3]. Figure 1(a) shows the volumetric composition of the optimized UHPC mixture which is going to be characterized in the current study. Steel fibres were added to UHPC in volume fraction of 3% to manufacture a UHPFRC mixture, by replacing an equivalent volume of aggregates.

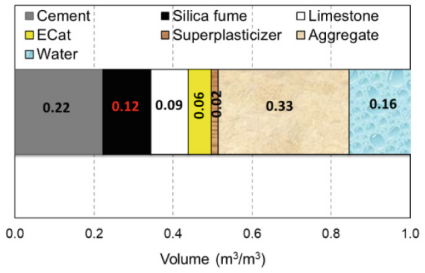

a)

Step	Task	Duration
1)	add ECat + water1 and mix	5 min
2)	add sand +powder materials and mix	2.5min+*+2.5min
3)	add water2 +75 % superpl. and mix	2.5 min
4)	add 25 % superpl. and mix	3.5min

water1= (80% mixing water + water for Ecat absorption);water 2=20% mixing water; (*) stoppage to scrape material adhering to the mixing bowl; mixing at low speed (140 ± 5 rotations·min^{-1})

b)

Fig. 1. (a) Mixture proportions of non-proprietary UHPC tested, in terms of volume; (b) Mixing sequence.

2.2 Test Methods

The UHPC mixture was produced according to the mixing procedure described in Fig. 1(b), using a mixer in accordance with the standard EN 196-1. The UHPFRC mixture preparation followed the same mixing procedure, except for the fibres incorporation during 2 min before the end of the mixing process.

Immediately after mixing, the slump-flow diameter was measured using a truncated cone (ϕ_{upper} = 70 mm; ϕ_{lower} = 100 mm; h = 60 mm), without any compaction

energy. The autogenous shrinkage of UHPC mixture was measured based on the ASTM C1698, using sealed corrugated tubes of 440 mm length and 28.5 mm average diameter. After filling the tubes, each specimen was measured, weighted and kept inside a chamber with controlled temperature (23 °C ± 1 °C). Shrinkage deformations were recorded continuously using linear variable differential transformers (LVDTs) and a data Taker DT500 acquisition system, up to 7 days. The final setting time, determined according to the standard EN 196-3, was considered as "time-zero" for the autogenous shrinkage evaluation. The Elasticity Modulus Measurement based on Ambient Response Method (EMM-ARM) [4] was used to continuously monitor the E-modulus evolution of UHPC since casting. The EMM-ARM is based on the identification of the resonant frequency of the testing mould (plastic hollow cylinder in simply supported conditions, filled with the sample to be tested immediately after mixing), which evolves along time due to the progress of hydration reactions. By monitoring the accelerations of the composite beam at mid-span, it is possible to perform the modal identification and to evaluate the first flexural resonance frequency of the beam. The E-modulus of the UHPC mixture could be inferred with basis on the dynamic equations of motion of the testing system [4].

Cubic specimens (50 mm) were produced to assess the compressive strength evolution up to 90 days. Specimens were kept under water in a chamber under controlled temperature (20 °C ± 2 °C) until testing age. The uniaxial tensile test (UTT) was carried out using six dog bone-shaped UHPFRC specimens, with a tested section length of 92 mm and cross section of 30 mm × 40 mm, after 28 curing days in a controlled environment room (temperature = 20 °C ± 2 °C and HR > 95%). Specimens were tested at a constant displacement rate of 0.003 mm/s. The elongation of the specimens was measured using four LVDT's system coupled along the tested section length of the specimen.

Concerning the durability, several tests were carried out on sound UHPC specimens to assess its resistance to the penetration of aggressive agents, as well as, the proneness to expansive reactions. The corresponding experimental plan is detailed in Table 1. Accelerated carbonation tests are also underway, but no carbonation front was detected in the specimens until the current date (9 months).

3 Results and Discussion

3.1 Flowability and Early Ages Properties

Both UHPC and UHPFRC mixtures exhibited high viscosity and good deformability with final spread diameters of 312.0 mm and 282.5 mm, respectively. Taking in consideration, the low water to binder ratio and high binder content in UHPC one would anticipate a large early autogenous shrinkage. In fact, the most typical UHPC mixtures (cement + large amounts of SF) reach values as high as 1119 μm/m at 7 days ("Previous UHPC" in Fig. 2(a)) [5]. Figure 2(a) shows that the UHPC mixture under study ("New UHPC") exhibits significantly less autogenous shrinkage (about 700 μm/mm at 7 days) attributed to the significant amount of water absorbed by ECat. The amount of extra water absorbed by ECat in the current mixture was 46.6 L/m^3, which is similar to

the water absorption capacity of superabsorbent polymers or lightweight aggregates often used for internal curing in UHPC [3]. The temperature increase inside the thin autogenous shrinkage test samples was very small (1 °C to 2 °C), thus no temperature correction was included.

Young Modulus evolution curve presented in Fig. 2(b) shows an initial dormant period, with duration close to 3 h, after which a strong evolution of the E-modulus was observed up to about 9 h, after the end of mixing. After this stage, a dramatic reduction in the slope of Young Modulus evolution occurs, and a Young modulus of about 36 GPa was achieved after 7 days. In the same figure, the E-modulus evolution of a conventional mortar (w/c = 0.40) is also plotted, showing a dormant period significantly longer and a rate of E-modulus evolution clearly slower. The addition of fibres in UHPFRC did not significantly influence its elastic modulus, but further reduces the autogenous shrinkage due to the locally shrinkage-restraining effect of fibres [3]. Both autogenous shrinkage and Young's modulus evolution will influence the development of self-induced stresses in the presence of external restraint, which will determine the risk of cracking at early ages.

Table 1. Durability testing plan carried out on sound UHPC specimens.

Durability indicator	Test standard/ technique	Testing age	Number of specimens	Specimens geometry
Total porosity and pore size distribution	MIP Poremaster-60 equipment	28, 90 days	2	Cylinder h = 30 mm, Ø = 9 mm
Water permeable porosity	Vacuum saturation approach	28 days	6	Cylinders h = 30 mm, Ø = 50 mm
Water absorption by capillarity	RILEM TC 116-PCD	28 days (+14 days at 40 °C, until constant mass)	5	Prisms 40 × 40 × 45 mm^3
Resistance to chlorides penetration	NT Build 492	28 days	6	Cylinders h = 50 mm, Ø = 100 mm
Resistance to sulphate attack	Portuguese specification E-462	–	6	Prisms 20 × 20 × 160 mm^3
Risk of alkali-silica reaction	ASTM C 1260	28 days*	3	Prisms 25 × 25 × 285 mm^3

(*) Specimens were subjected to heat curing according to the procedure proposed in ASTM C1260.

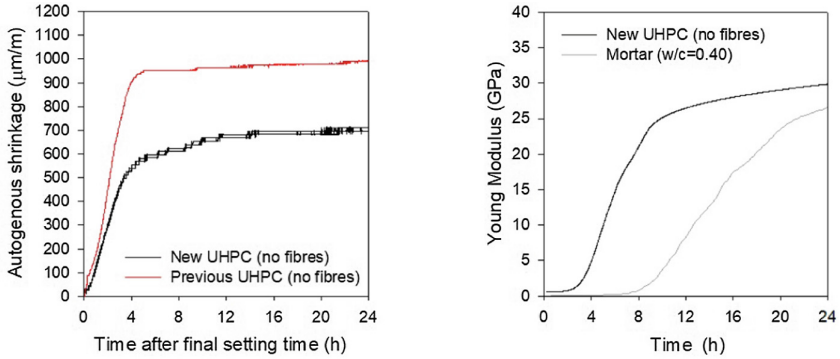

Fig. 2. (a) Autogenous shrinkage and (b) E-modulus evolution of UHPC up to 24 h.

3.2 Mechanical Performance

Figure 3(a) shows the increase in compressive strength of the UHPFRC mixture under study, up to 90 days. Compressive strengths of 147 MPa and 156 MPa were achieved, respectively, after 28 days and 90 days, without special curing conditions. Concerning the tensile behaviour, Fig. 3(b) shows that the UHPFRC exhibited a uniaxial tensile peak stress and a peak strain ranging from 11 MPa to 15 MPa and 0.27% to 0.47%, respectively, at 28 days, which compare well with results reported in the literature for UHPFRCs with other cementitious matrixes and same fibre content [6]. A significant tensile-hardening branch was observed in most specimens, particularly, for the specimens with more favourable fibres orientation.

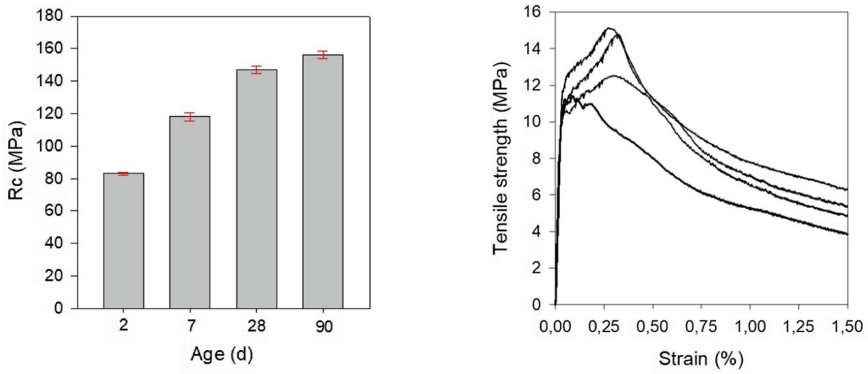

Fig. 3. (a) Compressive strength of the UHPFRC mixture at different ages and (b) UTT curves at 28 days of replicate UHPFRC specimens.

3.3 Durability Indicators

Whereas typical UHPFRCs (incorporating cement + large amounts of SF) are cured thermally, the UHPC under study was not and, therefore, it was expected to be more porous. The average water permeable porosity of UHPC was 14% and total porosity assessed by MIP was 4.8%, after 28 days of wet curing. Figure 4(a) shows only a small percentage of the total porosity corresponds to capillary pores (0.01 μm–1 μm). A further reduction in pore sizes and capillarity porosity was observed after 90 days of curing, which can be attributed to the pozzolanic effect of SF and ECat. The average water sorptivity coefficient of UHPC was 0.014 mg/(mm^{2}min$^{-1/2}$), which is approximately 6 times lower compared to that of good quality conventional concrete (w/c = 0.40). Likewise, UHPC showed low chloride diffusion coefficient of 1.99 × 10^{-12} m^2/s, on average. Figure 4(b) shows the expansion of the small UHPC prisms during ASR testing. The average expansion value measured of 0.0180%, after 14 days of testing, is much lower than the limit of 0.10% as prescribed in the ASTM C1260-94 standard. Thus, it seems there is no risk of physical damage due to the deleterious expansion associated to the ASR occurrence. The UHPC prisms of 20 mm × 20 mm × 160 mm were immersed in a sodium sulphate solution (Na_2SO_4, 16 g SO_4^{2-} per litre) and the length variation was regularly measured. The results indicate no significant expansion (0.002%) or visual deterioration, even after 26 weeks of immersion.

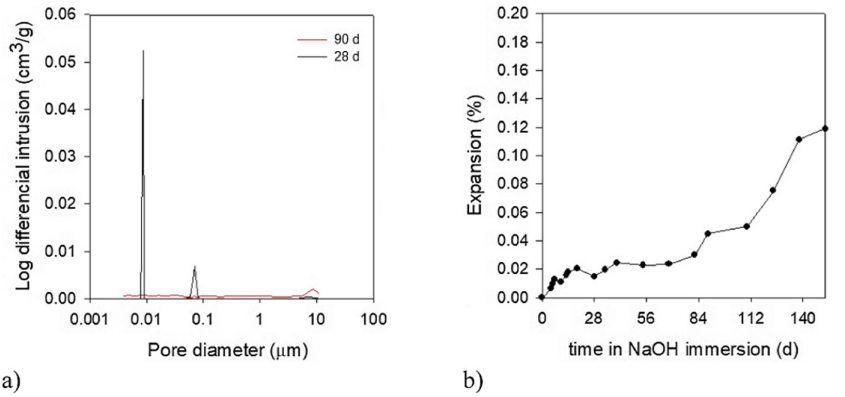

Fig. 4. (a) MIP curves of the UHPC after 28 and 90 days of water curing at 20 °C; (b) Change in the specimens' length due to the occurrence of ASR in the UHPC.

4 Conclusions

The current work investigated the performance of a non-proprietary UHPC mixture based on rational selection and proportioning of raw materials and using normal curing conditions. The incorporation of ECat, and the corresponding extra water that the ECat is able to absorb, lead to a significant reduction of the autogenous shrinkage of UHPC, while maintaining excellent workability in the fresh state. The high strength and

durability of typical UHPFRCs are highly dependent on thermal treatment. Despite being cured at 20 °C in a wet chamber, the investigated UHPFRC achieved a compressive strength of 147 and 156 MPa after 28 and 90 days, respectively; and exhibited a tensile strain-hardening behaviour with multiple micro-cracking formation. MIP testing and water sorptivity coefficient results showed that the primary reason for UHPC enhanced durability is its highly dense matrix phase, caused by a very low water to binder ratio and by the presence of very active pozzolans (silica fume and ECat) that gave rise to a very low capillary porosity. Accelerated testing also revealed that the studied UHPC presents a very good performance in terms of resistance to expansive reactions, namely, alkali-silica and external sulphates attack.

Acknowledgements. This work was financially supported by: UID/ECI/04708/2019- CONSTRUCT funded by national funds through the FCT/MCTES (PIDDAC); the project POCI-01-0145-FEDER-031777– UHPGRADE funded by FEDER funds through COMPETE2020 - Programa Operacional Competitividade e Internacionalização (POCI) and by national funds (PIDDAC) through FCT/MCTES; and by FCT PhD scholarship PD/BD/113636/2015-Doctoral Program EcoCoRe. Collaboration and materials supply by Sines Refinery/Galp Energia, Secil, Omya Comital, Sika, Bekaert and Euromodal is gratefully acknowledged.

References

1. Wang D, Shi C, Wu Z, Xiao J, Huang Z, Fang Z (2015) A review on ultra high performance concrete: part II. Hydration, microstructure and properties. Constr Build Mater 96:368–377
2. Shi C, Wu Z, Xiao J, Wang D, Huang Z, Fang Z (2015) A review on ultra high performance concrete: part I. Raw materials and mixture design. Constr Build Mater 101:741–751
3. Matos MA, Nunes S, Costa C, Aguiar José Luís B (2019) Spent equilibrium catalyst as internal curing agent in UHPFRC. Cem Concr Compos 104:103362
4. Granja J, Azenha M (2017) Towards a robust and versatile method for monitoring E-modulus of concrete since casting: enhancements and extensions of EMM-ARM. Strain 53:e12232
5. Mafalda Matos A, Nunes S, Costa C (2016) Mitigation of early age shrinkage of UHPFRC by using spent equilibrium catalyst. In: International RILEM conference materials, systems and structures in civil engineering 2016 segment on service life of cement-based materials and structures
6. Abrishambaf A, Pimentel M, Nunes S (2017) Influence of fibre orientation on the tensile behaviour of ultra-high performance fibre reinforced cementitious composites. Cem Concr Res 97:28–40

The Applicability of Reclaimed Concrete Granulate to SCC

Maciej Urban(✉) and Małgorzata Lenart

Faculty of Civil Engineering, Chair of Building Materials Engineering,
Cracow University of Technology,
ul. Warszawska 24 st., 31-155 Cracow, Poland
{maurban, mlenart}@pk.edu.pl

Abstract. Reclaimed aggregate granulate production is one of the most promising methods of utilization of unused fresh concrete. Its main advantage, as compared to other technologies, is the 100% reusability of the base material. Here, 2-component admixture technology was chosen. According to its producer, its usability is restricted to an S4 consistence maximum. The authors' intention was to perform a preliminary investigation to check whether it is possible to broaden this limit to SCC. It is an important task, as, time to time, it occurs that a delivery of SCC has to be rejected on-site. During this study fresh SCC was tested as well as compressive strength development (up to 90 days) and splitting tensile strength was checked after 28 days of hardening. Two SCC compositions were tested: one similar to low-cement content Eco-SCC and the second, similar to a typical binder-rich SCC. The granulate composition was obtained by thinning SCC of intermediate composition with dry aggregate to the level which enables the maintenance of an original aggregate grading curve after granulate hardening. Next, for simplicity, the granulate for the main research programme was produced from traditional concrete of S1 consistence, based on the same aggregate composition as SCC and the same paste content as in the thinned SCC. Two moisture content levels were tested: natural and wetted to the maximum water absorbability level of the coarse granulate. The results showed that it was possible to obtain well-workable SCC containing up to 15%–30% replacement by the natural state granulate, and up to 45% replacement using the wetted one. All granulate containing SCCs had the strength development not worsened in comparison to the base compositions.

Keywords: Self-compacting concrete · Sustainable development · Reclaimed concrete granulate · Not-used concrete recycling · Fresh concrete recycling

1 Introduction

The idea of sustainable development is not only developed for environment protection aiming to preserve for future generations as many goods as are necessary to develop our civilisation [1, 2]. It is a legal requirement and is defined in the EU 305/2011 Regulation [3]. The Seventh Basic Requirement for Building Objects refers to the sustainable utilization of natural resources. It is the foundation of many research

V. Mechtcherine et al. (Eds.): RheoCon 2019/SCC 2019, RILEM Bookseries 23, pp. 560–567, 2020.
https://doi.org/10.1007/978-3-030-22566-7_65

programmes aiming to enable the utilization of building industry demolition waste in new concrete, e.g. [4, 5]. The same applies to reclaimed aggregate, i.e. aggregate obtained from unused concrete [6]. The EN 206 standard permits the use of only the aggregate reclaimed by washing or crushing. The aggregate obtained from fresh concrete residues (left due to any reason after concreting) by its granulation (and consecutive crushing after hardening) also fulfils this requirement. The main advantage of this technology is the 100% reuse of base material, in contrast to the washing method where only approx. 80% of base material is reusable (i.e. aggregate and a part of water). Unfortunately, the usability of admixtures applied to granulate concrete is typically limited to S4 consistence (acc. to EN 206). Then, it is an open question if this technology can be also applied (probably with some restrictions) to self-compacting concrete (SCC) or, in this case, the washing technology is the only solution. The main problematic factors in SCC case (compared to traditional concrete) include: much higher paste, superplasticizer and water contents (see e.g. [7]). The answer to this question was laid as the basis for the preliminary research programme reported here.

2 Research Programme

The granulate was produced by 2 dedicated admixtures set technology: polymeric superabsorbent (typical dosage: 1 kg/m^3) and a setting accelerator based on calcium aluminate hydrate and sodium silicate (typical dosage: 6 kg/m^3).

Two SCC base compositions were assumed: one similar to low-cement content Eco-SCC (i.e. binder content around 300 kg/m^3, see e.g. [8]), and the second, similar to typical binder-rich SCC (i.e. of c.a. 550 kg/m^3 of binder, see e.g. [7, 9]). The granulate was obtained by the thinning SCC of intermediate composition with dry natural aggregate to the level which enables the maintenance of the original aggregate grading curve after granulate hardening. Next, for simplicity, the granulate for the main research programme was produced from traditional concrete of S1 consistence, based on the same aggregate composition as in all types of SCC and the same paste content as in the thinned SCC. It was composed of pure cement to avoid obtaining a too low cement content.

It was assumed that, for the granulate properties stability reasons, a mature material was to be used. That is why, it was tested after 1 day, 7 days and 14 days of hardening/drying in the laboratory (c.a. 20 °C, 45% RH). 14 day-old granulate was chosen for the main research programme. The programme was performed by partial natural aggregate replacement using both natural-wet and pre-wetted granulate (details: see Sect. 4.2). Consistency drop caused by higher water demand and higher water absorbability of granulate was corrected by superplasticizer. The maximum natural aggregate replacement level was assessed by the possibility of obtaining the assumed consistence range. All the series were tested after 7 days, 28 days, and 90 days of water curing at 20 °C. Compressive strength testing (all ages) and splitting tensile testing (after 28 days only) were performed.

3 Materials

Natural rounded aggregate (NRA) of Carpathian flysch origin from a single source (a river bed) was used. It was delivered divided into four groups of fractions (0 mm–0.5 mm, 0.125 mm–2 mm, 2 mm–8 mm and 8 mm–16 mm). Aggregate composition was obtained by void content in a loose state minimisation, according to the procedure described in [9]. The final aggregate grading curve is shown in Fig. 1. Paste was composed following the unique method described in detail in [9], using cement type CEM II/B-S 32.5R (f_{cm} = 47.5 MPa), commercial limestone powder dedicated to SCC (Lhoist Poland) and polycarboxyether type superplasticizer.

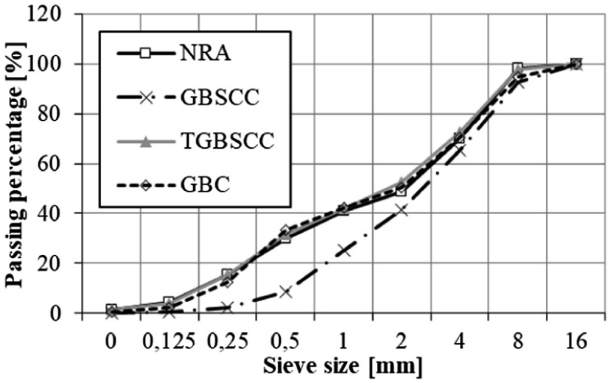

Fig. 1. Grading curves of natural rounded aggregate (NRA) and granulates obtained from: SCC mix (GBSCC), thinned SCC mix (TGBSCC) and equivalent traditional concrete (GBC).

4 Testing Methods, Procedures and Results

4.1 Fresh SCC

Self-compactibility of concrete mixes was assessed according to European standards (EN-206 and EN-12350 parts 8-11). Slump flow D_0 [mm] and t_{500} [s], V-funnel t_V and flow ability in L-box (PL2 class) were tested. It was assumed that all types of base SCCs have to fulfil SF2, VF2, PL2 requirements. For granulate SCCs PL2 this requirement was not checked to simplify the procedure, as it was decided not to include a consistence loss test in the reported research stage. That is why, forming was performed just after finishing the fresh concrete properties check, i.e. approx. 20 min–30 min after the start of mixing.

4.2 Base SCC and Granulate Mixes

Compositions of all base mixes are listed in Table 1. GBSCC was thinned by an additional portion of NRA (50%) resulting in the obtaining of traditional concrete (V_{paste} = 260 [dm^3/m^3], VeBe time 5 s), referred to hereafter as TGBSCC. Next,

granulate base concrete (GBC) was prepared maintaining w/c and V_{paste} on the established levels, but with a higher superplasticizer content to obtain better workability.

4.3 Granulate

Granulate was prepared from 3 mixes: GBSCC, TGBSCC and GBC. It was produced according to the producer's requirements, i.e. superabsorbent added first (1 kg/m^3) plus 2 min–3 min of mixing (in a counter-current mixer) followed by a hardening accelerator addition (6 kg/m^3) plus an additional 2 min–3 min of mixing. Granulates were poured in laboratory onto foil to a depth of 5 cm–10 cm thickness and left for approximately 24 h to harden (dry). After this period the layer was crushed with a shovel and put into an open container. All granulates were compared by sieve analysis acc. to EN 933-1 after 24 h of hardening, see Fig. 1. TGBSCC and GBC granulates curves are almost 100% coincident and very close to NRA. Consequently, GBC granulate was chosen for the main research programme.

Table 1. Compositions of base mixes and their properties in the fresh state.

Component/Proportion/Test	ECO-SCC (ESCC)	Granulate base SCC (GBSCC)	Binder-rich SCC (BRSCC)	Granulate base concrete (GBC)
Cement [kg/m^3]	300	365	450	308
Limestone powder [kg/m^3]	180	215	135	-
Water [kg/m^3]	180	182.5	175	154
Aggregate [kg/m^3]	1700	1590	1615	1960
Superplasticizer [kg/m^3]	3.00	5.10	5.60	3.85
V_{paste} [dm^3/m^3]	350	389	380	260
w/c [−]	0.60	0.50	0.39	0.5
w/b [−]	0.38	0.32	0.30	-
sp = %b [−]	0.625	0.90	0.95	1.25
Slump flow D_0 [mm]	670	750	740	30*
t_{500} [s]	3.75	4.0	6.7	-
V-funnel t_v [s]	10.2	10	19	-
L-box PL2 class [%]	82	92	80	-

*Slump [mm]

Next, for the chosen granulate water content (acc. to EN 1097-5) after 24 h and 14 days of hardening, as well as 24 h water absorption and density (acc. to EN 1097-6) after 7 days and 14 days of hardening (on fractions 0,063/4 mm and 4/31,5 mm separately) were assessed. These results are shown in Table 2. They indicate that 14 day-old granulate can be treated as a mature one. Consequently, in the main programme 14–17 day-old granulate was used. Due to the important water absorbability rise of granulate in comparison to NRA it was decided to use both dry (D) and

pre-wetted (W) granulate. The wetted state was assumed to be equal to WA_{24} value for 4/16 fraction. Pre-wetting was performed 24 h before use. As the density difference between NRA and granulate was relatively small, it was decided to calculate the replacement level by oven-dried (105 °C) granulate mass.

Table 2. Comparison of particle density and water content of GBC granulate and NRA.

Grain sizes [mm]	GBC granulate		Natural rounded aggregate		
	0.063/4	4/16	0/2	2/8	8/16
Particle density [Mg/m^3]	2.63	2.60	2.66	2.64	2.63
Water absorption WA_{24} [%] (7/14 days)	11.1/10.7	6.1/6.1	0.6	3.0	2.0
Water content [%] (1/14 days)	11.5/2.5		n.a.		

4.4 Fresh Granulate SCC

To simplify the mixing procedure (in 25 dm^3 laboratory counter-current mixer), all dry constituents were premixed first, followed by the addition of all fluid constituents in one move. The first important observation was that the mixing process had to last much longer (at least 5 min) in comparison to the base SCC (approx. 2 min). At the very beginning the concrete mix consistency was low, but after 3–4 min of mixing, the fluidity rose to the expected level. This suggests that at the beginning of mixing the granulate acts like a porous lightweight aggregate consuming a significant amount of paste but after a prolonged intense mixing smaller grains (sticking previously to the coarser one) tend to be abraded and the paste is released. Both "W" and "D" series behaved in the same way suggesting that superabsorbent particles tend to absorb water very quickly, without causing the delayed workability loss. The test results are shown in Table 3.

Table 3. Compositions and strength test results of granulate containing SCCs.

Mix symbol	sp [%]b	D_0 [mm]	t_{500} [s]	t_V [s]	f_{cm}^7 [MPa]	f_{cm}^{28} [MPa]	f_{cm}^{90} [MPa]	$f_{ct\ sp}$ [MPa]
ESCC-0	0.625	670	3.75	10.2	26.0*	39.3*	48.2*	3.7
ESCC-5W	0.65	670	5.2	15.5	31.6	47.5	56.7	3.7
ESCC-5D	0.75	690	4.5	14	30.1	45.6	50.5	3.65
ESCC-15W	0.7	660	5.2	23	32.6	47.9	55.7	3.5
ESCC-15D	0.825	690	5.2	13	32.6	48.1	58.8	3.5
ESCC-30W	0.75	700	3.9	12	29.4	44.5	53.4	3.5
ESCC-30D	0.9	670	6.2	18	29.1	43.9	54.8	4.1
ESCC-45W	0.75	650	5.6	20.5	30.3	42.9	55.7	3.65
BRSCC-0	0.95	740	6.7	19	52.8*	71.2*	75.8*	4.55
BRSCC-5W	1.0	700	7.7	27.5	56.1	70.2	83.0	5.25
BRSCC-5D**	1.1	840	4.5	19	–	–	–	–
BRSCC-5D	1.05	760	8.4	24	55.1	68.3	78.1	4.4
BRSCC-15W	1.05	700	11.2	28.5	53.7	64.7	79.3	4.9

(*continued*)

Table 3. (*continued*)

Mix symbol	sp [%]b	D_0 [mm]	t_{500} [s]	t_V [s]	f_{cm}^{7} [MPa]	f_{cm}^{28} [MPa]	f_{cm}^{90} [MPa]	$f_{ct\ sp}$ [MPa]
BRSCC-15D	1.1	700	9.0	25	54.0	68.3	84.1	5.3
BRSCC-30W	1.1	750	5.9	17.5	52.6	56.3	69.0	5.2
BRSCC-45W	1.1	705	9.0	23.5	49.7	60.7	71.3	4.2

*Doubled number of tested specimen
**Not formed due to too high fluidity

Notations of mixes contain the base mix abbreviation plus (after the dash) the percentage of NRA replacement by the granulate and the method of granulate preparation. For instance, notation ESCC-15W means that 15% of pre-wetted granulate and 85% of NRA (by mass) in ECO-SCC was used. The top granulate addition level was limited by the possibility of obtaining the assumed consistency range. In all cases, increased sp dose either did not allow the maintenance of $t_V < 25$ s (dry granulate), or caused serious sedimentation recorded as V-funnel blocking (the wet one). It must be mentioned that all the mixes were very sensitive to sp content in terms of the consistency range requirement fulfilment (see BRSCC-5D example in Table 3).

4.5 Hardened SCC

The concrete was moulded into 100 mm cubes, stripped after 24 h in a laboratory, and cured to the date of the test in water at 20 °C. A compressive strength test was performed after 7 days, 28 days and 90 days of hardening using 3, 6 and 3 cubes, respectively. In "0" series the sample number was doubled. A splitting tensile strength test was performed on 3 cubes, after 28 days of curing. The results are shown in Table 3, Figs. 2 and 3.

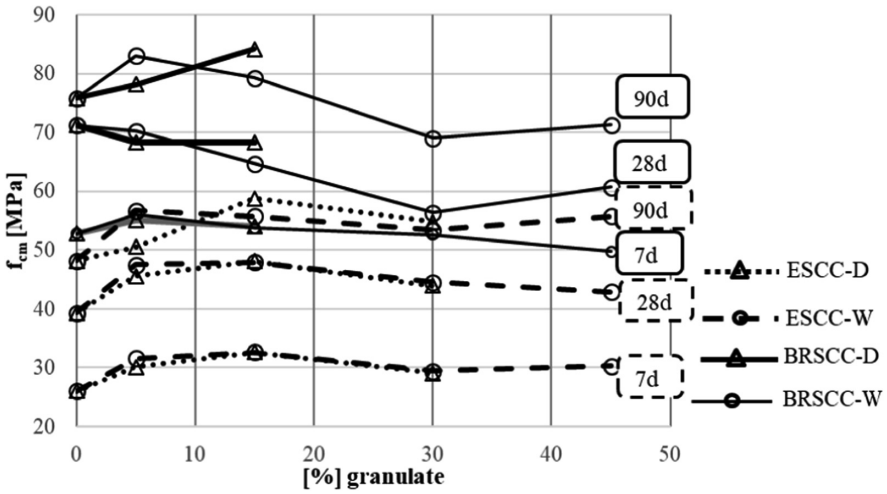

Fig. 2. Compressive strength test results for 7, 28 and 90 day-old specimens.

5 Analysis

The basis observation (Figs. 2 and 3) is the lack of influence (or even a slightly positive influence) of granulate addition level on the concrete strength. Identical results (obtained on mortars) are reported in [6]. Only one case of concrete strength lowering was observed: BRSCC, the top two granulate contents (30% and 45%) (Fig. 2). The most probable cause of this phenomenon is higher w/c ratio of granulate (0.5) than of the base mix (0.39). In the case of ESCC mix, a concrete strength rise was observed for the whole range of granulate replacement levels. The additional proof of this phenomenon is illustrated by "W" and "D" series comparisons (Figs. 2 and 3). There is almost no influence of granulate preparation method, with a slight tendency of a concrete strength rise for "D" series (comparing to the "W" one) for the highest granulate replacement levels. It coincides with the above mentioned observations made during the mixing process: a small grain cover on the coarsest one is sheared during mixing so that it has no influence on the aggregate – paste bond in a hardened composite. Unfortunately, checking this phenomenon by MRI is not possible yet as it is very hard to distinguish between granulate based paste and the SCC one. Thus, the granulate wetting process had a positive effect only on the lowering of the superplasticizer content. Its influence on strength was neutral or slightly negative. It is then possible that at least part of granulate wetting water has to be included in the total water content in the granulate-based mix. However, this needs additional proof.

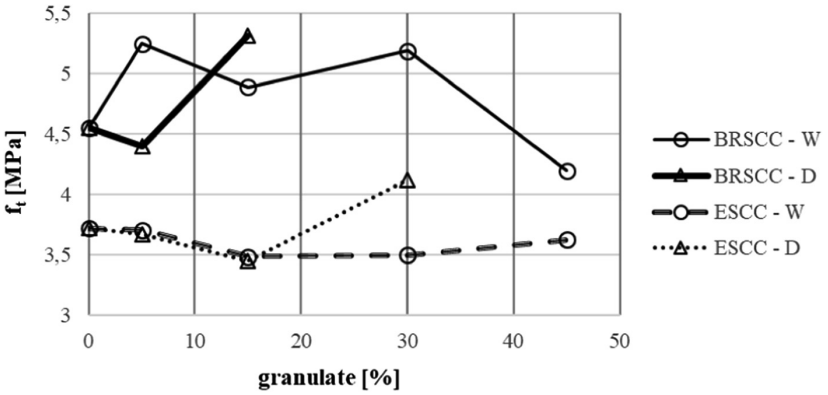

Fig. 3. Splitting tensile strength results (28 days).

Taking the above aspects into consideration, the observed fluctuation of $f_{ct\ sp}$ and f_{cm}^{7} i f_{cm}^{90} for BRCC-5 has to be treated as accidental fluctuation caused by a small number of tested samples. The time-strength development (Fig. 2) is also 100% coincident with the above mentioned observations. There is no any sight of internal curing occurrence (i.e. there is no evidence of strength rise acceleration caused by gradual water release from aggregate pores during the hardening process). Only steeply rising difference between "W" and "D" series was registered.

6 Conclusions

The conducted experiments led to the following conclusions:

(1) A high-quality granulate produced from unused SCC can be obtained by the use of double admixtures approach in a typical way (superabsorbent and setting accelerator set was applied here). The only modification needed is to thin fresh SCC with an additional portion of original aggregate (in a quantity allowing the obtaining of the original aggregate grading curve in the hardened granulate).
(2) The granulate obtained by this method can be used for a new SCC production following two tips:
   - superplasticizer content has to be enhanced to compensate the higher water demand of granulate,
   - the mixing process should be much longer (2–3 times compared to the base mix) to abrade granulate grains (avoiding paste entrapment inside the grains).
(3) The pre-wetting of granulate had a positive effect on superplasticizer content lowering and maximum allowable granulate content enhancement only. The influence of this pre-treatment for concrete strength was negligible (high pre-wetted granulate content resulted in a slight tendency to lower the strength).
(4) Not-worsened performance of granulate containing SCC was obtained up to natural aggregate replacement level approaching 50%.

References

1. Ortiz O, Castells F, Sonnemann G (2009) Sustainability in the construction industry: a review of recent developments based on LCA. Constr Build Mater 23:28–39
2. Hunashikatti GM, Pradhan S, Barai SV (2018) Partially hydrated recycled aggregate concrete: a systematic approach towards sustainable development. Constr Build Mater 186:537–549
3. Regulation (EU) No 305/2011 of the European Parliament and of the Council of 9 March 2011 laying down harmonised conditions for the marketing of construction products and repealing Council Directive 89/106/EEC
4. Xu G, Shen W, Zhang B, Li Y, Ji X, Ye Y (2018) Properties of recycled aggregate concrete prepared with scattering-filling coarse aggregate process. Cem Concr Comp 93:19–29
5. Thomas C, Setién J, Polanco JA, de Brito J, Fiol F (2019) Micro- and macro-porosity of dry- and saturated-state recycled aggregate concrete. J Cleaner Prod 211:932–940
6. Lenart M, Gruszczyński M (2017) Application of aggregate recycled from concrete mix as an example of implementation of sustainable development strategy in building engineering. In: Hager I (ed.) Energy efficient, sustainable building materials and products. Cracow University of Technology, pp 137–152
7. Domone PL (2006) SCC: an analysis of 11 years of case studies. Cem Concr Comp 28:197–208
8. Urban M (2018) Low cement content SCC (Eco-SCC) – the alternative for ready-mix traditional concrete. In: MATEC web of conferences, vol 163, p 01004
9. Urban M (2015) The new conception of SCC composition design: theoretical background, evaluation, presentation of procedure and examples of usage. Mater Struct 48:1321–1341

Modelling and Numerical Simulations of Rheological Behaviour

Particle Interactions in Silica Systems in Presence of Superplasticizer

Simon Becker[1], Zichen Lu[2], Sarah Leinitz[3], Wolfram Schmidt[3], Dietmar Stephan[2], and Regine von Klitzing[1(✉)]

[1] Soft Matter at Interfaces, Department of Physics, TU Darmstadt, Alarich-Weiss-Str. 10, 64287 Darmstadt, Germany
becker@fkp.tu-darmstadt.de, klitzing@smi.tu-darmstadt.de
[2] Department of Civil Engineering, Building Materials and Construction Chemistry, TU Berlin, Gustav Meyer Allee 25, 13355 Berlin, Germany
[3] Bundesanstalt für Materialforschung und -prüfung (BAM), Unter den Eichen 87, 12205 Berlin, Germany

Abstract. The flowability of cement paste is of great importance in today's construction industry and is influenced by additives such as superplasticizers (SP). One type of SPs are polycarboxylate ether type SPs. These additives electrostatically bind with the negatively charged carboxylic groups at the backbone to the positively charged clinker phases.

To model positively charged clinker phases with adsorbed SP, silicon wafers are pre-coated with cationic polyethylenimine (PEI) and SP is adsorbed onto the coated surface (Si/PEI/SP). Two different polycarboxylate ether type (PCE) SP are compared – one for ready-mix concrete and one for precast concrete. In this preliminary study the interaction forces between Si/PEI/SP surface and a silica microsphere (colloidal probe) are investigated under mild physico-chemical conditions (pH $\sim$6, ion concentration $<10^{-5}$ M) using Colloidal Probe Atomic Force Microscopy (CP-AFM).

The interaction force between the model surfaces is attractive for low concentration of SP. The force changes from attractive to repulsive by increasing amount of SP. The force upon approach reveals a biexponential behavior. The exponential decay at large and short surface separations are attributed to electrostatic and steric interactions, respectively. The steric forces of the SP for ready-mix concrete show a steeper onset than the SP for precast concrete.

The quantification of these interaction forces will be compared to rheological measurements of similar systems. Furthermore, the parameters will be changed to better approach the conditions in real systems, i.e. higher pH and ionic strength. This helps to understand how the forces on the nanoscale influence the macroscopic rheology.

Keywords: Interfacial forces · Silica beads · Superplasticizer · AFM

V. Mechtcherine et al. (Eds.): RheoCon 2019/SCC 2019, RILEM Bookseries 23, pp. 571–579, 2020.
https://doi.org/10.1007/978-3-030-22566-7_66

1 Introduction

Controlling the rheological behavior of cement pastes is of great importance in nowadays building industry. For this purpose, additives such as superplasticizers (SP) are used. While for precast concrete a fast increase of the flowability right after addition is needed, ready-mix concrete demands a longer durability of the fluidizing effect.

Depending on the type of SP different forces dominate the working mechanism. The dispersing effect of naphthalene sulfonates has been attributed mainly to electrostatic forces, whereas for copolymers consisting of acrylic acid-acrylic acid ester the working mechanism is suggested to be caused by steric forces [1] as well as for grafted polyethylene oxide side chains [2]. Similar findings are suggested by [3].

The investigation of interparticle forces in these systems is demanding due to the roughness of the particles and the high reactivity of the clinker phases with water which leads to increasing pH and ion concentration. Therefore, inert model substrates are used, such as calcite, MgO, mica and quartz. However, the negatively charged PCE is preferably adsorbed on positively charged (model) surfaces such as MgO, while the adsorption onto negatively charged surfaces (mica, calcite, quartz) is less pronounced [4]. Atomic force microscopy (AFM) on MgO substrates using a flattened tip showed an increase in the repulsive force between the tip and the MgO substrate with increasing amount of PCE in pure water or artificial pore solution (pH $\sim$12, high ion concentration $>10^{-1}$ M) [5]. This effect was more pronounced for shorter side chains than for longer ones. Not only adsorbed SP does contribute to a decrease of the viscosity of cement pastes. For longer durability of the dispersing effect (i.e. low viscosity) also non-adsorbed SP can be beneficial [6]. Furthermore non-adsorbed polymers in combination with adsorbed SP are capable of increasing the fluidity of cement pastes [7]. Forces between two model substrates can be measured using a colloidal probe of the desired material by conducting Colloidal Probe AFM (CP-AFM). Recently, colloidal probes of ordinary Portland cement (OPC) were produced using spray drying and first CP-AFM measurements in non-aqueous solution were carried out [8]. Comparison of rheometry and CP-AFM show an increase for the shear resistance of glass bead suspensions with an increase of the adhesive force between two glass beads by increasing salt concentration [9]. The addition of SP leads to its partial adsorption at the surface and decreases the particles ζ-potential [4]. The remaining free SP affect the electrostatic screening of the interaction between the two surfaces. Eliminating the effect of free SP in solution also revealed electrosteric repulsion between MgO surfaces with adsorbed SP investigated by CP-AFM using freeze granulated MgO colloidal probes [10]. The aim of the present study is also to separate both effects but using silica CPs.

To later mimic the positively charged patches of the clinker phases in the present study a planar silicon wafer was pre-coated with cationic polyethylene imine (PEI). The SP was adsorbed onto the prepared surface then. The interfacial force between the modified silicon wafer and a silica microsphere was measured with a CP-AFM under mild physico-chemical conditions (pH $\sim$6, ion concentration $<10^{-5}$ M) in deionized water without free SP. These conditions are far from those in real cementitious systems which are governed by high ion concentrations and high pH ($\sim$12 or higher) but should be used for first characterization of different SP in the silica system. The quantitative behavior of the force between both surfaces is investigated and compared for two types of SP – one for ready-mix concrete and one for precast concrete.

2 Materials and Methods

2.1 Materials and Preparation of Planar SP Surface

The nonporous silica particles (later referred to as colloidal probe) with a nominal diameter of 6.7 μm were purchased from BangsLab and the cantilevers (HQ:CSC38: tipless Cr-Au) from MikroMasch. The silicon wafers were from Siltronic AG. The sulfuric acid (96%, Carl Roth), hydrogen peroxide (30%, Carl Roth) were purchased from Merck, the polyethylenimine (PEI, 750 000 g/mol, branched, 50 wt% in H_2O) from Sigma-Aldrich. The deionized water was provided by the Milli-Q Integral-3 (18.2 MΩcm resistivity, Millipore, Merck, pH 6.1–6.3).

The polycarboxylate ether (PCE) SP for ready-mix concrete (low M_w) and for precast concrete (high M_w) were provided by BASF.

The wafers were etched for 30 min in piranha solution (1:1-vol.% sulfuric acid (96%) and hydrogen peroxide (30%)). To obtain positively charged surfaces the wafers were spin coated (2000 rpm, 30 s) with PEI (0.01 mono-M solution) three times. They were rinsed with Milli-Q water after each run in order to remove non-fixed PEI.

SP was adsorbed by storing the PEI coated wafers for 30 min in a distinct aqueous SP solution with Milli-Q water and a certain concentration of SP. In case of precast SP the concentrations were 0.001, 0.01, 0.05, 0.1, 0.5 and 1 vol.%, respectively and for ready-mix SP the concentrations were 0.001, 0.01, 0.1, 0.5 and 1 vol.%. All wafers were rinsed with Milli-Q water afterwards and dried by nitrogen flow. The modified Silicon wafers are referred to Si/PEI/SP.

2.2 AFM Measurements

The colloidal probe (silica sphere, diameter: 6.7 μm) was attached to the tipless cantilever as described elsewhere [11, 12]. The forces between the surfaces were measured using CP-AFM (MFP-3D, Asylum Research) [13, 14]. The experiments were carried out in Milli-Q water. It is important to emphasize that there was no SP added to the solution. If referred to, i.e. 0.001 vol.% SP this means the used concentration during preparation of the wafers.

For each type of SP one cantilever-colloidal probe pair was used. The force constant of the cantilever was determined using the Sader method [15], yielding the spring constants k = 96 pN/nm (precast) and k = 89 pN/nm (ready-mix). The surface was approached by a speed of 200 nm/s. Each recorded deflection vs. z-sensor curve was transformed individually to force vs. distance using the algorithm described by [16].

The force curves reflect at least 40 force curves combined (shown in the results in pale colour). These curves were smoothed by a binomial smoothing function (10^3 data points, displayed in intense colour in the results section).

3 Results

To avoid repetitions and for the sake of shortness the SP for precast concrete will be denoted as “precast SP” whereas the SP for ready-mix concrete can be referred to as “ready-mix SP”. The first part of the results focuses on the qualitative behaviour of the concentration dependence of the force for both types of SP. A quantitative investigation of the force by approach is then given in the second part of the results.

Figure 1 shows force vs. separation curves for both SP at three different concentrations. The force was divided by the radius of the colloidal probe for comparability [17]. Here, both the approach curves and the retraction curves are shown. For the lowest concentration of the precast SP (top row) an attractive net force could be measured for approach and retraction. For the intermediate concentration during approach no net attractive force could be detected, whereas the retraction showed slight attraction. For the highest concentration a net repulsive force over a large distance up to 100 nm was measured. By retraction a similar mean behaviour (dark blue) is shown with little individual force curves showing pulling events with repulsive force (light blue dots). While for the precast SP the mean approach and mean retraction curves overlay the ready-mix shows even for the highest concentration a reduced force by retraction.

The Fig. 1 bottom row shows the force vs. separation curves for the ready-mix SP. In this case for the concentration of 0.01 vol.% there is a slight adhesion unlike for the precast SP.

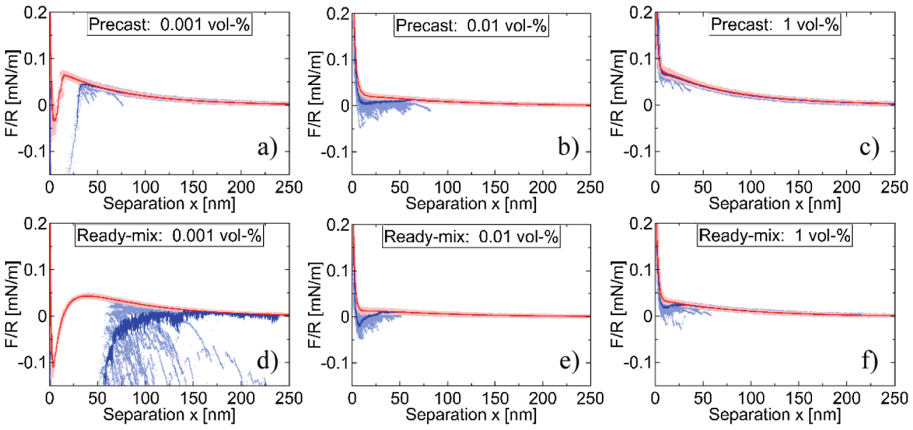

Fig. 1. Force curves of the colloidal probe (silica sphere) against a Si/PEI/SP wafer modified with three different concentrations of precast SP (a–c) and ready-mix SP (d–f). Red curve shows force during approach, blue for retraction. The smoothed force curves are depicted in intense color i.e. red or blue, whereas the master curves without smoothing are depicted in light red and light blue. (Color figure online)

Figure 2 depicts the force curves during approach for both SPs. The approach curve for the lowest dosage of SP (0.001 vol.%) displays a jump-into-contact at a distance of 14–16 nm from the surface – reflecting a strong attractive force. Higher dosages (>0.001 vol.%) show overall a net repulsive behaviour during approach.

The force changes non-monotonously with the concentration. Up to a concentration of 0.1 vol.% the force decreases and above this concentration the force increases with increasing SP concentration.

The effect of the SP concentration on the force is more pronounced for the precast SP which has the lower charge per mass but longer side chains.

On a logarithmic scale the forces reveal a biexponential behaviour (see Fig. 2; bottom row) with an exponential decrease at a distance in the order of 1 nm and a second decay in the order of 50–100 nm. The curves are fitted using a biexponential fit of the form

$$F/R = A_1 \exp\left(-\frac{x}{\xi_1}\right) + A_2 \exp\left(-\frac{x}{\xi_2}\right),$$

where x denotes the separation, F the force and R the effective radius of the colloidal probe, i.e. for sphere-plate geometry the radius of the silica micro sphere.

Figure 3a shows the fitted decay lengths ξ_1 and ξ_2 of the respective exponential functions. The corresponding amplitudes A_1 and A_2 of the exponential functions are depicted in Fig. 3b.

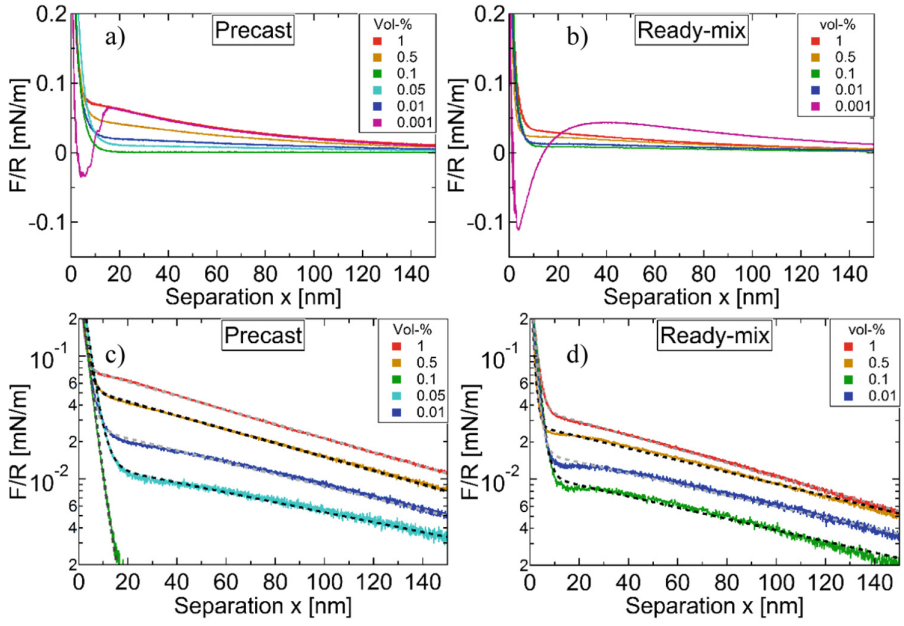

Fig. 2. Smoothed force curves for the approach of the colloidal probe towards Si/PEI/SP wafers for precast (a, c) and ready-mix (b, d) SP. The force over effective radius is plotted against separation of surfaces: Linear force scale (a, b) and logarithmic force scale (c, d). Colour coded is the concentration of SP at Si/PEI. (Color figure online)

Note that due to the small amplitude for a separation larger than 20 nm the second part could not be fitted for a concentration of 0.1 vol.%. The low value of A_2 is indicated in Fig. 3b. The biexponential fit describes the experimental data for small and large distances. In the region in which the dominating exponential function changes, the fit overestimates the force. There is no systematic influence of the SP concentration on both decay lengths. The mean values are $\bar{\xi}_2 = 83 \pm 11$ nm and $\bar{\xi}_1 = 2.0 \pm 0.6$ nm for the precast SP and $\bar{\xi}_2 = 84 \pm 17$ nm and $\bar{\xi}_1 = 1.5 \pm 0.3$ nm for the ready-mix SP.

It is worth noticing that ξ_2 shows no systemic dependence of the type of SP, whereas there is a trend that ξ_1 is slightly higher for the precast SP. Furthermore, the decay in the precast system shows at short distances a slight maximum for intermediate concentrations. The ready-mix system shows a similar behaviour except for the highest concentration.

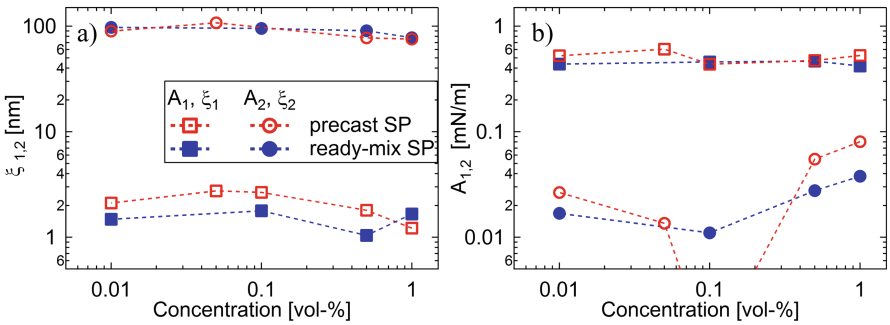

Fig. 3. Fit parameters (a) ξ_1 (squares), ξ_2 (circles), (b) A_1 (squares) and A_2 (circles) for biexponential fit of the approach force curves (0.01 vol.%–1 vol.%) for precast SP (open symbols) and for ready-mix SP (closed symbols). Note the missing fit parameter ξ_2 for 0.1 vol.% for the precast SP (explanation see text).

Both types of SP show a force minimum at intermediate concentrations for the long-range part (fit parameter A_2). For the ready-mix the minimum is flat while the precast SP shows a deeper minimum. For the concentration of 0.1 vol.% the second exponential cannot be fitted since the second decay could not be resolved due to the small values of F/R and as a consequence of this the scattering of the data. Therefore, the fitting parameter A_2 cannot be evaluated due to the scattering but the plateau value can be estimated to be less than 10^{-2} mN/m. The effect of the SP concentration on the decay length ξ_2 is negligible while the Amplitude A_2 shows a dependence on the concentration of the precast but no strong dependence on the ready-mix concentration.

4 Discussion

At low SP concentration a strong attraction is measured for both types of SP. It is assumed to be caused by the PEI coating of the surface. At low concentrations the adsorbed SP on the surface is not able to overcompensate the positive charge of the

PEI, which results in an attraction between the negatively charged silica colloidal probe and the positively charged Si/PEI/SP surface (see schematic Fig. 4). This can be seen by the jump-into-contact for 0.001 vol.% for both types of SP. Besides this assumption it cannot be excluded that the attractive force is of Van-der-Waals type. If the electrostatic force is rather low, the Van-der-Waals force exceeds this one resulting also in a strong attractive force.

Increasing the adsorbed amount of SP decreases the positive charge of the Si/PEI/SP surface. Therefore, for intermediate concentration there is no jump-into-contact by approach but still small attraction measurable for retraction.

For high amount of SP the two types of SP show different behaviour. For the precast SP repulsion is measured both for approach and retraction. In case of the ready-mix SP the approach is repulsive, whereas some individual curves for the retraction show attraction (see Fig. 2). Obviously, the longer side chains of the pre-cast SP show a stronger ability to prevent an attraction than the ready-mix SP.

The force curves show a biexponential decay. It is assumed that the second (long-ranged) decay indicates electrostatic repulsion and that the corresponding length ξ_2 can be considered as screening length, i.e. Debye length $\kappa^{-1} = \sqrt{\frac{\varepsilon_0 \varepsilon_r k_B T}{2 N_A e^2 I}}$ with the vacuum permittivity ε_0, the relative permittivity ε_r, the Boltzmann constant k_B, the absolute temperature T, the elementary charge e, Avogadro's constant N_A and the ionic strength I in mol/m^3. A Debye length in the range of 84 ± 17 nm as obtained in the present study corresponds to an ionic strength in the order of 10^{-5} M which is slightly higher than the ionic strength of Milli-Q water (pH 5.5). In this context the measured decay lengths for both SP reflect well the electrostatic repulsion between two likely charged surfaces across water.

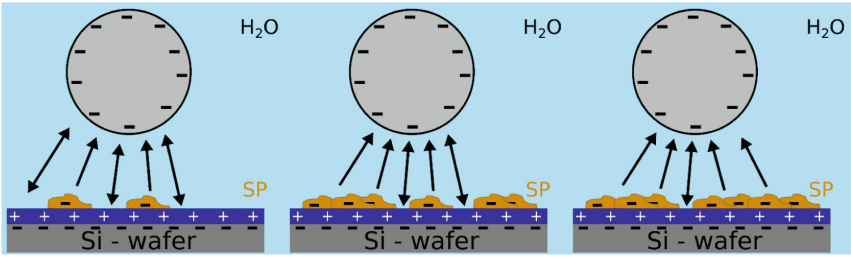

Fig. 4. Schematic representation of the Si/PEI/SP wafer surface. The concentration of SP increases from left to right. The arrows indicate the repulsive (→) and attractive (↔) interaction.

The first (short-ranged) exponential decay ξ_1 is in the range of nm. It is assumed to be caused by the steric forces induced by the polymer coating of the surface i.e. by the side chains of the SP [7]. According to this the decay length of the steric force is proportional to the brush thickness, i.e. the side chain length of the SP. Therefore ξ_1 should be longer for the precast SP due to its longer side chain. This is the case although the effect is rather minor (2 nm vs. 1.5 nm).

The amplitudes A_1 and A_2 do not behave as expected. Due to the higher amount of charge per mass and shorter side chains in case of the ready-mix SP one would expect a higher coverage of the surface by the ready-mix SP. Therefore, the amplitude A_1 of the steric force should be higher for the ready-mix SP than for the precast SP. A_2 changes non-monotonously with the SP concentration with a minimum at intermediate SP concentration which is also not understood yet.

Nevertheless for high SP concentrations, i.e. 0.5 to 1 vol.% the repulsive force increases, which can be roughly compared to 1 and 2 g/L of SP in deionised water investigated by Ferrari et al. [5]. For small side chains the qualitative behaviour seems to fit the results of the present work, whereas for long side chains there are deviations. One difference in the experiments is free SP in the study of 2011 whereas in the present study just adsorbed SP was used. Further experiments have to be carried out to have a look whether free SP could be the reason for this discrepancy.

To summarize the behaviour of the absolute values for the forces, especially the amplitudes of the exponentially decaying forces (steric and electrostatic ones) is not clear. More information has to be gained about the adsorbed amount of the SPs.

5 Conclusion

In this work, forces in silica systems containing different superplasticizers (SP) are successfully measured using Colloidal Probe Atomic Force Microscopy (CP-AFM). Positively charged patches of clinker particles are mimicked using silicon wafers coated with positively charged polyethylenimine (PEI) under mild conditions. Superplasticizer (SP) – i.e. SP for ready-mix concrete or SP for precast concrete – are then adsorbed at different concentrations. The interaction between both surfaces exhibits an attractive force (adhesion) at low concentration of added SP. This is attributed to insufficient coating of SP and therefore no overcompensation of the PEI's positive charge. The attractive force during retraction is reduced with increasing concentration of SP. The repulsive force at approach shows a biexponential behavior for both types of SP with two different decay lengths. At large surface separations the decay length ξ_2 is independent of the type and concentration of SP used. The force is attributed to an electrostatic interaction and the fitted Debye length is in the order of the one in pure water. The interaction for small surface separation is attributed to steric (i.e. entropic) interactions. For both side chain length and the highest concentrations of SP the overall force increases with SP concentration, which was also found by Ferrari et al. [5] for the small side chains, whereas for long side chains this tendency could not be investigated. In order to evaluate differences between the results of both SPs and former work deeper insight into the adsorbed amount is needed. Further investigations on the rheology of alike systems have to be done and be compared to the findings of this work as well as the parameter range has to be extended to include high pH and high ion concentrations.

Acknowledgment. The authors would like to thank the "Deutsche Forschungsgemeinschaft" (DFG) for the financial support of the priority programme SPP2005 "Opus Fluidum Futurum" (KL 1165/24-1). BASF is acknowledged for providing two superplasticizers.

References

1. Uchikawa H, Hanehara S, Sawaki D (1997) The role of steric repulsive force in the dispersion of cement particles in fresh paste prepared with organic admixture. Cem Concr Res 27(1):37–50
2. Yoshioka K, Sakai E, Daimon M, Kitahara A (1997) Role of Steric Hindrance in the Performance of Superplasticizers for Concrete. J Am Ceram Soc 80(10):2667–2671
3. Stephan D, Krelaus R, Schmidt M (2008) Direct measurement of particle-particle interactions of fines for UHPC using AFM technology. In: Proceedings of Second International Symposium on Ultra High Performance Concrete, Kassel University Press, Kassel, pp 375–381
4. Ferrari L, Kaufmann J, Winnefeld F, Plank J (2010) Interaction of cement model systems with superplasticizers investigated by atomic force microscopy, zeta potential, and adsorption measurements. J Colloid Interface Sci 347(1):15–24
5. Ferrari L, Kaufmann J, Winnefeld F, Plank J (2011) Multi-method approach to study influence of superplasticizers on cement suspensions. Cem Concr Res 41(10):1058–1066
6. Sakai E, Yamada K, Ohta A (2003) Molecular Structure and Dispersion-Adsorption Mechanisms of Comb-Type Superplasticizers Used in Japan. J Adv Concr Technol 1(1):16–25
7. Lange A, Plank J (2016) Contribution of non-adsorbing polymers to cement dispersion. Cem Concr Res 79:131–136
8. Ivanov D, Becker S, Lu Z, Pirharati ME, Kwade A, Krauss H-W, Stephan D, von Klitzing R, Schilde C (2019) Synthesis and analyss of spherical cementitious model particles. In: RheoCon & SCC 2019. Springer
9. Glotzbach C, Stephan D, Schmidt M (2013) Measuring interparticle forces: Evaluation of superplasticizers for microsilica via colloidal probe technique. Cem Concr Compos 36(1):42–47
10. Kauppi A, Andersson KM, Bergström L (2005) Probing the effect of superplasticizer adsorption on the surface forces using the colloidal probe AFM technique. Cem Concr Res 35(1):133–140
11. Schön S, von Klitzing R (2018) A simple extension of the commonly used fitting equation for oscillatory structural forces in case of silica nanoparticle suspensions. Beilstein J Nanotechnol 9(1):1095–1107
12. Füllbrandt M, Kesal D, von Klitzing R (2015) Multiscaling Approach for Non-Destructive Adhesion Studies of Metal/Polymer Composites. ACS Appl Mater Interfaces 7(30):16247–16256
13. Kappl M, Butt HJ (2002) The colloidal probe technique and its application to adhesion force measurements. Part Part Syst Charact 19(3):129–143
14. Butt HJ, Cappella B, Kappl M (2005) Force measurements with the atomic force microscope: Technique, interpretation and applications. Surf Sci Rep 59:1–152
15. Sader JE, Chon JWM, Mulvaney P (1999) Calibration of rectangular atomic force microscope cantilevers. Rev Sci Instrum 70(10):3967–3969
16. Senden TJ (2001) Force microscopy and surface interactions. Curr Opin Colloid Interface Sci 6(2):95–101
17. Ducker WA, Senden TJ, Pashley RM (1991) Direct measurement of colloidal forces using an atomic force microscope. Nature 353(6341):239–241

Fresh Concrete Pumping Arrest Investigation for Thixotropy by a CFD Modelling Approach

Robin De Schryver(✉), Khadija El Cheikh, Mert Y. Yardimci, Karel Lesage, and Geert De Schutter

Magnel Laboratory for Concrete Research, Ghent University, Ghent, Belgium
robin.deschryver@ugent.be

Abstract. Concrete pumping operations determine construction speed, finishing quality, durability and even structural integrity. When pumping operations cannot be continued, most problems occur due to complex time-dependent transformations. This causes significant industrial costs (e.g. material and delay). Since time-dependent aspects are currently not fully understood and cannot be predicted, a way to quantify time-dependent aspects is needed. Therefore, we make an attempt by numerical simulation by comparing thixotropic cases with different pumping arresting times. After an introduction to fresh concrete rheology and numerical modelling, ten representative thixotropy cases are analysed.

Despite some unresolved numerical instabilities, the numerical framework allows to estimate pumping pressure peaks after resting time. The results evaluate a thixotropy model, which is generally applicable for less thixotropic SCC's. It is clear that flow re-initiation after rest in concrete pumping is poorly understood. Numerical simulation could be one approach for further analysis and is potentially important for practice. Future work such as simulation of concrete mixers, pressure increase after pumping arrest, formwork pressure decay and leakage are therefore recommended.

Keywords: Fresh concrete · Thixotropy · Concrete pumping · Numerical CFD simulation

1 Introduction

Transportation, pumping and other execution technologies in concrete construction are key elements to ensure structural integrity and durability. During pumping, time-dependent effects of concrete (e.g. thixotropy) can cause costs due to blocking of pipelines [1]. However, time-dependent aspects are poorly understood and cannot reliably be predicted [2–5].

To be able to interpret presented results, one must understand the nature of fresh concrete in terms of rheology or flow behaviour. Rheology studies shear stresses (τ) as a function of applied shear rates ($\dot{\gamma}$) in fluid materials. This function is a so-called flow curve and is an attempt to describe the true nature of flow.

Concrete flow is generally quantified in a steady-state situation (i.e. temporal equilibrium). It is generally accepted that fresh concrete flow behaves according to a Bingham model (1), modified Bingham model or a Herschel-Bulkley model [6, 7],

V. Mechtcherine et al. (Eds.): RheoCon 2019/SCC 2019, RILEM Bookseries 23, pp. 580–587, 2020.
https://doi.org/10.1007/978-3-030-22566-7_67

even though fresh concrete can show non-linear behaviour due to shear thickening (i.e. increasing local viscosity) [2]. Current rheological devices used for cementitious materials mostly attempt to measure yield stress (τ_0) and plastic viscosity (μ) for a Bingham model (1).

$$\tau = \tau_0 + \mu\dot{\gamma} \tag{1}$$

Most problems in concrete pumping do not occur in such an ideal temporal equilibrium state, but are caused due to time-dependent effects [1]. Thixotropy is a reversible time effect defined by the formation of an internal structure due to flocculation at rest, which can deflocculate under shear action [6, 8–11]. This leads to an increase in flow resistance after rest and a decrease in viscosity under shear action. Although, it is often stated that time-dependent effects can be omitted (time period < 30 min–60 min), this is not the case for significant thixotropy (and/or hydration). In theory, there should not be any delay between pumping batches, but in practice it can be significant (15 min–45 min). These delays define as pumping arresting times. When fresh concrete is at rest in pipelines and formworks, time effects can no longer be overlooked from prediction point of view.

Despite numerous rheological investigations, time-dependency is not often considered. Time-dependent rheological models model an internal structure by an evolution equation, whether it is an explicit definition or an implicit one [9, 12–15].

A way to quantify time-dependent aspects is needed. Instead of inconvenient experiments, we make an attempt by numerical simulation. We analyse time-dependent features and compare numerical cases with different pumping arresting times. After an introduction to numerical modelling principles, different representative cases are analysed for time-dependency. An evaluation of the modelling capability concludes this work.

2 Numerical Methodology

Investigation of pumping arresting times involves a model of macroscopic scale. Therefore, Computational Fluid Dynamics (CFD) modelling is an adequate method, since fluid is modelled as a continuum by macroscopic behaviour properties. It transforms so-called constitutive equations derived from physics into discrete algebraic equations which can be solved by numerical discretisation (e.g. finite volume method) [3, 16–18]. The obtained solution therefore describes intrinsic physics, but is in fact an approximated solution. Accuracy depends on discretisation (mesh), solving algorithm (solver), solver settings and imposed assumptions. It does not mean that numerical results are useless or irrelevant, but it actually means that they provide main physical trends.

In CFD, Partial Differential Equations (PDE's (2) & (3)) are typically obtained from physics. Discrete control volumes are considered to which conservation laws apply [19].

$$\nabla \vec{v} = 0 \tag{2}$$

$$\partial_t \vec{v} + (\vec{v}\nabla)\vec{v} = \vec{g} - \nabla p + \mu' \Delta \vec{v} \tag{3}$$

Open source software OpenFOAM® is used in this framework allowing to solve for scalar pressure field p (kinematic pressure relative to density ρ) and velocity vector field $\vec{v}$. An incompressible solver 'nonNewtonianIcoFoam' is used.

This solver uses a general Newtonian approach (i.e. linearization to an apparent Newtonian viscosity μ'). We implemented thixotropy via linking the thixotropic internal structure λ to viscosity μ' [19]. We used a simplified Roussel model (4) to describe thixotropic behaviour [9]. This means the yield stress τ_0 increases linearly at rest by characteristic flocculation time T and has a deflocculation rate α (for time periods ca. <60 min [9, 20, 21]).

$$\begin{cases} \tau = \tau_0(1+\lambda) + \mu\dot{\gamma} \\ \frac{\partial \lambda}{\partial t} = \frac{1}{T} - \alpha\dot{\gamma}\lambda \end{cases} \tag{4}$$

Boundary Conditions (BC) determine how a simulation domain is connected to the 'outer world' and are important for the simulation. The BC's for pipe flow in this work:

- Pipe inlet: constant uniform velocity (U_0), zero gradient pressure, constant uniform internal structure parameter (λ_0).
- Pipe wall: zero wall velocity, zero gradient pressure, zero gradient internal structure parameter.
- Pipe outlet: zero gradient velocity, constant uniform pressure, zero gradient internal structure parameter.

Spatial discretisation (81000 volumes) is based on a mesh design analysis and temporal discretisation is (manually) controlled by the CFL (Courant-Friedrichs-Lewy) number.

3 Pumping Arrest Investigation

3.1 Investigation Methodology

Quantification in rheological devices may be highly complicated and values may differ significantly, leading to significant discrepancies in results from experiments and numerical simulations. This work attempts to evaluate model values representative for SCC in general.

In steady-state, the simplified Roussel model coincides with the Bingham model. All other parameters (Table 1) are chosen as a practical SCC reference via [9]. An initial internal structure λ_0 of 0.33 is used for pumping (after concrete mixing ca. 10 s^{-1} [9]).

Table 1. Overall case parameters are chosen on basis of a practical SCC reference [9].

Q [l/s]	$D = 2R$ [mm]	L [m]	U_0 [m/s]	ρ [kg/m^3]	τ_0 [Pa]	μ [Pa.s]	T [s]	α [-]	$A_{thix} = \frac{\tau_0}{T}$ [Pa/s]	λ_0 [-]
10	125	4	0.814	2400	30	20	60	0.005	0.5	0.33

After a first phase of pipe flow (0–60 s), pumping is arrested and a waiting period is induced by addition of an equivalent thixotropic internal structure ($\Delta\lambda_a = t_a/T$). Ten different waiting periods are considered for simulation (Table 2).

Table 2. Pumping arrest induces a thixotropic structural build-up which serves as an interpretation reference for other thixotropic fluids with equivalent arresting times.

Case	Pipe									
	1	2	3	4	5	6	7	8	9	10
Arresting time t_a [min]	0	1	2	3	4	5	10	15	30	45
Thixotropic structure $\Delta\lambda_a$ [-]	0	1	2	3	4	5	10	15	30	45

After pumping arrest, flow is re-initiated in the simulation and a pressure loss peak is expected in this second simulation phase (60 s–70 s). The longer the arresting time t_a, the higher the expected pressure loss peak, which is estimated by an analytical quantification based on the Buckingham-Reiner equation (5) for a Bingham model [5]. This expression is an approximation, since higher order terms of $\Delta p/L$ have been omitted and a thixotropic increase of yield stress has been considered by λ, violating the steady-state assumption. To make it generally applicable for pipe flow, pressure losses (Δp) are transformed in a relative ($1/L$) kinematic ($1/\rho$) form [m/s^2].

$$\frac{\Delta p}{L\rho} = \frac{1}{\rho}\left(\frac{8}{3}\frac{\tau_0(1+\lambda)}{R} + \frac{8\mu Q}{\pi R^4}\right) \tag{5}$$

Pipe pressure losses obtained from the simulations are computed by taking the average pressure difference of the pipe cross-section in fully-developed state (longitudinal).

3.2 Results

During the first simulation phase (0–60 s), pipe flow starts from its initial (thixotropic) state (λ = 0.33). Concrete (SCC) pipe flow is laminar (i.e. Reynolds number (12.2) smaller than 2300 [19]). This implies a linear pressure loss profile and a quadratic velocity profile, disregarding a plug in steady-state (Fig. 1) [22]. Despite time-dependent rheology aspects, steady-state (i.e. temporal equilibrium) is still obtained. As new material is

flowing in, pre-existing (thixotropically aged) material is flowing out. Material attached to pipe walls reaches a temporal equilibrium state under high shear, while material central in the pipe (bulk) is subjected to minor shear (or none for a plug) until it flows out. Thus a steady-state can indeed be obtained, because only a limited time is able to act on the bulk material (cfr. Eulerian character of simulation). Since the shear rate is the highest near the pipe wall, the internal thixotropic structure is demolished and a lower viscosity is obtained than in the bulk where no significant shear is present. This is reminiscent to lubrication layer effects, which omitted in this work [23, 24].

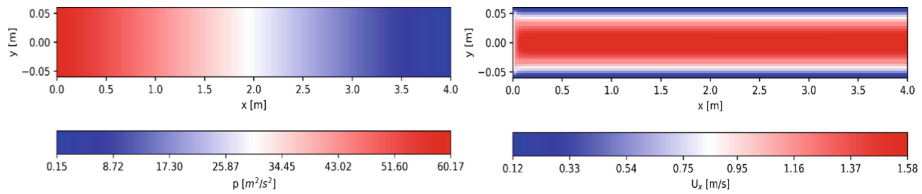

Fig. 1. Laminar pipe flow results in (left) a linear pressure profile and (right) a quadratic velocity profile (in function of pipe radius (y) and pipe length (x)).

In the second simulation phase after arrest (60 s–70 s), the pumping arresting time caused thixotropic build-up of the internal structure λ. Due to this, the overall rheological properties of the concrete have changed and more flow resistance is expected, thus higher pressure losses are expected to re-initiate pumping. During pumping re-initiation, two distinct flow regions can be observed (Fig. 2), i.e. one flow front where new material is inflowing and another where aged material is outflowing.

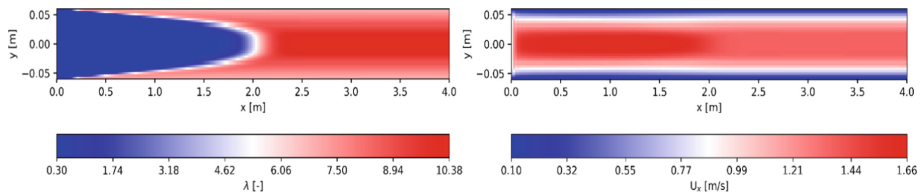

Fig. 2. (left) The thixotropic internal structure λ profile (60.5 s) and (right) the velocity profile (60.5 s) clearly distinguish two different flow regions: new vs. aged concrete.

Even though new material (i.e. freshly mixed $\lambda = 0.33$) is flowing in, thixotropically aged material sticks to pipe walls. Therefore, aged material has to undergo shear-induced breakdown before the pipe flow reaches its steady-state equilibrium. Hence, a gradual pressure loss decay is observed after 60 s (Fig. 3), even after the pipe has been refilled (62.5 s) by new concrete. An apparent bifurcation point occurs at the instant when the aged concrete plug flows out (ca. 62.5 s), since the pressure loss in Fig. 3 is calculated from the pipe end.

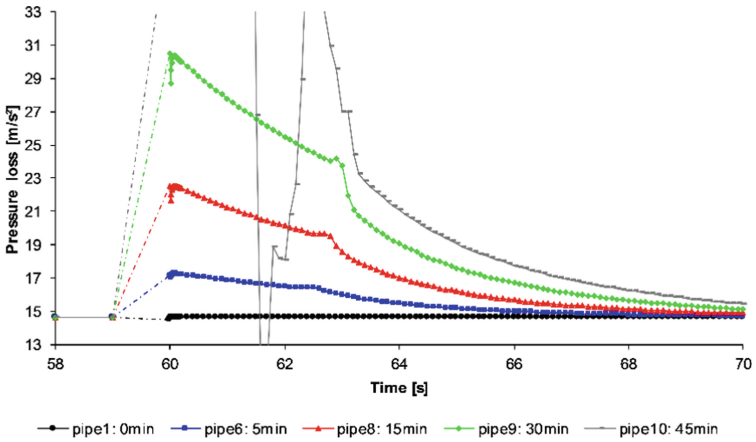

Fig. 3. Thixotropic aged material sticks to the pipe walls, causing a gradual decay in relative kinematic pressure loss, even after the pipe has been refilled (62.5 s) by new concrete.

The numerical pressure losses (Table 3, obtained at 60.1 s) are in range of the estimations by the modified Buckingham-Reiner equation. This equation does not return reliable values, because implied steady-state conditions are violated. Therefore, it rather returns a reference for the generally expected range of pressure losses. The nature of the simulation results is also questionable, because unresolved numerical stability problems are observed for the longest waiting time (45 min). The pressure peaks due to thixotropic materials under influence of pumping waiting times should thus be further investigated to gain meaning for practice. Another important aspect of thixotropic simulation could be simulation of formwork pressure decay and leakage.

Table 3. A relative kinematic pressure loss comparison (at 60.1 s) shows that the simulation is capable to simulate pressure re-initiation peaks for a thixotropic structure increase $\Delta\lambda_a$ up to 30.

Pressure loss	Pipe									
	1	2	3	4	5	6	7	8	9	10
Thixotropic structure $\Delta\lambda_a$ [-]	0	1	2	3	4	5	10	15	30	45
Buckingham-Reiner $\frac{\Delta p}{L\rho}$ [m/s^2]	14.4	15.0	15.5	16.0	16.6	17.1	19.8	22.4	30.4	38.4
Numerical simulation $\frac{\Delta p}{L\rho}$[m/s^2]	14.6	14.7	15.2	15.7	16.2	16.7	17.3	19.9	22.5	/

Once a stable simulation can be sustained, pressure losses and general flow behaviour can be revealed. Flow behaviour such as structural build-up as well as breakdown processes may be of great importance for practice. For instance, in the simulation of concrete (truck) mixers, rheometers (breakdown) and pumping or formwork pressure decay (build-up).

4 Summary and Conclusion

Fresh concrete can be modelled by a Bingham model in case of temporal equilibrium, or including thixotropy by a Roussel model. Independent of the considered model, one should be aware that rheological models are always assumed material behaviour and can only approximate the true rheological nature of materials. Future work could include a comparison between different rheological models.

Numerical software OpenFOAM® used in this work, allows custom implementations of thixotropic behaviour. As any software, it is based on constitutive equations to solve a physical problem. This means that numerical results are only an approximate solution compared to reality, but they do return general behavioural trends. A future validation is therefore indispensable.

Numerical simulation of pumping pressures after a thixotropic arresting time is possible. However, the modelling capability is limited due to some instabilities. The origin of this numerical artefact is not clear and requires more investigation.

Nevertheless, the obtained results evaluate a general thixotropy model, which is also applicable for less thixotropic SCC's, via transforming pumping arresting times to an equivalent increase in thixotropic structure λ_a. It is clear that flow re-initiation in concrete pumping is poorly understood and needs further elaboration with regard to practice. Numerical CFD simulation could be one approach for further analysis and simulation of concrete mixers (structural breakdown), pressure increase after pumping arrest or formwork pressure decay and leakage (structural build-up) are important for the future.

Acknowledgement. This work is a deliverable of the ERC Advanced Grant project 'SmartCast'. This project has received funding from the European Research Council (ERC) under the European Union's Horizon 2020 research and innovation programme (grant agreement No. 693755). This support is gratefully acknowledged.

References

1. De Schutter G (2017) Thixotropic effects during large-scale concrete pump tests on site. In: International conference on advances in construction materials systems ICACMS, vol 2, pp 1–7
2. Feys D (2009) Interactions between rheological properties and pumping of self-compacting concrete, Ghent University. http://hdl.handle.net/1854/LU-948561
3. Roussel N, Gram A (2014) Simulation of fresh concrete flow. Springer, Dordrecht

4. Roussel N, Gram A, Cremonesi M, Ferrara L, Krenzer K, Mechtcherine V, Shyshko S, Skocec J, Spangenberg J, Svec O, Thrane LN, Vasilic K (2016) Numerical simulations of concrete flow: a benchmark comparison. Cem Concr Res 79:265–271
5. Tichko S (2015) Hydrodynamic modelling of the flow of self-compacting concrete in formworks
6. Barnes HA (1997) Thixotropy - a review. J nonNewton Fluid Mech 70:1–33
7. Roussel N (2007) Correlation between yield stress and slump: comparison between numerical simulations and concrete rheometers results. Mater Struct 39:501–509
8. Mewis J, Wagner NJ (2009) Thixotropy. Adv Colloid Interface Sci 147–148:214–227. https://doi.org/10.1016/j.cis.2008.09.005
9. Roussel N (2006) A thixotropy model for fresh fluid concretes: theory, validation and applications. Cem Concr Res 36:1797–1806
10. Flatt RJ, Roussel N, Cheeseman CR (2012) Concrete: an eco material that needs to be improved. J Eur Ceram Soc 32:2787–2798
11. Roussel N (2011) Thixotropy: from measurement to casting of concrete. In: Understanding the Rheology of Concrete, pp 286–295. https://doi.org/10.1016/B978-0-85709-028-7.50011-X
12. Wallevik JE (2004) Microstructure-rheology: thixotropy and workability loss. Nord Concr Res 31:16. http://www.nvtf.org/ikbViewer/Content/224632/I09 - Wallevik 2004-06-07.pdf
13. Wallevik JE (2009) Rheological properties of cement paste: thixotropic behavior and structural breakdown. Cem Concr Res 39:14–29
14. Mujumdar A, Beris AN, Metzner AB (2002) Transient phenomena in thixotropic systems. J Nonnewton Fluid Mech 102:157–178
15. Wallevik JE (2005) Thixotropic investigation on cement paste: experimental and numerical approach. J Nonnewton Fluid Mech 132:86–99
16. Sjodin B (2016) What's the difference between FEM, FDM, and FVM? http://www.machinedesign.com/fea-and-simulation/what-s-difference-between-fem-fdm-and-fvm
17. Jarny S, Roussel N, Rodts S, Bertrand F, Le Roy R, Coussot P (2005) Rheological behavior of cement pastes from MRI velocimetry. Cem Concr Res 35:1873–1881
18. Roussel N, Geiker MR, Dufour F, Thrane LN, Szabo P (2007) Computational modeling of concrete flow: general overview. Cem Concr Res 37:1298–1307
19. Welty JR, Wicks CE, Wilson RE, Rorrer GL (2008) Fundamentals of momentum, heat, and mass transfer. Wiley, London
20. Roussel N (2007) Rheology of fresh concrete: from measurements to predictions of casting processes. Mater Struct 40:1001–1012
21. Lecompte T, Perrot A (2017) Non-linear modeling of yield stress increase due to SCC structural build-up at rest. Cem Concr Res 92
22. De Schutter G, Feys D (2016) Pumping of Fresh Concrete: Insights and Challenges, RILEM Tech. Lett., vol 1, p 76
23. Feys D (2012) Understanding the pumping of conventional vibrated and self-compacting concrete
24. Choi MS, Kim YJ, Kwon SH (2013) Prediction on pipe flow of pumped concrete based on shear-induced particle migration. Cem Concr Res 52:216–224

Numerical Simulation of the Flow Behavior of Newtonian Fluids in a Wide Gap Rheometer by CFD

Mahmoud Eslami Pirharati[1(✉)], Dimitri Ivanov[2], Hans-W. Krauss[1], Carsten Schilde[2], and Dirk Lowke[1]

[1] Institute of Building Materials, Concrete Construction and Fire Safety, Technische Universität Braunschweig, Brunswick, Germany
m.eslami@ibmb.tu-bs.de
[2] Institute of Particle Technology, Technische Universität Braunschweig, Brunswick, Germany

Abstract. Wide gap coaxial rheometers with vane-in-cup systems are widely used to determine rheological properties of cement paste, mortar and concrete. Available analytical models allow the calculation of average shear stress with acceptable accuracy. However, they exhibit serious oversimplifications, e.g. torque contributions of other parts than the vertical cylinder equivalent surface or neglecting of stress peaks. Hence, the accuracy of calculated shear stress values may be questionable depending on the actual purpose.

In the present contribution, experimental investigations of Newtonian fluids in a wide gap rheometer with both, a coaxial smooth steel cylinders and a vane-in-cup system, are presented. Accuracy of analytical models is discussed with respect to shear rate distributions over gap and over cylinder resp. vane probe surfaces determined from Computational Fluid Dynamics (CFD) simulations. A modified analytical model is proposed. As will be shown, the averaged shear rates over one revolution calculated from CFD simulations are comparable with the modified analytical model. Further results are discussed and an outlook for future research is given.

Keywords: Wide gap rheometer · CFD · Vane-in-cup · Newtonian fluids

1 Introduction

Wide gap rheometers with vane-in-cup systems are commonly used to determine rheological properties of non-Newtonian fluids such as cement paste, mortar or concrete. In contrast to more complex geometrical setups (helix, fishbone, etc.), vane-in-cup systems can be evaluated similarly to coaxial cylinders systems allowing the calculation of basic rheological properties such as viscosity or shear stress. The main advantages of vane-in-cup systems are the elimination of wall slip and the highly reduced disturbance of the sample during immersion [1, 2]. On the other hand, complexity of material flow behavior increases due to the stress peaks at the vane tips and the material flow around the tips. Ovarlez et al. [3] studied the local flow properties of different fluids in a vane-in-cup setup by means of MRI technique, revealing that shear

V. Mechtcherine et al. (Eds.): RheoCon 2019/SCC 2019, RILEM Bookseries 23, pp. 588–595, 2020.
https://doi.org/10.1007/978-3-030-22566-7_68

flow in a six-bladed vane-in-cup geometry varies in radial and tangential directions, e.g. the material enters deeply the region between the blades of vane probe [3]. Hamedi et al. [4] recommended correction factors for the torque contribution of individual probe surfaces in different geometrical setups based on material flow CFD simulations in a wide and a narrow gap rheometer.

The aim of the present contribution is to validate the accuracy of analytical models with respect to the real material flow behavior in a wide gap vane-in-cup rheometer determined by CFD simulations in comparison with smooth coaxial cylinders. As a first step, Newtonian materials are investigated here. One important goal is the reliable prediction of material shear rate history during rheometer testing at different points of interest in the sample volume (i.e. of 3D material flow). This is prerequisite to enable precise results on the effect of shear rate history on the in-situ particle size distribution, e.g. monitored by a laser system (an ongoing step of current research work, not shown here). First, analytical solutions for the prediction of rheological properties in coaxial rheometers are presented and the basic model simplifications and constraints are discussed. Then, details on the numerical CFD simulations, the experimental setup and the materials used are given. Finally, the experimental and numerical results on Newtonian fluids are presented and the validity of analytical calculations is discussed based on those results. A linear modification factor (percentage of applied torque on the lateral surface of cylinder resp. vane probe) is recommended to improve the analytical model's accuracy.

2 Analytical Models

Assuming laminar flow, no slip boundary conditions and constant shear stress distribution at the vertical cylinder surface the shear stress at given radius can be calculated analytically by Eq. 1 [1, 5, 6], where τ is the shear stress at radius R, T is the torque (constant at all radii) and h is the height of the inner cylinder. Note, that Eq. 1 takes into account the torque contribution of the lateral surface of inner cylinder only [5, 7].

Newtonian fluids exhibit a linear relationship between shear stress τ and shear rate $\dot{\gamma}$ expressed by the dynamic viscosity μ of the fluid as follows $\tau = \mu\dot{\gamma}$ [1, 8]. For Newtonian fluids the relationship between torque, rotational velocity and geometrical parameters in a coaxial cylinders rheometer is given by the expression in Eq. 2, where ω is the rotational velocity, and R_i and R_o are the inner and outer radii, respectively [9, 10]. Replacing $\tau = \mu\dot{\gamma}$ in Eq. 1, the shear rate distribution can be calculated as a function of radius for Newtonian fluids, see Eq. 3. Due to the fact that torque is constant over radius, shear rate decreases non-linearly with increasing radius [7].

$$\tau = \frac{T}{2\pi R^2 h} \tag{1}$$

$$\omega = \frac{T}{4\pi\mu h}\left[\frac{1}{R_i^2} - \frac{1}{R_o^2}\right] \tag{2}$$

$$\dot{\gamma} = \frac{T}{2\pi\mu R^2 h} \tag{3}$$

3 Numerical Simulations

3D numerical simulations of the flow behavior of Newtonian fluids in a wide gap rheometer have been carried out with the commercial software ANSYS Fluent Academic Research 18.0, using a finite volume method (FVM). Two different modules in ANSYS Workbench R18.1 (ANSYS Design Modeler and ANSYS Meshing), were utilized to design geometries and generate the mesh, respectively.

Though wall slip at the outer cylinder was eliminated in experiments using lamellae (see Fig. 1 and Sect. 4), their influence on shear flow is not considered here because shear stress distribution near the inner cylinder is of central interest. Hence, the radial position of the outer lamellae tips (R = 135/2 mm) is considered as the outer radius in simulations and analytical calculations. The outer cylinder was defined as "rotating walls" and the inner cylinder walls as stationary. No slip boundary conditions were imposed at all walls. Further, laminar flow model was chosen assuming steady flow. Tetrahedral elements were used to discretize the geometry 3D domain. The simulations were performed for two different geometries, see Sect. 4. Note, that an adequate mesh resolution is crucial for quality and accuracy of CFD simulation results. Here, the mesh independent study was conducted with respect to the numerical torque value, with the main idea to achieve results independent from the number of cells. The total number of cells for vane-in-cup and coaxial cylinders systems are 2173209 and 2339159, respectively.

To validate the accuracy of the analytical model, first the torque contributions of the individual surfaces of the rotating tools (lateral, top, bottom and pin) were determined from CFD simulations for both setups. The torque values are directly achieved from "Function Calculator" section in CFD-Post, for more detailed information see [11].

4 Experimental Program

The rheological experiments were conducted with a wide gap rheometer Viskomat XL (Schleibinger [12]) using two different setups, (a) vane-in-cup system and b) a coaxial smooth steel cylinders system. The Viskomat XL is a Couette type rheometer with rotating cup and stationary inner geometry, where torque is recorded [13]. The dimensions of the two different rheometer setups are displayed in Fig. 1. The cylinder in setup b (Fig. 1b) had an identical height and diameter as the vane probe (Fig. 1c). At the outer cylinder, vertical lamellae were fixed to eliminate wall slip. Two silicone oils (Newtonian fluids) AK 5000 and AK 10000, with a density of 970 kg/m^3 were used for experiments. The filling height was 140 mm. The temperature was controlled during testing (T = 20 °C ± 0.5 °C). A downward ramp profile (steps: 80, 70, 60, 50, 40, 30, 20, 10, 8, 6, 4, 2, 1, 0.1 rpm) was used, with every step being hold for 15 s. Each test was repeated 3 times at minimum.

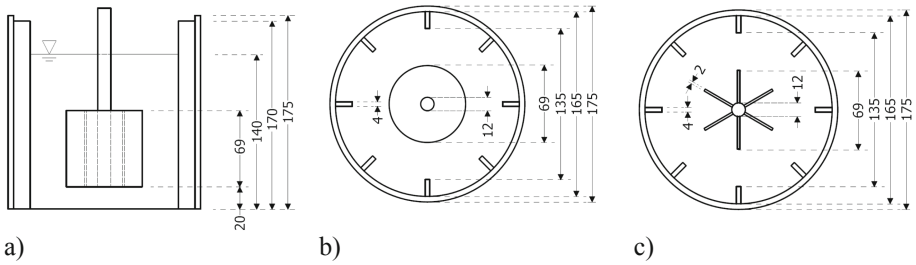

Fig. 1. Scheme of both setups investigated, with 8 vertical lamellae fixed at the outer cylinder and a filling height of 140 mm; (a) vertical cut, (b) top view of the coaxial cylinders setup, (c) top view of the vane-in-cup system (6 blades).

The average values of measured torque within the last 2 s at each profile step were determined and used as results. The viscosity and shear rate distribution over gap for both, vane-in-cup and coaxial cylinders setups were calculated analytically at 60 rpm from Eqs. 2 and 3, respectively.

5 Results and Discussion

5.1 Torque Contribution of Individual Surfaces

The CFD simulations reveal that about 95% of total torque results from the lateral surface in case of the vane-in-cup setup, whereas only 80% of total torque results from the lateral surface in case of smooth coaxial cylinders, see Table 1. As stated before, the analytical model takes into account torque contributions of the vertical surfaces only, neglecting the contribution of the top and bottom surfaces. We propose to introduce a correction factor X to modify the analytical model with respect to the torque contributions of the bottom and top surfaces, as follows: X = the percentage of applied torque only over lateral surface.

Table 1. Relative torque contribution of the different parts of inner geometry (percentages).

Material	Rel. torque X [%] at surfaces				Total torque T (Nmm)	
	Top	Lateral	Bottom	Pin	CFD	Experiment
Coaxial cylinder						
SO AK 5000	8.5	80.6	10.1	0.8	62.6	64.6
SO AK 10000	8.4	80.7	10.0	0.9	125.0	137.2
Vane probe						
SO AK 5000	1.9	94.7	2.2	1.2	47.2	47.4
SO AK 10000	1.9	94.6	2.2	1.3	94.3	101.7

With the correction factor X Eq. 3 is modified as follows:

$$\dot{\gamma} = X \frac{T}{2\pi\mu R^2 h} \tag{4}$$

Note, that the correction factor is different for the two setups investigated here. However, nearly identical factors were found for the two silicone oils ($X_{\text{coax,cyl}} = 0.8$, $X_{\text{vane}} = 0.94$). To generalize the findings on the correction factor X further investigations on other Newtonian fluids and on elastic-viscoplastic suspensions should be conducted. Moreover, the ratio between total torque measured in case of the vane-in-cup and coaxial cylinders setups defined as $T_{\text{vane}}/T_{\text{coax,cyl}}$ is 0.73 and 0.74 for silicone oils AK 5000 and AK 10000, respectively.

5.2 Shear Rate Distribution

The radial shear rate distributions are calculated from CFD simulations at three different heights of the cylinder resp. vane probe, see Fig. 2a. Furthermore, radial shear rate distributions are calculated for two angles in case of the vane probe setup, namely (a) along the vane blades (line A–B in Fig. 2b) and (b) in the middle between two vane blades (line C–D in Fig. 2b). The resulting radial shear rate distributions for the coaxial smooth cylinders setup are displayed in Fig. 3 and for the vane-in-cup setup in Fig. 4.

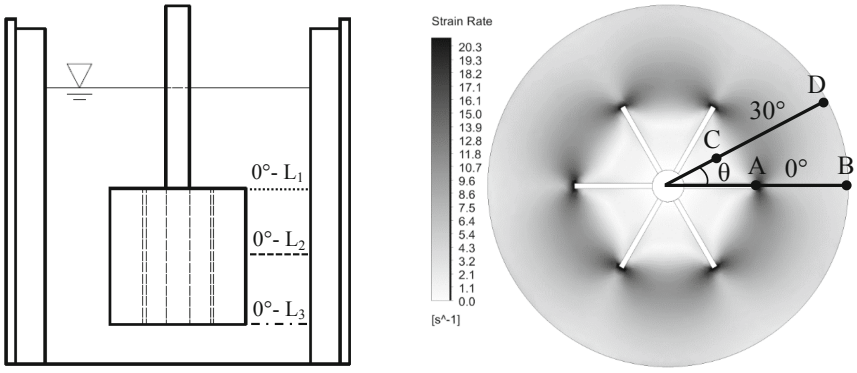

a) b)

Fig. 2. (a) Schematic definition of three different lines: top corner (0°- L_1), middle (0°- L_2) and bottom corner (0°- L_3) of the vane probe; (b) Shear rate distribution at middle height of the vane probe for SO AK 5000 along the vane blades (line A–B) and between the vane blades (line C–D).

In case of the vane-in-cup setup, the material shows largely inhomogeneous flow behavior caused by the blades of the vane probe. In Fig. 2b the shear rates are displayed for a horizontal section in the middle height of the vane probe. As expected, much higher shear rates occur at the tips of the vane blades compared to the middle between the blades. Moreover, the concentrated shear rates at point A show a sharp decrease in radial direction (A–B), whereas shear rates decrease only slightly in radial

direction at line C–D. In Fig. 3 the shear rate distributions at different height positions from CFD results as well as the analytical and modified analytical models are displayed for the coaxial smooth cylinder setup. At the top and bottom corners of the cylinder marked shear rate peaks occur, followed by a sharp decrease in radial direction compared to the middle cylinder height.

Obviously, the shear rate distribution calculated by the modified analytical model ($X = 0.80$) is in very good agreement with numerical results at middle height of the cylinder. However, if more precise information on the shear rate distributions, e.g. at other radial, vertical or tangential positions, are required, CFD simulations should be preferred.

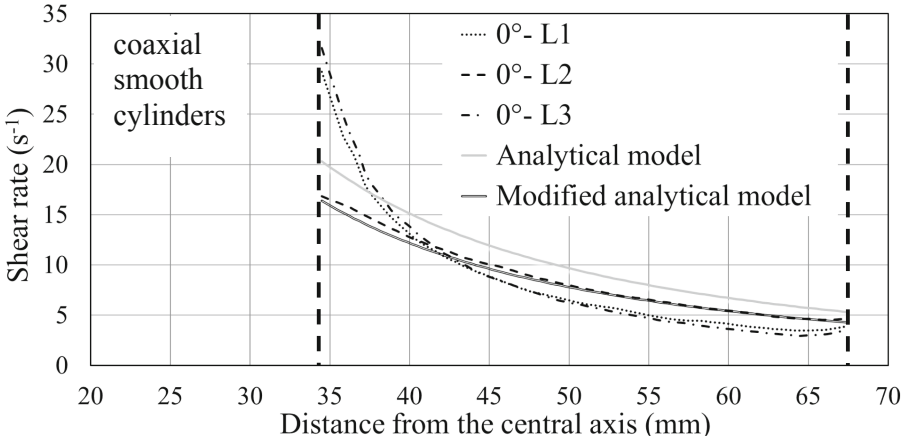

Fig. 3. Comparison of shear rate distributions over gap from numerical and analytical calculations for the coaxial smooth cylinders setup (SO AK 5000); inner and outer walls are indicated by vertical dashed lines.

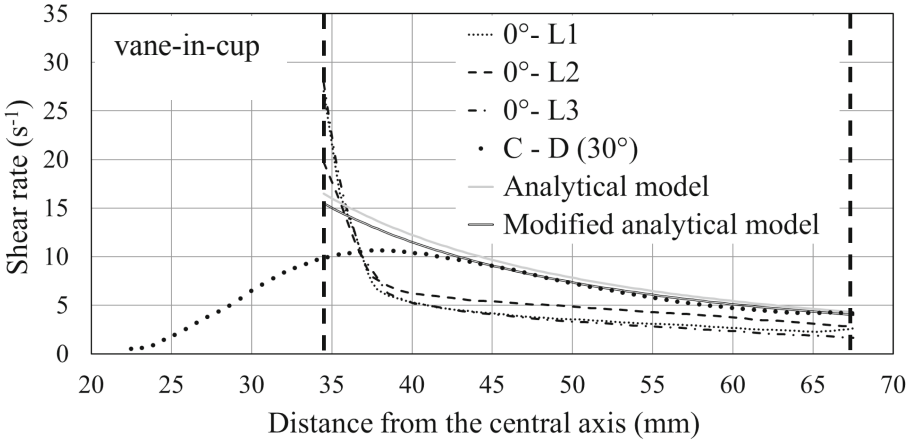

Fig. 4. Comparison of shear rate distributions over gap from numerical and analytical calculations for the vane probe setup (SO AK 5000); inner and outer walls are indicated by vertical dashed lines.

Figure 4 gives the shear rate distributions over gap for the vane-in-cup setup determined by numerical and analytical calculations at three different height positions (along the vane blades) compared to the position at 30° between the vane blades (at middle height). Again, marked shear rate peaks at the vane blade tips can be observed, followed by a strong decrease with increasing radius. On the other hand, shear rates along line C–D are comparable to results of the modified analytical model (smooth cylinder assumption).

However, when rotating along one circumference the material is exposed to different shear rate states in rheometer tests with vane-in-cup setup. As shown in Figs. 2b and 4, the concentrated shear rates at point A increase the non-linear decrease of shear rate in radial direction (A–B) in comparison with the shear rate decrease in radial direction at line (C–D). Hence, shear rate history of the material at different partial volumes is of interest for the determination of exact shear boundary conditions. In Fig. 5 the shear rate history of the material is displayed over one revolution at different positions in the middle height of the vane probe, (a) at 1 mm distance from the vane tip, (b) in the middle of the gap, and (c) at 3 mm distance from the lamellae tip at the outer cylinder.

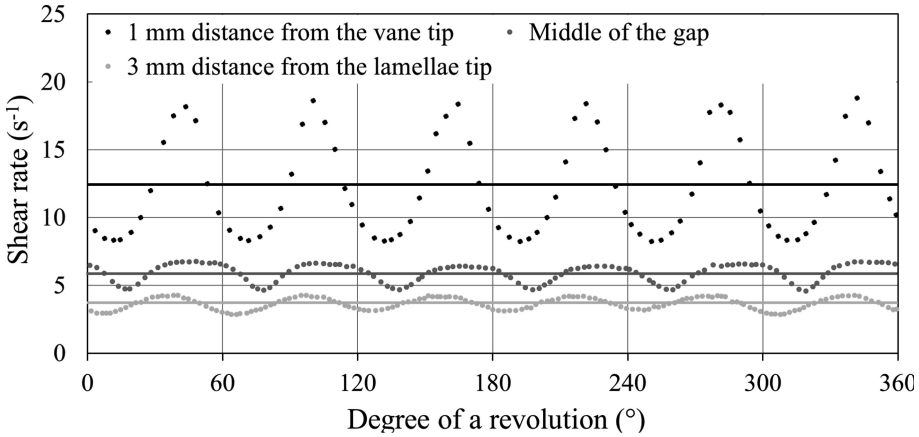

Fig. 5. Shear rate distributions (dotted lines) and average values (horizontal full lines) over one revolution at three different radial positions from CFD simulations.

Finally, to better understand the influence of the vane blade tips, the shear rate histories of the material for one revolution at three different positions over gap and the average value of shear rate histories were determined by CFD simulations, see Fig. 5. The results show that the average shear rates at the three positions over one revolution are in good agreement to the results of the modified analytical model.

6 Conclusions and Outlook

A series of experiments, 3D numerical analysis and analytical calculations have been carried out to determine shear rate and torque distributions in case of Newtonian materials for two rheometer setups. As demonstrated, 3D CFD simulations are suitable to investigate the shear rate history in different sample partial volumes, enabling a better physical understanding of the material flow behavior. Due to several simplifying assumptions, analytical models generally exhibit less precision. However, accuracy of the modified analytical model may be sufficient for many purposes, e.g. when an estimate of the average shear rate is of interest. In case of the vane-in-cup setup, shear rate distributions along the radial line between two vane blades give comparable results to the modified analytical model. Furthermore, the averaged shear rate distributions over one revolution at different positions were in good agreement with results from the modified analytical model. Future investigations will focus on 3D CFD simulations of non-Newtonian (Bingham) materials flow behavior in wide gap rheometers with vane-in-cup setup with the help of a User-defined Function (UDF). Moreover, the results on the shear rate distributions in the sample will be used to integrate a laser probe into the rheometer to assess the relation between shear history and in-situ particle size distribution.

References

1. Koehler EP, Fowler DW (2004) Development of a portable rheometer for fresh portland cement concrete, Research report ICAR-105-3
2. Rabia A, Yahiaoui S, Djabourov M, Feuillebois F, Lasuye T (2014) Optimization of the vane geometry. Rheol Acta 53:357–371
3. Ovarlez G, Mahaut F, Bertrand F, Chateau X (2011) Flows and heterogeneities with a vane tool: magnetic resonance imaging measurements. J Rheol 55:197–223
4. Hamedi N, Revstedt J, Tornberg E, Innings F (2014) A new numerical method for correction of wide gap rheometry data by CFD. Transactions of the Nordic Rheology Society, vol 22
5. Tattersall GH, Banfill PFG (1983) The rheology of fresh concrete, pp 53–57
6. Wallevik OH, Feys D, Wallevik JE, Khayat KH (2015) Avoiding inaccurate interpretations of rheological measurements for cement-based materials. Cem Concr Res 78:100–109
7. Feys D, Wallevik JE, Yahia A, Khayat KH, Wallevik OH (2013) Extension of the Reiner-Riwlin equation to determine modified Bingham parameters measured in coaxial cylinders rheometers. Mater Struct 46:289–311
8. Munson BR, Young DF (2002) Fundamentals of fluid mechanics, pp 16–18
9. Estellé P, Lanos C, Perrot A, Amziane S (2008) Processing the vane shear flow data from Couette analogy. Appl Rheol 18(3):34037
10. Steffe JF (1996) Rheological methods in food process engineering, 2nd edn. Freeman Press, East Lansing
11. ANSYS Inc. (2009) ANSYS FLUENT 12.0, user's guide, pp 147–148
12. Schleibinger Testing Systems. http://www.schleibinger.com/cmsimple/
13. Schramm G (1998) A practical approach to rheology and rheometry, pp 36–39

Segregation of Granular Material During the Transport in Pipes

Martin A. Haustein(✉) and Rüdiger Schwarze

Institute of Mechanics and Fluid Dynamics, TU Bergakademie Freiberg, Freiberg, Germany
martin.haustein@imfd.tu-freiberg.de

Abstract. Concrete is a material known for its complex rheology and segregation behavior. Especially near the wall, a zone depleted of coarse aggregates is found – the lubrication layer. The mechanism for the formation of the lubrication layer depends on hydrodynamic effects as well as on the particle/particle interactions.

An apparatus for the optical investigation of coarse glass particles dispersed in Newtonian and non-Newtonian model liquids was designed to observe the migration. Due to a pneumatic pumping of the suspension, the flow regime can be varied from constant to pulsating. Besides to measurements of the pressure loss during the pumping, the measurement area is optically accessible. The flow in the tube is measured by particle image velocimetry (PIV) and particle tracking velocimetry (PTV). With these techniques it is possible to visualize the velocity field in the near wall region and to track the position of particles.

The results of these measurements should be part of a benchmarking process of numerical simulations. Based on measurements and corresponding numerical simulations, we want to develop a rheological description of the lubrication layer near to the pipe wall.

Keywords: Lubrication layer · Segregation · PIV/PTV · Pumping · Model fluid

1 Introduction

Concrete has been one of the most important building materials for the last 2000 years. It is a highly polydisperse mixture of sand, gravel, cement, water and chemical additives, that can modify the complex rheology and material properties of the system [1–4]. The particle size has a nearly continuous distribution from a few micrometers to more than one centimeter. The transport of concrete is usually realized by using concrete pumps. One of the most common type of pumps for this purpose is a double piston pump, which leads to a pulsating flow regime compared to a uniform pumping as it would be the case for a peristaltic pump [5].

An important process that takes place during the pumping of concrete is the development of a lubrication layer near the tube wall. The polydisperse mixture is segregating and the coarse aggregates (>1 mm) migrate into the center of the tube, while the mortar remains at the wall. This reduces the pumping pressure significantly and allows the transport over longer distances possible. On the contrary, the material

V. Mechtcherine et al. (Eds.): RheoCon 2019/SCC 2019, RILEM Bookseries 23, pp. 596–601, 2020.
https://doi.org/10.1007/978-3-030-22566-7_69

becomes inhomogeneous during this process, which can modify the long term stability and workability of the building material.

The formation of this lubrication layer was analyzed by experimental [6–8] as well as numerical investigations [9]. Choi et al. found with the help of ultra sound velocimetry a thickness of this layer of ca. 2 mm [10]. Furthermore, investigations with PIV in an open channel were carried out by Le et al. They measured the velocity profile near the pipe wall with high accuracy and determined the thickness of the layer to be 2 mm independently of the aggregate size [11].

Nevertheless, the exact mechanism leading to the formation of the lubrication layer is still a topic of recent research. Especially the influence of the pulsating flow rate, as it is found during the pumping with double-piston pumps, is still a pending problem. In this paper, we will present an experimental setup that enables us to investigate optically the motion of the particles during the pumping process. A liquid can be used, which is able to mimic characteristic rheological properties of concrete, like a yield stress and shear thinning behavior. Additionally, the fluids refractive index is matched to the index of borosilica-glass to allow optical access. With this apparatus it should be prospectively possible to investigate the mechanisms leading to formation of the lubrication layer, as well as to describe the velocity fields in the material during the pumping process.

2 Experimental Setup

The experimental setup for the optical investigation of the lubrication layer, as well as the liquid used to model the concrete, has to match a large variety of demands. The tube for the measurement must be transparent, so that the camera can observe the near-wall layer and the processes in it. Furthermore, the fluid needs to be pumped in a way that can mimic typical pumping regimes, that means with a pulsating flow rate as well as with linear

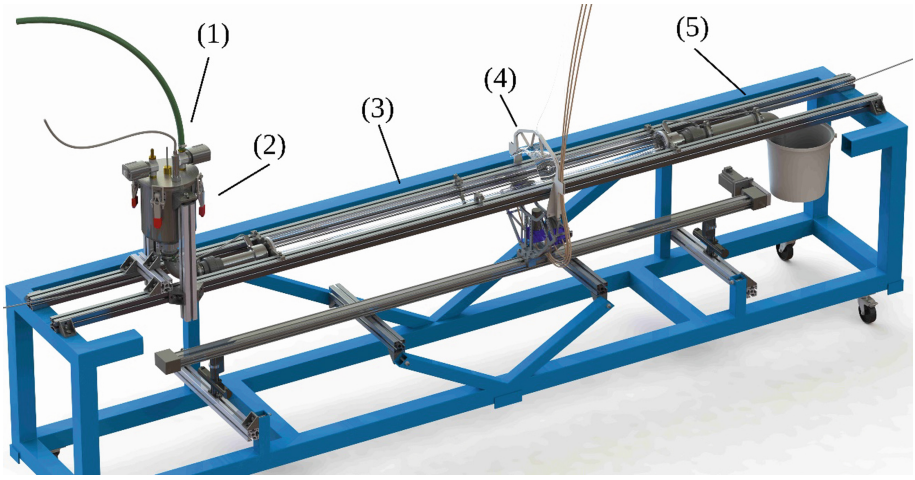

Fig. 1. CAD-Modell of the experimental setup for the optical investigation of particles during the pumping process. (1) Pressure supply (2) Liquid storage vessel (3) Transparent measurement pipe (4) Movable camera positioning system (5) Outlet.

pumping. The pumping of a suspension of coarse particles is a demanding task, since the usage of classical valves is not possible, because of the blockage of the mechanical components. Furthermore, the usage of a piston in the granular material can lead to abrasion and damaging of the pumping aggregate. A simple approach for that is the usage of a pneumatic pumping system. In this way we can avoid the usage of a piston, and modify the pumping velocity by modifying the pumping pressure. The final setup is shown in Fig. 1.

The key parts of this experiments are the storage vessel that can be pressurized by using four magnetic valves and the measurement pipe made of glass. The modulation of the pumping pressure can be used to realize either a linear or a pulsating pumping regime by using a constant pressure or a sinusoidal pressure curve, respectively. The liquid is accelerated due to the pressure difference between inlet and outlet. Three pressure sensors are installed in the system (M11 sensor from WIKA), one for the pressure regulation in the reservoir, one at the inlet of the measurement tube and one at the end. This gives us the possibility to investigate the pressure loss during the material transport.

Two mvBlueCOUGAR-XD BC-XD104G cameras from MATRIX VISION GmbH were installed at a movable carriage driven by an IGUS linear motor, as well as two LEDs opposed to the lenses for transmitted light photography. By making the camera system movable, we can reduce the relative velocity between the particles and the optical system. This reduces the image frame rate needed for a higher time resolution in the PIV measurements.

The observation of particles near the tube wall is difficult due to distortions of the curved interface. For this reason, the glass tube is installed in an octagon-shaped outer pipe that is filled with glycerin. Thus, the cameras observe the flow through a borosilicate glass tube that matches the refractive index of glycerin. Hence, the distortions of the spherical pipe are reduced and the fluid is observable.

The liquid should model concrete and its basic rheological properties. Furthermore it needs to contain particles, which represent the coarse aggregates. To use the technique of particle image velocimetry (PIV) inside a tube filled with a suspension, it is significant to match the refractive index of the fluid, the aggregates, the tube and every other material between the location to be investigated and the camera system. The key challenge is here to find a non-Newtonian liquid, that's refractive index n_D can be matched to borosilicate glass ($n_D = 1.4730$) and retains the rheological properties needed. As aggregates, spherical borosilicate particles of 1 mm diameter (Schäfer Glas) are used. These particles are made from the same material like the glass tube and have thus nearly the same refractive index. As fluid, a mixture of 3% Carbomer (Carbopol ETD 2050 Polymer, Lubrizol), 40% Saccharose and water is prepared to obtain a highly viscous gel that models the mortar content of the liquid. The refractive index of this gel is matched to the glass beads with Thio-Diethanol (95%, Sigma Aldrich). First measurements were also possible with the pure Newtonian fluid glycerin. Using this liquid, it is possible to analyze the particle movement without the influence of the complex, non-Newtonian behavior. The results obtained in that way will be compared to the particle movement and velocity fields in a concrete-like suspension as described above.

The pictures taken during the measurement are post-processed with the *Davis* software from LaVision [12] for PIV. Using the cross-correlation between a series of pictures, the velocity field near the wall is obtained. In the central part of the tube, it is not possible to get such a field due to the overlapping motion of the not completely transparent particles.

Inhomogeneity's of the glass hinder the simultaneous match of all particles. For a determination of the velocity field in the pipe center, the apparatus has to be modified to use the light-sheet method. This could help to diminish the reduced depth of field.

PTV will be simplified by adding larger, black particles of 2 mm diameter. The position of these can be tracked easily by an appropriate software like *trackpy* [13]. Since the particle diameter is known, the software is able to find the large tracers selectively and reconstruct the particle trajectory.

3 Results

In the following section, the results of a typical measurement in a purely Newtonian liquid (Glycerin 97%) with 30% glass beads of 1 mm diameter will be presented. Additionally, a few 2 mm glass beads in black are added for a simplified PTV-measurement. For the investigations, the pressure in the reservoir p_0 is increased linearly until an absolute pressure of 2 bar is reached in the inlet vessel. The measurement is started by rapidly opening the outlet valve. After that, the suspension is free to flow through the pipe.

The pressure is afterwards modulated with a sinusoidal function of 2 Hz and an amplitude of 0.2 bar to mimic the pulsating pumping with a double piston pump. After ca. 3 s, the initial transient time is over and the optical measurement is started. The pressure loss Δp is recorded during the whole measurement time. Starting with the first pressure pulse, the movement of the carriage is started with a constant velocity of 0.2 m/s. The velocity needed for the specific setup is determined by a preliminary test with a stationary carriage position. The liquid is observed during the pulsation with two cameras and an image frame rate of 100 Hz.

A measurement of Δp is shown in Fig. 2. The pressure pulsation is clearly visible in the system. Hereby the pressure loss follows immediately the pressure pulsation in the inlet vessel p_0. A pneumatic pumping of the granular material is thus possible, and able to mimic the behavior of a double piston pump.

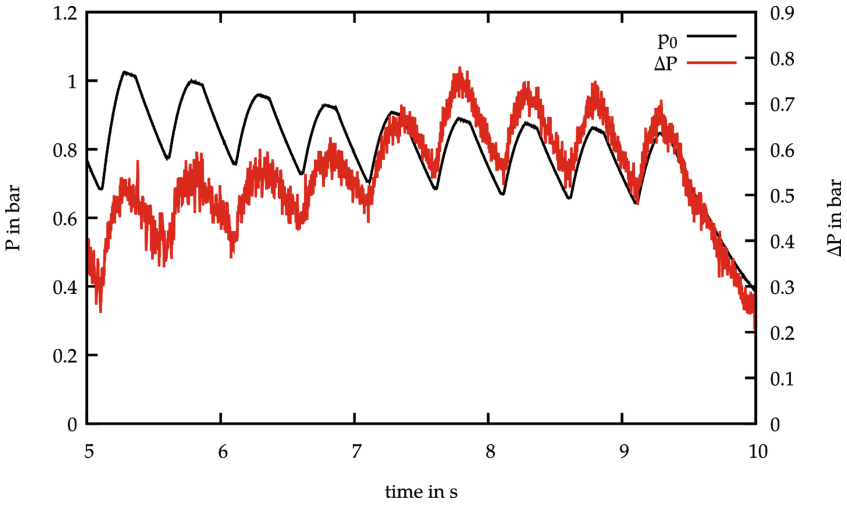

Fig. 2. Pressure in the inlet vessel p_0 and pressure loss Δp during the measurement.

A typical picture of the camera obtained during an experiment is shown in Fig. 3a. The pipe boundary is visible at the bottom and the top. Furthermore, the larger tracking particles for the PTV are shown with their position detected automatically by *trackpy*. This is possible for particles in the tube center and at the wall. The velocity in the center of the tube can be estimated by analysing the trajectory of the larger particles. In the case shown, a velocity of 0.18 m/s is determined under the assumption that the black particles are inside of the pulg flow. The particle position is determined for every snapshot. In the upper and lower part of the tube, the small 1 mm particles are distinguishable. In the center of the tube, this is not possible, since the opacity hinders the reliable identification of single particles. The small particles can be used to derive the velocity field near the wall by using PIV as shown in Fig. 3b. Since only data for the particles at the wall are processable, the data for the bulk flow is not shown here. The velocity field was calculated as statistical average of a large number of snapshots. For the purpose of visualization, a typical snapshot used for the PIV was underlayed. In contrast to PIV measurements in air, where the scattered light of small particles is detected, and a few tracer particles have to be in the interrogation window, the information content in the measurements shown here is much larger. The edges of the glass beads give ample information for the cross correlation algorithm, so that the interrogation window can be much smaller than the glass beads.

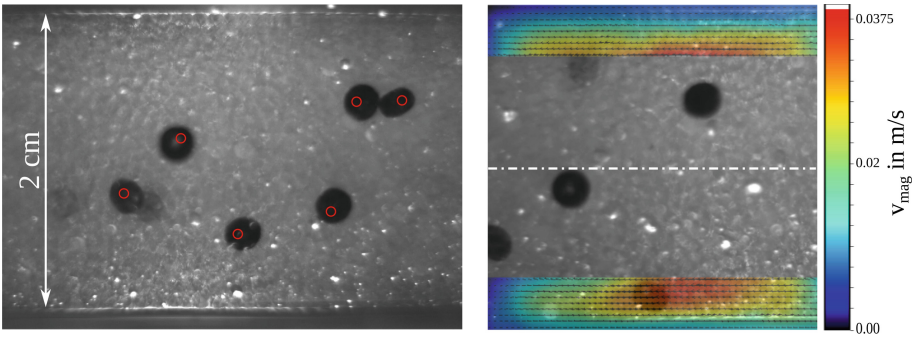

Fig. 3. Typical snapshots taken from a measurement at different times for (a) Tracking of black particles of 2 mm diameter and automatically detected positions by the trackpy software (b) Mean velocity field in the near wall area from the PIV data determined by the DAVIS software.

4 Conclusion

In this study we present an apparatus for the optical measurement of the particle motion in highly concentrated suspensions. With this, it was possible to pump the liquid pneumatically in a manner similar to the pumping of concrete with a double-piston pump. Additionally, it was possible to detect the pressure loss in the measurement-pipe during the experiment. By using a linear motor for moving the cameras during the fluid

motion, it was possible to reduce the relative velocity of the optical systems and the particles in the suspension. Thus, a lower frame rate was needed for the investigations.

Pictures taken by two cameras were used to investigate the flow field in the pipe near the wall and for the tracking of particles. The automatic detection and tracking of black particles is even in highly concentrated suspensions possible. The exact trajectory will be helpful in further studies to understand the migration of particles. Hence, the movement of coarse aggregates can be visualized under similar conditions like during the pumping of concrete. Furthermore, the analysis of the velocity field near the wall is possible, although the quality of the pictures and the illumination has to be further improved for more reliable data, which is part of ongoing work.

Acknowledgement. The authors would like to thank the German Research Foundation (DFG) for supporting the scientific work in terms of the Priority Programme "Opus Fluidum Futurum – Rheology of the reactive, multiscale, multiphase construction materials" (SPP2005, Subproject "Rheology of the lubrication layer based on a two-phase liquid-granular flow approach") Moreover, the authors thank Martin Botsch for his work on the construction and development of the measurement system.

References

1. Mai C, Kadri E, Ngo T, Kaci A, Riche M (2014) Estimation of the pumping pressure form concrete composition based on the identified tribological parameters. Adv Mater Sci Eng 2014:1–18
2. Camiletti J, Soliman AM, Nehdi ML (2013) Effects of nano- and micro-limestone addition on early-age properties of ultra-high-performance concrete. Mater Struct 46:881–898
3. Kwon S, Jang K, Kim J, Shah S (2016) State of the art on prediction of concrete pumping. Int J Concr Struct M 10:75–85
4. Yammine J, Chaouche M, Guerinet M, Moranville M, Roussel N (2008) From ordinary rhelogy concrete to self compacting concrete: a transition between frictional and hydrodynamic interactions. Cem Concr Res 38:890–896
5. Binns T (2003) Pumped concrete. In: Newman J, Choo BS (eds) Advanced concrete technology, pp 15/1–15/33. Butterworth-Heinemann
6. Choi MS, Kim YJ, Kim JK (2014) Prediction of concrete pumping using various rheological models. Int J Concr Struct Mater 8:269–278
7. Feys D, De Schutter G, Verhoeven R (2013) Parameters influencing pressure during pumping of self-compacting concrete. Mater Struct 46:533–555
8. Secrieru E, Khodor J, Schröfl C, Mechtcherine V (2018) Formation of lubricating layer and flow type during pumping of cement-based materials. Constr Build Mater 178:507–517
9. Jo SD, Park CK, Jeong JH, Lee SH, Kwon SH (2011) A computational approach to estimating a lubricating layer in concrete pumping. CMC-Comput Mater Con 27:189–210
10. Choi M, Roussel N, Kim Y, Kim J (2013) Lubrication layer properties during concrete pumping. Cem Concr Res 45:69–78
11. Le HD, Kadri EH, Aggoun S, Vierende J, Troch P, De Schutter G (2015) Effect of lubrication layer on velocity profile of concrete in a pumping pipe. Mater Struct 48:3991–4003
12. Davis. https://www.lavision.de/en/products/davis-software/
13. Allan D, Caswell T, Keim N, van der Wel C (2016) Trackpy V0.4.1 Zenodo. http://doi.org/10.5281/zenodo.1226458

Synthesis and Analysis of Spherical Cementitious Model Particles

Dimitri Ivanov[1(✉)], Simon Becker[2], Zichen Lu[3], Mahmoud Eslami Pirharati[4], Arno Kwade[1], Hans-W. Krauss[4], Dietmar Stephan[3], Regine von Klitzing[2], and Carsten Schilde[1]

[1] Institute for Particle Technology, TU Braunschweig, Brunswick, Germany
d.ivanov@tu-braunschweig.de
[2] Soft Matter at Interfaces, TU Darmstadt, Darmstadt, Germany
[3] Institute for Building Materials and Construction Chemistry, TU Berlin, Berlin, Germany
[4] Institute of Building Materials, Concrete Construction and Fire Safety, TU Braunschweig, Brunswick, Germany

Abstract. A new model system of spray dried particles was developed for the characterization of cementitious materials by Colloidal Probe Atomic Force Microscopy (CP-AFM). Prior to the current work it was not feasible to use CP-AFM with cementitious materials due to their inhomogeneous nature and non-sphericity. With the help of spray drying, it is possible to produce spherical and homogeneous particles with different roughness. Ordinary Portland Cement (OPC) is the examined material in this work.

The model particles are produced in multiple steps. First, the original OPC particles are sieved and nano-ground in ethanol using a planetary ball-mill. After spray drying the cementitious nanosuspension, the chemical composition of the model particles' surface as well as the bulk chemical composition are determined using X-ray Photoelectron Spectroscopy (XPS) and X-ray fluorescence measurements (XRF). Furthermore, the shape, size and roughness of the spray dried particles are estimated by Scanning Electron Microscopy (SEM) and laser diffraction analysis. Finally, first CP-AFM measurements are performed to access the interaction forces between the model particles in ethanol.

The experimental results show that the median primary particle sizes produced by nano-grinding are below 200 nm while the diameter of the spray dried particles are in the range of 10 µm. Furthermore, the results show that particles produced from OPC seem to have a lower content in calcium oxide (CaO) at the surface regions compared to the bulk cement. Possible reasons for these findings are discussed.

Keywords: Spray drying · Colloidal probe AFM · Portland cement

1 Introduction

The rheology of cement pastes and concrete is highly influenced by interparticle forces like van der Walls attraction or electrostatic repulsion. Colloidal Probe Atomic Force Microscopy (CP-AFM) is suitable for determining these forces. For CP-AFM round

V. Mechtcherine et al. (Eds.): RheoCon 2019/SCC 2019, RILEM Bookseries 23, pp. 602–609, 2020.
https://doi.org/10.1007/978-3-030-22566-7_70

particles are required to achieve reliable precision of measurements. Therefore, it is basically impossible to measure the long-range forces of cementitious materials because of the inhomogeneous nature of the original particles. To solve this challenge, spherical cement particles have to be produced. The first approach was made by [1] with a dry impact blending method described in [2]. However, the blended particles do not exhibit proper sphericity for reliable CP-AFM measurements. In this work spray drying is introduced as a suitable method to produce spherical particles feasible for CP-AFM. The spray dried particles are further called model particles.

Figure 1 depicts the original OPC and the corresponding model particles in Scanning Electron Microscopy (SEM) images. Obviously, the OPC particles exhibit a marked non-sphericity and a high roughness.

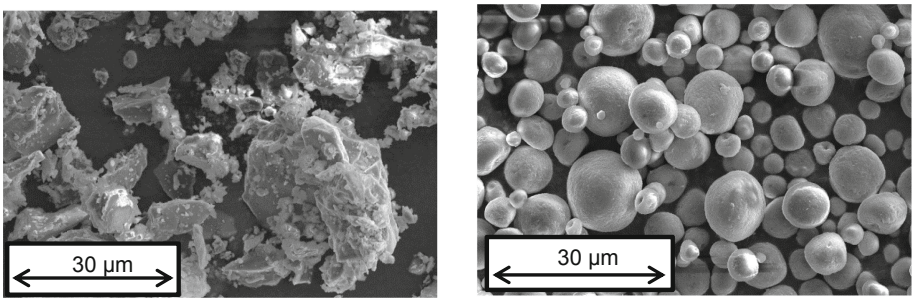

Fig. 1. SEM images of (a) original OPC (b) model particles.

2 Necessary Steps for the Production of Model Particles

The steps for the production of the model particles is to sieve the OPC, then to grind it with ethanol before spray drying. All the described steps are shown in Fig. 2.

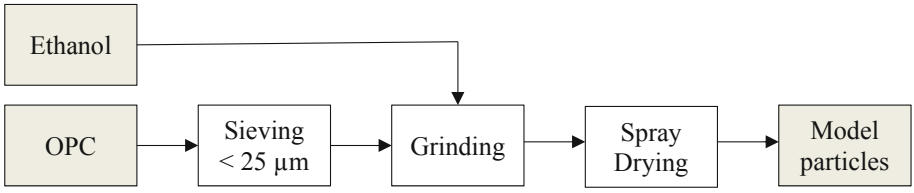

Fig. 2. Process chain for the production of spherical model particles.

For the production of the model particles, in the first step the original OPC particles are sieved through a 25 µm sieve to avoid a coarse particle fraction which cannot be ground to nanometre sized particles at the given stress energies of the small grinding media, which are used in the grinding experiments to realize high stress number.

The sieved material is then dispersed within ethanol as a solvent phase and ground up to 22 h in a planetary ball-mill using a x_{50} of 315 µm grinding media until achieving median primary particle sizes below 200 nm. The particle size was adjusted by varying the grinding time. Hereby, the primary particle size determines the roughness of the final spray dried particles.

Finally, the nanometre sized primary particles suspended in ethanol are spray dried via a co-current spray dryer (Procept). A bi-fluid nozzle is used to atomise the liquid into small droplets with a narrow droplet size distribution. Then these droplets are dried by the surrounding air stream. While the droplets' size is being reduced due to evaporation of the ethanol the primary particles are compacting until they form dense packed agglomerates due to low attractive interparticle interaction forces within the ethanol phase.

In this work the primary particle suspension has a solid content of 5% and the used nozzle has a diameter of 0.6 mm. The critical process parameter is the drying temperature. The higher the temperature the faster the ethanol evaporates in non-spherical model particles. Thus, in this work the suspension is spray dried at a minimum temperature of 60 °C where an entire evaporation of the solvent can be guaranteed.

3 Characterization of Model Particles

In Fig. 3 the corresponding particle size distribution (PSD) of the original OPC (a), the model particles (b) and the ground cement of two different batches (c, d) are given.

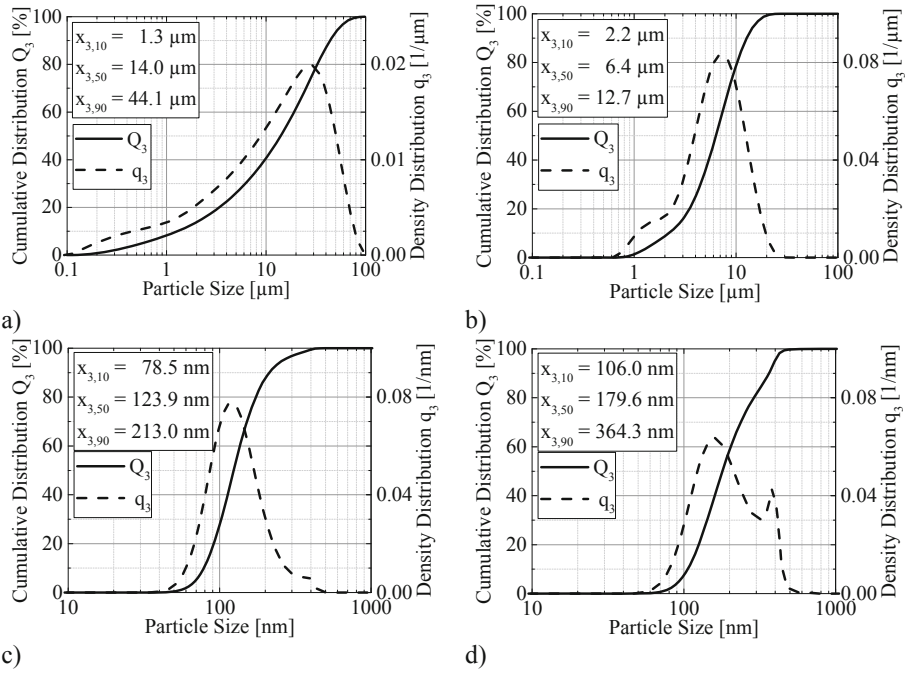

Fig. 3. PSD of (a) the original OPC (b) the model particles (c) the ground cement (d) the ground cement second batch.

For the measurement of the PSD a laser diffraction device was used (MasterSizer 3000) for the original OPC and the model particles and a dynamic light scattering device (Nanophox) for the ground primary particles. Different devices were used due to different limitations of the accessibility of the particle size. The grinding process reduces the particle size by a factor of 100. Furthermore, the distribution is narrower which is a common effect of small grinding media and long grinding times [3]. The PSD of the model particles is narrower than the pre-sieved OPC, which facilitates CP-AFM measurements because it is easier to find particles of the same size.

Larger ground primary particles result in an increased surface roughness of the model particles, as proven by the SEM images in Fig. 4. In Fig. 4 (a) the x_{50} of the ground primary particles is around 124 nm while the x_{50} of the primary particles of the rougher model particles in Fig. 4 (b) is at around 180 nm. The different roughness is an important parameter for a systematic characterization of the particle interaction forces between cementitious particles using CP-AFM.

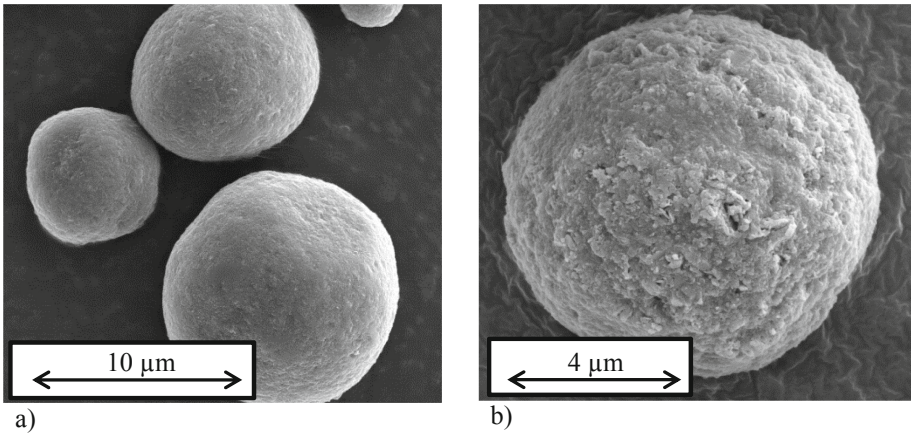

Fig. 4. (a) Smooth model particles ($x_{50,primary}$ = 124 nm) (b) Rough model particles ($x_{50,primary}$ = 180 nm).

It was observed that while OPC particles are grey, the model particles have a dark yellow colour. One of the possible reasons for this discrepancy could be a different chemical composition. Therefore, X-ray fluorescence (XRF) measurements were conducted to get the spectrum of the complete OPC. For the characterization of the model particles only measurement of the surface composition was necessary to support AFM experiments, which basically determine the surface forces between two particles. Therefore, the model particles were additionally characterized with X-Ray Photoelectron Spectroscopy XPS, whereby only several nanometres of the particles surface are penetrated [4]. The results from both methods are given in Table 1.

The results indicate that the model particles consist of less Calcium oxide (CaO) and more Silicon dioxide (SiO_2) at the particle surface than the bulk of original material.

One reason for this effect could be the sieving process. Possibly the coarser cement particles have a higher content in CaO than smaller ones, resulting in a lower Calcium content of the fine-grained sieved material. However, additional Energy Dispersive X-Ray Spectroscopy (EDS) measurements have shown that there is no significant difference between the chemical composition of the original OPC and the sieved OPC. Furthermore, the sieved material has the same colour as the original OPC.

Another reason could be the different grindablity of CaO and SiO_2 rich particles or different reagglomeration tendencies during or after the grinding process. As a consequence, a segregation during the spray drying process could lead to a core shell structure with primary particles of different chemical compositions, due to the fact that coarser primary particles assemble in the core of the model particles while the smaller particles accumulate preferentially in the outer shell [5].

Table 1. Chemical composition of the OPC and the model particles.

Oxide	OPC with measured with XRF	Model particles measured with XPS
CaO	64.78%	49.26%
SiO_2	20.40%	33.67%
Al_2O_3	5.28%	12.34%
Fe_2O_3	2.63%	0.39%
MgO	1.40%	0.00%
SO_3	2.42%	4.34%

4 Colloidal Probe Atomic Force Microscopy (CP-AFM)

For CP-AFM measurements the spray dried OPC particles have been attached to a tipless cantilever (HQ:CSC38:tipless Cr-Au from MikroMasch©) with an epoxy resin (UHU© Endfest, hardening time > 24 h) and with help of a motorized micromanipulator (MP-225, Sutter Instrument Company) for positioning. The cantilever with the attached colloidal probe is shown in Fig. 5. The force constant of the cantilever has been determined using the Sader method [6] yielding a value of k = 15.3 pN/nm.

The silicon (SK Siltron Co. Ltd. Korea) waver has been etched for 30 min in piranha solution containing equal volumes of sulfuric acid (96%, Carl Roth) and hydrogen peroxide (30%, Carl Roth). Before the measurements the wafer has been cleaned for 20 min by an air plasma (Femto, Diener electrectronic).

The AFM measurements for the spray dried particles have been carried out in the PEEK Fluid Cell with a PEEK cantilever holder. The forces have been measured between the silicon waver and the spray dried OPC particle in absolute ethanol (Emsure ®, Merck, Darmstadt) with an approach speed of 200 nm/s. The force curves have been calculated by assuming the constant compliance region from 100 nm–200 nm (of Z-sensor movement) from the onset of the force. The transformation from deflection and z-sensor to force and separation has been done using the algorithm described for example by Senden [7].

In first measurements it could be shown that it is possible to measure forces of the model particles in non-aqueous solutions, i.e. ethanol. Immobilizing the cement particle at the cantilever worked out and the probe stayed fixed at the cantilever during the measurements, i.e. it did not detach from the cantilever.

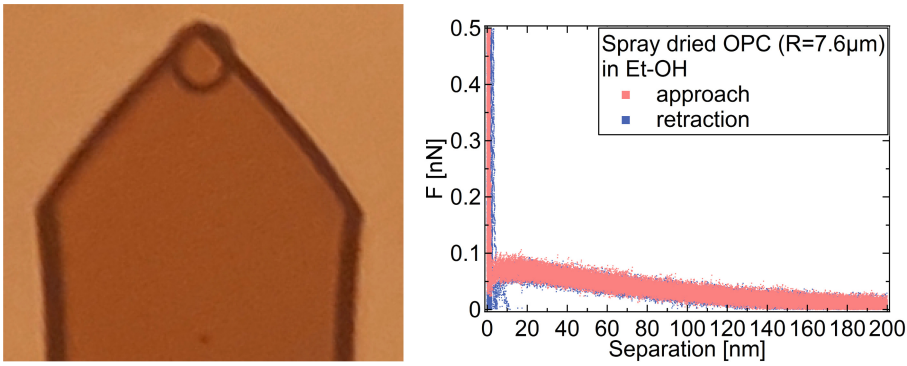

a) b)

Fig. 5. (a) Cantilever with glued spray dried OPC particle attached to the end of the tip. Lightmicroscope image looking through the cantilever from below. (b) Force vs. Separation for spray dried OPC in pure ethanol. At least 25 force curves overlaying are shown for each approach and retraction.

The force curves for approach and retraction are depicted in Fig. 5(b). The interaction forces between the particle and the planar surface are small at large distances but show an exponential increase when approaching. The increase can be fitted by an exponential function up to 20 nm of separation yielding a decay length of approximately 90 nm.

If the system is considered as a charged sphere and a charged surface which interact across an electrolyte the Debye length is given by

$$\kappa^{-1} = \sqrt{\frac{\varepsilon_0 \varepsilon_r k_B T}{e^2 N_A I}}$$

with the vacuum permittivity ε_0, the relative permittivity ε_r, the Boltzmann constant k_B, the absolute temperature T, the elementary charge e, Avogadro's constant N_A and the ionic strength I in mol/m^3.

Therefore, the decay length of 90 nm for this system is in the order of magnitude of the Debye length for the interaction of a silica colloidal probe and a silicon wafer in pure water (pH 5, Debye length about 100 nm). This silica-silicon system is the *drosophila* for colloidal probe AFM measurements.

Following this argumentation, since the dielectric constant of ethanol is about factor three smaller than the one of water the, Debye length in ethanol should be by factor $\sqrt{3}$ smaller than in water. However, the ionic strength in ethanol is unknown.

Since the OPC particles are patchy particles consisting of different charged domains the net charge depends on the concentration of each phase. One would expect that due to an averaging of the charge the net charge of the OPC particle is lower than for a typical silica probe. According to the microscope image and the given width of the cantilever of 32.5 µm the diameter of the spray dried particle is estimated to 5.5 µm–7.6 µm. Comparing F/R to typical values for silica system shows a force which is by one order of magnitude lower than comparable silica systems [8].

5 Summary and Conclusion

In this work spherical cement model particles were produced from original OPC by spray drying for the purpose of measuring the forces between cementitious materials with CP-AFM. This approach has the advantage, that spherical and smooth model particles can be produced from the inhomogeneous and non-spherical cementitious materials, which will help gaining further knowledge of the rheology of cementitious pastes by improving and hence developing improved rheological models for cementitious materials. Furthermore, this method can be used to calibrate the long-range forces in numerical simulations. Before the spay drying process the cement was sieved and ground to nanometre size. It was demonstrated, that by this method, model particles with different roughness can be produced.

A challenge is the segregation of primary particles of different size possibly resulting in varying surface compositions which do not fully represent the original material. This aspect needs further investigation. One possible solution could be coating of silica beads with primary particles, giving the advantage that segregation effects would be largely reduced or excluded.

Further investigations will include the production of model particles from pure clinker and the individual clinker phases to further investigate the interparticle forces acting between cementitious materials. Further investigations on the statistics of the interparticle forces for different OPC particles will be carried out. Moreover, the particle interactions in ethanol systems with a defined amount of salt have to be done for the comparison with well-known systems.

Acknowledgment. The authors gratefully acknowledge for the financial support by Deutsche Forschungsgemeinschaft within the priority program SPP 2005 “Opus Fluidum Futurum”.

References

1. Tanaka I, Suzuki N, Ono Y, Koishi M (1998) Fluidity of spherical cement and mechanism for creating high fluidity. Cem Concr Res 28:63–74
2. Tanaka I, Koishi M, Shinohara K (2002) A study on the process for formation of spherical cement through an examination of the changes of powder properties and electrical charges of the cement and its constituent materials during surface modification. Cem Concr Res 32:57–64
3. Stadler R, Polke R, Schwedes J, Vock F (1990) Naßmahlung in Rührwerksmühlen. Chem Ing Tech 62:907–915

4. Benko E, Barr TL, Hardcastle S, Hoppe E, Bernasik A, Morgiel J (2001) XPS study of the cBN-TiC system. Ceram Int 27:637–643
5. Zellmer S, Garnweitner G, Breinlinger T, Kraft T, Schilde C (2015) Hierarchical structure formation of nanoparticulate spray-dried composite aggregates. ACS Nano 11:10749–10757
6. Sader J, John E, Chon J, Mulvaney P (1999) Calibration of rectangular atomic force microscope cantilevers. Rev Sci Instrum 70:3967–3969
7. Senden T (2001) Force microscopy and surface interactions. Curr Opin Colloid Interface Sci 6:95–101
8. Ducker W, Senden T, Pashley R (1991) Direct measurement of colloidal forces using atomic force microscope. Nature 353:239–241

Comparison of Water-Isopropanol Replacement and Lyophilisation for Hydration Stop of Cementitious Suspensions

Patrick A. Kißling[1(✉)], Dario Cotardo[3], Tabea von Bronk[3], Ludger Lohaus[3], and Nadja C. Bigall[1,2(✉)]

[1] Institute of Physical Chemistry and Electrochemistry, Leibniz Universität Hannover, Hannover, Germany
{patrick.kissling, nadja.bigall}@pci.uni-hannover.de
[2] Laboratory of Nano and Quantum Engineering, Leibniz Universität Hannover, Hannover, Germany
[3] Institute of Building Materials Science, Leibniz Universität Hannover, Hannover, Germany

Abstract. For modern concrete technology, rheology is crucial for characterizing the properties of fresh concrete on the basis of physically defined parameters. These properties can be influenced by many factors, but have an effect on paste level predominantly. To obtain an understanding of influencing factors such as the underlying kinetics and mechanisms at the initial colloidal scale a time variant analysis of cementitious suspensions is needed. In this article, a method to stop the hydration process of cementitious suspensions at any time by gradual water-isopropanol replacement and lyophilisation is demonstrated. Therefore, three different methods for hydration stop are investigated, namely water-isopropanol exchange, lyophilisation as well as a combination of both, and compared to pristine (non-reacted) cement particles. Analysis of dried samples leads to the observation that direct lyophilisation leads to particles of similar size as the pristine cement particles. Water-isopropanol replacement as well as water-isopropanol exchange with subsequent lyophilisation, instead, leads to a very broad particle size distribution with larger particles, which might be attributed to secondary agglomerations of particles. We further investigate the three different hydration stop methods by evaluating the pore size distribution by means of nitrogen physisorption. Additionally, scanning electron microscopy (SEM) as an imaging method is used.

Keywords: Rheology · Hydration stop · Time variant analysis · Cementitious suspension · Freeze drying/lyophilisation

1 Introduction

For understanding the fundamental processes in modern concrete technology, characterizing the properties of fresh concrete on the basis of physically defined parameters is of utmost importance. For example, rheological properties can be influenced by various factors. Many of them having an effect on paste level predominantly.

V. Mechtcherine et al. (Eds.): RheoCon 2019/SCC 2019, RILEM Bookseries 23, pp. 610–618, 2020.
https://doi.org/10.1007/978-3-030-22566-7_71

Thus, parameter studies are preferably carried out on paste level. Also for reasons of practicability, with particular focus on limiting the test duration and the handling in general, more extensive concrete variations are often performed on paste level and not on concrete level. Nevertheless, concrete remains the real object of reflection of concrete technology. In general, it is the aim to obtain an understanding of influencing factors such as the underlying kinetics and mechanisms at the initial colloidal scale, and later on to transfer these influences to paste, mortar and concrete level. The cross-scale transfer from colloidal suspension to paste, mortar, and concrete is a challenge for concrete technology since it involves several orders of magnitudes on the size scale ranging from nanometres to metres. In order to characterize a colloidal suspension taking into account the hydration process, a time dependent (kinetic) analysis is needed. This scrutiny can be achieved by hydration stop at defined times after adding water to the mixture. The state of the art for such a hydration stop is based on water exchange with organic solvents, mostly isopropanol [1]. However, kinetic aspects of the mixing of isopropanol with the reaction of water should be considered. Alternatively, to get rid of liquid water as quickly as possible freezing at a high rate can be considered. Due to quick freezing in liquid nitrogen N_2(l), vitreous water is formed. Previous works concentrating on biological samples have shown that such vitreous water does not change the sample's morphology [2, 3] and can easily be evaporated by subsequent lyophilisation [3]. The motive for this procedure was, that after this freeze-type quenching the structural analysis of the dried system can be performed with relatively slow analytic methods, such as N_2-physisorption and X–ray diffraction (XRD). In addition, imaging methods such as scanning electron microscopy (SEM) and transmission electron microscopy (TEM) can be employed. The present article focuses on the question, whether the properties of dried suspensions after water-isopropanol replacement are comparable to the properties of freeze-dried suspensions. The second focus lies on finding the most sensitive method for hydration stop of cementitious suspensions.

2 Experimental

2.1 Chemicals

CEM I 42.5 R from HeidelbergCement AG was stored at ambient temperature (20 °C ± 2 °C) and humidity (18%–45%). Anhydrous isopropanol ($\geq$ 99.95%) and anhydrous copper sulphate ($\geq$ 98%) from Carl Roth, Millipore water (18.2 MΩ*cm) cleaned by Arium 611DI from Sartorius and liquid nitrogen ($\geq$ 99.999%) from Linde were used.

2.2 Cementitious Suspensions and Mixing Program

Following the mixing program shown in Table 1, 610 g CEM I 42.5 R and 305 g Millipore water – precooled to 10 °C – was mixed with a balloon whisk using a Kenwood KitchenAid KM336 S Chef Classic to simulate concrete mixing as usually performed at larger scales. During the first ten minutes, the mixture's temperature rose

to 20 °C. The last step of slow stirring at level 2 (approx. 72 rpm) was performed for different times (6, 26, 56, and 86 min) in order to investigate the reaction kinetic. All dried samples were stored at 19.2 °C ± 0.4 °C in a dry nitrogen atmosphere for 0 to 2 days before any characterization method.

2.3 Procedure for Freeze-Dried Samples

After a total reaction duration of 10 min, 30 min, 60 min, and 90 min after adding water (related to slow stirring at level 2 for 6 min, 26 min, 56 min, and 86 min, respectively), 10 mL of the cementitious suspension were taken with an Eppendorf pipette and instantly dropped into N_2(l) (approx. 100 mL in a precooled flask for approx. 20 min). Each sample was freeze-dried using an Alpha 1-2 LDplus from Christ for 36 h at $1.5 \cdot 10^{-2}$ mbar.

2.4 Procedure for Water-Isopropanol Replaced Samples

10, 30, 60 and 90 min after adding water to the mixture, 10 mL of the cementitious suspension were taken with an Eppendorf pipette, instantly dropped into 50 mL anhydrous isopropanol and stirred for 10 min at 50 rpm with a magnetic stirrer. Afterwards using a Buchner funnel the water-isopropanol suspension was filtrated (mesh size 4 µm to 12 µm). The sample was washed three times by adding 10 mL isopropanol. Approximately half of each (humid) sample was taken and dropped into N_2(l) (approx. 100 mL in a precooled flask for approx. 20 min). Each sample was freeze-dried using an Alpha 1-2 LDplus from Christ for 36 h at $1.5 \cdot 10^{-2}$ mbar. The other half was stored under ambient conditions (19.2 °C ± 0.4 °C) for 36 h. To exclude an impact of the big mesh size on the particle size distribution, the experiment was repeated using a smaller filter (mesh size 0.1 µm); no changes to the size distribution were observed. Secondly, in all cases the filtrate was not turbid. Therefore, particles smaller than 1 µm can be excluded.

Table 1. Mixing program for cementitious suspensions.

Type	Duration	Mode (Kenwood KitchenAid) [rpm]
Dry mixing of CEM I	60 s	Level 2 [approx. 72]
Adding water	30 s	Level 2 [approx. 72]
Pre-homogenisation	15 s	Level 2 [approx. 72]
Homogenisation	15 s	Level maximum [approx. 220]
Stop and sting manually	60 s	Off
Homogenisation II	120 s	Level maximum [approx. 220]
Slow stirring	Until stopped	Level 2 [approx. 72]

2.5 Characterization

Nitrogen (N_2)-physisorption was performed at a NOVA 3000 from Quantachrome operating at 77 K. Prior to physisorption measurements, the samples were degassed under vacuum at 298 K for 24 h. Specific surface areas and volumes were estimated by applying the Brunauer-Emmett-Teller (BET) [4] equation, pore volumina at $p/p_0 = 0.95345$ respectively by applying Density Functional Theory (DFT) [5, 6] as well as pore size distributions by applying Barrett-Joyner-Halenda (BJH) [7].

The morphologies of the dried samples were investigated by scanning electron microscopy (SEM) using a JOEL JSM 6700F, equipped with a cold field emission gun electron source. The acceleration voltage was 2 kV for each measurement. The powder was dropped on a sticky carbon patty. Excess of powder was blown away by a compressed air gun and a conductive carbon layer was sputtered.

By evaluation of eight SEM pictures at a magnification of 1000 times with ImageJ 1.52a, for each sample, a particle size distribution was determined.

The anhydrousity of the samples was tested by adding anhydrous copper sulphate to small amounts of the samples (colour change to blue for humid samples).

3 Results and Discussion

Following the mixing program shown in Table 1, cementitious suspensions were mixed with a water to cement mass ratio of *w/c* = 0.5 and the hydration process was stopped at four defined times. The hydration stop was induced either by lyophilisation after freezing in N_2(l) (**L**), or by a water-isopropanol exchange (**I**), or last by a gradual water-isopropanol replacement combined with freezing in N_2(l) and lyophilisation (**IL**). This allows analysing the suspension with N_2-physisorption and SEM in order to evaluate the influence of the hydration process and the used hydration stop method on changes to morphology, porosity and crystal phases.

In order to rate the possibility of further hydration processes after drying, a copper sulphate test was conducted. This test showed, that in case of isopropanol exchange (**I**), residual water was present, while methods involving lyophilisation (**L** and **IL**) yielded totally dry samples. Consequently, in the latter two cases further growth (after employing the hydration stop method) can be excluded, while in case of **I** hydration reactions might still occur.

Therefore, to get a quick overview about the expected changes of porosity due to hydration, the nitrogen ad- and desorption behavior was examined. The evaluation of the isotherms shows a small hysteresis, which varies at its width for the three different methods (Fig. 1a) used. The broadest hysteresis appears by using the gradual **IL** method. This effect is especially pronounced after a reaction time of 60 min (Fig. 1b).

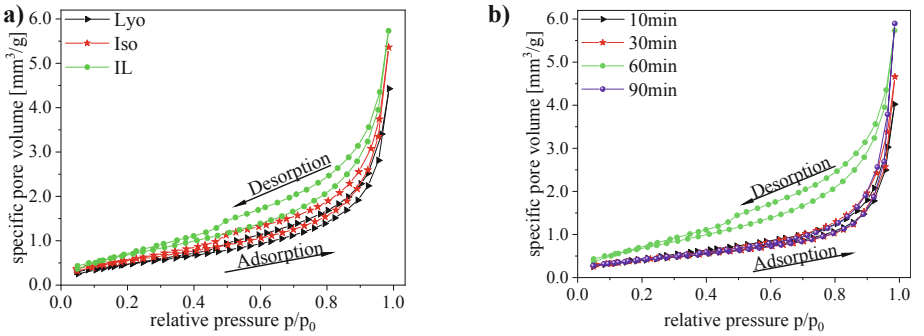

Fig. 1. N_2-physisorption measurement for comparison of isotherms of (**a**) hydrated CEM I stopped at 60 min and (**b**) time dependent comparison of method **IL**.

The N_2-physisorption measurements show also that independent of the used hydration stop method during the reaction the specific surface area (**SSA**) as well as the specific volume (**SV**) of the cement paste rises and drops after a maximum at 60 min (Fig. 2). These findings can be explained by looking at the reaction's course. During hydration, early hydration products were formed on the surface of the cement particles, which leads to an increase of the **SSA**. It can be assumed that this process is more dominant than the agglomeration of the cement particles, which occurs simultaneously during the reaction. A possible reason for this effect could be the reduced hydration kinetics at the dormant stage, which has been reported to be between 30 and 90 min [8]. A possible reason for the decay of the **SSA** and **SV**, hypothetically, is that the early hydration products on the surface had no more open surface to grow on, which resulted in a growing together into a layer, leading to a decreased specific surface area.

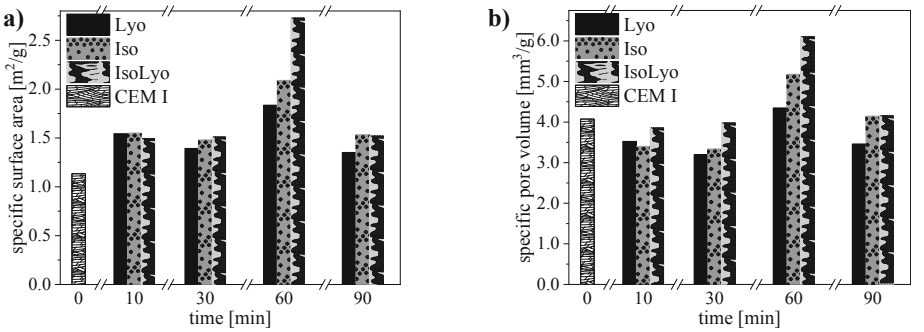

Fig. 2. N_2-physisorption; (**a**) specific surface area and (**b**) specific volume of raw and hydrated CEM I; hydration stopped at four times by three methods (**L, I & IL**).

The pore size distribution (**PSD**) after 60 min reaction time, derived from N_2-physisorption measurements is shown in Fig. 3. Compared to the starting material CEM I, with a mean pore size d_{50} = 4.89 nm ± 0.12 nm, the **PSD** after hydration becomes broader with a shift of the mean pore size to d_{50} = 5.77 nm ± 0.12 nm.

The broadening can be explained by the presence of various hydration products leading to a larger surface roughness and hence to both a larger **SSA** and a larger amount of small pores. This find derives from the agglomeration of cement particles during the dormant phase of the hydration process. In this period the surface is passivated [8] leading to usage of inner material for incorporating water into the crystal structure and respectively to bigger pore sizes.

For the sake of clarity, we note that the shown **PSD** cannot directly be transferred to mortar, as it is most likely that the drying leads to different pore sizes compared to mortar. The reason is that during the first hours no robust structure building occurs, which in turn conserves the pore structure during treating the sample.

Despite the slight differences discussed in the previous paragraphs, it can be derived that (as after 60 min) the change of pores in the nanometre range along with the change of surface area is of the same order of magnitude for all three hydration stop techniques. This is an indication that all three methods indeed lead to a reaction stop. This result is supported by SEM images. Here, at higher magnifications (see Fig. 4 bottom), grains or particles of similar morphology on the sub-micron range can be found on the larger particles in all three cases. The presence of these grains, which is likely to result in a nanoscopic **PSD** (Fig. 3), is much less pronounced for the pristine sample (**CEM I**).

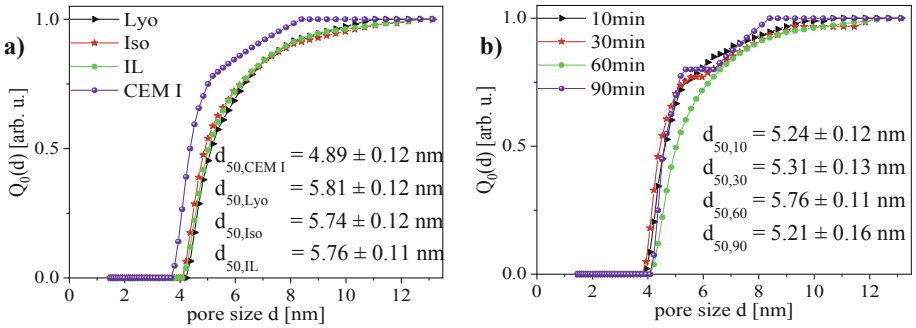

Fig. 3. N_2-physisorption; pore size distribution of (**a**) hydrated CEM I stopped at 60 min compared to non-hydrated CEM I and (**b**) time dependent comparison of method **IL**.

At lower magnification (Fig. 4 top), however, SEM analysis reveals significant differences in the sizes of larger particles. The results are quantitatively analysed by particle size distribution from these samples, see Fig. 5. The size distributions of the pristine sample (**CEM I**) and the lyophilised sample (**L**) are similar. Instead, samples treated with isopropanol (**I** and **IL**) have larger particle sizes. Since the larger particles are likely to be agglomerations of smaller particles, there are two possible ways to interpret the strong difference in results upon adding or not adding isopropanol:

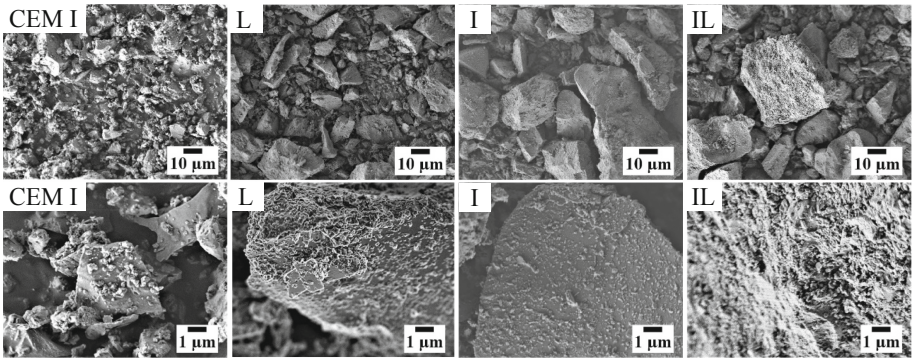

Fig. 4. SEM pictures of raw (**CEM I**) and hydrated cement; hydration stopped at 60 min by three different methods (**L, I & IL**); top row shows 1.000 times magnification and bottom row 10.000 times.

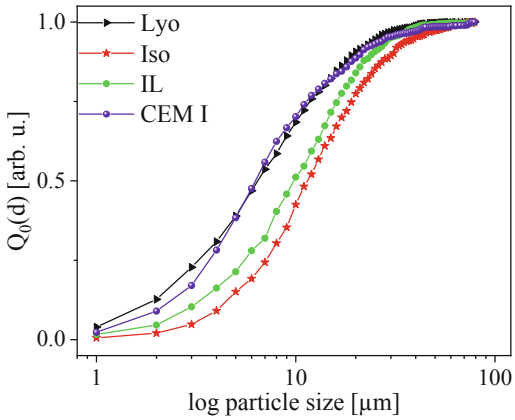

Fig. 5. Particle size distribution of hydrated CEM I stopped at 60 min using **Iso**, **Lyo** and **IL** compared to non-hydrated CEM I at low magnification.

(1) In the lyophilisation method, likely during the freezing of the sample, particles (especially the larger, agglomerated ones) are prone to shear forces, which leads to destroying of the agglomerates. If vitreous ice is indeed formed, however, this effect is unlikely to occur, since in this case no ice crystallites would be formed and the particles should be homogenously distributed in the ice without further movement (and, therefore, the shear forces would be considered to be low). This would mean that if this reason applies, no vitreous ice but ice crystallites have been formed, which would mean that for an improved hydration quenching procedure even faster freezing conditions would have to be employed. An argument against this explanation is that, since the size distribution of the lyophilised (**L**) and the pristine sample (CEM I) overlap, it would mean that all agglomerates

would have been completely destroyed again using the freezing/lyophilisation method. Id est, both effects of agglomeration during reaction and grinding using this method would be of equal magnitude and exactly compensating each other, which we consider not very likely.

(2) Upon adding isopropanol to the colloidal suspension, agglomeration of particles takes place. This would mean, larger particles found in Fig. 4 top might not be present prior to adding isopropanol. This would, however, point towards the direction, that the hydration stop induced via adding isopropanol can be misleading when it comes to the interpretation of certain processes during cementitious growth. An argument for reason 2 would be, that isopropanol may not dilute the cementitious dispersion and by this quenches the reaction but also may lead to reduced repulsion (likewise by change of polarity and viscosity of the liquid phase) of the dispersed particles and therefore the formation of such larger agglomerated particles.

Under the given parameter set, it is not possible to judge, which of these two explanations is the correct one. Further works, exempli gratia in combination with in situ analysis, will reveal more insight into this question.

4 Conclusion

In summary, the used hydration stop methods, namely lyophilisation of samples frozen in liquid nitrogen (**L**), isopropanol-water exchange (**I**), as well as the combination of both routes (**IL**), has a slight impact on the specific surface area, the specific volume, and the pore size distribution. By employing isopropanol (**I**), water remains in the system even after the drying procedure, which leads to an incompletely quenched hydration. For the intended time variant (kinetic) investigations of cementitious growth, this route is thus less suitable than quenching by fast freezing and lyophilisation (**IL**) or lyophilisation (**L**). Regarding the observation of microscale particle agglomerates, it still needs to be clarified whether adding isopropanol causes their presence or whether stop by lyophilisation leads to a de-agglomeration of already agglomerated particles. If the latter case would apply, the **IL** route (combination of both methods) would be the preferable route, since it would enable to nearly instantly stop the hydration process without a change in morphology and particle size distribution. If the first case would apply, it would mean that employing isopropanol could be disadvantageous for investigating the cementitious growth behaviour on the micrometre scale.

Acknowledgments. Financial support from the German Research Foundation (DFG) within the framework of SPP 2005 (BI 1708/5-1 and LO 751/26-1), as well as from the project BI 1708/4-1.

The authors thank A. Feldhoff and J. Caro for access to SEM and A. Schlosser and M. Jahns for help with nitrogen physisorption measurements.

References

1. Scrivener K, Bazzoni A, Mota B, Rossen JE (2015) A practical guide to microstructural analysis of cementitious materials. CRC PR INC, Boca Raton, pp 359–362
2. Dowell LG, Rinfret AP (1960) Low-temperature forms of ice as studied by x-ray diffraction. Nature 188:1144–1148
3. Rey L (1975) Freezing and freeze-drying. Proc R Soc Lond B 191:9–19
4. Brunauer S, Emmett PH, Teller E (1938) Adsorption of gases in multimolecular layers. J Am Chem Soc 60:309–319
5. Dreizler RM, Gross EKU (1990) Density functional theory: an approach to the quantum many-body problem. Springer, Heidelberg
6. Gelb LD, Gubbins KE, Radhakrishnan R, Sliwinska-Bartkowiak M (1999) Phase separation in confined systems. Rep Prog Phys 62:1573–1659
7. Barrett EP, Joyner LG, Halenda PP (1951) The determination of pore volume and area distributions in porous substances. I. Computations from nitrogen isotherms. J Am Chem Soc 73(1):373–380
8. Locher FW (2000) Zement - Grundlagen der Herstellung und Verwendung, Bau + Technik

Rheological Properties of Silica Beads in the Presence of Different Polymers and Electrolyte

Zichen Lu[1(✉)], Simon Becker[2], Sarah Leinitz[3], Regine von Klitzing[2], Wolfram Schmidt[3], and Dietmar Stephan[1]

[1] Building Materials and Construction Chemistry, Technische Universität Berlin, Berlin, Germany
zichen.lu@tu-berlin.de
[2] Soft Matter at Interfaces, Department of Physics, Technische Universität Darmstadt, Darmstadt, Germany
[3] Bundesanstalt für Materialforschung und -prüfung (BAM), Berlin, Germany

Abstract. Properties of interstitial liquid phase in cement paste, including the species and concentrations of polymers and ion etc., play an important role for the rheological properties of cementitious materials. In order to better understand their effect, an inert model substance, spherical silica beads (SBs) with defined surface and granulometry were used in the presence of electrolytes ($CaCl_2$) and/or different polymers, including polycarboxylate superplasticizer (PCE) and polyethylene glycol (PEG). It was found the presence of Ca^{2+} greatly increases the viscosity and yield stress of silica beads paste (SBP), which is proportional to the [Ca^{2+}]. For the effect of PCE, the addition of PCE is beneficial to the flowability of SBP, but a high dosage of PCE leads to a reversal effect. Furthermore, the yield stress firstly increases and then decreases with increasing [Ca^{2+}] under the same dosage of PCE. The addition of PEG always increases the yield stress of SBP, regardless of the ion concentration and the presence or not of PCE.

Keywords: Rheological properties · Ions · Superplasticizer · Silica beads

1 Introduction

The rheological properties of cementitious materials are very important for their application [1]. Normally, the force between the different particles is one key factor to determine the rheological performance of cementitious materials and many different forces may exist, for example, the attractive van der Waals force, the repulsive electrical double layer force, steric forces, bridging effects and depletion forces etc. [2, 3]. However, due to the complexity of cementitious system, the rheological performance originated from the interaction force can be determined by many factors, such as the water to cement ratio (W/C) [4], mineral admixtures [5], polymers [6] etc. Finally, varied rheological performance of cementitious materials can be observed [7, 8]. A cementitious system is composed of two main phases: the solid phase, including the cement grains, hydration products, supplementary binding materials, and the adsorbed

V. Mechtcherine et al. (Eds.): RheoCon 2019/SCC 2019, RILEM Bookseries 23, pp. 619–627, 2020.
https://doi.org/10.1007/978-3-030-22566-7_72

polymers etc., and the interstitial liquid phase, namely the pore solution, which contains different types of ions and un-adsorbed polymers. Unfortunately, most of the studies on the rheology of cementitious materials focus on the solid phases and not many literatures [9] have been published so far on the interstitial liquid phase.

In order to retain the workability of cement paste, especially at quite low W/C (e.g. self-compacting concrete), a large amount of superplasticizer (SP) is needed, which in turn leads to many un-adsorbed SP molecules remaining in the interstitial liquid phase. For the un-adsorbed polymer in solution, Liu et al. found that the viscosity of cement paste was increased with the increasing polycarboxylate superplasticizer (PCE) dosage under the W/C of 0.16 [10]. Matsuzawa et al. [11] further point out that the effect of over-dosed PCE depends on their structure, which also determines the adsorption ability of PCE on the surface of cement grains. If replacing the over-dosed PCE by polyethylene glycol (PEG, which is the main composition of PCE's side chain and normally regarded as non-adsorbing polymer), Lange et al. [12] found that the addition of PEG is beneficial to the fluidity improvement of cement paste, which is ascribed to the lubrication effect. Jiang [13] found a similar effect and attributed it to the shield effect of PEG on the carboxylate group existing in PCE, which prevents the agglomeration of cement grains caused by the complexation of PCE with calcium in pore solution or on the surface of cement grains. However, Bessaies-Bey et al. [2] found the addition of PEG with high molecular weight increases the yield stress of cement paste, which comes from the increasing depletion force caused by the high polymer concentration in pore solution. Obviously, no certain conclusion has been obtained on how the different polymer in liquid phase affects the rheological properties of cement paste.

Another important component in the interstitial solution is various ions with different concentration, which is steadily changing during cement hydration [14]. Certainly, the ions in the solution can interact with polymers and cement grains through different mechanisms [15]. Hence the question is raised on how these ions and polymers in solution independently and together affect the rheology of cementitious materials.

Due to the complexity of cement, inert spherical silica beads were used in this study. The ion type and concentration were controlled by the addition of soluble calcium salt with certain concentration to investigate the interaction of ions in pore solution with the polymer and their final effect on the rheological performance. Three polymers, including one PCE and two PEGs (with different molecular weight), were investigated.

2 Experimental

2.1 Materials

Silica beads (SBs, Sigmund Lindner GmbH, Germany) with spherical shape (Fig. 1) and three polymers (as shown in Table 1, one polycarboxylate superplasticizer (PCE) from BASF and two PEGs from Millipore Corporation) were used. The average particle size (d_{50}) of SBs is 6.5 μm and the density is 2.5 kg/dm^3. Calcium chloride with analytical pure grade and deionised water (DI water) was used directly.

2.2 Methods

2.2.1 Sample Preparation

The mass ratio of polymer to SBs was chosen at 0.02, 0.1 and 0.8 wt.-% respectively and water to silica beads ratio was 0.24. A certain amount of PCE or PEG was weighed and then dissolved into the solution (DI water, calcium chloride with certain concentration). After that, 600 g SBs was added into the solution and agitated by Hobart mixer at low rate (62 rpm) and high rate (125 rpm) for 1 min respectively under constant ambient temperature of 20 °C.

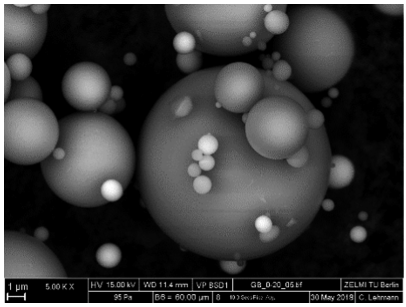

Fig. 1. SEM of silica beads.

Table 1. Basic physical parameters of the used polymers

Sample	Solid content (%)	Mw	PEO units
PCE	22.6	28000	18
PEG1	100	35000	680
PEG2	100	3000	68

2.2.2 Experiment

The rheology measurement was conducted at 20 °C with the vane-in-cup geometry of rheometer HAAKE RheoStress 600 (Thermo Electron Corporation). The paste was measured by a circle shear rate ramp from 0 s^{-1} to 8.378 s^{-1} and then to 0 s^{-1} in 7 min. The last point at each shear rate at the decreasing shear rate ramp was recorded to present the rheological performance of silica bead paste (SBP).

The same sample preparation method as described in Sect. 2.2.1 was used for the adsorption and zeta potential measurement. For the adsorption measurement, supernatant was obtained by the centrifugation and filtration (0.45 μm syringe filter). A Total Organic Carbon (TOC) analyser was used to measure residual PCE in the solutions and then the adsorbed amount was calculated. For the zeta potential measurement, electroacoustic method (DT-310, Dispersion Technology USA) was used and the temperature was kept at 20 °C during measurement. Each measurement was repeated three times and the average value was calculated.

3 Results and Discussions

3.1 Effect of Polymer on Rheological Performance of SBP

The effect of different polymers on the rheological performance of SBP is shown in Fig. 2. Compared to the reference sample, the addition of PCE could greatly decrease the yield stress and viscosity (The yield stress and viscosity was obtained according to

the simulation using Herschel Bulkley's equation ($\tau = \tau_0 + k\dot{\gamma}^n$) to the shear rate and shear stress curve as shown in Fig. 2. The values are not shown in this paper). However, with the increasing dosage of PCE, both the yield stress and the viscosity were firstly decreased and then increased, which is consistent with the literature [10]. Like the condition in cement paste, the decreasing yield stress is believed to be caused by the adsorption of PCE on the surface of SBs. The increasing yield stress of SBP is most likely caused by the depletion force due to the increasing amount of PCE molecules in the pore solution [2]. For the two PEGs, when the dosage is low (0.02 wt.-%), the addition of PEG has nearly no effect on the rheological performance, regardless of their molecular weight. However, with the increasing dosage of PEG, the addition of PEG leads to higher yield stress and viscosity. PEG with higher molecular weight shows a stronger effect. Many papers discussed the adsorption of PEG on silica beads, either through the formation of hydrogen bonding between ether group contained in PEG and the silanol group on the surface of silica beads [16] or through the affinity of the terminal hydroxyl group in PEG molecule to the SB surface [17]. Furthermore, it was reported that the adsorption can improve the flowability of the paste [17], which is not found in this study. It indicates that the PEG may not be adsorbed on the SBs, which may be caused by the deprotonation of the silanol group under the high pH in solution (about 11.5) [18], and/or the short time between mixing and measurement for the adsorption of PEG. Based on this, the high PEG concentration in pore solution triggers the high depletion force and then leads to high viscosity and yield stress with the increasing dosage.

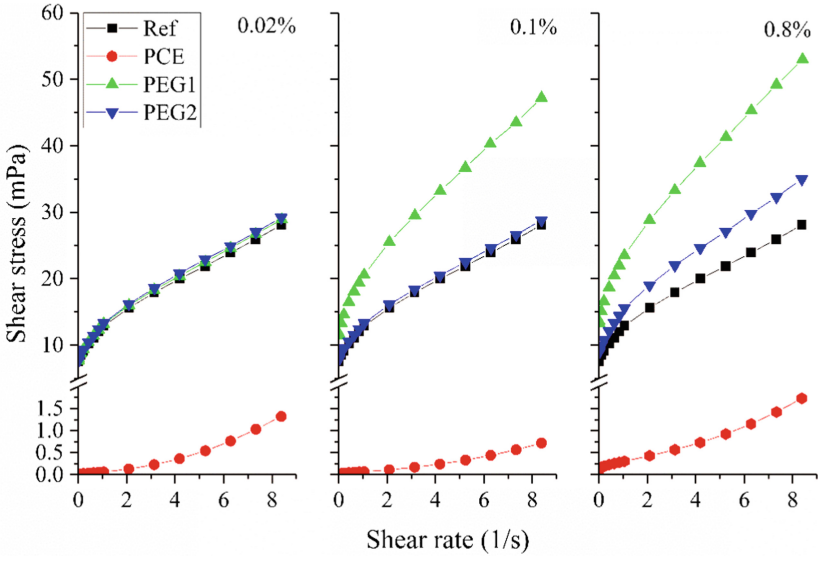

Fig. 2. Effect of different polymers on the rheological performance of SBP.

3.2 Effect of Ion Concentration on Rheological Performance of SBP

The effect of calcium ion under varied concentration on the rheological performance of SBP is shown in Fig. 3a. With the increasing [Ca^{2+}], both the yield stress and viscosity are clearly increased. According to the DLVO theory, it may be argued that the increasing yield stress and viscosity is caused by the decreasing absolute zeta potential of SBP. In order to clarify it, the zeta potential of SBP with the increasing [Ca^{2+}] are measured and shown in Fig. 3b. It is shown that, with the increasing [Ca^{2+}], the zeta potential of silica beads was gradually changed from negative to positive and the absolute value was firstly decreased and then increased, which is believed to be caused by the uptake of Ca^{2+} to the surface of SBs. The lowest zeta potential of $\sim$2.6 mV was achieved when the [Ca^{2+}] is 125 mmol/L. However, if we compare the rheological results, it is found that SBP with [Ca^{2+}] of 200 mmol/L shows the highest yield stress and viscosity, which indicates that the electrostatic force is not the only factor to determine the particle interaction and the [Ca^{2+}] plays the most important role here, which may be caused by the extraction of water layer on the surface of silica beads [19].

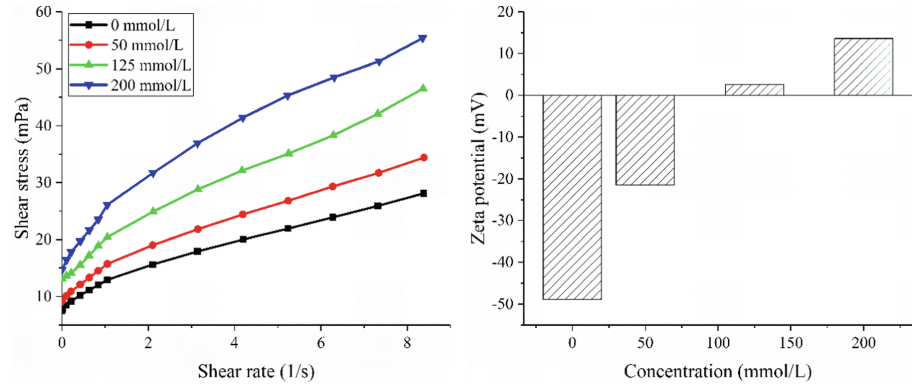

Fig. 3. (a) Effect of calcium ion with different concentrations on the rheological performance of SBP; (b) Zeta potential of SBP along with the increasing [Ca^{2+}].

3.3 Combined Effect of Ion and Polymer Concentration

The combined effect of polymer and ion on the rheological performance of SBP is shown in Fig. 4. For the samples with 0.1 and 0.8 wt.-% PCE, it is found the yield stress always firstly increases and then decreases along with the increasing [Ca^{2+}], which is contrary to the phenomenon found without addition of PCE (Fig. 3a). If partial PCE (0.7 wt.-%) was replaced by the PEG, the gradual increasing yield stress was observed again, just like the phenomenon found for the samples without PCE. In addition, PEG with higher molecular weight always leads to higher yield stress.

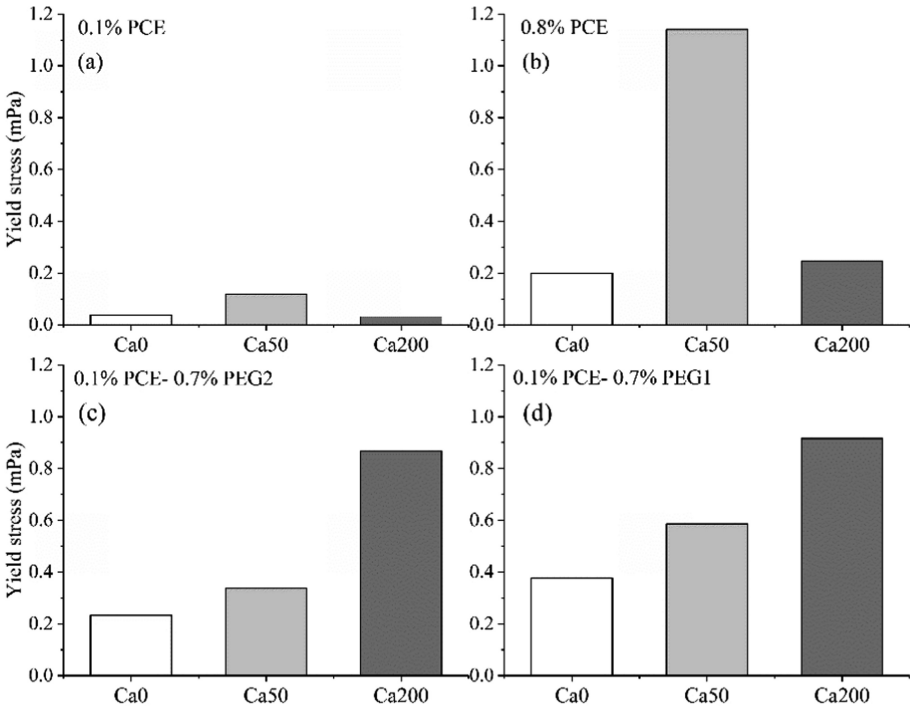

Fig. 4. Combined effect of different polymers and ion concentration on the yield stress of SBP.

Normally polymer adsorption on the surface of cement grains plays the essential role for their dispersing ability. Hence, the adsorption isotherm was measured under different PCE dosages and the results are shown in Fig. 5.

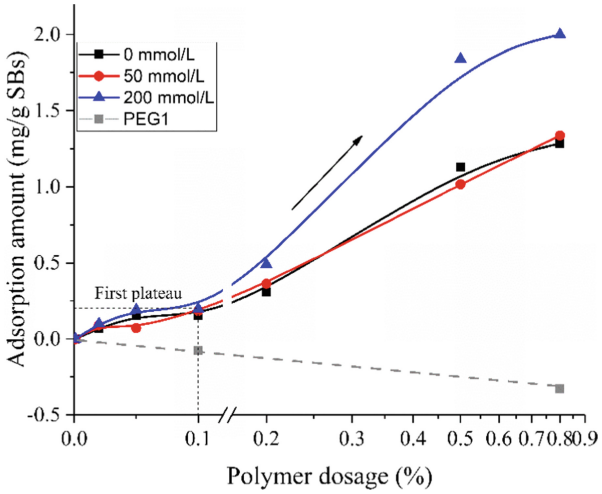

Fig. 5. Adsorption isotherm of PCE and PEG under different dosages.

For the reference sample, along with the increasing PCE dosage, the adsorption amount of PCE is clearly increased and then the adsorption equilibrium seems to be reached at the dosage of 0.1 wt.-%. If the dosage of PCE is further increased, the adsorption amount was further increased. In addition, PEG shows nearly no adsorption ability on SBs and therefore no improvement on rheological performance could be found, which matches well with our former rheological results (shown in Fig. 2).

When taking the effect of calcium ions into account, compared to the samples with different [Ca^{2+}], it is found that [Ca^{2+}] of 50 mmol/L has no obvious effect on the adsorption of PCE. However, [Ca^{2+}] of 200 mmol/L significantly increases the adsorption amount, especially when the dosage is higher than 0.2 wt.-%. As shown in Fig. 4b, obviously the increasing adsorption amount of 0.75 mg/g is beneficial for the improvement on flowability of SBP when the PCE dosage is 0.8 wt.-%. Considering the high positive zeta potential for SBP with [Ca^{2+}] of 200 mmol/L as shown in Fig. 3b, it is reasonable to conclude that the increasing adsorption is caused by the bridge of calcium ions on the surface of SB grains [18] with the carboxylate groups contained in the PCE. It should also be mentioned that, when the dosage of PCE is 0.1 wt.-%, the PCE's adsorption amount in both SBPs with [Ca^{2+}] of 50 mmol/L and 200 mmol/L seems similarly but still SBP with [Ca^{2+}] of 50 mmol/L shows higher yield stress. It indicates that besides the increasing adsorption amount under higher [Ca^{2+}], some other factors may exist to affect the rheological performance of SBP, which needs to further investigation. If we compare the measured yield stress shown in Fig. 4a with Fig. 4c and d, with the precondition of same PCE dosage but increasing PEG dosage, it is shown that regardless of the calcium concentration, the addition of PEG could greatly increase the yield stress, which is believed to be caused by the depletion effect as described in literature [2]. However, if we compare Fig. 4b with Fig. 4c and d, which is with the same total polymer dosage but different types of polymer, it is found that for the [Ca^{2+}] of 50 mmol/L, the replacement of PCE by PEG could decrease the yield stress, but the contrary phenomenon was found for the [Ca^{2+}] of 0 mmol/L and 200 mmol/L.

Adsorption results have shown that the adsorption amount of PCE on the SBs increases with the dosage and PEG cannot be adsorbed. It indicates that, compared to the sample with only PCE at the dosage of 0.8 wt.-%, more polymers will be left in pore solution for the samples with the replacement of PCE by PEG (as shown in Fig. 4c and d). For the paste with large amount of non-adsorbing polymers, if depletion force plays the key role for the increasing yield stress, as discussed in literature [2], the yield stress shown in Fig. 4c and d should always be higher than that in Fig. 4b regardless of the concentration of calcium ion (depletion force is mainly decided by the radius of grains, neighbouring particles distance and the number density of polymer [2]), which is contrary to the phenomenon found for the [Ca^{2+}] of 50 mmol/L. It indicates that, for the paste with large amount of non-adsorbing polymer in solution, the depletion force is not the only factor to determine the increase in yield stress. The interaction between polymer, ion and grains also plays a vital role for the final rheological performance, which depends on the structure and type of polymer and the type and concentration of ions in solution.

4 Conclusion

Based on the results above, the following conclusions can be obtained.

(1) Increasing dosage of PCE firstly decreases and then increases the yield stress and viscosity of SBP, while the addition of PEG just increases the yield stress along with the dosage. The PEG with higher molecular weight shows stronger ability.
(2) Without the addition of polymer, increasing [Ca^{2+}] always leads to high yield stress and viscosity. However, if PCE is involved, the increasing [Ca^{2+}] firstly increases the yield stress and then decreases it, which may originate from the increasing PCE adsorption with the high concentration of calcium ion.
(3) Depletion forces caused by the non-adsorbing polymer in solution are not the only factor to determine the increasing yield stress when the total polymer dosage is increased from 0.1 to 0.8 wt.-%. The interaction between polymer, ion and grains also play a vital role for the final rheological performance. Hence the properties of the interstitial liquid phase should be taken into consideration for the investigation on the rheological performance of paste.

Acknowledgement. The author would like to thank the funding from German Research Association (DFG) for the project program *Opus Fluidum Futurum – Rheology of reactive, multiscale, multiphase construction materials (SPP 2005)* (Project number 387092747) and the supply of cement and superplasticizer from HeidelbergCement and BASF, respectively.

References

1. Roussel N (2012) Understanding the rheology of concrete. Woodhead Publishing, Cambridge
2. Bessaies-Bey H, Palacios M, Pustovgar E, Hanafi M, Baumann R, Flatt RJ, Roussel N (2018) Non-adsorbing polymers and yield stress of cement paste: effect of depletion forces. Cem Concr Res 111:209–217
3. Johnson SB, Franks GV, Scales PJ, Boger DV, Healy TW (2000) Surface chemistry - rheology relationships in concentrated mineral suspensions. Int J Miner Process 58:267–304
4. Felekoğlu B, Türkel S, Baradan B (2007) Effect of water/cement ratio on the fresh and hardened properties of self-compacting concrete. Build Environ 42:1795–1802
5. Senff L, Labrincha JA, Ferreira VM, Hotza D, Repette WL (2009) Effect of nano-silica on rheology and fresh properties of cement pastes and mortars. Constr Build Mater 23:2487–2491
6. Lu Z, Kong X, Zhang C, Xing F, Zhang Y (2017) Effect of colloidal polymers with different surface properties on the rheological property of fresh cement pastes. Colloid Surf A-Physicochem Eng Asp 520:154–165
7. Papo A, Piani L (2004) Effect of various superplasticizers on the rheological properties of Portland cement pastes. Cem Concr Res 34:2097–2101
8. Yahia A (2011) Shear-thickening behavior of high-performance cement grouts - influencing mix-design parameters. Cem Concr Res 41:230–235
9. Schmidt W, Leinitz S, Mota B, Crasselt C (2018) Influence of the aqueous phase of cement phase on the rheology in the presence of PCE. In: Proceedings twelfth international conference, Beijing, China, October 2018

10. Liu J, Wang K, Zhang Q, Han F, Sha J, Liu J (2017) Influence of superplasticizer dosage on the viscosity of cement paste with low water-binder ratio. Constr Build Mater 149:359–366
11. Matsuzawa K, Shimazaki D, Kawakami H, Sakai E (2018) Influence of non-adsorbed polymers on fluidity of cement paste. In: Proceedings of 12th international conference on superplasticizers and other chemical admixtures in concrete, Beijing, China, October 2018
12. Lange A, Plank J (2016) Contribution of non-adsorbing polymers to cement dispersion. Cem Concr Res 79:131–136
13. Jiang L (2017) Study on the structure-property relationships of polycarboxylate superplasticizer, viscosity modifying agent and nucleation accelerator, Ph.D thesis, Tsinghua University
14. Lu Z, Kong X, Zhang C, Jansen D, Neubauer J, Goetz-Neunhoeffer F (2019) Effects of two oppositely charged colloidal polymers on cement hydration. Cem Concr Compos 96:66–76
15. Zhang Y, Kong X (2015) Correlations of the dispersing capability of NSF and PCE types of superplasticizer and their impacts on cement hydration with the adsorption in fresh cement pastes. Cem Concr Res 69:1–9
16. Hommer H (2009) Interaction of polycarboxylate ether with silica fume. J Eur Ceram Soc 29:1847–1853
17. Zaman AA (2000) Effect of polyethylene oxide on the viscosity of dispersions of charged silica particles: interplay between rheology, adsorption, and surface charge. Colloid Polym Sci 278:1187–1197
18. Merlin F, Guitouni H, Mouhoubi H (2005) Adsorption and heterocoagulation of nonionic surfactants and latex particles on cement hydrates. J Colloid Interf Sci 281:1–10
19. Amiri A, Øye G, Sjöblom J (2009) Influence of pH, high salinity and particle concentration on stability and rheological properties of aqueous suspensions of fumed silica. Colloid Surf A-Physicochem Eng Asp 349:43–54

A Plasticity Theory Approach for the Stability Analysis of Vertical Layers of Concrete in the Fresh State

Giacomo Torelli(✉) and Janet M. Lees

University of Cambridge, Cambridge, UK
gt384@cam.ac.uk

Abstract. The industrial production of cement is currently responsible for around 5% of global CO_2 emissions. Hence, the development of technologies aimed at minimizing the use of cement in concrete structures, while preserving their strength and durability properties, plays a vital role in the reduction of carbon emissions. The use of cement in concrete structures can be minimized through the manufacture of functionally layered structural elements where concrete with high cement content is used rationally only when it contributes significantly to the performance of the structure. In functionally layered concrete, horizontal variation in material composition can be achieved by casting adjacent vertical layers of different materials. Removable vertical panels can be used to demarcate the mixes during casting. A good bond between the layers can be achieved by removing the panels prior to concrete hardening. However, a major problem with this application is the control of the fresh-state deformations of the adjacent vertical layers. This study investigates the fundamental problem of fresh state stability of concrete prisms that consist of two vertical layers of different mixes. A novel limit-state approach based on plasticity theory is formulated to assess the stability of the system as a function of material properties and geometry. The relationship between material parameters, system stability and geometry is determined and the formulated limit-state approach is validated against experimental results.

Keywords: Concrete · Stability · Plasticity · Rheology · Limit-state analysis

1 Introduction

Concrete is the most widely used construction material in the world. The manufacture of cement, the key constituent of concrete, is energy intensive and accounts for around 5% of global CO_2 emissions related to human activities [1]. Minimizing the use of cement in concrete structures is thus a great opportunity to reduce the global CO_2 emissions.

The use of cement can be minimized by manufacturing functionally layered concrete elements, i.e. concrete elements composed of various layers of different concrete mixes. In this way, mixes with high cement content can be used only where they are needed. The material composition of concrete elements is commonly varied in the vertical direction by sequentially casting horizontal layers of different concrete mixes. Nevertheless, relatively little attention has been paid to the possibility of varying the

V. Mechtcherine et al. (Eds.): RheoCon 2019/SCC 2019, RILEM Bookseries 23, pp. 628–635, 2020.
https://doi.org/10.1007/978-3-030-22566-7_73

material composition in the horizontal direction by casting adjacent vertical layers of different mixes. This concept represents a clear opportunity to further optimize the use of cement in structural elements such as beams, columns and walls. If, for example, a relatively low water/cement ratio is needed in a vertical concrete cover to minimize porosity and maximize durability, concrete with high cement content can be used only in that region.

However, the major obstacle in the implementation of this concept is the control of the fresh state deformations of the vertical layers. Indeed, if the mixes are fluid enough, global instability phenomena can occur following the removal of a panel where heavier mixes tend to flow underneath lighter mixes. As a consequence, the desired spatial variation in concrete composition may be compromised. Accurate understanding of the parameters driving the fresh state instability of vertical layers of concrete is thus needed.

This paper presents an original analytical method to investigate the fundamental problem of the fresh state stability of two adjacent vertical layers of different concrete mixes (see Fig. 1). Two limit-state models, based on the upper and lower bound theorems of plasticity are developed to capture the relationship between system geometry, material parameters and the stability of the system. The newly formulated analysis method is validated and discussed in light of experimental results.

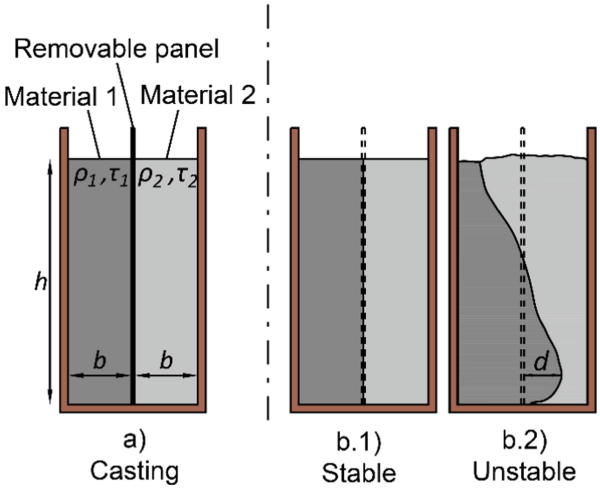

Fig. 1. (a) Casting, (b.1) stable fresh state behavior, and (b.2) unstable fresh state behavior of an element composed of two vertical layers of different mixes.

2 Modelling Approach

Fresh cementitious materials are commonly modelled as yield stress fluids. That is, they are assumed to behave as solids for low stresses and to flow when a threshold shear stress, referred to as yield stress τ, is exceeded. Experimental flow curves relating shear stress and shear rate can be approximated by a Herschel-Bulkley model:

$$\tau > \tau_0 \rightarrow \tau = \tau_0 + k\dot{\gamma}^n \tag{1}$$

where τ_0 is the yield stress, $\dot{\gamma}$ is the shear rate, k is the consistency index, and n is the flow index. The material parameters τ_0, k and n can be controlled by selecting the appropriate mix constituents and their relative proportions [2–5].

In this work it is assumed that, when the yield stress is exceeded, flow occurs at small shear rates. From Eq. 1 it can be seen that for small shear rates the shear stress tends to τ_0. Under these assumptions, the behaviour of the material is modelled through the theory of perfect plasticity. An exact analysis of a plastic body would require that equilibrium, compatibility and constitutive equations be satisfied simultaneously [6–8]. An alternative to a full plastic analysis is to focus on the stability limit state. This approach is justified when phenomena occurring prior to collapse are not of interest. The stability limit state of a plastic body can be studied through the upper and lower bound methods of plasticity theory [7, 9]. The upper bound method allows an upper bound of the exact collapse load to be determined by ignoring the equilibrium conditions. By contrast, the lower bound method allows a lower bound of the exact collapse load to be determined by ignoring the compatibility conditions.

Two models, based on the upper and lower bound theorems of plasticity, are formulated here to assess the relationships between material properties, geometry, boundary conditions and stability of the system presented in Fig. 1.

3 Plastic Models

3.1 Upper Bound Model

An upper bound model is developed that assumes the activation of the compatible mechanism shown in Fig. 2a. The kinematic model consists of four rigid blocks (A, B, E, D) and two radial shear zones (C_1 and C_2). In such a mechanism a heavier material would flow underneath a lighter material. In line with the definition of the model, it is assumed that the shear stress developing on slip surfaces between blocks is the yield stress of the material. At the walls, a fraction f of the yield stress of the material is considered, while the minimum yield stress of the two materials is assumed to develop at the interface between the materials. Equating external and internal work for the mechanism reported in Fig. 2a, leads to:

$$\tau_s = m_U \Delta\rho \tag{2}$$

where τ_s is the sum of the yield stresses τ_1 and τ_2 of material 1 and 2 respectively, $\Delta\rho$ is the difference in density between the two materials and m_U is here defined as upper-bound stability coefficient:

$$m_U = \frac{g}{k_{U1} + k_{U2} + k_{U3}} \tag{3}$$

where g is the gravitational acceleration and k_{U1}, k_{U2}, and k_{U3} are:

$$k_{U1} = \frac{\left(2+\frac{\pi}{2}\right)b}{bh-\frac{\sqrt{2}}{4}b^2}; \quad k_{U2} = \frac{f\left(h-\frac{b}{\sqrt{2}}\right)}{bh-\frac{\sqrt{2}}{4}b^2}; \quad k_{U3} = \frac{\frac{2\alpha}{\alpha+1}\left(h-\frac{b}{\sqrt{2}}\right)}{bh-\frac{\sqrt{2}}{4}b^2} \tag{4}$$

where b is the width of the column, h the height of the system and α is defined as the ratio between the smaller and the larger of the two yield stresses τ_1 and τ_2.

Equation 2 is an expression for the sum τ_s of yield stresses of the two materials that gives an unstable upper bound system for a given difference in density $\Delta\rho$ and geometry. The terms k_{U1}, k_{U2} and k_{U3} represent three different contributions to the stability of the system. Specifically, k_{U1} accounts for the energy needed to activate the internal slip surfaces and to deform the radial shear zones, k_{U2} captures the effects of friction at the walls, and k_{U3} accounts for the impact of the stress at the interface between the two materials on the stability of the system.

3.2 Lower Bound Model

A lower bound model is developed by defining an equilibrium stress state that does not violate the yield condition of the two materials. A simplified stress state that accounts for the effects of friction at the wall and at the interface between the materials (see Fig. 2b) was assumed. The friction stresses at the point of slip correspond to the kinematic mechanism reported in Fig. 2a and are applied as distributed loads p_1 and p_2 across the thickness of the columns, where:

$$p_1 = \frac{f\tau_1+\tau_{\min}}{b}; \quad p_2 = \frac{f\tau_2+\tau_{\min}}{b} \tag{5}$$

It is thus assumed that replacing the friction stresses acting on the upper part of the system with an equivalent distributed load does not significantly affect the solution. Under these assumptions, the defined equilibrium stress state presents a vertical stress discontinuity at the interface of the two materials. The vertical and horizontal directions are the directions of the principal stresses. To obtain a lower bound solution the materials are assumed to reach their yield strengthen shear at the base of the system. Writing the horizontal equilibrium for two elements A and B at the base of the columns (see Fig. 2b) leads to:

$$\tau_s = m_L \Delta\rho \tag{6}$$

where:

$$m_L = \frac{g}{k_{L1}+k_{L2}+k_{L3}} \tag{7}$$

$$k_{L1} = \frac{2}{h}; \quad k_{L2} = \frac{f\left(\frac{h}{b}-\frac{1}{\sqrt{2}}\right)}{h}; \quad k_{L3} = \frac{\frac{2\alpha}{\alpha+1}\left(\frac{h}{b}-\frac{1}{\sqrt{2}}\right)}{h} \tag{8}$$

Equation 6 expresses the sum τ_s of yield stresses of the two materials that gives a stable lower bound system for a given difference in density $\Delta\rho$ and geometry.

The two models described by Eqs. 2 and 6 suggest that for a given geometry and set of boundary conditions, the stability of the system can be controlled by varying the sum τ_s of the yield stresses of the materials and their difference in density $\Delta\rho$. Specifically, the two models indicate that for a given geometry, fresh state deformations of the system decrease with increasing stability coefficient m, defined as:

$$m = \frac{\tau_s}{\Delta\rho} \tag{9}$$

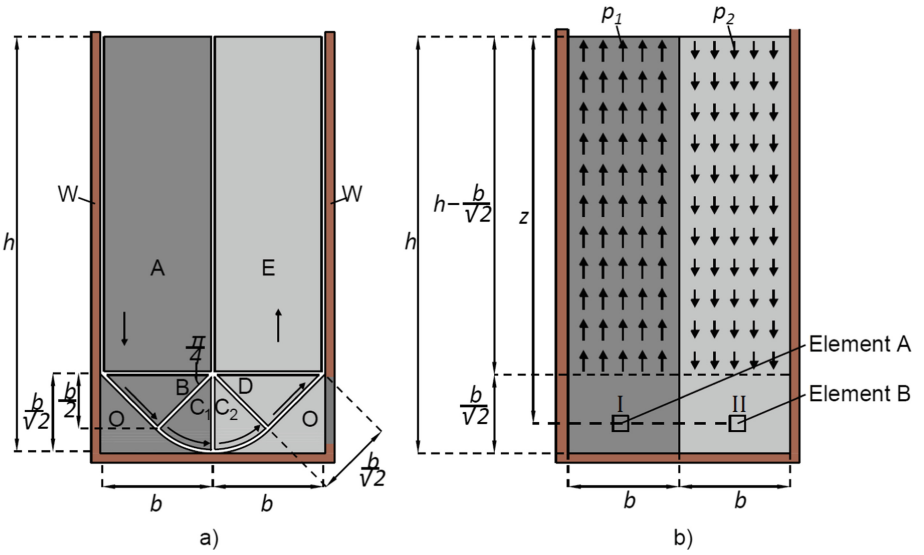

Fig. 2. (a) Mechanism and (b) Equilibrium stress state.

4 Validation Against Experiments

The bound models presented in Sect. 3 have been validated against a set of experiments on two vertical layers with tailored cementitious mixes having various yield stresses and densities. The reference tests are reported in [10, 11]. In these experiments, a system having a column width of b = 80 mm and a height of h = 300 mm was considered. Twelve tests were performed across 24 mix compositions with a wide range of densities and yield stresses. The density of the materials was varied by adding foam to the mixes, while the yield stress was varied by altering the water content and using a polycarboxylate ether (PCE) superplasticizer. The mixes were designed to achieve sums of the yield stresses ranging from 60 Pa to 248 Pa and differences in densities of up to 378 kg m^{-3}. This led to stability coefficients m ranging from 0.18 Pa m^3 kg^{-1} to 1.28 Pa m^3 kg^{-1}. As an indicator of the stability of the system, the maximum

horizontal displacement d of the interface between the two layers was measured in each test. A full description of the experimental methods is reported in [11].

Equations 3 and 7 were used to calculate an upper and a lower bound stability coefficient.

A friction coefficient of $f = 1$ was considered, representing no-slip boundary conditions at the wall. Coefficients $\alpha = 0.83$ and $\alpha = 0.22$ were selected for the upper and lower bound respectively. Such values represent the maximum and minimum coefficients α for the mixes studied experimentally. Hence, they allow to obtain indicate bounds for all tests. The calculated upper and lower bound stability coefficients were $m_U = 0.28$ Pa m^3 kg^{-1} and $m_L = 0.48$ Pa m^3 kg^{-1} respectively.

Figure 3 plots the experimentally measured maximum horizontal displacement d (see Fig. 1b) against the stability coefficient m, together with the limit lines representing the analytically calculated upper and lower bound stability coefficients m_U and m_L. The plot suggests that, according to the formulated bound models, a relationship exists between the difference in density $\Delta\rho$ of the two materials, the sum τ_s of their yield stresses, and the stability of the system. The displacements decrease with an increase in the stability coefficient m. Specifically d decreases sharply for stability coefficients m up to about 0.4 Pa m^3 kg^{-1} and more gradually for higher values of m. Figure 3 shows that the formulated upper and lower bound models bracket the regions of transition from unstable to stable behaviour.

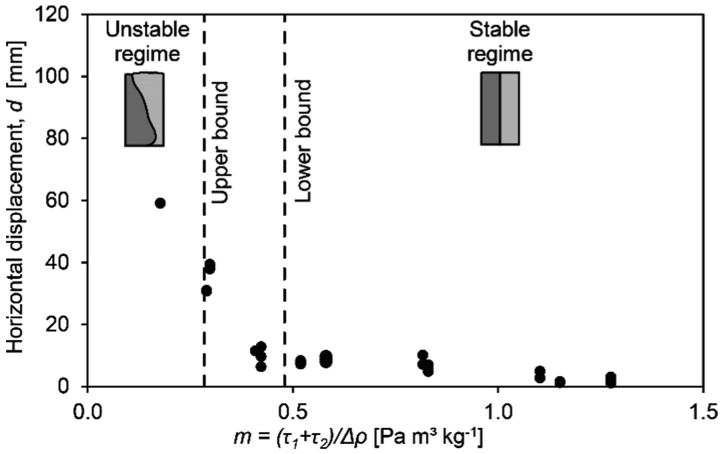

Fig. 3. Maximum horizontal displacement d as a function of the stability coefficient.

5 Discussion

Both the formulated analytical models and the experimental results suggest that, for a given system geometry, the stability of the system in the fresh state can be controlled by tailoring the material properties of the two mixes. The fresh state behaviour of the two columns is driven by the sum of the yield stresses τ_s and the difference in density

$\Delta\rho$ between the two mixes (see Fig. 3). The difference in density $\Delta\rho$ is proportional to the forces driving instability while the sum of yield stresses τ_s is an effective indicator of ability of the system to withstand shear stresses in the stable regime. Accordingly, the stability capacity of the system can be expressed through a stability coefficient m, defined here as the ratio between the sum τ_s of the yield stresses and the difference in densities $\Delta\rho$.

For a given geometry and set of boundary conditions, the two bound models allow for the assessment of two limit values of the stability coefficient within which plastic collapse is expected to occur. The calculated upper and lower bound solutions give an indication of the experimentally identified transition regime between stable and unstable conditions, represented by stability coefficients around 0.4 Pa m^3 kg^{-1} (see Fig. 3). This confirms that, in the case of slow flows, plasticity theory can be adopted to study the fluid behaviour of cementitious materials.

6 Conclusions

The following conclusions can be drawn from the present study:

- Two novel limit state models based on plasticity theory have been formulated to study the fresh state behaviour of a system composed of two vertical columns of different cementitious mixes. The models suggest that, for a given geometry and set of boundary conditions, the stability capacity of the system can be increased by either increasing the sum τ_s of the yield stresses of the materials or by minimizing their difference in density $\Delta\rho$.
- Such trends are confirmed experimentally. Specifically, it was shown that for a given geometry, fresh state deformations of the system decrease with increasing stability coefficient m, defined here as the ratio between the sum τ_s of the yield stresses and the difference in density $\Delta\rho$.
- The proposed bound models are indicative of the experimentally determined transition region between stable and unstable regimes. Thus, they can be adopted to design stable or unstable systems.

7 Acknowledgements

The authors would like to acknowledge the financial support of EPSRC - the Engineering and Physical Sciences Research Council (UK) [Project reference number: EP/N017668/1].

References

1. Boden T, Andres R, Marland G (2013) Global, regional, and national fossil-fuel CO2 emissions. Oak Ridge, Tennessee, U.S.A. Carbon dioxide information analysis center, Oak Ridge National Laboratory, U.S. Department of Energy

2. Banfill PFG (2006) Rheology of fresh cement and concrete. In: Rheology reviews. The British Society of Rheology, pp 61–130
3. Tattersall GH, Banfill PFG (1983) The rheology of fresh concrete. Pitman Books Limited, Boston
4. Tattersall GH (2014) Workability and quality control of concrete. CRC Press, Boca Raton
5. Wallevik OH (1990) The rheology of fresh concrete and its application on concrete with and without silica fume
6. Calladine CR (2010) Plasticity for engineers. Woodhead Publishing, Cambridge
7. Chen WF (2013) Limit analysis and soil plasticity. Elsevier Science, Amsterdam
8. Chen WF (2000) Plasticity, limit analysis and structural design. Int J Solids Struct 37:81–92
9. Heyman J (2008) Basic structural theory. Cambridge University Press, Cambridge
10. Torelli G, Lees JM (2019) Functionally graded concrete elements composed of vertical layers of different mixes. In: Proceedings of Guimarães IABSE symposium 2019, Guimarães, Portugal
11. Torelli G, Lees JM (2019) Fresh state stability of vertical layers of concrete. Cem Concr Res 120:227–243

Hydrating Cement Particle Interaction Model for Yield Stress Analysis

Neven Ukrainczyk(✉), Antonio Caggiano, Diego Said Schicchi, Albrecht Gilka-Bötzow, and Eddie Koenders

Institute of Construction and Building Materials, Technische Universität Darmstadt, Darmstadt, Germany
ukrainczyk@wib.tu-darmstadt.de

Abstract. This study overviews existing methods for analyzing cement paste yield stress, and presents a new approach based on micro-structural computation. The proposed model explicitly considers cement particle interactions, both the colloidal and the nucleated gel ones. A new algorithm is proposed based on flocculating of poly-dispersed hard spheres in a simulation box, followed by nucleation of mono-sized nano-gel particles. The obtained virtual microstructures are than used as an input for a mechanical approach, which is conceptualized for simulating sliding kinematics needed to initiate the flow of the percolated solid network, i.e. to reach the paste yield stress. The microstructural modeling tool provides insights on how the localized gel is bridging the cement particles, responsible for the yield stress properties of bulk cement paste. Thus, it provides a promising new approach for quantifying the evolution of the bridging strength with nucleation (shear rest) time, enabling parametrization of the mechanical yield stress computation at micro-structural scale.

Keywords: Cement flocculation · Particle based model · Boundary nucleation and growth · Microstructure · Yield stress

1 Introduction

The time dependent behavior of cementitious materials has attracted the attention of many researchers [1–3], while modeling approaches are scarce [4–8]. In particular, Hattori and Izumi [6] explain the effect in terms of (de-)flocculation processes. In their approach, particle-connections are described by an analytical function for the coefficient of friction between particles. It considers the number of primary (dispersed) particles in a unit volume, the initial degree of agglomeration (defined as the ratio of the number of junctions to the number of particles), and the agglomeration rate. Their proposed equation can reproduce the different hysteresis loops observed in experiments with rheometers [3].

Flatt and Bowen [4] developed a yield stress model (Yodel) for particles forming an attractive, i.e. only non-contact, interaction network derived by means of statistical-geometrical considerations. The yield stress is expressed as a function of the particle volume fraction, percolation threshold, maximum attractive inter-particle forces, median particle radius calculated on a volume basis and the particle coordination

V. Mechtcherine et al. (Eds.): RheoCon 2019/SCC 2019, RILEM Bookseries 23, pp. 636–643, 2020.
https://doi.org/10.1007/978-3-030-22566-7_74

number, which gives the number of contacts between particles. Maximum packing fraction and minimum inter-particle separation distance have to be used as fitting parameters. The model accurately predicts the dependence of yield stress on the solids volume fraction; however, the scaling of yield stress is not directly predicted from particle size, but from the radius of curvature at the point of particle contact. The Yodel considers the yield stress from colloidal stresses only, while contact between particles due to nucleation gel is not included.

Wallevik [7] used a semi-microstructural (statistical) approach to extend the so-called Hattori–Izumi theory [6] by adding different types of flocculation/nucleation connections, both reversible and permanent. This model is based on spherical and mono-dispersed particles and gives the number of particle connections, whose dynamic change is described by differential kinetic rate equations and interlinked with a continuum flow equation via apparent viscosities. Three types of yield stresses (and plastic viscosity) variables were introduced analytically, related to (1) the number of permanent linkages; (2) the number of reversible linkages and (3) the chemically formed breakable linkages.

Roussel et al. [5] considered a conceptual geometrical model where the nucleation gel links the monodispersed (d = 10 μm) cement particles as homogeneous cylinders, whose cross section (order of few nm) increases due to the ongoing formation of nucleation gel. This paper extends such an approach by employing a poly-dispersed particle model to explicitly describe flocculation and nucleation induced microstructures, for the first time.

Description of cement particle flocculation in 3D particle microstructural models was simulated using a Monte Carlo approach [9]. In [9], random moves of isolated cement particles and identified clusters are iterated, and according to the square-well potential, when any of two particles approach each other with a distance smaller than the critical, they will form a flocculated cluster.

This work presents a micro-structural computational approach for analyzing cement paste yield stress, explicitly considering cement particle interactions, including both the colloidal and the nucleated gel actions. The model is able to calculate the development of the micro-structure as a function of the particle size distribution, water cement ratio, size of maximal particle which flocculates (and minimum distance between flocculated particles), and volume of nucleated gel.

2 Micro-structural Modeling Approach

The particle interaction fundamentals, responsible for time-dependent rheological behavior of cement suspensions, are modelled using in-house developed particle packing routines in Matlab. Micro-to-nano-sized particle structures are used as a starting point to develop new modules related to rheology. As part of this paper, a commonly used cement hydration particle model (e.g. [10, 11]) is extended with: (1) a flocculation algorithm, (2) an Boundary Nucleation and Growth (BN&G) module that describes the nucleation induced bridging of the binder particles and (3) a rheological module for early age rheological behavior of the obtained virtual microstructures (Fig. 1). All three modules are described further in detail.

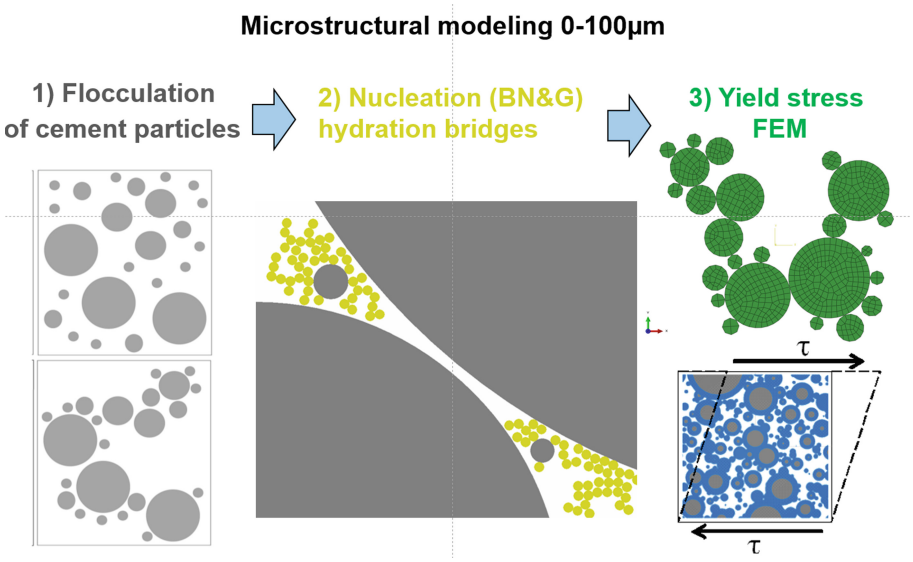

Fig. 1. The new poly-dispersed particle modeling approach proposed for elucidating time-dependent rheology ageing: interaction of cement and nucleation particles during the dormant hydration period.

2.1 Flocculation of Cement Particles

For implementing particle models, an initial randomly distributed cement particle structure is formed in a predefined representative volume element (RVE in 3D) or surface (in 2D) based on particle algorithm for non-overlapping placement of poly-dispersed particles [10] including periodic boundary conditions and a proposed flocculation algorithm. The starting point for the micro-scale particle modelling is that spherical particles are randomly positioned from bigger to smaller inside a predefined volume/surface (100 μm edge), following a certain particle size distribution. The number of particles per fraction is approximated by the Rosin-Rammler function [10]. The volume of all particles in a fraction of an individual component V is calculated by dividing the total fractional weight by its specific density. Then, dividing V by the volume of one single particle V_0, gives the number of particles in a certain fraction [10]. The selection of the lower particle size is based on computational time convenience, whereas the upper particle size depends on the size of the RVE. Every particle has its defined position (x and y in 2D) and radii. For cement particles below about 10 μm in diameter, colloidal properties will be considered, controlled by the action of the total (surface) potential energy. For larger particles ($d_c \sim > 10$ μm) the kinetic energy, or inertia, starts to dominate over the potential energy, so flocculation by soft colloidal linkages can be disregarded [2, 4, 5]. Flocculation of small cement particles to form larger agglomerates (flocs) is driven by van der Waals attractive forces [4, 5]. For flocculated systems, van der Waals inter-particle forces are dominating over Brownian forces, which are thus neglected. To speed up calculations and make them available for aggregation of nano-nucleation particles, particles are directly placed at equilibrium distances randomly around the outer surface of randomly chosen bigger cement particle.

The particle flocculation algorithm is proposed as follows:

1. Randomly place bigger particles (d_c>1-10μm)
2. If d<d_crit: Random attachment on smaller particles
   a. Random pick of a placed cement particle
   b. Random positioning on circumference of the picked (bigger) particle
   c. Overlap?
      i. Yes: GOTO step b)
      ii. No: store *Particle*(x, y, *radii*)
3. Loop (a-c) until all *cement particles are* placed

2.2 Nucleation Hydration: Nano-Particle Bridging of Cement Particles

After having generated the initial (flocculated) cement particle structure, hydration algorithms are invoked to simulate the stepwise evolution of the particle hydration process by the associated addition of nucleation 'nano-'particles following boundary nucleation and growth (BN&G) mechanism, whilst forming a nucleating virtual microstructure. Nucleation bridges as a function of hydration (rest) time is simulated by invoking the particle flocculation algorithm described in Sect. 2.1, extending it for (BN&G) aggregation of 'nano-'particles, based on volume balance and morphology approach for nucleation of (e.g. C-S-H and ettringite cement hydration products) on particle surfaces, both cement and nucleate particles. Therefore, initially cement particles are biased, i.e. have higher probability to be picked, as there are more of them than gel particles. Latter, with increasing degree of hydration, gel particles are becoming more and more biased, as the number of gel particles very soon prevails over the initial cement particles. The volume balance approach is simply based on expansion factor and density of gel nucleates [10, 11]. Incremental volume for each reaction iteration step is calculated proportionally to the degree of hydration (*DoH*), which is linearly increased (stepwise, e.g. in 10 steps) until reaching the maximum value of about *DoH* = 5% [11]. This maximum value for hydration degree corresponds to end of dormant (workable) period, i.e. begin of cement setting. Because of such a low reaction degree, and uncertainties about densities of nucleation gel, volume change of cement particles due to dissolution reaction was neglected. From the incremental gel volume, the number of nucleate gel particles for iteration step is obtained by defining their monodisperse size to be d_{nano} = 5 nm [11], or bigger for computational convenience. The amount of aggregated nucleation gel particles is numerically quantified (e.g. using a neighbour search algorithm) and analysed for local nano-structure morphology. This bridging morphological information is then correlated to the strength of the bridges between cement particles.

2.3 Yield Stress Computational Analysis

The virtual particle structure is transformed into a network of interacting cement particles, using FEM (Fig. 4) and/or DEM, where the cement particles are connected by (initially only) van-der-Walls attractive forces and/or with hydration gel bridges. Those

inter-particle connections, being weaker for the attractive forces and increase in strength with nucleation, still exhibit the weakest point of the elements forming the percolated network of particles. The FEM shear simulation on this network of connected cement particles can simulate the shear force needed to initiate the flow of the microstructure, i.e. the cement paste yield stress. Microstructural system is sheared by applying an external shear force using slow (stepwise) deformations, so the stress is spread only through the percolating network. In a general case, having a random angle Θ between the applied shear and the particle interaction orientation, the shear stress, which can effectively be used to separate the two cement particles is multiplied by a factor of $\cos(\Theta)$. This means that the stress is equal to zero (or maximum) if the cement particles are aligned in (or perpendicular to) the direction in which stress is applied.

3 Results and Discussion

The effect of flocculation is demonstrated by running two simulations (Fig. 2). The first one mimics a fully dispersed case (Fig. 2 down parts) obtained by fully random placement of cement particles for all sizes. On the other side, the upper figures show the flocculated case, where the cement particles having $d_{crit.} < 5$ µm are positioned using the above proposed flocculation algorithm. Results show formation of flocculated percolated network, which is connected via soft colloidal (van-der-Waals) forces.

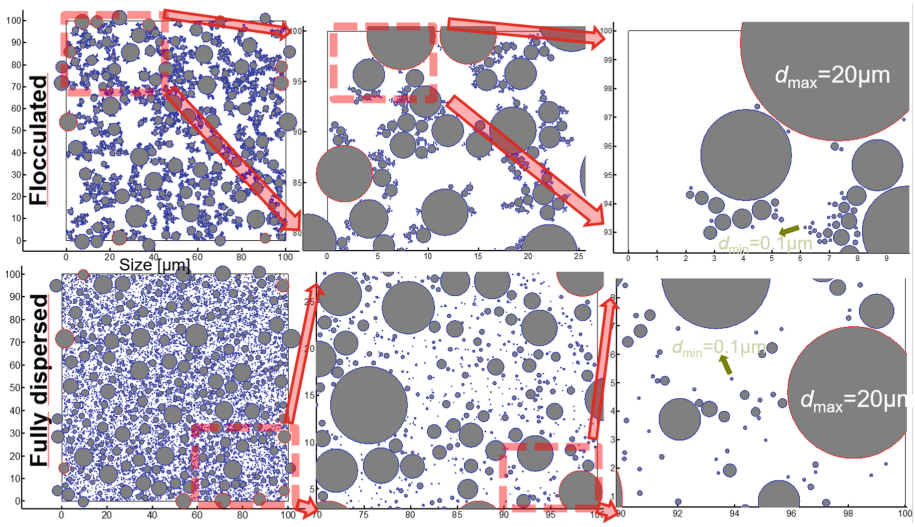

Fig. 2. Flocculation effects on cement microstructure (left: 100 µm × 100 µm simulation boxes, water-cement ratio of 0.45): (down) fully dispersed cement particles; (up) cement particles having $d_{crit.} < 5$ µm flocculate forming a percolated network via soft colloidal (van-der-Waals) interactions.

Figure 3 shows typical results from boundary nucleation and growth (BN&G) simulation, where the yellow nano-particles are aggregated by their sequential positioning near the surfaces of existing cement or gel particles. The simulation was run on the same initial flocculated microstructure from Fig. 2 (top), using 100 μm × 100 μm simulation box having a water-to-cement ratio of 0.45. The nucleation simulation was run until achieving a degree of hydration DoH = 5%, where the amount of aggregated gel particles was calculated based on a volume expansion factor (3.24) and nucleate density (1.2 g/cm^3). The results with zoom-in show how the yellow nucleation gel nano-particles are linking the cement particles to form a percolated rigid network. With the increasing degree of hydration (DoH = 0%–5%, not shown here but one can compare Figs. 2 and 3 for DOH = 0 and 5%), increases the number of the yellow nucleation gel particles. This results in an increased strength of each individual interaction bridges in a unique way, which can now be correlated with this microstructural configuration, as discussed in next.

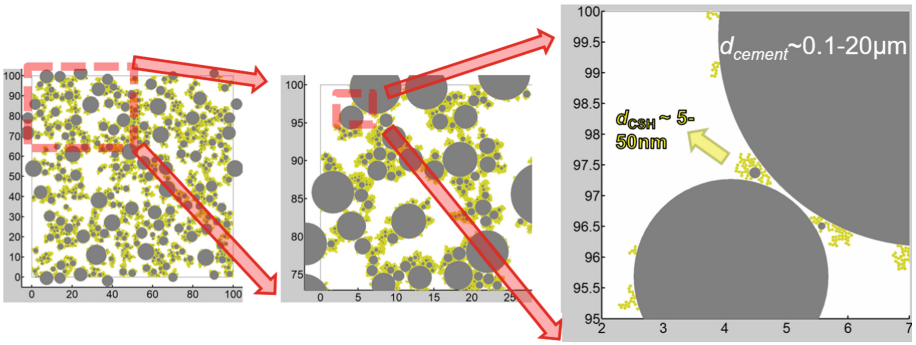

Fig. 3. Boundary nucleation and growth (BN&G) simulation by aggregation of (yellow) nano-particles. Nucleation particles are linking the cement particles to form a percolated rigid network; with increasing the degree of hydration (DoH = 0%–5%) increases the number of nucleation particles, resulting in increased strength of interaction bridges. (Color figure online)

In the case of nucleated bridges, the microstructure for yield stress analysis has to be simplified (Fig. 4). This is done by considering only an assembly of cement particles explicitly (Fig. 4 middle and right). The huge number of nano-particles (yellow, left in Fig. 4) is taken into account (up-scaled) implicitly via the interaction forces (strength of the bridges), as described in Sect. 2.3, where the bridging strength between cement particles is correlated with the local morphological configuration of the nano-particle aggregates. Morphological information on percolated nucleation hydration bridges is used to quantify the increased strength of interaction bridges with hydration to get the cement particle interaction input parameters for FEM yield stress microstructural analysis. On a cement particle scale, one applies an external shearing force, and calculates the changes in interaction energy and stress-strain distributions throughout the interconnected particle network.

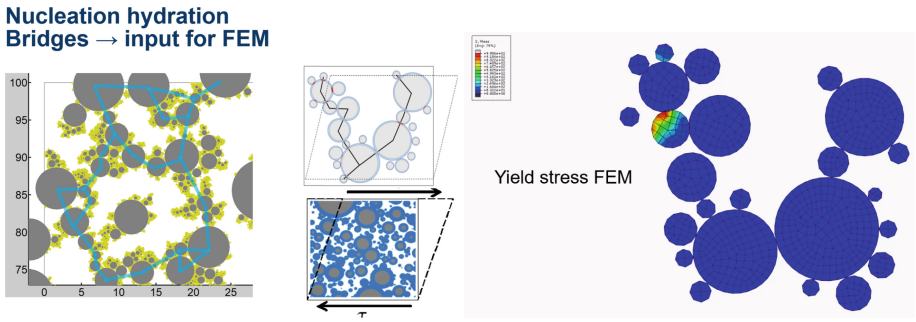

Fig. 4. Morphological information on percolated nucleation hydration bridges is used to quantify the increased strength of interaction bridges with hydration to get the cement particle interaction input parameters for FEM yield stress microstructural analysis. (Color figure online)

4 Conclusions

This paper proposes a micro-structural computational approach for analyzing cement paste yield stress. The approach explicitly considers cement particle interactions including both the colloidal and the nucleated gel interactions between particles.

A new flocculation particle based algorithm is described, based on placement of poly-dispersed hard spheres in a box, followed by nucleation of mono-sized nano-gel particles. A Boundary Nucleation and Growth process was considered, capturing the importance of morphology during evolution of the nano-scale gels. The model is able to calculate the development of the micro-structure as a function of the particle size distribution, water cement ratio, size of maximal particle which flocculates, minimum distance between flocculated particles, and volume of nucleated gel. A mechanical approach on this percolated particle network is proposed for simulating sliding kinematics needed to initiate the flow of the microstructure, i.e. to reach the paste yield stress. The model provides insights on how the localized colloidal and gel bridges are percolating cement particles, responsible for the yield stress properties of bulk cement paste. Currently, research is ongoing on how to parametrize the FEM yield stress using the bridging gel configurations, to correlate the amount and morphological configuration of nucleation particles (bridging the cement particles) with the micro-mechanical properties of the cement particle interactions.

Acknowledgement. Supported by National German DFG organization under Project number 387065993 titled '*Form filling ability of fresh concrete: A time and hydration dependent approach'*, as part of DFG SPP 2005 program.

References

1. Ahari RS, Erdem TK, Ramyar K (2015) Thixotropy and structural breakdown properties of self consolidating concrete containing various supplementary cementitious materials. Cem Concr Comp 59:26–37

2. Zingg A et al (2008) The microstructure of dispersed and non-dispersed fresh cement pastes —new insight by cryo-microscopy. Cem Concr Res 38:522–529
3. Banfill PFG (2006) Rheology of fresh cement and concrete. Rheol Rev 61:61–130
4. Flatt RJ, Bowen P (2006) Yodel: a yield stress model for suspensions. J Amer Ceram Soc 89:1244–1256
5. Roussel N et al (2012) The origins of thixotropy of fresh cement pastes. Cem Concr Res 42:148–157
6. Hattori K, Izumi K (2007) A rheological expression of coagulation rate theory. J Disper Sci Tech 3:129–145
7. Wallevik JE (2009) Rheological properties of cement paste: thixotropic behavior and structural breakdown. Cem Concr Res 39:14–29
8. Wallevik J, Rheocenter I, Iceland IC (2011) The particle flow interaction theory–thixotropic behaviour and structural breakdown. In: Proceedings of 36th conference on our world of concrete and structures, pp 978–981
9. Zheng J, Zhang J, Scherer GW (2012) Prediction of the degree of hydration at initial setting time of cement paste with particle agglomeration. Cem Concr Res 42:1280–1285
10. Ukrainczyk N, Koenders E (2014) Representative elementary volumes for 3D modeling of mass transport in cementitious materials. Model Sim Mater Sci Eng 22(3):035001:1–24
11. Prabhu A et al (2018) A multi-scale approach for percolation transition and its application to cement setting. Sci Rep 8(1):15830

Measuring Thixotropic Properties in a Truck Mixer - Analysis by Numerical Simulation Using the PFI Material Model

Jon Elvar Wallevik(✉)

ICI Rheocenter, Innovation Center Iceland, Reykjavik, Iceland
jon.w@innovation.is

Abstract. Currently, 3D printing is getting an increasing attention as it can offer new advantages over the traditional construction methods. However, to be functional as a "printing-material", the applied cement based material must possess a certain degree of thixotropic behavior. To speed up quality control at job site, it is relevant to investigate the possibility of using the truck mixer to measure such properties. This is the topic of the current paper, done by using computational fluid dynamics (CFD). With this, the overall test environment is thoroughly controlled and the experimental error is avoided, thus allowing the truck's true potential to be examined.

Keywords: Concrete mixing truck · Thixotropy · 3D printing · CFD

1 Introduction

Today, 3D printing is getting an increasing attention, as it can offer new advantages over the traditional construction methods [1]. Examples of benefits are reduced manpower, cost, new choices in building shape and shorter construction time [1, 2]. However, to be functional as a "printing-material", the applied cement based material must possess a certain degree of thixotropic behavior [1]. In particular, a thixotropic buildup must recover under static conditions after the extrusion process [2]. Thixotropy is in some cases quantified by measuring the area of what is called the "thixotropic loop" [3]. In general, the test procedure in a rheometer consists of registering the torque, while increasing the angular velocity (of the rotating part) in steps and thereafter decreasing it in steps. During such stepwise increase, thixotropic- and structural breakdown occurs, however not fast enough to reach equilibrium (or steady state). The measured torque is thus always higher than what would be obtained if equilibrium is reached. During the stepwise decrease in angular velocity, thixotropic rebuild occurs (but not structural rebuild, c.f. Sect. 2), which may or may not be fast enough for equilibrium to be reached. The area enclosed by the two curves is calculated and considered as a measure of thixotropic behavior (i.e. large area means highly thixotropic material, while small area represents material with low thixotropic behavior). Although this method does not give intrinsic physical values, it can provide comparative values [3]. The aim of the current work is to investigate the possibility of using the truck mixer to measure a thixotropic loop. This is done by using computational

V. Mechtcherine et al. (Eds.): RheoCon 2019/SCC 2019, RILEM Bookseries 23, pp. 644–651, 2020.
https://doi.org/10.1007/978-3-030-22566-7_75

fluid dynamics (CFD). With this, the overall test environment is thoroughly controlled and the experimental error is avoided, thus allowing the truck's true potential to be examined. The outcome of this (in Sect. 5) is compared to the outcome of a traditional rheological test (in Sect. 3).

2 Material Model

The material model used in this work is the Particle Flow Interaction theory (PFI-theory) [4]. It is an intrinsic physical rheological model that calculates the combined process of thixotropic behavior and structural breakdown. These concepts were proposed by Hattori and Izumi [5, 6] and by Tattersall and Banfill [7–9], respectively.

Thixotropy: In the PFI-theory, the thixotropic behavior of cement paste is related to coagulation (i.e. flocculation or agglomeration, c.f. IUPAC definition), dispersion (i.e. deflocculation) and re-coagulation of the cement particles. This is in accordance with the original idea presented by Hattori and Izumi [5]. Here, the term "coagulation" describes the occurrence when two (or more) cement particles come into a contact with each other for some duration of time; i.e. when the cement particles become "glued" to each other and work is required to separate them. As illustrated in Fig. 1, the particles become glued together as a result of the total potential energy interaction V_T that exists between them.

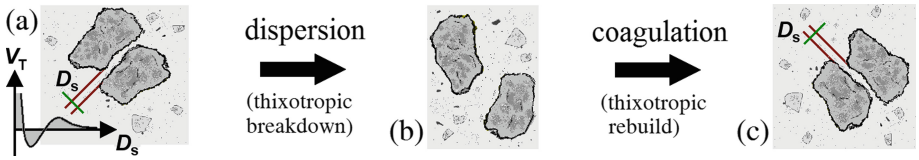

Fig. 1. (a) Coagulation by V_T, (b) dispersion by agitation (c) re-coagulation by V_T. The term D_s is the clear distance between the particles (see [10]).

Structural breakdown: In most time dependent models for cement based materials, only thixotropic behavior is assumed. The structural breakdown phenomenon seems to be less known, less used and is unfortunately often confused with thixotropy. The term structural breakdown was introduced by Tattersall in 1954–1955 [7, 8]. Because no recovery in torque was measured in the corresponding rheological experiment, structural breakdown was considered to be a phenomenon different from thixotropic behavior [7–9, 11–13]. More precisely, structural breakdown is not the same as thixotropic breakdown [7, 8]. The latter is related to behavior generated by the total potential energy V_T that exists between cement particles (i.e. van der Waals attraction, electrostatic repulsion and steric hindrance), while the former is not. A proposed mechanism of structural breakdown was given in 1983 in a textbook by Tattersall and Banfill [9]. There, it was attributed to the process of breaking certain linkages (i.e. connections) between the cement particles formed by the hydration process. The idea was that when a pair or more of cement particles came into contact with water,

hydration products (in the form of membrane) formed around both of them, making the cement particles link together, shown in Fig. 2a. With agitation of the cement paste (i.e. shearing), such formed linkages would then break, meaning that the bridging membrane is ruptured and the cement particles separate, shown in Fig. 2b (see Fig. 3.13 in [9] for the original illustration). Other possible mechanisms for structural breakdown are shown in Fig. 2 and explained in [14]. The point is that the structural breakdown is related to the breaking of breakable connections, made by chemical products, i.e. early C-S-H [15], syngenite [16], ettringite and so forth [14]. Because the growth rate of the hydration products, or "buildup of structure due to hydration of cement minerals" [11], the "structural buildup" is much slower process relative to thixotropic buildup.

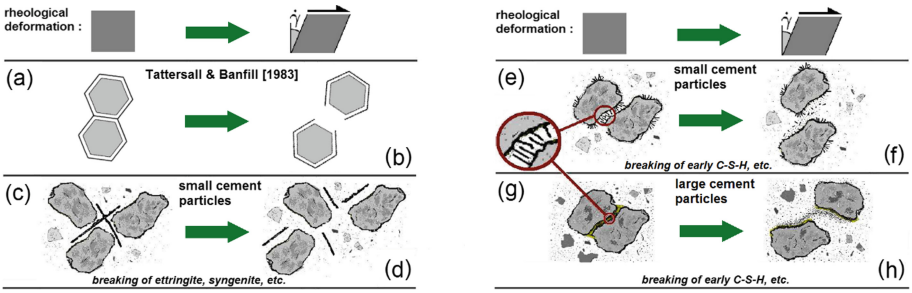

Fig. 2. Hypotheses about the various mechanism of structural breakdown [14].

In the PFI-theory, the shear stress τ is calculated by the following equation:

$$\tau = (\tau_0 + \tilde{\tau}_0 + \hat{\tau}_0) + (\mu + \tilde{\mu} + \hat{\mu})\dot{\gamma} \tag{1}$$

For a given rheological test, the terms τ_0 and μ are constants, $\tilde{\tau}_0$ and $\tilde{\mu}$ is the thixotropic contribution and the terms $\hat{\tau}_0$ and $\hat{\mu}$ the contribution of structural breakdown [4].

3 Traditional Rheological Tests

Here, the PFI material parameters are obtained from actual measurements made with a coaxial cylinders viscometer (see the illustration in Fig. 3c). The raw data is in terms of registered torque (inner cylinder), while the angular velocity (outer cylinder) is changed in steps. The steps are 0.63, 1.51, 2.39, 3.20, 4.08, 3.20, 2.39, 1.51, 0.63 and 2.70 rad/s. Also, this profile is shown with the red colored line in Fig. 3a.

The rheological tests were conducted on cement paste, mixed either with a high molecular weight Na-lignosulfonate, LS (Figs. 3a–b) or with a naphthalene type of superplasticizer, SNF (Figs. 3c–d). For both cases, the dosage is at 0.5% sbwc. Results apply either at 72 or at 102 min after water addition. The w/c is at 0.3 and the cement type is CEM I 42.5R. The PFI material parameters are extracted from the torque values in Figs. 3a–d and are available in Tables 2 and 3 in [4]. These values are used in the

truck mix simulations in Sect. 5. In Figs. 3e–h, the corresponding thixotropic loop areas are calculated (points are calculated from the average torque values shown as black line segments in Figs. 3a–d). The obtained values are 0.28, 0.25, 0.53 and 0.78 Nm/s for the LS and SNF, at 72 min and 102 min after water addition. The objective is to see if these results can be reproduced with the truck mixer.

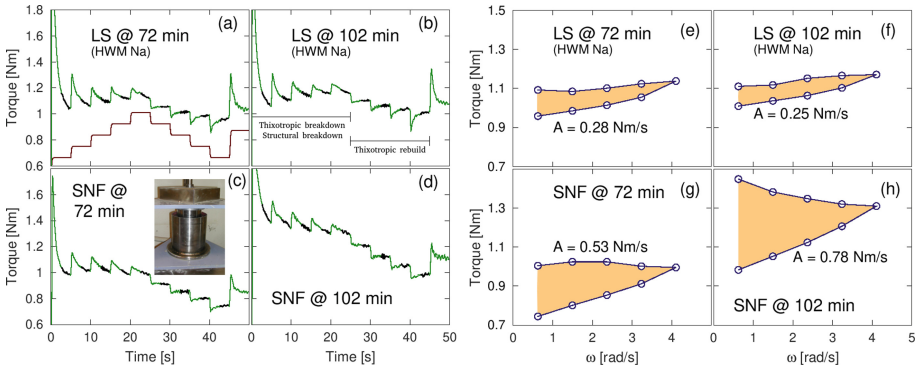

Fig. 3. Experimental data from traditional rheological tests [4] (to the left) and the corresponding thixotropic loop areas A (to the right). (Color figure online)

4 Truck Mixer as a (Thixotropic) Rheometer

Usually, the rheological data of the truck mixer is obtained by logging the hydraulic pressure required to rotate the drum at a specific angular velocity ω. Since the pressure is related to movement of piston(s) inside the drum drive motor, work is being conducted (over a time interval), meaning that the hydraulic pressure is related to power. Here, the power requirement (in kilowatts) to turn the drum is calculated, during a "thixotropic loop". That is, the test procedure consists of registering the power, while the drum angular velocity is changed in steps. The steps are the same as described in Sect. 3, except values are reduced by half (i.e. 0.315, 0.755, 1.195 rad/s and so forth). The reduction is done to avoid centrifuging the test material. The material parameters used in the simulations are obtained from Tables 2 and 3 in [4] and correspond to the results shown in Figs. 3a–d above. The amount of test material used in the drum is $V = 5.4\ \mathrm{m}^3$.

Figure 4 shows the drum geometry used in this work. It is commercially available and produced in Germany. The geometrical drum volume is $15.7\ \mathrm{m}^3$, but the max rated drum capacity is $9\ \mathrm{m}^3$. In general, the nominal range of drum speed is between 0 rpm and 14 rpm (i.e. from 0 to 0.23 rps), but in the current work the maximum speed is slightly higher or about 19 rpm (i.e. 0.32 rps). The inclination of the drum relative to the horizontal is 11°. The number of cells used in the drum is about 60.000, but also a high resolution simulation has been done, which consists of about 400.000 cells (not reported here). The solver was created within the OpenFOAM framework and compiled on the

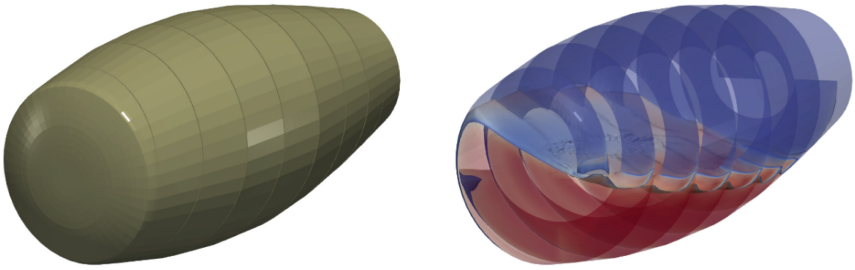

a) b)

Fig. 4. The geometry of the drum applied in the current work (a) and the quantity of test material used, namely $V = 5.4\ \mathrm{m}^3$ (b).

supercomputer "Garpur" (http://ihpc.is). For further information about the technical aspect of the calculation, like solution methods and boundary conditions, see [17].

The volume of a material body (also, material volume) is here designated with V and its bounding surface with ∂V. The material body represents a fixed number of fluid (or continuum) particles [10, 18, 19]. In this work, the material volume is chosen as consisting of all the test material inside the drum, namely $V = 5.4\ \mathrm{m}^3$. The power (i.e. rate of work) exerted on the material volume V, from its surroundings, is here designated with P [W] and is given by Eq. (2) [10, 19].

$$P(t) = \iiint_V \rho\, \mathbf{g} \cdot \mathbf{v}\, dV + \iint_{\partial V} \mathbf{t} \cdot \mathbf{v}\, dA \tag{2}$$

Since V is here chosen as all the test material inside the drum, the term P represents the power used by the drum (i.e. by the drum drive motor) in moving/shuffling/rotating/deforming the cement based material inside it. It should be clear that a negative value for P is possible and would signify that the test material is doing work on the drum (and thus in turn, on the drum drive gearbox). This happens for example when the gearbox is trying to reduce the drum's angular velocity, a process hampered by the already existing angular momentum of the test material. The term $\mathbf{t} = \mathbf{n} \cdot \boldsymbol{\sigma}$ in the above equation, is named traction [20, 21] and describes the force per unit area [$\mathrm{N/m}^2$] applied at the boundary ∂V, from the outer surroundings of the material volume V (i.e. in this case, applied by the steel drum wall on the test material). The term $\boldsymbol{\sigma}$ is the (total) stress tensor [Pa]. The term $\mathbf{n}$ is a unit normal vector located at the boundary ∂V pointing away from the material volume V. The terms ρ, $\mathbf{g}$, and $\mathbf{v}$ are the density [$\mathrm{kg/m}^3$], gravity [$\mathrm{m/s}^2$] and velocity [m/s]. As shown in [10] (pp. 386–389), through the mechanical energy equation, Eq. (2) can be transformed into the following equation:

$$P(t) = \iiint_V \rho \frac{d}{dt}\left[\frac{\mathbf{v} \cdot \mathbf{v}}{2}\right] dV + \iiint_V \eta \dot{\gamma}^2 dV \tag{3}$$

Here, Eq. (3) is used in calculating the power. The term $\dot{\gamma}$ is the shear rate [s^{-1}], $\eta = \tau/\dot{\gamma}$ is the apparent viscosity [Pa · s] and τ is the shear stress [Pa] by Eq. (1).

5 Results and Discussion

As already mentioned, the PFI material parameters used in the drum simulations are obtained from the torque data presented in Figs. 3a–d. The same torque data is used in generating the thixotropic loop areas in Figs. 3e–h. For the lignosulfonate cases (LS), the obtained thixotropic loop values are 0.28 Nm/s and 0.25 Nm/s, at 72 min and 102 min after water addition, respectively. This means that although there exists some thixotropic behavior (as well as structural breakdown) present for the LS case, there is no significant change in thixotropic loop areas A with time elapsed since water addition. However, for the SNF case (Figs. 3g–h), the loop values are 0.53 Nm/s and 0.78 Nm/s, at 72 min and 102 min after water addition, respectively. That is, when using the SNF superplasticizer, the thixotropic behavior (and structural breakdown) is both larger and is increasing with time from water addition. Thus, one could conclude that the SNF superplasticizer is better suited when making cement based material for 3D printing. The above is an example of comparative performance analysis of two different superplasticizers, relative to thixotropic behavior and structural breakdown, made with a traditional rheometer. The question is, can the truck mixer reproduce these results?

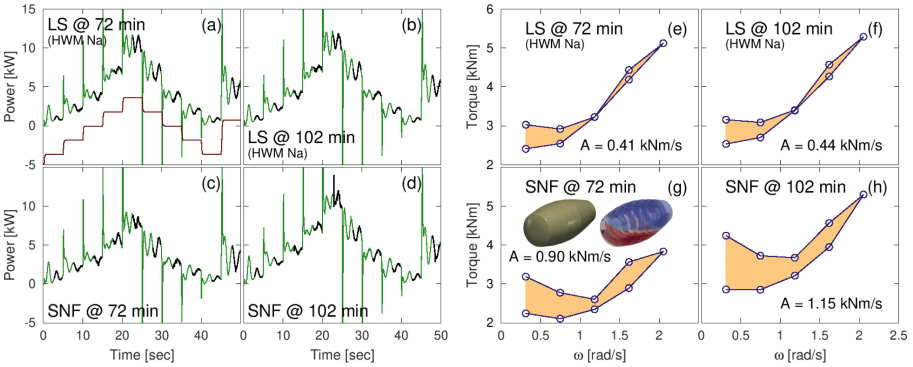

Fig. 5. Power values by Eq. (3) for the truck mixer (a) to (d) and the corresponding thixotropic loop areas A (e) to (h).

Figures 5a–d shows the power as a function of time by Eq. (3), for the same cases as shown in Figs. 3a–d, respectively. In Figs. 5e–h, the corresponding thixotropic loop areas are calculated (points are calculated from the average power values shown as black line segments in Figs. 5a–d). In Fig. 5, the conversion from power P to torque T (i.e. from illustrations a–d to illustrations e–h) is by $P = \omega\, T$, where ω is the drum's angular velocity. The obtained thixotropic loop values are 0.41, 0.44, 0.90 and 1.15 kNm/s for the LS and SNF, at 72 min and 102 min after water addition. In Fig. 6, these values are plotted against values obtained with the rheometer in Sect. 3. With correlation of $R^2 = 0.97$, a good match is achieved and thus the same conclusion can be made with the truck mixer as with the traditional rheometer, namely that the SNF is

better suited for 3D printing. However, one should keep in mind that the correlation between the two devices is only based on four data points. Thus, the generality of the results presented here is limited to this.

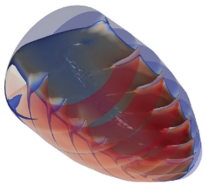

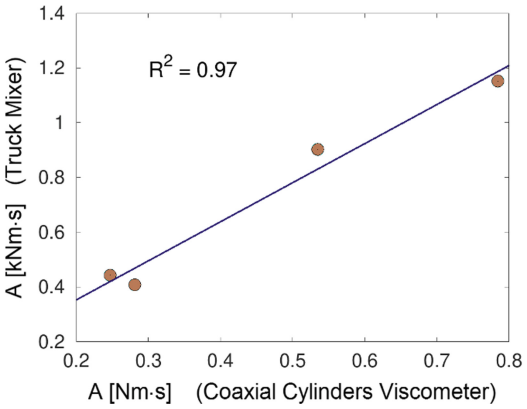

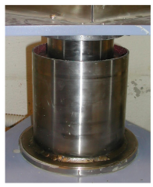

Fig. 6. Comparison of thixotropic loop values *A*, between the truck mixer and values generated by the coaxial cylinder viscometer.

6 Summary and Conclusion

In this work, the truck mixer could almost completely reproduce the results for the thixotropic loop obtained by the traditional rheometer. That is, with either results, one could conclude that the SNF superplasticizer is better suited (relative to the LS) when making cement based material for 3D printing. This conclusion relies of course on the assumption that a large thixotropic loop area is a good indicator of such suitability, which may not be true. Regardless, for a specific concrete family, exclusively developed and produced for 3D printing, such thixotropic loop area *A*, could aid in the overall quality control at job site. More specifically, if such control could be executed with a truck mixer, it would save labor and valuable decision time (i.e. batch acceptance or rejection) and ultimately money.

Acknowledgement. This work has been funded by the Icelandic Centre for Research –RANNIS (163382-051/52/53) and Norcem AS (Heidelberg Cement Group). Simulations were performed on resources provided by the Icelandic High Performance Computing (IHPC) - http://ihpc.is.

References

1. De Schutter G, Lesage K, Mechtcherine V, Nerella VN, Habert G, Agusti-Juan I (2018) Vision of 3D printing with concrete - technical, economic and environmental potentials. Cem Concr Res 112:25–36
2. Roussel N (2018) Rheological requirements for printable concretes. Cem Concr Res 112:76–85

3. Roussel N (2006) A thixotropy model for fresh fluid concretes: theory, validation and applications. Cem Concr Res 36:1797–1806
4. Wallevik JE (2009) Rheological properties of cement paste: thixotropic behavior and structural breakdown. Cem Concr Res 39:14–29
5. Hattori K, Izumi K (1991) Rheology of fresh cement and concrete, in rheology of fresh cement and concrete. In: Proceedings of the international conference organized by The British Society of Rheology, University of Liverpool, E & FN Spon, London, 16–29 March 1990, pp 83–92
6. Hattori K, Izumi K (1982) A rheological expression of coagulation rate theory, parts 1–3. J Dispersion Sci Technol 3(2):129–193
7. Tattersall GH (1955) The rheology of Portland cement pastes. Br J Appl Phys 6:165–167
8. Tattersall GH (1955) Structural breakdown of cement pastes at constant rate of shear. Nature 175:166
9. Tattersall GH, Banfill PFG (1983) The rheology of fresh concrete. Pitman Books Limited, London
10. Wallevik JE (2003) Rheology of particle suspensions - fresh concrete, mortar and cement paste with various types of lignosulfonates. Dr.ing. thesis, Department of Structural Engineering, The Norwegian University of Science and Technology, Trondheim. https://ntnuopen.ntnu.no
11. Banfill PFG, Saunders DC (1981) On the viscometric examination of cement pastes. Cem Concr Res 11(3):363–370
12. Banfill PFG (1991) The rheology of fresh mortar. Mag Concr Res 43(154):13–21
13. Banfill PFG (2003) The rheology of fresh cement and concrete - a review. In: Proceedings of the 11th international congress on the chemistry of cement: cement's contribution to the development in the 21st Century, Durban, 11–16 May 2003
14. Wallevik JE (2011) Particle flow interaction theory - thixotropic behavior and structural breakdown. In: Proceedings of 36th conference on our world of concrete and structures, Singapore, 14–16 August 2011, p 103. ISBN 978-981-08-9528-0
15. Scrivener KL, Juilland P, Monteiro PJM (2015) Advances in understanding hydration of Portland cement. Cem Concr Res 78:38–56
16. Kubens S (2010) Interaction of cement and admixtures and its effect on rheological properties. Ph.D. thesis, Faculty of Civil Engineering, Bauhaus University, Weimar, Germany
17. Wallevik JE, Wallevik OH (2017) Analysis of shear rate inside a concrete truck mixer. Cem Concr Res 95:9–17
18. Haug E, Langtangen HP (1997) Basic equations in Eulerian continuum mechanics. In: Dæhlen M, Tveito A (eds) Numerical methods and software tools in industrial mathematics. Birkhauser, Boston
19. Mase GT, Mase GE (1999) Continuum mechanics for engineers, 2nd edn. CRC Press LLC, Boca Raton
20. Mase GE (1970) Schaums outline series: theory and problems of continuum mechanics. McGraw-Hill Inc., New York
21. Malvern LE (1969) Introduction to the mechanics of continuous medium. Prentice-Hall Inc., Englewood Cliffs

Computational Segregation Analysis During Casting of SCC

Jon Elvar Wallevik[1(✉)], Wassim Mansour[2], and Olafur Haralds Wallevik[1,2]

[1] ICI Rheocenter, Innovation Center Iceland, Reykjavik, Iceland
jon.w@innovation.is
[2] School of Science and Engineering, Reykjavik University, Reykjavik, Iceland

Abstract. Uneven aggregate distribution can increase the local porosity and thus the permeability of concrete. Varying content of mortar causes heterogeneous shrinkage and creep in a given element. Moreover, high heterogeneity will increase the probability that these phenomena yield high internal stress gradients and thus cracking. In this work, a status is given about the development of a concrete casting solver within the OpenFOAM framework that can calculate the coarse aggregate distribution as a function of time. The aim is to predict the effect of segregation by gravity as well as by the shear rate induced particle migration. Case examples show that the latter can play a very important role in affecting the aggregate variation within a concrete element.

Keywords: CFD · Coarse aggregates · Segregation · Rheology

1 Introduction

The load carrying capacity and service life of concrete structure is very much dependent on the quality and success of concrete placement into formwork at jobsite [1]. In recent years numerical modeling of concrete placement has demonstrated great potentials to become an important tool for optimization of such process [2, 3]. Researchers from various part of the world have started to work on such casting prediction tools using different computational fluid dynamics (CFD) software [4]. But lot of work is still to be done to understand the large scale behavior of the flow processes involved [4], especially in terms of calculating the coarse aggregate concentration as a function of location and time [5]. In particular, variation in aggregate distribution can increase the local porosity and thus the permeability of concrete. This can also cause heterogeneous shrinkage and creep in a given concrete element. Moreover, high heterogeneity will increase the probability that these phenomena yield high internal stress gradients and thus suffer cracking with reduction in load carrying capacity of the concrete structure as a result [1].

The Self Compacting Concrete (SCC) is a very fluid concrete and thus was expected to be the answer to casting problems. However, experience has shown that even for such type of material, there will always exist a formwork and steel bars configuration in which casting problems may occur [4]. Furthermore, these casting problems may not be fully resolved unless one can calculate the aggregate

V. Mechtcherine et al. (Eds.): RheoCon 2019/SCC 2019, RILEM Bookseries 23, pp. 652–659, 2020.
https://doi.org/10.1007/978-3-030-22566-7_76

concentration as a function of time and location and especially its response to different types of obstacles.

In the current project, a multiphase transient simulator is being developed that models the dynamics of multiple fluid phases during casting of concrete. The development is realized within the OpenFOAM framework, which uses the finite volume method (FVM). One of the aims with the solver is to simulate operational problems related to uncertainties in casting predictions. This includes the effect of the settlement of aggregates by gravity (i.e. segregation) as well as the effect of shear rate induced particle migration [6–8]. Improved prediction accuracy of transient multiphase flow allows for the design of more complex and durable concrete structures and additionally allows ready-mix plants to investigate the effect of stability variation during casting of a large/difficult structure.

2 Theoretical Background

The numerical solver encompasses two theories. The first one is the Computational Fluid Dynamics (CFD) of transient viscoplastic fluid with open (free) boundary, thus dividing the system between the atmospheric air and a viscoplastic fluid (e.g. fresh concrete). This is what could be considered as a standard Volume of Fluid approach (VOF) [9]. The second theory is the implementation of field equation for particle distribution into the numerical framework to be able to calculate segregation within the viscoplastic fluid (e.g. segregation of concrete), including the shear rate induced particle migration [6–8]. The approach used in treating the aggregate segregation is based on the Drift Flux Method (DFM), which is derived from the so-called two-fluid model [10, 11].

As stated above, a standard VOF approach is mixed with the DFM (both implemented by the FVM). The former calculates the flow of two fluids that do not generally intermix (immiscible) and thus usually have a clear boundary between them, e.g. concrete and atmospheric air. For the second part of the solver, where the DFM is applied, the phases are generally in an intermixed (miscible) state, e.g. coarse aggregates suspended in mortar. Three phases are involved in the solver, in which atmospheric air is the first phase (with a volume fraction of α_2). The viscoplastic fluid (volume fraction α_1), which could for example represent fresh concrete, is divided between a matrix phase (also, *continuous phase*) and a particle phase (also, *dispersed phase*), which constitute the second and the third phase, respectively (with volume fractions α_c and α_d).

It is straightforward to show that $\alpha_1 + \alpha_2 = 1$ and $\alpha_c + \alpha_d = \alpha_1$. Thus, it is sufficient only to solve the phase transport equations for α_1 and α_d as shown with Eq. (1) [10, 12].

$$\frac{\partial(\alpha_1\rho_1)}{\partial t} + \nabla\cdot(\alpha_1\rho_1\mathbf{U}) = S_1 \quad \text{and} \quad \frac{\partial\alpha_\mathrm{d}}{\partial t} + \nabla\cdot\left(\alpha_\mathrm{d}\mathbf{U} + \alpha_\mathrm{d}\frac{\rho_\mathrm{c}}{\rho_1}\mathbf{V}_\mathrm{dj}\right) = S_2 \qquad (1)$$

The mixture density is given by $\rho = \alpha_1\rho_1 + \alpha_2\rho_2 = (\alpha_d\rho_d + \alpha_c\rho_c) + \alpha_2\rho_2$, the term $\mathbf{U}$ is the velocity of the flow, obtained by Eq. (2), while $\mathbf{V}_\mathrm{dj}$ is the drift velocity [10, 11]. The terms S_1 and S_2 are source terms, only active at the thin interface between

phase 1 and 2 (i.e. between fresh concrete and atmospheric air) and the purpose of this, is to maintain a sharp interface between the two phases [12]. With $S_1 = 0$ and $S_2 = 0$ in most of the fluid domain, the equations in Eq. (1) are hyperbolic in nature and thus solved with a special advection scheme named the Flux Corrected Transport [13, 14].

The momentum equation currently used in the solver is given by Eq. (2) and includes both aspects of the VOF [9] as well as of the DFM [10, 11]. The complete derivation of Eq. (2) will be available in [15].

$$\frac{\partial(\rho\mathbf{U})}{\partial t} + \nabla\cdot(\rho\mathbf{U}\mathbf{U}) + \nabla\cdot\left(\left[\frac{\alpha_\mathrm{d}}{\alpha_1-\alpha_\mathrm{d}}\frac{\rho_\mathrm{c}\rho_\mathrm{d}}{\rho_1}\right]\mathbf{V}_\mathrm{dj}\mathbf{V}_\mathrm{dj}\right) = -\nabla p + \nabla\cdot\mathbf{T} + \rho\mathbf{g} + \mathbf{F}_s. \quad (2)$$

The terms p and $\mathbf{U}$ are the pressure and velocity. Here, these two last terms are not calculated separately for each phase, but solved as a single entity by Eq. (2). The term $\mathbf{g}$ is gravity and $\mathbf{F}_\mathrm{s}$ is the force exerted by surface tension between the two phases α_1 and α_2 and is calculated by the CSF model of Brackbill et al. [16].

The constitutive equation consists of the Generalized Newtonian Model [17] (GNM) and is given by $\mathbf{T} = 2\eta\dot{\boldsymbol{\epsilon}}$, where $\dot{\boldsymbol{\epsilon}}$ is known as the rate of deformation tensor [18]. Here, the apparent viscosity is given by $\eta = \alpha_1\eta_1 + \alpha_2\eta_2$, where η_2 is the viscosity of the atmospheric air, while η_1 is the apparent viscosity of the fresh concrete. For the latter, the following is applied [19]:

$$\eta_1 = \mu(0)\left(1-\frac{\phi}{\phi_m}\right)^{-2.5\phi_m} + \frac{\tau_0(0)}{\dot{\gamma}}\sqrt{(1-\phi)\left(1-\frac{\phi}{\phi_m}\right)^{-2.5\phi_m}}. \quad (3)$$

In the above equation, ϕ_m is the dense packing fraction of the mono sized spherical particles [19]. For the results shown here, ϕ is set equal to α_d, namely the volume fraction of the dispersed phase. This means that the $\mu(0)$ and $\tau_0(0)$ refer to the 0–11 mm mortar. The shear rate in Eq. (3), is calculated as explained in [20] and is in general highly non-uniform and time dependent. As mentioned above, the term $\mathbf{V}_\mathrm{dj}$ in Eq. (1) is the drift velocity of the dispersed phase [10, 11]. For cases of fresh concrete, this velocity can be approximated with the settling velocity $\mathbf{V}_\mathrm{s}$ (i.e. the "observed" segregation) [15], here calculated by

$$\mathbf{V}_\mathrm{s} = \mathbf{V}_\mathrm{s}^\mathrm{GR} + \mathbf{V}_\mathrm{s}^\mathrm{SR}, \text{ where } \mathbf{V}_\mathrm{s}^\mathrm{GR} = \frac{\mathbf{g}(\rho_d-\rho_c)a^2}{18\mu_s} \text{ and } \mathbf{V}_\mathrm{s}^\mathrm{SR} = -k\nabla\dot{\gamma}. \quad (4)$$

The velocity term $\mathbf{V}_\mathrm{s}^\mathrm{GR}$ represents settling by gravity and is obtained from [19], while $\mathbf{V}_\mathrm{s}^\mathrm{SR}$ represents settling by the shear rate induced particle migration (see [6–8]). The quantity k used in $\mathbf{V}_\mathrm{s}^\mathrm{SR}$, represents the migration coefficient [6]. The term a in the above equation is the characteristic particle diameter of the dispersed phase (the coarse aggregates) and μ_s is the local surrounding viscosity of the continuous phase (the mortar phase) calculated as η_1/δ where δ is an empirical parameter greater than 1 [19].

3 An Example: Casting of a Wall Section

Several different types of formwork geometries have been used for testing of the current solver. Here, a wall segment is used, shown in Fig. 1. Its length is 10 m, height is 4 m and thickness is 30 cm. The concrete is being pumped into the formwork from the left side, in which the drop height is about 2 m. The inflow rate is such that it takes about 80 s to fill the formwork. Placing the hose at this height is done to put a certain strain on the solver. The number of cells in the current case is about 420.000 and the calculations were performed on resources provided by the Icelandic High Performance Computing.

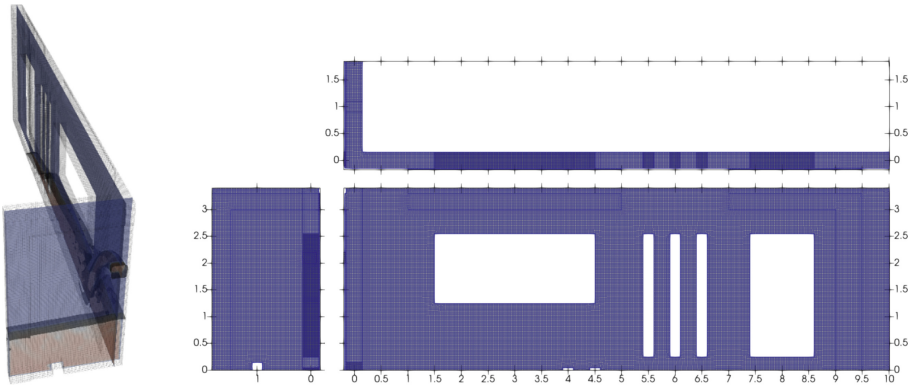

Fig. 1. Geometry of the wall section used in the simulation tests.

Figures 2 and 3 show a simulation result in which the flowing material is SCC with $D_{\max}$ of 16 mm. The following parameters are used: $\phi_m = 0.75$, $\delta = 1.5$ (see [19]), $\mu(0) = 50$ Pa·s, $\tau_0(0) = 10$ Pa, $a = 13$ mm, $\rho_d = 2700$ kg/m^3, $\rho_c = 2200$ kg/m^3 and $k = 1.4 \cdot 10^{-5}$ m^2.

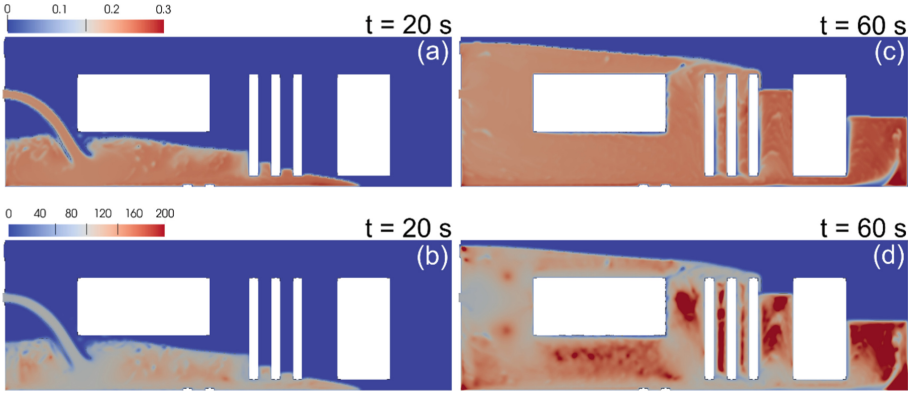

Fig. 2. Solid concentration of coarse aggregates α_d (illustrations (a), (c)) and value of the apparent viscosity η (illustrations (b) and (d)). (Color figure online)

3.1 Solid Concentration of the 11–16 mm Aggregates

Figures 2a and c show the distribution of α_d (in the wall center cross-section of Fig. 1) at 20 s and 60 s after start of pumping, i.e. of the 11–16 mm aggregate phase.

The color bar shown in the top-left part of Fig. 2a, applies to both illustrations (a) and (c). The dark red color, namely $\alpha_d = 0.3$, represents higher compaction (or concentration) of coarse aggregates, while the dark blue color, $\alpha_d = 0$, represents area that is completely absent of coarse aggregates. At such location, only mortar (i.e. fine concrete <11 mm) remains. In the light brown color range, the solid concentration is close to $\alpha_d \approx 0.2$, which means homogeneous concrete, or rather an initial state of concentration of coarse aggregates. Finally, the blue color above the concrete represents the atmospheric air, or α_2.

Figures 2b and d shows the range of values for the apparent viscosity $\eta = \alpha_1\eta_1 + \alpha_2\eta_2$, in which η_2 is viscosity of the atmospheric air, while η_1 is that of the fresh concrete calculated by Eq. (3). The color bar shown in the top-left part of Fig. 2b, applies to both illustrations (b) and (d) and demonstrates the range in units of Pa·s, from 0 (atmospheric air) to 200 Pa·s. It should be noted that the maximum value can reach up to and above 2000 Pa·s, occurring in the very dark red areas in Fig. 2d.

3.2 Settling Velocity

Figure 3 refers to the same simulation case as shown in Fig. 2, however, now illustrating the settling velocity $\mathbf{V}_s$ by Eq. (4). More specifically, Figs. 3a and c show settling by the shear rate induced particle migration $\mathbf{V}_s^{SR}$, while Figs. 3b and d show settling by gravity $\mathbf{V}_s^{GR}$. In all cases, only the vertical component of $\mathbf{V}_s$ is shown, which is natural for the gravity segregation, while not so for the shear rate induced particle migration. That is, the latter exhibits vector components in all directions. However, as its vertical component is (mostly) the dominating one, it is the only one shown.

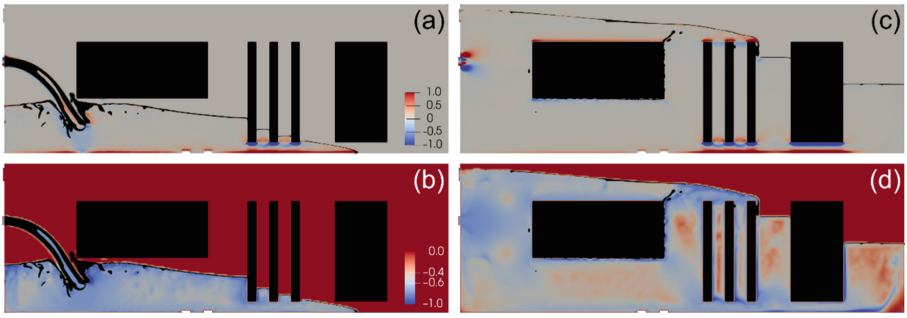

Fig. 3. Settling speed by $\mathbf{V}_s^{SR}$ (illustrations (a), (c)) and by $\mathbf{V}_s^{GR}$ ((b) and (d)). (Color figure online)

The color bar shown in the bottom-right part of Fig. 3a, applies to both illustrations (a) and (c) and demonstrates the range of vertical settling speed of $\mathbf{V}_s^{SR}$, from 1 mm/s

(upward settling) down to −1 mm/s (downward settling). For dark blue and dark red areas in (a) and (c), the settling speed (absolute values) are higher than 1 mm/s. Likewise, the color bar shown in the bottom-right part of Fig. 3b, applies to both illustrations (b) and (d) and demonstrates the range of vertical settling of $\mathbf{V}_s^{GR}$, from 0 mm/s (no settling) down to −1 mm/s (downward settling).

3.3 Example of Segregation Analysis

When looking at Fig. 2a, at 20 s after start of pumping, only minor variations in coarse aggregate concentration α_d emerges. However, at 60 s (Fig. 2c), in the area around the doorway entrance, a higher concentration of coarse aggregates is present. Also, at the bottom, to the right of the doorway, there is a section (or actually a thin streak), where coarse aggregates are totally absent. To understand what is happening, one has to examine the results in Figs. 3a and c. From these, it is clear that the highest value of shear rate induced particle migration $\mathbf{V}_s^{SR}$ is occurring below the three parallel windows as well as below the doorsteps. There, the fresh concrete is being segregated at the highest rate and thereafter transported "downstream" by the general flow, thus generating sections either absent of coarse aggregates or containing to much coarse aggregates. In this calculation, it is interesting how little damage is being done by gravity $\mathbf{V}_s^{GR}$. One can increase this effect for example by increasing δ in Eq. (4), or by reducing η_1 Eq. (3) (see Figs. 2b and d) through reduction in $\tau_0(0)$ and/or $\mu(0)$. However, although apparently not so destructive (for the current case), one should keep in mind that segregation by gravity can be very active after casting, while not so for the shear rate induced particle migration $\mathbf{V}_s^{SR}$. That is, although $\mathbf{V}_s^{GR}$ is occurring at a slower rate, it will have a longer time period to operate relative to $\mathbf{V}_s^{SR}$. Enabling the current solver to calculate such stagnate condition is currently being experimented with.

3.4 Code Verification

As mentioned in the beginning of this article, the current solver is a mixture of VOF and DFM. As a part of the code verification, the aim is to compare the output of the current solver with the outcome of well-known and verified solvers.

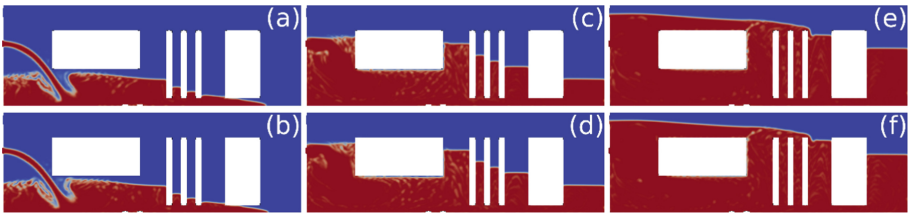

Fig. 4. Comparison of a standard VOF solver (illustrations (a), (c) and (e)) with the current solver (illustrations (b), (d) and (f)).

For the VOF part, the comparison is made to the interFoam solver (OpenFOAM). The latter is a VOF solver only and thus the settling velocity Eq. (4) must be set equal to zero. Also, the apparent viscosity η_1 must be set to something that both solver can handle, meaning that Eq. (3) cannot be used. Here, a standard Bingham model is applied, with plastic viscosity of 50 Pa·s and yield stress of 10 Pa. The outcome of such comparison is shown in Fig. 4, which demonstrates the solid concentration of α_1, (i.e. fresh concrete). Illustrations (a), (c) and (e) are results generated by interFoam and refer to 20, 40 and 60 s after start of pumping, with the same inflow rate as applies in Figs. 2 and 3. Illustrations (b), (d) and (f) are results of α_1 at the same time points, generated by the current solver. As shown, the outcome of the two solvers are the same. Other cases have also been successfully tested. For the DFM comparison, the obvious candidate within the OpenFOAM is the settlingFoam (its newest version is known as the driftFluxFoam). This is however more complicated as this solver cannot handle open boundaries (i.e. VOF). However, a case setup is being devised in which both settlingFoam and the current solver can operate, for a valid comparison.

4 Summary and Conclusion

The aim of the project has been to create a multiphase transient simulator that can model the segregation of the fresh concrete both by gravity (i.e. segregation) as well as by the shear rate induced particle migration. The current aim is to demonstrate the potential of the solver, which will be freely available (with documentation) with the project conclusion [15]. For the present tests shown here, emphasis has been on using difficult flow condition with complex geometry and already accepted material models (e.g. Eqs. (3) and (4)). With this, current case examples show that the shear rate induced particle migration can play a very important role in affecting the aggregate variation within a concrete element.

Acknowledgement. This work has been funded by the Icelandic Centre for Research - RANNIS (grant numbers 163382-051/052/053), Readymix Abu Dhabi and Norcem AS (Heidelberg Cement Group). Simulations were performed on resources provided by the Icelandic High Performance Computing (IHPC) - http://ihpc.is.

References

1. Spangenberg J, Tutum C, Hattel J, Roussel N, Geiker M (2011) Optimization of casting process parameters for homogeneous aggregate distribution in self-compacting concrete: a feasibility study. In: Proceedings of the 6th IEEE congress on evolutionary computation
2. Vasilic K, Roussel N, Meng B, Kuhne H-C (2009) Computational modelling of SCC flow: reinforcement network modelled as porous medium. In: Proceedings of the 3rd international RILEM symposium on rheology of cement suspensions such as fresh concrete, Reykjavik, Iceland, 19–21 August 2009. RILEM Publications S.A.R.L. ISBN 978-2-35158-091-2
3. Thrane LN (2007) Form filling with self-compacting concrete. Ph.D. thesis, Danish Technological Institute - Technical University of Denmark, Lyngby

4. Roussel N (2009) Computational modelling of SCC flow: reinforcement network modelled as a porous medium. In: Proceedings of the 3rd international RILEM symposium on rheology of cement suspensions such as fresh concrete, Reykjavik, Iceland, 19–21 August 2009. RILEM Publications S.A.R.L. ISBN 978-2-35158-091-2
5. Spangenberg J (2012) Numerical modelling of form filling with self-compacting concrete. Ph.D. thesis, Department of Mechanical Engineering, Technical University of Denmark (DTU), Lyngby
6. Barnes HA, Hutton JF, Walters K (1989) An introduction to rheology. Elsevier Science, Amsterdam
7. Wallevik JE (2003) Rheology of particle suspensions - fresh concrete, mortar and cement paste with various types of lignosulfonates. Dr.ing. thesis, Department of Structural Engineering, The Norwegian University of Science and Technology (NTNU), Trondheim. https://ntnuopen.ntnu.no
8. Spangenberg J, Roussel N, Hattel JH, Stang H, Skocek J, Geiker MR (2012) Flow induced particle migration in fresh concrete: theoretical frame, numerical simulations and experimental results on model fluids. Cem Concr Res 42:633–641
9. Hirt CW, Nichols BD (1981) Volume of fluid (VOF) method for the dynamics of free boundaries. J Comput Phys 39:201–225
10. Ishii M (1975) Thermo-fluid dynamic theory of two-phase flow. Eyrolles, Paris
11. Brennan D (2001) The numerical simulation of two-phase flows in settling tanks. Ph.D. thesis, Department of Mechanical Engineering, Imperial College of Science, London
12. Klostermann J, Schaake K, Schwarze R (2013) Numerical simulation of a single rising bubble by VOF with surface compression. Int J Numer Meth Fluids 71(8):960–982
13. Boris JP, Book DL (1973) Flux-corrected transport I: SHASTA, a fluid transport algorithm that works. J Comput Phys 11:38–69
14. Zalesak ST (1979) Fully multidimensional flux-corrected transport algorithms for fluids. J Comput Phys 31:335–362
15. Source code manual and source code and for project "RANNIS 163382-051/052/053", to be released in early 2020 at www.vvpf.net
16. Brackbill JU, Kothe DB, Zemach C (1992) A continuum method for modeling surface tension. J Comput Phys 100:335–354
17. Tanner RI, Walters K (1998) Rheology: an historical perspective. Elsevier Science B.V., Amsterdam
18. Malvern LE (1969) Introduction to the mechanics of continuous medium. Prentice-Hall Inc., Englewood Cliffs
19. Spangenberg J, Roussel N, Hattel JH, Sarmiento EV, Zirgulis G, Geiker MR (2012) Patterns of gravity induced aggregate migration during casting of fluid concretes. Cem Concr Res 42:1571–1578
20. Wallevik JE (2014) Effect of the hydrodynamic pressure on shaft torque for a 4-blades vane rheometer. Int J Heat Fluid Flow 50:95–102

Author Index

V. Mechtcherine et al. (Eds.): RheoCon 2019/SCC 2019, RILEM Bookseries 23, pp. 661–663, 2020.
https://doi.org/10.1007/978-3-030-22566-7